

Proceedings of the annual meeting
of the French Society of Astronomy & Astrophysics
Paris, June 20-23, 2011



Credit: S. Cnudde

Contents

Table of contents	i
Participant list	x
SF2A — Joint session (S00)	1
Orbital characterization of β Pictoris b <i>H. Beust, G. Chauvin, and A.-M. Lagrange</i>	3
Retrieving cosmological signal using cosmic flows <i>V. Bouillot, and J.-M. Alimi</i>	9
Planetary migration and accretion <i>A. Crida</i>	15
Planck SZ clusters <i>M. Douspis</i>	21
R&D activities for astronomy and astrophysics in France <i>P. Kern</i>	27
Properties of unusual void LSBs versus cosmological simulations predictions <i>J.-M. Martin, S. A. Pustilnik, and A. Y. Kniazev</i>	37
Particles acceleration at relativistic shocks and high energy astrophysics <i>G. Pelletier, and M. Lemoine</i>	39
Stellar physics with Gaia <i>B. Plez</i>	47
Large extragalactic and cosmological surveys (S01)	53
Results from the first three years of operation of the Supernova Legacy Survey (SNLS) <i>C. Balland, and the SNLS collaboration</i>	55
A Bayesian approach to gravitational lens model selection <i>I. Balmès, and P.-S. Corasaniti</i>	59
Coincident searches between gravitational waves and high-energy neutrinos with the ANTARES and LIGO/Virgo detectors <i>B. Bouhou, the ANTARES Collaboration, the LIGO Scientific Collaboration, and the Virgo Collaboration</i>	63
Galaxies and cosmology with the projects Physics of the Accelerating Universe (PAU) and Dark Energy Survey (DES) <i>F. J. Castander, on behalf of the PAU, and DES collaborations</i>	69
Constraining type Ia supernova models with SNLS spectra <i>F. Cellier-Holzem, and C. Balland</i>	73
A reionisation scenario from HII regions mergers histories <i>J. Chardin, and D. Aubert</i>	77

The influence of the environment in compact galaxy groups: an infrared perspective <i>V. Charmandaris, and T. Bitsakis</i>	81
The star formation rate density and dust attenuation evolution over 12 Gyr with the VVDS surveys <i>O. Cucciati, L. Tresse, O. Ilbert, and O. Le Fèvre</i>	85
Querying for heavily obscured AGN via high 9.7 μ m optical depths: results from the 12 μ m, GOODS, and FLS Spitzer spectroscopic samples <i>K. M. Daszra, I. Georgantopoulos, A. Pope, and M. Rovilos</i>	91
LBGs properties from $z\sim 3$ to $z\sim 6$ <i>S. de Barros, D. Schaerer, and D. P. Stark</i>	95
A panchromatic study of two pairs of galaxy clusters <i>F. Durret, T. F. Laganá, M. Haider, C. Adami, and E. Bertin</i>	101
A project for an infrared synoptic survey from Antarctica with the Polar Large Telescope (PLT) <i>N. Epchtein, L. Abe, W. Ansorge, M. Langlois, I. Vauglin, S. Argentini, I. Esau, C. David, I. Bryson, G. Dalton, and et al</i>	107
Non-thermal physics of galaxy clusters <i>C. Ferrari</i>	111
Evolution as a confounding parameter in scaling relations for galaxies <i>D. Fraix-Burnet</i>	115
Mapping the dust properties of nearby galaxies with Herschel and LABOCA <i>M. Galametz, M. Albrecht, R. Kennicutt, F. Bertoldi, F. Walter, A. Weiss, D. Dale, B. Draine, G. Aniano, C. Engelbracht, and et al</i>	119
The DAFT/FADA Survey status and latest results <i>L. Guennou</i>	125
Prospects for the cosmological application of polarized Lyman-alpha radiation <i>M. Hayes, and C. Scarlata</i>	129
The formation of large galactic disks: revival or survival? <i>F. Hammer, M. Puech, H. Flores, E. Athanassoula, Y. B. Yang, J. L. Wang, M. Rodrigues, and S. Fouquet</i>	135
High- z galaxies behind the lensing cluster A2667 <i>N. Laporte, R. Pelló, D. Schaerer, J. Richard, F. Boone, J.-P. Kneib, and E. Egami</i>	141
The baryon fraction in five galaxy groups <i>N. Martinet, F. Durret, T. F. Laganá, and G. B. Lima Neto</i>	147
The Next Generation Virgo Cluster Survey: status and first results <i>S. Mei, L. Ferrarese, A. Boselli, S. Boissier, F. Bournaud, J. C. Cuillandre, P.-A. Duc, E. Ferrière, R. Gavazzi, S. D. J. Gwyn, and et al</i>	153
Bulge Formation Patterns in APM-SPH simulations: Questions to Be Answered by Future Missions <i>A. Obreja, R. Domínguez-Tenreiro, M. Doménech-Moral, F. J. Martínez-Serrano, and A. Serna</i>	157
Extragalactic science with EMIR-GTC <i>R. Pelló, F. Garzón, M. Balcells, F. Boone, N. Cardiel, J. G. Cuby, J. Gallego, R. Guzmán, M. Hayes, P. Hudelot, and et al</i>	161

Galaxies and cosmology with ALMA <i>P. Planesas</i>	169
Early-type galaxies: mass-size relation at $z \sim 1.3$ for different environments <i>A. Raichoor, S. Mei, S. A. Stanford, B. P. Holden, F. Nakata, P. Rosati, F. Shankar, M. Tanaka, H. Ford, M. Huertas-Company, and et al</i>	175
Local host galaxy properties of type Ia supernovae from the Nearby SuperNovae Factory <i>M. Rigault, Y. Copin, G. Aldering, P. Antilogus, C. Aragon, C. Baltay, S. Bongard, C. Buton, A. Canto, M. Childress, and et al</i>	179
Morphological classification of galaxy clusters <i>F. Rostagni, C. Benoist, and S. Maurogordato</i>	185
Instrumental calibration of wide field imagers <i>F. Villa, and the SNDice collaboration</i>	191
Lyman horizons in the early phases of the epoch of reionization <i>P. Vonlanthen, and B. Semelin</i>	197
Helio- and astero-seismology, advances and perspectives in the context of new space missions and ground-based instruments (S02)	201
The helium shells of HeI and HeII at solar minimum: New results from eclipse flash spectra of 2008- 2010 <i>C. Bazin, S. Koutchmy, and P. Lamy</i>	203
Calibrating 15 years of GOLF data <i>G. R. Davies, and R. A. García</i>	207
Seismic inference on the core of the subgiant HD 49385 via mixed modes <i>S. Deheuvels</i>	211
Nonlinear simulations of the convection-pulsation coupling <i>T. Gastine, and B. Dintrans</i>	215
Seismic analysis of two solar-type stars observed by <i>Kepler</i> <i>S. Mathur</i>	221
Red giants unveiled <i>B. Mosser</i>	225
Pulsation modes detected by CoRoT in the hot Be star HD 51452 <i>C. Neiner, M. Floquet, and the CoRoT Be team</i>	231
Surface convection: from the Sun to red giant stars <i>L. Piau, P. Kervella, S. Dib, and P. Hauschildt</i>	235
Photospheric motions from an observational point of view: HINODE and SDO satellite observations <i>T. Roudier</i>	241
Stellar activity cycles and asteroseismology <i>D. Salabert</i>	245
Rotation on the oscillation spectrum of solar-like stars <i>J. C. Suárez, M.-J. Goupil, D. R. Reese, R. Samadi, F. Lignières, M. Rieutord, and J. Lochard</i>	249

Diffusion-induced iron accumulations and thermohaline convection in A type stars : asteroseismic implications <i>S. Théado, S. Vauclair, G. Alecian, and F. LeBlanc</i>	253
Main lessons from GOLF/SOHO instrument on dynamics of the radiative zone, fundamental physics and energetics <i>S. Turck-Chièze, R. A. García, L. Piau, and S. Couvidat</i>	257
Stellar and interstellar physics for the modelling of the galaxy and its components (S03)	261
Orbit of potentially hazardous asteroids using Gaia and ground-based observations <i>D. Bancelin, D. Hestroffer, and W. Thuillot</i>	263
The H α Balmer line as an effective temperature criterion <i>R. Cayrel, C. Van't Veer-Menneret, N. F. Allard, and C. Stehlé</i>	267
Calibration of the Gaia RVS from ground-based observations of candidate standard stars <i>L. Chemin, C. Soubiran, F. Crifo, G. Jasiewicz, D. Katz, D. Hestroffer, and S. Udry</i>	271
The dependence of the galactic star formation laws on metallicity <i>S. Dib, L. Piau, S. Mohanty, and J. Braine</i>	275
Collision rates and the determination of atmospheric parameters <i>A. Spielfiedel, N. Feautrier, M. Guitou, and A. K. Belyaev</i>	283
Kinematic imprints from the bar and spiral structures in the galactic disk <i>F. Figueras, T. Antoja, O. Valenzuela, M. Romero-Gómez, B. Pichardo, and E. Moreno</i>	287
Dust mass in simulations of galaxies <i>N. Gaudin, and H. Wozniak</i>	291
Determination of the ages of stars from their position in the HR diagram <i>C. Guédé, Y. Lebreton, and G. Dréan</i>	295
The Milky Way stellar populations in CFHTLS fields <i>M. Guittet, M. Haywood, and M. Schultheis</i>	299
New SB2 binaries for accurate stellar masses with Gaia <i>J.-L. Halbwachs, F. Arenou, B. Famaey, P. Guillout, Y. Lebreton, and D. Pourbaix</i>	303
Chemical abundances of A-type dwarfs in the young open cluster M6 <i>T. Kılıçoğlu, R. Monier, and L. Fossati</i>	307
Probing the thick disc formation scenarios outside the solar neighbourhood <i>G. Kordopatis, A. Recio-Blanco, P. de Laverny, G. Gilmore, V. Hill, R. F. G. Wyse, A. Helmi, A. Bijaoui, C. Ordenovic, M. Zoccali, and et al</i>	311
Gaia: luminosity calibrations and distances in the Galaxy and Local Group <i>X. Luri, and C. Turon</i>	315
Carbon-enhanced metal-poor stars: witnesses of the first generation of stars <i>T. Masseron</i>	321
Spitzer characterization of dust in the ionized medium of the Large Magellanic Cloud <i>D. Paradis, R. Paladini, A. Noriega-Crespo, G. Lagache, A. Kawamura, T. Onishi, and Y. Fukui</i>	325

Galactic dust properties <i>D. Paradis, and the Hi-GAL team</i>	329
SPADES: a Stellar PArameters DEtermination Software <i>H. Posbic, D. Katz, E. Caffau, P. Bonifacio, L. Sbordone, A. Gomez, and F. Arenou</i>	333
The physical parameters of the low-mass multiple system LHS1070 from Spectral synthesis analysis <i>A. S. Rajpurohit, C. Reylé, M. Schultheis, C. Leinert, and F. Allard</i>	339
Simulating the Galaxy and applications to the preparation of the Gaia mission <i>A. C. Robin, C. Reylé, CU2, and Gaia-DPAC consortium</i>	345
Evolution of our galaxy and others with the high-resolution version of the code PÉGASE <i>B. Rocca-Volmerange, A. Sourie, A. Karamelas, M. Kontizas, and P. Tsalmantza</i>	349
Preliminary determination of the Non-LTE Calcium abundance in a sample of extremely metal-poor stars* <i>M. Spite, F. Spite, P. Bonifacio, E. Caffau, S. Andrievsky, S. Korotin, R. Cayrel, and P. François</i>	353
A.S. Gaia: 2007-2011 and perspectives <i>C. Turon, F. Arenou, and M. Haywood</i>	357
Atmosphere-Ionosphere coupling: atmospheric electricity (TLEs, TGFs, lightning) and the upper atmosphere physics and chemistry (S04)	361
Natural lightning flashes: from observation to modeling <i>E. Defer, T. Farges, C. Barthe, C. Bovalo, J.-P. Pinty, M. Chong, S. Soula, and P. Ortéga</i>	363
Solar-terrestrial relations and space weather (S05)	367
SOHO observations of oscillatory motions in an eruptive filament: Intensity and velocity variations <i>K. Bocchialini, S. Koutchmy, and J. Solomon</i>	369
Automated detection and tracking of solar and heliospheric features in the frame of the European project HELIO <i>X. Bonnin, J. Aboudarham, N. Fuller, C. Renie, D. Perez-Suarez, P. Gallagher, P. Higgins, L. Krista, A. Csillaghy, and R. Bentley</i>	373
Compressible turbulence in astrophysics <i>S. Galtier, and S. Banerjee</i>	379
The early Earth as a planet in the making (S06)	381
Ghosts in Saturn's rings <i>K. Baillié, J.E. Colwell, and L.W. Esposito</i>	383
Solar physics at the advent of the European Solar Telescope (S07)	387
Reconstruction of the solar coronal magnetic field, from active region to large scale <i>T. Amari, A. Canou, F. Delyon, J. J. Aly, P. Frey, F. Alauzet, and SDO/HMI Team</i>	389
Adaptive optics system performances and large field of view spectropolarimetric observations <i>G. Aulanier, and G. Molodij</i>	395

Magnetohydrodynamics turbulence: waves or eddies? <i>S. Galtier, and B. Bigot</i>	399
Scattering polarization of molecular lines at the solar limb <i>I. Milić, and M. Faurobert</i>	401
Simulations of the solar atmosphere and solar limbs <i>L. Piau, R. F. Stein, S. Melo, S. Turck-Chièze, G. Thuillier, and A. Hauchecorne</i>	407
Circumstellar matter with ALMA and HERSCHEL (S08)	411
Observational studies of intermediate-mass protostars with PdBI, 30m, and Herschel <i>T. Alonso-Albi, and A. Fuente</i>	413
An HI 21-cm line survey of evolved stars <i>E. Gérard, T. Le Bertre, and Y. Libert</i>	419
Molecular emission in chemically active protostellar outflows <i>B. Lefloch</i>	423
Stripping a debris disk by gravitational interaction with an inner planet <i>E. Morey, and J.-F. Lestrade</i>	429
Stellar physics (PNPS) (S10)	433
Theoretical analysis of the He ₂ line at 585 Å <i>N. F. Allard, F. X. Gadéa, A. Monari, and B. Deguilhem</i>	435
Absorption profiles of the potassium 4s – 4p and 4p – 5s lines perturbed by helium <i>N. F. Allard</i>	439
Critical layers for internal waves in stellar radiation zones <i>L. Alvan, and S. Mathis</i>	443
Characterisation of SPH noise in simulations of protoplanetary discs <i>S. E. Arena, J.-F. Gonzalez, and E. Crespe</i>	449
Planetary migration in weakly magnetized turbulent discs <i>C. Baruteau, S. Fromang, R. P. Nelson, and F. Masset</i>	455
Planets formed by gravitational instability should rapidly migrate inward <i>C. Baruteau, F. Meru, and S.-J. Paardekooper</i>	459
Numerical modelling of the accretion column in magnetic cataclysmic variables <i>C. Busschaert, C. Michaut, E. Falize, B. Loupiau, A. Ravasio, A. Dizière, H. C. Nguyen, and M. Koenig</i>	463
The Rossby wave instability in 2D viscous protoplanetary discs <i>E. Crespe, J.-F. Gonzalez, and S. E. Arena</i>	469
Numerical simulations of magnetic relaxation in rotating stellar radiation zones <i>V. Duez</i>	475
Infrared excess and extended emission around Cepheids <i>A. Gallenne, P. Kervella, and A. Mérand</i>	479

SPEC3D: a three-dimensional radiative transfer code for astrophysical and laboratory applications <i>L. Ibgui, I. Hubeny, T. Lanz, and C. Stehlé</i>	485
Angular momentum transport in stellar interiors <i>S. Mathis</i>	491
Long-term magnetic monitoring of 19 Sun-like stars <i>A. Morgenthaler, P. Petit, J. Morin, M. Aurière, and B. Dintrans</i>	497
Evidence for dynamo bistability among very low mass stars <i>J. Morin, X. Delfosse, J.-F. Donati, E. Dormy, T. Forveille, M. M. Jardine, P. Petit, and M. Schirmer</i>	503
Progress on Magnetism in Massive Stars (MiMeS) <i>C. Neiner, E. Alecian, S. Mathis, and the MiMeS collaboration</i>	509
The fluid equilibrium tide in stars and giant planets <i>F. Remus, S. Mathis, and J.-P. Zahn</i>	515
The equilibrium tide in viscoelastic parts of planets <i>F. Remus, S. Mathis, J.-P. Zahn, and V. Lainey</i>	519
High energy and cosmic phenomena (PCHE) (S12)	523
Ultra fast variability monitoring with CTA <i>J. Biteau, and B. Giebels</i>	525
Search for lorentz invariance violation with AGNs: a prospect for CTA <i>J. Bolmont, and A. Jacholkowska</i>	529
Data analysis method for the search of point sources of gamma rays with the HAGAR telescope array <i>R. J. Britto, B. S. Acharya, G. C. Anupama, P. Bhattacharjee, V. R. Chitnis, R. Cowsik, N. Dorji, S. K. Duhan, K. S. Gothe, P. U. Kamath, and et al</i>	535
Status of the Himalayan Gamma-Ray Observatory (HIGRO) and observaton with HAGAR at very high energies <i>R. J. Britto, B. S. Acharya, G. C. Anupama, N. Bhatt, P. Bhattacharjee, S. Bhattacharya, V. R. Chitnis, R. Cowsik, N. Dorji, S. K. Duhan, and et al</i>	539
The W49 region as seen by H.E.S.S. <i>F. Brun, M. de Naurois, W. Hofmann, S. Carrigan, A. Djannati-Ataï, S. Ohm, and H.E.S.S. Collaboration</i>	545
Prospects for dark matter searches with CTA <i>P. Brun</i>	549
Lepto-hadronic modelling of blazar emission <i>M. Cerruti, A. Zech, C. Boisson, and S. Inoue</i>	555
Collective excitations in the neutron star inner crust <i>L. Di Gallo, M. Oertel, and M. Urban</i>	559
Self-consistent spectra from GRMHD simulations with radiative cooling: A link to reality for Sgr A <i>S. Drappeau, S. Dibi, J. Dexter, S. Markoff, and P. C. Fragile</i>	563
Detection of a relativistic iron line in MXB 1728–34 with <i>XMM-Newton</i> <i>E. Egron, T. Di Salvo, L. Burderi, A. Papitto, L. Barragán, T. Dauser, J. Wilms, A. D’Ai, A. Riggio, R. Iaria, and et al</i>	567

Thermal evolution of neutron stars and constraints on their internal properties <i>M. Fortin, J. L. Zdunik, P. Haensel, and J. Margueron</i>	573
Accurate black hole mass measurements for thermal AGNs and the origin of the correlations between black hole mass and bulge properties <i>C. M. Gaskell</i>	577
Modeling X-ray polarimetry while flying around the misaligned outflow of NGC 1068 <i>R. W. Goosmann, and G. Matt</i>	583
Fermi Large Area Telescope observations of gamma-ray pulsars <i>L. Guillemot, the Fermi LAT Collaboration, the LAT Pulsar Timing Consortium, and the LAT Pulsar Search Consortium</i>	587
Do Fermi-LAT observations really imply very large Lorentz factors in GRB outflows ? <i>R. Hascoët, F. Daigne, R. Mochkovitch, and V. Vennin</i>	593
Modeling the polarization of radio-quiet AGN: from the optical to the X-ray band <i>F. Marin, and R. W. Goosmann</i>	597
Neutrino transport in gravitationnal supernovæ simulations : a simplified treatment via a leakage scheme <i>B. Peres, J. Novak, and M. Oertel</i>	601
Particle transport at relativistic shocks <i>I. Plotnikov</i>	605
Some recent results of the Codalema Experiment <i>A. Rebai, and the CODALEMA collaboration</i>	609
Optical follow-up of high energy neutrinos detected by the ANTARES telescope <i>M. Vecchi, M. Ageron, C. Akerlof, I. Al Samarai, S. Basa, V. Bertin, M. Boer, J. Brunner, J. Busto, D. Dornic, and et al</i>	615
The galactic center region viewed by H.E.S.S.. <i>A. Viana</i>	621
Gravitation, reference, astronomy, and metrology (AS-GRAM) (S15)	627
Updated orbit of Apophis with recent observations <i>D. Bancelin, F. Colas, W. Thuillot, D. Hestroffer, and M. Assafin</i>	629
Relativistic astrometry and time transfer functions <i>S. Bertone, and C. Le Poncin-Lafitte</i>	635
Statistical analysis on the uncertainty of asteroid ephemerides <i>J. Desmars, D. Bancelin, D. Hestroffer, and W. Thuillot</i>	639
Analytical expression of the potential generated by a massive inhomogeneous straight segment <i>N.-E. Najid, and E. Elourabi</i>	643
In-flight calibration of the MICROSCOPE space mission instrument: development of the simulator <i>E. Hardy, A. Levy, G. Métris, A. Robert, M. Rodrigues, and P. Touboul</i>	647
Testing gravitation in the Solar System with radio science experiments <i>A. Hees, P. Wolf, B. Lamine, S. Reynaud, M. T. Jaekel, C. Le Poncin-Lafitte, V. Lainey, and V. Dehant</i>	653

The first measurement of the Galactic aberration by the VLBI <i>S. B. Lambert</i>	659
Measuring the absolute non-gravitational acceleration of a spacecraft: goals, devices, methods, performances <i>B. Lenoir, B. Christophe, and S. Reynaud</i>	663
GETEMME: a mission to explore the martian satellites <i>C. Le Poncin-Lafitte, and the GETEMME core team</i>	669
Development of techniques to study the dynamic of highly elliptical orbits <i>G. Lion, and G. Métris</i>	673
ACES-PHARAO : Microwave link data processing <i>F. Meynadier, P. Delva, C. Le Poncin-Lafitte, P. Laurent, and P. Wolf</i>	679
The gravitational potential of axially symmetric bodies from a regularized green kernel <i>A. Trova, J.-M. Huré, and F. Hersant</i>	685
Towards constraining the central black hole's properties by studying its infrared flares with the GRAVITY instrument <i>F. H. Vincent, T. Paumard, G. Perrin, E. Gourgoulhon, F. Eisenhauer, and S. Gillessen</i>	689
Discussions EJSM JGO after Decadal Survey US - towards a new mission scenario? (S16)	695
Quantifying the measurement requirements needed to understand the origin of the Galilean satellite system <i>O. Mousis, J. H. Waite, and J. I. Lunine</i>	697
Author Index	701

Participant list

Ouali **ACEF** (ouali.acef at obspm.fr)
Ixandra **ACHITOUV** (ixandra.achitouv at obspm.fr)
Ahmed **REBAI** (ahmed.rebai at subatech.in2p3.fr)
Hauchecorne **ALAIN** (alain.hauchecorne at latmos.ipsl.fr)
Francis **ALBAREDE** (albaredede at ens-lyon.fr)
Javier **ALCOLEA** (j.alcolea at oan.es)
Georges **ALECIAN** (georges.alecian at obspm.fr)
Olga **ALEXANDROVA** (olga.alexandrova at obspm.fr)
Emilio J. **ALFARO** (emilio at iaa.es)
Safwan **ALJBAAE** (safwan.aljbaae at obspm.fr)
Nicole **ALLARD** (nicole.allard at obspm.fr)
Carlos **ALLENDE-PRIETO** (callende at iac.es)
Tomás **ALONSO** (t.alonso at oan.es)
Lucie **ALVAN** (lucie.alvan at cea.fr)
Tahar **AMARI** (amari at cpht.polytechnique.fr)
Nicolas **ANDRÉ** (nicolas.andre at cesr.fr)
Serena **ARENA** (serena.arena at ens-lyon.fr)
Frédéric **ARENOU** (Frederic.Arenou at obspm.fr)
Nick **ARNDT** (arndt at ujf-grenoble.fr)
Andres **ASENSIO RAMOS** (aasensio at iac.es)
Frédéric **AUCHÈRE** (frederic.auchere at ias.u-psud.fr)
Guillaume **AULANIER** (guillaume.aulanier at obspm.fr)
Michel **AURIERE** (michel.auriere at ast.obs-mip.fr)
Hervé **AUSSEL** (herve.aussel at cea.fr)
Carine **BABUSIAUX** (carine.babusiaux at obspm.fr)
Annie **BAGLIN** (annie.baglin at obspm.fr)
Kévin **BAILLIÉ** (kevin.baillie at gmail.com)
Christophe **BALLAND** (balland at lpnhe.in2p3.fr)
Jean **BALLET** (jballet at cea.fr)
Irène **BALMÈS** (irene.balmes at obspm.fr)
David **BANCELIN** (bancelin at imcce.fr)
Caroline **BARBAN** (caroline.barban at obspm.fr)
Matteo **BARSUGLIA** (barsuglia at apc.univ-paris7.fr)
Mathieu **BARTHELEMY** (mathieu.barthelemy at obs.ujf-grenoble.fr)
Jacques-olivier **BARUCH** (duee28 at noos.fr)
Clement **BARUTEAU** (C.Baruteau at damtp.cam.ac.uk)
Stephane **BASA** (stephane.basa at oamp.fr)
Cyrille **BAZIN** (bazin at iap.fr)
Jean-philippe **BEAULIEU** (beaulieu at iap.fr)
Laurène **BEAUVALET** (beauvalet at imcce.fr)
Slimane **BEKKI** (slimane.bekki at latmos.ipsl.fr)
Soraya **BELHEOUANE** (soraya.belheouane at obspm.fr)
Luis **BELLOT RUBIO** (lbellot at iaa.es)
Txitxo **BENITEZ** (benitez at iaa.es)
Latifa **BENJOUALI** (latifa.benjouali at uam.es)
Gelly **BERNARD** (bgelly at themis.iac.es)
Stefano **BERTONE** (stefano.bertone at obspm.fr)
Nicolas **BESSOLAZ** (Nicolas.Bessolaz at cea.fr)
Hervé **BEUST** (Herve.Beust at obs.ujf-grenoble.fr)
Lionel **BIREE** (lionebiree at hotmal.fr)
Jonathan **BITEAU** (biteau at in2p3.fr)
Guillaume **BLANC** (blanc at apc.univ-paris7.fr)
Elisabeth **BLANC** (elisabeth.blanc at cea.fr)
Pierre-louis **BLELLY** (pierre-louis.blelly at cesr.fr)

Janne **BLICHERT-TOFT** (jblicher at ens-lyon.fr)
Thomas **BOCH** (thomas.boch at astro.unistra.fr)
Yann **BOEHLER** (yann_boehler at msn.com)
Samuel **BOISSIER** (samuel.boissier at oamp.fr)
Catherine **BOISSON** (catherine.boisson at obspm.fr)
Julien **BOLMONT** (bolmont at in2p3.fr)
Véronique **BOMMIER** (V.Bommier at obspm.fr)
Piercarlo **BONIFACIO** (Piercarlo.Bonifacio at obspm.fr)
Pascal **BONNEFOND** (Pascal.Bonnefond at obs-azur.fr)
Caroline **BOT** (caroline.bot at astro.unistra.fr)
Boutayeb **BOUHOUE** (bouhou at apc.univ-paris7.fr)
Vincent **BOUILLOT** (vincent.bouillot at obspm.fr)
Francois **BOULANGER** (francois.boulanger at ias.u-psud.fr)
Patrick **BOUMIER** (patrick.boumier at ias.u-psud.fr)
Anne **BOURDON** (anne.bourdon at em2c.ecp.fr)
Herve **BOUY** (hbouy at cab.inta-csic.es)
Felipe **BRAGA RIBAS** (felipe.ribas at obspm.fr)
Jonathan **BRAINE** (braine at obs.u-bordeaux1.fr)
Florence **BRAULT** (brault at iap.fr)
Carine **BRIAND** (carine.briand at obspm.fr)
Danielle **BRIOT** (danielle.briot at obspm.fr)
Richard **BRITTO** (britto at tifr.res.in)
Yann **BROUET** (yann.brouet at obspm.fr)
Allan Sacha **BRUN** (sacha.brun at cea.fr)
Pierre **BRUN** (pierre.brun at cea.fr)
Francois **BRUN** (francois.brun at llr.in2p3.fr)
Eric **BUCHLIN** (eric.buchlin at ias.u-psud.fr)
Pascale **BUKHARI** (Pascale.bukhari at cnrs-dir.fr)
Denis **BURGARELLA** (denis.burgarella at oamp.fr)
Michel **BUSQUET** (busquet at artepinc.com)
Clotilde **BUSSCHAERT** (clotilde.busschaert at obspm.fr)
Elisabetta **CAFFAU** (Elisabetta.Caffau at obspm.fr)
Laurent **CAMBRESY** (cambresy at astro.unistra.fr)
Arnaud **CANTO** (canto at lpnhe.in2p3.fr)
Nicole **CAPITAINE** (nicole.capitaine at obspm.fr)
Fabienne **CASOLI** (fabienne.casoli at cnes.fr)
Francisco Javier **CASTANDER** (fjc at ieec.uab.es)
Thibault **CAVALIÉ** (cavalie at obs.u-bordeaux1.fr)
Cécile **CAVET** (cecile.cavet at obspm.fr)
Roger **CAYREL** (roger.cayrel at obspm.fr)
Baptiste **CECCONI** (baptiste.cecconi at obspm.fr)
Flora **CELLIER-HOLZEM** (cellier at lpnhe.in2p3.fr)
Matteo **CERRUTI** (matteo.cerruti at obspm.fr)
Corinne **CHARBONNEL** (Corinne.Charbonnel at unige.ch)
Jonathan **CHARDIN** (jonathan.chardin at astro.unistra.fr)
Stéphane **CHARLOT** (charlot at iap.fr)
Vassilis **CHARMANDARIS** (vassilis at physics.uoc.gr)
Eric **CHASSANDE-MOTTIN** (ecm at apc.univ-paris7.fr)
Marc **CHAUSSIDON** (chocho at crpg.cnrs-nancy.fr)
Gael **CHAUVIN** (gael.chauvin at obs.ujf-grenoble.fr)
Touhami **CHERRAK** (touhami.cherrak at etu.univ-lehavre.fr)
Olivier **CHESNEAU** (Olivier.Chesneau at oca.eu)
Igor **CHILINGARIAN** (igor.chilingarian at astro.unistra.fr)
Arnaud **CHULLIAT** (chulliat at ipgp.fr)
Andrea **CIARDI** (andrea.ciardi at obspm.fr)

Claude CAMY-PEYRET (claude.camy-peyret at upmc.fr)
Nicolas CLERC (nicolas.clerc at cea.fr)
Manuel COLLADOS (mcv at iac.es)
Suzy COLLIN-ZAHN (suzy.collin at obspm.fr)
Francoise COMBES (francoise.combes at obspm.fr)
Thierry CORBARD (thierry.corbard at oca.eu)
Nicole CORNILLEAU-WEHRLIN (nicole.cornilleau at lpp.polytechnique.fr)
Patrick COTE (Patrick.Cote at nrc-cnrc.gc.ca)
Clément COURDE (clement.courde at oca.eu)
Régis COURTIN (regis.courtin at obspm.fr)
Morgane COUSIN (morgane.cousin at ias.u-psud.fr)
Athéna COUSTENIS (athena.coustenis at obspm.fr)
Elisabeth CRESPE (elisabeth.crespe at ens-lyon.fr)
Aurélien CRIDA (crida at oca.eu)
Francoise CRIFO (francoise.crifo at obspm.fr)
Pierre CRISTOFARI (pierre.cristofari at apc.univ-paris7.fr)
Olga CUCCIATI (olga.cucciati at oamp.fr)
Jean-charles CUILLANDRE (jcc at cfht.hawaii.edu)
Louis D'HENDECOURT (ldh at ias.u-psud.fr)
Frédéric DAIGNE (daigne at iap.fr)
Emmanuel DARTOIS (emmanuel.dartois at ias.u-psud.fr)
Kalliopi DASYRA (kalliopi.dasyra at obspm.fr)
Guy DAVIES (grd349 at gmail.com)
Stephane DE BARROS (stephane.debarros at unige.ch)
Hervé DE FERAUDY (herve.deferaudy at latmos.ipsl.fr)
Amaury DE KERTANGUY (amaury.dekertanguy at obspm.fr)
Estelle DÉAU (estelle.deau at jpl.nasa.gov)
Frederic DEBRAINE (fdebraine at free.fr)
Thibaut DECRESSIN (thibaut.decressin at unige.ch)
Eric DEFER (eric.defer at obspm.fr)
Bernard DEGRANGE (degrange at llr.in2p3.fr)
Sebastien DEHEUVELS (sebastien.deheuvels at yale.edu)
Jose Carlos DEL TORO (jti at iaa.es)
Lauriane DELAYE (lauriane.delaye at obspm.fr)
Dominique DELCOURT (dominique.delcourt at lpp.polytechnique.fr)
Florent DELEFLIE (Florent.Deleflie at imcce.fr)
Pacôme DELVA (pacome.delva at obspm.fr)
Sylvie DERENNE (sylvie.derenne at upmc.fr)
Daniel DEVOST (devost at cfht.hawaii.edu)
Luc DI GALLO (digallo_luc at obspm.fr)
Paola DI MATTEO (paola.dimatteo at obspm.fr)
Sami DIB (s.dib at imperial.ac.uk)
Salomé DIBI (s.dibi at uva.nl)
Didier BARRET (didier.Barret at cesr.fr)
Olivier DO CAO (olivier.do-cao at cea.fr)
Herve DOLE (herve_dole at yahoo.com)
Catherine DOUGADOS (catherine.dougados at obs.ujf-grenoble.fr)
Marian DOUSPIS (marian.douspis at ias.u-psud.fr)
Samia DRAPPEAU (s.drappeau at uva.nl)
Pierre DROSSART (pierre.drossart at obspm.fr)
Marie-lise DUBERNET (marie-lise.dubernet at obspm.fr)
Thierry DUDOK DE WIT (ddwit at cnrs-orleans.fr)
Vincent DUEZ (vduetz at astro.uni-bonn.de)
Florence DURRET (durret at iap.fr)
Fabrice DURUISSEAU (fabrice.duruisseau at etu.univ-orleans.fr)

Elise **EGRON** (elise.egron at dsf.unica.it)
David **EHRENREICH** (david.ehrenreich at obs.ujf-grenoble.fr)
El Haj **EL OURABI** (elourabi2000 at yahoo.fr)
Thomas **ELGHOZI** (thomas.elghozi at gmail.com)
Maryame **ELMOUTAMID** (maryame.elmoutamid at obspm.fr)
Nicolas **EPCHEIN** (epchtein at unice.fr)
Michel **ERIC** (eric.michel at obspm.fr)
Cyril **ESCOLANO** (cyril.escolano at univ-montp2.fr)
Pierre **EXERTIER** (Pierre.Exertier at obs-azur.fr)
Emeric **FALIZE** (Emeric.Falize at obspm.fr)
Thomas **FARGES** (thomas.farges at cea.fr)
Marianne **FAUROBERT** (marianne.faurobert at unice.fr)
Nicole **FEAUTRIER** (nicole.Feautrieer at obspm.fr)
Stephen **FEGAN** (sfegan at llr.in2p3.fr)
Chiara **FERRARI** (chiara.ferrari at oca.eu)
Francesca **FIGUERAS SIÑOL** (cesca at am.ub.es)
Patrick **FLEURY** (patrick.fleury at moulinfleury.net)
Bernard **FOING** (Bernard.Foing at esa.int)
Dominique **FONTAINE** (dominique.fontaine at lpp.polytechnique.fr)
Pascal **FORTIN** (fortin at llr.in2p3.fr)
Morgane **FORTIN** (morgane.fortin at obspm.fr)
Thierry **FOUCHET** (Thierry.Fouchet at obspm.fr)
Sylvain **FOUQUET** (sylvain.fouquet at obspm.fr)
Didier **FRAIX-BURNET** (fraix at obs.ujf-grenoble.fr)
Nicolas **FULLER** (nicolas.fuller at obspm.fr)
Stefano **GABICI** (stefano.gabici at apc.univ-paris7.fr)
Maud **GALAMETZ** (mgalamet at ast.cam.ac.uk)
Alexandre **GALLENNE** (alexandre.gallenne at obspm.fr)
Louis-jonardan **GALLIN** (gallin.louis.j at gmail.com)
Sébastien **GALTIER** (sebastien.galtier at ias.u-psud.fr)
Rafael A. **GARCIA** (rgarcia at cea.fr)
Martin **GASKELL** (martin.gaskell at uv.cl)
Thomas **GASTINE** (gastine at mps.mpg.de)
Nicolas **GAUDIN** (nicolas.gaudin at astro.unistra.fr)
Anne-lise **GAUTIER** (anne-lise.gautier at obspm.fr)
Jean **GAY** (jean_gay_astro at yahoo.fr)
Françoise **GENOVA** (genova at astro.u-strasbg.fr)
Eric **GERARD** (eric.gerard at obspm.fr)
Maryvonne **GERIN** (maryvonne.gerin at ira.ens.fr)
Berrie **GIEBELS** (berrie at in2p3.fr)
Julien **GIRARD** (julien.girard at obspm.fr)
Ana **GOMEZ** (ana.gomez at obspm.fraeg11)
René **GOOSMANN** (rene.goosmann at astro.unistra.fr)
Eric **GOURGOULHON** (eric.gourgoulhon at obspm.fr)
Philippe **GRANDCLÉMENT** (philippe.grandclement at obspm.fr)
Pierre **GRATIER** (gratier at iram.fr)
Isabelle **GRENIER** (isabelle.grenier at cea.fr)
Sandrine **GRIMALD** (grimald at cesr.fr)
Marie-hélène **GRONDIN** (grondin at astro.uni-tuebingen.de)
Céline **GUÉDÉ** (celine.guede at obspm.fr)
Loïc **GUENNOU** (loic.guennou at oamp.fr)
Jérôme **GUILLET** (jg613 at cam.ac.uk)
Lucas **GUILLEMOT** (guillemo at mpifr-bonn.mpg.de)
Sylvain **GUIRIEC** (sylvain.guiriec at lpta.in2p3.fr)
Mélanie **GUITTET** (melanie.guittet at obspm.fr)

Jean-louis HALBWACHS (jean-louis.halbwachs at astro.unistra.fr)
Francois HAMMER (francois.hammer at obspm.fr)
Emilie HARDY (emilie.hardy at onera.fr)
Romain HASCOËT (hascoet at iap.fr)
Matthew HAYES (matthew.hayes at ast.obs-mip.fr)
Misha HAYWOOD (Misha.Haywood at obspm.fr)
Guillaume HÉBRARD (hebrard at iap.fr)
Aurélien HEES (ahees at oma.be)
Daniel HESTROFFER (hestro at imcce.fr)
Mohammad HEYDARI-MALAYERI (m.heydari at obspm.fr)
Alain HILGERS (alain.hilgers at esa.int)
Ugo HINCELIN (Ugo.Hincelin at obs.u-bordeaux1.fr)
Deirdre HORAN (deirdre at llr.in2p3.fr)
Anne Marie HUBERT (anne-marie.hubert at obspm.fr)
Marc HUERTAS-COMPANY (marc.huertas at obspm.fr)
Nathalie HURET (nhuret at cnrs-orleans.fr)
Rodrigo IBATA (ibata at astro.u-strasbg.fr)
Laurent IBGUI (laurent.ibgui at obspm.fr)
Ismael PÉREZ-FOURNON (ipf at iac.es)
Karine ISSAUTIER (karine.issautier at obspm.fr)
Jerome BUREAU (jerome.bureau at upmc.fr)
Christine JOBLIN (christine.joblin at cesr.fr)
Eric JOSSELIN (eric.josselin at univ-montp2.fr)
David KATZ (david.katz at obspm.fr)
Pierre KERN (pierre.kern at obs.ujf-grenoble.fr)
Pierre KERVELLA (pierre.kervella at obspm.fr)
Elena KHOMENKO (khomenko at iac.es)
Tolgahan KILIÇOĞLU (tkilicoglu at ankara.edu.tr)
Karl-ludwig KLEIN (Ludwig.klein at obspm.fr)
Jurgen KNODLSEDER (Jurgen.Knodlseder at cesr.fr)
Georges KORDOPATIS (Georges.Kordopatis at oca.eu)
Serge KOUTCHMY (koutchmy at iap.fr)
Catherine KRAFFT (catherine.krafft at lpp.polytechnique.fr)
Benjamin L'HUILLIER (benjamin.lhuillier at obspm.fr)
Olivier LA MARLE (olivier.lamarle at cnes.fr)
Hélène LAFFON (laffon at llr.in2p3.fr)
Guilaine LAGACHE (guilaine.lagache at ias.u-psud.fr)
Sébastien LAMBERT (sebastien.lambert at obspm.fr)
Astrid LAMBERTS (astrid.lamberts at obs.ujf-grenoble.fr)
Ariane LANÇON (ariane.lancon at astro.unistra.fr)
Arnaud LANDRAGIN (arnaud.landragin at obspm.fr)
Nicolas LAPORTE (nicolas.laporte at ast.obs-mip.fr)
Chantal LATHUILLERE (chantal.lathuillere at obs.ujf-grenoble.fr)
Philippe LAURENT (plaurant at cea.fr)
Thibaut LE BERTRE (thibaut.lebertre at obspm.fr)
Gaéтан LE CHAT (gaetan.lechat at obspm.fr)
Olivier LE CONTEL (olivier.lecontel at lpp.polytechnique.fr)
Bertrand LE FLOCH (lefloch at obs.ujf-grenoble.fr)
Christophe LE PONCIN-LAFITTE (christophe.leponcin-lafitte at obspm.fr)
Loic LE TIRAN (loic.le-tiran at obspm.fr)
Francois LEBLANC (francois.leblanc at latmos.ipsl.fr)
Vianney LEBOUTEILLER (vianney.lebouteiller at cea.fr)
Jean-pierre LEBRETON (jean-pierre.lebreton at cnrs-orleans.fr)
Marianne LEMOINE-GOUMARD (lemoine at cenbg.in2p3.fr)
Benjamin LENOIR (benjamin.lenoir at onera.fr)

Sylvie LEON-HIRTZ (sylvie.leon at cnes.fr)
Agnès LEVY (agnes.levy at onera.fr)
Yannick LIBERT (libert at iram.fr)
Roxanne LIGI (roxanne.ligi at oca.eu)
Jean LILENSTEN (jean.lilensten at obs.ujf-grenoble.fr)
Guillaume LION (Guillaume.Lion at oca.eu)
Arturo LOPEZ ARISTE (arturo at themis.iac.es)
Xavier LURI (xluri at am.ub.es)
Anne-lise MAIRE (anne-lise.maire at obspm.fr)
Lucie MAQUET (lucie.maquet at imcce.fr)
Aurélie MARCHAUDON (aurelie.marchaudon at cnrs-orleans.fr)
Frédéric MARIN (frederic.marin at astro.unistra.fr)
Douglas MARSHALL (douglas.marshall at cesr.fr)
Jean-michel MARTIN (jean-michel.martin at obspm.fr)
Claire MARTIN ZAIDI (claire.martin-zaidi at obs.ujf-grenoble.fr)
Nicolas MARTINET (nicolas.martinet at obspm.fr)
Maria Jesus MARTINEZ GONZALEZ (marian at iac.es)
Fabrice MARTINS (fabrice.martins at univ-montp2.fr)
Bernard MARTY (bmarty at crpg.cnrs-nancy.fr)
Jean-louis MASNOU (jean-louis.masnou at malix.univ-paris1.fr)
Thomas MASSERON (thomas.masseron at ulb.ac.be)
Stéphane MATHIS (stephane.mathis at cea.fr)
Savita MATHUR (savita at ucar.edu)
Sean MATT (smatt at spacescience.org)
Israel MATUTE (matute at iaa.es)
Anaëlle MAURY (amaury at eso.org)
Farida MAZOUZ (farida.mazouz at latmos.ipsl.fr)
Heloïse MEHEUT (meheut at space.unibe.ch)
Simona MEI (simona.mei at obspm.fr)
Michel MENVIELLE (michel.menvielle at latmos.ipsl.fr)
Gilles METRIS (Gilles.Metris at oca.eu)
Frédéric MEYNADIER (Frederic.Meynadier at obspm.fr)
Francois MIGNARD (francois.mignard at oca.eu)
Ivan MILIC (milic at aob.rs)
Habibollah MINOO (hminoo at orange.fr)
Marc-antoine MIVILLE DESCHENES (mamd at ias.u-psud.fr)
Jacques MOITY (jacques.moity at obspm.fr)
Guillaume MOLODIJ (guillaume.molodij at obspm.fr)
Michel MONCUQUET (michel.moncuquet at obspm.fr)
Richard MONIER (Richard.Monier at unice.fr)
Maurice MONNERVILLE (maurice.monnerville at univ-lille1.fr)
Miguel MONTARGÈS (miguel.montarges at obspm.fr)
David MONTES (dmg at astrax.fis.ucm.es)
Estelle MORAUX (emoraux at obs.ujf-grenoble.fr)
Alessandro MORBIDELLI (morby at oca.eu)
Etienne MOREY (etienne.morey at obspm.fr)
Audrey MORGENTHALER (amorgent at ast.obs-mip.fr)
Julien MORIN (jmorin at cp.dias.ie)
Benoît MOSSER (benoit.mosser at obspm.fr)
Martine MOUCHET (martine.mouchet at obspm.fr)
Denis MOURARD (denis.mourard at oca.eu)
Olivier MOUSIS (olivier.mousis at obs-besancon.fr)
Coralie NEINER (Coralie.Neiner at obspm.fr)
Quang NGUYEN-LUONG (quang.nguyen-luong at cea.fr)
Jerome NOVAK (jerome.novak at obspm.fr)

Aura **OBREJA** (aura.obreja at uam.es)
Pierre **OCVIRK** (pierre.ocvirk at astro.unistra.fr)
Micaela **OERTEL** (micaela.oertel at obspm.fr)
Grasset **OLIVIER** (olivier.grasset at univ-nantes.fr)
Rhita-maria **OUAZZANI** (rhita-maria.ouazzani at obspm.fr)
Laurent **PAGANI** (laurent.pagani at obspm.fr)
François **PAJOT** (francois.pajot at ias.u-psud.fr)
Pere L. **PALLÉ** (pere.l.palle at iac.es)
Deborah **PARADIS** (paradis at cesr.fr)
Etienne **PARIAT** (etienne.pariat at obspm.fr)
Michel **PARROT** (mparrot at cnrs-orleans.fr)
Sébastien **PEIRANI** (peirani at iap.fr)
Guy **PELLETIER** (Guy.Pelletier at obs.ujf-grenoble.fr)
Roser **PELLO** (roser at ast.obs-mip.fr)
Aurelie **PENIN** (aurelie.penin at ias.u-psud.fr)
Bruno **PERES** (bruno.peres at obspm.fr)
Jérôme **PETY** (pety at iram.fr)
Laurent **PIAU** (laurent.piau at latmos.ipsl.fr)
Bernard **PICHON** (Bernard.Pichon at oca.eu)
Monique **PICK** (monique.pick at obspm.fr)
Arnaud **PIERENS** (arnaud.pierens at obs.u-bordeaux1.fr)
Marguerite **PIERRE** (mpierre at cea.fr)
Jean-louis **PINÇON** (jlpincon at cnrs-orleans.fr)
Rui **PINTO** (rui.pinto at cea.fr)
Frédéric **PITOUT** (pitout at cesr.fr)
Pere **PLANESAS** (p.planesas at gmail.com)
Bertrand **PLEZ** (bertrand.plez at univ-montp2.fr)
Illya **PLOTNIKOV** (illya.plotnikov at obs.ujf-grenoble.fr)
Hélène **POSBIC** (helene.posbic at obspm.fr)
Dominique **PROUST** (dominique.proust at obspm.fr)
Denis **PUY** (Denis.Puy at univ-montp2.fr)
Manso Sainz **RAFAEL** (rsainz at iac.es)
Anand **RAICHOOR** (anand.raichoor at brera.inaf.it)
Séverine **RAIMOND** (severine.raimond at latmos.ipsl.fr)
Arvind Singh **RAJPUROHIT** (arvind at obs-besancon.fr)
Clara **RÉGULO** (crr at iac.es)
Françoise **REMUS** (francoise.remus at obspm.fr)
Matthieu **RENAUD** (mrenaud at lupm.univ-montp2.fr)
Vincent **REVERDY** (vincent.reverdy at obspm.fr)
Anthony **REY** (anthony.rey at etu.univ-lehavre.fr)
Céline **REYLÉ** (celine at obs-besancon.fr)
Mickael **RIGAULT** (rigault at ipnl.in2p3.fr)
Laurie **RIGUCCINI** (laurie.riguccini at cea.fr)
Francois **RINCON** (rincon at ast.obs-mip.fr)
Isabelle **RISTORCELLI** (Isabelle.Ristorcelli at cesr.fr)
Patxi **RITTER** (patxi.ritter at cnrs-orleans.fr)
Annie **ROBIN** (annie.robin at obs-besancon.fr)
Brigitte **ROCCA** (rocca at iap.fr)
Jerome **RODRIGUEZ** (jrodriguez at cea.fr)
Sébastien **RODRIGUEZ** (sebastien.rodriguez at cea.fr)
Florent **ROSTAGNI** (rostagni at oca.eu)
Daniel **ROUAN** (daniel.rouan at obspm.fr)
Thierry **ROUDIER** (roudier at ast.obs-mip.fr)
Frédéric **ROYER** (frederic.royer at obspm.fr)
Jose Alberto **RUBINO-MARTIN** (jose.alberto.rubino at iac.es)

Sylvie SAHAL-BRÉCHOT (sylvie.sahal-brechot at obspm.fr)
Fouad SAHRAOUI (fouad.sahraoui at lpp.polytechnique.fr)
David SALABERT (salabert at oca.eu)
Salomé LILIENFELD (salome.lilienfeld at numericable.fr)
Réza SAMADI (reza.samadi at obspm.fr)
Paola SARTORETTI-CHARLOT (paola.sartoretti at obspm.fr)
François-xavier SCHMIDER (schmider at unice.fr)
Juergen SCHMIDT (jschmidt at agnld.uni-potsdam.de)
Brigitte SCHMIEDER (brigitte.schmieder at obspm.fr)
Fabian SCHUSSLER (fabian.schussler at cea.fr)
Sébastien PAYAN (sebastien.payan at upmc.fr)
Romain SELIER (romain.selier at obspm.fr)
Clea SERPOLLIER (clea.serpollier at gmail.com)
Amanda SHAMIRYAN (shamiryan.a at gmail.com)
Enrique SOLANO (esm at cab.inta-csic.es)
Laurence SOULAT (laurence.soulat at unice.fr)
Annie Myriam SPIELFIEDEL (annie.spielriedel at obspm.fr)
Francois SPITE (francois.spite at obspm.fr)
Monique SPITE (monique.spite at obspm.fr)
Grazyna STASINSKA (grazyna.stasinska at obspm.fr)
Chantal STEHLE (chantal.stehle at obspm.fr)
Thierry STOLARCZYK (thierry.stolarczyk at cea.fr)
Antoine STRUGAREK (antoine.strugarek at cea.fr)
Juan Carlos SUÁREZ (jcsuarez at iaa.es)
Sylvestre MELODY (melody.sylvestre at gmail.com)
Sylvie THÉADO (stheado at ast.obs-mip.fr)
Michel TAGGER (michel.tagger at cnrs-orleans.fr)
Radwan TAJEDDINE (tajeddin at imcce.fr)
Cyril TASSE (cyril.tasse at obspm.fr)
Test TEST (knodlseder at cesr.fr)
Rémi THIÉBLEMONT (remi.thieblemont at cnrs-orleans.fr)
Laurent THIRKELL (thirkell at cnrs-orleans.fr)
William THUILLOT (thuillot at imcce.fr)
Gabriel TOBIE (gabriel.tobie at univ-nantes.fr)
Guillaume TRAP (trap at apc.univ-paris7.fr)
Laurence TRESSE (laurence.tresse at oamp.fr)
Gerard TROTTET (gerard.trottet at obspm.fr)
Audrey TROVA (Audrey.Trova at obs.u-bordeaux1.fr)
Philip TUCKEY (philip.tuckey at obspm.fr)
Sylvaine TURCK-CHIEZE (sylvaine.turck-chieze at cea.fr)
Catherine TURON (catherine.turon at obspm.fr)
David VALLS-GABAUD (david.valls-gabaud at obspm.fr)
Peggy VARNIERE (varniere at apc.univ-paris7.fr)
Manuela VECCHI (vecchi at cppm.in2p3.fr)
Christian VEILLET (veillet at cfht.hawaii.edu)
Aion VIANA (aion.viana at cea.fr)
Luis VIEIRA (luis.vieira at cnrs-orleans.fr)
Francesca VILLA (villa at lpnhe.in2p3.fr)
Frédéric VINCENT (frederic.vincent at obspm.fr)
Patrick VONLANTHEN (patrick.vonlanthen at obspm.fr)
Peter WOLF (peter.wolf at obspm.fr)
Melody WOLK (wolk at iap.fr)
Hervé WOZNIAK (herve.wozniak at astro.unistra.fr)
Xavier BONNIN (xavier.bonnin at obspm.fr)
Philippe YAYA (pyaya at cls.fr)

Jean-paul ZAHN (jean-paul.zahn at obspm.fr)

Ivan ZOLOTUKHIN (ivan.zolotukhin at obspm.fr)

Yannis ZOUGANELIS (yannis.zouganelis at lpp.polytechnique.fr)

Session SF2A

Joint session

ORBITAL CHARACTERIZATION OF β PICTORIS B

H. Beust¹, G. Chauvin¹ and A.-M. Lagrange¹

Abstract. The young planet β Pictoris b offers the rare opportunity to monitor a large fraction of its orbit using the imaging technique over a reasonable timescale. Using NACO at VLT, we obtained repeated follow-up imaging observations of the β Pic system in the K_s and L' filters over 2010 and 2011. Together with past measurements, we have conducted an homogeneous analysis of data, that covers more than 8 yrs. We then derived the most probable orbital solutions that fit our measurements using a least-square algorithm and a Markov-Chain Monte Carlo approach. The solutions favor a low-eccentricity orbit $e \lesssim 0.2$, with semi-major axis between 8–11.5 AU corresponding to orbital periods of 15–25 yrs. Our solutions also favor highly inclined solution with a peak around $i = 88.5^\circ$ revealing a probable tilt with a perfectly edge-on configuration. We also derive prediction for transiting events. The solution is consistent with the planet being responsible for the 1981 transiting event. Finally, the planet seems compatible with former predictions linked with the cometary activity in the β Pic system.

Keywords: techniques: high angular resolution, stars: low-mass, brown dwarfs, stars: planetary systems

1 Introduction

Thanks to its probable moderate orbital period (~ 20 yrs), the recently imaged giant exoplanet β Pic b (Lagrange et al. 2009, 2010) offers a rare opportunity to rapidly constrain its orbital and physical properties, and connect them to the characteristics of the β Pic circumstellar environment.

Since the recovery of the planet (Lagrange et al. 2010), we have initiated an astrometric monitoring campaign, using NACO at VLT. In Sect. 2, we describe observations of 2010 and 2011 and we present our data analysis. In Sect. 3, we present the results of using a least-square algorithm and a Markov-Chain Monte Carlo approach. In Sect 4, we discuss the consequences of our results in the context of previous astrometric studies, and their implications regarding the previous indications for the presence of a giant planet orbiting β Pic.

2 Observations and data analysis

To pursue the monitoring of the β Pic b astrometry, we used the NaCo high contrast Adaptive Optics (AO) imager of the VLT-UT4 (Rousset et al. 2002; Lenzen et al. 2002). The follow-up observations were obtained at five different epochs between September 2010 and March 2011, using the angular differential imaging (ADI) mode of NaCo. For accurate astrometry, two observing set-ups were used, the L' filter with the L27 camera and the K_s filter with the S27 camera. The NaCo detector cube mode was in addition used for frame selection. At the end, the typical observing sequence represented a total of a 200–250 cubes, i.e, a total integration time of 35–50 min for an observing sequence of 1–1.5 hrs on target. A typical exposure time of 0.15s and 0.2s was respectively used in K_s and L' -filters to saturate the PSF core by a factor 100 (a few pixels in radius) to improve the dynamics of our images.

For the present study, we processed the data of the new observations of β Pic b obtained in September 28, 2010, November 16, 2010, November 17, 2010, February 1st, 2011 and March 26, 2011. Previous archived data including available astrometric calibrations, and obtained between November 2003 and April 2010, were also re-processed (see Table 1). The best astrometric measurements (in terms of observing conditions and stability)

¹ UJF-Grenoble 1 / CNRS-INSU, Institut de Planétologie et d'Astrophysique de Grenoble (IPAG) UMR 5274, Grenoble, F-38041, France

Table 1. NaCo astrometric measurements of β Pic b relative to β Pic

UT Date	Mode Obs/Filter/Obj	Platescale (mas)	True North (deg)	$\Delta\alpha$ (mas)	$\Delta\delta$ (mas)	separation (mas)	PA (deg)
10/11/03	Field/ L' /L27	27.11 ± 0.04	0.29 ± 0.07	233 ± 22	341 ± 22	413 ± 22	34.42 ± 2.82
25/10/09	Field/ L' /L27	27.11 ± 0.05	-0.08 ± 0.10	-153 ± 14	-257 ± 14	299 ± 14	210.74 ± 2.60
29/12/09	ADI/ L' /L27	27.10 ± 0.04	-0.06 ± 0.08	-163 ± 9	-260 ± 8	306 ± 9	212.07 ± 1.51
10/04/10	ADI/ K_s /S27	27.01 ± 0.04	-0.26 ± 0.09	-173 ± 7	-300 ± 7	346 ± 7	209.93 ± 1.26
28/09/10	ADI/ L' /L27	27.11 ± 0.04	-0.36 ± 0.11	-193 ± 11	-331 ± 11	383 ± 11	210.28 ± 1.57
16/11/10	ADI/ K_s /S27	27.01 ± 0.05	-0.25 ± 0.07	-207 ± 8	-326 ± 10	387 ± 8	212.41 ± 1.35
17/11/10	ADI/ L' /S27	27.10 ± 0.04	-0.25 ± 0.07	-209 ± 13	-330 ± 14	390 ± 13	212.34 ± 1.92
01/02/11	ADI/ K_s /S27	27.01 ± 0.04	-0.32 ± 0.10	-211 ± 19	-350 ± 10	408 ± 9	211.13 ± 1.33
26/03/11	ADI/ K_s /S27	27.01 ± 0.04	-0.35 ± 0.10	-214 ± 12	-367 ± 14	426 ± 13	210.13 ± 1.83

were kept at each epoch. Data obtained on November 16, 2010 and November 17, 2010 were both reduced to check the consistency of the results with both observing setups ($L'/L27$ and $K_s/S27$) used for this study.

The difficulty to derive the planet’s position relative to the star was to accurately estimate both the individual detector position of the saturated central star, and the planet position affected by the stellar residuals. We have fitted with a Moffat function the non-saturated part of the stellar PSF wing. To derive the planet position and flux, we used a grid of 5000 fake planets injected one-by-one in the data to derive the best solution minimizing the residuals in a region covering the companion ADI signature. The results are given in Table 1.

3 Orbital fit

a (AU)	P (yr)	e	i ($^\circ$)	Ω ($^\circ$)	ω ($^\circ$)	t_p (yr JD)	χ^2
11.2	28.3	0.16	88.8	-147.73	4.0	2013.3	5.37
8.8	19.6	0.021	88.5	-148.24	-115.0	2006.3	6.70

Table 2. Orbital solutions for β Pic b. **Top :** the best χ^2 model obtained with the LSLM algorithm; **bottom :** a typical “most probable” orbit according to the MCMC fit. Note that we do not give error bars here, as these are supposed to be described by the MCMC distribution.

We assumed for β Pic b an orbit described in a referential frame $OXYZ$ where the XOY plane corresponds to the plane of the sky, and where the Z -axis points towards the Earth. The position angle measurements (Table 1) are consistent with a quasi edge-on configuration of the orbit, which matches the position angle of the β Pic circumstellar disk (Olofsson et al. 2001). To best fit our measurements, we considered the planet’s inclination i as a free parameter.

A Keplerian model was fitted to our $(\Delta\delta, \Delta\alpha)$ results of Table 1 to constrain the orbital period P (or equivalently the semi-major axis a , using the stellar mass $M_* = 1.75 M_\odot$), the eccentricity e , the inclination i , the longitude of ascending node Ω (measured from North), the argument of periastron ω and the time for periastron passage t_p . We used two complementary fitting methods: a least-square Levenberg-Marquardt (LSLM) algorithm (Press et al. 1992) to search for the model with the minimal χ^2 , and a more robust statistical approach using the Markov-Chain Monte Carlo (MCMC) Bayesian analysis technique (Ford 2005, 2006).

The best LSLM χ^2 solution found, and a typical example of “most probable orbit” according to the result of the MCMC study, are given in Table 2. These orbits are plotted in Fig. 2, in a plane containing the line of sight, as well as the positions of the planet at various observing dates. The combined results of both fitting methods are also shown in Fig. 1. Surprisingly, the best LSLM model does not fall in the most probable peak, although this model obviously achieves actually the best χ^2 among our whole distribution. This discrepancy shows that our data are still too sparse to derive a deep χ^2 minimum. Consequently, our confidence in the LSLM approach must be low. This validates the MCMC approach, which better explores the parameter space. Considering the MCMC results, we first note that the semi-major axis is fairly well constrained by the fit. The most probable range is 8–11.5 AU (periods between 15–25 AU). Similarly, most eccentricities fall between 0 and ~ 0.17 . Solutions with higher semi-major axes and higher eccentricities cannot be completely excluded. They correspond to orbits with a periastron passage at ~ 9 AU to the SW side of the disk around 2009. Regarding the inclination, the

statistical distribution appears extremely concentrated close to 90° . The inclination nevertheless peaks at $\sim 88.5^\circ$, revealing a probable $\sim 1.5^\circ$ tilt with respect to a strict edge-on configuration. The statistical distribution of the argument of periastron ω is more erratic. Our results are in agreement with the orbital solution found by Currie et al. (2011) using a similar Monte Carlo technique, but using fewer data points. Interestingly, their results concerning the inclination are almost identical. Our semi-major axis range is nevertheless better constrained thanks to our extended data set.

4 Discussion

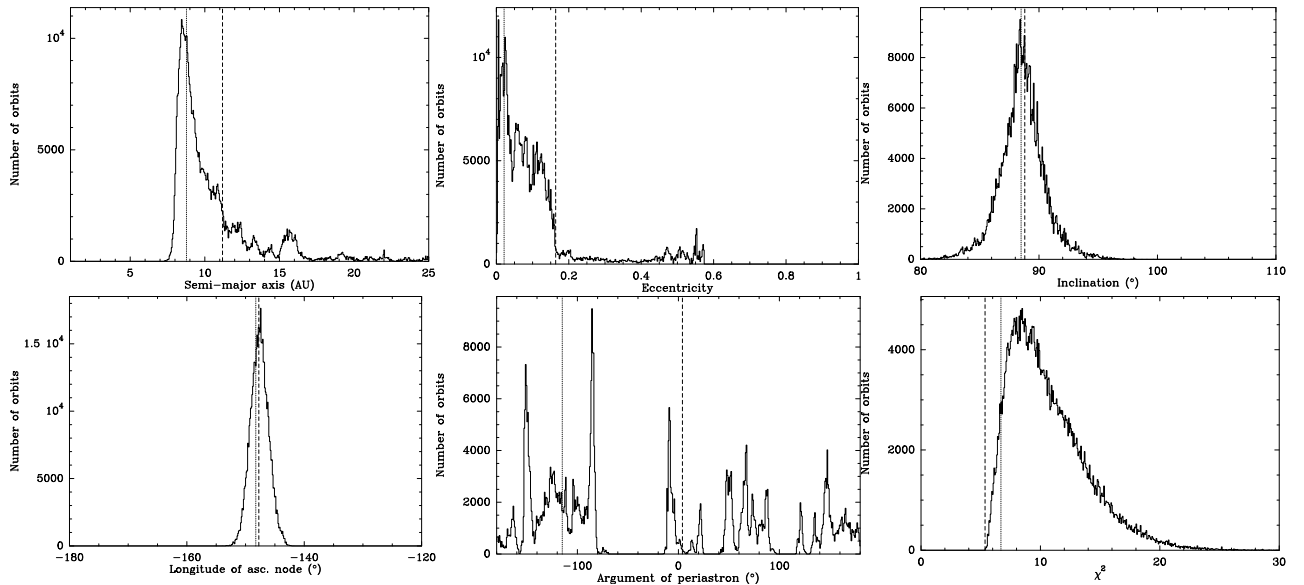


Fig. 1. Results of the MCMC fit of the astrometric data of β Pic b: statistical distribution of the orbital elements **Top left:** a ; **top middle:** e ; **top right:** i ; **bottom left:** Ω ; **bottom middle:** ω . **Bottom Right:** We also show the distribution of χ^2 of the solutions obtained. On each plot, the dashed line indicates the position of the best LSLM χ^2 model obtained, and the dotted line shows the position of the most probable orbit of Table 2.

From our previous orbital fit analysis, three important outcomes arise: the semi-major axis of β Pic b falls very probably in the range 8–11.5 AU, the eccentricity is most probably $\lesssim 0.2$, and the orbit is likely to have a $\sim 1.5^\circ$ tilt with respect to strict edge-on configuration. The existence of a giant planet orbiting β Pic had already been suggested by various previous studies. The main indirect signs pointed out are i/ the inner warped component of the β Pic circumstellar disk, together with additional asymmetries observed in the outer part (Mouillet et al. 1997; Kalas & Jewitt 1995), ii/ the photometric transit-like event observed in 1981 (Lecavelier des Etangs et al. 1997), and iii/ the cometary activity observed in the absorption spectrum of β Pic (Ferlet et al. 1987; Lagrange et al. 1996; Petterson & Tobin 1999). We discuss below how each of these observing facts may be related to the existence, and the orbital and physical properties of β Pic b.

4.1 Disk – Planet configuration

Dedicated scattered-light studies have accurately and morphologically detailed the view of the β Pic disk (Kalas & Jewitt 1995; Heap et al. 2000; Golimowski et al. 2006). They mainly show a nearly edge-on disk composed of a main disk observed beyond 80 AU, and an inner warped component (at less than 80 AU), and inclined by $2–5^\circ$ with respect to the main disk position angle. Simulations of Mouillet et al. (1997); Augereau et al. (2001) showed that the presence of a planet orbiting the star at 10 AU, misaligned with the main disk, could actually form and sustain the β Pic inner warped disk. (Currie et al. 2011) recently claimed evidence for a misalignment between the planet and the inner warped disk of β Pic concluding that the planet was orbiting inside the main disk’s orbital plane. We however do not confirm these results. This work and our $K_s/S27$ measurements of November 16, 2011 with a dedicated analysis for the disk orientation, shows that the projected separation of

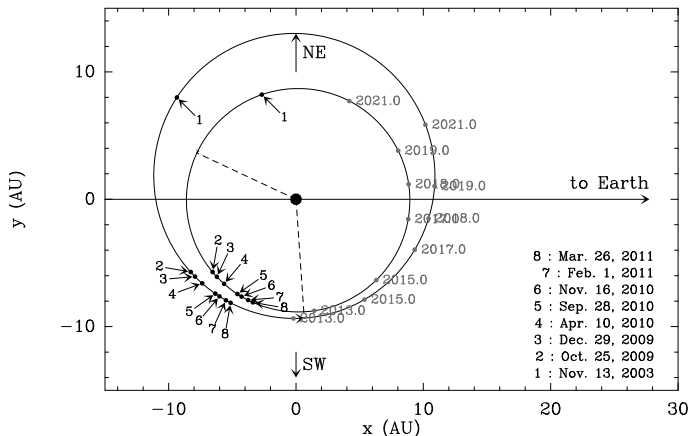


Fig. 2. Plots of the orbit of Table 2 with their orientation with respect to the line of sight. The larger orbit is the best LSLM χ^2 model and the smaller one is an example of most probable orbit obtained with the MCMC approach (Table 2). In each case, the dashed line shows the location of the periastron. The position of the planet at different observation epochs is shown as black dots along the orbit, and predictions for the upcoming years are shown in grey.

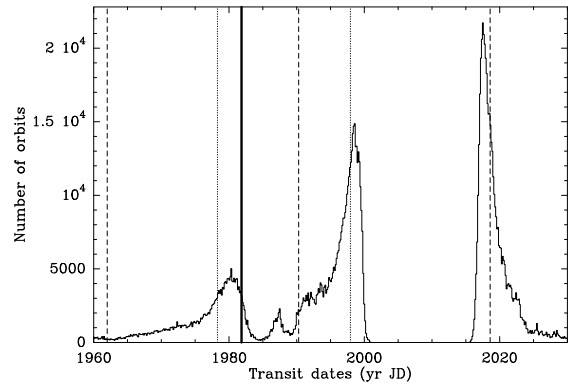


Fig. 3. MCMC distribution of the transit dates of β Pic b in front of the line of sight. The plotting conventions are the same as in Fig. 1. In addition, the date of the transit predicted by Lecavelier des Etangs et al. (1997) is marked with a thick vertical line.

β Pic b is actually located above the midplane of the main disk, supporting the planet being located in the warped component, and therefore being responsible for the inner warped morphology of the β Pic disk.

4.2 1981 Transiting event

Photometric follow-up of β Pic was made by Geneva observatory between 1975 and 1982. Lecavelier des Etangs et al. (1995) reports significant variations in November 1981 with a peculiar transit-like event on November 10, 1981. Lecavelier des Etangs et al. (1997) showed in that a planet with 2–4 times the radius of Jupiter, orbiting at ~ 9 AU at most could well be responsible for the photometric variations they report. Lecavelier des Etangs & Vidal-Madjar (2009) investigated this issue on the sole basis of the 2003 detection (Lagrange et al. 2009) of β Pic b. They found that a transit of β Pic b in November 1981 could be compatible with a quadrature position in November 2003, assuming a semi-major axis in the range [7.6–8.7] AU, without being able to definitely conclude. We reinvestigate this issue on the basis on our orbital fit. Figure 3 shows the MCMC distribution of the predicted transit dates of β Pic b between 1960 and 2030, assuming that the inclination is close enough to 90° to allow a transit of the clear zone around the planet at each orbit. We note that the most recent (~ 1999) and next (~ 2018) transits are somewhat well constrained. We also note a broader peak in ~ 1980 corresponding to the transit preceding the most recent one. The suggested transit date of November 1981 falls to the right edge in that peak (although not in the center). Therefore, the current orbital properties of β Pic b are still compatible with the planet being responsible for the 1981 transiting event.

4.3 The β Pic cometary activity

Transient redshifted spectral events have been regularly monitored in the absorption spectrum of β Pic (Ferlet et al. 1987; Lagrange et al. 1996; Petterson & Tobin 1999), and were attributed to the sublimation of numerous star-grazing planetesimals crossing the line of sight, also referred to as the Falling Evaporating Bodies (FEBs) phenomenon (Beust et al. 1996). Their origin was tentatively related to mean-motion resonances with a Jovian planet orbiting the star (Beust & Morbidelli 1996, 2000; Thébault & Beust 2001; Beust & Valiron 2007). Several constraints could be actually deduced from dynamical studies of the FEBs scenario, suggesting that: (i) The planet responsible for the phenomenon is massive enough (\sim Jovian) to allow numerous enough bodies to be trapped in the mean-motion resonances under consideration; (ii) its orbit is slightly eccentric ($e \gtrsim 0.05$ – 0.1) to allow bodies trapped in the resonances to see their eccentricity pumped up (Beust & Morbidelli 1996, 2000); (iii) the longitude of periastron of the planet with respect to the line of sight $m_{\text{was}} \sim -70^\circ \pm 20^\circ$ (Thébault

& Beust 2001), to enable the statistics of the Doppler velocities of the FEB spectral signatures to match the observed ones (strongly biased towards redshifts); (iv) the planet location was not further away than ~ 20 AU, otherwise the FEBs could hardly get into the dust sublimation zone.

The β Pic b planet has orbital and physical properties obviously compatible with constraints (i) and (iv). The situation is less straightforward for the constraints (ii) and (iii). Eccentricities larger than ~ 0.05 – 0.1 are actually fully compatible with our fit, but circular orbits are not excluded. Finally, the longitude of periastron ϖ measured from the line of sight is related to the argument of periastron ω from our fit. ω is measured from the XOY plane of our referential frame, i.e., the plane of the sky. Assuming an edge-on orientation of the disk, then we have $\omega = \varpi + \pi/2$. Thus $\varpi \simeq 70^\circ \pm 20^\circ$ means $\omega \simeq 20^\circ \pm 20^\circ$. Unfortunately, our constraint on ω is still too low to state whether this constraint is fulfilled or not. This is partly due to our still too weak constraint on the eccentricity itself. Further measurements are needed to refine this analysis.

5 Conclusion

We report the results of new follow-up observations of the astrometric positions of β Pic b relative to β Pic We then used to orbital fit techniques to derive the most probable orbital solutions for the β Pic b planet, including a least-square algorithm and Markov-Chain Monte Carlo Bayesian analysis. The latter approach gives us more robust and reliable results. The most probable solutions favor a low-eccentricity orbit $e \lesssim 0.2$, with semi-major axis between 8–11.5 AU corresponding to orbital periods of 15–25 yrs, and an inclination with a $\sim 1.5^\circ$ tilt with respect to strict edge-on configuration. The current orbital solution of β Pic b is consistent with the planet being responsible for the inner disk warp and the 1981 transiting event. Finally, it also supports β Pic b as the possible origin of the cometary activity observed in the β Pic system. Further deep imaging characterization should help reducing the orbital parameters space of β Pic b once the planet will have passed the next quadrature (most probably in 2013).

References

- Augereau J.-C., Nelson R.P., Lagrange A.-M., Papaloizou J.C.B., Mouillet D., 2001, *A&A* 370, 447
 Beust H., Lagrange A.-M., Plazy F. Mouillet D., 1996, *A&A* 310, 181
 Beust H. & Morbidelli A., 1996, *Icarus* 120, 358
 Beust H., Morbidelli A., 2000, *Icarus* 143, 170
 Beust H., Valiron P., 2007, *A&A* 466, 201
 Crida A., Masset F., Morbidelli A., 2009, *ApJ* 705, L148
 Currie T., Thalmann C., Matsumura S., et al., 2011, *ApJL*, 736, L33
 Ferlet R., Hobbs L.M., Vidal-Madjar A., 1987, *A&A* 185, 267
 Ford E.B., 2005, *AJ* 129, 1706
 Ford E.B., 2006, *ApJ* 642, 505
 Golimowski D. A., Ardila D. R., Krist J. E. et al. 2006, *AJ*, 131, 3109
 Heap S.R., Lindler D.J., Lanz T.M., et al., 2000, *ApJ* 539, 435
 Kalas P. & Jewitt D. 1995, *AJ* 110, 794
 Kalas P., Graham J.R., Chiang E., et al., 2008, *Science* 322, 1345
 Lagrange A.-M., Plazy F., Beust H., et al., 1996, *A&A* 310, 547
 Lagrange A.-M., Gratadour D., Chauvin G., 2009, *A&A* 493, L21
 Lagrange A.-M., Bonnefoy M., Chauvin G., et al., 2010, *Science* 329, 57
 Lecavelier des Etangs A., Deleuil M., Vidal-Madjar A., et al., 1995, *A&A* 299, 557
 Lecavelier des Etangs A., Vidal-Madjar A., Burki G., et al., 1997, *A&A* 328, 311
 Lecavelier des Etangs A., Vidal-Madjar A., 2009, *A&A* 497, 557
 Lenzen R., Hartung M., Brandner et al. 2002, *SPIE*, Vol. 4841
 Mouillet D., Larwood J.D., Papaloizou J.C.B., Lagrange A.-M., 1997, *MNRAS* 292, 896
 Olofsson G., Liseau R., Brandeker A., 2001, *ApJ* 563, 77
 Petterson O.K.L., Tobin W., 1999, *MNRAS* 304, 733
 Press W.H., Teukolsky S.A., Vetterling W.T., Flannery B.P., 1992, *Numerical Recipes* (Cambridge Univ. Press.)
 Rousset G., Lacombe F., Puget P., et al., 2002, *SPIE*, Vol. 4007
 Thébault P., Beust H., 2001, *A&A* 376, 621

RETRIEVING COSMOLOGICAL SIGNAL USING COSMIC FLOWS

V. Bouillot¹ and J.-M. Alimi¹

Abstract. To understand the origin of the anomalously high bulk flow at large scales, we use very large simulations in various cosmological models. To disentangle between cosmological and environmental effects, we select samples with bulk flow profiles similar to the observational data Watkins et al. (2009) which exhibit a maximum in the bulk flow at $53 \text{ h}^{-1} \text{ Mpc}$. The estimation of the cosmological parameters Ω_M and σ_8 , done on those samples, is correct from the *rms* mass fluctuation whereas this estimation gives completely false values when done on bulk flow measurements, hence showing a dependance of velocity fields on larger scales. By drawing a clear link between velocity fields at $53 \text{ h}^{-1} \text{ Mpc}$ and asymmetric patterns of the density field at $85 \text{ h}^{-1} \text{ Mpc}$, we show that the bulk flow can depend largely on the environment. The retrieving of the cosmological signal is achieved by studying the convergence of the bulk flow towards the linear prediction at very large scale ($\sim 150 \text{ h}^{-1} \text{ Mpc}$).

Keywords: cosmology

1 Introduction

Velocity fields are unique probes for cosmology. Since it traces the growth of structures, velocity fields enable us to constraint dark energy models. Moreover, bulk flow (i.e. the dipole of the peculiar velocity fields) is a sensitive probe of matter fluctuation on large scales. Recent measurements (Watkins et al. 2009), based on the compositing of several peculiar velocity surveys, have exhibited a large deviation from the concordance Λ CDM model prediction. As a matter of fact, a convergence of the bulk flow toward the linear prediction of the Λ CDM model is far from being observed at $50 \text{ h}^{-1} \text{ Mpc}$. This was claimed to be a challenge to Λ CDM.

A usual method to study the convergence of the velocity of the Local Group toward the CMB dipole is also to reconstruct peculiar velocities from redshift surveys using linear theory. A recent example is the reconstruction of the velocity fields of the 2MASS Redshift Survey (Erdođdu et al. 2006). However, linear theory is not valid when dealing with large density fluctuations as the Virgo cluster or the Shapley cluster and may lead to anomalously high velocity fields. To obtain a better reconstruction of the velocity fields, a possible solution is to use Lagrangian methods, e.g. Monge-Ampère-Kantorovich method, which enable to better take into account the nonlinear regime. This issue has been widely developed by Lavaux et al. (2010). Those types of reconstruction are in agreement with Watkins et al. (2009), especially on the existence of a maximum in the bulk flow.

In this proceeding, we highlight the dependance of the bulk flow on the environment. This dependance must be carefully studied to understand the role of cosmology in the observed deviations from predicted velocity fields. To separate cosmological and environmental effects, we use very large simulations done according to various cosmological scenarii. In those simulations, we select samples with bulk flow profiles similar to the measurements of Watkins et al. (2009) (see Fig. 1). We first describe the numerical simulations used in this study as well as the method used to compute observables. In a second part, we introduce the notion of density field asymmetry in spheres. This enables us to describe the environmental dependance of the bulk flow at intermediate scales. Finally, we conclude in section 4 with a brief discussion and summary.

¹ Laboratoire Univers et Théories (LUTH), UMR 8102 CNRS, Observatoire de Paris, Université Paris Diderot, 5 place Jules Janssen, 92190 Meudon, France

Parameters	Λ CDM	RPCDM	SUCDM
Ω_m	0.26	0.23	0.25
α	0	0.5	1
σ_8^{lin}	0.80	0.66	0.73
w_0	-1	-0.87	-0.94
w_1	0	0.08	0.19

Table 1. Cosmological parameters selected for the realistic models. These are flat models ($\Omega_{Q(\Lambda)} = 1 - \Omega_m$), with a spectral index $n_s = 0.963$, $A_S = 2.1 \times 10^{-9}$, $h = 0.72$, $\Omega_b h^2 = 0.02273$, and $\tau = 0.087$.

2 Numerical set-up

2.1 The Dark Energy Universe Simulation Series

The Dark Energy Universe Simulation Series (Alimi et al. 2010; Rasera et al. 2010) is a series of N-body simulations realized in three different realistic cosmological scenarii namely Λ CDM model, Ratra-Peebles and Supergravity quintessence models. The cosmological parameters used in those simulations are fixed in order to have realistic cosmological models (i.e. in agreement with SNe, CMB and BAO). Their values, fitted on the CMB and supernovae data with a likelihood analysis, are given in Table 1. The simulations followed 1024^3 dark matter particles from $z = 92$ to the present day within a cubic region of $648h^{-1}$ Mpc on a side. About 0.5 million dark matter haloes that contain more than 100 particles are detected at $z = 0$ according to a friends-of-friends (FOF) algorithm with a linking length $b = 0.2$ (Davis et al. 1985). In this proceeding, we present the analysis on Λ CDM only. The inclusion of other cosmologies will be done in a forthcoming paper (Alimi et al. in prep).

2.2 Computing numerical bulk flow

The peculiar velocity of galaxies \mathbf{u} can be seen as the departure from an idealized isotropic expansion and thus can be expressed as a sum of two terms: $\mathbf{u}(\mathbf{r}) = \mathbf{u}(0) + \mathbf{v}(\mathbf{r}) - H_0 \mathbf{r}$, with $\mathbf{v}(\mathbf{r})$ representing the global motion of galaxies and $H_0 \mathbf{r}$ the mean Hubble expansion. The bulk (i.e. volume average) flow is defined as the mean of $\mathbf{v}(\mathbf{r})$ in a sphere of growing radius.

Having the tridimensional velocity fields of N_h objects in a sphere of radius R centered on the Local Group, observers can express the bulk flow as:

$$v_{bulk}(R) = \left\| \frac{1}{N_{h,r < R}} \sum_i^{N_{h,r < R}} \vec{v}_i \right\| \quad (2.1)$$

This quantity can be computed exactly in numerical simulations. We choose to throw randomly 20,000 centers in the computational volume and compute bulk flows in increasing radii for each of these centers.

A statistical definition of the bulk flow, formally equivalent to the root mean square mass fluctuation σ_R , can be given:

$$v_{bulk} = \sqrt{\langle \bar{v}^2 \rangle} = \sqrt{\frac{1}{2\pi^2} \int_0^\infty dk k^2 P_v(k) \hat{W}(kR)^2} \quad (2.2)$$

This definition is of utmost importance since it links the velocity power spectrum to the bulk flow, doing a statistical mean on all possible environments. Therefore, a departure from this prediction is deeply linked with environmental effects.

From our 20.000 objects (i.e. centers), we extract two subsets:

1. Centers with a bulk flow close to the linear prediction (at 95% confidence level);
2. Centers with a bulk flow close to the observational data based on the measurements of Watkins et al. (2009) (at 95% confidence level). This sample is called *realistic* since its mean bulk flow profile is in agreement with the observations with specially a minimum at $16 h^{-1}$ Mpc and a bump at $53 h^{-1}$ Mpc (Fig. 1 right).

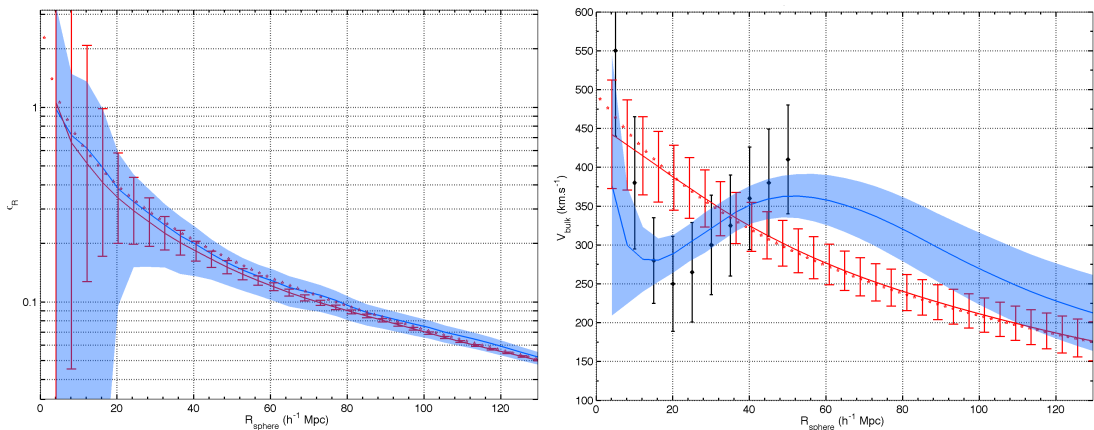


Fig. 1. **Left:** σ_R vs the radius of spheres. **Right:** Bulk flow vs radius of spheres. The linear prediction is shown with red stars, the linear subset is in red and the realistic sample in blue. Error bars correspond to the scattering of the bulk flows.

Computing mean and standard variances of the bulk flow and the *rms* mass fluctuation for both classes, we obtain Figure 1. On this figure, we see clearly the agreement between the mean behavior of the realistic (blue) and the observational (red) data for the σ_R and the strong disagreement between the realistic data and the linear prediction for the bulk flow.

Such a discrepancy finds its origin in the definition of the matter and velocity fields. In fact, the *rms* mass fluctuation is undistinguishable from one subset to the other one since it only keeps track of local overdensities. Since the density contrast is not very sensitive to large scales, it converges quickly towards the linear prediction and both subsets have the same behavior. On the contrary, the bulk flow, computed from vectorial quantities, has kept the imprint of the directional information: it gives an hint on the amplitude of the density field. Therefore, we have to quantify the position of overdensities in a given direction with respect to the opposite direction i.e. the asymmetry of the matter field in a sphere.

3 Environmental effects

The asymmetry in a sphere of (equivalently in a shell at) radius R_0 is defined by a vector which norm (named the asymmetry index) can be defined mathematically as followed:

$$A_{R_0} = \max_{\phi_0 \in [0, 2\pi], \theta_0 \in [0, 2\pi]} \left\{ \frac{1}{\rho_{mean}} \iint_{S^2/2} \rho_{<R_0}(\theta + \theta_0, \phi + \phi_0) - \rho_{<R_0}(\pi - (\theta + \theta_0), \pi + (\phi + \phi_0)) d\Omega \right\}, \quad (3.1)$$

ρ_A being the density in a shell at radius A , $\rho_{<R_0}$ the density from 0 to radius R_0 and (θ, ϕ) the direction of the density field.

Physically, the asymmetry index characterizes the deviation from a symmetric sphere. A symmetric environment will be characterized by an asymmetry index equal to zero whereas a highly asymmetric environment exhibits an asymmetry index close to one. The direction of the asymmetry corresponds to find the direction of the densest hemisphere, which is a function of ϕ_0 and θ_0 *.

The numerical computation of the mean asymmetry index (Figure 2) exhibits three zones. From 12 to 40 h^{-1} Mpc, the observational set and the linear sample show the same tendency i.e. a linear behavior. From 40 to 76 h^{-1} Mpc, the observational subset is more symmetric than the linear sample. Finally, from 76 to 128 h^{-1} Mpc, the observational subset is more asymmetric than the linear sample. Since matter sources velocity fields, the latter should therefore be linked with the bump of the bulk flow. In fact, an alignment of the bulk flow and the asymmetry should be observed at large scales. This link is particularly enhanced between the scale of the

*This issue as well as the equivalence between the characterization of the environment by the center of mass or the asymmetry index will be discussed in a forthcoming paper (Bouillot et al. in prep). Intuitively, the more symmetric a sphere is, the nearer the center of mass to the geometric center is.

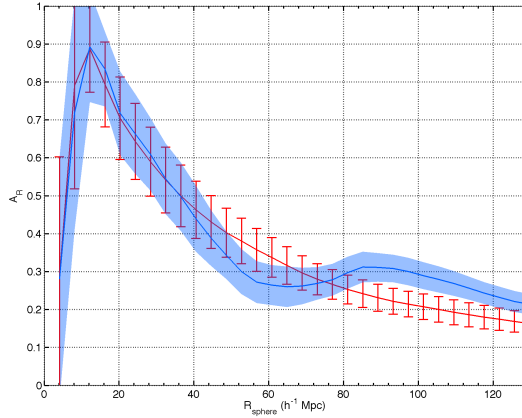


Fig. 2. Asymmetry index vs radius of the sphere for realistic subsets.

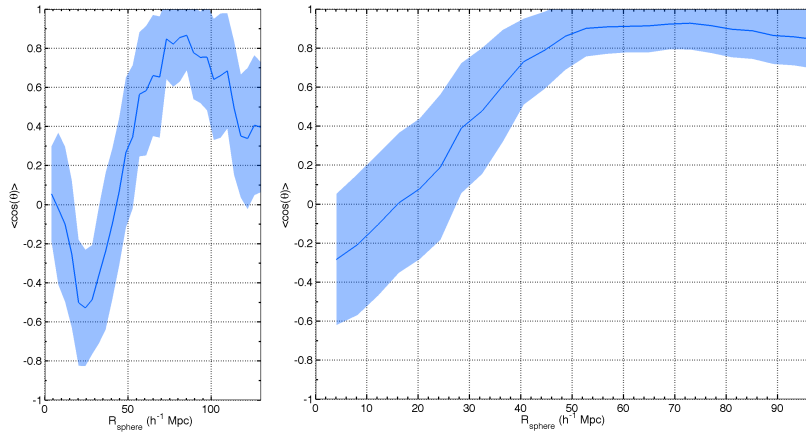


Fig. 3. Asymmetry index vs radius of the sphere for linear (red) and realistic (blue) subsets.

maximum of the bulk flow and the scale of the maximum of the asymmetry index.

To exhibit this alignment scale of the asymmetry vector and the bulk flow at $53 \text{ h}^{-1} \text{ Mpc}$, we compute the normalized scalar product of the bulk flow at $53 \text{ h}^{-1} \text{ Mpc}$ and the asymmetry in a shell (instead of a sphere). This will show the sourcing scale of the bulk flow. Left panel of Figure 3 gives the value of this particular scale: $85 \text{ h}^{-1} \text{ Mpc}$ [†].

Once the bulk flow is aligned at high scales, the direction of the bulk flow remains roughly the same. As a matter of fact, the direction of the bulk flow should remain aligned with the direction of the asymmetry at higher scales. Performing a shift δR of the asymmetry index, the alignment of the bulk flow along the direction of the asymmetry at higher scale can be visualized. This is shown on the right panel of Figure 3 with the computation of the scalar product of the bulk flow at radius R and the asymmetry in a sphere at radius $R + \delta R$ with $\delta R = 32 \pm 4.1 \text{ h}^{-1} \text{ Mpc}$.

4 Conclusion

By building samples with bulk flow profiles in agreement with the observations, we show that the anomalously high bulk flow detected in observational datasets is mainly due to environmental effects. Those effects are shown by quantifying the asymmetric tridimensional distribution of matter. In particular, a bump of the bulk

[†]The fact that this scale corresponds exactly to the scale of the maximum of the asymmetry index is pure luck and do not have any physical meaning.

flow at $53 \text{ h}^{-1} \text{ Mpc}$ is explained by an asymmetric distribution of matter at $85 \text{ h}^{-1} \text{ Mpc}$. The major result is that, by studying the distribution of matter, one can infer the position of the maximum of the bulk flow, hence constraining cosmological models. In other words, the study of the matter field of redshifts surveys can give us the scale of the position of the maximum of the bulk flow without ultra-deep velocity surveys. Far from this scale, a convergence towards the linear prediction is observed and therefore, only the cosmological signal remains (Alimi et al. in prep).

References

- Alimi, J.-M., Bouillot, V., Füzfa, A., & Rasera, Y. 2012, MNRAS (in prep)
- Alimi, J.-M., Füzfa, A., Boucher, V., et al. 2010, MNRAS, 401, 775
- Bouillot, V., Alimi, J.-M., Rasera, Y., & Füzfa, A. 2012, MNRAS (in prep)
- Davis, M., Efstathiou, G., Frenk, C. S., & White, S. D. M. 1985, ApJ, 292, 371
- Erdoğdu, P., Lahav, O., Huchra, J. P., et al. 2006, MNRAS, 373, 45
- Lavaux, G., Tully, R. B., Mohayaee, R., & Colombi, S. 2010, ApJ, 709, 483
- Rasera, Y., Alimi, J.-M., Courtin, J., et al. 2010, in American Institute of Physics Conference Series, Vol. 1241, American Institute of Physics Conference Series, ed. J.-M. Alimi & A. Füzfa, 1134–1139
- Watkins, R., Feldman, H. A., & Hudson, M. J. 2009, MNRAS, 392, 743

PLANETARY MIGRATION AND ACCRETION

A. Crida¹

Abstract. In this plenary session talk, I review some of the most important recent progresses in planetary science. I focus here on two aspects linked to planetary formation.

In section 2, I present the issue of planetary migration of type I. After an introduction to planet-disk interactions, I present the differential Lindblad torque, responsible for a too fast inward migration of terrestrial planets. Then, the corotation torque is presented. It is shown that the total torque is positive in the inner regions of the disk, and negative in the outer regions, leading to a convergence of terrestrial planets to an equilibrium radius.

In section 3, I present a new scenario for the formation of Saturn's rings and satellites. New results suggest that the rings were initially very massive, made of pieces of the icy mantle of differentiated satellite that migrated into Saturn at the time of solar system formation. These rings then spread viscously, and reach the observed mass and density in about 4 Gyrs. As a by-product of this spreading, all the satellites inside the orbit of Titan form beyond the Roche limit and then migrate to their present position.

Keywords: planetary formation, planetary migration, protoplanetary disks, planet-disk interactions, planet: Saturn, Saturn: rings

1 Introduction

Planetary formation takes place in proto-planetary disks. These disks of gas and dust around young stars have typically an aspect ratio of the order of $H/r \approx 0.05$, which translates into a temperature of the order of $T = 150 \text{ K} \times (1 \text{ AU}/r)$, where r is the distance to the central star and H the scale height of the disk. These disks spread, and accrete into the star, and finally vanish in a few million years. Meanwhile, in the proto-planetary disks, the heavy elements condensate and agglomerate to form planets. From micro-metric grains to giant planets, this is 14 orders of magnitude to grow!

It is generally considered that this takes place at first in 5 steps:

- Condensation to micrometer grains of solids,
- Sedimentation of the grains onto the mid-plane,
- Aggregation up to mm-cm dust packets,
- Formation of planetesimals of a few km,
- Formation of embryos of more than a few thousand km.

Then, if an embryo is massive enough (about 10 Earth masses), it accretes a gaseous envelope, that slowly grows and cools. At some point, the hydrostatic equilibrium of the envelope is not possible anymore, and it collapses. This leads to the formation of a giant gaseous planet, in the most accepted model by Pollack et al. (1996). So, planet formation must take place inside the gas disk. In this review, I won't discuss the complex processes of planet formation, but I present the interactions between a planet or an embryo and the gaseous protoplanetary disk. The latest results on planetary migration are shown, and the perspectives are drawn.

In section 3, I will also discuss recent results about the formation of Saturn's rings and satellites system, in which migration and accretion are the key.

¹ University of Nice Sophia-antipolis / C.N.R.S. / Observatoire de la Côte d'Azur, 06304 NICE cedex 4, France

2 Planetary migration

The gravity of a planet perturbs the trajectory of the gas particles. This leads to the formation of a one armed spiral wave, the *wake* (see Fig. 1, left panel). Due to the Keplerian rotation, the wave is leading the planet in the inner part of the disk, and trailing behind the planet in the outer disk.

This wave is a pressure-supported, density wave. It represents a mass excess with respect to the unperturbed disk. Therefore, the wave and the planet gravitationally attract each other. This results in a torque and orbital angular momentum transfer. The basic result is that the inner disk gives angular momentum to the planet, and the planet gives angular momentum to the outer disk.

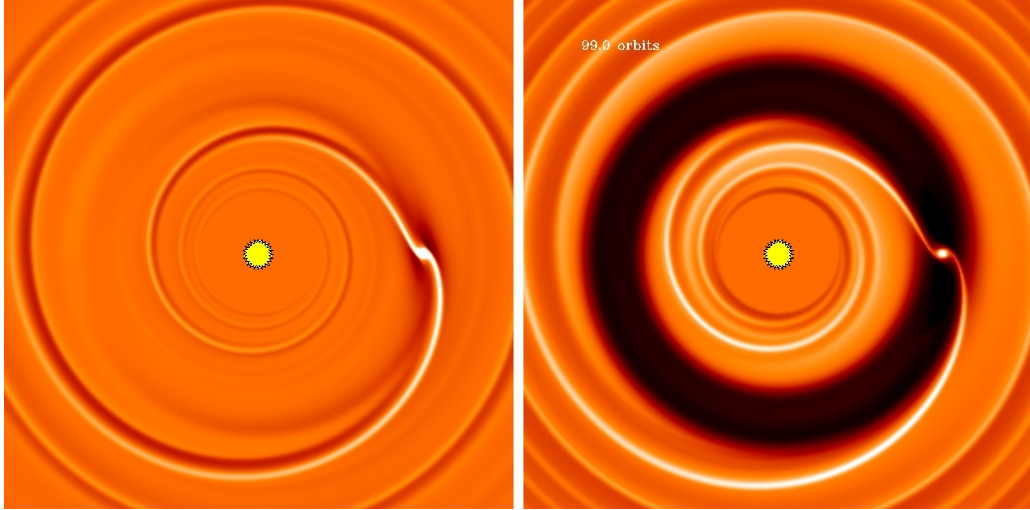


Fig. 1. Examples of planet-disk interaction. The star is in the center of the square, and the planet is in the middle of the white blob on the right. The rotation is counter-clockwise. The color represents the gas density: light for high density, dark for low density. Images by F. Masset, modified by A. Crida. **Left:** Wake created by a terrestrial planet. **Right:** Gap opened by a giant planet.

2.1 Type II migration

If the planetary torque is massive enough (case of a giant planet), this results in the opening of a gap around the planetary orbit (Lin & Papaloizou 1986a; Takeuchi et al. 1996; Crida et al. 2006): the inner disk is repelled inward, and the outer disk outward (see right panel of figure 1).

In this case, the planet is locked in the gap, and follows the viscous evolution of the disk. This drives the planet towards the central star on a viscous time-scale (of the order of a million years). This is called *type II migration* (Lin & Papaloizou 1986b, see also Crida & Morbidelli (2007)).

This is consistent with the observation of hot Jupiters: giant planets observed within 0.1 AU from their host star, where they couldn't form because there is not enough solid material to form a massive core.

2.2 Type I migration

If the planet is not massive enough, the profile of the disk is not changed, and the perturbation remains linear (figure 1, left panel). Nonetheless, angular momentum is exchanged, and the planet should migrate with respect to the gas disk. This is *type I migration* (Ward 1997).

2.2.1 Differential Lindblad torque

In the linear case, Ward (1986) has demonstrated that the torque from the outer disk always dominates that from the inner disk. The total torque felt by the planet, called the *differential Lindblad torque*, is thus negative. It reads (Tanaka et al. 2002):

$$\Gamma_{dLt} = -(3.2 + 1.468\alpha)\Gamma_0 \quad (2.1)$$

where $\alpha = d \log \Sigma / d \log r$, Σ being the surface density of the gas disk, and

$$\Gamma_0 = \left(\frac{M_p}{M_*} \right)^2 \Sigma r_p^4 \Omega_p^2 \left(\frac{H}{r} \right)^{-2} \quad (2.2)$$

where M_p is the mass of the planet, M_* the mass of the central star, r_p is the radius of the planetary orbit, and Ω_p is the angular velocity of the planet.

Application The migration speed is proportional to the planet mass. As a consequence, an Earth mass planet in a typical protoplanetary disk at 1 AU is lost into the Sun in about 2×10^5 years. This is a problem: no planet should survive!

2.2.2 Corotation torque

Not only the inner and outer disk should be considered, but also the horseshoe region. As shown in the left panel of figure 2, it is the region around the planetary orbit where gas particles have a horseshoe-shaped orbit, well-known in the restricted three-body problem.

Gas particles on these orbits on average co-rotate around the central star with the planet. Particles slightly outside the planetary orbit are caught up by the planet. The planet being behind them, it exerts a negative torque on them. Thus, these particles are sent onto a smaller orbit, inside the planetary orbit. Then, they orbit around the star faster than the planet does. In the frame rotating with the planet, they make a U-turn. They eventually catch up with the planet, that accelerates them and sends them back on an outer orbit, in an other U-turn. This results in angular momentum exchange, and a torque on the planet, called the *corotation torque* or more precisely the *horseshoe drag* (Paardekooper & Papaloizou 2009, and references therein).

Assume that the radial entropy gradient is negative. Then at the U-turn leading the planet, colder gas is sent from outside to inside the planetary orbit. And behind the planet, gas from the inner hotter region is sent to the colder outer region. Pressure equilibration after the U-turn leads to density variation, to balance the temperature difference. Thus, the hot plume trailing behind the planet becomes under-dense, while the cold plume leading the planet is over-dense. The result is a strong positive torque in non isothermal disks, first discovered by Paardekooper & Mellema (2006).

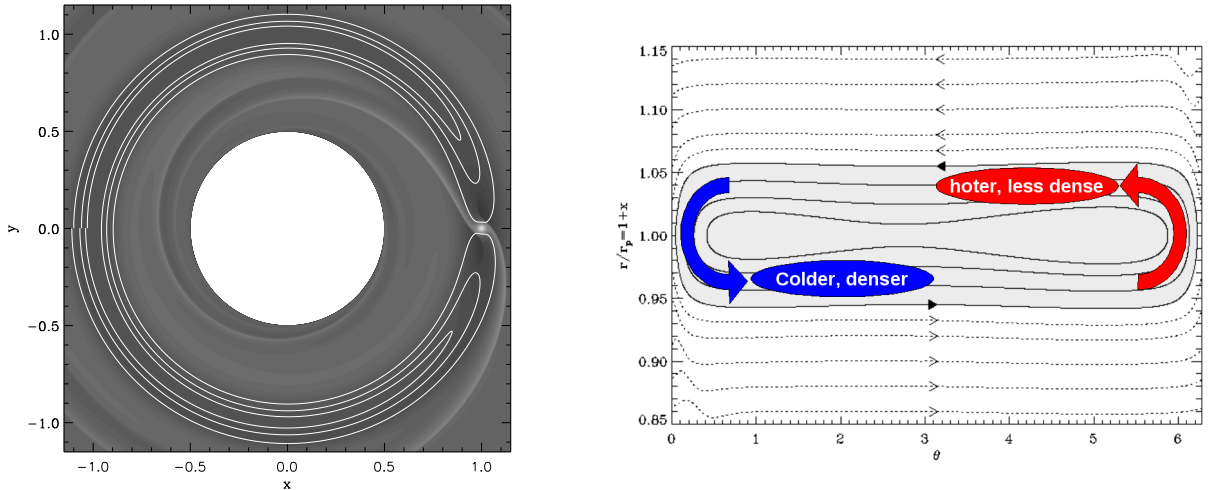


Fig. 2. Left: Horseshoe-shaped orbits, seen in Cartesian coordinates $x - y$. **Right:** The horseshoe orbits in the $\theta - r$ plane; the U-turns of cold and hot gas are shown on the left and right, respectively. Images by F. Masset, modified by A. Crida.

This effect has been studied by many authors, as it appears to be a possible solution to the too fast inward type I migration problem (e.g. Baruteau & Masset 2008; Kley & Crida 2008; Masset & Casoli 2009). Finally,

Paardekooper et al. (2010) have derived an expression for the type I torque, that takes the thermal part of the corotation torque into account :

$$\gamma\Gamma = -(0.9 + \alpha + 1.7\beta - 7.9\xi/\gamma)\Gamma_0 \quad (2.3)$$

where γ is the adiabatic index, $\beta = d \log T / d \log r$, and $\xi = \beta - (\gamma - 1)\alpha$.

2.2.3 Saturation of the corotation torque

The “thermal corotation torque” described above requires some conditions. First, the disk should not be completely adiabatic ; otherwise, after a few libration periods, the horseshoe region will be well-mixed, and uniformly warm. No more hot/cold plume, no more positive torque. This is called the *saturation* of the corotation torque (see Paardekooper et al. 2011). It cancels the positive torque. To prevent saturation, the initial entropy gradient needs to be restored (e.g. Kley & Crida 2008).

On the other hand, the cooling/heating should not be too fast ; otherwise by the time gas particles make a U-turn, they reach the local temperature at their destination radius. The disk should not be locally isothermal either.

These conditions can be summed up in conditions on the cooling time, compared to the libration and U-turn times :

$$\tau_{U\text{-turn}} < \tau_{\text{cooling}} < \tau_{\text{libration}} \quad (2.4)$$

2.2.4 Saving the planets

In the inner regions of the protoplanetary disk, the density is high, the opacity too, and the cooling time is therefore relatively long, at least longer than the U-turn time. Migration should be directed outwards.

In the outer parts of the disk, the opacity is low, and the cooling efficient. The gas is almost locally isothermal, and the cooling time is smaller than the U-turn time. Migration should be directed inwards.

In the end, there should be a convergence radius, where planets or embryos should gather. It could be of the order a few AUs, according to some preliminary works by Mordasini et al., who even find 2 such equilibrium radii, because the opacity is not a monotonic function of r (private communication).

In conclusion, it seems that the problem of the dramatic loss of terrestrial planets by type I migration is solved, thanks to the theoretical breakthroughs of the past five years.

There seems to be locations in the disk where terrestrial planets gather. These equilibrium radii are most likely sweet spots for the fast formation of massive embryos, the future cores of the giant planets. However, the interactions between these embryos should be taken into account, and the influence of the mass of the planet on the equilibrium radius should be inquired. In the coming years, research in planetary migration and formation will address this question. It should lead to a better understanding of the formation of giant planets, with interesting applications to the Solar System and exoplanetary systems.

3 Formation of Saturn’s system

Recent articles published in 2010 have changed our understanding of the system of Saturn. Put together, these new results draw a global picture and a completely new scenario for the formation of Saturn’s rings and satellites. Of course, some caveats still need to be addressed, but this is very promising.

3.1 Formation of massive, icy rings

At the end of their formation, giant planets are surrounded by a circum-planetary disk of gas and dust, like a miniature proto-planetary disk. In this disk, planetary formation takes place, leading to the formation of a satellites system around the planet. Due to type I migration, many satellites are lost into the central planet (Canup & Ward 2002). It is assumed here that type I migration is directed inwards in the circum-planetary disk.

Canup (2010) suggests that the last massive, differentiated satellite that migrated towards Saturn was “peeled off” by the tides of Saturn (see also Crida & Charnoz 2010). Indeed, the Roche radius for ice is located at about 140 000 km from Saturn, while the Roche radius for silicates is at about 90 000 km. Canup suggests that this

was the radius of Saturn at the time of its formation. Consequently, a differentiated satellite with an icy mantle and a silicate core (like Titan) that migrates inside 140 000 km, would lose its mantle, while its core would fall into Saturn, as shown in numerical simulations.

The final result is a massive ring of ice blocks between Saturn and the Roche limit, and nothing else between this ring and Titan... This scenario explains the composition of the rings (amazingly more than 90% water ice).

3.2 *Viscous spreading of massive rings*

Salmon et al. (2010) have studied the viscous spreading of Saturn's rings. Applying Daisaka et al. (2001)'s prescription for the viscosity in (non) self-gravitating disks, they find that the present rings could be as old as the Solar System. In fact, the more massive the rings are, the more viscous they are, and the faster they spread. Thus, whatever their initial mass, they should reach in less than 4 billion years a density profile such that their Toomre parameter Q is of the order of 2 everywhere. This corresponds quite well to the presently observed profile.

This result enables to bridge the gap between the massive rings formed in Canup's scenario 4.5 Gyrs ago, and the present rings.

3.3 *Satellites formation from the viscous spreading the rings*

As the rings spread, what happens to the material of the rings that flows beyond the Roche radius ? By definition of the Roche radius, it can form gravitational aggregates. Such aggregates migrate outwards (due to the positive torque from the inner disk, the rings). As they migrate outward, they also merge with each other, and grow, which increases their migration speed.

Charnoz et al. (2010) have shown that the small moons of Saturn, orbiting just outside the rings (namely Janus, Epimetheus, Pandora, Prometheus, and Atlas), formed this way. It is well reproduced by numerical simulations, and it explains at the same time their surface properties, composition, density, shape, orbital radii... As a consequence, they actually formed only a few to a hundred million years ago.

Charnoz et al. (2011) extend this result to all the satellites inside the orbit of Titan. Starting from massive rings as in section 3.1, it is possible to form the mid-sized moons (Rhea, Dione, Tethys, Enceladus, Mimas), in less than 3.5 Gyrs*. In fact, this would also explain the origin of the silicate cores of these bodies: chunks of silicates are likely to have been present in the rings at their formation. They would have formed gravitational aggregates, acquired an ice shell, and migrated through the rings. Some of them migrated outwards, and ended out of the rings, giving birth to the embryos of the mid-sized moons. Then they went on migrating outwards, accreting ice aggregates coming out of the rings.

3.4 *Conclusion*

This new scenario for the origin of Saturn's ring and satellite system could solve a long-standing mystery of planetary science. It provides the rings with an age, gives a satisfactory explanation for the composition of the rings, and their resistance to meteoritic pollution (in massive rings, the pollution is diluted). It also shows that many satellites of Saturn are actually much younger than the Solar System.

The idea of satellite formation from the spreading of a ring of solid particles beyond its outer edge at the Roche limit (a "tidal disk"), is particularly appealing, and could be applied to other planets. An analytical model has just been developed by Crida & Charnoz (2011). This field is going to be very active in the next years, improving our understanding of satellite formation in the Solar System.

A. Crida thanks the organizers of the "journées de la SF2A 2011", and the french national program of planetary science (PNP), for the invitation to present this review talk in plenary session.

References

- Baruteau, C. & Masset, F. 2008, ApJ, 672, 1054
 Canup, R. M. 2010, Nature, 468, 943

*This requires however that the tides of Saturn are about ten times more efficient than previously thought, but we have good reasons to believe that for Saturn, $Q = 1680$. See coming work by Lainey et al. and Mathis et al.

- Canup, R. M. & Ward, W. R. 2002, *AJ*, 124, 3404
- Charnoz, S., Crida, A., Castillo-Rogez, J. C., et al. 2011, *Icarus*, 216, 535
- Charnoz, S., Salmon, J., & Crida, A. 2010, *Nature*, 465, 752
- Crida, A. & Charnoz, S. 2010, *Nature*, 468, 903
- Crida, A. & Charnoz, S. 2011, in EPSC-DPS joint meeting 2011, Vol. 6, #1082
- Crida, A. & Morbidelli, A. 2007, *MNRAS*, 377, 1324
- Crida, A., Morbidelli, A., & Masset, F. 2006, *Icarus*, 181, 587
- Daisaka, H., Tanaka, H., & Ida, S. 2001, *Icarus*, 154, 296
- Kley, W. & Crida, A. 2008, *A&A*, 487, L9
- Lin, D. N. C. & Papaloizou, J. 1986a, *ApJ*, 307, 395
- Lin, D. N. C. & Papaloizou, J. 1986b, *ApJ*, 309, 846
- Masset, F. S. & Casoli, J. 2009, *ApJ*, 703, 857
- Paardekooper, S.-J., Baruteau, C., Crida, A., & Kley, W. 2010, *MNRAS*, 401, 1950
- Paardekooper, S.-J., Baruteau, C., & Kley, W. 2011, *MNRAS*, 410, 293
- Paardekooper, S.-J. & Mellema, G. 2006, *A&A*, 459, L17
- Paardekooper, S.-J. & Papaloizou, J. C. B. 2009, *MNRAS*, 394, 2283
- Pollack, J. B., Hubickyj, O., Bodenheimer, P., et al. 1996, *Icarus*, 124, 62
- Salmon, J., Charnoz, S., Crida, A., & Brahic, A. 2010, *Icarus*, 209, 771
- Takeuchi, T., Miyama, S. M., & Lin, D. N. C. 1996, *ApJ*, 460, 832
- Tanaka, H., Takeuchi, T., & Ward, W. R. 2002, *ApJ*, 565, 1257
- Ward, W. R. 1986, *Icarus*, 67, 164
- Ward, W. R. 1997, *Icarus*, 126, 261

PLANCK SZ CLUSTERS

M. Douspis^{1,2}

Abstract. We present here the first results on galaxy clusters detected by the *Planck* satellite through the Sunyaev–Zeldovich (SZ) effect from its six highest frequencies. We show the properties of the first all sky SZ sample (Planck Early SZ sample, ESZ) and how the new discovered clusters are mostly morphologically disturbed. Finally, we present results on the scaling relations between SZ and X-ray or optical cluster properties.

Keywords: Cosmology, Galaxy clusters

1 Introduction

In January 2011, Planck* delivered to the community the first data and accompanying papers. The Early Release Compact Source Catalogue (ERCSC, Fig. 1) contains three type of samples: the first type consists in a sample of compact sources per frequency (from 30 GHz to 857 GHz), the second one is the Early Cold Core (ECC) sample, and the last one in the Early SZ (ESZ) cluster sample. On top of the technological, spatial, and human achievement, *Planck* is also a scientific success with the publication of 20 articles so far, based only on 10 months of observations.

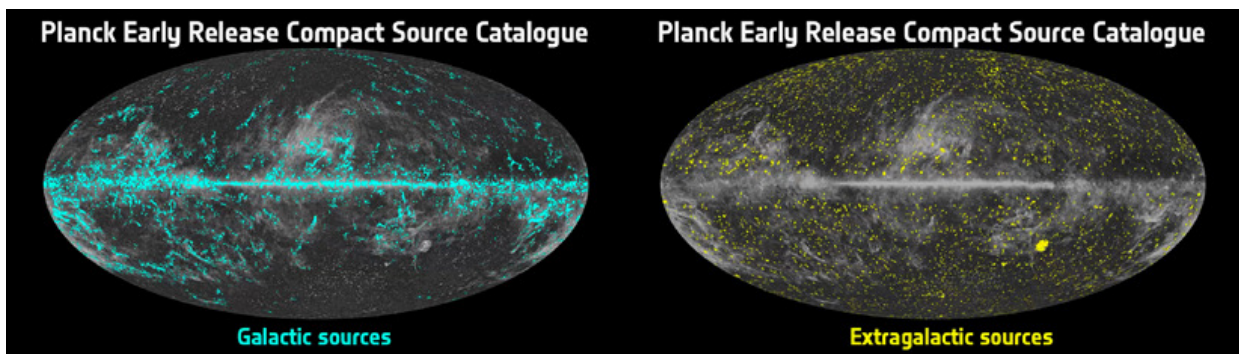


Fig. 1. Left: Planck ERCSC galactic sources. **Right:** Planck ERCSC extragalactic sources.

Among the Planck early papers on extragalactic science, five are presenting results on galaxy clusters (Planck Collaboration 2011b,c,d,e,f) including the description of the ESZ and new XMM confirmed clusters, SZ/X-ray and SZ/optical scaling laws.

¹ IAS, Université Paris Sud 11, CNRS, 91400 Orsay, France

² on behalf of the Planck Collaboration, www.rssd.esa.int/

**Planck* (<http://www.rssd.esa.int/Planck>) is a project of the European Space Agency (ESA) with instruments provided by two scientific consortia funded by ESA member states (in particular the lead countries France and Italy), with contributions from NASA (USA) and telescope reflectors provided by a collaboration between ESA and a scientific consortium led and funded by Denmark.

2 Clusters and SZ effect

The clusters of galaxies are the largest virialized structures of the universe and are thus very sensitive to the primordial fluctuations and the evolution of the universe. They are composed of dark matter ($\approx 80\%$), hot gas ($\approx 15\%$), and stars (galaxies). The dark matter component is responsible for most of the potential well with the gas component. The latter is the source of the X-ray and SZ emissions, enabling the observation of the clusters. The smallest component, galaxies and stars, revealed the existence of clusters through the first means of observation in visible wavelengths. Galaxy counts enable the characterization of clusters even today.

The Sunyaev-Zeldovich effect emerges when light of the CMB travels through hot gas in clusters of galaxies. It is caused by the inverse Compton effect, where the electrons of the hot gas interact with (scatter) the CMB photons. This interaction has a very specific signature in the microwave spectrum, predicted already by Sunyaev & Zeldovich (1972); Sunyaev & Zeldovich (1980), showing up as a distortion of the blackbody spectrum that translates into a “hole in the sky” at frequencies below 217 GHz and a “bump” above this frequency. The frequencies of *Planck* channels were specifically chosen to observe this effect. Figure 2 shows a cluster (Abell 2319) as seen by *Planck* between 44 GHz and 545 GHz. Note the negative (resp. positive) signal below (resp. above) 217 GHz. At the latter frequency, the SZ signal is expected to be null.

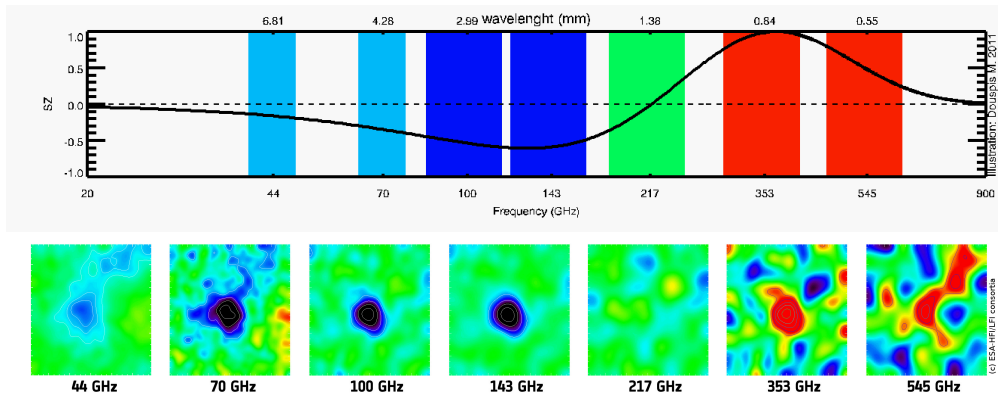


Fig. 2. Abell 2319 seen by *Planck* between 44 GHz and 545 GHz.

3 Planck SZ clusters

Using this specific SZ signature, *Planck* was designed to be able to detect numerous clusters (Aghanim et al. 1997). Unfortunately, not all are showing up as Abell 2319. The signal is indeed quite weak and is contaminated by foregrounds (our Galaxy, and nearby radio/IR galaxies) and backgrounds (CMB and CIB). As described later, the published Planck clusters have a signal-to-noise ratio (S/N) greater than 6. This means that the S/N per frequency is of the order of 1. This has led us to develop a specific approach for detecting, validating and confirming clusters.

We use a multi-matched filter (MMF) method (Melin et al. 2006) to detect the clusters. It is taking advantage of the spectral signature (SZ signature without relativistic effects) and the spatial signature (universal spherical profile from X-ray observations, Arnaud et al. 2010) of the clusters detected by Planck. As optimal as the method can be, a process of validation is still necessary to remove false detections. This is done in two steps. First a cross-check with internal Planck catalogues (cold cores, solar system objects, bad pixels) is performed, then cross-checks with existing external catalogues and data (SDSS, RASS) are performed to classify the known clusters and the new candidate clusters. Finally, follow-up observations has been done in optical, SZ and mainly in X-ray with XMM-Newton, to confirm our candidate clusters.

3.1 Planck Early SZ cluster sample

These detection, validation, and confirmation steps have led to the production of the Planck Early SZ Cluster sample (ESZ). It contains 199 clusters, 10 of which, confirmed by XMM-Newton have a $S/N < 6$. The 189 clusters with S/N greater than 6 are divided in 169 known clusters (in X-ray, optical or SZ) and 20 new Planck clusters. At the time of the release only 11 were confirmed by XMM-Newton. Since then, 6 more have been confirmed by

SPT and AMI (Story et al. 2011; AMI Consortium et al. 2011). The sample is available as part of the Planck Early Release Compact Source Catalogue (ERCSC, Planck Collaboration 2011a) at rssd.esa.int/Planck. The distribution on the sky of these clusters is shown in Fig. 3.

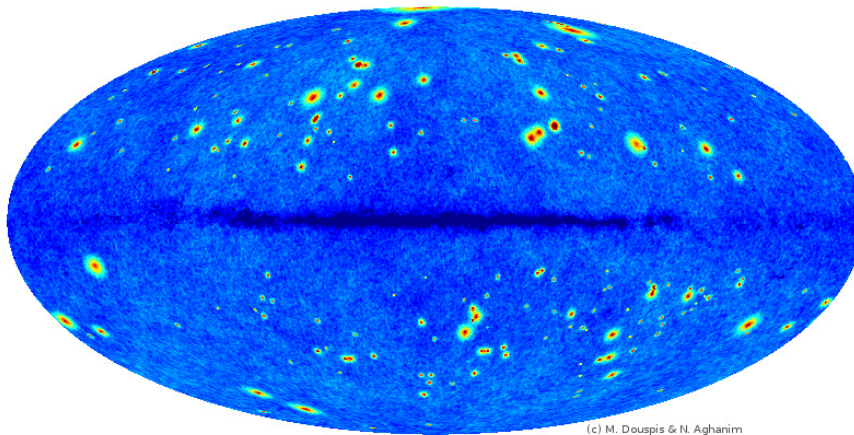


Fig. 3. Distribution on the sky of the Planck ESZ clusters (the signal has been amplified to be seen).

The ESZ clusters have relatively low redshift; 86% of them have $z < 0.3$. Their masses span more than a decade up to $1.5 \cdot 10^{15} M_{sol}$, and a large fraction of new Planck detected clusters are massive ($> 9 \cdot 10^{14} M_{sol}$). Planck has thus a unique capability to detect the rarest and most massive clusters over the full sky.

3.2 SZ clusters properties

Observing galaxy clusters in SZ opens a new observational window to understand not only the clusters themselves but also the evolution of our Universe. As described earlier, Planck has detected new clusters, sometimes massive. Why have they not been detected already in X-ray? Is this a new population of clusters, or the gas (responsible for both X-ray and SZ emissions) properties differ from what we think? As massive objects, clusters are sensitive to cosmological initial conditions and cosmic evolution. To use clusters for cosmological studies we need to relate their mass to our observation (SZ effect or Y-parameter). But is SZ effect a good proxy for the mass? How does the SZ signal relates to the X-ray luminosity, to the richness of clusters? The Planck ESZ clusters and Planck data are and will help in answering these questions.

3.3 New Planck clusters

The new Planck confirmed clusters have been compared with REXCESS X-ray detected clusters. *Planck* clusters show a more complex morphology, being sometimes really diffuse, extended, disturbed, and also double or triple. For the same given mass, they are also sub-luminous in X-ray compared to the REXCESS ones. Their electronic density profiles is on average lower in the center than the REXCESS ones (see Fig. 4).

Multiwavelength studies will help understand these properties. For example, Bagchi et al. (2011) have observed one the XMM confirmed Planck new clusters and found radio arcs. Such findings, revealing shocks and/or merger, would imply higher temperature areas, that could enhance the SZ signal and explain why these clusters are seen in SZ and not in X-ray. More dedicated multiwavelength studies are thus needed to better understand these clusters.

3.4 Scaling relations

In order to use clusters as cosmological probes, one needs to relate the observed properties (being X-ray luminosity, optical richness, or obviously SZ signal) to the mass of the clusters. It is usually assumed that X-ray luminosity is a good proxy for the mass. We thus looked at the relation between SZ signal and X-ray luminosity

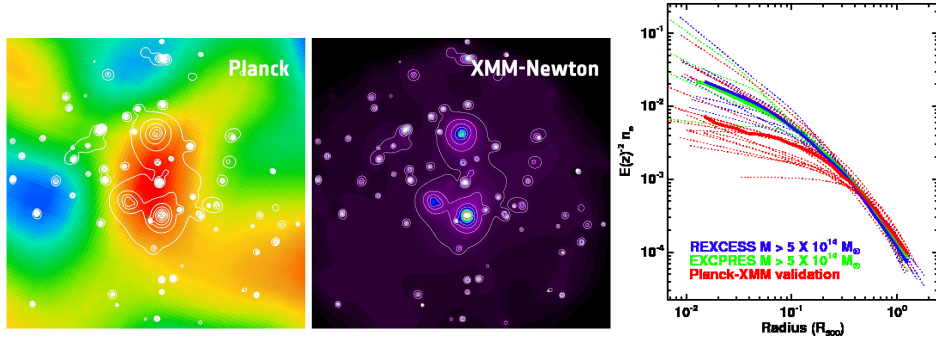


Fig. 4. Left: Planck SZ and XMM X-ray images of PLCKG214.6+37.0 Right: electronic density profiles of Planck and REXCESS clusters

on one side and SZ signal and optical richness on the other side. For this, we used two cluster catalogues. The first one is a meta-catalogue of ~ 1600 homogenized X-ray clusters (Piffaretti et al. 2010). The other one is an optical catalogue based on SDSS of ~ 13000 clusters between $0.1 < z < 0.3$. From these two catalogues, using the universal pressure profile, we computed the expected SZ signal per bin in X-ray luminosity or richness. We then compared these expected values with the ones observed by Planck at the positions of the catalogue clusters. The results are shown in Fig. 5.

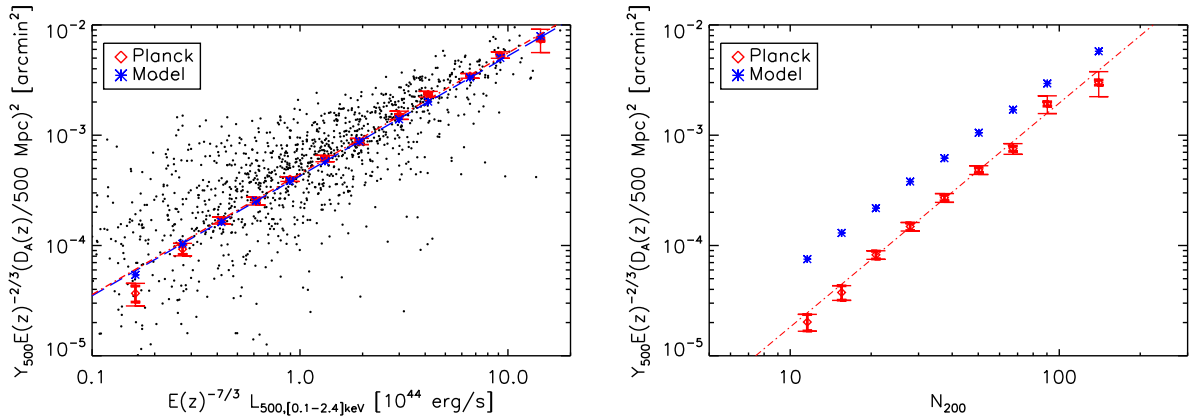


Fig. 5. Left: Scaling relation between X-ray luminosity and *Planck* SZ flux Right: Scaling relation between the optical richness (N_{200}) and *Planck* SZ flux

The first result shown in these figures is that the SZ signal is observed and detected for the first time at really low masses $\sim 5 \cdot 10^{13} M_{sol}$, with a precision 10 times better than WMAP.

It is also shown that the predicted signal inferred from X-ray luminosity is in perfect agreement with that observed by Planck. This agreement, expected by the fact that the gas is responsible for both signals, is furthermore good at all masses (luminosity). It has also been checked with several catalogues and ESZ subsamples (Planck Collaboration 2011e). This comforts us in the fact that the X-ray luminosity is a good mass proxy for clusters. The good quality of the data allows us now to study the dispersion and evolution with redshift of the X-SZ relation.

A good correlation is also found between the SZ signal and the optical richness of clusters. But, besides this good correlation, the expected signal inferred from the richness is a factor of 2 higher (at $N_{200} = 50$) than that observed. This disagreement remains unexplained, and studies are ongoing to understand the role of selection effects, the disagreement between X-ray and lensing masses, or any other explanation.

4 Conclusions

Planck has delivered a unique all sky sample of 199 galaxy clusters observed in SZ. This is the most complete and homogeneous sample of massive SZ clusters at moderate redshift ($z < 0.5$). For 80% of the sample, this is the first SZ measure, increasing by a factor 2 the number of observed clusters in SZ.

Planck offers thus a new window for the study of galaxy clusters. The newly discovered clusters seem to have a more complex morphology and a lower luminosity than the usual X-ray clusters.

The predicted signal inferred from X-ray observations is in very good agreement with the observed SZ signal, even to lower masses, leading to a good understanding of the gas properties in clusters. Conversely, the optical richness of clusters does not seem to probe correctly the SZ signal. This discrepancy is still under study by both optical and SZ clusters communities.

The next release of Planck data will occur in January 2013. The SZ cluster sample will obviously be expanded, especially towards higher redshift (see e.g. Planck Collaboration et al. (2011), and Fig. 6). It will be used for cosmology, studies of the diffuse SZ, and more detailed studies of particular clusters.

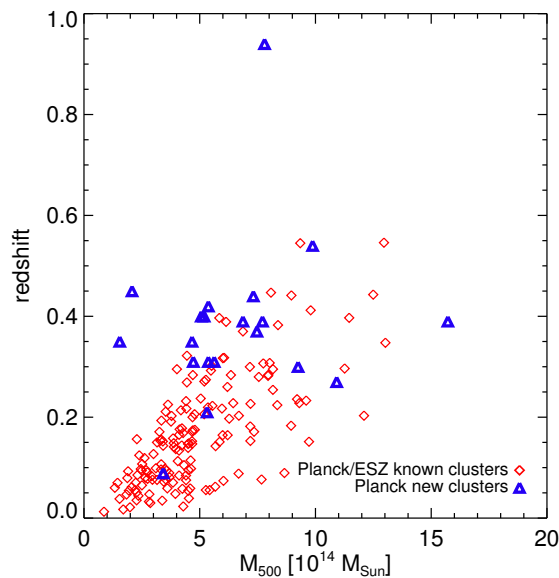


Fig. 6. Redshift–mass distribution of the ESZ sample as well as the new $z \sim 1$ clusters of Planck Collaboration et al. (2011)

The authors thank N. Schartel, ESA XMM-Newton project scientist, for granting the Director Discretionary Time used for confirmation of SZ Planck candidates. This research has made use of the following databases: SIMBAD, operated at CDS, Strasbourg, France; the NED database, which is operated by the Jet Propulsion Laboratory, California Institute of Technology, under contract with the National Aeronautics and Space Administration; BAX, operated by the Laboratoire d’Astrophysique de Tarbes-Toulouse (LATT), under contract with the Centre National d’Etudes Spatiales (CNES), SZ repository operated by IAS Data and Operation Center (IDOC) under contract with CNES. The authors acknowledge the use of software provided by the US National Virtual Observatory. A description of the Planck Collaboration and a list of its members, indicating which technical or scientific activities they have been involved in, can be found at <http://www.rssd.esa.int/Planck>.

References

- Aghanim, N., de Luca, A., Bouchet, F. R., Gispert, R., & Puget, J. L. 1997, *A&A*, 325, 9
 AMI Consortium, Hurley-Walker, N., Brown, M. L., et al. 2011, *MNRAS*, 414, L75
 Arnaud, M., Pratt, G. W., Piffaretti, R., et al. 2010, *A&A*, 517, A92
 Bagchi, J., Sirothia, S. K., Werner, N., et al. 2011, *ApJ*, 736, L8+
 Melin, J., Bartlett, J. G., & Delabrouille, J. 2006, *A&A*, 459, 341
 Piffaretti, R., Arnaud, M., Pratt, G. W., Pointecouteau, E., & Melin, J. 2010, arXiv e-print, [arXiv:1007.1916](https://arxiv.org/abs/1007.1916)

- Planck Collaboration. 2011a, Planck early results 07: The Early Release Compact Source Catalogue (Submitted to A&A, [arXiv:astro-ph/1101.2041])
- Planck Collaboration. 2011b, Planck early results 08: The all-sky early Sunyaev-Zeldovich cluster sample (Submitted to A&A, [arXiv:astro-ph/1101.2024])
- Planck Collaboration. 2011c, Planck early results 09: XMM-Newton follow-up for validation of Planck cluster candidates (Submitted to A&A, [arXiv:astro-ph/1101.2025])
- Planck Collaboration. 2011d, Planck early results 10: Statistical analysis of Sunyaev-Zeldovich scaling relations for X-ray galaxy clusters (Submitted to A&A, [arXiv:astro-ph/1101.2043])
- Planck Collaboration. 2011e, Planck early results 11: Calibration of the local galaxy cluster Sunyaev-Zeldovich scaling relations (Submitted to A&A, [arXiv:astro-ph/1101.2026])
- Planck Collaboration. 2011f, Planck early results 12: Cluster Sunyaev-Zeldovich optical Scaling relations (Submitted to A&A, [arXiv:astro-ph/1101.2027])
- Planck Collaboration, Aghanim, N., Arnaud, M., et al. 2011, ArXiv e-prints, [arXiv:1106.1376]
- Story, K., Aird, K. A., Andersson, K., et al. 2011, ApJ, 735, L36+
- Sunyaev, R. A. & Zeldovich, I. B. 1980, ARA&A, 18, 537
- Sunyaev, R. A. & Zeldovich, Y. B. 1972, Comments on Astrophysics and Space Physics, 4, 173

R&D ACTIVITIES FOR ASTRONOMY AND ASTROPHYSICS IN FRANCE

P. Kern¹

Abstract. This report provides the output of a survey performed in 2010 on the R&D activities for Astronomy and Astrophysics. This prospective exercise ended by a national Symposium that gathered all the actors of the discipline in Grenoble for 4 days in May 2011. This report gives also the main conclusions issued from the working groups of the Symposium.

Keywords: R&D, R&T, instrumentation, technology

1 Introductions: Outlines

After its 2009 prospective exercise, the division Astronomy/Astrophysics of CNRS/INSU * requested a review of the R&D activities in the laboratories of the discipline. R&Ds provide very efficient supports to the instrumental developments performed in France. Instrumentation is one of the domains of excellence of the French astronomy highlighted by the very strong French presence for the design and the construction of ground based and space borne instruments dedicated to the major European observation facilities.

R&D is also a real research topic from which emerges innovations sometimes published in international peer reviewed journals of the corresponding discipline. The French R&D activity has a strong international profile.

The requested review work was carried out in two stages, first by means of a survey conducted in 2010 among all the involved laboratories and then through a Symposium held in Grenoble (May 9 to 13, 2011).

The investigative work and the organization of the conference was made by a group of twenty scientists and engineers, with representatives of all laboratories, of each R&D theme and some representatives of the national agencies such as CNES, the national technology platforms as RENATECH (see <http://www.rtb.cnrs.fr>) or CEA/LETI and OPTITEC/POPSUD as a competitive cluster.

This work involved the R&D teams from the laboratories. Their contributions were solicited through the survey that was coordinated at the laboratory scale by their technical managers. This survey gathered answers from more than 20 laboratories, describing their R&D actions. As a final event of this exercise more than 220 people attended the R&D Symposium over 4 days (see <http://retd-insu-2011.obs.ujf-grenoble.fr/>).

These two exercises provided a comprehensive overview that highlights the wealth of the activities, of the results and the interdisciplinary collaborations with laboratories outside of the discipline or with industrial partners.

2 The survey of the R&D in the laboratories

The survey was managed at the laboratory scale by the technical managers in two steps, an initial one to identify all the actions and a second one to homogenize the data returned in the answers, in order to obtain comparable informations.

We present here the information gathered over a period of almost 4 years:

- **21 laboratories** answered to this survey, and **140 actions** are identified.
- More than **400 scientists, engineers, and technicians** are involved in all laboratories.

¹ UJF-Grenoble 1 / CNRS-INSU, Institut de Planétologie et d'Astrophysique de Grenoble (IPAG), UMR 5274, BP 53, F-38041 Grenoble cedex 9, France, e-mail: Pierre.Kern@obs.ujf-grenoble.fr

* INSU: Institut National des Sciences de l'Univers see also <http://www.insu.cnrs.fr>

- This corresponds to an overall budget of **7.5M Euros /year** with a support of almost **125 FTE/year**.
- **63 academic partners** contribute to these actions, including **25 foreign partners** (UK, Italy, Germany, USA, Netherlands, Spain, Australia, ...).
- **61 industrial partners** are identified, some of them contributing to several actions.
- **Access to technologic platforms** outside of the laboratories is required for more than 36 actions.

Indeed the final application of most of these R&Ds is related to **instrumentation for astrophysics**, but some **valorizations** succeed to bring the developed technology to other field of science (medical, aeronautics, laser, biology ...).

2.1 Domain of investigation

The graph of Fig. 1 presents the domains of investigation of the all the actions, reported in number of actions (and not in overall budget). For the analysis we use the domains corresponding to the main technics used for astrophysical investigations. The optics domain cover the largest part of the developments. Detection is also a large domain of investigation covering all the wavelengths from high energy to radio wavelengths.

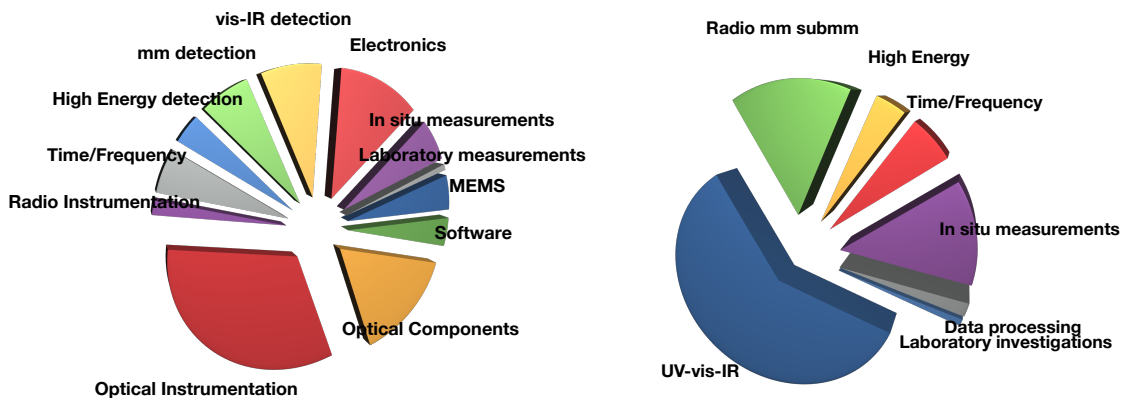


Fig. 1. Repartition of the actions in the various thematics (**left**) and domains (**right**)

2.2 Manpower

We identified more than 400 persons involved in R&D actions, a large part of them being engineers and technicians. It corresponds to an effort of 500 FTE on the period of analysis (125 FTE/year).

Many R&D activities are also carried by PhD students. 71 PhD thesis are identified with various supports from Universities, CNES, CNRS, and Industrial partners. Co-funding are required for CNES and CNRS. CIFRE supports allow PhD directly hired by the companies. More and more PhD supports are coming from EU programs or ANR. A few PhD supports are provided by ESO. Indeed in many cases, PhD thesis are a good way for the investigation of new technologies. It allows a well defined effort on a 3 years time scale.

The repartition according to staff's position is summarized in Fig. 2.

2.3 The partners

More than half of the actions is carrying in collaboration with industrial partners, large groups, SMEs or spinoffs.

More than one third of the actions involves academic partners outside of INSU in France including ONERA and CEA. Collaborations with foreign partners are also a significant part. Indeed the collaborations with academic partners are more often devoted to initial developments.

A large dozen of actions is supported by RENATECH through a RTB funding. RENATECH is the French network of the large technologic facilities supported by CNRS (PTA/Grenoble, LAAS/Toulouse, IEF/Orsay, LPN/Nozay, IEMN/Lilles, FEMTO-ST/Besançon) and LETI (MINATEC/Grenoble) (see <http://www.rtb.cnrs.fr>).

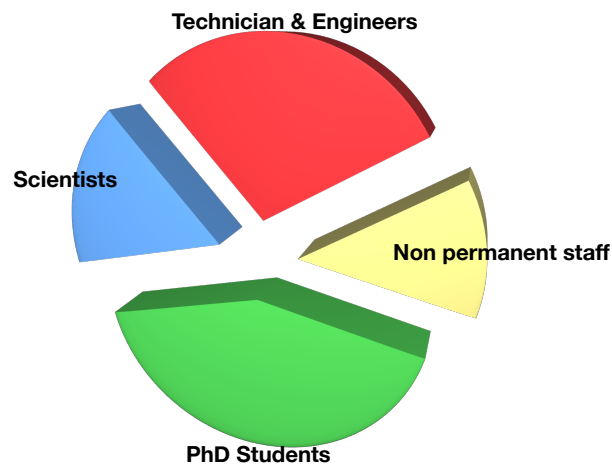


Fig. 2. Staff involved in the R&D in the laboratories

2.4 Synergies with other application domains

For a long time astrophysics has been benefiting from the technological efforts made by other disciplines: this applied to military optronics in the eighties mainly for detection and adaptive optics more specifically for the IR domain. It applied also to optical telecom in the nineties especially for optical interferometry using integrated optics technology.

In an other hand the developments done by the discipline allow fruitful transfers toward other domains of applications: Ophthalmology from adaptive optics, optics manufacturing, Time/Frequency measurements, Spectroscopy and more recently aeronautics through the valorization of a high speed detector.

2.5 Localization on the national area

Fig. 3 presents the repartition of the R&D actions in the French laboratories. The major actors are the laboratories involved in the realization of the instrumentation for the large telescopes and for space missions. Indeed it corresponds often to the preparation of future programs on a top-down process, but it corresponds also to bottom-up developments where new ideas arise from the instrumental groups, including developments not directly linked to well identified instrumental programs.

We keep here both descriptions in term of number of actions and in term of budgets, to avoid the bias of very expensive developments like for instance the new detector developments.

The analysis shows also that R&D activity has been growing in several places since a few years. It is identified in several laboratories as an essential support to instrumental activities including information services.

2.6 Funding

In the recent years there has been a diversification of sources of budget as for other research domains. Apart the usual funding coming from space agencies (CNES and ESA mainly) or INSU, several new tools were provided to the teams to fund there research: ANR, FUI (Fond Unique Interministériel), EU Framework Programs (FP7 currently until 2013). This diversification induces a difficulty to manage the R&D programs at the national scale, and to focus it mainly in support to the large instrumental programs. Forthcoming new tools of "initiatives d'excellence" will even reinforce this effect. It underline the importance of an efficient animation by INSU, to keep the best coordination between the laboratories and to provide the right support to the main projects of the discipline. Fig. 4 presents the fundings that have been used for the R&D actions reported by the survey. The main funding devoted to R&D programs are the following:

- R&T CNES 2011: 2,394 M€
 - Astronomy Astrophysics: 0,88 M€
 - Planetology: 0,4 M€

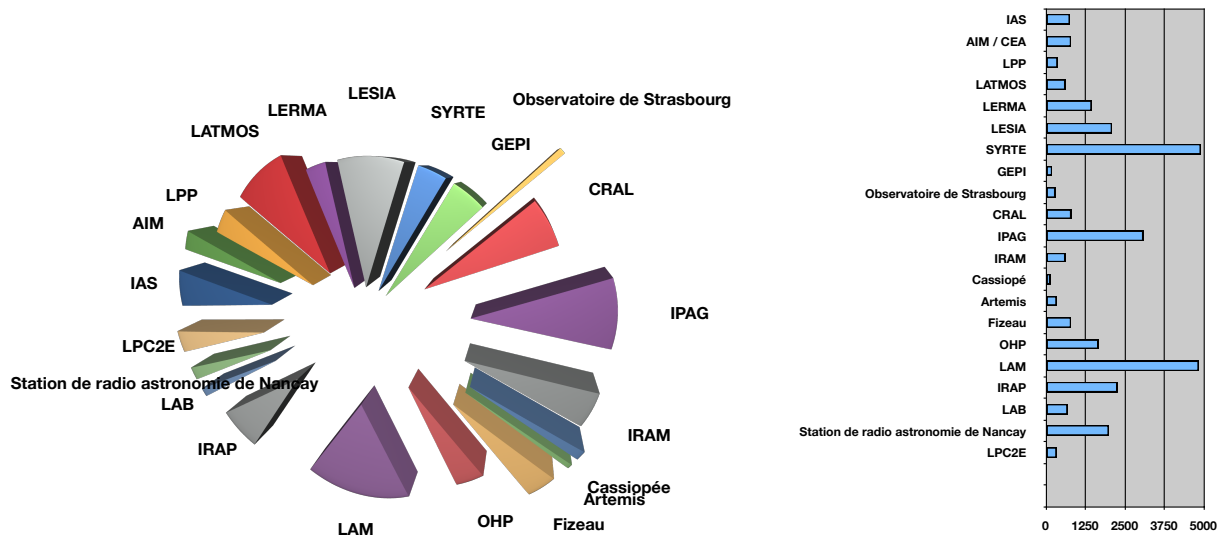


Fig. 3. Repartition of the R&D actions in the French laboratories reported to the number of actions (**left**) and to the considered budget (**right**).

- Fundamental Physics: 0,45 M€
- Solar Physics: 0,29 M€
- Exobiology: 0,245 M€
- R&D INSU AA (R&D + ELT/SKA + VLTI) (2010/2011): 400k€/ 200k€
- ANR (20 actions mentioned) and FUI (4) corresponding for both cases to allocations of 2,9M€.
- ESO and ESA Contributions, Projects. As a reminder the French contributions to the agencies (info prospective INSU) are ESA/65M€ for the mandatory program, ESO/20M€, CNES/62M€,
- EU FP7 budget for the 2003-2009 period (actions related to Astronomy and Astrophysics) is almost 50M€.

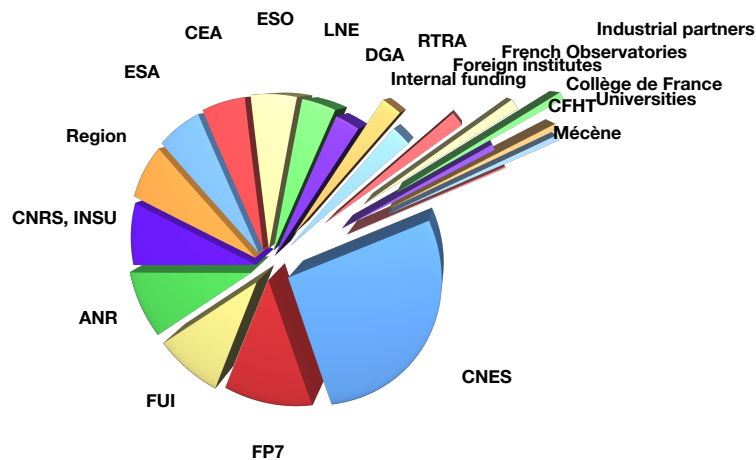


Fig. 4. Funding supports

3 The Symposium

3.1 Attendees

More than 220 persons participated to this four day Symposium. It includes representatives from:

- the laboratories of the disciplines (most of the INSU/AA laboratories were represented),
- the main organism partners (CEA, LETI, ONERA)
- the agencies (CNES, ESO),
- the technologic facilities, mainly RENATECH
- industrial partners from main groups, SME and spinoffs.

3.2 The program of the Symposium

The detailed program of the whole Symposium is reported in Table 1. The program during the 4 days included:

- A first half day of presentation of the instrumental needs. It addressed ground based facilities (ESO), space program needs (CNES), a reminder of the conclusions of the INSU-AA prospective exercise.
- One day for a full review of the R&D programs for all instrumental themes, done mainly by the members of the scientific committee via 20 keynote presentations.
- At the end of the second day, a presentation of the national means available for technological realization.
- A full day of workshops addressing the organization of the R&D in Astronomy, with four groups, each addressing one of the following themes:
 - Organization within the laboratories
 - Technologies means available inside and outside of the laboratories
 - International collaborations
 - R&D and large instrumental programs
- The last day was devoted to the relations with the industrial partners, through keynote presentations (Large groups, SMEs, Spin-offs) and round table: (1) common projects and answers to agencies call for tenders, (2) common research through PhD, (3) transfers of technologies and knowledge).
- This last day ended by a concluding talk that summarizes the conclusions of the 4 workshops of the wednesday, and drew some first recommendations.

3.3 Wednesday Workshop

The four workshops were organized by a team of a few engineers and scientists from the organization committee with additional persons when necessary to complete the expertise.

The conclusions of these workshops were presented in a plenary session during the last day of the workshop. It was discussed from the **top down R&Ds** generated by the main instrumental programs as well as the **bottom up R&Ds** that arise from the research teams. These two processes must be supported since they are both essential for the discipline, the efforts must not be centered only on program driven R&Ds. Agencies and laboratories must keep availability and funding for up stream developments in order to anticipate long term programs.

Some specific recommendations were issued from each workshop:

1. Programs impact:

Jean Gabriel Cuby (LAM), Thomas Foujols (LATMOS), Martin Giard (IRAP), Michel Piat (APC)

- Need to bring out the observational barriers in each scientific theme. Such concerns could be addressed via the INSU/AA national programs.

Table 1. Detailed program of the Symposium

Introduction of the Symposium		
Instrumentation priorities INSU/AA prospective	Martin Giard	IRAP
R&D in the laboratories main numbers	Pierre Kern	IPAG
ESO/VLT and ELT instrumental requirements	Norbert Hubin	ESO
Space programs and CNES R&T	Pierre Gilles Tizien	CNES
Thematic survey		
Optical Telescopes	Marc Ferrari	LAM
Planetary exploration	Sylvestre Maurice	IRAP
Gamma nuclear astronomy	Peter Von Balmoos	IRAP
radio mm/sub-mm R&D	Michel Guélin	IRAM/LERMA
Optical Interferometry	Denis Mourard	OCA
Signal processing software	Eric Slezak	OCA
Time-Frequency	Noel Dimarcq	SYRTE
Ondes gravitational waves	Hubert Halloin	APC
Optical Spectroscopy	Jean Gabriel Cuby	LAM
Radio telescope Back-end	Marc Torres	IRAM
Adaptive Optics	Gérard Rousset	LESIA
High dynamic Imagery	Pierre Baudoz	LESIA
Virtual Observatory, inter-operability, new interactions user/data	Françoise Genova	Observatoire de Strasbourg
Gamma high energy-very high energy astronomy	Pascal Vincent	LPNHE
BF Radio-astronomy	Steve Torchinsky	Station de Nancy
Astronomy X	Olivier Limousin	CEA
Heterodyne mm detection	Yan Delorme	LERMA
UV-Vis-IR detection	Philippe Feautrier	IPAG
mm direct detection	Michel Piat	APC
Cryogeny for detection	Philippe Camus	Institut Néel
Presentation of the national technology facilities		
General presentation of RENATECH	Michel de Labachellerie	FEMTO-ST
The platforms of the RENATECH network	Hugues Granier	LAAS
Examples of developments for INSU/AA programs		
- Arrays of bolometers at LETI	Louis Rodriguez	CEA
- UV Filtres at FEMTO-ST		IAS
- Nano-technologies for submm detection at LPN	Roland Lefevre	LERMA
IRAM: a dedicated platform	Karl Schuster	IRAM
GDR CNRS Micro Nano Systems	Jean-Louis Leclercq	ECL
Industrial partners		
Air Liquide	Sébastien Triqueneaux	
CILAS	Jean Jacques Roland	
SAGEM REOSC	Roland Geyl	
SESO	Gilbert Dahan	
SODERN	Roland Legoff	
μQuanS	Bruno Desruelle	
THALES	Jean-Jacques Juillet	
ONERA	Vincent Michau	

- Need technology demonstrators before the main programs. It concerns ground based instruments, balloon as well as space missions. The difficulty has been identified on the CNES side, a working group is constituted.
- Increase the coupling between the CNES thematic groups and R&D, with suitable comments on actual relevance.
- Need of feedbacks from proposal and/or from the competitive phases A toward required R&D.

2. Organization

Françoise Genova (observatoire de Strasbourg), Guy Guyot (INSU), Pascal Jagourel (GEPI), Roger Pons (IRAP)

- The volume of activities in the laboratories is varying depending on project activities. The dynamic between R&D programs and project activities must be balanced accordingly.
- The organization of R&D within the discipline must be improved:
 - At the local level, laboratories must define their strategy for R&T.
 - The definition of a national strategy seems all the more necessary as funding opportunities become more and more diverse.
 - An overall coordination of INSU R&T in addition to the INSU/AA coordination mentioned above could be useful.
- The organization of such a R&D Symposium before the next INSU/AA prospective is requested as an input to the prospective exercise (skills, highlights, strategic lines would be defined at the Symposium)
- Then such Symposium must remain recurrent.
- R&T Actions:

Actions must be quickly known in laboratories. They must have an appropriate project structure: definition of the objectives, milestones, regular reflection on their pursuit (decision to end, realization phase, valorization outside of Astronomy, ... and confrontation with project / laboratory / national strategy). The special conditions of different types of funding must be taken into account.
- Staff:

This activity is performed by "instrumentalists" researchers AND engineers/technicians specialists, as well as PhD students. If the laboratory wishes to retain the expertise after the projects at least one permanent scientist or engineer must follow the activity.

Regarding to the staff careers, the criterion "project management" should not be the sole criterion for promotions of the engineers and technicians. The difficulties for the careers of engineers and technicians are specific and the R&D activity must be taken into account. It must be noticed that instrumentation is a **Researcher profiles** for Astronomy and Astrophysics.

3. Technology facilities:

Marc Ferrari (LAM), Louis Rodriguez (SAP/CEA)

The teams involved in technology developments for Astronomy and Astrophysics use either national facilities as the one of RENATECH/CNRS network or MINATEC/LETI or the means (pooled or not) of INSU laboratories.

A lack of knowledge of the capacities and capabilities of the existing facilities was observed. The situation was already known, but strongly arose from the discussion. It was suggested to:

- Provide an information about these facilities, mainly in INSU laboratories, but also about the national Centrals
- Maintain a national census of the proximity platforms.
- Setting up a network / forum about technology means.
- Centralize the information at CNRS / INSU level through a dedicated and unique website.

The need for recognition of the technical staff of the technology centers was also underlined. The support to R&D or community is poorly (or not!) recognized, in particular when it is performed for other institutes. We need to find another measure of the impact of the activity that the publications in peer review papers.

The difficulties to maintain the manufacturing processes was also identified. Is it the role of technology centers to maintain the technologies required by astronomical instrumentation? The question is to identify

if it must be done by the INSU laboratories themselves using dedicated means. For most of the cases this support is too expensive for INSU.

Another point is to define the boundary between laboratories and national platforms means. We must keep the critical steps and key technologies in the labs to ensure the product realization for incoming large projects.

The need of a new job was identified: "technology project manager". It must probably be supported at the INSU level in order to insure the legitimacy with respect to Renatech. Such people will insure multi-lab and multi-core role.

Finally one identified that two operation modes are used by the technology platforms: "Do it Yourself" or "Do Not Touch Anything". Necessarily an intermediate mode is often necessary for a suitable operation for INSU developments, in order to associate researchers/technologists from INSU laboratories for the developments.

4. International

G rard Beaudin (LERMA), Marc Ollivier (IAS), Denis Mourard (OCA), G rard Rousset (LESIA)

- Observations

European Union tools are important sources of funding for R&D. FP7 EU programs are well suited to prepare the positioning for the construction and access to the instruments. The international positioning is one of the criteria for the evaluation of the laboratories.

Throughout the difficulties we identified:

- Regarding to responses to EU call for tenders (CFT) rules are numerous and the structure is complex.
- Heavy project management,
- Regarding to the intellectual property, special attentions should be given to the dissemination of ideas.
- EU tends to focus on targeted call for tenders
- France is misplaced in the European lobbying
- International activities are not well recognized for the career progression.

- Recommendations:

It is essential to insure the sustainability and to capitalize the experience by a permanent staff especially for administration AND project management. A strengthening of the support by CNRS regional delegations will be invaluable.

International collaboration require to sign:

- a confidentiality agreement from the beginning of the project preparation,
- a Memorandum of Understanding (MoU) for the responses to the CFT,
- a consortium agreement for the realization.

Laboratory staff must be encouraged to become "expert" to understand the logic of the EU CFT and to increase the chances of success

We enjoin CNRS to support white programs of the EU in order to stimulate new ideas.

Mount specific training for the preparation and the management of international projects:

- Ongoing training for the laboratory staff
- University education for future research players

4 Conclusions of the discussions during the Symposium

The following conclusions were issued from the works of the 4 workshops and of final discussion within the organization committee.

R&D is an essential element of the activity in Astronomy, for the preparation of future projects to push the technologies to their limits, and enable technological breakthroughs. It exist an actual virtuous circle between the scientific needs, instruments realization, and R&D activities. Instrumental research is one of the strengths

of French research in astronomy. Large sectors of R&D excellence includes many domains (components, test benches, system analysis, simulations, software ...)

It is necessary to maintain a coordinating role to INSU.

The diversity of funding tools increases, including for phase A studies devoted to space missions and ground based instruments, in particular to remove the technological show stoppers. These new fundings authorize R&D programs that could not be possible 10 years ago. In essence R&D activities are not supposed to succeed in all cases (which are not necessarily failures). The role of the partnership with the main agencies is essential especially CNES and INSU for space. The integration in European programs is excellent (EU, ESA, ESO).

The group underlines the interdisciplinary of the activities including with industrial partners. The rich relationships with industry is far from a simple delivery service. It must be considered to use alternate indicators able to put a better emphasis on this efficient partnerships beyond the usual indicators of the social and economic impact. R&D provides a good potential for use outside of the discipline. Concerning the signal processing, a structure must be created, especially for the dissemination of the knowledge in the community (creation of a CNRS/Specific Action)

5 Conclusions

The Symposium responded to a strong demand of the community. The last Symposium organized by INSU on this subject was in 1999 in Boussens. Most of the laboratories answered to the survey, and send several representatives to the Symposium. The high quality of the talks and of the associated posters was emphasized by the attendees. The Symposium provided also an excellent occasion for multiple discussions between various teams that are not usually meeting since they are not working in the same domain.

The strong evolution of the national landscape was enlighten by the exercise. Especially the support is now coming from a much larger number of funding partners and agencies. It is essential to take the best benefits of this evolution whereas we maintain the main objectives of INSU/AA missions.

This overall R&D survey brings a first step toward a better organization at the national scale, through the potential of INSU and its laboratories.

The main support of the Symposium was provided by CNRS (Formation Permanente) and by INSU. Additional supports were also given by CEA/SAP, CEA/LETI, CNES, Thales, POPSud, Université Joseph Fourier.

PROPERTIES OF UNUSUAL VOID LSBDS VERSUS COSMOLOGICAL SIMULATIONS PREDICTIONS

J.-M. Martin¹, S. A. Pustilnik² and A. Y. Kniazev³

Abstract. We present the study of several unusual galaxies - low-mass, Low Surface Brightness Dwarfs (LSBD) ($M_{\text{bary}} \sim 3 \times 10^7$ to $\sim 3 \times 10^9 M_{\odot}$, and $M_{\text{B}} \sim -(12-14.5)$) which reside in the nearby Lynx-Cancer void. We confront their properties with the results from recent cosmological simulations, predicting both dynamical properties of low-mass objects and connecting their formation and evolution. In particular, we compare the rotational velocity, the baryonic mass and total dynamical mass with the predictions of Hoefl & Gottloeber (2010), which take into account the suppression of gas accretion onto the low-mass DM halos.

Keywords: galaxies: voids

1 Introduction

Models of galaxy formation (in the context of the popular Λ CDM cosmology) were rather successful for the description of large scale distribution of matter. Λ CDM based N-body cosmological simulations of large volumes show structures and objects quite similar to the observed realm of galaxies. However, this is valid only for large structures and rather massive galaxies. At smaller scales and for low-mass galaxies the situation is not that good. The known problems include the so-called "overabundance problem" and the question of sub-halos around massive galaxies (e.g. Klypin et al. (1999) and Tikhonov & Klypin (2009)), and the low-mass end of galaxy mass/luminosity function in the field/voids. The number of visible objects with $M_{\text{B}} < -14$, which probably form a complete sample in the nearby Lynx-Cancer void (see Pustilnik & Tepliakova (2011)) is several times smaller than the number of DM halos expected from the high-resolution Λ CDM simulations by Gottlöber et al. (2003). It is not clear whether this indicates the real limits of the Λ CDM cosmology and requires the extension of the paradigm, or that the failures of Λ CDM simulations are caused by a still too low spatial resolution and a poor understanding of the underlying physics of galaxies and star formation. However, improvement of our knowledge of the low-mass galaxies, including a more precise determination of their dynamics and evolutionary paths should be crucial for current and future comparison with various model predictions. Since dwarf galaxies are more sensitive to external tidal perturbations which change their dynamics and SF, one should try to avoid interacting objects as much as possible in order to form a good observational dataset. It is natural to assume that the mutual effects of galaxy encounters are minimal in the most rarefied regions - i.e. large voids outlined by filaments and walls, in which the matter density can be as low as 0.1 of the mean density. The detailed study of the least massive void galaxies can give us a valuable material to confront their properties and spatial distribution with the results of state-of-art cosmological simulations.

2 First results

In the context of the study of the Lynx-Cancer void deep sample of ~ 80 galaxies from Pustilnik & Tepliakova (2011) we have identified a half-dozen faint LSB dwarfs with extremely low metallicities, $12+\log(\text{O}/\text{H}) \lesssim 7.30$

¹ Observatoire de Paris, GEPI, 5 place Jules Janssen, F92195 Meudon, France and Observatoire de Paris, USN, Route de Souesmes, F-18330 Nançay, France

² Special Astrophysical Observatory of RAS, Nizhnij Arkhyz, Karachai-Circassia 369167, Russia

³ South African Astronomical Observatory, PO Box 9, 7935 Observatory, Cape Town, South Africa and Southern African Large Telescope Foundation, PO Box 9, 7935 Observatory, Cape Town, South Africa

(Pustilnik et al. (2011)). These galaxies are gas-dominated ($f_{gas} \gtrsim 0.95$), and the ages of the oldest visible stellar populations are in the range of ~ 1 to ~ 3 Gyr (for part of them). They are probably the best galaxies in order to compare their dynamics and baryonic content with the predictions of the modern models. In the figure 1 we present 4 dwarf galaxies from the Lynx-Cancer void sample (J0723+3621, J0737+4724, J0852+1350, J0926+3343) with the range of $M_{bary} = (0.4-4) \times 10^8 M_{\odot}$ and with $V_{rot} = 24-50 \text{ km s}^{-1}$. The predictions of M_{bary}/M_{tot} for the void dwarfs have been published by Hoeft & Gottlöber (2010) in the context of Λ CDM simulations taking into account the gas heating by the UV background. Model and observational ratios match together if one takes into account the expected large ratio between the linear scales of DM mass estimates in models (R_{virial}) and observations ($R(HI)$). Surprisingly, for the discussed LSBs this ratio varies between ~ 1 for $V_{rot} \sim 50 \text{ km s}^{-1}$ to ~ 5 for $V_{rot} \sim 24-30 \text{ km s}^{-1}$: this might indicate that a more careful analysis of the modeling basic assumptions is needed.

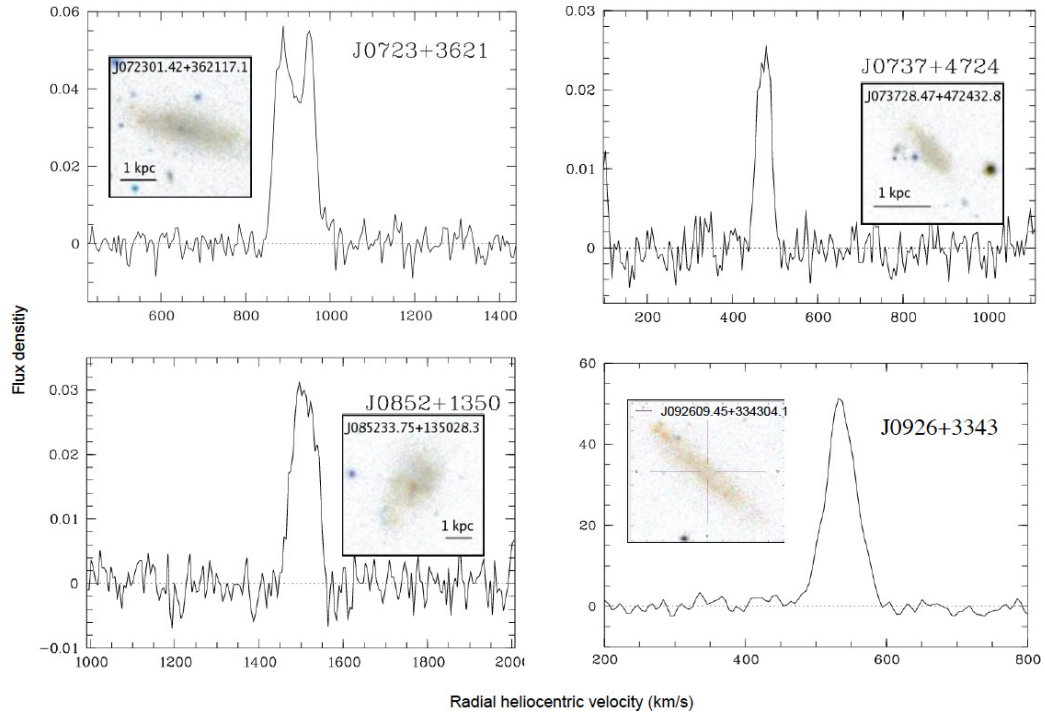


Fig. 1. HI spectra and SDSS images of 4 dwarf galaxies from the Lynx-Cancer void sample. Flux densities are given in Jy (except for J0926+3343, which has a mJy scale). 21-cm spectra have been obtained with the Nançay Radio Telescope and the standard spectral correlator. Radial velocities and abundances have been obtained with the SAO 6m telescope and/or with the SDSS database.

Authors thank the Nançay Radio Telescope Time Allocation Committee and director for generous allocation of observation time.

References

- Gottlöber, S., Lokas, E.L., Klypin, A., Hoffman, Y. 2003, MNRAS, 344, 715
 Hoeft, M., Gottlöber, S. 2010, Advances in Astronomy, vol. 2010, id.693968
 Klypin, A., Kravtsov, A.V., Valenzuela, O., Prada, F. 1999, ApJ, 522, 82
 Pustilnik, S.A., Tepliakova, A.L. 2011, MNRAS, 415, 1188
 Pustilnik, S. A., Martin, J.-M., Tepliakova, A. L., Kniazev, A. Y. 2011, MNRAS, 417, 1335
 Tikhonov, A.V., Klypin, A. 2009, MNRAS, 395, 1915

PARTICLES ACCELERATION AT RELATIVISTIC SHOCKS AND HIGH ENERGY ASTROPHYSICS

G. Pelletier¹ and M. Lemoine²

Abstract. High energy astrophysical phenomena stem from the generation of powerful flows emanating from Super Nova explosions, Gamma Ray Bursts, from ejections in the environment of Black Holes or Neutron Stars that lead to the formation of very strong shocks where particle acceleration takes place. The new developments in these issues are based on the interdependence between the shock structure, the generation of supra-thermal particles and the generation of turbulence. This view started with the studies of Super Nova Remnants, both with X-ray observations and with theoretical investigations, that concluded that the magnetic field is largely amplified by MHD instabilities in the precursor. It is thought, and numerical simulations support that view, that the penetration of supra-thermal particles in the shock precursor generates a magnetic turbulence which in turn produces the scattering process needed for particle acceleration through the Fermi process. This successful development inspired similar investigations for the termination shock of Gamma Ray Bursts. However in ultra-relativistic shocks, difficulties arise with the transverse magnetic field that puts a limitation to particle penetration upstream and that drags particles in the downstream flow and makes shock recrossing difficult. It turns out that only fast enough micro-turbulence can make the Fermi process operative when its level is high enough. This very challenging requirement can nevertheless be fulfilled naturally, as proved by recent numerical simulations. These points are briefly discussed in the presentation and astrophysical consequences are drawn. In particular, it is shown that ultra-relativistic shocks are very efficient electron accelerators and radiation emitters, but poor proton accelerators. It turns out that mildly relativistic shocks inside relativistic flows are better candidates for the generation of UHE-Cosmic Rays. The acceleration performance depends essentially of two parameters: the conversion factor of incoming energy at a shock into magnetic turbulence (this number is provided by the numerical simulations) and the jet power. The Pierre Auger Observatory suggests that the UHECR spectrum is enriched with heavy elements at high energies. What we know about the closest Radio-jets, as those of Centaurus A, together with the theoretical view, indicates that UHECRs can be accelerated up to a few $Z \times 10^{18} eV$, and iron nuclei ($Z=26$) from these nearby radio galaxies can populate the UHE-Cosmic Rays, as long as they are not photo-dissociated. Nevertheless a significant proton contribution can come from GRB internal shocks as well.

Keywords: high energy astrophysics, Fermi acceleration, turbulence, UHE-cosmic rays, SNRs, GRBs, jets

1 Introduction

Strong shocks occurring in astrophysical flows often generate power law distributions of very high energy particles. This is the origin of most high energy phenomena in astrophysics. The favored mechanism for that supra-thermal particle generation is the famous Fermi process. It works with the scattering of high energy particles off magnetic disturbances that allows them to cross the shock back and forth and thus to gain energy. Many works have been done in the 80-ties and 90-ties by assuming a pre-existing magnetic turbulence. However, it turns out that the pre-existing turbulence is generally not strong enough to account for the acceleration performance. The X-ray observations with the satellites XMM and Chandra of Super Nova Remnants (Cassam-Chenaï et al. 2004) have stimulated the studies of particle acceleration at shocks by revealing an important fact, namely that the magnetic field is largely amplified in the vicinity of the forward shock. New developments of the theory of magnetic field amplification by Cosmic Rays have shown that the penetration of accelerated

¹ Institut de Planétologie et d'Astrophysique de Grenoble, 38041 Grenoble, France

² Institut d'Astrophysique de Paris, CNRS – UPMC, 75014 Paris, France

particles in the shock upstream flow can generate a magnetic turbulence that reaches a level much larger than the intensity of the ambient mean field (Bell 2004; Pelletier et al. 2006). In producing turbulence the cosmic rays component loses a fraction of its global energy but increases the maximum energy of its spectrum. Roughly the maximum energy achieved by the Fermi process is close to $\epsilon_{max} = Ze\bar{B}r_s$, where r_s is the shock radius (typically of a few pc at the beginning of the Sedov phase) and \bar{B} is the rms turbulent field that can reach an intensity of few hundreds of μ Gauss, much larger than the value of $2 - 3 \mu$ Gauss of the ambient magnetic field in the Galaxy, which allows Super Nova Remnants to generate cosmic rays that cover the various “knees” of the spectrum from the proton knee around $10^{15} - 10^{16}$ eV up to the iron knee 26 times higher. According to theory and numerical simulations, one expects that a SNR shock converts 10 percent of its incoming energy flux into cosmic rays and a few percent into magnetic turbulence.

These results incited similar investigations for the termination shock of GRBs with the expectation of getting a much larger efficiency and of solving the enigma of UHE-Cosmic Ray generation. However several difficulties raised in the physics of relativistic shocks. Very encouraging results were obtained at the beginning of the century which extended the theory of Fermi process to the case of relativistic shocks and predicted the formation of a power law energy spectrum with an index $s = 2.2 - 2.3$ and an acceleration time as fast as the Larmor time (Gallant et al. 1999; Kirk et al. 2000; Achterberg et al. 2001; Bednarz & Ostrowsky 1998; Ellison & Double 2002; Pelletier 2003). But disappointment came once the effect of the ambient magnetic field had been taken into account, because it inhibits the Fermi process even when one considers a strong Kolmogorov turbulence (Niemiec et al. 2006; Lemoine et al. 2006).

In the following, it will be shown how the paradigm of the three interdependent aspects of collisionless shock physics works successfully in the absence of any mean field: structure with a partial reflection on a barrier, supra-thermal particle generation, magnetic turbulence generation. Then the scattering issue in the presence of a mean magnetic field will be addressed and the requirement for circumventing the inhibition effect will be stated. Then an unusual fact in astrophysics will be emphasized, namely the necessity of considering some unavoidable micro-physics, that turns out to be crucial not only for the relativistic shock formation but also for making the Fermi process operative and producing high energy particles. The termination shocks of Gamma Ray Bursts will be discussed together with the determination of its performance for electron acceleration and gamma-ray emission, and for proton acceleration. Finally the generation of UHE-Cosmic Rays will be addressed.

2 Successful Fermi process at very low magnetization

The most favored process for the generation of supra-thermal power law distributions is the Fermi process at shocks. The plasma flow that experiences a shock is supposed to carry a frozen in turbulent magnetic field under astrophysical conditions. High energy particles (some injection mechanism is expected at non-relativistic shocks) scatter off magnetic perturbations with a mean free path much larger than the shock thickness, so that they can cross the shock front back and forth. They undergo elastic interactions with magnetic disturbances with respect to their proper frame, however upstream magnetic perturbations move forward faster than downstream ones, and thus a particle that undergoes a Fermi cycle—i.e. a cycle upstream-downstream-upstream or downstream-upstream-downstream—because of its scattering, gains energy.

At a non-relativistic shock of speed, $\beta_s = V_s/c \ll 1$, the average gain per cycle is small, $G = 1 + \frac{4}{3} \frac{r-1}{r} \beta_s$ (where r is the compression ratio, that reaches the value 4 when the shock is adiabatic and strong). However this is compensated by a large number of shock crossings; indeed the escape probability (i.e. the probability for a particle to be entrained by the downstream flow and to not come back to the shock front) is weak, $P_{esc} = 4\beta_s/r$; the return probability P_{ret} is thus large. A power law distribution of energy is set up with an index that is a simple function of the compression ratio, in the non-relativistic case:

$$s = 1 - \frac{\ln P_{ret}}{\ln G} \simeq 1 + \frac{3}{r-1} . \quad (2.1)$$

Strong adiabatic shocks provide a particle spectrum with an universal index, $s \simeq 2$, which is modified by losses, radiation losses for the electrons, expansion or escape for protons. For instance protons accelerated in a Super Nova Remnant gain energy until their Larmor radius becomes larger than the shock radius during the Sedov phase, which leads to $\epsilon_{max} = Ze\bar{B}r_s$, where \bar{B} is the rms field intensity at the shock. The spectrum is then steepened by the effect of diffusive propagation and escape of particles from the Galaxy.

A sizable fraction of the incoming energy flux is converted into cosmic ray pressure:

$$P_{cr} = \xi_{cr} \rho_u V_s^2 \text{ with } \xi_{cr} \sim 0.1 . \quad (2.2)$$

The successive Fermi cycles produce a precursor of supra-thermal particles (mostly protons) of large extension (the diffusion length increases with the particle energy) and this penetration in the upstream medium (the ambient medium for an external shock) triggers an MHD turbulence through two types of streaming instability, one is resonant and has been considered for many years (see for instance Kenzie & Völk 1982), the other is non-resonant and has been considered more recently (Bell 2004; Pelletier et al. 2006). That latter case is quite interesting, first because it is a simple and robust mechanism based on the supplementary Lorentz force associated with the plasma current that compensates the cosmic ray current, second because it leads to a turbulent field of large intensity; indeed this latter can become much larger than the ambient magnetic field. The theory indicates that the fraction of incoming energy flux converted into magnetic energy can reach $\xi_B \sim \beta_s$, which is a few percent in Super Nova Remnants, where one defines

$$\frac{\bar{B}^2}{4\pi} = \xi_B \rho_u V_s^2 . \quad (2.3)$$

A very important remark is that the efficiency of the Fermi process depends on the efficiency of the scattering process. By the way, the mechanism of Fermi acceleration is a simple process, but the scattering is the main issue for particle acceleration.

As for relativistic shocks, there are similarities and some differences with the non-relativistic ones, as summarized in Table 1. There are strong arguments that there is a significant generation of magnetic turbulence at the external shock of a Gamma Ray Burst (Li & Waxman 06) and there is an obvious power law distribution of ultra-relativistic electrons that synchrotron radiate, with an index compatible with the theory of Fermi process at ultra-relativistic shocks ($s = 2.2 - 2.3$). The ambient magnetic field is very low and at first approximation can be neglected. A remarkable work was published in 2008 by A. Spitkovsky (Spitkovsky 2008) that fully validates the paradigm that combines three fundamental processes: the formation of a collisionless relativistic shock front with reflected particles, the generation of magnetic turbulence and the generation of a power law distribution through Fermi process. This is a PIC (Particles In Cell) simulation of the development of a collisionless shock in a pair plasma (electrons and positrons) that runs with a Lorentz factor Γ_s of a few tens ($\Gamma_s \equiv (1 - \beta_s^2)^{-1/2}$). The flow of reflected particles interacts with the flow of passing particles leading to streaming type instabilities, and the Weibel branch of instability describes the formation of intense small scale magnetic filaments. The relevant scale of the physics is the inertial length (or skin depth) $\delta \equiv \frac{c}{\omega_p}$. The spatial growth of the magnetic micro-turbulence produces a partial reflection of the incoming particles, which allows the formation of a shock front, and self-consistently, the reflected particles generate the required level of micro-turbulence. Similarly as the non-relativistic case, conversion parameters ξ_{cr}, ξ_B can be defined in the ultra-relativistic case:

$$P_{cr} = \xi_{cr} \rho_u \Gamma_s^2 c^2 \quad (2.4)$$

$$\frac{\bar{B}^2}{4\pi} = \xi_B \rho_u \Gamma_s^2 c^2 \quad (2.5)$$

And the simulations indicate that $\xi_{cr} \sim 0.1$ and $\xi_B \sim 1 - 10\%$, similarly to the non-relativistic case. However a parameter scan needs to be done. Actually the physics is being developed in the two extremes, non-relativistic and ultra-relativistic, that allows some approximations, but not yet in the case of mildly relativistic shocks. The supra-thermal spectrum obtained in the simulation is close to the theoretical prediction with an index $s \simeq 2.4$.

Table 1. Comparison non-relativistic shocks and relativistic shocks.

At non-relativistic shocks	At relativistic shocks
weak escape probability	significant escape probability
many cycles of weak energy gain	few cycles of large energy gain
power law distribution ϵ^{-s} with $s \simeq 2$	power law distribution ϵ^{-s} with $s \sim 2.3$
upstream distribution weakly anisotropic	upstream distribution strongly anisotropic
partial reflection at shock front	partial reflection at shock front
generation of MHD turbulence upstream	generation of e.m. micro-turbulence upstream
acceleration time $t_{acc} \sim \tau_s / \beta_s^2$	acceleration time $t_{acc} \sim \tau_s$

Similar results were obtained later with PIC simulation involving a plasma of electrons and ions of $10 - 100 m_e$ (Sironi & Spitkovsky 2009).

3 Opening phase space with finite magnetization

Many astrophysical shocks form in a plasma having a significant magnetization. The physics becomes more complex with a finite ambient mean field; it is controlled by the important “magnetization” parameter σ :

$$\sigma \equiv \frac{B_{t,f}^2}{4\pi\rho_u\Gamma_s^2c^2} = \frac{B_0^2 \sin^2 \theta_B}{4\pi\rho_u c^2}, \quad (3.1)$$

where B_0 is the field measured in the upstream flow frame (generally the ambient field), and $B_{t,f}$ is the transverse component of the mean field measured in the front frame. Like in non-relativistic shocks, the angle of the field lines with respect to the shock normal is very important. But whereas most non-relativistic shocks are in the so-called “sub-luminal” configuration, i.e. that the angle θ_B is not too close to 90° and thus particles can flow along the field lines, in ultra-relativistic shocks, it suffices that the field angle θ_B be larger than $1/\Gamma_s$ to stop the motions of particles returning upstream. A generic ultra-relativistic shock is thus “supra-luminal”, and the magnetic field in the front frame can be considered as almost perpendicular, because its transverse component is amplified by a factor Γ_s . This field orientation is a serious hindrance for the development of Fermi cycles. A particle that enters the downstream flow of speed $c/3$ is dragged by the frozen in magnetic field and cannot easily come back upstream; it can be shown that it can come back just one time (Lemoine et al. 2006). Once upstream, it eventually comes back downstream, but in a subset of phase space that does not allow it to make a second cycle. It might be thought that a strong turbulence could make an efficient scattering allowing it to make several cycles. But an usual turbulent MHD state with a large scale coherence length behaves like an ordered magnetic field for such particles, because their penetration length upstream ($\ell_p = m_p c^2 / \Gamma_s e B_0$, measured in co-moving upstream frame) is much shorter than the coherence length of turbulence (Lemoine et al. 2006). The coherence length ℓ_c is formally defined as the range of the field correlation; the field self-correlation function being $C(r)$, assuming an isotropic turbulent state (it can easily be properly modified in the case of anisotropic turbulence):

$$\ell_c \equiv \int_0^\infty C(r) dr ; \quad (3.2)$$

this can be expressed in term of an integral over the turbulence spectrum, and one finds that for a spectrum in $k^{-\beta}$ the correlation length is located in the large wavelengths part for $1 < \beta < 2$, as is the case of a Kolmogorov spectrum; for $0 \leq \beta \leq 1$, the coherence length is in the shortest wavelengths part of the spectrum.

Moreover the expected duration of the cycle would be much shorter than the eddy turn over time of large scale vortices. The requirement for a scattering process off magnetic turbulence is quite challenging (Pelletier et al. 2009), for not only the intensity of the turbulent field must be much larger than the mean field, but also the coherence length must be shorter than a Larmor radius. When a scattering process develops, the opening of phase space for getting an operative Fermi process is achieved if the scattering frequency is larger than the Larmor pulsation in the mean field. Short scale turbulence leads to a scattering frequency $\nu_s \propto \epsilon^2$, whereas the Larmor pulsation $\omega_L \propto \epsilon$; thus the range of particle energies for which the phase space is unlocked and Fermi process operative, is such that $\epsilon < \epsilon_{scatt} \equiv Ze(\bar{B}^2/B_0)\ell_c$.

The investigation of ultra-relativistic collisionless shocks started at the beginning of the 90-ties with J. Arons and co-workers, in the case of high magnetization ($\sigma > 0.03$ say). The results, obtained mostly in 1D-PIC simulations, revealed the interesting physics of those shocks (Gallant et al. 1992;). The loop of particles reflected by a magnetic barrier is responsible for a Synchrotron Maser Instability that generates an intense electro-magnetic wave propagating upstream and downstream. The shock radiates a coherent wave upstream with an energy flux, which corresponds to the conversion of the incoming energy by a factor $\sim 0.1\sigma$. The downstream wave is absorbed at synchrotron resonance and heats the plasma that displays a Maxwell-Jüttner distribution. These studies have been done for electron positron plasma first, which is relevant for the termination shock of the pulsar wind nebulae. When the plasma is composed of electrons and protons, the upstream coherent waves exerts a ponderomotive force on electrons which locally separates them from protons and so generates an electrostatic wake-field. The electrons undergo relativistic oscillations in this wave-field and are thus strongly heated until equipartition with protons that are slowed down. These physics has been confirmed by more precise 2D-PIC simulations, performed recently (Sironi & Spitkovsky 2011).

At lower magnetization, nothing happens except the thermalization of protons ($T_p \simeq 0.2\Gamma_s m_p c^2$), until one comes to a very low critical value of the magnetization where the Fermi process starts. Actually one needs a very low magnetic field to get a penetration length of supra-thermal particles upstream large enough for having a significant interaction of those particles with the incoming plasma and having a growth of micro-instabilities.

Fermi process works with the magnetic component of micro-turbulence at inertial scale $\sim \delta \equiv c/\omega_{pi}$. In principle it starts at even smaller scale, the inertial scale of electrons, however electrons are efficiently heated by the electric component of micro-turbulence and then the precursor becomes composed of electrons and protons of similar mass, like a pair plasma. This is a very interesting outcome that simplifies these physics which rapidly evolves towards physics similar to that occurring in a pair plasma. Thus the PIC simulations developed in a pair plasma are also valuable to understand the physics of shocks in electron-proton plasmas. Then a distribution function displaying a thermal part and a supra-thermal part with a power law is obtained.

The transition towards the Fermi process is determined by the micro-instabilities that can grow when the upstream penetration of reflected particles is long enough. The fastest instabilities (Buneman instability, Oblique Two Stream instability, see Bret et al. (2005)) seem to essentially pre-heat the incoming electrons almost up to equipartition with protons. However more simulations are necessary to clarify this important point. Also laboratory experiments are envisaged to check the capability of the micro-turbulence excited by a beam of protons to efficiently heat the electron population (V. Tikhonchuk). The generation of magnetic micro-turbulence by Weibel instability, which is also studied in laboratory experiments, is thought to be the main ingredient to form the collisionless shock and to produce the Fermi process; however this is also under study by PIC simulations. The generation of magnetic micro-turbulence occurs when the magnetization parameter goes below the following critical value (Lemoine & Pelletier 2009), as confirmed by numerical simulations (Sironi & Spitkovsky 2011):

$$\sigma < \sigma_{crit} \equiv \frac{\xi_{cr}}{\Gamma_s^2} . \quad (3.3)$$

Numerical simulations show that the level reached by that Weibel turbulence is such that $\xi_B = 1 - 10\%$, which insures shock formation and Fermi process. Then there exists a large energy range for particle scattering when $\sigma \ll \xi_B^2$.

The main issue with Fermi process based on scattering off micro-turbulence is that the scattering frequency decreases as ϵ^{-2} . The performance of Fermi process at non-relativistic shocks is that the scattering off large scale, say Kolmogorov, turbulence is fairly low (much weaker than the Larmor pulsation in the mean field) but decreases slowly, like $\epsilon^{-1/3}$. Thus if we compare the Fermi process at relativistic shocks with the process at non-relativistic shock, this is like the hare and the tortoise: the scattering, and thus the acceleration rhythm, at relativistic shocks is very fast at low energy and decreases rapidly as energy increases, whereas, at non-relativistic shocks, it is slow at low energy but continues at higher energies with a moderate decline of its efficiency.

4 Electron acceleration at relativistic shocks and radiation (GRBs)

The external shock that starts the afterglow emission of Gamma Ray Bursts (GRBs) gives rise to an efficient acceleration of electrons. If they thermalize with protons (as reasonably expected), their temperature is already very high at the beginning of the afterglow:

$$T_e \sim T_p = \frac{\Gamma_s}{3\sqrt{2}} m_p c^2 ; \quad (4.1)$$

which corresponds to a few tens of GeV. Intense short scale magnetic turbulence develops because the interstellar magnetization parameter is very low, $\sigma \sim 10^{-9}$, whereas the critical value $\sigma_{crit} \sim 10^{-6}$, with $\Gamma_s \sim 300$.

What kind of radiation can be expected in such small scale field, much more intense than the mean field? This depends on a so-called ‘‘wiggler’’ parameter a :

$$a \equiv \frac{e\bar{B}\ell_c}{m_e c^2} \sim \xi_B^{1/2} \Gamma_s \frac{m_p}{m_e} . \quad (4.2)$$

This parameter measures the capability of the magnetic force to deviate a relativistic electron of Lorentz factor γ by an angle $1/\gamma$ (this is the reason for which γ does not appear in the definition). When $a > 1$ the magnetic field produces a single deviation of the electron in the emission cone of half angle $1/\gamma$, whereas when $a < 1$ the electron can undergo several wiggles in the emission cone. When a is large, the emission behaves like a normal synchrotron radiation in a mean field, except that there is no polarization. When a is small, the emission is of ‘‘jitter’’ type (Medvedev 2000). Thus the emission caused by shocked and accelerated electrons at a relativistic shock is ‘‘synchrotron-like’’, and the analysis of the emitted spectrum provides a diagnosis of the magnetic turbulence.

It is quite remarkable that there exists an almost universal energy limit for the electron radiating in the intense small scale field (in agreement with (Kirk & Reville 2010):

$$\gamma_{\max} \sim \left(\frac{4\pi e^2 \ell_c}{\sigma_T m_e c^2} \right)^{1/3} \sim \left(\frac{m_p/m_e}{nr_e^3} \right)^{1/6} \sim 10^6 . \quad (4.3)$$

The corresponding maximum energy for the emitted photons is

$$\epsilon_{\gamma, \max} = \sqrt{\pi} \xi_B \frac{\Gamma_s^2}{\gamma_{\max}} \frac{m_p c^2}{\alpha_f} \simeq 2 \times \left(\frac{\xi_B}{10^{-2}} \right)^{1/2} \left(\frac{\Gamma_s}{300} \right)^2 \text{GeV} . \quad (4.4)$$

Thus a single synchrotron-like spectrum extending up to several GeV, even possibly a few tens, can be expected and thus is compatible with observations. So the performance of relativistic shocks for electron acceleration and radiation is excellent. The conversion factor into radiation is $\xi_{\text{rad}} \sim \xi_B \sigma_T n_0 r_s < \gamma_e^2 >$, and at the beginning of the afterglow $\xi_{\text{rad}} \sim \xi_B \sim 1 - 10\%$.

5 Relativistic shock and supra-thermal protons in GRBs

As mentioned previously, because the scattering time and thus the acceleration time increase with ϵ^2 , the Fermi process at relativistic shocks is not expected to be an efficient accelerator of protons towards the highest energies. That acceleration is limited by expansion losses of time scale r_s/c in observer frame. At the terminal shock of GRBs at the beginning of the afterglow, the maximum energy achieved is

$$\epsilon_{\max} = Z \Gamma_s^{3/2} \xi_B^{1/2} \sqrt{\frac{r_s}{\delta_i}} m_p c^2 \sim Z \times 1.7 \times 10^7 \text{GeV} . \quad (5.1)$$

This has to be compared with the scattering limit $\epsilon_{\text{scatt}} = Z \frac{\xi_B}{\sqrt{\sigma}} \Gamma_s^2 m_p c^2 \sim Z \times 3 \times 10^7 \text{GeV}$. These numbers are not much better than the Hillas limit in the ambient mean field: $\epsilon_{\text{Hillas}} = Z \Gamma_s e B_0 r_s \sim Z \times 0.3 \times 10^7 \text{GeV}$. Thus although an energy of order 10^{16} eV is achieved, which is something, the result is far from the goal of UHE-range. The relativistic shocks are poor protons or nuclei accelerators.

6 About the origin of UHE-Cosmic Rays

Precise performances of mildly or sub-relativistic shocks are not yet known and require more numerical simulations. However some reasonable guess are permitted by extrapolating what we know about the two extremes: non-relativistic and ultra-relativistic shocks. The main guess is that we can expect a magnetic field amplification at shocks with a conversion factor $\xi_B = 1 - 10\%$, occurring in MHD regime without severe limitation due to the super-luminal configuration, especially for oblique internal shocks (termination shocks in the hot spots of FR2 jets might be super-luminal). These assumptions can be applied to internal shocks of AGN jets (in particular in Blazars jets), and to internal shocks of GRBs; the limitation of the acceleration of protons and nuclei is essentially the escape of particles at the edge of the flow. For a relativistic jet of radius r_j , with a large bulk Lorentz factor Γ_j and a kinetic power $P_{\text{jet}} \simeq \rho_0 c^3 \Gamma_j^2 \pi r_j^2$ (ρ_0 being the co-moving density), the maximum energy given by assuming acceleration at the Bohm limit, i.e. an acceleration timescale $t_{\text{acc}} = r_L/c$ in the co-moving frame, the maximum energy in the observer frame reads (in agreement with Lemoine & Waxman 2009):

$$\epsilon_{\max} \simeq \Gamma_j Z e \bar{B} r_j \simeq Z \times 10^{19} \left(\frac{\xi_B}{10^{-2}} \frac{P_{\text{jet}}}{10^{45} \text{erg/s}} \right)^{1/2} \text{eV} . \quad (6.1)$$

Here we assumed that $\gamma_s(\gamma_s - 1) \simeq 1$ so that $\bar{B}^2/4\pi \simeq \xi_B \rho_0 c^2$.

The jets of FR2 radiogalaxies have a power $P_{\text{jet}} = 10^{44} - 10^{46} \text{erg/s}$, hence they might produce UHECRs. GRBs flows carrying internal shocks can be even more efficient accelerators, depending of the duration of the flow for a given energy. For instance, a GRB of apparent isotropic luminosity $P_{\text{jet}}/(\theta_j^2/4) \sim 10^{52} \text{erg/s}$ (θ_j being the half opening angle of the flow $> 1/\Gamma_j$) with $\Gamma_j \sim 100$ may produce particles with energy as high as $Z \times 10^{21} \text{eV}$ for a similar conversion factor $\xi_B = 0.01$. Thus mildly or sub-relativistic shocks in a relativistic flow are more efficient accelerators of protons than ultra-relativistic shocks and are excellent candidates for being sources of UHECRs, thanks to the magnetic field amplification at shocks.

Now if we consider FR1-jets, they are less powerful than the FR2, with $P_{jet} = 10^{42} - 10^{43} \text{ erg/s}$ and they are sub-relativistic. The maximum energy achieved in those jets is one order of magnitude lower than that achieved in FR2-jets. This can be compensated by the generation of UHECRs in the form of iron nuclei ($Z=26$). For instance, we have fairly precise VLBI measurement of the radius of Centaurus A at several distances from the nuclei, together with estimate of the magnetic field responsible for synchrotron emission; this leads to an estimate of the product $B r_j \simeq 2 \times 10^{-3} G \times pc$. The Hillas criterium leads to $\epsilon_{\max} \simeq Z \times 2 \times 10^{18} eV$ (see (Lemoine & Waxman 2009)), which is consistent with a significant amplification of the magnetic field at internal shocks. The most recent VLBI map of Centaurus A, done by the TANAMI project, reveals structures in the flow, suggesting internal shocks. The recent data analysis of Pierre Auger Observatory suggests an enrichment of the UHECR spectrum with heavy elements at higher energies and also a possible correlation with Centaurus A. However it is very difficult to understand the observed pattern of anisotropy if one assumes that the observed particles are heavier than hydrogen (Lemoine & Waxman 2009). In this sense, a contribution of protons coming from more remote and more powerful sources appears unavoidable. A recent spectrum fitting ((Aloisio et al. 2011)) strongly suggests that the spectrum displays a proton cut off around $10^{18} eV$ and another one around $3 \times 10^{19} eV$ associated with iron nuclei. Another recent work ((Ptuskin et al. 2011)) strongly suggests that local radio-galaxies can contribute to the UHE spectrum with iron nuclei.

7 Conclusion and prospect

The triangular dependence of collisionless shock structure with a reflecting barrier for a part of incoming particles, with generation of supra-thermal particles and the generation of magnetic turbulence is a successful paradigm that applies to astrophysical shocks, both non-relativistic and relativistic. Numerical and theoretical works are making significant progress for both understanding the physics and providing quantitative results useful for astrophysical investigations. This includes not only the spectrum index and cut off of the distribution of accelerated particles, but also the conversion factors into cosmic rays, magnetic turbulence and radiation. This is the only beginning of these studies, that require more PIC simulations and new types of hybrid codes involving relativistic MHD coupled with PIC codes for cosmic rays.

The new results that have already been obtained with these approaches are important. First the strong amplification of the magnetic field at SNRs received theoretical and numerical support; the astrophysical consequences are interesting, especially for understanding of the galactic contribution of the Cosmic Ray spectrum. Secondly it has been understood and confirmed by PIC simulations that the Fermi process does not work at relativistic shocks with magnetization of order unity, which is supposed to be a frequent situation in high energy astrophysics, as for instance in FR2 hot spots, in Blazars, in Pulsar Wind Nebulae (we will discuss again this point further on). Thirdly the radiation process that takes place in most high energy astrophysical sources is produced by relativistic electrons scattered in an intense short scale magnetic turbulence; this leads to reconsider the radiation physics in this context and to use it as a diagnosis of the magnetic turbulent state.

There are many opened questions in that field, that can be organized as follows.

- We do not understand yet the process of electron heating and also we have to check whether the electron temperature reaches equipartition with the proton one (we recall that in GRB termination shocks, at the beginning of the afterglow, the electron temperature could reach a few tens of GeV!). This will require more PIC simulations. Moreover experiments with powerful lasers are envisaged: intense protons beam can be produced by high energy laser like LMJ in Bordeaux (however still subrelativistic), and it would be possible to look whether triggering electronic turbulence can leads to a thermalization process (V. Tikhonchuk) during the interaction with a target plasma.
- Till now the shock fronts have been considered as stationary, whereas we know from space plasma physics that most shocks are experiencing a reformation process, which has an impact on particle acceleration (Lembège & Savoini 1992). This issue is currently under investigation for relativistic shocks (Lembège, Plotnikov).
- The physics of mildly or sub-relativistic shocks is not yet done. Even if we might draw some hints by knowing what happens in non-relativistic strong shocks and in ultra-relativistic shocks, for which analytical studies can be developed, we need quantitative results. This is important because those shocks are frequently encountered in high energy astrophysics and are probably the sources of UHE Cosmic Rays. Not only PIC, but also Relativistic MHD code (Casse & Marcowith) and special hybrid codes will be useful for these investigations.

- The classification of relativistic shocks as a function of their magnetization is still very recent, and we need to explore more completely the properties of each class. For instance at high magnetization we know that the Fermi process is impossible and that an intense coherent wave is generated. When the plasma is composed of protons and electrons, a wake field is also generated; this has been studied by two simulations only, and one shows a thermalization process only, whereas the other one indicates also the formation of a power law tail. At intermediate magnetization, a simulation says that nothing happens but the thermalization of protons. This needs to be checked by other simulations and other codes. At low magnetization, where micro-turbulence develops together with the Fermi process, many opened questions remain that could be clarified by appropriate codes (PIC and hybrid RMHD+PIC).
- A special investigation of magnetic reconnections occurring downstream a relativistic shock is a new topic, motivated by at least three reasons. First at high magnetization, in Blazars for instance, we can observe power law distributions with an index smaller ($s \simeq 1.5$) than the one predicted by Fermi process. In the termination shock of Pulsar Wind Nebulae (Y. Gallant, private communication), we can also observe broken spectra with a low energy part with an index $s \simeq 1.5$ and a high energy part compatible with a Fermi process with an index $s \simeq 2.2$. It is thought that the hard spectra are produced by reconnections driven by the compression of a relativistic shock. This is particularly relevant in the case of a Pulsar Wind Nebula (Petri & Lyubarsky 2007) because of the striped structure of the flow where the magnetic field changes its orientation periodically. Moreover dramatic gamma-ray flares have recently been observed in the Crab Nebula (Lemoine-Goumard, this meeting).

The new trend in these topics is the important role imputed to micro-physics phenomena, which have a direct astrophysical impact, as this talk is supposed to show. These developments incite some interests in several communities including Space Plasma Physics and Laser-Plasma Physics communities, Astro-Particle and High Energy Astrophysics communities. This is a very stimulating phase of research.

References

- Achterberg, A., Gallant, Y., Kirk, J. G., Guthmann, A. W. 2001, MNRAS 328, 393
 Aloisio R., Berezhinsky V., Gazizov A., 2011, Astroparticle Phys., 34, 620
 Bednarz, J., & Ostrowski, M. 1998, Phys. Rev. Lett., 80, 3911
 Bell, A. 2004, MNRAS, 353, 550
 Bret, A., Firpo, M.-C., Deutsch, C. 2004, Phys. Rev. E, 70, 046401
 Cassam-Chenaï G.; Decourchelle, A.; Ballet, J.; Hwang, U.; Hughes, J. P.; Petre, R., et al. 2004, A&A, 414, 545
 Ellison, D., & Double, G. 2002, Astroparticle Physics, 18, 213
 Gallant, Y. A., & A. 1999, MNRAS, 305, L6
 Gallant, Y.A., Hoshino M., Langdon A.B., Arons J., Max C.E. 1992, ApJ, 391, 73.
 Hoshino, M., Arons J. 1991, Phys. Fluids B, 3, 818
 Kirk, J., Guthmann, A., Gallant, Y., & Achterberg, A. 2000, ApJ, 542, 235
 Kirk J., Reville B. 2010, ApJ, 710, 16
 Lembège, B., Savoini P. 1992, Phys. Fluids, 4, 3533
 Lemoine, M., Pelletier, G. 2003, ApJ, 589, L73
 Lemoine, M., Pelletier, G., Revenu, B. 2006, ApJ, 645, L129
 Lemoine, M., Waxman E. 2009, JCAP, 11, 009
 Lemoine, M., & Waxman, E. 2009, JCAP, 11, 9
 Mc Kenzie, J.F., Völk, H.J. 1982, A&A, 116, 191
 Medvedev, M. V. 2000, ApJ, 540, 704
 Niemec, J., Ostrowski, M., Pohl, M. 2006, ApJ, 650, 1020
 Pelletier G., Lemoine M., & Marcowith A. 2006, A&A, 453, 181
 393, 587
 Pétri, J., Lyubarsky Y. 2007, A&A, 473, 683
 Ptuskin V.S., Rogovaya S.I., Zirakashvili V.N., 2011, astro-ph, arXiv:1105.4491
 Spitkovsky, A., 2008, ApJ, 673, L39
 Sironi, L., Spitkovsky, A. 2011, ApJ, 726, 75

STELLAR PHYSICS WITH GAIA

B. Plez¹

Abstract. Gaia will provide a three-dimensional map of our Galaxy, with unprecedented positional and radial velocity measurements for about one per cent of the Galactic stellar population. Combined with astrophysical information derived from spectroscopy and photometry for each star, this will lead to a detailed understanding of the formation, and dynamical and chemical evolution of our Galaxy. Other scientific products include extra-solar planets, minor bodies in the solar system, or distant quasars. The contribution of Gaia to stellar physics is less publicized, although very significant. I show here a number of illustrative examples. For example, we will have access to very precise HR diagrams with very large sample of stars allowing extensive tests of fine effects in stellar evolution. Accurate parameters (esp. luminosities, and masses) will allow the independent determination of surface gravities, the characterization of non-LTE effects, and the derivation of more accurate chemical abundances. We will be able to quantify transport processes in various populations of stars, and shed new light on abundance anomalies. In addition, the preparation of Gaia induces a very large effort devoted to homogenize the stellar parameters of a great number of reference stars, and the development of performant tools designed to automatically extract parameters from tremendous amounts of spectra.

Keywords:

1 Introduction

Gaia's main goal is to provide high-precision astrometric data (positions, parallaxes, and proper motions) for one billion objects in the sky. These data, together with multi-epoch photometric and spectroscopic data will allow us to reconstruct the formation history, structure, and evolution of the Galaxy. Many other exciting breakthroughs will also result from this tremendous data set of unprecedented accuracy, in the fields of, e.g., exoplanets, fundamental physics, solar system science, dark matter, the cosmological distance scale (Perryman et al. 2001). In the study of the Galaxy, stars are used as markers of the kinematics, and chemistry. The purpose of this paper is to show that stars will be studied by Gaia as targets per se. We will gain insight into various aspects of stellar physics, thanks to the knowledge of many accurate distances, luminosities, radii, and masses. In addition the preparation of the Gaia mission generates an enormous amount of efforts aimed at a better understanding of stars, and at the development of extremely performant tools for the analysis of stellar observations. I will illustrate these two points through selected examples in the following.

2 What will Gaia provide for stellar physics studies?

Gaia aims at measuring parallaxes of one billion stars with an accuracy better than 300 micro-arcsec, for a complete magnitude limited sample down to $V=20$. The accuracy will be 20 mas (milli-arcsec) for 26 million stars down to $V=15$. As an illustration this translates to 2% errors for Sun-like stars at 1 kpc, 5% errors for red giants out to 2.5 kpc, and M-L dwarfs distances with 3% errors within 100 pc. In total, distances will be known to better than 1% for 11 million stars, and to better than 10% for 150 million stars. Proper motions should be 50% more accurate than parallaxes. The RVS (radial velocity spectrometer) will collect radial velocities down to $V=16$, with an accuracy of 1 to 10 km/s. Details about all these numbers can be found in Turon et al. (2012), and at <http://www.rssd.esa.int>. This unprecedented data set will allow the determination of accurate luminosities for a very large sample of stars. Luminosity (L) is the most commonly missing parameter

¹ LUPM, UMR 5299, CNRS, Université Montpellier 2, 34095 Montpellier, France

in Galactic star studies. Luminosities combined with effective temperatures (T_{eff}) derived from photometry or spectroscopy will give radii (R). With precise masses (M) from the numerous binaries, this will lead to surface gravities (g) independently of ill-controlled hypotheses, as is the case when they are spectroscopically derived, due to NLTE effects. An aspect not to underestimate is the possibility to increase the scientific return using Gaia data in synergy with asteroseismology data that provide strong constraint on other combinations of stellar parameters such as the mean density, M/R^3 or the state of evolution. The multiple epochs of observation (80 per object on average) will allow the study of stellar variability, and of rare types of stars in short evolutionary stages. It is estimated that about 18 million variables will be observed and characterized (Eyer & Cuypers 2000).

3 Examples in the field of stellar evolution

One field that will greatly benefit from Gaia results is stellar structure and evolution. Modeling stellar evolution requires the inclusion of the the most up-to-date physics, e.g., equation of state, nuclear reaction rates, opacities, atomic diffusion, atmosphere models. Special difficulties are encountered for cool, dense stars, late stages of evolution, and of course when very accurate modeling is demanded by very high-quality observations, as in the case of the Sun (Lebreton 2005, 2008). Atmospheres are a particularly critical ingredient as they constitute the boundary condition of the stellar interior, they provide the transformation from theoretical (L , T_{eff}) to observed quantities like magnitudes, colors, and bolometric corrections. Finally, the stellar parameters T_{eff} , $\log g$, chemical composition, are mostly derived from spectroscopic or photometric observations using calculated spectra from model atmospheres. Despite great recent progress (opacities, 3D hydrodynamical models, NLTE calculations), there are still relatively large systematic errors for, e.g., cool giants, hot stars, very metal-poor stars.

3.1 Isochrones: calculations and observations

Stellar evolution models provide stellar parameters like $L(t)$, $R(t)$, $T_{\text{eff}}(t)$, $Z(t)$, that must be confronted to quantities derived from observations, in order to estimate ages, masses, helium content, or metallicities. One widely used, and in principle straightforward way to derive a star's age, mass and initial metal content is to compute isochrones for a distribution of initial masses and just place the star in the magnitude- T_{eff} diagram. This is not as easy as it seems, nor unambiguous. Isochrones overlap on the main sequence, around the turn-off, and on the red giant branch (RGB). But even outside these domains, there is a need for very precise, and accurate L , T_{eff} , and metallicity determinations (Jørgensen & Lindegren 2005). Gaia will dramatically increase the precision of luminosity determinations through better distance measurements, and indirectly also the precision of stellar parameter determinations (see section 4), thus allowing better age determinations (Lebreton & Montalbán 2009). Nevertheless, only the combination with asteroseismology will allow to lift degeneracies in the HR diagram (Lebreton 2011; Gilliland et al. 2011).

3.2 Validation of stellar evolution models

Before these models can be used on a large scale they must be validated using well observed, well constrained systems, of which the Sun, and the α Cen binary are among the few that can be used nowadays.

The case of the Sun is much debated, with the most recent atmospheric abundance determinations (Asplund et al. 2005; Grevesse et al. 2010) leading to discordance of the observed and predicted sound speed profile, and of the depth of the lower boundary of the convection zone. The progress we anticipate Gaia will induce in our understanding of stellar structure on one hand, and of line formation and NLTE effects on the other hand will certainly impact the work on the Sun.

The basic parameters of the α Cen system are known within very small error bars. For the A and B components the masses are $M_A = 1.105 \pm 0.007$, $M_B = 0.934 \pm 0.006 M_{\odot}$ (Pourbaix et al. 2002), and the interferometrically derived radii are $R_A = 1.224 \pm 0.003$, $R_B = 0.863 \pm 0.005 R_{\odot}$ (Kervella et al. 2003), resulting in surface gravities $\log g_A = 4.307 \pm 0.005$, $\log g_B = 4.538 \pm 0.008$ (in c.g.s. units). Porto de Mello et al. (2008) recently published a very careful spectroscopic study of the system leading to $T_{\text{eff A}} = 5824 \pm 26$ K, and $T_{\text{eff B}} = 5223 \pm 62$ K. At least for α Cen B, this is not compatible with the hotter $T_{\text{eff B}}$ derived from the very well known luminosity and radius. The fit of isochrones on the system's data leads to different ages for the components. The most probable explanation put forward by Porto de Mello et al. (2008) is that the estimated temperature of the B component is too low. In addition a review of all abundance determinations for this system show a very large scatter (up to 0.4 dex for Ti). To impose a consistent solution for all parameters of

this system brings a strong constraint on atmosphere and evolution models. The important point is that with Gaia we will have many other systems with well determined masses, luminosities, and radii, distributed all over the HR diagram. This will allow stringent tests of the models.

Another contribution of Gaia will be to bring accurate distances for a rich variety of clusters. Clusters are a very powerful way of testing stellar evolution models, as different physical processes dominate the isochrones shape in different parts of the HR diagram. The lower main sequence is impacted by the uncertainties in the calculation of spectra and atmosphere models. The description of convection affects the main sequence around solar-type stars, and rotation and overshooting affect the upper main sequence, and the turn-off, not to forget the effect of the equation of state, opacities, and nuclear reaction rates. The calibration of models on a large number of clusters will open the way to exciting science, as can be seen in the case of the best studied cluster, the Hyades. In addition to the very precise Hipparcos dynamical parallaxes, the presence of the spectroscopic eclipsing binary HD 27130, with very accurate masses and luminosities, allows to delineate the He content of the stars from the isochrones fit (Lebreton et al. 2001). As a consequence of the fit of the tight observational sequence Lebreton et al. (2001) can also discuss details of the physical ingredients used in the models (mixing-length parameter, model atmospheres, equation of state). This illustrates well what will be possible with the Gaia data on clusters.

4 Gaia and the determination of accurate chemical abundances

The chemical composition of stars is a central piece of information, and considerable work has been devoted to improve the quality of the determinations that are made through the analysis of stellar spectra. Most of the time the stellar parameters T_{eff} and $\log g$ are derived from the spectra together with the abundances. However, model atmospheres suffer from approximations (e.g. LTE) that may induce systematic errors in the results. One enlightening example is given by the case of Procyon, a single-lined nearby binary, for which an astrometric determination of the gravity ($\log g = 4.05$), strongly disagrees with a spectroscopic determination based on the ionization equilibrium of iron ($\log g = 3.6$), as is discussed in detail by Fuhrmann et al. (1997). This is a well known manifestation of NLTE: the Fe I/Fe II, or any other element ratio depend critically on inelastic collisions with hydrogen. The cross-sections are not well known, and extremely difficult to calculate or to measure for many atoms, although progress has been made recently (Barklem et al. 2011). The Drawin (1969) approximation of the H-collision cross-sections is commonly used, often with a scaling factor, S_{H} , with values from 0 (no collisions), to about 3, which tends towards the LTE situation. Korn et al. (2003) derived a value $S_{\text{H}} = 3$ from a careful study of iron lines in a few (4) reference stars with known distances (thus L), T_{eff} (thus R), and masses (thus g). They show that the set of fundamental parameters (of which the distance is a critical one) is only compatible with the NLTE Fe I/Fe II ratio calculated using $S_{\text{H}} = 3$. This kind of work can be done today only on a small number of stars. Gaia will provide very large such samples, that will allow a breakthrough in this domain, especially if combined with interferometric and astero-seismologic data.

5 Transport processes and abundance anomalies

The increasing quality of observational data, and refinements in analysis techniques have unveiled abundance peculiarities that require new mechanisms to be taken into account, i.e. mixing, and diffusion. The work of Spite et al. (2007) on field metal-poor red giant stars uncovered two well-separated groups, one with a high N/C, and a low $^{12}\text{C}/^{13}\text{C}$ ratios, and no detectable Li, showing the sign of CN-processing, and mixing. In higher metallicity stars ($[\text{Fe}/\text{H}]=-1.5$), Gratton et al. (2000) showed that extra mixing happens at the bump, as explained by thermohaline mixing (Charbonnel & Zahn 2007; Cantiello & Langer 2010). In the more metal-poor stars of the Spite et al. (2007) sample, however, unmixed stars are found above the bump and mixed stars seem to exist below the bump. In addition variation in Al and Na abundances indicate very deep mixing in some cases. Firm conclusions cannot be drawn, as there exist the possibility that the spectroscopically derived gravities may suffer from uncertainties. More importantly the distances, and thus the luminosities may be in error. Also, the position of the bump is dependent on metallicity and not well defined yet at very low metallicity. Some stars of the sample might also be AGB or RHB stars and not on the RGB. Halo stars are within reach of Gaia, and this question should be settled once good distances are secured for a large number of field metal-poor stars.

5.1 *The case of Li*

Another illuminating example of the contribution of Gaia to stellar physics concerns element diffusion inside stars. The radial chemical composition of stars is not homogeneous, even outside the regions where nuclear reactions operate. In radiative zones, gravitational settling competes with radiative acceleration leading to sometimes strong abundance gradients. The surface composition of a star does not always reflect its inner content. This is particularly critical in the case of Li, the surface abundance of which measured in very metal-poor stars is a factor of 2 or 3 lower than the primordial abundance that is compatible with standard BBN and the WMAP measurements of the cosmic microwave background (Sbordone et al. 2010). Current models including diffusion predict moderate abundance modifications, due to the inclusion of additional turbulent mixing which is unfortunately tuned with a free parameter. The calibration of the amount of turbulent mixing was made by Korn et al. (2006, 2007) using a sequence of stars in the NGC 6397 cluster. The model tuned to match the observed Mg, Ca, Ti, and Fe abundances does explain sub-primordial Li in these cluster stars, offering a solution to this Li problem, as was already suggested by Richard et al. (2005). This work needs to be extended to more metal-poor stars, as the amount of turbulent mixing might be metallicity dependent. As shown in Sbordone et al. (2010) the Spite plateau dissolves at metallicities below -2.5 , and even more below $[\text{Fe}/\text{H}]=-3.0$, further deepening the mystery of primordial Li. To study the effect of element diffusion at such low metallicities demands to know precisely the evolutionary status of field stars, the distances, and luminosities of which are poorly known. Again, Gaia data will be decisive in the solution of this question.

6 Gaia preparation

Apart from much awaited contributions from Gaia science data, the preparation of the mission itself is developing into a full industry of new tools, and approaches in our way of doing stellar physics.

6.1 *Global stellar parametrizers*

The paramount size of the sample of RVS data to be analyzed calls for innovative methods to, e.g., quickly derive stellar parameters from spectra (and in the case of Gaia RVS, relatively low resolution, and restricted range spectra). A number of algorithms (Global Stellar Parametrizers - GSP-spec) have been developed based on optimization (minimization of distance between observations and reference spectra), projection (the observations are projected on a set of vectors defined during a learning phase), or classification (pattern recognition). They prove to be very efficient, once tested and calibrated on well studied samples of spectra. The two algorithms Matisse (Recio-Blanco et al. 2006) and Degas using the two latter methods compare well with published data when applied to spectral libraries (Kordopatis et al. 2011). Their performances are characterized in terms of accuracy depending on the SNR, and the resolution of the spectra, and the position of the star in the HR diagram. Kordopatis et al. (2011) claim that the results are sufficiently accurate down to SNR as low as 20 for galactic archaeology work, opening new horizons in this field. These tools are absolutely indispensable to deal with the extremely large coming surveys, including Gaia. These algorithms are already used to derive stellar parameters (T_{eff} , $\log g$, abundances) from in particular the ESO archive of spectra.

6.2 *Large homogeneous samples of stars*

As is mentioned above, the accuracy to which GSP's will deliver their results is largely dependent on the spectra they are trained on, and on the stellar parameters attached to them. As GSP's are trained on synthetic spectra that are not error-free, systematic errors in astrophysical parameters (AP) may arise. A high quality external calibration with reference stars is therefore mandatory. A Work Package within CU8 of the DPAC of Gaia ("provide calibration of training data") has undertaken this task. The objective is to determine high quality AP's on an homogeneous scale. A few tens of stars that can be studied at very high resolution with a variety of techniques, but too bright for Gaia, will serve as fundamental calibrators. On this basis, AP's will be differentially determined for 500 to 5000 primary calibrators. Then, thousands of secondary calibrators will allow a large scale validation in a large range of stellar parameters, as, e.g., the 90 000 SDSS stellar spectra discussed by Re Fiorentin et al. (2007). Also, many large samples analyzed in recent years by various authors will be homogenized using the tools described above, coupled with the detailed study of primary calibrators. This is an unprecedented major effort, extremely important to validate stellar models, and that will impact stellar physics at large.

6.3 3D hydrodynamical models, photocenters, and parallax accuracies

The preparation for Gaia also benefits from efforts to develop more ambitious models of stellar atmospheres and interiors. 3D hydrodynamical simulations of red giants and supergiants atmospheres dominated by granulation are now able to make quantitative predictions on the size of granules, their intensity contrast, the shifts and asymmetries affecting spectral line, and their time scales. Chiavassa et al. (2011) have showed that the fluctuations in the position of the photocenter of red supergiants are of the order of a fraction of an AU. This will result in systematic errors in Gaia's parallax determinations of the order of 5%. In return Gaia measurements will help verify these predictions on a large number of stars, which can not be done with, e.g., interferometers from the ground, as it necessitates repeated observations of a number of stars during a few years.

7 Conclusions

Gaia will increase our sample of binary systems with masses known to the 1% level from 100 to about 17 000. It will bring us 11 million stars with parallaxes at the 1% level, to compare with the 700 we have today, of which 100 000 will have a 0.1% accuracy. We will have parallaxes for types of stars for which we have none today (subdwarfs, subgiants). The distance to individual stars in 20 globular clusters (100 to 100 000 stars per cluster) will be determined to better than 10%. It is obvious that this will revolutionize our view of the Galaxy and its evolution. I have shown here that the tremendous Gaia data set, combined with interferometric (R/d), and astero-seismologic (e.g., M/R^3) data will also allow stringent tests, and validations of models of the interior and atmosphere of stars. This will ultimately lead to a much improved quantitative understanding of the physical processes at work in stars.

Stellar physics is a broad field the diversity of which no one can fully embrace. On many topics discussed here I am merely the carrier of others words. Many colleagues helped me while preparing this paper, and without them the task would have been much heavier. Be they all thanked here: Alain Jorissen, Andrea Chiavassa, Andreas Korn, Caroline Soubiran, François Spite, Mathias Schultheis, Monique Spite, Olivier Richard, Patrick de Laverny, and not the least Yveline Lebreton. I thank the AS Gaia and the SF2A for inviting me, and the AS Gaia for providing financial support. Special thanks to Catherine Turon, who so kindly insisted that I gave this talk at the Annual Meeting of the SF2A. I truly enjoyed it.

References

- Asplund, M., Grevesse, N., & Sauval, A. J. 2005, in *Astronomical Society of the Pacific Conference Series*, Vol. 336, *Cosmic Abundances as Records of Stellar Evolution and Nucleosynthesis*, ed. T. G. Barnes III & F. N. Bash, 25
- Barklem, P. S., Belyaev, A. K., Guitou, M., et al. 2011, *A&A*, 530, A94
- Cantiello, M. & Langer, N. 2010, *A&A*, 521, A9
- Charbonnel, C. & Zahn, J.-P. 2007, *A&A*, 467, L15
- Chiavassa, A., Pasquato, E., Jorissen, A., et al. 2011, *A&A*, 528, A120
- Drawin, H. W. 1969, *Zeitschrift für Physik*, 228, 99
- Eyer, L. & Cuypers, J. 2000, in *Astronomical Society of the Pacific Conference Series*, Vol. 203, *IAU Colloq. 176: The Impact of Large-Scale Surveys on Pulsating Star Research*, ed. L. Szabados & D. Kurtz, 71–72
- Fuhrmann, K., Pfeiffer, M., Frank, C., Reetz, J., & Gehren, T. 1997, *A&A*, 323, 909
- Gilliland, R. L., McCullough, P. R., Nelan, E. P., et al. 2011, *ApJ*, 726, 2
- Gratton, R. G., Sneden, C., Carretta, E., & Bragaglia, A. 2000, *A&A*, 354, 169
- Grevesse, N., Asplund, M., Sauval, A. J., & Scott, P. 2010, *Ap&SS*, 328, 179
- Jørgensen, B. R. & Lindegren, L. 2005, *A&A*, 436, 127
- Kervella, P., Thévenin, F., Ségransan, D., et al. 2003, *A&A*, 404, 1087
- Kordopatis, G., Recio-Blanco, A., de Laverny, P., et al. 2011, *ArXiv e-prints*, 1109.6237
- Korn, A. J., Grundahl, F., Richard, O., et al. 2006, *Nature*, 442, 657
- Korn, A. J., Grundahl, F., Richard, O., et al. 2007, *ApJ*, 671, 402
- Korn, A. J., Shi, J., & Gehren, T. 2003, *A&A*, 407, 691
- Lebreton, Y. 2005, in *ESA Special Publication*, Vol. 576, *The Three-Dimensional Universe with Gaia*, ed. C. Turon, K. S. O'Flaherty, & M. A. C. Perryman, 493
- Lebreton, Y. 2008, in *IAU Symposium*, Vol. 248, *IAU Symposium*, ed. W. J. Jin, I. Platais, & M. A. C. Perryman, 411–416
- Lebreton, Y. 2011, *ArXiv e-prints*, 1108.6153

- Lebreton, Y., Fernandes, J., & Lejeune, T. 2001, *A&A*, 374, 540
- Lebreton, Y. & Montalbán, J. 2009, in *IAU Symposium*, Vol. 258, *IAU Symposium*, ed. E. E. Mamajek, D. R. Soderblom, & R. F. G. Wyse, 419–430
- Perryman, M. A. C., de Boer, K. S., Gilmore, G., et al. 2001, *A&A*, 369, 339
- Porto de Mello, G. F., Lyra, W., & Keller, G. R. 2008, *A&A*, 488, 653
- Pourbaix, D., Nidever, D., McCarthy, C., et al. 2002, *A&A*, 386, 280
- Re Fiorentin, P., Bailer-Jones, C. A. L., Lee, Y. S., et al. 2007, *A&A*, 467, 1373
- Recio-Blanco, A., Bijaoui, A., & de Laverny, P. 2006, *MNRAS*, 370, 141
- Richard, O., Michaud, G., & Richer, J. 2005, *ApJ*, 619, 538
- Sbordone, L., Bonifacio, P., Caffau, E., et al. 2010, *A&A*, 522, A26
- Spite, M., Bonifacio, P., Cayrel, R., et al. 2007, in *IAU Symposium*, Vol. 239, *IAU Symposium*, ed. F. Kupka, I. Roxburgh, & K. Chan, 280–285
- Turon, C., Luri, X., & Masana, E. 2012, in *The fundamental distance scale: state of the art and the Gaia perspectives*, ed. M. Marconi, G. Clementini & E. Brocato, *Astrophysics and Space Science Conference Series*, in press

Session 01

Large extragalactic and cosmological surveys

RESULTS FROM THE FIRST THREE YEARS OF OPERATION OF THE SUPERNOVA LEGACY SURVEY (SNLS)

C. Balland^{1,2} and the SNLS collaboration

Abstract. Type Ia supernovae (SNe Ia) currently provide the most direct evidence for an accelerating Universe and for the existence of an unknown dark energy driving the expansion. The Supernova Legacy Survey (SNLS) is a five-year project which has delivered around 500 high-redshift SNe Ia light curves and spectra in the redshift range $0.2 < z < 1.0$ in order to constrain the dark energy equation-of-state, w . The cosmological results obtained with the data of the first 3 years of the survey are presented.

Keywords: type Ia supernovae, cosmology, dark energy, SuperNova Legacy Survey

1 Cosmology with Type Ia supernovae

Type Ia supernovae (SNe Ia) are thought to be the result of the thermonuclear explosion of a carbon-oxygen white dwarf reaching the Chandrasekhar mass limit. Observationally, they are rare (roughly one per galaxy and per thousand years), very bright ($L \sim 10^{10} L_{\odot}$) and transient (~ 1 month) events. Cosmological tests based on measuring their luminosity distance, which encodes the history of the universal expansion, rely on the assumption that they are standard candles. If true, the comparison of their fluxes at different redshifts gives access to the ratio of their luminosity distances as a function of the cosmological parameters governing the expansion of the universe. Namely, for two SNe Ia at z_1 and z_2 :

$$\frac{d_L(z_1)}{d_L(z_2)} = \left(\frac{\phi_2}{\phi_1}\right)^{1/2} = \mathcal{F}(z_1, z_2, \Omega_M, \Omega_X, w),$$

where d_L and ϕ are the luminosity distance and apparent flux of the supernovae. Ω_M and Ω_X are the matter and dark energy density parameters. $w = p/\rho$ is the equation-of-state parameter, where p and ρ are the pressure and density of dark energy.

SNe Ia are actually known for not being standard candles: a dispersion of $\sigma(L_{max}) \sim 40\%$ in their absolute B-band luminosity at maximum light exists. However, two empirical correlations between their physical properties and brightness are used to standardize them. One of these two correlations relates the light curve shape – the so-called ‘stretch’ parameter s – to the absolute magnitude of a SN Ia: the brighter the supernova, the slower the decrease of its luminosity with time. The other correlation involves the color c of a supernova: brighter supernovae are also found bluer. The use of these empirically established ‘brighter-slower’ and ‘brighter-bluer’ relationships allows one to reduce $\sigma(L_{max})$ to 15%, leading to a 5% precision in distance measurements (Guy et al. 2010). Distance and redshift measurements of a large number of SNe Ia are used to build a redshift-distance (Hubble) diagram over a large redshift range. Combined with other probes, this diagram is used to constrain the equation-of-state of the dark energy (e.g., Astier et al. 2006; Kowalski et al. 2008; Kessler et al. 2009; Sullivan et al. 2011).

¹ LPNHE, 4 place Jussieu, 75252 Paris Cedex 05, France

² Université Paris 11, Orsay, F-91405, France
email: balland@lpnhe.in2p3.fr

2 The SNLS survey

The Supernova Legacy Survey (SNLS) is a five year french-canadian program than ran from 2003 to 2008, dedicated to the measurement of distant ($0.2 < z < 1.0$) SNe Ia light curves and spectra. It consisted in an imaging survey on the Canada France Hawaii telescope (CFHT) as part of the deep component of the CFHT-Legacy Survey, and a spectroscopic survey on 8/10-m diameter telescopes.

The SNLS imaging survey was a 5 year "rolling search" using MEGACAM at the prime focus of the CFHT. Each lunar month (~ 18 nights), repeated observations (every 3 to 4 nights) of two 1 square degree fields (out of the 4 fields of the CFHT-LS Deep survey) were performed in 4+1 filters ($griz+u$) for as long as the fields stayed visible (i.e., ~ 6 months). With this technique, about 500 SNe Ia were observed and spectroscopically confirmed between 2003 and 2008, with early, pre-discovery SN photometry, leading to well sampled and measured light curves.

The SNLS spectroscopic survey primarily aimed at identifying the type of the SN and determining its redshift. It has also permitted detailed studies in the UV and optical part of SN spectra (e.g., Ellis et al. 2008; Sullivan et al. 2009; Balland et al. 2009). Spectra have been obtained at the VLT (during two large programs in service observing mode for a total of 480 hours of spectroscopy time between 2003 and 2007), at Gemini North and South (60 hours per semester) and Keck (30 hours during one semester).

3 Implementing the cosmological test

In SNLS, we have set up two independent analysis pipelines (one in France, one in Canada) for the photometric calibration, the SN photometry, the light curve fitters and the spectroscopic identification. Extensive comparisons between the two analyses allowed us to select at each step the most performant approach. When no objective reason for selecting one approach over the other was found, the differences were accounted for as systematics in our analysis. The uncertainties (both statistical and systematics) are included in the SNLS cosmological fits as a full variance-covariance matrix (available to the community; Conley et al. 2011). We describe the key ingredients of our analysis in the following.

3.1 Photometric and SN flux calibration

The SNLS 3 year analysis has led to a precise control of focal plane non-uniformities. Dithered observations of dense stellar fields have permitted to solve the non uniformities of the instrumental response. Variations in the instrumental response up to 8% difference along the focal plane and up to 4 nm in the effective wavelength of filters have been found and corrected for (Regnault et al. 2009).

A key feature of our cosmological test is that it relies on the comparison of low redshift SNe Ia with the high redshift homogenous sample of SNLS SNe Ia. Nearby SNe Ia are usually calibrated against the Landolt UBVRI system. To avoid introducing additional systematic uncertainties between distant and nearby SN fluxes, SNLS supernovae are also calibrated against Landolt stars. Color-color diagrams are used to translate Landolt UBVRI colors into MEGACAM $griz$ colors using piece-wise linear transformations. To obtain ratios of distances of SNe at low and high redshift, the ratio of fluxes of a reference star spectrum used as a calibrator is needed. For this purpose, we use BD+17° 4708 as its colors fall in the same range as our observations of Landolt stars so that no extrapolation in colour-colour diagrams are required. This significantly reduces the systematic uncertainty associated with flux calibration compared to the 1st year analysis that relied on Vega colors (Regnault et al. 2009).

3.2 Light curve fitter and distance estimate

To measure the flux ratio of SNe at different redshifts in the same wavelength range and at the same phase*, it is necessary to interpolate light curve measurements obtained in different rest-frame bands with various time sampling. We use an empirical model of the SNe Ia spectral sequence that takes into account the diversity of SNe Ia via three parameters: a global luminosity offset x_0 , a single shape parameter x_1 (related to the stretch s) and a global colour c . As an empirical model of the SNe Ia spectral sequence $\phi(SN, \phi, \lambda)$, we use SALT2 (Guy et al. 2007):

$$\phi(SN, \varphi, \lambda) = x_0[M_0(\varphi, \lambda) + x_1M_1(\varphi, \lambda) + \dots] \times \exp[c.CL(\lambda)]. \quad (3.1)$$

*The phase φ is the number of rest-frame days elapsed since B-band maximum light.

$CL(\lambda)$ is a colour variation law and $\{M_i\}$ is a set of linear principal components. Note that the color law does not assume any specific reddening by dust or intrinsic color variation. In particular, it does not follow a Cardelli extinction law. This model is trained both on nearby and distant (SNLS) SNe Ia. Using SNLS SNe Ia in the training process allows us to constrain the bluer part of the rest-frame spectrum without using observer frame U-band photometry, which is noticeably difficult to calibrate. The regular redshift sampling yields an accurate photometric scan of the SNe Ia spectra. Note that the light curve fit performed with this model is independent of any distance estimate.

As a distance estimate, we use the rest-frame B-band distance modulus μ_B :

$$\mu_B(z, \Omega_M, \Omega_X, w) = m_B - [M_B - \alpha.(s - 1) + \beta.c],$$

with m_B the apparent peak magnitude in rest-frame B-band and M_B the absolute B-band peak magnitude for a "standard" SN Ia ($s = 1$; $c = 0$). The terms $\alpha.(s - 1)$ and $\beta.c$ represent the way we implement the light curve shape and color corrections. β accounts for host galaxy dust extinction as well as for any intrinsic color property of SNe Ia. M_B , α and β are empirical coefficients fitted along with cosmology.

3.3 Environmental dependance of supernova properties

When one splits SNe Ia samples according to supernova host properties (host color, star formation rate, luminosity, stellar mass ...), differences in shape are found (Sullivan et al. 2006). The shape parameter is found larger in blue, highly star forming, less massive and fainter hosts: SNe Ia are brighter in these galaxies. However, after correction for the brighter-slower correlation, SNe Ia are found brighter in massive, early-type hosts (Sullivan et al. 2010). We perform an improved cosmological analysis by taking this effect into account. We consider two M_B parameters to be fitted along with the cosmological parameters: one for high-mass galaxies, and one for low-mass galaxies, with a split mass of $10^{10} M_\odot$ separating the two groups (Sullivan et al. 2011).

3.4 Spectroscopic identification

VLT spectra of the SNLS 3 year SNe Ia were analyzed with an optimized spectral extraction based on the use of the photometric profile of the host galaxy measured on deep stacked reference images as a model of the underlying galaxy. With this technique, host separation is very efficient in about 75% of cases (Baumont et al. 2008). In the remaining cases, no separate extraction of the SN and the host is attempted.

To identify the SN type, a simultaneous fit of the SN light curve and spectrum using SALT2 has been performed. A host component is added to the SALT2 SN Ia model and the best-fit host contribution to the full spectrum is obtained by χ^2 minimization. This procedure allows us to separate the host from the supernova component at the stage of identification in the spectra for which no separate extraction was possible.

4 Latest cosmological results from the SNLS

4.1 SNe Ia only constraints

The left panel of Fig. 1 presents an up-to-date Hubble diagram of SNe Ia from Conley et al. (2011). It compiles 242 SNLS, 123 nearby ($z \sim 0.05$), 93 SDSS-II ($z = 0.1 - 0.4$) and 14 HST ($z = 0.7 - 1.4$) SNe Ia, for a total of 472 SNe Ia. The regular sampling of data with redshift shows that the former gap at intermediate redshift has now been filled. The best-fit cosmological model and residuals are also plotted (see Conley et al. 2011 for details). Using SNe Ia alone, the universal acceleration is detected at the level of more than 99,9 %, including systematic effects. Assuming a flat universe, our results are consistent with the dark energy being a cosmological constant. Under this assumption, we find that $\Omega_M = 0.18 \pm 0.1$, $w = -0.91^{+0.17}_{-0.24}$ (syst. + stat). Assuming $\Omega_M = 0.27$, we obtain $w = -1.08 \pm 0.1$ (syst. + stat.). Including systematic uncertainties almost double the area of the confidence ellipses in the parameter planes under investigation. 97% of the systematics originate from calibration uncertainties, despite the considerable effort put in obtaining better than 1% accuracy on fluxes (Regnault et al. 2009). Uncertainties in the host split relationship and Malmquist bias come far behind as the second sources of systematics: each contributes 0,6% of the total systematic budget.

4.2 Using SNe Ia with other probes

Supplementing the supernova data with external probes such as baryon acoustic oscillations (BAO/DR7) and WMAP7, we find that the data are again consistent with the dark energy being a cosmological constant (Sullivan

et al. 2011). Contours in the $w-\Omega_M$ plane are shown in the right panel of Fig. 1. Assuming flatness, we find $w = -1.061 \pm 0.069$ (a 6.5% measurement of the dark energy equation-of-state parameter) and $\Omega_M = 0.269 \pm 0.015$. Relaxing the flatness hypothesis, we find $w = -1.069 \pm 0.091$; $\Omega_M = 0.271 \pm 0.015$ and $\Omega_k = -0.002 \pm 0.006$ (Ω_k is the curvature density). The total error increases up to 9% in this latter case. Parameterizing the time evolution of w as $w(a) = w_0 + w_a(1 - a)$, where a is the scale factor of the universe, gives $w_0 = -0.905 \pm 0.196$, $w_a = -0.984^{+1.094}_{-1.097}$ in a flat universe. Clearly, our data do not constrain the time evolution of w .

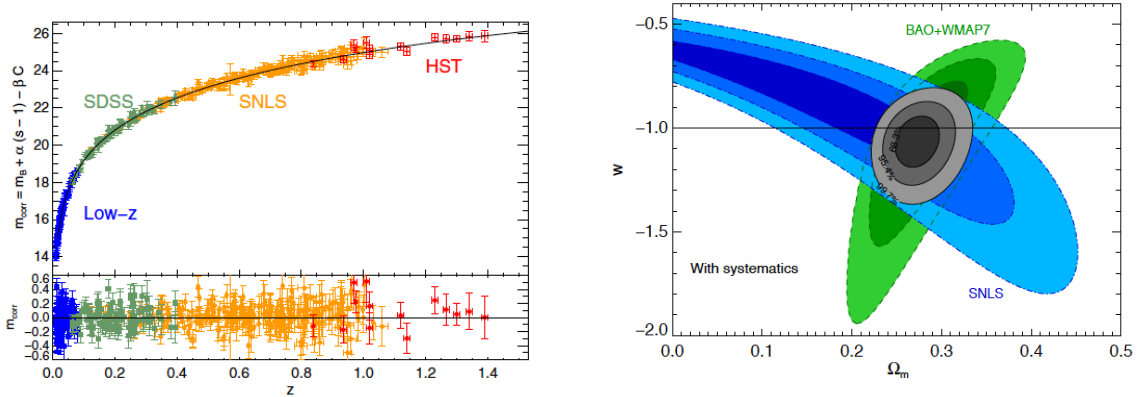


Fig. 1. Left: The Hubble diagram of SNe Ia (Conley et al. 2011). **Right:** Contours in the $w-\Omega_M$ plane. The blue areas are 68, 95 and 99% confidence level constrains from SNLS. The green areas show the constrains from baryon acoustic oscillations BAO/DR7 and WMAP7. The combined contours are shown in grey (Sullivan et al. 2011).

5 Conclusion

We have used the 3 year SNLS supernova sample along with nearby, intermediate and high redshift external SNe Ia samples to constrain the cosmological parameters governing the universal expansion. The SNLS sample is the largest, highest-quality of moderate to high redshift SN Ia sample. From SNe Ia samples only, we obtain w at a precision of 0.1 for a flat universe given a Ω_M measurement. Combining the supernova data with external probes (BAO and WMAP7), we obtain, for a flat universe, a precision of 5.5% on w (stat. only) increasing to $\sim 6.5\%$ if we include systematics. Refinements in the future will include a joint analysis of the 5 years of SNLS (~ 500 SNe Ia) with SDSS (~ 300 SNe Ia), taking full advantage of inter-calibration possibilities between the two experiments.

References

- Astier, P., Guy, J., Regnault, N., et al. 2006, A&A, 447, 31
- Balland, C., Baumont, S., Basa, S., et al. 2009, A&A, 507, 85
- Baumont, S., Balland, C., Astier, P., et al. 2008, A&A, 491, 567
- Conley, A., Guy, J., Sullivan, M., et al. 2011, ApJS, 192, 1
- Ellis, R. S., Sullivan, M., Nugent, P. E., et al. 2008, ApJ, 674, 51
- Guy, J., Astier, P., Baumont, S., et al. 2007, A&A, 466, 11
- Guy, J., Sullivan, M., Conley, A., et al. 2010, A&A, 523, A7
- Kessler, R., Becker, A. C., Cinabro, D., et al. 2009, ApJS, 185, 32
- Kowalski, M., Rubin, D., Aldering, G., et al. 2008, ApJ, 686, 749
- Regnault, N., Conley, A., Guy, J., et al. 2009, A&A, 506, 999
- Sullivan, M., Conley, A., Howell, D. A., et al. 2010, MNRAS, 406, 782
- Sullivan, M., Ellis, R. S., Howell, D. A., et al. 2009, ApJ, 693, L76
- Sullivan, M., Guy, J., Conley, A., et al. 2011, ApJ, 737, 102
- Sullivan, M., Le Borgne, D., Pritchett, C. J., et al. 2006, ApJ, 648, 868

A BAYESIAN APPROACH TO GRAVITATIONAL LENS MODEL SELECTION

I. Balmès¹ and P.-S. Corasaniti¹

Abstract. Over the past decade advancements in the understanding of several astrophysical phenomena have allowed us to infer a concordance cosmological model that successfully accounts for most of the observations of our universe. This has opened up the way to studies that aim to better determine the constants of the model and confront its predictions with those of competing scenarios. Here, we use strong gravitational lenses as cosmological probes. Strong lensing, as opposed to weak lensing, produces multiple images of a single source. Extracting cosmologically relevant information requires accurate modeling of the lens mass distribution, the latter being a galaxy or a cluster. To this purpose a variety of models are available, but it is hard to distinguish between them, as the choice is mostly guided by the quality of the fit to the data without accounting for the number of additional parameters introduced. However, this is a model selection problem rather than one of parameter fitting that we address in the Bayesian framework. Using simple test cases, we show that the assumption of more complicate lens models may not be justified given the level of accuracy of the data.

Keywords: Bayes' factor, strong lensing, model selection

1 Introduction

Over the past years, our understanding of the universe has greatly improved. The concordance model explains most of the cosmological observations. We have now entered a phase where finding new observational ways of measuring the constants of this model as well as confronting predictions with those of competing scenarios is crucial to further advance the research in cosmology. Strongly lensed quasars constitute such a cosmological probe.

In a strong gravitational lens, each image is the result of a different light-path. As a result, if the source behind the lens has a variable luminosity, as quasars do, it will manifest with a time delay between the two images.

This time delay Δt depends on the gravitational potential of the lens, and the underlying cosmological model.

The time delay between two images A and B is:

$$\Delta t_{A,B} = (1 + z_l) \frac{d_l d_s}{d_{ls}} \left(\frac{1}{2} ((\theta_A - \beta)^2 - (\theta_B - \beta)^2) + \psi(\theta_A) - \psi(\theta_B) \right) \quad (1.1)$$

where $\Delta t_{A,B}$, z_l , θ_A and θ_B are observables, β , $\psi(\theta_A)$ and $\psi(\theta_B)$ depend on the lens model and d_l , d_s and d_{ls} depend on cosmology.

Using the above relation, we can derive constraints on cosmological parameters, provided we assume a lens model. Time delays are particularly sensitive to the value of the Hubble constant H_0 .

Unfortunately, a change in the lens model can shift the inferred value of H_0 by a factor of two. Hence, the modeling of the lens, as well as a robust discrimination between lens models, is critical to the study of time delays.

Here, we first discuss the lens models used in our study, then describe our methodology based on Bayesian statistical analysis, and finally present our results.

¹ Laboratoire Univers et Théories (LUTH), UMR 8102 CNRS, Observatoire de Paris, Université Paris Diderot, 5 place Jules Janssen, 92190 Meudon, France

2 Numerous Lens Models

A large number of lens models have been proposed in a vast literature. Given the fact that observables are limited to the position of the images, their time delay and their flux ratio (or magnification), we restrict our analysis to simple examples characterized by a few parameters. In particular we consider two models for lenses with two images, so called “double” lenses (for a review on lensing, see Kochanek (2006)).

1. Power-law model: assume a density profile $\varrho \propto r^{-n}$, with n a free parameter. For $n = 2$, it describes an isothermal lens. In order to assess the dependance on the prior parameter interval we assume two different priors: $0 < n < 3$ (large) and $1 < n < 3$ (small).
2. Power-law model with external shear: assume the previous model with the addition of shear accounting for environmental effect on the lens. This adds two parameters: the strength of the shear γ , and its direction. Expected values for the shear vary up to $\gamma \simeq 0.1$, therefore we assume three different priors on γ : $\gamma < 0.1$, < 0.2 and < 0.5 respectively. This allow us to test the shear strength up to nearly unrealistic values.

3 Our method

To discriminate between different models, we use the Bayes’ factor. The reader can find a more complete review on that subject in Trotta (2008), but it seems useful here to remind a few facts on Bayesian analysis.

Bayesian statistical analysis derives from Bayes’ theorem:

$$P(A|B, I) = \frac{P(B|A, I)P(A|I)}{P(B|I)} \quad (3.1)$$

A well known application of this theorem is parameter estimation. If we take $A = \{\theta\}$ to be a set of parameters in a model, and $B = D$ data resulting from an experience or an observation, then the Bayes’ theorem tells us how our prior knowledge on the parameters $P(\{\theta\}|I)$ is transformed into a new posterior $P(\{\theta\}|D, I)$ by the likelihood $P(D|\{\theta\}, I)$. Here I can be written M_0 , and represents a particular model as well as general background information: before this particular observation, we already had certain expectations about the parameters A , coming from our knowledge of the physical world, or from the model we are trying to fit. For example, we might expect a mass to be positive. The resulting equation can be written:

$$P(\{\theta\}|D, M_0) = \frac{P(D|\{\theta\}, M_0)P(\{\theta\}|M_0)}{P(D|M_0)} \quad (3.2)$$

But consider another alternative. If we take A to represent a certain model M_0 , and B to represent our data set, we know have:

$$P(M_0|D, I) = \frac{P(D|M_0, I)P(M_0, I)}{P(D|I)} \quad (3.3)$$

The term $P(D|M_0, I)$ can be calculated from the previous equation 3.2: it is the denominator of the right-hand-side. $P(M_0|I)$ is our prior belief on the model M_0 to provide the correct description of the data. $P(D|I)$ could be problematic, but we can get rid of it by considering two models, and studying their relative probability:

$$\frac{P(M_0|D, I)}{P(M_1|D, I)} = \frac{P(D|M_0, I)}{P(D|M_1, I)} \frac{P(M_0|I)}{P(M_1|I)} \quad (3.4)$$

The first term on the right-hand-side of this equation, $P(D|M_0, I)/P(D|M_1, I)$ is what is called the Bayes’ factor between models M_0 and M_1 . Supposing we have the same prior belief on the two models, it represents their relative probability, and quantify the ability of one model to account for the observations, with respect to the other model.

An important advantage of the Bayes’ factor over other methods such as χ^2 or information criterion, is that the Bayes’ factor takes into account a term akin to the Occam’s razor idea: models with more parameters, though they usually fit the data better, should not always be preferred. In terms of model selection the improvement on the quality of the fit should be discounted by the increased volume of the prior model parameter space.

In our particular case, we calculated the Bayes’ factor for the lens models (1) and (2), taking as constraints either the time delay measurement alone, or the time delay combined with flux ratio measurements.

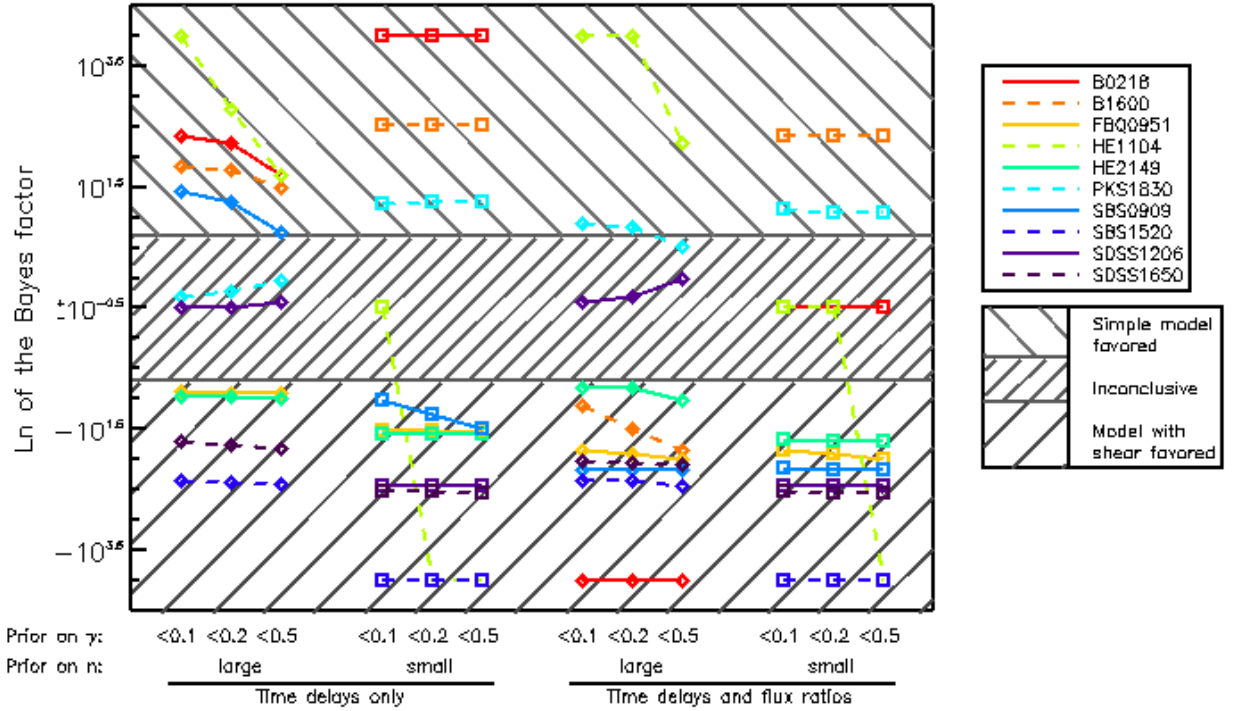


Fig. 1. Bayes' factor between model 1 and 2, with different priors. We plot $\ln(B_{1,2})$ on a logarithmic scale. Each color represents a different lens.

4 Our results

Results are summarized in Fig. 1. Large Bayes' factors favor the simpler model, model 1. Above (below) a certain threshold, the evidence in favor of model 1 (2) is considered strong. In-between, the evidence is inconclusive, and no model can be preferred. In the following, we highlight a few relevant aspects.

4.1 Effect of the prior on n

The lens data set is mainly composed of galaxies, which we expect to be nearly isothermal. Nevertheless, our analysis show that few of them are in fact well described by a power-law model with a reduced prior on n , while the majority favors the more complex model, which also include the shear: the effects of the environment can not, in general, be taken as negligible. In the case of the larger prior, $0 < n < 3$, the number of lenses well described by the power-law increases.

4.2 Effect of the prior on γ

In more than half of the cases, allowing higher (unrealistic) shear strength does not change the Bayes' factor. This is a consequence of Occam's razor: as the parameter space grows, the fit gets better and better, but this effect is compensated for by the Bayes' factor.

In about a quarter of the cases, widening the prior on γ favors the more complex model, as the fit gets sufficiently better to over-compensate for the Occam's razor term.

4.3 Effect of the flux ratios

Time delays depend on the gravitational potential of the lens, whereas flux ratios depend on its second derivative. Furthermore, they are subject to a number of local phenomena (microlensing, absorption...) that do not affect time delays. Therefore, flux ratios can be hardly described with a smooth model, eventually requiring a more

complex modeling than needed by time delays. This is consistent with our findings: in fact, adding flux ratios as a constraint leads to having less lenses accurately described by model 1, since $\ln B_{1,2}$ decreases.

5 Conclusion

Bayesian techniques are a good way to discriminate between lens models and allow us to decide which double lenses can be accurately modeled by a simple power-law model. With the result from this analysis, we now have a good sample of double lenses, together with lens models, to determine cosmological parameters more accurately.

I. Balmès is supported by a scholarship of the "Ministère de l'Éducation Nationale, de la Recherche et de la Technologie" (MENRT).

References

- Kochanek, C. S. 2006, in Saas-Fee Advanced Course 33: Gravitational Lensing: Strong, Weak and Micro, ed. G. Meylan, P. Jetzer, P. North, P. Schneider, C. S. Kochanek, & J. Wambsganss, 91–268
- Trotta, R. 2008, *Contemporary Physics*, 49, 71

COINCIDENT SEARCHES BETWEEN GRAVITATIONAL WAVES AND HIGH-ENERGY NEUTRINOS WITH THE ANTARES AND LIGO/VIRGO DETECTORS

B. Bouhou¹, the ANTARES Collaboration, the LIGO Scientific Collaboration and the Virgo Collaboration

Abstract. A multi-messenger approach with gravitational-wave transients and high-energy neutrinos is expected to open new perspectives in the study of the most violent astrophysical processes in the Universe. In particular, gamma-ray bursts are of special interest as they are associated with astrophysical scenarios predicting significant joint emission of gravitational waves and high-energy neutrinos. Several experiments (e.g. ANTARES, IceCube, LIGO and Virgo) are currently recording data and searching for those astrophysical sources. In this report, we present the first joint analysis effort using data from the gravitational-wave detectors LIGO and Virgo, and from the high-energy neutrino detector ANTARES.

Keywords: Multi-messenger astronomy, high-energy neutrino, gravitational waves

1 Introduction

With the construction of the ANTARES neutrino telescope (Aguilar et al. 2011a) in the Mediterranean Sea and IceCube at the South Pole, together with the interesting sensitivity reached by the LIGO (Abbott et al. 2004) and the Virgo (Acernese et al. 2008) detectors, the multi-messenger astronomy with gravitational waves (GW) and high-energy neutrinos (HEN) is entering a very promising era.

ANTARES is an array of 12 strings spaced over an area of 0.1 km², each one holding 75 optical modules. The main goal of the experiment is to search for HEN of astrophysical origin (i.e. with energies > 100 GeV) by detecting the Cerenkov photons produced by relativistic muons induced by neutrino charged current interaction in the vicinity of the detector. The detector was completed on May 30, 2008 but it started recording data in an incomplete configuration since Jan 30, 2007.

The US project LIGO and European Virgo are Michelson-Morley interferometers, using a very sophisticated technology to measure any variation in the arms length due to the passage of GWs, which are a ripples of space-time caused by accelerating masses. LIGO and Virgo follow the similar operational design but include differences in the arm length for instance (4 km for LIGO and 3 km for Virgo). The interferometer is maintained on the nominal working point where the light beams from each arm interfere destructively, i.e the dark fringe. If a GW passes through the detector it produces a differential strain between the two arms, and hence a change in the phase shift between beams at recombination. This small perturbation results in a fluctuation in the light power after recombination which is converted into the GW strength or strain with $h_{strain} = 2\Delta L/L$, where ΔL is the change in separation of two masses at distance L . Those detectors have reached their initial sensitivity and are currently being upgraded to improve their sensitivity by one order of magnitude.

A working group gathering people from the network of experiments ANTARES, IceCube, LIGO and Virgo study the connections between GWs and HENs emitted by astrophysical phenomena such as gamma-ray burst. In Sec. 2 we discuss the GW and HEN joint search strategy and in Sec. 3 we describe the analysis of the first combined 2007 data sample from ANTARES (5L), LIGO (S5) and Virgo (VSR1).

¹ AstroParticule et Cosmologie (APC) Université Paris-Diderot, 10 rue Alice Domon et Léonie Duquet, 75205 Paris Cedex 13 FRANCE
bouhou@apc.univ-paris7.fr

2 Joint search with ANTARES, LIGO and Virgo data

2.1 Feasibility and data sets

We search for time and spatial coincidences between GW and HEN signals. This is feasible since ANTARES and LIGO/Virgo (Van Elewyck et al. 2009; Chassande-Mottin et al. 2010) share a common view of $\sim 30\%$ of the sky and several periods of concomitant data takings can be identified. In late 2007 ANTARES, IceCube, LIGO and Virgo completed a first concomitant data taking period. LIGO completed the fifth "science run", S5, from November 4, 2005 until September 30, 2007. The first Virgo Science Run (VSR1), covered the period from May 18, 2007 until September 30, 2007 (Abadie et al. 2010). During this period, ANTARES was operating in 5 active detection strings (5L) and IceCube in 22 active strings. The concomitant set of ANTARES (5L), VSR1 and S5 data, covers the period between January 27th and September 30th, 2007. A second step will concern the analysis of the sixth LIGO science run, S6, covering the period from July 7, 2009 until December 31, 2010, the second Virgo science run VSR2, covering the period from July, 2009 until December 31 and ANTARES 10L and 12L from the end of December 2007 up to now. Future schedules involving next-generation detectors with a sensitivity increased by at least one order of magnitude (such as KM3NeT and the Advanced LIGO/Advanced Virgo projects (Smith 2009)) are likely to coincide as well. A time chart of the experiments is shown in Fig. 1. Here we report on the first data set taken in 2007.

	2007	2008	2009	2010	2011	2012	2013	2014	2015	2016	
ANTARES	5L	10L	12L							KM3NeT	
Ice Cube	9s	22s	40s	59s	79s	Ice Cube 86 strings					
LIGO	S5			S6					Advanced LIGO		
VIRGO	VSR1			VSR2	VSR3				Advanced VIRGO		

Fig. 1. Time chart of the ANTARES, IceCube, KM3NET, LIGO and the Virgo experiments.

2.2 Time and spatial coincidence between gravitational waves and high-energy neutrinos

2.2.1 Time search window

Gamma-Ray Bursts (GRBs) are a promising class of extragalactic joint sources of GW and HEN. GRBs are commonly explained by invoking jets of relativistic particles ejected by a yet-to-be-determined "central engine(s)". The observed gamma-rays result from the decay of shock accelerated electrons in the jets. Similarly HENs are expected to be produced by accelerated protons in the same relativistic shocks. The astrophysical systems mentioned as possible central engines are coalescing binaries involving black holes and/or neutron stars or the collapse of massive spinning stars, both expected sources of GW. GRBs provide an interesting astrophysical scenario where the delay between GW and HEN emissions can be characterized. A conservative estimate of this delay determines the baseline duration over which GW and HEN are declared in coincidence. A statistical estimate has been obtained by Baret et al. (2011). In this article, the authors considered the durations of the different emission processes from GRBs (see Fig. 2), mainly observed by BATSE, Swift and Fermi LAT to infer the size of the time search window. This leads to an upper bound on the size of the time search window. The latter is $\Delta t_{GW+HEN} = [-500s, +500s]$ which is conservative enough to encompass most theoretical models of GW and HEN emissions for GRBs.

2.2.2 Angular search window

The angular search window (ASW) is the error distribution of the HEN direction, β , where $\beta = |\theta_{true}^\nu - \theta_{rec}^\mu|$, with θ_{true}^ν is the true zenith angle of the HEN and θ_{rec}^μ is the zenith angle of the reconstructed muon track. The angular resolution is usually defined by the median of β obtained from a Monte-Carlo simulation sample.

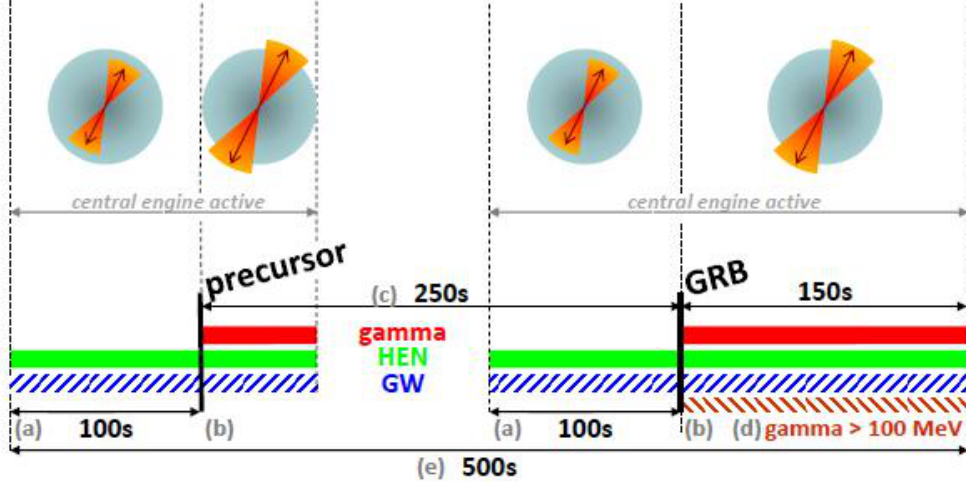


Fig. 2. Overview of the GRB emission processes and GW/HEN time search window. (a) Active central engine before the relativistic jet has broken out of star; (b) Active central engine with relativistic jet broken out of star; (c) Delay between onset of precursor and main burst; (d) Duration corresponding to 90% of GeV photon emission; (e) Time span of central engine activity. Possible GW/HEN emission between the precursor and the main GRB (no emission is shown on the figure) has no effect on the estimated time window. Overall, the considered processes allow for a maximum of 500s between the observation of a HEN and a GW transient, setting the time search window to $[-500s; 500s]$. (top) Schematic drawing of plausible emission scenario. For both precursor and main GRB, after the central engine drives an outflow that breaks out after $\leq 100s$. (Adapted from Baret et al. (2011)).

Fig. 3 left shows an example of β in a bin of declination and Fig. 3 right illustrates the angular resolution as a function of the log-energy. The angular resolution is limited by the detector geometry and by the propagation characteristics of the Cerenkov light in the medium (i.e., photon scattering and absorption). For the cuts defined for this analysis (see Sec. 3.1), the angular resolution is about one degree for events reconstructed with three lines and more above 100 TeV and of 2.5 degrees at low energies. For events reconstructed with two lines, it ranges from about 2 to 3 degrees.

The radius used for the joint analysis is defined as the 90% quantile of β (denoted $ASW_{GW+HEN}^{90\%}$). The value of this radius is calculated in bins of the reconstructed declination and in bins of number of hits used in the reconstruction. The distribution of β is fitted by a log-normal distribution on an event-by-event basis (see Fig. 3).

The coincidence search strategy is as follows: we first select a set of HEN candidates by applying the procedure and cuts detailed in Sec. 3.1 and estimate for each candidate its time of arrival, its ASW and the parameters of the corresponding log-normal fit. These parameters are fed to a search pipeline which tests the presence of a coincident GW signal consistent in time (i.e., within the time coincidence window defined in Sec. 2.2.1) and direction (i.e., within the angular search window defined in Sec. 2.2.2). In practice, we use the so-called X-pipeline (Sutton et al. 2010) algorithm to search coherently the GW data and scan the sky area centered at HEN sky location within a radius $ASW_{GW+HEN}^{90\%}$ (see Sec. 3.2). At this point, it is interesting to note that $ASW_{GW+HEN}^{90\%}$ is comparable in size to the typical GW error box (obtained when reconstructing the source direction from the triangulation of GW data).

3 Data analysis of ANTARES 5L–LIGO/Virgo S5/VSR1 data set

3.1 Selection of the high-energy neutrino candidates

The ANTARES neutrino telescope recorded data from January 1st to December 3rd 2007 with 5 lines. The data sample used in this analysis covers the period between 1st January and 30 September, 2007, as it overlaps with LIGO S5 and Virgo VSR1. These data are sampled using several selection criteria, trigger levels and selection cuts, used to discard the background present at the ANTARES site. Trigger decisions are based on the calculations done at three levels. The first level of trigger is a simple threshold of about 0.5 photo-electron (pe)

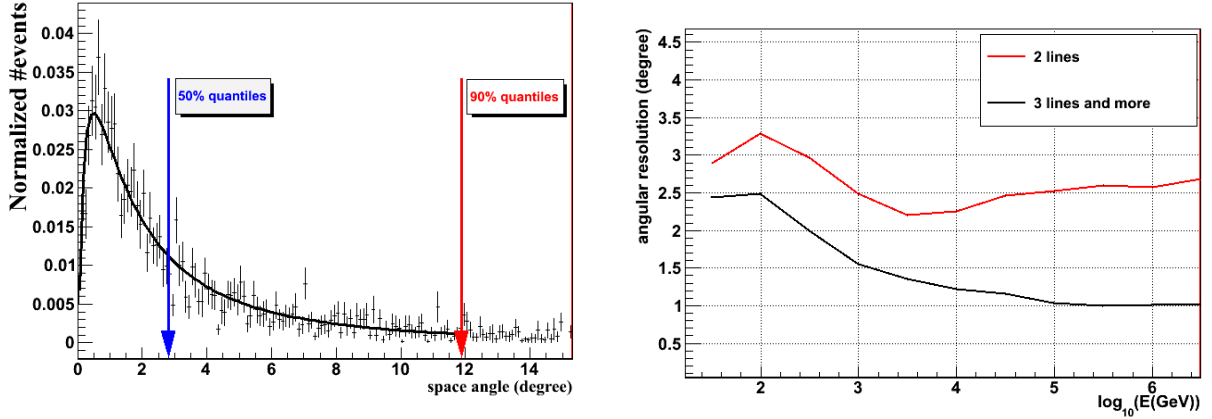


Fig. 3. Left: The error distribution on the neutrino direction for declination between -20 and -10 degrees for event with 7 hits along with its log-normal fit. Right: The angular resolution for ANTARES 5L data represented as function of the true neutrino energy, for events reconstructed with exactly 2 lines (red curve) and for events reconstructed with 3 lines and more (black curve).

equivalent charge applied to the analog signal of the photo-multiplier tubes (Ageron et al. 2007). The second level trigger is based on coincident hits in the same storey within 20 ns, and hits with large charge (greater than 3 pe or 10 pe depending on the detector configuration). The third level evaluates the characteristics of the hits from the second trigger level. The track reconstruction is based on the χ^2 -minimization approach implemented in the track reconstruction algorithm (Aguilar et al. 2011b). Events are identified as sets of hits (direct Cerenkov photons) in a time window of $2.2\mu\text{s}$ (Aguilar et al. 2011c) over the full detector. For the background estimation, various samples of neutrinos and atmospheric muons were simulated and used for data vs. Monte-Carlo comparisons. Various parameters are used to select up-going neutrino candidates and reject physical background (i.e. atmospheric neutrinos and down-going atmospheric muons that are misreconstructed as up-going). Those include the χ^2 of the best fit track, the number of hits used in the fit and the estimated direction of the reconstructed track. For this analysis we define two cut values on the χ^2 depending on the track direction, i.e. $\chi^2 \leq 1.8$ when $\theta \leq 80^\circ$ and $\chi^2 \leq 1.4$ when $80^\circ \leq \theta \leq 90^\circ$ where the contamination from down-going muons is higher (see Fig. 4). The values of the χ^2 cuts were optimized based on the maximization of the model discovery potential according to a standard E^{-2} spectrum (Becker 2008). With these cuts around 20% of contamination from atmospheric muons remains in the final selected sample.

After applying the set of selections exposed in the previous section, a sample of 216 neutrino candidates is selected. Each candidate is defined by its arrival time t_{HEN} in the detector, its direction $(\delta_{HEN}, \alpha_{HEN})$ and the radius $ASW_{HEN}^{90\%}$. The distribution of selected HEN candidates is in good agreement with the expected distribution of (upward-going) atmospheric neutrinos. A small fraction of the HEN candidates may however be of cosmic origin and this can be determined by the detection of a GW counterpart as discussed in the next section.

3.2 Searching for gravitational waves associated with high-energy neutrinos

The GW data used in this analysis were collected during LIGO Virgo S5 VSR1. Combined with ANTARES 5L this yields ~ 103 days of lifetime. We used the so-called X-pipeline algorithm (Sutton et al. 2010) to search for unmodelled GW bursts (duration ≤ 1 s) in association with each of the selected 216 HEN candidates. For this analysis the circular polarization of the impinging GW is assumed. The 1000 second duration data segments around the HEN trigger time t_{HEN} defines the “on-source” segments. The “on-source” data from all available GW detectors are searched coherently over the sky region identified by the $ASW_{GW+HEN}^{90\%}$ (see Sec. 2.2.2). The same analysis is applied to two “off-source” segments (3 hour duration) surrounding the “on-source” region.

The X pipeline estimates the significance of each GW candidate event detected in the “on-source” by computing the rate of occurrence of a similar transient in the “off-source” segments. The list of final candidate events is subjected to additional checks that may result in vetoing events overlapping in time with known instrumental or environmental disturbances (Abbott et al. 2010).

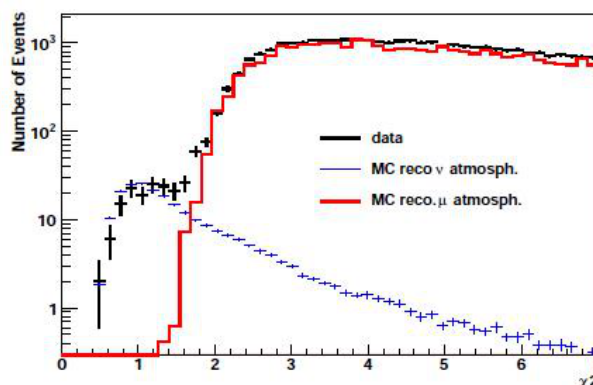


Fig. 4. Distribution of the up-going HEN events as a function of the track quality parameter χ^2 . The distributions obtained with Monte-Carlo simulations are compared to the data.

The first joint GW and HEN analysis is complete and is currently under internal review. The final results will be published in an article in preparation. We could however estimate the search sensitivity for various emission models. As stated earlier, coalescing binaries of neutron stars are of particular interest for this study as they may be associated with the release of GRBs. We estimated the distance reach for those sources to be ~ 8 Mpc (inferred from GW data only). Using typical assumptions on the HEN production in association with GRB, we obtain a similar distance reach (for at least one neutrino observed by ANTARES). We conclude that the distance reach of the joint search is of the same order.

The authors gratefully acknowledge the support of the United States National Science Foundation for the construction and operation of the LIGO Laboratory, the Science and Technology Facilities Council of the United Kingdom, the Max-Planck-Society, and the State of Niedersachsen/Germany for support of the construction and operation of the GEO600 detector, and the Italian Istituto Nazionale di Fisica Nucleare and the French Centre National de la Recherche Scientifique for the construction and operation of the Virgo detector. The authors also gratefully acknowledge the support of the research by these agencies and by the Australian Research Council, the International Science Linkages program of the Commonwealth of Australia, the Council of Scientific and Industrial Research of India, the Istituto Nazionale di Fisica Nucleare of Italy, the Spanish Ministerio de Educación y Ciencia, the Conselleria d'Economia Hisenda i Innovació of the Govern de les Illes Balears, the Foundation for Fundamental Research on Matter supported by the Netherlands Organisation for Scientific Research, the Polish Ministry of Science and Higher Education, the FOCUS Programme of Foundation for Polish Science, the Royal Society, the Scottish Funding Council, the Scottish Universities Physics Alliance, The National Aeronautics and Space Administration, the Carnegie Trust, the Leverhulme Trust, the David and Lucile Packard Foundation, the Research Corporation, and the Alfred P. Sloan Foundation.

The authors also acknowledge the financial support of the funding agencies for the construction and operation of the ANTARES neutrino telescope: Centre National de la Recherche Scientifique (CNRS), Commissariat à l'énergie atomique et aux énergies alternatives (CEA), Agence National de la Recherche (ANR), Commission Européenne (FEDER fund and Marie Curie Program), Région Alsace (contrat CPER), Région Provence-Alpes-Côte d'Azur, Département du Var and Ville de La Seyne-sur-Mer, France; Bundesministerium für Bildung und Forschung (BMBF), Germany; Istituto Nazionale di Fisica Nucleare (INFN), Italy; Stichting voor Fundamenteel Onderzoek der Materie (FOM), Nederlandse organisatie voor Wetenschappelijk Onderzoek (NWO), the Netherlands; Council of the President of the Russian Federation for young scientists and leading scientific schools supporting grants, Russia; National Authority for Scientific Research (ANCS), Romania; Ministerio de Ciencia e Innovación (MICINN), Prometeo of Generalitat Valenciana (GVA) and Multi-Dark, Spain. They also acknowledge the technical support of Ifremer, AIM and Foselev Marine for the sea operation and the CC-IN2P3 for the computing facilities.

This work has received support from the Groupement de Recherche Phénomènes Cosmiques de Haute Energie. This publication has been assigned LIGO Document Number LIGO-P1100127.

References

- Abadie, J. et al. 2010, *Astrophys. J.*, 715, 1453
- Abbott, B. et al. 2004, *NUCL. INSTRUM. METH. A*, 517, 154
- Abbott, B. P. et al. 2010, *Astrophys. J.*, 715, 1438
- Acernese, F. et al. 2008, *Class. Quantum Gravity*, 25, 114
- Ageron, M. et al. 2007, *Nucl. Instrum. Meth.*, A578, 498
- Aguilar, J. et al. 2011a, *Nucl. Instrum. Meth.*, A656, 11
- Aguilar, J. A. et al. 2011b, *Astropart. Phys.*, 34, 652
- Aguilar, J. A. et al. 2011c, *Astropart. Phys.*, 34, 539

- Baret, B. et al. 2011, *Astropart. Phys.*, 35, 1
Becker, J. K. 2008, *Phys.Rept.*, 458, 173
Chassande-Mottin, E. et al. 2010, *J. Phys.: Conf. Ser.*, 243
Smith, J. R. 2009, *Class. Quant. Grav.*, 26, 114013
Sutton, P. J. et al. 2010, *New J. Phys.*, 12, 053034
Van Elewyck, V. et al. 2009, *Int. J. Mod. Phys.*, D18, 1655

GALAXIES AND COSMOLOGY WITH THE PROJECTS PHYSICS OF THE ACCELERATING UNIVERSE (PAU) AND DARK ENERGY SURVEY (DES)

F. J. Castander¹, on behalf of the PAU and DES collaborations

Abstract. Dark energy poses one of the biggest challenges to our understanding of the universe. Currently, many projects and surveys are flourishing trying to investigate its nature. Here we briefly review the Dark Energy Survey (DES), one of the most comprehensive dark energy imaging surveys that will start observations in the near future. We also present the Physics of the Accelerating Universe (PAU) survey, which features the use of narrow band filters to obtain precise photometric redshifts to sample cosmic structure.

Keywords: cosmology, galaxy surveys, dark matter, dark energy

1 Introduction

The realization that the universe was accelerating came as a surprise more than ten years ago. Today, all cosmological observations seem to ratify this picture where the universe is dominated by some strange form of peculiar energy that drives the universe to accelerate its expansion rate. Conversely, it may happen that this acceleration is just a consequence of the laws of gravity departing from our standard understanding provided by general relativity. The investigation of what causes this accelerated expansion is driving current observational cosmological projects. In order to probe the universe we can measure its expansion rate and its growth of structure rate. The most constraining observables include supernovae, clusters of galaxies, the clustering of galaxies, weak lensing, the integrated Sachs-Wolfe effect (e.g., Albrecht et al. 2006). Most of them require to sample large volumes and large redshift epochs to be most efficient. For good enough statistics enough objects need to be sampled, which often means sampling many galaxies. It is also necessary to measure their distances and shapes. There are many projects focus on carrying out such extensive and comprehensive surveys. Here we will focus on two of them, the Dark Energy Survey and the Physics of the Accelerating Universe Survey.

2 The Dark Energy Survey

The Dark Energy Survey (DES*, Dark Energy Survey Collaboration 2005) is one of the most comprehensive photometric dark energy surveys planned in the near future. The DES collaboration comprises over 120 members in more than 15 institutions spread over 5 countries. The DES is constructing a new large area camera DECam (see Figure 1) to be mounted at the prime focus of the Blanco 4m telescope at Cerro Tololo, Chile. The camera includes a newly designed corrector that delivers a 2.2 degrees diameter field of view which is densely covered by 62 science CCDs, supplemented by others used for guiding, monitoring the wave front and focusing. The detectors are 2k by 4k fully depleted CCDs which make them very sensitive to red wavelengths. The camera is equipped with a set of grizY filters. DECam is now at its latest stages of construction. The installation at the 4m telescope is scheduled for January 2012. The camera is expected to be fully operational by the middle of 2012.

The DES is also implementing a data management system to handle the survey image reduction. At the same time, CTIO/NOAO is preparing the observatory and improving the telescope performance for the arrival of DECam.

¹ Institut de Ciències de l'Espai (IEEC/CSIC), Campus UAB, 08193 Bellaterra, Barcelona, Spain

*<http://www.darkenergysurvey.org>

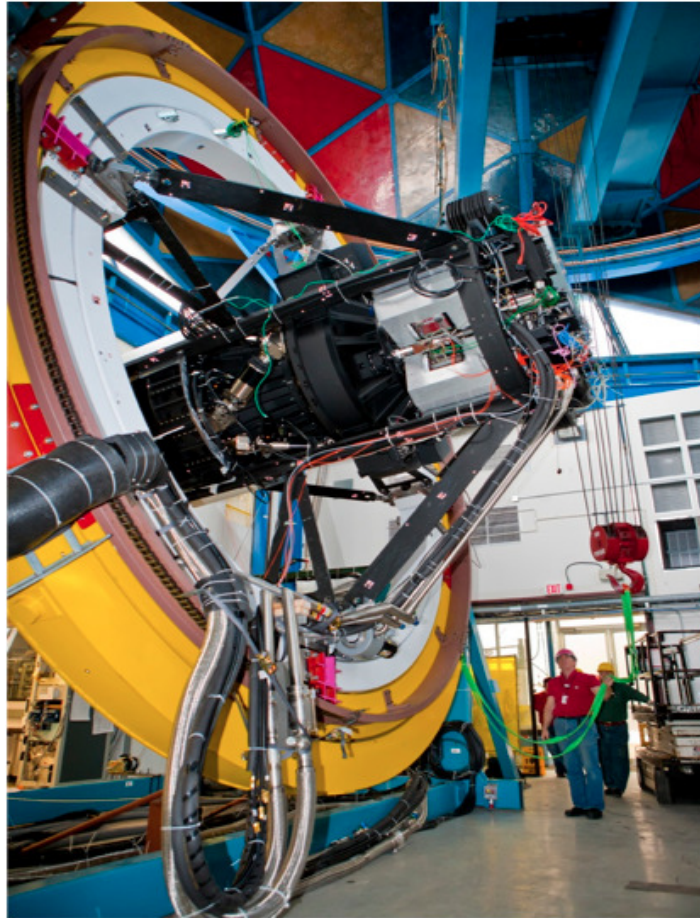


Fig. 1. DECam mounted on the Telescope Simulator at Fermilab in early 2011

The DES will use 525 nights to map 5000 deg^2 in 5 bands, *grizY*, down to an approximate depth of $i \sim 24$. Additionally it will sample 30 deg^2 repeatedly to search for supernovae in 10 separate fields. Two of these SNe fields will be imaged deeply and the rest will be shallower. The main science driver of DES is to characterize dark energy using four cosmological probes. DES will detect a hundred thousand galaxy clusters to redshifts $z \sim 1$ and will use the evolution of their abundance to test cosmology. For that purpose it needs to calibrate the relation between its detection method (optical searches based on colour and spatial distribution) and mass. It will overlap with the SPT SZ survey and therefore will benefit with cross checks and calibrations with the SZ decrement. Cluster weak lensing measurements will also be used to calibrate the cluster masses. Another probe will be weak lensing. DES will measure shapes for $\sim 3 \times 10^8$ galaxies at mean redshift $z \sim 0.7$ and use them to compute the cosmic shear angular power spectrum. Additionally it will use the bispectrum and the galaxy-shear signal to determine dark energy. DES will also use the clustering of galaxies to constrain cosmology. In particular, it will measure the baryon acoustic oscillation scale at different photometric redshifts bins. It will also study redshift space distortions. Another cosmological probe will be the use of supernovae. With its dual strategy search (deep and shallow) DES expects to detect around 4000 well-sampled SNe out to $z = 1$.

DES will be a photometric survey and therefore will need to rely on photometric techniques to estimate the redshift to the observed objects. The VISTA Hemisphere Survey (VHS[†]) has already started observations and will eventually map the whole DES area in the *J*, *H* and *K* filters. The addition of near infrared data improves the photo-*z* performance that is expected to have an RMS scatter below 10%. For clusters it will be lower, of the order of 2%. This precision is sufficient for the dark energy probes to be used provided that the error

[†]<http://www.ast.cam.ac.uk/~rgm/vhs/>

distributions are sufficiently well measured.

In order to understand the constraints that can be possible to place on dark energy, the DES team is developing a comprehensive simulation effort.

Another important component of DES is a data management system to be able to cope with the vast amounts of data that the survey will generate. In this context, a community pipeline is being developed for external users of DECam.

The DES is expected to start in September 2012 and will release their data 12 months after the data are taken.

3 The Physics of the Accelerated Universe Survey

The basics requirements for a cosmological survey are to cover large volumes, sample enough objects, measure distances and shapes and in the case of supernovae have appropriate time coverage/cadence. Photometric surveys are very efficient in sampling large volumes and many galaxy tracers. However, they perform poorly in determining redshifts. On the other hand, spectroscopic surveys can determine very accurately redshift, but struggle to obtain large number of objects and sample large volumes. The Physics of the Accelerated Universe Survey (PAU[‡]) is designed to straddle between both concepts trying to sample large volumes with good enough redshift accuracy. In fact, many cosmological applications do not require extremely accurate redshift determinations. For example, the lensing efficiency kernel is very broad and therefore individual distances need not be good. The baryon acoustic oscillations feature has an intrinsic width and sampling it with a much better distance resolution is therefore inefficient. The PAU survey intends to sample a large area of the sky using narrow band filters to obtain good photometric redshifts to constrain cosmology.

The PAU survey collaboration is building a new large field of view camera (PAUCam, Casas et al. 2010, see Figure 2) to be installed at the William Herschel Telescope (WHT) at the Observatorio del Roque de los Muchachos in La Palma, Spain. The camera will be installed at the prime focus and will use its current corrector that delivers a 1 deg diameter field of view with the inner 40arcmin without any vignetting. PAUCam will have 18 $2k \times 4k$ CCDs in its focal plane. These detectors are red sensitive fully depleted CCDs supplied by Hamamatsu. The camera will be equipped with 36 narrow band filters of 100 Å width covering the wavelength range from 4800 to 8400 Å and six standard broad band filters (ugrizY). PAUCam is currently undergoing construction that is expected to finish by the end of 2012.

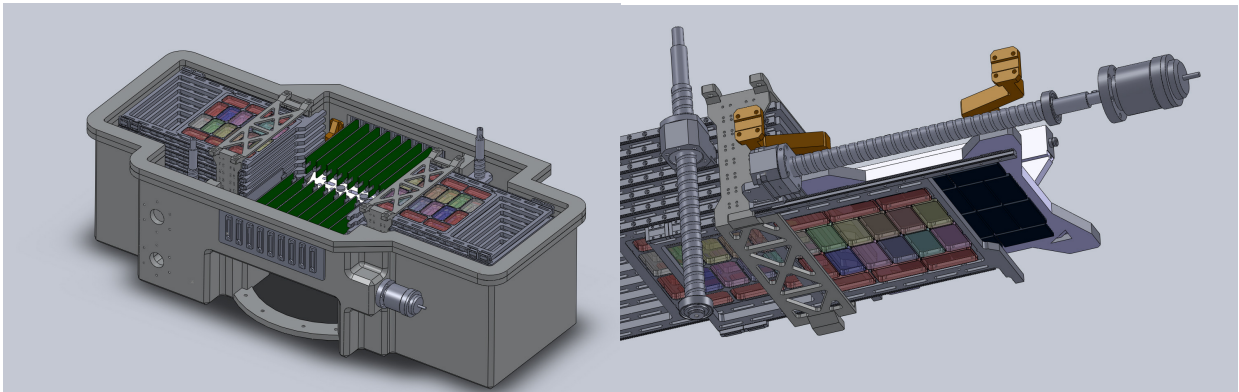


Fig. 2. Left: Rendering of the PAU Camera interior. **Right:** Image of the camera filter trays.

The PAU Camera will have a surveying power of 2 deg^2 per night imaging down to $i \sim 22.5$ in the narrow band filters and down to $i \sim 24$ in the broad band filters. The PAU survey team expects to conduct a wide area survey with all the narrow band and broad band filters in the camera of at least 200 deg^2 down to the previous quoted depth. The exact reach will depend on how much time can be used for the survey, though. Each filter tray has eighteen positions for filters, one for each CCD. We intend to place 6 narrow band and 2 broad band filters in the central eight positions (those without vignetting) of each tray. We define our survey strategy based on these eight central detectors. Nominal survey procedures with similar exposures in six different filter

[‡]<http://www.pausurvey.org/>

trays result in two different samples of galaxies. One shallower sample detected in the both the broad band and narrow band filters for which we would obtain photometric redshifts with $\delta z \sim 0.0035 \times (1+z)$ accuracy. And another deeper sample with galaxies just detected in the broad band filters with photometric redshift accuracy of $\delta z \sim 0.05 \times (1+z)$. We intend to study the redshift space distortions (RSD) and the weak lensing (WL) magnification of the sample and use them to place cosmological constraints. The expected performance is presented in Gaztañaga et al. (2011), where the method is explained in detail. Briefly, we will measure the RSD of the shallower sample and the WL (either by measuring magnification and/or shear) of the deeper one. We will cross-correlate different redshift bins of both samples. This technique enables to produce figure of merits on w and γ that are one order of magnitude better than if analysed separately (see Figure 3).

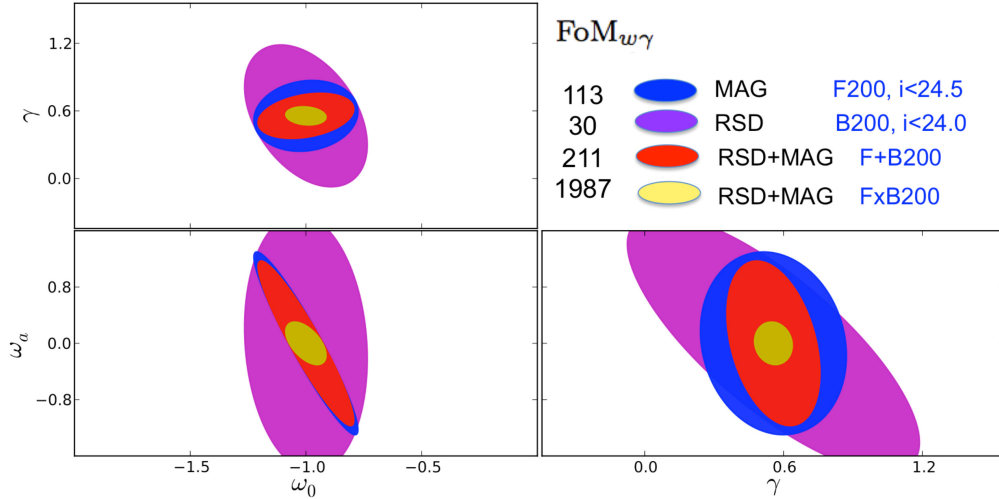


Fig. 3. Expected cosmological constraints for the dark energy equation of state (w_0 and w_a) and the growth rate of structure (γ) from the PAU survey covering 200 deg^2 . From Gaztañaga et al. (2011)

4 Conclusions

We have presented to upcoming surveys designed to measure the expansion rate and the growth rate of the universe to constraint dark energy. Both surveys are constructing large field of view cameras to conduct comprehensive surveys. DES will produce a photometric catalogue of 5000 deg^2 and will use four different probes to constrain dark energy. The PAU Survey straddles in between photometric and spectroscopic surveys. It will produce a shallower with good redshift determinations sample and a deeper one with poorer redshift accuracies in the same area. The PAU survey expects to exploit the benefits of conducting both surveys in the same area.

FJC acknowledges financial support from the Spanish Ministerio de Ciencia e Innovación (MICINN), project AYA2009- 13936, Consolider-Ingenio CSD2007- 00060, European Commissions Marie Curie Initial Training Network CosmoComp (PITN-GA-2009-238356), and research project 2009-SGR-1398 from Generalitat de Catalunya

References

- Albrecht, A., Bernstein, G., Cahn, R., & et al. 2006, arXiv:astro-ph/0609591
 Casas, R., Ballester, O., Cardiel-Sas, L., & et al. 2010, SPIE, 3757735, 107
 Dark Energy Survey Collaboration. 2005, arXiv:astro-ph/0510346
 Gaztañaga, E., Eriksen, M., Crocce, M., & et al. 2011, arXiv:astro-ph/1109.4852

CONSTRAINING TYPE IA SUPERNOVA MODELS WITH SNLS SPECTRA

F. Cellier-Holzem¹ and C. Balland¹

Abstract. The use of type Ia supernovae for cosmology is limited today by systematic uncertainties. To reduce these uncertainties and standardize these objects, we have to better understand their physical properties. For this purpose, we compare type Ia supernova spectra from the SuperNova Legacy Survey with the predictions of two supernova explosion models (a deflagration and a delayed detonation models) in order to constrain and improve them.

Keywords: type Ia supernova, cosmology, SuperNova Legacy Survey, supernova formation models

1 Cosmological context and aim

The use of type Ia supernovae (SNeIa) allows to constrain the accelerated expansion of the universe via the cosmological parameters (Riess et al. 1998; Perlmutter et al. 1999). Using the first three year data set of the Supernova Legacy Survey (SNLS), supplemented with nearby, intermediate and high redshift supernovae, Conley et al. (2011) obtain $w = -0.91_{-0.20}^{+0.16}(stat)_{-0.14}^{+0.07}(sys)$ assuming a flat universe. A better knowledge of type Ia supernova properties will permit to reduce the systematic uncertainties in the future. Supernova formation models producing spectra and light-curves, will help us to understand the SNeIa. In the present study, we compare SNLS spectra with synthetic spectra produced by a pure deflagration model (W7) and a delayed detonation model (DD25) (Nomoto et al. 1984; Khokhlov 1991; Hoefflich et al. 2002). We evaluate how observations can discriminate models, in order to constrain and improve them.

2 Explosion models : W7 and DD25

We use two synthetic spectra samples : one combined W7 with the radiative transfer code *Phoenix*, the other combined DD25 (with $\rho_{tr} = 25.10^6 g.cm^{-3}$, the transition density between the deflagration and the detonation) with the same radiative transfer code *. These spectra are produced from 5 to 50 days since the beginning of the explosion for W7 and from 7 to 50 days for DD25, with a regular sampling near the maximum light. Both models describe the explosion of a carbon and oxygen white dwarf reaching Chandrasekhar mass limit : a nuclear explosion producing intermediate and iron peak elements. The burning front is a key parameter governing the final element composition as predicted by the models. A different burning front velocity implies differences between the two models. These differences are shown in Fig. 1 where we overlap a DD25 and a W7 spectrum at maximum light (~ 18 days).

The differences are more pronounced in the UV part of the spectra ($\lambda < 4300\text{\AA}$), in particular for the absorption depth of calcium II at $\lambda \sim 3700\text{\AA}$ and the peak amplitude at $\lambda \sim 4150\text{\AA}$. In the same spirit, differences are noticed with two peaks at $\lambda \sim 3200\text{\AA}$ and $\lambda \sim 2900\text{\AA}$. The spectrum produced by W7 is more structured than the DD25 spectrum : spectral structures are missing in the DD25 spectrum (peaks in W7 spectrum at $\lambda \sim 3400\text{\AA}$ and $\lambda \sim 3650\text{\AA}$). Clearly, the UV spectral zone will be discriminant for the models.

¹ Laboratoire de Physique Nucléaire et Hautes Énergies (LPNHE), Paris, France

*We thank Dr. D. Jack and Prof. Dr. P. Hauschildt for providing us the synthetic spectra

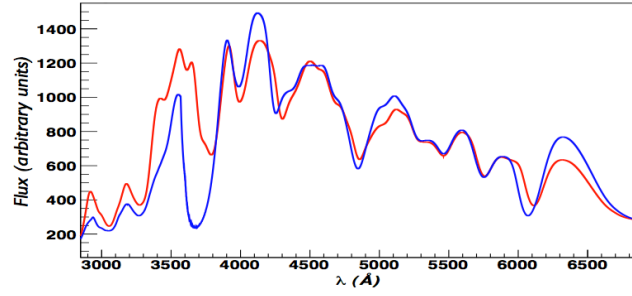


Fig. 1. Overlap of 18 days W7 (red line) and 18 days DD25 (blue line) spectra showing the spectral differences between the models.

3 SNLS spectra

The SNLS is a 5 year experiment aiming at measuring the luminosity distance of a large number of intermediate and high redshift SNeIa in order to constrain cosmological parameters (Astier et al. 2006; Sullivan et al. 2006; Guy et al. 2010). Conducted from 2003 to 2008, this experiment is split in two surveys :

- an imaging survey with the Canada-France-Hawaii Telescope (CFHT) in Hawaii, to detect the supernovae and monitor their light-curves in several photometric bands,
- a spectroscopic program with the Very Large Telescope (VLT), Gemini and Keck telescopes to confirm the nature of the SNeIa candidates and measure their redshift.

SNLS measured 242 SNeIa during the first three years of operation. For the present study, we use an homogenous subset of 51 SNeIa spectra measured at the VLT for which a separate extraction of the supernova and the host galaxy is possible to limit the host contamination (Balland et al. 2009). This spectra are measured in a large range of redshift ($0.15 < z < 1.0$) with a regular phase distribution ($-8d < phase < 13d$) where the phase is the number of rest-frame days elapsed since the B-band maximum date.

4 Observations vs Models

4.1 Fitting SNLS spectra with synthetic spectra

In this section, we compare SNLS spectra with the models. We perform a χ^2 minimization fit of each SNLS spectrum by the two synthetic spectra samples (W7 and DD25). We do the fit at each W7 and DD25 spectrum phase. In some cases, W7 is the best fit, as shown in Fig. 2 for SN 04D2cf, a supernova at $z = 0.368$ with a phase of 8.48 days. This is clearly visible in the UV part, where the Ca II absorption line ($\lambda \sim 3700\text{\AA}$) and the amplitudes of the peaks around the silicon II feature ($\lambda \sim 4000\text{\AA}$) are well reproduced by W7 (on the left panel of Fig. 2) and not by DD25 (on the right panel of Fig. 2).

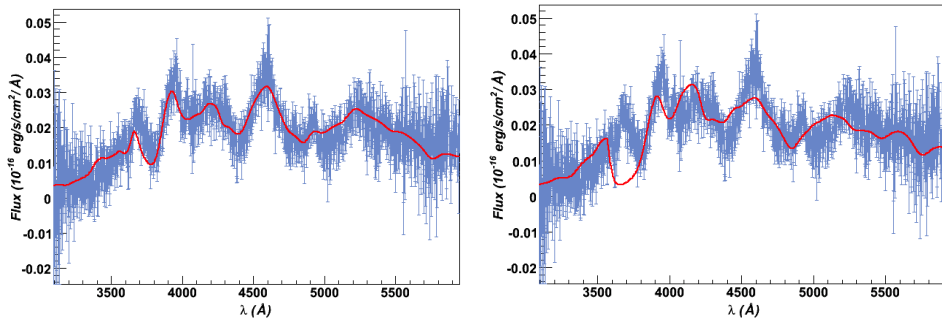


Fig. 2. SN 04D2cf (blue) at $z=0.368$ with phase=8.48 days, fitted by the models (red). **Left:** 24 days W7 spectrum (best fit) **Right:** 20 days DD25 spectrum.

On the contrary, for some supernovae, DD25 is favoured by the data, as shown in Fig. 3 for SN 04D2an, a supernova at $z = 0.362$ with a phase of -3.39 days. Again, the UV part is the discriminant zone of the spectrum.

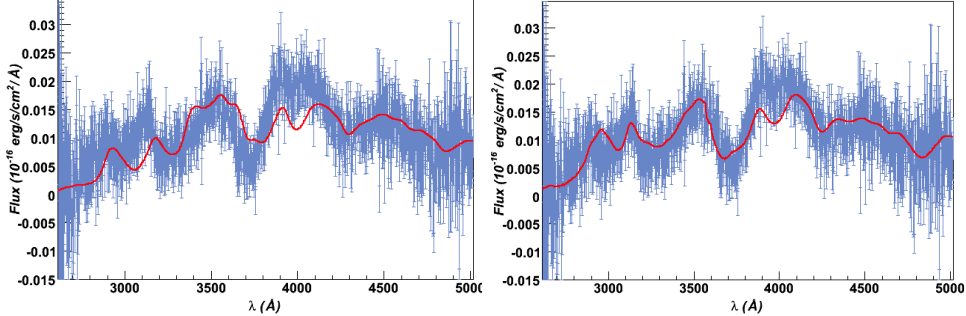


Fig. 3. SN 04D2an (blue) at $z=0.362$ with phase= -3.39 days, fitted by the models (red). **Left:** 16 days W7 spectrum **Right:** 14 days DD25 spectrum (best fit).

4.2 Do the data really discriminate the models ?

We test the null hypothesis that the models reproduce equivalently well the data. For this purpose, we perform a F-Test : for each fit, we compute the χ^2 ratio $F = \chi_1^2 / \chi_2^2$ where 1 is the model with the smaller χ^2 (W7 or DD25). This F quantity follows a Fisher probability law. If the F probability $P(F) \simeq 1$, the hypothesis is true and the data cannot discriminate the models. On the contrary if $P(F) \ll 1$, the hypothesis is false and one of these two models is favoured (model with the smallest χ^2). We consider that observations can discriminate models when the probability is smaller than 5% (choosing another cut do not change the results). Among the 51 observed spectra, 21 pass this cut. We end up with two subsamples : one for the W7 best fit spectra, and the other for DD25.

We now investigate if these subsamples represent different populations of type Ia supernovae. For this purpose, we compare the average photometric properties of these two subsamples (Table 1).

	$\langle M_B \rangle$	$\langle s \rangle$	$\langle c \rangle$	host type
W7 (13 spectra)	-19.20 ± 0.04	1.014 ± 0.024	-0.021 ± 0.018	50% early-type - 50% spiral
DD25 (8 spectra)	-19.30 ± 0.04	1.048 ± 0.022	0.003 ± 0.021	17% early-type - 83% spiral

Table 1. Average photometric properties of the two subsamples best fitted by W7 or DD25 (errors are errors on the mean).

First, we compare the average absolute magnitude $\langle M_B \rangle$ of the two subsamples (column 2 of Table 1). We find that DD25 fits better brighter SNeIa (with a smaller M_B , $\langle M_B \rangle = -19.30 \pm 0.04$) than W7 ($\langle M_B \rangle = -19.20 \pm 0.04$).

Column 3 of Table 1 shows the average stretch $\langle s \rangle$ (stretch is a light-curve shape parameter). SNeIa best fitted by DD25 have a marginally higher stretch ($\langle s \rangle = 1.048 \pm 0.022$) than SNeIa best fitted by W7 ($\langle s \rangle = 1.014 \pm 0.024$). This is consistent with the well known *brighter-slower* empirical correlation observed for SNeIa.

Another empirical correlation, called *brighter-bluer*, exists for SNeIa between the luminosity and the color c . Column 4 of Table 1 shows that there is not significant difference between the color of the W7 ($\langle c \rangle = -0.021 \pm 0.018$) and the DD25 subsample ($\langle c \rangle = 0.003 \pm 0.021$).

Finally, column 5 of Table 1 shows a correlation between the SNeIa and the host galaxy : brighter supernovae are preferentially in spiral galaxy and fainter SNeIa in early type galaxy (elliptic). It seems that DD25 reproduces this tendency (83% in an spiral galaxy) but it is less visible for W7 (50% in an early type galaxy).

To summarize, W7 fits better on average fainter supernovae with a smaller stretch and DD25, brighter supernovae in spiral galaxy with an higher stretch. We do not find color difference between the subsamples best fitted by W7 and DD25.

4.3 Why is a model favoured by the data ?

As stated earlier, a large of W7 and DD25 spectral differences can be attributed to the Ca II feature ($\lambda \sim 3700\text{\AA}$). We compute the equivalent width of Ca II (EW Ca) for synthetic spectra. The time evolution of EW Ca is shown on the left panel of Fig. 4. Notice that EW Ca for DD25 is twice as big as for W7 : the Ca II absorption line predicted by DD25 is deeper than for W7. The right panel of Fig. 4 shows the EW Ca computed for the observed spectra best fitted by W7 (red points) and for spectra best fitted by DD25 (blue points) for phases from -5 days to 12 days. DD25 is clearly favoured by earlier phases spectra because the EW Ca for W7 spectra is too small compared to the data. For post maximum phases, the EW Ca for DD25 spectra is too big compared to the data and W7 is thus favoured.

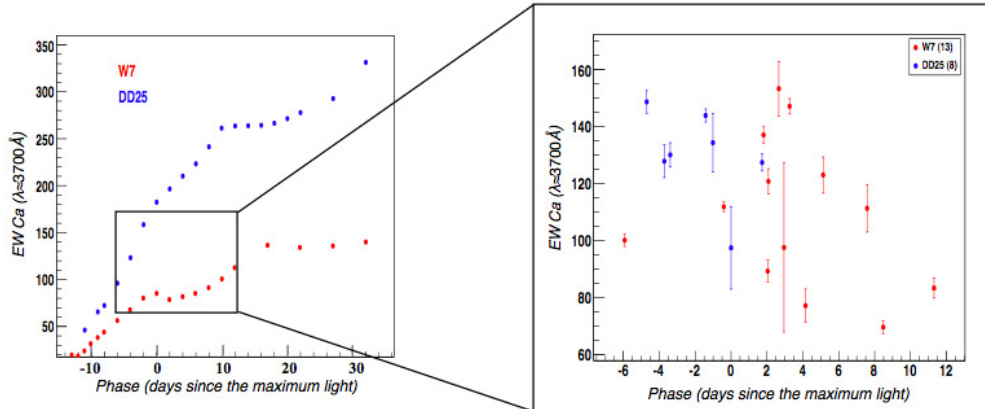


Fig. 4. Time evolution of EW Ca **Left:** for W7 (red) and DD25 (blue) model spectra **Right:** Same as left for the two observed spectra subsamples best fitted by W7 (red) and DD25 (blue). The ranges of EW Ca values and phases match those shown in the box on the left panel.

5 Conclusions

We have shown that SNLS spectral data have the power to discriminate some models. Better quality spectra from the SuperNova Factory (SNFactory) will allow us to confirm this result in the near future. We also plan to use a larger set of models to broaden the physical parameter space describing SNeIa. Our goal is to improve these models, reproduce the differences between SNeIa and understand their physical properties for a better calibration of SNeIa for cosmological use.

References

- Astier, P., Guy, J., Regnault, N. et al. 2006, A&A, 447, 31
- Balland, C., Baumont, S., Basa, S. et al. 2009, A&A, 507, 85
- Conley, A., Guy, J., Sullivan, M. et al. 2011, ApJS, 192, 1
- Guy, J., Sullivan, M., Conley, A. et al. 2010, A&A, 523, A7
- Hoefflich, P., Gerardy, C. L., Fesen, R. A. et al. 2002, ApJ, 568, 791
- Khokhlov, A. M. 1991, A&A, 245, 114
- Nomoto, K., Thielemann, F.-K., & Yokoi, K. 1984, ApJ, 286, 644
- Perlmutter, S., Aldering, G., Goldhaber, G. et al. 1999, ApJ, 517, 565
- Riess, A. G., Filippenko, A. V., Challis, P. et al. 1998, AJ, 116, 1009
- Sullivan, M., Howell, D. A., Perrett, K. et al. 2006, ApJ, 131, 960

A REIONISATION SCENARIO FROM HII REGIONS MERGERS HISTORIES

J. Chardin¹ and D. Aubert¹

Abstract. We describe a methodology to analyse the reionisation in numerical simulations. We particularly focus on the merger history of HII regions during the process. For this purpose, we identified the HII regions using a *friend-of-friend* algorithm and then derived the merger tree of these regions. By investigating the properties of evolving ionised regions thanks to the merger tree, we propose a typical scenario of the reionisation.

Keywords: Reionisation, HII regions, first stars, Methods: numerical

1 Introduction

Recent progress in numerical simulations (see Trac & Gnedin 2009 for a complete review of these models) permit us to add radiative transfer runs on hydrodynamics data. In this context, one challenge is to describe the chrono-geometry of the reionisation process through cosmological simulations. This will be an helpful tool in order to overtake forthcoming observations with new large-area radio interferometers like SKA (<http://www.skatelescope.org/>) and LOFAR (<http://lofar.org/>).

We aim here at investigating the time sequence of the reionisation in simulations. For this purpose, we adopt an alternative method by tracking the HII regions and derivating their merger tree. As a result, we embrace a ‘local’ perspective with histories of reionisation instead of ‘global’ rationale commonly used. We apply this technique to a large-scale cosmological simulation of reionisation and propose a scenario in this context.

2 Methodology

2.1 Simulation

This work was developed on a numerical simulation of reionisation fully described in Aubert & Teyssier (2010). The hydrodynamic of the gas is performed with the RAMSES code (Teyssier 2002) and the radiative transfer is post-processed with the ATON code (Aubert & Teyssier 2008). The simulation is a comoving 50 Mpc/h box produced on a 1024^3 coarse grid. The simulation is performed from $z \sim 14$ to $z \sim 6$ when the reionisation is achieved.

2.2 Friend-of-friend algorithm

The first step of our purpose is the identification of individual HII regions in each snapshots of the simulation. The rule we adopt is that each cell of our cosmological box with a ionisation fraction $x > 0.5$ is considered as ionised. Then, when we encounter a ionised cell we allocate to it an identification number corresponding to the ionised region being tested. With the help of a *friend-of-friend* algorithm we allocate to the ionised nearest neighbors of this cell the identification of the HII regions being explored. We are thus able to separate all the ionised region and to keep track of each of them with the identification number.

¹ Observatoire Astronomique de Strasbourg, Université de Strasbourg, CNRS UMR 7550, 11 rue de l’Université, F-67000 Strasbourg, France

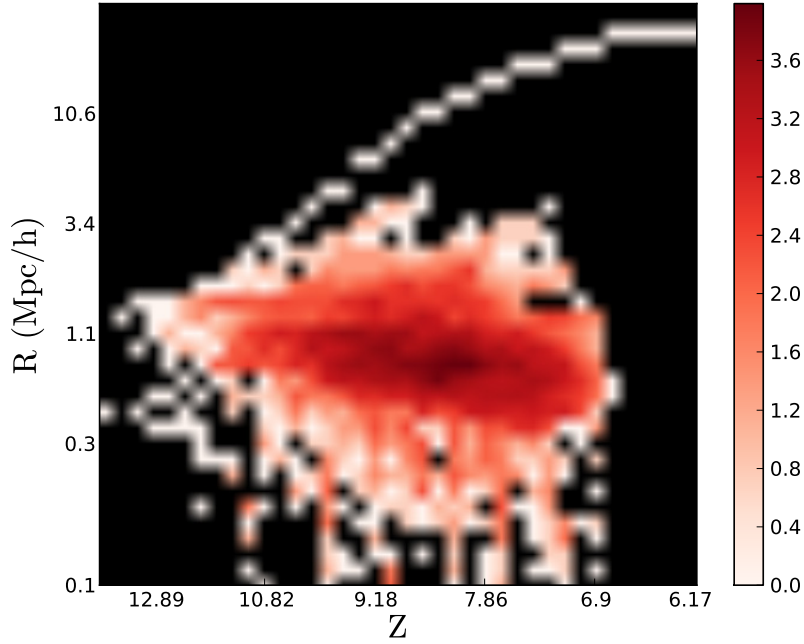


Fig. 1. Redshift radius distribution of HII regions. The color code is an arbitrary logarithm scale of the number of counts.

2.3 Merger tree

The second step is the derivation of the merger tree of these regions to follow them with time. In order to follow the evolution of the properties of each HII region we track the evolution of its identification number. In practice, we extract where are located the cells of an HII region at time t and look at the identification number that they received at time $t + 1$. We then link the two identification number between the two snapshots. We repeat this process for all the HII regions and between all the snapshots of the simulation.

3 Results

3.1 HII regions size

By firstly focusing on the size distribution of HII region with redshift (figure 1), we find that the typical radius of ionised patches is ~ 1 Mpc/h during the entire period simulated. Moreover, we observe that HII regions reach rarely a radius above 3 Mpc/h. We also find the emergence of a single dominant HII region in size which appear early in the simulated reionisation. We are able to follow this particular region with the merger tree and we will show that it has a key role in our reionisation scenario. Intuitively, the ionised regions reach the critical value of 3 Mpc/h in radius before merging with the main one.

3.2 Analysing the merger tree

Thanks to the merger tree we can investigate some properties related to the HII regions. We summarize them below:

- The number of new HII regions between two snapshots.
- The number of ionised regions resulting from mergers between two snapshots.
- The number of parents involved for an HII region resulting from mergers.
- The number of mergers that occurs between two snapshots.

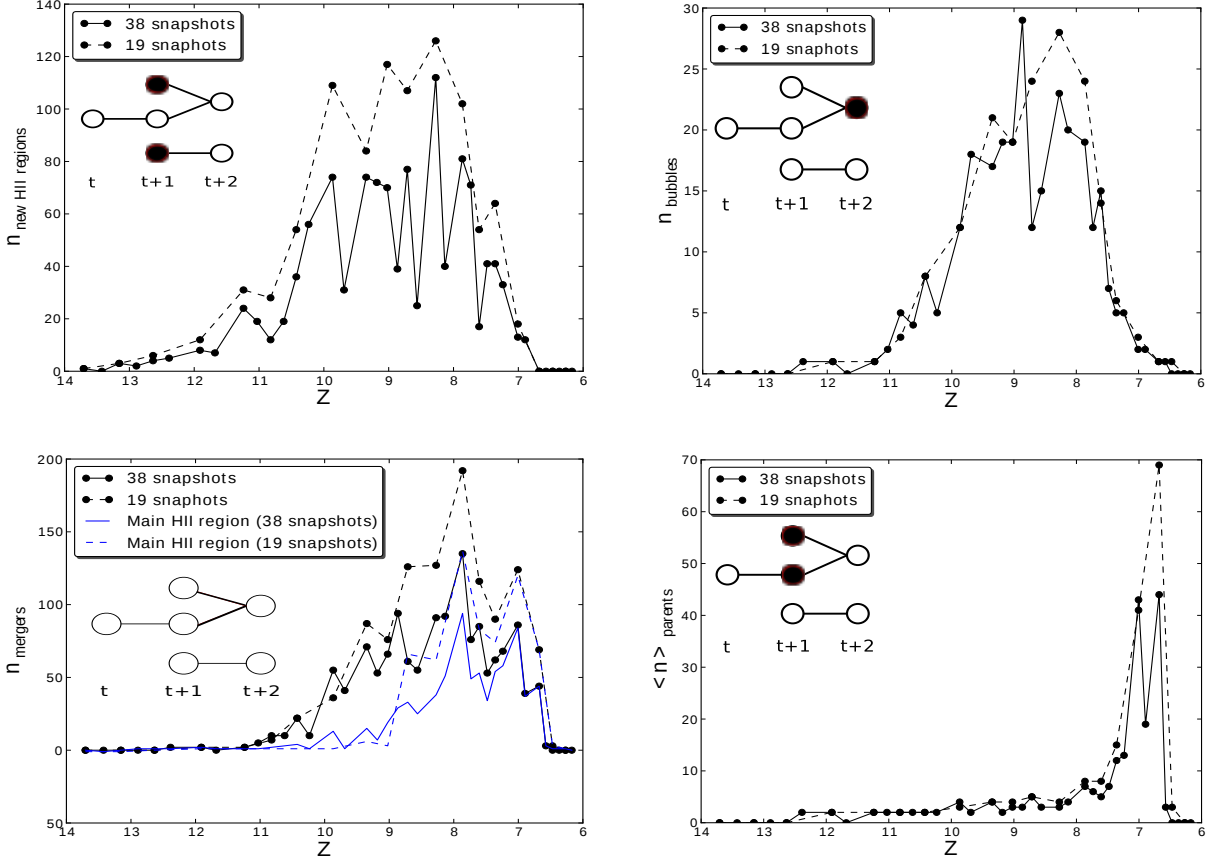


Fig. 2. The redshift evolution of the typical properties investigated by the merger tree. The number of new HII regions (*top left*), the number of HII regions resulting from merger (*top right*), the number of mergers that occur between two snapshots (*bottom left*) and the average number of parents for HII regions resulting from mergers (*bottom right*). We represent also the number of mergers involving the main HII region with the blue line in the *bottom left* panel. Each little diagram represent the typical HII regions considered.

In figure 2 we can see the redshift evolution of these properties for two snapshots sampling (for the 38 snapshots of our simulation and by taking one snapshot over two which correspond to 19 snapshots).

We see that the merger process is concentrated between $z \sim 11$ and $z \sim 7$ by looking at the *top right* and *bottom left* panel of figure 2. From $z \sim 9$ mergers are dominated by the main HII regions and at $z \sim 7$ this region is responsible of all the mergers (*bottom left* of figure 2).

We remark that there is a significant number of birth of HII regions up to $z \sim 7$ (*top left*). But at the same time the merger process is also very marked. An explanation is that the merger seems to be localized in a certain region of space. These concentrated merger would build the main HII region in a clustered area.

In the *bottom right* panel we see that the averaged number of parents for ionised regions resulting from mergers growth dramatically. This would be the moment where the main HII region merge very efficiently with the other remaining. This moment could be seen as the end of the reionisation in terms of HII regions.

3.3 A reionisation scenario

From the properties analysed in the previous section, we are able to propose a reionisation scenario in terms of HII regions in the context of our simulation. We propose to summarize here the main key period that emerge from the curve in figure 2:

- Between $14 > z > 12$ the first sources begin to appear in the simulated volume.

- Between $12 > z > 11$ the sources birth is marked but the merger process between them is not efficient.
- Between $11 > z > 8.5$ the first merger appear locally and lead to the construction of a main HII region in size.
- At $z \sim 8$, the space is saturated in terms of isolated HII regions. This is the typical turning point where the merger process dominate the HII regions formation rate.
- Between $8 > z > 7$ there is a intense period of merger mainly dominated by the main region.
- At $z \sim 7$, the main HII region finally merge with the others remaining. This can be seen as the redshift of reionisation in terms of HII regions.

4 Conclusions

By applying a new technique to characterize the chronology and the geometry of reionisation, we have determined some key period in the course of the process. We have also proposed a scenario for the particular case of our simulation. In the future, we will apply systematically this technique in order to understand how the physical ‘ingredients’ in the simulation will influence the chrono-morphology of the reionisation. Finally, the merger tree developed promise to be an helpful tool for other kind of work like the reionisation around particular objects in the simulations. We will in forthcoming work use it to characterize the ‘HII region object’ in regard to the cosmological environment where it is expanding.

We want to thank B.Semelin, P Ocvirk, R. Teyssier and H. Wozniak for comments and discussion. This work is supported by the LIDAU ANR.

References

- Aubert, D. & Teyssier, R. 2008, MNRAS, 387, 295
Aubert, D. & Teyssier, R. 2010, ApJ, 724, 244
Teyssier, R. 2002, A&A, 385, 337
Trac, H. & Gnedin, N. Y. 2009, ArXiv e-prints (astro-ph/0906.4348)

THE INFLUENCE OF THE ENVIRONMENT IN COMPACT GALAXY GROUPS: AN INFRARED PERSPECTIVE

V. Charmandaris¹ and T. Bitsakis²

Abstract. We present a comprehensive study on the influence of the environment of compact galaxy groups to the evolution of their members using a multi-wavelength analysis, from the UV to the far-IR, on a sample of 32 Hickson Compact Groups (HCGs) containing 135 galaxies. Fitting the SEDs of all galaxies with the state-of-the-art model of da Cunha et al. (2008) we can accurately calculate their mass, SFR, and extinction, as well as estimate their infrared luminosity and dust content. We contrast our findings with control samples of field galaxies, early-stage interacting pairs, and galaxies in clusters.

We find that classifying the evolutionary state of HCGs as dynamically “old” or “young” depending on whether or not they contain more than 25% of early-type galaxies is physical and consistent with past classifications based on their gas content. Late-type galaxies in dynamically “young” groups have sSFR, as well as NUV-r and mid-infrared colors, which are similar to those of field and early stage interacting pairs. However, late-type galaxies in dynamically “old” groups have redder NUV-r colors, as they have likely experienced several tidal encounters in the past and built up their stellar mass, and they display lower sSFRs. Finally our model suggests that in 13 groups, 10 of which are dynamically “old”, there is diffuse dust in the intragroup medium.

All these evidence point to an evolutionary scenario in which it takes time for the group environment to visibly affect the properties of its members. Early on the influence of close companions to group galaxies is similar to the one of galaxy pairs in the field. However, as the time progresses, the effects of tidal torques and minor merging shape the morphology and star formation history of the group galaxies, leading to an increase of the fraction of early type members and a rapid built up of the stellar mass in the remaining late type galaxies.

Keywords: Infrared: galaxies, Galaxies: evolution, Galaxies: interactions, Galaxies: star formation

1 Introduction

It has become increasingly evident that interactions and merging of galaxies have contributed substantially to their evolution, both in terms of their stellar population as well as their morphological appearance. Compact galaxy groups, with their high galaxy density and signs of tidal interactions among their members, are ideal systems to study the impact on environment to the evolution of galaxies. The Hickson Compact Groups (HCGs) are 100 systems of typically 4 or more galaxies in a compact configuration on the sky (Hickson 1982) They contain a total of 451 galaxies and are mostly found in relatively isolated regions where no excess of surrounding galaxies can be seen, reflecting a strong local density enhancement. The HCGs occupy a unique position in the framework of galaxy evolution, bridging the range of galaxy environments, from field and loose groups to cores of rich galaxy clusters. The fact that the original selection of the HCG members did not include redshift information, led to the inclusion of interlopers among them, the most famous being NGC 7320 in Stephan’s Quintet (HCG 92). This led to a debate as to whether compact groups are line-of-sight alignments of galaxy pairs within loose groups, or filaments seen end-on (Mamon 1986; Hernquist et al. 1995). However, the detection of hot X-ray gas in $\sim 75\%$ of the HCGs by Ponman et al. (1996) implies that they reside in a massive dark matter halo and thus are indeed physically dense structures. Numerical simulations indicate that in the absence

¹ Department of Physics & ITCP, University of Crete, GR-71003, Heraklion, Greece, and Chercheur Associé, Observatoire de Paris, F-75014, Paris, France

² Department of Physics, University of Crete, GR-71003, Heraklion, Greece

of velocity information, raising the minimum surface brightness criterion for the group used by Hickson would help eliminate interlopers (see McConnachie et al. 2008).

Because of the nature of these groups, the high density enhancements in addition to the low velocity dispersions ($\sim 250 \text{ km s}^{-1}$), make them ideal to study the effects of galaxy interactions. Hickson (1982) found that the majority of HCGs display an excess of elliptical galaxies, $\sim 31\%$ of all members compared to the field, while the fraction of spiral galaxies and irregular is only 43%, nearly a factor of two less of what is observed in the field. Optical imaging by Mendes de Oliveira & Hickson (1994) showed that 43% of all HCG galaxies display morphological features of interactions and mergers, such as bridges, tails and other distortions. Similar indications of interactions are seen in maps of the atomic hydrogen distribution in selected groups by Verdes-Montenegro et al. (2001). Moreover, Hickson (1989) found that the fractional distribution of the ratio of far-infrared (far-IR) to optical luminosity in HCG spiral galaxies is significantly larger than that of isolated galaxies, suggesting that for a given optical luminosity, spiral galaxies in groups have higher infrared luminosities. Comparison of HCG spirals with those in clusters of galaxies from Bica & Giovanelli (1987) reveals that the distributions of the IR to optical luminosity, as well as the 60 to $100 \mu\text{m}$ far-IR color are similar. Finally, nuclear optical spectroscopy studies indicate that almost 40% of the galaxies within these groups display evidence of an active galactic nucleus (AGN, Martinez et al. 2010; Shimada et al. 2000). All these clues are consistent with an evolutionary pattern where tidal encounters and the accretion of small companions by the group members, redistribute the gas content of the groups and affect the morphology of their members.

Verdes-Montenegro et al. (2001) and Borthakur et al. (2010) have proposed an evolutionary sequence for the HCGs based on the amount and spatial distribution of their neutral atomic gas. Using HI maps they classified the groups into three phases based on the ratio of the gas content within the galaxies over the total observed in the group. However, a necessary step to determine the evolutionary state of HCGs, is the analysis of not just the morphology of the group members, but of their stellar population and star formation history. In the present paper we summarize the work of Bitsakis et al. (2010) and Bitsakis et al. (2010) who presented a complete multiwavelength analysis and theoretical modeling of the spectral energy distribution (SED) of a compact group sample and we refer the reader to these papers for more details. The sample was constructed from the original Hickson (1982) catalogue of 100 groups, using as criterion the availability of high spatial resolution 3.6 to $24 \mu\text{m}$ mid-infrared imagery from the Spitzer Space Telescope archive, as well as UV imaging from GALEX. The infrared data are essential to probe the properties of the energy production in nuclei of galaxies, some of which may be enshrouded by dust, while the UV is necessary to properly estimate the effects of extinction and accurately account for the global energy balance when we model their SED. These constraints resulted in a sample of 32 compact groups containing 135 galaxies, 62 (46%) of which are early-type (E's & S0's) and 73 (54%) are late-type (S/SB's & Irr's). We collected a wealth of NUV/FUV (GALEX), optical (SDSS), near-IR (J,H,Ks), mid-IR (Spitzer), and far-IR (IRAS/Akari) for our sample, fitted their SED using the model of da Cunha et al. (2008), and derived their physical properties, such as: the stellar mass, star formation rate (SFR), specific SFR (sSFR), L_{IR} , and extinction (A_V). We compared our findings with a number of control samples including the well known SINGS, and LVL Spitzer samples, isolated galaxies, early-stage interacting systems (Smith et al. 2007), as well as galaxies in clusters (Haines et al. 2008).

2 HCG late-type galaxies

In order to study the star formation properties of HCGs groups, (Bitsakis et al. 2010) separated them into dynamically “young” and dynamically “old”. We classified a group as dynamically “young” if at least 75% of its galaxies are late-type. Conversely, a group is dynamically “old” if more than 25% of its galaxies are early-type. The fact that the group environment has played an important role in the evolution of its member galaxies, is evident since the fraction of early-type systems in groups is higher than what is found in the field. So one would expect that because of their proximity, the late-type galaxies in groups would display different star formation properties from the ones in the field. It is known that the sSFR, is a tracer of the star formation history of a galaxy, and galaxies in compact groups do experience multiple encounters with the various group members. We display in Fig. 1a (left) a histogram of the sSFR of the late type galaxies in our sample and compare it with late-type galaxies in the field, as well as early-stage interacting systems. Galaxies in dynamically “young” groups have a median sSFR of $8.51^{+4.07}_{-2.75} \times 10^{-11} \text{ yr}^{-1}$, while for galaxies in the dynamically “old” groups $\text{sSFR} = 2.75^{+2.03}_{-1.16} \times 10^{-11} \text{ yr}^{-1}$. Similarly, galaxies in interacting pairs have a $\text{sSFR} = 11.20^{+3.67}_{-2.70} \times 10^{-11} \text{ yr}^{-1}$ and in field galaxies $\text{sSFR} = 15.30^{+5.65}_{-4.29} \times 10^{-11} \text{ yr}^{-1}$. An analysis using two sided KS test indicates that there is no statistical difference between the samples of late-type galaxies in dynamically “young” HCGs and those of the

SINGs and interacting pair samples ($P_{KS} > 0.80$). However, the same KS test reveals that the late-type galaxies in dynamically “old” groups, having a median sSFR which is more than three times lower, can not be drawn from same parent distribution as the other three samples ($P_{KS} \sim 10^{-3}$). Investigating in more detail the reason for this disparity, we find that it cannot be attributed to depressed SFR but instead it is due to a substantially more massive stellar content ($\sim 3 \times 10^{10} M_{\odot}$), similar to what is found early-type systems.

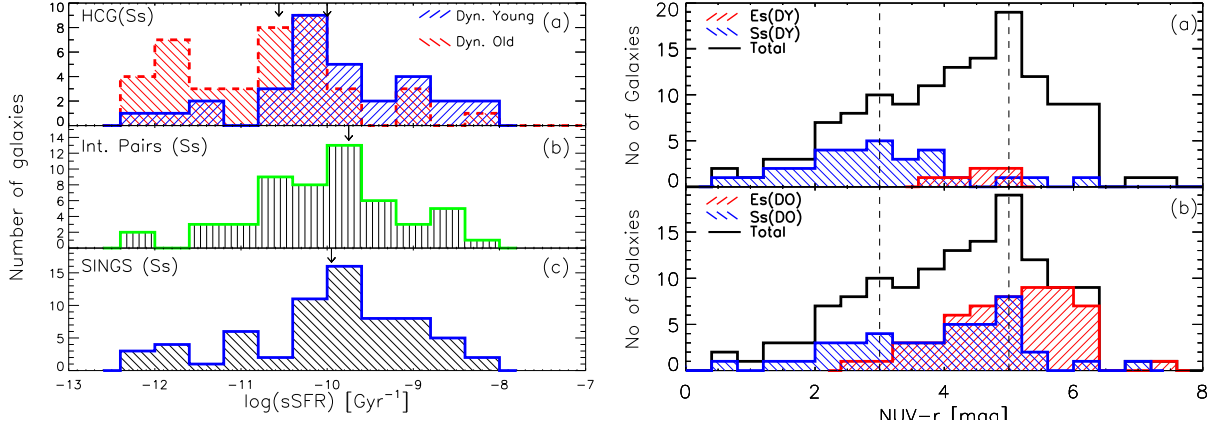


Fig. 1. Left: Histograms of the specific star formation, sSFR, of the late-type galaxies our three samples, estimated by modelling their SED. The top plot displays in blue the histogram of the sSFR of the 31 late-type galaxies found in dynamically-young, spiral-dominated groups. Over-plotted in red is the corresponding histogram of the 42 galaxies in dynamically-old elliptically dominated groups. The middle and bottom plots present the histograms of the 52 late-type galaxies in the Smith et al. (2007) interacting galaxy pairs, as well as the 71 SINGs late-type galaxies. The arrows indicate the median sSFR value of each distribution. **Right:** a) NUV-r histogram of our HCG galaxy sample shown in black solid line. The corresponding histograms of the early- and late-type galaxies found in dynamically “young” groups are shown with the red and blue shaded areas respectively. b) Same as in a), but for the galaxies in dynamically “old” groups. The region of $3 < \text{NUV-r} < 5$, identified as “green valley”, is marked with the vertical dashed lines.

3 Bimodality in HCG galaxy colors

In order to explore the color variations as a function of the evolution state of the groups, we plot in Fig. 1 (right) the histograms of the early- and late-type galaxies found in the dynamically “young” and “old” groups respectively. Observing the top right panel we find that almost 60% the late-type galaxies in dynamically “young” groups are located within the “blue cloud” and 43% of them, for which nuclear spectra were available, host an AGN in their nucleus. There are also three outlier galaxies which have red NUV-r colors ($> 5 \text{ mag}$). It is possible, that these systems have built up their stellar mass in the past and their UV/optical colors are currently dominated by emission from old stars. In addition, past tidal interactions probably stripped some of their gas in the intragroup medium decreasing the fuel necessary for current star formation. In dynamically “old” groups the late-type galaxies are redder and as we can see in Fig. 1 (bottom-right panel) most of them ($> 63\%$) are located within the “green valley”. As in dynamically “young” groups there are also four galaxies in these groups which are found in the “red sequence”. Since dust appears to affect the UV colors of HCG galaxies, we used our SED models and produced an extinction corrected NUV-r histogram similar to Fig. 1 (right). Furthermore, one could suggest the use of their mid-IR colors, because they trace the light which was originally absorbed by the dust grains in the UV-optical. In Fig. 12 of Bitsakis et al. (2011) we present an IRAC $f_{8.0\mu\text{m}}/f_{4.5\mu\text{m}}$ vs $f_{5.8\mu\text{m}}/f_{3.6\mu\text{m}}$ diagram and note that most of the late-type galaxies are located in the upper right quadrant of the plot (also displaying $\text{NUV-r} < 2.5$), while most of the early-types (which have $\text{NUV-r} > 3.5$) are in the lower left. This suggest that the color bimodality observed in the extinction corrected UV/optical colors, is also observed in the mid-IR and emerges from the same physical properties of the galaxies.

4 Conclusions

Based on the analysis of 135 galaxies residing in 32 Hickson Compact Groups Bitsakis et al. (2011) conclude the following:

- The classification of the evolutionary state of HCGs according to the fraction of their early-type members appears to be physical and is in general agreement with previous classifications. The study of their properties suggest that dynamically “old” groups are more compact and have higher velocity dispersions. They also display higher stellar masses than the “young” ones, while both have similar HI mass distributions. However, “old” groups have nearly an order of magnitude larger dynamical masses than “young” groups.
- The late-type galaxies in dynamically “old” groups display lower sSFRs since the multiple past interactions have already converted a fraction of their gas into stars increasing their stellar masses. This is also the main reason why these galaxies show redder NUV/optical colors than field spirals. However, there are few spiral galaxies in these groups which display even redder colors. They all have very small SFRs, similar to early-type systems. We speculate that tidal interactions must have stripped the gas out of their disk suppressing their star formation activity.
- Most early-type galaxies in dynamically “old” groups, seem to migrate from the star-forming to the quiescent galaxy colors, even though a fraction of them ($\sim 25\%$) display bluer colors and higher star formation activity than normal field ellipticals possibly due to gas accretion from other group members as well as merging of dwarf companions.
- Late-type galaxies in dynamically “young” groups have similar star formation properties to field spirals, as well as in early-stage interacting pairs.
- Even though nearly 46% of the HCG members have an optically identified AGN, we find no evidence of enhanced AGN activity at any stage of the group evolution, or the optical/mid-IR colors of the galaxies.
- Our analysis suggests that the reported lower density of galaxies in the IRAC color-color diagram is caused by the morphological natural bimodality of galaxies and it is similar to what is also observed in the UV-optical colors.
- Our SED model suggests that in 13 groups, 10 of which are dynamically “old”, there is diffuse cold dust in the intragroup medium.

References

- Bitsakis, T., Charmandaris, V., Le Floch, E., et al. 2010, *A&A*, 517, 75
 Bitsakis, T., Charmandaris, V., da Cunha, E., et al. 2011, *A&A*, (in press arXiv:1107.3418)
 Bica, M. D., & Giovanelli, R. 1987, *ApJ*, 321, 645
 Borthakur, S., Yun, M. S., & Verdes-Montenegro, L. 2010, *ApJ*, 710, 385
 da Cunha, E., Charlot, S., Elbaz, D. 2008, *MNRAS*, 388, 1595
 Haines, C. P., Gargiulo, A. & Merluzzi, P. 2008, *MNRAS*, 385, 1201
 Hernquist, L., Katz, N., & Weinberg, D. H. 1995, *ApJ*, 442, 57
 Hickson, P. 1982, *ApJ*, 255, 382
 Hickson, P., Kindl, E. and Auman, J. R. 1989, *ApJ*, 70, 687
 Mamon, G. A. 1986, *ApJ*, 307, 426
 Martinez, M. A., Del Olmo, A., Coziol, R., Perea, J. 2010, *AJ*, 139, 1199
 Martinez-Badenes et al. 2011, *A&A*, (submitted)
 McConnachie, A. W., Ellison, S. L., & Patton, D. R. 2008, *MNRAS*, 387, 1281
 Mendes de Oliveira, C. & Hickson, P. 1994, *ApJ*, 427, 684
 Ponman, T. J., Bourner, P. D. J., Ebeling, H., Bohringer, H. 1996, *MNRAS*, 283, 690
 Shimada, M., Ohya, Y., Nishiura, S., Murayama, T., & Taniguchi, Y. 2000, *AJ*, 119, 2664
 Smith, B. J., Struck, C., Hancock, M., et al. 2007a, *AJ*, 133, 791
 Verdes-Montenegro, L., Yun, M. S., Williams, B. A., et al. 2001, *A&A*, 377, 812

THE STAR FORMATION RATE DENSITY AND DUST ATTENUATION EVOLUTION OVER 12 GYR WITH THE VVDS SURVEYS

O. Cucciati¹, L. Tresse¹, O. Ilbert¹ and O. Le Fèvre¹

Abstract.

We investigate the cosmic star formation rate density (SFRD) over ~ 12 Gyr ($0.05 \leq z \leq 4.5$), combining the VVDS Deep ($17.5 \leq I_{AB} \leq 24.0$) and Ultra-Deep ($23.00 \leq i'_{AB} \leq 24.75$) surveys. We obtain a single homogeneous spectroscopic redshift sample, totalizing about 11000 galaxies. We estimate the rest-frame FUV luminosity function (LF) and luminosity density (LD), extract the dust attenuation of the FUV radiation using SED fitting, and derive the dust-corrected SFRD. We find a constant and flat faint-end slope α in the FUV LF at $z < 1.7$. The absolute magnitude M_{FUV}^* brightens in the entire range $0 < z < 4.5$, and at $z > 2$ it is on average brighter than in the literature, while ϕ^* is smaller. Our total LD shows a robust peak at $z \simeq 2$, and the SFRD history peaks as well at $z \simeq 2$. This peak is produced by the decreasing contribution at $z < 2$ of galaxies with $-21.5 \leq M_{FUV} \leq -19.5$ mag. As times goes by, the total SFRD is dominated by fainter and fainter galaxies. Moreover, at $z > 2$ the SFRD is entirely shaped by the high specific SFR galaxies. The presence of a fast rise at $z > 2$ and of a clear peak at $z \simeq 2$ of the SFRD is compelling for models of galaxy formation. The mean dust attenuation A_{FUV} of the global galaxy population rises by 1 mag from $z = 4.5$ to $z = 2$, reaches its maximum at $z = 1$ ($A_{FUV} \simeq 2.2$ mag), and then decreases by 1.1 mag down to $z = 0$. The dust attenuation maximum is reached 2 Gyr after the SFRD peak, implying a contribution from the intermediate-mass stars to the dust production at $z < 2$.

Keywords: cosmology: observations, galaxies: evolution, luminosity function, high-redshift - star formation

1 Data analysis

This work is extensively described in Cucciati et al. (2011). We use ~ 11000 galaxies with spectroscopic redshift within $0.05 < z \leq 4.50$ taken from the VVDS Deep ($17.5 \leq I_{AB} \leq 24.0$, ~ 2100 arcmin²) and Ultra-Deep ($23.00 \leq i'_{AB} \leq 24.75$, ~ 500 arcmin²) surveys (Le Fèvre et al. 2005 and Le Fèvre et al. in prep.). We use the available photometric data (the *BVI* with CFHT-12K camera, the *u*r'i'z'* with the MEGACAM camera and the *JHK_s* bands with the WIRCAM camera,) to derive the FUV-band intrinsic luminosities with a SED fitting technique (Algorithm for Luminosity Function, ALF, Ilbert et al. 2005). We choose the template library from Bruzual & Charlot (2003) modulated by the attenuation of the intrinsic stellar continuum, $A(\lambda) = k(\lambda)E(B-V)$, where $E(B-V)_{star}$ is the intrinsic colour excess of the stellar continuum of a galaxy, and $k(\lambda)$ is the starburst reddening curve in Calzetti et al. (2000).

In this work, we have primarily estimated the rest-frame FUV luminosity functions (LF) and densities (LD) to derive the SFRD history. The recent SFR is traced by the intrinsic non-ionising ultraviolet stellar continuum (91.2 – 300 nm) of galaxies. Within this UV range, the far UV radiation (FUV-150) is a better SFR indicator than the near UV radiation (NUV-250), because the NUV is contaminated by evolved stars, while the FUV is dominated by the radiation from new, massive, short-lived stars (see, e.g., Madau et al. 1998).

The galaxy luminosity function (LF) usually follows a Schechter (1976) function characterised by a break luminosity, L^* , a faint-end slope, α , and a normalisation density parameter, ϕ^* . We derive the FUV-band LF in 10 different redshift bins, using our code ALF that includes the non-parametric $1/V_{max}$, SWML, and C^+ and the parametric STY luminosity function estimators (see Appendixes in Ilbert et al. 2005, and references therein). Our LF parameters are estimated with data brighter than the LF bias limit. We compute the rest-frame FUV

¹ Laboratoire d'Astrophysique de Marseille (UMR 6110), CNRS-Université de Provence, 38 rue Frédéric Joliot-Curie, F-13388 Marseille Cedex 13, France

LFs using a unique merged catalogue which includes both the Deep and Ultra-Deep surveys, for a total covered magnitude range of $17.5 \leq I_{AB} \leq 24.75$. This way, we exploit both the large magnitude range covered by the Deep survey and the depth reached by the Ultra-Deep survey. This leads us to a robust determination of the LF shape and normalisation.

We derive the mean comoving luminosity density (LD) in each redshift bin as $LD = \int_{L_{faint}}^{L_{bright}} \phi(L) L dL$, where $\phi(L)$ is the luminosity function assuming a Schechter (1976) functional form. We set $L_{faint} = 10^{15} \text{ W Hz}^{-1}$ and $L_{bright} = 10^{25} \text{ W Hz}^{-1}$ (corresponding to $M_{faint} \sim -3.4$ and $M_{bright} \sim -28.4$). Our LD uncertainties include errors from the STY LF fit, errors due to cosmic variance, Poisson noise, and errors associated to our weighting scheme.

We derived the FUV-band dust attenuation A_{FUV} in the following way. Our template SED fitting assigns to each galaxy a value of $E(B - V)_{star}$ chosen from a grid of five possible values (0.1, 0.2, 0.3, 0.4, 0.5). In each studied redshift bin, we compute our resulting average $E(B - V)_{star}$. Then, to compute the mean A_{FUV} in each redshift bin, we follow the prescription in Calzetti et al. (2000), that is, $A(\lambda) = E(B - V)_{star} k(\lambda)$. Fig. 1 shows our A_{FUV} determination as a function of redshift.

We computed the dust corrected SFRD from our LD, transforming FUV fluxes into star formation rates with the FUV-SFR calibration of Madau et al. (1998), and correcting for the dust attenuation. We use the formula $SFRD(z) = 1.4 \cdot 10^{-28} LD_{FUV}(z) 10^{0.4 A_{FUV}(z)}$, where the SFRD is in $M_{\odot} \text{ yr}^{-1} \text{ Mpc}^{-3}$ units and the LD in $\text{erg s}^{-1} \text{ Hz}^{-1} \text{ Mpc}^{-3}$. Our SFRD is shown in Fig. 2 and Fig. 3.

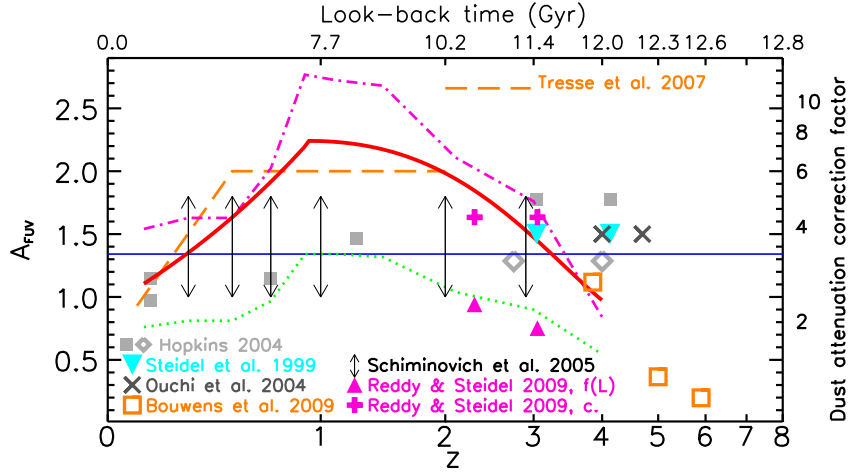


Fig. 1. Dust attenuation A_{FUV} in magnitudes as a function of redshift as found in this work (thick solid red curve). Magenta dot-dashed curve: average A_{FUV} determined in this work using the recipe in Meurer et al. (1999), based on the β slope. Green dotted curve: same as the dot-dashed one, but using the recipe in Cortese et al. (2006). Thin blue horizontal solid line: constant A_{FUV} computed with the Calzetti's law using one single typical value of $E(B - V)$ ($=0.13$). The right $y - axis$ shows the multiplicative factor to be applied to the observed luminosities, i.e., $10^{0.4 A_{FUV}}$. All the other symbols represent dust attenuations found in literature, as indicated in the labels.

2 Results

Our result is an improvement with respect to the similar study of the FUV-band LD in Tresse et al. (2007), that was based on our first VVDS-Deep spectroscopic sample (Le Fèvre et al. 2005) and our UVBRI photometric sample (Le Fèvre et al. 2004). Our findings can be summarised as follows.

- We find a flat and constant faint-end slope in the FUV-band LF at $z < 1.7$ ($\alpha \sim 1$). We verified that this is unlikely to be the result of missing faint galaxies from our I -band selection, and that dust may have a role. At $z > 1.7$, we set α evolving with $(1 + z)$, and this way it becomes as steep as -1.73 at $z \simeq 4$, consistent with values from deep photometric studies. M_{FUV}^* increases by ~ 4 mag from $z \sim 0$ to $z \sim 4.5$, while ϕ^* starts decreasing at $z > 0.7$. We find that at $z = 2, 3, 4$ our M_{FUV}^* is on average brighter than what has been found in previous works, and that ϕ^* is on average smaller, in particular at $z \sim 4$.

- We derived the evolution of the dust-attenuation in the FUV-band (A_{FUV} , see Fig. 1) in the range $0.05 < z \leq 4.5$, using a SED fitting method, in a consistent way from a single survey with a well controlled selection function. We find a continuous increase of A_{FUV} by ~ 1 mag from $z \sim 4.5$ to $z \sim 1$, then a decrease by the same amount from $z \sim 1$ to $z \sim 0$. This is the first time that the A_{FUV} evolution has been assessed homogeneously on such a broad redshift range.
- We traced the dust-corrected SFRD evolution over the past ~ 12 Gyr (see Fig. 2 and 3). Thanks to the homogeneity of our data over such a cosmic time, we have been able to unveil the presence of a peak at $z \sim 2$ in the cosmic SFR history. This peak is preceded by a rapid increase by a factor 6 from $z \sim 4.5$, then followed by a general decrease by a factor 12 to $z \sim 0$. We remark that the epoch of the peak of the dust-corrected SFRD ($z \sim 2$) does not coincide with that of the maximum of the dust attenuation evolution ($z \sim 1$), and that a peak at $z \sim 2$ is already present in the evolution of our LD.
- We find that as times goes by, the total SFRD is dominated by fainter and fainter galaxies. Moreover, the presence of a SFRD peak at $z \sim 2$ is due to a similar peak within the population of galaxies with $-21.5 \leq M_{FUV} \leq -19.5$, while the most extreme star-forming galaxies reaches their maximum activity at higher redshift (see Fig. 4). Finally, we find that the shape of the SFRD evolution at $z > 2$ is entirely due to galaxies with large specific SFR.

Our data therefore consistently show a peak in the LD and SFRD at $z \sim 2$, where the LF is well constrained. While the decrease in SFRD at $z > 2$ is not in question, the exact amplitude of this decrease remains to be investigated, as the faint end slope of the LF is still unconstrained even from our very deep spectroscopic survey.

3 Conclusions

The correct determination of the shape of the SFRD evolution is necessary to understand which physical processes mostly affect galaxy evolution. The SFRD is the result of the transformation of gas into stars and therefore requires a significant gas reservoir to sustain a strong star formation rate for a long time. A number of processes are expected to modify the gas reservoir hence the SFR, including the efficiency of star formation, cold accretion along the cosmic web filaments, mergers with gas-rich galaxies, stellar feedback, SN feedback blowing gas out from the galaxy core, AGN feedback, cosmic photoionizing radiation, or environment effects which may result in star formation quenching (e.g., among many others, White & Frenk 1991; Efstathiou 1992; Cole et al. 1994, 2000; Di Matteo et al. 2005; Baugh 2006; Cox et al. 2008; Dekel et al. 2009; de Ravel et al. 2009). The exact balance of these different processes along cosmic time will result in the observed SFRD. The SFRD peak that we find at $z \simeq 2$ is produced by intermediate luminosity galaxies, requiring that significant gas reservoirs still exist at this epoch and are probably replenished by cold accretion and wet mergers, while feedback or quenching processes are not yet strong enough to lower the SF. Knowing the SFRD, we may hope to identify the relative contribution of these different processes at different epochs.

Using simulations (semi-analytical galaxy evolution models, smoothed particle hydrodynamics simulation), several authors have attempted to reproduce the observed Cosmic Star Formation History with theoretical predictions (e.g. Baugh et al. 2005; Somerville et al. 2008; Hopkins et al. 2010; van de Voort et al. 2011). As a recent example, Weinmann et al. (2011) start from a standard model of galaxy evolution, and produce slightly different versions of it by tuning one or more ingredients at a time (such as star formation efficiency, stellar feedback, merger processes...). All of their models (see their Fig. 10) reproduce qualitatively the fast SFRD increase from $z \sim 0$ to $z \sim 1$, but at $z > 1$ the predicted SFRDs have different behaviours, showing growths at different rates, in some cases a plateau, and a more or less delayed decrease at higher redshifts. It is worth noticing that one of the models (where feedback has been tuned) predicts a sharp peak in the SFRD evolution at $z \sim 1.5$, qualitatively similar to the one that we find at $z \sim 2$. It is not the aim of this work to compare in details our findings with model predictions, and we will address this issue in more details in a future work. Here we want only to stress the importance of bringing strong observational constraints on the SFRD from a unique and homogeneous galaxy sample covering a large cosmic time of ~ 12 Gyr, which will need to be reproduced by next generation models.

Another remarkable finding of our work is that the peak of the dust and the SFR do not coincide, differently from what one could have naively thought in the case the dust is immediately released into the ISM a short time after supernova explosions of massive, short-lived stars which dominate the SFR. These two peaks are separated by ~ 2.5 Gyr, which is a long period if one considers that the dust production rate peak is below 1 Gyr for

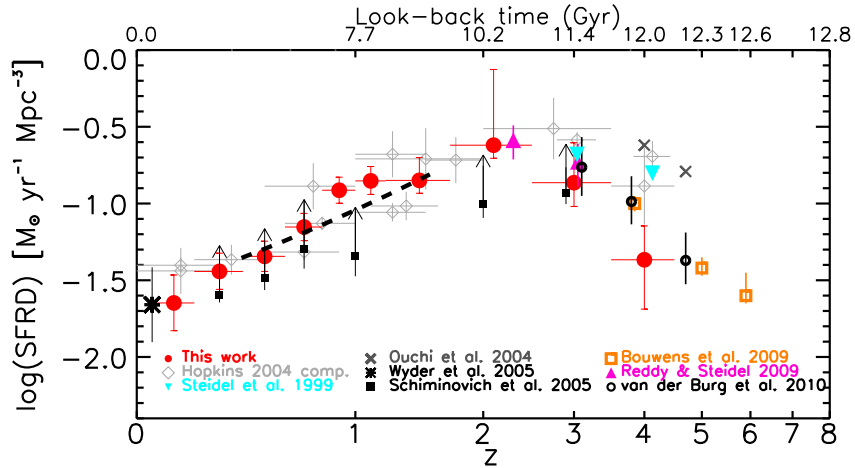


Fig. 2. Total dust-corrected UV-derived SFRDs as a function of redshift from the VVDS Deep+Ultra-Deep sample (red filled circles). Uncertainties are explained in the text. The black dashed line is the SFRD(z) implied from the stellar mass density in Ilbert et al. (2010). We overplot other results from the literature, as detailed in the labels. All SFRDs in this plot are derived using the FUV-band LDs converted into SFRD with the scaling relation from Madau et al. (1998). All data have been homogenised with the same IMF (Salpeter 1955).

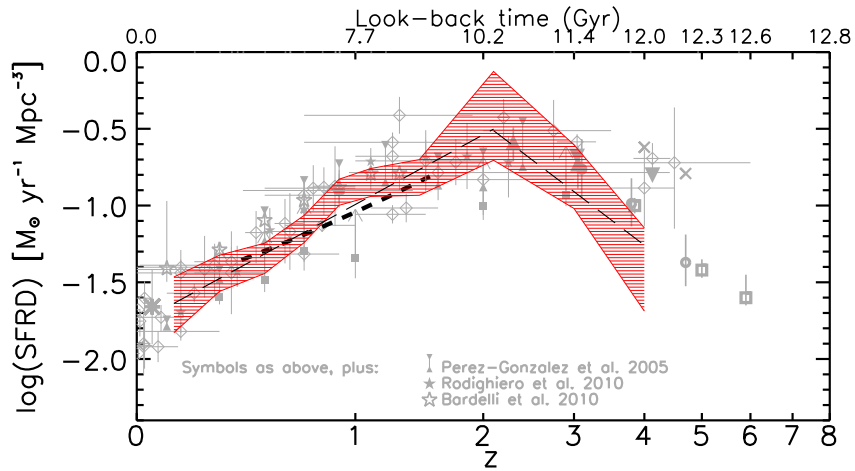


Fig. 3. Total dust-corrected UV-derived SFRDs as a function of redshift from the VVDS Deep+Ultra-Deep sample (red shaded area, corresponding to red circles and error bars in Fig. 2). The two long-dashed lines represent two fits to our SFRDs in the form $\propto (1+z)^\beta$ (see text for details). Gray points are from literature, derived from various SFR calibrators (UV, emission lines, IR, radio): they include the literature points as in Fig. 2, plus other works as in the labels.

SNII, but it is at 3-4Gyr for low-mass stars (see Dwek 1998). Nevertheless the dust reaches a sort of plateau from $z \sim 1.5$ (with a maximum at $z \sim 1$), i.e. 1 Gyr after the peak of the SFRD. Recently, Fukugita (2011) suggested that the dust must survive on much longer time scales than what has been previously thought and that half of the dust could be produced by SNII and the other half by low-mass (1-8 solar masses), long-lived stars. If we assume that the SNII dust production peaks very shortly after the SFRD peak, then the dust peak that we observe at $z \sim 1$ is likely due to intermediate-mass, long-lived stars producing their peak of dust on a delayed time. Surely, like in the case of the SFRD evolution, our findings about the general evolution of the FUV-band dust attenuation in such a broad cosmic epoch (~ 12 Gyr) will constitute an important reference for future models.

We thank S. Boissier for useful discussions. OC thanks V. Buat, D. Burgarella and L. Cortese for interesting conversations. This

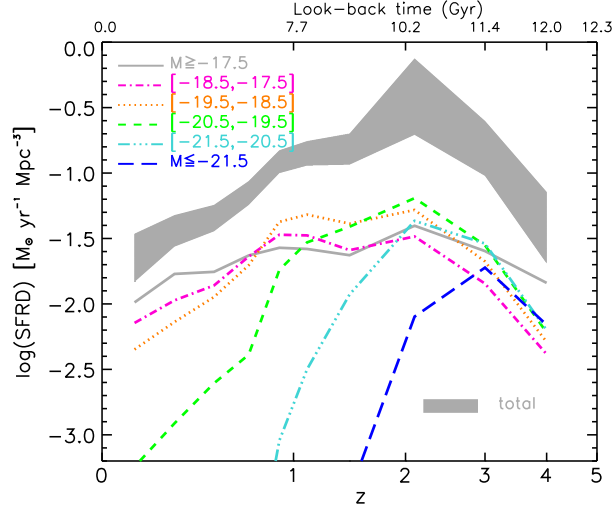


Fig. 4. The dust-corrected SFRD from galaxies in different FUV-band luminosity bins, as described in the labels. The background gray shaded area is the total SFRD.

work has been partially supported by the CNRS-INSU and its Programme National Cosmologie-Galaxies (France) and by INAF grant COFIN 2010.

References

- Baugh, C. M. 2006, Reports on Progress in Physics, 69, 3101
- Baugh, C. M., Lacey, C. G., Frenk, C. S., et al. 2005, MNRAS, 356, 1191
- Bruzual, G. & Charlot, S. 2003, MNRAS, 344, 1000
- Calzetti, D., Armus, L., Bohlin, R. C., et al. 2000, ApJ, 533, 682
- Cole, S., Aragon-Salamanca, A., Frenk, C. S., Navarro, J. F., & Zepf, S. E. 1994, MNRAS, 271, 781
- Cole, S., Lacey, C. G., Baugh, C. M., & Frenk, C. S. 2000, MNRAS, 319, 168
- Cortese, L., Boselli, A., Buat, V., et al. 2006, ApJ, 637, 242
- Cox, T. J., Jonsson, P., Somerville, R. S., Primack, J. R., & Dekel, A. 2008, MNRAS, 384, 386
- Cucciati, O., Tresse, L., Ilbert, O., et al. 2011, ArXiv:1109.1005
- de Ravel, L., Le Fèvre, O., Tresse, L., et al. 2009, A&A, 498, 379
- Dekel, A., Birnboim, Y., Engel, G., et al. 2009, Nature, 457, 451
- Di Matteo, T., Springel, V., & Hernquist, L. 2005, Nature, 433, 604
- Dwek, E. 1998, ApJ, 501, 643
- Efstathiou, G. 1992, MNRAS, 256, 43P
- Fukugita, M. 2011, ArXiv e-prints
- Hopkins, P. F., Younger, J. D., Hayward, C. C., Narayanan, D., & Hernquist, L. 2010, MNRAS, 402, 1693
- Ilbert, O., Salvato, M., Le Flo'c'h, E., et al. 2010, ApJ, 709, 644
- Ilbert, O., Tresse, L., Zucca, E., et al. 2005, A&A, 439, 863
- Le Fèvre, O., Vettolani, G., Garilli, B., et al. 2005, A&A, 439, 845
- Le Fèvre, O., Vettolani, G., Paltani, S., et al. 2004, A&A, 428, 1043
- Madau, P., Pozzetti, L., & Dickinson, M. 1998, ApJ, 498, 106
- Meurer, G. R., Heckman, T. M., & Calzetti, D. 1999, ApJ, 521, 64
- Salpeter, E. E. 1955, ApJ, 121, 161
- Schechter, P. 1976, ApJ, 203, 297
- Somerville, R. S., Hopkins, P. F., Cox, T. J., Robertson, B. E., & Hernquist, L. 2008, MNRAS, 391, 481
- Tresse, L., Ilbert, O., Zucca, E., et al. 2007, A&A, 472, 403
- van de Voort, F., Schaye, J., Booth, C. M., & Dalla Vecchia, C. 2011, MNRAS, 415, 2782
- Weinmann, S. M., Neistein, E., & Dekel, A. 2011, ArXiv:1103.3011
- White, S. D. M. & Frenk, C. S. 1991, ApJ, 379, 52

QUERYING FOR HEAVILY OBSCURED AGN VIA HIGH $9.7\mu\text{m}$ OPTICAL DEPTHS: RESULTS FROM THE $12\mu\text{m}$, GOODS, AND FLS SPITZER SPECTROSCOPIC SAMPLES

K. M. Dasyra^{1,2}, I. Georgantopoulos^{3,4}, A. Pope⁵ and M. Rovilos⁶

Abstract. To optimally identify candidates of the Compton-thick (CT) active galactic nuclei (AGN) that contribute to the unresolved X-ray background in infrared surveys, a tracer of column density is desirable in addition to an AGN indicator. In a recent study, we aimed to test whether the $9.7\mu\text{m}$ silicate absorption feature can be used for this purpose when seen at high optical depths. We found that the extreme criterion of optical thickness at $9.7\mu\text{m}$ is efficient in identifying CT objects among local AGN. Having identified six of the nine CT AGN in the $12\mu\text{m}$ sample with *Spitzer* and X-ray spectra, we expanded this analysis at intermediate/high z , using all GOODS and FLS sources with *Spitzer* and X-ray observations. We found 12 sources with $\tau_{9.7} > 1$ that host an AGN between $0.8 < z < 2.7$. Four of them are likely to be CT according to their low X-ray to $6\mu\text{m}$ luminosity ratio. Surveys with complete coverage in both mid-infrared spectra and X-ray data can provide large populations of such sources, as at least 5-9% of all infrared bright galaxies in the GOODS and FLS samples are $\tau_{9.7} > 1$ AGN.

Keywords: galaxies: active, infrared: galaxies, X-rays: galaxies

1 Introduction

Observational evidence points out to the existence of a population of active galactic nuclei (AGN) that is yet unidentified due to extreme dust obscuration. The observed space density of black holes in the local Universe cannot be accounted for, unless AGN with column densities of $>10^{24}\text{ cm}^{-2}$ exist (Comastri 2004; Merloni & Heinz 2008). At such high column densities, the circumnuclear medium is Compton thick (CT). CT AGN are thought to account for the unresolved cosmic X-ray background (Churazov et al. 2007), producing 10–20% of the total 30 keV flux (Gilli et al. 2007; Treister et al. 2009). Identifying these sources and adding them to the comparison of the black hole accretion rate with the star formation rate history of the Universe is essential, as they are thought to be primarily missing at $z < 1$ (Gilli et al. 2007; Treister et al. 2009), i.e., after the bulk of the stellar mass assembly (Marconi et al. 2004; Merloni et al. 2004; Gruppioni et al. 2011).

The sources missing from the cosmic X-ray background can be sought for in the cosmic background at infrared (IR) or longer wavelengths, as it is in these wavelengths that the radiation absorbed by the dust is re-emitted. Mid-IR excess (e.g., Lacy et al. 2004; Stern et al. 2005; Daddi et al. 2007; Fiore et al. 2008) and radio excess (Del Moro et al. 2012, in preparation) techniques have been used for this purpose. However, they do not preferentially select type 2 over type 1 AGN. We recently argued that in addition to an AGN tracer, a high column density indicator can be used to efficiently query for CT objects (Georgantopoulos et al. 2011). The latter was chosen to be the optical depth of the silicate feature at $9.7\mu\text{m}$, $\tau_{9.7}$, when seen in absorption. Even though the $9.7\mu\text{m}$ and X-ray column densities are uncorrelated at moderate optical depths (Shi et al. 2006; Wu et al. 2009), the bulk of the silicates can still be in a compact, circum-nuclear distribution in front

¹ Observatoire de Paris, LERMA (CNRS:UMR8112), 61 Av. de l'Observatoire, F-75014, Paris, France

² Laboratoire AIM, Irfu/Service d' Astrophysique, CEA Saclay, Orme des Merisiers, 91191 Gif sur Yvette Cedex, France

³ INAF-Osservatorio Astronomico di Bologna, Via Ranzani 1, 40127, Italy

⁴ Institute of Astronomy & Astrophysics, National Observatory of Athens, Palaia Penteli, 15236, Athens, Greece

⁵ Department of Astronomy, University of Massachusetts, Amherst, MA01003, USA

⁶ Max Planck Institut für Extraterrestrische Physik, Giessenbachstraße, 85748, Garching, Germany

of a bright continuum source (Soifer et al. 2002; Tristram et al. 2007). They have even been suggested to be located in the AGN torus because their feature is often seen in emission in type-1 AGN and in absorption in type-2 AGN (Shi et al. 2006; Hao et al. 2007), in agreement with the Antonucci & Miller (1985) unification scheme. We specifically examined how frequently do the local AGN with the most extreme mid-IR obscuration, simply defined as those that are optically thick ($\tau > 1$) at $9.7 \mu\text{m}$, have X-ray column densities $> 10^{24} \text{ cm}^{-2}$. We then applied this criterion to query for CT candidates among distant AGN samples.

2 Sample selection

2.1 The $12 \mu\text{m}$ sample

To quantify the fraction of CT AGN that are identified using the $\tau_{9.7} > 1$ criterion, we used all local $12 \mu\text{m}$ -selected Seyferts (Rush et al. 1993) with *Spitzer* IRS spectroscopy (Wu et al. 2009). Re-analysis of these spectra indicated that 11 out of the 103 Seyferts in this sample have $\tau_{9.7} > 1$. Nine of those have X-ray spectra that are necessary to determine their X-ray column densities (e.g., Brightman & Nandra 2011; Georgantopoulos et al. 2011).

2.2 The GOODS and FLS samples

To identify AGN in the distant Universe that are deeply obscured in the mid-IR (Fig. 1; left panel), we used two surveys with *Spitzer* IRS spectroscopy and X-ray data. The Great Observatories Origins Deep Survey (GOODS) covering the *Chandra* Deep Fields (CDF) North and South, and the First Look Survey (FLS). The two surveys were complementary in providing targets. The FLS is a 4 deg^2 shallow survey, whose 220 IRS spectra were flux-limited to a depth of 0.9 mJy (mainly presented in Yan et al. 2007; Sajina et al. 2007; Dasyra et al. 2009). Its X-ray coverage was nonetheless sparse (Bauer et al. 2010). On the other hand, the GOODS area ($\sim 900 \text{ arcmin}^2$ in total) has the deepest mid-IR and X-ray observations available, but a sparse (not flux-limited) IRS spectroscopic coverage of 150 sources (Pope et al. 2012, in preparation).

Overall, 7 $\tau_{9.7} > 1$ AGN with X-ray data were identified in GOODS North and South, and 5 in the FLS. The common criterion that we applied to classify distant sources as AGN was the lack of strong polycyclic aromatic hydrocarbon (PAH) emission, due either to the dilution of the PAHs into the AGN continuum or to the potential destruction of the PAHs by the AGN radiation. It translated to 6.2 (or 11.3) μm equivalent widths $< 0.3 \mu\text{m}$. Several other direct AGN indicators were subsequently found in our sources, including the detection of narrow-line-region lines with widths $> 500 \text{ km s}^{-1}$, the unambiguous need for an AGN-heated dust component in the spectral energy distribution (SED) fitting (Fig. 1; right panel), and the X-ray luminosity L_X values themselves, which exceeded $10^{42.5} \text{ erg s}^{-1}$ for many sources.

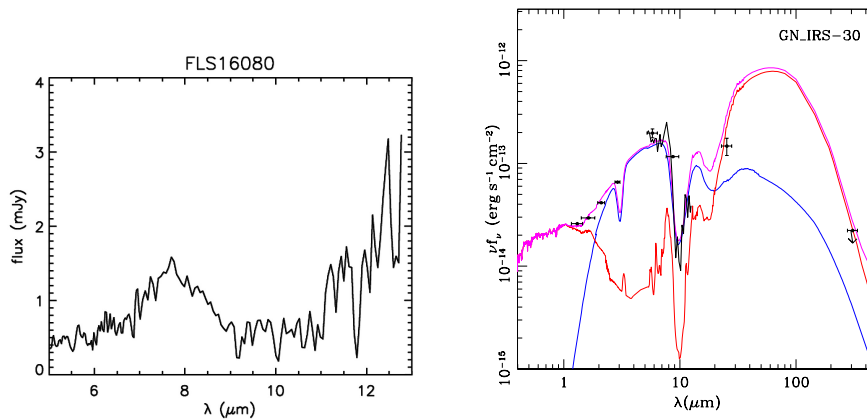


Fig. 1. Left: The mid-IR spectrum of a distant $\tau_{9.7} > 1$ AGN in the FLS (Sajina et al. 2007). **Right:** SED decomposition of a GOODS $\tau_{9.7} > 1$ source using an AGN (blue) and a starburst (red) component. The sum of the two is shown in magenta (Georgantopoulos et al. 2011).

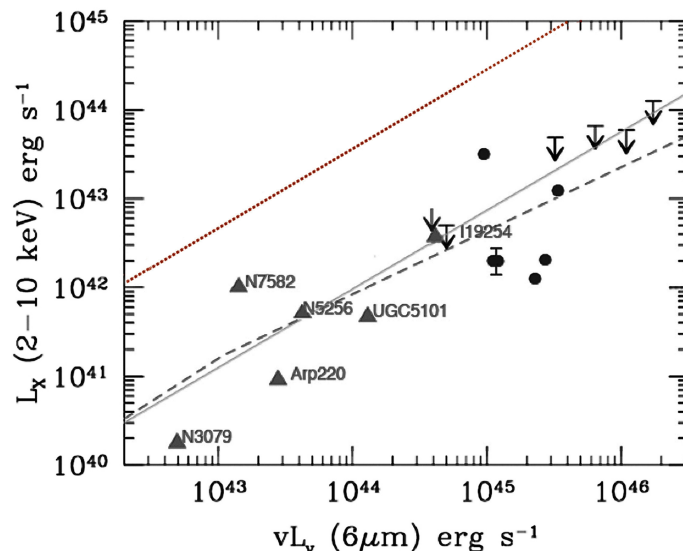


Fig. 2. Observed L_X vs $\nu L_\nu(6\mu\text{m})$ diagram (adapted from Georgantopoulos et al. 2011). The solid and dashed lines indicate the area below which CT AGN lie, found for different AGN samples (Maiolino et al. 2007; Fiore et al. 2009, respectively) and for a fixed fraction, 0.03, of the intrinsic L_X value being ascribed to the 2-10 keV reflection component luminosity. For comparison, a relation with similar slope to that in Maiolino et al. (2007) that fits the intrinsic (extinction-corrected) X-ray and $6\mu\text{m}$ luminosities of Seyfert 1 and 2 galaxies (Lutz et al. 2004) is shown with a dotted line. Local CT AGN with $\tau_{9.7}>1$ from the $12\mu\text{m}$ sample are shown as triangles. Distant CT AGN candidates in GOODS and FLS are plotted with circles (or arrows for limits).

3 Results

Nine sources hosting a CT nucleus are known to exist in the sub-sample of $12\mu\text{m}$ Seyferts with both IRS and X-ray spectra. These were identified through the detection of (i) a high ($\sim 1\text{ keV}$) equivalent-width (EW) $\text{FeK}\alpha$ line, (ii) a flat X-ray spectrum (with index $\Gamma \sim 1$ or flatter), which is attributed to reflection from the back side of the torus, or (iii) an absorption turnover at high energies (Akylas & Georgantopoulos 2009). Six of the nine sources matching these criteria were found to also have $\tau_{9.7}>1$, suggesting that the identification of CT AGN using this $\tau_{9.7}$ threshold can be promising despite the different spatial distributions of the media responsible for the X-ray and IR obscuration.

The application of the same $\tau_{9.7}$ threshold for the GOODS and FLS samples enabled us to identify 12 CT AGN candidates at $0.8 < z < 2.7$. Because reliable X-ray spectra could not be derived for them, we used the observed L_X , integrated over the 2-10 keV range, vs $\nu L_\nu(6\mu\text{m})$ diagram (Lutz et al. 2004) to assess which sources could be hosting a CT nucleus. With increasing obscuration, L_X drops and $L_\nu(6\mu\text{m})$ increases, making the AGN move from the relation that is appropriate for the intrinsic (obscuration-corrected) luminosities (Fig. 2; dotted line) to the bottom-right part of the diagram. The boundary of the locus of CT AGN (solid line) is computed using the X-ray and $6\mu\text{m}$ luminosities of the AGN presented in Maiolino et al. (2007). Given that this boundary depends on the SED and extinction properties of the objects in the chosen sample, we also computed it for the AGN in Fiore et al. (2009, shown with a dashed line, and additionally taking into account a luminosity evolution). We placed the 6 local $\tau_{9.7}>1$ CT AGN from the $12\mu\text{m}$ sample on this diagram, and found that 5 of them are indeed below or close to either boundary. For the distant sources, we find that 4 of the 12 candidates are well within the CT range. Several more could be in it, given the proximity of their upper limits to the boundary. It is thus possible, that the fraction of actual CT AGN among these candidates is high. This remains to be confirmed with deep X-ray spectra.

Volume-density wise, our technique could provide a non-negligible fraction of the evasive AGN population. Of the 220 FLS IR-bright galaxies with IRS spectra, 20 satisfied both our $\tau_{9.7}$ and weak PAH emission criteria. The use of other, direct AGN tracers could make this fraction exceed 9%, as CT AGN can also be residing in strong starbursts (with $\tau_{9.7}>1$). In the combined GOODS North and South fields, the fraction of all 150 IR-bright galaxies with $\tau_{9.7}>1$ was 10% (15 sources), with 5% (7) of the sources having weak PAH emission

(Georgantopoulos et al. 2011). Potential $\tau_{9.7}>1$ (AGN or starburst) candidates in GOODS were found to correspond to 8–16% of the galaxies with only broad-band *Spitzer* and *Herschel* data (Magdis et al. 2011). Even in the local Universe, IR-bright galaxies are frequently optically thick at $9.7\ \mu\text{m}$ (Imanishi 2009).

4 Conclusions

While not all CT sources have $\tau_{9.7}>1$ due to the clumpy structure of their obscuring medium, the efficiency of identifying them by querying for AGN that are optically thick at $9.7\ \mu\text{m}$ can be high. Six of the nine Seyferts in the local $12\ \mu\text{m}$ sample that are known to be CT from their X-ray spectral properties and that have *Spitzer* IRS spectra satisfied this criterion. In the GOODS and FLS surveys, we found twelve sources that are classified as AGN and that have $\tau_{9.7}>1$, four of which are likely to be CT according to their low X-ray to $6\ \mu\text{m}$ luminosity ratio. While the number of sources presented in this work is limited due to the lack of either X-ray or IR data, the technique has the potential to provide large samples of CT AGN candidates.

This work was supported by the European Community through the Marie Curie Intra-European Fellowships (IEF) 2009-235038 and 2008-235285, which were awarded to K. D. and I. G., respectively, under the 7th Framework Programme (2007-2013).

References

- Akylas, A., & Georgantopoulos, I., 2009, *A&A*, 500, 999
 Antonucci, R., & Miller, J. 1985, *ApJ*, 297, 621
 Bauer, F. E., Yan, L., Sajina, A., Alexander, D. M., 2010, *ApJ*, 710, 212
 Brightman, M. & Nandra, K. 2011, *MNRAS*, 413, 1206
 Comastri, A. 2004, *ASSL*, 308, 245
 Churazov, E., Sunyaev, R., Revnivtsev, M., et al. 2007, *A&A*, 467, 529
 Daddi, E., Alexander, D. M., Dickinson, M., et al., 2007, *ApJ*, 670, 173
 Dasyra, K. M., Yan, L., Helou, G., et al., 2009, *ApJ*, 701, 1123
 Fiore, F., Grazian, A., Santini, P., et al., 2008, *ApJ*, 672, 94
 Fiore, F., Puccetti, S., Brusa, M., et al. 2009, *ApJ*, 693, 447
 Hao, L., Weedman, D. W., Spoon, H. W. W., et al. 2007, *ApJ*, 655, L77
 Georgantopoulos, I., Dasyra, K. M., Rovilos, E., et al. 2011, *A&A*, 531, 116
 Gilli, R., Comastri, A., Hasinger, G., 2007, *A&A*, 463, 79
 Gruppioni, C., Pozzi, F., Zamorani, G., Vignali, C. 2011, *MNRAS*, 416, 70
 Imanishi, M., 2009, *ApJ*, 694, 751
 Lacy, M., Storrie-Lombardi, L. J., Sajina, A., et al. 2004, *ApJS*, 154, 166
 Lutz, D., Maiolino, R., Spoon, H. W. W., Moorwood, A. F. M., 2004, *A&A*, 418, 465
 Magdis, G. E., Elbaz, D., Dickinson, M. et al. 2011, *A&A*, 534, 15
 Maiolino, R., Shemmer, O., Imanishi, M., et al. 2007, *A&A*, 468, 979
 Marconi, A., Risaliti, G., Gilli, R., Hunt, L.K., Maiolino, R., Salvati, M. 2004, *MNRAS*, 351, 169
 Merloni, A., Rudnick, G., Di Matteo, T. 2004, *MNRAS*, 354, L37
 Merloni, A. & Heinz, S., 2008, *MNRAS*, 388, 1011
 Rush, B., Malkan, M.A., Spinoglio, L., 1993, *ApJS*, 89, 1
 Shi, Y., Rieke, G. H., Hines, D. C., et al., 2006, *ApJ*, 653, 127
 Sajina, A., Yan, L., Armus, L. et al. 2007, *ApJ*, 664, 713
 Soifer, B.T., Neugebauer, G., Matthews, K., Egami, E., Weinberger, A.J., 2002, *AJ*, 124, 2980
 Stern, D., Eisenhardt, P., Gorjian, V., et al. 2005, *ApJ*, 631, 163
 Treister, E., Urry, C. M., Virani, S., 2009, *ApJ*, 696, 110
 Tristram, K. R. W., Meisenheimer, K., Jaffe, W., 2007 *A&A*, 474, 837
 Wu, Y., Charmandaris, V., Huang, J., Spinoglio, L., Tommasin, S., 2009, *ApJ*, 701, 658
 Yan, L., Sajina, A., Fadda, D., et al., 2007, *ApJ*, 658, 778

LBGS PROPERTIES FROM $Z \sim 3$ TO $Z \sim 6$

S. de Barros¹, D. Schaerer^{1,2} and D. P. Stark³

Abstract. We analyse the spectral energy distribution (SED) of U , B , V and i -dropout samples from GOODS-MUSIC and we determine their physical properties, such as stellar age and mass, dust attenuation and star formation rate (SFR). Furthermore, we examine how the strength of Ly α emission can be constrained from broad-band SED fits instead of relying in spectroscopy. We use our SED fitting tool including the effects of nebular emission and we explore different star formation histories (SFHs). We find that SEDs are statistically better fitted with nebular emission and exponentially decreasing star formation. Considering this result, stellar mass and star formation rate (SFR) estimations modify the specific SFR (SFR/ M_*) - redshift relation, in compared to previous studies. Finally, our inferred Ly α properties are in good agreement with the available spectroscopic observations.

Keywords: Galaxies: starburst, Galaxies: ISM, Galaxies: high-redshift, Ultraviolet: galaxies

1 Introduction

Understanding how galaxies assemble their mass is an important goal in high redshift studies (Stark et al. 2009). Using new SED modeling techniques taking into account nebular emission (Schaerer & de Barros 2009, 2010), we present preliminary results of a study of a large sample of high redshift galaxies. We find that statistically, the model which provides the best fit is a model including nebular emission, with an exponentially decreasing star formation history. This implies a new estimation on age, stellar mass and SFR. Also, we here demonstrate that the properties of Ly α can also be inferred from broad-band observations, at least statistically for large samples. This allows us, for example, to determine trends of Ly α with redshift and other parameters, without resort to spectroscopy.

We adopt a Λ -CDM cosmological model with $H_0=70$ km s⁻¹ Mpc⁻¹, $\Omega_m=0.3$ and $\Omega_\Lambda=0.7$.

2 Data and method

We have used the GOODS-MUSIC catalog of Santini et al. (2009) for the GOODS-South field, providing photometry in the U , B_{435} , V_{606} , i_{776} , z_{850} , J , H , K , bands mostly from the VLT and HST, and the 3.6, 4.5, 5.8 and 8.0 μ m bands from the IRAC camera onboard *Spitzer*. Using standard criteria as in Stark et al. (2009), we have selected U , B , V and i -drop galaxies. To reduce the contamination rate, we have only retained the objects whose median photometric redshifts agree with the targetted redshift range. We are thus left with a sample of 389, 705, 199 and 60 galaxies at $z \sim 3$, $z \sim 4$, $z \sim 5$ and $z \sim 6$.

Our SED fitting tool as already being described in Schaerer & de Barros (2009) and Schaerer & de Barros (2010), here, we briefly summarize.

We use a recent, modified version of the Hyperz photometric redshift code of Bolzonella et al. (2000), taking into account nebular emission (lines and continua) which can impact broad band photometry and derived properties (Schaerer & de Barros 2009, 2010; Ono et al. 2010). We consider a large set of spectral templates (Bruzual & Charlot 2003), covering different metallicities and a wide range of star formation (SF) histories (exponentially decreasing, constant and rising SF) and we add the effects of nebular emission.

¹ Observatoire de Genève, Université de Genève, 51, Ch. des Maillettes, CH-1290 Versoix, Switzerland

² Laboratoire d'Astrophysique de Toulouse-Tarbes, Université de Toulouse, CNRS, 14 Avenue E. Belin, 31400 Toulouse, France

³ Kavli Institute of Cosmology and Institute of Astronomy, University of Cambridge, Madingley Road, Cambridge CB30HA, UK

We adopt a Salpeter IMF (Salpeter 1955) from 0.1 to 100 M_{\odot} , and we properly treat the returned ISM mass from stars. IGM is treated following Madau (1995) and the extinction is described by the Calzetti law (Calzetti et al. 2000). Nebular emission from continuum processes and lines is added to the spectra predicted from the GALAXEV models as described in Schaerer & de Barros (2009). We define three models:

- Reference model: constant star formation, age > 50 Myr and solar metallicity.
- Decreasing model: exponentially decreasing star formation ($\text{SFR} \propto \exp(-t/\tau)$). Metallicity and τ are free parameters, τ varying from 10 Myr to ∞ ($\text{SFR} = \text{constant}$).
- Rising model: we use the mean rising star-formation history from the simulations of Finlator et al. (2011). Metallicity is a free parameter.

Furthermore, we define two options: first, +NEB which indicates that we include nebular emission, with all lines except $\text{Ly}\alpha$, since this line may be attenuated by radiation transfer processes inside the galaxy or by the intervening intergalactic medium and second, +NEB+ $\text{Ly}\alpha$ which indicates that we include nebular emission, with all lines. In all cases, we consider $z \in [0,10]$ in steps of 0.1 and $A_V \in [0,4]$ mag in steps of 0.1.

To determine properly confidence intervals for all the parameters, we ran 1000 Monte Carlo simulations for each object by perturbing the input broadband photometry assuming the photometric uncertainties are Gaussian. This procedure provides the probability distribution of the physical parameters for each source and for the ensemble of sources.

3 Fit quality

For the four samples and each SFH (see figure 1 for Rising model, we find similar results for all SFHs), $\sim 35\%$ (30%-39%) of the objects are best fitted without taking into account nebular emission. This fraction is independent of parameters like M_{1500} or the filter's number available. For the three SFH, in U , B , V and i -dropout, we found respectively 68%, 71%, 71% and 77% common objects best fitted without nebular emission and 85%, 80%, 94% and 88% common objects best fitted taking into account nebular emission.

$\text{H}\alpha$ is a strong line at 656.4 nm (reference frame) and must affect $3.5\mu\text{m}$ - $4.6\mu\text{m}$ color for objects between $z=3.8$ and $z=5$ (Shim et al. 2011). We selected B -dropout objects with $3.6\mu\text{m}$ and $4.5\mu\text{m}$ available data (excluding non-detections) and with median redshift between 3.8 and 5. We obtain a subsample of 303 objects, with similar distribution for the best fits ($\sim 35\%$ - $\sim 65\%$). Figure 1 shows that objects best fitted with nebular emission are almost all blue objects, which can be easily explain by strong nebular emission. We define two categories of objects: Wneb, which are objects best fitted without nebular emission and Sneb, which are objects best fitted with nebular emission, choosing arbitrarily the "Decreasing model" to do this selection, considering the similarity between these two categories among the SFHs.

Wneb objects show a slight χ_r^2 improvement (15% to 25% lower) for models without nebular emission in comparison with the χ_r^2 for models including nebular emission. At the opposite, Sneb objects show a large improvement of the χ_r^2 for models including nebular emission (36% to 51% lower). In all cases, we find lowest χ_r^2 with Decreasing/Rising models and Sneb are significantly best fitted with Decreasing+NEB/+NEB+ $\text{Ly}\alpha$ models.

4 Star formation rate and stellar mass

Considering Wneb and Sneb, if these two populations have respectively intrinsic weak and strong nebular emission lines, we expect to find two different SFR estimations (or other difference on physical properties), with a larger SFR for Sneb. Actually, we find a difference between these two populations at each redshift. In Figure 2, we show for $z \sim 4$ that Reference model doesn't permit any distinction between the two populations while with Decreasing+NEB model, Wneb objects have a median SFR lower (by a factor 4) than Sneb.

For example, at $z \sim 4$, considering respectively Decreasing+NEB and Rising+NEB model, median SFR is increased by 15% (180%) and the median stellar mass is decreased by more than 50% (60%). A direct consequence is that we establish a different sSFR-redshift relation (see Figure 3) in comparison with previous study (González et al. 2010).

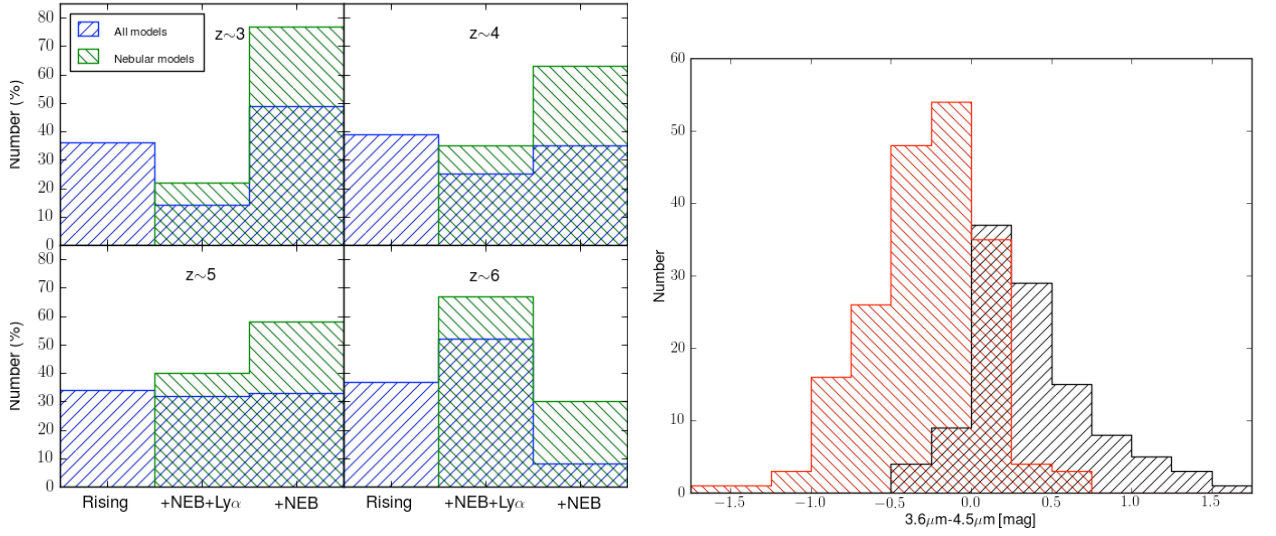


Fig. 1. Left: In blue: best fits distribution among Rising, Rising+NEB+Ly α and Rising+NEB model and in green: best fits distribution between Rising+NEB+Ly α and Rising+NEB model. **Right:** $3.6\mu\text{m}-4.5\mu\text{m}$ color histogram for a sub-sample of $z \in [3.8, 5]$ objects. In red, best fitted objects with nebular emission and black, best fitted objects without nebular emission.

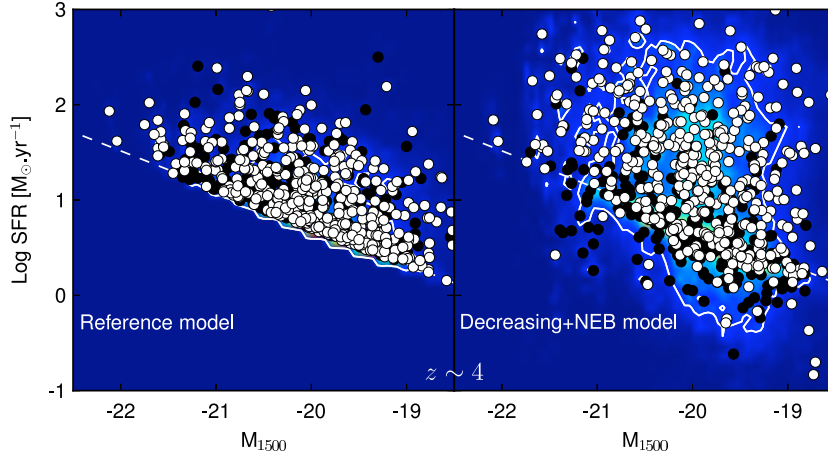


Fig. 2. Composite probability distribution of M_{1500} and SFR for the Reference and Decreasing+NEB model for the sample at $z \sim 4$ as determined for each galaxy from our 1000 Monte Carlo simulations. The points overlaid show the median value properties for each object in the sample, black dots for Wneb and white dots for Sneb. The overlaid contour indicate the 68% integrated probabilities on the ensemble properties measured from the centroid of the distribution. The dashed line represents the Kennicutt relation (Kennicutt 1998).

5 Constraint on Ly α

In some models, we introduce an additional free parameter, a variable Ly α strength described by the relative Ly α escape fraction $f_{Ly\alpha}^{rel} \in [0, 1]$, defined by $L(Ly\alpha) = f_{Ly\alpha}^{rel} \times L^B(Ly\alpha)$, where L^B is the intrinsic Ly α luminosity of the spectral template given by its Lyman continuum flux and the case B assumption and $L(Ly\alpha)$ is the adopted Ly α luminosity for the spectral template (before any additional attenuation with the Calzetti law, assumed to affect stars and gaz in the same manner). Values $f_{Ly\alpha}^{rel} < 1$ therefore describe an additional reduction of Ly α

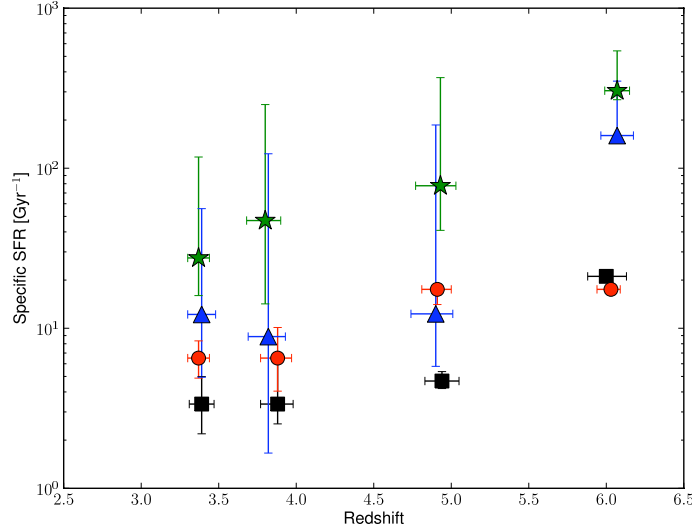


Fig. 3. Evolution of the specific SFR with redshift. Black squares: Reference model, red dots: Reference+NEB model, blue triangles: Decreasing+NEB model and green stars: Rising+NEB model. +NEB models are used for all redshift except $z \sim 6$, for which we use +NEB+Ly α models.

beyond the attenuation suffered by the UV continuum.

Overall it turns out that $f_{Ly\alpha}^{rel}$ is not well constrained for individual objects. For each sample, however, the pdf shows two relative maxima close to $f_{Ly\alpha}^{rel} = 0$ and 1, whose relative importance varies between the samples. To quantify this behaviour further, regardless of the detailed shape of the pdf, we count the number of objects with $EW(Ly\alpha) > 50 \text{ \AA}$. We define the corresponding fraction of Ly α objects as $r_{Ly\alpha} = N(EW(Ly\alpha))/N_{tot}$. In Figure 4, we plot $r_{Ly\alpha}$ as a function of the absolute UV magnitude for the sample of $z \sim 3, 4$ and 5. We find that the fraction of objects showing Ly α emission increases with redshift and at each redshift, we find that Ly α emission is more common in galaxies with fainter UV magnitudes. These two main results are in good agreement with previous spectroscopic studies (Stark et al. 2011; Shapley et al. 2003; Hayes et al. 2011), showing that photometric data can also provide information on Ly α emission.

6 Conclusions

Using an updated version of the Hyperz photometric redshift code of Bolzonella et al. (2000) adding nebular emission (lines and continua) to the spectral templates (Schaerer & de Barros 2009, 2010), we have analysed a large sample of Lyman-break selected galaxies at $z \sim 3-6$ in the GOODS-S field, for which deep multi-band photometry from the U -band to $8 \mu\text{m}$ is available.

We find that at each redshift, an exponentially decreasing star formation history with nebular emission provides statistically better SED fits than models with constant or rising star formation. Furthermore, decreasing and rising star formation with nebular emission are the only models coherent with $3.6-4.5 \mu\text{m}$ color which is likely influenced by H α emission at $z \sim 4$ (Shim et al. 2011). These results have direct consequences on physical parameters estimation like stellar mass and SFR, which imply possibly a new mass assembly interpretation (de Barros et al. 2011, in preparation). Finally, we show that significant trends of Ly α strength with redshift and with UV magnitude can be inferred from broad-band photometry observations of large samples of galaxies using our models (Schaerer et al. 2011, accepted).

We acknowledge the GOODS-MUSIC collaboration. The work of SdB and DS is supported by the Swiss National Science Foundation. DPS is supported by an STFC postdoctoral research fellowship.

References

Bolzonella, M., Miralles, J., & Pelló, R. 2000, A&A, 363, 476

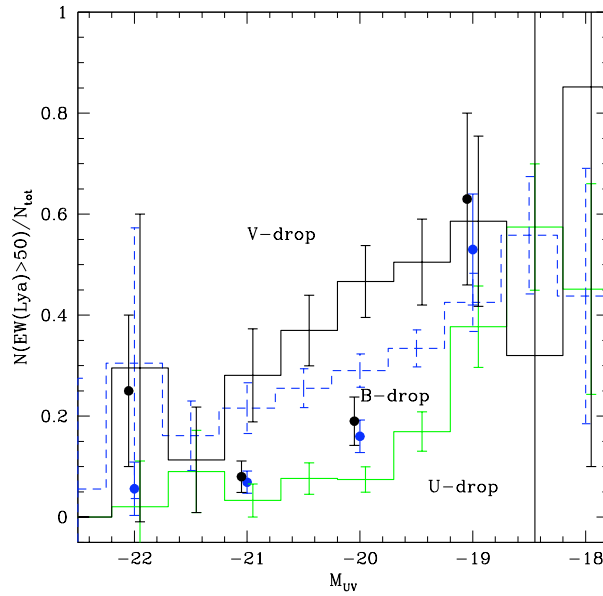


Fig. 4. Fraction of galaxies with a large Ly α equivalent width $EW(Ly\alpha) > 50 \text{ \AA}$ compared to the observed fraction derived from follow-up spectroscopy of $z \sim 4$ (blue points) and 5 (black points) LBGs (data for B and V drops from Stark et al. (2010))

Bruzual, G. & Charlot, S. 2003, MNRAS, 344, 1000

Calzetti, D., Armus, L., Bohlin, R. C., et al. 2000, ApJ, 533, 682

Finlator, K., Oppenheimer, B. D., & Davé, R. 2011, MNRAS, 410, 1703

González, V., Labbé, I., Bouwens, R. J., et al. 2010, ApJ, 713, 115

Hayes, M., Schaerer, D., Östlin, G., et al. 2011, ApJ, 730, 8

Kennicutt, Jr., R. C. 1998, ARA&A, 36, 189

Madau, P. 1995, ApJ, 441, 18

Ono, Y., Ouchi, M., Shimasaku, K., et al. 2010, ApJ, 724, 1524

Salpeter, E. E. 1955, ApJ, 121, 161

Santini, P., Fontana, A., Grazian, A., et al. 2009, A&A, 504, 751

Schaerer, D. & de Barros, S. 2009, A&A, 502, 423

Schaerer, D. & de Barros, S. 2010, A&A, 515, A73

Shapley, A. E., Steidel, C. C., Pettini, M., & Adelberger, K. L. 2003, ApJ, 588, 65

Shim, H., Chary, R.-R., Dickinson, M., et al. 2011, ApJ, 738, 69

Stark, D. P., Ellis, R. S., Bunker, A., et al. 2009, ApJ, 697, 1493

Stark, D. P., Ellis, R. S., Chiu, K., Ouchi, M., & Bunker, A. 2010, MNRAS, 408, 1628

Stark, D. P., Ellis, R. S., & Ouchi, M. 2011, ApJ, 728, L2

A PANCHROMATIC STUDY OF TWO PAIRS OF GALAXY CLUSTERS

F. Durret¹, T. F. Laganá², M. Haider³, C. Adami⁴ and E. Bertin¹

Abstract.

We have analysed the properties of two pairs of intermediate redshift clusters Abell 222/223 and Abell 1758 North/South, based on XMM-Newton data, deep multi-wavelength optical imaging with CFHT/ Megacam, and, for the second pair, numerical simulations. Temperature and metallicity maps of the X-ray gas show striking features, particularly in one of the members of each pair, implying ongoing mergers at least in Abell 223 and in Abell 1758 North. The comparison of the metallicity map of the latter cluster with the results of numerical simulations suggests that in the metal rich regions, winds have been more efficient in transporting metal enriched gas to the outskirts than ram pressure stripping. Optical galaxy luminosity functions (GLFs) tend to show dips and wiggles, as well as an excess of bright galaxies over a Schechter function fit, confirming the merging structure of each of these four clusters.

Keywords: clusters of galaxies, optical, X-rays

1 Introduction

Environmental effects are known to have an influence on galaxy evolution, and can therefore modify galaxy luminosity functions (hereafter GLFs). This is particularly obvious in merging clusters, where GLFs may differ from those in non-merging (relaxed) clusters. The GLFs also allow us to trace the cluster-formation history, as shown for example for Coma (Adami et al. 2007).

This dynamical history can also be derived by analysing the temperature and metallicity distributions of the X-ray gas in clusters. These maps have revealed that in many cases clusters with emissivity maps that show a fairly relaxed appearance could have very disturbed temperature and metallicity distributions, implying they have undergone one or several mergers in the last few Gyr. The temperature distribution of the intra-cluster medium (ICM) provides insight into the process of galaxy cluster merging and on the dissipation of the merger energy in form of turbulent motion. Metallicity maps can be regarded as a record of the integral yield of all the stars that have released their metals through supernova explosions or winds during the cluster evolution. The comparison of these maps with the results of hydrodynamical numerical simulations allows us to characterize the last merging events that have taken or are taking place.

We briefly present here our results for two pairs of moderately distant clusters, where the effects of merging are expected to be even stronger: Abell 222/223 (redshift $z=0.21$) and Abell 1758 North/South ($z=0.279$). Our studies are based on archive XMM-Newton X-ray data and archive CFHT/Megacam optical images in the g and r bands. A full description of their properties can be found in Durret et al. (2010) and Durret et al. (2011).

2 X-ray temperature and metallicity maps

The X-ray temperature and metallicity maps of A222/223 are shown in Fig. 1. Abell 222 appears fairly isothermal when compared to Abell 223, but neither of these clusters presents a cool-core, precluding a fully

¹ UPMC Université Paris 06, UMR 7095, Institut d'Astrophysique de Paris, 98bis Bd Arago, F-75014, Paris, France

² IAG, USP, R. do Matão 1226, 05508-090, São Paulo/SP, Brazil

³ Inst. of Astro and Particle Physics, University of Innsbruck, A-6020 Innsbruck, Austria

⁴ LAM, OAMP, Pôle de l'Etoile Site Château-Gombert, 38 rue Frédéric Joliot-Curie, 13388 Marseille Cedex 13, France

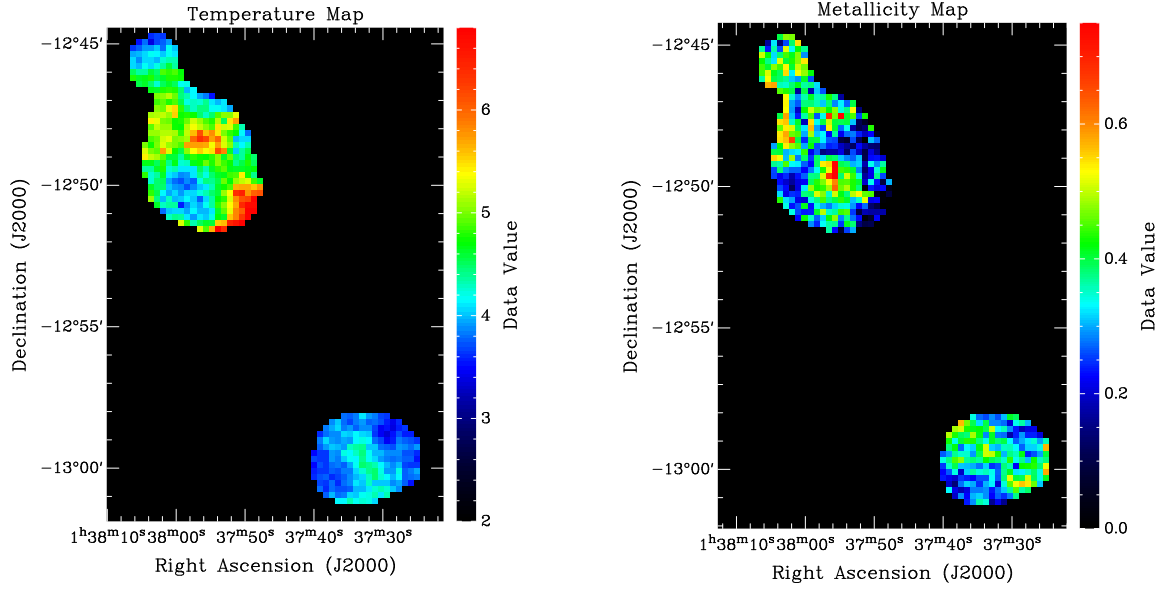


Fig. 1. Left: Temperature map of A222 (bottom right cluster) and A223 (top left). **Right:** Corresponding metallicity map.

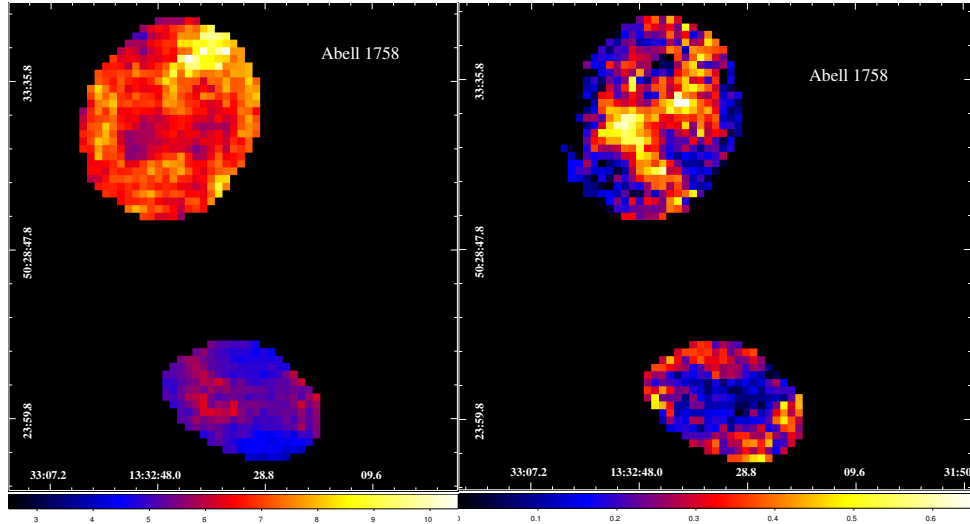


Fig. 2. Left: Temperature map of A1758N (top cluster) and S (bottom). **Right:** Corresponding metallicity map.

relaxed state even in A222. The overall temperature map of Abell 223 is strongly inhomogeneous and shows a large number of sub-structures. The metallicity map, shows a metallicity enhancement in the central region of Abell 223.

The gas temperature maps of A1758N/S displayed in Fig. 2 do not present prominent inhomogeneities, except for a hotter blob in the northwest of Abell 1758 North. The North cluster is hotter (with temperatures in the range of 6-7 keV) and the South one cooler ($kT = 4-5$ keV). The hotter blob in the northwest of Abell 1758 North could be explained by heating of the gas in that region by the movement of the northwest system towards the north, as proposed by David & Kempner (2004). The most striking features are seen in the metallicity maps. The metallicity map of the South cluster is even more unusual, because it shows a deficit of metals in the central region. This deficit is probably the signature of an interaction with the central object that could have expelled metals towards the outskirts. We also detect two elongated regions of high metallicity in the North

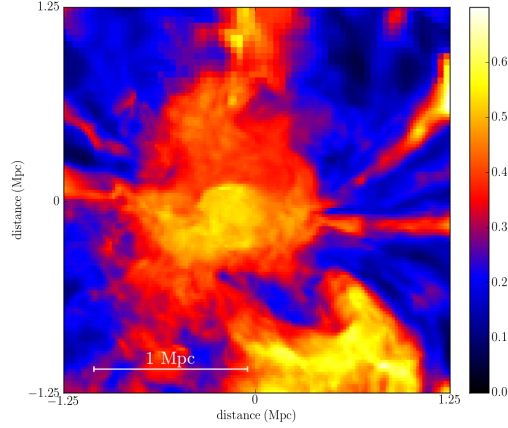


Fig. 3. Metal distribution predicted by numerical simulations for A1758 North

cluster, suggesting that it has been crossed by at least two smaller clusters.

To better understand the nature of the most prominent features exhibited in the metallicity map of the North cluster, we performed five simulations with different initial conditions. Among these five simulations, we found one metal distribution that quite reasonably reproduces the elongated region of high abundance found observationally for the North cluster, although without a perfect spatial correlation (see Fig. 3). The results of our numerical simulations allow us to distinguish the role of metal transportation processes such as galactic winds and ram-pressure stripping. These phenomena act in different regions of the cluster, and it appears that in the metal-rich elongated regions of the North cluster winds are more efficient in transporting enhanced gas to the outskirts than ram-pressure stripping.

3 Galaxy luminosity functions

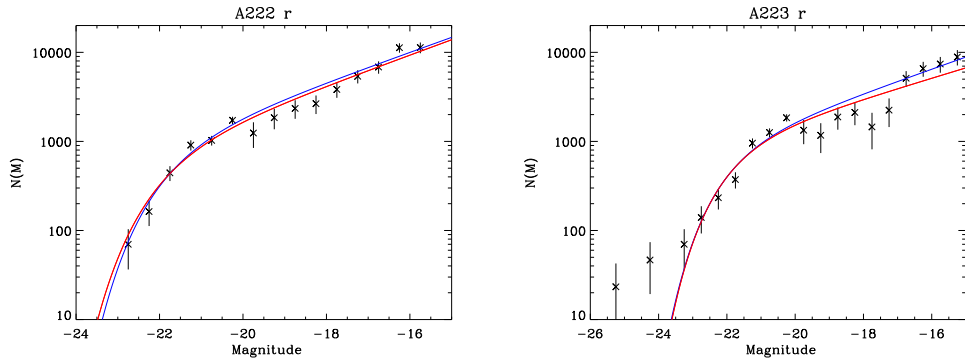


Fig. 4. Left: Galaxy luminosity function of A222 in the r band. **Right:** Galaxy luminosity function of A223 in the r band. The blue and red colours correspond to the best Schechter function fits obtained for two different background galaxy subtractions.

Abell 222 appears to be smaller and less massive than Abell 223. The galaxy luminosity functions (GLF) in the r band are shown in Fig. 4 for these two clusters. For Abell 222, the GLF is quite well fit by a Schechter function, while Abell 223 presents a “perturbed” GLF, with dips and wiggles, and an excess of bright galaxies over a single Schechter fit.

As seen in Fig. 5, the GLF of Abell 1758 North also shows an excess of galaxies over a Schechter function in the brightest magnitude bins, as well as a possible and unexplained excess of galaxies around $M_{r'} \sim -17.5$. In contrast, for Abell 1758 South, which is metal-poorer than the North cluster, the GLF is not as well fit by

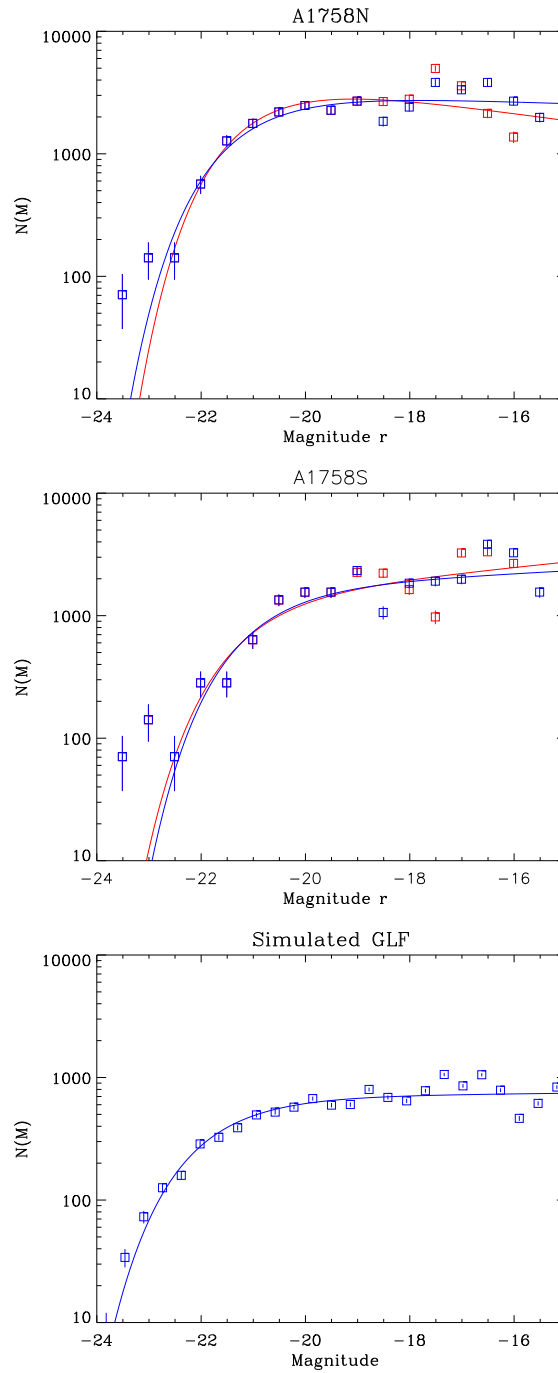


Fig. 5. Top: Galaxy luminosity function of A1758 North in the r band. **Middle:** Galaxy luminosity function of A1758 South in the r band. The blue and red symbols correspond to two different galaxy selections and the corresponding curves show the best Schechter function fits. **Bottom:** Simulated galaxy luminosity function for A1758 with best Schechter fit superimposed.

a Schechter function, and also shows an excess at bright magnitudes. The somewhat perturbed shapes of the GLFs of both clusters agree with the assumption that they are both undergoing merging processes.

The numerical simulations computed to account for the metallicity map of A1758 North also allowed us to simulate an optical GLF, and the result is consistent with the observed GLF, as seen when comparing the left and right panels of Fig. 5.

4 Discussion

The metallicity enhancement in the central region of A223 can be explained by the fact that this cluster has more very bright galaxies than A222. Assuming ram-pressure stripping with tidal disruption of the bright galaxies near the cluster center as a mechanism for metal injection, one would indeed expect this cluster to have a higher central metallicity than A222. The combined analysis of X-ray and optical data argues for a scenario in which the two clusters are beginning to collide. A223 presents signs of interaction in both wavelength ranges, and has probably been crossed by a small cluster heading north east, while A222 does not show strong evidence for interaction, except for the absence of a cool-core.

For A1758, signs of merger(s) are detected in the optical and the X-ray wavelength ranges in both subclusters, meaning that both galaxies and gas are still out of equilibrium. The presence of two elongated regions of high metallicity in the North cluster suggest that at least two smaller clusters have crossed the North cluster. Our temperature and metallicity maps agree with the scenarios proposed by David & Kempner (2004), who derived that the North cluster is in the later stages of a large impact parameter merger between two 7 keV clusters, while the South cluster is in the earlier stages of a nearly head-on merger between two 5 keV clusters.

The present study confirms that the analysis of temperature and metallicity maps of the X-ray gas, coupled with numerical simulations, can bring important knowledge on the formation history and evolution of individual clusters. In particular, these maps allow to show evidence for merging events even when emissivity maps show no clear evidence for substructures. A complementary approach to the study of merging clusters is the analysis of optical GLFs. It indeed appears that the GLFs of clusters revealing evidence for merging show dips and wiggles, together with an excess of galaxies over a Schechter function in the brightest magnitude bins. This could be used as a test for recent merging events in clusters where the evidence for mergers is not obvious.

References

- Adami C., Durret F., Mazure A. et al. 2007, *A&A* 462, 411
David L.P. & Kempner J. 2004, *ApJ* 613, 831
Durret F., Laganá T. F., Adami C., Bertin E. 2010, *A&A* 517, 94
Durret F., Laganá T. F., Haider M. 2011, *A&A* 529, 38
Wright E.L. 2006, *PASP*, 118, 1711

A PROJECT FOR AN INFRARED SYNOPTIC SURVEY FROM ANTARCTICA WITH THE POLAR LARGE TELESCOPE (PLT)

N. Epchtein¹, L. Abe¹, W. Ansorge², M. Langlois³, I. Vauglin³, S. Argentini⁴, I. Esau⁵, C. David⁶, I. Bryson⁷, G. Dalton⁷, M. C. B. Ashley⁸ and J. S. Lawrence⁹

Abstract. The *Polar Large Telescope (PLT)* aims at performing a new generation of astronomical *Infrared Synoptic Survey from Antarctica (ISSA)*. It would carry out for the first time large scale periodic imaging surveys at $\sim 0.3''$ angular resolution in the short thermal infrared (2-5 μm) range benefiting from the extremely dry, cold, and stable polar atmosphere. The PLT consists of a 2.5m class telescope equipped with a 250-Mpixel infrared camera. The survey would produce diffraction limited images at 2 μm covering a total of ~ 5000 square degrees, explore the time domain from seconds to years down to $m_{AB}=25.5$ in K_d , generate alerts of transients and react quickly to alerts from other ground based or space borne facilities.

Keywords: Infrared Surveys, Telescope, Antarctic Astronomy

1 An Infrared Synoptic Survey from Antarctica

Large scale astronomical surveys in the infrared (TMSS, IRAS, 2MASS, DENIS, UKIDSS, Spitzer, VISTA, WISE, AKARI, etc..) have lead to enthralling breakthroughs in most critical areas of astrophysics during the last half century (see *e.g.*, Price 2009, and references therein for a review). All-sky or large sky fractions surveys beyond the K_s band (cut-off at 2.3 μm) from the Earth are unfortunately hampered by the excessive level of the sky thermal background emission and are therefore impracticable. On the other hand, a space mission cannot provide at the same time, wide field coverage AND high angular resolution.

The Antarctic Plateau actually offers an interesting option, because of its unique atmospheric properties (Burton 2010). One of the greatest advantages over conventional ground sites is indeed the low sky brightness in the near infrared (Walden *et al.* 2005; Philips *et al.* 2009). This property is particularly beneficial to the exploitation of the “hot” part of the 2 μm window between 2.3 and 2.5 μm that the K_s filter cuts-off to get rid of excessive thermal background, and to a lesser extent the 3 μm window. Moreover, Antarctic sites which have been already assessed such as Dome C or Dome A feature a turbulent layer by far much thinner (a few meters up to a few tens of meters) than above any other sites on the ground (Aristidi *et al.* 2009). The PLT is aimed at exploiting these properties to provide superb images at $\sim 0.3''$ resolution and carry out the first *Infrared Synoptic Survey from Antarctica (ISSA)*.

Moreover, the PLT, like the LSST, will explore the time domain through repeated visits of a selection of large areas of the sky, to track possible transients, monitor large numbers of variable objects, emit alerts and respond to alerts of other ground based or space surveyors at other wavelengths.

¹ CNRS-Laboratoire H. Fizeau, UNS, F06000-Nice, France, (epchtein@unice.fr)

² RAMS-CON Management consultants, D85617-Assling, Germany

³ CRAL, Observatoire de Lyon, France

⁴ CNR-ISAC, Rome, Italy

⁵ Nansen Environmental and Remote Sensing Center, Bergen, Norway

⁶ IPEV, Brest, France

⁷ STFC, UK

⁸ School of Physics, UNSW, Sydney, Australia

⁹ Australian Astronomical Observatory

2 Science Cases

The scientific niches for a 2 metre class telescope in Antarctic environment have been detailed in 3 papers (see Lawrence *et al.* 2009abc) for the Australian project PILOT and in the final report of the specialized working group of the EC network ARENA (Burton *et al.*, 2010). However, the PLT science cases significantly differ from the PILOT ones, because, i) it focuses on a smaller range of wavelengths, ii) it features a much larger FOV, and iii) it explores the time domain for the first time in the infrared.

At the present time three main astrophysical fields would greatly benefit from the PLT. These topics are in common with other instruments that will operate at the same period, and in particular the LSST. The PLT and the LSST data would thus be managed using similar procedures. Both surveys will be able to alert each other during the overlapping period of operation for an optimal follow-up of transient events.

2.1 Distant Universe

PLT is particularly appropriate to the exploration of the distant universe, notably wherever the dust extinction strongly hampers the optical observations, such as the disks and bulges of galaxies where the largest space density of stars -and thus of SN candidates - are found. Moreover, it will explore the time dimension during a period of 10 years at different time resolutions. The most promising domains encompass:

- a survey for pair-instability supernovae (via a dedicated periodically repeated wide field survey) and γ -ray burst afterglows (via alerts from high energy satellites, LSST detections), events which represent the final evolutionary stages of the first stars to form in the Universe,
- an ultra-deep survey to study galaxy structure, formation, and evolution via the detection of large samples of high redshift galaxies,
- a near-infrared search for Type Ia supernovae to obtain light curves that are largely unaffected by dust extinction and reddening, allowing tighter constraints to be placed on the expansion of the Universe and a study of a sample of moderate-redshift galaxy clusters aimed at understanding galaxy cluster growth, structure, and evolution.

2.2 Stellar formation and evolution, galactic ecology

Deep thermal infrared imaging is ideally suited to probe:

- the stellar content of our Galaxy and galaxies of the local groups, especially young stellar objects, stars in the late stage of evolution and very low mass stars. Repeated observations will provide hundred of thousands of light curves that will improve our knowledge of the mass loss process, enrichment of the interstellar medium in heavy elements and the internal physical processes occurring in the Asymptotic Giant Branch phase,
- disk of galaxies of the local group to study the processes of galaxy formation and evolution,
- nearby satellite galaxies to trace their outer morphology, structure, age and metallicity,
- repeatedly surveying the Magellanic Clouds in order to understand the star formation and evolution processes in galaxies of different metallicities. The Magellanic Clouds are continuously observable in excellent condition from Antarctica.

2.3 Very low mass stars, exoplanets and small bodies of the solar system

Areas in which PLT would be a very powerful tool are:

- the search for free-floating planetary-mass objects,
- the follow-up of gravitational microlensing candidate detections based on alerts from dedicated survey telescopes,
- a collection of high precision photometric infrared light curves for secondary transits of previously discovered exoplanets. PLT will have the possibility of observing nearly continuously during the antarctic winter and possibly all year round in the 3 μ m window,
- the identification and infrared characterization of small bodies of the solar system (transneptunians, Gould belt, geocruisers...) in close connection with the LSST.

3 Instrumental Concept

3.1 Telescope

The telescope baseline benefits from the earlier PILOT phase A study (UNSW-AAO) (Lawrence *et al.* 2009abc), although it is optimized for the 2-4 μm , thus somewhat relaxing the optical constraints. The main characteristics of the telescope are summarized in Tab.1. One of the two Nasmyth foci would be equipped with the IR camera covering the 2-5 μm range and the second focus could possibly feed, in the future, another instrument such as *e.g.*, a mid-IR camera (8-30 μm) or a near-IR Integral Field Spectrograph.

The height above the ice at which the telescope would be set up is absolutely critical, for two main reasons, i) the turbulent ground layer (TGL) thickness at Dome C is as low as about 30 m with possible important fluctuations, ii) the temperature gradient may rise sharply in the TGL and strong variations of temperature often occur, especially in winter. Setting the telescope above the boundary layer, for instance on top of a ~ 30 m tower, is thus essential, but one must also definitely stabilize its temperature. A solution to fix the temperature of the telescope by blowing cold air from the ground level has been proposed in the PILOT phase A study.

Field of View	$\geq 1^\circ$
Effective clear aperture	$\sim 2.5\text{m}$
Configuration	Ritchey-Chrétien, double Nasmyth foci
Etendue	$5\text{m}^2\text{deg}^2$
Spectral range	2-5 μm
Sky coverage	5000°^2
Final f ratio	f/5
Diameter of 80% encircled energy spot	$\leq 0.2''$

Table 1. Main characteristics of the telescope

3.2 Infrared Camera

Thanks to recent developments in the industrial production of larger infrared arrays (currently 4, but soon up to 16 Mpixels), it has been possible to develop facilities for surveys in the near infrared that are comparable to those in the visible, although at much higher cost. A reasonable trade-off between cost and performances points toward a 256-Mpixel FPA. The basic specifications of the PLT infrared camera are displayed in Tab. 2. A Ground Layer Adaptive Optics (GLAO) system would possibly equip the camera to alleviate residual turbulence above the telescope, or relax the constraint on the height of the tower (Travouillon *et al.* 2009).

Array type	HgCdTe HAWAII 4RG
Array size	$4k \times 4k$
FPA configuration	16 chips buttable end to end
Pixel size	10 μm
Pixel scale	$\leq 0.15''$
Final PSF FWHM	$0.3''$
Field of view of the camera	$40' \times 40'$
Filter set (3 minimal)	K_d, L_s, L'
Possible additional filters	K, K_s , M', Grism, narrow bands
Read out time (typical)	5 sec
Integration time per frame (typical)	100 s

Table 2. Main characteristics of the PLT near infrared camera

4 Performances and Operations

The PLT would be the most sensitive instrument ever installed on the ground at 2 μm pushing the limit at least 2 magnitudes below the VISTA achievement (Dalton *et al.* 2010). Table 3 summarizes the point source

and extended object limiting sensitivities (in AB magnitudes) for a 5σ , 1 hour integration, assuming that the sky background is summed over 4 times the FWHM disc (for point sources), that the telescope temperature is stabilized at 227K with 5% emissivity, and the overall optical efficiency is 50% (including throughput, detector efficiencies, and secondary mirror obscuration) (adapted from Lawrence *et al.* 2009abc).

Band	λ (μm)	R ($\lambda/\Delta\lambda$)	FWHM ($''$)	m_{AB} mag.	m_{AB} /arc ²
K_d	2.40	10	0.32	25.3	24.7
L'	3.76	5.8	0.40	21.2	20.8
M	4.66	19	0.46	19.6	19.4

Table 3. Expected sensitivity of the PLT

The PLT would operate all year round during a foreseen 10-yr period. Dark time would be mostly dedicated to the 2 μm window, while bright time (summer and twilight) would be exclusively dedicated to the 3-5 μm range. Since PLT is not intended to make an *all-sky* survey, like LSST, the number of visits of each sky area will depend on their extension, and special scientific requests. The PLT would produce about 1 Tbyte of raw data per day (Tab.4). For lack of high-flow internet connection in Antarctica, they should be massively processed on-site. PLT data are planned to be eventually archived at the CC-IN2P3 in Lyon, already involved in the LSST data management, and would be made accessible to the community through a VO model.

	PLT	LSST
Image exposure time	30s	30s ($2 \times 15\text{s}$)
FOV (sq. deg.)	0.5	10
Sky coverage (sq. deg.)	5 000	20 000
Coverage time	4×24 hours	3 nights
Raw pixel data per 24 h period	0.5 to 1 Tb	15 Tb
Yearly archive rate	100 to 200 Tb	5.6 Pb
Number of visits per year (<i>indicative for PLT</i>)	25 @ K_d / 90 @ L' , M	100
Number of filters (baseline, mini, goal)	4, 3, 6	5, 3, 6
Image quality (average, maxi, goal) (arcsec)	0.40, 0.45, 0.35	0.56, 0.59, 0.53

Table 4. PLT and LSST observing strategies and data flows.

The PLT consortium involves ten research laboratories, agencies and industrial companies, and more than 50 researchers and engineers from 3 laboratories of the French CNRS, [*Fizeau (Nice)*, *CRAL (Lyon)*, *CC-IN2P3 (Lyon)*], the Institute of Atmospheric Sciences and Climate (*ISAC, Rome*) of the Italian CNR, European Industrial Engineering (EIE, Mestre, Italy), the Fraunhofer Institute (IPA) in Stuttgart, Germany, Institut Paul-Emile Victor (Brest, France), the Nansen Environmental and Remote Sensing Center (Bergen, Norway), RAMS-CON Management Consultants (Assling, Germany), SAFRAN (REOSC) France, the Science and Technology Facilities Council (STFC) and the University of New South-Wales (UNSW), Sydney, Australia.

The members of the PLT Design Study proposal and in particular M. Carbillet, C. Genthon, T. Le Bertre, R. Lemrani, B. Le Roux, G. Marchiori, J. Montnacher, P. Prugniel, K. Rachwal, & E. Ruch, are warmly thanked for their contributions to the project.

References

- Aristidi E., Fossat E. Agabi, A. *et al.*, 2009, A&A, 499, 955
 Burton, M.G., 2010, Astron. Astrophys. Rev., 18, 417
 Burton, M.G., *et al.*, 2010, Procs. third ARENA Conference on “An Astronomical Observatory at Concordia(Dome C, Antarctica)” *Spinoglio L., Epchtein N., (eds.)*, EDP EAS Publication Series, Vol. 40, 125
 Dalton G., 2010, Proc. SPIE Vol. 7735, 77351J
 Lawrence J. *et al.*, 2009, PASA, 46, 379(a), 397(b), 415(c)
 Philips A., Burton M.G., Ashley M.C.B., *et al.*, 2009, ApJ, 527, 1009
 Price, S.D., 2009, Space Sc. Rev 142, 233
 Travouillon T., Jolissaint L., Ashley M.C.B. *et al.*, 2009, PASP, 121, 668
 Walden V.P., *et al.*, 2005, PASP, 117, 300

NON-THERMAL PHYSICS OF GALAXY CLUSTERS

C. Ferrari¹

Abstract. Deep radio observations of galaxy clusters have revealed the existence of diffuse radio sources related to the presence of relativistic electrons and weak magnetic fields in the intracluster volume. Non-thermal intracluster phenomena are reviewed, together with the importance for this research field of joint radio, mm, X- and Gamma-ray observations of galaxy clusters.

Keywords: galaxies: clusters: general, radio continuum: galaxies

1 Introduction

Galaxy clusters are complex gravitationally bound astrophysical objects, whose huge masses ($M_{cl} \approx 10^{13} - 10^{15} M_{\odot}$) are principally made of dark matter ($\sim 80\% M_{cl}$). Their dominant baryonic component is a hot and tenuous intracluster medium (ICM) that we observe in X-rays ($\sim 15\% M_{cl}$). Radio observations have pointed out that the volume in between cluster galaxies may also host a non-thermal component, i.e. weak magnetic fields ($\approx \mu\text{Gauss}$) and relativistic particles ($\approx \text{GeV}$). At present, non-thermal emission has been detected in approximately 10% of known clusters, in particular in massive major mergers (Ferrari et al. 2008).

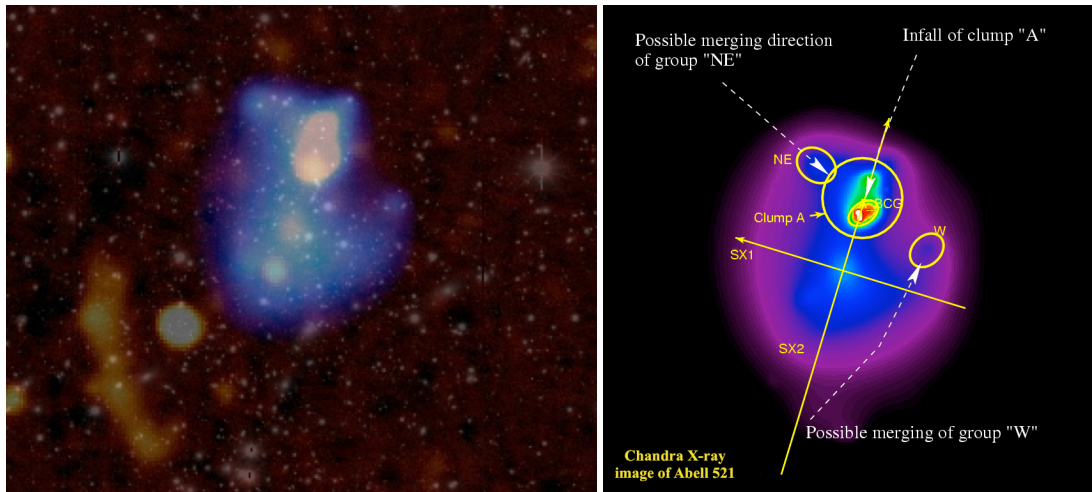


Fig. 1. **Left:** composite image of the galaxy cluster Abell 521, observed in optical (*ESO*, white), X-rays (*Chandra*, blue) and radio (*VLA*, brown). (Adapted from Ferrari et al. 2003, 2006). **Right:** multiple merging scenario for Abell 521 reconstructed by comparing optical and X-ray observations of the cluster (from Ferrari et al. 2006).

Actually, in agreement with the expectation of the hierarchical scenario of structure formation emerging from the concordant cosmological model, the comparison of X-ray and optical observations with results coming from numerical simulations has now clearly proven that galaxy clusters form through merging of less massive systems (e.g. Maurogordato et al. 2011, see also right panel of Fig. 1)).

¹ Université de Nice Sophia Antipolis, CNRS, Observatoire de la Côte d'Azur, Laboratoire Cassiopée, Nice, France

2 Detection of the non-thermal intracluster component

2.1 Radio observations

In 1959 Large et al. mapped for the first time the Coma cluster at radio wavelengths. Despite the very low resolution of their observations ($\sim 40 \times 56$ arcmin²), they discovered the presence of a resolved and thus extended source at the cluster centre. The nature of this diffuse radio emission remained unclear until 1970, when Willson confirmed its detection and pointed out that the extended source was related to intergalactic emission rather than integrated radiation from unresolved radio galaxies. Since then extended radio sources permeating the central volume of clusters are usually referred as “radio halos” or as “radio mini-halos”, depending on their size (≥ 1 Mpc vs. $\lesssim 500$ kpc). Elongated radio sources in the cluster periphery are known as “radio relics”. These sources are generally characterized by steep synchrotron spectra, indicative of aging of relativistic particles (bottom left panel of Fig. 2).

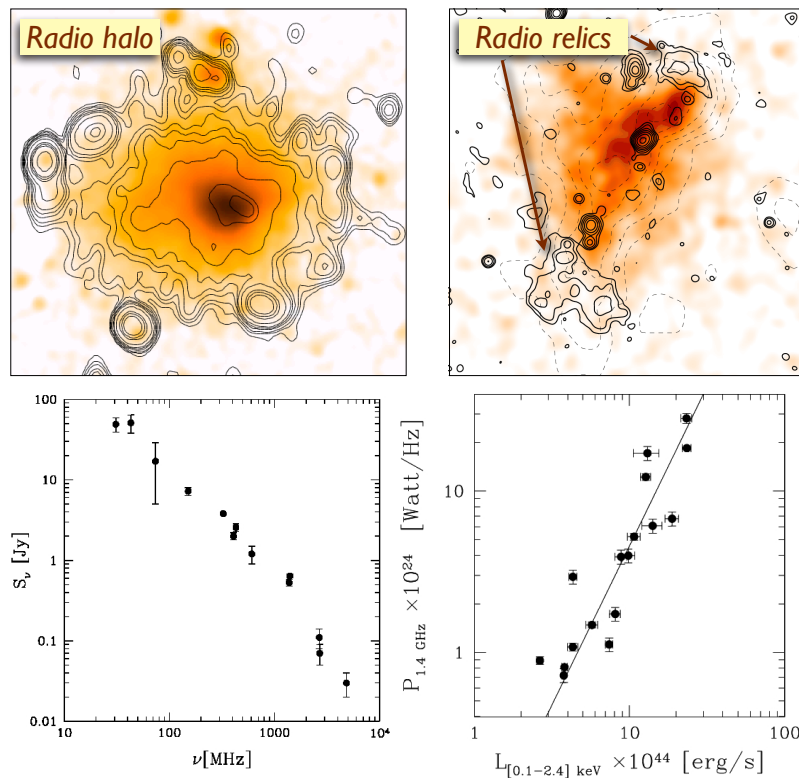


Fig. 2. **Top:** Radio contours overlaid on the X-ray image of Abell 2163 (*left*) and ZwCl 2341.1+0000 (*right*) (adapted from Feretti et al. 2001; Bourdin et al. 2011; van Weeren et al. 2009). **Bottom:** Spectrum of the radio halo in the Coma cluster (*left* – adapted from Thierbach et al. 2003). Radio power at 1.4 GHz of radio halos vs. cluster X-ray luminosity (*right* – adapted from Cassano et al. 2006).

Up to now Mpc-scale intracluster radio sources have been detected only in merging galaxy clusters. Their radio power generally correlates with the X-ray luminosity of the host clusters (see bottom right panel of Fig. 2). Recent results claim however the detection of a few systems lying outside the expected radio vs. X-ray correlation. These clusters are under- or over-powerful at radio wavelengths with respect to their X-ray luminosity (Russell et al. 2011; Giovannini et al. 2011).

2.2 Hard X-ray and Gamma-ray observations

If, as detailed in previous sections, X-ray and radio observations have revealed the presence of a highly ionized thermal plasma as well as of relativistic electrons and magnetic fields in the intracluster volume, galaxy clusters are also expected to host relativistic protons and ultra-relativistic electrons (e.g Brunetti et al. 2009). Besides synchrotron radio emission from GeV electrons and intracluster magnetic fields, non-thermal emission from galaxy clusters is thus expected in other bands of the electromagnetic spectrum (Ferrari et al. 2008; Brunetti et al. 2009, and references therein):

- Hard X-rays (HXR) from inverse Compton (IC) scattering of CMB photons by GeV electrons or from synchrotron emission of TeV electrons;

- Gamma-rays from IC scattering of CMB photons by TeV electrons or from inelastic collision of cosmic ray protons with the ions of the CMB. Some gamma-ray emission is also expected from interactions of relativistic electrons and protons with MHD intracluster turbulence.

Evidence of non-thermal (IC) HXR emission from several clusters hosting diffuse radio sources has been obtained mostly through the X-ray satellites *Beppo-SAX* and *RXTE* (Fusco-Femiano et al. 1999; Rephaeli et al. 1999). The detection and nature (thermal or non-thermal) of the HXR excess in galaxy clusters is however strongly debated (Ferrari 2009, and references therein). Up to now, only upper-limits have been derived for the Gamma-ray emission of galaxy clusters (e.g. Ackermann et al. 2010), which imply a cosmic-ray energy density less than 5-20% of the thermal cluster energy density.

3 Open questions and perspectives

The origin of the intracluster non-thermal component observed at radio wavelengths is one of the main open questions of current cluster studies.

Magnetic fields at the observed intensity level ($\approx 1 \mu\text{Gauss}$) could result from amplification of seed fields through adiabatic compression, turbulence and shear flows associated to the hierarchical structure formation process. Seed fields could fill the entire volume of the universe, having been created by primordial processes or through different physical mechanisms (such as the “Biermann battery” effect in merger and accretion shocks, or the outflow from AGN and starburst galaxies in proto-clusters at $z \approx 4 - 6$. See Dolag et al. 2008, for a review).

Different mechanisms can produce cosmic-rays in galaxy clusters. Primary relativistic electrons can be accelerated by processes internal to cluster galaxies and then ejected into the intracluster volume. The expected diffusion velocity of relativistic particles being of the order of the Alfvén speed ($\sim 100 \text{ km/s}$), cosmic rays need ≥ 10 Gyr to propagate over radio halo and relic extensions. The radiative lifetime of relativistic electrons is however much shorter ($\lesssim 0.1$ Gyr) due to IC and synchrotron energy losses*. Cosmic-ray electrons, thus, cannot simply be ejected by active galaxies and propagate over the cluster volume, but they have to be continuously (re-)accelerated *in situ* (see Ferrari et al. 2008, and references therein). Electrons can be (re-)accelerated by shocks and turbulence generated in the ICM by major cluster mergers (Ensslin et al. 1998; Brunetti et al. 2001), or they could have a secondary origin, resulting from hadronic collisions between relativistic protons and ions of the ICM (Dennison 1980). Current radio observational results are mostly in agreement with the first hypothesis (e.g. Brunetti et al. 2008). In particular, intracluster electron re-acceleration would be related to shocks in the case of radio relics, or turbulence in the case of halos and mini-halos. Since most of Mpc-scale radio sources have been detected in luminous merging systems, the energy required to produce radio emitting cosmic-rays would come most likely from the huge gravitational energy released during cluster mergers ($\approx 10^{64}$ ergs). In the case of mini-halos it has been suggested that a population of relic electrons ejected by a central AGN are most likely re-accelerated by MHD turbulence within the central cold cluster region (Gitti et al. 2002).

In a recent work, we have shown for the first time the importance of combining radio and mm studies of galaxy clusters in order to understand the physical mechanisms lying behind electron acceleration (Ferrari et al. 2011). A high-pressure region in the ICM of the galaxy cluster RXJ1347-1145 has been pointed out by mm *MUSTANG* observations through the Sunyaev-Zel’dovich effect (Mason et al. 2010). This galaxy cluster was known to host a radio mini-halo, whose cosmic-ray electron origin was attributed to ICM turbulence at the center of the cluster (Gitti et al. 2007). Our low-frequency (240 MHz and 610 MHz) *GMRT* observations point out the existence of an excess radio emission corresponding to the high pressure region of the ICM (see Fig. 3), which is in turn most likely associated to a shock front resulting from a cluster merger (Ferrari et al. 2011).

This result indicates that the diffuse radio source at the center of RXJ1347-1145 presents intermediate properties between classical radio mini-halos and relics. The acceleration of electrons in this system results from the combination of different physical mechanisms, suggesting that, if up to now we have observed the “tip of the iceberg” of non-thermal cluster emission, joint multi-wavelength studies of clusters through new radio, mm and X-ray instruments (e.g. *LOFAR*, *Planck*, *NuSTAR* . . .) will probably allow us to get a clearer characterization of the physics driving non-thermal intracluster phenomena. Traditional classifications of diffuse intracluster radio sources will lead to a more general view of multi-scale, complex radio emission, deeply connected to the thermo-dynamical history of each cluster.

I acknowledge financial support by the “*Agence Nationale de la Recherche*” through grant ANR-09-JCJC-0001-01.

*Note that, compared to electrons, cosmic ray protons have much longer lifetimes, comparable to the Hubble time.

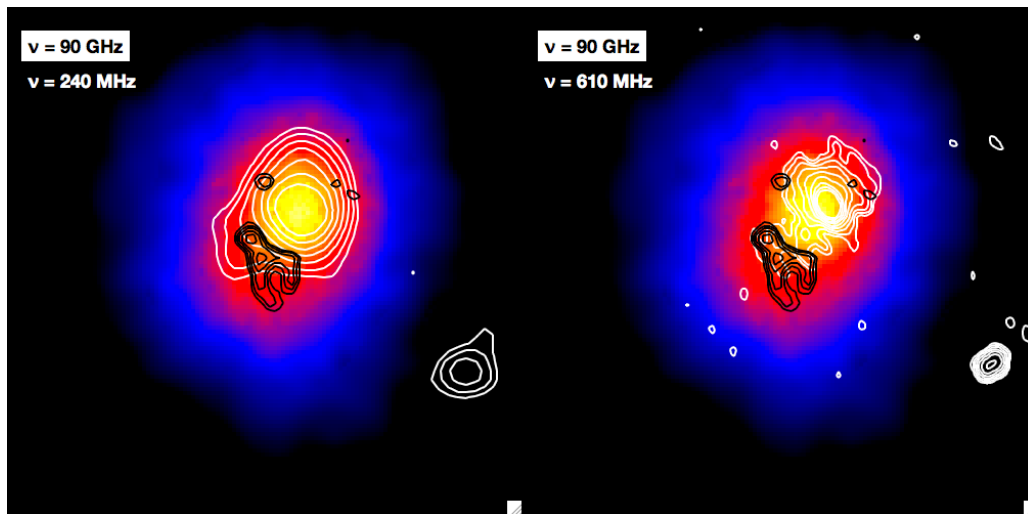


Fig. 3. X-ray image of RXJ1347-1145 with *MUSTANG* 90 GHz contours in black, indicating the presence of a high-pressure ICM region, possibly related to hot shocked gas (Mason et al. 2010). GMRT 240 MHz (*left*) and 610 MHz (*right*) contours are also superimposed (in white). The first radio contours is at 5σ level (with 0.9 and 0.1 mJy/beam noise level at 240 and 610 MHz, respectively). (Adapted from Ferrari et al. 2011).

References

- Ackermann, M., Ajello, M., Allafort, A., et al. 2010, *ApJ*, 717, L71
- Bourdin, H., Arnaud, M., Mazzotta, P., et al. 2011, *A&A*, 527, A21
- Brunetti, G., Blasi, P., Cassano, R., & Gabici, S. 2009, in *American Institute of Physics Conference Series*, Vol. 1112, American Institute of Physics Conference Series, ed. D. Bastieri & R. Rando, 129–137
- Brunetti, G., Giacintucci, S., Cassano, R., et al. 2008, *Nature*, 455, 944
- Brunetti, G., Setti, G., Feretti, L., & Giovannini, G. 2001, *MNRAS*, 320, 365
- Cassano, R., Brunetti, G., & Setti, G. 2006, *MNRAS*, 369, 1577
- Dennison, B. 1980, *ApJ*, 239, L93
- Dolag, K., Bykov, A. M., & Diaferio, A. 2008, *Space Sci. Rev.*, 134, 311
- Ensslin, T. A., Biermann, P. L., Klein, U., & Kohle, S. 1998, *A&A*, 332, 395
- Feretti, L., Fusco-Femiano, R., Giovannini, G., & Govoni, F. 2001, *A&A*, 373, 106
- Ferrari, C. 2009, in *American Institute of Physics Conference Series*, Vol. 1126, American Institute of Physics Conference Series, ed. J. Rodriguez & P. Ferrando, 277
- Ferrari, C., Arnaud, M., Etori, S., Maurogordato, S., & Rho, J. 2006, *A&A*, 446, 417
- Ferrari, C., Govoni, F., Schindler, S., Bykov, A. M., & Rephaeli, Y. 2008, *Space Sci. Rev.*, 134, 93
- Ferrari, C., Intema, H. T., Orrù, E., et al. 2011, *ArXiv e-prints*
- Ferrari, C., Maurogordato, S., Cappi, A., & Benoist, C. 2003, *A&A*, 399, 813
- Fusco-Femiano, R., dal Fiume, D., Feretti, L., et al. 1999, *ApJ*, 513, L21
- Giovannini, G., Feretti, L., Girardi, M., et al. 2011, *A&A*, 530, L5
- Gitti, M., Brunetti, G., & Setti, G. 2002, *A&A*, 386, 456
- Gitti, M., Ferrari, C., Domainko, W., Feretti, L., & Schindler, S. 2007, *A&A*, 470, L25
- Large, M. I., Mathewson, D. S., & Haslam, C. G. T. 1959, *Nature*, 183, 1663
- Mason, B. S., Dicker, S. R., Korngut, P. M., et al. 2010, *ApJ*, 716, 739
- Maurogordato, S., Sauvageot, J. L., Bourdin, H., et al. 2011, *A&A*, 525, 79
- Rephaeli, Y., Gruber, D., & Blanco, P. 1999, *ApJ*, 511, L21
- Russell, H. R., van Weeren, R. J., Edge, A. C., et al. 2011, *MNRAS*, L297
- Thierbach, M., Klein, U., & Wielebinski, R. 2003, *A&A*, 397, 53
- van Weeren, R. J., Röttgering, H. J. A., Bagchi, J., et al. 2009, *A&A*, 506, 1083
- Willson, M. A. G. 1970, *MNRAS*, 151, 1

EVOLUTION AS A CONFOUNDING PARAMETER IN SCALING RELATIONS FOR GALAXIES

D. Fraix-Burnet¹

Abstract. Early-type galaxies are characterized by many scaling relations. Evolutionary classifications find that some of these correlations are indeed generated by diversification. With a simple mathematical formalism, we show (Fraix-Burnet 2011) that even the so-called fundamental plane, a relatively tight correlation between three variables, can be easily explained as the artifact of the effect of another parameter influencing all, without any physical hypothesis. In other words, the fundamental plane is probably a confounding correlation, i.e. not physically causal. The complexity of the physics of galaxies and of their evolution suggests that the confounding parameter must be related to the level of diversification reached by the galaxies. Galaxy mass, central black hole mass or the gas fraction during the last big merger are shown to be possible confounding factors. Consequently, many scaling relations for galaxies are probably evolutionary correlations that are explained by the statistical general evolution of most properties of galaxies. This effect makes the observables not independent, so that it must be removed before statistical and physical inferences could be made.

Keywords: galaxies: fundamental parameters, methods: statistical, galaxies: evolution, galaxies: formation

1 The fundamental plane as a confounding correlation

The fundamental plane for early-type galaxies is a correlation between effective radius, the central velocity dispersion and the surface brightness within the effective radius (Djorgovski & Davis 1987; Dressler et al. 1987). Let us consider that the effective radius r_e , the central velocity dispersion σ and the luminosity L are all power-law functions of a same generic parameter \tilde{X} :

$$\begin{cases} r_e &= A_1 \tilde{X}^p \\ \sigma &= A_2 \tilde{X}^s \\ L &= A_3 \tilde{X}^t \end{cases} \quad (1.1)$$

The surface brightness μ_e can be expressed as

$$\begin{aligned} \mu_e &= -2.5 \log(L/\pi r_e^2) + m \\ &= (-2.5t + 5p) \log \tilde{X} + 2.5 \log(\pi) + m \end{aligned} \quad (1.2)$$

where m is a constant of normalisation. Any linear correlation of the form

$$\log r_e = a \log \sigma + b \mu_e + c \quad (1.3)$$

translates to

$$\begin{cases} p &= sa + (-2.5t + 5p)b \\ \log A_1 &= a \log A_2 + b (2.5 \log(\pi A_1^2/A_3) + m) + c. \end{cases} \quad (1.4)$$

If a solution can be found for a and b from Eq. 1.4, then the equation of the fundamental plane Eq. 1.3 is obtained. Conversely, the observations provide a , b and c , so that it is possible to derive p , s and t . There is no need of any further assumption to explain the fundamental plane.

¹ Université Joseph Fourier - Grenoble 1 / CNRS, Institut de Planétologie et d'Astrophysique de Grenoble, BP 53, F-38041 Grenoble cedex 9, France, e-mail: fraix@obs.ujf-grenoble.fr

Here are a few examples for \tilde{X} , the relations being constrained only by observations or numerical simulations and Eq. 1.4:

$$\begin{cases} r_e \propto f_{starburst}^{-1} \\ \sigma \propto f_{starburst}^1 \\ L \propto f_{starburst}^{0.8} \end{cases} \quad (1.5)$$

$$\begin{cases} r_e \propto M_{BH}^{0.63} \\ \sigma \propto M_{BH}^{0.28} \\ L \propto M_{BH}^{0.83} \end{cases} \quad (1.6)$$

$$\begin{cases} r_e \propto (1+z)^{-0.5} \\ \sigma \propto (1+z)^{0.4} \\ L \propto (1+z)^{0.25} \end{cases} \quad (1.7)$$

2 Evolutionary correlations

In the course of diversification, many properties of galaxies change, and they tend to statistically change in a more or less monotonous way. It seems difficult to avoid the evolution to act as a confounding factor. It is a well-known problem of comparative methods in phylogeny (e.g. Felsenstein 1985).

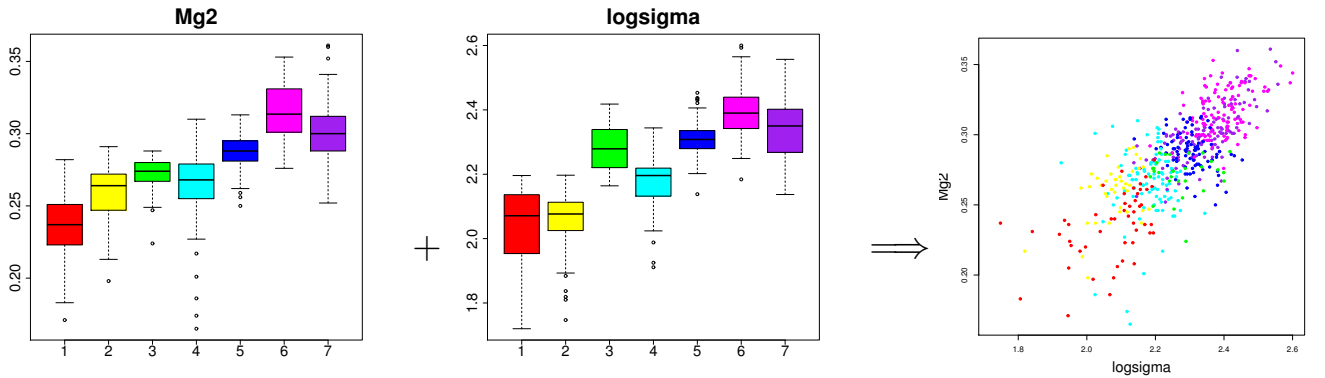


Fig. 1. Two parameters (Mg_2 , left, and σ , middle) evolving as a function of an other parameter (here the level of diversification) necessarily produce a correlation in the corresponding scatter plot (right).

We thus propose that the main confounding parameter is

$$\tilde{X} = T$$

with T an indicator of the level of diversification, being something like an evolutionary clock not necessarily easily related to time or redshift.

Indeed, the evolutionary clock, i.e. the factor $\tilde{X} = T$, can be hidden, not understandable analytically and not directly observable.

Diversification cannot be summarized with only one simple property (like redshift or mass) because galaxies are too complex objects and do not evolve linearly in a unique way. In some diagrams, that is for some set of variables, a particular property could crudely depict the general trend of diversification. In the case of r_e , σ and μ_e , and to a first approximation, mass could well represent a satisfactory driving parameter for the fundamental plane correlation, but it is certainly not unique. Since it is only approximate, some dispersion is expected. Hence, dispersion may be explained by the statistical (non-causal) nature of the correlation and the heterogeneity of the samples as far as diversification is concerned (Fraix-Burnet et al. 2010).

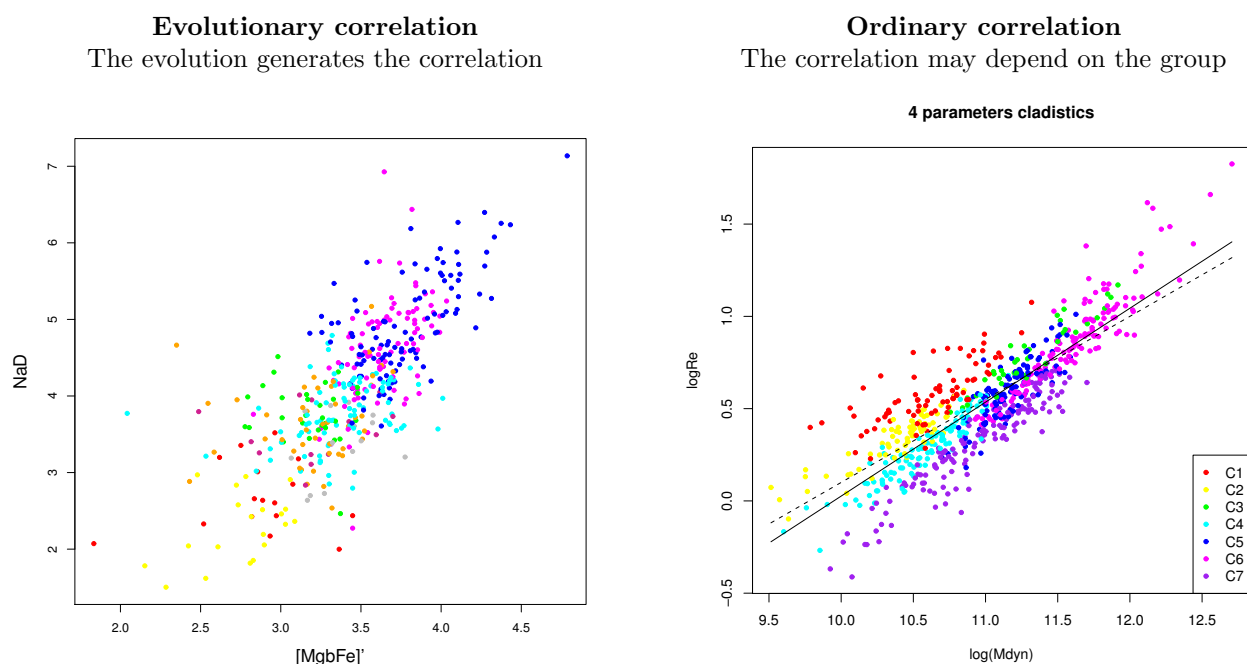


Fig. 2. Illustration of two kinds of correlations. **Left:** The evolutionary correlation can be identified by the groups (indicated by their colors) nearly ordered according to their level of diversification. **right:** An ordinary correlation is independent of diversification, but may or may not exist globally and/or within each group.

A lot of observables evolve with diversification, at least statistically, so that we should not be surprised by the many scaling relations found for galaxies and the difficulty to pinpoint the driving parameters and mechanisms. We also better understand why several characteristic parameters (mass, luminosity, metallicity...) and also the samples themselves have been found to influence the shape of the fundamental plane without providing a clearer picture of its origin. Physics can only be investigated when confounding factors have been eliminated. This here requires an evolutionary classification that gathers objects according to their history.

This work is published in Fraix-Burnet (2011).

References

- Djorgovski, S. & Davis, M. 1987, ApJ, 313, 59
 Dressler, A., Lynden-Bell, D., Burstein, D., et al. 1987, ApJ, 313, 42
 Felsenstein, J. 1985, The American Naturalist, 125, 1
 Fraix-Burnet, D. 2011, MNRAS: Letters, 416, L36
 Fraix-Burnet, D., Dugué, M., Chattopadhyay, T., Chattopadhyay, A. K., & Davoust, E. 2010, MNRAS, 407, 2207

MAPPING THE DUST PROPERTIES OF NEARBY GALAXIES WITH HERSCHEL AND LABOCA

M. Galametz¹, M. Albrecht², R. Kennicutt¹, F. Bertoldi², F. Walter³, A. Weiss⁴, D. Dale⁵, B. Draine⁶, G. Aniano⁶, C. Engelbracht⁷, J. Hinz⁷ and H. Roussel⁸

Abstract. We combine Spitzer, Herschel and LABOCA observations from 24 to 870 μm for 11 galaxies of the KINGFISH Herschel Key programme dedicated to the observations of 61 nearby galaxies of various metallicities and levels of star formation activity. We perform a global two-temperature fitting of the Spectral Energy Distributions of the galaxies to study the cold dust properties and probe the variations in the emissivity index of grains inferred by the use of submm data. Using the resolution of Spitzer and Herschel observations, we also produce dust temperature maps of the galaxies and perform a local study of the variations of cold dust properties within the galaxies. We finally build extrapolated maps at 870 μm and compare them with our LABOCA observations. Some of our galaxies exhibit an excess at 870 μm compared to fluxes inferred from the modeling. This excess decreases (and even disappears in some cases) when a lower emissivity index is used, for instance $\beta=1.5$ in lieu of the standard value of 2 commonly used in current SED models. The cause for such excess still has to be investigated.

Keywords: ISM, dust, submillimeter, Herschel, LABOCA, SED model

1 Introduction

An exhaustive inventory of the dust temperature distribution and heating processes is essential to understand the physics of the Interstellar Medium (ISM). Numerous studies have pointed out the necessity of both far-infrared (FIR) and submillimeter (submm) observations to constrain the thermal dust emission of galaxies and probe the dust grain properties such as temperature, emissivity or mass (Gordon et al. 2010, among others). *Herschel* is currently mapping nearby galaxies in the 70 to 500 μm wavelength range. Early science results led to the detection of colder dust ($T < 20\text{K}$) than previously assumed in nearby galaxies. Those studies investigated the cold dust temperature dependence on morphological type and bars (Engelbracht et al. 2010), radius (Pohlen et al. 2010), star formation or global starlight (Bendo et al. 2011; Galametz et al. 2010). Submm observations of low-metallicity galaxies have also suggested that cold dust properties could differ from standard ones and led to the detection of an excess (Dumke et al. 2004; Galliano et al. 2003, 2005; Bendo et al. 2006; Marleau et al. 2006; Galametz et al. 2009; O’Halloran et al. 2010; Bot et al. 2010). In the present work, we combine *Herschel* observations of 11 nearby galaxies obtained as part of the KINGFISH programme (Key Insights on Nearby Galaxies: A Far-Infrared Survey with Herschel, PI: R. Kennicutt) with LABOCA maps at 870 μm to probe the spatially-resolved cold dust properties and investigate potential submm excess emission in our targets.

¹ Institute of Astronomy, University of Cambridge, Madingley Road, Cambridge CB3 0HA, UK

² Argelander-Institut für Astronomie, Abteilung Radioastronomie, Auf dem Hügel, D-53121 Bonn, Germany

³ Max-Planck-Institut für Astronomie, Königstuhl 17, D-69117 Heidelberg, Germany

⁴ Max-Planck-Institut für Radioastronomie, Auf dem Hügel 69, D-53121 Bonn, Germany

⁵ Department of Physics & Astronomy, University of Wyoming, Laramie, WY 82071, USA

⁶ Department of Astrophysical Sciences, Princeton University, Princeton, NJ 08544, USA

⁷ Steward Observatory, University of Arizona, Tucson, AZ 85721, USA

⁸ Institut d’Astrophysique de Paris, F-75014 Paris, France

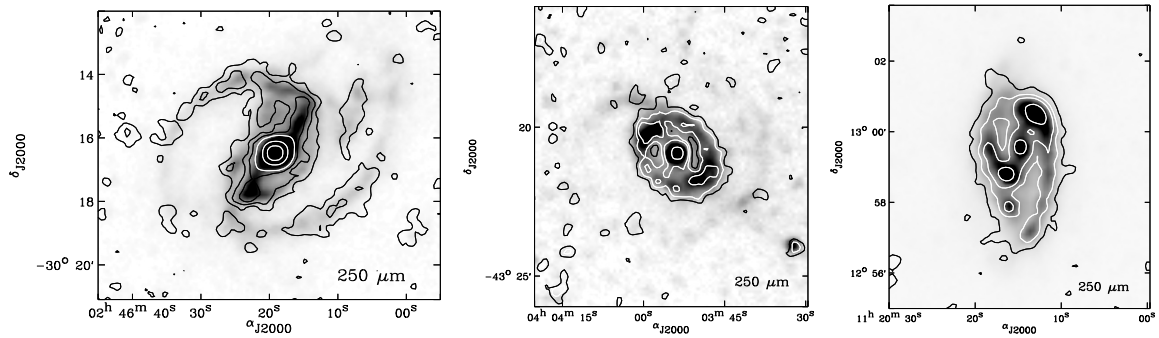


Fig. 1. KINGFISH SPIRE 250 μm observations with 870 μm contours overlaid. **Left:** NGC 1097. Contours indicate flux densities of 4, 10, 17, 30, 100 and 200 mJy.beam^{-1} , **Middle:** NGC 1512. Contours indicate flux densities of 3.5, 6.5, 10 and 25 mJy beam^{-1} . **Right:** NGC 3627. Contours indicate flux densities of 10, 30, 50 and 100 mJy beam^{-1} .

2 Herschel and LABOCA observations

The *Herschel* PACS and SPIRE observations have been obtained as part of the KINGFISH programme (see Kennicutt et al. 2011, for a description of the survey). PACS observes at 70, 100 and 160 μm with FWHMs of 5.2", 7.7" and 12" respectively (Poglitsch et al. 2010). The Scanamorphos technique was used to process the data from Level 1 (Roussel et al. 2011 in prep). The PACS calibration uncertainties are $\sim 10\%$ at 70 and 100 μm and $\sim 20\%$ at 160 μm . SPIRE produces maps at 250, 350 and 500 μm , with FWHMs of 18", 25" and 36" respectively (Griffin et al. 2010). Calibration uncertainties are estimated to be $\sim 7\%$ for the three wave bands. Complementary data with LABOCA at 870 μm were also obtained for the same sample. A complete description of the LABOCA data reduction can be found in Albrecht et al. (in prep). The full width half maximum (FWHM) of the point spread function (PSF) at 870 μm is $\sim 19''.2$. The resolution of LABOCA is similar to that of SPIRE 250 μm . SPIRE 250 μm maps with LABOCA contours overlaid are shown in Fig. 1.

3 Global dust properties

To study the global dust temperatures of our sample, we perform a two-temperature (warm and cold) modeling with a combination of modified blackbodies. We add *Spitzer* and IRAS data to sample the dust thermal emission of our galaxies from 24 to 870 μm . The notation T_c will refer to the temperature of cold dust hereafter. The emissivity index of the warm dust (β_w) is fixed to a standard emissivity index of 2 (Li & Draine 2001) while that of the cold dust (β_c) is free. Figure 2 *left* shows the global SED of NGC 3627. The bottom panel indicates the residuals from the fit. For NGC 1097, NGC 1512, NGC 3351 or NGC 3621, the warm component contributes to more than 50% of the 70 μm flux, justifying the use of a warm component in the fitting. We observe strong variations of the cold dust emissivity within our sample, with β_c varying between 0.96 to 2.12 (consistent, within the error bars, with the expected range for emissivities). The LABOCA 870 μm flux strongly influences the parameters derived in some cases like NGC 1512 (steeper emissivity required). We note that the 500 μm flux density is systematically underestimated by the model when the LABOCA flux is used in the modeling. This excess is lower than 20% for most of the galaxies but reaches 40% for NGC 1512. We find that the derived T_c are higher when β_c is free compared to values derived if β_c is fixed to a standard value of 2. In that last case, the use of LABOCA data only weakly influences the T_c estimate (less than 4%).

Instrumental uncertainties can lead to an anti-correlation between T and β (Shetty et al. 2009). In order to study this dependence and quantify the errors bars of our results, we generate for each galaxy 2000 sets of modified constraints randomly varying within error bars. Correlations between SPIRE calibration errors are taken into account when generating the new datasets. We apply our two-temperature fit to the 2000 modified sets. Figure 2 *right* shows the parameter distribution of the 2000 runs in a $T_c - \beta_c$ parameter space for NGC 3627. The green crosses indicate the 2000 (T_c, β_c) combinations derived when the correlation between SPIRE calibration uncertainties is taken into account and the black crosses the 2000 combinations where SPIRE fluxes are modified independently. We overlay the median temperature and emissivity index in red. Taking into account the correlations between SPIRE calibration uncertainties clearly shrinks the ranges of values reached by T_c and β_c but does not influence the median values derived (less than 2% difference).

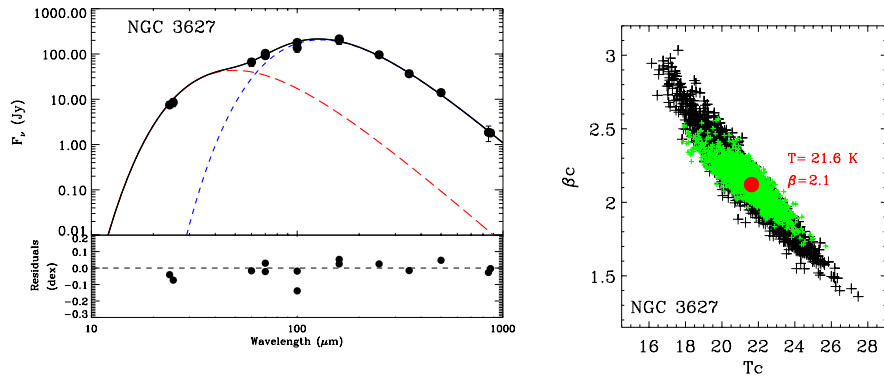


Fig. 2. Left: Two-temperature fits for NGC 3627 ($\beta_w=2$, β_c free). Data are overlaid with black circles. The bottom panel indicates the residuals from the fit. **Right:** (T_c , β_c) combinations derived from 2000 randomly modified datasets for NGC 3627. Median values are overlaid in red. See text for details on definitions and colors.

4 Resolved temperature maps

We use the same two-temperature modeling technique to derive temperature maps. MIPS, PACS and SPIRE maps are convolved to the SPIRE 500 μm resolution and projected to a common sample grid with a pixel size of $18''$. We first use a fixed $\beta_c (=2)$ to obtain a robust determination of the cold dust temperature distribution. LABOCA data are not used in the fitting but combined with the procedure results to derive excess maps at 870 μm (see the next section). Figure 3 *left* shows the temperature map of NGC 3627. SPIRE 250 μm contours are overlaid to enable a comparison of the temperature distribution with submm emission. We observe a smooth variation of the cold dust temperature distribution within our galaxies, with temperature maxima towards the center and towards star forming regions, and temperatures decreasing in the outer parts of galaxies. The choice of $\beta_c=2$ influences the temperatures derived. The temperature range is globally scaled to higher values if $\beta_c < 2$ or lower values if $\beta_c > 2$. If we let T_c and β_c vary, the temperature distributions derived from the modeling are more homogenous than those obtained with a fixed β_c , with a disappearance of the galaxy structure in extended objects. The temperature distribution seems also more erratic for low-surface brightnesses. This effect was pointed out by Planck Collaboration et al. (2011b) in the LMC and by Foyle et al. 2011 (submitted) in M83.

These discrepancies between temperature maps of course questions the physical sense of letting both temperature and emissivity vary at the same time, knowing the possible correlation between those parameters. Figure 3 shows the T - β diagram gathering pixels with 500 μm $3\text{-}\sigma$ detection for our sample. Galaxies are color-coded. The distribution of pixels in the T - β plane significantly differs from galaxy to galaxy, with a wide range of emissivity values for galaxies such as NGC 628, NGC 1097, NGC 3621 or NGC 7793, or more homogeneous values for NGC 1512, NGC 3351 or NGC 3627. An anti-correlation is clearly observed between temperature and emissivity, with higher emissivity values in colder ISM elements. The trend does not disappear if we restrict ourselves to the brightest pixels (so good confidence in the flux densities). It thus seems unlikely that this anti-correlation is only linked with Eddington bias (i.e. uncertainties on measurements) even if this assumption is difficult to assess. Moreover, a $18'' \times 18''$ pixel corresponds to a large ISM element for the galaxies of our sample - $18''$ corresponds to ~ 0.8 kpc at the distance of NGC 3627 - and thus to a large mixture of dust temperatures. The anti-correlation could then be artificially created by the addition of several dust temperatures, with a flattening of the slope when cold dust is present along the line of sight. Studies on resolved structures in the Milky Way (e.g. Paradis et al. 2009; Planck Collaboration et al. 2011a) or in closest galaxies like the Magellanic Clouds are crucial to better disentangle these explanations.

5 Investigations on a submm excess

Previous submm observations have led to the detection of an excess compared to extrapolations from *Spitzer*-based fits, especially in low-metallicity galaxies. This excess is poorly understood and a spatially-resolved study is necessary to understand its origin and link it with the properties of the environment. One of the major

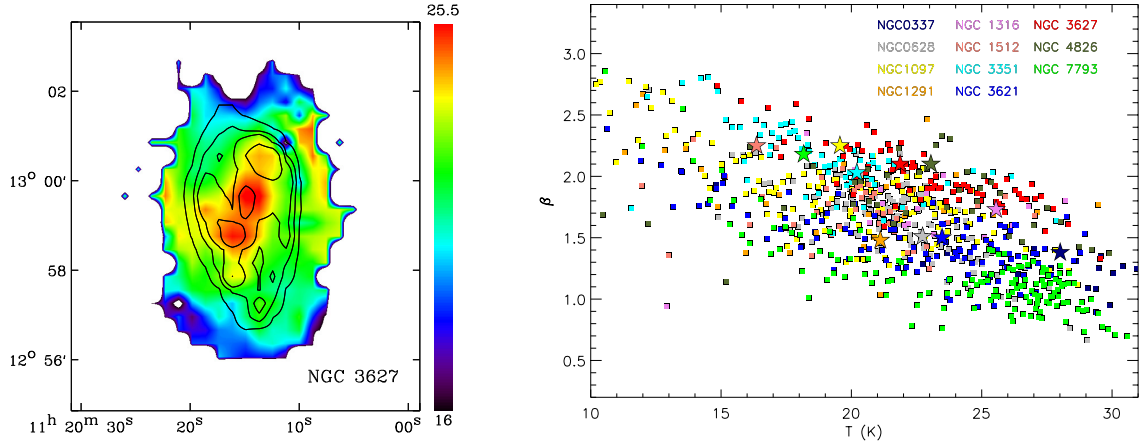


Fig. 3. Left: Temperature maps in Kelvin derived with $\beta_c = 2$. SPIRE 250 μm contours are overlaid. **Right:** Temperature dependence of the spectral index in our sample. Global estimates are shown with stars. Squares are pixel-by-pixel values (pixel size: 18'') averaged 3-by-3 for clarity.

interests of our study is that submm excess was never detected in a normal spiral galaxy before. For that matter, none of our galaxies show an excess at 870 μm when studied globally. The resolutions of *Herschel* and LABOCA maps enable us for the first time to study if an excess is detected at local scales. We use the previous modeling technique (based on data up to 500 μm) to extrapolate a 870 μm map. β_c is fixed to 2, 1.5 or used as a free parameter. We convolve and regrid our LABOCA maps to match our 18'' pixel grid and calculate the LABOCA excess compared to the extrapolated maps at 870 μm . A pixel-by-pixel SED modeling of the whole KINGFISH sample using the more complex Draine & Li (2007) dust models is performed in Aniano et al. (in prep). We extrapolate 870 μm maps from their procedure and compare them with our LABOCA data as well.

Figure 4 shows the 870 μm excess maps in absolute scale (LABOCA maps - extrapolated maps) obtained using our two-temperature fits with β_c fixed to 2, 1.5 or free. Some extended galaxies possess a clear 870 μm excess that seems to follow the bright structures of the galaxies (NGC 337, NGC 1097, NGC 1512, NGC 3627, NGC 4826) while others do not present such an excess (e.g. NGC 628). The 870 μm maps extrapolated using $\beta_c = 1.5$ are brighter than those using $\beta_c = 2$ due to the flatter submm slope induced by the modeling technique. The excess derived using $\beta_c = 1.5$ is thus systematically lower than that with $\beta_c = 2$ and disappears in some cases (e.g. NGC 1512, NGC 3621). The excess maps derived using the Draine & Li (2007) formalism are most of the time in between the two models with $\beta_c = 2$ and $\beta_c = 1.5$. It might be explained by the fact that in the wavelength range covered by SPIRE, their SEDs are similar to modified blackbodies with $\beta_c = 2$ but more flexible due to the mixture of temperatures it includes. We remind the reader that those models also incorporate modifications in the amorphous silicate opacity at $\lambda > 250 \mu\text{m}$, in order to better match the average high Galactic latitude dust emission spectrum measured by COBE-FIRAS (Wright et al. 1991; Reach et al. 1995; Finkbeiner et al. 1999) and thus already include a ‘‘submm excess’’ (lower than 12 % at $\lambda > 250 \mu\text{m}$).

We are still investigating the origin of the 870 μm excess. Several sources of line emission can contaminate the 870 μm flux and contribute to the excess, for instance the $^{12}\text{CO}(3-2)$ line whose rest wavelength (867 μm) falls into the LABOCA spectral bandpass. Two galaxies (NGC 1512 and NGC 3621) do not have any CO measurements while half of our sample only possess single-point $^{12}\text{CO}(3-2)$ or $^{12}\text{CO}(1-0)$ measurements toward the center. Four galaxies (NGC 337, NGC 628, NGC 3351 and NGC 3627) have been mapped in $^{12}\text{CO}(3-2)$ and/or in $^{12}\text{CO}(2-1)$ as part of the James Clark Maxwell Telescope Nearby Galaxies Legacy Survey (NGLS; Wilson et al. 2009) and HERA CO Line Extragalactic Survey (HERACLES; Leroy et al. 2009) respectively. Those maps will help us to quantify the contribution of the $^{12}\text{CO}(3-2)$ line to the 870 μm flux directly or using CO line ratios. Secondary sources of contamination are the synchrotron emission from relativistic electrons moving in a uniform magnetic field or thermal bremsstrahlung emission (free-free) from electrons in the hot ionized gas. Those contributions will be estimated using available radio and $\text{H}\alpha$ maps of the galaxies. Only then will we be able to properly quantify the relative excess of our galaxies at 870 μm .

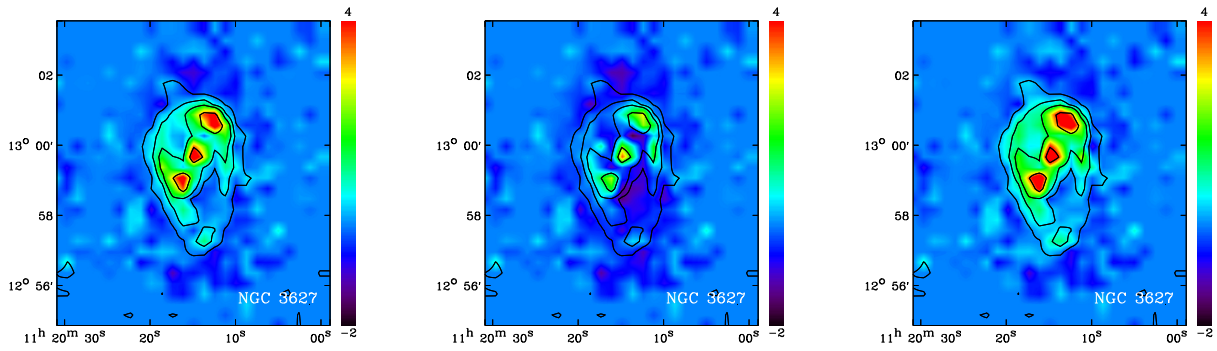


Fig. 4. Excess map at $870 \mu\text{m}$ of NGC 3627 (in MJy sr^{-1}) derived using our two-modified blackbody procedure with, from left to right, β_c fixed to 2, fixed to 1.5 or free.

References

- Bendo, G. J., Boselli, A., Dariush, A., et al. 2011, arXiv:1109.0237
 Bendo, G. J., Dale, D. A., Draine, B. T., et al. 2006, *ApJ*, 652, 283
 Bot, C., Rubio, M., Boulanger, F., et al. 2010, *A&A*, 524, A52+
 Draine, B. T. & Li, A. 2007, *ApJ*, 657, 810
 Dumke, M., Krause, M., & Wielebinski, R. 2004, *A&A*, 414, 475
 Engelbracht, C. W., Hunt, L. K., Skibba, R. A., et al. 2010, *A&A*, 518, L56+
 Finkbeiner, D. P., Davis, M., & Schlegel, D. J. 1999, *ApJ*, 524, 867
 Galametz, M., Madden, S., Galliano, F., et al. 2009, *A&A*, 508, 645
 Galametz, M., Madden, S. C., Galliano, F., et al. 2010, *A&A*, 518, L55+
 Galliano, F., Madden, S. C., Jones, A. P., Wilson, C. D., & Bernard, J.-P. 2005, *A&A*, 434, 867
 Galliano, F., Madden, S. C., Jones, A. P., et al. 2003, *A&A*, 407, 159
 Gordon, K. D., Galliano, F., Hony, S., et al. 2010, *A&A*, 518, L89+
 Griffin, M. J., Abergel, A., Abreu, A., et al. 2010, *A&A*, 518, L3+
 Kennicutt, Jr., R. C. et al. 2011, submitted to *PASP*
 Leroy, A. K., Walter, F., Bigiel, F., et al. 2009, *AJ*, 137, 4670
 Li, A. & Draine, B. T. 2001, *ApJ*, 554, 778
 Marleau, F. R., Noriega-Crespo, A., Misselt, K. A., et al. 2006, *ApJ*, 646, 929
 O'Halloran, B., Galametz, M., Madden, S. C., et al. 2010, *A&A*, 518, L58+
 Paradis, D., Bernard, J.-P., & Mény, C. 2009, *A&A*, 506, 745
 Planck Collaboration, Abergel, A., Ade, P. A. R., et al. 2011a, arXiv:1101.2037
 Planck Collaboration, Ade, P. A. R., Aghanim, N., et al. 2011b, arXiv:1101.2046
 Poglitsch, A., Waelkens, C., Geis, N., et al. 2010, *A&A*, 518, L2+
 Pohlen, M., Cortese, L., Smith, M. W. L., et al. 2010, *A&A*, 518, L72+
 Reach, W. T., Dwek, E., Fixsen, D. J., et al. 1995, *ApJ*, 451, 188
 Shetty, R., Kauffmann, J., Schnee, S., Goodman, A. A., & Ercolano, B. 2009, *ApJ*, 696, 2234
 Wilson, C. D., Warren, B. E., Israel, F. P., et al. 2009, *ApJ*, 693, 1736
 Wright, E. L., Mather, J. C., Bennett, C. L., et al. 1991, *ApJ*, 381, 200

THE DAFT/FADA SURVEY STATUS AND LATEST RESULTS

L. Guennou¹

Abstract. We present here the latest results obtained from the American French collaboration called the Dark energy American French Team/French American DArk energy Team (DAFT/FADA). The goal of the DAFT/FADA collaboration is to carry out a weak lensing tomography survey of $z = 0.4-0.9$ rich clusters of galaxies. Unlike supernovae or other methods such as cluster of galaxy counts, weak lensing tomography is purely based on geometry and does not depend on knowledge of the physics of the objects used as distance indicators. In addition, the reason for analyzing observations in the direction of clusters is that the shear signal is enhanced by about 10 over the field. Our work will eventually contain results obtained on 91 rich clusters from the HST archive combined with ground based work to obtain photo-zs. This combination of photo-z and weak lensing tomography will enable us to constrain the equation of state of dark energy. We present here the latest results obtained so far in this study.

Keywords: cosmology, dark energy, gravitational lensing: weak, galaxies: clusters: general

1 The DAFT/FADA survey

1.1 Overview

The discovery ten years ago of the acceleration of the expansion of the Universe (Riess & al. 1998) which is typically explained by assuming that most of its energy is in the form of an unknown dark energy (DE), is one of the most puzzling issues of modern cosmology. Efforts have therefore been undertaken, such as the Dark Energy Task Force (Albrecht & al. 2006) or the ESA-ESO working group on fundamental physics (Peacock & al. 2006) to design projects to measure DE and determine its nature. As highlighted by these reports, understanding DE requires big surveys to overcome cosmic variance and shot noise as well as new experiments to control the unknown systematic uncertainties. In this context, galaxy clusters, together with several other probes, are expected to play a major role (e.g. Nichol 2007). These objects have indeed long held a place of importance in astronomy and cosmology. Zwicky (e.g. Zwicky F. 1933) inferred from observations of the Coma cluster that the matter in our universe could be in the form of a dark component (this component was first supposed to be low surface brightness diffuse light). Galaxy clusters can also be used to test the redshift-distance relation (e.g. Supernovae as standard candles, Baryon Acoustic Oscillations or weak lensing tomography with clusters, e.g. Hu 1999) or the growth of structures through weak lensing, cluster number counts, or integrated Sachs-Wolfe effect. Clusters are also intrinsically interesting in many aspects, including the influence of environment on galaxy formation and evolution. Building a detailed picture of galaxy and large-scale structure growth (e.g. clusters) is therefore necessary to understand how the Universe has evolved. The Dark energy American French Team (DAFT, in French FADA) has started a large project to characterize statistically high redshift galaxy clusters, infer cosmological constraints from weak lensing tomography, and understand biases relevant for constraining DE and cluster physics in future cluster and cosmological experiments. This work is based on a sample of 91 high redshift ($z = [0.4; 0.9]$), massive ($\geq 3 \times 10^{14} M_{\odot}$) clusters with existing HST imaging, for which we are presently performing complementary multi-wavelength imaging. This will allow us in particular to estimate accurate photometric redshifts for as many galaxies as possible. The requested accuracy depends on both our ability to discriminate between cluster and background field galaxies without losing too many objects and on the weak lensing tomography method internal parameters. Catalogs of cluster galaxies (e.g. Adami & al. 2008) typically show photometric redshifts spanning a total ($\sim 3\sigma$) interval of ± 0.15 in photo-z. This means that the

¹ Laboratoire Astrophysique de Marseille, 13388 Marseille, France

goal of our survey is to have photometric redshifts with a 1σ precision better than 0.05. With such a precision, the photo- z uncertainties would not be the expected dominant source of errors in our method. Our goal is to describe the method used to obtain these photometric redshifts on all the available clusters at the moment. This will allow us in the future to combine photo- z with weak lensing shear measurements to carry out tomography and build mass models for clusters.

1.2 Obtained results

We computed photo- z s with the LePhare package for ten relatively distant cluster lines of sight selecting B, V, R, I, F814W, z , Spitzer IRAC 3.6 μm , and 4.5 μm images. These images were reduced and aligned at the pixel scale using the SCAMP and SWarp tools. The zero points of the various bands were adjusted by LePhare using publicly available spectroscopy. The photo- z s prove to be reliable in the $z \sim [0.4, 1.5]$ redshift range and in the magnitude range F814W $\sim [19.5, 24.5]$. They are also relatively reliable in the $z \sim [3.75, 6.0]$ redshift range and in the magnitude range F814W $\sim [19.5, 24.]$. We remarked that catastrophic errors mainly occurred towards the high photometric redshifts (at $z \geq 1.5$). This will obviously not affect our survey when limiting our analysis to the $[0.4, 1.5]$ redshift range. The only consequence would be to remove a small number of galaxies. If we also consider the $z \sim [3.75, 6.0]$ redshift range, we will include in our future weak lensing analyses some galaxies (of the order of 2% from the spectroscopic redshift sample estimate) with completely wrong redshifts. Given the limited amount of such galaxies, the consequences on our survey will however remain limited. We achieved a photo- z precision of the order of 0.05 for the full sample. This precision is degraded by a factor of two when considering blended objects.

2 Other work: IntraCluster Light

2.1 Overview

Another important aspect of this survey is the search for intracluster light (hereafter ICL) which provides a complementary way of determining the mechanisms occurring inside galaxy clusters, as well as constraining the properties and formation history of the ICL. These studies promise to yield possible answers to many fundamental questions about the formation and evolution of galaxy clusters and their constituent galaxies. In addition, it is important to determine how and when the ICL formed, and the connection between the ICL and the central brightest cluster galaxy (see e.g. González & al. 2005). Cosmological N-body and hydrodynamical simulations are beginning to predict the kinematics and origin of the ICL (see e.g. Dolag & al. 2010). The ICL traces the evolution of baryonic substructures in dense environments and can thus be used to constrain some aspects of cosmological simulations that are uncertain, such as the modeling of star formation and the mass distribution of the baryonic light-emitting component in galaxies. The study by Da Rocha & al. (2005) also produced important results about the significant presence of ICL in groups, which are crucial if we assume that groups are the basic building blocks of clusters, that are able to bring their own ICL to the cluster-building process. From a technical point-of-view, modern CCD cameras now allow us to study the properties of the diffuse light in clusters, i.e. its morphology, radial distribution, and colors, in a quantitative way (e.g. Uson & al. 1991; Bernstein & al. 1995; Gregg & West al. 1998; Mihos & al. 2005; Zibetti & al. 2005; González & al. 2007; Krick & Bernstein 2007; Rudick & al. 2010). However, accurate photometric measurements of the diffuse light are difficult to perform because its surface brightness is typically fainter than 1% of that of the night sky, and it can be difficult (especially at high redshift) to distinguish the extended outer halos of the brightest cluster galaxies (BCGs) in a cluster core from the stars floating freely in the cluster potential. This explains why, until now, most studies of the ICL have been performed on galaxy clusters at redshifts below $z \sim 0.3$ (see e.g. Toledo & al. 2011). However, since it is crucial to understand how the evolution of galaxy clusters affects that of the ICL, we must study the ICL within a range of clusters at various redshifts. It would be ideal to investigate as much as possible the period between $z=0.3$ and $z \sim 2$, and investigate clusters since their birth. We propose here to fill part of this gap in the 0.4-0.8 redshift range for a sample of ten clusters. This redshift range is sufficient to cover about half of the typical cluster lifetimes.

2.2 Obtained results

We studied the diffuse light in ten different clusters in one band up to $z \sim 0.8$ based on deep HST ACS images and in three of them (up to $z \sim 0.58$) in two bands with FORS2 data. However, these deep data would not have

been sufficient if we were not using a very sensitive wavelet-detection technique, the `ov_wav` method (Pereira & al. 2003; Da Rocha & al. 2005), itself a variant of the à trous wavelet transform described by Starck et al. (1998, see also Starck & Murtagh (2002)). This method is independent of both the galaxy and star modelling, and of the sky level subtraction.

To help us analyze the mechanisms taking place in galaxy clusters, and place constraints on their formation history and physical properties, we have searched for intracluster light (ICL) in ten galaxy clusters at redshifts $0.4 < z < 0.8$. For the first time, we have detected significant diffuse light sources in an unprecedentedly high redshift bin $z=[0.4,0.8]$ based on very deep HST ACS images to which we have applied a very sensitive wavelet detection method. So our study represents a significant step forward in measuring any ICL evolution with redshift.

In the F814W filter, we have detected diffuse light sources in all the clusters with typical sizes of a few tens of kpc (assuming that the diffuse light sources are at the cluster redshifts). The ICL detected by stacking the ten F814W images shows a very clear 8σ detection in the source center extending over a $\sim 50 \times 50$ kpc² area. The total absolute magnitude of this source is -21.6 in the F814W filter, equivalent to about two L^* galaxies for each of the 10 clusters.

Finally, besides the extended ICL, we have also found Wavelet-detected compact objects (WDCOs). Since these sources are very faint, we only considered those detected in both the HST/ACS/F814W and FORS2/V-band filters, in the three clusters for which sufficiently deep data in both bands are available. The fit of a two-dimensional Gaussian plus a constant background on each of the WDCO images suggests that they are very unlikely to be faint Galactic stars. On the other hand, part of the WDCOs are located on the cluster red sequences in color-magnitude diagrams and their spatial distribution also suggests that they could be very faint compact galaxies belonging to the considered clusters and comparable to faint Local Group Dwarfs.

References

- Adami C., Ilbert O., Pell ÌÀ R., et al. 2008, *A&A*, 491, 681
 Albrecht A., Bernstein G., Cahn R., et al. 2006, astro-ph:0609591
 Bernstein G.M., Nichol R.C., Tyson J.A., et al. 1995, *AJ*, 110, 1507
 Da Rocha C., Mendes de Oliveira C. 2005, *MNRAS*, 364, 1069
 Dolag K., Murante G., Borgani S., 2010 *MNRAS*, 405, 1544
 González A.H., Zabludoff A.I., Zaritsky D. 2005, *ApJ*, 618, 195
 González A.H., Zaritsky D., Zabludoff A.I. 2007, *ApJ*, 666, 147
 Gregg M.D., West M.J. 1998, *Nature*, 396, 549
 Hu W. 1999 *ApJ*, 522, L21
 Krick J.E., Bernstein R.A. 2007, *AJ*, 134, 466
 Mihos J.C., Harding P., Feldmeier J., Morrison H. 2005, *ApJ*, 631, L41
 Nichol R. 2007, *Cosmic Frontiers ASP Conference Series*, 379, 89
 Peacock J.A., Schneider P., Efstathiou G., et al. 2006, *Fundamental Cosmology*, ESA-ESO Working Groups, Report No.3 (also <http://www.stecf.org/coordination/esaeso/cosmology.php>)
 Pereira D.N.E. 2003, Undergraduate thesis, Univ. Federal do Rio de Janeiro, Brazil
 Riess A.G., Filippenko A.V., Challis P. 1998A, *J* 116,1009
 Rudick C.S., Mihos J.C., Harding P., et al. 2010, *ApJ*, 720, 569
 Starck J.-L. & Murtagh F. D. 2002, *Astronomical Image and Data Analysis*, Springer
 Toledo I., Melnick J., Selman F. et al. 2011, *MNRAS*, 414, 602
 Uson J.M., Boughn S.P., Kuhn J.R. 1991, *ApJ*, 369, 46
 Zibetti S., White S.D.M., Schneider D.P., Brinkmann J. 2005, *MNRAS*, 358, 949
 Zwicky F. 1933, *Helvetica Physica Acta*, 6, 110

PROSPECTS FOR THE COSMOLOGICAL APPLICATION OF POLARIZED LYMAN-ALPHA RADIATION

M. Hayes¹ and C. Scarlata²

Abstract. We discuss the nature of various flavors of Lyman-alpha ($\text{Ly}\alpha$) emitting objects at high redshift. We provide a brief overview of $\text{Ly}\alpha$ radiative transport, giving particular consideration to polarization, and discuss the requirements to obtain net polarization on the emitted radiation. We present and discuss the current status of $\text{Ly}\alpha$ polarimetric observations, focusing on a single resolved Lyman-alpha blob at a redshift of 3. Finally we discuss some future prospects and further possible application of $\text{Ly}\alpha$ polarimetry, and similar methods for different galaxies.

Keywords: galaxies: high-redshift, galaxies: Lyman-alpha emitters, galaxies: specific: LAB1, methods: observational

1 Introduction – Lyman-alpha things at high-redshift

The H I Lyman-alpha ($\text{Ly}\alpha$) emission line is a versatile and intriguing spectral feature, used with high efficiency in the selection of high-redshift (z) galaxies. It has the advantage of enabling us to probe farther down the mass function than effectively any other selection method (E.g. Cantalupo et al. 2007; Rauch et al. 2008; Hayes et al. 2010), while at luminosities ~ 3 dex higher extended (> 100 kpc) $\text{Ly}\alpha$ halo emission is also found associated with the most luminous high- z radio galaxies (HzRG; Villar-Martín et al. 2002; van Ojik et al. 1997; Christensen et al. 2006). Furthermore, $\text{Ly}\alpha$ selection digs out a more enigmatic population of objects, that appear similar in luminosity and morphology to HzRG haloes, but instead are radio quiet. These objects, usually dubbed $\text{Ly}\alpha$ blobs (LAB; Francis et al. 1996; Steidel et al. 2000), show great diversity in their properties, which has fueled debate about how they relate to populations of less luminous compact $\text{Ly}\alpha$ -emitters (LAEs) and HzRGs, whether they are a homogeneous population at all, and even about what powers them.

LABs have been studied extensively over the past decade. It is clear that they are rare and highly clustered, suggesting that (like HzRGs) they live at the peaks of the underlying matter distribution (Matsuda et al. 2004; Yang et al. 2009; Francis et al. 1997; Prescott et al. 2008). However, LABs do not present with a common set of counterpart galaxies, with some hosting star forming Lyman break galaxies, some hosting radio quiet AGN, and more curiously, some with no counterpart galaxies detected at any wavelength (Nilsson et al. 2006; Smith & Jarvis 2007). This sets up the framework for the debate upon what drives the luminous $\text{Ly}\alpha$ emission, and various mechanisms have been proposed. That the $\text{Ly}\alpha$ photons could be produced by photoionization from hot stars and/or AGN (Steidel et al. 2000) is energetically viable for LABs hosting LBG or AGN counterparts, but implies that the UV-luminous systems must be heavily enshrouded by dust for those that do not. The necessary luminosities in most cases are so high that thermal dust emission should cause them to be bright in the IR and sub-mm, which indeed some are but others still are not. Alternatively it has been argued that the extended emission could be caused by shock heating inside an expanding shell driven by the supernova winds produced by an intense bout of star formation (Taniguchi & Shioya 2000; Mori et al. 2004). As with photoionization, this also requires the internal power source to be hidden from view in many cases. Completely circumventing this problem, the energy may not come from within the nebula itself but from without: the $\text{Ly}\alpha$ may be the result of intergalactic gas accreting onto a dark matter halo, heating, and subsequently cooling through $\text{Ly}\alpha$ (Haiman et al. 2000; Fardal et al. 2001; Yang et al. 2006).

¹ Université de Toulouse; UPS-OMP; IRAP; Toulouse, France / CNRS; IRAP; 14, avenue Edouard Belin, F-31400 Toulouse, France

² Minnesota Institute for Astrophysics, University of Minnesota, Minneapolis, MN 55455, USA

The last model is of particular interest in light of recent theoretical studies that showed a substantial fraction of the in-falling gas may not shock heat to the virial temperature of the halo, but could possibly arrive at the centre predominantly along cold (10^4 K) filaments in the cosmic web (Kereš et al. 2005; Dekel et al. 2009; Brooks et al. 2009). Results of hydrodynamical simulations coupled with Ly α radiative transfer show that such cold streams are spatially extended Ly α sources with properties similar to those observed in Ly α blobs (Yang et al. 2006; Dijkstra & Loeb 2009). These scenario is also able to reconcile the puzzling fact that while some of the blobs are not associated with any galaxies some others are associated with powerful dust-enshrouded active galaxies (both star-forming and AGN-like activity, e.g., Scarlata et al. 2009). Now we have at least three plausible mechanisms by which LABs could be powered although it is important to remember that (a) not all LABs need to be powered by the same mechanism and (b) just because some counterparts are energetically capable of powering the LABs, does not necessarily imply that they do. Indeed further observational tests are needed. These may come in the form of other emission lines in the UV (Prescott et al. 2009; Scarlata et al. 2009), or rest frame optical (Yang et al. 2011). Recently, however, Dijkstra & Loeb (2008) suggested a further observable to help in discriminating between models: the polarization signal on the Ly α line itself.

2 Polarizing Lyman-alpha

Ly α photons may scatter wherever they encounter neutral hydrogen, causing their propagation in HI to pose a diffusion-like problem (Osterbrock 1962; Auer 1968; Adams 1972; Harrington 1973). Feedback – the return of kinetic energy to the interstellar medium – seems to be at play in every star-forming galaxy, introducing velocity shifts between the neutral ISM and the nebulae in which Ly α is produced. Resonance scattering (in the core of the frequency redistribution profile and coherent in the rest frame) upon bulk accelerated gas will therefore shift Ly α photons to frequencies at which they encounter subsequent neutral gas at substantially lower optical depths, greatly enhancing the likelihood of transmission. This is thought to be the origin of the red-shifting of Ly α compared with other spectral tracers (Kunth et al. 1998; Shapley et al. 2003; Tapken et al. 2007; Steidel et al. 2010; McLinden et al. 2011). However a frequency shift may be introduced even if the scattering medium is static, due to the natural redistribution profile of the transition. Wing scattering is much less frequent than resonance scattering, but the net effect is again to shift the photon to optically thin frequencies, which is thought to be the origin of double-peaked Ly α profiles (e.g. Tapken et al. 2004).

However besides frequency redistribution, there are further important differences between the core and wing scatterings, that result from quantum mechanical differences in the hyperfine splitting of the $^2P_{1/2}$ and $^2P_{3/2}$ levels. Scatterings in the core obey an isotropic phase function and on re-emission have no preferred direction for the electric field vector, whereas scatterings in the wing are analogous to Rayleigh scattering (Stenflo 1980). Wing scatterings through the $^1S_{1/2} \leftrightarrow ^2P_{3/2}$ channel (a) have a preferential scattering angle of $\pm\pi/2$ and (b) can carry a high degree of linear polarization, P , up to $\approx 40\%$ (Chandrasekhar 1960). The pertinent question to observers then becomes whether astrophysical bodies are able to systematically polarize Ly α . What is needed is a geometry in which photons that have scattered through an angle of 90° are preferentially observed. In the case of a point source of photons that is surrounded by a spherically symmetric scattering medium, any photon that is emitted in the plane of the sky and is subsequently observed must have scattered through a net angle of 90° (see Bower 2011 for an illustration).

Rybicki & Loeb (1999) first visited the problem of Ly α photons scattering in a neutral (i.e. pre-reionization), predicting that P should be substantial; small centrally but $P \approx 30 - 40\%$ at observable radii. Furthermore, at these radii they predicted the angle of the polarization vector, χ , should orientate tangentially to the circle centered upon the central source. This scenario was re-visited by Dijkstra & Loeb (2008), who suggested IGM-scattered Ly α should be polarized to much lower levels, but made further predictions for scattering in outflowing neutral shells, and for Ly α photons produced in situ at large radii by cooling gas that inflows along spherically symmetric trajectories. The results suggested that the new scenarios should both result in little Ly α polarization at small impact factors, but P that increases to measurable values near the limb. These two scenarios can then be further disentangled by the variation of P across the line profile, which should reverse based upon the direction in which the gas is flowing. However, it has been further mentioned (Dijkstra & Loeb 2009) that should the accretion be filamentary, emergent P could be reduced to unmeasurable levels by the low volume filling factor of the neutral gas. Finally Lee & Ahn (1998) have suggested that moderate polarization signals ($P \sim 5\%$) may be measurable even for spatially unresolved systems, provided the underlying geometry is sufficiently anisotropic. Clearly these theoretical treatments of polarization have evolved to the point where they need to be tested.

3 The status of Lyman-alpha polarimetric observations

This is a fledgling field with only two journal articles, and the reader is referred directly to Prescott et al. (2011) and Hayes et al. (2011); here we briefly summarize. Both observations targeted individual LABs known to have counterparts. Prescott et al. (2011) observed LABd05 from Dey et al. (2005) – a system known to host a strong active nucleus – with the SPOL instrument at the 2.3 meter Bok telescope. They reported a total aperture integrated polarization signal consistent with zero $\lesssim 5\%$ within a radius of 4 arcsec. By performing partial azimuthal averaging over several radial bins they found $P < 12\%$ (1σ) at 4 arcsec.

Hayes et al. (2011, Fig 1) observed the system LAB1 from Steidel et al. (2000) – an LAB known to host several Lyman break galaxies – with the FORS2 instrument at the 8.2 metre VLT. We reported integrated $P = 11.9 \pm 2\%$ inside a radius of 7 arcsec, but note that due to the different method of photometric analysis this is not directly comparable with Prescott’s upper limit. The morphology of significantly polarized radiation is rather revealing, and shows that significantly polarized regions tend to avoid the highest Ly α surface brightness, emanating instead from more diffuse regions. We did find evidence of P systematically increasing with radius, with a peak azimuthally averaged P of almost 20%. Furthermore we found evidence that, whenever Ly α does show a significant polarization, the angle χ is consistently aligned tangentially with both the overall (circular) azimuthal direction, and also with isophotal contours in the local surface brightness. All of these measurements are in qualitative agreement with a scenario in which there is a preferential direction of the incoming radiation field as it impinges upon the HI scattering medium. We have made the reduced data-products publicly available*.

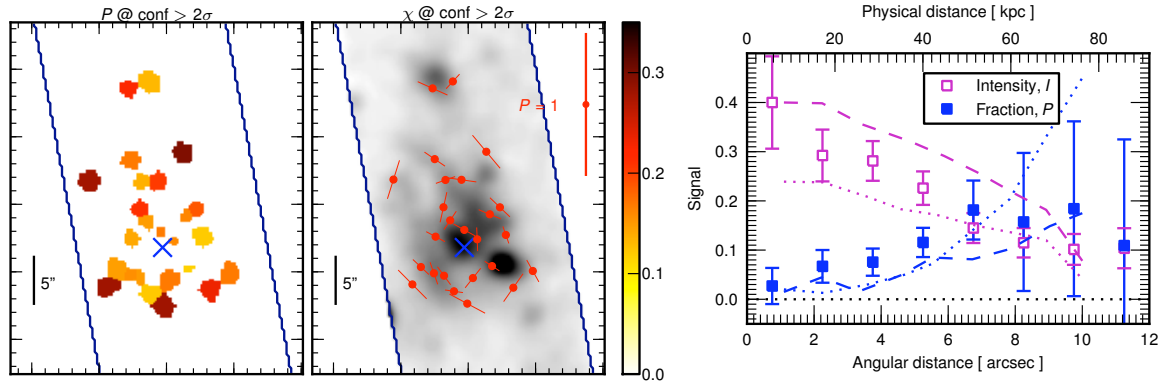


Fig. 1. The observed Ly α polarization of LAB1 (Hayes et al. 2011). The *left* panel shows P for resolution elements in which it was measured to be significant ($P/\Delta P > 2$). The polarized bins clearly avoid the regions of higher surface brightness (c.f. the Ly α image in the *centre* panel), and form an broken ring. Polarized Ly α can be seen from both LAB1 (central main structure) and also LAB8 (smaller structure towards the top). The *centre* panel shows the angle of the polarization vector, χ , for the same bins as the *left* image; χ orientates tangentially to both the overall geometry of the systems and also against the steepest gradients in local surface brightness. *Right* shows the radial distribution profile of the Ly α surface brightness (magenta) and P (blue), measured in concentric annuli centered on the blue cross shown in the *centre* panel. P increases with radius to an angle of about 7 arcsec (≈ 45 kpc) beyond which surface brightness decreases to a level where a meaningful estimate of P is no longer attainable.

4 Prospects and future application

To date, Ly α polarization studies have only employed imaging mode, which is not surprising given the daunting prospect of differential analysis of low surface brightness spectra from $z > 2$ sources. Nevertheless, spectropolarimetry of Ly α may hold substantial promise for more general application. Firstly spectral mode derestricts the observer in terms of the available redshifts and narrowband filters, but more importantly the scattering processes from which the polarization arises also broaden the line and introduce characteristic features (blue bumps and both a knee and ankle on the red side; Verhamme et al. 2006). Thus it is plausible that while the

*<http://obswww.unige.ch/people/matthew.hayes/LymanAlpha/LabPol/>

line-integrated signal may be low, the polarization signal may reach over 60% in certain features (Dijkstra & Loeb 2008), which will manifest as substantial observational differences at various angles of the wave plate.

Suggestion that Extremely Large Telescopes (ELT) could be used to extend such studies raises the question of whether such an instrument will ever become a reality. Of proposed E-ELT instruments[†], the *Exo-Planet Imaging Camera and Spectrograph (EPICS)*, Kasper et al. 2008) includes the *EPOL* polarimeter (Keller et al. 2010) and looks like a possibility. Other ELT instruments for which polarimetric capabilities have been discussed include the *Planet Formation Imager* and *Second-Earth Imager for TMT (SEIT)* for the *Thirty Meter Telescope*, and the *Giant Magellan Telescope* lists polarimetry among the necessities to meet their high level science requirements. This field is currently motivated almost exclusively by exo-planetary science (scattering of stellar light in planetary atmospheres) but it is the development of the instrumentation that is paramount. We cannot say whether we will be able to turn *EPICS* directly to a Ly α galaxy; it should be optically possible, but may require tweaks in the design and/or additional settings. In this eventuality the level of detailed work we undertook on LAB1 (Hayes et al. 2011) could be performed in around four hours. Consequently a moderately sized ELT programme dedicated to Ly α polarimetry could quite easily target a full distribution of selected targets, and even reach full statistical significance.

ELT speculation aside, there is still much left to do with 8 m telescopes. Two Ly α -emitting sources (LAB1 and LAB8) have been studied in depth (Hayes et al. 2011), and one (LABd05) has shallow constraints (Prescott et al. 2011). Yet over 2000 compact LAEs and ~ 100 LABs are known. We cannot state that the current results generalize to all LABs, and many complicating factors could result in both higher and lower polarization levels. LAB1 is known to host LBGs, while others harbor AGN (Dey et al. 2005; Wilman et al. 2005; Geach et al. 2009), composite populations (Colbert et al. 2011), or nothing measurable. Moreover, LABs were first targeted with the polarimeter due to their apparent enigmatic and controversial status regarding homogeneity and energy balance. HzRG haloes are less controversial – there is no energetic problem – but have not been tested. Ly α emission in these cases is likely the result of in situ ionization, coupled with shock excitation/ionization from feedback and where tested, Ly α seems to be if anything less polarized than the continuum (Cimatti et al. 1998; Vernet et al. 2001). These spectroscopic results could indeed suggest that HzRGs are fundamentally different to LAB1, although the observations and analysis methods are not directly comparable. Compact Ly α sources also remain unexplored with the polarimeter. Targeting resolved objects ensures that even if the system is completely spherically symmetric, analysis can be performed in individual regions where the Stokes vectors do not all cancel, and polarization can be detected. However that LAEs and Ly α transport are spherically symmetric does not sound likely to be the case in general, and symmetry is most likely broken on unresolved scales. Thus we may also expect a measurable polarization signal from LAEs (Lee & Ahn 1998).

Interpretation in the field of optical polarimetry of high- z sources has never been straightforward and whatever results from future Ly α polarimetry, the interpretation will again be challenging. Current state-of-the-art simulations assume density and kinematic structures that vary smoothly and continuously, which is unlikely to be the case in real galaxies. The smooth spherically symmetric accretion of gas is currently disfavored, with multi-phase filamentary streams preferred. Any superwind ejected by the galaxy is also unlikely to remain stable when encountering the circumgalactic medium, and clumpy outflows such as those favored by Steidel et al. (2011) may be prevalent. What is urgently needed is for the implementation of Ly α polarization in all Ly α radiative transport codes (without accelerators!), and predictions to be made with various application. This includes systematic explorations in clumpy media that brute force the parameter space of clump distribution and covering fraction, and detailed post-processing of cosmological simulations. With limited instrumentation and demanding observations, and a complex problem with few constraints, we need dedicated theoretical and observational developments that proceed in parallel.

We thank Brian Siana for his collaboration on the polarization programmes and Mark Dijkstra, Peter Laursen, and Anne Verhamme for useful discussions. M.H. received support from Agence Nationale de la Recherche (reference ANR-09-BLAN-0234-01).

References

- Adams, T. F. 1972, ApJ, 174, 439
 Auer, L. H. 1968, ApJ, 153, 783
 Bower, R. 2011, Nature, 476, 288

[†]<http://www.eso.org/sci/facilities/eelt/instrumentation/>

- Brooks, A. M., Governato, F., Quinn, T., Brook, C. B., & Wadsley, J. 2009, *ApJ*, 694, 396
- Cantalupo, S., Lilly, S. J., & Porciani, C. 2007, *ApJ*, 657, 135
- Chandrasekhar, S. 1960, *Radiative transfer* (New York: Dover)
- Christensen, L., Jahnke, K., Wisotzki, L., & Sánchez, S. F. 2006, *A&A*, 459, 717
- Cimatti, A., di Serego Alighieri, S., Vernet, J., Cohen, M., & Fosbury, R. A. E. 1998, *ApJ*, 499, L21
- Colbert, J. W., Scarlata, C., Teplitz, H., et al. 2011, *ApJ*, 728, 59
- Dekel, A., Birnboim, Y., Engel, G., et al. 2009, *Nature*, 457, 451
- Dey, A., Bian, C., Soifer, B. T., et al. 2005, *ApJ*, 629, 654
- Dijkstra, M. & Loeb, A. 2008, *MNRAS*, 386, 492
- Dijkstra, M. & Loeb, A. 2009, *MNRAS*, 400, 1109
- Fardal, M. A., Katz, N., Gardner, J. P., et al. 2001, *ApJ*, 562, 605
- Francis, P. J., Woodgate, B. E., & Danks, A. C. 1997, *ApJ*, 482, L25
- Francis, P. J., Woodgate, B. E., Warren, S. J., et al. 1996, *ApJ*, 457, 490
- Geach, J. E., Alexander, D. M., Lehmer, B. D., et al. 2009, *ApJ*, 700, 1
- Haiman, Z., Spaans, M., & Quataert, E. 2000, *ApJ*, 537, L5
- Harrington, J. P. 1973, *MNRAS*, 162, 43
- Hayes, M., Östlin, G., Schaerer, D., et al. 2010, *Nature*, 464, 562
- Hayes, M., Scarlata, C., & Siana, B. 2011, *Nature*, 476, 304
- Kasper, M. E., Beuzit, J.-L., Verinaud, C., et al. 2008, in *Society of Photo-Optical Instrumentation Engineers (SPIE) Conference Series*, Vol. 7015, *Society of Photo-Optical Instrumentation Engineers (SPIE) Conference Series*
- Keller, C. U., Schmid, H. M., Venema, L. B., et al. 2010, in *Society of Photo-Optical Instrumentation Engineers (SPIE) Conference Series*, Vol. 7735, *Society of Photo-Optical Instrumentation Engineers (SPIE) Conference Series*
- Kereš, D., Katz, N., Weinberg, D. H., & Davé, R. 2005, *MNRAS*, 363, 2
- Kunth, D., Mas-Hesse, J. M., Terlevich, E., et al. 1998, *A&A*, 334, 11
- Lee, H. & Ahn, S. 1998, *ApJ*, 504, L61
- Matsuda, Y., Yamada, T., Hayashino, T., et al. 2004, *AJ*, 128, 569
- McLinden, E. M., Finkelstein, S. L., Rhoads, J. E., et al. 2011, *ApJ*, 730, 136
- Mori, M., Umemura, M., & Ferrara, A. 2004, *ApJ*, 613, L97
- Nilsson, K. K., Fynbo, J. P. U., Møller, P., Sommer-Larsen, J., & Ledoux, C. 2006, *A&A*, 452, L23
- Osterbrock, D. E. 1962, *ApJ*, 135, 195
- Prescott, M. K. M., Dey, A., & Jannuzi, B. T. 2009, *ApJ*, 702, 554
- Prescott, M. K. M., Kashikawa, N., Dey, A., & Matsuda, Y. 2008, *ApJ*, 678, L77
- Prescott, M. K. M., Smith, P. S., Schmidt, G. D., & Dey, A. 2011, *ApJ*, 730, L25
- Rauch, M., Haehnelt, M., Bunker, A., et al. 2008, *ApJ*, 681, 856
- Rybicki, G. B. & Loeb, A. 1999, *ApJ*, 520, L79
- Scarlata, C., Colbert, J., Teplitz, H. I., et al. 2009, *ApJ*, 706, 1241
- Shapley, A. E., Steidel, C. C., Pettini, M., & Adelberger, K. L. 2003, *ApJ*, 588, 65
- Smith, D. J. B. & Jarvis, M. J. 2007, *MNRAS*, 378, L49
- Steidel, C. C., Adelberger, K. L., Shapley, A. E., et al. 2000, *ApJ*, 532, 170
- Steidel, C. C., Bogosavljević, M., Shapley, A. E., et al. 2011, *ArXiv e-prints*
- Steidel, C. C., Erb, D. K., Shapley, A. E., et al. 2010, *ApJ*, 717, 289
- Stenflo, J. O. 1980, *A&A*, 84, 68
- Taniguchi, Y. & Shioya, Y. 2000, *ApJ*, 532, L13
- Tapken, C., Appenzeller, I., Mehlert, D., Noll, S., & Richling, S. 2004, *A&A*, 416, L1
- Tapken, C., Appenzeller, I., Noll, S., et al. 2007, *A&A*, 467, 63
- van Ojik, R., Roettgering, H. J. A., Miley, G. K., & Hunstead, R. W. 1997, *A&A*, 317, 358
- Verhamme, A., Schaerer, D., & Maselli, A. 2006, *A&A*, 460, 397
- Vernet, J., Fosbury, R. A. E., Villar-Martín, M., et al. 2001, *A&A*, 366, 7
- Villar-Martín, M., Vernet, J., di Serego Alighieri, S., et al. 2002, *MNRAS*, 336, 436
- Wilman, R. J., Gerssen, J., Bower, R. G., et al. 2005, *Nature*, 436, 227
- Yang, Y., Zabludoff, A., Jahnke, K., et al. 2011, *ApJ*, 735, 87
- Yang, Y., Zabludoff, A., Tremonti, C., Eisenstein, D., & Davé, R. 2009, *ApJ*, 693, 1579
- Yang, Y., Zabludoff, A. I., Davé, R., et al. 2006, *ApJ*, 640, 539

THE FORMATION OF LARGE GALACTIC DISKS: REVIVAL OR SURVIVAL?

F. Hammer¹, M. Puech¹, H. Flores¹, E. Athanassoula², Y. B. Yang¹, J. L. Wang¹, M. Rodrigues¹
and S. Fouquet¹

Abstract. Using the deepest and the most complete set of observations of distant galaxies, we investigate how extended disks could have formed. Observations include spatially-resolved kinematics, detailed morphologies and photometry from UV to mid-IR. Six billion years ago, half of the present-day spiral progenitors had anomalous kinematics and morphologies, as well as relatively high gas fractions. We argue that gas-rich major mergers, i.e., fusions between gas-rich disk galaxies of similar mass, can be the likeliest driver for such strong peculiarities. This suggests a new channel of disk formation, e.g. many disks could be reformed after gas-rich mergers. This is found to be in perfect agreement with predictions from the state-of-the-art Λ CDM semi-empirical models: due to our sensitivity in detecting mergers at all phases, from pairs to relaxed post-mergers, we find a more accurate merger rate. The scenario can be finally confronted to properties of nearby galaxies, including M31 and galaxies showing ultra-faint, gigantic structures in their haloes.

Keywords: galaxies; galaxy formation; spirals; M31

1 Introduction

Seventy two percent of local galaxies with $M_{stellar} > 2 \times 10^{10} M_{\odot}$ are disk-dominated. Thin disks are fragile to collisions with other galaxies that can easily destroy them (Toth & Ostriker 1992). Λ CDM predicts a high level of merger activity on all scales and this makes it difficult for the corresponding simulations to reproduce such a large number of large disks with small bulge fraction. This is illustrated by the tidal torque theory (Peebles 1976; White 1984), which assumes that the angular momentum of disk galaxies had been acquired by early interactions: related simulations provide too small disks with too small angular momentum, compared to observations.

What do we learn from observations? The situation seems somewhat confused with discordant results on the real impact of mergers, either minor or major. Thus, the role of mergers in the evolution of disk galaxies remains uncertain. Discordant results can be attributed to the following reasons:

- differences between galaxy sample selection, for example various stellar/baryonic mass ranges;
- different methodologies to characterize a merger (pair technique, automatic classification methods such as concentration-asymmetry and GINI-M20, decision tree methods, etc.);
- different methodologies to classify "normal" galaxies, especially disk galaxies: either automatic classification or systematic comparison to local templates and use of spatially-resolved kinematics to verify the presence of rotation;
- the depth and spatial resolution of the images to which the above methodologies have been applied.

In this paper, we present the results of the IMAGES survey that encompasses the deepest and the most complete set of measurements of galaxies at $z=0.4-0.8$. The explicit goal of IMAGES is to gather enough constraints $z=0.4-0.8$ galaxies to directly link them to their descendants, the local galaxies. Its selection is limited by an absolute J-band magnitude ($M_J(AB) < -20.3$), a quantity relatively well linked to the stellar mass (Yang et al. 2008, hereafter IMAGES-I), leading to a complete sample of 63 galaxies with $M_{stellar} > 1.5 \times 10^{10} M_{\odot}$, and with an average value similar to the Milky Way mass. The set of measurements includes:

¹ GEPI, Observatoire de Paris, CNRS, 5 Place Jules Janssen, 92195 Meudon, France

² LAM, CNRS/UMR6110 and Université de Provence, 38 rue Frédéric Joliot-Curie, 13388 Marseille Cédex 13, France

- ACS imagery from GOODS (3 orbits in b, v, i and z) to recover color-morphology comparable to the depth and resolution (<400 pc) of the SDSS (Delgado-Serrano et al. 2010);
- spatially-resolved kinematics from FLAMES/GIRAFFE (from 8 to 24hrs integration) to sample gas motions at ~ 7 kpc resolution scale (IMAGES I);
- deep VLT/FORS2 observations (3hrs with two grisms at $R=1500$) to recover the gas metal abundances (Rodrigues et al. 2008, hereafter IMAGES-IV);
- Spitzer $24\mu\text{m}$ observations of the GOODS field to estimate the extinction-corrected star formation rates as well as Spitzer IRAC and GALEX deep observations of the field to provide photometric points to constraint the spectral energy distribution.

Taken together, these measurements ensure that the IMAGES sample is collecting an unprecedented amount of data with depth and resolution comparable to what is currently obtained for local galaxies. For example IMAGES is hardly affected by cosmological dimming, because 3 HST/ACS orbits ensure the detection of the optical disk of the Milky Way after being redshifted to $z \sim 0.5$. In section 2 we present the morphological and kinematical properties of distant galaxies, and propose a scenario to relate them to their present-day mass analogues. In section 3 we discuss these results in the context of the Λ CDM model. In section 4 we verify whether this link is robust when compared to the detailed observations of nearby spirals and their haloes.

2 What is the past history of giant spiral galaxies?

Progenitors of present-day giant spirals are similar to galaxies having emitted their light ~ 6 Gyr ago, according to the Cosmological Principle. The IMAGES sample is then unique to sample these progenitors: Fig. 1 presents the results of a morphological analysis of 116 SDSS galaxies (top) and of 143 distant galaxies including those from IMAGES (bottom) for which depth, spatial resolution and selection are strictly equivalent (Delgado-Serrano et al. 2010). Methodology for classifying the morphologies follows a semiautomatic decision tree, which uses as templates the well known morphologies of local galaxies that populate the Hubble sequence, including the color of their sub-components (Delgado-Serrano et al. 2010, see their Fig. 4). Such a conservative method is the only way for a robust morphological classification, and indeed, the Delgado-Serrano et al. (2010) results are similar to those of experts in the field (e.g., van den Bergh 2002). The second step in classifying the nature of distant galaxies is to compare the morphological classification to the spatially-resolved kinematics. The latter provides a kinematical classification of velocity fields ranging from rotation, perturbed rotation or complex kinematics (Flores et al. 2006; Yang et al. 2008). Neichel et al. (2008) robustly established that peculiar morphologies coincide well with anomalous kinematics and vice versa: 95% and 86% of galaxies with complex kinematics and perturbed rotations have peculiar morphologies, respectively. On the other hand 80% of galaxies with robust rotation show spiral morphologies.

Neichel et al. (2008) also verified whether such a situation is preserved when using automatic classification methods such as concentration-asymmetry and GINI-M20. The answer is negative, and these methods overestimate the number of spirals by a factor of two, a problem already identified by Conselice et al. (2005). Such methods are interesting because they can be applied to a much larger number of galaxies than the 143 galaxies studied by Delgado-Serrano et al. (2010). However their limitations in distinguishing peculiar from spiral morphologies lead to far larger uncertainties than the Poisson statistical noise in Delgado-Serrano et al. (2010).

Fig. 1 presents the global evolution of the Hubble sequence during the past 6 Gyr. The link between the two Hubble sequences (past and present-day) is marginally affected by very recent mergers (number density evolution) or by stellar population evolution (luminosity or stellar mass evolution). While the former is limited by the expected decrease of mergers at recent epochs, the latter is precisely compensated by the evolution of the M_{stellar}/L_K ratio (Delgado-Serrano et al. 2010, see their sect. 5.3). As a result the fraction of E/S0 has not evolved, while half of the spirals were not in place 6 Gyr ago, or in other words, half of the spiral progenitors have either peculiar morphology and/or anomalous kinematics.

The remarkable agreement between morphological and kinematical classifications implies that dynamical perturbations of the gaseous component at large scales are linked to peculiar morphological distribution of the stars. This indicates a common process at all scales for gas and stars in these galaxies. Which physical processes may be responsible of this morpho-kinematic behavior? Most anomalous galaxies reveal peculiar large-scale gas motions that cannot be caused by minor mergers: although they can affect locally the dispersion map they do not affect the large scale rotational field over several tens of kpc (Puech et al. 2007). Internal fragmentation

This has led our team to test and then successfully model five of the IMAGES galaxies as consequences of major mergers (Peirani et al. 2009; Yang et al. 2009; Hammer et al. 2009b; Puech et al. 2009; Fuentes-Carrera 2010) using hydrodynamical simulations (GADGET2 and ZENO). However the amount of data to be reproduced per galaxy is simply enormous, leading to 21 observational constraints to be compared to 16 free model parameters in the specific case of Yang et al. (2009). We have then limited our subsequent analysis to the 33 galaxies belonging to the CDFS for reasons of data homogeneity. A comparison of their morpho-kinematics properties to those from a grid of simple major merger models based on Barnes (2002), provided convincing matches in about two-thirds of the cases. This implies that a third of $z=0.4-0.75$ spiral galaxies are or have been potentially involved in a major merger. Since major mergers can easily destroy thin rotating disks, this creates an apparent tension between the large fraction of present-day disks and their survival within the Λ CDM (e.g., Stewart et al. 2009). On the other hand this appears consistent with expectations from Maller, Dekel, & Somerville (2002) i.e., that: "the orbital angular momentum from major mergers may solve the spin catastrophe".

3 Are disks surviving or reviving after a merger?

Barnes (2002) described the re-formation of disks after major mergers, assuming a Milky Way gas fraction (12%) in the progenitors. With larger gas fraction the rebuilt disk can be more prominent and in case of extremely high gas fraction, could dominate the galaxy (Brook et al. 2004; Springel & Hernquist 2005; Robertson et al. 2006). After a gas-rich merger a prominent gaseous disk can form, which could be the progenitor of some present-day disks. These models could appear to be of relatively limited significance given the very large assumed gas fractions (up to 90%). In fact observations of distant galaxies indicate gas fractions that may exceed 50% at $z \sim 1.5-2$ (Daddi et al. 2010; Erb et al. 2006), and it is unclear whether or not higher gas fractions may be common at those redshifts. It could be possible to circumvent this difficulty, perhaps through tuning some physical ingredients in the models, e.g. a feedback more efficient within the central region (Governato et al. 2009), or a star formation less efficient at earlier epochs (Hammer et al. 2010). Such methods are not necessarily wrong, but their additional value is limited since they have been designed intentionally to preserve the gas before the merger or to remove the gas from the central regions to redistribute it to the newly formed disk.

Important progress is expected on both observational and theoretical sides: a confirmation/infirmation of the IMAGES result has to be done by an independent team, although it needs to avoid automatic procedures that often degrade the significance of astrophysical data. With this, the so numerous unstable, anomalous progenitors of present-day spirals, with behavior so similar to major mergers will be the major constraint for disk galaxy formation theories. Why IMAGES is finding so many galaxies (a third to half of the spiral progenitors) that can be attributed to a major merger phase? In fact the morpho-kinematic technique used in IMAGES is found to be sensitive to all merger phases, from pairs to post-merger relaxation. Puech et al. (2011) has compared the merger rate associated with these different phases, and found a perfect match with predictions by state-of-the-art Λ CDM semi-empirical models (Hopkins et al. 2010) with no particular fine-tuning. Thus, both theory and observations predict an important impact of major mergers for progenitors of present-day spiral galaxies: the Hubble sequence made of elliptical and spiral galaxies could be just a vestige of merger events (Hammer et al. 2009b).

Athanassoula (2010) described the different physical processes leading to the formation of elliptical and spiral galaxies. Since the "merger hypothesis" by Toomre & Toomre (1972), it is often accepted that elliptical galaxies may be the product of a major merger between two gas-poor spiral galaxies. It appears more and more plausible that some spiral galaxies could also result from a gas-rich merger of two smaller spiral galaxies. An increasing number of cosmological simulations lead to the formation of late-type disk galaxies after major mergers (Font et al. 2011; Brook et al. 2011). There are still some important questions on precisely how galaxies dominated by thin disks can be generated by such violent processes. We also need to examine whether this scenario can be reconciled with observations of large disks in present-day spiral galaxies.

4 Can a rich merger history be reconciled with observations of nearby spirals?

Having a tumultuous merger history 6 Gyr ago should have left some imprints in many present-day spiral galaxies. Let us consider our nearest neighbour, M31. Quoting van den Bergh (2005): "Both the high metallicity of the M31 halo, and the $r^{1/4}$ luminosity profile of the Andromeda galaxy, suggest that this object might have formed from the early merger and subsequent violent relaxation, of two (or more) relatively massive metal-rich

ancestral objects.” In fact the considerable amount of streams in the M31 haunted halo could be the result of a major merger instead of a considerable number of minor mergers (Hammer et al. 2010). This alternative provides a robust explanation of the Giant Stream discovered by Ibata et al. (2001): it could be made of stars returning from a tidal tail that contains material previously stripped from the lowest mass encounter prior to the fusion. In fact stars in the Giant Stream (Brown et al. 2007) have ages older than 5.5 Gyr, which is difficult to reconcile with a recent collision that is expected in a case of a minor merger (e.g., Font et al. 2008). This constraint has let Hammer et al. (2010) to reproduce the M31 substructures (disk, bulge & thick disk) as well as the Giant Stream after a 3:1 gas-rich merger for which the interaction and fusion may have occurred 8.75 ± 0.35 and 5.5 ± 0.5 Gyr ago, respectively. Besides this, the Milky Way may have had an exceptionally quiet merger history (e.g., Hammer et al. 2007).

Further away from the Milky Way, Martínez-Delgado et al. (2010) conducted a pilot survey of isolated spiral galaxies in the Local Volume up to a low surface brightness sensitivity of ~ 28.5 mag/arcsec² in the *V* band. They found that many of these galaxies have loops or streams of various shapes. These observations are currently considered as evidencing the presence of minor mergers in spiral galaxies. For example, NGC5907 is showing the most spectacular loops that have been modelled by a very minor merger (mass ratio is 4000:1) by Martínez-Delgado et al. (2008). Instead of that, Wang et al. (2011) recently succeed to model the NGC5907 galaxy and their associated loops by assuming a 3:1 gas-rich major merger during the past 8-9 Gyr, for which the loops are caused by returning stars from tidal tails.

There is still a considerable work to do to establish firmly which process is responsible for the tumultuous history of nearby spirals that is imprinted into their haloes. In most cases (Martínez-Delgado et al. 2010), there is no hint of the residual of the satellite core that is responsible of the faint structures discovered in the nearby spiral haloes. If confirmed, this may be problematic for the minor merger scenario. On the other hand, the major merger alternative still faces the problem of reconstructing thin disks that are consistent with the observed ones. However, numerical simulations are rapidly progressing, and AREPO-like simulations (Keres et al. 2011) provide much higher resulting angular momentum when compared to GADGET, and thus thin disks that could resemble much more to the observed ones. Another important advance is provided by Spitzer observations of edge-on spirals (Comerón et al. 2011), indicating more massive thick disks than previously reported, these structures being naturally expected in the case of major mergers.

5 Conclusion

The first proposition that major mergers could be responsible of the re-formation of $\sim 70\%$ of present-day galactic disks (Hammer et al. 2005), was at that time only based on the coeval evolution of morphologies, star formation density and merger rate. Subsequent morpho-kinematic analyses are providing a much more robust confirmation and accuracy to this scenario. It now receives much more attention from both the theoretical side – with an impressive number of articles aiming at reforming spiral galaxies after a collision – and from the observational side – with a large number of papers discussing the influence of mergers in galaxy formation.

Here we plead for the use of a complete set of (observationally), well-determined parameters to characterize distant galaxies. Galaxies are made of hundred billions of stars and distant galaxies contain an equivalent amount of mass of gas. As such they are complex objects and, to be relevant, analyses should include detailed characterizations of their morphologies, kinematics, star formation and gas and stellar masses. Very large surveys are very powerful in gathering huge number of galaxy spectra, although they often lead to oversimplifications related to automatic procedures in characterizing galaxies.

Having characterized distant galaxies with unprecedented details through the IMAGES project, this supports that a third to a half of spiral progenitors were in a merger phase at $z=[0.4-0.75]$. This can potentially reconcile the Λ CDM scenario, predicting a large fraction of mergers, with the very large fraction of large disks in present-day galaxies with masses similar to that of the Milky Way. Consequences of a disk reformation after a merger episode could have important impacts in modern cosmology.

F.H. thanks Collen Sharkey and his team at the Hubble European Information Centre for their remarkable work to disseminate science and for the reprocessing of the Fig. 5 of Delgado et al. (2010). We thank Yanchun Liang and Benoit Neichel who have noticeably contributed to the success of the IMAGES project.

References

Athanassoula E. 2010, *Astronomical Society of the Pacific*, 421, 157

- Barnes, J.E. 2002, MNRAS, 333, 481
- Brook, C. B., Kawata, D., Gibson, B. K., & Freeman K. 2004b, ApJ, 612, 894
- Brook, C. B., Stinson, G., Gibson, B. K. et al. 2011, MNRAS, in press (arXiv:1105.2562)
- Brooks, A. M., Governato, F., Quinn, T., Brook, C. B., Wadsley, J. 2009, ApJ, 694, 396
- Brown, T. M., et al. 2007, ApJ, 658, L95
- Comerón, S., Elmegreen, B. G., Knapen, J. H. et al., 2011, ApJ, in press, (arXiv:1108.0037)
- Conselice C. J., Bundy K., Ellis R. S. et al., 2005, ApJ, 628, 160
- Daddi, E., Bournaud, F., Walter, F. et al. 2010, ApJ, 713, 686
- Delgado-Serrano, R., Hammer, F., Yang, Y. B., Puech, M., Flores, H., Rodrigues, M. 2010, A&A, 509, 78
- Erb, D. K., Shapley, A. E., Pettini, et al. 2006, ApJ, 644, 813
- Flores, H., Hammer, F., Puech, M., Amram, P., & Balkowski, C. 2006, A&A, 455, 107
- Font, A. S., Johnston, K. V., Ferguson, A. M. N., et al. 2008, ApJ, 673, 215
- Font, A. S., McCarthy, I. G., Crain, R. A. et al. 2011, MNRAS, 416, 2802
- Fuentes-Carrera, I. et al., A&A, 513, 43
- Governato, F., Brook, C. B., Brooks, A. M. et al., 2009, MNRAS, 398, 312
- Hammer, F., Gruel, N., Thuan, T.X., et al. 2001, ApJ, 550, 570
- Hammer, F., Flores, H., Elbaz, D., Zheng, X. Z., Liang, Y. C., & Cesarsky, C. 2005, A&A, 430, 115
- Hammer, F., Puech, M., Chemin, L., Flores, H., & Lehnert, M. 2007, ApJ, 662, 322
- Hammer F., Flores H., Yang Y. B., et al. 2009a, A&A, 496, 381
- Hammer F., Flores H., Puech, M., Athanassoula, E. Yang Y. B., et al. 2009b, A&A, 507, 1313
- Hammer, F., Yang, Y. B., Wang, J. L., Puech, M., Flores, H., Fouquet, S, 2010, ApJ, 725, 542
- Hopkins, P. F., Bundy, K., Croton, D. 2010, ApJ, 715, 202
- Ibata, R., Irwin, M., Lewis, G., Ferguson, A. M. N., & Tanvir, N. 2001, Nature, 412, 49
- Keres, D., Katz, N., Fardal, M., Dave, R., Weinberg, D. H. 2009, MNRAS, 395, 160
- Keres, D., Vogelsberger, M., Sijacki, D., Springel, V., Hernquist, L. 2011, MNRAS, submitted (arXiv:1109.4638)
- Liang, Y. C., Hammer, F., & Flores, H. 2006, A&A, 447, 113
- Maller A. H., Dekel A., Somerville R., 2002, MNRAS, 329, 423
- Martínez-Delgado, D., Peñarrubia, J., Gabany, R. J., Trujillo, I., Majewski, S. R., & Pohlen, M. 2008, ApJ, 689, 184
- Martínez-Delgado, D., et al. 2010, AJ, 140, 962
- Neichel, B., et al. 2008, A&A, 484, 159 (IMAGES-II)
- Peebles, P.J.E., 1976 ApJ, 205, 109
- Peirani S., Hammer F., Flores H., Yang Y., Athanassoula E., 2009, A&A, 496, 51
- Puech, M., Hammer, F., Flores, H., Neichel, B., Yang, Y., Rodrigues, M. 2007, A&A, 476, 21
- Puech, M. et al. 2008, A&A, 484, 173 (IMAGES-III)
- Puech M., Hammer F., Flores H., Neichel B., Yang Y., 2009, A&A, 493, 899
- Puech M., Hammer F., Flores, H., Delgado, R., Rodrigues, M., Yang, Y. B., 2010, A&A, 510, 68
- Puech M., 2010, MNRAS, 406, 535
- Puech M., Hammer, F., Hopkins, P. F., Athanassoula, E., Flores, H., Rodrigues, M., Wang, J. L. 2011, ApJ, submitted
- Robertson, B., Bullock, J. S., Cox, et al., 2006, ApJ, 645, 986
- Rodrigues, M. et al. 2008, A&A, 492, 371 (IMAGES-IV)
- Springel, V., Hernquist, L. 2005, ApJ, 622, 9
- Stewart, K., & Bullock, J. S., Wechsler, R., Maller, A. 2009, ApJ, 702, 307
- Toomre, A., Toomre, J. 1972, ApJ, 178, 623
- Toth, G., & Ostriker, J. P. 1992, ApJ, 389, 5
- van den Bergh S. 2002, PASP, 114, 797
- van den Bergh, S., 2005, in The Local Group as an Astrophysical Laboratory, ed. M. Livio & T. M. Brown (Cambridge: Cambridge Univ. Press), P.1-15 (astro-ph /0305042)
- Wang, J. L., Hammer, F., Athanassoula, E., Puech, M., Yang, Y. B., Flores, H. 2011, A&A, submitted
- White, S. D. M., 1984 ApJ 286 38
- Yang, Y. B. et al. 2008, A&A, 477, 789 (IMAGES-I)
- Yang, Y., Hammer, F., Flores, H., Puech, M., Rodrigues, M. 2009, A&A, 501, 437

HIGH- Z GALAXIES BEHIND THE LENSING CLUSTER A2667

N. Laporte¹, R. Pelló¹, D. Schaerer², J. Richard³, F. Boone¹, J.-P. Kneib⁴ and E. Egami⁵

Abstract. We have conducted a survey aimed at identifying a sample of $z \sim 7-10$ candidates accessible to detailed spectroscopic studies. The deep survey on A2667 covers a large field of view with HAWK-I and FORS2 at ESO/VLT between 0.8 and $2.5\mu\text{m}$ (typical depth $m(\text{AB})=27.5$ at 3σ). 13 sources were identified based on the Lyman Break technique, namely 1 J -drop, 8 Y -drops and 4 z -drops over the ~ 45 arcmin² field of view. Optical and near-IR data were combined with Spitzer and Hubble Space Telescope data, when available, in order to determine photometric redshifts. Although the best-fit is always obtained for a high- z solution, this sample shows a relatively high contamination level from extreme mid- z interlopers which may also be present in other surveys. This is demonstrated by the recent detection of two candidates by Herschel and LABOCA, making the high- z identification unlikely. Waiting for a complete spectroscopic follow up, we have used different criteria to account for this contamination and to derive new constraints on the bright end of the UV LF from $z \sim 7$ to 9, using a MC approach based on the redshift probability distributions. Our results are consistent with a significant evolution in the density of bright galaxies beyond $z \sim 8$, whereas no clear evolution is observed between $z \sim 7$ and 8.

Keywords: gravitational lensing: strong, galaxies: high-redshift, dark ages, reionization, first stars

1 Introduction

Understanding the formation of the first luminous sources in the Universe is one of the most important goal in modern astrophysics. Since few years, considerable advances have been made in the search for and study of the first galaxies, by pushing the farthest candidates at $z \sim 10$ (Bouwens et al. 2011). At the same time, the number of confirmed galaxies at $z \geq 6.0$, taking benefit from the use of the new instruments, as VIMOS@Keck or X-Shooter@VLT (Richard et al. 2011), has greatly increased. We have recently published the first results on the search for high- z galaxies around the lensing cluster A2667 (Laporte et al. 2011, hereafter paper 1) using the Lyman Break Technique (Steidel et al. 1995) and the lensing cluster as a gravitational telescope (Zwicky 1937). In this paper we briefly present the main results of the search for $z \geq 6.5$ sources behind A2667, and then focus on the determination of their Luminosity Function (hereafter LF) and its evolution. In the following, we use the concordance cosmology with $\Omega_{\Lambda}=0.7$, $\Omega_M=0.3$ and $H_0=70\text{km.s}^{-1}.\text{Mpc}^{-1}$.

2 High- z sample selection

2.1 Observational data

Our project is based on the photometric pre-selection of candidates using deep optical and near-IR images taken with HAWK-I (filters Y , J , H and K_s) and FORS2 (I and z bands) on the VLT combined with Spitzer data (3.6, 4.5, 5.8, 8.0 and $24\mu\text{m}$) when available. The reader is invited to refer to paper 1 for a complete description of images properties and data processing.

¹ IRAP, 14 Avenue Edouard Belin, 31400 Toulouse & CNRS; IRAP; 14, avenue Edouard Belin, F-31400 Toulouse, France

² Geneva Observatory, 51 Ch; des Maillettes, CH-1290 Versoix, Switzerland

³ Institute for Computational Cosmology, Department of Physics, University of Durham, DH1 3LE, UK

⁴ Laboratoire d Astrophysique de Marseille, CNRS - Universitt'e Aix-Marseille, 38 rue Fr't'ed't'eric Joliot-Curie, 13388 Marseille Cedex 13, France

⁵ Steward Observatory, University of Arizona, 933 North Cherry Avenue, Tucson, AZ 85721, USA

2.2 Selection criteria

The spectral energy distribution (SED) of star-forming high- z galaxies is characterized by a strong break bluewards of Lyman-alpha and a blue continuum redwards. We used different filter combinations to identify galaxy samples fulfilling these criteria at different redshifts. In order to select sources at $z \geq 8$, we have imposed as detection criteria: $m_{H,K} \geq 5\sigma$ and $m_{I,z} \leq 2\sigma$. At redshift 7 these criteria become : $m_{Y,J} \geq 5\sigma$ and $m_I \leq 2\sigma$. According to the general considerations described above, the selection function is based on the position of galaxies on color-color diagrams defined from MC simulations and filter transmissions (Tab 1). Using these color selection, we have found 13 bright sources namely 1 J - drop, 8 Y -drops and 4 z -dropouts (some of them are shown on Fig 1). The magnitude in the H-band range between 23.35 and 26.51 and magnification factors are relatively modest (from 1.01 to 1.37).

	$z \geq 9$	$z \geq 8$	$z \geq 7$
Color Criteria	$J - H \geq 0.76$	$Y - J \geq 0.8$	$z - Y \geq 1.0$
	$H - K \leq 0.5$	$J - H \leq 1.2$	$Y - J \leq 1.2$
	$J - H \geq 1.3(H - K) + 0.76$	$Y - J \geq 1.25(J - H) + 0.8$	$z - Y \geq (Y - J) + 0.6$

Table 1. Color selection criteria adopted as a function of redshift

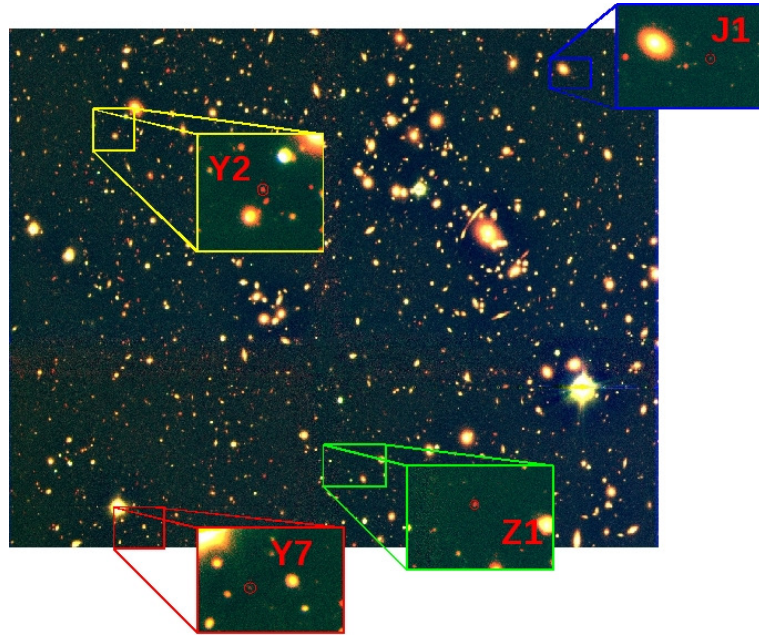


Fig. 1. Color image of Abell2667 including 4 sources from the high- z sample, presented in details in Laporte et al. (2011)

2.3 Contamination

Considering the evolving Luminosity Function (LF) from Bouwens et al. (2008), we expect to detect ~ 5 high- z sources in the field of A2667 in this range of magnitude, suggesting a strong contamination by low/mid- z interlopers. The SED-fitting work and photometric redshift including all optical and near IR data yield a best solution at high- z in all cases. When applying a luminosity prior and/or additional information (see below), only half of the sample survives. Indeed, a recent study of 2 sources from the sample (Boone et al. 2011) using submillimeter data from Herschel (instruments PACS and SPIRE) and LABOCA with wavelength ranging from 100 to $870\mu\text{m}$ has shown that standard templates from the literature fail to reproduce the visible photometry observed even if the far-IR/submillimeter data are correctly adjusted with ULIRGS or SMGs at $z \sim 2$. Due to the shape of their SED in optical and near-IR domain, these two objects appear as extreme sources which could contaminate other high- z samples.

3 Luminosity Functions

In this section we first present the main steps used to determine the LF. The results obtained at $z > 7$ will be presented together with a discussion on the evolution of the LF between $z \sim 7$ and 9

3.1 Method

We have used a method based on MC simulations to compute the LF following Bolzonella et al. (2002). This method is based on the probability distributions derived when computing photometric redshifts. Number densities were corrected from incompleteness as a function of magnitude and redshift, and error bars were derived according to Trenti & Stiavelli (2008) including cosmic variance and Poisson uncertainties.

The method includes the following steps: i) For each source and at each iteration, a probability a is randomly selected between 0 and 1; ii) According to the cumulated redshift probability distribution, a redshift z is attributed as follows $z \Rightarrow P(z) = a$; iii) The UV luminosity L_{1500} is derived as a function of redshift, taking into account the restframe SED and correcting for the magnification value; iv) The number of sources in each luminosity bin is determined, corrected for incompleteness, and finally translated into a number density using the corresponding (lensing corrected) covolume. The typical number of iterations is 1000 to derive a LF in a redshift bin.

3.2 Results

As explained above, we have found one J -dropout candidate (called J1 and presented in Fig 1) over our ~ 45 arcmin² field of view. This is one of the candidates for which a spectroscopic follow up is needed to conclude about its redshift and nature. For this reason, two cases have been considered: either J1 is a genuine high- z galaxy or it is a mid- z interloper instead (i.e. no J -dropout is found around A2667 up to the limits of this survey). In the former case, the number density is $\Phi(M = -21.5 \pm 0.5) = (6.76 \pm 5.0) 10^{-7} \text{Mpc}^{-3}$, which is consistent with upper limit from Bouwens et al. (2008) and points from Lorenzoni et al. (2010). In the later case, if no J -drop is found around A2667, we are able to give a strong constraint on the bright part of the LF considering a Poisson distribution. We found, at 68% confidence level, a limit of $\Phi(M = -21.5 \pm 0.5) \leq (5.17 \pm 5.0) 10^{-6} \text{Mpc}^{-3}$ which is also consistent with previous references (Fig 2 bottom left)

At $z \sim 8$, we have found 8 Y -dropouts with magnitude ranging between 23.35 and 25.40. We expect up to 75% contamination in this redshift bin. Waiting for additional (spectroscopic) data, we have performed different tests. The best results are obtained when applying a selection based on the optical χ^2 method following Bouwens et al. (2010). Two points are obtained with this new sub-sample: $\Phi(M = -22.0 \pm 0.25) = (0.18_{-0.16}^{+2.8}) 10^{-5} \text{Mpc}^{-3}$ and $\Phi(M = -21.5 \pm 0.25) = (0.12_{-0.1}^{+1.5}) 10^{-4} \text{Mpc}^{-3}$. These new results are consistent with McLure et al. (2010) and previous references (Fig 2 top right).

At lower redshift, $z \sim 7$, after removing Z1 from our sample based on its detection at 24 microns and the IR SED (see Boone et al. (2011)), we computed the LF from the 3 remaining objects and were able to give one point in the bright end of the LF : $\Phi(M = -21.25 \pm 0.25) = (8.5 \pm 7.6) 10^{-5} \text{Mpc}^{-3}$. This new result is consistent with results from Castellano et al. (2010) and Ouchi et al. (2009) (Fig 2 top left).

3.3 Evolution of the LF from $z \sim 7$ to 9

To study the evolution of the LF beyond $z \sim 7$, the usual parametrization based on the Schechter function (Schechter 1976) was used :

$$\Phi(M) = \Phi^* \frac{\ln(10)}{2.5} (10^{-0.4(M-M^*)})^{\alpha+1} \exp -10^{-0.4(M-M^*)} \quad (3.1)$$

A χ^2 minimization procedure was used to determine the best-fit LF parameters (namely Φ^* , M^* , and α), by combining our own results with those found by previous authors (see references in Sect. 3.2). Fig 2 displays three LFs (at $z \sim 7$, 8 and 9) together with the 68% likelihood contour from which error bars on each parameters are deduced. Tab. 2 summarizes these results as a function of redshift. Our observations cover the bright end of the LF and are therefore insensitive to the faint-end slope α . This value is assumed fixed at $z \sim 9$ for consistency, and the best-fit value at $z \sim 7$ and $z \sim 8$ is also consistent as expected with previous authors.

Given the error bars, the LF does not seem to evolve significantly between $z \sim 7$ and 8. This finding is consistent with results from Bouwens et al. (2010) who found no evidence of an evolution of the LF in this

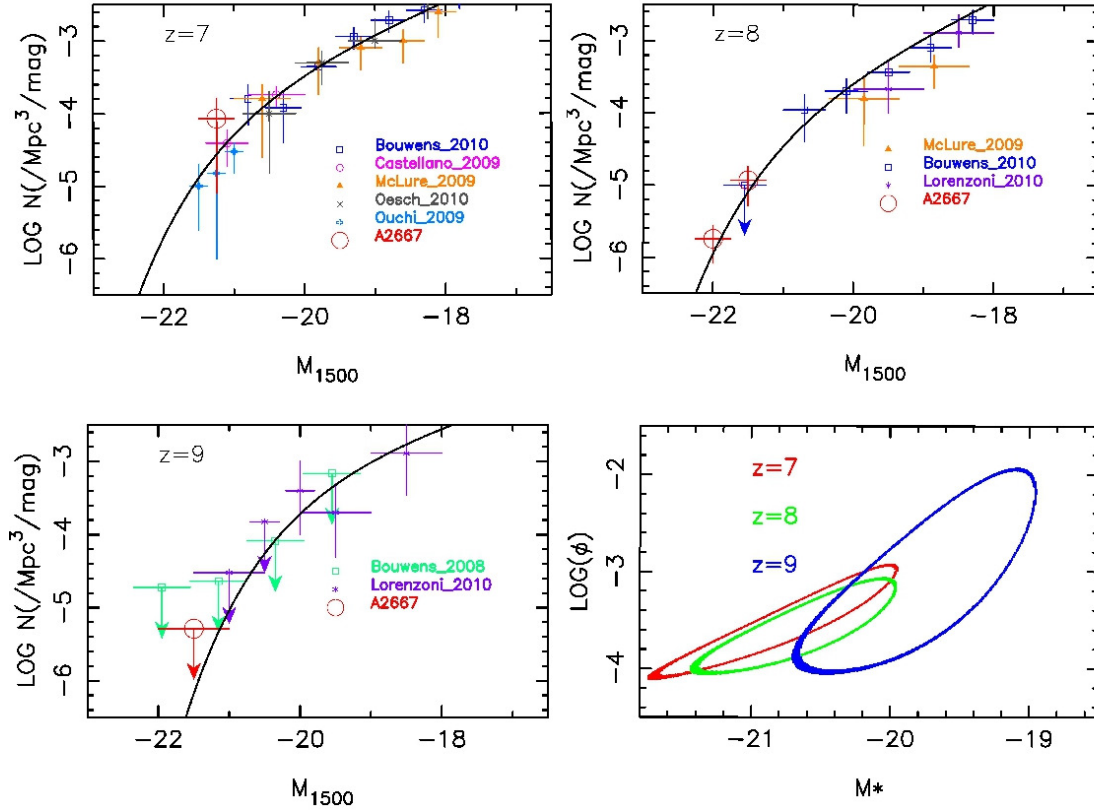


Fig. 2. LF at $z \sim 7$ (top-left), $z \sim 8$ (top-right) and $z \sim 9$ (bottom-left). Solid lines display the best-fit Schechter parametrization. At $z \sim 9$, the upper limit is shown. The 68% likelihood contours on the Schechter parameters are shown in the bottom-right panel

Redshift	M^*	Φ^* 10^{-3}Mpc^{-3}	α
$z \sim 7$	-20.53 ± 0.18	$0.40^{+0.4}_{-0.2}$	-2.00 ± 0.21
$z \sim 8$	-20.51 ± 0.35	$0.30^{+0.26}_{-0.14}$	-2.14 ± 0.20
$z \sim 9$	-19.52 ± 0.33	$1.37^{+1.7}_{-0.8}$	-1.74 (<i>fixed</i>)

Table 2. Parametrization of the LF using results from this work, together with Ouchi et al. (2009), Castellano et al. (2010), McLure et al. (2010), Bouwens et al. (2010), Lorenzoni et al. (2010), Bouwens et al. (2008)

redshift domain. A strong evolution between $z \sim 8$ and 9, with a sharp decrease in the number density of bright galaxies beyond $z \sim 8$, as expected by hierarchical models of galaxy formation.

4 Conclusions

The photometric survey conducted with HAWK-I and FORS2 on A2667 allowed us to identify a sample of 13 high- z candidates ($z \geq 6.5$) namely 1 J -drop, 8 Y -drops and 4 z -drops using a color selection based on the Lyman Break Technique (Laporte et al. 2011). This sample suffers from a relatively high contamination level from extreme mid- z interlopers, as demonstrated by the recent detection of two candidates by Herschel and LABOCA, making the high- z identification unlikely (Boone et al. 2011). Waiting for a complete spectroscopic follow up, we have used different criteria to account for this contamination and to derive new constraints on the bright end of the UV LF from $z \sim 7$ to 9, using a MC approach based on the redshift probability distributions. Our results are consistent with a significant evolution in the density of bright galaxies beyond $z \sim 8$, whereas no

clear evolution is observed between $z \sim 7$ and 8.

Part of this work was supported by the French Centre National de la Recherche Scientifique (CNRS), the French Programme National de Cosmologie et Galaxies (PNCG), as well as by the Swiss National Science Foundation. We acknowledge support for the International Team 181 from International Space Science Institute (ISSI) in Berne. This work received support from Agence Nationale de la Recherche (ANR) bearing the reference ANR-09-BLAN-0234. This paper is based on observations collected at the European Southern Observatory (ESO), Chile (71.A-0428,082.A-0163).

References

- Bolzonella, M., Pelló, R., & Maccagni, D. 2002, *A&A*, 395, 443
Boone, F., Schaerer, D., Pello, R., et al. 2011, ArXiv e-prints : 1108.2406
Bouwens, R. J., Illingworth, G. D., Franx, M., & Ford, H. 2008, *ApJ*, 686, 230
Bouwens, R. J., Illingworth, G. D., González, V., et al. 2010, *ApJ*, 725, 1587
Bouwens, R. J., Illingworth, G. D., Labbe, I., et al. 2011, *Nature*, 469, 504
Castellano, M., Fontana, A., Paris, D., et al. 2010, *A&A*, 524, A28
Laporte, N., Pelló, R., Schaerer, D., et al. 2011, *A&A*, 531, A74
Lorenzoni, S., Bunker, A., Wilkins, S., et al. 2010, ArXiv e-prints
McLure, R. J., Dunlop, J. S., Cirasuolo, M., et al. 2010, *MNRAS*, 403, 960
Ouchi, M., Mobasher, B., Shimasaku, K., et al. 2009, *ApJ*, 706, 1136
Richard, J., Kneib, J.-P., Ebeling, H., et al. 2011, *MNRAS*, 414, L31
Schechter, P. 1976, *ApJ*, 203, 297
Steidel, C. C., Pettini, M., & Hamilton, D. 1995, *AJ*, 110, 2519
Trenti, M. & Stiavelli, M. 2008, *ApJ*, 676, 767
Zwicky, F. 1937, *ApJ*, 86, 217

THE BARYON FRACTION IN FIVE GALAXY GROUPS

N. Martinet^{2,1}, F. Durret², T. F. Laganá³ and G. B. Lima Neto³

Abstract. Using ESO 2.2m/WFI optical data in two bands, we computed the galaxy luminosity functions of five groups of galaxies, selecting group members with the color-magnitude relation. By integrating the luminosity function, we calculated the stellar masses of our groups. We then calculated the X-ray gas mass and the total group mass from the density and temperature profiles obtained from XMM-Newton X-ray data. This enabled us to derive the baryon fraction in our groups and to compare it with those from other studies of groups and clusters.

Keywords: groups of galaxies, optical, X-rays

1 Introduction

Groups of galaxies are composed of a few to a few tens of galaxies in gravitational quasi-equilibrium. As for clusters, their principal baryonic constituents are the stellar matter, mainly inside galaxies and the intracluster gas. The former is detected through optical observations (among other wavelength) and the latter mainly through X-rays.

These data give access to the fraction of baryons inside groups. Similar studies have been conducted on clusters of galaxies (e.g. Laganá et al. 2008, Giodini et al. 2009) and on small clusters (e.g. Vikhlinin et al. 2006, Sun et al. 2009, Andreon 2010). In most cases, only the gas mass is calculated. Then, the stellar mass is considered as one fifth or one sixth of the gas mass, and the baryon fraction is estimated.

This last assertion, true for clusters, is discussed in the case of groups. We confirm here that the stellar matter contributes as much as the gas to the baryon budget in the case of groups. This could be a first step to answering recent questions about the nature of groups. Are they scaled-down clusters or are they more specific objects?

We present here the methods we used to estimate the baryon fractions of five groups of galaxies: NGC4325, HCG62, HCG42, NGC5044 and NGC5846. This work was based on ESO 2.2m/WFI data in the B and Rc optical bands and XMM-Newton X-ray data. Our results are put in perspective with other baryon fractions of low mass clusters.

2 Optical analysis

Optical WFI images are treated using SExtractor (Bertin & Arnouts 1996), SCAMP (Bertin 2006) and SWarp (Bertin 2002). Then, R and B magnitudes of objects are extracted via the MAG_AUTO keyword of SExtractor. Magnitudes are corrected for airmass and extinction. This last correction is done with the extinction maps from Schlegel et al. (1998).

The analysis leading to an estimate of the stellar mass is done following statistical methods used for clusters (see e.g. Durret et al. 2009). Galaxies are separated from stars based on their central surface brightness. We checked that the number of stars found per square degree is consistent with the Besançon catalog (Robin et al. 2003). Galaxies belonging to the group are then selected from a (B-R) versus R color magnitude relation based on galaxies with spectroscopic redshifts (Fig. 1, left). One can note that statistical subtraction of galaxy counts

¹ ENS de Cachan, 94230 Cachan, France

² UPMC Université Paris 06, UMR 7095, Institut d'Astrophysique de Paris, 98bis Bd Arago, F-75014, Paris, France

³ IAG, USP, R. do Matão 1226, 05508-090, São Paulo/SP, Brazil

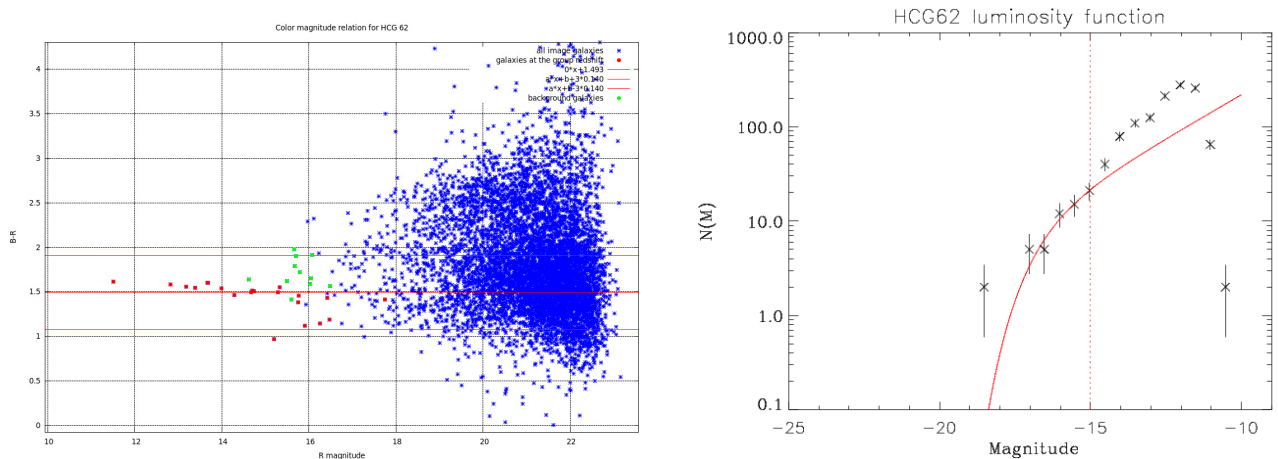


Fig. 1. **Left:** HCG62 B-R vs. R color magnitude relation. Red dots are the galaxies which belong to the group according to their spectroscopic redshift. Red lines indicate the $\pm 3\sigma$ red sequence. Green dots are background galaxies with a measured spectroscopic redshift. **Right:** HCG62 R-band luminosity function. The red curve is the Schechter fit of the data down to an absolute magnitude of -15 (dotted line)

is not possible in the case of groups due to the small number of galaxies. After selecting the galaxies belonging to the group, we can plot the luminosity function of the groups in their r_{2500} radius (the radius at which the group reaches 2500 times the critical density of the Universe) and fit them with a Schechter function. One can see on the right side of Fig. 1 that the Schechter function is divided in two parts. The bright part corresponds to the bright galaxies and seems to be the Schechter function of the group, while the faint part shows higher counts dominated by background galaxies. An estimate of the mass is obtained by integration of this function. Luminosities are converted into masses using different M/L ratios for elliptical and spiral galaxies. These ratios are taken from Kauffmann et al. (2003) and the fraction of spiral galaxies from Osmond & Ponman (2004).

However, these statistical methods, which are applicable for clusters, are not well suited to groups. This can be seen if we plot the color-magnitude relation for all the galaxies with known redshift. One can see on the left part of Fig. 1 that background galaxies (green dots) are not well separated from galaxies belonging to the group (red dots). In the case of clusters, those background galaxies can be neglected (at least at relatively bright magnitudes) due to their faint number compared to the large amount of cluster galaxies. Taking this into account, a Schechter function cannot correctly fit the data and we finally calculated the mass in a different way, by considering that the stellar mass is the mean of an upper and lower limit. The lower limit is obtained by simply adding the masses of the galaxies belonging to the group according to their spectroscopic redshift. The upper limit is obtained by adding the masses of all the galaxies within the red sequence limits (color magnitude best fit $\pm 3\sigma$). The error bars, given by the differences between the upper and mean values, are considerably below the error bars due to the missknowledge of the mass to luminosity ratios.

3 X-ray analysis

XMM-Newton X-ray data were reduced using the standard procedure with the SAS package*. The time intervals of high particle background (flares) have been removed and we have produced clean event files for the pn, MOS1 and MOS2. We have used normalized blank-fields† to compute the necessary background spectra.

The temperature profiles were determined in concentric circular rings around the centre where, for each ring we have extracted the spectra from all EPIC cameras and produced the appropriated RMF and ARF. For each ring we have fitted the spectra using XSPEC 12, with a plasma emission model MEKAL and photoelectric absorption model PHABS.

The gas density profile was deprojected from the radial surface brightness profiles, which were measured using the task ELLIPSE from IRAF. We have used exposure map corrected [0.5–8.0 keV] images from the MOS

*See <http://xmm.esac.esa.int/sas/current/howtouseasas.shtml>

†See http://xmm2.esac.esa.int/external/xmm_sw_cal/background/index.shtml

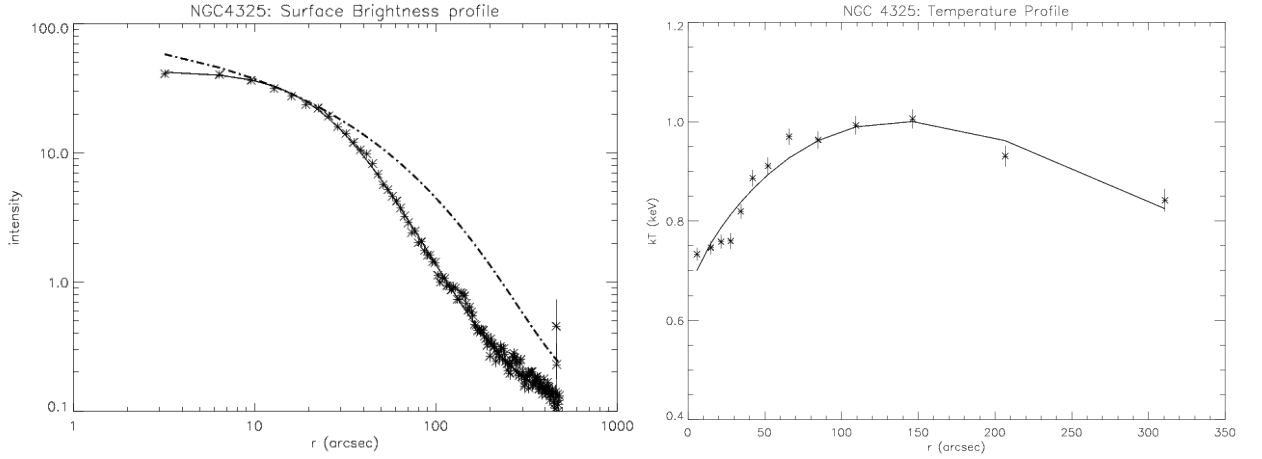


Fig. 2. Left: NGC4325 surface brightness profile. The full curve corresponds to the beta-model while the dashed curve corresponds to the Sersic model. **Right:** NGC4325 temperature profile.

cameras, since they present less bad columns and pixels than the pn camera.

The mean temperature was used to estimate the r_{2500} radius of each group via a $kT-r_{2500}$ scaling relation drawn from Sun et al. (2009). The surface brightness profile is well fitted by a β -model (see left part of Fig. 2):

$$\Sigma(r) = \Sigma_0 \left(1 + \left(\frac{r}{r_c}\right)^2\right)^{-3\beta + \frac{1}{2}} \quad (3.1)$$

where r_c is the core radius, β a shape parameter and Σ_0 the central surface brightness. The temperature profile is then fitted by the following expression from Laganá et al. (2008):

$$T_{2D}(r) = \frac{T_0 \left(\alpha \sqrt{\frac{r}{r_t} + \frac{r}{r_t}} + 1\right)}{\left(\frac{r}{r_t}\right)^2 + 1} \quad (3.2)$$

where r_t is a scale parameter, T_0 the central temperature and α a shape parameter. Assuming the β -model, one can get the gas density profile from the surface brightness profile.

$$\rho(r) = \rho_0 \left(1 + \left(\frac{r}{r_c}\right)^2\right)^{-\frac{3\beta}{2}} \quad (3.3)$$

where r_c and β are the parameters of the β -model fitting the surface brightness profile and ρ_0 is calculated taking into account the normalization parameter in XSPEC. The gas mass in a radius of r_{2500} is simply obtained by integrating the density profile over a sphere of radius r_{2500} .

Assuming the gas is a perfect gas in hydrostatic equilibrium in the Newtonian potential of the group, one can write the following equation for the dynamical mass:

$$M_{dyn}(r) = -\frac{r^2 k T(r)}{m_H G \mu} \left(\frac{1}{\rho(r)} \frac{d\rho(r)}{dr} + \frac{1}{T(r)} \frac{dT(r)}{dr} \right) \quad (3.4)$$

where m_H , G , μ and k are respectively the proton mass, the gravitational constant, the average molar mass and the Boltzmann constant. We thus calculate the total mass within r_{2500} using the density and temperature profiles.

4 Discussion

The method described above enables us to calculate the fraction of baryons in stars ($f_{stars} = \frac{M_{stars}}{M_{tot}}$), in gas ($f_{gas} = \frac{M_{gas}}{M_{tot}}$) and the total baryon fraction ($f_{baryons} = f_{stars} + f_{gas}$) within a sphere of radius r_{2500} (see Table 1). The values given in Table 1 are somewhat lower than cluster values found in the literature. However, a comparison is possible by considering the evolution of these fractions with the total mass of groups or clusters, as shown in Fig. 3.

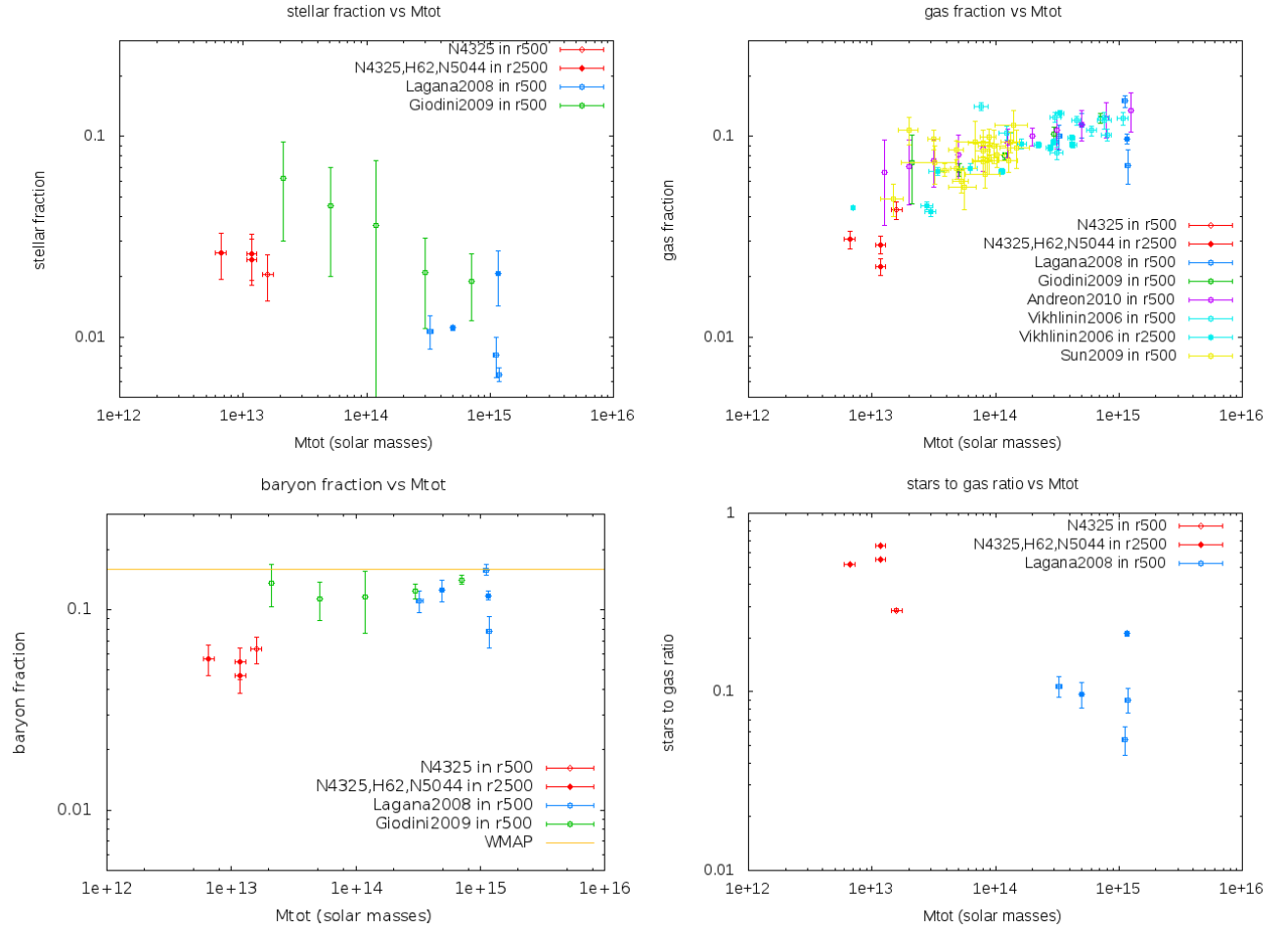


Fig. 3. **Top left:** Stellar fraction vs total mass. **Top right:** Gas fraction vs total mass. **Bottom left:** Baryon fraction vs total mass. **Bottom right:** stellar to gas mass ratio vs total mass. Open circles are calculated in r_{500} while full circles are in r_{2500} in all figures.

One can notice the different trends of each curve: the stellar fraction decreases with total mass, while the gas fraction increases with total mass. This result lets us think that stars and gas exchange some matter, perhaps by gas accretion or supernova explosions. We plotted values in r_{500} and in r_{2500} . As group studies are only beginning, many results are only given in r_{500} , the usual radius of cluster studies in the literature. We see that our values are in good agreement with values taken from the literature concerning the gas fraction in both r_{500} (Vikhlinin et al. 2006, Sun et al. 2009, Giodini et al. 2009, Andreon 2010) and r_{2500} (Vikhlinin et al. 2006). However, we found lower stellar fractions than those predicted by other studies (Giodini et al. 2009).

This is not surprising for groups calculated within r_{2500} as Giodini et al. worked within a bigger radius: r_{500} , and thus their groups contain much more baryons. However, we calculated NGC4325 values within r_{500} and it still has lower stellar and baryon fractions. The main argument that could account for this result is the contribution of diffuse light, which has been neglected due to the difficulty to detect it. Diffuse light is the part of stellar matter which is not in a galaxy but is located in the intracluster medium. As groups are less dominated by gravitation than clusters, this diffuse light could account for much more missing baryons in groups than in clusters. For example, Da Rocha et al. (2008) showed that this matter could account for almost half of the total stellar mass in some groups. As a result of our lower stellar masses, our baryon fractions are also lower than expected from the literature (Giodini et al. 2009).

Diffuse light could therefore be a major constituent of the baryon fraction and thus partially explain the lack of baryons compared to the WMAP value ($\frac{\Omega_B}{\Omega_M} = 0.16$, Dunkley et al. 2009). Another explanation for this lack of baryons could be that we do measurements in a small radius (r_{2500} or r_{500}) while the WMAP value is

Table 1. Baryon fractions in r_{2500} for a sample of four groups (the quality of the X-ray data for HCG42 was not sufficient to derive the gas and total masses). NGC5846 is not distant enough to be studied in this radius, so it is analyzed in $0.67r_{2500}$). We also give values in r_{500} for NGC4325.

Groups	z	r_{2500}	T_X	M_{tot} ($10^{11}M_{\odot}$)	f_{stars}	f_{gas}	$f_{baryons}$
NGC4325	0.0257	171	0.84 ± 0.01	118 ± 11.8	0.0243 ± 0.0063	0.0224 ± 0.002	0.0467 ± 0.0083
HCG62	0.0137	168	0.81 ± 0.03	66 ± 6.6	0.0262 ± 0.0068	0.0306 ± 0.0031	0.0568 ± 0.0099
HCG42	0.0133	157	0.69 ± 0.02				
NGC5044	0.0093	175	0.88 ± 0.03	118 ± 11.8	0.0259 ± 0.0067	0.0288 ± 0.0029	0.0547 ± 0.0096
NGC5846	0.0057	155	0.67 ± 0.01	77.5 ± 7.8	0.0107 ± 0.0028	0.0068 ± 0.0007	0.0175 ± 0.0035

Groups	z	r_{500}	T_X	M_{tot} ($10^{11}M_{\odot}$)	f_{stars}	f_{gas}	$f_{baryons}$
NGC4325	0.0257	364	0.84 ± 0.01	159 ± 15.9	0.0204 ± 0.0053	0.0430 ± 0.0043	0.0634 ± 0.0096

obtained for all the sky.

Finally, we plotted the ratio of the stellar mass to gas mass against the total mass. While comparing our sample with clusters of Laganá et al. (2008), we can conclude that this ratio decreases with total mass. This underlines the importance of calculating accurately the stellar mass in the case of groups. In most cluster studies the stellar mass is simply estimated as one sixth of the gas mass while here it almost reaches one half (and this without taking into account diffuse light).

References

- Andreon, S. 2010, MNRAS, 407, 263
 Bertin, E 2002, ASP, Vol. 281, p. 228
 Bertin, E. 2006, ASP, Vol. 351, p. 112
 Bertin, E. & Arnouts, S. 1996, A&AS 317, 393
 Da Rocha, C., Ziegler, B.L., Mendes de Oliveira, C. 2008, MNRAS, 388, 1433
 Dunkley J. et al. 2009, ApJS, 180, 306
 Durret, F., Slezak, E. & Adami, C. 2009, A&A, 506, 637
 Giodini, S., et al. 2009, ApJ, 703, 982
 Kauffmann, G., et al. 2003, MNRAS, 341, 33
 Laganá T. F., Lima Neto G. B., Andrade-Santos, F., and Cypriano E. S. 2008, A&A, 485, 633
 Osmond, J. P. F., Ponman, T. J. 2004, MNRAS, 350, 1511
 Robin, A. C., Reylé, C., Derrière, S., Picaud, S. 2003, A&A, 409
 Schlegel, D.J., Finkbeiner, D. P., Davis, M. 1998, ApJ, 500, 525
 Sun, M., et al. 2009, ApJ, 693, 1142
 Vikhlinin A., et al. 2006, ApJ, 640, 691

THE NEXT GENERATION VIRGO CLUSTER SURVEY: STATUS AND FIRST RESULTS

S. Mei¹, L. Ferrarese², A. Boselli³, S. Boissier³, F. Bournaud⁴, J. C. Cuillandre⁵, P.-A. Duc⁵, E. Ferrière⁵, R. Gavazzi⁶, S. D. J. Gwyn², P. Hudelot⁶, O. Ilbert³, A. Lançon⁷, M. Huertas-Company¹, Y. Mellier⁶, M. Milkeraitis⁸, R. Muñoz⁷, T. H. Puzia¹⁹, L. van Waerbeke⁸, B. Vollmer⁷, D. Woods⁸, C. Balkowski¹, M. L. Balogh⁹, N. Ball², J. P. Blakeslee², C. Carignan¹⁰, R. G. Carlberg¹¹, S. G. Chapman¹², P. Côté², S. Courteau¹³, T. J. Davidge², S. Demers¹⁴, P. R. Durrell¹⁵, T. Erben¹⁶, E. Emsellem¹⁷, G. Gavazzi¹⁸, H. Hoekstra¹⁹, A. Jordán²⁰, J. J. Kavelaars², L. MacArthur², A. W. McConnachie², D. McLaughlin²¹, J. C. Mihos²², C. Peng², E. W. Peng²³, M. Sawicki²⁴, D. Schade², L. Simard², J. E. Taylor²⁵, J. L. Tonry²⁶, R. B. Tully²⁵, W. van Driel¹ and C. D. Wilson²⁷

Abstract. We present recent results from the Next Generation Virgo Cluster Survey (NGVS). NGVS is a CFHT MegaCam large program to observe the Virgo Cluster from its core to virial radius, for a total coverage of 104 square degrees. The survey is performing deep imaging (10 sigma detection for point sources of 25.9 mag in the g-band) in five band-passes (u*,g',r',i',z') and will reach a depth never attained before

¹ GEPI, Observatoire de Paris, CNRS, Univ. Paris Diderot, 5 Place J. Janssen, 92190 Meudon Cedex, France

² Herzberg Institute of Astrophysics, National Research Council of Canada, Victoria, BC, V9E 2E7, Canada - Department of Physics and Astronomy, University of Victoria, Box 3055, Victoria, BC V8W 3P6, Canada

³ Laboratoire d'Astrophysique de Marseille, OAMP, Université Aix-Marseille, France

⁴ CEA, IRFU, SAp, 91191 Gif-sur-Yvette, France

⁵ Canada-France-Hawaii Telescope Corporation, Kamuela, HI 96743, USA

⁶ Institut d'Astrophysique de Paris, UMR7095 CNRS — Université Paris 6, 98bis Bd Arago, 75014 Paris, France

⁷ Observatoire Astronomique & CNRS UMR7550, Université de Strasbourg, 11 rue de l'Université, Strasbourg F-67000, France

⁸ University of British Columbia, Department of Physics and Astronomy, 6224 Agricultural Road, Vancouver, B.C. V6T 1Z1, Canada

⁹ Department of Physics and Astronomy, University of Waterloo, Waterloo, Ontario N2L 3G1, Canada

¹⁰ Laboratoire d'Astrophysique Expérimentale, Observatoire du Mont Mégantic, PQ, Canada- Département de Physique, Université de Montréal, CP 6128, Station Centreville, Montréal, PQ H3C 3J7, Canada

¹¹ Department of Astronomy and Astrophysics, University of Toronto, Toronto, ON M5S 3H4, Canada

¹² Institute of Astronomy, Madingley Road, Cambridge, CB3 0HA, UK

¹³ Department of Physics, Engineering Physics and Astronomy, Queen's University, Kingston, ON, Canada

¹⁴ Département de Physique, Université de Montréal, CP 6128, Station Centreville, Montréal, PQ H3C 3J7, Canada

¹⁵ Department of Physics and Astronomy, Youngstown State University, Youngstown, OH, USA

¹⁶ University of Bonn, Germany

¹⁷ Université de Lyon 1, CRAL, Observatoire de Lyon, 9 av. Charles André, F-69230 Saint-Genis Laval; CNRS, UMR 5574; ENS de Lyon, France - European Southern Observatory, Karl-Schwarzschild-Str. 2, 85748, Garching, Germany

¹⁸ Università degli Studi di Milano-Bicocca, Piazza della Scienza 3, 20126 Milano, Italy

¹⁹ Leiden University, Leiden Observatory, Niels-Borhweg 2, 2333CA, Leiden, the Netherlands

²⁰ Departamento de Astronomía y Astrofísica, Pontificia Universidad Católica de Chile, Santiago 22, Chile

²¹ Astrophysics Group, Lennard-Jones Laboratories, Keele University, Keele, Staffordshire, ST5 5BG, UK

²² Department of Astronomy, Case Western Reserve University, Cleveland, OH

²³ Department of Astronomy, Peking University, Beijing 100871, China

²⁴ Department of Astronomy and Physics, St. Mary's University, Halifax, NS B3H 3C3, Canada

²⁵ Department of Physics and Astronomy, University of Waterloo, 200 University Avenue West, Waterloo, Ontario N2L3G1, Canada

²⁶ Institute for Astronomy, 2680 Woodlawn Dr., University of Hawaii, Honolulu, Hawaii, 96822, USA

²⁷ Department of Physics and Astronomy, McMaster University, Hamilton, ON L8S 4M1, Canada

in optical studies of the Virgo cluster. The program's main scientific objectives are: the characterization of the faint-end of the galaxy luminosity function, the characterization of galaxy scaling relations from low to high masses, the cluster/intracluster medium/galaxy connection, the role of environmental effects in galaxy evolution, and the fossil record of star formation and chemical enrichment in dense environments. Numerous ancillary projects — from a survey of the Galactic halo to a cosmic shear measurement of the matter power spectrum on large scales — are also under way. We present the status of the survey and multi-wavelength projects, and results on recently detected high-redshift galaxy clusters.

Keywords: Galaxy clusters, galaxies, evolution

1 Introduction

The Next Generation Virgo Cluster Survey (NGVS; Ferrarese et al. 2011) is a large program at the Canada France Hawaii Telescope (PI: Laura Ferrarese), and aims to observe 104 square degrees of sky within the virial radius of the Virgo cluster in five spectral bandpasses (u' , g , r , i , z') with the instrument Megaprime. The program involves around 50 scientists from more than 20 institutions. Observations have started in December 2008 and are scheduled to be completed by June 2012. The current status of the survey is shown in Fig. 1.

The main goals of the survey are the characterization of (1) the faint-end of the galaxy luminosity function, (2) galaxy scaling relations from low to high masses, (3) the cluster/intracluster medium/galaxy connection, (4) the role of environment in galaxy evolution, and (5) the fossil record of star formation and chemical enrichment in dense environments. Numerous ancillary projects — from a survey of the Galactic halo to a cosmic shear measurement of the matter power spectrum on large scales — are also under way.

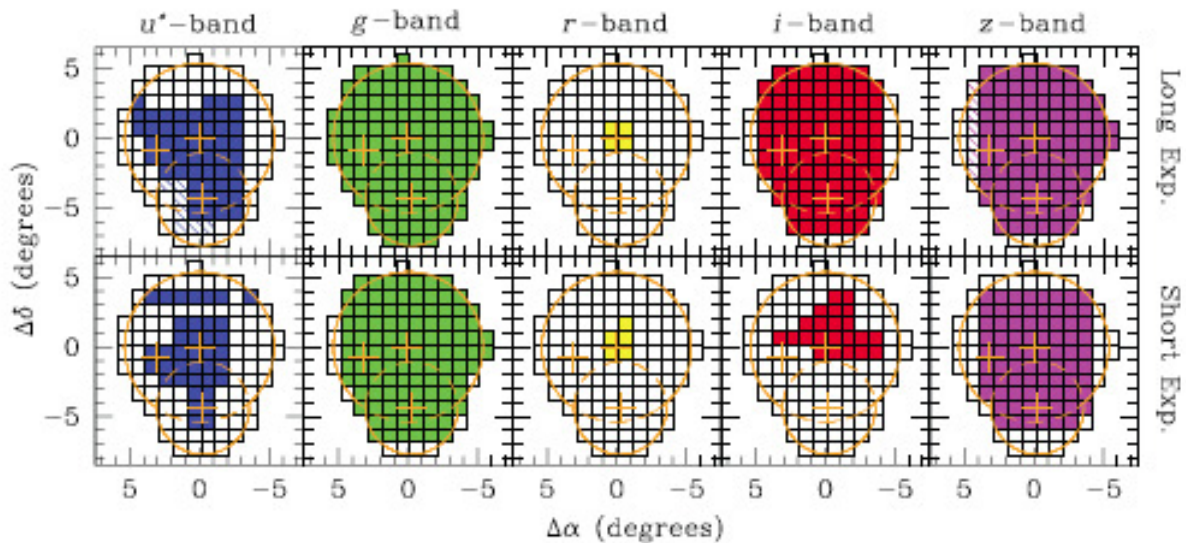


Fig. 1. NGVS observing status as of September 2011 (Ferrarese et al. 2011). Empty squares show Megacam pointings. Long and short exposures (see Ferrarese et al. 2011 for details) are shown in the top and bottom rows, for the five bandpasses covered by the survey. Fields for which observations have been completed are indicated by colored filled squares, while only partial data have been obtained for dashed fields. The orange outline indicates the virial radii of Virgo A and B subclusters, while the crosses mark the location of M87 to the North, M49 to the South and M60 to the East.

2 New adapted observational strategies

The NGVS observational strategy has been optimized to reach very faint surface brightness levels, thus allowing us to characterize the outer haloes of galaxies and detect low surface brightness, diffuse features, such as tidal tails and intracluster light. The main challenge is to characterize and correct for scattered light contamination

in the raw frames. This is achieved thanks to a dedicated data acquisition strategy that allows a real time sampling of the scattered light component, which is then removed during data processing. The final images attain a surface brightness of $\mu_g = 29$ mag arcsec $^{-2}$. The individual frames are processed at CFHT using a newly developed pipeline (Elixir-LSB, Cuillandre et al., in prep.; Fig. 2).

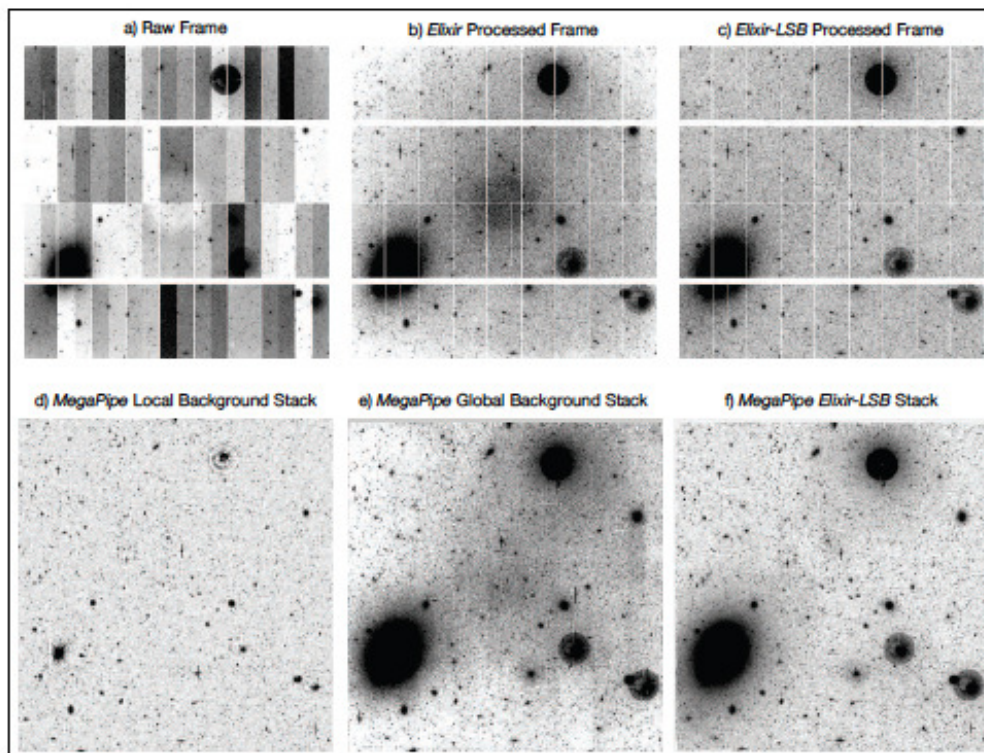


Fig. 2. The *Elixir-LSB* pipeline results are shown (top), compared to the standard Megapipeline reduction (bottom). The top row shows, from left to right, a raw, Elixir and Elixir-LSB processed single frame. The bottom row shows, from left to right, MegaPipe *local background*, *global background* and *Elixir-LSB* stacks obtained by combining all five long g-band dithered frames obtained for a NGVS field (Cuillandre et al., in preparation; see Ferrarese et al. 2011 for details).

3 Multi-wavelength follow-up of the Virgo Cluster

Two imaging programs designed to complement the NGVS data have been undertaken in the past year: the NGVS-IR (NGVS-Infrared) and GUViCS (GALEX Ultraviolet Virgo Cluster Survey).

The NGVS-IR survey (coPI: Ariane Lançon and Thomas Puzia) covers the Virgo central 4 deg 2 in the K-band with 34 pointings ($4 \times 2048 \times 2048$ pixels) of CFHT/WIRCAM, each observed 108 times with non-redundant offsets. Acquisition started in December 2009, and was completed in June 2010. The observational strategy includes nodding, within the target area, between relatively empty fields and crowded ones, in order to sample the sky in every pixel at a frequency comparable to that of the large near-IR sky brightness variations.

GUViCS (PI: Alessandro Boselli; Boselli et al. 2011) observations were completed in 2010 and processed by the standard GALEX pipelines. Photometry and cut-offs were extracted for extended objects following standard procedures. This includes flux extraction of pointlike and extended sources, low surface brightness features, not homogeneously provided by the standard GALEX pipelines. For extended sources we reconstruct the NUV and FUV radial profiles, necessary for the determination of the structural parameters used in the construction of several scaling relations (e.g the effective radius and surface brightness) and in the comparison with model predictions. We determined the FUV and NUV luminosity functions of the Virgo cluster core for all cluster members and separately for early- and late-type galaxies for the central 12 sq. deg. (Boselli et al. 2011).

4 Background galaxy clusters

Among the ancillary projects, we briefly describe detections of background high-redshift galaxy clusters. With the depth and spectral energy distribution coverage of the NGVS, we expect to detect 5-10 background galaxy clusters per square degree, with masses above $M \approx 5 \times 10^{13} M_{\odot}$ over the redshift range $0.1 < z < 1$. This will give a total of 500 to 1000 background galaxy clusters. Fig. 3 shows examples of clusters in the range $0.4 < z < 0.8$ identified in the NGVS using the 3D-Matched-Filter cluster finding algorithm of Milkeraitis et al. (2010) and an independent red sequence based algorithm (Mei et al. 2011). Based on a preliminary analysis, and on results from surveys with similar depth and spectral coverage (e.g., Ilbert et al. 2006; Coupon et al. 2009), we expect to measure reliable photometric redshifts and select cluster populations to a depth of $i \approx 22.5$ mag.

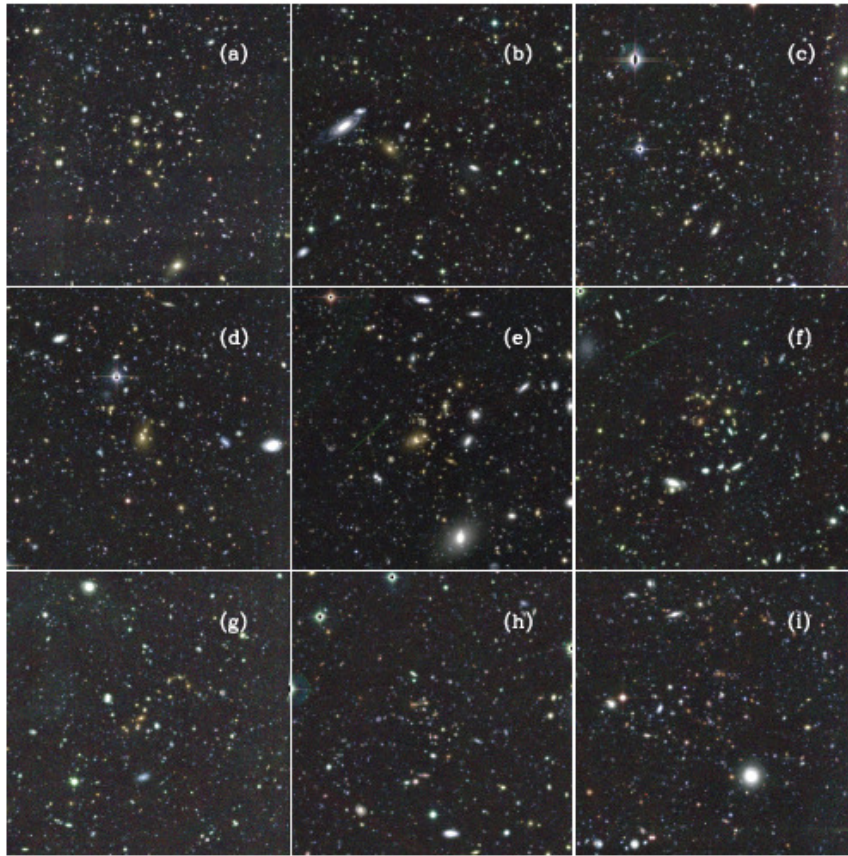


Fig. 3. Examples of background galaxy clusters identified in the NGVS using the 3D-Matched-Filter cluster finding algorithm of Milkeraitis et al. (2010) and the red sequence based algorithm of Mei et al. (2011). Each image measures 1.5 X 1.5 Mpc in size and the detections are in the redshift range $0.4 < z < 0.8$.

References

- Boselli, A., Boissier, S., Heinis, S., et al. 2011, A&A, 528, A107
 Coupon, J., Ilbert, O., Kilbinger, M., et al. 2009, A&A, 500, 981
 Ferrarese, L. et al. 2011, ApJS, submitted
 Ilbert, O., Arnouts, S., McCracken, H. J., et al. 2006, A&A, 457, 841
 Mei, S. et al. 2011, ApJ, submitted
 Milkeraitis, M., van Waerbeke, L., Heymans, C., et al. 2010, MNRAS, 406, 673

BULGE FORMATION PATTERNS IN AP³M-SPH SIMULATIONS: QUESTIONS TO BE ANSWERED BY FUTURE MISSIONS

A. Obreja¹, R. Domínguez-Tenreiro¹, M. Doménech-Moral², F. J. Martínez-Serrano² and A. Serna²

Abstract. The few observations of bulges available suggest a bi-modality in their properties, feature we have also found in high resolution hydrodynamical simulations in a cosmological context. The latter gives important information about bulge formation processes, facilitating the comparison with available observational data, as well as serving as guideline for future observational strategies. We conclude that in this particular field, there is much need for more in depth observations of large samples in order to distinguish among the variety of possible bulge formations paths.

Keywords: theory, galaxies, bulges, structure, kinematics, abundances

1 Introduction

It has been a long-standing matter of debate whether elliptical galaxies (Es from now on) and classical bulges of spirals (see bulge classification in Kormendy & Kennicutt 2004) share a similar formation history, since they have in common at least part of their observed properties. For example, both types of objects seem to share the same fundamental plane, their rotational support correlates with their shape in a similar manner, and both are α -element enhanced.

Concerning observational studies of spiral galaxies in particular, stellar population studies of external bulges, as well as of the Milky Way Bulge, showed that many classical bulges appear as an older and kinematically hotter population superimposed on a secondary, younger one with kinematics more similar to disks, in resemblance with the blue cores found in some Es. Also, the two populations have different metallicities and α -element enhancements, their mixing leading to a wide range of observed abundance gradients.

In the case of Es, analytical models as well as N-body simulations revealed that the halo mass assembly process follows a two-phase scenario, with a first violent one characterized by high mass aggregation rates and resulting from collapse-like and merger events, and a latter one with lower mass aggregation rates (Wechsler et al. 2002; Zhao et al. 2003). This scenario was confirmed later on in hydrodynamical simulations (Domínguez-Tenreiro et al. 2006, 2011; Oser et al. 2010).

In this frame, our objective is to test whether this two-phase formation scenario, proposed for Es, could also explain the up-to-now observations of classical bulges. Therefore, we want to know if it can account for the characteristics of bulge observations, like the duality in stellar populations (Ellis et al. 2001; Thomas & Davies 2006; Carollo et al. 2007), the variety of age and metallicities gradients (MacArthur et al. 2009; Sánchez-Blázquez et al. 2011), or some secular-like morphologies (Prugniel et al. 2001; Peletier et al. 2007).

2 Theoretical Approach to Bulge Formation

Bulge formation has been linked to apparently diverging processes like hierarchical structure formation and monolithic collapse, or to secular instabilities of the galactic disks. However, not one such process alone can explain the diversity of bulge shapes, sizes, abundances, kinematics and profiles observed, although these observations are still scarce. For this reason, hydrodynamical simulations in a cosmological context are a powerful

¹ Departamento de Física Teórica, Universidad Autónoma de Madrid, 28049 Cantoblanco, Madrid, Spain

² Departamento de Física y Arquitectura de Computadores, Universidad Miguel Hernández, 032202 Elche, Alicante, Spain

tool to disentangle the variety of possible paths leading to bulge formation. Progress in this topic requires increasing the observational data on bulges, not only in number but in spacial and spectral resolution as well.

The simulations we have analyzed have been performed using an OpenMP parallel version of the DEVA code (Serna et al. 2003), in which special emphasis was put on conservation laws. The chemical feedback and cooling methods have been described in Martínez-Serrano et al. (2008). In brief, the statistically implemented chemical evolution accounts for the full dependence of metal production on the detailed composition of the stellar particles, the metals diffusing among gas particles. A probabilistic approach for the delayed gas restitution from stars reduces the statistical noise, allowing the study of the chemical structure of small scale structures –like bulges– at an affordable computational cost.

Low-resolution simulations that consisted of different Monte Carlo realizations of the same cosmological model: a flat Λ CDM (with $\Omega_\Lambda = 0.723$, $\Omega_m = 0.277$, $\Omega_b = 0.04$, and $h = 0.7$) within a periodic box of 10 Mpc per side were performed (Doménech-Moral et al. 2011). Afterwards, massive gas-rich objects with a prominent gas disk at $z = 0$ were selected from high (HD) and low density (LD) regions, and resimulated at high resolution. The baryonic mass of these galaxies is of the order of $10^{10} M_\odot$, with a mass resolution of $\sim 10^5$ (baryons) and $10^6 M_\odot$ (DM), respectively. The minimum SPH smoothing length is $0.2 h^{-1}$ kpc, while the star formation (SF) follows a Kennicutt–Schmidt-like law with an efficiency ≤ 0.01 and a density threshold $\sim 10^{-25} \text{ g cm}^{-3}$.

Doménech-Moral et al. (2011) analyzed the disk galaxies simulated as described above from the point of view of their fine structure. They identified different components (thin and thick disc, halo, bulge) with properties in good consistency with observations, in particular bimodal bulge metallicities and $[\alpha/\text{Fe}]$ distributions, that they interpret as resulting from fast and slow modes of SF. In our work, we study in detail the intrinsic properties of these simulated (classical) bulges, specifically focusing on the mass-averaged three-dimensional sizes, shapes and kinematics, as well as their stellar ages and abundances, in connection with their formation history.

3 Bulge Formation Patterns

In order to see how bulges actually get assembled, we looked at the snapshots of the simulated objects between a redshift of ~ 9 to the present epoch. In this manner, we were able to identify the two mass aggregation modes which were also found in simulations of Es. Thus, we noticed a first fast collapse phase with high mass aggregation rates and violent episodes of star formation, and a secondary quieter mode in which gas is more continuously accreted on the central, already formed, old, stellar spheroid, being slowly transformed into stars. Given this behavior, we look for a criteria which we could use to separate the bulge stars formed in these two phases, and therefore constructed the star formation rate histories (SFRHs) and the mass assembly tracks (MATs) of the simulated objects. An example of such a plot for a particular object is given in the left panel of Fig. 2, where we can observe a correlation between the dark matter halo major mergers and the peaks in the star formation rate at the bulge scale, the latter appearing as a delayed consequence of the former. Also, the MAT jumps at the galaxy (dashed cyan lines) and virial radius (solid black line) scales are correlated with those at the bulge scale (solid red, green, blue, magenta and orange lines), therefore reinforcing the importance of cosmological gas inflow on bulge formation. Therefore, we separated the old from the young stellar bulge at $z = 0$ based on the point where the SFR tail begins, point also correlated with the beginning of the slowly increasing plateau in the MAT at the bulge scale, exemplified in the figure by the vertical dashed line.

We should mention that for objects in high density environments, the slow phase of bulge assembly can show imprints of major mergers with associated starbursts. In these cases, we considered the bulge stars forming during these SFR maxima as a distinct component, which we dubbed “intermediate”.

In order to exemplify the two modes of bulge formation, we constructed Fig. 1, in which we give a redshift sequence of a particular projection in position of an object from a low-density region, LD-5101A. Basically, the two left-most panels correspond to redshifts from the fast phase, while the two right-most ones to z s from the slow mode. In this case, the temporal separation between the old (red) and the young one (blue) stellar population is $z \sim 2.1$ and roughly corresponds to the center-right snapshot. The center-left panel also corresponds to an important point in the bulge evolution, at this redshift the SFR attaining its highest value. In this snapshot we see the old bulge condensed at the densest points of the flow converging regions, while the young bulge-to-be stars are still found as gaseous particles spanning a much wider volume. These different aggregation modes of the old and young bulge can be distinguished, however, from much earlier on (see left panel in the same figure).

Even before the beginning of the slow mode, the old bulge is in place as a spheroid, the gas which will come to form the young bulge stars appearing as a disk-like structure centered on this spheroid. This behavior can be seen in the center-right panel of Fig. 1. The $z = 1.14$ snapshot depicts a stage in which the young bulge is

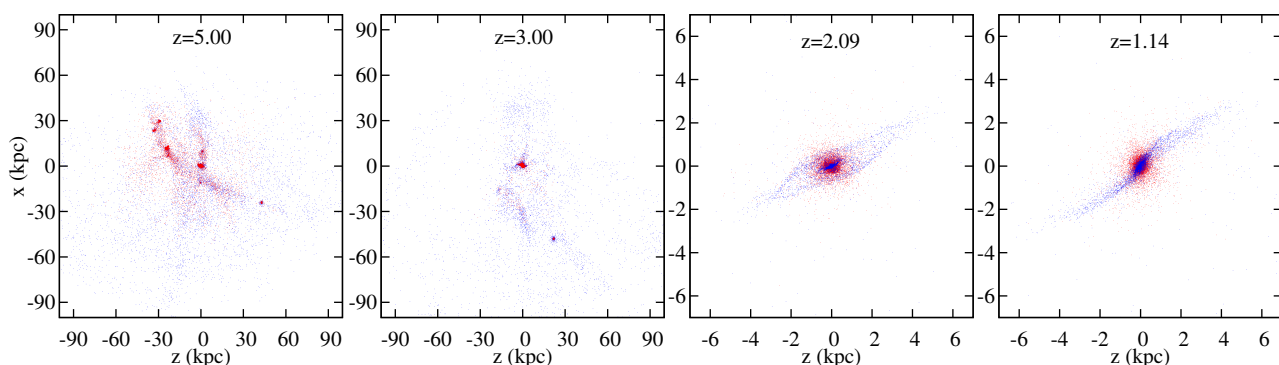


Fig. 1. Position projections of old (red) and young (blue) bulge-to-be stellar particles at $z = 0$ at four different redshifts for object LD-5101A.

still clearly structured as a disk, this particular redshift corresponding to the moment when approximately half of the young bulge is already found as stellar particles. By redshift 0, all these particles will be found as stars within a sphere of 1.85 kpc (for LD-5101A), the young bulge still “remembering” its distinct formation pattern.

These bulge assembly patterns resemble the two phases found by Domínguez-Tenreiro et al. (2006, 2011) for more massive spheroids, the main difference being the fact that, in the case of massive ellipticals almost all the gas is transformed into stars at the flow converging regions along the first phase, while no such exhaustive gas consumptions occurs for bulges.

4 Properties of Simulated Bulges

In the simulated bulges, the sizes, shapes, kinematics, stellar ages and metal contents of the stellar populations formed in these distinct phases can be well distinguished. In this respect, we found the youngest component to be more centrally concentrated, with disk-like morphology, more rotationally supported, with roughly solar metallicities and sub-solar α -element enhancements. The oldest population, in contrast, is more spheroid-like, has clearly sub-solar metallicities and larger α -element enhancements.

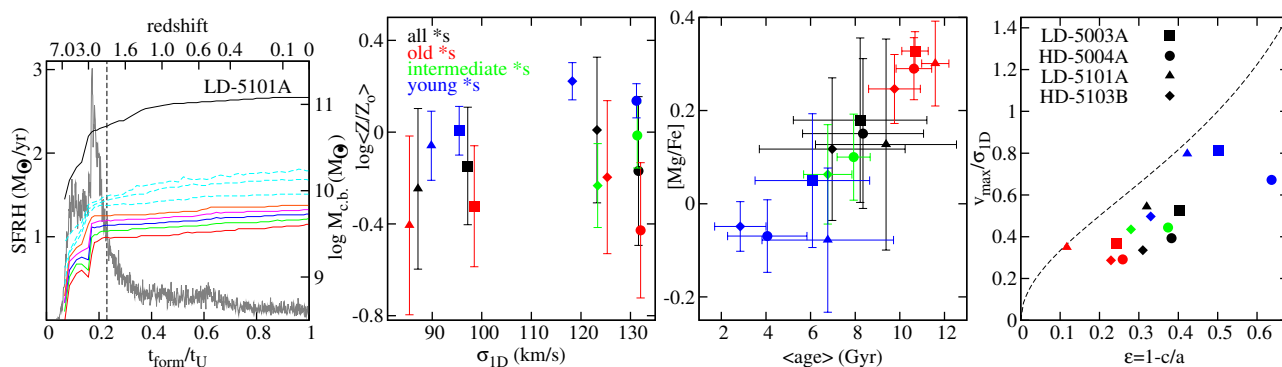


Fig. 2. **Left:** SFRH of bulge HD-5101A (grey line) superimposed on the temporal evolution of cold gas plus stellar mass inside fix radii (solid black for total mass inside the virial radius, dashed cyan for radii exceeding r_{bulge} , and solid red, green, blue, magenta and orange for radii roughly within r_{bulge} with the radius increasing from bottom to top); the vertical black dashed line marks the separation between the old and the young bulges. **Center-left:** average metallicity vs. 1D velocity dispersion. **Center-right:** $[Mg/Fe]$ vs. average age. **Right:** Rotational support vs. shape parameter.

These findings are exemplified in Fig. 2, where we give some of the global properties of both bulges as well as their distinct stellar components at redshift 0. The center-left panel for e.g. shows the average metallicity versus the 1D velocity dispersion, in which a clear trend can be noted, Z increasing with σ_{1D} (more rapidly for the younger components), as well as with the age.

Additionally, the center-right panel gives the $[Mg/Fe]$ as a tracer of α -enhancement versus average stellar

age, in which is obvious that the α -enhancement is an age effect, the youngest a population the lower its average [Mg/Fe]. The right-most panel comes to sustain our argument that the younger bulge is more rotationally supported and more oblate than the old one. The shape parameter, ε in this case, was computed from the principal axis lengths of the inertia tensor. In this last panel, we can see that all four bulges, as well as their different components appear below the curve of oblate spheroids flattened only by rotation (dashed black curve), the shape parameter together with the amount of rotational support increasing with the average stellar age.

These global properties predicted by simulations can be used to design effective observational strategies for bulges, in order to take advantage of the ever more powerful instruments both on Earth as well as in space, easing in this manner the cumbersome task of comparing observations with theoretical predictions.

5 Conclusions

We find our sample bulges to have a mass-dominant old stellar population, formed at high z in a fast collapse-like event, and one or two younger populations formed later on, during a second phase generally characterized by lower mass assembly and SF rates. The bulge stars resulting from the fast mode form an object with properties similar to low mass spheroids, while those which are a consequence of the later slow mode show global characteristics more typical of disks. The variety of processes which can act during the second phase (minor and major mergers, disk secular instabilities, satellite incorporation) together with continuous gas accretion result in objects with different characteristics, that fit well with the important dispersion in bulge properties observationally found. We also noticed correlations between the evolution of the DM halo and the SFR at the bulge scale, reinforcing the importance of cosmologically driven processes in bulge formation. These results are not only important for testing the physical conditions necessary for bulges formation, but also as guidelines for observational strategy designs, field in which there is room for ample improvements.

From an observational perspective although much progress has been made with surveys like SAURON, there still remain some important questions regarding bulge formation and evolution mechanisms. Some of them are related to the role of major mergers in galaxy evolution or to the process of satellite cannibalism. Equally important are also the bars, for e.g. their frequency with redshift and their life cycle. In this latter issue, a better understanding of the intrinsic properties of pseudobulges would provide much insight into the bulge classification schemes. On the other hand, although we have today the hierarchical structure formation paradigm, the details of cold gas inflows, an important mechanism in bulge formation, are not yet fully understood. Least but not last, bulges are thought to evolve in some sort of correlation with the massive black holes they host, problem which is still far from being successfully tackled.

Solving these problems requires high resolution spatial and spectroscopic surveys, extended in redshift as much as possible. In this respect, the HST's survey mission CANDELS, the Wide-field Infrared Survey Explorer (WISE), or the Next Generation Virgo cluster Survey (NGVS) at CFHT will add important observational data to that provided up to now by telescopes like Spitzer, Hershel, WHT or Gemini-North.

References

- Carollo, C. M., Scarlata, C., Stiavelli, M., Wyse, R. F. G., & Mayer, L. 2007, *ApJ*, 658, 960
 Doménech-Moral, M., Martínez-Serrano, F., Domínguez-Tenreiro, R., & Serna, A. 2011, *MNRAS*, submitted
 Domínguez-Tenreiro, R., Oñorbe, J., Martínez-Serrano, F., & Serna, A. 2011, *MNRAS*, 413, 3022
 Domínguez-Tenreiro, R., Oñorbe, J., Sáiz, A., Artal, H., & Serna, A. 2006, *ApJ*, 636, 77
 Ellis, R. S., Abraham, R. G., & Dickinson, M. 2001, *ApJ*, 551, 111
 Kormendy, J. & Kennicutt, Jr., R. C. 2004, *ARA&A*, 42, 603
 MacArthur, L. A., González, J. J., & Courteau, S. 2009, *MNRAS*, 395, 28
 Martínez-Serrano, F. J., Serna, A., Domínguez-Tenreiro, R., & Mollá, M. 2008, *MNRAS*, 388, 39
 Oser, L., Ostriker, J. P., Naab, T., Johansson, P. H., & Burkert, A. 2010, *ApJ*, 725, 2312
 Peletier, R. F., Falcón-Barroso, J., Bacon, R., et al. 2007, *MNRAS*, 379, 445
 Prugniel, P., Maubon, G., & Simien, F. 2001, *A&A*, 366, 68
 Sánchez-Blázquez, P., Ocvirk, P., Gibson, B. K., Pérez, I., & Peletier, R. F. 2011, *MNRAS*, 415, 709
 Serna, A., Domínguez-Tenreiro, R., & Sáiz, A. 2003, *ApJ*, 597, 878
 Thomas, D. & Davies, R. L. 2006, *MNRAS*, 366, 510
 Wechsler, R. H., Bullock, J. S., Primack, J. R., Kravtsov, A. V., & Dekel, A. 2002, *ApJ*, 568, 52
 Zhao, D. H., Mo, H. J., Jing, Y. P., & Börner, G. 2003, *MNRAS*, 339, 12

EXTRAGALACTIC SCIENCE WITH EMIR-GTC

R. Pelló¹, F. Garzón², M. Balcells², F. Boone¹, N. Cardiel³, J. G. Cuby⁴, J. Gallego³, R. Guzmán⁵, M. Hayes¹, P. Hudelot⁶, J.-P. Kneib⁴, N. Laporte¹, J. F. Le Borgne¹, Y. Mellier⁶, M. Prieto², J. Richard⁷, D. Schaerer⁸, L. Tresse⁴, the GOYA/EMIR and REGALDIS collaborations

Abstract. EMIR is a wide-field, near-IR spectrograph currently under development for the Nasmyth focus of the Spanish 10.4m GTC at Canary Islands. EMIR will provide imaging and multi-slit spectroscopy in the $\sim 1\text{-}2.5$ micron domain at a resolution of $R \sim 5000\text{-}4000$. This paper reviews the status of the project, including instrumental developments and main science drivers, focusing the GOYA Survey, a scientific program to be developed mainly using the guaranteed time of the international consortium building EMIR. The GOYA project addresses the formation and evolution of galaxies, in particular the structure, dynamics and integrated stellar populations of galaxies at high redshift. One of the main goals of the GOYA survey is the identification and study of $z \geq 7$ sources, both in lensing clusters and in the field. The aim is to build up a statistically significant sample of galaxies with secure redshifts, and to study their physical properties using their broad-band spectral energy distribution in one hand, and their emission line properties on the other hand. The first results obtained from our photometric surveys in lensing fields and in the blank field CFHT WIRCAM Ultra Deep Survey (WUDS), which are intended to provide a robust selection of targets for GOYA, are also presented and briefly discussed.

Keywords: surveys, galaxies: high-redshift, gravitational lensing: strong, cosmology: dark ages, reionization, first stars

1 Introduction

EMIR is a wide-field, near-IR spectrograph currently under development for the Nasmyth focus of the Spanish GTC at Canary Islands*. EMIR is being built by a consortium led by the IAC, including Spanish and French institutions (Garzón et al. 2006), mainly funded by GRANTECAN and the *Plan Nacional de Astronomía y Astrofísica*. It is one of the first fully cryogenic multi-object spectrographs to be operated on a 10m-class telescope, with the proper resolution to achieve an efficient OH-line suppression. The design of EMIR was determined by its main scientific drivers around the study of distant galaxies, in particular the GOYA project (see e.g. Guzmán 2003; Balcells 2003).

This paper presents an overview of the GOYA Survey with EMIR, a scientific program to be carried out mainly using the guaranteed time of the international consortium building EMIR. The observing strategy for target selection will be also presented, in particular the characteristics of our photometric CFHT WIRCAM Ultra Deep Survey (WUDS), which is intended to provide a robust selection of targets for GOYA. We focus on

¹ Université de Toulouse; UPS-OMP; CNRS; IRAP; 14, avenue Edouard Belin, 31400 Toulouse, France

² Instituto de Astrofísica de Canarias, c/Vía Lactea s/n, 38205 La Laguna, Tenerife, Spain

³ Departamento de Astrofísica y CC de la Atmósfera, Universidad Complutense de Madrid, Av Complutense s/n, 28040 Madrid, Spain

⁴ Laboratoire d'Astrophysique de Marseille, OAMP, Université Aix-Marseille & CNRS, 38 rue Frédéric Joliot Curie, 13388 Marseille Cedex 13, France

⁵ Department of astronomy, University of Florida, 211 Bryant Space Science Center, Gainesville, FL 32611-2055, USA

⁶ Institut d'Astrophysique de Paris, UMR7095 CNRS, Université Pierre & Marie Curie, 98 bis boulevard Arago, 75014 Paris, France

⁷ Centre de Recherche Astrophysique de Lyon, University of Lyon, 9 Avenue Charles André, 69230 Saint Genis Laval, France

⁸ Geneva Observatory, 51, Ch. des Maillettes, 1290 Versoix, Switzerland

*<http://www.gtc.iac.es/en/pages/gtc.php?lang=EN>

Table 1. Characteristics of EMIR

<u>Spectral Range</u>	0.9-2.5 microns	<u>MOS Mode</u>		<u>Imaging</u>	
<u>Spectral Resolution</u>	5000, 4250, 4000 (JHK)	FOV	6×4 arcmin ²	FOV	6×6 arcmin ²
<u>Spectral Coverage</u>	1 spectral window/exp.	<u>Sensitivity</u>	continuum	<u>Sensitivity</u>	
<u>Detector</u>	HAWAII2 2048 ²	$\overline{K}_{AB} \sim 22$	in 2h S/N~5	$\overline{K}_{AB} \sim 24.7$	1h, S/N~5
<u>Image Scale</u>	0.2 arcsec/pixel		emission lines	0.6 arcsec	aperture
<u>Image Quality</u>	$\theta_{80} < 0.3$ arcsec	1.4×10^{-18}	erg/s/cm ² S/N~6		

a particularly important science case for GOYA/EMIR, aimed at constraining the abundance and properties of the first star-forming galaxies in the Universe. WUDS and the complementary photometric survey in lensing clusters are specifically tailored to identify the brightest galaxies at ≥ 7 , accessible for observations with EMIR, and therefore to set strong constraints on the cosmic Star Formation Rate (SFR) and the bright end of the Luminosity Function (LF), taking advantage from our privileged access to EMIR/GTC for a precise redshift determination and subsequent emission-line studies.

In Sect. 2 we summarize the present state of the art regarding the development of EMIR for the GTC. The GOYA Survey is introduced in Sect. 3. Sect. 4 describes the particular science case around the first star-forming galaxies in the Universe. We present in this section the REGALDIS Project, in preparation for the GOYA Survey, as well as the technical aspects regarding the selection of high- z galaxies, and the current results achieved in this framework, both in lensing fields and in the blank field of WUDS. Conclusions and perspectives are given in Sect. 5.

2 EMIR at the GTC

The Gran Telescopio Canarias (known as GTC) is a single-dish 10.4m telescope on the island of La Palma (Spain). It started its scientific operations in March 2009 (first light in July 2007). Only one instrument, OSIRIS, is currently available, and a second one, CanariCam, is presently being commissioned. The next and last first-generation instrument will be EMIR (2012). Observing time with GTC is available to astronomers from the partner institutions in Spain, México and U. of Florida, as well as to european astronomers as part of the ESO-GTC collaboration, in addition to International Time Programs.

EMIR will provide imaging and multi-slit spectroscopy in the ~ 1 -2.5 micron domain for up to 50 targets using a cryogenic multi-slit mask, at a resolution of $R \sim 5000$ -4000. Table 1 summarizes the main characteristics of this instrument, and Fig. 1 presents the general layout, together with several subsystems shown in thumbnails. Among the key modules of EMIR are the cryogenic configurable slit unit, and the detector translation unit (respectively CSU and DTU in Fig. 1). For these new mechanical concepts, extremely long phases of prototyping, testing and qualification were required before the final acceptance. A particularly demanding development in the optical design corresponds to the “pseudo-grisms”, i.e. large grisms with a high refractive index which are needed to meet the specifications. All these critical elements were developed in close collaboration with industrial partners. More details can be found in Garzón et al. (2006) and Garzón et al. (2007).

The development plans and schedule till the first light of EMIR can be summarized as follows. During 2011, the pseudo-grisms developed at LAM (Marseille) will be integrated into the EMIR grism unit (GU in Fig. 1) and tested under cryogenic conditions. Also the development of the EMIR cryostat and auxiliary elements such as EIT (EMIR Integration Tool), ETT (EMIR Transport Tool),..., is expected to be completed by the end of September 2011. The final integration phase of EMIR subsystems and verification phase should start in October 2011, for a period of about one year. The EMIR commissioning phase at GTC is expected to start during the last quarter of 2012, with a first scientific light in mid-2013.

3 The GOYA Survey

The Galaxy Origins and Young Assembly (GOYA) Survey[†] is a scientific program to be developed mainly using the guaranteed time of the international consortium building EMIR. The GOYA project addresses the formation

[†]<http://www.astro.ufl.edu/GOYA/home.html>

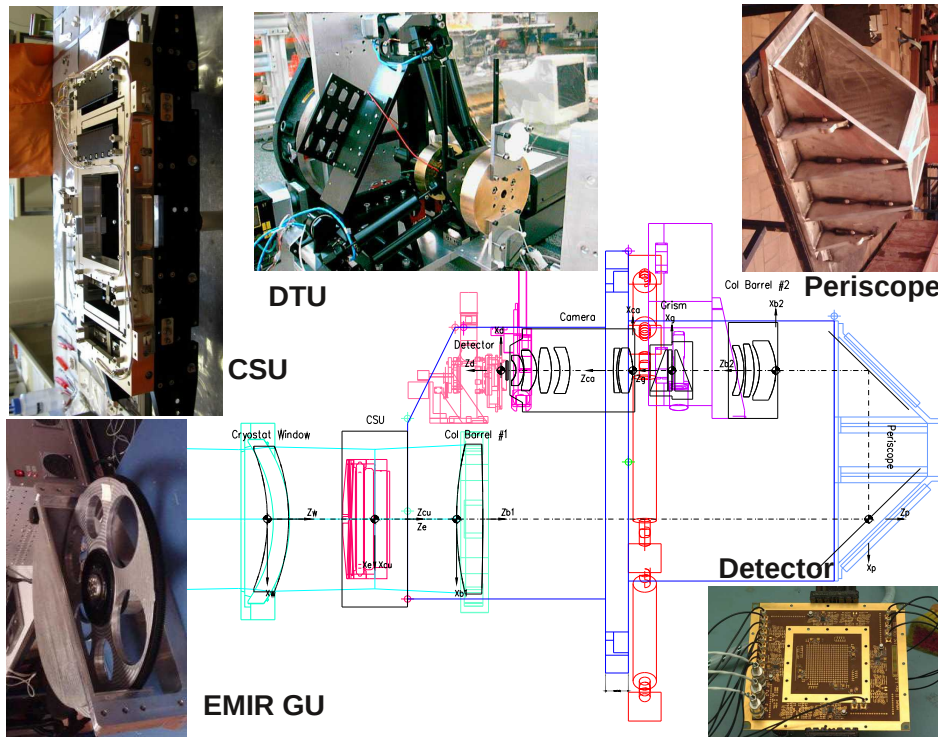


Fig. 1. EMIR layout. Several subsystems are shown in thumbnails.

and evolution of galaxies, in particular the structure, dynamics and integrated stellar populations of galaxies at high redshift. Indeed, near-IR spectroscopy is needed to target the relevant spectral features providing physical diagnostics (SFR, reddening, metal abundances, AGN contribution,...) all the way from the local universe to the highest redshifts. The main goals of the GOYA Survey can be summarized as follows:

- The characterization of the early-type population of galaxies at $1 \leq z \leq 2$. This epoch is particularly important for the formation of the red sequence. Ages and metallicities will be derived using different spectral indicators (e.g. Δ_{4000} , H_{β} , $Mg2$, Fe lines...), as well as kinematical properties and virial masses. Scaling laws will be obtained providing the empirical relations between structural and kinematical properties and stellar population parameters (see also Balcells 2007; Domínguez-Palmero et al. 2008).
- The characterization of the star-forming galaxies at the epoch of maximum activity ($1 \leq z \leq 5$), using emission-line indicators to trace the evolution of different properties: SFR densities (based on H_{α} , [OII], [OIII],...), metallicity, extinction (H_{α}/H_{β}), kinematics and virial masses (velocity widths). The efficiency of EMIR and the typical density of sources should allow us to address the clustering properties of these populations. (see also Gallego 2003).
- The parameterization of the growth of SMBH in AGNs at the epoch of maximum QSO activity ($1 \leq z \leq 4$). This includes the determination of SMBH masses.
- The identification and study of the first galaxies in the universe ($z \geq 7$; see Sect. 4).

In preparation for the exploitation of EMIR, the GOYA team carried out different wide-field photometric surveys in the optical and near-IR bands, mainly using the WHT (see e.g. Vallbe I Mumbrú et al. 2007; Cristóbal-Hornillos et al. 2003), including our CFHT WIRCAM Ultra Deep Survey (WUDS; see Sect. 4.1). These surveys are needed for an appropriate target selection, because most science cases of GOYA require a stellar-mass preselection and a redshift determination before using EMIR (either photometric or spectroscopic redshift). Needless to say that GOYA observations will be optimized to fulfill different science cases in a single shot/mask. This requires a careful sample selection and mask design.

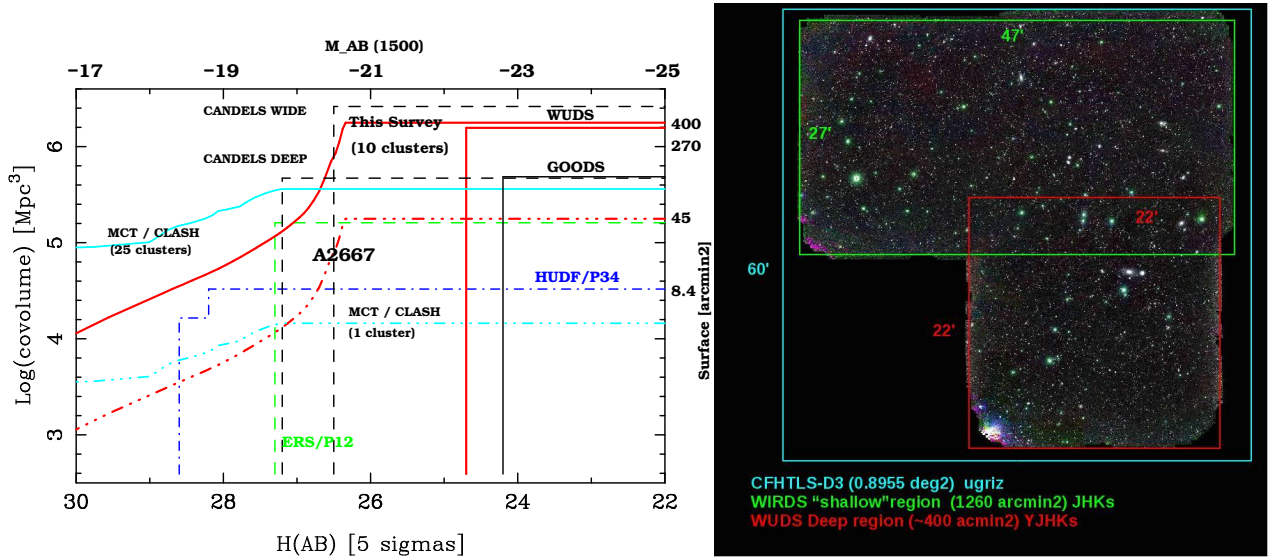


Fig. 2. Left: Characteristics of the $z \geq 7$ survey (thick red lines) compared to other surveys. The effective (unlensed) area and the $z \sim 7-9$ covolume sampled by each survey is given as a function of effective H magnitude limit (5σ) and corresponding $M_{AB}(1500\text{\AA})$. The different surveys are: our CFHT/WUDS survey (solid red line); the survey on A2667 (red dash-dotted line); the HST/MCT CLASH Survey (cyan, 1 cluster like A2667 and the whole survey); and the compilation of deep imaging *JHK* data available for dropout searches (from Wilkins et al. 2010): GOODS field (solid thin black line), ERS/P12 (dashed green line), and HUDF/P34 fields (dot-dashed blue line). **Right:** Layout of the WUDS Survey showing the regions covered by the deep and wide regimes as compared to the CFHTLS-D3 field (Groth Strip).

4 An important Science Case for EMIR/GTC: Constraining the abundance and properties of the first star-forming galaxies

One of the main goals of the GOYA survey is the identification and study of $z \geq 7$ sources. This is an important challenge for modern cosmology, as star-forming sources at $z \sim 7-12$ could have been responsible for a significant part of the cosmic reionization. Detailed studies of these “primordial” systems require the use of new ground-based and space facilities becoming available during the last few years (e.g. VLT/Hawk-I, HST/WFC3, Herschel,...), including ALMA and EMIR. The REGALDIS project[‡] was born in 2009 precisely to take advantage from our privileged access to these key facilities (through granted -open or guaranteed- time) to build up a statistically significant sample of galaxies with secure redshifts, together with an additional sample of candidates based on photometric redshifts and wide multi-wavelength coverage. The aim is to study the physical properties of these galaxies using their broad-band spectral energy distribution in one hand, and their emission line properties on the other hand.

The abundance and properties of $z \sim 7-12$ galaxies have been discussed during the last few years in a context of international competition, based on deep photometric observations in the near-IR, both in blank and lensing fields (e.g. Bouwens et al. 2008; Richard et al. 2008; Bouwens et al. 2011, and the references therein). There is increasing evidence for a strong evolution in the UV LF between $z \sim 7-10$ and $z \sim 3-4$, the SFR density being smaller at very high- z up to the limits of the present surveys, in particular towards the bright end of the LF, in such a way that cosmic reionization should be dominated by low-luminosity galaxies. The extent of this effect is still a matter of debate. Together with field-to-field variance, there are two main issues. The first one is the limited surface covered by current “deep” surveys, both space or ground-based (i.e. lensing or in blank fields), compared to the needs in order to derive statistically significant results. Another issue is the lack of secure spectroscopic confirmation for all present $z \geq 7$ samples, and this is where an efficient facility such as EMIR is needed.

[‡]<http://regaldis.ast.obs-mip.fr/>

4.1 Photometric selection of high- z galaxies

The selection of high- z galaxies is based on the Lyman-break or dropout technique. Different redshift intervals within $6 \leq z \leq 12$ can be defined using an appropriate set of near-IR filters in combination with optical data (see e.g. Laporte et al. 2011). An homogeneous and deep coverage of the near-IR domain is crucial to achieve a reliable identification of high- z photometric candidates.

As shown by Maizy et al. (2010), the presence of a strong lensing cluster along the line-of-sight strongly improves the global efficiency of the survey with respect to blank fields, in particular to explore the $z \sim 6 - 12$ domain, and for relatively “shallow” surveys (i.e., the typical near-IR ground-based surveys). However, although lensing clusters are more efficient to conduct detailed (spectroscopic) studies in this redshift domain and to explore the faint-end of the LF, observations of wide blank fields are complementary to set reliable constraints on the brightest end of the UV LF, given the strong field to field variance in number counts in this regime. Our project combines the two approaches. Observations of lensing clusters with FORS2 + Hawk-I at VLT, and new (ACS and WFC3) HST images (cycle 17, PI J.P. Kneib) are being gathered in the framework of REGALDIS, together with Spitzer/IRAC+MIPS imaging data and Herschel data from the “Herschel Lensing Survey” (HLS Egami et al. 2010), available for all our target clusters, and ongoing APEX/LABOCA observations (see Boone et al. 2011).

The blank-field counterpart is our WIRCAM Ultra Deep Survey (WUDS) at CFHT, which is also intended to provide a robust selection of targets for other science cases of GOYA. The survey was specifically tailored to set strong constraints on the cosmic SFR and the bright end of the LF. WUDS has been carried out on the CFHTLS-D3 field (Groth Strip), in 4 near-IR bands (YJHK_s), the same bands used in lensing studies. The right panel in Fig. 2 provides the layout of the survey, showing the regions covered by the deep (WUDS) and wide (WIRDS) regimes. Data processing was performed at Terapix/IAP and CFHT. The final version of the stacked images was made available to the collaboration end 2010, and a public release of these data is foreseen by the end 2011. The typical depth for the ~ 400 arcmin² “deep” area reaches between ~ 26.8 in Y and J, and ~ 26 in H and K_s (AB, 3σ in $1''.3$ aperture), for a completeness level of $\sim 80\%$ at Y ~ 26 and H and K_s ~ 25.2 , and excellent seeing conditions (ranging between $0''.55$ and $0''.66$). The corresponding depth of the CFHTLS-D3 images in this region ranges between 28.6 and 29 in *ugr*, 28.2 in *i* and 27.1 in *z* (same S/N ratio and aperture). The WUDS survey will be presented in a forthcoming paper.

Fig. 2 displays a comparison between our survey (lensing and WUDS fields) and other surveys in the $z \sim 7 - 9$ redshift domain. In the case of the CLASH Survey, we assumed that all clusters are as efficient as A2667, which is a rather optimistic assumption. The present survey will cover the same volume as all the presently available deep HST (ACS+WFC3) fields, but it is a factor of ~ 7 larger at $M_{AB}(1500\text{\AA}) \leq -20.3$ (i.e. $\gtrsim L^*$ at $z \sim 7 - 9$). As compared to the large ongoing HST “Multi-cycle Treasury” (MCT) programs, and in particular the CLASH survey with ACS and WFC3, our survey is quite complementary. It will cover an **effective** volume which is ~ 5 times larger at $z \sim 7 - 9$ in the intermediate-luminosity domain ($M_{AB} \sim -20.5$ to -23). It is therefore better-suited to trace the most sensitive region of the LF, and also for the selection of spectroscopic targets. Only the CANDELS Survey with HST is expected to provide a similar and larger area. However, all HST surveys lack deep data in the K-band, which is particularly useful to identify high- z sources and to determine the slope of the UV continuum.

4.2 First results in lensing & WUDS fields

We have obtained a complete dataset at ~ 0.8 - 2.5 microns with ESO/VLT HAWK-I and FORS2 on the lensing cluster A2667, as part of the REGALDIS project (see Laporte et al. 2011). The selection function is based on deep *I*, *z*, *Y*, *J*, *H* and *Ks*-band images (AB ~ 26 - 27 , 3σ), including IRAC data between 3.6 and $8 \mu\text{m}$, and MIPS $24 \mu\text{m}$ when available. 13 candidates are selected within the $\sim 7' \times 7'$ field of view of HAWK-I (~ 33 arcmin² of effective area once corrected for contamination and lensing dilution at $z \sim 7 - 10$), namely 1 *J*-drop, 8 *Y*-drops and 4 *z*-drops. Fig. 3 displays the brightest 10 optical-dropouts reported by (Laporte et al. 2011), with $H_{AB} = 23.4$ to 25.2 and magnification factors between 1.1 and 1.4. Best-fit photometric redshifts are obtained at high- z for all these candidates using a variety of template SEDs ($z \sim 7.5$ to 9), with a less significant solution at $z \sim 1.7$ to 2.8. Several of these sources seem too bright to be at $z \geq 7.5$, suggesting some contamination by mid- z interlopers which must be also present in other current surveys. Indeed, two candidates from Laporte et al. (2011) have been recently detected in the Herschel and LABOCA/APEX IR bands, making the high- z identification unlikely (Boone et al. 2011).

Regarding the contamination by mid- z interlopers, it could be between ~ 50 - 75% depending on the redshift

bin, based on the comparison with the WUDS results on a larger field of view. Indeed, preliminary results using the same color selection (but the 5 optical bands of the CFHTLS-D3 instead of 2 in A2667) indicate 3 J -drop (+1 dubious), 13 Y -drops and 12 z -drops (+3 dubious) within the deep WUDS region. This means a relatively low density of potential targets for this programme (typically ~ 0.1 target/arcmin, i.e. ~ 2 -3 targets within the EMIR FOV). The number of potential targets in a lensing field is expected to be at least a factor of 2 (and up to a factor of 5) larger within the EMIR FOV, depending on the depth of the selection window.

The first results obtained on the LF of $z \gtrsim 7$ galaxies based on A2667 observations are consistent with a sharp decrease in the number of bright galaxies beyond $z \sim 8$, in agreement with other previous findings (e.g. Bouwens et al. 2011, see also Laporte et al., this conference).

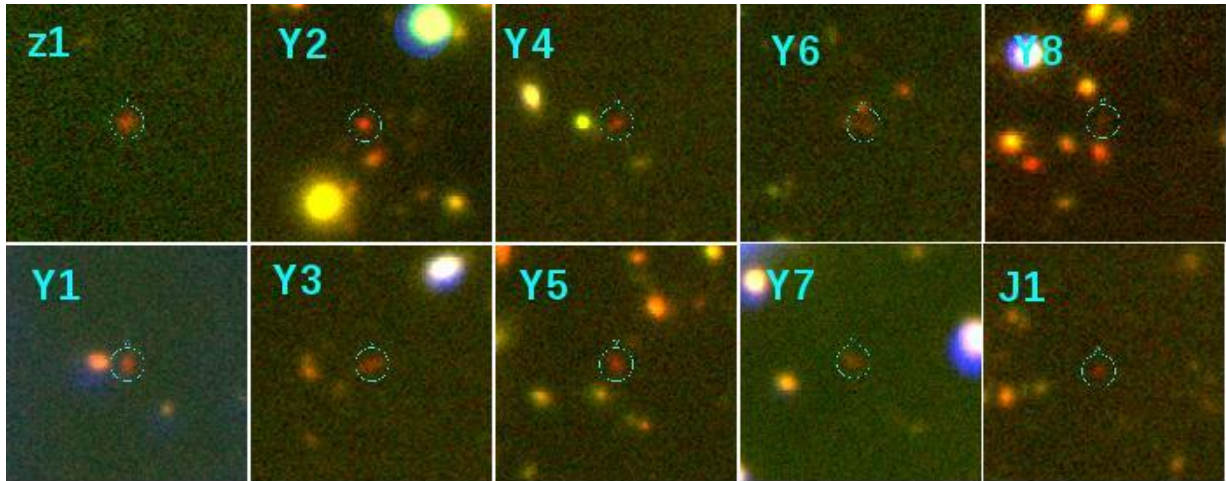


Fig. 3. Color thumbnails showing the 10 brightest optical-dropouts found in the lensing cluster A2667 (see Laporte et al. 2011, for more details).

5 Conclusions and Perspectives

Due to a lack of efficient near-IR spectrographs, very few galaxies at $z \gtrsim 7$ have been spectroscopically confirmed till now. The identification and study of the first galaxies require an extensive multi-wavelength coverage of their SED. Detailed studies of spectral signatures for $z \gtrsim 7$ galaxies, including a precise redshift determination, need near-IR observations at wavelengths beyond 1 micron. Spectroscopy is mandatory for (at least) a robust/reference sample of photometric candidates. It is also needed to understand the nature of (extreme) mid- z interlopers presently found in deep surveys. The arrival of EMIR/GTC, and the start of the spectroscopic part of the GOYA Survey in 2013, is expected to introduce a substantial progress in this area. The spectroscopic follow up of WUDS candidates in particular is already planned with EMIR/GTC.

Our ongoing photometric survey for the selection of $z \geq 7$ candidates, combining both lensing and blank fields, is quite complementary with respect to large HST “Multi-cycle Treasury” (MCT) programs, in particular the CLASH survey. It is therefore better-suited to trace the $L \gtrsim L^*$ region of the LF, and also for the selection of spectroscopic targets for EMIR and ALMA.

Part of this work was supported by the French CNRS, the French Programme National de Cosmologie et Galaxies (PNCG), as well as by the Swiss National Science Foundation. We acknowledge support from the Spanish Programa Nacional de Astronomía y Astrofísica under grant AYA 2006-02358. Partially funded by the Spanish MEC under the Consolider-Ingenio 2010 Program grant CSD2006-00070: First Science with the GTC (<http://www.iac.es/consolider-ingenio-gtc/>). This work received support from Agence Nationale de la recherche bearing the reference ANR-09-BLAN-0234. This paper is based on observations collected at the European Space Observatory, Chile (71.A-0428, 082.A-0163). Based on observations obtained with WIRCam, a joint project of CFHT, Taiwan, Korea, Canada, France, and the Canada-France-Hawaii Telescope (CFHT) which is operated by the National Research Council (NRC) of Canada, the Institut National des Sciences de l’Univers of the Centre National de la Recherche Scientifique of France, and the University of Hawaii.

References

- Balcells, M. 2003, in *Revista Mexicana de Astronomía y Astrofísica Conference Series Vol. 16*, ed. J. M. Rodríguez Espinosa, F. Garzon Lopez, & V. Melo Martin, p. 69
- Balcells, M. 2007, in *Revista Mexicana de Astronomía y Astrofísica Conference Series Vol. 29*, ed. R. Guzmán, p. 126
- Boone, F., Schaerer, D., Pelló, R., et al. 2011, ArXiv e-prints astro-ph/1108.2406
- Bouwens, R. J., Illingworth, G. D., Franx, M., & Ford, H. 2008, *ApJ*, 686, 230
- Bouwens, R. J., Illingworth, G. D., Labbe, I., et al. 2011, *Nature*, 469, 504
- Cristóbal-Hornillos, D., Balcells, M., Prieto, M., et al. 2003, *ApJ*, 595, 71
- Domínguez-Palmero, L., Balcells, M., Erwin, P., et al. 2008, *A&A*, 488, 1167
- Egami, E., Rex, M., Rawle, T. D., et al. 2010, *A&A*, 518, L12
- Gallego, J. 2003, in *Revista Mexicana de Astronomía y Astrofísica Conference Series Vol. 16*, ed. J. M. Rodríguez Espinosa, F. Garzon Lopez, & V. Melo Martin, p. 221
- Garzón, F., Abreu, D., Barrera, S., et al. 2006, in *Society of Photo-Optical Instrumentation Engineers (SPIE) Conference Series, Vol. 6269*, Society of Photo-Optical Instrumentation Engineers (SPIE) Conference Series
- Garzón, F., Abreu, D., Barrera, S., et al. 2007, in *Revista Mexicana de Astronomía y Astrofísica Conference Series Vol. 29*, ed. R. Guzmán, p. 12
- Guzmán, R. 2003, in *Revista Mexicana de Astronomía y Astrofísica Conference Series Vol. 16*, ed. J. M. Rodríguez Espinosa, F. Garzon Lopez, & V. Melo Martin, p. 209–212
- Laporte, N., Pelló, R., Schaerer, D., et al. 2011, *A&A*, 531, A74
- Maizy, A., Richard, J., de Leo, M. A., Pelló, R., & Kneib, J. P. 2010, *A&A*, 509, A105
- Richard, J., Stark, D. P., Ellis, R. S., et al. 2008, *ApJ*, 685, 705
- Vallbe I Mumburú, M., Balcells, M., & Gallego, J. 2007, in *Astronomical Society of the Pacific Conference Series, Vol. 379*, *Cosmic Frontiers*, ed. N. Metcalfe & T. Shanks, p. 352
- Wilkins, S. M., Bunker, A. J., Ellis, R. S., et al. 2010, *MNRAS*, 403, 938

GALAXIES AND COSMOLOGY WITH ALMA

P. Planesas¹

Abstract. Intensive work is being carried out at the Joint ALMA Observatory in order to bring four bands of a 16-antenna mm/submm interferometer into scientific operation. Specific tests of the advertised capabilities for Early Science are being carried out as well as further tests in order to bring ALMA into full operation as planned. Some of the measurements were taken towards extragalactic objects. In fact, the high sensitivity, high angular resolution, high image fidelity, and high mapping speed, together with a large frequency coverage, will make ALMA the right instrument for high redshift studies, and detailed dynamical and chemical studies of nearby galaxies.

Keywords: galaxies, high-redshift, cosmology, observatories, ALMA

1 Introduction

The Atacama Large Millimeter/submillimeter Array (ALMA), the larger astronomical project in existence (cf. <http://www.almaobservatory.org>), is planning to start the Early Science readiness Cycle 0 on fall 2011 (cf. <http://www.almascience.org>). The capabilities of the instrument will be limited (to four frequency bands and to 16 antennas, giving about one third of the full collecting area of the final 50 antenna main array) and observations will be conducted on a best effort basis. Nevertheless, almost one thousand proposals were submitted by the end on June by astronomers of all over the world, showing the large interest of the community in using this instrument, specially for extragalactic and cosmology research. In fact, if the 2009 ALMA Design Reference Science Plan (hereafter DRSP, <http://www.eso.org/sci/facilities/alma/science/drsp/>) and the 600 notices of intent received by end of April 2011 were good indicators, extragalactic and cosmology will account for about half the number of proposals*, a share that could well be maintained when ALMA delivers its full performance in a couple of years.

2 The Joint ALMA Observatory science teams

The construction and commissioning of an observatory is not only a task of constructors and technical staff, but of astronomers as well. The effort of assembling and characterizing the individual radiotelescopes started by the beginning of 2008, carried out by the Assembly, Integration and Verification (AIV) team, that included a handful of astronomers. A larger team is currently carrying out the Commissioning and Science Verification (CSV) tasks in order to have the interferometer ready for Early Science and also testing additional capabilities planned for the final instrument. The Science Operations team, involved in both the AIV and CSV tasks, is getting the knowledge to perform all sorts of observations and analysis to deliver the data to the final users, via the ALMA Regional Centers (ARCs). Astronomers in the ARCs actively collaborate in the CSV tasks either remotely or by spending short periods in Chile. The current JAO staff in Chile includes around 35 astronomers.

By the time of the Paris meeting, the AIV team had already fully checked (control, tracking, pointing, switching, on-the-fly mapping, tuning, spectral checks, interferometry) and optimized (surface, focus) 15 antennas to within science specifications. They had subsequently been delivered to the ALMA Operations Site (AOS) at 5000 m above sea level and integrated in the interferometer being tested by the CSV team. Tests at baselines up to 600 m long were carried out successfully. Measurements of continuum and line sensitivity,

¹ Observatorio Astronómico Nacional (IGN), Alfonso XII, 3, 28014 Madrid, Spain

*It turned out to be: Cosmology and the high redshift universe 20%; Galaxies and galactic nuclei 27%.

Table 1. Band 3 at 115 GHz: FOW, angular and linear resolution

	Field of view	$z=0.0036$ (Virgo cluster)	$z=2$
12 m antenna	54''	4.0 kpc	458 kpc
	Angular resolution	$z=0.0036$ (Virgo cluster)	$z=2$
Early Science compact (125 m)	4.30''	320 pc	36 kpc
Early Science extended (400 m)	1.34''	100 pc	11 kpc
Full operations most extended (16 km)	34 mas	2.5 pc	285 pc
For band 6 at 230 GHz (CO 2–1 rest frequency): divide by 2			
For band 7 at 345 GHz (CO 3–2 rest frequency): divide by 3			
For band 9 at 692 GHz (CO 6–5 rest frequency): divide by 6			

frequency resolution, imaging fidelity and dynamic range, and amplitude calibration, bandpass calibration and positional accuracy were done.

Several end-to-end projects were selected out of a suggestion list made by the ALMA science teams and the community, including nearby as well as high-redshift galaxies. When possible, the observations were compared for consistency with the results obtained with other instruments, either interferometers (IRAM Plateau de Bure, SMA) or single dish telescopes (IRAM Pico de Veleta, APEX). Continuum-like and low frequency resolution CO measurements in all bands were done towards NGC 253. HCN and HCO⁺ absorption lines discovered by Wiklind & Combes (1998) at $z = 0.8858$ towards the $z = 2.5$ gravitationally lensed quasar PKS 1830-211 were measured too. And the 158 micron [CII] line redshifted at $z = 4.43$ towards the gravitationally lensed quasar host BRI 0952-0115 discovered by Maiolino et al. (2009) was also measured, in band 7. All these observations were done with a handful of antennas so providing only a glimpse of what ALMA Early Science can produce.

Some datasets have been made publicly available (cf. <http://almascience.eso.org/alma-data/>). They are provided as a means for the user to become acquainted with the ALMA data structure, observing strategies and reduction techniques. In fact, the early band 3 observations of the luminous galaxy NGC 3256 (a merger of two gas-rich galaxies, now in its later stages) come with a detailed data reduction tutorial (<http://casaguides.nrao.edu/index.php?title=NGC3256Band3>).

3 The Early Science instrument

Sixteen 12-m antennas in a single array will provide 120 baselines, that allow for a rather fast mapping speed. Two configurations will be available, a compact one with baselines up to 125 m and an extended one providing a 3 times better angular resolution (cf. Table 1). Observations will consist of single fields or small mosaics of up to 50 pointings.

All the antennas are equipped with at least four observing bands, covering partially the frequencies between 84 and 720 GHz (or wavelengths between 417 micron and 3.6 mm). This ensures that at all redshifts (except for tiny gaps) at least two CO transitions can be observed (Fig. 1, left panel). In the future, all antennas will be equipped with band 4, 8 and 10 receivers, consequently at least three CO transitions will be available at any redshift lower than 7.3 (Fig. 1, right panel), allowing for excitation studies or line SED determinations. In Early Science up to 4 basebands (or spectral windows) of bandwidth 0.06 to 2 GHz and resolution 0.015 to 1 MHz will be available simultaneously, providing a spectral resolution in the range $R = 10^{4.9} - 10^{7.7}$ and a velocity resolution down to 0.006 km s^{-1} .

Some intense fine structure atomic lines (e.g. [CII] at $157.74 \mu\text{m}$, [OIII] at $88.35 \mu\text{m}$ and [OI] at $63.18 \mu\text{m}$) can also be observed with ALMA in some frequency ranges, provided that the redshift is large enough (Fig. 2), e.g. the [CII] line can be observed in band 9 for $1.64 < z < 2.16$ or in bands 6 and 7 for $4.1 < z < 8.0$. This line, the main coolant of the interstellar medium (ISM), may be better than CO lines to study the extreme redshifts, i.e. the Epoch of Cosmic Reionization at $z > 6$ (bands 6, 4 and 3).

At full operations the ALMA main array will consist of 50 12-m antennas, providing more than a thousand simultaneous baselines. The maximum baseline will be extended to 16 km, providing milliarcsecond resolution. An additional 16 antenna compact array (ACA) with baselines up to 50 m will be available. Bands 4 and 8 will be added first, plus band 10 and possibly band 5 in a few antennas. A more versatile use of the correlator will provide up to 32 spectral windows within a 8 GHz passband. True continuum, full polarization and solar observations will be available, as well as increased mosaicing possibilities.

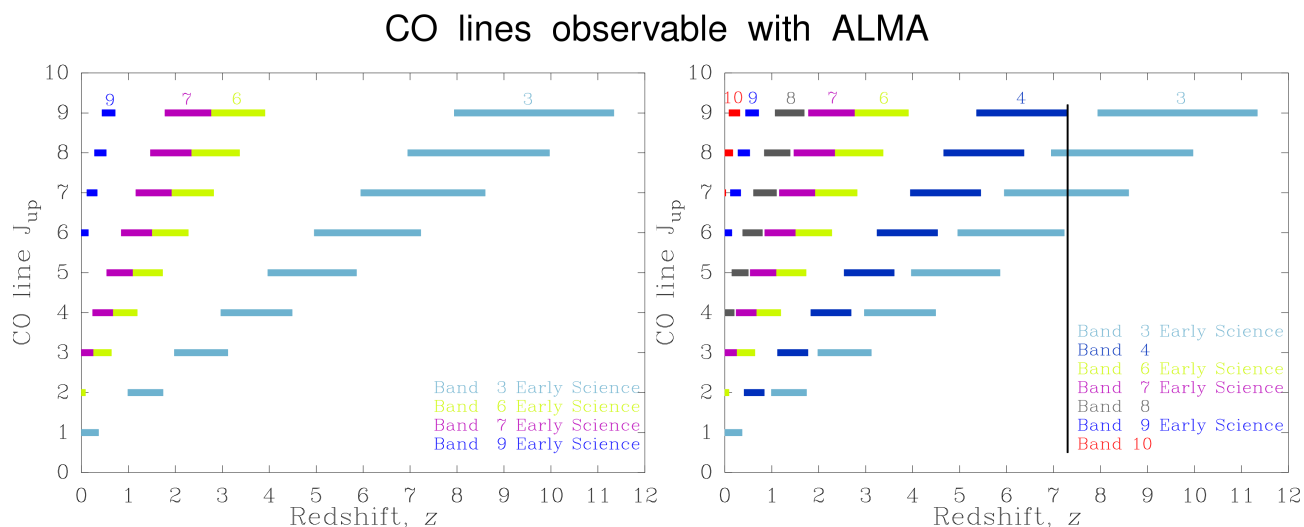


Fig. 1. CO lines observable with ALMA receivers as a function of redshift up to $z = 12$. **Left:** receivers available in Early Science. **Right:** with all receivers currently being build. The vertical line at $z = 7.30$ shows the redshift limit for three different CO lines being observable towards a high redshift object.

Some atomic lines observable with ALMA

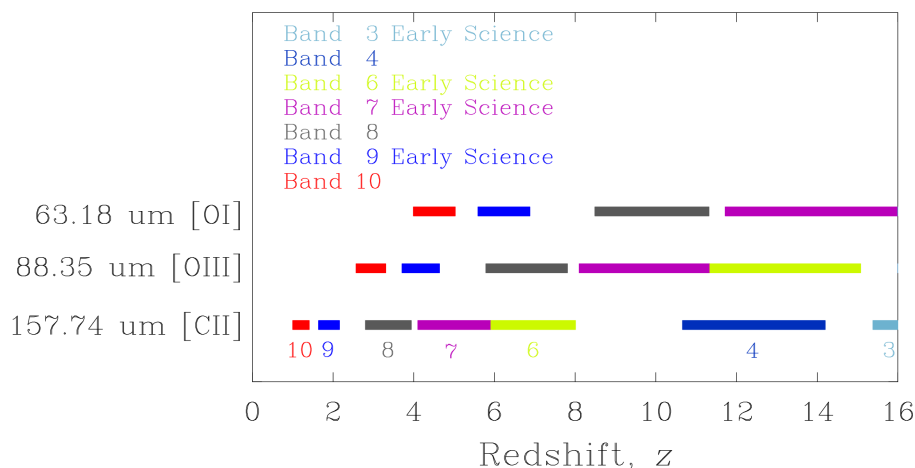


Fig. 2. Redshift ranges (up to $z = 16$) for the observation of some atomic fine structure lines with the ALMA receivers currently installed or being build.

4 Extragalactic science with ALMA at full operations

The high sensitivity (collecting area of 5.600 m^2), high angular resolution ($0.21'' \lambda_{\text{mm}}/L_{\text{km}}$), large frequency coverage (almost full from 84 to 500 GHz, plus the 602-720 GHz and 787-950 GHz windows) and high mapping speed (~ 1200 baselines), together with the high quality of the site ($< 1 \text{ mm}$ of water vapour for most of the operational time, cf. <http://www.apex-telescope.org/sites/chajnantor/atmosphere/pwvvar/>), will make ALMA the right instrument for high redshift studies, and detailed dynamical and chemical studies of nearby galaxies. In particular, the negative K-correction will allow to study the continuum SED of starburst galaxies with nearly equal sensitivity in the redshift range 1 – 10 for wavelengths longer than 0.8 mm, that is up to band 7. A further consequence is that, in contrast to what is observed in the optical, we expect to see many more objects with high redshifts (say $z > 1.5$) than at lower redshifts.

A little survey of what has been proposed in the past (e.g. the previously quoted DRSP, Maiolino 2008, Bachiller and Cernicharo 2008) can give some insight of scientific goals that will be achievable with ALMA at full operations. Some large scientific projects that could be carried out by continuum observations (using mainly

the higher frequency bands) at high redshift follow:

1. Ultradeep surveys of well studied fields (UDF, COSMOS, GOODS-S) to probe the formation and evolution of galaxies, targeting the highest redshifts.
2. Unbiased surveys to detect submillimeter galaxies (SMGs) and determine their size, likely followed by redshift and dynamical mass determinations using bands 3 and 6 spectroscopic measurements. The goal is to study galaxy evolution and the epochs of higher rates of (dust obscured) star formation.
3. Ultradeep surveys through clusters to image magnified background galaxies to determine the properties of the population of faint, young galaxies.
4. Detection (band 6) and multicolor images (bands 3 to 6) of selected sources (from Spitzer, Planck, LBGs or SMGs catalogs) to determine their SED and characterize the star formation rate history.
5. Map the dust emission of gravitational lenses (high bands) to better constrain the shape of their lensing potential.
6. Study merging clusters and the fine structure of clusters via the Sunyaev-Zel'dovich effect (band 3).

The expected detection sensitivity in radio continuum is $5\sigma = 0.11$ mJy/beam in 1 hour in band 7 (0.35 mJy/beam for Early Science) for two 8 GHz bandwidth polarizations and 1 mm of water vapour.

The molecular gas content and properties will be studied at all redshifts in spectroscopic mode. The expected sensitivity varies strongly with the angular resolution, that is with the maximum baseline length (L_{\max}). In bands 3 to 6, for a velocity resolution of 10 km s^{-1} and the compact configuration ($L_{\max} = 150$ m), we expect a brightness temperature line detection sensitivity of $3\sigma \sim 10$ mK in one hour (in 4 hours for the Early Science compact configuration). To estimate the sensitivity for other configurations, consider that the line sensitivity scales as L_{\max}^2 .

One of the three main scientific requirements for the ALMA design was that it must be able to map the CO and [CII] spectral lines in a Milky Way galaxy at a redshift of $z = 3$ in less than 24 hours, so normal galaxies can be studied at moderate redshifts. Galaxies with a richer interstellar medium can be studied at even larger redshifts. Some spectroscopic projects that can be undertaken are:

1. Single line (CO) blind surveys of SMGs to get their redshift distribution.
2. Line studies (CO, HCN, HCO^+ , CN, H_2O) of SMGs to search for dense gas and, perhaps, determine a chemical classification.
3. Coolant line ([OI], [CII]) studies of the interstellar medium in high- z ULIRGs and ISM-rich objects.
4. Search for high- z line emitting galaxies and also moderate- z field galaxies, in order to characterize their properties.
5. Detect rare molecules at high redshift via molecular absorption towards QSOs, a procedure that can also be applied to the nearby Magellanic Clouds.
6. Study the shape distortion and gas kinematics in lensing systems.
7. Map the CO distribution in order to determine dynamical masses, e.g. towards moderate and high- z ULIRGs and infrared luminous QSOs.

The high image reconstruction fidelity provided by ALMA, specially when combining the main array and ACA data, will be of great importance in nearby galaxy studies. The high sensitivity will allow the study of large samples. In fact, it has been estimated that all spirals within $1 - 25$ Mpc can be mapped at $1''$ angular resolution and 10 km s^{-1} velocity resolution in less than two months (Sakamoto 2008). Large, massive ($5 \cdot 10^6 M_{\odot}$) giant molecular clouds (GMCs) can be detected at a 200 Mpc distance (that of Mrk 231) in one hour with ALMA. Projects involving individual GMCs:

1. Study the distribution, kinematics and chemistry of GMCs and the interstellar medium in a variety of galaxy types and environments.

2. Resolve GMCs to determine virial masses and contribute to the determination of the integrated CO $1 \rightarrow 0$ line emission to H_2 column density conversion factor $\chi_{1\ 0}$ in galaxies with different metallicity.
3. Extend the GMC studies to higher CO $J+1 \rightarrow J$ transitions in order to study the line excitation conditions and establish the conversion factors $\chi_{J+1\ J}$ required for high- z studies.

Studies of the nuclei of nearby galaxies suitable for ALMA:

1. Resolve the nuclear molecular torus of nearby AGNs down to a few parsecs.
2. Study outflow and feedback processes in the vicinity of AGNs and at larger scales, as they could play a key role in galaxy evolution.
3. Study the star formation efficiency in normal, starburst and infrared luminous galaxies and, specifically, determine the role of the dense molecular gas.
4. Resolve circumnuclear starburst rings down to individual GMC complexes, and study the gas distribution and kinematics in relation to star formation processes and to gas flows, e.g. those induced by bars.
5. Study the dense gas content and its physical conditions via multitransition observations, and probe the environment via multiline studies that allow to discriminate between shocks, PDRs and XDRs.
6. Studies of the chemical complexity of the interstellar medium in a variety of galaxy types, using several lines in a number of molecules, high angular resolution to identify their location and extend, and high sensitivity to detect the less abundant ones.
7. Study the kinematics and dynamics of the ISM at small to large scale in nearby isolated and interacting galaxies.

References

- Bachiller, R. and Cernicharo, J., (eds.) 2008, *Science with the Atacama Large Millimeter Array* (Heidelberg: Springer)
- Maiolino, R. 2008, *New A Rev.*, 52, 339
- Maiolino, R., Caselli, P., Nagao, T., et al. 2009, *A&A*, 500, L1
- Sakamoto, K. 2008, *Ap&SS*, 313, 245
- Wiklind, T. & Combes, F. 1998, *ApJ*, 500, 129

EARLY-TYPE GALAXIES: MASS-SIZE RELATION AT $Z \sim 1.3$ FOR DIFFERENT ENVIRONMENTS

A. Raichoor¹, S. Mei¹, S. A. Stanford², B. P. Holden³, F. Nakata⁴, P. Rosati⁵, F. Shankar⁶, M. Tanaka⁷, H. Ford⁸, M. Huertas-Company¹, G. Illingworth³, T. Kodama⁴, M. Postman⁹, A. Rettura², J. P. Blakeslee¹⁰, R. Demarco¹¹, M. J. Jee³ and R. L. White⁹

Abstract. We combine multi-wavelength data of the Lynx superstructure and GOODS/CDF-S to build a sample of 75 visually selected early-type galaxies (ETGs), spanning different environments (cluster/group/field) at $z \sim 1.3$. By estimating their mass, age (SED fitting, with a careful attention to the stellar population model used) and size, we are able to probe the dependence on the environment of the mass-size relation. We find that, for ETGs with $10^{10} < M/M_{\odot} < 10^{11.5}$, (1) the mass-size relation in the field did not evolve overall from $z \sim 1.3$ to present; (2) the mass-size relation in cluster/group environments at $z \sim 1.3$ lies at smaller sizes than the local mass-size relation ($R_{e,z \sim 1.3}/R_{e,z=0} \sim 0.6-0.8$).

Keywords: galaxies: clusters: individual (RX J0849+4452, RX J0848+4453), galaxies: evolution, galaxies: formation, galaxies: high-redshift, galaxies: fundamental parameters

1 Introduction

In recent years, studies have unveiled the existence at $z \sim 1-2$ of a population of massive spheroidal galaxies with small size, hence called compact (e.g., Daddi et al. 2005; Buitrago et al. 2008; Cimatti et al. 2008; van Dokkum et al. 2008; Damjanov et al. 2009; Saracco et al. 2010; Strazzullo et al. 2010, and also references therein). When comparing those high redshift galaxies with local ones of similar mass, it appears that their sizes are smaller by a factor of $\sim 2-3$ and up to 5 (van Dokkum et al. 2008).

The formation of compact galaxies might be a consequence of mergers of gas-rich subunits at high redshift (e.g., Khochfar & Silk 2006) and/or cold flows (e.g., Bournaud et al. 2011), resulting in an intense starburst and compact quiescent remnant due to highly dissipative processes. The picture concerning the subsequent evolution of compact galaxies down to $z = 0$ is more difficult to draw. The comparison of high redshift to local samples may be affected by two selection biases: age selection bias against young galaxies in high redshift samples (e.g. Valentinuzzi et al. 2010) and progenitor bias due to morphological evolution (e.g., van Dokkum & Franx 2001). Within this context, it is still unclear which part of the galaxy population went through evolution and which mechanism contributed to it. If the compact galaxy population requires evolution, one efficient process may be minor dry mergers (Naab et al. 2009; Shankar et al. 2011).

¹ GEPI, Observatoire de Paris, Section de Meudon, 5 Place J. Janssen, 92190 Meudon Cedex, France

² Department of Physics, University of California, 1 Shields Avenue, Davis, CA 95616, USA

³ UCO/Lick Observatories, University of California, Santa Cruz 95065, USA

⁴ Subaru Telescope, National Astronomical Observatory of Japan, 650 North A'ohoku Place, Hilo, HI 96720, USA

⁵ European South Observatory, Karl-Schwarzschild -Str. 2, 85748, Garching, Germany

⁶ Max-Planck-Institut für Astrophysik, Karl-Schwarzschild-Str. 1, 85748, Garching, Germany

⁷ Institute for the Physics and Mathematics of the Universe, The University of Tokyo, 5-1-5 Kashiwanoha, Kashiwa-shi, Chiba 277-8583, Japan

⁸ Department of Physics and Astronomy, Johns Hopkins University, Baltimore, MD 21218, USA

⁹ Space Telescope Science Institute, 3700 San Martin Drive, Baltimore, MD 21218, USA

¹⁰ Herzberg Institute of Astrophysics, National Research Council of Canada, Victoria, BC V9E 2E7, Canada

¹¹ Department of Astronomy, Universidad de Concepción, Casilla 160-C, Concepción, Chile

To go deeper in understanding these mechanisms, it is useful to study the mass-size relation (MSR) as a function of environment. Until now, few studies have covered the full range of environment when studying the mass-size relation at $z > 1$. In the local universe, Maltby et al. (2010) found that the MSR does not depend on the environment for ETGs.

In Raichoor et al. (2011a), we presented a unique homogeneous sample of ETGs probing cluster, group and field environments at $z \sim 1.3$. Our study relies on high-quality multi-wavelength data covering the Lynx supercluster, a structure at $z = 1.26$ made of two clusters and at least three groups, spectroscopically confirmed (Stanford et al. 1997; Rosati et al. 1999; Nakata et al. 2005; Mei 2011).

We here use this sample to study the influence of environment on the structural parameters of ETGs at high redshift as a function of mass and environment. The estimates of ETG sizes from *HST*/ACS images combined with stellar population parameters (Raichoor et al. 2011a) allow us to build the MSR (Raichoor et al. 2011b).

2 Data and sample selection

This work relies on optical/near-infrared ($Ri_{775z_{850}}JK_s[3.6\mu\text{m}][4.5\mu\text{m}]$) images of the Lynx supercluster (Raichoor et al. 2011a) and of the Great Observatories Origins Deep Survey (GOODS; Giavalisco et al. 2004) observations of the Chandra Deep Field South (CDF-S; Giavalisco et al. 2004; Nonino et al. 2009; Retzlaff et al. 2010, Dickinson et al., in preparation). The sample consists of 75 ETGs (30 in the Lynx clusters, 18 in the Lynx groups and 27 in the CDF-S) selected in redshift ($0.92 \leq z_{phot} \leq 1.36$ for the Lynx ETGs and $1.1 \leq z_{spec} \leq 1.4$ with $\langle z_{spec} \rangle = 1.239 \pm 0.082$ for the CDF-S), in magnitude ($z_{850} \text{ (AB)} \leq 24$) and in morphology (E/S0 types based on visual inspection of z_{850} -band of *HST*/ACS images). ETGs belonging to the Lynx clusters and groups are identified in Mei (2011) by a Friend-Of-Friend algorithm (Geller & Huchra 1983).

At $z_{850} = 24$ mag, Lynx samples are complete and our CDF-S sample is more than 70% complete. The Lynx cluster, group, and CDF-S field samples have similar spectral coverage and are almost complete at $z_{850} = 24$ mag, thus providing a homogeneous and consistent sample. Our sample has spectroscopic redshifts for 20/30 ETGs in the clusters, 8/18 ETGs in the groups (Mei 2011) and 27/27 ETGs in the field.

3 Analysis

We estimate stellar masses and stellar population ages (Raichoor et al. 2011a) by fitting the SED with different stellar population models: Bruzual & Charlot (2003), Maraston (2005), and an updated version [CB07] of Bruzual & Charlot (2003) that implements a new modeling of the TP-AGB phase. We hereafter refer to those models as BC03, MA05 and CB07, respectively. For SED fitting we used a Salpeter (1955) IMF, solar metallicity, exponentially declining star-formation histories $\psi(t) \propto e^{-t/\tau}$ with a characteristic time $0.1 \leq \text{SFH } \tau \text{ (Ga)} \leq 5$, and no dust.

We estimate the sizes of our ETGs (Raichoor et al. 2011b) in the *HST*/ACS z_{850} band images, the closest to the rest-frame *B*-band in our sample. We fit with a Sersic (1968) $r^{1/n}$ profile the observed two-dimensional surface brightness distributions, using the GALFIT (Peng et al. 2002) software.

4 Results

4.1 Dependence on the stellar population models

We observe that the difference in predicted masses (and ages) between models depends on the ETG's age, as can be seen in Fig.1, where we plot the ratio of the masses predicted with two models versus the age. The modeling of this TP-AGB phase has a significant impact on the derived masses and ages for galaxies observed at high redshift: BC03 models seem to underestimate the impact of the TP-AGB phase, which explains why the inferred masses (and ages) are higher than those inferred with MA05/CB07 (especially around ~ 1 Ga, where the TP-AGB phase is the more active). While recent models from MA05 and CB07 offer better modeling of the TP-AGB phase with respect to less recent BC03 models, we still observe some discrepancies between their predictions.

4.2 Mass-size relation at $z \sim 1.3$

We plot in Fig.2, for the three environments and the three models, the normalized distributions of the size ratio $R_e/R_{e, \text{valen.}}$, which represents the ratio between the size of our ETGs and the one predicted by the local MSR

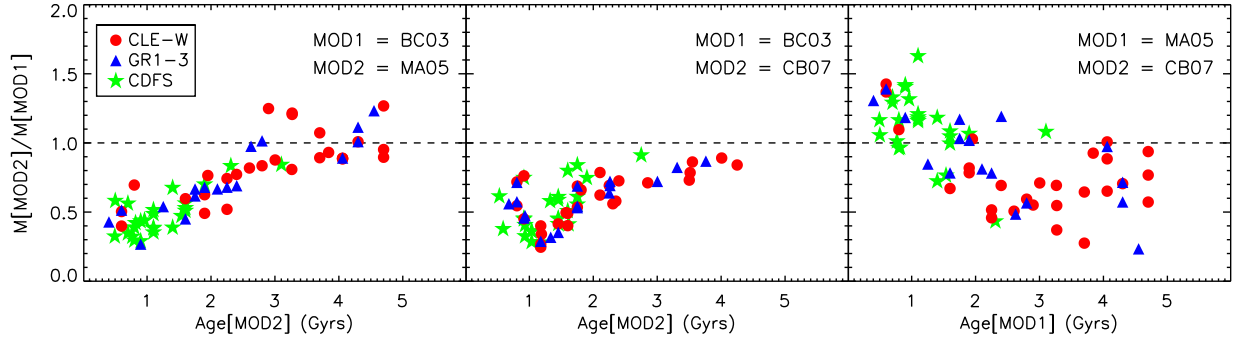


Fig. 1. Dependence of the estimated mass on the stellar population models (BC03/MA05/CB07). Mass ratios as a function of age. Lynx cluster ETGs are the red dots, Lynx group ETGs are the blue triangles and CDF-S ETGs are the green stars. For our sample, typical mass uncertainty is 40%-60% and typical age uncertainty is 1-1.5 Ga.

of Valentinuzzi et al. (2010) at similar masses. Despite the dependence on the model, there is a general trend : most of the cluster and group ETGs lie below local MSRs. We observe that cluster and group size ETG ratios are mostly below 1 with a narrow distribution that peaks around 0.6-0.8, whereas field ETG size ratios have a more widespread distribution, peaking around 0.7-1.1. *At a given mass, ETGs in denser environments tend to have smaller sizes at $z \sim 1.3$ than in the local Universe.*

More precisely, when considering stellar masses estimated with MA05/CB07 models, we observe that our field $z \sim 1.3$ ETGs lie on a MSR in agreement with the local one, whereas our cluster/group $z \sim 1.3$ ETGs lie on a MSR with sizes smaller than the local MSR ($R_{e,z \sim 1.3}/R_{e,z=0} \sim 0.6-0.8$).

When using MA05/CB07 models and looking at the dependence of the size ratio $R_e/R_{e,Valen}$ on the redshift of formation z_{form} , we find that compact ETGs do not have a preferred z_{form} and we observe a near absence of ETGs with $z_{form} > 3$ and a high size ratio ($R_e/R_{e,Valen} > 2$).

5 Conclusion

We have studied a sample of 75 ETGs spanning a wide range of environments (cluster, group, and field) at $z \sim 1.3$, combining optical/near-infrared observations of the Lynx supercluster, with data on the GOODS/CDF-S field. We estimated the mass and age of our ETGs with SED fitting using BC03, MA05 and CB07 stellar population models, and their size by fitting a Sérsic profile to the *HST*/ACS z_{850} images. We first study the dependence of the derived stellar mass (and age) on the stellar population model used, and then we probe the dependence on the environment of the MSR.

When we compare the MSR of cluster and group ETGs vs field ETGs, we find that, at similar masses, cluster and group ETGs are more compact than field ETGs. Our results are mainly driven by galaxies with masses $M < 2 \times 10^{11} M_{\odot}$. Since in the local Universe, the ETG MSR does not depend on environment, our results imply that, for our mass range ($10^{10} < M/M_{\odot} < 10^{11.5}$), an evolution in the MSR of cluster and group ETG size is required to explain current observations, while field ETGs show a MSR that is compatible with the local one. The evolution of the MSR in dense environments might reflect either an evolution in size of the pristine population or the transformation of ETG progenitors that are not classified as ETG at $z \sim 1.3$ or the accretion of a new population of larger ETGs.

The HAWK-I Distant Cluster Survey (P.I.: C. Lidman), with a multi-wavelength coverage (*HST*, VLT, *Spitzer*) of 10 rich clusters between $z = 0.8$ and $z = 1.4$, will bring crucial observations on the detailed evolution of the MSR in dense environments during a key epoch of galaxy assembly.

References

- Bournaud, F., Chapon, D., Teyssier, R., et al. 2011, ApJ, 730, 4
- Bruzual, G. & Charlot, S. 2003, MNRAS, 344, 1000
- Buitrago, F., Trujillo, I., Conselice, C. J., et al. 2008, ApJ, 687, L61
- Cimatti, A., Cassata, P., Pozzetti, L., et al. 2008, A&A, 482, 21

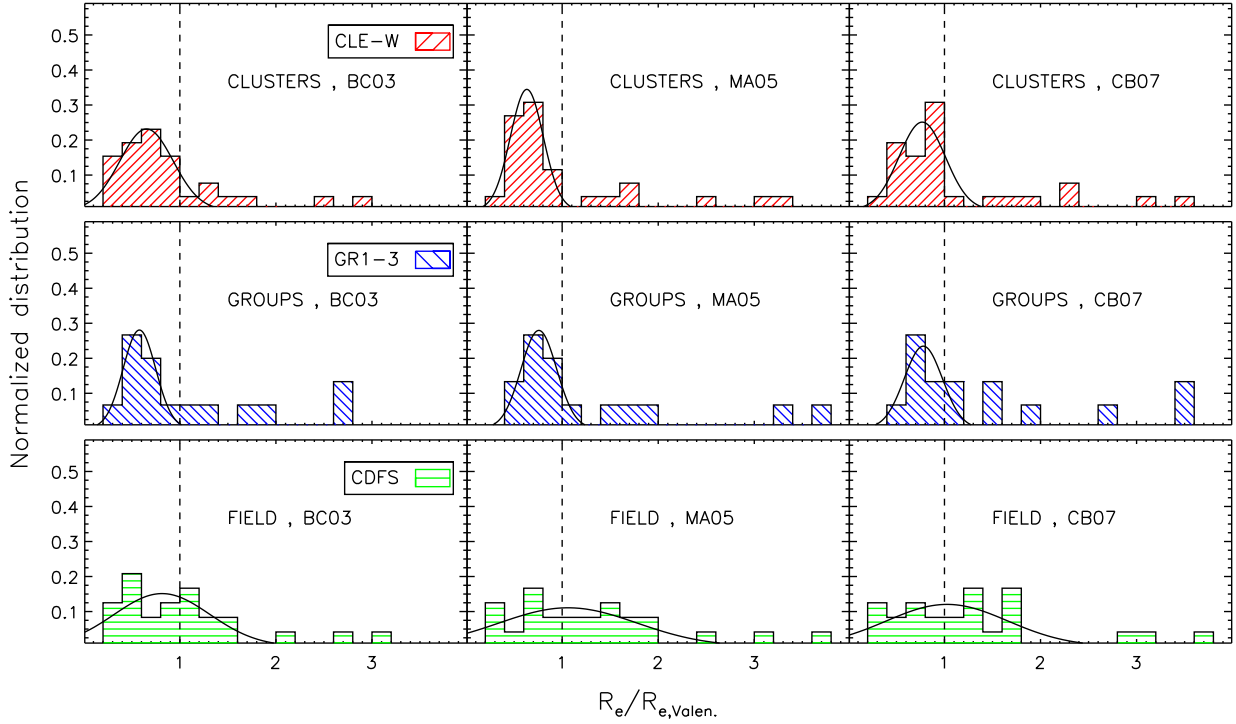


Fig. 2. Size ratio $R_e/R_{e,Valen}$ normalized distributions derived with the three stellar population models (BC03/MA05/CB07), split by environments: Lynx cluster ETGs (*top panels*), Lynx group ETGs (*middle panels*) and CDF-S ETGs (*bottom panels*). $R_e/R_{e,Valen}$ represents the ratio between the size of our ETGs and the one predicted by the local MSR of Valentinuzzi et al. (2010). The black solid line represents the best-fit gaussian to the distributions.

- Daddi, E., Renzini, A., Pirzkal, N., et al. 2005, ApJ, 626, 680
 Damjanov, I., McCarthy, P. J., Abraham, R. G., et al. 2009, ApJ, 695, 101
 Geller, M. J. & Huchra, J. P. 1983, ApJS, 52, 61
 Giavalisco, M., Ferguson, H. C., Koekemoer, A. M., et al. 2004, ApJ, 600, L93
 Khochfar, S. & Silk, J. 2006, MNRAS, 370, 902
 Maltby, D. T., Aragón-Salamanca, A., Gray, M. E., et al. 2010, MNRAS, 402, 282
 Maraston, C. 2005, MNRAS, 362, 799
 Mei, S., 2011 ApJ, submitted
 Naab, T., Johansson, P. H., & Ostriker, J. P. 2009, ApJ, 699, L178
 Nakata, F., Kodama, T., Shimasaku, K., et al. 2005, MNRAS, 357, 1357
 Nonino, M., Dickinson, M., Rosati, P., et al. 2009, ApJS, 183, 244
 Peng, C. Y., Ho, L. C., Impey, C. D., & Rix, H. 2002, AJ, 124, 266
 Raichoor, A., Mei, S., Nakata, F., et al. 2011a, ApJ, 732, 12
 Raichoor, A., Mei, S., Stanford, S., et al. 2011b, ApJ, in press, arXiv:1109.0284
 Retzlaff, J., Rosati, P., Dickinson, M., et al. 2010, A&A, 511, A50+
 Rosati, P., Stanford, S. A., Eisenhardt, P. R., et al. 1999, AJ, 118, 76
 Salpeter, E. E. 1955, ApJ, 121, 161
 Saracco, P., Longhetti, M., & Gargiulo, A. 2010, MNRAS, 408, L21
 Sersic, J. L. 1968, Atlas de galaxias australes (Córdoba: Observatorio Astronómico)
 Shankar, F., Marulli, F., Bernardi, M., et al. 2011
 Stanford, S. A., Elston, R., Eisenhardt, P. R., et al. 1997, AJ, 114, 2232
 Strazzullo, V., Rosati, P., Pannella, M., et al. 2010, A&A, 524, A17+
 Valentinuzzi, T., Fritz, J., Poggianti, B. M., et al. 2010, ApJ, 712, 226
 van Dokkum, P. G. & Franx, M. 2001, ApJ, 553, 90
 van Dokkum, P. G., Franx, M., Kriek, M., et al. 2008, ApJ, 677, L5

LOCAL HOST GALAXY PROPERTIES OF TYPE IA SUPERNOVAE FROM THE NEARBY SUPERNOVAE FACTORY

M. Rigault¹, Y. Copin¹, G. Aldering², P. Antilogus³, C. Aragon², C. Baltay⁴, S. Bongard³, C. Buton⁵, A. Canto³, M. Childress^{2,6}, N. Chotard¹, H. K. Fakhouri^{2,6}, E. Gangler¹, E. Y. Hsiao², M. Kerschhaggl⁵, M. Kowalski⁵, S. Loken², P. Nugent^{7,8}, K. Paech⁵, R. Pain³, E. Pecontal⁹, R. Pereira¹, S. Perlmutter^{2,6}, D. Rabinowitz⁴, K. Runge², R. Scalzo^{4,10}, G. Smadja¹, C. Tao^{11,12}, R. C. Thomas⁷, B. A. Weaver¹³ and C. Wu^{3,14}

Abstract. Type Ia supernovae are key tools to study accelerating expansion of the Universe. However despite active research, physics of such objects remain uncertain. To better understand potential systematics we investigate on local host galaxy properties. In this preliminary analysis, we find gas derived quantities such as metallicity and star formation rate compatible to those present in literature. Finally we show a relationship between SALT2 color and x_1 with star formation activity.

Keywords: Observational cosmology, Type Ia supernovae, Host galaxy, Gas properties

1 Introduction

Type Ia supernovae (SNe Ia) were key luminosity distance indicators in the discovery of the accelerating expansion of the Universe (Riess et al. 1998; Perlmutter et al. 1999). As their intrinsic peak luminosity variations are small – less than 0.15 magnitude after standardization – SNe Ia are used as cosmological standard candles. Despite ongoing research, the physical nature of progenitor system and the explosion mechanism remain however uncertain.

In recent years, numerous samples of SNe Ia have been observed and approximately 600 spectroscopically-confirmed SNe Ia are available for cosmological analyses (Amanullah et al. 2010). With such a large sample, investigating systematic uncertainties has grown into a major preoccupation. In particular, global host properties might have an important impact on the properties and standardization of SNe Ia (Howell et al. 2006; Lampeitl et al. 2010; Sullivan et al. 2010; Konishi et al. 2011).

The *Nearby Supernovae Factory* collaboration (SNfactory, Aldering et al. 2002) has collected a sample of more than 200 SN Ia spectrophotometric time series. Each series typically consists of 15 spectra plus two or

¹ Université de Lyon, 69622 Lyon, France; Université de Lyon 1, Villeurbanne; CNRS/IN2P3, Institut de Physique Nucléaire de Lyon

² Physics Division, Lawrence Berkeley National Laboratory, 1 Cyclotron Road, Berkeley, CA 94720, USA

³ LPNHE, Université Pierre et Marie Curie Paris 6, Université Paris Diderot Paris 7, CNRS-IN2P3, 75252 Paris Cedex 05, France

⁴ Department of Physics, Yale University, New Haven, CT 06250-8121, USA

⁵ Physikalisches Institut Universität Bonn, Nussallee 12 53115 Bonn, Germany

⁶ Department of Physics, University of California Berkeley, 366 LeConte Hall MC 7300, Berkeley, CA, 94720-7300, USA

⁷ Computational Cosmology Center, Lawrence Berkeley National Laboratory, 1 Cyclotron Road, Berkeley, CA 94720, USA

⁸ Department of Astronomy, University of California, Berkeley, CA 94720-3411, USA

⁹ Observatoire de Lyon, Saint-Genis Laval, 69230 Lyon, Université de Lyon, 69003 Lyon, France

¹⁰ Australian National University, Mt. Stromlo Observatory, The RSAA, Weston Creek, ACT 2611 Australia

¹¹ Tsinghua Center for Astrophysics, Tsinghua University, Beijing 100084, China

¹² Centre de Physique des Particules de Marseille, 163, avenue de Luminy - Case 902 - 13288 Marseille Cedex 09, France

¹³ New York University, Center for Cosmology and Particle Physics, 4 Washington Place, New York, NY 10003, USA

¹⁴ National Astronomical Observatories, Chinese Academy of Sciences, Beijing 100012, China

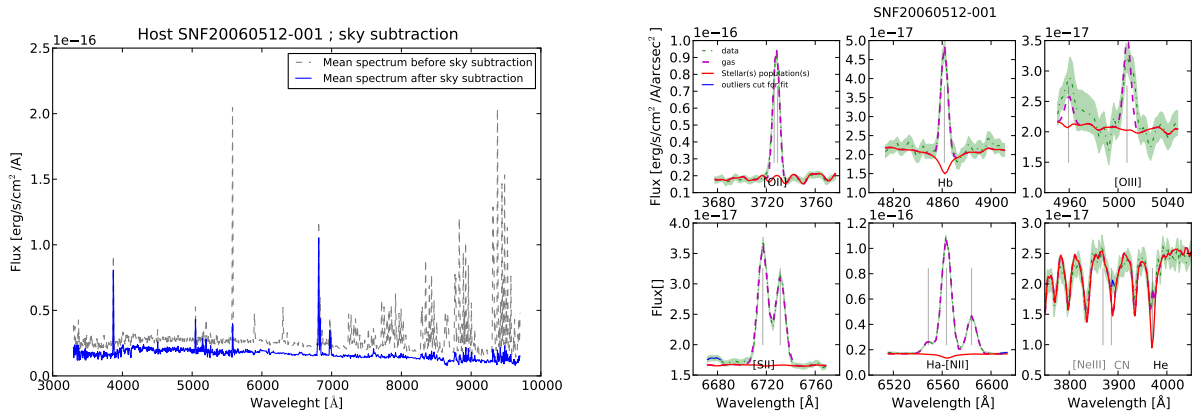


Fig. 1. Left: Mean spectra extracted from merged cube of both B and R channels for the darkest observation night of SNF20060512-001 host galaxy. The gray dashed-line represent the host galaxy + sky spectrum while the blue solid-line is the galaxy spectrum obtained after sky subtraction. **Right:** Zooms on relevant part of the galaxy spectrum. The data is the dashed-point green line with best ULYSS fit split in two component: the SSP is the solid-red line while the gas is plotted in dashed-magenta line.

more local host observations taken at least one year after the explosion (final references). SNfactory observations are made using an Integral Field Spectrograph (IFS) with a field-of-view (FoV) of few arcsec, allowing to collect simultaneously SN Ia point source as well as its local environment. This peculiarity offers unique conditions that might help to constrain progenitor populations better than a global host study.

We present our data sample and the local host galaxy spectrum extraction in § 2; § 3 exposes the method used to measure the gas emission and we discuss our results in § 4.

2 Data analysis

The spectra was obtained by the SNfactory collaboration between 2004 and 2010 with the *SuperNovae Integral Field Spectrograph* (SNIFS, Lantz et al. 2004), a fully integrated instrument optimized for automated observations of point sources on a structured background over an extended optical window at moderate spectral resolution. The IFS possesses a fully-filled $6''4 \times 6''4$ spectroscopic FoV subdivided into a grid of 15×15 spatial elements (spaxels). The dual-channel spectrograph covers simultaneously 3200–5200 Å (B-channel) and 5100–10000 Å (R-channel). More details about SNIFS are presented in Thomas et al. (2011), and the software pipeline is summarized in Aldering et al. (2006). The inter-channel dichroic implies a 200 Å wide range around 5100 Å with a bigger variance and some yet unresolved data-reduction issues. This impacts the measurement of H_β and [OIII] for redshifts $0.028 < z < 0.07$ and $z < 0.038$, respectively. Thus, excepted for highest signal over noise ratio spectra, this domain can not be directly used for analysis yet.

SNIFS does not have a sky channel, and given its small FoV, it is usually impossible to isolate a pure sky signal as can be done in long slit spectrography. We therefore developed a technique to model the sky contribution on the observed spectra. This model is obtained from studies of night skies observed during standard star exposures. We use more than 1000 spectra and feed them to a Principal Component Analysis (PCA) to extract relevant contributions. The PCA will be performed independantly on the red sky emission lines (PCA_R) – after subtraction of a 4^{th} -order Legendre polynomial continuum – and the blue continuum plus lines (PCA_B). The resulting sky model is therefore a linear combination of 18 parameters: 8 PCA_R coefficients plus a 4^{th} -order Legendre polynomial for the R-channel, and 5 PCA_B coefficients for the B-channel.

The sky subtraction algorithm for a given x, y, λ cube is then the following. First extract the mean spectrum of the say 10 spaxels with the lowest galaxy signal, to get an high contrast “raw sky”. In this sky, galaxy signal, in particular gas emission lines, could still remain. To avoid subtracting this galaxy signal, we then fit our sky model to this raw sky to get the “modeled sky”: since host gas emission lines are not part of the model, the modeled sky will not have any galaxy feature. We can then proceed by subtracting the spatially uniform sky model from each spaxels of the observed cube. Fig. 1 shows the result of such a sky subtraction. The strong emission lines that disappear above 7200 Å are atmospheric lines modeled in the PCA_R , whereas the remaining lines are gas galactic emission.

To increase the signal over noise ratio of the host galaxy spectrum, we add to final references the “galaxy + SN” cubes from which the SN point source was subtracted. A “super cube” is created by merging all sky- (and potentially SN-) subtracted cubes after proper Atmospheric Differential Refraction (ADR) correction and registration. We discard cubes with strong flux residuals at the SN location (from PSF subtraction leftovers), and cubes with strong dichroic effects.

Finally, we extract the mean local galaxy spectrum at the SN location from brightest spaxels in the IFS FoV. This spectrum represent the brightest contribution of the galaxy to the direct environment of the SN.

3 Fitting emission lines

A galaxy is a combination of various physical elements that have a different incidence on the observed spectrum: stars create a black body continuum with an absorption structure depending on their age and metallicity; the gas contributes for emission lines, as a function of its metallicity and ionization; the dust absorbs light over the whole wavelength range. The dust absorption law is supposed to be a Cardelli law (Cardelli et al. 1989, $R_V = 3.1$).

In order to get accurate fluxes of gas emission lines, it is necessary to fit all galaxy components together. To do so, we use a modified version of the *University of Lyon Spectroscopic analysis Software** (ULySS, Koleva et al. 2008, 2009). This allows us to fit a single stellar population (SSP) or a combination of multiple SPs (MSP) simultaneously with a set of emissions lines together with a multiplicative continuum that corrects both for dust extinction and large scale flux mismatch. Fig. 1 shows zooms of relevant elements of the host spectrum adjusted by ULySS in rest frame after Milky-Way dereddening. We see that some lines are unaffected by the underlying stellar continuum – such as [NII] or [OII] – while others – such as H_β – are sensitive to the SSP (or MSP) estimate.

Emission lines give information about physical properties such as the extinction through the color excess $E(B - V)$, the star formation rate (SFR) or the gas metallicity ($\log(O/H) + 12$). $E(B - V)$ is computed using Balmer’s emission lines, namely H_α , H_β or H_γ which have predictable ratios. Comparing the theoretical relationship to the observed ones yields to $E(B - V)$ (Osterbrock 1989; Gordon et al. 2003) assuming $R_V = 3.1$. After extinction correction, we measure the SFR from H_α luminosity (Kennicutt 1998). To get an intensive value, we divide this quantity with the physical observed surface to define the $SFR_{SD}[M_\odot a^{-1} kpc^{-2}]$ (SD for Surface Density, Konishi et al. 2011). Finally, the gas metallicity is obtained using the Kewley & Dopita (2002) [OII]/[NII] method. Due to the distance between these two lines, this method is very sensitive to the $E(B - V)$ estimate. We therefore limit our sample to the 53 host in which a precise measurement of $E(B - V)$ is possible. However, we add 12 hosts for the SFR study since it is barely dependent on the measured extinction. Added spectra are those removed because of strong dichroic effect – preventing accurate measurement of H_β – but with a good H_α detection.

4 Results

Fig. 2 shows the repartition of gas properties of the SN Ia direct environment for hosts where $E(B - V)$ can be measured. We plot for comparison the same quantities as presented by Konishi et al. (2011) for SDSS global host gas properties.

Our local gas analysis gives us a maximal probability of $E(B - V)$ at 0.45 with a few negative measurement and an upper distribution tail extending to 1. This distribution is in a good agreement with the compared literature. The galaxy spectra are then corrected for this extinction. Since $E(B - V)$ should be positive, the small number of negative measurements are set to zero.

As in Konishi et al. (2011) the SFR_{SD} presence probability reaches a maximum at $0.12 M_\odot a^{-1} kpc^{-2}$ and raises up to 3. Lowest values are found in well detected hosts but with very thin gas presence, e.g. in elliptical galaxies, or in low detection hosts which limit our capacity to get accurate measurement of very low SFR_{SD} .

The local gas metallicity distribution peaks at 9.0 dex in agreement with the existing literature. Moreover we seem to have a second peak at 8.6 which could arise from our metallicity estimate method that begin to degenerate with lower metallicities around this value. The few points bellow 8.5 should not be taken into consideration regarding the [NII]/[OII] Kewley & Dopita (2002) metallicity estimation.

*<http://ulyss.univ-lyon1.fr>

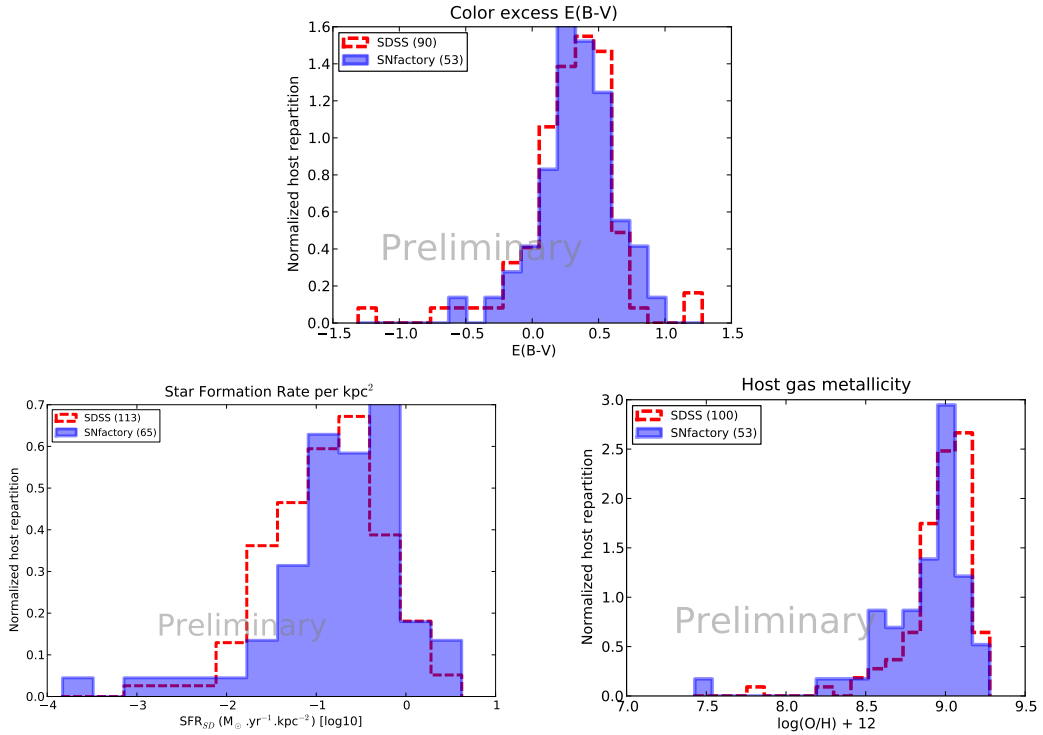


Fig. 2. For the three plots, our local host gas properties are represented in filled blue histograms for the 53 SN Ia host spectra. Empty dashed-red histogram represent same quantities from SDSS SN Ia host global analysis added for comparison (Konishi et al. 2011) ($0.05 < z < 0.4$). **Upper panel:** The color excess $E(B - V)$. **Left bottom panel:** The Star Formation Rate per Surface Density SFR_{SD} . **Right bottom panel:** The gas metallicity $\log(O/H) + 12$.

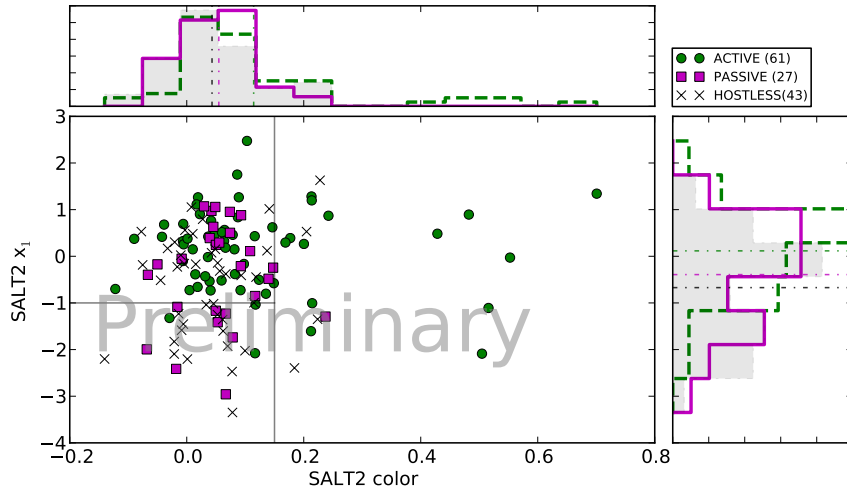


Fig. 3. The SALT2 x_1 and color repartition split as function of the SNe Ia host activity sub-classification: in circle-green “active” galaxies, in square-magenta “passive” ones and black cross for “hostless” SNe. Upper and right histograms are repartition of the SALT2 x_1 and color, respectively, for the three subclasses: dashed-green lines for “active”, solid-magenta lines for “passive” and filled histograms for “hostless”.

We then split our host galaxy sample in three categories: “active” (defined as galaxies with a $SFR_{SD} \geq 10^{-1.3}$, 61 hosts), “passive” ($SFR_{SD} < 10^{-1.3}$, 27 hosts) and “hostless” (host without any detected signal in our FoV, 27 hosts). Note that if no galaxy signal has been detected, this corresponds to the absence of H_α , thus supposing $SFR_{SD} \ll 10^{-1.3}$: this hostless subclass could be assimilated to the passive one.

We now investigate the SN Ia properties as function of the host activity sub-classification. Fig. 3 shows the repartition of SALT2 (Guy et al. 2007) x_1 and color for our SN sample, split with respect to the host activity. This can be compared to Fig. 2 of Lampeitl et al. (2010) for the the SDSS global host study.

We can do two comments on Fig. 3. 1. SNe Ia with a color larger than 0.15 are mostly from active hosts. 2. as found by Lampeitl et al. (2010), low-stretch ($x_1 < -1$) SNe Ia tend to be found in “passive” hosts – i.e. old stellar population – or “hostless” hosts – i.e. supposedly passive local environment.

5 Conclusion

SNfactory offers the unprecedented possibility to study SN Ia local host properties. After extraction of the mean local host spectrum we investigated the gas characteristics by measuring $E(B - V)$, SFR_{SD} and $\log(O/H) + 12$. We have found a repartition of those quantities in our sample in good agreement with existing literature looking at global host properties. Having split our 119 hosts into three subsamples according to their star formation activity, we notice, as observed by Lampeitl et al. (2010), that passive hosts galaxies tend to form lower SALT2 x_1 SNe Ia, and that all but one SNe Ia with $c > 0.15$ are coming from active galaxies.

Further studies on local host properties are in progress. As our IFS allows us to investigate gradient properties such as the H_α spatial distribution around the SN locations, studying structures could give us a better understanding of the direct environment of the SN progenitors.

References

- Aldering, G., Adam, G., Antilogus, P., et al. 2002, SPIE, 4836, 61
Aldering, G., Antilogus, P., Bailey, S., et al. 2006, ApJ, 650, 510
Amanullah, R., Lidman, C., Rubin, D., et al. 2010, ApJ, 716, 712
Cardelli, J. A., Clayton, G. C., & Mathis, J. S. 1989, ApJ, 345, 245
Gordon, K. D., Clayton, G. C., Misselt, K. A., Landolt, A. U., & Wolff, M. J. 2003, ApJ, 594, 279
Guy, J., Astier, P., Baumont, S., et al. 2007, A&A, 466, 11
Howell, D. A., Sullivan, M., Nugent, P. E., et al. 2006, Nature, 443, 308
Kennicutt, R. C. 1998, ApJ, 498, 541
Kewley, L. J. & Dopita, M. A. 2002, ApJS, 142, 35
Koleva, M., Prugniel, P., Bouchard, A., & Wu, Y. 2009, A & A, 501, 1269
Koleva, M., Prugniel, P., Ocvirk, P., Le Borgne, D., & Soubiran, C. 2008, MNRAS, 385, 1998
Konishi, K., Cinabro, D., Garnavich, P. M., et al. 2011, 1101.4269
Lampeitl, H., Smith, M., Nichol, R. C., et al. 2010, ApJ, 722, 566
Lantz, B., Aldering, G., Antilogus, P., et al. 2004, Proc. SPIE, 5249, 146
Osterbrock, D. 1989, Astrophysics of gaseous nebulae and active galactic nuclei (Mill Valley CA: University Science Books)
Perlmutter, S., Aldering, G., Goldhaber, G., et al. 1999, ApJ, 517, 565
Riess, A. G., Filippenko, A. V., Challis, P., et al. 1998, ApJ, 116, 1009
Sullivan, M., Conley, A., Howell, D. A., et al. 2010, MNRAS, 406, 782
Thomas, R. C., Aldering, G., Aragon, C., et al. 2011, arXiv:1109.1312

MORPHOLOGICAL CLASSIFICATION OF GALAXY CLUSTERS

F. Rostagni¹, C. Benoist¹ and S. Maurogordato¹

Abstract. We perform a quantitative morphological classification of a sample of low redshift galaxy clusters extracted from the SDSS C4 cluster catalogue. Clusters with a high spectroscopic coverage were selected. A wavelet based algorithm was applied allowing to detect and quantify 3D substructures and analyze the large scale environment of these clusters. Based on this classification, we study the correlation between cluster morphology and spectral properties of galaxy members.

Keywords: Galaxies: clusters: general, large scale structure of universe

1 Introduction

Galaxy clusters are the largest gravitationally bound systems of the universe. According to the standard model of cosmology they have been formed recently through a hierarchical growth in which smaller units, the galaxies, assemble together. Numerous observations in X-rays (Jones & Forman 1999) as well as in optical (Geller & Beers 1982; Dressler & Shectman 1988) show that there are substructures in a non negligible fraction of clusters, revealing that clusters are currently in a non relaxed dynamical state. Not only substructures reveal clusters dynamical state but also they can lead to wrong estimation of cluster physical properties, such as their mass for instance. For this reason, the use of galaxy clusters as probe to evaluate the cosmological parameters must be done carefully. Thus quantifying cluster dynamical state is of prime importance to measure their mass correctly.

Several previous works were performed in order to establish cluster morphological classifications. First galaxy cluster classifications were done using cluster galaxy content. Bautz & Morgan (1970) developed a classification based on three classes of clusters plus two intermediate ones according that a cluster contains a cD (class I), the cluster BCG is intermediate between a cD and a Virgo-type giant elliptical (class II) and the cluster contains no dominant galaxy (class III). Also Rood & Sastry (1971) defined the famous “tuning fork” classification.

Due to projection effects optical cluster classifications were forsaken and X-rays observations were used to analyze cluster dynamical state through the gas. Furthermore the gas enables to have an idea about cluster stage of merging process that is observed while galaxies do not. Moreover X-rays give a continuous distribution (gas photons or temperature) while optical gives only points (position of galaxies) which made more difficult the statistical analysis of the galaxy distribution than the one of the gas. It is in this context that several powerful statistical tools were developed to analyze cluster morphology in X-rays. Mohr et al. (1993) used the centroid shift to constrain the dynamical state of 5 clusters observed with the *Einstein Observatory*. This technique was also used on more clusters (Jones & Forman 1999; Schuecker et al. 2001). Buote & Tsai (1996) developed the power ratio method, consisting in measuring the ratio between statistical moments of cluster X-ray luminosity. Cluster ellipticity was also used to assess cluster relaxation (Kolokotronis et al. 2001; Melott et al. 2001; Plionis 2002).

Thanks to the development of multi-object spectroscopy numerous galaxy redshifts could have been measured and these redshifts enable to disentangle piled up structures along the line of sight, solving the problem of projection effects on galaxies. First analyses of galaxy redshifts were made in the beginning of the nineties. Several statistical tools were developed to evaluate cluster properties along the line of sight (e.g. Beers et al. 1990) and to check the gaussianity of their redshift distribution (e.g. Ashman et al. 1994). Later new analyses

¹ Université de Nice-Sophia Antipolis, Observatoire de la Côte d’Azur, CNRS UMR 6202 Cassiopée, boulevard de l’Observatoire 06304 Nice Cedex, France

of galaxy projected distribution were performed. The main idea of these is to transform galaxy positions into a continuous distribution function. Adaptive kernels have been used (Ramella et al. 2007) in this purpose like wavelet analysis (Ferrari et al. 2005; Flin & Krywult 2006).

The aim of the present analysis is to establish a new cluster classification based on galaxies. In this analysis, galaxy position and redshift are used to finely characterize cluster optical morphology. In future works, this classification will be used to study the impact of cluster morphology on cluster galaxy members and to try to constrain cosmological parameters using clusters more precisely by removing complex systems or by assessing more accurate mass measurements.

In this paper, the assumption of a flat universe with $H_0 = 70 \text{ km s}^{-1}$, $\Omega_M = 0.3$ and $\Omega_\Lambda = 0.7$ is done.

2 Data description

Currently the Sloan Digital Sky Survey (Abazajian et al. 2004) is the best sky survey for the local universe. Miller et al. (2005) developed the C4 cluster finder algorithm and detected 749 clusters in SDSS DR2. C4 clusters are the baseline of the present analysis. Photometric and spectroscopic information of all galaxies falling within 5 Mpc from C4 cluster centers have been extracted into *C4 fields*. Only galaxies brighter than $r' = 17.77$ were selected as SDSS spectroscopy is complete up to this magnitude. As galaxy redshift will be used to analyze cluster morphology high spectroscopic completeness is required (at least 60% was chosen) and numerous galaxies are needed (at least 50 was chosen). These two first criteria plus the removal of overlaps reduced the cluster sample from 749 to 179 fields. Sample clusters have redshifts ranging from 0.0294 to 0.1386, the median being 0.0834.

3 Morphological classification

Galaxy cluster morphology consists in measuring deviations from a relaxed cluster, typically by detecting substructures within clusters. The presence of substructures has been detected in X-rays and in optical but mainly in projection on the sky plane and in other studies along the line of sight with galaxy velocities only. The development of multi-object spectroscopy enables the measurement of numerous galaxy redshifts giving access to the information along the line of sight together with the galaxy positions. The aim of this analysis is to classify clusters into five categories: relaxed clusters, bimodal major mergers, minor mergers, multiple mergers and clusters in virialisation phase.

To do so, not only detecting substructures in the projected sky plane and along the line of sight is performed but also measuring deviations from a relaxed cluster other than substructures. Namely the detection of substructures along the line of sight is based on the assumption that an ideal relaxed cluster has a gaussian velocity distribution, thus detecting deviations from gaussianity in the velocity distribution means that a cluster is not relaxed. In that purpose numerous statistical tests have been developed (see Beers et al. 1990, for instance). Here the assumption of gaussian velocity distribution is done and a gaussian mixture will be used to describe cluster galaxy velocities. Every cluster will be decomposed in gaussian peaks along the line of sight, some clusters will consist in one gaussian peak, others in two, three etc... Clusters presenting one gaussian peak may be "relaxed". Indeed at this stage no information in projection on the sky plane has been used thus these clusters may correspond to bimodal clusters in projection on the sky plane and the gaussian hypothesis may not be correct for these clusters. For single gaussian clusters their gaussianity has to be evaluated. This is done by computing the χ^2 between the gaussian fit and the velocity distribution: bad χ^2 values ($\chi^2 \geq 0.2$) means that the velocity distribution does not follow a gaussian law.

The analysis of galaxy positions is more complex than for redshifts. Actually for redshifts it is quite easy because their expected distribution is a gaussian law and several tools have been developed in that purpose. For galaxy positions, the expected distribution is the universal NFW profile (Navarro et al. 1995). However this distribution is much more complex than a gaussian law and it is not possible, today, to describe a data set by a mixture of NFW profiles. In fact a continuous field is required to analyze galaxy positions instead of a discrete data set. There are several ways to transform galaxy positions into their underlying distribution. Based on a multi-scale approach cluster density maps have been computed. The detailed description of the algorithm can be found in Ferrari et al. (2005). Briefly, it involves a wavelet decomposition of the galaxy positions performed on scales from which the significant structures are recombined to give the final map (following Eq. (C7) in Fadda et al. 1998). The scales correspond to the size of structures that will be reconstructed in the final image. Clusters and groups of galaxies have masses ranging between $10^{13} M_\odot$ and $10^{15} M_\odot$ and thus have sizes ranging

between 0.3 Mpc and 2 Mpc. With a multi-scale approach, interesting scales can be selected and only these ones can be used to compute the final image, thus only structures with size between 0.3 Mpc and 2 Mpc will be considered. The computed image is a 10 Mpc square to detect cluster environment.

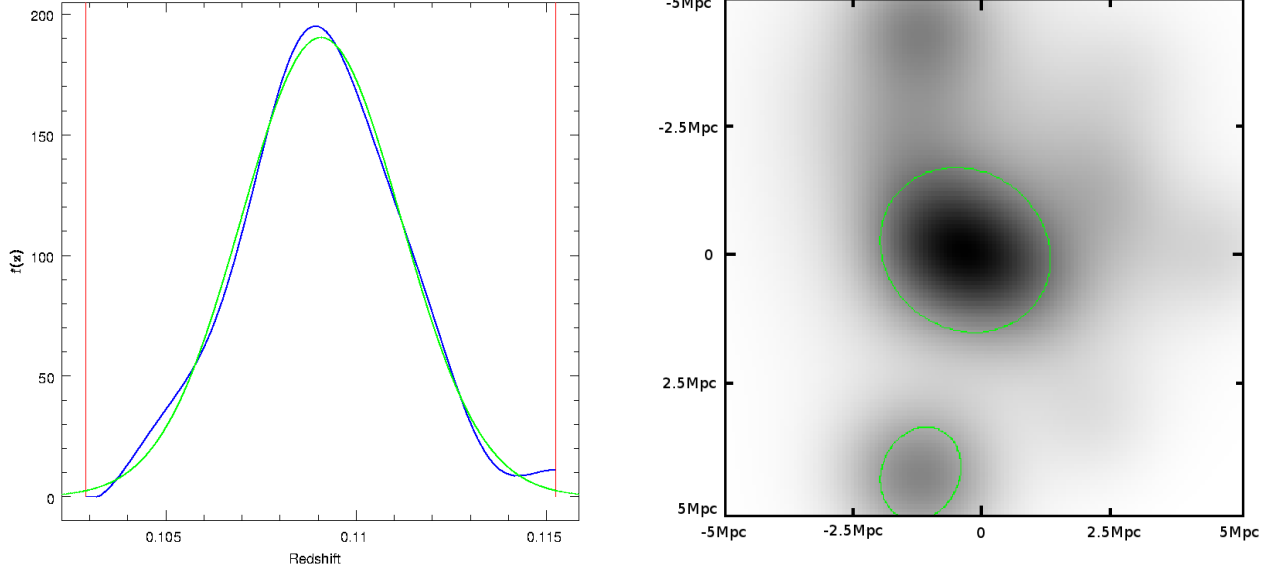


Fig. 1. Example of a relaxed cluster: cluster C4 0090. On the **left** panel its redshift distribution function (blue) reveals one gaussian peak (green) indicating no interaction along the line of sight. The red vertical lines indicates cluster redshift interval. On the **right** panel its density map reveals only two significant clumps (in green), but the distance between the clumps is too large with respect to their virial radius to indicate an interaction between them. Thus without interaction this cluster is classified as relaxed.

The right panel of Figure 1 shows the density map of C4 cluster 0090. On the right panel the density map reveals two significant clumps. The central clump on density maps is the main cluster, the others may be other clusters, or groups or substructures in the vicinity of the main cluster. The number of clumps is important for morphology but not all clumps are physically significant: only the ones close enough from the main cluster are interacting with it. The interaction depends on the distance between clumps but also on their mass. The criterion used for interaction is

$$d \leq r_{vir,1} + r_{vir,2}$$

where d is the physical distance between the main clump and the other clump and $r_{vir,i}$ is the virial radius of the clump. Furthermore the ellipticity of the cluster is an indication of its dynamical state. An ideal relaxed cluster has to be spherical and in projection has to appear circular. Large ellipticities ($\epsilon \geq 0.3$) indicate a non relaxed state of clusters. This parameter has to be taken into account for the morphology.

Finally clusters will be classified according to the following scheme:

- relaxed clusters: clusters presenting one gaussian peak ($\chi^2 \leq 0.2$) and one isolated clump ($\epsilon \leq 0.3$) in projection;
- bimodal major mergers: clusters presenting two massive components (with mass ratio greater than 1:2) (i) one gaussian peak (χ^2) and two massive interacting clumps, (ii) two close gaussian peaks and one clump in projection or (iii) two gaussian peaks corresponding to two massive clumps in projection;
- minor mergers: clusters having in their surrounding one or more structures with mass ratio between 1:2 and 1:5, they correspond to several gaussian peaks or several clumps in projection;
- multiple mergers: clusters having in their surroundings at least one other massive (with mass ratio greater than 1:2) cluster and one or several clumps less massive (with mass ratio between 1:2 and 1:5);
- clusters in virialisation phase or in merging state that do not allow to detect substructures: clusters with non gaussian peak or with a high ellipticity ($\epsilon \geq 0.3$).

4 Application to C4 clusters

The extraction method of galaxies in SDSS give fields of galaxies, *i.e.* a cone of galaxies, whose angular size corresponds to an angular size of 5 Mpc at the C4 cluster redshift. To disentangle piled up structures along the line of sight and keep only the cluster (namely to remove projection effects) galaxy redshift was used. The galaxy redshift distribution function (hereafter RDF) for each field has been computed using a multi-scale approach in the same way as for density maps but in one dimension. The redshift distribution function of the C4 cluster 0090 is represented in the left panel of Figure 1. By computing the RDF cluster redshift interval can be determined. Indeed the reconstruction algorithm removes the constant contribution of the signal and keeps only 3σ significant structures which means that the computed RDFs are composed by regions with significant signal delimited by regions with no signal. Clusters being galaxy concentration in the redshift space they contribute significantly to the RDF. In one field there may be several redshift regions with significant signal. The one containing the most galaxies appears to have the closest redshift to the corresponding C4 cluster thus this region will be the cluster redshift interval. In this interval of redshifts, galaxy redshifts will be analyzed to determine if they correspond to one or more gaussian peaks and if a single peak is found if this one is really gaussian or not. The decomposition of the RDF into a gaussian mixture is done by EMMIX software (McLachlan & Peel 1999). EMMIX detects all gaussian peaks nevertheless not all peaks are physically significant and only peaks more massive than $10^{13} M_{\odot}$ are considered. EMMIX gives the three important parameters of the gaussian peaks: the mean, the standard deviation and the number of objects belonging to the peak. To assess the quality of the fit, χ^2 were computed between EMMIX gaussian fit and the RDF computed with the wavelet analysis. If the gaussian hypothesis is not correct for a cluster, its EMMIX fit will not be accurate and then its χ^2 will be high. The threshold value chosen to consider a cluster to be well fitted by a gaussian mixture is 0.2: higher values mean that cluster can not be described by a gaussian mixture.

Following the analysis along the line of sight, cluster density maps have been computed as described in section 3. The detection of clumps on density maps has been done using SExtractor software (Bertin & Arnouts 1996). SExtractor fits detections (clumps) in an image by ellipses and gives all their geometrical parameters (position, semi-major and minor axes, orientation ...) and "physical" parameters (FWHM, flux in an isocontour ...). Here the important parameters are the geometrical ones and the FISO parameter which is the flux in the lowest isocontour of clumps. Density maps being the projected galaxy distribution function, the FISO parameter measures the number of galaxies in the clumps. The cluster is the clump with the most galaxies thus the highest FISO. Only clumps that may be significantly interacting with the main cluster are kept, clumps with $FISO \geq 0.1 FISO_{cluster}$. The interaction between clumps has to be verified as indicated in section 3. Virial radii are computed using Finn et al. (2008) formula (their Eq. 4). Galaxies are affected to their clumps and clump velocity dispersion is computed. Finally for isolated clusters (no cluster close and massive enough to interact) their ellipticity is compared to 0.3.

With cluster environment along the line of sight and in projection and the indication of gaussianness and ellipticity, the 179 clusters were classified into the 5 categories. 59 clusters (33%) are relaxed, 10 (6%) are major bimodal mergers with mass ratio greater than 1:2. 56 clusters (31%) are minor mergers with mass ratio comprised between 1:2 and 1:5. 36 clusters (20%) are multiple mergers with at least one major merger and at least one minor merger. The last 18 clusters (10%) are in virialisation phase.

5 Conclusion

33% of relaxed clusters is in good agreement with previous studies which find between 30% and 70% of relaxed clusters in the local universe (Dressler & Shectman 1988). This classification gives a statistical sample of clusters to study environment effects on galaxies according to their cluster dynamical state and see if (i) there is a correlation between the cluster morphology and the fraction of star forming galaxies and if (ii) the cluster morphology has an impact on the distribution of star forming galaxies: if they are distributed rather in cluster outskirts or innerparts.

References

- Abazajian, K., Adelman-McCarthy, J. K., Agüeros, M. A., et al. 2004, AJ, 128, 502
 Ashman, K. M., Bird, C. M., & Zepf, S. E. 1994, AJ, 108, 2348
 Bautz, L. P. & Morgan, W. W. 1970, ApJ, 162, L149

- Beers, T. C., Flynn, K., & Gebhardt, K. 1990, *AJ*, 100, 32
- Bertin, E. & Arnouts, S. 1996, *A&AS*, 117, 393
- Buote, D. A. & Tsai, J. C. 1996, *ApJ*, 458, 27
- Dressler, A. & Shectman, S. A. 1988, *AJ*, 95, 985
- Fadda, D., Slezak, E., & Bijaoui, A. 1998, *A&AS*, 127, 335
- Ferrari, C., Benoist, C., Maurogordato, S., Cappi, A., & Slezak, E. 2005, *A&A*, 430, 19
- Finn, R. A., Balogh, M. L., Zaritsky, D., Miller, C. J., & Nichol, R. C. 2008, *ApJ*, 679, 279
- Flin, P. & Krywult, J. 2006, *A&A*, 450, 9
- Geller, M. J. & Beers, T. C. 1982, *PASP*, 94, 421
- Jones, C. & Forman, W. 1999, *ApJ*, 511, 65
- Kolokotronis, V., Basilakos, S., Plionis, M., & Georgantopoulos, I. 2001, *MNRAS*, 320, 49
- McLachlan, G. & Peel, D. 1999, *Journal of Statistical Software*, 4, 1
- Melott, A. L., Chambers, S. W., & Miller, C. J. 2001, *ApJ*, 559, L75
- Miller, C. J., Nichol, R. C., Reichart, D., et al. 2005, *AJ*, 130, 968
- Mohr, J. J., Fabricant, D. G., & Geller, M. J. 1993, *ApJ*, 413, 492
- Navarro, J. F., Frenk, C. S., & White, S. D. M. 1995, *MNRAS*, 275, 720
- Plionis, M. 2002, *ApJ*, 572, L67
- Ramella, M., Biviano, A., Pisani, A., et al. 2007, *A&A*, 470, 39
- Rood, H. J. & Sastry, G. N. 1971, *PASP*, 83, 313
- Schuecker, P., Böhringer, H., Reiprich, T. H., & Feretti, L. 2001, *A&A*, 378, 408

INSTRUMENTAL CALIBRATION OF WIDE FIELD IMAGERS

F. Villa¹ and the SNDice collaboration

Abstract. Photometric calibration is becoming a crucial issue in various cosmological measurements, such as the measurement of the cosmological parameters with Type Ia Supernovae (SNe Ia). To achieve the accuracy level of $\sim 0.1\%$ required by future surveys, several collaborations are studying new instrumental calibration strategies. We report on the SNDice project. SNDice is a very stable illuminating system installed at the Canada-France-Hawaii Telescope (CFHT). The goal is to demonstrate that, with such an instrument, it is possible to monitor the instrument response with a precision of 0.01% , and to deliver a flux calibration accurate at the 0.1% level.

Keywords: Type Ia Supernovae, calibration, SNDice

1 Introduction

Type Ia Supernovae are one of the most powerful cosmological probes to study the properties of Dark Energy (Sullivan et al. 2011; Conley et al. 2011; Guy et al. 2010; Amanullah et al. 2010). The next generation of very large surveys (DES, Euclid, LSST) will detect and study thousands of SNe Ia. The measurement of the Dark Energy Equation of State will reach a statistical precision of 1% or better (Abell et al. 2009).

The challenge is now to reduce systematic uncertainties to a comparable level. The dominant contribution to the systematic error budget is the photometric calibration of the imagers. Future surveys will require a flux calibration accurate at the per-mil level. This seems difficult to obtain with the traditional techniques relying on standard star observations. For this reason, supernova surveys are exploring alternative approaches. For instance, the SNLS collaboration began to invest in the SNDice project. SNDice is a demonstrator, designed and built at LPNHE in Paris, which was installed in 2008 in the enclosure of the Canada-France-Hawaii Telescope (CFHT) in Mauna Kea (Hawaii) (Juramy et al. 2008; Barrelet & Juramy 2008). The goal is to show that it is possible to obtain a photometric calibration accurate at the 0.1% level or better.

In what follows, we present the design of the SNDice instrument. We review the many applications of the system, such as the monitoring of the telescope readout electronics, the study of the camera uniformity and the measurement of the imager passbands. Finally, we detail the analysis of the SNDice data and explain how this strategy may be an alternative to the traditional calibration techniques.

2 The SNDice instrument

SNDice (SuperNova Direct Illumination Calibration Experiment) is a photometric calibration device which has been optimized to study the MegaCam imager (Boulade et al. 2003). The instrument consists in a calibrated light source composed of 24 narrow spectrum (Fig. 1 *right*) LEDs ($\delta\lambda/\lambda \sim 7\%$). Their emission wavelengths cover the MegaCam bandwidth from the UV to the IR. LEDs have been chosen for the stability of their emission and their spectral properties. Each LED emits a 1° wide conical beam which illuminates the whole CCD camera. Each LED beam covers a ~ 30 cm wide area on the primary mirror and generates a nearly flat illumination on the focal plane. In each LED channel, a calibration photodiode is placed off-axis in front of the LED to monitor the light output as a function of time and input current. Finally, the light source can be oriented to allow one to align SNDice and MegaCam optical axes.

In 2008, a prototype of SNDice was installed in the CFHT enclosure. Since then, SNDice is taking data and two upgrades of the motorization were made.

¹ Laboratoire de Physique Nucléaire et de Hautes Energies, Tour 22, 1er étage, 4 Place Jussieu, 75252 Paris Cedex, France

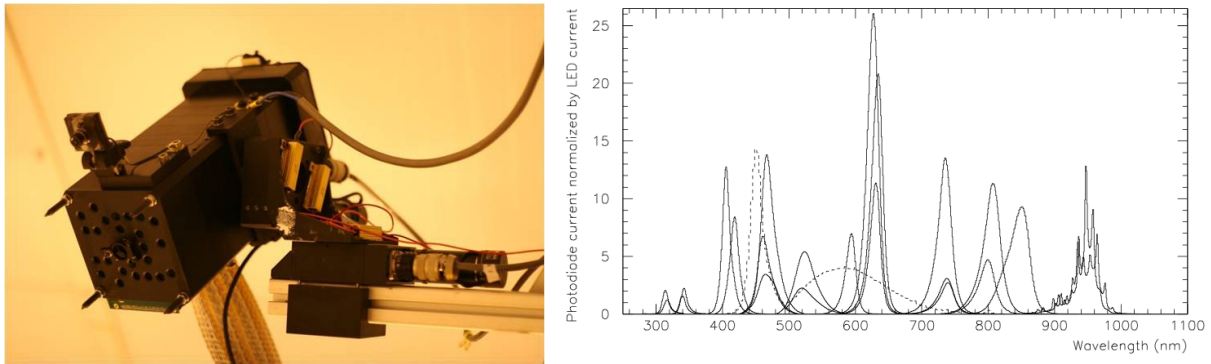


Fig. 1. Left: The SNDice demonstrator in the CFHT enclosure. **Right:** Spectra of the 24 LEDs composing the light source.

3 Test bench studies

Prior to its installation, the SNDice instrument has been characterized and calibrated on a precision test bench at LPNHE. The main products of these studies are:

- maps of the radiant intensity of each LED beam, accurate at the 0.1% level,
- spectra of each LED, measured with a similar precision.

The calibration was performed on short range and long range distances. The short range measurements have been done on a 2.5 m test bench enclosed in a black box. A 12 m-long black tube was used for the long range calibration. In both configurations, the light source was placed at a fixed position in the black box. The photometric calibration of each LED was done using a NIST (National Institute of Standard of Technology) photodiode. This photodiode was mounted on a 3D motorization including a 1.5 m-long axis for motion parallel to the light source axis. Each LED beam was mapped in a 30×30 cm² region perpendicular with respect to the source axis. The short distance setting allowed us to map each LED beam, whereas the long distance configuration was necessary to reproduce the study at a distance similar to CFHT focal length. LED spectra have been calibrated to determine their variations as a function of temperature.

The illuminating system has been proved to be stable at the 0.01% level.

4 The monitoring of MegaCam

The response function of MegaCam is likely to change over time. First, the gains of the readout electronics are subject to variations over time scales of a few hours. Second, the transmission of the instrument degrades slowly over time. This affects the zero points of the instrument, as well as the flat-field structure. Given its 0.01% stability, SNDice is a good tool to measure these effects.

As an example, the gains of the 72 amplifiers of the MegaCam CCDs have been measured throughout one year of data acquisitions. The average values of the gains for 2010 are showed on the left panel of Fig. 2. Since the SNDice illumination of the focal plane is uniform, the amplifier gains have been obtained through the variance of the Poissonian distribution of the fluxes measured in each pixel. The monitoring of the readout electronics reached a precision such that it was possible to study the gain variability from one run to another. Variations up to 1% have been highlighted. The values for February 2010 and July 2010 are showed on the right panel of Fig. 2. The gain variations are correlated for the nearby amplifiers.

5 The SNDice exposures

Fig. 3 (*left*) gives an example of a SNDice exposure. As we will see in this section, each exposure encodes a lot of information on the imager internals.

First, one can see differences from amplifier to amplifier. These are due to the gain differences from one amplifier to another, and also to variations of quantum efficiencies from one CCD to another. By requiring that

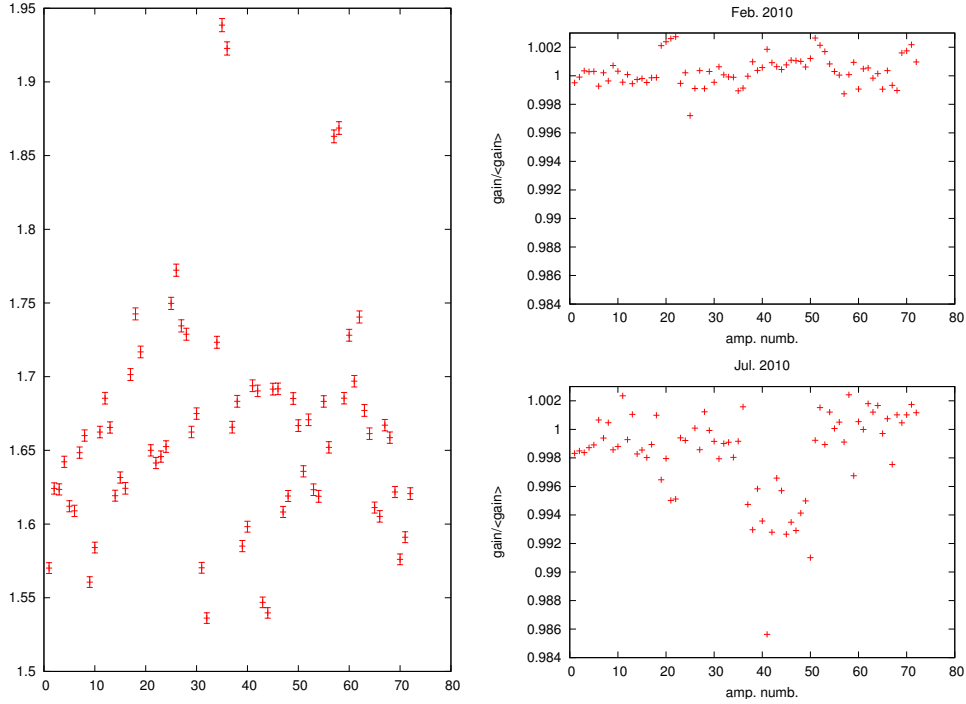


Fig. 2. Left: The gains averaged over time for the 72 amplifiers. **Right:** On the top panel, the gain values for data taken on February 2010; on the bottom panel, gains measured on July 2010. The precision of the SNDice system allowed one to study gain variations at the 0.1% level with respect to the average value over the year. Correlations between nearby amplifiers have been found.

the focal plane illumination is continuous, it is possible to determine the relative ratios of the gains and CCD quantum efficiencies and to monitor their variations.

The diffraction patterns caused by imperfections and dusts settled on the optics are another feature present on raw images. Fortunately, it is quite easy to deal with this effects by resampling the images in “superpixels” and by calculating the median of the fluxes in each “superpixel”.

Once these sources of non-uniformities are accounted for, one can see that the exposure integrates not only the direct light, but also the light from internal reflections within the imager. As an example, in Fig. 3 (*right*) one sees clearly the reflexion of the focal plane on the cryostat window. Also, it is easily visible the “pincushion” due to light reflected by the filter and lens L4 of the wide field corrector. Depending on the focal plane position and on the illuminating LED, the indirect light may represent 0.5% to 20% of the direct light. Hence, we need a model to disentangle the direct and indirect light. Note that any flat-field is similarly affected by internal reflections. However, due to the very simple design of SNDice, it is possible to build a model of the reflections, that can predict the illumination on a point (x,y) of the focal plane. This model can be written as:

$$\Phi_{\text{ADU}}(x, y) = g_{\text{amp}} \int \varepsilon_{\text{CCD}}(\lambda) \cdot T(\lambda, \mathbf{x}) \cdot \mathcal{B}(\lambda, \mathbf{x}) d(\lambda) + \text{reflections}(\mathbf{x}) + \text{dust diffractions}$$

where $\mathcal{B}(\lambda, \mathbf{x})$ is the model of the LED quasi-Lambertian beam.

6 Modeling the focal plane illumination

The determination of the illumination $\mathcal{B}(\lambda, \mathbf{x})$ on the focal plane depends on the measurement of the LED beam at the source and on its propagation through the optics. The illumination delivered by SNDice is well known thanks to the test bench. To predict the beam shape after the optics, it is necessary to simulate the propagation. To do this, the main tool is a very simple ray-tracer simulating the SNDice-MegaCam system. This software is based on C++ CERN ROOT libraries. As shown in Fig. 4 (*left*), it is able to reproduce MegaCam optics and to model direct and secondary paths of the SNDice light propagation through them. Finally we are able to simulate

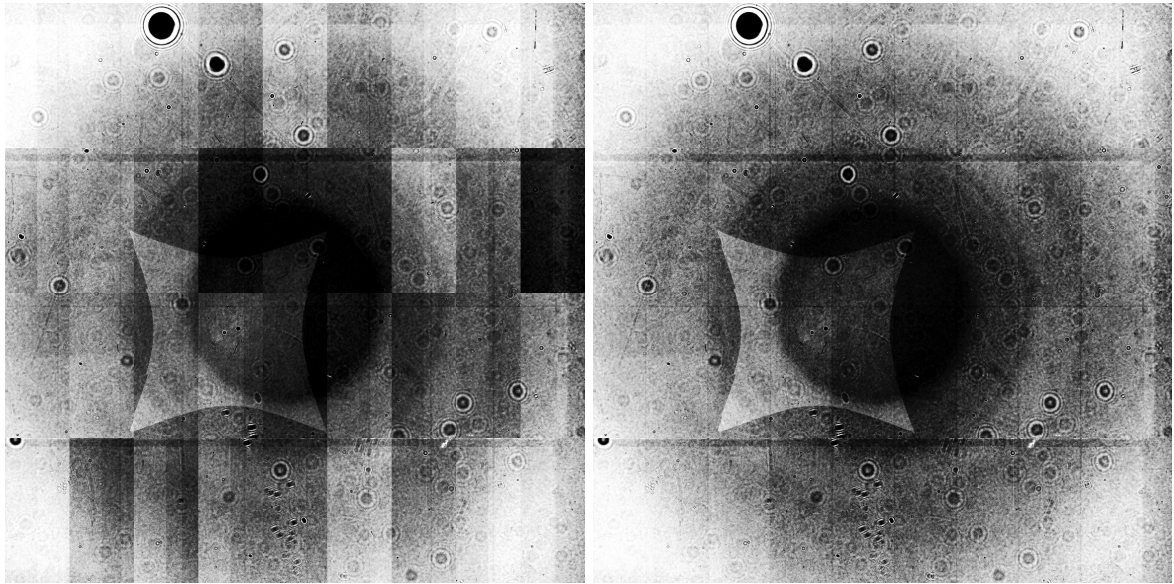


Fig. 3. Left: Raw SNDice exposure: the dominant effect are the differences from an amplifier to another. These non-uniformities are caused by the different gains of the readout electronics and the variations of the quantum efficiencies from a CCD to another. The diffraction patterns caused by dusts or imperfections on the optical path are visible too. **Right:** SNDice exposure after the correction for the gains and the CCD quantum efficiencies. The correction highlights other effects due to reflections in the optics (the central “pincushion” due to the light reflected by the curved surface of lens L4, the reflection of lens L3 on the lower left corner of the focal plane) as well as the radial variation of passband transmission.

an exposure to distinguish between direct illumination, see Fig. 4 (*center*), and reflection contamination, shown in Fig. 4 (*right*), (which can reach up to 20% of the direct light intensity). The determination of the direct

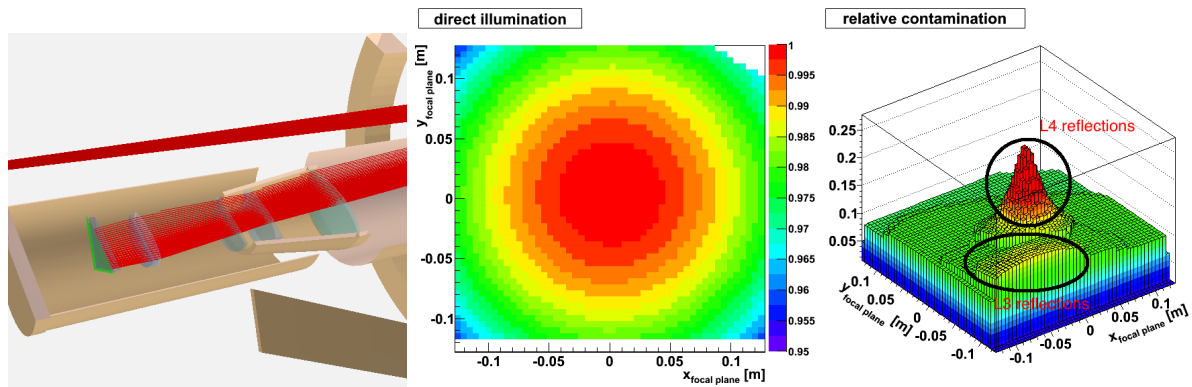


Fig. 4. Left: Simulation of the SNDice beam illuminating the primary mirror. **Center:** The direct illumination of the focal plane. Determining the amount of the direct contribution is a crucial point to gain in precision. **Right:** Spatial distribution of the internal reflection relative contamination on the MegaCam focal plane. The hugest contributions are the reflections due to the curved surfaces of L4 and L3 lenses.

illumination on the focal plane is the crucial measurement to improve the precision of the photometric calibration through the optimization of the flat-fielding technique.

7 Conclusions and perspectives

The analysis of SNDice exposures is an ongoing work. Once the determination of the reflection contamination is achieved, next steps will be the study of the MegaCam focal plane uniformity and the optimization of the

flat-fielding procedure with SNDice exposures.

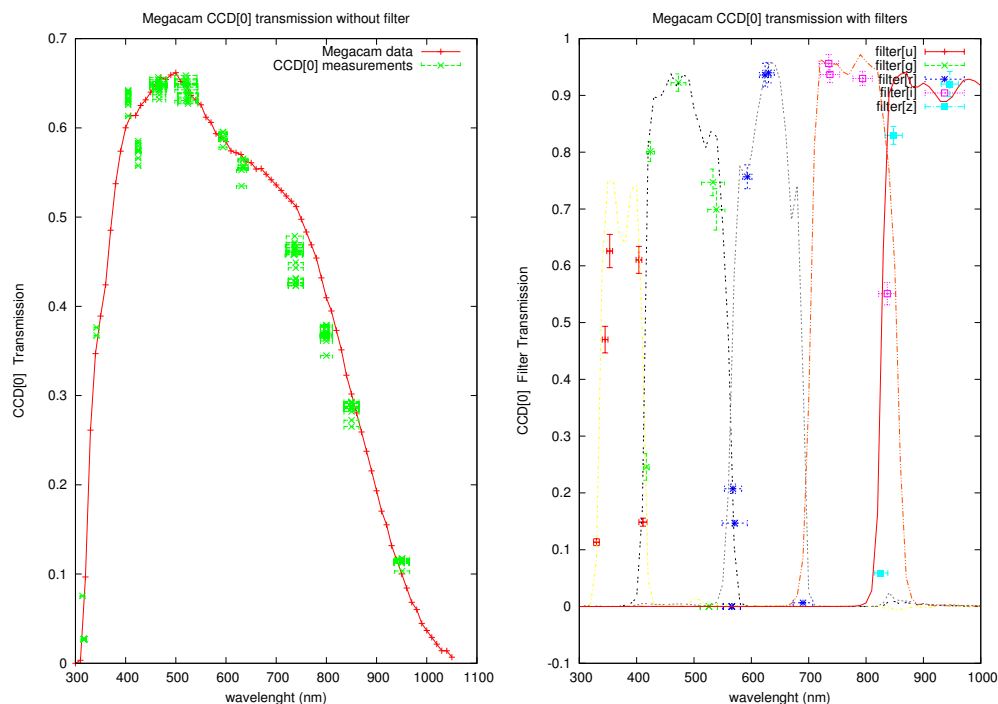


Fig. 5. Left: Open transmission. **Right:** Filter responses: the curves are the theoretical transmissions, the points are the measurements of the 24 LEDs fluxes.

Furthermore, there are ongoing studies on the determination of the normalized transmissions of the imager passbands. Preliminary results are shown in Fig. 5. On the left, the open transmission of the MegaCam is displayed: it has been obtained comparing the MegaCam flux on CCD #0 to the flux measured by the control photodiode mounted in front of the LED. The plot in Fig. 5 (right) shows the filter transmissions measured on CCD #0 as the flux ratio of an exposure taken with filter over one without filter. The aim of the study on the filters is the extraction of normalized passband transmissions with an accuracy better than 1%. The achievement of this analysis depends on the measurement of the variation of LED spectra as function of temperature (test bench studies at LPNHE).

References

- Abell, P. A., Allison, J., Anderson, S. F., et al. 2009, LSS Science Book, Version 2.0, ArXiv e-prints 0912.0201
- Amanullah, R., Lidman, C., Rubin, D., et al. 2010, ApJ, 716, 712
- Barrelet, E. & Juramy, C. 2008, Nuclear Instruments and Methods in Physics Research A, 585, 93
- Boulade, O., Charlot, X., Abbon, P., et al. 2003, in SPIE Conference Series, Vol. 4841, SPIE Conference Series, ed. M. Iye & A. F. M. Moorwood, p. 72
- Conley, A., Guy, J., Sullivan, M., et al. 2011, ApJS, 192, 1
- Guy, J., Sullivan, M., Conley, A., et al. 2010, A&A, 523, A7
- Juramy, C., Barrelet, E., Schahmaneche, K., et al. 2008, in SPIE Conference Series, Vol. 7014, SPIE Conference Series, ed. I.S. McLean & M. Casali, p. 701451
- Sullivan, M., Guy, J., Conley, A., et al. 2011, ApJ, 737, 102

LYMAN HORIZONS IN THE EARLY PHASES OF THE EPOCH OF REIONIZATION

P. Vonlanthen¹ and B. Semelin^{1,2}

Abstract. It has been shown that the radial profile of the Lyman- α flux around light sources emitting in the Lyman band during the early phases of the epoch of reionization is characterized by a series of step-like discontinuities. This property originates in the fact that the neutral intergalactic medium is optically thick at the frequencies of all the Lyman-series lines. We show that, through unsaturated Wouthuysen-Field coupling, these spherical discontinuities are also present in the redshifted 21 cm signal of neutral hydrogen. We use realistic 3D numerical simulations with full radiative transfer calculation in the first five Lyman lines in order to study the properties of these discontinuities and the possibility for detection with the future Square Kilometre Array. Although challenging, these observations could provide a diagnostic tool to disentangle the cosmological signal and residuals from imperfect foreground removal.

Keywords: Radiative transfer, intergalactic medium, large-scale structure of Universe, dark ages, reionization

1 The 21 cm signal

The epoch of reionization is the period in the history of our universe during which the neutral intergalactic medium underwent a major phase transition and became progressively ionized under the influence of the first light sources. This epoch is constrained by a few number of observations only and its most promising probe is the future observation of the redshifted 21 cm line corresponding to the transition between the two hyperfine levels of the HI electronic ground state. The differential brightness temperature of this signal, compared to the cosmic microwave background (CMB), is determined by the following expression (see e.g. Madau et al. 1997; Ciardi & Madau 2003):

$$\delta T_b = 28.1 x_{\text{HI}} (1 + \delta) \left(\frac{1+z}{10} \right)^{1/2} \frac{T_s - T_\gamma}{T_s} \left(\frac{\Omega_b}{0.042} \frac{h}{0.73} \right) \left(\frac{0.24}{\Omega_m} \right)^{1/2} \left(\frac{1 - Y_p}{1 - 0.248} \right) \text{mK}, \quad (1.1)$$

where x_{HI} is the neutral hydrogen fraction, $(1 + \delta)$ the fractional baryon overdensity at redshift z , T_γ the CMB temperature, and T_s the spin temperature, which is related to the ratio of the densities of HI atoms in the two hyperfine levels. Ω_b , Ω_m , h , and Y_p denote the usual cosmological parameters. From that equation, we clearly see that observations of the line are only possible when the spin temperature is different from the CMB temperature. Three processes can excite the hyperfine levels: absorption of CMB photons, collisions, and the Wouthuysen-Field effect. The latter is a radiative coupling mechanism which mixes the two hyperfine levels through absorption and reemission of Ly α photons (Wouthuysen 1952; Field 1958). Thus, the spin temperature can be written as

$$T_s^{-1} = \frac{T_\gamma^{-1} + x_\alpha (T_c^{\text{eff}})^{-1} + x_c T_k^{-1}}{1 + x_\alpha + x_c}, \quad (1.2)$$

where T_c^{eff} is the effective color temperature of the UV radiation field, T_k the gas kinetic temperature, x_α the coupling coefficient for Ly α pumping, and x_c the coupling coefficient for collisions. Once the first radiation

¹ LERMA, Observatoire de Paris, 61 av. de l'Observatoire, 75014 Paris, France

² Université Pierre et Marie Curie, 4 Place Jules Janssen, 92195 Meudon Cedex, France

sources appear, the Wouthuysen-Field mechanism is the dominant effect likely to decouple the spin temperature and the CMB temperature. In relation with the local Ly α flux, x_α can be written as

$$x_\alpha = \frac{16\pi^2 T_\star e^2 f_\alpha}{27 A_{10} T_\gamma m_e c} S_\alpha J_\alpha, \quad (1.3)$$

with e the electron charge, f_α the Ly α oscillator strength, $A_{10} = 2.85 \times 10^{-15} \text{ s}^{-1}$ the spontaneous emission factor of the 21 cm transition, m_e the electronic mass, c the speed of light and J_α the angle-averaged specific intensity of Ly α photons by photon number. $T_\star = h\nu_{10}/k_B = 0.0682 \text{ K}$ is the temperature corresponding to the energy difference between the two hyperfine levels, with h the Planck constant, $\nu_{10} = 1420.4057 \text{ MHz}$ the hyperfine transition frequency and k_B the Boltzmann constant. Finally, the backreaction factor S_α accounts for spectral distortions near the Ly α resonance that are caused by recoils and spin diffusivity.

2 Goal of the study

Our goal is to study the role of higher-order Lyman-series photons in the determination of the differential brightness temperature of the 21 cm signal of HI. We are motivated by the fact that the local Ly α photon intensity around primordial sources is made of two contributions (Hirata 2006; Pritchard & Furlanetto 2006):

1. Photons emitted below the Ly β frequency that redshift to the Ly α frequency as they propagate in the intergalactic medium (IGM);
2. Photons emitted between Ly β and the Lyman limit that redshift until they reach the nearest Lyman resonance. Because the IGM is optically thick to all the Lyman lines, these photons are absorbed. The subsequent radiative cascades have a given probability to end with the emission of extra Ly α photons.

As a consequence, the radial profile of the Ly α flux around sources emitting in the Lyman band shows a series of steps at the positions of the so-called Lyman horizons, i.e. at distances from the source where photons emitted just below the Ly $(n+1)$ frequency reach the Ly n frequency. Because of the Wouthuysen-Field effect, similar structures appear in the redshifted 21 cm signal. We perform realistic numerical simulations including hydrodynamics and 3D radiative transfer of both ionizing and Lyman band photons, using the code LICORICE (Semelin et al. 2007; Baek et al. 2009; Iliev et al. 2009). The simulated volumes have a minimum size of $100 h^{-1}$ comoving Mpc. We take into account the first five Lyman-series lines and include the backreaction effect using the simple analytical fit from Hirata (2006). We consider here purely stellar sources (no X-rays), characterized by a Salpeter IMF with masses in the range 1-120 M_\odot .

3 Lyman horizons

We clearly detect Lyman horizons in the early phases of our simulations. As an example, Fig. 1 shows a map of the quantity* ($-\delta T_b \times r^2$) at $z = 13.42$, with r the distance to the source center, in arbitrary units (Vonlanthen et al. 2011). The source (white spot) is the first to light up at $z = 14.06$ in a $100 h^{-1}$ comoving Mpc simulation. The Ly ϵ , Ly δ and Ly γ horizons are marked with white, yellow and red arrows respectively. The slice thickness is $2 h^{-1}$ comoving Mpc and the colorscale is logarithmic. Note that there is no Ly β horizon. Indeed, because of quantum selection rules, a Ly β photon cannot produce a Ly α photon. The sizes of the horizons can be precisely computed. In the redshifts of interest for this study ($z \approx 14-10$), the result is in the range 50-59 comoving Mpc for the Ly γ discontinuity, 27-31 comoving Mpc for Ly δ , and 16-19 comoving Mpc for Ly ϵ , assuming standard values for the cosmological parameters.

Furthermore, we find that detection of these features are seriously affected by the appearance of other nearby sources. This is illustrated in the left panel of Fig. 2, in which we plot the gradient of the spherically averaged δT_b profile around the same source as in Fig. 1. The four panels show the profile at different redshifts, from $z = 13.22$ to $z = 11.64$. At early times, Lyman horizons are detected as peaks in the δT_b gradient at the predicted positions (indicated by arrows). But as more and more sources light up, fluctuations in the Ly α background around individual sources appear, which translates into similar fluctuations in the 21 cm signal. We find that the Ly ϵ and Ly δ discontinuities can be detected during an interval $\Delta z \sim 2$ after the first source

*As δT_b is approximately proportional to r^{-2} , mapping the product of the differential brightness temperature and r^2 will straighten up the radial profiles and improve visualization.

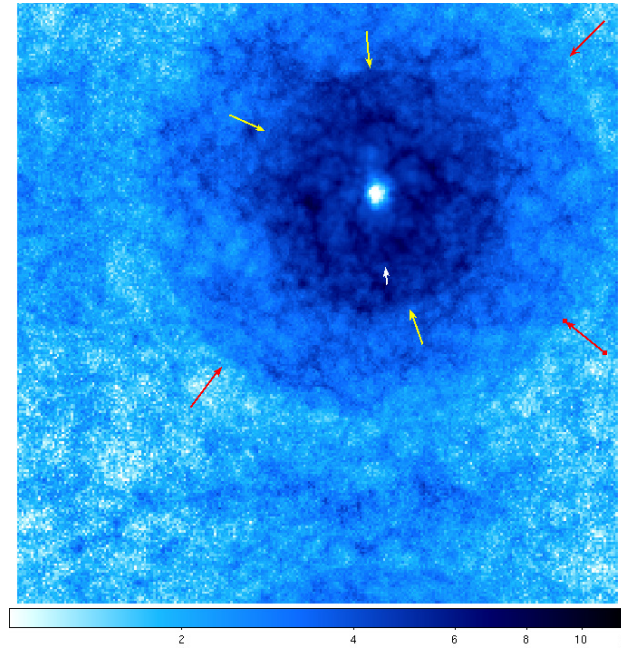


Fig. 1. Map of the quantity $-\delta T_b \times r^2$ at $z = 13.42$, with r the distance to the source center, in arbitrary units. We indicate the positions of the Ly ϵ , Ly δ and Ly γ horizons with white, yellow and red arrows respectively.

lights up, with temperature jumps in the range 2-4 mK. The Ly γ horizon is weaker and is observable during an interval $\Delta z < 1.5$ only.

Stacking all the individual profiles inside the simulation box at a given redshift allows us to extend the detectability period for the Ly δ and Ly ϵ horizons to $\Delta z \sim 4$, that is for $10 < z < 14$ in our simulations.

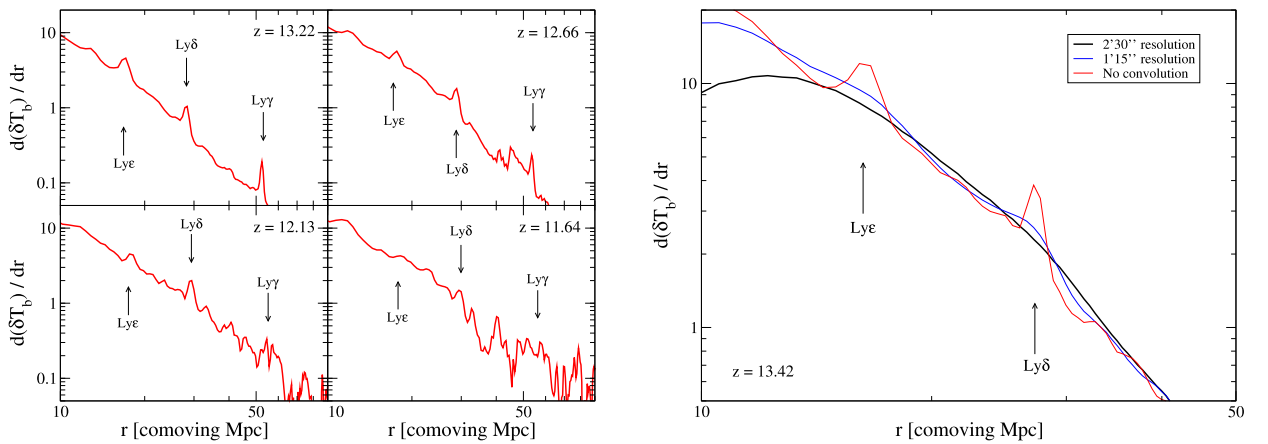


Fig. 2. Left: Gradient of the spherically averaged profile of the differential brightness temperature, around the same source as in Fig. 1. The four panels show the profile at different redshifts. Arrows indicate the predicted positions of the first three horizons. **Right:** The thick black line shows the gradient of the δT_b stacked profile in a $200 h^{-1}$ comoving Mpc simulation at $z = 13.42$, with SKA-like noise, assuming a field of view of 400 deg^2 , and a $2'30''$ resolution. The horizons are wiped off by the limited SKA resolution. The blue line assumes an optimistic $1'15''$ resolution. The red line shows, for comparison, the gradient of the profile without noise nor resolution effect.

4 Detection with the Square Kilometre Array?

Detection of these distinctive rings in the future 21 cm observations would be of great interest for people involved in the very difficult task of foreground removal. Indeed, these structures of known sizes at a given redshift could provide a diagnostic tool for the cosmological origin of the detected signal after removal procedures.

For that reason, we investigated the possibility for detection with the planned Square Kilometre Array (SKA). In order to do so, we included in our simulated data the effect of both SKA noise and resolution. The effect of noise can be softened if we consider a large field of view (several hundreds of square degrees) and stacking of the radial profiles around sources. The most limiting factor will probably be the limited resolution of the instrument. Indeed, assuming the currently favored design, the 5-km core translates into a resolution between $2'$ and $3'$ in the range $10 < z < 14$. The right panel of Fig. 2 shows that such a resolution completely erases the Lyman horizons (black line). However, if we optimistically assume a resolution that is twice better (corresponding to a 10-km core), then the Ly δ horizon can be observed as a wide and weak hump (blue line).

We conclude from this figure that detection of the Lyman horizons in the early phases of the epoch of reionization using the SKA will be a challenging task. It could be possible for the Ly δ horizon with a resolution of the order of one arcminute.

This work was realized in the context of the LIDAU project. The LIDAU project is financed by a French ANR (Agence Nationale de la Recherche) funding (ANR-09-BLAN-0030). PV acknowledges support from a Swiss National Science Foundation (SNSF) post-doctoral fellowship. This work was performed using HPC resources from GENCI-[CINES/IDRIS] (Grant 2011-[x2011046667]).

References

- Baek, S., Di Matteo, P., Semelin, B., Combes, F., & Revaz, Y. 2009, *A&A*, 495, 389
Ciardi, B. & Madau, P. 2003, *ApJ*, 596, 1
Field, G. B. 1958, *Proc. I. R. E.*, 46, 240
Hirata, C. M. 2006, *MNRAS*, 367, 259
Iliev, I. T., Whalen, D., Mellema, G., et al. 2009, *MNRAS*, 400, 1283
Madau, P., Meiksin, A., & Rees, M. J. 1997, *ApJ*, 475, 429
Pritchard, J. R. & Furlanetto, S. R. 2006, *MNRAS*, 367, 1057
Semelin, B., Combes, F., & Baek, S. 2007, *A&A*, 474, 365
Vonlanthen, P., Semelin, B., Baek, S., & Revaz, Y. 2011, *A&A*, 532, A97
Wouthuysen, S. A. 1952, *AJ*, 57, 31

Session 02

Helio- and astero-seismology, advances and perspectives in the context of new space missions and ground-based instruments

THE HELIUM SHELLS OF HE I AND HE II AT SOLAR MINIMUM: NEW RESULTS FROM ECLIPSE FLASH SPECTRA OF 2008- 2010

C. Bazin^{1,2}, S. Koutchmy³ and P. Lamy⁴

Abstract. Flash spectra taken at high frame rate during the total solar eclipse of August 1st 2008 in Siberia and during the July 11th 2010 in French Polynesia are compared in the context of the quiet Sun near the minimum of activity. They both reveal the weak Paschen α 468.6 nm ionized helium line, seen as a helium shell in layers up to the 8 Mm heights. The preliminary evaluated effective height of the He I 4713 shell is 1.8 Mm and it is approximately 2.0 Mm for the He II 4686 emissions outside polar regions. These lines can be measured only in eclipse conditions, when the parasitic scattered light is negligible for very low solar fluxes corresponding to the coronal levels. Many faint lines are also seen in emission such as Ba +, Ti +, Fe +, but with a much lower radial extension. They were observed to be superposed to F-lines when defining the solar limb using the continuum background. A cartoon is proposed to describe the structuration of these low layers and to illustrate the contribution of the magnetic field. These observations are important new insights for understanding (i) the magnetic field inference in the very low layers of the solar transition region and (ii) the ionisation mechanisms producing the big jump of the temperature towards the corona, including the source of heating.

Keywords: ionized helium He II 4686, total solar eclipses, flash spectra, helium shells, solar transition region, intensity profiles, layers, faint emission lines

1 Observations and analysis of the helium shells

The faint emission lines and the helium lines were identified in the flash spectra at the last total eclipse of July 2010. (Mitchell 1935) (Bazin et al. 2009), (Hirayama & Irie 1984), (Zirin 1975), (Zirin 1975). The extension of the He I shell is evaluated to be 1.8 Mm and it is 2.0 Mm for the He II second helium shell. This result is almost in agreement of what was known for the helium He I shell D3 bright line (Avrett & Koutchmy 1989). But this difference of the extension is linked with the higher temperatures, and the ionisation potential of He II Paschen α is 54 eV, and 24 eV for the He I line (Athay 1965), (Koutchmy et al. 2009).

2 Cartoon of the TR of the layers above the limb.

We show the low layers of the transition region, and the field lines of the emerging magnetic field.

The red lines indicate the magnetic boundaries of the more dense plasma (Athay & Menzel 1956). Black lines are the magnetic lines of force. η means the filling factor or heterogeneity factor, and β is the ratio of gas pressure to magnetic pressure. (Bazin et al. 2009).

References

- Athay, R. 1965, ApJ, 142, 755
Athay, R. & Menzel, D. 1956, ApJ, 123, 285

¹ UPMC Univ Paris 06, UMR 7095, Institut d'Astrophysique de Paris, F-75014, Paris, France

² CNRS, UMR 7095, Institut d'Astrophysique de Paris, F-75014, Paris, France

³ Institut d'Astrophysique de Paris, F-75014, Paris, France

⁴ LAM-OAMP-UMR 6110-CNRS Pole de l'Etoile Site de Chateau-Gombert 38, rue Frederic Joliot-Curie 13388 Marseille cedex 13 France

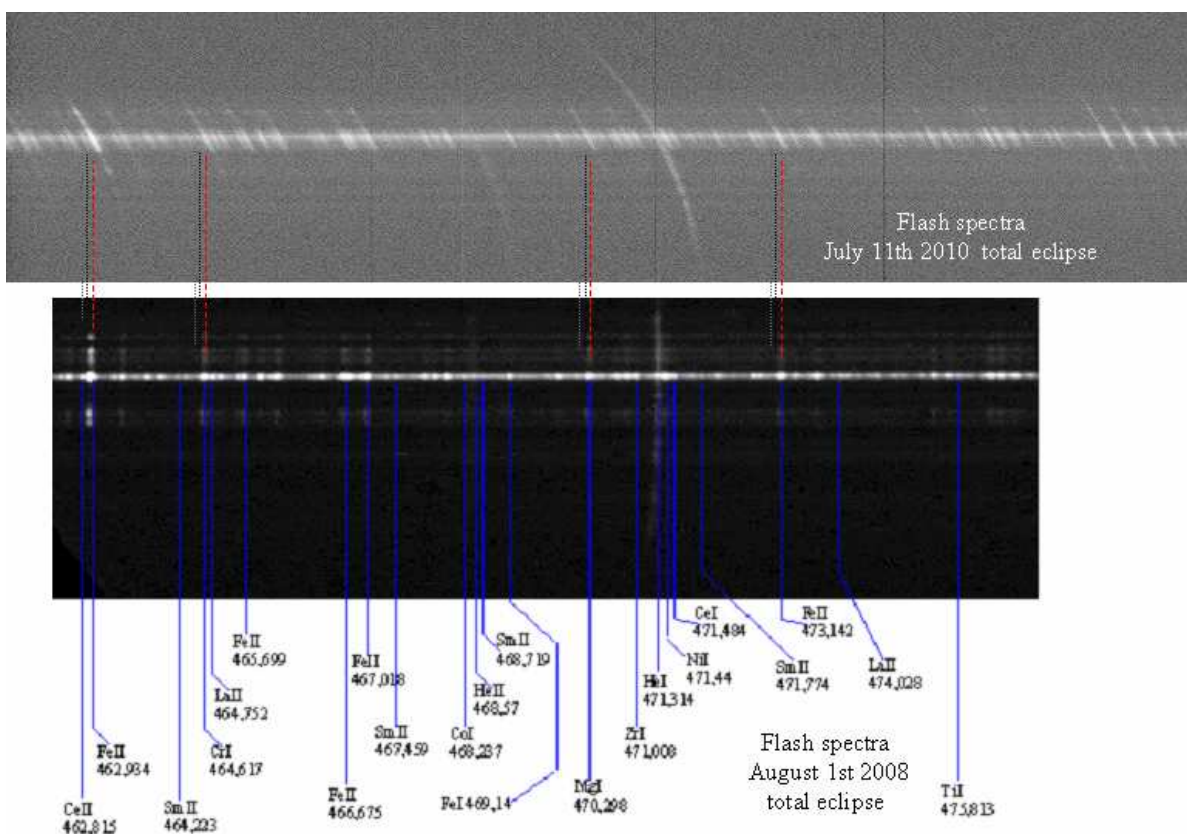


Fig. 1. Flash spectrum at the 2008 and 2010 total eclipses.

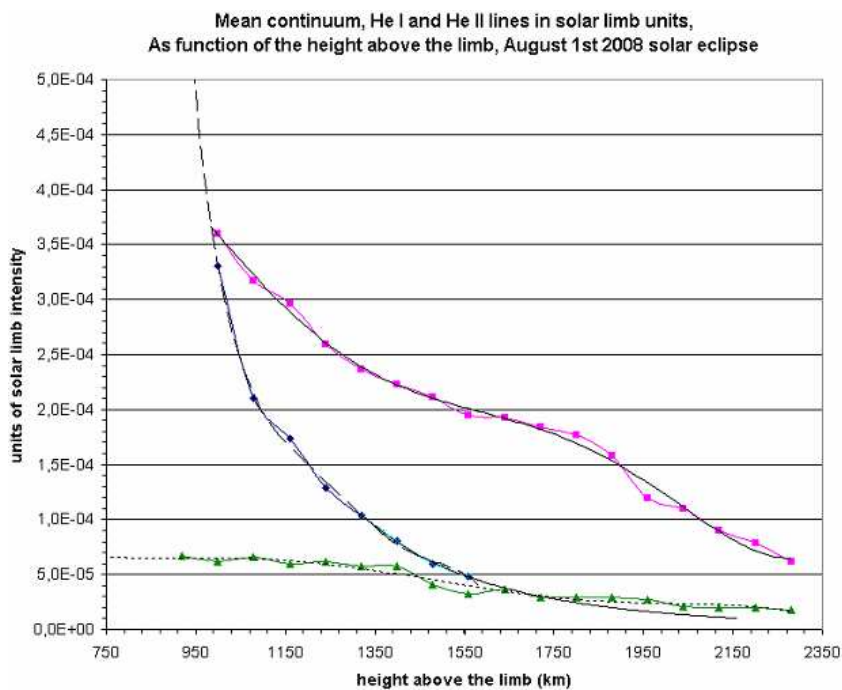


Fig. 2. Intensity profiles of the helium lines and continuum at the August 1st 2008 total eclipse

Avrett, E. & Koutchmy, S. 1989, Bulletin of the American Astronomical Society, 21, 828

Bazin, C., Koutchmy, S., & Tavabi, E. 2009, in Solar Wind and space environment interaction, ed. H. Hady & L. Dame

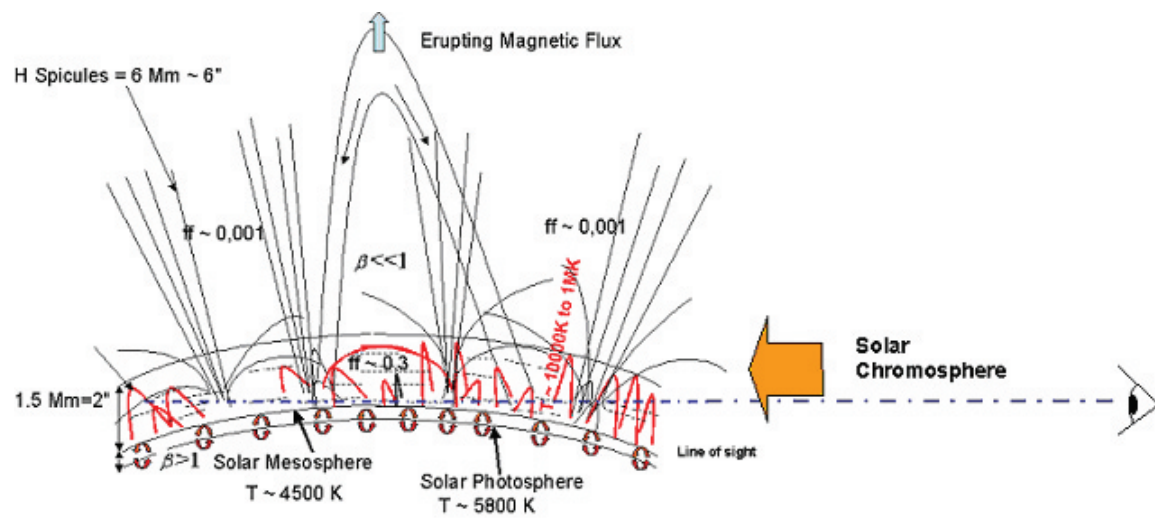


Fig. 3. Cartoon to show the low layers of the transition region (TR) including the emergence of flux tubes.

(Dordrecht/Boston/London), 100–106

Hirayama, T. & Irie, M. 1984, *SoPh*, 90, 291

Koutchmy, S., Mouette, J., & Bazin, C. 2009, *Observations et Travaux*, 71, 2

Mitchell, S. 1935, *Publications of the Leander McCormick Observatory*, 5, 51

Zirin, H. 1975, *ApJ*, 199, 63

CALIBRATING 15 YEARS OF GOLF DATA

G. R. Davies¹ and R. A. García¹

Abstract. The GOLF resonant scattering spectrophotometer aboard SoHO has now provided 15 years of continuous high precision Sun-as-a-star radial-velocity measurements. This length of time series provides very high resolution in the frequency domain and is combined with very good long-term instrumental stability. These are the requirements for measuring the low-l low-frequency global oscillations of the Sun that will unlock the secrets of the solar core. However, before the scientifically interesting gravity and mixed modes of oscillation fully reveal themselves, a correction and calibration of the whole data set is required. Here we present work towards producing a 15 year GOLF data set corrected for instrumental ageing and thermal variation.

Keywords: Sun, helioseismology, instrumentation

1 Introduction

The Global Oscillations at Low Frequency (GOLF) instrument measures the Sun-as-a-star radial velocity field (Gabriel et al. 1995, 1997). Raw measurements are made in intensity and then corrected and calibrated to produce final residual velocities (García et al. 2005). The ability of this calibration process to produce high quality and very long time series (15 years) is important as GOLF is forced to operate in a single wing mode (Pallé et al. 1999). The scientific motivation for an improved calibration comes from the need for a stable 15 year time series. This will allow detailed analysis of the impact of the solar cycle on helioseismic parameters (Broomhall et al. 2009b; Salabert et al. 2009) and the detection of new low-frequency oscillations. Low-frequency oscillations have low signal-to-noise ratios making their detection a significant challenge. Recent reports on the signature of g modes (Turck-Chièze et al. 2004) and their fingertips (García et al. 2007, 2008) sparked much debate. An improvement in GOLF performance at low frequency could reveal the secrets of the solar core.

2 GOLF observations

GOLF makes measurements of intensity, I , integrated over narrow bands in wavelength, λ , and integrated over the visible surface of the solar disk, S . We can state this as a simple model,

$$I = \int_{\lambda} \int_S I_{\odot}(\lambda, S, v_{\text{los}}) W(\lambda, S, v_{\text{los}}) d\lambda dS, \quad (2.1)$$

where I_{\odot} is the solar D1 and D2 absorption line spectrum, W is the instrumental weighting, and v_{los} is the line-of-sight velocity between GOLF and the Solar surface. Given the measured intensity, the solar line function, and the instrumental weighting it would be possible to determine v_{los} . However, all three components contain some level of uncertainty and/or cannot be sufficiently modeled (Ulrich et al. 2000). So we make simplifications and propose a method that relies on the following statement: a well corrected instrument will give intensity measurements that are only a function of v_{los} . This gives us the definition of a parameter for good - the correspondence of intensity and line-of-sight velocity.

To achieve the best possible GOLF signal-to-noise ratio, it is necessary to correct for long term instrumental effects and to provide a stable calibration that minimizes non-solar variation in mode amplitude. Previous work

¹ Laboratoire AIM, CEA/DSM-CNRS-Université Paris Diderot; IRFU/SaP, Centre de Saclay, 91191 Gif-sur-Yvette Cedex, France

has tackled these two aspects one after another. However, the gain of the instrument (photons detected divided by photons collected) and the instrument sensitivity (dI/dv_{los}) are coupled. The two processes must be treated concurrently to give an optimum calibration. Figure 1 shows GOLF raw-intensity measurements as a function of time. There are two processes that are clearly visible: the yearly variation in the Sun-instrument line-of-sight velocity; and the ageing of the instrument. Further to this there is a less obvious variation of instrumental gain which is a function of the temperature of the instrument.

To account for all effects present in Fig. 1 we modify equation 1. We add the ageing of the instrument

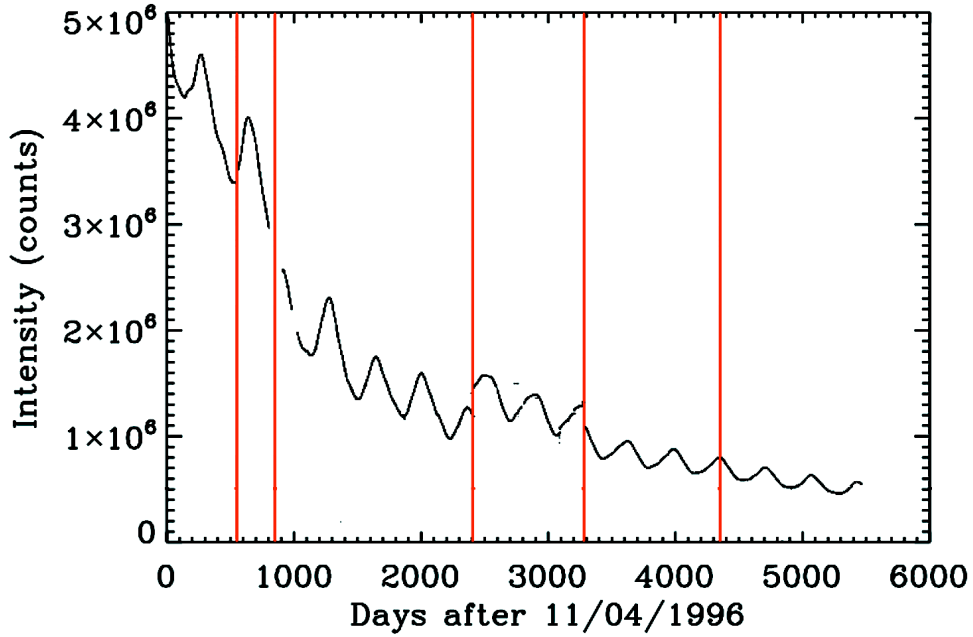


Fig. 1. GOLF raw-intensity measurements as a function of time. Red lines mark breaks in continuity due to instrumental adjustments. The obvious effects displayed are the ageing of the photomultiplier tubes (PMT near exponential decay), the Sun-instrument line-of-sight velocity (one year period), and the discontinuities due switching between the “red” and “blue” wings and PMT high voltage adjustment.

(probably dominated by the ageing of the photomultiplier tubes) $P(t)$, the variation in flux as a function of the spacecraft-Sun distance $F(d)$, and the variation in gain due to the changes in instrument temperature $K(T)$. This gives

$$I = P(t)F(d)K(T) \int_{\lambda} \int_S I_{\odot}(\lambda, S, v_{\text{los}}) W(\lambda, S, v_{\text{los}}) d\lambda dS. \quad (2.2)$$

Given the simple model of the the underlying system and a goodness-of-fit parameter, we can use the 15 years of GOLF observation to determine instrumental parameters. First we must define the parameters and functions describing the instrument.

The ageing of the instrument is expected to be dominated by the exponential loss of efficiency in GOLF’s photomultiplier tubes. From GOLF’s measurements we find that the rate of ageing varies as a function of time. To describe this in the simplest possible manner we use the following function,

$$P(t) = p_0 \exp -(t(p_1 + p_2 t)). \quad (2.3)$$

The change in flux due to the variation in the spacecraft-Sun distance is determined by the solid angle presented by the GOLF aperture. It is trivial to how that

$$F(d) = f_0^2/d^2, \quad (2.4)$$

where f_0 is a reference distance.

For the gain of the instrument due to temperature we use the form of García et al. (2005),

$$K(t) = 1 - k_1(T - k_0) - k_2(T - k_0)^2, \quad (2.5)$$

where k_0 is a reference temperature. Variations in instrumental gain due to temperature have a number of possible sources: variation in the vapour cell stem temperature; variation in the detector temperature (PMT and counting electronics); and other sources including the temperature of the interference filters. Rather than considering a function for each temperature we note that each of the measured temperatures (particularly the cell stem and detectors) are well correlated. Using this we apply a single correction using only the stem temperature, which is the measured temperature with the greatest precision.

We must also describe the sensitivity of the instrument (dI/dv_{los}). In this work we use the derivative of a fourth order polynomial as we know this has been successfully applied to similar but ground based instruments (Elsworth et al. 1995; Broomhall et al. 2009a),

$$\frac{dI}{dv_{\text{los}}} = \sum_{i=1}^4 a_i i v_{\text{los}}^{i-1}. \quad (2.6)$$

We have developed more sophisticated models of the instrumental sensitivity that require more space for description than is available here. The full description will be presented in Davies et al. (in prep.).

3 Results

We show an example of the new correction and calibration technique applied to 387 days of GOLF data. Figure 2 shows the strong correspondence between the Sun-instrument line-of-sight velocity and the calibrated velocities returned by the new method. In addition, Fig. 2 shows the residual velocities (measured velocity less v_{los}) which show both the impact of solar surface activity (period around 13 days) and solar oscillations (period of about 5 minutes and amplitude of a few m s^{-1}). Figure 3 shows the power spectrum of the residual velocities. The frequency domain again shows the presence of solar surface activity and solar oscillations.

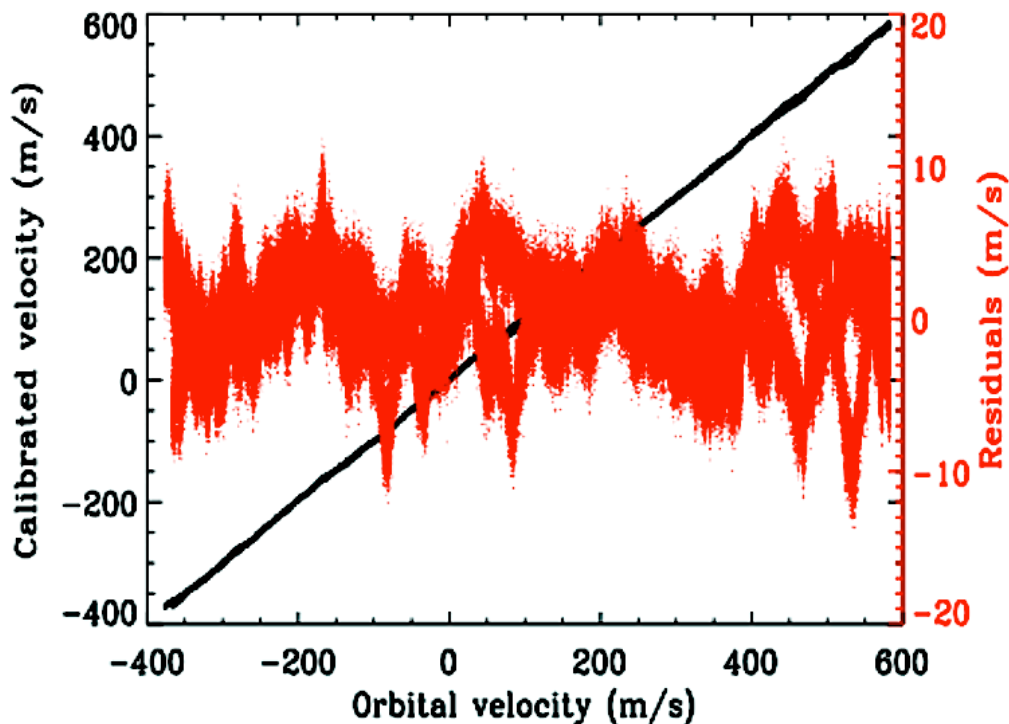


Fig. 2. Calibrated velocity as a function of Sun-instrument line-of-sight velocity. Residual velocities shown in red with scale on the right ordinate. The impact of solar surface activity in the residuals can be clearly seen as a near 13 day period fluctuation. The magnitude of the solar oscillation signal is a few m s^{-1} .

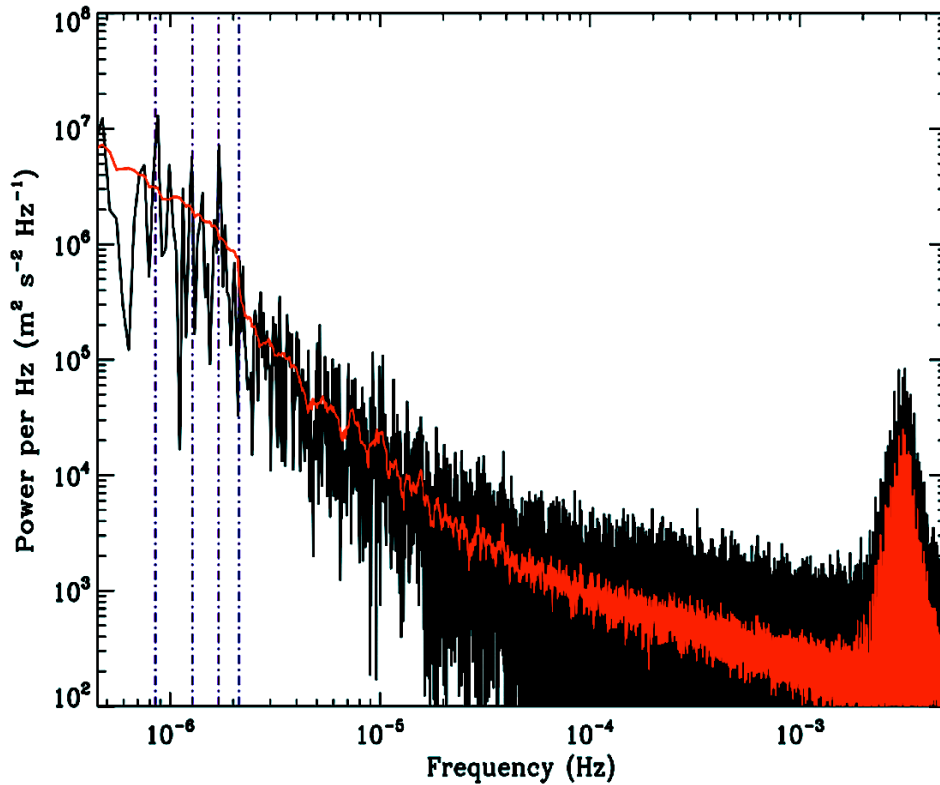


Fig. 3. Power spectrum of the 387 day residuals using the new correction and calibration method. Black: power spectrum. Red: 20 point boxcar smoothed power spectrum. Vertical lines: overtones of the Carrington rotation rate (highlighting peaks in the power spectrum due to solar surface activity). The “five minute” modes are clearly visible at high frequency (≈ 3 mHz).

4 Conclusions

Here we present work focusing on achieving a stable correction and calibration of GOLF data that could be applied to 15 years of observations. We demonstrate that we can achieve a good correspondence between the Sun-instrument line-of-sight velocity and the calibrated velocity. The calibrated velocities show the signatures of both solar surface activity and solar oscillations.

The GOLF instrument is a cooperative effort of many individuals, to whom we are indebted. SoHO is a mission of international cooperation between ESA and NASA. The authors thanks the support of the CNES.

References

- Broomhall, A.-M., Chaplin, W. J., Davies, G. R., et al. 2009a, MNRAS, 396, L100
 Broomhall, A.-M., Chaplin, W. J., Elsworth, Y., Fletcher, S. T., & New, R. 2009b, A&A, 503, 241
 Elsworth, Y., Howe, R., Isaak, G. R., et al. 1995, A&AS, 113, 379
 Gabriel, A. H., Charra, J., Grec, G., et al. 1997, Sol. Phys., 175, 207
 Gabriel, A. H., Grec, G., Charra, J., et al. 1995, Sol. Phys., 162, 61
 García, R. A., Jiménez, A., Mathur, S., et al. 2008, Astronomische Nachrichten, 329, 476
 García, R. A., Turk-Chièze, S., Boumier, P., et al. 2005, A&A, 442, 385
 García, R. A., Turk-Chièze, S., Jiménez-Reyes, S. J., et al. 2007, Science, 316, 1591
 Pallé, P. L., Régulo, C., Roca Cortés, T., et al. 1999, A&A, 341, 625
 Salabert, D., García, R. A., Pallé, P. L., & Jiménez-Reyes, S. J. 2009, A&A, 504, L1
 Turk-Chièze, S., García, R. A., Couvidat, S., et al. 2004, ApJ, 604, 455
 Ulrich, R. K., García, R. A., Robillot, J.-M., et al. 2000, A&A, 364, 799

SEISMIC INFERENCE ON THE CORE OF THE SUBGIANT HD 49385 VIA MIXED MODES

S. Deheuvels¹

Abstract. We report the detection of mixed modes in the oscillation spectrum of the CoRoT target HD 49385. We propose a new grid-search method specifically designed to handle stars with mixed modes, which we apply to HD 49385.

Keywords: Stars: oscillations, Stars: interiors, Stars: evolution, Stars: individual: HD 49385

1 Introduction

As a star evolves, the density in the core keeps increasing, which causes the frequencies of gravity modes (g modes) to increase. They eventually become of the same order of magnitude as pressure modes (p modes). When the frequency of a g mode becomes close to that of a p mode of same degree ℓ , the two modes undergo an *avoided crossing* at the end of which they have exchanged natures. During this process, the modes have a *mixed* character: they behave as g modes in the core and as p modes near the surface. These mixed modes have a very high potential for core diagnostics because they are sensitive to the core while having much higher amplitudes than pure g modes, which are still impossible to detect in solar-like pulsators. Their existence in stars has been theoretically known since Osaki (1975) discovered them in stellar evolution models. However, until very recently, the quality of the observed oscillation spectra was too low to detect and fully exploit mixed modes. The development of space missions CoRoT and Kepler has opened new opportunities.

We here report the detection of mixed modes in the oscillation spectrum of the CoRoT target HD 49385. We then propose a new approach to grid-search modeling specifically designed to handle stars with mixed modes, which we apply to HD 49385.

2 Detection of an $\ell = 1$ avoided crossing in the spectrum of HD 49385

The star HD 49385 is a solar-like pulsator, which was observed with the CoRoT satellite over a period of 137 days with a duty cycle close to 90%. Its oscillation spectrum was analyzed by Deheuvels et al. (2010) who unambiguously identified modes of degrees $\ell = 0, 1$, and 2 over nine radial orders. The authors estimated the frequencies of these modes by fitting Lorentzian profiles to the power spectrum. The mode frequencies are plotted in Fig. 1 in the traditionally used *échelle diagram*. This representation makes use of the fact that in solar-like pulsators, p modes of consecutive orders are spaced by the *large separation* $\Delta\nu$, which is roughly constant with frequency. To build an échelle diagram, the oscillation spectrum is divided in $\Delta\nu$ -wide sections, which are then piled up onto one another. That way, modes of similar degree form vertical ridges, as can be seen in Fig. 1. Deheuvels et al. (2010) identified several unaccounted for features in this diagram. First, the curvature of the $\ell = 1$ ridge unexpectedly differs from that of the $\ell = 0$ ridge at low frequency. Then, several modes were detected outside the identified ridges.

Deheuvels & Michel (2010) investigated the possibility that these peculiar features might be caused by mixed modes. They proposed a toy model, which demonstrated that $\ell = 1$ avoided crossings induce a specific distortion of the $\ell = 1$ ridge that is very comparable to the one that we observe in the spectrum of HD 49385. They then found a post-main-sequence (PoMS) model with an $\ell = 1$ avoided crossing that reproduces both the spectroscopic constraints and the observed shape of the $\ell = 1$ ridge in the échelle diagram (model plotted in red in Fig. 1). This enabled them to establish the firm detection of $\ell = 1$ mixed modes in the oscillation spectrum of HD 49385, as well as the PoMS status of the star.

¹ Department of Astronomy, Yale University, P.O. Box 208101, New Haven, CT 06520-8101, USA

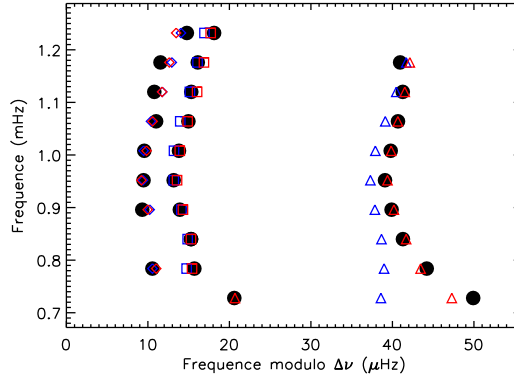


Fig. 1. Échelle diagram of the oscillation spectrum of HD 49385, folded with a large separation of $\Delta\nu = 56.3 \mu\text{Hz}$. The frequencies of a MS model (blue) and a PoMS model (red) have been overplotted (see text for a description of the models). Squares represent $\ell = 0$ modes, triangles $\ell = 1$ modes and diamonds $\ell = 2$ modes.

3 A new approach to grid-search modeling for stars with mixed modes

We now present a thorough modeling of HD 49385, trying to fit stellar models to the properties of the observed avoided crossing. It is the first time such a study is attempted. The main difficulty we encountered is that avoided crossings occur on a very short timescale (typically of the order of 1 Myr or less) compared to the stellar evolution timescale. Applying a traditional grid-search method with a time step of the order of the avoided crossing timescale is infeasible, because it would require the computation of a tremendously large number of models. On the other hand, with a larger time step, the probability of finding models that correctly reproduce the frequency of the avoided crossing is very low and we therefore miss the best-fit models.

We thus adapted the grid-of-model approach to the special case of stars with mixed modes. The method is described in detail in Deheuvels et al. (2011) but we here give a brief overview of how it works. As the star evolves from the MS to the PoMS, the most central regions keep contracting. As a result, the frequencies of g modes monotonically increase because of the growing central density. Therefore, for a given physics, there exists *only one age* for which the frequency of the observed avoided crossing ν_{cross} is reproduced. The location in the HR diagram of the models which verify this condition is represented by the red dashed line in Fig. 2. But also, as the star evolves, the outer layers expand and the radius increases, which causes the large separation to monotonically decrease. Hence, there is *only one age* for which the models reproduce the observed large separation $\Delta\nu$. The models that verify this second condition are located on the blue dashed line in Fig. 2. From Fig. 2, it is obvious that, for a given physics, there is *only one stellar mass* for which both the frequency of the avoided crossing and the large separation match the observations. We therefore proposed to reduce the dimensions of the model space by eliminating the mass and age from the set of free parameters, these two quantities being each time determined by $\Delta\nu$ and ν_{cross} . Since the age is no longer a free parameter of the fit, this approach solves the problem of the definition of a time step for the grid of models.

4 Application to the case of HD 49385

We applied the method presented in Sect. 3 to the case of HD 49385. The properties of our models are described in Deheuvels et al. (2011). We computed two grids of models, one assuming the mixture of Grevesse & Noels (1993) (further noted GN93) and the other the more recent mixture of Asplund et al. (2005) (further noted AGS05). We varied the values of the mixing length parameter α_{conv} , the helium abundance Y_0 , the metallicity (Z/X) and the amount of overshooting α_{ov} . For each point in the grids, an optimization was performed to determine the stellar mass and age that fit $\Delta\nu$ and ν_{cross} simultaneously (for details on this optimization, see Deheuvels et al. 2011). We then computed a χ^2 function to estimate the agreement between the models and the observations (both spectroscopic and seismic).

We showed that by using this technique, we were able to constrain the stellar mass, radius, and age very tightly: we obtained $M = 1.25 \pm 0.05 M_{\odot}$ (precision of 4%), $R = 1.94 \pm 0.03 R_{\odot}$ (precision of 1.5%), and $\tau = 5.02 \pm 0.26 \text{ Gyr}$ (precision of 5%) for HD 49385. Interestingly, we also managed to obtain valuable

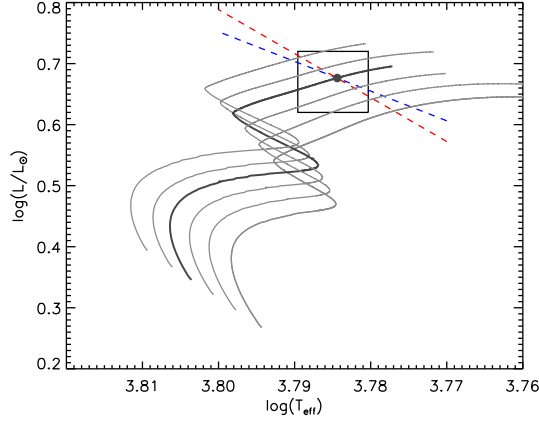


Fig. 2. Evolutionary tracks in the HR diagram of models with masses ranging from $1.2 M_{\odot}$ to $1.3 M_{\odot}$, for a given physics. The box corresponds to the observational values of the effective temperature and luminosity of the star within $1\text{-}\sigma$ error bars. The dashed lines indicate the location of models which reproduce the observed values of the large separation (blue) and the frequency of the avoided crossing (red). The model for which both conditions are verified is plotted in dark grey.

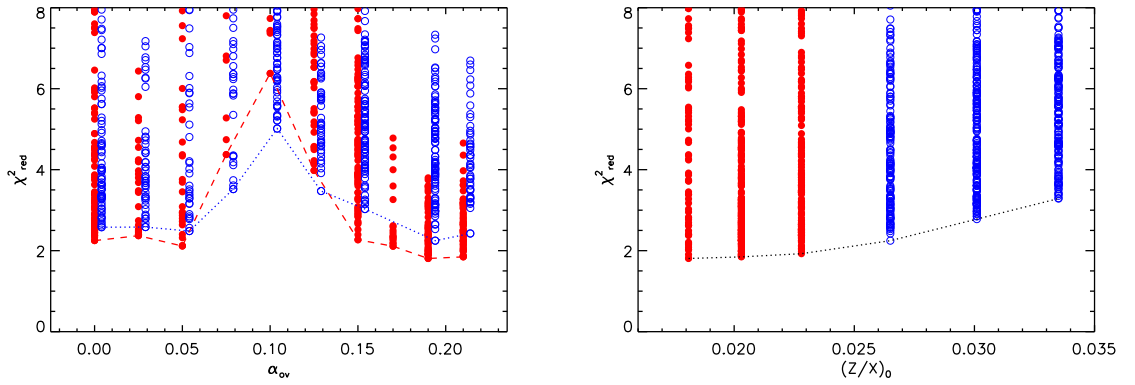


Fig. 3. Left: Values of the χ^2 function for the models computed with the mixture of GN93 (blue empty circles) and that of AGS05 (red filled circles) as a function of the amount of overshooting. The best-fit models for each value of α_{ov} have been linked. **Right:** Same as the left panel, representing the values of the χ^2 function as a function of metallicity.

information about several physical processes that remain theoretically uncertain.

4.1 Constraints on the amount of core overshooting

In stars that have a convective core, the distance over which convective elements penetrate in the radiative region owing to inertia, known as *core overshooting*, is difficult to predict theoretically. This can result in an uncertainty in the stellar ages of up to 30% (Michel et al. 2006). For HD 49385, we showed that the amount of overshooting had to be either very small (distance of penetration lower than $0.05 H_P$, where H_P is the pressure scale height) or moderate (about $0.2 H_P$). This can be clearly seen in Fig. 3. The existence of two minima in Fig. 3 is explained in Deheuvels et al. (2011).

4.2 Constraints on the abundance in heavy elements

The abundance in heavy elements at the surface of the Sun, which had been estimated to about $(Z/X) = 0.0245$ by GN93, has recently been revised by AGS05, who found a much lower value — $(Z/X) = 0.0165$. However, this new value is in disagreement with helioseismology (see Basu & Antia 2008 for a review) and the solar metallicity still remains uncertain. This generates large uncertainties in stellar structure, e.g. in the determination of

radiative opacities and the efficiency of nuclear reactions. Because of the degeneracy of stellar models, it is very hard to constrain the value of (Z/X) in stars, even with the help of seismology. For HD 49385, we showed that the abundances of AGS05 are in closer agreement with the observations than those of GN93 (see Fig. 3).

4.3 Constraints on the efficiency of convection

Since we are still lacking a proper treatment of convection in stars, stellar models usually resort to the simplistic mixing length theory, and use a solar calibrated value for the mixing length parameter α_{conv} . In the case of HD 49385, no satisfactory model can be found if we use α_{\odot} . Using the full-spectrum theory (FST) proposed by Canuto et al. (1996), the best-fit models are obtained for a mixing length parameter of $\alpha_{\text{conv}} = 0.55 \pm 0.04$, whereas a calibration for the Sun gives $\alpha_{\odot} = 0.64$. It is interesting to note that Piau et al. (2011) also found sub-solar mixing length parameters for subgiants using a different approach.

5 Why are the stellar parameters so well-constrained in HD 49385?

Given that it is usually very hard to obtain information about the physical processes that we mentioned above with regular main sequence stars, one might wonder why it is possible for HD 49385. This is of course linked with the detection of mixed modes, and it was investigated in details in Deheuvels et al. (2011). There are mainly two reasons. First, the frequency of the observed avoided crossing reduces the dimensions of the model space, as shown in Sect. 3, which lifts some degeneracies between the models. Secondly, the intensity of the distortion in the $\ell = 1$ ridge that we mentioned in Sect. 2 depends on the strength of the coupling between the p-mode cavity and the g-mode cavity in the star. We have shown in Deheuvels et al. (2011) that this coupling is tightly related to the stellar mass. This provides an additional constraint, which we have proven to be crucial to discriminate between the different models.

6 Conclusions

We have performed a thorough modeling of HD 49385, trying to fully exploit the potential of the detection of $\ell = 1$ mixed modes in the oscillation spectrum of the star. For this purpose, we have developed a new optimization method specifically suited to model stars with mixed modes. We then successfully applied it to HD 49385. We obtained very precise values of the stellar mass ($M = 1.25 \pm 0.05 M_{\odot}$), radius ($R = 1.94 \pm 0.03 R_{\odot}$), and age ($\tau = 5.02 \pm 0.26 \text{ Gyr}$) for the star. We also showed that the recently revised abundances of AGS05 offer a closer agreement with the observations than those of GN93. We had to invoke sub-solar values of the mixing length parameter ($\alpha_{\text{conv}} = 0.55 \pm 0.04$). We found two families of solution with either a very small amount of core overshooting ($\alpha_{\text{ov}} < 0.05$) or a moderate one ($\alpha_{\text{ov}} = 0.19 \pm 0.01$).

This study confirms to a large degree that stars with mixed modes have a very high potential in terms of asteroseismic diagnostics. We note that the space mission Kepler has already claimed the detection of mixed modes in several solar-like pulsators (Chaplin et al. 2010) and it will be very interesting to apply the method that we proposed here to these targets.

References

- Asplund, M., Grevesse, N., & Sauval, A. J. 2005, in *Cosmic Abundances as Records of Stellar Evolution and Nucleosynthesis*, ed. T. G. Barnes III & F. N. Bash, (ASPC, San Francisco), Vol. 336, 25
- Basu, S. & Antia, H. M. 2008, *Phys. Rep.*, 457, 217
- Canuto, V. M., Goldman, I., & Mazzitelli, I. 1996, *ApJ*, 473, 550
- Chaplin, W. J., Appourchaux, T., Elsworth, Y., et al. 2010, *ApJ*, 713, L169
- Deheuvels, S., Bruntt, H., Michel, E., et al. 2010, (D10), *A&A*, 515, A87
- Deheuvels, S. & Michel, E. 2010, *Ap&SS*, 328, 259
- Deheuvels et al. 2011, accepted in *A&A*, in press
- Grevesse, N. & Noels, A. 1993, in *Origin and Evolution of the Elements*, ed. N. Prantzos, E. Vangioni-Flam, & M. Casse (Cambridge University Press, New York), 15–25
- Michel, E., Baglin, A., Auvergne, M., et al. 2006, in *ESA Special Publication*, Vol. 1306, ESA Special Publication, ed. M. Fridlund, A. Baglin, J. Lochar, & L. Conroy, 39–+
- Osaki, J. 1975, *PASJ*, 27, 237
- Piau, L., Kervella, P., Dib, S., & Hauschildt, P. 2011, *A&A*, 526, A100+

NONLINEAR SIMULATIONS OF THE CONVECTION-PULSATION COUPLING

T. Gastine¹ and B. Dintrans²

Abstract. In cold Cepheids close to the red edge of the classical instability strip, a strong coupling between the stellar pulsations and the surface convective motions occurs. This coupling is by now poorly described by 1-D models of convection, the so-called "time-dependent convection models" (TDC). The intrinsic weakness of such models comes from the large number of unconstrained free parameters entering in the description of turbulent convection. A way to overcome these limits is to compute two-dimensional direct simulations (DNS), in which all the nonlinearities are correctly solved. Two-dimensional DNS of the convection-pulsation coupling are presented here. In an appropriate parameter regime, convective motions can actually quench the radial pulsations of the star, as suspected in Cepheids close to the red edge of the instability strip. These nonlinear simulations can also be used to determine the limits and the relevance of the TDC models.

Keywords: Convection , Instabilities , Stars: oscillations , Methods: numerical , Stars: Variables: Cepheids

1 Introduction

The cold Cepheids located close to the red edge of the classical instability strip have a large surface convective zone that affects their pulsation properties (e.g. the reviews of Gautschy & Saio 1996; Buchler 2009). The first calculations, that assumed *frozen-in* convection, predicted a cooler red edge than the observed one. Indeed, as already stated by Baker & Kippenhahn (1965), a non-adiabatic treatment of the convection-pulsation coupling is mandatory to predict the red edge location with a better accuracy.

Several time-dependent convection (TDC) models were therefore developed to address this coupling (e.g. Stellingwerf 1982; Kuhfuß 1986; Xiong 1989) and succeeded in reproducing the correct location of the red edge, despite their disagreements with the physical origin of the mode stabilisation (e.g. Bono et al. 1999; Yecko et al. 1998; Grigahcène et al. 2005).

However, all these formulations involve many free and degenerate parameters (e.g. the seven dimensionless α coefficients used by Yecko et al. 1998) that are either fitted to the observations or hardly constrained by theoretical values. Nevertheless, another way to tackle this problem is to compute 2-D and 3-D direct numerical simulations (DNS) that correctly take into account the nonlinearities involved in this coupling. Results of such pioneering 2-D nonlinear simulations of the convection-pulsation coupling are presented in the following.

2 The convection-pulsation coupling

Our system corresponds to a local zoom around an ionisation region responsible for the driving of the acoustic modes excited by the κ -mechanism. It is composed of a 2-D cartesian layer filled with a monatomic and perfect gas. The opacity bump associated with this ionisation zone is modelled by a temperature-dependent radiative conductivity profile $K(T)$ (for further details, see Gastine & Dintrans 2008a). In addition to the κ -mechanism, the conductivity profile is deep enough to locally get a superadiabatic temperature gradient, meaning that convective motions develop there, according to Schwarzschild's criterion. A strong coupling between convection and the acoustic oscillations therefore develops.

The hydrodynamical equations are then advanced in time with the high-order, finite-difference pencil code*, which is fully explicit except for the radiative diffusion term that is solved implicitly thanks to a parallel alternate

¹ Max-Planck-Institut für Sonnensystemforschung, Max-Planck-Strasse 2, 37191 Katlenburg-Lindau, Germany

² Institut de Recherche en Astrophysique et Planétologie, CNRS/Université de Toulouse, 14 Av. Edouard Belin, 31400 Toulouse, France

*See <http://www.nordita.org/software/pencil-code/> and Brandenburg & Dobler (2002).

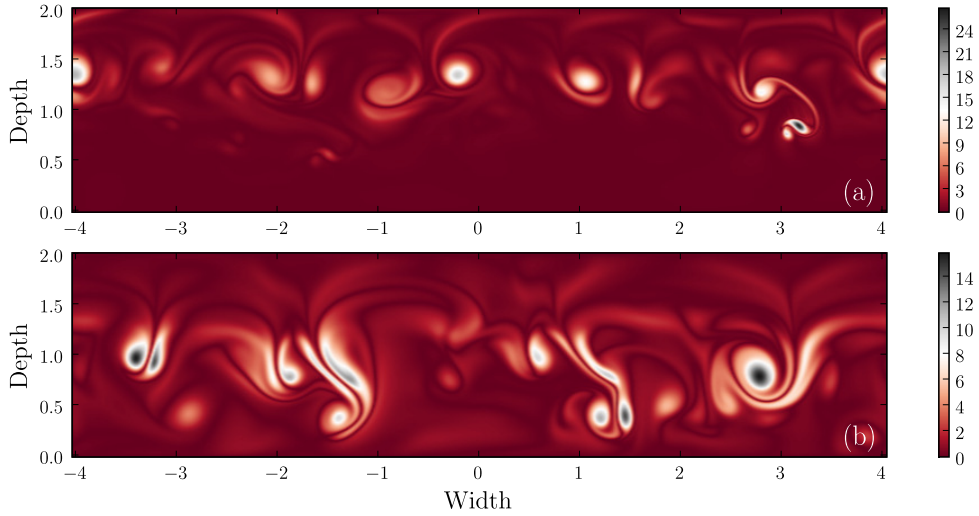


Fig. 1. Snapshot of the modulus of the vorticity field $|\vec{\nabla} \times \vec{u}|$ in the G8 (a) and in the G8H8 simulations (b).

direction implicit (ADI) solver (Gastine & Dintrans 2008a). The simulation box spans about 10% of the star radius around the ionisation region. In order to ensure that both thermal relaxation and nonlinear saturation of the κ -mechanism are achieved, the simulations are computed over more than 4000 days (corresponding roughly to 1500 periods of oscillation, see Gastine & Dintrans 2011a).

Figure 1 displays a snapshot of the vorticity field for two simulations discussed in (Gastine & Dintrans 2011a), namely G8 (upper panel) and G8H8 (lower panel). This vorticity field highlights the convective motions that are approximately localised in the middle of the layer, where the radiative conductivity is minimum. Differences in the typical length-scale of convection are noticeable between these two DNS: convective eddies are smaller scale in the G8 simulation than in the G8H8 one. Accordingly, the overshooting of convective elements into the lower stably stratified layer is also more pronounced in the latter simulation.

Beyond these qualitative differences, a good way to compare these simulations is to study the temporal evolution of average quantities, such as the vertical mass flux ρu_z . Indeed, as we are considering simulations with both convective motions and oscillations of acoustic modes, it is relevant to use a simple diagnostic that roughly separates their relative contributions. Because the convective plumes have both ascending and descending motions, the average vertical mass flux filters out their contribution and is therefore a good proxy of the amplitude of the acoustic modes. The left panel of Fig. 2 therefore displays the temporal evolution of ρu_z for the two simulations discussed before. An oscillatory behaviour is observed in both cases due to the radial oscillations of the fundamental acoustic mode excited by κ -mechanism. In the G8 simulation, the amplitude first grows exponentially until reaching the nonlinear saturation regime. At first glance, this time evolution looks very similar to what has been already observed in purely radiative simulations of Gastine & Dintrans (2008b), that is, a linear growth of the amplitude and a saturation at a well-defined value. In contrast, the dynamics of the G8H8 simulation differ radically from the previous one as the amplitude remains weak and is highly modulated over time. No clear nonlinear saturation is observed in this case, meaning that the acoustic oscillations are more influenced by convective motions than in the previous DNS.

To separate more precisely the relative contributions of the acoustic modes and the convective motions to the energy budget, the velocity field of each simulations is projected onto an acoustic subspace built from normal eigenmodes (see Bogdan et al. 1993). Thanks to this formalism, it is possible to extract the time evolution of the kinetic energy contained in each acoustic mode found in the nonlinear simulation. The right panel of Fig. 2 displays the time evolution of the energy contained in the fundamental acoustic mode normalised by the total kinetic energy. In the G8 simulation, the acoustic energy linearly increases until its nonlinear saturation, in a similar way to what has been previously observed with the time evolution of ρu_z . Once this saturation is reached, 70% of the kinetic energy is contained in the radial oscillations of the fundamental acoustic mode, while the remaining is in the convective plumes. In other words, the acoustic oscillations are not affected much by the convective motions in this simulation. In contrast, this acoustic energy ratio remains very weak in the

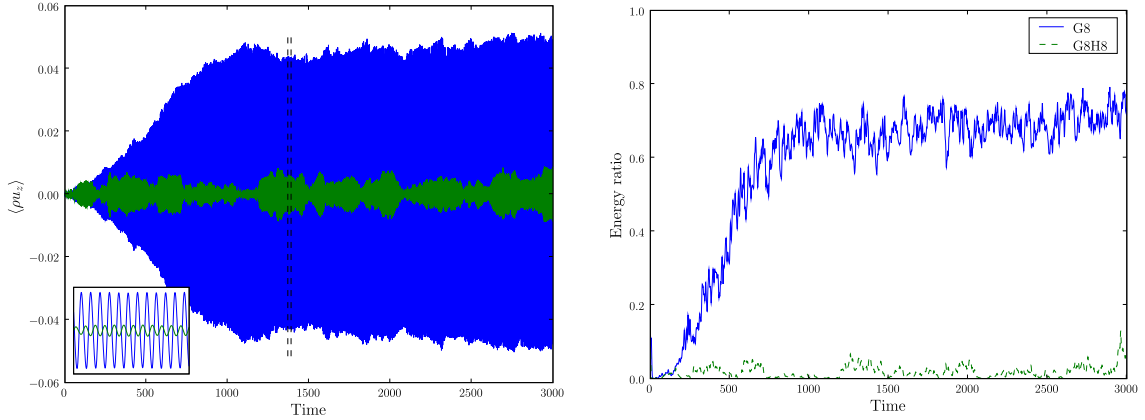


Fig. 2. *Left panel:* Temporal evolution of the mean vertical mass flux ρu_z for the two simulations G8 (solid blue line) and G8H8 (solid green line). The two vertical dashed black lines define the boundaries of the zoom displayed in the bottom left corner. *Right panel:* temporal evolution of the energy contained in acoustic modes normalised by the total kinetic energy for the two simulations G8 (solid blue line) and G8H8 (dashed green line).

other simulation. Despite some transient increases during which non-trivial values ($\simeq 10\%$) are obtained, the average ratio is less than 5%, and convective motions contains the bulk of the kinetic energy. In this case, the radial oscillations excited by the κ -mechanism are thus quenched by convective plumes. This situation is relevant to the physics of Cepheids close to the red edge of the instability strip, where the unstable acoustic modes are supposed to be damped by the surface convective motions. This convective quenching of the acoustic oscillations may be the direct signature of the different density contrasts in the G8 and the G8H8 simulations: in fact, weaker stratification (as in G8H8) leads to bigger vortices (see Fig. 1b), meaning that the energy is contained in larger convective structures. In our DNS, the amplitude of the κ -mechanism seems to be controlled by the screening effect due to these large convective vortices (Gastine & Dintrans 2011a).

3 Limits of time-dependent convection models

The nonlinear simulations of the convection-pulsation coupling, where the acoustic modes strongly modulate the convective motions over time (as in the G8 simulation) are also good candidates to test and compare the relevance of different prescriptions of 1-D time-dependent convection (TDC) models. We focus here on two popular formulations widely used in Cepheids models, namely the TDC model of Stellingwerf (1982) and the one of Kuhfuß (1986). In these formulations, a single equation for the turbulent kinetic energy \mathcal{E}_t is added to the classical mean-field equations and the main second-order correlations, such as the convective flux, are expressed as a function of \mathcal{E}_t only:

$$\begin{cases} \mathcal{F}_{\text{St}}(z, t) = \alpha_{\text{St}} \frac{A}{B} \mathcal{E}_t \text{sign}(\nabla - \nabla_{\text{ad}}) \sqrt{|\nabla - \nabla_{\text{ad}}|}, \\ \mathcal{F}_{\text{Ku}}(z, t) = \alpha_{\text{Ku}} A \sqrt{\mathcal{E}_t} (\nabla - \nabla_{\text{ad}}), \end{cases} \quad (3.1)$$

where $\nabla = d \ln T / d \ln p$, $\nabla_{\text{ad}} = 1 - c_v / c_p$ and

$$\mathcal{E}_t(z, t) = \left\langle \frac{u_z'^2}{2} \right\rangle, \quad A = c_p \langle \rho \rangle \langle T \rangle \quad \text{and} \quad B = \sqrt{c_p \langle T \rangle \nabla_{\text{ad}}}, \quad (3.2)$$

where p is the pressure, ρ the density, and the brackets denote a horizontal average. Each of these two TDC expressions thus involves one dimensionless parameter (α_{St} and α_{Ku} , respectively) that is poorly constrained by theory (Yecko et al. 1998). The nonlinear results of the G8 simulations are compared to these TDC recipes by computing χ^2 -statistics to extract the optimum α coefficients corresponding to each formulation.

Figure 3 compares the convective flux in the DNS with the two TDC prescriptions computed with the best fit values α_{St} and α_{Ku} obtained in (Gastine & Dintrans 2011b). Stellingwerf's formulation seems to give a better agreement with the nonlinear simulation than Kuhfuß's one. Indeed, the Kuhfuß model overestimates

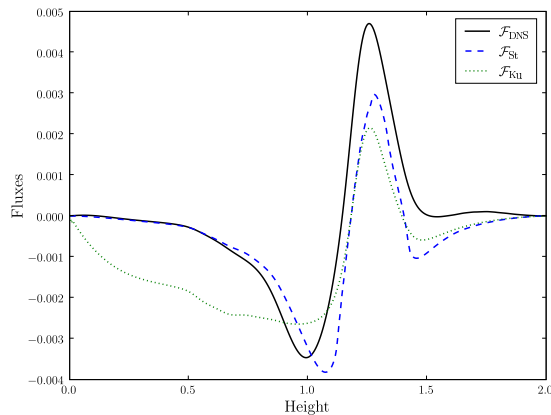


Fig. 3. Mean convective flux in the G8 simulation (solid black line), compared with the best TDC predictions based on the models of Stellingwerf (dashed blue line) and Kuhfuß (dotted green line).

the overshooting as the (negative) convective flux remains non-negligible until the bottom of the radiative zone. In contrast, the Stellingwerf profile accounts for the local penetration of convective plumes better and shows the same exponential-like decay in the negative convective flux when sinking in the radiative zone. However, the two models are fairly similar in the bulk of the convective zone, where convection is fully developed. One also notes that they both predict a negative flux at the top of the convective zone, which is an upper overshooting of convective motions near the surface that is not observed in the DNS.

4 Conclusion

The main weakness of all theories of 1-D time-dependent convection lies in the large number of free parameters involved in the description of convection. New constraints must therefore be found to reduce the intrinsic degeneracy of these models and to check the relevance of the different assumptions underlying these parametrisations.

Nonlinear 2-D direct numerical simulations are a useful way to address the convection-pulsation coupling that occurs in cold Cepheids. These simulations show a variable influence of convection onto the acoustic modes excited by κ -mechanism: (*i*) either the amplitude of the acoustic modes remains very weak and convective motions quench the oscillations ; (*ii*) or the kinetic energy is mainly contained in the acoustic modes and convective plumes are strongly modulated over time by the radial oscillations. While the former situation is relevant to the stabilisation of the oscillations of Cepheids close to the red edge, the latter is a good candidate to draw the limits of current TDC recipes. Focusing on two such widely used models, Stellingwerf's formulation is found to give a better agreement with the nonlinear results than does Kuhfuß's.

This first comparison of TDC with nonlinear 2-D simulations emphasises how DNS can be helpful to validate and improve the future 1-D models of convection.

This work was granted access to the HPC resources of CALMIP under the allocation 2010-P1021 (<http://www.calmip.cict.fr>).

References

- Baker, N. & Kippenhahn, R. 1965, ApJ, 142, 868
- Bogdan, T. J., Cattaneo, F., & Malagoli, A. 1993, ApJ, 407, 316
- Bono, G., Marconi, M., & Stellingwerf, R. F. 1999, ApJS, 122, 167
- Brandenburg, A. & Dobler, W. 2002, CoPhC, 147, 471
- Buchler, J. R. 2009, in American Institute of Physics Conference Series, Vol. 1170, American Institute of Physics Conference Series, ed. J. A. Guzik & P. A. Bradley, 51–58
- Gastine, T. & Dintrans, B. 2008a, A&A, 484, 29
- Gastine, T. & Dintrans, B. 2008b, A&A, 490, 743
- Gastine, T. & Dintrans, B. 2011a, A&A, 528, A6
- Gastine, T. & Dintrans, B. 2011b, A&A, 530, L7

- Gautschy, A. & Saio, H. 1996, *ARA&A*, 34, 551
- Grigahcène, A., Dupret, M.-A., Gabriel, M., Garrido, R., & Scuflaire, R. 2005, *A&A*, 434, 1055
- Kuhfuß, R. 1986, *A&A*, 160, 116
- Stellingwerf, R. F. 1982, *ApJ*, 262, 330
- Xiong, D. 1989, *A&A*, 209, 126
- Yecko, P. A., Kolláth, Z., & Buchler, J. R. 1998, *A&A*, 336, 553

SEISMIC ANALYSIS OF TWO SOLAR-TYPE STARS OBSERVED BY *KEPLER*S. Mathur¹

Abstract. After more than one year of operation, the Kepler photometer has already provided exquisite data of solar-type stars. During the survey phase, 42 stars have been continuously observed. It appeared that five stars show evidence of oscillations, even though they are rather faint (magnitudes from 10.5 to 12). We will show the results of the seismic analysis of the light curves of two of these stars, which have been observed during more than 8 months. This analysis led to the determination of the acoustic-mode global parameters (mean large separation, mean small separation...), lists of frequencies built by comparing the results of several teams, some parameters of the modes, and the rotation period of the stellar surface.

Keywords: asteroseismology, solar-type stars, data analysis, oscillations

1 Introduction

Interferometry, spectroscopy, and spectro-polarimetry are the classical methods to characterize stars, giving us information about mass and radius, the stellar atmosphere, rotation and magnetic activity. Over the past decade, *asteroseismology* has emerged as a powerful new tool allowing us to directly probe the stellar interior.

A star is a resonant cavity where two types of waves can propagate. Acoustic (p) modes are excited in the convective zone and sustained by pressure. These modes are equally spaced in frequency and we define the mean large frequency separation, $\langle \Delta\nu \rangle$, that is the mean root square of the density. The mean small frequency separation, $\langle \delta_{02} \rangle$, is very sensitive to the structure of the star, and thus to its age. Gravity (g) modes propagate in the radiative zone and are sustained by buoyancy, rendering them evanescent in the convective zone. As such, g modes in solar-type stars are very difficult to detect, since they reach the stellar surface with very low amplitudes (García et al. 2007; Appourchaux et al. 2010). Finally there are mixed modes, which are sustained by both pressure and buoyancy, making them sensitive to both the core and the envelope of a star. These modes are very precious, as they carry information on the stellar core and reach the stellar surface with larger amplitudes than pure g modes (e.g. Beck et al. 2011; Bedding et al. 2011; Mosser et al. 2011).

The ground-based observing campaigns (e.g. Arentoft et al. 2008) and space-based photometric observations with instruments such as WIRE (Wide-Field Infrared Explorer Bruntt et al. 2007) and MOST (Microvariability and Oscillations of STars Walker et al. 2003) allowed us to study these solar-like oscillations in a few tens of stars. The CoRoT mission (Convection, Rotation, and Transits Baglin et al. 2006) increased the number of main-sequence solar-like pulsators known thanks to longer continuous observations. Depending on the signal-to-noise ratio, it was possible to estimate the global parameters of the p modes (García et al. 2009; Mosser et al. 2009; Mathur et al. 2010a) and even resolve the individual modes (e.g. Ballot et al. 2011).

The *Kepler* mission (Borucki et al. 2010), launched in March 2009 into an Earth-trailing orbit, was designed to search for Earth-like exoplanets. It is a photometer composed of 42 CCDs (now 38) that will monitor the brightness of more than 150,000 stars in the direction of Cygnus and Lyra for at least 3.5 years. An additional program was introduced to apply asteroseismic methods to the target stars. Around 2000 solar-type stars have been observed for one month during the first year of survey and solar-like oscillations were detected in around 600 stars. With this large number of stars, we can start to do “ensemble” asteroseismology leading to very interesting results (Chaplin et al. 2011), which are important for our understanding of stellar evolution. Among the stars continuously observed during the survey phase, five present solar-like oscillations: two F-type stars (KIC 11234888 and KIC 10273246) and two G-type stars (KIC 11395018 and KIC 10920273). We refer to Mathur et al. (2011a) and Campante et al. (2011) for a detailed analysis of these stars. We present here the results of the analysis of two of these solar-type stars, KIC 11395018 and KIC 11234888, that have been observed for more than eight months.

¹ High Altitude Observatory, NCAR, P.O. Box 3000, Boulder, CO 80307, USA

2 Analysis of the *Kepler* targets

In each observation quarter (of ~ 3 months), a few hundreds of stars are observed by *Kepler* in short cadence (58.85 s) (Gilliland et al. 2010). The *Kepler* Science Office provides light curves that are corrected for instrumental effects and that are optimized for exoplanet transits search (Jenkins et al. 2010). However, it can happen that the low-frequency signals of some stars are filtered out. Thus, within the Kepler Asteroseismic Scientific Consortium (KASC, Kjeldsen et al. 2010), the Working Group # 1 (which focuses on oscillations in main-sequence solar-type stars) developed their own method for the corrections. The raw light curves are corrected for three types of instrumental perturbations: outliers, jumps, and drifts, following the methods described in García et al. (2011). The data of each *Kepler* quarter are concatenated after equalizing their mean values by fitting a 6th order polynomial to each segment. To remove the low-frequency instrumental trends, a high-pass filter is applied.

Several teams (Huber et al. 2009; Mosser & Appourchaux 2009; Roxburgh 2009; Campante et al. 2010; Hekker et al. 2010; Mathur et al. 2010b) analyzed the light curves to retrieve the global parameters of the p modes. We were able to measure the mean large frequency separation $\langle \Delta\nu \rangle$, the frequency of maximum oscillation power ν_{\max} , the mean small separation $\langle \delta_{02} \rangle$, and the mean linewidth $\langle \Gamma \rangle$. We obtained $\langle \Delta\nu \rangle = 47.76 \pm 0.99 \mu\text{Hz}$ and $\langle \Delta\nu \rangle = 41.74 \pm 0.94 \mu\text{Hz}$ for KIC 11395018 and KIC 11234888 respectively. We determined the mean values of the small separation, $\langle \delta_{02} \rangle = 4.12 \pm 0.035 \mu\text{Hz}$ and $2.38 \pm 0.19 \mu\text{Hz}$ respectively for KIC 11395018 and KIC 11234888, as well as the mean linewidth of the modes, $\langle \Gamma \rangle = 0.84 \pm 0.02 \mu\text{Hz}$ and $0.86 \pm 0.06 \mu\text{Hz}$ respectively.

We also fitted the granulation signal with a Harvey-like function (Harvey 1985; Mathur et al. 2011b), yielding the granulation time scale, τ_{gran} of 698 ± 33 s and 869 ± 89 s for KIC 11395018 and KIC 11234888 respectively.

To study the low-frequency region of the power spectrum, we used different high-pass filters so that the signal below $1 \mu\text{Hz}$ was conserved. We estimated the surface rotation period to 36 days for KIC 11395918. The data of KIC 11234888 were noisier than the rest of the data. So we only considered the last 7 months of data. Several peaks were present at low frequency suggesting that the surface of that star has a differential rotation (between 19 and 27 days).

In addition, several teams fitted the individual modes using different methods. The most common approach adopted was the maximum likelihood estimator method (e.g. Appourchaux et al. 1998). Another group used Bayesian Markov Chain Monte Carlo algorithms (MCMC; e.g. Handberg & Campante 2011). Finally a smaller group did not fit the individual modes but looked for the highest peaks in the power spectrum (e.g. Bonanno et al. 2008). Applying the method described in Mathur et al. (2011a), we selected the minimal and maximal lists of frequencies that provide very tight constraints to model the stars.

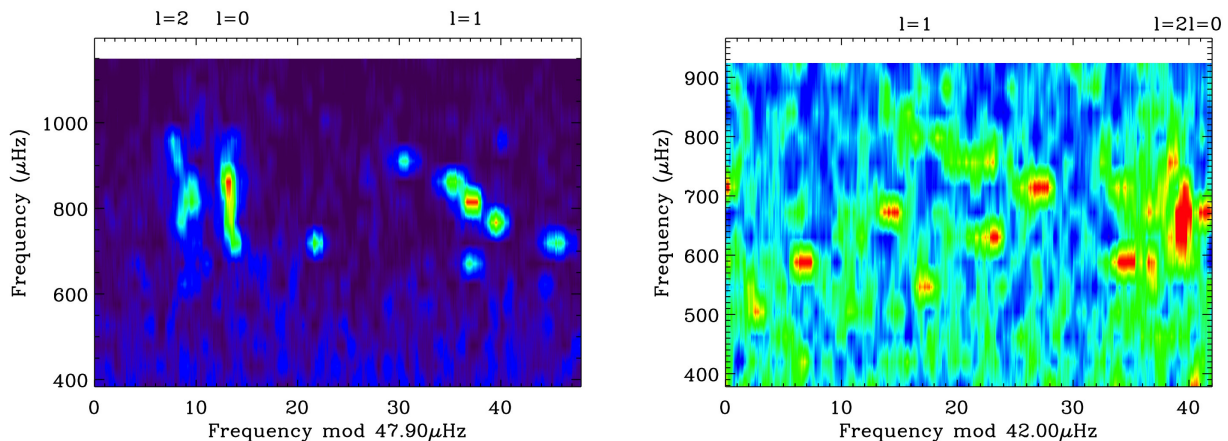


Fig. 1. **Left:** Echelle diagram of 8 months of data for KIC 11395018. **Right:** Echelle diagram of 8 months of data for the star KIC 11234888.

Figure 1 shows the échelle diagrams of the two stars. This diagram is computed as follows: we take segments in the power spectrum of width approximately $\langle \Delta\nu \rangle$ and stack them one on top of each other. The left panel shows the ridges $\ell = 0, 1$, and 2 for KIC 1139501. We can also note the presence of an avoided crossing, where an $\ell = 1$ is “bumped” because of the coupling between acoustic and gravity modes. The right panel shows that

KIC 11234888 has several avoided crossings. The presence of the mixed modes is very important to constrain the age of the star (see for example Metcalfe et al. 2010).

Finally, we were able to have a first estimate for the splitting and inclination angle of the star KIC 11395918 using the MCMC approach. It gave an estimation of the projected rotational splitting $\nu_s^* = \nu_s \sin(i)$ (where ν_s is the splitting) of $0.29 \pm 0.06 \mu\text{Hz}$ and an inclination angle $i > 20^\circ$, with a confidence level of 68 %.

3 Conclusions

We analyzed the power spectra of two solar-type stars observed by *Kepler* during approximately eight months. We obtained not only the first estimates of the p-mode global parameters but also the individual frequencies of the p modes. We identified 22 p modes in the range 600 to 1000 μHz for KIC 11395018 and 16 p modes in the range 500 to 900 μHz for KIC 11234888.

Using scaling relations (Kjeldsen & Bedding 2011; Huber et al. 2010; Verner et al. 2011), we can have a first estimate of the mass and radius of the stars. For KIC 11395018, we obtain: $M = 1.25 \pm 0.24 M_\odot$ and $R = 2.15 \pm 0.21 R_\odot$, while for KIC 11234888, we have $M = 1.33 \pm 0.26 M_\odot$ and $R = 2.4 \pm 0.24 R_\odot$.

These stars will be studied in more details using stellar modeling that combines the individual mode frequencies and the atmospheric parameters to retrieve precise estimates of the stellar parameters (Creevey et al. 2011, Brandão et al., in prep.; Doğan et al., in prep.).

This is the beginning of a new era as we are now able to measure the frequencies of p modes in a few hundreds of solar-type stars. This allow us to start testing and improving the stellar modeling codes with a very large sample of stars for the first time and to better understand stellar evolution.

Funding for this Discovery mission is provided by NASAs Science Mission Directorate. The author wishes to thank the entire Kepler team, without whom these results would not be possible. The author also thanks the members of the KASC Working Group 1, all funding councils and agencies that have supported the activities of KASC Working Group 1, and the International Space Science Institute (ISSI). NCAR is supported by the National Science Foundation.

References

- Appourchaux, T., Belkacem, K., Broomhall, A.-M., et al. 2010, *A&A Rev.*, 18, 197
- Appourchaux, T., Gizon, L., & Rabello-Soares, M.-C. 1998, *A&AS*, 132, 107
- Arentoft, T., Kjeldsen, H., Bedding, T. R., et al. 2008, *ApJ*, 687, 1180
- Baglin, A., Auvergne, M., Boisnard, L., et al. 2006, in *COSPAR, Plenary Meeting, Vol. 36, 36th COSPAR Scientific Assembly*, 3749
- Ballot, J., Gizon, L., Samadi, R., et al. 2011, *A&A*, 530, A97
- Beck, P. G., Bedding, T. R., Mosser, B., et al. 2011, *Science*, 332, 205
- Bedding, T. R., Mosser, B., Huber, D., et al. 2011, *Nature*, 471, 608
- Bonanno, A., Benatti, S., Claudi, R., et al. 2008, *ApJ*, 676, 1248
- Borucki, W. J., Koch, D., Basri, G., et al. 2010, *Science*, 327, 977
- Bruntt, H., Suárez, J. C., Bedding, T. R., et al. 2007, *A&A*, 461, 619
- Campante, T. L., Handberg, R., Mathur, S., et al. 2011, *ArXiv e-prints* 1108.3807
- Campante, T. L., Karoff, C., Chaplin, W. J., et al. 2010, *MNRAS*, 408, 542
- Chaplin, W. J., Kjeldsen, H., Christensen-Dalsgaard, J., et al. 2011, *Science*, 332, 213
- Creevey, O. L., Doğan, G., Frasca, A., et al. 2011, *A&A*, in press
- García, R. A., Hekker, S., Stello, D., et al. 2011, *MNRAS*, 414, L6
- García, R. A., Régulo, C., Samadi, R., et al. 2009, *A&A*, 506, 41
- García, R. A., Turck-Chièze, S., Jiménez-Reyes, S. J., et al. 2007, *Science*, 316, 1591
- Gilliland, R. L., Jenkins, J. M., Borucki, W. J., et al. 2010, *ApJ*, 713, L160
- Handberg, R. & Campante, T. L. 2011, *A&A*, 527, A56
- Harvey, J. 1985, in *ESA Special Publication, Vol. 235, Future Missions in Solar, Heliospheric & Space Plasma Physics*, ed. E. Rolfe & B. Battrock, 199
- Hekker, S., Broomhall, A., Chaplin, W. J., et al. 2010, *MNRAS*, 402, 2049
- Huber, D., Bedding, T. R., Stello, D., et al. 2010, *ApJ*, 723, 1607
- Huber, D., Stello, D., Bedding, T. R., et al. 2009, *Communications in Asteroseismology*, 160, 74

- Jenkins, J. M., Caldwell, D. A., Chandrasekaran, H., et al. 2010, *ApJ*, 713, L87
- Kjeldsen, H. & Bedding, T. R. 2011, *A&A*, 529, L8
- Kjeldsen, H., Christensen-Dalsgaard, J., Handberg, R., et al. 2010, *Astronomische Nachrichten*, 331, 966
- Mathur, S., García, R. A., Catala, C., et al. 2010a, *A&A*, 518, A53
- Mathur, S., García, R. A., Régulo, C., et al. 2010b, *A&A*, 511, A46
- Mathur, S., Handberg, R., Campante, T. L., et al. 2011a, *ApJ*, 733, 95
- Mathur, S., Hekker, S., Trampedach, R., et al. 2011b, *ApJ*, 741, 119
- Metcalfe, T. S., Monteiro, M. J. P. F. G., Thompson, M. J., et al. 2010, *ApJ*, 723, 1583
- Mosser, B. & Appourchaux, T. 2009, *A&A*, 508, 877
- Mosser, B., Barban, C., Montalbán, J., et al. 2011, *A&A*, 532, A86
- Mosser, B., Michel, E., Appourchaux, T., et al. 2009, *A&A*, 506, 33
- Roxburgh, I. W. 2009, *A&A*, 506, 435
- Verner, G. A., Elsworth, Y., Chaplin, W. J., et al. 2011, *MNRAS*, 415, 3539
- Walker, G., Matthews, J., Kuschnig, R., et al. 2003, *PASP*, 115, 1023

RED GIANTS UNVEILED

B. Mosser¹

Abstract. The CoRoT and Kepler missions provide us with thousands of red giant light curves that allow a very precise asteroseismic study of these objects. Before these space missions, the red giant oscillation patterns remained obscure. Now, these spectra are completely clear. Moreover, they unveil many crucial interior structure properties. For thousands of red giants, we can derive from the seismic data: precise estimates of the stellar mass and radius, the evolutionary status of the giants (with a clear difference between clump and RGB stars), the internal differential rotation, the mass loss, the distance of the stars... Analyzing this large amount of information is made easy by the identification of the largely homologous red giant oscillation pattern. This allows us, for instance, to identify rotation scaling relations, or to measure the mode visibility and the bolometric amplitudes. Fine details completing the red giant oscillation pattern then provide further information for a more detailed view on the interior structure.

Keywords: stars: oscillations, stars: interiors, stars: evolution, stars: late-type, methods: data analysis

1 Introduction

The CNES CoRoT and NASA *Kepler* missions provide us with thousands of high-precision photometric light curves for asteroseismic observations (Michel et al. 2008; Gilliland et al. 2010). A large part of the observed stars are red giants. Their observations have opened a new era in red giant asteroseismology since they give a precise view of pressure modes (p modes), corresponding to oscillations propagating essentially in the large stellar convective envelopes, as well as of mixed modes, corresponding to pressure waves coupled to gravity waves propagating in the core radiative regions.

First ground-based red giant seismic observations were restrained by a ‘short’ observation duration (of about 1 month) and a poor duty cycle (Frandsen et al. 2002). As a consequence, even if solar-like oscillations were undoubtedly detected, open questions remained, concerning the possible existence of non-radial modes and the measurement of the mode lifetimes in red giants. As a consequence, the physical output of this pioneering work remained unfortunately limited, but motivated a large interest. Red giant seismology has therefore been defined as an objective for the CoRoT and *Kepler* missions.

First CoRoT results on red giants have reported the presence of radial and non-radial oscillations in more than 300 giant stars (De Ridder et al. 2009). They have confirmed the solar-like oscillations, measured mode lifetimes of the order of a month, and found giants with a complex spectrum. This paper aims to summarize the major outputs of these space observations obtained with CoRoT and *Kepler*.

2 Scaling relations

Before addressing the full properties of a red giant oscillation spectrum (Fig. 1), we may focus on the global frequency parameters that describe solar-like oscillations. The central frequency ν_{\max} of the oscillation power excess is directly related to the photospheric acoustic cutoff frequency; the large separation $\Delta\nu$ of the pressure modes, measuring the travel time of a sound wave along the stellar diameter, is directly related to the mean value of the stellar density. Due to the amount of data, many automated codes have been developed for measuring these parameters (e.g. Mosser & Appourchaux 2009). The different methods have been extensively tested and

¹ LESIA - Observatoire de Paris, CNRS, Université Pierre et Marie Curie, Université Denis Diderot, 92195 Meudon cedex, France; e-mail: benoit.mosser@obspm.fr

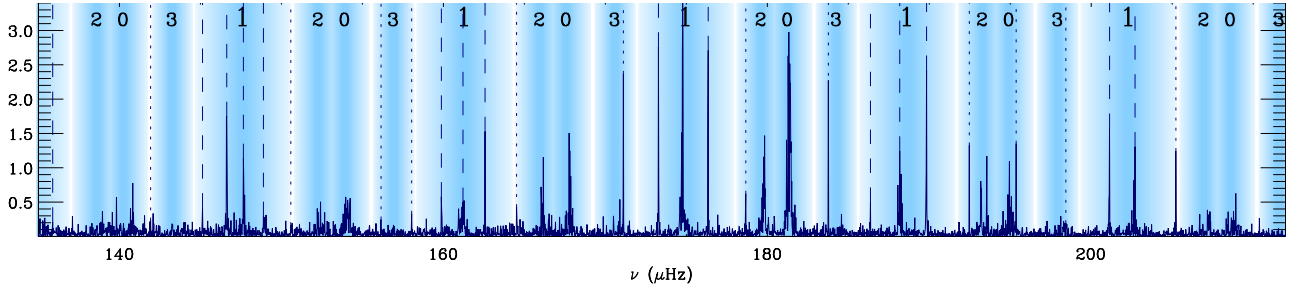


Fig. 1. Power density spectrum of an RGB star observed with *Kepler*. The degrees of the pressure modes are emphasized by the color code. The $\ell = 1$ mixed modes are identified by dashed and dotted vertical lines.

compared (Hekker et al. 2011b; Verner et al. 2011a). Hekker et al. (2009) have shown that $\Delta\nu$ and ν_{\max} are closely related, with a scaling relation of the form

$$\Delta\nu \propto \nu_{\max}^{\alpha} \quad (2.1)$$

The value of α is discussed below. The importance of the measurements of $\Delta\nu$ and ν_{\max} is emphasized by their ability to provide accurate estimates of the stellar mass and radius, as theoretically assessed by Belkacem et al. (2011):

$$\frac{R}{R_{\odot}} = r \left(\frac{\nu_{\max}}{\nu_{\max,\odot}} \right) \left(\frac{\Delta\nu}{\Delta\nu_{\odot}} \right)^{-2} \left(\frac{T_{\text{eff}}}{T_{\odot}} \right)^{1/2} \quad \frac{M}{M_{\odot}} = m \left(\frac{\nu_{\max}}{\nu_{\max,\odot}} \right)^3 \left(\frac{\Delta\nu}{\Delta\nu_{\odot}} \right)^{-4} \left(\frac{T_{\text{eff}}}{T_{\odot}} \right)^{3/2}. \quad (2.2)$$

The solar values are $\Delta\nu_{\odot} = 135.5 \mu\text{Hz}$ and $\nu_{\max,\odot} = 3050 \mu\text{Hz}$, whereas red giant values are much smaller, typically of about 4 and $40 \mu\text{Hz}$, respectively, at the red clump. Calibration with modelled stars has shown that the factors r and m are very close to 1. On the other hand, observations on cluster stars have proven that r and m have a weak dependence, limited to a few percents, in the evolutionary status (Miglio et al. 2011). Grid modelling reaches similar conclusion (White et al. 2011). As a consequence, mass and radius can be reliably estimated with asteroseismic measurements, with conservative uncertainties of about 15 and 7% respectively (Fig. 2a). Ongoing modelling will help to significantly reduce the systematic errors, hence the total uncertainties. We stress that these estimates do not depend on any distance measurements.

The scaling relation $M(\nu_{\max}, \Delta\nu, T_{\text{eff}})$ shows that the exponent of the scaling relation between ν_{\max} and $\Delta\nu$ in Eq. 2.1 is necessarily close to $3/4$, since it implies a relation between $\Delta\nu$ and ν_{\max} of the form:

$$\Delta\nu \propto \nu_{\max}^{3/4} M^{-1/4} T_{\text{eff}}^{3/8} \quad (2.3)$$

For red giants, Mosser et al. (2010) reported a clear correlation between T_{eff} and ν_{\max} : $T_{\text{eff}} \propto \nu_{\max}^{0.04}$. On the other hand, there is no relation between ν_{\max} and M since all stars ascend the RGB, with a negligible mass loss before the tip, so that one derives for red giant stars $\Delta\nu \propto \nu_{\max}^{0.745}$. Observations give very similar results, with an exponent α between 0.745 and 0.764, depending on the method (Huber et al. 2010).

For main-sequence stars, the relation between ν_{\max} and T_{eff} is more steep, and one must take into account the mass dependence in ν_{\max} . From previous CoRoT observations (Barban et al. 2009; García et al. 2009; Benomar et al. 2009; Gaulme et al. 2010; Ballot et al. 2011), we estimate that $T_{\text{eff}} \propto \nu_{\max}^{-0.25}$ and $M \propto \nu_{\max}^{-0.70}$, so that $\Delta\nu \propto \nu_{\max}^{0.83}$ on the main sequence. This is confirmed by the ensemble-asteroseismic results obtained with *Kepler* (Verner et al. 2011b).

Many other scaling relations between frequency and energy global parameters of the oscillations have been identified (Mosser et al. 2011c, and references therein). These scaling relations are not yet fully understood (e.g. Samadi et al. 2007; Stello et al. 2011). They certainly result from the largely homologous properties of the red giant envelope and also reflect the energy partition between convection and oscillations. The link between granulation and oscillations, both related to the convective flux, has been clearly exposed by Mathur et al. (2011), from *Kepler* observations and 3-D convection simulations. Similarly, Mosser et al. (2011c) have shown that the total energy in the oscillations is proportional to the total energy in the granulation. This emphasizes the interest of the scaling relations for the global understanding of the red giant interior structure.

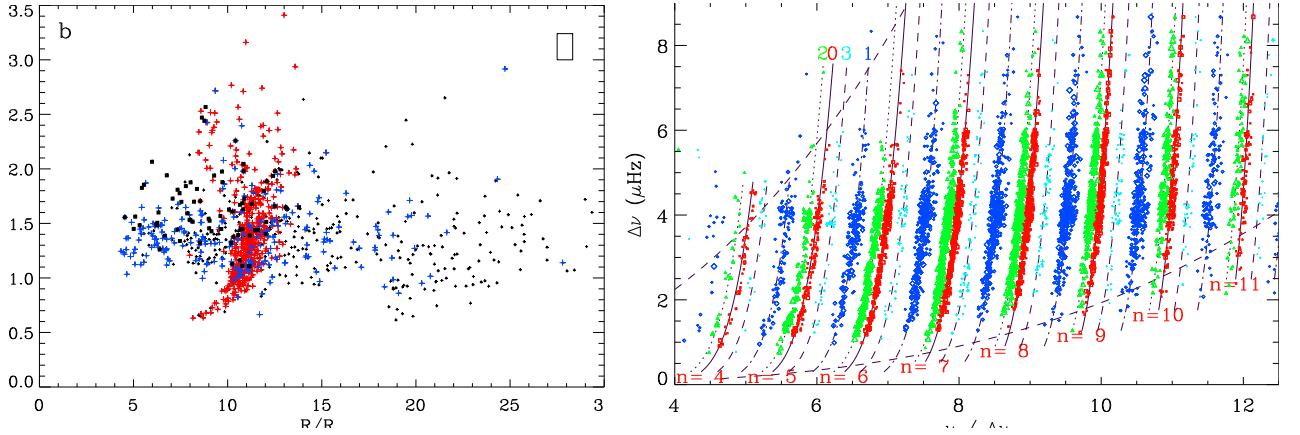


Fig. 2. a: Asteroseismic mass as a function of the asteroseismic radius, from Mosser et al. (2011c). The color code gives the evolutionary status; clump stars in red, giant-branch stars in blue, unknown status in dark grey. The population of giants with very low $\ell = 1$ amplitude is indicated with black squares. The rectangles indicate the mean value of the 1- σ error bars. **b:** Complete identification of the ridges, in red giant oscillation spectra observed with CoRoT and analyzed according to Mosser et al. (2011b). Each colour corresponds to a different mode degree (radial modes in red, dipole modes in dark blue, $\ell = 2$ modes in green, $\ell = 3$ modes in light blue). The dark dashed lines, derived from the scaling law dealing with the oscillation power excess, delineate the region where the modes have noticeable amplitudes (Mosser et al. 2010).

3 The pressure mode oscillation pattern

In this Section, we focus on the p-mode oscillation pattern. Many papers use the simplified form:

$$\nu_{n,\ell} = \left[n + \frac{\ell}{2} + \varepsilon \right] \Delta\nu - d_{0\ell}. \quad (3.1)$$

This form, adapted for red giants from the Tassoul asymptotic relation (Tassoul 1980), introduces mean values of the large separation $\Delta\nu$, of the dimensionless parameter ε , and of the difference $d_{0\ell}$ between non-radial and radial ridges. Various work has shown that all parameters are related to the large separation (Bedding et al. 2010; Mosser et al. 2010; Huber et al. 2010). A refined analysis has shown that a parametrization of the spectrum provides then a very precise measurement of the mean value of the large separation $\Delta\nu$, since it severely reduces the perturbation of the spectrum due to the stochastic excitation of the modes. It also allows an efficient automated identification of the eigenmodes (Fig. 1 and Fig. 2b). The universal red giant oscillation pattern is given by

$$\nu_{n,\ell} = \left[n + \frac{\ell}{2} + \varepsilon(\Delta\nu) - d_{0\ell}(\Delta\nu) + \frac{\alpha}{2} (n - n_{\max})^2 \right] \Delta\nu, \quad (3.2)$$

with $n_{\max} = \nu_{\max}/\Delta\nu$. The constant α , close to 0.008 for radial modes (Mosser et al. 2011b), accounts for the fact that the spacing between consecutive radial eigenfrequencies linearly varies with frequency. As a consequence, the mean large separations introduced by Eqs. 3.1 and 3.2 are not strictly equivalent. In practice, they are very close from each other, and different but very close (about 1%) to the definition related to the stellar acoustic diameter ($\Delta\nu = (2 \int_0^r dr/c)^{-1}$, with c the sound speed) which is considered in the mass and radius scaling relations.

With high-resolution oscillation spectra, it is now possible to investigate a more precise description of the local values of the large separations $\Delta\nu(\nu)$, defined as the spacing between consecutive eigenfrequencies with the same degree ℓ . A systematic modulation in the spectrum was early put in evidence (Mosser et al. 2010). The measurement of $\Delta\nu(\nu)$ for radial modes only (Mosser 2010) allows us to measure the modulation of the large separation due to the helium second-ionization region (Miglio et al. 2010).

4 Mixed modes

Mixed modes correspond to waves propagating as pressure waves in the convective envelope, and as gravity waves in the radiative region of the core. Such modes, with a huge number of nodes inside the core, are able

to analyze in great detail its structure. Their theoretical description can be found in Dupret et al. (2009) and references therein.

In red giants, they were first reported by Beck et al. (2011). The analysis by Bedding et al. (2011) and Mosser et al. (2011a) has shown that they are sensitive to the stellar evolutionary status, and allow us to make a clear difference between RGB stars (with an inactive helium core) and clump stars (burning the central helium). Recent work by Mosser et al. (2011c) shows that the mixed modes also precisely probe the thin shell where hydrogen is burning. Very different mixed-modes spectra are observed, which probably correspond to various situations occurring during the red giant evolution. Mosser et al. (2012) have shown that the mixed-mode eigenfrequency pattern can be modelled with a formalism close to what has been developed for pure p or g modes (Tassoul 1980). This is of great interest for identifying the mixed modes, since the coupling severely complicates their pattern. With the identification of mixed modes in a wide frequency range, we can now propose a direct measure of the g-mode spacing. This gives, for the first time, a clear insight on the red giant core. The mixed modes also directly probe the region where hydrogen burns in shell.

5 Mass loss, populations, red giants in cluster

With space-borne observations, asteroseismic observations now directly constrain the interior structure. We can for instance read in the radius-mass diagram shown in Fig. 2 the signature of the mass loss occurring at the tip of the red giant branch. Most of the stars ascending the RGB have a mass in the range $[1, 2 M_{\odot}]$. Lower mass stars are more rare, since they take time to evolve on the main sequence; higher mass stars evolving rapidly are rare too. After the tip (not yet probed by the data, due to a limit in frequency resolution), the distribution of the stellar mass in the clump starts at $0.6 M_{\odot}$. This means that significant mass loss has occurred at the tip of the RGB. We also note that the mass-radius relation is well defined for clump stars in the range $[0.6, 1.8 M_{\odot}]$. The RGB progenitors of these stars had a degenerate helium core, so that the helium ignition started abruptly. As a consequence of the helium flash, the cores of these stars have very similar masses and physical conditions; the equilibrium state of the envelope then yields the mass-radius relation. Above $1.8 M_{\odot}$, stars of the secondary clump have avoided the helium flash. Hence, the spread in the mass-radius relation is more important than for red-clump stars.

As a direct consequence of the measurement of the stellar radius (Eq. 2.2), the luminosity of the star can be derived from the Boltzmann law, hence its absolute magnitude and its distance. This allows us to probe the stellar population, especially in the different fields of CoRoT, with small galactic latitudes (Miglio et al. 2009). Red giants are also observed in clusters (Basu et al. 2011; Hekker et al. 2011a), with specific consequences due to the advantage of observing stars with similar age and initial composition (Stello et al. 2011).

6 A golden age for red giant asteroseismology

Many topics have not been developed in this rapid review on asteroseismology. A more complete view was given by Bedding (2011). It is worth noting that the modelling of individual stars has just started (Jiang et al. 2011; di Mauro et al. 2011). At the moment, grid modelling is prevailing (e.g. Kallinger et al. 2010). This means that the physics of the models is not specifically addressed. This will be done in a near future, for making the best of asteroseismic constraints, as already shown by Miglio et al. (2010) who showed how the modulation of the large separation directly probes the helium second-ionization region. A direct investigation of the physical conditions in the helium core will be provided by the mixed modes (Mosser et al. 2011c). Furthermore, the way these mixed modes are coupled to the pressure modes will test the shell where hydrogen is burning.

In the future, CoRoT observations are necessary to provide population studies, as shown by Miglio et al. (2009), with access to young populations in the Galactic disk not observed by *Kepler*. On the other hand, *Kepler* observation will benefit from a 4-year long duration, providing very high SNR spectra. They will give access to the inner rotation profile (Beck et al., accepted in Nature) and to the tip of the RGB, with a possible connection with ground-based observations (Dziembowski & Soszyński 2010).

The CoRoT space mission, launched 2006 December 27, was developed and is operated by the CNES, with participation of the Science Programs of ESA, ESAs RSSD, Austria, Belgium, Brazil, Germany, and Spain. Funding for the Discovery *Kepler* mission is provided by NASA's Science Mission Directorate. We gratefully acknowledge the entire CoRoT and *Kepler* teams, whose efforts have made these results possible.

References

- Ballot, J., Gizon, L., Samadi, R., et al. 2011, *A&A*, 530, A97
- Barban, C., Deheuvels, S., Baudin, F., et al. 2009, *A&A*, 506, 51
- Basu, S., Grundahl, F., Stello, D., et al. 2011, *ApJ*, 729, L10
- Beck, P. G., Bedding, T. R., Mosser, B., et al. 2011, *Science*, 332, 205
- Bedding, T. R. 2011, *ArXiv e-prints*
- Bedding, T. R., Huber, D., Stello, D., et al. 2010, *ApJ*, 713, L176
- Bedding, T. R., Mosser, B., Huber, D., et al. 2011, *Nature*, 471, 608
- Belkacem, K., Goupil, M. J., Dupret, M. A., et al. 2011, *A&A*, 530, A142
- Benomar, O., Baudin, F., Campante, T. L., et al. 2009, *A&A*, 507, L13
- De Ridder, J., Barban, C., Baudin, F., et al. 2009, *Nature*, 459, 398
- di Mauro, M. P., Cardini, D., Catanzaro, G., et al. 2011, *MNRAS*, 415, 3783
- Dupret, M., Belkacem, K., Samadi, R., et al. 2009, *A&A*, 506, 57
- Dziembowski, W. A. & Soszyński, I. 2010, *A&A*, 524, A88
- Frandsen, S., Carrier, F., Aerts, C., et al. 2002, *A&A*, 394, L5
- García, R. A., Régulo, C., Samadi, R., et al. 2009, *A&A*, 506, 41
- Gaulme, P., Deheuvels, S., Weiss, W. W., et al. 2010, *A&A*, 524, A47
- Gilliland, R. L., Brown, T. M., Christensen-Dalsgaard, J., et al. 2010, *PASP*, 122, 131
- Hekker, S., Basu, S., Stello, D., et al. 2011a, *A&A*, 530, A100
- Hekker, S., Elsworth, Y., De Ridder, J., et al. 2011b, *A&A*, 525, A131
- Hekker, S., Kallinger, T., Baudin, F., et al. 2009, *A&A*, 506, 465
- Huber, D., Bedding, T. R., Stello, D., et al. 2010, *ApJ*, 723, 1607
- Jiang, C., Jiang, B., Christensen-Dalsgaard, J., et al. 2011, *ArXiv e-prints*
- Kallinger, T., Mosser, B., Hekker, S., et al. 2010, *A&A*, 522, A1
- Mathur, S., Hekker, S., Trampedach, R., et al. 2011, *A&A*, in press
- Michel, E., Baglin, A., Auvergne, M., et al. 2008, *Science*, 322, 558
- Miglio, A., Brogaard, K., Stello, D., et al. 2011, *ArXiv e-prints*
- Miglio, A., Montalbán, J., Baudin, F., et al. 2009, *A&A*, 503, L21
- Miglio, A., Montalbán, J., Carrier, F., et al. 2010, *A&A*, 520, L6
- Mosser, B. 2010, *Astronomische Nachrichten*, 331, 944
- Mosser, B. & Appourchaux, T. 2009, *A&A*, 508, 877
- Mosser, B., Barban, C., Montalbán, J., et al. 2011a, *A&A*, 532, A86
- Mosser, B., Belkacem, K., Goupil, M., et al. 2010, *A&A*, 517, A22
- Mosser, B., Belkacem, K., Goupil, M. J., et al. 2011b, *A&A*, 525, L9
- Mosser, B., Elsworth, Y., Hekker, S., et al. 2011c, *ArXiv e-prints*
- Mosser, B., Goupil, M., Belkacem, K., et al. 2012, submitted to *A&A*
- Samadi, R., Georgobiani, D., Trampedach, R., et al. 2007, *A&A*, 463, 297
- Stello, D., Huber, D., Kallinger, T., et al. 2011, *ApJ*, 737, L10
- Tassoul, M. 1980, *ApJS*, 43, 469
- Verner, G. A., Elsworth, Y., Chaplin, W. J., et al. 2011a, *MNRAS*, 415, 3539
- Verner, G. A., Elsworth, Y., Chaplin, W. J., et al. 2011b, *MNRAS*, 892
- White, T. R., Bedding, T. R., Stello, D., et al. 2011, *ArXiv e-prints*

PULSATION MODES DETECTED BY COROT IN THE HOT BE STAR HD 51452

C. Neiner¹, M. Floquet² and the CoRoT Be team

Abstract. HD 51452 is a hot Be star observed by CoRoT and simultaneous spectroscopy. This star shows pulsation p modes of β Cephei type as expected for this spectral type, as well as g modes with lower frequencies, which are not expected in such stars. We investigate whether this is due to the rotational flattening of the star, allowing for cooler regions at the equator from which SPB-type g -modes excited by the κ mechanism could arise, but conclude that the detected modes are rather stochastic g -modes.

Keywords: stars: emission-line, Be – stars: individual: HD 51452 – stars: oscillations – Stars: rotation

1 Introduction

Be stars are known to pulsate. As of today, the driving mechanism of pulsations in Be stars is thought to be the κ mechanism, i.e. an effect of the opacity of iron-peak elements in the envelope of the star (Dziembowski & Pamiatnykh 1993; Dziembowski et al. 1993). This mechanism only occurs when the opacity bump coincides with the adiabatic and non-adiabatic transition zone. Pressure (p) and gravity (g) modes can then be auto-excited, depending on the depth at which the iron opacity bump is situated in the envelope, i.e. depending on the temperature of the star. In the Milky Way, p -modes are observed in stars down to the B3 spectral type, while g -modes are observed from the B2 spectral type downwards.

2 Observations of HD 51452

HD 51452 is a hot Be star observed with the CoRoT satellite during 114.4 consecutive days. Simultaneously, ground-based observations have been obtained during about 1 month in spectroscopy with HARPS (ESO) and SOPHIE (OHP). Additional spectra from the BeSS database have also been collected, more scarcely but over the whole CoRoT run.

HD 51452 is a B0IVe star as shown by Frémat et al. (2006). For such a hot star, the κ mechanism can create p -modes of pulsations, but cannot excite g -modes. Nevertheless, the pulsation analysis of the CoRoT data of HD 51452 shows that several frequencies below 2 c d^{-1} , i.e. in the frequency domain usually attributed to g -modes, are detected (see Fig. 1) in addition to frequencies of fainter amplitude in the p -mode domain. HD 51452 thus appears as a hybrid pulsator despite its hot spectral type, which is incompatible with the limits of the instability strips determined from theory or observed so far in the Milky Way (e.g. Miglio et al. 2007).

3 Discussion

3.1 Flattening of the star

Since HD 51452 rotates close to its critical velocity, the star is very flattened and its temperature is very different at the pole and at the equator. One possible explanation is therefore that the temperature in the equatorial region is low enough to allow the excitation of g -modes by the κ mechanism, while p -modes would be excited in the rest of the star. The inclination angle at which we observe the star is around ~ 45 degrees, and the observer thus indeed sees both the pole and equator of the star. Accordingly, the spectra reflects the average temperature

¹ LESIA, Observatoire de Paris, CNRS UMR 8109, UPMC, Université Paris Diderot; 5 place Jules Janssen, 92190 Meudon, France

² GEPI, Observatoire de Paris, CNRS UMR 8111, Université Paris Diderot; 5 place Jules Janssen, 92190 Meudon, France

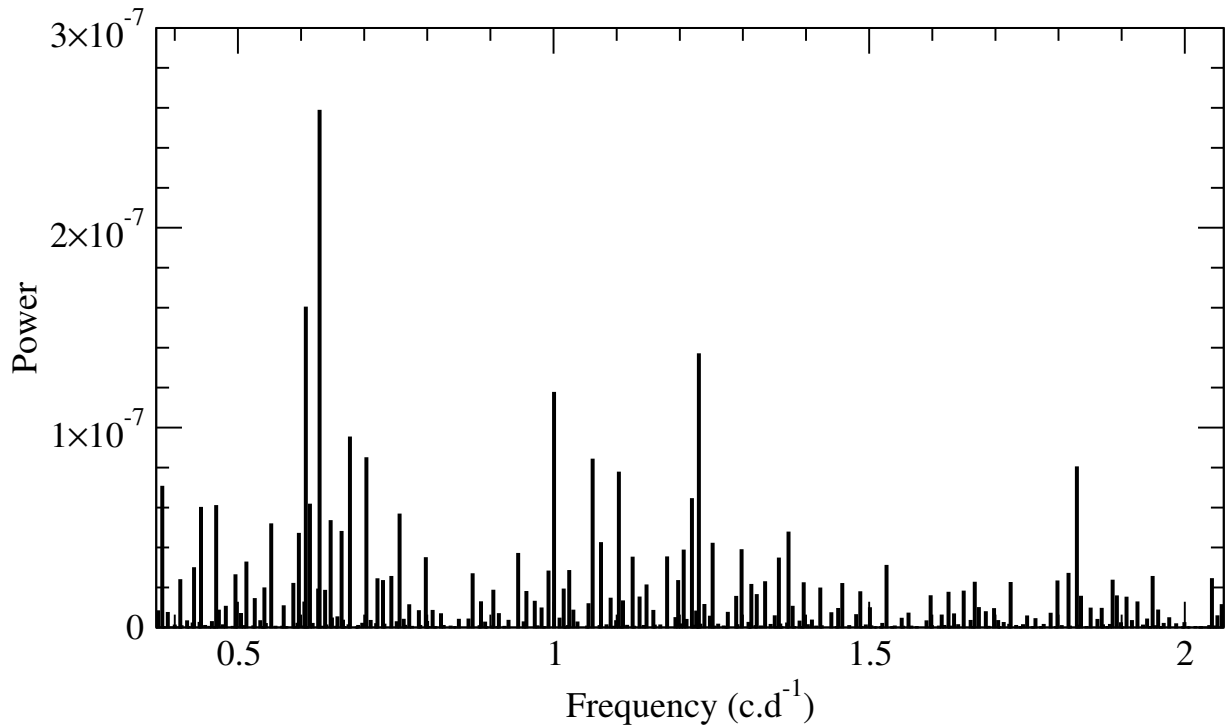


Fig. 1. Power spectrum of the CoRoT data, showing the frequency region $f=0.5$ to 2 c d^{-1} where g -modes are detected.

at the stellar surface. A difference of more than 10000 K would be required between the temperature at the poles and at the equator for the latter to be cool enough to host g -modes. Such a steep profile of temperature is unlikely even with a very strong flattening.

3.2 Stochastic modes

The low frequencies detected in the CoRoT data of HD 51452 should thus be attributed to another excitation mechanism than the κ mechanism. Stochastic low radial order g modes can be excited in the convective core of Be stars while asymptotic g modes can be excited by the iron ionization opacity peak in the sub-surface convection zones (Samadi et al. (2010), see also Cantiello et al. (2011)). Moreover, the convective sub-surface layer is thicker at the equator than at the poles in Be stars because of their rapid rotation and flattening. Stochastic g -modes thus appear has a realistic explanation for the presence of low frequencies in this star. However, the impact of rapid rotation on the excitation of stochastic g modes has only been studied for lower mass stars so far (Belkacem et al. 2009). Note that stochastic g -waves are also put forward as an explanation (Neiner et al. 2011) for the CoRoT observations of the outbursting Be star HD 49330 (Huat et al. 2009; Floquet et al. 2009).

4 Conclusions

HD 51452 is a hot Be star hosting g -modes. Considering the temperature of the star, these modes cannot be driven by the κ mechanism. However, stochastic g modes are predicted by recent theoretical work in early-type stars, and the rapid rotation of HD 51452 may facilitate the presence of a sub-surface convective zone. Thus HD 51452 is probably the first Be star for which stochastic g modes are clearly detected.

The CoRoT space mission, launched on December 27th 2006, has been developed and is operated by CNES, with the contribution of Austria, Belgium, Brasil, ESA (RSSD and Science Program), Germany and Spain. We wish to thank the CoRoT team for the acquisition and reduction of the CoRoT data.

References

- Belkacem, K., Mathis, S., Goupil, M. J., & Samadi, R. 2009, *A&A*, 508, 345
- Cantiello, M., Braithwaite, J., Brandenburg, A., et al. 2011, in *IAU Symposium*, ed. C. Neiner, G. Wade, G. Meynet, & G. Peters, Vol. 272, 32
- Dziembowski, W. A., Moskalik, P., & Pamyatnykh, A. A. 1993, *MNRAS*, 265, 588
- Dziembowski, W. A. & Pamiatnykh, A. A. 1993, *MNRAS*, 262, 204
- Floquet, M., Hubert, A.-M., Huat, A.-L., et al. 2009, *A&A*, 506, 103
- Frémat, Y., Neiner, C., Hubert, A.-M., et al. 2006, *A&A*, 451, 1053
- Huat, A.-L., Hubert, A.-M., Baudin, F., et al. 2009, *A&A*, 506, 95
- Miglio, A., Montalbán, J., & Dupret, M.-A. 2007, *Communications in Asteroseismology*, 151, 48
- Neiner, C., Saio, H., Lovekin, C., Mathis, S., & Lee, U. 2011, *A&A*, in preparation
- Samadi, R., Belkacem, K., Goupil, M. J., et al. 2010, *Ap&SS*, 328, 253

SURFACE CONVECTION: FROM THE SUN TO RED GIANT STARS

L. Piau¹, P. Kervella², S. Dib³ and P. Hauschildt⁴

Abstract. We check how the change in surface conditions between the Sun and red giant branch stars changes the characteristic surface convection length scale to be used in models. We investigate the question in the case of the mixing length theory and of the phenomenology of full spectrum of turbulence. For the observational part, we rely on independent measurements of effective temperatures and interferometric radii of nearby red giants. We find that the local red giant branch cannot be explained taking into account the solar calibrated convective length scale.

Keywords: surface convection, Sun, red giant stars, interferometry

1 Introduction

In low mass stars the effective temperature and the radius estimate the efficiency of surface convection. The Sun and the red giant branch stars (hereafter RGBs) have very different surface conditions. A red giant surface gravity and energy flux are much smaller than the solar ones. The purpose of the work we present is to check how this changes the surface convection efficiency. First we build calibrated solar models using the mixing length theory (hereafter MLT) or the phenomenology of full spectrum of turbulence by Canuto, Goldman & Mazzitelli (1996) (hereafter CGM) for surface convection. Then relying on the same input physics, we build red giant models. The red giant models radii and effective temperatures are compared to an observational sample of 38 objects for which the radii are known directly through interferometry to better than 10 percent. Absolute luminosities and effective temperatures of these objects are also accurately known. In the next section we give the main ingredients of the models affecting the radius and effective temperature and address the solar calibration. In section 3 we describe the RGBs giant sample. Section 4 investigates the changes in characteristic convection length scale from the Sun to RGBs. We conclude in section 5.

2 Models inputs and solar convection length scale

The radii of solar and RGBs models are tuned by the outer thermal gradient. It depends on four ingredients:

1. The opacities. We rely on the OPAL opacities and, below 5600K, on the Ferguson et al. (2005) opacities. The composition is either assumed to be solar with $X=0.7392$, $Z=0.0122$ (Asplund et al. 2005) or slightly subsolar at $[\text{Fe}/\text{H}]=-0.17$. The metal repartition is always the one of Asplund et al. (2005).
2. Convection efficiency to transport energy. The poor efficiency of outer convection induces the subsurface superadiabatic gradient which in turn sets the entropy of the deep convection zone. A lower entropy level of the deep convection zone means a less dense envelope and thus a wider radius and a lower effective temperature. To model the inefficient convection we use two simplified local treatments of convection: the mixing length theory (Böhm-Vitense 1958) and the full spectrum of turbulence of Canuto, Goldman & Mazzitelli (1996). For both treatments the characteristic convection length scale Λ is assumed to be a constant fraction of the local pressure scale height: $\Lambda = \alpha H_p$.

¹ LATMOS, 11 Boulevard d'Alembert, 78280 Guyancourt, France

² LESIA, Observatoire de Paris, CNRS UMR 8109, UPMC, Université Paris Diderot, 5 place Jules Janssen, 92195 Meudon, France

³ Astrophysics Group, Imperial College of Science, Technology and Medicine, London SW7 2AZ, United Kingdom

⁴ Hamburger Sternwarte, Gojenbergsweg 112, 21029 Hamburg, Germany

3. Atmospheric effects. At the edge of the star the diffusion approximation does not hold for photons and lines strongly affect the radiative transfer: these effects are expressed by the temperature-optical depth relations that are provided by atmosphere models. We use two series of non-grey atmosphere models as outer boundary conditions. The first series of relations ($T(\tau)^4 = T_{\text{eff}}^4 f_{\text{grid}}(\tau)$) is computed with the PHOENIX/1D atmosphere code where the convection is handled using the MLT. The second series of temperature-optical depth relations is computed with the Atlas12 atmosphere code (Castelli 2005). We modified Atlas12 to use the CGM prescription. Each type of atmosphere models are used with the corresponding phenomenology of convection in the deeper regions as is necessary for consistency in the models (Montalbán et al. 2004).
4. The equation of state influences the radius through the adiabatic exponents. We use the OPAL EoS.

We assume that $L_{\odot} = 3.846 \cdot 10^{33} \text{ ergs}^{-1}$ and $R_{\odot} = 6.9599 \cdot 10^{10} \text{ cm}$ and begin the solar evolution on the zero age main sequence. The calibration in luminosity, radius, and metal-to-hydrogen ratio $\frac{Z_{\text{surf}}}{X_{\text{surf}}}$ are achieved to better than 10^{-4} at the age of 4.6 Ga for both MLT and CGM convection prescriptions. In the MLT framework we obtain $\alpha_{\text{mlt}\odot} = 1.98$, in the CGM framework we obtain $\alpha_{\text{cgm}\odot} = 0.77$.

3 The red giant sample

We first queried the CHARM2 catalogue (Richichi et al. 2005) to obtain all direct measurements of giant and subgiant angular diameters up to 2004, with effective temperatures in the range from 5000 K to 5500 K. We then searched the literature for more recent observations, and added the measurement of γ Sge, δ Eri, ξ Hya, and the recent high accuracy CHARA/FLUOR measurements of ϵ Oph and η Ser. The conversion of uniform disk angular diameters to limb-darkened values was done using linear limb-darkening coefficients by Claret et al. (1995), which are based on stellar atmosphere models by Kurucz (1993). Our sample contains 38 giant and subgiant stars with spectral types from G5 to M0. The distances to the selected stars range from 11 to 110 pc. Thanks to this proximity, we neglected the interstellar reddening for the computation of the bolometric luminosity. The accurate parallaxes and interferometric angular radii estimates allow the objects to have a relative uncertainty in the linear radius smaller than 10%. The average metallicity is slightly subsolar $[\text{Fe}/\text{H}] = -0.17$ with no object below -0.44 and no object above 0.04 but one exception at 0.13.

4 Red giant branch calibration

We model RGB stars up to 10^3 solar luminosity with exactly the same physics as in the solar models. The microscopic diffusion is accounted for in any model warmer than 5000 K following Proffitt & Michaud (1993). This is important in order to obtain correct ages as diffusion speeds up the main sequence evolution. After the first dredge-up though ($T_{\text{eff}} < 5000 \text{ K}$) diffusion effects become negligible. Provided the atmosphere boundary models and the opacity tables are unchanged, there are three main model inputs that change the position of the RGB: the mass, the metallicity and the surface convection characteristic length scale. The latter parameter is what we want to constrain. As mentioned above the more efficient the convection, the smaller the radius and the higher the effective temperature at a given luminosity. The metallicity of the sample is known and is therefore no hurdle. The masses of the stars however are not known: unlike RGB stars of a globular or a Galactic cluster, the RGB stars of the sample are field stars that presumably have different masses and ages. Yet it is possible to set an upper limit to the age of local red giants or equivalently a lower limit to their masses. The limit is given by the age of the Galactic disk and the evolutionary timescale of its low mass stars: for objects in the slightly subsolar metallicity range ($-0.25 < [\text{Fe}/\text{H}] < -0.14$), Liu & Chaboyer (2000) suggest a maximum age of $11.7 \pm 1.9 \text{ Ga}$. In this study, we consider models that have reached $10^3 L_{\odot}$ on the RGB by that age as our RGB stars exhibits $[\text{Fe}/\text{H}] = -0.17$ on average. We can set broader upper limits to the local Galactic disk age: it is certainly younger than the Universe $13.7 \pm 0.1 \text{ Ga}$ (Komatsu et al. 2009). In the next subsections we focus on the lower envelope of the RGB i.e. on these stars with the lower effective temperature or larger radii at a given luminosity (see Figure 1). They are also the oldest and lowest mass stars of the sample.

4.1 Mixing length theory

Figure 2 (left panel) shows the six lower envelope stars of the RGB and features different evolutionary tracks. Let's define $\chi_1^2 = \sum_{i=1}^N (1/N) [(T_{\text{eff}}^{\text{mod}} - T_{\text{eff}}^{\text{obs}}) / \Delta T_{\text{eff}}^{\text{obs}}]^2$, where $T_{\text{eff}}^{\text{obs}}$, $T_{\text{eff}}^{\text{mod}}$ and $\Delta T_{\text{eff}}^{\text{obs}} = 130 \text{ K}$ are respectively the

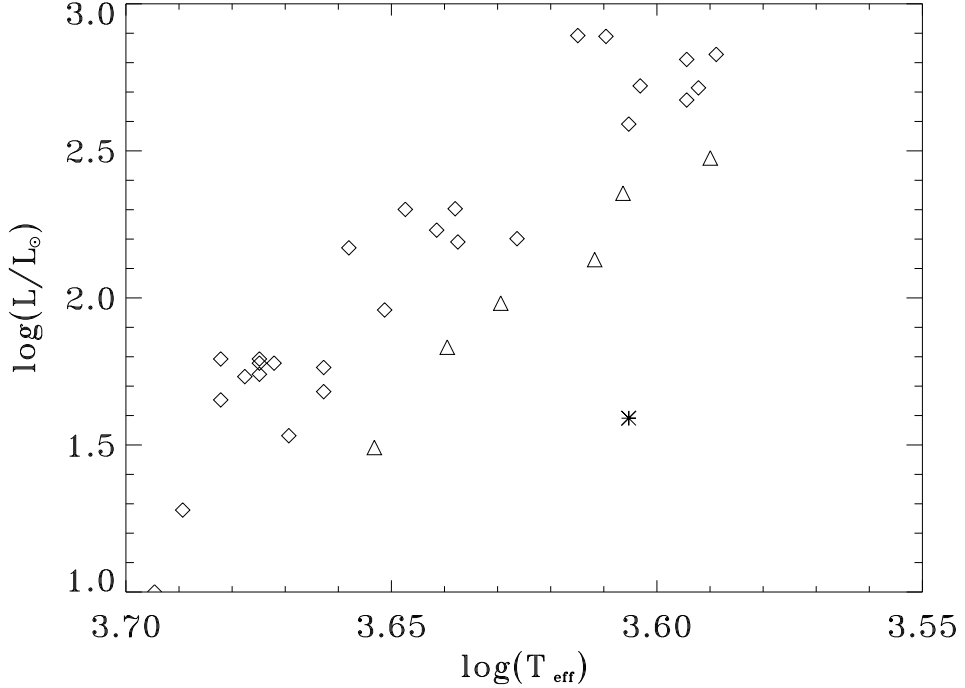


Fig. 1. HR diagram of the RGB stars sample. The triangles define the lower envelope of the RGB in the sense that they show the stars with the lowest effective temperature for a given luminosity.

observed T_{eff} of an object, the T_{eff} of the model having the same luminosity as the object and the uncertainty on the observed T_{eff} . N is the number of objects considered. Figure 2 (left panel) models in solid line, dashed line and dotted line all use the solar calibrated value of $\alpha_{\text{mlt}} = 1.98$. The solid line track corresponds to a $0.95M_{\odot}$ star reaching 10^3L_{\odot} at ≈ 11.5 Ga. This model has $[\text{Fe}/\text{H}] = -0.17$ and an helium fraction $Y=0.2582$. It is clearly too warm to fit the lower envelope of the RGB: $\chi_1^2=3.8$. The dashed and dotted lines correspond to less massive and helium poorer stars with $0.9M_{\odot}$ and $Y=0.2482$ respectively. The lower mass model is extreme in the sense that it reaches 10^3L_{\odot} at ≈ 13.9 Ga (or 10^2L_{\odot} at ≈ 13.88 Ga), which is older than the current age estimate of the Universe. The helium poor model is also extreme in the sense that its helium fraction nearly is that of Big Bang nucleosynthesis (Coc et al. 2004) and evidently cannot be lowered any further. Both two last models are in slightly better agreement with the data than the former one. Yet they do not provide a good fit to the observations. This demonstrates that mass or helium fraction cannot be changed to improve the agreement to the observations. Models with lower α_{mlt} than the solar value provide much better fits to the data. The three dotted-dashed line is the track of the model with $\alpha_{\text{mlt}} = 1.68$, $0.95M_{\odot}$, and $[\text{Fe}/\text{H}] = -0.17$. This model reaches 10^3L_{\odot} at 11.5 Ga and has $\chi_1^2=0.16$. The long-dashed line model has $\alpha_{\text{mlt}} = 1.68$, $1.13M_{\odot}$, and $[\text{Fe}/\text{H}] = 0$. It reaches 10^3L_{\odot} at 7.5 Ga and has $\chi_1^2=0.078$. The analysis in the HR diagram suggests a smaller than solar calibrated characteristic length scale for the MLT.

4.2 Full spectrum of turbulence phenomenology

We will now perform a similar analysis as above but regarding the CGM phenomenology. Furthermore, instead of using T_{eff} we will use the interferometric radii. We therefore do not set ourselves in the HR diagram but in a luminosity vs. square of radius diagram (see Figure 2 right panel). Let's define $\chi_2^2 = \sum_{i=1}^N (1/N)[(R_{\text{mod}}^2 - R_{\text{obs}}^2)/\Delta R_{\text{obs}}^2]^2$. Once again N is the number of objects considered. R_{obs} , R_{mod} and ΔR_{obs} are respectively the observed radius of an object, the radius of the model having the same luminosity as the object and the uncertainty on the observed radius. Figure 2 (right panel) shows the nine stars with the largest radii at given luminosities. They were selected by considering the nine largest deviations to a linear fit of the whole sample in the luminosity vs. square radius diagram. The solid line track in Figure 2 (right panel) corresponds to a

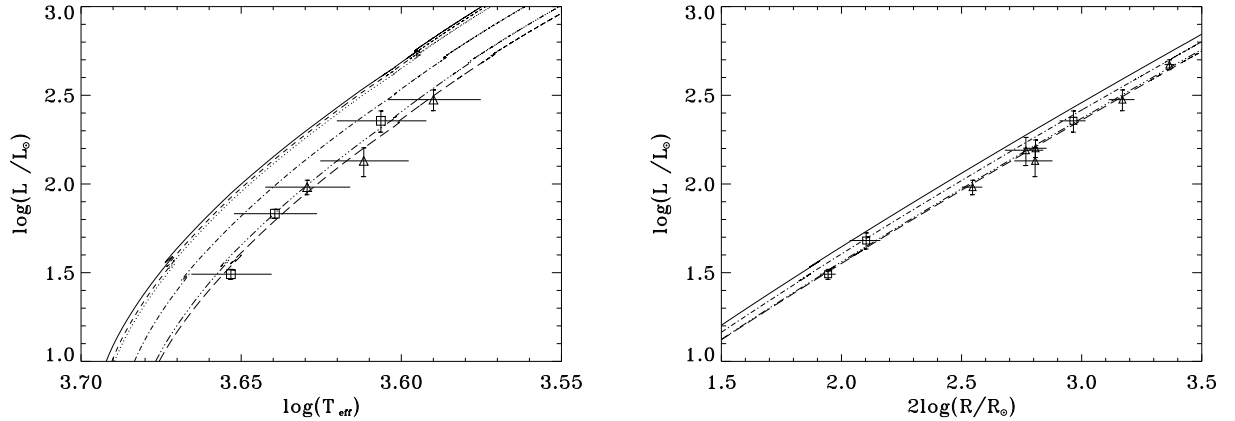


Fig. 2. Left: Position of the six lower envelope stars of the sample with T_{eff} errorbars and various evolutionary tracks computed using the MLT. See text for a description of the corresponding models. **Right:** Position of the nine stars of the sample with largest radii and errorbars. The various evolutionary tracks in overplot were computed using the CGM. See text for a description of the corresponding models.

0.95 M_{\odot} star reaching 10^3L_{\odot} at ≈ 11.6 Ga. This model has $[\text{Fe}/\text{H}] = -0.17$, an helium fraction $Y=0.2582$ and the solar-calibrated value $\alpha_{\text{cgm}} = 0.77$. This model corresponds to too small radii to fit the lower envelope of the RGB: $\chi_2^2 = 7.2$. As in the case of the MLT, changes in mass and helium fraction are unable to significantly improve the agreement to the data and we will not discuss them. On the opposite if we decrease α_{cgm} down to 0.62 we recover a good agreement to the observations. The three dotted-dashed line is the track of the model with $\alpha_{\text{cgm}} = 0.62$, 0.95 M_{\odot} , and $[\text{Fe}/\text{H}] = -0.17$. This model reaches 10^3L_{\odot} at 11.8 Ga and has $\chi_2^2=0.70$. The long-dashed line model has $\alpha_{\text{mlt}} = 0.62$, 1.17 M_{\odot} , and $[\text{Fe}/\text{H}] = 0$. It reaches 10^3L_{\odot} at 6.9 Ga and has $\chi_2^2=0.40$. The analysis in the luminosity radius diagram suggests a smaller than solar calibrated characteristic length scale for the CGM.

5 Conclusion

We modelled the Sun and local RGB stars in order to check if the change in surface conditions implies a change of the characteristic convection length scale Λ for two local treatments of convection: the MLT and the CGM. In both cases we assume $\Lambda = \alpha H_p$. Therefore we do not consider the original version of the CGM where the characteristic convection length scale is the distance to the boundary with the region stable with respect to convection. At a given absolute luminosity α tunes the position of the RGB in effective temperature and in radius. We have accurate data on absolute luminosities, effective temperatures and radii of all RGB stars we consider. The location of the coolest stars or equivalently the largest radii stars of the sample suggest a decrease in surface characteristic length scale with respect to its solar calibrated value. We have shown the decrease to be required for the MLT in the HR diagram and for the CGM in the luminosity radius diagram. However we could have inverted the diagrams with respect to the convection treatments, the result would have been similar. The reader will find many more details in Piau et al. (2011) where we also specifically address the three RGB stars of the sample with asteroseismic mass estimates. The combination of interferometric and asteroseismic data clearly opens up new perspectives in the understanding of stellar fundamental parameters and how they can be used to constrain stellar physics (Huber et al. 2011).

This work has been supported by LATMOS of Centre National de la Recherche Scientifique and the Centre National d'Etudes Spatiales for the scientific return of the Picard mission.

References

- Asplund, M., Grevesse, N., Sauval, J., 2005, ASP Conference Series, Vol XXX.
 Böhm-Vitense, E., 1958, Zs. f. Ap., 46, 108

- Canuto, V. M., Goldman, I., Mazzitelli, I., 1996, *ApJ*, 473, 550
- Castelli, F., 2005, *MSAIt*, 8, 25
- Claret, A., Diaz-Cordoves, J., Gimenez, A. 1995, *A&A Suppl. Ser.*, 114, 247
- Coc, A., Vangioni-Flam, E., Descouvemont, P., Adahchour, A., Angulo, C., 2004, *ApJ*, 600, 544
- Ferguson, J. W., Alexander, D., Allard, F. Barman, T. Bodnarik, J., Hauschildt, P., et al. , 2005, *ApJ*, 623, 585
- Huber, D., et al., 2011, in preparation
- Komatsu, E., Dunkley, J., Nolta, M. R., Bennett, C. L., Gold, B., Hinshaw, G., and 13 coauthors, 2009, *ApJS*, 180, 330
- Kurucz, R. L., 1993, CD-ROM 13, Cambridge, SAO
- Liu, W. M., Chaboyer, B., *ApJ*, 2000, 544, 818
- Montalban, J., D'Antona, F., Kupka, F., Heiter, U., 2004, *A&A*, 416, 1081
- Piau, L., Kervella, P., Dib, S., Hauschildt, P., 2011, *A&A*, 526, 100
- Proffitt, C. R., Michaud, G., 1993, *ASP Conference Series*, Vol. 40, 246
- Richichi, A., Percheron, I., Khristoforova, M. 2005, *A&A*, 431, 773

PHOTOSPHERIC MOTIONS FROM AN OBSERVATIONAL POINT OF VIEW: HINODE AND SDO SATELLITE OBSERVATIONS

T. Roudier¹

Abstract. Thanks to the Solar Optical Telescope onboard HINODE, we mainly aim at the understanding of temporal evolution and spatial characterization of solar granular and supergranular features and their relation with magnetic field. We study the photospheric motions and the network magnetic field interactions using the Tree of Fragmenting Granules (TFGs). The mutual interactions of the TFGs tend to expulse corks outside of them on 3h-4h and concentrate the corks on supergranular scale in approximately 6h-8h to form the magnetic network. Then, the long living families contribute to form the magnetic network. The measurement of the horizontal velocities by the proper motion of granules over the full Sun with SDO data, allow us to determine, for the first time, the solar differential rotation directly at the central meridian. During the starting phase of the solar cycle 24, the solar differential rotation seems to show some modification which must be confirmed.

Keywords: Sun granulation, Sun photosphere, Sun rotation

1 Introduction

Understanding the distribution and diffusion of magnetic flux at the solar surface is of primary importance to describe many aspects of solar magnetism and activity, and notably requires to uncover the physical nature of flows at various scales which contribute to the transport of magnetic elements. The movements of the solar plasma generate magnetic field at different depths in the convection zone. The determination of these convective motions below the surface is a challenge which can be done using helioseismology but only in the first Megameters. However, today we can access to the solar surface motions over the entire solar disk.

Answering these questions requires high-resolution observations of the solar surface dynamics on a large field of view and for several consecutive hours. We present new observations from the HINODE and SDO satellites which fulfill some of these requirements.

2 Supergranulation and TFGs evolution from HINODE observation

The solar surface is now described as being structured in several sizes of “convective” scale: granulation, meso-granulation and supergranulation. From these three types of observed scale, only the physical nature of the solar granulation is really determined today. Hence, from many points of view, supergranulation is an essential element of the surface or atmospheric magnetic activity of the Sun. Its physical nature is still in debate and new measurements are required in order to progress in the understanding of its physical origin.

3D analysis (x, y, t) of the granular intensity field demonstrates that a significant fraction of the granules in the photosphere are organized in the form of Tree of Fragmenting Granules (TFGs, Roudier et al. 2003). A TFG consists of a family of repeatedly splitting granules, originating from a single granule (see Fig. 1).

The typical size of mature TFGs indicate that they trace some mesoscale rising plumes. In the old debate on the specificity of mesogranulation as a genuine scale of sub-photospheric convection rather than a mere extension of granular flow, TFGs point towards the genuine scale. Following the evolution of TFGs on two days showed their distribution among a supergranule which basically advects them. The use of floating corks demonstrates

¹ Institut de Recherche en Astrophysique et Planétologie, Université de Toulouse, CNRS, 14 avenue Edouard Belin, 31400 Toulouse, France

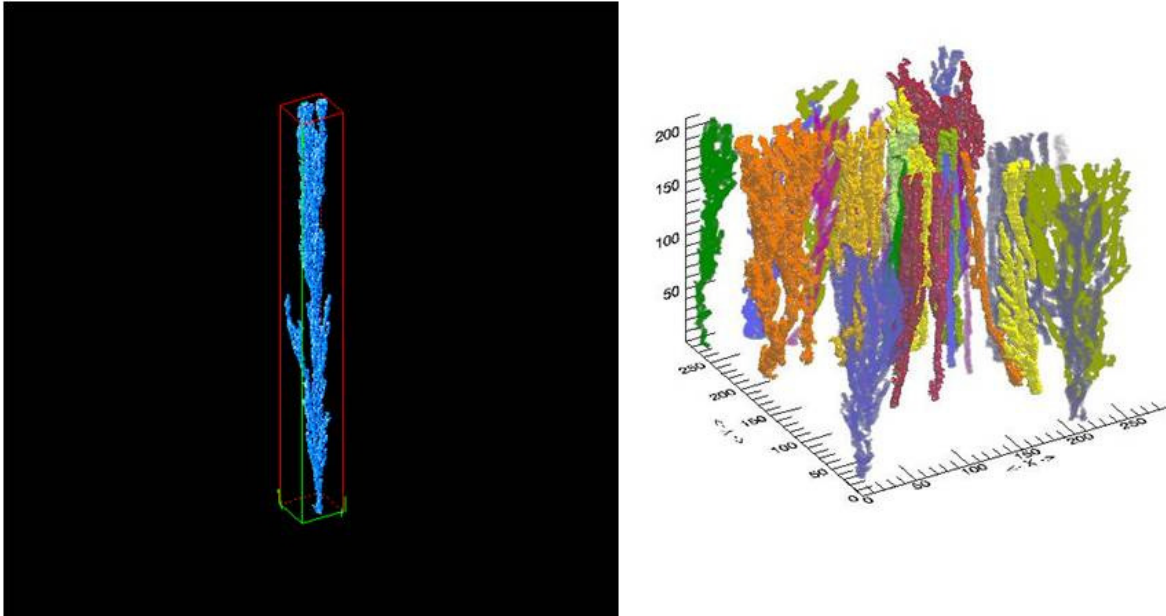


Fig. 1. Left: 3D (x, y, t) representation of a TFG with a lifetime of 8h10 which influenced a total area of $15'' \times 17''$. **Right:** Example of the 3D (x, y, t) evolution of different families in the same field.

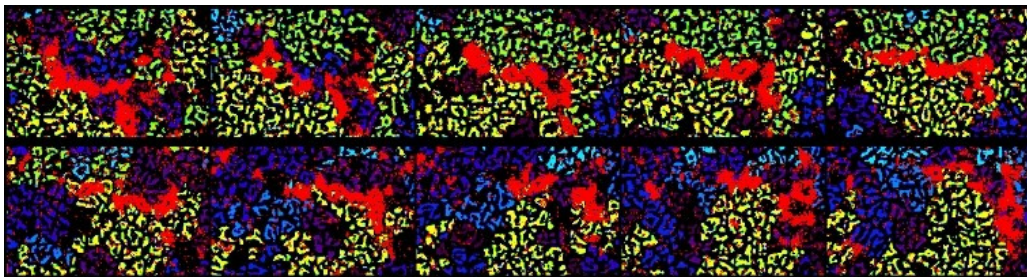


Fig. 2. Longitudinal magnetic field evolution, over ten hours, at the edge of a TFG (yellow). Time step between frame is 1 hour and the starting frame is on top left.

that final state of passively advected quantities like a magnetic field is a patchy distribution on the boundaries of a supergranule. This is confirmed by the observed evolution of the longitudinal magnetic field which is always located in the boarder of the TFGs (Fig. 2).

This is in agreement with the possibility that supergranulation is an emergent length scale building up as small magnetic element are displaced by TFGs flow, occasionally colliding and aggregating to form larger magnetic clusters with granulation which, can seed the supergranular downflow structure.

The temporal evolution of the magnetic elements, corks and TFGs are available at: <http://www.lesia.obspm.fr/perso/jean-marie-malherbe/papers/Hinode2008/>

3 Horizontal velocities over the Sun surface

For the first time, the motion of granules (solar plasma) has been followed over the full Sun surface, using SDO white light data. Horizontal velocity fields are derived from image correlation tracking using a new developed version of the Coherent Structure tracking (CST) algorithm (Rieutord et al. 2007). The spatial and temporal resolutions of the horizontal velocity map are respectively 2.5 Mm and 30 min (Figs. 3 and 4).

The measurement of the horizontal velocities over 24h at the central meridian, allowed us, for the first time,

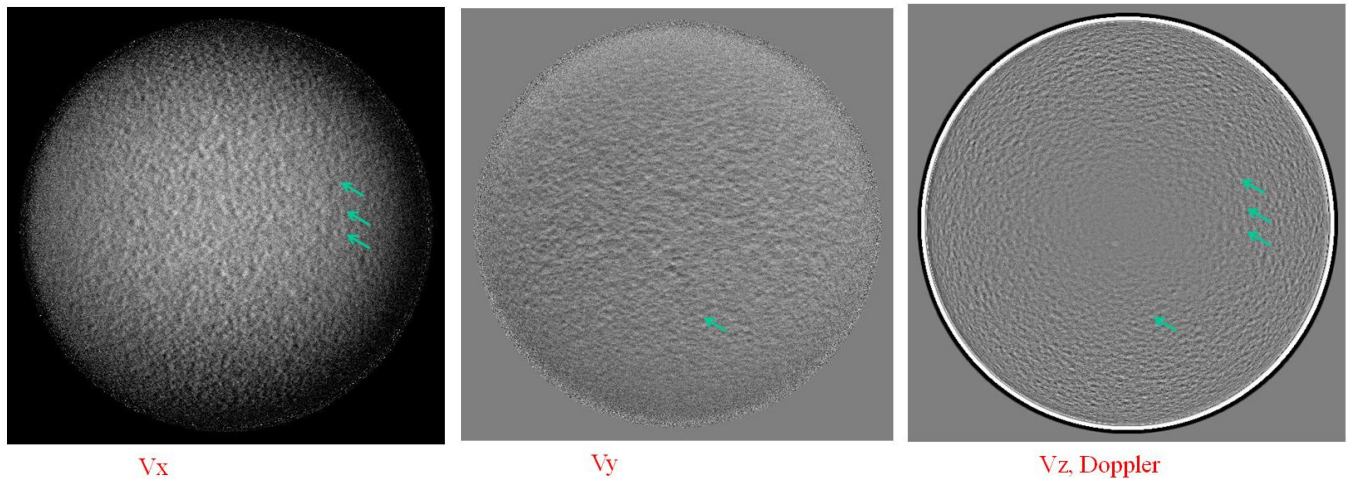


Fig. 3. **Left:** Full Sun V_x and **(Center)** V_y component from 2-hour sequence, spatial resolution = 2.5 Mm. Green arrows indicate the location of supergranule which are also visible **(Right)** on the Doppler map (2-hour sequence) where solar rotation has been removed.

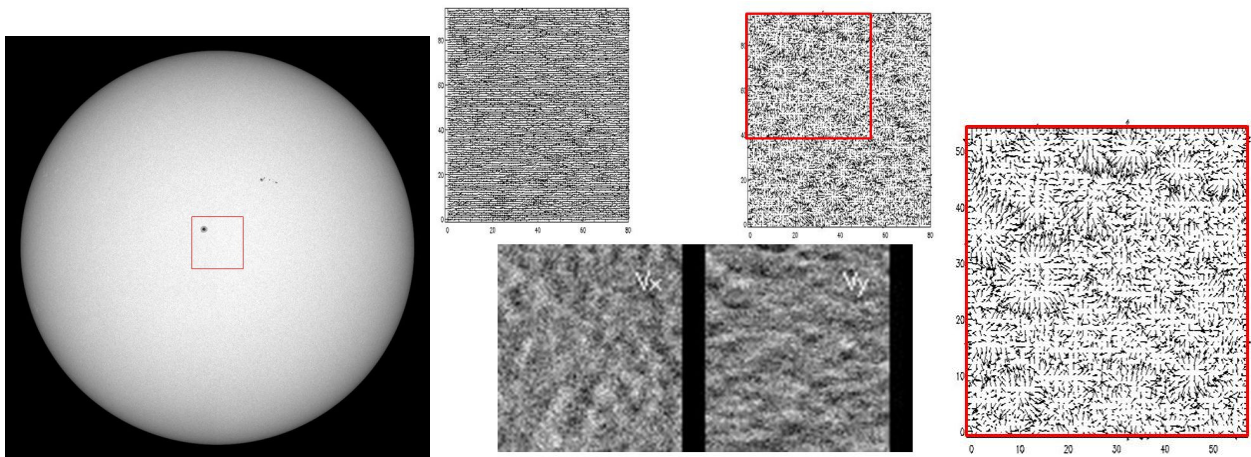


Fig. 4. **Left:** White light SDO observation on August 31, 2010. **Center:** Horizontal velocities (1-h sequence) details around sunspot with and without solar rotation (top left) and V_x and V_y component (bottom left), **Right:** Enlargement of flow fields around sunspot where divergent structures and also the sunspot moat are clearly visible. The field of view is $3.3' \times 3.3'$ and the spatial step is 2.5 Mm.

to determine the solar rotation from the granule displacement. Fig. 5 shows the differential rotation computed for four different dates close to the solar minimum. Our results are in agreement on April 10, 2010 with an error bar of 0.06 km/s, with the spectroscopic determination of the solar rotation (Howard et al. 1970) but the rotation seems faster with an equatorial velocity of 1.99 km/s for the other dates.

The daily Wolf number are respectively 8, 14, 33, 26 and monthly 8, 16.1, 41.6. The solar differential rotation change in time particularly at high latitudes, but we need extensive analysis to confirm that variations. Today 1h20min are necessary to treat 30 min of observation. Improvements of the code are in progress. When the computation duration will be reasonable, the CST code will be implemented in the German Data Center for SDO and also given to Joint Science Operations Center), and will be available to solar community.

4 Conclusions

Thanks to a long 48 hours time sequence obtained with the SOT onboard HINODE, we confirm the organization of flows at the surface of the quiet Sun in the form of Trees of Fragmenting Granules. We quantified the contri-

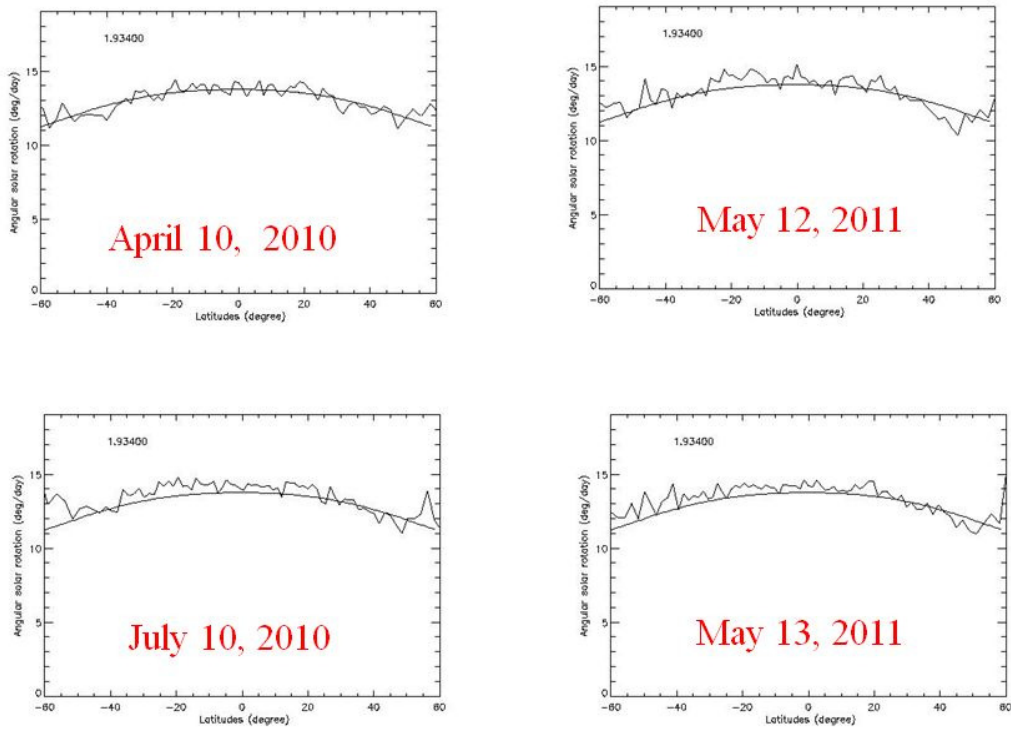


Fig. 5. Solar differential rotation from april 2010 to May 2011. The solid line is the rotation law determined by spectroscopic method (Howard et al. 1970) which is: $\omega = 13.76 - 1.74 \times [\sin(l)]^2 - 2.19 \times (\sin(l))^4$ (where l is the latitude and ω is the angular velocity in deg/day), giving an equatorial velocity of 1.93 km/s.

bution of these families to magnetic field diffusion in the quiet Sun and their role in building the photospheric network Roudier et al. (2003). The overlap between the distribution of floating corks and magnetic elements shows that magnetic fields get advected like a passive quantity before they end-up in a patchy distribution on supergranules boundaries. Presumably, these patches correspond to stable downwards flows that might be stabilized by the dynamical feedback provided by magnetic field concentrations.

For the first time, with the help of SDO white light data, the motions of granules (solar plasma) have been used to determine the projected velocities on the sky, over the full Sun surface. Many studies can be made at all spatial and temporal scales such as the determination of the photospheric velocity field before, during and after an eruption (and CME). These subjects concern the solar weather research.

We thank the Hinode team for letting us use their data. Hinode is a Japanese mission developed and launched by ISAS/JAXA, collaborating with NAOJ as a domestic partner, NASA and STFC (UK) as international partners. Support for the post-launch operation is provided by JAXA and NAOJ (Japan), STFC (U.K.), NASA, ESA, and NSC (Norway). We thank the HMI team members for their hard work. This work was supported by the CNRS Programme National Soleil Terre.

References

- Howard, R. and Harvey, J. 1970, *Sol. Phys.*, 12, 23
 Rieutord, M., Roudier, T., Roques, S., Ducottet, C. 2007, *A&A*, 471, 687
 Roudier, T., Lignières, F., Rieutord, M., Brandt, P. N., Malherbe, J. M. 2003, *A&A*, 409, 299

STELLAR ACTIVITY CYCLES AND ASTEROSEISMOLOGY

D. Salabert¹

Abstract. The success of helioseismology is due to its capability to accurately measure the p -mode parameters of the solar eigenmode spectrum, which allow us to infer unique information about the internal structure and dynamics of the Sun from its surface all the way down to the core. It has contributed greatly to a clearer understanding of the Sun and provided insights into the complex solar magnetism, by means for instance of the variability of the characteristics of the p -mode spectrum. Indeed, variations in the mean strength of the solar magnetic field lead to significant shifts in the frequencies of even the lowest-degree p modes with high levels of correlation with solar surface activity proxies. These frequency shifts are explained to arise from structural changes in the outer layers of the Sun during the 11-year activity cycle, which is understood to be driven by a dynamo process. However, clear differences between p -mode frequencies and solar surface activity during the unusually extended minimum of cycle 23 were observed. The origin of the p -mode variability is thus far from being properly understood and a better comprehension of its relationship with solar and stellar activity cycles will help us in our understanding of the dynamo processes. Spectroscopic measurements of Ca H and K emission lines revealed magnetic activity variations in a large sample of solar-type stars with timescales ranging from 2.5 and 25 years. This broad range of cycle periods is thought to reflect differences in the rotational properties and the depths of the surface convection zones with various masses and ages. However, spectroscopic measurements are only good proxies of surface magnetic fields. The recent discovery of variations with magnetic activity in the p -mode oscillation frequencies of the solar-like star HD 49933 observed by CoRoT, with a frequency dependence comparable in shape to the one observed in the Sun, opens a new era in the study of the physical phenomena involved in the dynamo processes. Current and future asteroseismic observations will contribute to probe stellar cycles in a wide variety of solar-type stars.

Keywords: solar-type stars, activity, oscillations

1 Introduction

The Sun is a variable star with an 11-year cyclic variation of its magnetic activity. Signatures of its variability can be seen in several activity proxies, the most famous being the number of spots on the surface of the Sun. Other indices such as the 10.7-cm radio flux or the irradiance for instance also show this 11-year periodicity. The 11-year magnetic cycle is theoretically understood to be driven by a magnetic dynamo process located at the bottom of the convective zone (Svalgaard et al. 2005; Dikpati & Gilman 2006). Attempts have been made to provide prediction of the cycle properties based on dynamo models but these are not conclusive yet. Indeed, different conclusions were obtained for the new cycle 24, for which these models had not predicted the long and deep minimum of cycle 23.

Although spots on solar-type stars cannot be directly observed, stellar magnetic cycles have been already reported. Indeed, the associated areas of concentrated magnetic field produce strong emission in the Ca II H and K spectral lines, which were proven to be a good proxy of surface magnetic fields (Leighton 1959). Surveys from the Mount Wilson and Lowell Observatories (northern-hemisphere targets) along with long-term monitoring campaigns with SMARTS 1.5-m telescope at CTIO (southern-hemisphere targets) have revealed that many solar-type stars exhibit long-term cyclic variations in their Ca II H and K emission lines, analogous to the solar variations (Wilson 1978; Baliunas et al. 1995; Metcalfe et al. 2009). The complete sample includes cycle periods covering a range between 2.5 to 25 years. Recently, Metcalfe et al. (2010) discovered an even

¹ Université de Nice Sophia-Antipolis, CNRS UMR 6202, Observatoire de la Côte d'Azur, BP 4229, 06304 Nice Cedex 4, France

shorter activity cycle of 1.6 years in the exoplanet hosting F8V star HD 17051. Moreover, it has been observed that the periods of the activity cycles increase proportional to the stellar rotational periods along two distinct paths in main-sequence stars: the relatively young, active sequence, and the older, less active sequence (Saar & Brandenburg 1999; Böhm-Vitense 2007). Relations between mean level of magnetic activity, rotation rate, and periods of the observed activity cycle generally support a dynamo interpretation. However, spectroscopic measurements are only good proxies of surface magnetic fields.

The recent discovery, using asteroseismic observations, of variations with magnetic activity in the p -mode oscillation frequencies of the solar-like F5V star HD 49933 (García et al. 2010), with a frequency dependence comparable in shape to the one observed in the Sun (Salabert et al. 2011), opens a new era in the study of the physical phenomena involved in the dynamo processes. Indeed, through the precise measurements of oscillation parameters, the seismic observables provide unique information about the interior of the stars and for the determination of key parameters for the study of stellar activity, such as the depth of the convection zone, the characteristic evolution time of the granulation, the differential rotation, or the sound-speed as a function of the star's radius (see the preliminary work on HD 49933 by Ceillier et al. 2011). All these new observables will impose new constraints to the theory (e.g. Chaplin et al. 2007a; Metcalfe et al. 2007). Long, high-quality photometric observations such as the ones collected by the space-based Convection, Rotation, and planetary Transits (CoRoT, Baglin et al. 2006) and *Kepler* (Koch et al. 2010) missions will contribute to probe stellar cycles in a wide variety of solar-type stars.

2 Variability of the oscillation parameters with solar magnetic activity

The success of helioseismology is due to its capability to accurately measure the p -mode parameters of the solar eigenmode spectrum, which allow us to infer unique information about the internal structure and dynamics of the Sun from its surface all the way down to the core. It has contributed greatly to a clearer understanding of the Sun and provided insights into the complex solar magnetism, by means for instance of the variability of the characteristics of the p -mode spectrum. Evidence of p -mode frequency changes with solar activity, first revealed by Woodard & Noyes (1985), were established by Pallé et al. (1989) with the analysis of helioseismic observations spanning the complete solar cycle 21 (1977–1988). As longer, higher quality, and continuous helioseismic observations became available, the solar p -mode frequencies proved to be very sensitive to the solar surface activity (e.g., Anguera Gubau et al. 1992; Régulo et al. 1994; Jiménez-Reyes et al. 2001; Gelly et al. 2002; Salabert et al. 2004; Chaplin et al. 2007b, and references therein) with high levels of correlation with solar surface activity proxies. The low-degree, p -mode frequencies change by about $0.4\mu\text{Hz}$ between the minimum and the maximum of the solar cycle with correlation levels with surface activity proxies higher than 0.9. Moreover, Howe et al. (2002) showed that the p -mode frequencies are shifted in presence of surface magnetic activity, varying with close temporal and spatial distributions. However, clear differences were observed between the frequency shifts and the surface activity of the Sun during the unusually extended and deep minimum of cycle 23 (Howe et al. 2009; Salabert et al. 2009; Broomhall et al. 2009; Jain et al. 2011). Although the form and the dependence of the shifts indicate a near-surface phenomenon explained to arise from changes in the outer layers of the Sun, the origin of the frequency shifts is far from being properly understood. Moreover, a quasi-biennial signal in the solar frequencies was recently observed by Fletcher et al. (2010), indicating the possible action of a second dynamo seated near the bottom of the layer extending 5% below the solar surface.

The other p -mode oscillation parameters such as the amplitude, the lifetime, and the asymmetry, were also observed to vary with solar activity (Chaplin et al. 2000; Komm et al. 2002; Salabert et al. 2003; Salabert & Jiménez-Reyes 2006; Jiménez-Reyes et al. 2007). For example, the mode amplitudes decrease with increasing solar activity by about 40% from minimum to maximum of the 11-year cycle. The temporal variations between frequency and amplitude are therefore anticorrelated.

3 Signatures of stellar magnetic activity using asteroseismic observations

The solar-like F5V star HD 49933 observed by the CoRoT satellite (Appourchaux et al. 2008; Benomar et al. 2009) is the first star after the Sun for which variability of the p -mode parameters with magnetic activity was observed (García et al. 2010). Indeed, the p -mode frequencies and amplitudes vary with time with a clear anti-correlation between both parameters as observed in the Sun (e.g. Salabert et al. 2003). These temporal variations suggest a cycle period of at least 120 days. Preliminary spectroscopic measurements with of the Ca II H and K emission lines had shown that HD 49933 is an active star, with a Mount Wilson S-index of 0.3. Follow-

up long-term monitoring confirms the existence of a short activity cycle (T. Metcalfe, private communication, 2011). Incoming observations (both asteroseismic and spectroscopic) will help us to determine more accurately the period and the properties of this magnetic activity cycle. Salabert et al. (2011) showed that the frequency shifts measured in HD 49933 present a frequency dependence with a clear increase with frequency, reaching a maximal shift of about $2\mu\text{Hz}$ around $2100\mu\text{Hz}$, which shows a similar pattern as in the Sun. That indicates then the presence of similar physical phenomena driving the frequency shifts of the oscillation modes as the ones taking place in the Sun, which are understood to reflect structural changes in and just below the photosphere with stellar activity if we suppose similar mechanisms as in the Sun (e.g., Goldreich et al. 1991). However, the frequency shift measured in HD 49933 is at least five times larger than in the Sun, which reaches about $0.5\mu\text{Hz}$ at $3700\mu\text{Hz}$ between the maximum and the minimum of the 11-year solar cycle (e.g. Salabert et al. 2004). This observation supports the scaling proposed by Metcalfe et al. (2007), who predicted that stars hotter and more evolved than the Sun (like HD 49933) should have larger frequency shifts than in the Sun. Preliminary structure models of HD 49933 were computed by Ceillier et al. (2011) in order to study the effects of sound-speed perturbations in the near surface layers on the p -mode frequencies. This will provide for instance insights on the properties of the convective zone of HD 49933 and on the depth at which the magnetic field perturbs the modes.

Three other solar-like stars observed by CoRoT have been studied, for which spectropolarimetric measurements from the NARVAL instrument (Aurière 2003) located at the Pic du Midi Observatory are available: HD 181420 (Barban et al. 2009), HD 49385 (Deheuvels et al. 2010), and HD 52265 (Ballot et al. 2011). Although HD 181420 and HD 49385 seem to be in a quiescence state, HD 52265 shows small temporal variations of the p -mode parameters, suggesting a modest increase of magnetic activity, also indicated by the spectroscopic observations (Mathur et al. 2011).

4 Conclusions

Asteroseismology provides not only invaluable information to infer the structure and the dynamics of the interior of the stars but also key parameters for the study of stellar magnetic activity cycles in a wide variety of solar-type stars imposing new observational constraints to the theory. Studies of stellar activity cycles will bring important inferences for the modeling of dynamo processes and will put the Sun and its 11-year activity cycle into context. The solar-like F star, HD 49933, is the first star after the Sun for which variations of the oscillation parameters with magnetic activity have been observed. Although these changes follow analogous patterns as in the Sun, they suggest a short cycle period, which is confirmed by spectroscopic observations. They also support that stars hotter and more evolved than the Sun should have larger frequency shifts. This is important for CoRoT and *Kepler* when searching for similar frequency shifts as it suggests that the shifts should be easier to detect in the F stars. Also, as short activity cycles seem to be more common than expected, the CoRoT and *Kepler* (and future) missions should potentially be able to observe a large number of full cycles. Such studies will also provide inputs to explore the impacts of magnetic activity on possible planets hosted by these stars.

The author acknowledges the financial support from the Centre National d'Etudes Spatiales (CNES).

References

- Anguera Gubau, M., Pallé, P. L., Pérez Hernandez, F., Régulo, C., & Roca Cortés, T. 1992, *A&A*, 255, 363
- Appourchaux, T., Michel, E., Auvergne, M., et al. 2008, *A&A*, 488, 705
- Aurière, M. 2003, in Proceedings of the conference Magnetism and Activity of the Sun and Stars, ed. J. Arnaud & N. Meunier (EAS Publications Series, Vol. 9) 105
- Baglin, A., Michel, E., Auvergne, M., & The CoRoT Team 2006, in Proceedings of SOHO 18/GONG 2006/HELAS I, Beyond the spherical Sun, ESA SP-624, ed. K. Fletcher, & M. Thompson (ESA Special Publication, Noordwijk), 34
- Baliunas, S.L., Donahue, R.A., Soon, W.H., et al. 1995, *ApJ*, 438, 269
- Ballot, J., Gizon, L., Samadi, R., et al. 2011, *A&A*, 530, A97
- Barban, C., Deheuvels, S., Baudin, F., et al. 2009, *A&A*, 506, 51
- Benomar, O., Baudin, F., Campante, T. L., et al. 2009, *A&A*, 507, L13
- Böhm-Vitense, E. 2007, *ApJ*, 657, 486
- Broomhall, A.-M., Chaplin, W. J., Elsworth, Y., Fletcher, S. T., & New, R. 2009, *ApJ*, 700, L162

- Ceillier, T., Ballot, J., García, R. A., et al. 2011, in Proceedings of the 2nd CoRoT symposium, Transiting planets, vibrating stars, and their connection, ed. A. Baglin, M. Deleuil, E. Michel, & C. Moutou, to be published
- Chaplin, W. J., Elsworth, Y., Isaak, G. R., Miller, B. A., & New, R. 2000, MNRAS, 313, 32
- Chaplin, W. J., Elsworth, Y., Houdek, G., & New, R. 2007a, MNRAS, 377, 17
- Chaplin, W. J., Elsworth, Y., Miller, B. A., Verner, G. A., & New, R. 2007b, ApJ, 659, 1749
- Deheuvels, S., Bruntt, H., Michel, E., et al. 2010, A&A, 515, A87
- Dikpati, M., & Gilman, P. A. 2006, ApJ, 649, 498
- Fletcher, S. T., Broomhall, A.-M., Salabert, D., et al. 2010, ApJ, 718, L19
- García, R. A., Mathur, S., Salabert, D., et al. 2010, Science, 329, 1032
- Gelly, B., Lazrek, M., Grec, G., et al. 2002, A&A, 394, 285
- Goldreich, P., Murray, N., & Willette, G. 1991, ApJ, 370, 752
- Howe, R., Komm, R. W., & Hill, F. 2002, ApJ, 580, 1172
- Howe, R., Christensen-Dalsgaard, J., Hill, F., et al. 2009, ApJ, 701, L87
- Jain, K., Tripathy, S. C., & Hill, F. 2011, ApJ, 739, 6
- Jiménez-Reyes, S. J., Corbard, T., Pallé, P. L., Roca Cortés, T., & Tomczyk, S. 2001, A&A, 379, 622
- Jiménez-Reyes, S.J., Chaplin, W.J., Elsworth, Y., et al. 2007, ApJ, 654, 1135
- Koch, D. G., Borucki, W. J., Basri, G., et al. 2010, ApJ, 713, L79
- Komm, R., Howe, R., & Hill, F. 2002, ApJ, 572, 663
- Leighton, R. B. 1959, ApJ, 130, 366
- Mathur, S. et al. 2011, Submitted to A&A
- Metcalfe, T. S., Dziembowski, W. A., Judge, P. G., & Snow, M. 2007, MNRAS, 379, L16
- Metcalfe, T. S., Judge, P. G., Basu, S., et al. 2009, arXiv:0909.5464
- Metcalfe, T. S., Basu, S., Henry, T. J., et al. 2010, ApJ, 723, L213
- Pallé, P. L., Régulo, C., & Roca Cortés, T. 1989, A&A, 224, 253
- Régulo, C., Jiménez, A., Pallé, P. L., Pérez Hernandez, F., & Roca Cortés, T. 1994, ApJ, 434, 384
- Saar, S.H., & Brandenburg, A. 1999, ApJ, 524, 295
- Salabert, D., Jiménez-Reyes, S. J., & Tomczyk, S. 2003, A&A, 408, 729
- Salabert, D., Fossat, E., Gelly, B., et al. 2004, A&A, 413, 1135
- Salabert, D., & Jiménez-Reyes, S. J. 2006, ApJ, 650, 451
- Salabert, D., García, R. A., Pallé, P. L., & Jiménez-Reyes, S. J. 2009, A&A, 504, L1
- Salabert, D., Régulo, C., Ballot, J., García, R. A., & Mathur, S. 2011, A&A, 530, A127
- Svalgaard, L., Cliver, E. W., & Kamide, Y. 2005, Geophys. Res. Lett., 32, 1104
- Wilson, O. C. 1978, ApJ, 226, 379
- Woodard, M. F., & Noyes, R. W. 1985, Nature, 318, 449

ROTATION ON THE OSCILLATION SPECTRUM OF SOLAR-LIKE STARS

J. C. Suárez¹, M.-J. Goupil², D. R. Reese², R. Samadi², F. Lignières^{4,3}, M. Rieutord^{3,4} and J. Lochard²

Abstract. One of the main sources of uncertainty in the asteroseismic models of solar-like stars is the poor match between predicted oscillation frequencies and observed ones in the very high frequency domain. Today, such deviation is usually corrected by fitting the affected frequencies with polynomials which are then physically explained by possible effects of turbulence, diffusion, etc., i.e., the so-called “surface effects”. In this work, we show that the effect of the stellar deformation due to rotation is of the same order or even larger than the aforementioned surface effects. Moreover, we show that rotation effects, even for the low velocities generally observed in solar-like stars, becomes important for the asteroseismic analysis and cannot be neglected when modeling such stars.

Keywords: oscillations, rotation, pulsation, solar-like stars, stellar structure, stellar evolution

1 Introduction

Asteroseismology is nowadays the unique tool to probe the stellar interiors and hence provide information on both stellar structure and evolution. Today, stellar physics witnesses a significant boost (see Suárez 2010, for a short review), thanks to the space era, where satellites like *MOST* (Walker et al. 2003), *CoRoT* (Baglin 2003), and *Kepler* (Gilliland et al. 2010), are providing asteroseismic data with unprecedented accuracy (see eg. Poretti et al. 2011; Catanzaro et al. 2011; Balona et al. 2011; Breger et al. 2011; Chaplin et al. 2010a; García Hernández et al. 2009; Bruntt et al. 2007, to name a few).

One of the main source of uncertainty in asteroseismology comes from the effect of rotation, which not only interacts with other physical processes, but also affects the form of the resonant cavity (see eg. Goupil et al. 2005; Goupil 2009). For slow-to-moderately rotating stars, like solar-like stars, the oscillation computation is undertaken using the perturbation approach (see eg. Soufi et al. 1998; Suárez 2002). It has been shown that for such rotators, rotation effects cannot be neglected for asteroseismic studies (e.g. Suárez et al. 2009; Briquet et al. 2009; Casas et al. 2009, 2006; Suárez et al. 2006a, 2007; Rodríguez et al. 2006b,a; Poretti et al. 2005).

Analysis of low-mass models for different turbulent diffusion coefficients (Mathis et al. 2007) revealed that rotation may increase the horizontal transport and the rotational effects upon frequencies. Moreover, it has been found that the effects of rotationally-induced mixing in solar-type stars is not strong enough to impose a rigid rotation, as opposed to the solar case (see e.g. Eggenberger & Carrier 2006, who studied the solar-like star β Virginis).

Furthermore, excited modes in solar-like stars are high-order (therefore high-frequency) p modes with small inertia. Since they propagate mainly through the outer layers of the star, their frequencies are more sensitive to changes in the surface physical properties, where the centrifugal force becomes more efficient. The present work examines and evaluates the effects of rotation in this high-frequency domain, and its impact on the different seismic diagnostics techniques based on the asymptotic properties of the oscillations. The main results have been published in the paper Suárez et al. (2010) (hereafter S10).

¹ Instituto de Astrofísica de Andalucía (CSIC), CP3004, Granada, Spain

² Observatoire de Paris, LESIA, CNRS UMR 8109, 92195 Meudon, France

³ Université de Toulouse, UPS, Laboratoire d’Astrophysique de Toulouse-Tarbes (LATT), 31400 Toulouse, France

⁴ CNRS, Laboratoire d’Astrophysique de Toulouse-Tarbes (LATT), 31400 Toulouse, France

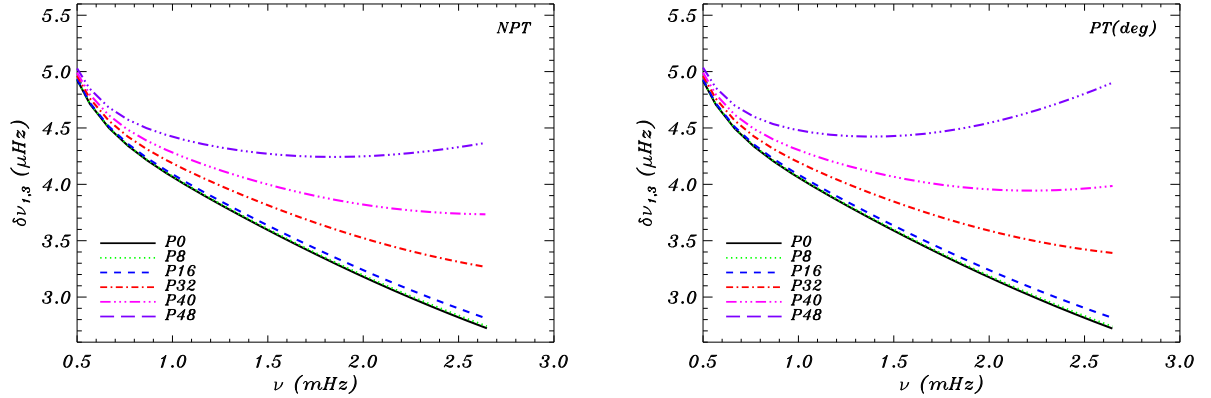


Fig. 1. Small spacings $\delta\nu_{1,3}$ as a function of the oscillation frequency, calculated using NP (left panel) and P (right panel, including near degeneracy effects) approaches. Different line types correspond to spacings computed for different rotational velocities. Figures taken from S10.

2 Perturbative vs. non-perturbative approaches

This work has been performed using 1D asteroseismic models, i.e. equilibrium models plus their corresponding oscillation models following the perturbative approach. These were computed using the evolutionary code CESAM (Morel 1997), and the adiabatic oscillation code FILOU (Suárez 2002; Suárez & Goupil 2008), following the prescriptions by the ESTA/CoRoT team (Moya et al. 2008). The equilibrium models take the rotation into account by including an effective gravity (due to the centrifugal force), but without modifying the spherical symmetry. Depart from spherical symmetry were considered in the oscillation computations, as well as the effect of near degeneracy (more details in Suárez et al. 2006b). The perturbative approach (from now on P approach) is only valid for a certain range of star distortion and frequency domain as explained in (Lignières et al. 2006; Reese et al. 2006) from which a complete calculation (non-perturbative approach, NP) is necessary. The first semi-empirical determination of such a limit was obtained for the well-known δ Scuti star Altair (Suárez et al. 2005), but no equivalent had been done so far for solar-type stars. In the present work we show that the P approach is valid up to $v_{\text{rot}} = 40 - 50 \text{ km s}^{-1}$, which can be illustrated in the comparison of small spacings shown in Fig. 1. This frequency spacing is expected to be small when the star does not rotate. However, the figure shows how such spacings are no longer small when increasing the rotational velocity. As can be seen, both P and NP predict almost identical results, except for higher velocities where slight differences come up. Both calculations are based on a polytropic model of index $n = 3$ with $M = 1.3 M_{\odot}$ and $R = 1.276 R_{\odot}$. The characteristics of all P and NP models are listed in Table 1 of S10.

3 Effect of rotation on diagnostics of echelle diagrams

One of the most frequently used techniques for seismic diagnostics of solar-like stars is the representation of the oscillation frequencies in the so-called echelle diagram which consists in depicting the oscillation frequencies as a function of the same frequencies modulo $\Delta\nu$.

Figure 2 shows such diagrams calculated for a realistic model of a solar-like star (see Table 1 in S10), assuming a uniform rotation of 32 km s^{-1} . It can be seen that ridges are altered significantly towards the highest frequency domain. In S10, it is shown that for rotational velocities of about 16 km s^{-1} and higher, diagnostics on large spacings and on modal identification through echelle diagrams can be altered by the presence of the $m \neq 0$ components of the rotationally split modes. These effects are detectable in the observed frequency range (from ν_{max} to higher frequencies). More specifically we found that the larger the rotational velocity of the star is, the more chances the observed ridges in echelle diagrams correspond to $\ell = 0$ and/or $\ell = |m|$ modes. This is in agreement with the empirical correlation found by Suárez et al. (2002) between the amplitudes of p modes with the angle of inclination i (details in S10).

The effect of rotation on the oscillations may go from a few μHz up to $20 - 30 \mu\text{Hz}$ for the largest rotational velocity considered (around 50 km s^{-1}). This is of the same order or even larger than the so-called *surface*

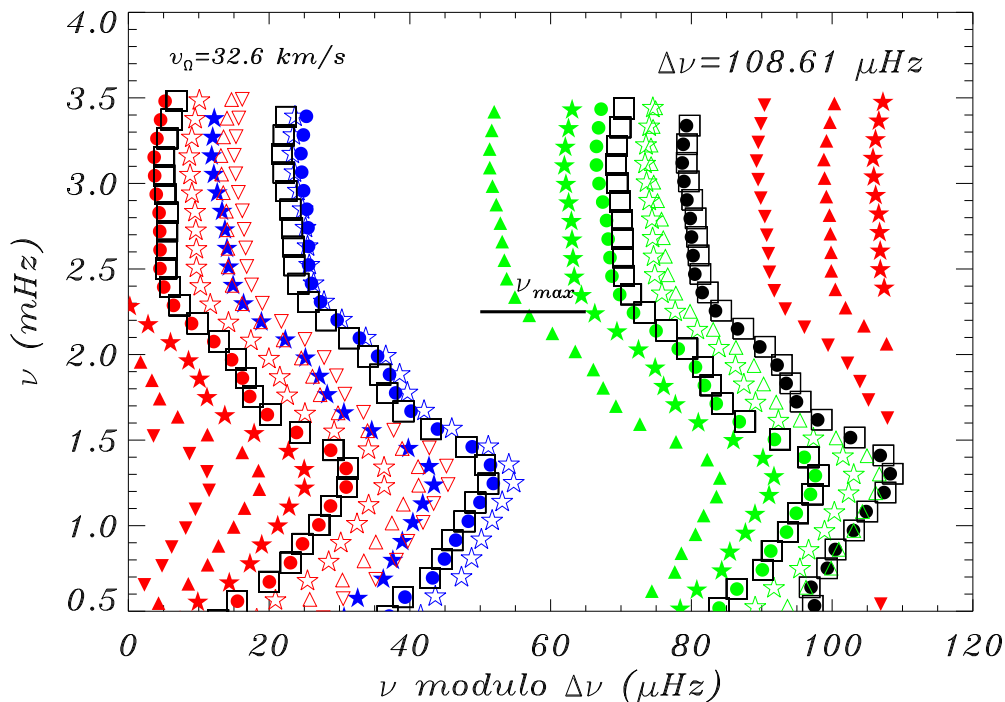


Fig. 2. Echelle diagrams for the uniformly-rotating models. Open squares correspond to ridges of the non-rotating stellar reference model. Black and green symbols represent $\ell = 0$ and $\ell = 2$ modes, respectively. Blue and red symbols represent $\ell = 1$ and $\ell = 3$ modes, respectively. Filled circles represent both $\ell = 0$ and $m = 0$ modes. For the rest of modes, filled and empty symbols represent the $-m$ and $+m$ frequencies, respectively. Stars, triangles, and inverted triangles represent modes with $|m| = 1, 2,$ and $3,$ respectively. The small horizontal line shows the location of the ν_{max} frequency. Figure taken from S10.

effects. These later are, for instance, the turbulence (Straka et al. 2006) (up to $5 \mu\text{Hz}$, from ν_{max} to higher frequencies). Moreover microscopic diffusion might also contribute to such surface effects (Thoul & Montalbán 2007; Théado et al. 2005) which are of the order of a few μHz .

In addition, other wisely used diagnostic tools based on frequency combinations in asymptotic regime are also altered, so their use, and more importantly the physical conclusions obtained with them must be considered with care (see Sect. 2 of S10).

4 Conclusions

The main conclusion of the present work is that rotation should be considered as one of the so-called surface effects because their effects on the oscillation spectrum of solar-like stars are of the order or even larger than other physical effects considered to explain such discrepancies between predicted and observed frequencies in the high-order frequency domain. As a consequence, this also indicates that the Sun asteroseismic standard model should be revised. In general, rotation effects, particularly structure distortion due to the centrifugal force must be taken into account for a proper analysis and interpretation of the Sun and solar-like stars, even if their rotational velocity is small. This result might also be important for asteroseismic studies aiming at characterizing with high accuracy the exo-planetary systems around solar-like stars (see García et al. 2011; Chaplin et al. 2010b; Metcalfe et al. 2010; Stello et al. 2009, as examples of studies based on Kepler data).

JCS acknowledges support from the “Instituto de Astrofísica de Andalucía (CSIC)” by an “Excellence Project post-doctoral fellowship” financed by the Spanish “Conjunción de Innovación, Ciencia y Empresa de la Junta de Andalucía” under project “FQM4156-2008”. JCS also acknowledges support by the Spanish “Plan Nacional del Espacio” under project ESP2007-65480-C02-01, and financial support from CNES. DRR acknowledges support from the CNES through a post-doctoral fellowship.

References

- Baglin, A. 2003, *Advances in Space Research*, 31, 345
- Balona, L. A., Pigulski, A., Cat, P. D., et al. 2011, *MNRAS*, 413, 2403
- Breger, M., Balona, L., Lenz, P., et al. 2011, *MNRAS*, 414, 1721
- Briquet, M., Uytterhoeven, K., Morel, T., et al. 2009, *A&A*, 506, 269
- Bruntt, H., Stello, D., Suárez, J. C., et al. 2007, *MNRAS*, 378, 1371
- Casas, R., Moya, A., Suárez, J. C., et al. 2009, *ApJ*, 697, 522
- Casas, R., Suárez, J. C., Moya, A., & Garrido, R. 2006, *A&A*, 455, 1019
- Catanzaro, G., Ripepi, V., Bernabei, S., et al. 2011, *MNRAS*, 411, 1167
- Chaplin, W. J., Appourchaux, T., Elsworth, Y., et al. 2010a, *ApJ*, 713, L169
- Chaplin, W. J., Appourchaux, T., Elsworth, Y., et al. 2010b, *ApJ*, 713, L169
- Eggenberger, P. & Carrier, F. 2006, *A&A*, 449, 293
- García, R. A., Ceillier, T., Campante, T., et al. 2011, arXiv:1109.6488
- García Hernández, A., Moya, A., Michel, E., et al. 2009, *A&A*, 506, 79
- Gilliland, R. L., Brown, T. M., Christensen-Dalsgaard, J., et al. 2010, *PASP*, 122, 131
- Goupil, M. J. 2009, in *Lecture Notes in Physics*, Vol. 765, eds. J.-P. Rozelot & C. Neiner (Berlin: Springer), p. 45
- Goupil, M.-J., Dupret, M. A., Samadi, R., et al. 2005, *J. Astrophys. Astr.*, 26, 249
- Lignières, F., Rieutord, M., & Reese, D. 2006, *A&A*, 455, 607
- Mathis, S., Palacios, A., & Zahn, J.-P. 2007, *A&A*, 462, 1063
- Metcalfe, T. S., Monteiro, M. J. P. F. G., Thompson, M. J., et al. 2010, *ApJ*, 723, 1583
- Morel, P. 1997, *A&AS*, 124, 597
- Moya, A., Christensen-Dalsgaard, J., Charpinet, S., et al. 2008, *Ap&SS*, 316, 231
- Poretti, E., Rainer, M., Weiss, W. W., et al. 2011, *A&A*, 528, A147
- Poretti, E., Suárez, J. C., Niarchos, P. G., et al. 2005, *A&A*, 440, 1097
- Reese, D., Lignières, F., & Rieutord, M. 2006, *A&A*, 455, 621
- Rodríguez, E., Amado, P. J., Suárez, J. C., et al. 2006a, *A&A*, 450, 715
- Rodríguez, E., Costa, V., Zhou, A.-Y., et al. 2006b, *A&A*, 456, 261
- Soufi, F., Goupil, M. J., & Dziembowski, W. A. 1998, *A&A*, 334, 911
- Stello, D., Chaplin, W. J., Bruntt, H., et al. 2009, *ApJ*, 700, 1589
- Straka, C. W., Demarque, P., Guenther, D. B., Li, L., & Robinson, F. J. 2006, *ApJ*, 636, 1078
- Suárez, J. C. 2002, Ph.D. Thesis, ISBN 84-689-3851-3, ID 02/PA07/7178
- Suárez, J. C. 2010, *Lecture Notes and Essays in Astrophysics*, 4, 33
- Suárez, J. C., Bruntt, H., & Buzasi, D. 2005, *A&A*, 438, 633
- Suárez, J. C., Garrido, R., & Goupil, M. J. 2006a, *A&A*, 447, 649
- Suárez, J. C., Garrido, R., & Moya, A. 2007, *A&A*, 474, 961
- Suárez, J. C. & Goupil, M. J. 2008, *Ap&SS*, 316, 155
- Suárez, J. C., Goupil, M. J., & Morel, P. 2006b, *A&A*, 449, 673
- Suárez, J. C., Goupil, M. J., Reese, D. R., et al. 2010, *ApJ*, 721, 537
- Suárez, J.-C., Michel, E., Pérez Hernández, F., et al. 2002, *A&A*, 390, 523
- Suárez, J. C., Moya, A., Amado, P. J., et al. 2009, *ApJ*, 690, 1401
- Théado, S., Vauclair, S., Castro, M., Charpinet, S., & Dolez, N. 2005, *A&A*, 437, 553
- Thoul, A. & Montalbán, J. 2007, in *EAS Publications Series*, Vol. 26, eds. C. W. Straka, Y. Lebreton, & M. J. P. F. G. Monteiro, p. 25
- Walker, G., Matthews, J., Kuschnig, R., et al. 2003, *PASP*, 115, 1023

DIFFUSION-INDUCED IRON ACCUMULATIONS AND THERMOHALINE CONVECTION IN A TYPE STARS : ASTEROSEISMIC IMPLICATIONS

S. Théado^{1,2}, S. Vauclair^{1,2}, G. Alecian³ and F. LeBlanc⁴

Abstract. The radiative acceleration on iron inside stars may lead to an accumulation of this element in stellar internal layers. This iron accumulation may have many important consequences. It may lead to an extra convective zone, and in some cases it may help triggering stellar pulsations. In this framework diffusion induced-iron accumulations are sometimes invoked to reconcile seismic observations and stellar modelling. These accumulations provide a natural answer to the κ -mechanism boost required to explain the mode excitation in several kind of pulsating stars (e.g. β Cephei, SPB, sdB stars). However, the computations which have been done up to now ignore an important effect: the double-diffusive or “thermohaline” convection induced by the inverse μ -gradients. Radiative diffusion and thermohaline convection have been introduced in the Toulouse-Genève stellar evolution code. We present here stellar models computed in this context. We show how thermohaline convection modifies the iron profiles inside stars, with important consequences for the chemical stratification and the seismic properties of stars.

Keywords: stars:abundances, stars:oscillations, hydrodynamics, convection, asteroseismology

1 Introduction

The atomic diffusion theory predicts in A and hotter stars the occurrence of iron peak element accumulations in stellar interiors (Richer et al. 2000; Turcotte et al. 2000; Richard et al. 2001). Such accumulations, due to radiative diffusion effects are expected to take place in particular in the opacity bump region (around 200000K). In this region, the induced opacity increase may lead to local convection and may help triggering stellar oscillations through the iron κ -mechanism.

Asteroseismic observations support the iron accumulation theory in pulsating A and B type stars. The stability analysis of chemically homogeneous models fails to reproduce seismic observations in β Cephei, SPB and sdB stars (cf. Théado et al. 2009, and references therein for a review on this subject). Introducing iron accumulation profiles in the opacity bump region of models drastically improves the agreement between the theoretical and observed frequency spectra : e.g. Pamyatnykh et al. (2004); Bourge & Alecian (2006); Miglio et al. (2007) for the SPB and β Cephei stars and Charpinet et al. (1996, 1997); Brassard et al. (2001); Charpinet et al. (2001, 2005, 2006, 2008) for the sdB stars. These diffusion-induced iron accumulations provide a natural explanation to the κ -mechanism boost required to explain the mode excitation in A and B type stars.

However in all previous computations the question of the stability of the diffusion-induced iron accumulations was not adressed. In this framework a crucial process was ignored: the thermohaline convection.

2 The thermohaline instability

The iron accumulation due to radiative diffusion induces a local increase of the molecular weight μ . Metal-rich layers may then overlay regions with smaller molecular weights which results locally in μ -values increasing upward. As discussed in many papers (see Théado & Vauclair 2011, for a review on this subject), this situation

¹ CNRS; IRAP; Toulouse, France

² Université de Toulouse; UPS-OMP; IRAP; Toulouse, France

³ LUTH; Observatoire de Paris; CNRS, Université Paris Diderot; Meudon, France

⁴ Département de Physique et d’Astronomie, Université de Moncton, Canada

where a positive μ -gradient builds in a convectively stable region gives rise to a double diffusive instability called thermohaline convection. This instability takes the form of elongated cells called fingers. Since heat diffuses faster than the chemical composition these fingers sink because they grow increasingly heavier than their environment until they become turbulent and dissolve. The induced motions will result in a partial mixing of the stellar material which proceeds until a stable μ -stratification has been restored (i.e. $d \ln \mu / dr \leq 0$).

The effects of thermohaline convection as a mixing process in stars are far from trivial. They are traditionally modelled as a diffusive process. The relevant expression for the diffusion coefficient had long been a matter of debate (Ulrich 1972; Kippenhahn et al. 1980; Charbonnel & Zahn 2007). Recent 2D and 3D numerical simulations of the thermohaline instabilities (Denissenkov 2010; Traxler et al. 2011) seem to converge with similar orders of magnitude for the diffusion coefficient as that of Kippenhahn et al. (1980) (see also Théado & Vauclair 2011, for a detailed discussion about the Denissenkhov et al. and the Traxler et al. coefficients).

In the following, using the Kippenhahn et al. (1980) prescription for the mixing, we show how thermohaline convection may affect the diffusion-induced iron accumulations.

3 Computations

Two $1.7 M_{\odot}$ models were computed using the Toulouse-Geneva stellar evolution code TGEC (Hui-Bon-Hoa 2008; Théado et al. 2009). In the first model, atomic diffusion including radiative accelerations was introduced, in the second model, the effects of the thermohaline mixing were added. The two models were evolved from the ZAMS up to H core exhaustion.

The two models included the atomic diffusion of H, He, C, N, O, Ca and Fe followed separately. The radiative accelerations were computed following the semi-analytical prescription proposed by Alecian & LeBlanc (2002) and LeBlanc & Alecian (2004). The opacities were computed using the OPCDv3.3 codes and data (Seaton 2005) which allow re-computing in each shell of the model and for each timestep accurate opacities taking into account the modifications of the detailed composition of the stellar material. The initial metal mixture used in the computations was the Grevesse & Noels (1993) one with $X_0 = 0.7112$ and $Y_0 = 0.2714$.

The convective zones were instantaneously homogenized. The HI and HeII convective zones were assumed connected by overshooting. The iron convective zone which may appear in much deeper regions was assumed disconnected from the surface convective envelope because of the large distance between them. The effects of the thermohaline convection were introduced as a diffusion process using the diffusion coefficient proposed by Kippenhahn et al. (1980).

4 The thermohaline mixing effects

Figures 1 and 2 present the iron abundance and the molecular weight profiles inside the two models at various evolutionary steps along the main sequence phase. The two models reach the main sequence with chemically homogeneous envelopes. During the stellar evolution, He sinks and creates a stable μ -gradient ($d \ln \mu / dr < 0$) below the convective envelope of the two models, while the radiative diffusion induces an iron accumulation in the iron-peak element opacity bump ($\log T \simeq 5.2$). This iron enhancement leads to an opacity increase which results in a new convective zone already well developed at 299 Ma (cf. the plateau in the iron- and μ -profiles around $\log T = 5.3$). The models with and without thermohaline mixing are for now similar.

At 403 Ma, the two models (with and without thermohaline mixing) begin to differ. In the model without thermohaline mixing, the iron accumulation drastically increases with time up to a factor 95 at 1388 Ma. In this case the iron convective zone persists during most of the main sequence lifetime. The large iron accumulation leads to large inverse (i.e. positive) μ -gradients, highly unstable.

In the model including thermohaline convection, the μ -gradient is kept close to zero along the main sequence phase. As a result of the induced mixing the iron accumulation in the opacity bump is strongly reduced and never exceeds a factor 15. It is however important to stress that an iron accumulation still occurs. This model does not show a persistent iron convective zone: the opacity bump region undergoes alternatively convective and radiative episodes during the main sequence evolution.

5 Discussion-Conclusion

We have investigated the effects of thermohaline convection on diffusion-induced iron accumulations in A type stars. Our computations demonstrate that thermohaline convection drastically reduces the iron enhancement in

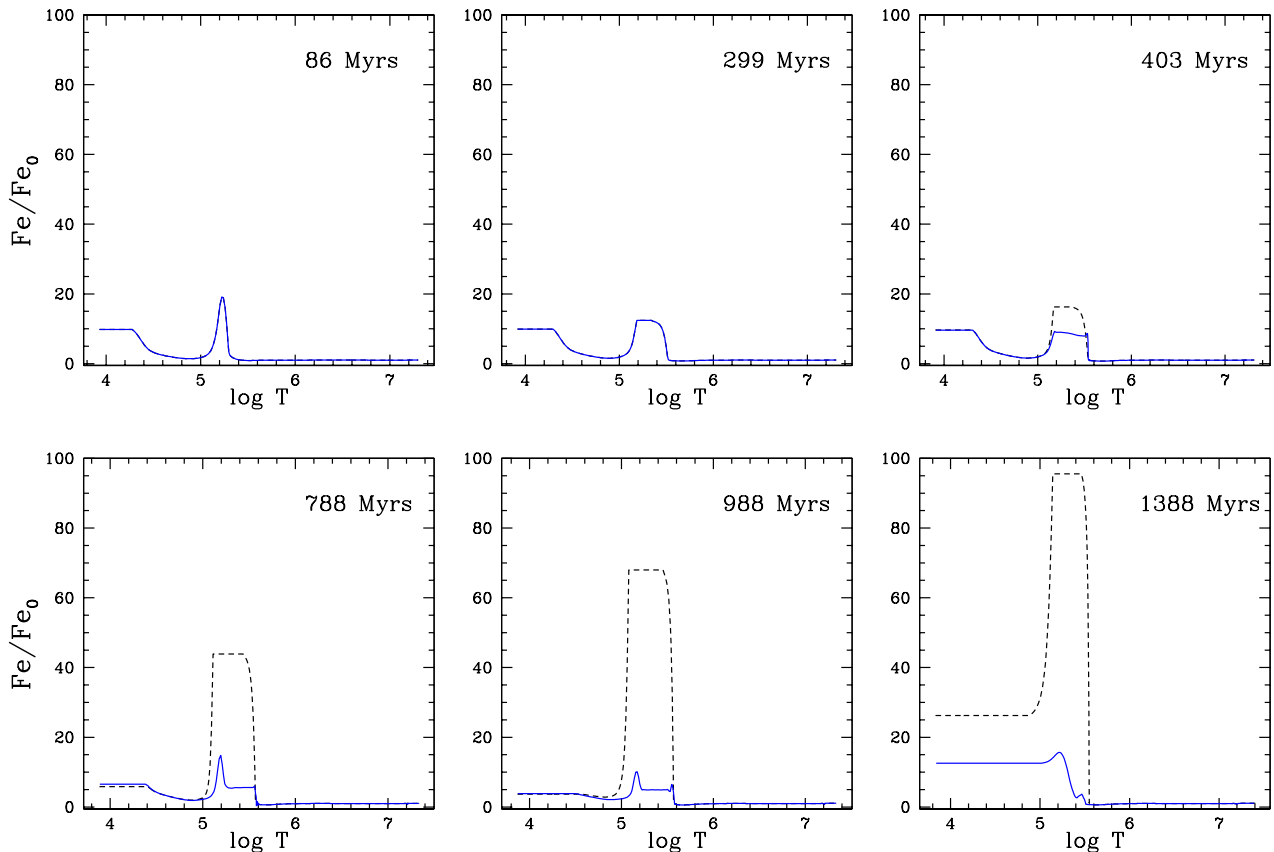


Fig. 1. Iron accumulation profiles in two $1.7 M_{\odot}$ models at different evolutionary steps. The dashed lines show a model including atomic diffusion (with radiative pressure effects), the solid lines present a model including both atomic diffusion and thermohaline mixing. Fe/Fe_0 represents the ratio between the current iron abundance and its initial value on the ZAMS.

the opacity bump region and that it also affects the iron convective zone boundaries. This process is expected to take place in all types of stars where heavy element accumulations occur (i.e. in F, A and B type stars). As a result the real iron accumulations in A and B type stars are probably smaller than those deduced from atomic diffusion computations. The effects of the thermohaline mixing on the iron abundance may have strong implications for the oscillations driven by the iron κ -mechanism, the influence of this mixing on the iron convective zone may also affect the oscillations excited through the convective blocking. As a consequence thermohaline instabilities must be introduced in the stellar evolutionary computations and the stability analysis of pulsating A and hotter stars (i.e. in β -Cephei, SPB, HgMn, sdB or γ -Doradus models).

References

- Alecian, G. & LeBlanc, F. 2002, MNRAS, 332, 891
 Bourge, P.-O. & Alecian, G. 2006, in *Astronomical Society of the Pacific Conference Series*, Vol. 349, *Astrophysics of Variable Stars*, ed. C. Aerts & C. Sterken, 201
 Brassard, P., Fontaine, G., Billères, M., et al. 2001, ApJ, 563, 1013
 Charbonnel, C. & Zahn, J.-P. 2007, A&A, 467, L15
 Charpinet, S., Fontaine, G., & Brassard, P. 2001, PASP, 113, 775
 Charpinet, S., Fontaine, G., Brassard, P., et al. 1997, ApJ, 483, L123
 Charpinet, S., Fontaine, G., Brassard, P., & Dorman, B. 1996, ApJ, 471, L103
 Charpinet, S., Fontaine, G., Brassard, P., Green, E. M., & Chayer, P. 2005, A&A, 437, 575
 Charpinet, S., Silvotti, R., Bonanno, A., et al. 2006, A&A, 459, 565
 Charpinet, S., van Grootel, V., Reese, D., et al. 2008, A&A, 489, 377

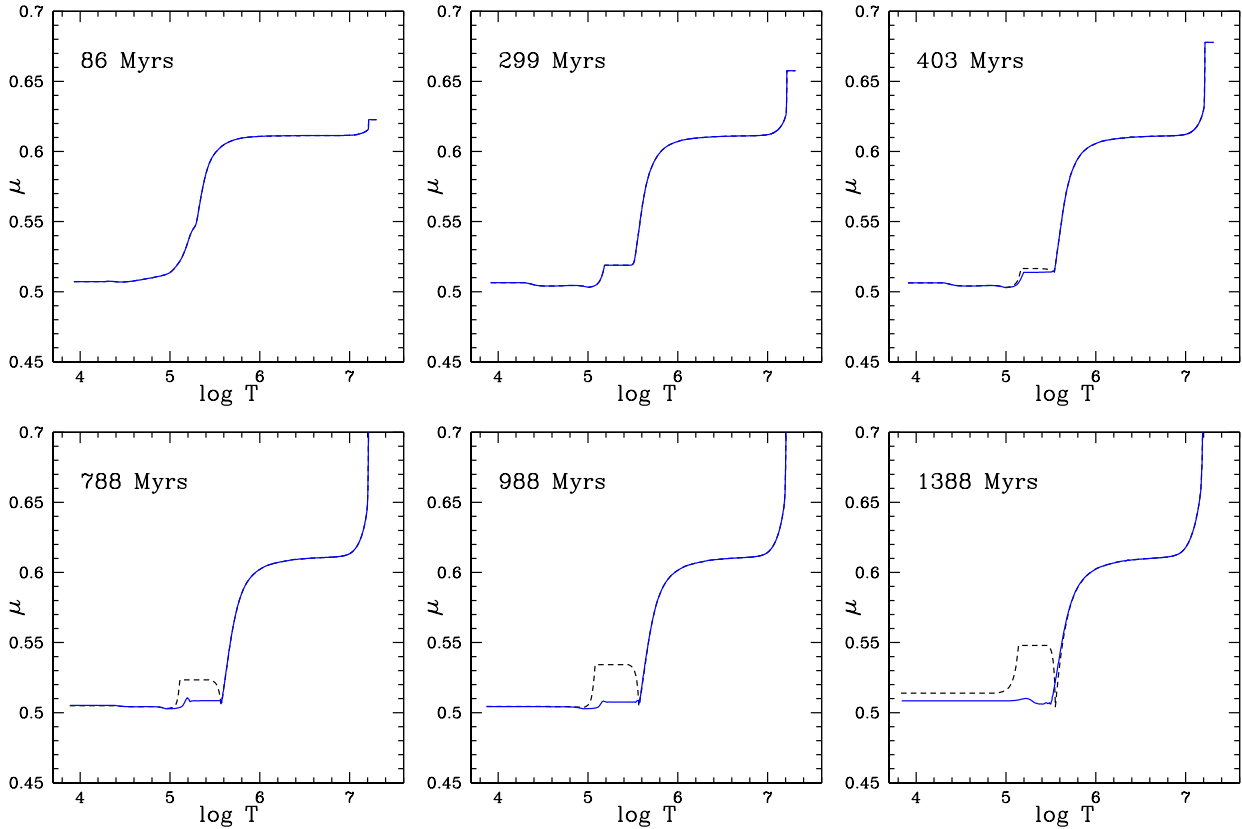


Fig. 2. Molecular weight profiles for the same models as presented on Fig. 1.

Denissenkov, P. A. 2010, *ApJ*, 723, 563

Grevesse, N. & Noels, A. 1993, in *Origin and Evolution of the Elements*, ed. N. Prantzos, E. Vangioni-Flam, & M. Cassé, 15–25

Hui-Bon-Hoa, A. 2008, *Ap&SS*, 316, 55

Kippenhahn, R., Ruschenplatt, G., & Thomas, H.-C. 1980, *A&A*, 91, 175

LeBlanc, F. & Alecian, G. 2004, *MNRAS*, 352, 1329

Miglio, A., Bourge, P.-O., Montalbán, J., & Dupret, M.-A. 2007, *Communications in Asteroseismology*, 150, 209

Pamyatnykh, A. A., Handler, G., & Dziembowski, W. A. 2004, *MNRAS*, 350, 1022

Richard, O., Michaud, G., & Richer, J. 2001, *ApJ*, 558, 377

Richer, J., Michaud, G., & Turcotte, S. 2000, *ApJ*, 529, 338

Seaton, M. J. 2005, *MNRAS*, 362, L1

Théado, S. & Vauclair, S. 2011, *ArXiv* 1109.4238

Théado, S., Vauclair, S., Alecian, G., & Le Blanc, F. 2009, *ApJ*, 704, 1262

Traxler, A., Garaud, P., & Stellmach, S. 2011, *ApJ*, 728, L29

Turcotte, S., Richer, J., Michaud, G., & Christensen-Dalsgaard, J. 2000, *A&A*, 360, 603

Ulrich, R. K. 1972, *ApJ*, 172, 165

MAIN LESSONS FROM GOLF/SOHO INSTRUMENT ON DYNAMICS OF THE RADIATIVE ZONE, FUNDAMENTAL PHYSICS AND ENERGETICS

S. Turck-Chièze¹, R. A. García¹, L. Piau² and S. Couvidat³

Abstract. The GOLF instrument aboard SoHO has reached its main objectives and reveals its power to constrain fundamental physics, energetics and dynamics of the radiative zone. The Standard Solar Model (SSM) is no more sufficient to interpret all the seismic observations of the solar radiative zone. We confront the main results of GOLF to models beyond the SSM assumptions. We discuss the missing processes and quantify some of them to build a more realistic view of our star. Present works on GOLF instrument are now turned on its capability to follow the solar activity and on a tentative to detect more gravity modes. All the results are useful for solar-like stars observed by COROT and KEPLER.

Keywords: helioseismology, sound speed, internal rotation, neutrinos, WIMPS, stellar modelling

1 Introduction

The SoHO satellite probes the Sun by acoustic modes with GOLF (Gabriel et al. 1995; García et al. 2005) and MDI (Scherrer et al. 1995) since more than 15 years. The GOLF instrument has been particular efficient to measure the low degree low order acoustic modes (Bertello et al. 2000; García et al. 2001; Gelly et al. 2002) and to detect the first gravity mode frequencies (Turck-Chièze et al. 2001, 2004; García et al. 2007, 2011). From these data, we deduce a sound speed profile and a rotation profile in the whole radiative zone.

On the other side, neutrino detections put other constraints on the solar core in total agreement with the helioseismic results, see the review of Turck-Chièze & Couvidat (2011) (TCC2011). The study of the gravitational moments shows also that the dynamical processes in the radiative zone cannot be forgotten (Duez, Turck-Chièze & Mathis 2011) and that the knowledge of the dynamics of the radiative zone depends on its history.

The Sun will stay for long the only star for which the internal radiative zone is known with such details even hopefully, thousand analogous stars begin to be studied by asteroseismology. We summarize here the main conclusions we have deduced from the analysis of the GOLF data.

1.1 Solar sound speed, density and rotation profiles in the radiative zone

The detection of the low order radial acoustic modes, that are not polluted by any surface solar cycle effect, has allowed a determination of the sound speed down to $0.06 R_{\odot}$ with high accuracy (Turck-Chièze et al. 2001) in integrating 5 years of data. The inversion of these data leads to an extremely precise vertical error bar but a non negligible horizontal error bar (see Figure 1). The profile in the core has been strictly confirmed after 30 years of measurements on ground by the BiSON network for the low degree modes (Basu et al. 2009). Figure 1 (*left*) shows the absolute value of the sound speed in the core. Figure 1 (*middle*) compares the sound speed and the density profiles to two models: the Solar Seismic Model (SSeM), adjusted on the observed sound speed (Turck-Chièze et al. 2001; Couvidat et al. 2003) in slightly modifying the input physics, and the SSM that integrates the updated physics including the new photospheric CNO estimate. Both solve the classical structural equations along time.

¹ CEA/DSM/IRFU/SAP-AIM, CE Saclay, Orme des Merisiers, 91191 Gif-sur-Yvette, France

² LATMOS, 11 Boulevard d'Alembert, 78280 Guyancourt, France

³ HEPL, Stanford University, USA

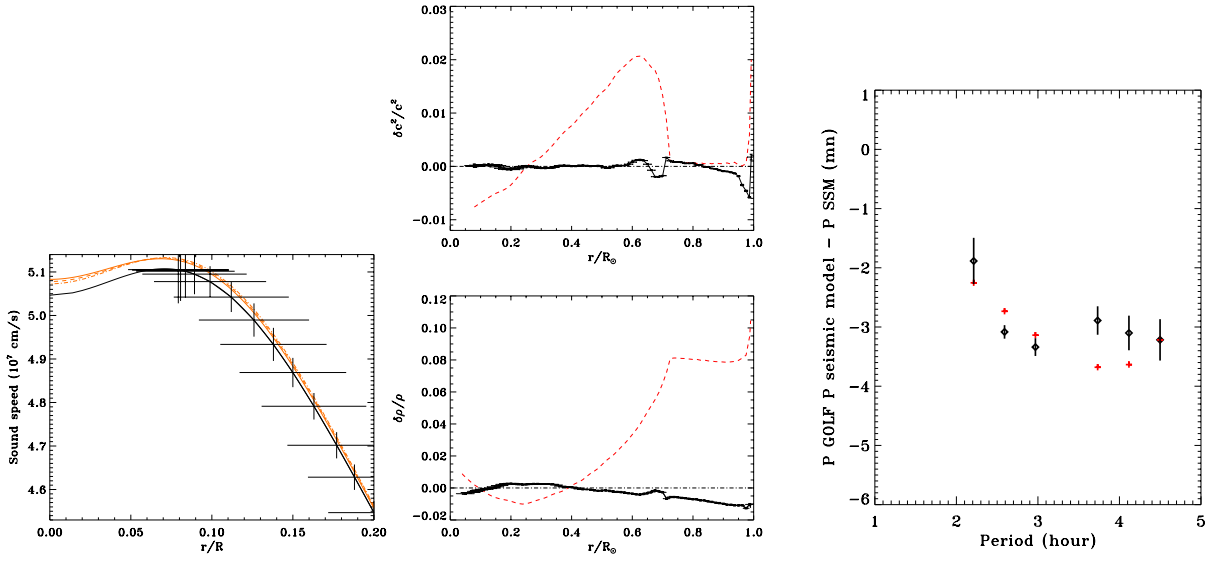


Fig. 1. Left: Zoom on the absolute value of the sound speed in the core, the vertical error bars are multiplied by 100 for their visibility. The extracted values are compared to the SSeM (in black) and to the SSM in orange + dashed lines for models with central luminosity increased by 2% and 5%. **Middle:** Differences in squared sound speed and density between GOLF+MDI/SoHO and solar model predictions. Seismic model: full line + seismic error bars, SSM model (—). Both curves are from Turck-Chièze, Piau & Couvidat (2011). **Right:** Difference of dipole gravity mode periods between SSM and GOLF (diamonds with error bars) or SSeM (red crosses) and SSM. See also Turck-Chièze et al. (2011).

From the same seismic data plus the first detected dipole gravity modes (García et al. 2007, 2011), we can also extract the rotation profile (Figure 2, *left*) down to the same region in the core. The error bars are still large due to the small number of modes detected. The latitudinal effect must be confirmed by the detection of more splitting values which will improve such profile. Nevertheless one observes clearly an increase in the solar core that succeeds to a quasi flat rotation in the rest of the radiative zone.

1.2 A zoom on the solar core: neutrinos, gravity modes and dark matter

We have now a lot of information from this region: 5 neutrino detectors sensitive to different energy of neutrinos, more than 20 radial acoustic modes and at least 6 dipole gravity modes and the related splittings. It is important to notice that they all agree together through the predictions of the SSeM that has been built to reproduce only the sound speed of the whole radiative zone. Figure 1 illustrates this point comparing the absolute sound speed with models and the large period difference of the gravity modes between SSM and SSeM but the proximity of the observational values of GOLF (Figure 1 *right*) with SSeM. TCC2011 show also in their table 9 the excellent agreement between the prediction of the emitted neutrinos and the 5 neutrino detectors. The central temperature is strongly constrained by the boron neutrino flux and the central density by the gravity mode frequencies, so the solar values must be well reproduced by the seismic model values: $T_C = 15.75 \cdot 10^6$ K and $\rho_C = 153.6 \text{ g cm}^{-3}$. This information is also useful for putting some constraints on the potential presence of dark matter (Turck-Chièze et al. 2011).

This seismic model has been extremely useful for its predictions but it is not a physical model of the Sun. It cannot predict any dynamical process that one needs to introduce in the radiative zone or at the surface. So step by step it will be replaced by more sophisticated model of the Sun.

2 The stars are rotating objects

For the first time, we get a complete solar internal rotation profile, so one needs to explore the transport of momentum due to rotation along stellar evolution. By chance, we also have some hints from other stars thanks to the splitting of their mixed modes for subgiant or red giant stars (Deheuvels et al. 2011; Beck et al. 2011).

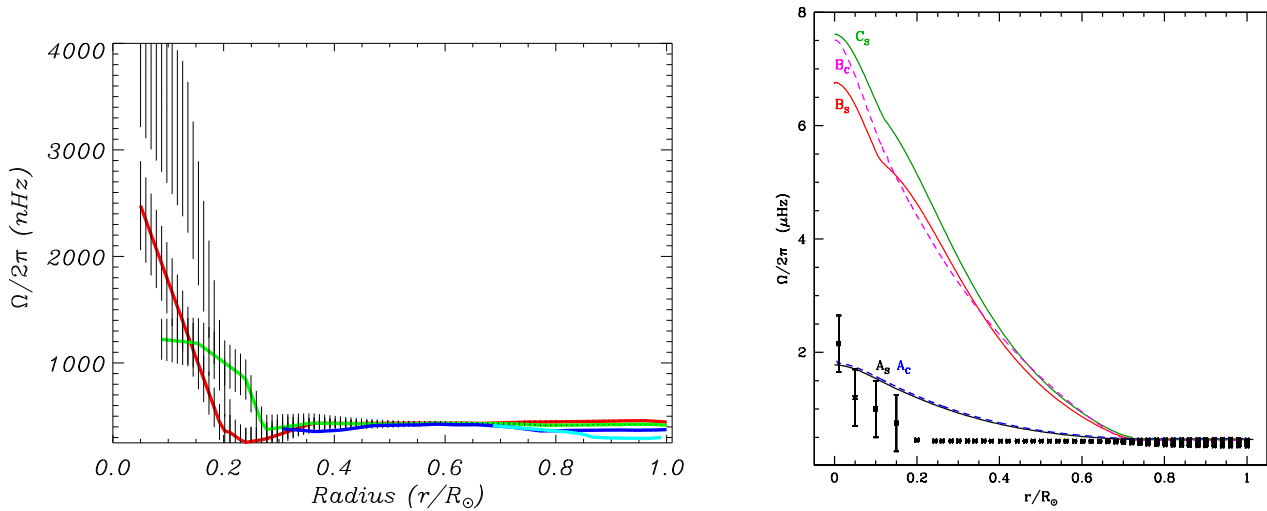


Fig. 2. Left: Radial rotation profile extracted from the first gravity dipole modes detected with the GOLF instrument and all the acoustic modes observed with GOLF+MDI. From García et al. (2011). **Right:** Comparison of the mean profile to different models (A, B and C) see text. From Turck-Chièze et al. (2010).

Let compare the obtained rotation profile to models including rotation and transport of rotation (Turck-Chièze et al. 2010). We have built several models to follow the time evolution of the rotation profile. In these computations, we have followed the internal structure of the pre-main sequence evolution corresponding to the decoupling of the star from the disk. We have built two classes of models. The first class (A) consists in purely academic models starting with a low rotation that evolves naturally toward the present external velocity of 2 km/s. The second class (B and C) has surface velocity of 20 to 50 km/s before the arrival on the main sequence and then are spin down by magnetic braking following the Skumanich (1972) law down to the present solar rotation. Models B and C are compatible with observations of Bouvier (2009). Our transport of momentum follows the prescription of Zahn (1992). The radial gradient of rotation is mainly established during the contraction phase, the first 45 Ma. Then the evolution of this profile is quite slow. Moreover, the meridional circulation associated to the rotation transport becomes quickly extremely slow in comparison with what one can observe in the convective zone. Figure 2 (*right*) illustrates our results. We note that the important gradient observed in the whole radiative zone, for models B (20 km/s at the arrival on the main sequence) and C (50 km/s) do not agree with the rotation profile observed by seismology. Models A agree better in the core but do not respect the observations of young stars nor the spin down observed along the main sequence. Moreover in the two kinds of modeling, one never reaches a flat rotation profile outside the nuclear core as it is well established now by MDI results (Korzennik & Eff-Darwich 2011).

So the progress done on the solar internal rotation profile by the detection of gravity modes coupled to acoustic modes is presently not understood. This year, asteroseismology adds new results: a gradient of about a factor 5 between core and surface in a subgiant star (Deheuvels et al. 2011) and a gradient of about a factor 10 in giants (Beck et al. 2011). These complementary observations are compatible with a slow transport effect along the main sequence coupled to an acceleration of the core rotation in red giants in comparison to the surface rotation. Such important results encourage certainly to go further on the dynamics of the radiative zone.

3 Young solar analogs, Missing Processes and Conclusion

The limitation of SSM appears also in its lack to model the young solar analogs. These stars are generally extremely active and their UV manifestation can be about 1000 times greater than the present solar activity.

As the internal rotation profile seems largely influenced by that stage of evolution, one needs to introduce the processes that are connected to that early activity. The energetic balance, in the SSM framework, is dominated by the nuclear production in the core and the transfer of energy by radiation. Part of the energy could be transformed through kinetic energy, magnetic one during the early stage where the Sun was mainly convective. Moreover the comparison between the central conditions of the Sun, verified by neutrinos and gravity modes,

and the external luminosity let place for small difference of several per cent which cannot be understood inside the assumptions of the SSM where radiative transfer is instantaneous.

Using young stellar analogues of the Sun and their time activity evolution laws, a greater initial mass than the one of the present Sun is possible, this produces an increase of luminosity with important consequences for the formation of planets. See Turck-Chièze, Piau & Couvidat (2011).

The building of dynamical models of solar-like stars consists also to introduce the presence of a fossil magnetic field built in the first stage when the star was still connected to the disk and largely convective. More and more indicators call for such a complex view of the radiative zone. We have begun to build some key ingredient to explore such possibility in using a magnetic field topology which takes into account poloidal and toroidal mixed fields (Duez, Mathis & Turck-Chièze 2010). The difficulty is to estimate the strength of such a field and to find some indirect manifestation of this field: we have thought to quadrupole moments but they are already rather properly explained by the rotation profile (Duez, Turck-Chièze & Mathis 2011) or to some effects on the quadrupole gravity modes but their identification is still puzzling (Turck-Chièze et al. 2004). We shall begin with toy models of transport of momentum by magnetic field and diffusion as suggested by Mathis & Zahn (2005). Other stars, observed in seismology, will help in this new progress to build more realistic representation of solar-like stars and the bridge between young stellar object and main sequence stars.

Conclusion: The main results obtained by GOLF instrument: the sound speed, density and rotation gradients are not presently explained. The missing dynamical processes are well identified and only partly introduced due to the lack of young stellar seismic constraints and solar quadrupole gravity mode splitting measurements. KEPLER for stars and GOLF-NG (Turck-Chièze et al. 2008) for gravity mode detection will help. In the meantime, we continue to improve the analysis of GOLF to hopefully detect these quadrupole modes.

This work was supported by CEA and the space agencies ESA and CNES. We are extremely grateful to NASA for their support on the SoHO satellite. We would like to thank J. Ballot, H. Dzitko, S. Mathur, P. Nghiem, who have actively participated to some of these works. S. Couvidat is now funded by NASA grant NAS5-02139 (HMI).

References

- Basu, S. et al. 2009, *ApJ*, 699, 1403
 Beck, P. G. et al. 2011, *Science*, 332, 205, 10.1126/science.1201939 and 4th KEPLER meeting
 Bertello, L. et al. 2000, *ApJ*, 535, 1066
 Bouvier, J. 2009, in *Stellar Magnetism*, eds. C. Neiner, J.-P. Zahn, EAS Publ. Series 2009, p. 199
 Couvidat, S., Turck-Chièze, S., & Kosovichev, A. G. 2003, *ApJ*, 599, 1434
 Duez, V., Mathis, S., Turck-Chièze, S. 2010, *MNRAS*, 402, 271, 29
 Duez, V., Turck-Chièze, S. Mathis, S. 2011, *ApJ*, in preparation
 Deheuvels S., et al. 2011, Contribution to the 4th KEPLER meeting
 Gabriel A. H. et al. 1995, *Sol. Phys.* 162, 61
 García, R. A. et al. 2001, *Sol. Phys.*, 200, 361
 García, R. A. et al. 2005, *A&A*, 442, 385
 García, R. A., et al. 2007, *Science*, 316, 1591
 García, R. A. et al. 2008, *Astron. Nach.* 329, 476
 García, R. A. et al. 2011, *SOHO24, JPCS*, 271, 12046
 Gelly, B. et al. 2002, *A&A*, 394, 285
 Korzennik, S. G. & Eff-Darwich A. 2011, *JPCS* 271, 012067
 Mathis, S. & Zahn J. P. 2005, *A&A*, 440, 653
 Scherrer, P. H. et al. 1995, *Sol. Phys.*, 162, 129
 Skumanich, A. 1972, *ApJ*, 171, 565
 Turck-Chièze, S., et al. 2001, *ApJ*, 555, L69
 Turck-Chièze, S., et al. 2004, *ApJ*, 604, 455
 Turck-Chièze, S., and the GOLF-NG collaboration 2006, *Advances in Space Research*, 38, 1812
 Turck-Chièze, S., and the GOLF-NG collaboration 2008, *Journal of Physics Conference Series*, 118, 012044
 Turck-Chièze, S., Palacios, A., Marques, J., Nghiem, P.A.P. 2010, *ApJ*, 715, 153
 Turck-Chièze, S., Piau, L. and Couvidat, S. 2011, *ApJ Lett*, 731, L29
 Turck-Chièze, S. and Couvidat, S. 2011, Report in Progress in Physics, 74, 086901
 Turck-Chièze, S., et al. 2011, *ApJ*, submitted
 Zahn J. P. 1992, *A&A*, 265, 115

Session 03

Stellar and interstellar physics for the modelling of
the Galaxy and its components

ORBIT OF POTENTIALLY HAZARDOUS ASTEROIDS USING GAIA AND GROUND-BASED OBSERVATIONS

D. Bancelin¹, D. Hestroffer¹ and W. Thuillot¹

Abstract. Potentially Hazardous Asteroids (PHAs) are Near Earth Asteroids characterized by a Minimum Orbital Intersection Distance (MOID) with Earth less to 0,05 A.U and an absolute magnitude $H < 22$. Those objects have sometimes a so significant close approach with Earth that they can be put on a chaotic orbit. This kind of orbit is very sensitive for exemple to the initial conditions, to the planetary theory used (for instance JPL's model versus IMCCE's model) or even to the numerical integrator used (Lie Series, Bulirsch-Stoer or Radau). New observations (optical, radar, flyby or satellite mission) can improve those orbits and reduce the uncertainties on the Keplerian elements.

Keywords: Gaia mission, b-plane, Potentially Hazardous Asteroids, orbit determination, astrometry

1 Introduction

Gaia is a 5-years astrometric mission scheduled for spring 2013. The main aim is to make a three dimensional map of our Galaxy. There are a lot of science outcomes from this mission: a better understanding of the star formation and the history of the Milky Way; study on stellar astrophysics, on the Galactic structure and on Binaries and Brown dwarfs. The Solar System Science goal is to map thousand of Main Belt Asteroids (MBAs), Near Earth Asteroids (NEAs) (including comets) and also planetary satellites. The principal purpose is orbital determination (better than 5 mas astrometric precision), determination of asteroid mass, spin properties and taxonomy. Besides, Gaia will be able to discover a few objects, in particular NEAs in the region down to the solar elongation (45°) which are harder to detect with current ground-based surveys. The aim of this study is to analyse the impact of Gaia data on the orbit of Potentially Hazardous Asteroids (PHAs) and also the advantage of combining space-based and ground-based data.

2 Statistical observations of NEAs by Gaia

During the 5-years mission, Gaia will continuously scan the sky with a specific strategy: objects will be observed from two lines of sight separated with a constant basic angle. Five constants already fixed determinate the nominal scanning law but two others are still free parameters: the initial spin phase (influencing the date of observations) and the initial precession angle (influencing the number of observations). These latter will be fixed at the start of the nominal scientific outcome (possibility of performing tests of fundamental physics) together with operational requirements (downlink to Earth windows). Hence several sets of observation will be provided according to the initial precession angle. Figure 1 shows the number of NEAs that would be observed by Gaia. This number represents about 30% of the NEAs population.

3 Astrometry for known PHAs

Asteroid Apophis is a PHA discovered in 2004 and was revealed to be a threatening asteroid for the Earth, since, because of a deep close encounter ($\sim 38000\text{km}$) with Earth in 2029, there is some risks of collision mainly in 2036. In order to better prepare future space missions towards this asteroid, it is important to well quantity the uncertainty in 2029. To better represent the state of an asteroid approaching the Earth, we better use the

¹ Institut de Mécanique Céleste et de Calcul de Éphémérides, 77 Avenue Denfert-Rochereau 75014 Paris, France

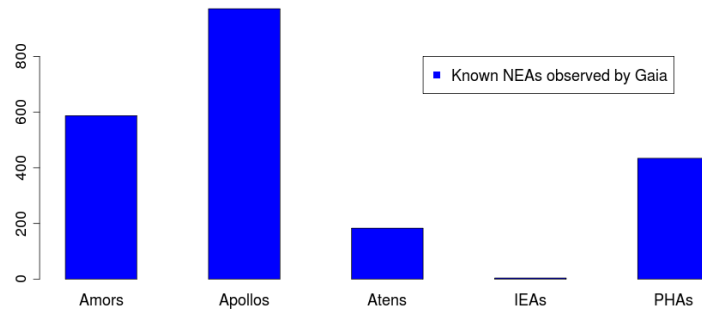


Fig. 1. Number of known NEAs possibly observed by Gaia

b-plane or target plane (Valsecchi et al. 2003) . It passes through the Earth’s center and is perpendicular to the geocentric velocity of the asteroid. In this plane, the asteroid will have two geocentric coordinates (ξ, ζ) . Thus the projection of the 6-dimension region uncertainty of the Keplerian elements in the 2029-b-plane is a 3σ ellipse uncertainty. Fig. 2 represents the 3σ ellipse in (ξ, ζ) in the 2029-b-plane with (blue) and without (grey) additional Gaia data. For completeness, we represented primary(\star) and secondary keyholes leading at collision at the ascending (\blacksquare) and descending node (\blacksquare). Keyholes are regions in the b-plane of 2029 where the asteroid has to pass in order to collide the Earth at some dates indicated in Fig. 2.

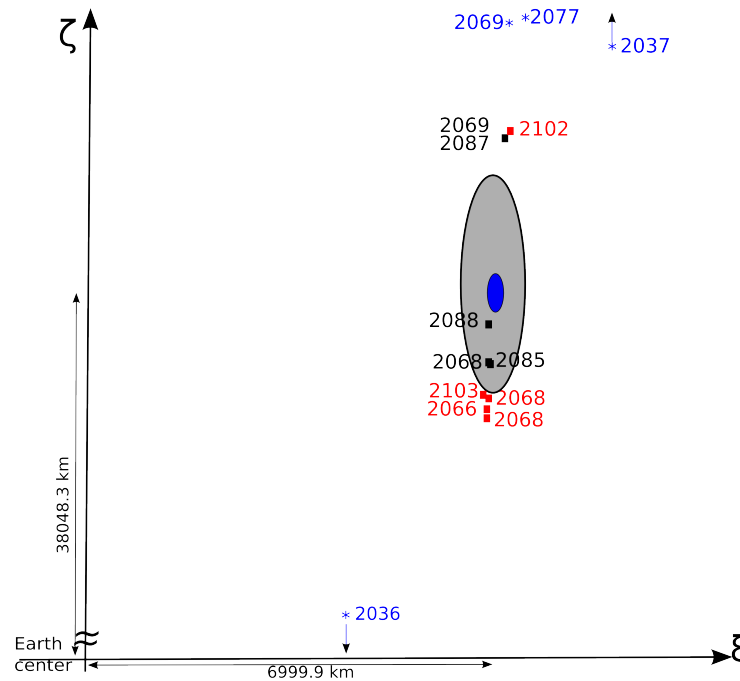


Fig. 2. 3σ ellipse uncertainty in the 2029-b-plane centered in the (ξ, ζ) nominal value: In blue: using Gaia data; in grey: without Gaia data. The positions of the center of keyholes are also represented.

As shown in the Tab. 1, Gaia data enable to reach the kilometer knowledge level on the accuracy of the orbit of Apophis in 2029.

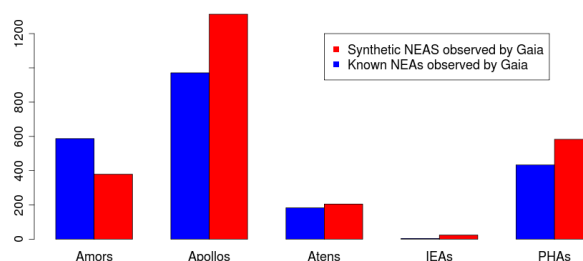
4 Astrometry for newly discovered PHAs

During the mission, we do expect Gaia to observe some new objects and among them new PHAs. But Gaia is not a follow-up mission and as a consequence, the newly discovered objects can rapidly be lost if no recovery process

Table 1. Impact of Gaia data on the size of the 3σ ellipse uncertainty in the 2029-b-plane.

b-plane uncertainty	Ground-based data only	Ground-based and Gaia data
σ_ξ (km)	10.5	0.3
σ_ζ (km)	87	1.4

of those potential alerts is done from Earth. We would like first to quantify the number of alerts expected. In a first approach, using a 20000-synthetic population of NEAs (Bottke et al. 2002) and comparing with Fig.1, we see that only a small number of alerts is expected: around one alert every four days. The statistical details are represented in Fig.3. Because of the scanning law, Gaia will provide only two (α, δ) observations (before being re-observed) and separated by $\Delta t \sim 1.5$ hours. When observing a new object, Gaia will send, within 24 h, the coordinates to Earth, where a preliminary short arc orbit can be computed, using Statistical Ranging method (Virtanen et al. 2001)

**Fig. 3.** Number of known and synthetic NEAs that would be observed by Gaia during the 5-years mission.

This yields to an (α, δ) prediction in the sky plane (\circ). As the (α, δ) distribution is large, we can extract its maximum likelihood (ML) and center a typical field of view ($24' \times 24'$) on this ML (\bullet) in order to know where to look in the sky and how long the object can still be recovered. This test is done with an hypothetical asteroid (1620) Geographos that would be discovered by Gaia. In Fig. 4, when comparing with the expected position of Geographos (\blacktriangledown), we can see that up to 7 days, the asteroid may be lost with this size of field of view.

When recovered, this asteroid will be followed at least one night (and preferably more) in order to have an orbit improvement. Fig. 5 shows the advantage of combining, in real-time, ground-based (with 0.5 arcsec accuracy) and space-based data (5 mas accuracy). One can see that the (α, δ) distribution is drastically reduced when adding additional ground-based observations (\circ).

5 Conclusions

Even if Gaia will not be a big NEAs discoverer, it will provide unprecedented accuracy for NEAs orbit's improvement. Besides, this study can be continued considering the astrometric reduction due to the stellar catalogue provided by Gaia. As a matter of fact, this catalogue will be more precise and dense and almost free of zonal errors. Thus, classical ground-based astrometry (and concerning hence more object down to fainter magnitude) will be improved.

The author are grateful to the DPAC members and CU4.

References

- Bottke, W. F., Morbidelli, A., Jedicke, R., et al. 2002, *Icarus*, 156, 399
Valsecchi, G. B., Milani, A., Gronchi, G. F., & Chesley, S. R. 2003, *A&A*, 408, 1179
Virtanen, J., Muinonen, K., & Bowell, E. 2001, *Icarus*, 154, 412

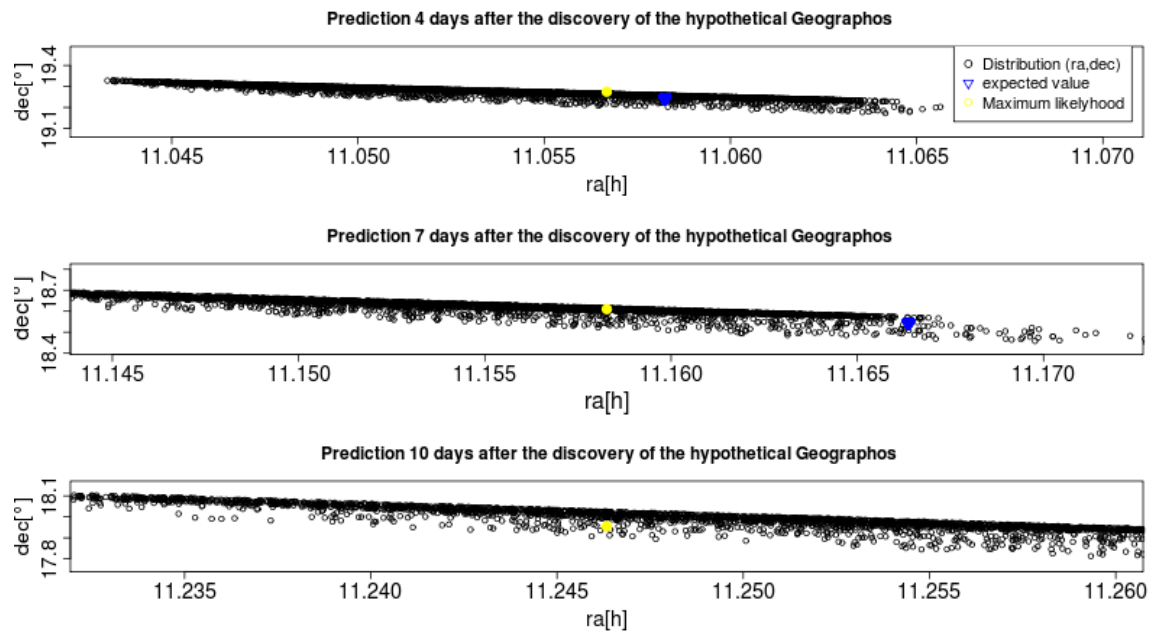


Fig. 4. Prediction on the sky plane of the hypothetical Geographos, until 10 days after its discovery by Gaia.

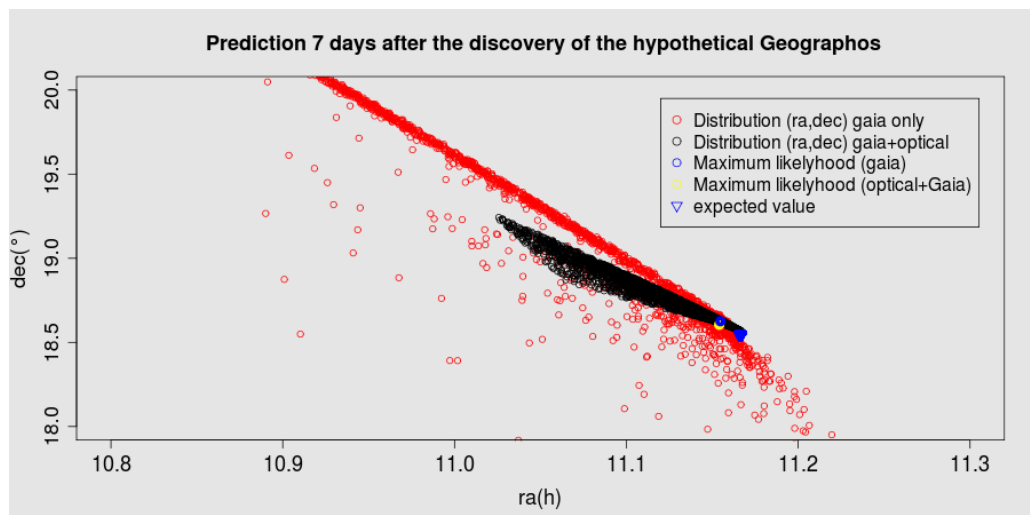


Fig. 5. Distribution (α, δ) combining ground and space-based data (\circ), 7 days after the hypothetical discovery of asteroid Geographos.

THE H α BALMER LINE AS AN EFFECTIVE TEMPERATURE CRITERION

R. Cayrel¹, C. Van't Veer-Menneret², N. F. Allard^{1,3} and C. Stehlé⁴

Abstract. For eleven stars with an accurate effective temperature derived from their apparent angular diameter we determine the effective temperature of the Kurucz Atlas9 model that provides the best fit of the computed theoretical H α profile (using the recent theoretical advances) with the corresponding observed profile, extracted from the S4N spectroscopic database. The two sets of effective temperatures have a significant offset, but are tightly correlated, with a correlation coefficient of 0.9976. The regression straight line of T_{eff}(direct) versus T_{eff}(H α) enables us to reach the true effective temperature from the spectroscopic observation of the H α profile, with an rms error of only 30 K. This provides a way of obtaining the true effective temperature of a reddened star.

Keywords: stars:atmospheres, stars:fundamental parameters, line:profile

1 Introduction

Already many authors have used the H α Balmer line as effective temperature criterion. Two events justify to derive a new calibration of H α versus effective temperature.

The first one is a continuous improvement in the physics of the broadening of the line, from 1999 to 2008. The second one is the enormous gain in the accuracy of apparent angular diameter measurements by interferometric methods. This enables to derive the effective temperatures of a dozen of stars with an accuracy of the order of one per cent by the relation:

$$T_{\text{eff}} = (4/\sigma)^{1/4} f_{\text{bol}}^{1/4} \theta^{-1/2}$$

where σ is the Stefan-Boltzmann constant, and f_{bol} and θ are respectively the apparent bolometric flux and limb-darkened angular diameter of the object. This is the so-called direct method, less model dependent than the Infrared Flux Method, largely used before. Our work has been to connect the effective temperature obtained by the direct method, to the effective temperature of the model giving the best fit between the computed and the observed profile of H α for this dozen of stars.

2 Effective temperatures from the H α fitting procedure

2.1 Observations

We selected the spectra of the S4N spectral library (Allende Prieto et al. 2004) for the 10 stars having apparent angular diameters measurements better than 2 per cent. These spectra are very suited for the study of the H α wings, usually difficult to get with cross-dispersed spectrographs.

2.2 Model atmosphere

We used Kurucz ATLAS9, BALMER9 codes, after incorporating the Stark broadening of Stehlé & Hutcheon (1999) and the collisional broadening by neutral H of Allard et al. (2008). We used a mixing length over pressure scale height ratio of 0.5.

¹ Observatoire de Paris, GEPI, UMR 8111, CNRS, 61, Avenue de l'Observatoire, F-75014 Paris, France

² Observatoire de Paris, GEPI, 5 Place J. Janssen, 92195 Meudon, France

³ Institut d'Astrophysique de Paris, F-75014 Paris, UMR 7095, CNRS, 98bis Boulevard Arago, F-750014 Paris, France

⁴ Observatoire de Paris, LERMA, 5 Place J. Janssen, 92195 Meudon, France

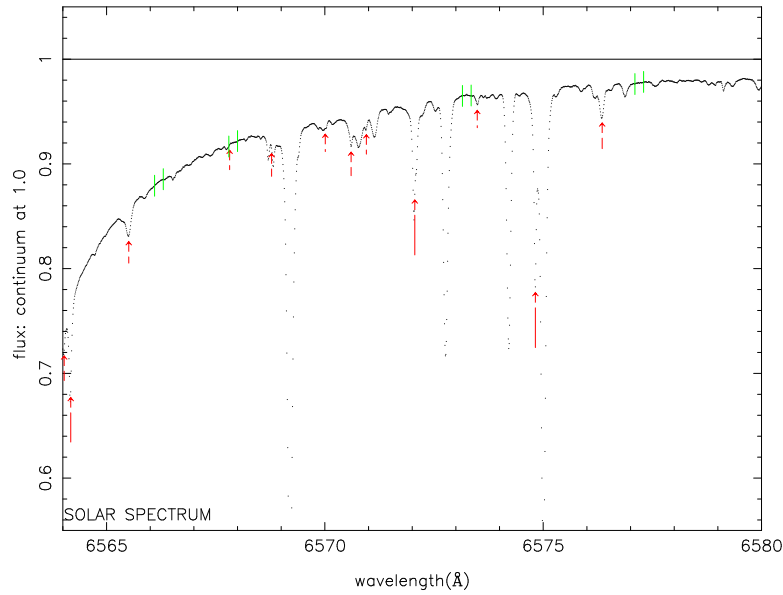


Fig. 1. Red wing of the observed solar $H\alpha$ profile. The windows free of other lines contamination are indicated by a couple of green vertical lines.

2.3 Fitting procedure

As done by Barklem et al. (2002) we have selected windows, where $H\alpha$ is not contaminated by other stellar lines (see Fig. 1). The telluric lines, indicated by red arrows, have been a worry as they move with the radial velocity of the object and must be avoided too. Some windows may be lost. Taking the parameters gravity and metallicity from the PASTEL database (Soubiran et al. 2010), we vary the effective temperature of the model until we get the best fit with the observed profile. See examples in Fig. 2. The procedure is repeated for the selected ten spectra from the S4N library plus the Sun.

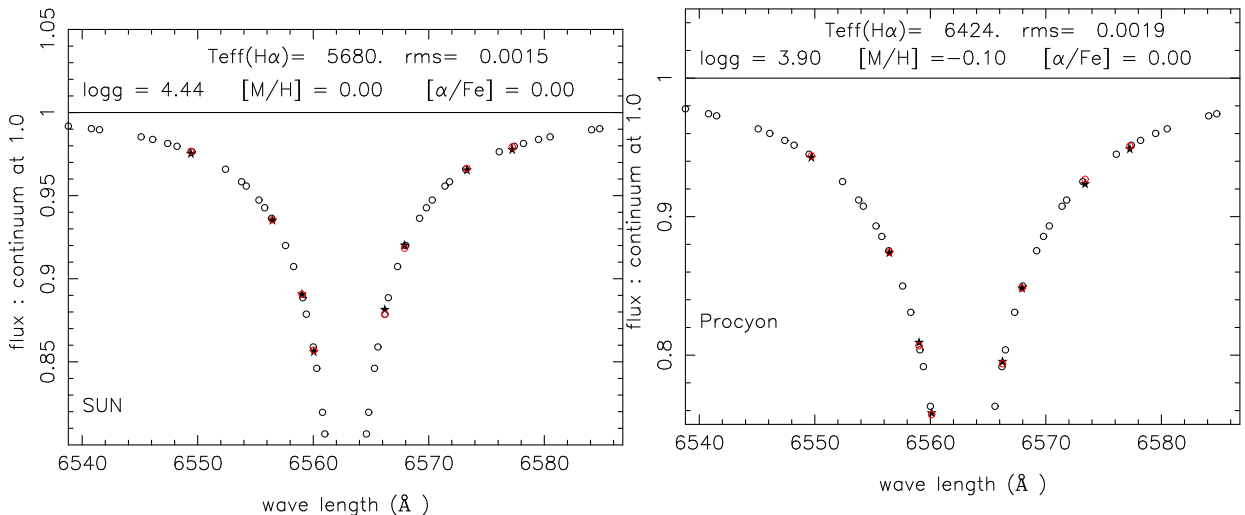


Fig. 2. Left: Fitting of the computed to the observed fluxes of the solar $H\alpha$ profile.

Right: Fitting of the computed to the observed fluxes on the $H\alpha$ profile of Procyon.

Open circles are the theoretical profile, the red ones corresponding to the wavelength of the observed points represented by full black stars.

3 $T_{\text{eff}}(\text{direct})$ and results

The apparent angular diameters have been taken from the literature. Most of them come from the Mount Wilson interferometer (now CHARA) and a few from the ESO VLTI. A list of them can be found in Casagrande et al. (2010). The apparent bolometric magnitudes have been derived from colour indices by relations established by Casagrande et al. (2010). The dispersion of the points around the regression line of $T_{\text{eff}}(\text{direct})$ versus $T_{\text{eff}}(\text{H}\alpha)$ is remarkably small, with a root mean square deviation of only 30 K. The relation between the two sets of effective temperatures is represented by:

$$T_{\text{eff}}(\text{direct}) = 20.3 + 1.014 \times T_{\text{eff}}(\text{H}\alpha)$$

The correlation coefficient between the two sets is 0.9976, a very tight connection (Fig. 3). The principal aim of our paper has been met, a simple procedure for deriving the true effective temperature from the observed H α Balmer line profiles, enabling to bypass the uncertainties in the amount of interstellar reddening, critical for temperatures derived from photometric indices. All the calibration stars are all at distances less than 15 parsecs, therefore not affected by reddening. The remaining interesting problem is to understand why the two sets of temperatures have an offset instead of being equal. This is clearly a problem for 3D hydrodynamical models, that we are investigating now.

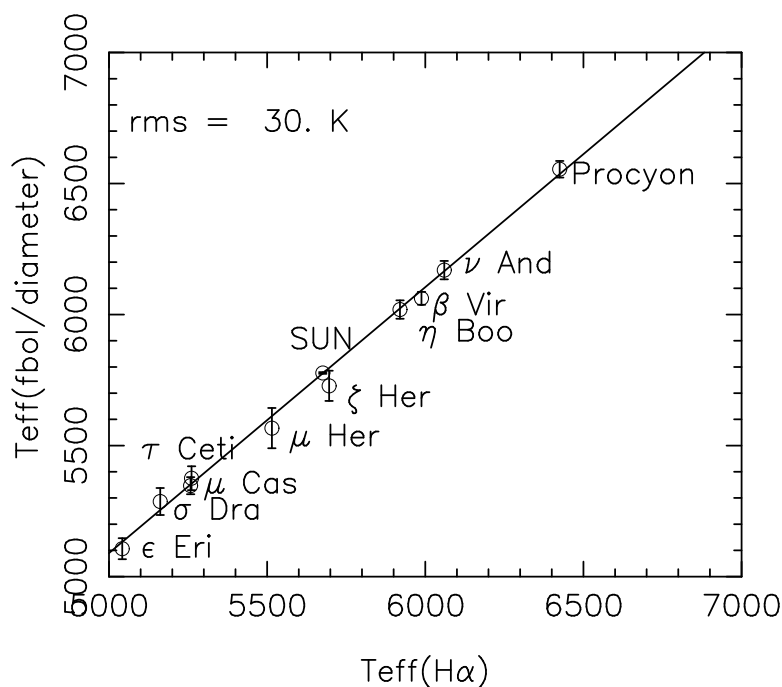


Fig. 3. Regression line between $T_{\text{eff}}(\text{H}\alpha)$ and $T_{\text{eff}}(\text{direct})$. The rms of the fit is 30 K.

The details of this research are available in Cayrel et al. (2011).

References

- Allard, N.F., Kielkopf, J.F., Cayrel, R., van 't Veer-Menneret, C. 2008, A&A 480, 581
 Allende Prieto, C., Barklem, P.S., Lambert, D.L., Cunha, K. 2004, A&A 420, 183 (S4N)
 Barklem, P.S., Stempels, H.C., Allende Prieto, C. et al. 2002 A&A 385,951
 Casagrande, L., Ramírez I., Meléndez, J. et al. 2010, A&A 512, 54
 Cayrel, R., van 't Veer-Menneret, C., Allard, N.F., Stehlé C. 2011, A&A 531, A83
 Soubiran, C., Le Campion, J.-F., Cayrel de Strobel, G., Caillo, A. 2010, A&A 515, A111
 Stehlé C., & Hutcheon, R. 1999, A&AS, 140, 93

CALIBRATION OF THE GAIA RVS FROM GROUND-BASED OBSERVATIONS OF CANDIDATE STANDARD STARS

L. Chemin¹, C. Soubiran¹, F. Crifo², G. Jasniewicz³, D. Katz², D. Hestroffer⁴ and S. Udry⁵

Abstract. The Radial Velocity Spectrometer (RVS) on board of Gaia will perform a large spectroscopic survey to determine the radial velocities of some 1.5×10^8 stars. We present the status of ground-based observations of a sample of 1420 candidate standard stars designed to calibrate the RVS. Each candidate star has to be observed several times before Gaia launch (and at least once during the mission) to ensure that its radial velocity remains stable during the whole mission. Observations are performed with the high-resolution spectrographs SOPHIE, NARVAL and CORALIE, completed with archival data of the ELODIE and HARPS instruments. The analysis shows that about 7% of the current catalogue exhibits variations larger than the adopted threshold of 300 m s^{-1} . Consequently, those stars should be rejected as reference targets, due to the expected accuracy of the Gaia RVS. Emphasis is also put here on our observations of bright asteroids to calibrate the ground-based velocities by a direct comparison with celestial mechanics. It is shown that the radial velocity zero points of SOPHIE, NARVAL and CORALIE are consistent with each other, within the uncertainties. Despite some scatter, their temporal variations remain small with respect to our adopted stability criterion.

Keywords: Galaxy: kinematics and dynamics, Galaxy: structure, Stars: kinematics and dynamics, Minor planets, asteroids: general, Surveys, Techniques: radial velocities

1 Generalities

The RVS is a slitless spectrograph whose spectral domain is 847-874 nm and resolving power $R \sim 11500$. The expected accuracy is 1 km s^{-1} for F0 to K0 stars brighter than $V=13$, and for K1 to K4 stars brighter than $V=14$.

The main scientific objectives of RVS are the chemistry and dynamics of the Milky Way, the detection and characterisation of multiple systems and variable stars (for more details, see Wilkinson et al. 2005). Those objectives will be achieved from a spectroscopic survey of:

- Radial velocities ($\sim 150 \times 10^6$ objects, $V \leq 17$)
- Rotational velocities ($\sim 5 \times 10^6$ objects, $V \leq 13$)
- Atmospheric parameters ($\sim 5 \times 10^6$ objects, $V \leq 13$)
- Abundances ($\sim 2 \times 10^6$ objects, $V \leq 12$)

Each star will be observed ~ 40 times on average by RVS over the 5 years of the mission.

¹ Laboratoire d'Astrophysique de Bordeaux, UMR 5804 (CNRS, Université Bordeaux 1), 33271 Floirac Cedex, France

² Observatoire de Paris, GEPI, UMR 8111 (CNRS, Université Denis Diderot Paris 7), 92195 Meudon, France

³ GRAAL, UMR5024, (CNRS, Université Montpellier 2), 34095 Montpellier Cedex 05, France

⁴ Observatoire de Paris, IMCCE, UMR8028 (CNRS, Université Pierre & Marie Curie Paris 6), 75014, Paris, France

⁵ Observatoire de Genève, 51 Ch. des Maillettes, 1290 Sauverny, Switzerland

2 Calibration of the Gaia RVS

Because the RVS has no calibration module on board, the zero point of its radial velocities has to be determined from reference sources. Ground-based observations of a large sample of well-known, stable reference stars as well as of asteroids are thus critical for the calibration of the RVS. A sample of 1420 candidate standard stars has been established (Crifo et al. 2009, 2010) and has to be validated by high spectral resolution observations.

Two measurements per candidate star are being made before Gaia is launched (or one, depending on already available archived data). Another measurement will occur during the mission. The measurements will allow us to check the temporal stability of radial velocities, and to reject any targets with significant RV variation.

3 Status of observations of stars

The ongoing observations are performed with three high spectral resolution spectrographs:

- SOPHIE on the 1.93-m telescope at Observatoire de Haute-Provence,
- NARVAL on the T telescope Bernard Lyot at Observatoire Pic-du-Midi,
- CORALIE on the Euler swiss telescope at La Silla.

As of June 2011 we have observed 995 distinct candidates with SOPHIE, CORALIE and NARVAL. The detailed observations per instrument are:

- 691 stars (1165 velocities) with SOPHIE
- 669 stars (945 velocities) with CORALIE
- 93 stars (98 velocities) with NARVAL

Figure 1 (left-hand panel) represents the spatial distribution in the equatorial frame of the sample and the number of measurements per object we have done so far with the three instruments.

In addition to those new observations, we use radial velocity measurements available from the spectroscopic archives of two other high-resolution instruments: ELODIE, which is a former OHP spectrograph, and HARPS which is currently observing at the ESO La Silla 3.6-m telescope. The archived data allow us to recover 1057 radial velocities for 292 stars (ELODIE) and 1289 velocities for 113 stars (HARPS).

Figure 1 (right-hand panel) summarizes the status of the total number of measurements for the sample of 1420 candidate stars performed with all five instruments.

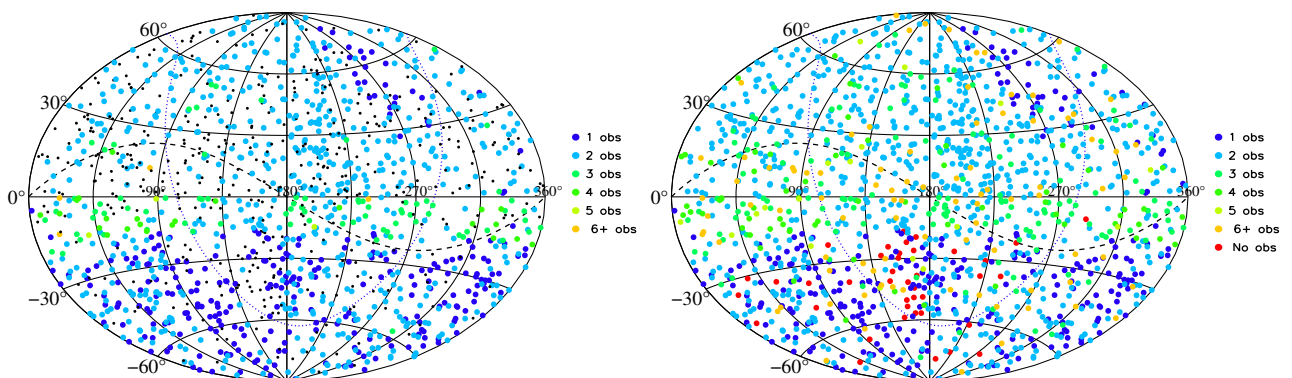


Fig. 1. Left panel: Current status of the number of observations available per candidate standard star observed with the SOPHIE, CORALIE and NARVAL instruments (995 distinct stars). Black dots indicate the locations of the 425 remaining sources from the sample of 1420 candidates. **Right panel:** Same as in left panel, but including archival data of the ELODIE and HARPS instruments as well. The maps are represented in the equatorial frame. The Ecliptic plane is shown as a dashed line and the Galactic plane as a dotted line.

4 How stable are the radial velocities of our candidates?

We have derived the variation of radial velocity of each star for which we have at least two velocity measurements separated by an elapsed time of at least 100 days. These stars represent a subsample of 1044 among 1420 targets. The variation is defined as the difference between the maximum and minimum velocities, as reported in the frame of the SOPHIE spectrograph. Its distribution is displayed in Figure 2.

A candidate is considered as a reference star for the RVS calibration when its radial velocity does not vary by more than an adopted threshold of 300 m s^{-1} . Such a threshold has been defined to satisfy the condition that the variation of the RV of a candidate must be well smaller than the expected RVS accuracy (1 km s^{-1} at best for the brightest stars). As a result, we find $\sim 7\%$ of the 1044 stars exhibiting a variation larger than 300 m s^{-1} , as derived from available measurements performed to date. Those variable stars will have to be rejected from the list of standard stars. Note that about 75% of the 1044 stars have very stable RV, at a level of variation smaller than 100 m s^{-1} .

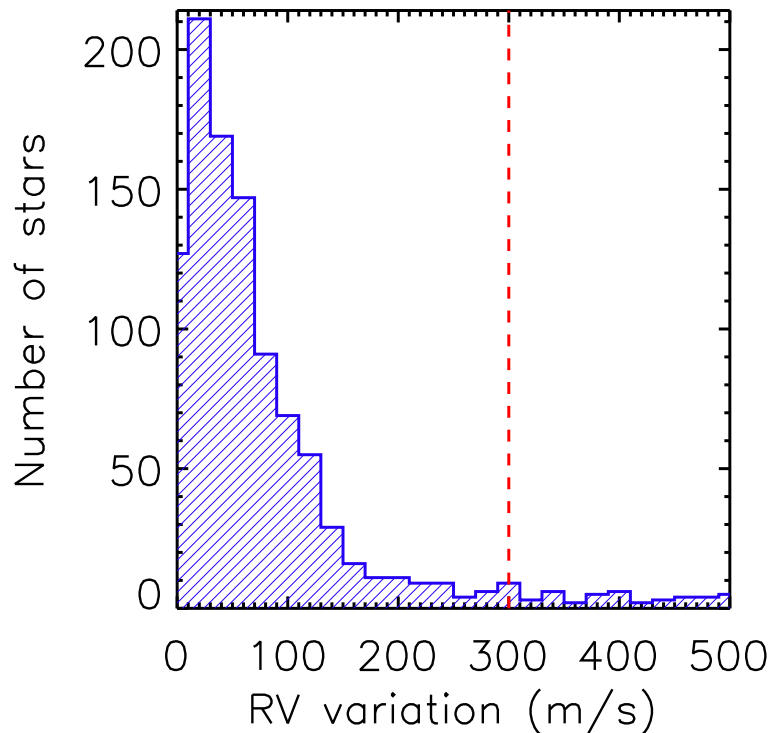


Fig. 2. Distribution of variations of radial velocities of candidate standard stars having at least two RV measurements separated by 100 days or more. A dashed line shows the adopted 300 m s^{-1} stability threshold.

5 Spectral observations of asteroids

Observations of asteroids are very important for the radial velocity calibration. Indeed they will be used to determine the zero-points of the RVs measured with SOPHIE, CORALIE and NARVAL (as well as the Gaia-RVS zero-point). Those goals will be achieved by comparing the spectroscopic RVs of asteroids from ground-based measurements with theoretical kinematical RVs from celestial mechanics. The theoretical RVs are provided by IMCCE and are known with an accuracy better than 1 m s^{-1} . About 280 measurements of 90 asteroids have been done so far.

As an illustration, Figure 3 (left-hand panel) displays the residual velocity (observed minus computed RVs) of asteroids observed by the SOPHIE instrument as a function of the observed RVs. The average residual of asteroids observed with SOPHIE is 30 m s^{-1} and the scatter is 38 m s^{-1} .

In Figure 3 (right-hand panel) we also show the variation of the residual RVs with time. It nicely shows how

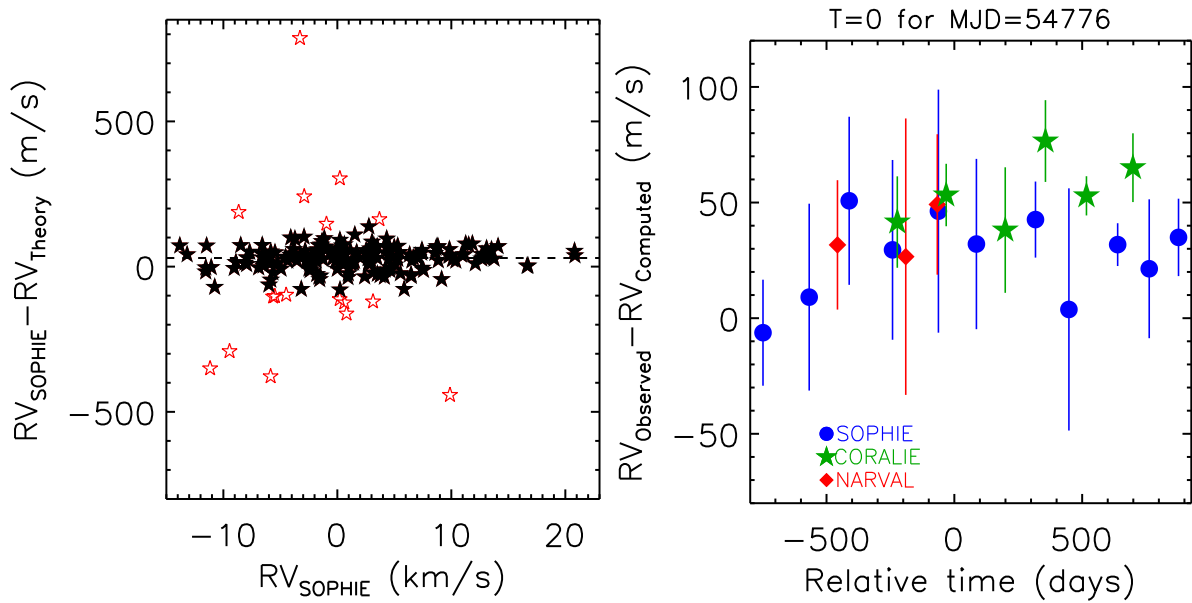


Fig. 3. Radial velocities of asteroids. **Left panel:** Residual velocities (observed minus computed) of asteroids as a function of their observed velocities (SOPHIE observations only). Red symbols are points deviant by more than 3σ . A horizontal dashed line represents the mean residual velocity of 30 m s^{-1} . **Right panel:** Comparison of residual velocities of asteroids for SOPHIE, CORALIE and NARVAL as a function of time for the various observing runs.

stable the RVs are as a function of time. The residual RVs are relatively constant within the quoted errors. The error-bars represent the dispersion of all measurements performed at each observational run. Their amplitude is mainly related to the conditions of observations that differ from one session to another (in particular the moonlight contamination). Though significant (between 10 and 50 m s^{-1}) those error-bars remain smaller than our target stability criterion of 300 m s^{-1} , which will enable us to determine correctly the RV zero point of each instrument.

Note also we have verified that intrinsic properties of asteroids (e.g. their size, shape, rotation velocity, albedo, etc...) have negligible systematic impacts on the determination of RVs zero points for the spectrographs. From now, observations of asteroids shall be performed with reduced moonlight contamination

We are very grateful to the AS-Gaia, the PNPS and PNCG for the financial support of the observing campaigns and the help in this project.

References

- Crifo F., Jasniewicz G., Soubiran C., et al., 2009, SF2A 2009 conference proceedings, 267
 Crifo F., Jasniewicz G., Soubiran C., et al., 2010, A&A, 524, A10
 Wilkinson M., et al., 2005, MNRAS, 359, 1306

THE DEPENDENCE OF THE GALACTIC STAR FORMATION LAWS ON METALLICITY

S. Dib¹, L. Piau², S. Mohanty¹ and J. Braine³

Abstract. We describe results from semi-analytical modelling of star formation in protocluster clumps of different metallicities. In this model, gravitationally bound cores form uniformly in the clump following a prescribed core formation efficiency per unit time. After a contraction timescale which is equal to a few times their free-fall times, the cores collapse into stars and populate the IMF. Feedback from the newly formed OB stars is taken into account in the form of stellar winds. When the ratio of the effective energy of the winds to the gravitational energy of the system reaches unity, gas is removed from the clump and core and star formation are quenched. The power of the radiation driven winds has a strong dependence on metallicity and it increases with increasing metallicity. Thus, winds from stars in the high metallicity models lead to a rapid evacuation of the gas from the protocluster clump and to a reduced star formation efficiency, as compared to their low metallicity counterparts. We derive the metallicity dependent star formation efficiency per unit time in this model as a function of the gas surface density Σ_g . This is combined with the molecular gas fraction in order to derive the dependence of the surface density of star formation Σ_{SFR} on Σ_g . This feedback regulated model of star formation reproduces very well the observed star formation laws in galaxies extending from low gas surface densities up to the starburst regime. Furthermore, the results show a dependence of Σ_{SFR} on metallicity over the entire range of gas surface densities, and can also explain part of the scatter in the observations.

Keywords: Stars: massive, winds; ISM: clouds, galaxies: star formation: star clusters

1 Introduction

Over the last two decades, the dependence of the star formation rate surface density (Σ_{SFR}) on the gas surface density (Σ_g) and eventually on other physical quantities has been extensively investigated both observationally (e.g., Kennicutt 1998; Wong & Blitz 2002; Boissier et al. 2003; Bigiel et al. 2008; Blanc et al. 2009; Onodera et al. 2010; Tabatabaei & Berkhuijsen 2010; Heiner et al. 2010; Schrubba et al. 2011; Bolatto et al. 2011) as well as theoretically and numerically (e.g., Tutukov 2006; Krumholz & Thompson 2007; Fuchs et al. 2009; Silk & Norman 2009; Krumholz et al. 2009a; Papadopoulos & Pelupessy 2010; Gnedin & Kravtsov 2011; Narayanan et al. 2011; Feldmann et al. 2011; Vollmer & Leroy 2011; Braun & Schmidt 2011; Monaco et al. 2011; Kim et al. 2011; Dib 2011a,b). Determining the rate of star formation in a given tracer of the gas surface density requires quantifying the fraction of that tracer as a function of the global gas surface density and a description of the efficiency at which the star forming gas is converted into stars per unit time. The relationship between Σ_{SFR} and the surface density of the molecular hydrogen gas Σ_{H_2} is given by:

$$\Sigma_{SFR} = \Sigma_g f_{H_2} \frac{SFE_\tau}{\tau}, \quad (1.1)$$

where $f_{H_2} = \Sigma_{H_2}/\Sigma_g$ is the molecular hydrogen mass fraction, SFE_τ is the star formation efficiency over the timescale τ . Krumholz & McKee (2005) proposed a theory in which supersonic turbulence is the dominant agent that regulates star formation in giant molecular clouds (GMCs). They derived a core formation efficiency per unit free-fall time, CFE_{ff} , which is given by $CFE_{ff} =$

¹ Astrophysics Group, Blackett Laboratory, Imperial College London, London SW7 2AZ; s.dib@imperial.ac.uk

² LATMOS, 11 Boulevard d'Alembert, 78280 Guyancourt, France

³ Laboratoire d'Astrophysique de Bordeaux, Université de Bordeaux, OASU CNRS/INSU, 33271 Floirac, France

$0.15\alpha_{vir}^{-0.68}\mathcal{M}^{-0.32}$, where α_{vir} and \mathcal{M} are the virial parameter and the *rms* sonic Mach number of the GMC, respectively*. By assuming that only a fraction of the mass of the cores ends up in the stars, this CFE_{ff} can be converted into a star formation efficiency $SFE_{ff} = \eta \times CFE_{ff}$ ($\eta \leq 1$). An alternative theory has been recently proposed by Dib et al. (2011) and Dib (2011a,b) in which the star formation rate in protocluster clumps is primarily regulated by feedback from massive stars and in particular through energy injection in the clumps by stellar winds. In the following sections, we briefly describe the main constituents of this model.

2 Feedback regulated star formation

The model follows the formation of dense gravitationally bound cores in a protocluster clump. Cores form in the clump with a given core formation efficiency per unit time and follow a local mass distribution that is the result of the gravo-turbulent fragmentation of the clump. In their series of models, Dib et al. (2011) varied the core formation efficiency per unit free-fall time (CFE_{ff}) between 0.1 and 0.3. This is consistent with the range of CFE_{ff} measured in numerical simulations which describe the gravo-turbulent fragmentation of magnetised, turbulent, and self-gravitating molecular clouds (e.g., Dib et al. 2008; Dib et al. 2010a). The gravitationally bound cores that are generated at every epoch have a mass distribution that is given by the gravo-turbulent fragmentation model of Padoan & Nordlund (2002). In this work, we leave out, for simplicity, the role played by gas accretion and coalescence in modifying the mass distribution of the cores. The interested reader is referred to Dib et al. (2007) and Dib et al. (2010b) for such models. Cores contract over a lifetime which is a few times their free-fall time before collapsing to form stars. Feedback from the most massive stars ($M_{\star} \geq 5 M_{\odot}$) is taken into account in the form of stellar winds. The formation of cores in the protocluster clump, and consequently star formation, are terminated whenever the fraction of the wind energy stored into motions that oppose gravity exceeds the gravitational energy of the clump. In order to calculate reliable estimates of the feedback generated by metallicity dependent stellar winds, we proceed in two steps. In the first step, we use a modified version of the stellar evolution code CESAM (see appendix 1 in Piau et al. 2011) to calculate a grid of main sequence stellar models for stars in the mass range [5-80] M_{\odot} (with steps of 5 M_{\odot}) at various metallicities $Z/Z_{\odot} = [1/10, 1/6, 1/3, 1/2, 1, 2]$ ($Z_{\odot} = 0.0138$). The evolution of massive stars is followed using the CESAM code for ~ 1 Myr, on the main sequence. The characteristic stellar properties, which are the effective temperature T_{eff} , the luminosity L_{\star} , and the stellar radius R_{\star} are then used in the stellar atmosphere model of Vink et al. (2001) in order to calculate the stellar mass loss rate \dot{M}_{\star} . Vink et al. (2001) did not derive the values of the terminal velocities of the winds (v_{∞}), therefore, we use instead the derivations of v_{∞} obtained by Leitherer et al. (1992).

The power of the stellar winds is given by $\dot{M}_{\star}v_{\infty}^2$. This quantity is displayed in Fig. 1 for the models with different metallicities. The values of $\dot{M}_{\star}v_{\infty}^2$ are fitted with fourth order polynomials (overplotted to the data) and whose coefficients are provided in Dib et al. (2011). The $\dot{M}_{\star}v_{\infty}^2 - M_{\star}$ relations displayed in Fig. 1 allow for the calculation of the total wind energy deposited by stellar winds. The total energy from the winds is given by:

$$E_{wind} = \int_{t'=0}^{t'=t} \int_{M_{\star}=5 M_{\odot}}^{M_{\star}=120 M_{\odot}} \left(\frac{N(M_{\star})\dot{M}_{\star}(M_{\star})v_{\infty}^2}{2} dM_{\star} \right) dt'. \quad (2.1)$$

We assume that only a fraction of E_{wind} will be transformed into systemic motions that will oppose gravity and participate in the evacuation of the bulk of the gas from the proto-cluster clump. The effective kinetic wind energy is thus given by:

$$E_{k,wind} = \kappa E_{wind}, \quad (2.2)$$

where κ is a quantity ≤ 1 (in this work, we use $\kappa = 0.1$ for all models). $E_{k,wind}$ is compared at every timestep to the absolute value of the gravitational energy, E_{grav} , which is calculated as being:

$$E_{grav} = -\frac{16}{3}\pi^2 G \int_0^{R_c} \rho_c(r)^2 r^4 dr. \quad (2.3)$$

*Padoan & Nordlund (2011) found a different dependence of the SFR on α_{vir} and \mathcal{M} . The results of their numerical simulations suggest that the SFR decreases with increasing α_{vir} but also that it increases with increasing \mathcal{M} .

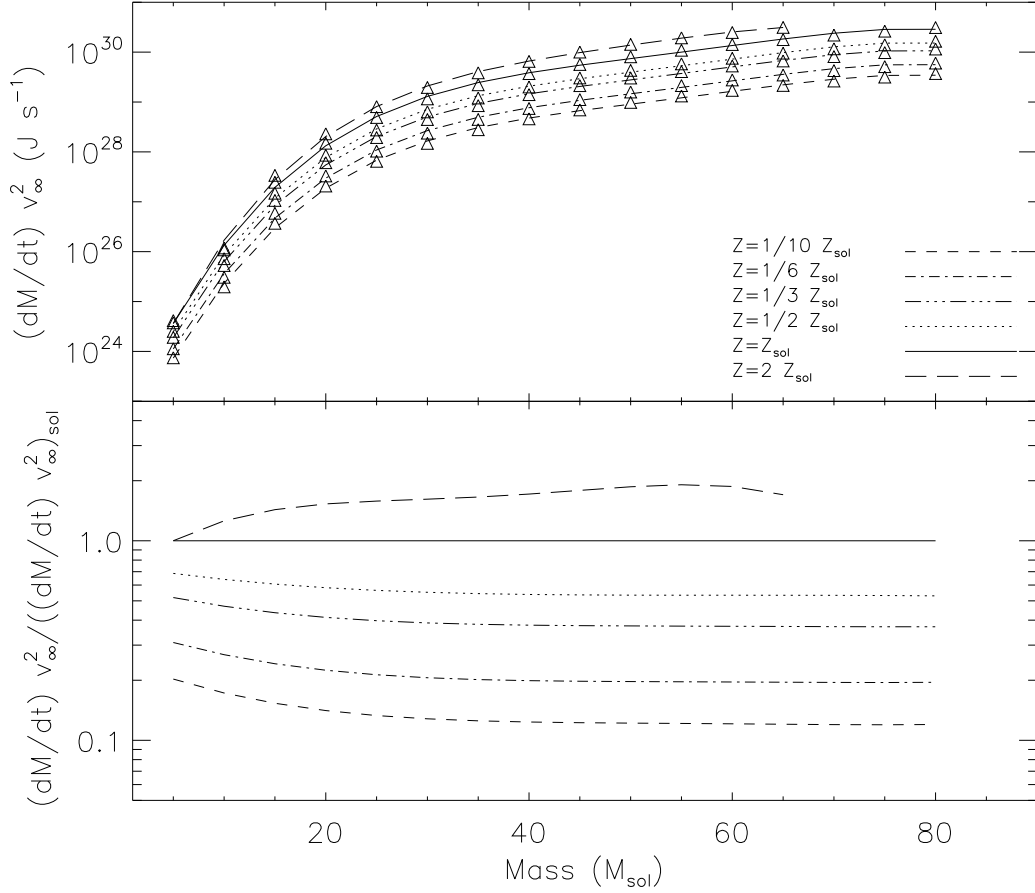


Fig. 1. The power of the stellar winds, or wind luminosities, for stars in the mass range $5\text{--}80 M_{\odot}$ on the main sequence, and for various metallicities. The stellar mass loss rates have been calculated using the stellar characteristics (effective temperature, stellar luminosity and radius) computed using the stellar evolution code CESAM coupled to the stellar atmosphere model of Vink et al. (2001). The values of v_{∞} have been calculated using the derivation by Leitherer et al. (1992). Over-plotted to the data are fourth order polynomials. The parameters of the fit functions can be found in Dib et al. (2011). Adapted from Dib et al. (2011).

Since higher metallicity stellar winds deposit larger amounts of energy in the clump than their lower metallicity counterparts, this leads them to evacuate the gas from the clump on shorter timescales. This in turn quenches the process of core and star formation earlier and sets a smaller final star formation efficiency, SFE_{exp} . Fig. 2 displays the dependence of SFE_{exp} and of the expulsion time, t_{exp} (expressed in units of the free-fall time t_{ff}), as a function of metallicity for clumps of various masses.

3 Metallicity dependent star formation laws

Using the above described model, it is possible to derive the dependence of Σ_{SFR} on Σ_g . The star formation rate surface density in the feedback regulated mode of star formation is given by:

$$\Sigma_{SFR} = \Sigma_g f_{H2} \frac{\langle SFE_{exp} \rangle}{\langle t_{exp} \rangle}, \quad (3.1)$$

where $\langle SFE_{exp} \rangle$ and $\langle t_{exp} \rangle$ are, respectively, the characteristic SFE_{exp} and the epoch at which gas is expelled from the protocluster region for the clump mass distribution associated with a given Σ_g . Writing $\langle t_{exp} \rangle$ in terms of the clump free-fall time $\langle t_{ff} \rangle$, Eq. 3.1 becomes:

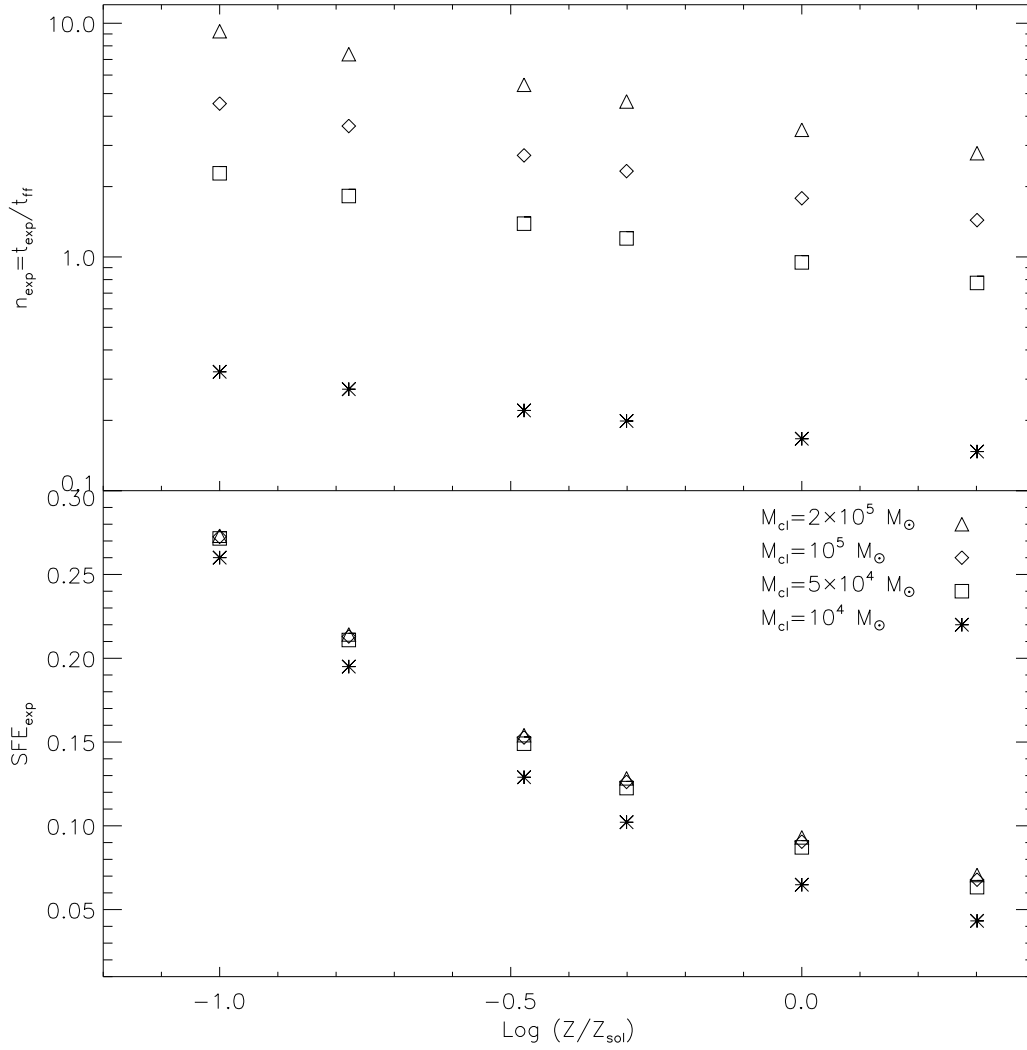


Fig. 2. Dependence of the quantities SFE_{exp} (final star formation efficiency) and $n_{exp} = t_{exp}/t_{ff}$ (ratio of the expulsion time to the free-fall time) for selected values of the protocluster forming clump masses and metallicities. These results are based on the models of Dib et al. (2011).

$$\begin{aligned} \Sigma_{SFR} &= \Sigma_g f_{H_2} \frac{\langle SFE_{exp} \rangle}{\langle n_{exp} \rangle} \frac{1}{\langle t_{ff} \rangle} \\ &= \Sigma_g f_{H_2} \frac{\langle f_{*,ff} \rangle}{\langle t_{ff} \rangle}. \end{aligned} \quad (3.2)$$

where $f_{*,ff}$ is the dimensionless star formation efficiency and which corresponds to the mass fraction of the molecular gas that is converted into stars per free-fall time t_{ff} of the clumps. $\langle f_{*,ff} \rangle$ and $\langle t_{ff} \rangle$ represent characteristic values of $f_{*,ff}$ and t_{ff} for the spectrum of clump masses found in the GMC for a given value of Σ_g . The quantity f_{H_2} is the mass fraction of the total gas that is in molecular form. In this work, we use the functional form of f_{H_2} obtained by Krumholz et al. (2009b) who derived f_{H_2} as a function of the gas surface density and metallicity (see their paper or Dib 2011 for the detailed formula). $\langle t_{ff} \rangle$ can be approximated by the free-fall time of the clump with the characteristic mass $t_{ff}(M_{char}) = 8 \Sigma_{cl}^{-3/4} M_{char,6}^{1/4}$ Myr where $M_{char,6} = M_{char}/10^6 M_{\odot}$. The characteristic mass M_{char} is given by :

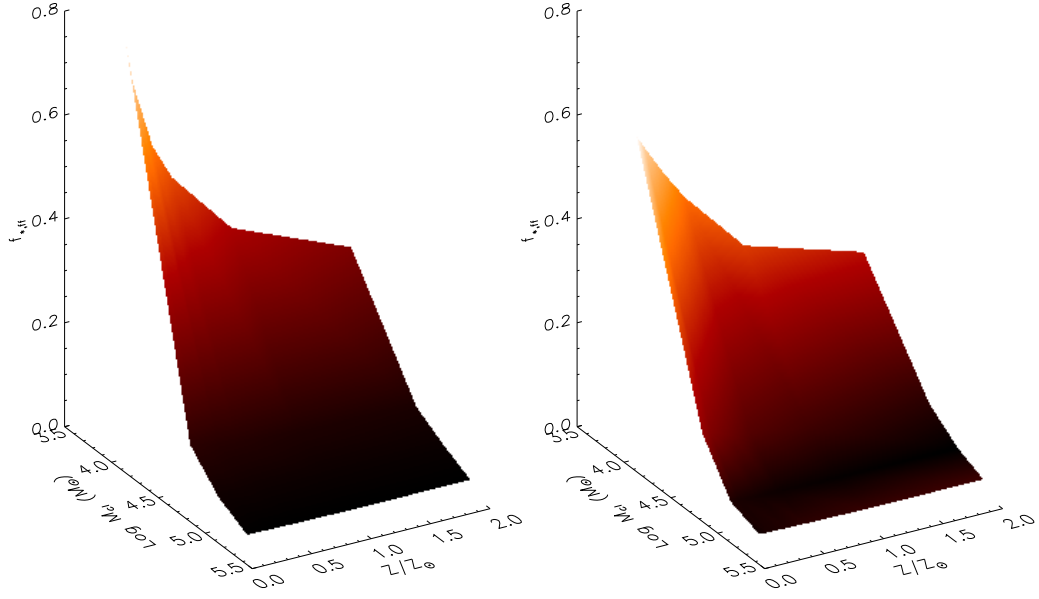


Fig. 3. Star formation efficiency per unit free-fall time in the protocluster clump in the metallicity-dependent feedback model. The star formation efficiencies per free-fell use a core-to-star efficiency conversion factor of 1/3. The left panel displays $f_{*,ff}$ as a function of both M_{cl} and $Z' = Z/Z_{\odot}$ in the original data, while the right panel displays the analytical fit function to this data set given in Eq. 3.5. Adapted from Dib (2011a).

$$M_{char} = \int_{M_{cl,min}}^{\max(M_{cl,max}, M_{GMC})} M_{cl} N(M_{cl}) dM_{cl}, \quad (3.3)$$

where $N(M_{cl})$ is the mass function of protocluster forming clumps which we take to be $N(M_{cl}) = A_{cl} M_{cl}^{-2}$, and A_{cl} is a normalisation coefficient given by $A_{cl} \int_{M_{cl,min}}^{\max(M_{cl,max}, M_{GMC})} N(M_{cl}) dM_{cl} = \epsilon$, where $0 < \epsilon < 1$ is the mass fraction of the GMCs that is in protocluster clumps at any given time. In this work we use $\epsilon = 0.5$. The minimum clump mass $M_{cl,min}$ is taken to be $2.5 \times 10^3 M_{\odot}$ (this guarantees, for final SFEs in the range of 0.05-0.3 a minimum mass for the stellar cluster of $\sim 50 M_{\odot}$) and the maximum clump mass is $10^8 M_{\odot}$. The characteristic GMC mass is determined by the local Jeans mass and is given by:

$$M_{GMC} = 37 \times 10^6 \left(\frac{\Sigma_g}{85 M_{\odot} \text{ pc}^{-2}} \right) M_{\odot}. \quad (3.4)$$

Fig. 4 (top) displays M_{char} as a function of Σ_g . The quantity $f_{*,ff} = SFE_{exp}/n_{exp}$ is displayed in Fig. 3 (left panel) as a function of mass and metallicity ($Z' = Z/Z_{\odot}$). These models use a value of $CFE_{ff} = 0.2$ and standard clump and core parameters (see Dib et al. 2001 and Dib 2011a,b for more detail). A fit to the (M_{cl}, Z') data points with a 2-variables second order polynomial yields the following relation shown in Fig. 3, right panel:

$$\begin{aligned} f_{*,ff}(M_{cl}, Z') = & 11.31 - 4.31 \log(M_{cl}) + 0.41 [\log(M_{cl})]^2 \\ & - 8.28 Z' + 3.20 Z' \log(M_{cl}) - 0.32 Z' [\log(M_{cl})]^2 \\ & + 2.30 Z'^2 - 0.89 Z'^2 \log(M_{cl}) + 0.08 Z'^2 [\log(M_{cl})]^2. \end{aligned} \quad (3.5)$$

Using Eq. 3.5, it is then possible to calculate $\langle f_{*,ff} \rangle$:

$$\langle f_{*,ff} \rangle (Z', \Sigma_g) = \int_{M_{cl,min}}^{\max(M_{cl,max}, M_{GMC})} f_{*,ff}(M_{cl}, Z') N(M_{cl}) dM_{cl}. \quad (3.6)$$

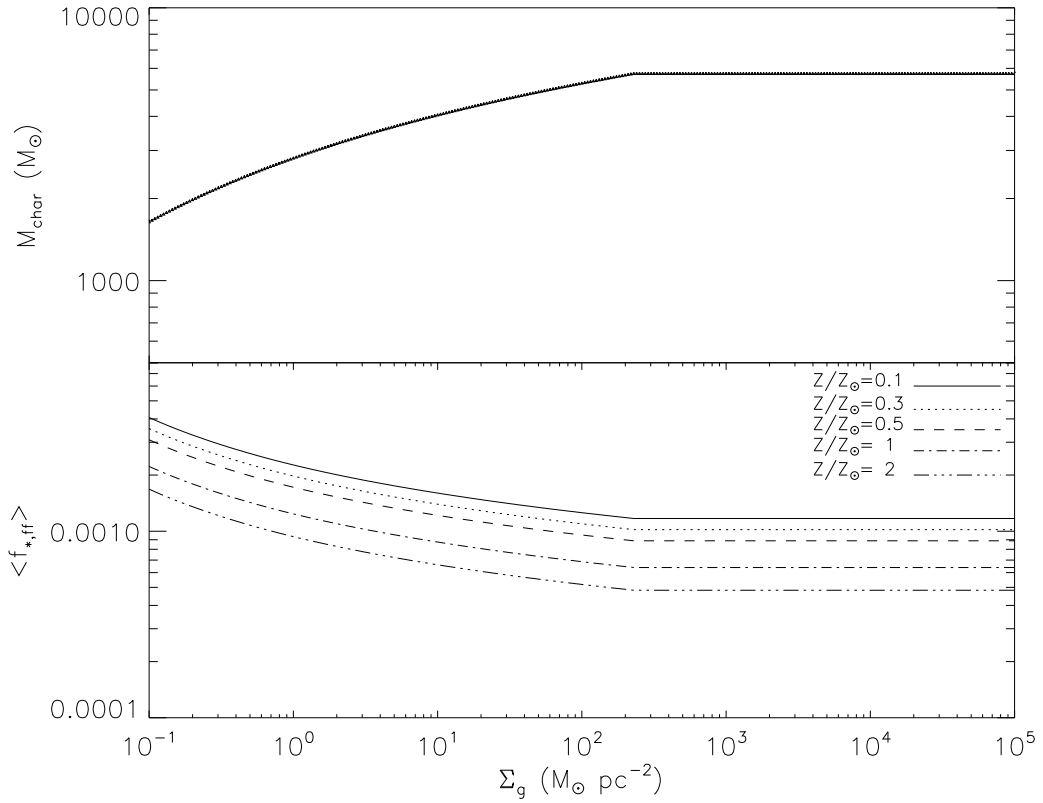


Fig. 4. Characteristic clump mass as a function of the gas surface density (Eq. 3.3, top panel) and the star formation efficiency per unit free-fall time in this feedback regulated model of star formation (lower panel). Adapted from Dib (2011a).

Fig. 4 (bottom) displays $\langle f_{*,ff} \rangle (Z', \Sigma_g)$ for values of Z' in the range $[0.1 - 2]$. We assume that there is a critical value of $\Sigma_g = 85 \text{ M}_\odot \text{ pc}^{-2}$ below which clumps are pressurised by their internal stellar feedback, such that $\Sigma_{cl} = \Sigma_{g,crit}$ where $\Sigma_g < \Sigma_{g,crit}$ and $\Sigma_{cl} = \Sigma_{GMC} = \Sigma_g$ when $\Sigma_g \geq \Sigma_{g,crit}$. With the above elements, the star formation law can be re-written as:

$$\Sigma_{SFR} = \frac{8}{10^6} f_{H_2}(\Sigma_g, c, Z') \Sigma_g \times \left\{ \begin{array}{ll} \frac{\langle f_{*,ff} \rangle (Z')}{M_{char,6}^{1/4}} & ; \frac{\Sigma_g}{85 \text{ M}_\odot \text{ pc}^{-2}} < 1 \\ \frac{\langle f_{*,ff} \rangle (Z')}{M_{char,6}^{1/4}} \left(\frac{\Sigma_g}{85 \text{ M}_\odot \text{ pc}^{-2}} \right)^{3/4} & ; \frac{\Sigma_g}{85 \text{ M}_\odot \text{ pc}^{-2}} \geq 1 \end{array} \right\}, \quad (3.7)$$

where Σ_{SFR} is in $\text{M}_\odot \text{ yr}^{-1} \text{ kpc}^{-2}$, M_{char} is given by Eq. 3.3, and $\langle f_{*,ff} \rangle$ by Eqs. 3.5 and 3.6. Fig. 5 displays the results obtained using Eq. 3.7 for Σ_g values starting from low gas surface densities up to the starburst regime. The results are calculated for the metallicity values of $Z' = [0.1, 0.3, 0.5, 1, 2]$. The results are compared to the sub-kpc data of Bigiel et al. (2008,2010) and to the normal and starburst galaxies results of Kennicutt (1998). The models fits remarkably well the observational results over the entire range of surface densities. Furthermore, the segregation by metallicity extends beyond the low surface density regime up to the starburst regime where a segregation in metallicity of ~ 0.5 dex is observed.

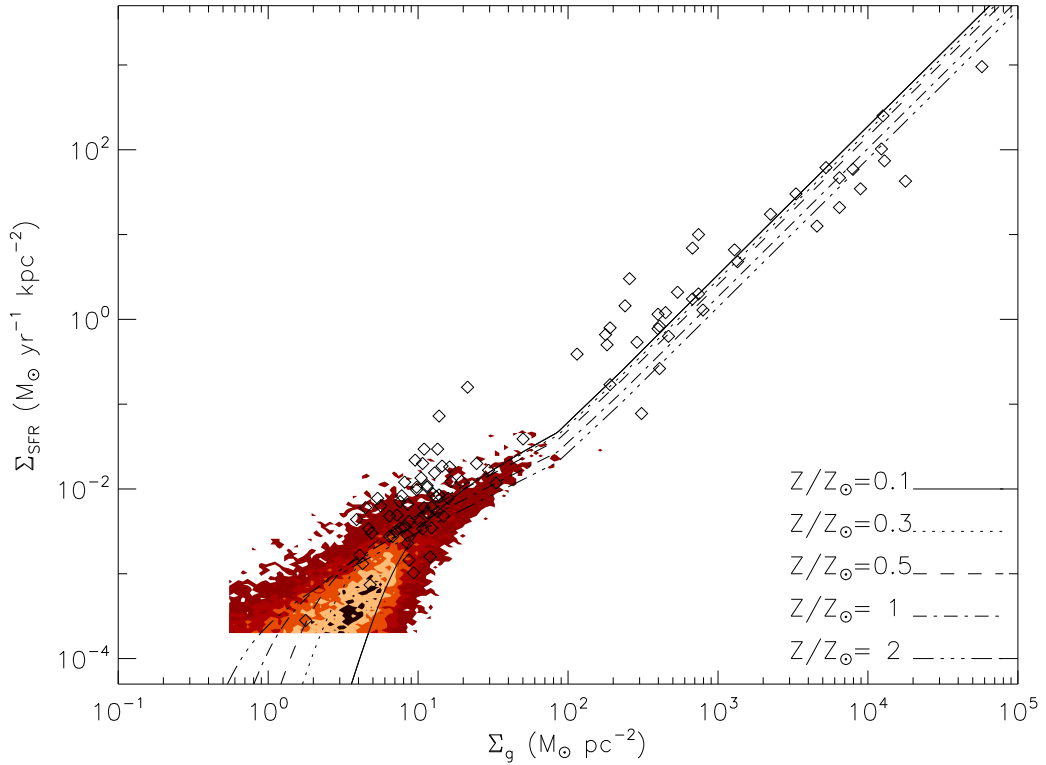


Fig. 5. Star formation laws in the feedback-regulated star formation model. Overplotted to the models are the normal and starburst galaxies data of Kennicutt (1998) and the combined sub-kpc data (4478 subregions) for 11 nearby galaxies from Bigiel et al. (2008,2010). The Bigiel et al. data is shown in the form of a 2D histogram with the colour coding corresponding, from the lighter to the darker colours to the 1,5,10,20, and 30 contour levels. The displayed theoretical models cover the metallicity range $Z' = Z/Z_{\odot} = [0.1, 2]$.

4 Conclusions

We have presented a model for star formation in protocluster clumps of different metallicities. The model describes the co-evolution of the dense core mass function and of the IMF in the clumps. Cores form uniformly over time in the clumps following a prescribed core formation efficiency per unit time. Cores contract over timescales which are a few times their free fall time before they collapse to form stars. Feedback from the newly formed OB stars ($> 5 M_{\odot}$) is taken into account and when the ratio of the cumulated effective kinetic energy of the winds to the gravitational energy of the system (left over gas+stars) reaches unity, gas is expelled from the clump and further core and star formation are quenched. The radiation driven winds of OB stars are metallicity dependent. Metal rich OB stars inject larger amount of energy into the clump than their low metallicity counterparts and thus help expel the gas on shorter timescales. This results in reduced final star formation efficiencies in metal rich clumps in comparison to their low metallicity counterparts. Both the final star formation efficiency and the gas expulsion timescales are combined for a grid of clump models with different masses and metallicities in order to calculate the star formation efficiency per unit time ($f_{*,ff}$) in this feedback regulated model of star formation. We calculate the characteristic value of $f_{*,ff}$ for a clump mass distribution associated with a gas surface density, Σ_g . This is combined with a description of the molecular mass fraction as a function of Σ_g and the assumption that there is a critical surface gas density ($\Sigma_g = 85 M_{\odot} \text{ pc}^{-2}$) above which the protocluster clumps and their parent giant molecular clouds switch from being pressurised from within by stellar feedback to being confined by the external interstellar medium pressure. The combination of these three elements allows us to construct the star formation laws in galaxies going from low gas surface densities up to the starburst regime. Our models exhibit a dependence on metallicity over the entire range of considered gas surface densities and fits remarkably well the observational data of Bigiel et al. (2008,2010) and Kennicutt (1998). This dependence on metallicity of the KS relation may well explain the scatter (or part of it) that is seen in the observationally derived relations.

I would like to thank the organizers of the workshop *Stellar and Interstellar physics for the modelling of the Galaxy and its components* for the opportunity to speak, and would like to acknowledge the generous financial support from the SF2A. S.D. and S.M. acknowledge the support provided by STFC grant ST/H00307X/1.

References

- Bigiel, F., Leroy, A., Walter, F. et al. 2008, *AJ*, 136, 2846
- Bigiel, F., Leroy, A., Walter, F. et al. 2010, *AJ*, 140, 1194
- Blanc, G. A., Heiderman, A., Gebhardt, K., Evans, N. J. II, & Adams, J. 2009, *ApJ*, 704, 842
- Boissier, S., Prantzos, N., Boselli, A., & Gavazzi, A. 2003, *MNRAS*, 346, 1215
- Bolatto, A. D., Leroy, A. K., Jameson, K. et al. 2011, *ApJ*, accepted, (arXiv:1107.1717)
- Boquien, M., Lisenfeld, U., Duc, P.-A. et al. 2011, *A&A*, 533, 19
- Braun, H., & Schmidt, W. 2011, *MNRAS*, submitted, (arXiv:1104.5582)
- Dib, S., Kim, J., & Shadmehri, M. 2007, *MNRAS*, 381, L40
- Dib, S., Brandenburg, A., Kim, J., Gopinathan, M., & André, P. 2008, *ApJ*, 678, L105
- Dib, S., Hennebelle, P., Pineda, J. E., Csengeri, T., Bontemps, S., Audit, E., & Goodman, A. A. 2010a, *ApJ*, 723, 425
- Dib, S., Shadmehri, M., Padoan, P., Maheswar, G., Ojha, D. K., & Khajenabi, F. 2010b, *MNRAS*, 405, 401
- Dib, S., Piau, L., Mohanty, S., & Braine, J. 2011, *MNRAS*, 415, 3439
- Dib, S. 2011a, *ApJ*, 737, L20
- Dib, S. 2011b, in *Stellar Clusters and Associations- A RIA workshop on GAIA*, (arXiv:1107.0886)
- Feldmann, R., Gnedin, N. Y., & Kravtsov, A. V. 2011, *ApJ*, 732, 115
- Fuchs, B., Jahrreiß, H., & Flynn, C. 2009, 137, 266
- Gnedin, N. Y., & Kravtsov, A. V. 2011, *ApJ*, 728, 88
- Heiner, J. S., Allen, R. J., & van der Kruit 2010, *ApJ*, 719, 1244
- Kennicutt, R. C. Jr. 1989, *ApJ*, 344, 685
- Kennicutt, R. C. Jr. 1998, *ApJ*, 498, 541
- Kim, C.-G., Kim, W.-T., Ostriker, E. C. 2011, *ApJ*, accepted, (arXiv:1109.0028)
- Krumholz, M. R. & McKee, C. F. 2005, *ApJ*, 630, 250
- Krumholz, M. R., & Thompson, T. A. 2007, *ApJ*, 669, 289
- Krumholz, M. R., McKee, C. F., & Tumlinson, J. 2009, *ApJ*, 699, 850
- Krumholz, M. R., McKee, C. F., & Tumlinson, J. 2009, *ApJ*, 693, 216
- Leitherer, C., Robert, C., & Drissen, L. 1992, *ApJ*, 401, 596
- Monaco, P., Murante, G., Borgani, S., & Dolag, K. 2011, *MNRAS*, accepted, (arXiv:1109.0484)
- Narayanan, D., Cox, T. J., Hayward, C. C., Hernquist, L. 2011, *MNRAS*, 412, 287
- Onodera, S., Kuno, N., Tosaki, T. et al. 2010, *ApJ*, 722, 127
- Padoan, P., & Nordlund, Å. 2002, *ApJ*, 576, 870
- Padoan, P., & Nordlund, Å. 2011, *ApJ*, 730, 40
- Papadopoulos, P. P. & Pelupessy, F. I. 2010, *ApJ*, 717, 1037
- Piau, L., Kervella, P., Dib, S., & Hauschildt, P. 2011, *A&A*, 526, 100
- Schruba, A., Leroy, A. K., Walter, F. et al. 2011, *AJ*, 142, 37
- Silk, J., & Norman, C. 2009, *ApJ*, 700, 262
- Tabatabaei, F. & Berkhuijsen, E. M. 2010, *A&A*, 517, 77
- Tutukov, A. V. 2006, *ARep*, 50, 526
- Vink, J. S., de Koter, A., & Lamers, H. J. G. L. M. 2001, *A&A*, 369, 574
- Vollmer, B., & Leroy, A. K. 2011, *AJ*, 141, 24
- Wong, T. & Blitz, L. 2002, *ApJ*, 569, 157

COLLISION RATES AND THE DETERMINATION OF ATMOSPHERIC PARAMETERS

A. Spielfiedel¹, N. Feautrier¹, M. Guitou² and A. K. Belyaev^{1,3}

Abstract. Non-LTE modelisation of stellar atmospheres requires an accurate knowledge of collisional rate coefficients (mainly with H atoms) that compete with radiative rates to populate the atomic levels. In the framework of the SAM-GAIA project, we carry out, with colleagues from Uppsala, St. Petersburg and Nice, an interdisciplinary work combining quantum chemistry, collision physics and astrophysical modeling. Present studies concern collisional excitation of Mg and O by H-atoms. In the particular case of Mg, 15 electronic states of the MgH molecule as well as the associated couplings that mix the states during the collision were calculated. The resulting cross sections and rate coefficients point out the sensitivity of the results with the quantum chemistry data. Our detailed calculations show that the usual approximate formulae (Drawin, Kaulakys) lead to errors by factors up to 10^6 . Consequences on atmospheric parameters are analyzed.

Keywords: atomic data, line: formation, stars: abundances

1 Introduction

Non-LTE modeling implies a competition between radiative and collisional processes. The radiative data are well known thanks to the Opacity and the Iron projects. The influence of inelastic hydrogen atom collisions dominant in cold atmospheres on non-LTE spectral line formation has been, and remains to be, a significant source of uncertainty for stellar abundance analyses, due to the difficulty in obtaining accurate data for such low-energy collisions, either experimentally or theoretically. For lack of a better alternative, the classical so-called Drawin formula is often used. The question is: does the Drawin formula provide reasonable estimates of this process? After a brief presentation of the different steps used to obtain accurate quantum calculations for collisions with H atoms (Section 2), the comparison with the approximate formulae is made in section 3. Finally, preliminary conclusions on stellar abundance determination are drawn.

2 Quantum mechanical calculations

There are two steps to compute collisional rate coefficients : the first one is the calculation of the interaction potentials between the studied atom and H atom and the determination of the couplings between these potentials which allow collisional transitions. This concerns quantum chemistry, and the main difficulty is to build large basis sets adapted to the study of high excited states : it is a real challenge for quantum chemistry. Dynamics using these molecular data constitutes the second step. Accurate collisional cross sections and rate coefficients are obtained using the quantum close-coupling approach. In order to account for the so-called electron translation effect, the coupled-channel equations are solved by means of the reprojecion method (Belyaev 2010). Calculations were recently done for Li (Belyaev & Barklem 2003) and Na (Belyaev et al. 2010). Mg-H collisions and molecular interactions between O and H atoms are under study. Future work will be devoted to study H-collisions for atomic Ca, Ca^+ ion and possibly iron.

When the two colliding atoms come close together, they form temporarily a molecule whose electronic symmetry

¹ LERMA, Paris Observatory, 92195 Meudon

² MSME, Paris-Est University, 77454 Marne-la-Vallée

³ Department of Theoretical Physics, Herzen University, 191186 St Petersburg, Russia

and spin multiplicity depend on the electronic states of the two partners. In the case of magnesium we have considered all states up to the 1D and now 3D states. This gives more than twenty molecular states to be calculated. Fig. 1 displays the corresponding $^2\Sigma^+$ potentials as function of the internuclear distance R . The more interesting aspect for these potentials is the existence for the $^2\Sigma^+$ states of a strong mixing with the Mg^+-H^- ionic state. This leads to an ion-pair production channel for Mg in collision with H atoms and to the reverse reaction. For the Π and Δ states, no such perturbation occurs. This perturbation may lead to large coupling terms among the $^2\Sigma^+$ states, mainly at large R distances between high excited states (Guitou et al. 2010). So large cross sections and rate coefficients between Mg excited states are expected (Guitou et al. 2011), as well as Mg^+ formation through ion-pair production (Barklem et al. 2011). Preliminary results* show that the dominant rates are those between the closest final states, large rates between atomic levels of different spin symmetry and an important contribution of ion-pair production are found.

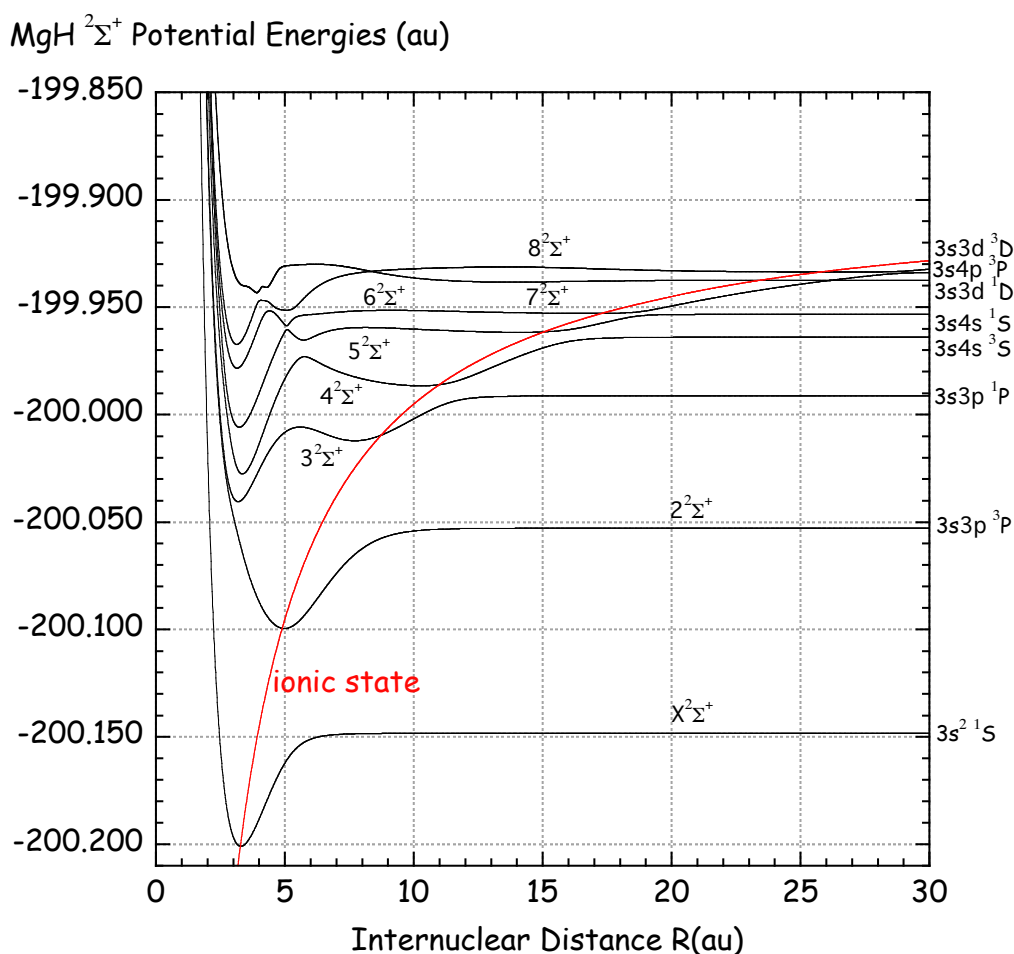


Fig. 1. $^2\Sigma^+$ electronic states as function of the internuclear distance. In red is displayed the ionic state

3 Comparison with approximate methods

It is important to compare accurate quantum rates with the results obtained using approximate formulae: the well known Drawin (1969) formula, which is an extension of the classical formula for ionization of atoms by electron impact, and the Kaulakys (1991) formula based on the free electron model applicable to Rydberg atoms. The Drawin formula gives rates proportional to the atomic oscillator strength (and thus equal to zero for spin

*Guitou, Belyaev, Barklem, Spielfiedel, Feautrier, unpublished 2011

forbidden transitions). In Fig. 2, which concerns collisions with Na atom (Lind et al. 2011), are plotted as function of the energy difference of the levels the ratio between Drawin and Kaulakys rates (right) and Drawin and quantum rates (left). Both approximate formulae give results far from the quantum one. This is expected as the detailed physics of the interactions is not at all introduced in the two models (Barklem et al. 2011). The same trends are found for collisions between H and Li and Mg atoms. The Drawin formula overestimates the rates by several orders of magnitude (up to 10^6). This is now well known, so in some modeling works the Drawin rates are multiplied by a corrective factor S_H ($0 \leq S_H \leq 1$). Comparison with accurate quantum results shows that S_H is different for different processes.

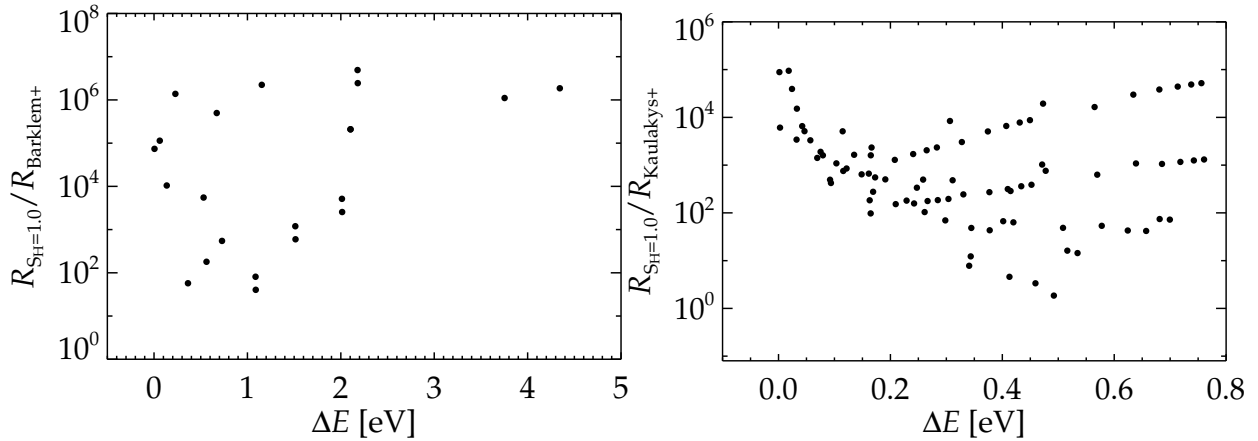


Fig. 2. Left: Drawin/quantum rates. Right: Drawin/Kaulakys rates.

4 Consequences on star atmosphere modeling

To date, no general conclusion on the effect of the new H-collisional rates seems possible as collisions compete with radiative processes for both excitation/deexcitation and ion-pair production of the species. As a consequence, the abundances depend non-linearly on many parameters: the physical conditions of the star atmosphere (temperature, gravity, metallicity), the number of atomic states included in the model, the radiative transfer and 1D or 3D modeling, the line considered for the diagnostics. However, some trends are available from recent studies on lithium, sodium, carbon and oxygen lines.

In a study relative to the Sun and to a sub giant metal-poor star, Barklem et al. (2003) show that H-collisions have a relatively small influence on the non-LTE predicted equivalent width of the resonance line for the Sun and larger effects for the metal-poor star. This is expected as collisional rate coefficients between the first atomic levels are very small and H atoms are not abundant in the Sun atmosphere. For a metal-poor star with low metallicity, the larger collisional effect is mainly due to mutual neutralisation with H^- which overpopulates the first levels. This last effect seems smaller for Na lines (Lind et al. 2011). In the absence of accurate H-collision rate coefficients for carbon and oxygen, Fabbian et al. (2006) and Fabbian et al. (2009) consider non-LTE abundance corrections using the Drawin formula with $S_H = 0$ (no collisions) and $S_H = 1$ (with H collisions). Both studies consider infra red lines, and large non-LTE effects (probably overestimated) are found for low metallicity stars.

5 Concluding remarks

H collisions play an important role for abundance determination of low metallicity stars when the diagnostics is obtained using lines between excited states. We note the importance of the 3D modeling. Preliminary results concerning lithium, sodium and magnesium show a large overestimation of the rate coefficients using the Drawin formula and the importance of ion-pair production by collisions with H atoms. These trends should be confirmed by studies on other atomic systems: work on oxygen is in progress and future work on neutral and ionized calcium is planned.

We would like to acknowledge support from French «Action Spécifique Gaia, Programme PNPS of the CNRS», the Chemical Institute of the CNRS, as well as collaboration with Paul Barklem (Uppsala, Sweden) and the SAM/GAIA team.

References

- Barklem, P., Belyaev, A., & Asplund, M. 2003, *A&A*, 409, L1
Barklem, P., Belyaev, A., Feautrier, N., et al. 2011, *A&A*, 530, A94
Belyaev, A. 2010, *Phys. Rev. A*, 82, 060701(R)
Belyaev, A. & Barklem, P. 2003, *Phys. Rev. A*, 68, 062703
Belyaev, A., Barklem, P., Dickinson, A., & Gadéa, F. 2010, *Phys. Rev. A*, 81, 032706
Drawin, H. 1969, *Zeitschrift fur Physik*, 225, 483
Fabbian, D., Asplund, M., Barklem, P., Carlsson, M., & Kiselman, D. 2009, *A&A*, 500, 1221
Fabbian, D., Asplund, M., Carlsson, M., & Kiselman, D. 2006, *A&A*, 458, 899
Guitou, M., Belyaev, A., Barklem, P., Spielfiedel, A., & Feautrier, N. 2011, *J. Phys. B*, 44, 035202
Guitou, M., Spielfiedel, A., & Feautrier, N. 2010, *Chem. Phys. Letters*, 488, 145
Kaulakys, B. 1991, *J. Phys. B*, 24, L127
Lind, K., Asplund, M., Barklem, P., & Belyaev, A. 2011, *A&A*, 528, A103

KINEMATIC IMPRINTS FROM THE BAR AND SPIRAL STRUCTURES IN THE GALACTIC DISK

F. Figueras¹, T. Antoja², O. Valenzuela³, M. Romero-Gómez¹, B. Pichardo³ and E. Moreno³

Abstract. At 140 years of the discovery of the moving groups, these stellar streams are emerging as powerful tools to constrain the models for the spiral arms and the Galactic bar in the Gaia era. From the kinematic-age-metallicity analysis in the solar neighbourhood it is now well established that some of these kinematic structures have a dynamical origin, different from the classical cluster disruption hypothesis. Test particle simulations allow us to definitively establish that these local structures can be created by the dynamical resonances of material spiral arms and not exclusively by the Galactic bar. First studies to evaluate the capabilities of the future Gaia data to detect and characterize moving groups at 2-6 kpc from the solar neighborhood are discussed.

Keywords: Galaxy: kinematics and dynamics, solar neighbourhood, spiral structure, Galactic bar

1 Introduction

In the last two decades the study of the Milky Way (MW) has experienced outstanding progress owing to the advent of high-quality observations, better models and methods, and the use of powerful computation facilities (e.g. Turon et al. 2008). In particular, the solar neighbourhood has been studied in depth thanks to the stellar positions and velocities from the Hipparcos mission and its complementary photometric and spectroscopic on-ground surveys. The rich kinematics and stellar chemical distribution in the solar neighbourhood may constitute a set of imprints and fossils left after several Galactic processes. The observations have revealed very interesting properties, one of the most intriguing features being what now is usually called moving groups (MG). These are stellar streams, gravitationally unbound, occupying extended regions of the Galaxy which are seen as overdensities in the velocity space. At present, the origin of these kinematic structures is far from being completely understood although it is more than 140 years since they were discovered (see Antoja et al. 2010a, for a historical review).

Several scenarios to understand their origin and evolution have been proposed since then: 1) cluster and star complex disruption; 2) orbital and resonant effects of the non-axisymmetric structure of the MW (spiral arms and bar): periodic orbits, chaos, precession of periodic orbits, transient spiral structure; 3) tidal debris of past accretion events and, 4) external dynamical effects on the disk resulting from interaction events. A combination of some of these options becomes a complex but fascinating scenario. Here we will comment on the work our team has been undertaken in the last five years, that is, the characterization of what we observe in the solar neighbourhood, how test particle simulations show that MGs can be induced by the MW bar and spiral arms and how the Gaia satellite* will see them in the next decade.

2 What we observe

In Antoja et al. (2008) we applied the Wavelet Denoising technique to an extensive compendium of stars – more than 24000 – in the solar neighbourhood to characterize MGs in the U-V-age-[Fe/H] space. We confirm that the

¹ Dept. d'Astronomia i Meteorologia & Institut de Ciències del Cosmos, Universitat de Barcelona, Martí i Franquès 1, E-08028 Barcelona, Spain.

² Kapteyn Astronomical Institute, University of Groningen, PO Box 800, 9700 AV Groningen, the Netherlands.

³ Instituto de Astronomía, Universidad Nacional Autónoma de México, A.P. 70-264, 04510, México, D.F., México

*<http://sci.esa.int/science-e/www/area/index.cfm?fareaid=26>

dominant kinematic structures in the U-V plane are the branches of Sirius, Coma Berenices, Hyades-Pleiades and Hercules. They all present a negative slope of $\sim 16^\circ$ in the U-V plane. These branches are present in all spatial regions studied and, although our data was well constrained to the solar neighbourhood, we detected for the first time a slight dependence of the kinematic branches on Galactic position. These studies is being now taken up again with a much more extended sample around the Sun using the recently published 3th release of RAVE radial velocity survey (Antoja et al., in prep.).

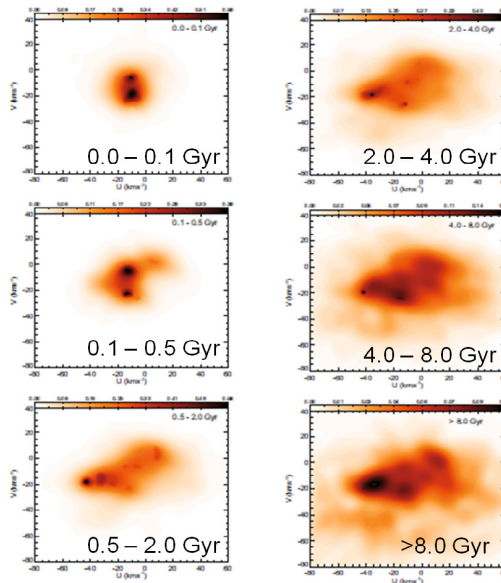


Fig. 1. Velocity distribution for different ages groups. See Antoja et al. (2008) for catalogue compilation.

From the Geneva Copenhagen Survey it is now well established that these kinematic branches have an extended age distribution (see Fig. 1). Even more, very promising recent spectroscopic studies have revealed that most groups are chemically inhomogeneous (Arcturus (Williams et al. 2009); Hercules (Bensby et al. 2007), among others). It is reasonable to think that the four scenarios mentioned above for the origin of MGs can coexist in the solar neighbourhood. HR1614 can be an example of a minor kinematic structure possibly originated from a cluster disruption; it has a low chemical and age scattering and, hence, it does seem to be remnant of a dispersed star-forming event (de Silva et al. 2007). But for sure, the observations available up to now show that many MGs, specially the above mentioned branches, have a large spread in ages and chemical composition indicating that, definitively, we shall rule out those models that propose that these kinematic structures are remnants of disk star clusters.

3 Moving groups induced by MW bar and spiral arms

We have performed numerical integrations of test particle orbits on the Galactic plane (2D), adopting the potential described in Antoja et al. (2011). There we have shown that studies with only spiral arms or only the bar are a valid way to understand the effects of each component in the velocity distribution, and eventually they could be used to constrain the characteristics of the bar and spiral arms.

3.1 Imprints from the Galactic bar

In Antoja et al. (2009) we show how the Galactic prolate bar (Pichardo et al. 2003), with a realistic orientation and density profile, triggers the already known bimodality in the velocity distribution (Kalnajs 1991). This is caused by a thin region of irregular orbits that are probably related to the bar 2:1 OLR. The central node of the bimodality is distorted through positive U. This distortion could be associated with the new observed group found at $(U, V) = (35, -20)$ km/s and with the elongation of the Coma Berenices branch. We also propose that the low angular momentum MGs, including Arcturus, could have two distinct viable origins related to the bar acting on a relatively hot stellar disk: 1) the dynamics of the bar could have a strong influence on the transient

kinematic groups at low angular momentum that are products of the ongoing phase mixing in an un-relaxed disk or 2) the bar also creates kinematic structures at low angular momentum that may be associated entirely with its induced resonant effects on the U-V plane. Bar resonances 3:1, 4:1 and 5:1 could be responsible for these kinematic groups at low angular momentum.

3.2 Imprints from the spiral arms

In Antoja et al. (2011) we studied the spiral arm influence on the solar neighbourhood stellar kinematics. We have seen that the spiral arms induce strong kinematic imprints in the solar neighbourhood for pattern speeds $\Omega_p \sim 15 - 19 \text{ km/s/kpc}$, close to the 4:1 inner resonance (see Fig. 2). No substructure is induced close to corotation or higher order resonances ($m > 6$) which, in the solar neighbourhood, corresponds to pattern speeds of $20 - 30 \text{ km/s/kpc}$.

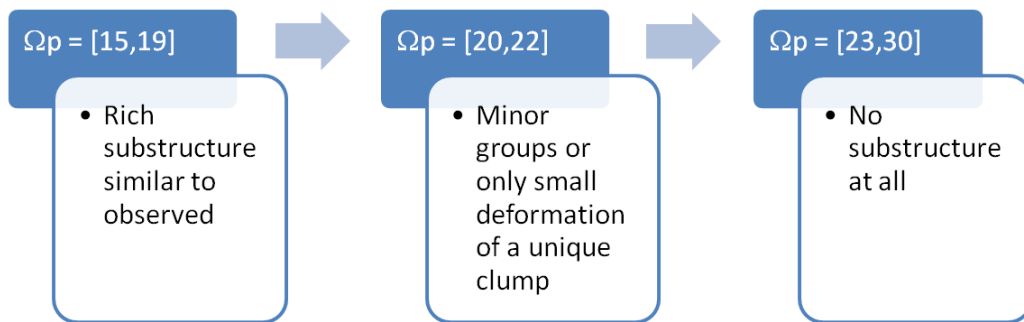


Fig. 2. Scheme of the relation between the MW pattern speed of the spiral arms and the existence of kinematic substructure in the solar neighbourhood.

We have observed that the velocity distribution is less sensitive to the relative spiral phase. More than 2 kpc in galactocentric azimuth are needed to detect a significant change in the velocity space. The strongest effects are detected near the arms. The effects of spiral arm density contrast has been also investigated. We observe that a higher density contrast increases the dispersion but maintains the geometry of the kinematic substructure, so concluding that the strength of the MW spiral pattern will be a parameter difficult to constrain using MGs.

4 Future Gaia capabilities

We can identify several scientific challenges for the coming years as far as MGs are concerned. A combination of chemical tagging, improved large-scale Galactic dynamics studies and cosmological simulations applied to the MW are required in order to disentangle the origin of the kinematic structures in the Galactic disk. New theoretical and observational strategies to approach the problem are needed in preparation for the upcoming Gaia and complementary surveys. A first attempt to evaluate how far Gaia will go in providing precise 3D velocity distributions was presented in Antoja et al. (2010b). We analyzed two regions, the Scutum Centaurus tangency $(l, b) = (305^\circ, 0^\circ)$ at $\sim 7 \text{ kpc}$ and the Perseus arm at the anticenter direction, at $\sim 2 \text{ kpc}$. Working in the space of the observables we confirm that the unprecedented Gaia accuracy in proper motions will allow to clearly identify the rich kinematic substructure in the Perseus arm at $\sim 2 \text{ kpc}$ from the Sun. That is Gaia errors hardly change or hide the kinematic structure obtained from our test particle simulations in this region. Concerning the detection of kinematic substructure in the Scutum Centaurus tangency, K giants in this far region will have a relative error in Gaia parallax of $\sim 60\%$, therefore IR photometric distances will be required. Looking again in the observable plane of radial velocities and proper motions, we checked that errors in radial velocity not larger than $2 - 3 \text{ km/s}$ are needed to detect the rich resonant kinematic structure in this region. The study of the phase space in those regions is critical to understand the kinematic behaviour and nature of the spiral pattern.

5 Conclusions

Our analysis of the observational sample and the test particle simulations indicates that it is very feasible that some of the MGs observed in the solar neighbourhood have a dynamical origin related with the effects induced by the spiral arms and the bar. However, several improvements are needed in order to definitively characterize the chemistry and the evolutionary state of the different kinematic groups. This is a statistical study which requires a large number of stars with accurate ages and chemical composition. Data from Multi-Object Spectrographs currently available and/or in preparation are promising for the analysis of chemical inhomogeneities in the kinematic groups. More complex is the derivation of accurate stellar ages, where large errors are present. Future Gaia data will require complementary age determinations from new tools like asteroseismology (Poretti et al. 2011) or stellar chronology with white dwarfs in wide binary systems (Garces et al. 2012), among others.

From our test particle studies we can confirm that MW spiral arms in the range of the observed spiral arms parameters favour the triggering of kinematics groups such as the ones observed in the solar neighbourhood. But can we at present constrain the spiral arms using the MGs? Our analysis demonstrates that groups such as the observed ones in the solar vicinity can be reproduced by different combinations of parameters, i.e. a degeneracy is present. Thus, data from velocity distributions at larger distances are needed for a definitive constraint. Work is in progress to map the evolution of these MGs at large scale on the Galactic disk both from test particle and N-body simulations.

Preliminary analysis of Gaia capabilities confirm that the stellar streams are emerging as powerful tools to constrain the models for the spiral arms and the Galactic bar in the Gaia era. It is mandatory to analyze carefully our modelled velocity distributions at large scale in the Galactic disk so as to find strategic places where the kinematic structures are particularly rich to discriminate among models and to constrain the spiral arm and the Galactic bar parameter space.

We acknowledge funding support from MICINN (Spanish Ministry of Science and Innovation) - FEDER through grant AYA2009-14648-C02-01 and CONSOLIDER CSD2007-00050, the European Research Council under ERC-StG grant GALACTICA-24027, Some of the simulations were run at the HP CP 4000 cluster (KanBalam) in the DGSCA/UNAM.

References

- Antoja, T., Figueras, F., Fernández, D., Torra, J., 2008, *A&A*, 490, 135
- Antoja, T., Valenzuela, O., Pichardo, B., Moreno, E., Figueras, F., Fernández, D., 2009, *ApJ*, 700, L78
- Antoja, T., Figueras, F., Torra, J., Valenzuela, O., Pichardo, B., 2010, *LNEA*, 4, 13
- Antoja, T., Figueras, F., Monguió, M., 2011, *EAS*, 45, 309
- Antoja, T., Figueras, F., Valenzuela, O. et al. 2011, *MNRAS*, arXiv:1106.1170
- Antoja, T., 2011, in “Kinematic groups across the MW disk: insights from models and from the RAVE catalogue” , proceedings of *Assembling the Puzzle of the Milky Way*, Editors: Céline Reylé, Annie Robin and Mathias Schultheis, *European Physical Journal*.
- Bensby, T., Oey, M. S., Feltzing, S., Gustafsson, B., 2007, *ApJ*, 655, L89
- De Silva, G. M., Freeman, K. C., Bland-Hawthorn, J., Asplund, M., Bessell, M. S., *AJ*, 133, 694
- Garces, A., Catalán, S., Ribas, I. <http://xxx.unizar.es/abs/1105.0287>
- Kalnajis, A.J., 1991, *Dynamics of Disk Galaxies*, ed. B. Sundelius, 323
- Pichardo, B., Martos, M., Moreno, E., Espresate, J., 2003, *ApJ*, 582, 230
- Poretti et al., 2011, <http://xxx.unizar.es/abs/1102.3085>
- Turon, C., Primas, F., Binney, J., et al., 2008, Report N. 4, ESA-ESO working Group, *Galactic Populations, Chemistry and Dynamics* vii, 3
- Williams, M. E. K., Freeman, K. C., Helmi, A., the RAVE collaboration, 2009, in “The Arcturus Moving Group: Its Place in the Galaxy” *The Galaxy Disk in Cosmological Context*, Proceedings of the International Astronomical Union, IAU Symposium, Volume 254. Edited by J. Andersen, J. Bland-Hawthorn, and B. Nordström, p. 139-144

DUST MASS IN SIMULATIONS OF GALAXIES

N. Gaudin¹ and H. Wozniak¹

Abstract. We have designed a model to compute dust abundances in chemodynamical N-body+SPH simulations. It includes the production by Asymptotic Giant Branch (AGB) stars, supernovae (SNe, type I and II), the destruction by shock induced by SNe and the growth of dust grains in the interstellar medium (ISM). The model takes advantage of the self-consistent chemodynamical code to compute the evolution of the dust mass: the two ISM phases, evolving stellar populations, and metal enrichment. We show that our model is able to reproduce the abundances of dust and its linear relation with the metallicity of the ISM, provided all dust processes are included. Moreover, some low-metallicity galaxies that are under-abundant in dust could be explained by our simulations as being dominated by the dust destruction in SNe shocks.

Keywords: dust, galaxies: evolution, methods: numerical

1 Introduction

Despite its low mass fraction the dust provides powerful clues for the chemical and physical description of the ISM (Savage & Sembach 1996; Jenkins 2009), and recently for constraining galactic evolution (Dwek et al. 2011).

To understand the life-cycle of dust in ISM, semi-analytic models of galactic evolution have been extensively used (Lisenfeld & Ferrara 1998; Tielens 1998; Hirashita et al. 2002; Morgan & Edmunds 2003; Zhukovska et al. 2008; Dwek & Cherchneff 2011). We present hereafter a model for dust production and destruction mechanisms, specially designed for self-consistent chemodynamical simulations of galaxies. The results obtained in simulation of a massive galaxy are discussed in section 3.

2 The Model

The evolution of a galaxy is simulated using PM+SPH code described in Michel-Dansac & Wozniak (2004). Wozniak et al. (2011) have updated the star formation recipes and the chemical evolution to take the stellar population evolution as well as the multiphase nature of the ISM into account. The new chemodynamical prescription includes star formation based on the local Jeans instability. Stellar populations have various metallicities and evolve over ~ 10 Gyr injecting energy and gas into ISM. The ISM has two gaseous phases. One represents the cold neutral medium with a fixed temperature (10^2 K). The second has a variable temperature ranging from 10^2 to 10^8 K, determined by solving the energy equilibrium. The cooling function is metallicity dependent. Heating from stars is also included. Phases exchange mass by condensation and evaporation mechanisms.

Our model (see Fig. 1, left) computes the dust mass with recipes adapted from semi-analytic models. The main difference is the local nature of our model. Indeed, contrary to the global galactic computation of semi-analytic models, our recipes computes dust mass for each SPH particles having a resolution varying from 10 pc (in the nucleus) to 1 kpc (in the outskirts). All assumptions of classical semi-analytic models of dust evolution have been adapted to the local conditions in simulations. A second difference comes from the physically motivated distinction of two ISM phases (the cold and the warm/hot). Our model takes advantage of this, providing dust mass separately for both phases.

We have performed simulations with different combinations of three basic processes: the production of dust by stars, the accretion in interstellar medium, and the destruction by SNe. The “stardust” is mainly produced by

¹ Observatoire Astronomique de Strasbourg, 11 rue de l’Université, 67000 Strasbourg, France

AGB stars and SNe (Cherchneff & Dwek 2010; Morgan & Edmunds 2003), we make use of data from Zhukovska et al. (2008) with metallicity dependent populations of stars, injecting dust in the two phases of our ISM as proportional to their respective volume. The production by growth of grains in ISM must be included to balance the low lifetime of dust (Draine et al. 2007). In our simulations, it is activated in cold phase above a threshold density of $n_{\text{H}} = 10^4 \text{ cm}^{-3}$. Our accretion recipe uses a simple assumption based on the collision rate between grains and particles of the gaseous phase, leading to:

$$\rho_d(t) = \frac{\rho_d(0)}{(1 - \rho_d(0)/\rho_M) e^{-t/\tau} + \rho_d(0)/\rho_M}, \quad (2.1)$$

where ρ_d is the local density of the dust component, ρ_M its maximal density which is the density of the accreting metal C, O, Mg, Si, Fe (Savage & Sembach 1996; Draine et al. 2007), and τ^{-1} the rate of accretion (proportional to the accreting metal density too). The destruction of dust occurs mainly in shocks produced by SNe. We use the destruction efficiency computed by Jones et al. (1994, 1996) and the shocked mass from Hirashita et al. (2002), to get a formula of destroyed mass of dust, proportional to the energy released by the SNe.

3 Discussion

We have performed four simulations with various combinations of active processes. The global evolution of simulations is plotted in Fig. 1 (right). Our simulations agree well with the observations from Lisenfeld & Ferrara (1998), Draine et al. (2007), and Engelbracht et al. (2008). The trend for the simulations, apart from the simulation with stardust and destruction only, is linear as predicted by the expected relation:

$$\frac{M_{\text{dust}}}{M_{\text{H}}} \approx 0.01 \frac{(O/H)}{(O/H)_{\text{MW}}}, \quad (3.1)$$

scaled from local Milky-Way models (see Draine et al. 2007). If destruction is activated and accretion is not, we obtain lower dust abundances conforming with the low-metallicity galaxies which are dust under-abundant.

We have shown that only the simulation which includes all the three creation and destruction mechanisms is able to reproduce the observed dust mass ratio as a function of metallicity (see Fig. 2). Especially, because of the lack of free parameters for destruction, we need to include accretion to obtain a reasonable mass of dust when the destruction process is activated. Moreover, it is noteworthy that the destruction has a visible effect in low metallicity region of our simulation with the full dust physics. This dust fraction, lower than that predicted by the linear relation, suggests that low-metallicity irregular dwarves could be dominated by the dust destruction. This will be checked by full self-consistent simulations of dwarf galaxies.

References

- Cherchneff, I. & Dwek, E. 2010, *ApJ*, 713, 1
 Draine, B. T., Dale, D. A., Bendo, G., et al. 2007, *ApJ*, 663, 866
 Dwek, E. & Cherchneff, I. 2011, *ApJ*, 727, 63
 Dwek, E., Staguhn, J. G., Arendt, R. G., et al. 2011, *ApJ*, 738, 36
 Engelbracht, C. W., Rieke, G. H., Gordon, K. D., et al. 2008, *ApJ*, 678, 804
 Hirashita, H., Tajiri, Y. Y., & Kamaya, H. 2002, *A&A*, 388, 439
 Jenkins, E. B. 2009, *ApJ*, 700, 1299
 Jones, A. P., Tielens, A. G. G. M., & Hollenbach, D. J. 1996, *ApJ*, 469, 740
 Jones, A. P., Tielens, A. G. G. M., Hollenbach, D. J., & McKee, C. F. 1994, *ApJ*, 433, 797
 Lisenfeld, U. & Ferrara, A. 1998, *ApJ*, 496, 145
 Michel-Dansac, L. & Wozniak, H. 2004, *A&A*, 421, 863
 Morgan, H. L. & Edmunds, M. G. 2003, *MNRAS*, 343, 427
 Savage, B. D. & Sembach, K. R. 1996, *ARA&A*, 34, 279
 Tielens, A. G. G. M. 1998, *ApJ*, 499, 267
 Wozniak, H., Champavert, N., & Feldner, H. 2011, in *EAS Publications Series*, Vol. 44, *EAS Publications Series*, ed. H. Wozniak & G. Hensler, 41–42
 Zhukovska, S., Gail, H.-P., & Trieloff, M. 2008, *A&A*, 479, 453

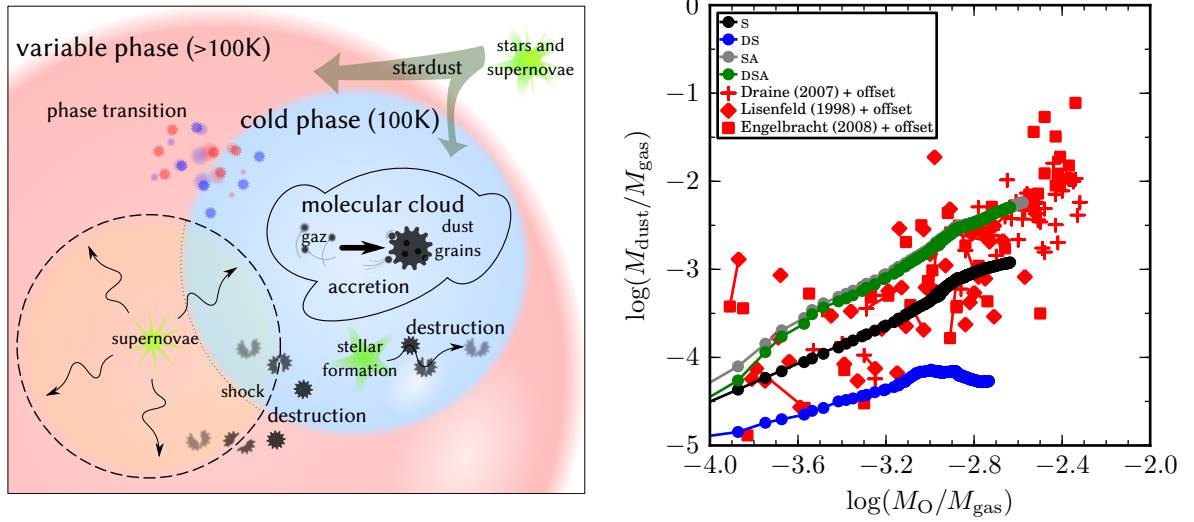


Fig. 1. Left: Sketch of physical processes involved to compute the evolution of the dust mass. **Right:** Evolution of our 4 simulations, snapshots every ~ 25 Myr. Simulations are labelled with the active processes: S for stardust, D for destruction, A for accretion. Data from observations (Lisenfeld & Ferrara 1998; Draine et al. 2007; Engelbracht et al. 2008), in red, have been homogenized applying an offset.

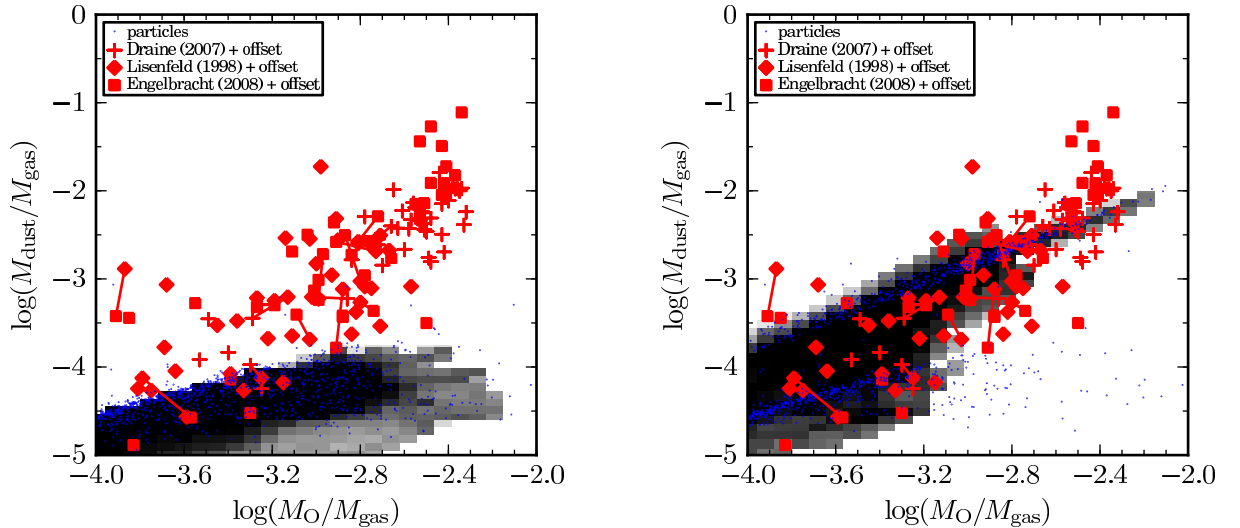


Fig. 2. 2D histograms of snapshots. **Left:** Simulation with stardust, SNe shock destruction, but without accretion. The observed dust abundance for high-metallicity galaxies is higher than the simulated value. All snapshots show similar behavior, we show here snapshot at $t = 264$ Myr. **Right:** Simulation with all the three dust processing active: destruction, stardust, and accretion. We take the snapshot at $t = 264$ Myr, few Myrs after the star formation rate maximum to have high dust destruction rate from SNe shocks.

DETERMINATION OF THE AGES OF STARS FROM THEIR POSITION IN THE HR DIAGRAM

C. Guédé¹, Y. Lebreton¹ and G. Dréan²

Abstract. The determination of stellar ages is fundamental to understand the formation and evolution of the Galaxy. We determine the age of stars by combining their position in the HR diagram with stellar evolutionary tracks or isochrones. The goal of this study is to prepare the tools that will be used to age-date stars after the Gaia mission.

Keywords: stars: fundamental parameters - methods: statistical - (stars:) Hertzsprung-Russell and C-M diagrams

1 Introduction

To understand the formation and evolution of the Galaxy it is necessary to determine the ages of its stars. There are several methods to determine the age of stars which are based on either the kinematics or expansion of stars, the lithium depletion, the gyrochronology, activity, asteroseismology or isochrones models. These methods are described by Soderblom 2010. Here we are interested in determining the ages of large samples of stars for which the method based on isochrones is applicable. The age of stars is determined by combining their position in the HR diagram and models isochrones (Ng & Bertelli 1998, Lachaume et al. 1999). We use a Bayesian estimation to determine the most probable age from stellar models (Pont & Eyer 2004, Jørgensen & Lindegren 2005 and Casagrande et al. 2011). We adapt this method to use the stellar evolutionary tracks instead of the isochrones. We compare our results to Casagrande et al. (2011) work to validate our tools. This method will be used to determine the ages of stars that will be observed by the Gaia mission.

In Section 2 we describe the Bayesian estimation and the methods that we use. In section 3 we compare the ages obtained with evolutionary tracks and with isochrones. Section 4 describes the age-mass relation and age-metallicity relation and the comparison of these relations with Casagrande et al. (2011) work.

2 Determination of ages

We determine the age of the stars from their position in the HR diagram and either stellar evolutionary tracks or isochrones. In the region of isochrones where the stars evolve very quickly (for example the turn-off) a star that we aim to date, can be adjusted by several isochrones. As an example in Fig 1 (Jørgensen & Lindegren 2005), for the star on the left there are three isochrones that adjust properly the star. Therefore, these stars have three possible ages. In this case, the question is how to choose the correct age? In order to answer this question we use a Bayesian approach: this method allows us to determine the most probable age with the *a priori* density function. The age of a star corresponds to the maximum of the *a posteriori* density function $f(T, [Fe/H], m)$, defined as

$$f(T, [Fe/H], m) \propto f_0(T, [Fe/H], m)L(T, [Fe/H], m) \quad (2.1)$$

where $f_0(T, [Fe/H], m)$ is the *a priori* density function, which depends on the Initial Mass Function, Stellar Formation Rate and initial metallicity distribution. We choose to adopt a flat stellar formation rate and a

¹ GEPI UMR 8111, Observatoire de Paris-Meudon , France

² LTSI, INSERM U642 Université de Rennes 1, France

flat initial metallicity distribution. For the initial mass function we use the same than Jørgensen & Lindegren (2005), which is defined as $\xi(m) = m^{-2.7}$ (it is based on the *IMF* of Kroupa et al. 1993). $L(T, [Fe/H], m)$ is the likelihood defined as

$$L(T, [Fe/H], m) = \left(\prod_{i=1}^n \frac{1}{(2\pi)^{\frac{1}{2}} \sigma_i} \right) \exp \left(\frac{-\chi^2}{2} \right) \quad (2.2)$$

where the χ^2 parameter is calculated for the temperature T_{eff} (or color) of the stars, the magnitude M_v (or luminosity) and the metallicity $[Fe/H]$. The σ_i are the corresponding observational errors. For the numerical implementation, we sum the *a posteriori* density function for the evolutionary track that have a metallicity measuring range between $[Fe/H]_{obs} \pm 3.5\sigma_{[Fe/H],obs}$ and for all masses. The age of the star corresponds to the maximum of the *a posteriori* density function.

The method of Jørgensen & Lindegren (2005) determines the age by using isochrones and we have adapted the program to determine the age directly from the evolutionary tracks. We compare both results in Section 3. This method is also well designed to calculate the mass of stars.

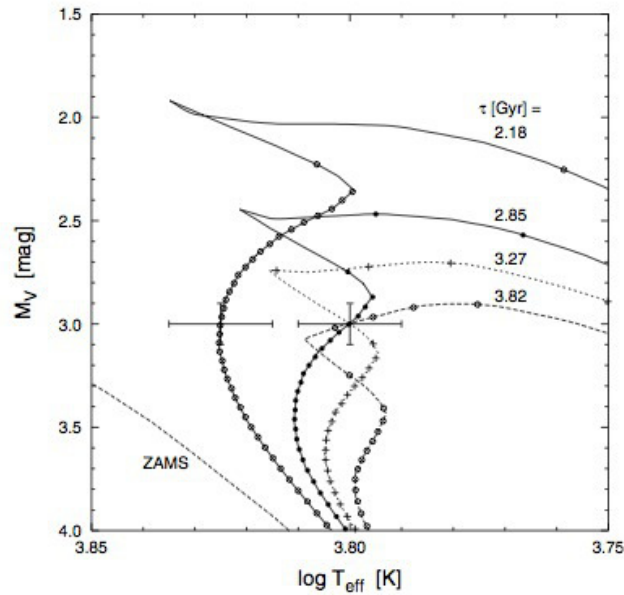


Fig. 1. Isochrones degeneracy in the HR diagram. After Jørgensen & Lindegren (2005)

3 Tracks vs. Isochrones

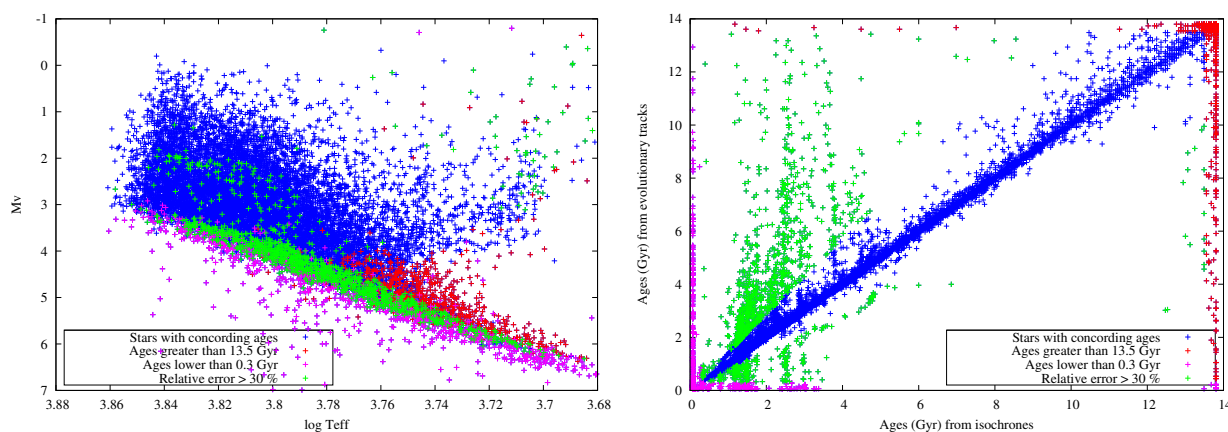
Traditionally, ages are derived from isochrones built by interpolation of stellar evolutionary tracks and provided by stellar modelers. To determine the ages we use the evolutionary tracks of Basti (Pietrinferni et al. 2004). We calculate the ages of 16 682 stars in the Geneva Copenhagen Survey of the solar neighborhood (Casagrande et al. 2011 but see also Holmberg et al. 2009). These stars are represented in a diagram $\log T_{eff} - M_v$ on the left Figure 2. We compare and classify the ages obtained with the isochrones and evolutionary tracks on the right Figure 2 and in the Table 1. We note that 72.2 % of the stars have similar ages : this shows that we have a good agreement between both methods. We note that the stars have different ages when they are located in the same region in the diagram $\log T_{eff} - M_v$, near the ZAMS. In the vicinity of the ZAMS, low mass stars evolve very slowly in the HR diagram so their age is poorly defined.

4 Age-mass relation and age-metallicity relation

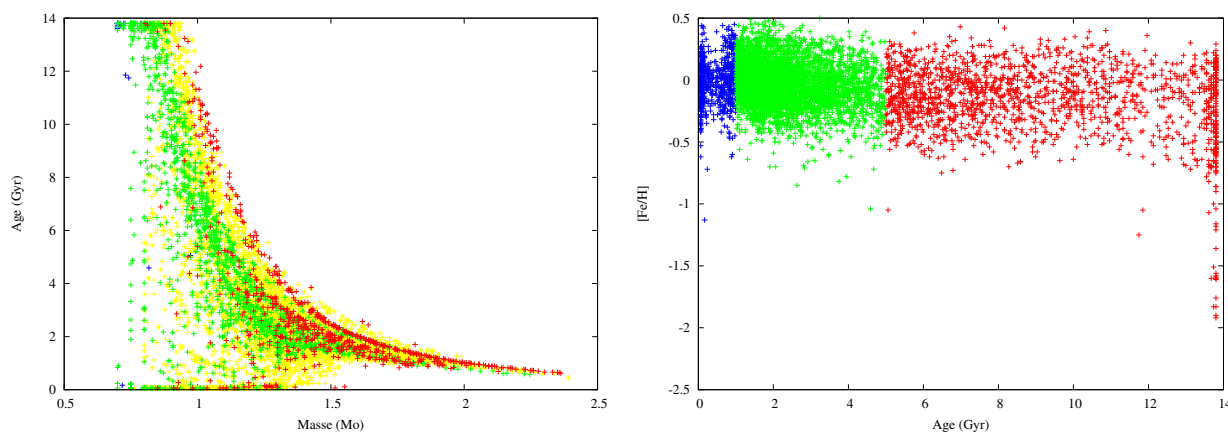
We present the age-mass relation (on the left Figure 3) and the age-metallicity relation (on the right Figure 3) with ages and masses calculated by us with the evolutionary tracks method, for 6670 stars in the GCS catalogue. We obtain a relation that is similar to Casagrande et al. (2011). For the age-metallicity relation we

Table 1. Results of the comparison for the ages obtained with the isochrones and evolutionary tracks.

Similar ages	72.2 %
Relative difference exceeding 30%	7.5 %
Ages lower than 0.3 Gyr	15.2 %
Stars with ages lower than 0.3 Gyr with both evolutionary tracks and isochrones	47 %
Ages greater than 13.5 Gyr	5.1 %
Stars with ages greater than 13.5 Gyr with both evolutionary tracks and isochrones	68 %


Fig. 2. Left Figure : HR diagram with (i) in red, stars with age > 13.5 Gyr, (ii) in pink stars with age < 0.3 Gyr, (iii) in green stars with ages differing by more than 30 % and (iv) in blue the stars having similar ages. Right Figure : comparison between ages from isochrones and ages from evolutionary tracks.

see a concentration of stars at solar metallicity and small ages: when the age increases there is a metallicity dispersion due to the radial mixing of the stars. The relation allows to demonstrate that a subsample of stars belongs to the thin disk (Haywood 2008).


Fig. 3. Left Figure: Mass-Age relation for ages and masses from the evolutionary tracks. Colors indicate increasing metallicity $[Fe/H]$ from metal-poor stars (in blue) to metal-rich stars (in red). Right Figure : Age- $[Fe/H]$ relation for ages from evolutionary tracks. In blue stars with age < 1 Gyr, in green stars with $1 \text{ Gyr} \leq \text{age} < 5$ Gyr, and in red stars with age ≥ 5 Gyr.

5 Conclusions

We adapted the method of Jørgensen & Lindegren (2005) to determine the age of stars from evolutionary tracks. The comparison of the isochrones ages with the evolutionary tracks ages shows that the results of both methods are similar except for the stars close to the ZAMS. In these regions, the stars have a low mass and they evolve very slowly, so their age is arduous to determine. The comparisons of our results with those of Casagrande et al. (2011) shows that we obtain the same trend for the age-mass and age-metallicity relations. These comparisons allow us to validate our program for age determination.

We warmly thank Misha Haywood for his advice and for discussions.

References

References

- Casagrande, L., Schönrich, R., Asplund et al. S. 2011, *A&A*, 530, A138
Haywood, M. 2008, *MNRAS*, 388, 1175
Holmberg, J., Nordström, B., & Andersen, J. 2009, *A&A*, 501, 941
Jørgensen, B. R., & Lindegren, L. 2005, *A&A*, 436, 127
Kroupa, P., Tout, C. A., & Gilmore, G. 1993, *MNRAS*, 262, 545
Lachaume, R., Dominik, C., Lanz, T., & Habing, H. J. 1999, *A&A*, 348, 897
Ng, Y. K., & Bertelli, G. 1998, *A&A*, 329, 943
Pont, F., & Eyer, L. 2004, *MNRAS*, 351, 487
Pietrinferni, A., Cassisi, S., Salaris, M. et al. 2004, *ApJ*, 612, 168
Soderblom, D. R. 2010, *ARA&A*, 48, 581

THE MILKY WAY STELLAR POPULATIONS IN CFHTLS FIELDS

M. Guittet¹, M. Haywood¹ and M. Schultheis²

Abstract. We investigate the characteristics of the thick disk in the Canada – France – Hawaii – Telescope Legacy Survey (CFHTLS) fields, complemented at bright magnitudes with Sloan Digital Sky Survey (SDSS) data. The $([\text{Fe}/\text{H}], Z)$ distributions are derived in the W1 and W3 fields, and compared with simulated maps produced using the Besançon model. It is shown that the thick disk, represented in star-count models by a distinct component, is not an adequate description of the observed $([\text{Fe}/\text{H}], Z)$ distributions in these fields.

Keywords: the Galaxy, the thick disk, $[\text{Fe}/\text{H}]$ abundance.

1 Introduction

Our knowledge of the characteristics of the thick disk remains limited in practically every aspects. Its structure on large scales ($> \text{kpc}$) is not well defined, either clumpy or smooth, and its connections with the collapsed part of the halo or the old thin disk are essentially not understood. The spectrum of possible scenarios proposed to explain its formation is still very large and really discriminant constraints are rare. The SDSS photometric survey has provided a wealth of new informations on the thick disk, see in particular Ivezić et al. (2008), Bond et al. (2010) and Lee et al. (2011). However, the data have barely been directly confronted to star-count models, and little insights have been given on how the thick disk in these models really represents the survey data. In the present work, we initiate such comparisons by comparing the Besançon model with metallicity and distance information in the W1 and W3 CFHTLS fields, and provide a brief discussion of our results.

2 Data description

Among the four fields that make the Wide Survey, W1 and W3 cover larger angular surfaces (72 and 49 square degrees) than W2 and W4 (both having 25 square degrees). They point towards higher latitudes (-61.24° and 58.39° respectively) and are consequently less affected by dust extinction, and contain a larger relative proportion of thick disk stars. We will therefore focus on W1 and W3. CFHTLS photometry starts at a substantially fainter magnitude than the SDSS, missing a large part of the thick disk. We complemented the CFHTLS catalogue at the bright end with stars from the SDSS not present in the CFHTLS fields. In the final catalogues, W1 contains $\sim 139\,000$ stars, with 16% from the SDSS, while $\sim 132\,000$ stars are found in W3 field, with 31% coming from the Sloan.

W1 and W3 are at large distances above the galactic plane. The dust extinction is very small at these latitudes. For example the Schlegel map (Schlegel et al. 1998) estimates for W1 an absorption coefficient A_v of 0.087 while Jones et al. (2011) give $A_v=0.113$. The extinction models of Arenou et al. (1992) or Hakkila et al. (1997) estimate A_v values to 0.1 and 0.054 respectively. We briefly discuss the effect of extinction on distance determination and metallicities in 4.1.

¹ GEPI, Observatoire de Paris, CNRS, Université Paris Diderot; 5 Place Jules Janssen, 92190 Meudon, France

² Observatoire de Besançon; 41 bis, avenue de l'Observatoire, 25000 Besançon, France

3 Comparisons between the Besançon model and CFHTLS/SDSS data: Hess diagrams

3.1 The Besançon model

Simulations were made using the Besançon model (Robin et al. (2003), Haywood et al. (1997), Bienayme et al. (1987)) online version. The model includes four populations: the bulge, the thin disk, the thick disk and the halo. The metallicities of the thick disk and the halo in the online version of the model (-0.78 and -1.78 dex respectively) were shifted (to -0.6 dex and -1.5 dex) to comply with more generally accepted values, and in particular with values derived from the Sloan data (see Lee et al. (2011), who shows that the thick disk have a metallicity $[\text{Fe}/\text{H}] = -0.6$ dex roughly independent of vertical distances, and (Ivezić et al. (2008), Bond et al. (2010), Sesar et al. (2011), Carollo et al. (2010) or de Jong et al. (2010) for the inner halo metallicity, estimated to be about -1.5 dex). The thick disk has a scale height of 800 pc and a local stellar density ρ_0 of 6.8 % of the local thin disk, while the stellar halo is described by a power law with a flattening and a local density of 0.6%. Simulations were made assuming photometric errors as described in the SDSS.

3.2 Hess diagrams

The distributions of CFHTLS/SDSS and model stars in the g versus $u-g$ color magnitude diagram (CMD) are shown in Fig. 1. For both diagrams, faint blue stars ($u-g \sim 0.9$, $g > 18$) are clearly discernible and correspond to the galactic halo. The concentration of stars at $g < 18$, $u-g \sim 1.1$, corresponds to disk stars and in particular thick disk stars. Because of the SDSS saturation at $g=14$ which does not allow to have a representative sample of thin disk stars, our data sample is mainly composed of thick disk and halo stars. The Besançon model shows a distinct separation between thin disk stars ($u-g \sim 1.3$, $g < 14-15$) and thick disk stars ($u-g \sim 1.1$, $15 < g < 18$) which cannot be checked with the present data.

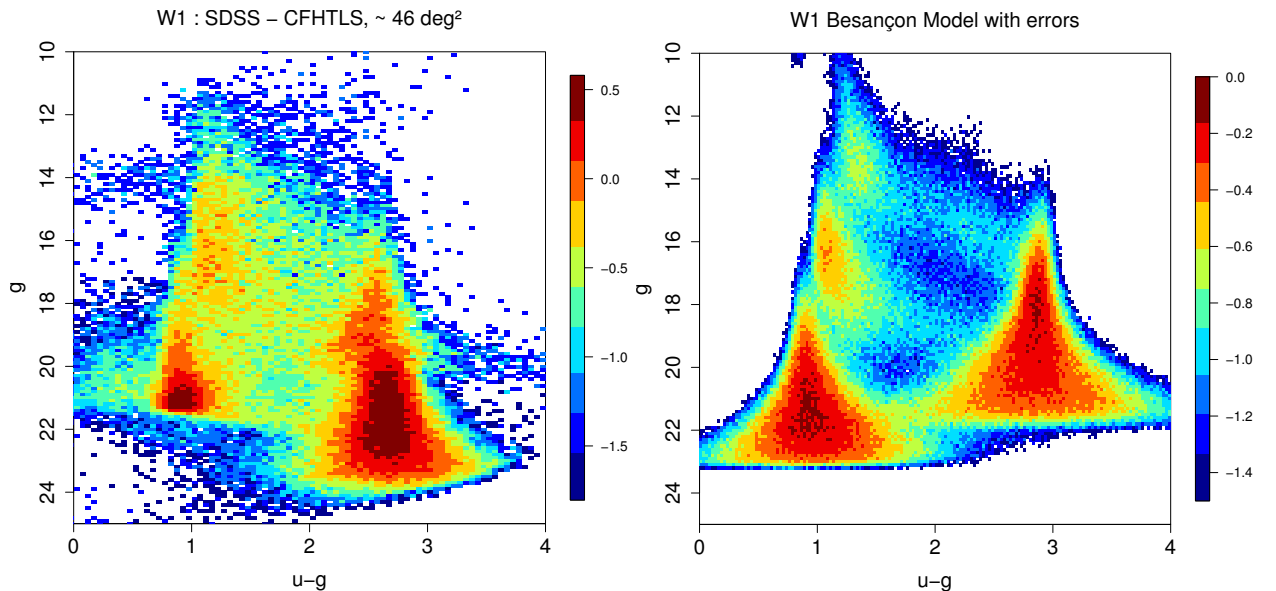


Fig. 1. Left: CFHTLS/SDSS $u-g$ Hess diagram in W1 field. **Right:** The same as the left graphic but for the Besançon model stars to which observational errors from SDSS data have been added. The successive ridge lines due to the thin disk, thick disk and the halo main sequence stars are clearly distinguishable between $0.7 < u-g < 1.5$.

4 Comparisons between the Besançon model and CFHTLS/SDSS data: ([Fe/H], Z) distributions

4.1 Metallicity and photometric distance determinations

Jurić et al. (2008) and Ivezić et al. (2008) have published calibrations of the metallicity and photometric parallax as a function of $ugri$ magnitudes. The metallicity calibration has been revised in Bond et al. (2010) :

$$[\text{Fe}/\text{H}] = A + Bx + Cy + Dxy + Ex^2 + Fy^2 + Gx^2y + Hxy^2 + Ix^3 + Jy^3 \quad (4.1)$$

where $x = u - g$, $y = g - r$ and $(A-J) = (-13.13, 14.09, 28.04, -5.51, -5.90, -58.58, 9.14, -20.61, 0.0, 58.20)$. This relation has been determined for F and G stars and is consequently applicable in the range : $0.2 < g - r < 0.6$ and $-0.25 + 0.5(u - g) < g - r < 0.05 + 0.5(u - g)$. This calibration only extends to -0.2 dex. Observed vertical distances Z have been calculated using $Z = D \sin(b)$, b being the latitude of the star. Photometric distances D , such as $m_r - M_r = 5 \log(D) - 5$, were determined using the absolute magnitude calibration of Ivezić et al. (2008) which depends on the metallicity and on $g - i$ colors.

For the highest extinction values given by Jones et al. (2011), the impact on metallicities, as can be estimated using Eq. 4.1 and the absolute magnitude relation of Ivezić et al. (2008) are at most of 0.15 dex near $g-r=0.5$ at solar metallicities and 0.1 dex at $[\text{Fe}/\text{H}] = -1$ dex. Distances will be affected at most by about 20% at solar metallicities and 15% at $[\text{Fe}/\text{H}] = -1$ dex at $g-r$ near 0.40-0.45.

4.2 ([Fe/H], Z) distributions

We generated catalogues with the model in the direction of W1 and W3, deriving the Z height above the plane from simulated distances and metallicities from the assumed metallicity distributions of each population. In Fig. 2 we present $([\text{Fe}/\text{H}], Z)$ distributions for both the data and the model. The dotted line is the median metallicity per bin of 0.5 kpc. The continuous line is the median metallicity for disk stars as shown by Bond et al. (2010) and follows rather well the disk distribution in our data. We find similar results as Bond et al. (2010) : the halo dominates the star counts above 3 kpc with a mean metallicity of about -1.5 dex. Sesar et al. (2011) studied the four CFHTLS Wide fields but with magnitudes corrected for ISM extinction. They found the mean halo metallicity in the range between -1.4 and -1.6 dex. Our estimate of the extinction effect would shift metallicities to about 0.15 dex at most, and shows that our mean halo metallicity is in good agreement with their estimates.

The interesting point worth of notice is the conspicuous, distinct, pattern that represents the thick disk in the model and which clearly is absent in the data. As expected, the standard thick disk model dominates the counts between 1 and 4 kpc, while in the data, the thick disk seems to be less extended, and does not appear as a distinct component between the thin disk and the halo. The vertical resolution of the observed distribution prevents any clear statement concerning the transition from the thin to thick disk, although it is apparent that the model is at variance with the data. This result raises the interesting question of the connections (or lack of) between the thin and thick disks. Almost since its discovery, it has been suggested that the thick disk is more akin to an extended thin disk (Norris 1987). Our knowledge of the thick disk more than twenty years later does not permit us to draw any firm conclusion on that point.

5 Conclusion

Investigation of the $([\text{Fe}/\text{H}], Z)$ distribution in the CFHTLS Wide fields does not seem to show a thick disc component as prominent and distinct as predicted by standard star-count models. The mean halo metallicity found to be -1.5 dex is in agreement with previous studies (e.g Bond et al. (2010), Sesar et al. (2011)). The behavior of models must be studied on more extensive data sets in order to assess the necessary adjustments and to better characterize the thick disk.

References

- Arenou, F., Grenon, M., & Gomez, A. 1992, *A&A*, 258, 104
 Bienayme, O., Robin, A. C., & Creze, M. 1987, *A&A*, 180, 94
 Bond, N. A., Ivezić, Ž., Sesar, B., et al. 2010, *ApJ*, 716, 1

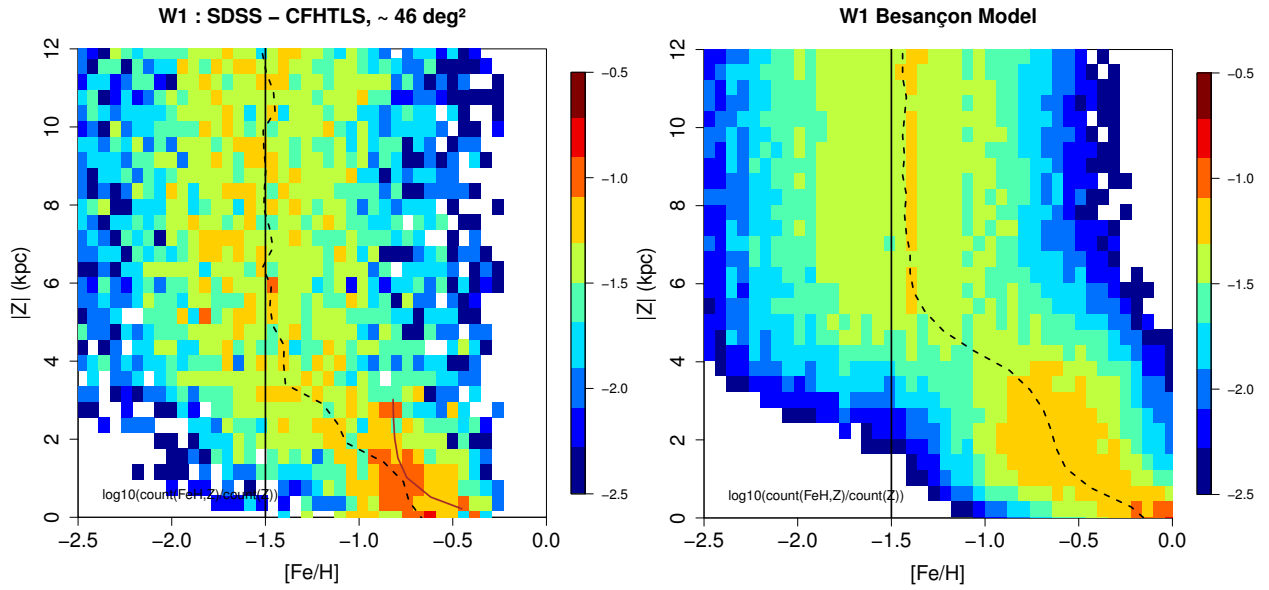


Fig. 2. Left: $([Fe/H], Z)$ distribution for CFHTLS/SDSS data in W1 field. **Right:** Besançon model $([Fe/H], Z)$ distribution in W1 field. The continuous line on the left plot shows the median metallicity formula (A2) derived by Bond et al. (2010). The dotted line represents the median metallicity per bin of 0.5 kpc.

- Carollo, D., Beers, T. C., Chiba, M., et al. 2010, *ApJ*, 712, 692
 de Jong, J. T. A., Yanny, B., Rix, H.-W., et al. 2010, *ApJ*, 714, 663
 Hakkila, J., Myers, J. M., Stidham, B. J., & Hartmann, D. H. 1997, *AJ*, 114, 2043
 Haywood, M., Robin, A. C., & Creze, M. 1997, *A&A*, 320, 428
 Ivezić, Ž., Sesar, B., Jurić, M., et al. 2008, *ApJ*, 684, 287
 Jones, D. O., West, A. A., & Foster, J. B. 2011, *AJ*, 142, 44
 Jurić, M., Ivezić, Ž., Brooks, A., et al. 2008, *ApJ*, 673, 864
 Lee, Y. S., Beers, T. C., An, D., et al. 2011, *ApJ*, 738, 187
 Norris, J. 1987, *ApJ*, 314, L39
 Robin, A. C., Reylé, C., Derrière, S., & Picaud, S. 2003, *A&A*, 409, 523
 Schlegel, D. J., Finkbeiner, D. P., & Davis, M. 1998, *ApJ*, 500, 525
 Sesar, B., Jurić, M., & Ivezić, Ž. 2011, *ApJ*, 731, 4

NEW SB2 BINARIES FOR ACCURATE STELLAR MASSES WITH GAIA*

J.-L. Halbwachs¹, F. Arenou², B. Famaey¹, P. Guillout¹, Y. Lebreton² and D. Pourbaix³

Abstract. The forthcoming Gaia mission will make possible the derivation of accurate stellar masses of binary components, by combining the astrometric measurements and the elements of SB2 orbits. We present a list of 16 long period SB1 systems observed with the T193/Sophie, and for which we measured the radial velocity of the secondary component, changing them in SB2. The 32 components of these systems could get masses with errors around 1 % when the Gaia astrometric measurements and a sufficient set of RV measurements will be available.

Keywords: binaries: spectroscopic, stars: fundamental parameters

1 Introduction

The Gaia astrometric measurements will make possible the derivation of masses of double-lined spectroscopic binary (SB2) components, with relative errors around 1 % (Halbwachs & Arenou 1999, 2009). For that purpose, a large observation programme was undertaken at the OHP observatory with the T193/Sophie in order to get very accurate SB orbital elements. Two hundred and eight target stars were selected among known SB, taken in the SB9 catalogue (Pourbaix & Tokovinin 2003; Pourbaix et al. 2004) and also in Halbwachs et al. (2003) and Halbwachs et al. (2011), but only 52, ie 25 % of them, were already known as SB2. The priority of the first ongoing observing runs is then to detect the secondary components of the SB1, changing them in SB2.

2 The observations

In order to optimize the observing time, ephemerides were computed and the SB are observed only when the radial velocities (RV) of the components are sufficiently different to allow the detection of the secondary. Since many SB have periods as long as a few years, this selection criterion results in observing only a part of the sample, and in accumulating measurements for the stars which are in the best conditions, instead of observing the others. After one year and one additional mission, totalizing 8 nights, 265 radial velocity (RV) measurements were obtained for 123 stars, 29 SB2 and 94 single-lined spectroscopic binaries (SB1). The signal-to-noise ratios (SNR) of the spectra were adapted to the magnitudes of the stars, and were chosen between 50 and 150.

3 Detection of the secondary components

For each observation, the SOPHIE automatic pipe-line provides the cross-correlation function (CCF) of the spectrum of the SB with a mask. This mask usually corresponds to a spectral type close to that of the primary component, but masks adapted to the presumed secondary were also used. For a SB1, the CCF is a single bell-shape dip, that may be approximately fitted with a normal distribution. For a SB2, the dip corresponding to the secondary component is also visible when it is not too close to that of the primary, and the resulting CCF looks like the sum of two normal distributions.

Among the 94 SB1 observed, 16 had a CCF exhibiting a small secondary dip aside from the primary one. These CCF are shown in Fig. 1.

A few cases in Fig. 1 deserve explanations:

* Based on observations performed at the Haute-Provence Observatory

¹ Observatoire Astronomique de Strasbourg, UMR 7550, 11, rue de l'université, F-67000 Strasbourg, France

² GEPI, Observatoire de Paris-Meudon, F-92195 Meudon Cedex, France

³ FNRS, Université libre de Bruxelles, CP226, boulevard du Triomphe, 1050 Bruxelles, Belgium

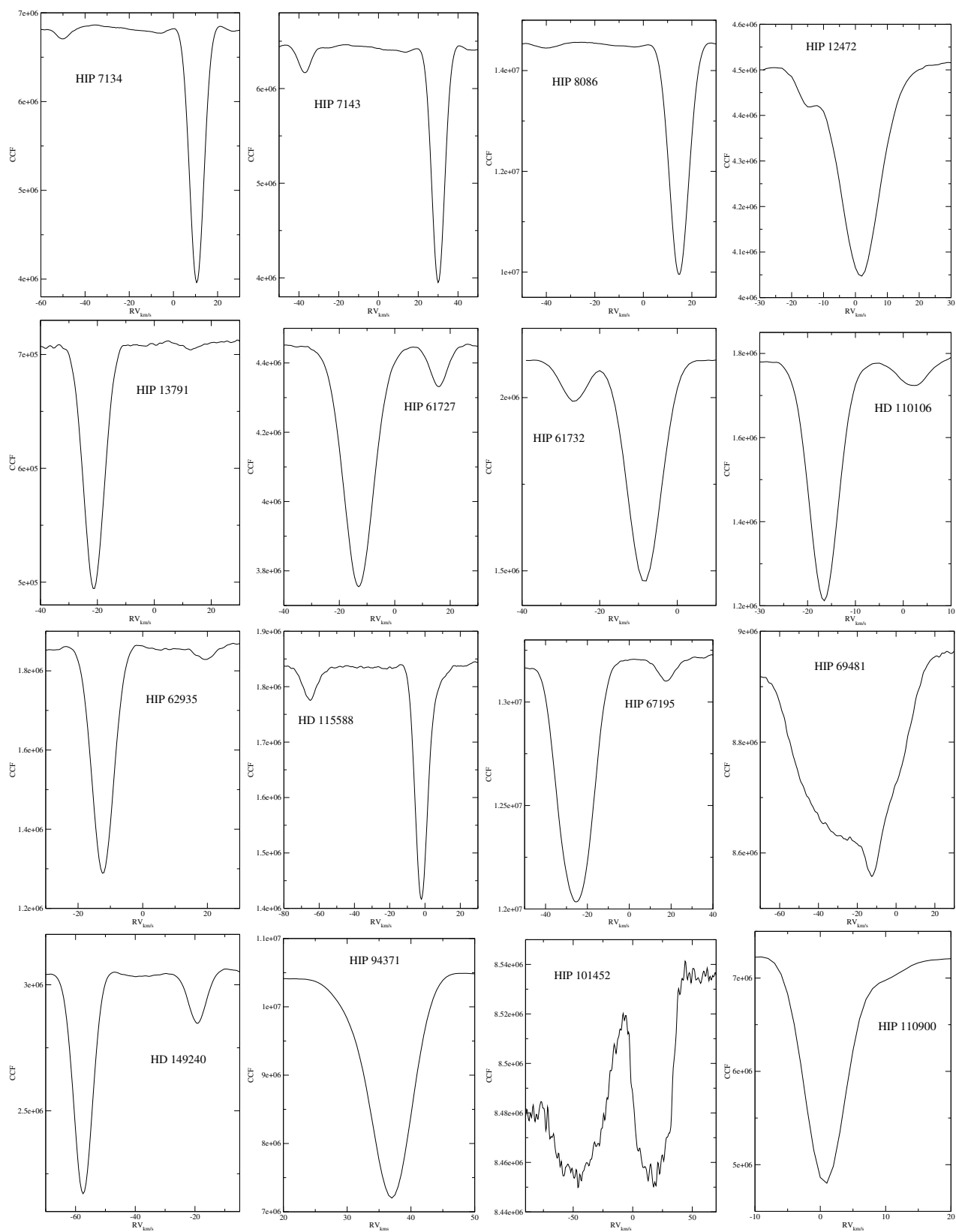


Fig. 1. The CCF of the new SB2. Small secondary dips are visible aside those of the primary components

Table 1. The mass ratios of the new SB2. Very uncertain estimations are indicated with a “:” in the place of the last digit.

Star	$q = \mathcal{M}_2/\mathcal{M}_1$	Star	$q = \mathcal{M}_2/\mathcal{M}_1$
HIP 7134	0.72	HIP 62935	0.71
HIP 7143	0.58	HD 115588	0.36
HIP 8086	0.5 :	HIP 67195	0.65
HIP 12472	0.68	HIP 69481	0.2 :
HIP 13791	0.53	HD 149240	0.42
HIP 61727	0.64	HIP 94371	0.9 :
HIP 61732	0.66	HIP 101452	0.92
HD 110106	0.75	HIP 110900	0.85

- HIP 8086: The secondary dip is very small, but it was observed at 3 different epochs, and its position is moving as expected. The detection is then certain.
- HIP 69481: A narrow secondary dip is emerging from a wide primary dip. A second observation, at another phase, confirms the detection.
- HIP 94371: Only one dissymmetric dip is visible, and the detection must still be confirmed.
- HIP 101452: An A0V-type star, at the very earliest limit of the range covered by SOPHIE. Since the earliest mask is F0, the CCF profile is not really the expected one, with a background much lower on the left side than on the right one.
- HIP 110900: The secondary dip is in the wing of the primary one, and it has to be confirmed.

4 Mass ratios of the new SB2

Since the barycentric velocities of the systems, V_γ , were already obtained with the elements of the SB1 orbits, the mass ratios may be obtained from one observation only. For that purpose, the velocities of the components were derived, fitting the CCF with two normal distributions subtracted to a linear background. The mass ratio is then $q = |V_1 - V_\gamma|/|V_2 - V_\gamma|$, where V_1 and V_2 are the RV of the primary and of the secondary component, respectively. The resulting q are in Table 1. It is worth noticing that these estimations are rather uncertain, since they are based on barycentric velocities obtained with another spectrograph than SOPHIE, and we still have too few measurements for correcting the systematic shift between our SOPHIE measurements and the ones used in the derivation of the SB orbit.

The mass ratios in Table 1 range from around 0.2 to 0.92, with a median around 0.65. We remind that, with spectrographs earlier than the CCD era, the luminosity ratio of binary star components generally prevents detection of secondaries with mass ratio smaller than 0.65 in the best conditions (Halbwachs et al. 2003). Therefore, half of the new SB2 detected with SOPHIE were obviously not detectable with the previous generation. Moreover, three new SB2 have a mass ratio well above this limit :

- HIP 101452. The primary is a A0p-type star, and its radial velocity, obtained in the past from photographic plates, was probably measured thanks to the peculiar lines of the spectrum. These lines could be missing in the secondary spectrum. The two components are clearly visible on the CCF obtained with an early-type mask.
- HIP 94371 and HIP 110900. If the secondary is confirmed in the future, it seems to be underluminous. It is obvious that the relation between the mass ratio and the visibility of the secondary is not unique: for instance, the secondary dip of HD 149240 ($q=0.42$) is much more visible than that of HIP 62935 ($q=0.71$).

5 Conclusions

Thanks to the ability of the SOPHIE spectrograph, the detection limit in mass ratio is shifted from around 0.7 to around 0.4. This leads to a selection of $52 + 16 = 68$ SB2, ie 136 stars for which we expect to derive the

masses with an accuracy near 1 % at the end of the Gaia mission. Since 62 SB1 remain to be measured, we still expect to find around 10 new SB2, leading to a total amount of a bit more than 150 individual masses. Since the combined astometric+spectroscopic solution will also provide the luminosity ratio of the components, the luminosities of the stars in the Gaia *G*-band will be obtained together with the masses. Therefore, the mass–luminosity relation will then be revisited thanks to our programme.

This programme is supported by the PNPS and by the AS-Gaia. We are grateful to the staff of the OHP for their kind assistance.

References

- Halbwachs, J.-L., Arenou, F. 1999, *Baltic Astronomy* 8, 301
- Halbwachs, J.-L., Arenou, F. 2009, *Proceedings SF2A 2009 – Scientific Highlights*, M. Heydary–Malayeri, C. Reylé et R. Samadi édr., p. 53
- Halbwachs, J.L., Mayor, M., Udry, S., Arenou, F. 2003, *A&A* 397, 159
- Halbwachs, J.L., Mayor, M., Udry, S. 2011, *MNRAS* (in preparation)
- Pourbaix, D., Tokovinin, A.A. 2003, The ninth catalogue of the orbital elements of spectroscopic binary stars, <http://sb9.astro.ulb.ac.be/>
- Pourbaix, D., Tokovinin, A.A., Batten, A.H. et al. 2004, *A&A* 424, 727

CHEMICAL ABUNDANCES OF A-TYPE DWARFS IN THE YOUNG OPEN CLUSTER M6

T. Kılıçoğlu¹, R. Monier² and L. Fossati³

Abstract. Elemental abundance analysis of five members in the open cluster M6 (age ~ 90 myr) were performed using FLAMES-GIRAFFE spectrograph mounted on 8-meter class VLT telescopes. The abundances of 14 chemical elements were derived. Johnson and Geneva photometric systems, hydrogen line profile fittings, and ionization equilibrium were used to derive the atmospheric parameters of the stars. Synthetic spectra were compared to the observed spectra to derive chemical abundances. The abundance analysis of these five members shows that these stars have an enhancement (or solar composition) of metals in general, with some exceptions. C, O, Ca, Sc, Ni, Y, and Ba exhibit the largest star-to-star abundance variations.

Keywords: stars: abundances - stars: chemically peculiar - open clusters and associations: individual: M6

1 Introduction

Stars members of an open cluster are generally assumed to share common properties: same initial chemical composition, same age and same distance. Thus open clusters appear to be unique laboratories to constrain evolutionary models via abundance determinations. Especially, early type main sequence members of open clusters of different ages are excellent laboratories to study the competition between radiative diffusion and mixing mechanisms. Abundance analysis of the open clusters (or moving groups) Ursa Major, Pleiades, Coma Berenices, Praesepe, Hyades, NGC 5460 were performed by Monier (2005), Gebran & Monier (2008), Gebran et al. (2008), Gebran et al. (2010), Fossati et al. (2011).

M6 (=NGC 6405) is an open cluster located about 450-500 pc (e.g. Talbert 1965; Vleeming 1974; Paunzen et al. 2006) away in the constellation Scorpio. The first photometric study of M6, including numbering system of the cluster, was performed by Rohlfs et al. (1959). Various ages between 50 and 140 myr were derived by several authors for M6 (e.g. Vleeming 1974; North & Cramer 1981; Paunzen et al. 2006; Landstreet et al. 2007). We averaged these ages and adopted 90 ± 30 myr. M6 is a rich, young, and relatively close cluster. Thus, its brightness allows us to obtain good quality spectra of many members.

2 Observations

The 104 possible member stars have been observed using FLAMES-GIRAFFE spectrograph with MEDUSA fibers, mounted at UT2 (Kueyen), the 8 meter class VLT telescope in May and June, 2007 (Fossati et al. 2008). The spectral regions cover three wavelength intervals: 4500-5100 Å, 5140-5350 Å, and 5590-5840 Å at resolving powers of about 7500, 25900, 24200, respectively. Some of the spectra have very low signal-to-noise ratio which prevent us from performing a detailed abundance analysis. Only 42 members have Geneva seven-color photometric measurements that can be used to derive fundamental parameters. The cluster members are identified according to Rohlfs et al. (1959) classification.

¹ Ankara University, Faculty of Science, Department of Astronomy and Space Sciences, 06100, Tandoğan, Ankara, Turkey

² Laboratoire Hippolyte Fizeau, Université de Nice - Sophia Antipolis, 06108 Nice Cedex 2, France

³ Department of Physics and Astronomy, Open University, Walton Hall, Milton Keynes MK7 6AA, UK.

3 Effective Temperatures and Surface Gravities

3.1 Johnson UBV and Geneva Seven-Colour photometric systems

We mainly used Geneva seven-colour photometry to derive atmospheric parameters. Johnson UBV observations were used to estimate effective temperature only for the stars lacking Geneva photometry. The photometric data was retrieved from the WEBDA database. We adopted the colour excesses of $E(B-V) = 0.15 \pm 0.01$ and $E(B2-V1) = 0.13 \pm 0.01$ for Johnson UBV and Geneva seven-colour photometric systems, respectively (e.g. Vleming 1974; Nicolet 1981; Ahumada & Lapasset 1995). The calibrations of Kunzli et al. (1997), and Popper (1980) were used during the calculations for Geneva and Johnson systems, respectively.

3.2 Balmer Lines

The Balmer lines of hydrogen are reliable diagnostics for atmospheric parameters. The Balmer profiles are sensitive to both effective temperature and surface gravity variations. At higher temperatures, hydrogen lines are more sensitive to surface gravity variations.

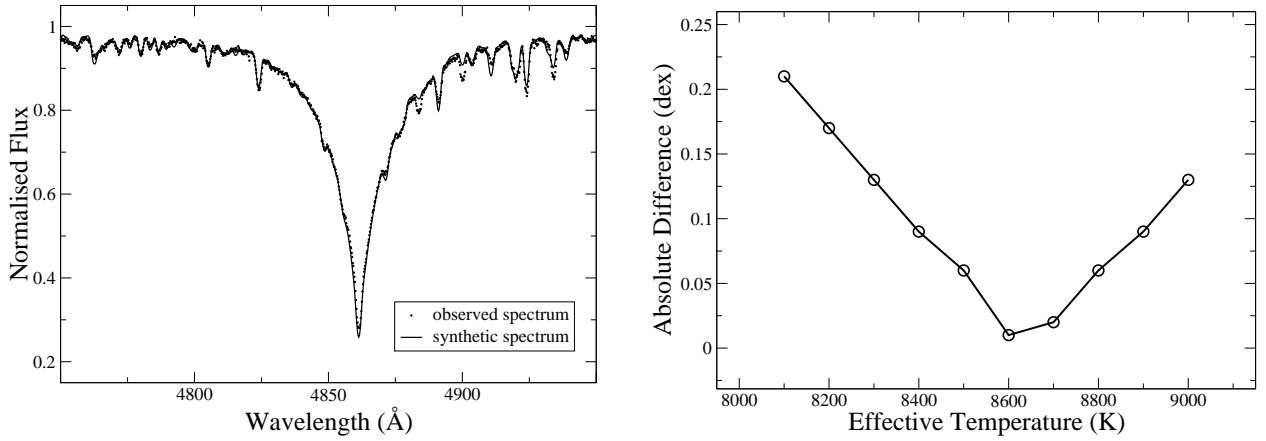


Fig. 1. Left: Comparison of the observed spectrum of NGC 6405 53 and the synthetic spectrum computed for $T_{\text{eff}} = 8100$ K, $\log g = 3.65$, and solar abundances. **Right:** Effective temperature versus absolute difference between the iron abundances (with respect to the Sun) derived by using Fe I and Fe II lines for NGC 6405 53.

In order to derive atmospheric parameters, we compared synthetic H_{β} profiles computed by SYNSPEC48 (Hubeny & Lanz 1992) to the observed H_{β} lines (Fig. 1, left). The H_{β} profiles of the analyzed early type stars appear to be narrower than those computed for the atmospheric parameters derived from the Geneva seven-colour photometry. This suggests that the actual surface gravities of these stars should be lower than those derived from Geneva photometry.

3.3 Ionisation Equilibrium

The hydrogen Balmer lines do not suffice to derive effective temperature and surface gravity simultaneously. In order to obtain these parameters precisely, we used ionization equilibrium of iron lines. We plotted the variation of the absolute value of $[\text{Fe}/\text{H}]_{\text{from Fe I lines}} - [\text{Fe}/\text{H}]_{\text{from Fe II lines}}$ as a function of effective temperature (Fig. 1, right).

As can be seen from Fig. 1, right for NGC 6405 53, the minimum of the curve shows that the effective temperature is close to 8650 K. This temperature is higher than the temperature derived from Balmer H_{β} lines (8100 K), while it is closer to the photometric temperature of 8380 K. The error of T_{eff} can be adopted as 150 K from Fig. 1, right.

4 Microturbulent Velocity

Microturbulent velocities should be derived as precisely as possible to derive reliable chemical abundances. In order to obtain this parameter, we used two methods. We first estimated the microturbulent velocity using

Pace et al. (2006)'s following calibration:

$$V_{\text{mic}} = -4.7 \log(T_{\text{eff}}) + 20.9 \text{ km s}^{-1}$$

Then, we plotted the standard deviations of the iron abundance calculated from many iron lines, according to various microturbulent velocity around that estimated value (Fig. 2, left). The minima in these plots yield the most likely microturbulent velocity. The shapes of the minima also indicate the accuracy of the microturbulent velocity. A sharp minimum provides a more precise value. The microturbulent velocities calculated by using this spectral method are consistent with those calculated from the calibration of Pace et al. (2006) in many cases.

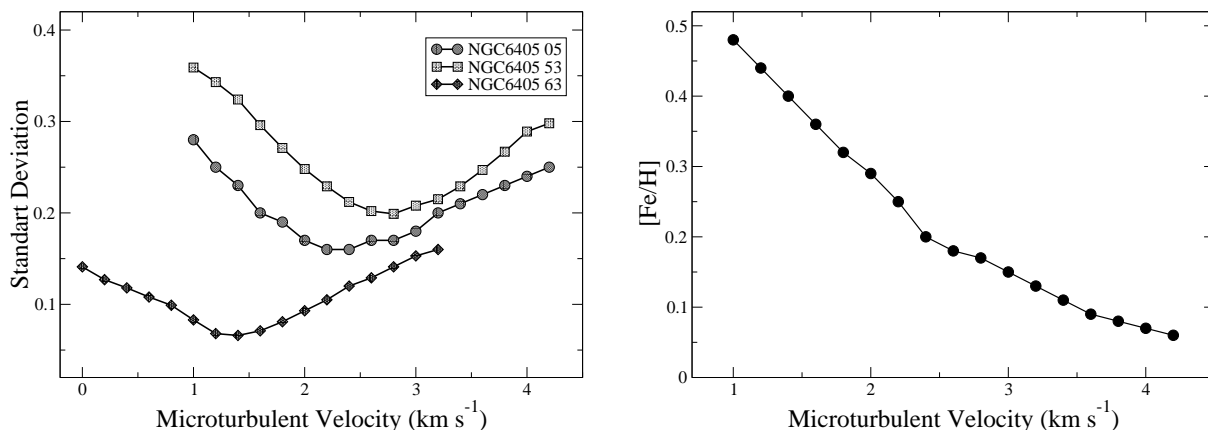


Fig. 2. Left: The standard deviation of the iron abundance derived from Fe I and Fe II lines versus microturbulent velocity for the three stars of the cluster. The standard deviations given for NGC 6405 53 were shifted by +0.05 for display purpose only. **Right:** Effective temperature versus absolute difference between the iron abundances (with respect to the Sun) derived by using Fe I and Fe II lines for NGC 6405 53.

In order to test the effects of microturbulence on the derived abundances, we performed the abundance analysis of unblended iron lines for assumed v_{mic} varying around the estimated value, in steps of 0.2 km s^{-1} for NGC 6405 05 (Fig. 2, right). A change of 0.2 km s^{-1} in microturbulence corresponds to an abundance change between 0.02-0.05 dex for this star.

5 Abundance Analysis

In order to perform the abundance analysis, we used model atmospheres and synthetic spectra. Model atmospheres were calculated by using ATLAS9 (Kurucz 1979), assuming a plane parallel geometry, a gas in hydrostatic and radiative equilibrium and LTE. During the computations, we used prescriptions of Smalley (2004) for the mixing length ratio. The atomic data was firstly constructed from Kurucz's gfhyperall.dat*, and then updated by using VALD, NIST databases and recent publications. Hyperfine structure was taken into account. Synthetic spectra are computed by using SYNSPEC48, assuming Grevesse & Sauval (1998) solar chemical composition.

6 Results and Discussion

Temperatures of 9100, 9400, 8650, 9400, 9900 K were adopted for the stars numbered 05, 47, 53, 71, and 95. Log g values are close to the value of 4.1, except no. 53 having lower value (3.65). We derived the abundances of 14 elements for the five members of M6 (Fig. 3). C, O and Ca abundances are close to solar or often slightly underabundant. All stars exhibit Sc deficiency, while Mg, Cr and Ni appear to be overabundant for the stars nos. 05, 47 and 53. Fe abundances are slightly scattered around the solar iron abundance. The largest star-to-star variations occur for the elements of C, O, Ca, Sc, Ni, Y and Ba.

*<http://kurucz.harvard.edu/LINELISTS.html>.

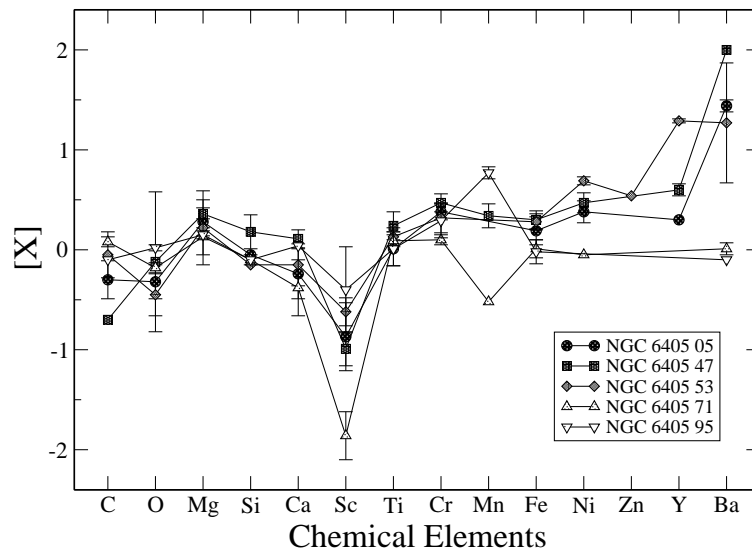


Fig. 3. The derived abundances of the elements with respect to the Sun for the five members of the cluster.

The abundances of the elements heavier than Mg are larger than solar for NGC 6405 47, except for Sc. The elements of Cr, Ni, Y and Ba are overabundant for this star. The abundance pattern for this star resembles that of a hot Am star.

The ongoing analysis of the remaining members will enable us to derive the general abundance pattern of the M6 cluster and address the chemical heterogeneity (star to star variations) of A stars in this open young cluster.

We kindly thank Pierre North for making his code CALIB available. This research was supported by the Scientific and Technological Research Council of Turkey (TÜBİTAK), and has used SIMBAD, WEBDA, VALD, and NIST databases.

References

- Ahumada, J. & Lapasset, E. 1995, *A&AS*, 109, 375
 Fossati, L., Bagnulo, S., Landstreet, J., et al. 2008, *A&A*, 483, 891
 Fossati, L., Folsom, C. P., Bagnulo, S., et al. 2011, *MNRAS*, 413, 1132
 Gebran, M. & Monier, R. 2008, *A&A*, 483, 567
 Gebran, M., Monier, R., & Richard, O. 2008, *A&A*, 479, 189
 Gebran, M., Vick, M., Monier, R., & Fossati, L. 2010, *A&A*, 523, A71+
 Grevesse, N. & Sauval, A. J. 1998, *Space Sci. Rev.*, 85, 161
 Hubeny, I. & Lanz, T. 1992, *A&A*, 262, 501
 Kunzli, M., North, P., Kurucz, R. L., & Nicolet, B. 1997, *A&AS*, 122, 51
 Kurucz, R. L. 1979, *ApJS*, 40, 1
 Landstreet, J. D., Bagnulo, S., Andretta, V., et al. 2007, *A&A*, 470, 685
 Monier, R. 2005, *A&A*, 442, 563
 Nicolet, B. 1981, *A&A*, 104, 185
 North, P. & Cramer, N. 1981, in *Liege International Astrophysical Colloquia*, Vol. 23, Liege International Astrophysical Colloquia, 55–59
 Pace, G., Recio-Blanco, A., Piotto, G., & Momany, Y. 2006, *A&A*, 452, 493
 Paunzen, E., Netopil, M., Iliev, I. K., et al. 2006, *A&A*, 454, 171
 Popper, D. M. 1980, *ARA&A*, 18, 115
 Rohlfs, K., Schrick, K. W., & Stock, J. 1959, *ZAp*, 47, 15
 Smalley, B. 2004, in *IAU Symposium*, Vol. 224, *The A-Star Puzzle*, ed. J. Zverko, J. Ziznovsky, S. J. Adelman, & W. W. Weiss, 131–138
 Talbert, F. D. 1965, *PASP*, 77, 19
 Vleeming, G. 1974, *A&AS*, 16, 331

PROBING THE THICK DISC FORMATION SCENARIOS OUTSIDE THE SOLAR NEIGHBOURHOOD

G. Kordopatis¹, A. Recio-Blanco¹, P. de Laverny¹, G. Gilmore², V. Hill¹, R. F. G. Wyse³, A. Helmi⁴, A. Bijaoui¹, C. Ordenovic¹, M. Zoccali⁵ and O. Bienaymé⁶

Abstract. The origin and evolution of the Milky Way remains one of the key unanswered questions in astrophysics. From a sample of roughly 700 stars selected in order to probe the galactic thick disc outside the solar neighborhood, we investigate the radial scale length and scale height of this structure, based on the spectroscopic measurement of its star members. Estimations of the scale height and scale lengths for different metallicity bins result in consistent values, with $h_R \sim 3.4 \pm 0.7$ kpc and $h_Z \sim 694 \pm 45$ pc, showing no evidence of relics of destroyed massive satellites and challenging the radial migration mechanisms as being the most important processes of creation of the thick disc.

Keywords: Galaxy: evolution – Galaxy: kinematics and dynamics – stars: abundances – methods: observational

1 Introduction

The existence of a thick disc for the Milky Way (Gilmore & Reid 1983), and for other disc galaxies (Yoachim & Dalcanton 2006) is rather clearly established nowadays. Nevertheless, its creation mechanisms still remain a riddle in the paradigm of a cold dark matter dominated Universe. For instance, Abadi et al. (2003) propose that the stars forming the thick disc mostly come from disrupted satellites, whereas Villalobos & Helmi (2008) predict that the pre-existing thin disc has been heated rapidly from successive accretions. On the other hand, Brook et al. (2004) suggest that a gas rich merger brought the necessary gas to form *in situ* the thick disc stars, before the gas have had completely settled into a thin disc. Finally, the simulations of Schönrich & Binney (2009) manage to form a thick disc without any external stimulus: stars migrate to larger heights from the inner parts of the Galaxy, due to resonances with the spiral arms and the central bar.

Typical F, G and K main sequence stars are particularly useful to study galactic evolution, since they are both numerous and long-lived, and their atmospheres reflect their initial chemical composition. However, a direct measurement of their spatial distribution requires accurate estimates of stellar distances, which is a delicate step involving (if the parallax is not available) the determination of precise stellar parameters (effective temperatures T_{eff} , surface gravities $\log g$, and metal content $[M/H]$).

In order to put more constraints on the thick disc properties, we explore spectroscopically the stellar contents outside the solar neighborhood, owing to an extensive use of the Ojha et al. (1996) catalogue in which are published the proper motions (μ_l , μ_b) and U,B,V colors of several thousand stars. Here, based on the spectroscopic observations of 700 of these stars towards the galactic coordinates $l \sim 277^\circ$, $b \sim 47^\circ$, we present a kinematic and chemical characterization of the thick disc.

¹ Université de Nice Sophia Antipolis, CNRS, Observatoire de la Côte d’Azur, Cassiopée UMR 6202, BP 4229, 06304 Nice, France

² Institute of Astronomy, University of Cambridge, Madingley Road, Cambridge CB3 0HA, UK

³ Johns Hopkins University, Baltimore, MD, USA

⁴ Kapteyn Astronomical Institute, University of Groningen, PO Box 800, 9700 AV Groningen, The Netherlands

⁵ Departamento de Astronomía y Astrofísica, Pontificia Universidad Católica de Chile, Av. Vicuña Mackenna 4860, Casilla 306, Santiago 22, Chile

⁶ Université de Strasbourg, Observatoire Astronomique, Strasbourg, France

2 The star sample

The target stars were selected having $14 \leq m_V \leq 18.5$ mag in order to probe the galactic thick disc and an acceptable signal-to-noise ratio ($S/N > 20$). According to the published values of Ojha et al. (1996), the magnitude precisions range from 0.02 mag for the brightest, to 0.05 mag for the faintest stars. Associated errors for the proper motions are estimated to be 2 mas/year.

The observations were obtained with VLT/FLAMES feeding the GIRAFFE spectrograph with the LR08 grating (8206-9400 Å, $R \sim 6500$). This setup contains the Gaia/RVS wavelength range (8475-8745 Å), and is similar to its low-resolution mode. In that wavelength range, the IR CaII triplet is predominant for most of the spectral types and luminosity classes as well as for very metal-poor stars. In addition, these strong features are still detectable even at low S/N, allowing a good radial velocity (V_{rad}) derivation and, combined with the other available lines, a good overall metallicity estimation.

Radial velocities have been derived by cross-correlating the spectra with a binary template of a K0 type star, reaching a mean estimated error of 4.7 km s^{-1} . We used the pipeline presented in Kordopatis et al. (2011a) to obtain the T_{eff} , $\log g$ and $[M/H]$ for our sample. This pipeline combines a local multi-linear regression method, MATISSE (Recio-Blanco et al. 2006), and an oblique decision-tree, DEGAS (Bijaoui et al. 2010) in order to normalize iteratively the spectra and derive accurately the stellar atmospheric parameters. The method has been tested on a set of 8×10^4 synthetic spectra, in order to establish the relative errors of our algorithm on the effects of the S/N and possible radial velocity shifts. We found that for an intermediate metallicity dwarf star, at $S/N \sim 50 \text{ pixel}^{-1}$ (which is the mean S/N of our spectra), accuracies of $\sim 108 \text{ K}$, 0.17 dex and 0.12 dex are achieved for T_{eff} , $\log g$ and $[M/H]$, respectively. In addition, the algorithm has been applied on two observed stellar libraries, the S^4N (Allende Prieto et al. 2004) and the CFLIB one (Valdes et al. 2004), showing no particular biases according to the S/N, the spectral type of the star or the metallic content.

2.1 Derivation of the stellar distances and velocities

At least until the ESA/Gaia mission, stellar distances for FGK targets far from the solar neighborhood have to be determined spectroscopically or photometrically. For instance, the atmospheric parameters determined in the previous section can be projected on a set of theoretical isochrones to derive the absolute magnitudes of the stars. Then, the line-of-sight distances can be derived, using the distance modulus.

We generated our own set of isochrones by using the *YYmix2* interpolation code, based on the Yonsei-Yale models (version 2, Demarque et al. 2004) combined with the Lejeune et al. (1998) colour table. To obtain the absolute magnitude M_v , the method of Zwitter et al. (2010) was used. This procedure consists in finding the most likely values of the stellar parameters, given the measured atmospheric ones, and the time spent by a star on each region of the H–R diagram.

The availability of the distances (D) then allows to estimate their galactic-centred cylindrical coordinates, which, combined with proper motions and radial velocities, provide the information required to calculate the full space motions of any star in the Galaxy. For our sample, the radial velocities are derived from the observed spectra, whereas magnitudes, colors and proper motions are taken from Ojha et al. (1996).

The errors on these kinematic data are estimated as follows: for each star, we make 5×10^3 Monte-Carlo realisations for D , μ_l , μ_b and V_{rad} , assuming Gaussian distributions around their adopted values, with a dispersion according to their estimated errors. For every realization, 6d phase-space parameters are computed, taking as a final value the mean of all the realisations, and as an error the standard deviation (see Kordopatis et al. 2011b).

3 Derivation of the radial scale lengths and scale heights

In what follows, we considered as thin disc the stars below 800 pc from the galactic plane, and as thick disc the stars between 1 and 3 kpc, in order to avoid a strong contamination from the other components. Supposing that the thick disc and the thin disc are in equilibrium, the velocity ellipsoids that were derived (corrected from the observational errors as in Jones & Walker 1988), can be used with the Jeans equation in order to infer an estimation of their radial scale lengths (h_R) and scale heights (h_Z). In cylindrical coordinates, the radial and azimuthal components of the Jeans equation are:

$$v_c^2 - \overline{v_\phi}^2 = \sigma_{V_R}^2 \left(\frac{\sigma_{V_\phi}^2}{\sigma_{V_R}^2} - 1 - \frac{\partial \ln(\rho \sigma_{V_R}^2)}{\partial \ln R} - \frac{r}{\sigma_{V_R}^2} \frac{\partial \sigma_{V_{R,Z}}^2}{\partial Z} \right) \quad (3.1)$$

$$\rho K_Z = \frac{\partial \rho \sigma_{V_Z}^2}{\partial Z} + \frac{1}{R} \frac{\partial R \rho \sigma_{V_{R,Z}}^2}{\partial R} \quad (3.2)$$

where ρ is the density of the considered galactic component, $V_c = 220 \text{ km s}^{-1}$ is the circular velocity at the solar radius, $\overline{V_\phi}$ is the mean rotational velocity of the stars having the $\sigma_{V_R}, \sigma_{V_\phi}, \sigma_{V_Z}$ velocity dispersions, $\sigma_{V_{R,Z}}^2 = \overline{V_R V_Z} - \overline{V_R} \overline{V_Z}$, and K_Z is the vertical galactic acceleration.

3.1 Radial scale lengths

We consider that $\rho(R) \propto \exp(-R/h_R)$, and that $\sigma_{V_R}^2$ has the same radial dependence as ρ (as in Carollo et al. 2010). Therefore, $\sigma_{V_R}^2 \propto \exp(-R/h_R)$. In addition, one can assume that the galactic potential is dominated by a centrally concentrated mass distribution and that the local velocity ellipsoid points towards the galactic centre (Gilmore et al. 1989; Siebert et al. 2008). In that case, the last term of Eq. 3.1 becomes:

$$\frac{r}{\sigma_{V_R}^2} \frac{\partial \sigma_{V_{R,Z}}^2}{\partial Z} \approx 1 - \frac{\sigma_{V_Z}^2}{\sigma_{V_R}^2} \quad (3.3)$$

Equation 3.1 can then be re-written as follows:

$$\frac{\sigma_{V_\phi}^2}{\sigma_{V_R}^2} - 2 + \frac{2R}{h_R} - \frac{v_c^2 - \overline{v_\phi}^2}{\sigma_{V_R}^2} + \frac{\sigma_{V_Z}^2}{\sigma_{V_R}^2} = 0 \quad (3.4)$$

Each of the terms of Eq. 3.4 have been measured in our data, leaving as the only free variable, the radial scale length h_R of the discs. With the values derived for the thick disc of $(\sigma_{V_R}; \sigma_{V_\phi}; \overline{V_\phi}) = (66 \pm 5; 57 \pm 4; -167 \pm 3) \text{ km s}^{-1}$, we find $h_R \sim 3.4 \pm 0.7 \text{ kpc}$. This results is found to be the upper end of the values cited in the literature (ranging from 2.2 kpc (Carollo et al. 2010) up to 3.6 kpc (Jurić et al. 2008), or even 4.5 kpc in the case of Chiba & Beers (2001)).

As far as the thin disc is concerned, using $(\sigma_{V_R}; \sigma_{V_\phi}; \overline{V_\phi}) = (43 \pm 2; 33 \pm 1; -204 \pm 1) \text{ km s}^{-1}$, we find that it has a smaller, though comparable radial extent (within our uncertainties) as the thick disc, with $h_R = 2.9 \pm 0.2 \text{ kpc}$. A smaller thin disc has been suggested by other recent observations (see Jurić et al. 2008), but once more, the value we derive is at the upper end of the previously reported values in the literature. Nevertheless, such an extended thin disc is plausible, since our data probe mainly the old thin disc, which is likely to be more extended than its younger part.

3.2 Scale heights

We assume that the last term of Eq. 3.2 is negligible, since we are far from the galactic centre, and that $\rho(Z) \propto \exp(-Z/h_Z)$. Equation 3.2 hence becomes:

$$\frac{\partial \ln \sigma_{V_Z}^2}{\partial Z} - \frac{1}{h_Z} + \frac{K_Z}{\sigma_{V_Z}^2} = 0 \quad (3.5)$$

We use $K_Z = 2\pi G \times 71 M_\odot \text{ pc}^{-2}$ derived by Kuijken & Gilmore (1991) at $|Z| = 1.1 \text{ kpc}$, but we note however, that this value of K_Z might differ at the distances where our targets are observed. We also use for the thick disc the value derived from our data of $\partial \sigma_{V_Z}^2 / \partial Z = 15 \pm 7 \text{ km s}^{-1} \text{ kpc}^{-1}$ and $\sigma_{V_Z} = 53 \pm 3 \text{ km s}^{-1}$. Hence, for the thick disc, we find $h_Z \sim 694 \pm 45 \text{ pc}$.

As far as the thin disc is concerned, we found that $\partial \sigma_{V_Z}^2 / \partial Z = 19 \pm 10 \text{ km s}^{-1} \text{ kpc}^{-1}$ and $\sigma_{V_Z} = 25 \pm 1 \text{ km s}^{-1}$, resulting in $h_Z = 216 \pm 13 \text{ pc}$. The derived values for both components are in good agreement with, for example, Jurić et al. (2008), who suggested a thin disc with $h_Z = 300 \text{ pc}$, and a thick disc having $h_Z = 900 \text{ pc}$.

4 Discussion

We computed the radial scale lengths and scale heights of the thick disc for different metallicity bins, using Eq. 3.4 and Eq. 3.5. The results are shown in Table 1, where the metallicity bins have been selected in order to include at least 30 stars each. Though we found that both h_R and h_Z increased with decreasing metallicity (except for the most metal poor bin), this trend is not strong enough to stand out significantly from the errors. We conclude that, within the errors, the same scale lengths and scale heights are found, which could be the

Table 1. Kinematic parameters, radial scale lengths and scale heights for different metallicity bins of the thick disc targets.

$[M/H]$ (dex)	N	$\overline{V_R}$ (km s ⁻¹)	σ_{V_R} (km s ⁻¹)	$\overline{V_\phi}$ (km s ⁻¹)	σ_{V_ϕ} (km s ⁻¹)	$\overline{V_Z}$ (km s ⁻¹)	σ_{V_Z} (km s ⁻¹)	h_R (kpc)	h_Z (pc)
-1.14	36	-5± 9	58± 11	-137± 11	61± 7	-7± 8	59± 7	1.9± 0.7	934± 166
-0.67	26	-3± 17	85± 17	-161± 11	54± 11	-4± 12	54± 8	4.0± 1.3	804± 181
-0.40	56	5± 8	81± 8	-168± 6	52± 5	-17± 6	45± 4	3.8± 0.9	610± 90
-0.11	37	6± 9	64± 8	-171± 7	50± 6	-18± 7	45± 5	3.1± 0.9	620± 97

signature of only one population. Indeed, if an important amount of relics of a destroyed massive satellite would exist in our line-of-sight, as suggested by Gilmore et al. (2002), one would expect them to have a different spatial distribution compared to the canonical thick disc, which we do not observe. Unless, of course, the satellite debris provides the dominant stellar population in the thick disc.

This result can also be discussed in the frame of a thick disc formed according to a radial migration scenario. In that case, the older stars being at the solar radius have come from the inner parts of the Galaxy, and are expected to have a higher vertical velocity dispersion and a different metallicity, and therefore, should exhibit scale heights dependent on metallicity. In particular, the model of Schönrich & Binney (2009) predicts a smaller scale height for the metal poor thick disc, compared to its metal rich counter part. Such a trend is not seen in our data (if it exists, it should be rather small), which challenges the migration scenario as being the most important process of creation of the galactic thick disc.

The authors would like to thank the MESOCENTRE de l'Observatoire de la Cote d'Azur, for computing the grid of synthetic spectra. We are grateful to B. Plez for his molecular line-lists and M. Irwin for letting us use the routine of sky subtraction. Finally, G.K. would like to thank the Centre National d'Etudes Spatiales (CNES) and the Centre National de Recherche Scientifique (CNRS) for the financial support.

References

- Abadi, M. G., Navarro, J. F., Steinmetz, M., & Eke, V. R. 2003, *ApJ*, 591, 499
- Allende Prieto, C., Barklem, P. S., Lambert, D. L., & Cunha, K. 2004, *A&A*, 420, 183
- Bijaoui, A., Recio-Blanco, A., de Laverny, P., & Ordenovic, C. 2010, in *ADA 6 - Sixth Conference on Astronomical Data Analysis*
- Brook, C. B., Kawata, D., Gibson, B. K., & Freeman, K. C. 2004, *ApJ*, 612, 894
- Carollo, D., Beers, T. C., Chiba, M., et al. 2010, *ApJ*, 712, 692
- Chiba, M. & Beers, T. C. 2001, *ApJ*, 549, 325
- Demarque, P., Woo, J.-H., Kim, Y.-C., & Yi, S. K. 2004, *ApJS*, 155, 667
- Gilmore, G. & Reid, N. 1983, *MNRAS*, 202, 1025
- Gilmore, G., Wyse, R. F. G., & Kuijken, K. 1989, *ARA&A*, 27, 555
- Gilmore, G., Wyse, R. F. G., & Norris, J. E. 2002, *ApJ*, 574, L39
- Jones, B. F. & Walker, M. F. 1988, *AJ*, 95, 1755
- Jurić, M., Ivezić, Ž., Brooks, A., et al. 2008, *ApJ*, 673, 864
- Kordopatis, G., Recio-Blanco, A., de Laverny, P., et al. 2011a, *ArXiv:1109.6237*
- Kordopatis, G., Recio-Blanco, A., de Laverny, P., et al. 2011b, *A&A*, submitted, *arXiv:1110.5221*
- Kuijken, K. & Gilmore, G. 1991, *ApJ*, 367, L9
- Lejeune, T., Cuisinier, F., & Buser, R. 1998, *A&AS*, 130, 65
- Ojha, D. K., Bienayme, O., Robin, A. C., Creze, M., & Mohan, V. 1996, *A&A*, 311, 456
- Recio-Blanco, A., Bijaoui, A., & de Laverny, P. 2006, *MNRAS*, 370, 141
- Schönrich, R. & Binney, J. 2009, *MNRAS*, 399, 1145
- Siebert, A., Bienaymé, O., Binney, J., et al. 2008, *MNRAS*, 391, 793
- Valdes, F., Gupta, R., Rose, J. A., Singh, H. P., & Bell, D. J. 2004, *ApJS*, 152, 251
- Villalobos, Á. & Helmi, A. 2008, *MNRAS*, 391, 1806
- Yoachim, P. & Dalcanton, J. J. 2006, *AJ*, 131, 226
- Zwitter, T., Matijević, G., Breddels, M. A., et al. 2010, *A&A*, 522, A54

GAIA: LUMINOSITY CALIBRATIONS AND DISTANCES IN THE GALAXY AND LOCAL GROUP

X. Luri¹ and C. Turon²

Abstract. The upcoming availability of the Gaia mission data will prompt a significant advancement in many areas of astrophysics and will specially have a huge impact in the determination of luminosity calibration and distances, thanks to the availability of very precise parallaxes.

Already the Hipparcos mission made a huge improvement in these areas with respect to the previous eras, but the advent of Gaia will represent an even larger improvement: the Gaia catalogue will contain about a billion objects, with more than 100 million of them with distances known to better than 10%, all over the Galaxy. All stellar distance indicators will be directly measured in very large number, providing a direct calibration of their luminosity and making possible detailed studies of the impacts of various effects linked to chemical element abundances or cluster membership. Furthermore, Gaia astrometry will be precise enough to reach the Large and Small Magellanic Clouds, allowing for the first time a direct parallax estimation of its distances.

In this paper we will review with the help of simulations the potential contributions of Gaia in these areas.

Keywords: Gaia, astrometry, luminosity calibration, distance scale

1 Introduction

The ESA Gaia astrometric mission has been designed for solving one of the most difficult yet deeply fundamental challenges in modern astronomy: to create an extraordinarily precise 3D map of about a billion stars throughout our Galaxy and beyond (Perryman et al. 2001).

The survey aims for completeness to $V_{lim} \sim 20-25mag$ depending on the color of the object, with astrometric accuracies of about $10\mu as$ at $15mag$ (see figure 1). In the process, it will map the stellar motion and provide the detailed physical properties of each star observed: characterizing their luminosity, temperature, gravity and elemental composition.

Additionally, it will perform the detection and orbital classification of tens of thousands of extra-solar planetary systems, and a comprehensive survey of some $10^5 - 10^6$ minor bodies in our solar system; furthermore, it will also include galaxies in the nearby Universe and distant quasars.

This massive stellar census will provide the basic observational data to tackle an enormous range of important problems related to the origin, structure and evolutionary history of our Galaxy and new tests of general relativity and cosmology, and in particular will make a substantial contribution to the determination of luminosity calibrations and the distance scale.

2 The Gaia simulator

Gaia will acquire an enormous quantity of complex and extremely precise data that will be transmitted daily to a ground station. By the end of Gaia's operational life, around 150 terabytes (10^{14} bytes) will have been transmitted to Earth: some 1,000 times the raw volume from the related Hipparcos mission.

¹ Dept. Astronomia i Meteorologia, Universitat de Barcelona, ICCUB/IEEC, 08028 Barcelona, Spain, xluri@am.ub.es

² GEPI - UMR 8111, Observatoire de Paris, CNRS, Université Paris Diderot, 5 Place Jules Janssen, 92190 Meudon, France, catherine.turon@obspm.fr

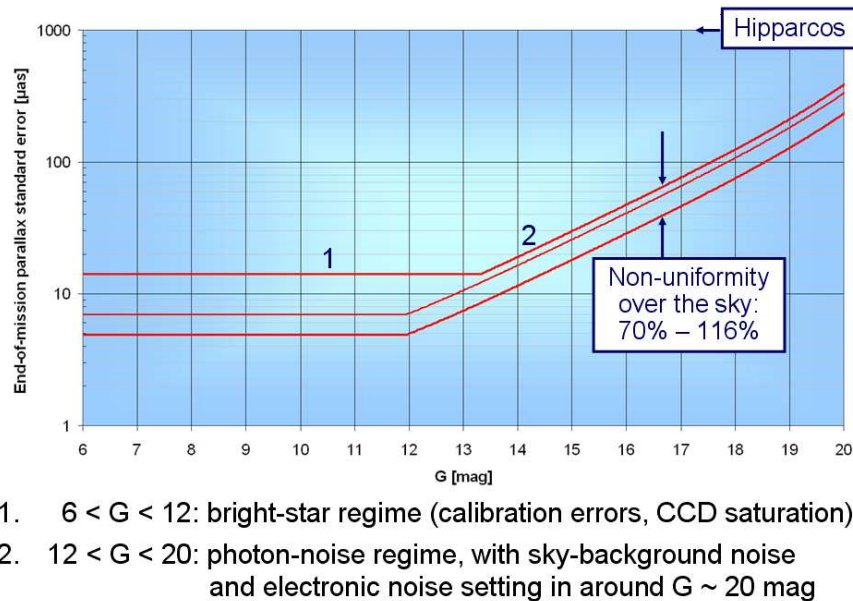


Fig. 1. End of life Gaia parallax errors (courtesy J. de Bruijne, ESA)

An extensive and sophisticated Gaia data processing mechanism is being developed to yield meaningful results from collected data. To allow its development and testing a system has been developed to generate the simulated Gaia data, the Gaia simulator.

The Gaia simulator has been organized around a common tool box (named GaiaSimu library) containing a universe model, an instrument model and other utilities, such as numerical methods and astronomical tools. This common tool box is used by several specialized components and one of its main components is the so-called Universe Model. It allows the simulation of the characteristics of all the different types of objects that Gaia will observe: their spatial distribution, photometry, kinematics and spectra. The universe model is designed to generate lists of astronomical sources whose distributions and the statistics of its observables are as realistic as possible.

The object generation process is divided into three main modules, Solar System, the Milky Way and extra-galactic objects. We will not deal here with the first and third modules and we present below a short summary of the second. For more details see (Robin et al. 2011).

2.1 The galaxy model

Galactic objects are generated from a model based on Besançon Galaxy Model (BGM) (Robin et al. 2003) which provides the distribution of the stars, their intrinsic parameters and their motions. The stellar population synthesis combines:

- Theoretical considerations such as stellar evolution, galactic evolution and dynamics.
- Observational facts such as the local luminosity function, the age-velocity dispersion relation, the age-metallicity relation.

The result is a comprehensive description of the stellar components of the Galaxy with their physical characteristics (e.g. temperature, mass, gravity, chemical composition and motions).

The Galaxy model is formed by four stellar populations constructed with different model parameters:

- The thin disc: young stars with high metallicities. It is additionally divided in seven isothermal components of ages varying from 0-0.15 Gyr for the youngest to 7-10 Gyr for the oldest. For computing the

scale height at the solar position as a function of age (Bienaymé et al. 1987), the Boltzmann equation (first moment at the first order with the plane parallel approximation) is used assuming an age-velocity dispersion relation deduced from Hipparcos observations (Gómez et al. 1997).

- The thick disc: in terms of metallicity, stars are at half-way between the thin disc and the stellar halo.
- The stellar halo (spheroid): old and metal poor stars.
- The outer bulge: old stars with metallicities similar to the ones in the thick disc.

The distribution in the Hess diagram split into several age bins is obtained from an evolutionary model which starts with a mass of gas, generates stars of different masses assuming an Initial Mass Function and a star formation rate history, and makes these stars evolve along evolutionary tracks. The evolution model is described in Haywood et al. (1997a,b). The evolutionary model produces a file describing the distribution of stars per element volume in the space (M_V, T_{eff}, Age). Similar Hess diagrams are also produced for the bulge, the thick disc and the spheroid populations, assuming a single burst of star formation and ages of 10 Gyr, 11 Gyr and 14 Gyr respectively.

The stellar luminosity function is the one of primary stars (single stars, or primary stars in multiple systems) in the solar neighborhood Reid et al. (2002).

It is worth noting that white dwarf (WD) are taken into account separately but self-consistently. Additionally, some rare objects such as Be stars, peculiar metallicity stars and Wolf Rayet stars have also been added.

In the end, each star from the generated catalogue has assigned intrinsic attributes (age, effective temperature, bolometric magnitude, U,V,W velocities, distance) and observational parameters (apparent magnitudes, colors, proper motions, radial velocities, etc) affected by the implemented 3D extinction model from Drimmel et al. (2003).

3 Simulation overview

The universe model generates a total number of 1,000,000,000 galactic objects at $G < 20$ of which 49% are single stars and 51% stellar systems formed by stars with planets and binary/multiple stars. Individually, the model has created 1,600,000,000 stars where 31.66% of them are single stars with magnitude G inferior to 20 (potentially observable by Gaia) and 68.34% correspond to stars in multiple systems. This last group is formed by stars that have magnitude G inferior to 20 as a system but, in some cases, its isolated components can have magnitude G superior to 20 and will not be individually detectable by Gaia.

3.1 Spatial distribution

Based on these simulations, the Gaia catalogue will sample a large fraction of the galactic volume, thoroughly mapping the solar neighborhood, providing large numbers of objects for a substantial part of the disk and reaching the central parts of the Galaxy although not the centre itself. In figure 2 the sampling of the Galaxy is depicted based on the simulation results.

3.2 The HR diagram

On the other hand, the stars in the catalogue will also fully cover the HR diagram, sampling even the regions with the rarest types of objects. This coverage is depicted in figure 3; the densest regions contain tens of millions of objects and even the rarest types (bottom of the main sequence, brightest giants) are represented with some hundreds of objects.

4 Consequences for the Luminosity calibrations and distance scale

Even though Hipparcos was a major improvement with respect to earlier ground-based astrometric observations, *only* about 30 000 stars (compared to a few hundreds before Hipparcos) obtained a relative precision on the trigonometric parallax better than 10 %, all of them are in the solar neighborhood, and very few standard candles are among them. On the other hand, many different photometric and spectroscopic systems have been used, resulting in the non-uniformity of the color or abundances scales, and have been compared with many different

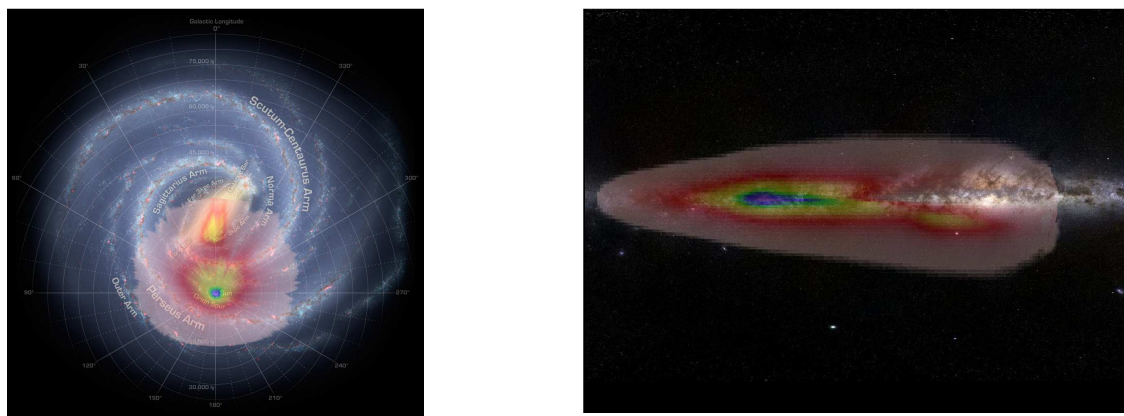


Fig. 2. These images show the expected 3D distribution in the Milky Way of the contents of the Gaia catalogue. They are an overlay of an artistic top view of our galaxy (NASA/JPL-Caltech/R. Hurt) and an illustration of a side view of the Galaxy (right, Gigagalaxy zoom, ESO/S. Brunier/S. Guisard: the Milky Way as seen from ESO, Chile) with the results of a simulation of the contents of the Gaia catalogue. The colors of the overlaid simulation show the expected density of the one-billion stars in the catalogue in different regions of the Milky Way, ranging from purple-blue very high densities around the Sun to pink low densities farther from it. The “spikes” pointing away from the Sun are due to windows in the interstellar extinction, allowing deeper observations. Notice in particular the region in yellow and red, just below the galactic center. It corresponds to the high-density bulge visible through an extinction window around the galactic central region. See http://www.rssd.esa.int/index.php?project=GAIA&page=picture_of_the_week&pow=141 for the full-resolution images.

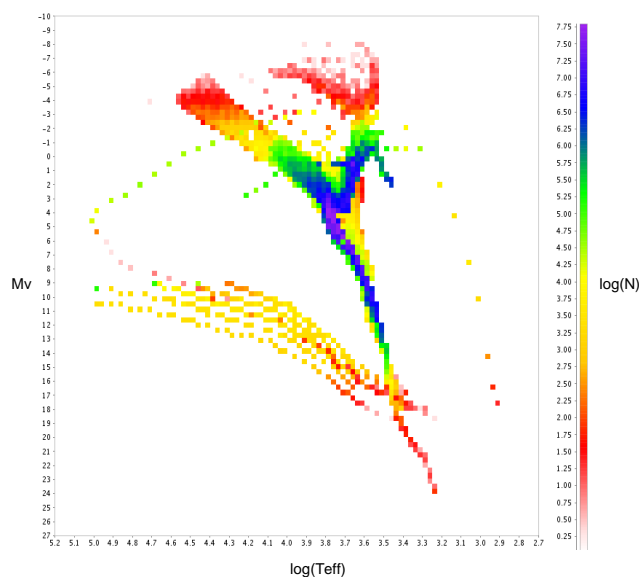


Fig. 3. The Gaia HR diagram. The figure shows the expected density of catalogue objects in the different regions of the HR diagram (single stars and components of systems alike). The color scale gives the decimal logarithm of the number of objects for each $[0.025K \times 0.37mag]$ box in the diagram; to properly interpret this figure it is important to take into account that the logarithmic scale strongly enhances the visibility of low-density areas that will be represented in the Gaia catalogue, which makes it somewhat unfamiliar compared with the usual HR diagrams.

models of stellar atmosphere, resulting in various transformations from color to the effective temperature and various estimations of the bolometric correction. Finally, it is difficult to safely compare observations between

Table 1. Luminosity calibrations: from Hipparcos to Gaia (adapted from Turon & Perryman 1999, and updated)

	Hipparcos (a)	Hipparcos re-reduction (b)	GAIA
$\sigma_\pi/\pi < 0.1\%$	-	3	$\sim 100\,000$ stars
$\sigma_\pi/\pi < 1\%$	442 stars	719 stars	$\sim 11 \times 10^6$ stars up to 1 – 2 kpc ($M_v < 0$) up to 0.5– 1 kpc ($M_v < 5$)
$\sigma_\pi/\pi < 10\%$	22 396 stars	30 579 stars	$\sim 150 \times 10^6$ stars up to 10–15 kpc ($M_v < -5$) up to 7–10 kpc ($M_v < 0$) up to 2– 3 kpc ($M_v < 5$)
Error on M_v ($V = 10$) due to error on π	0.5 mag at 100 pc		0.002-0.007 mag at 100 pc 0.2-0.7 mag at 10 kpc
Stellar populations	mainly disk		all populations, even the rarest
HR diagram $< 10\%$	$-4 < M_v < 13$ $-0.2 < B - V < 1.7$		all magnitudes all colors

(a)(Perryman et al. 1997; Perryman & ESA 1997)

(b)(van Leeuwen & Fantino 2005; van Leeuwen 2007)

themselves and with theoretical isochrones.

The remaining major sources of uncertainty are the location of the principal sequences of the Hertzsprung-Russell diagram (main sequence, subgiant branch, turn-off stars, red clump stars, blue supergiants) versus metallicity, age or detailed element abundances, the calibration of the period-luminosity(-color) relations of pulsating variable stars with respect to all effects likely to affect their absolute luminosity, the distance (and depth) of the Large Magellanic Cloud, whose Cepheids are often used as reference to derive relative distances to other galaxies.

As we have seen in the previous section the Gaia catalogue will abundantly cover all the above mentioned regions of the HR diagram, and will do it with much more precise astrometry than Hipparcos, as shown in table 1.

Therefore, a huge amount of extremely accurate trigonometric parallaxes will be available for very large samples of all galactic populations, allowing the direct distance determination of large samples of all kinds of stellar candles, and may even provide the first direct test of the universality of the period-luminosity(-color) relations. It will also provide a systematic diagnostic of the duplicity (multiplicity) of all observed targets and reliable abundances and ages for very large samples of field and cluster stars.

Furthermore, Gaia will also observe about 7.5 million stars in the Large Magellanic Cloud and about 1.5 million stars in the Small Magellanic Cloud. Although most of the individual parallaxes will have too large errors to be useful to determine the distance of the individual stars (see figure 4) taking all the millions of individual parallaxes together will allow to determine the mean parallax of the LMC with a relative error of about 0.5%, and that of the SMC with a relative error of about 1.5%. Even more, for the brightest objects in the clouds (including Cepheids) the Gaia parallax error will be still small enough (50% - 100%) to obtain useful distance estimations, allowing for the first time to directly study the 3D distribution of these objects.

5 Conclusions

The precise knowledge of distances is an essential clue to the calibration of the luminosities of stellar candles used to estimate the distances in the Universe, very far beyond the Local Group of galaxies. Hipparcos was a major step forward and the next, spectacular, step will be Gaia, with orders of magnitude improvement in the number of observed targets (from 118 000 for Hipparcos to 1 billion for Gaia) and in the accuracy (from 1 mas for Hipparcos to 10 μ as for Gaia), as well as its full coverage of the HR diagram and its direct reaching of the

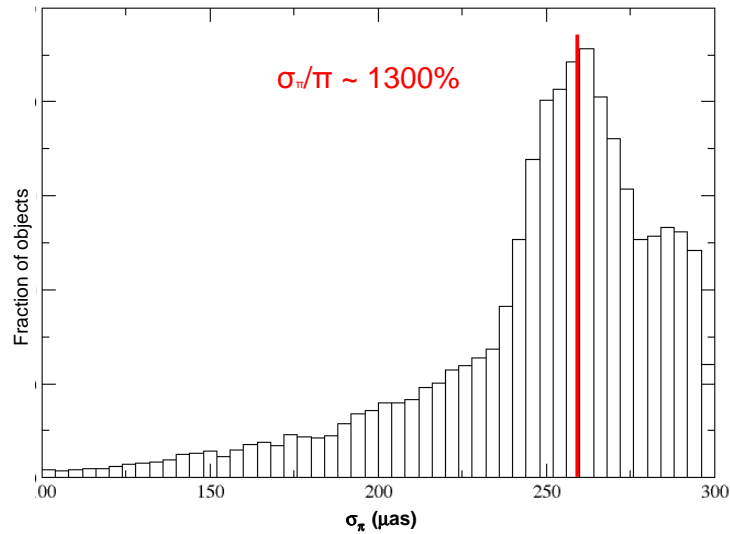


Fig. 4. Distribution of the errors in parallax for the simulated LMC objects. Notice that the maximum is at a relative error of 1300%, but that there is a significant tail of objects reaching low relative errors.

Large and Small Magellanic Clouds.

Finally, the other – also essential – characteristic of Gaia is its capability to obtain photometric and spectroscopic observations quasi-simultaneously with astrometric data. This is a key possibility for a complete study of stellar candles, especially because of the importance of metallicity effects on their luminosity, and holds the promise for a significant advance in the determination of luminosity calibrations and, with them, the distance scale of the universe.

This work was supported by the MICINN (Spanish Ministry of Science and Innovation) - FEDER through grant AYA2009-14648-C02-01 and CONSOLIDER CSD2007-00050. The simulations presented in this paper have been done in the supercomputer MareNostrum at Barcelona Supercomputing Center - Centro Nacional de Supercomputación (The Spanish National Supercomputing Center)

References

- Bienaymé, O., Robin, A. C., & Crézé, M. 1987, *A&A*, 180, 94
 Drimmel, R., Cabrera-Lavers, A., & Lopez-Corredoira, M. 2003, *A&A*, 409, 205
 Gómez, A. E., Grenier, S., Udry, S., et al. 1997, in *ESA Special Publication*, Vol. 402, *ESA Special Publication*, 621–624
 Haywood, M., Robin, A. C., & Creze, M. 1997a, *A&A*, 320, 428
 Haywood, M., Robin, A. C., & Creze, M. 1997b, *A&A*, 320, 440
 Perryman, M. A. C., de Boer, K. S., Gilmore, G., et al. 2001, *A&A*, 369, 339
 Perryman, M. A. C. & ESA, eds. 1997, *ESA Special Publication*, Vol. 1200, *The HIPPARCOS and TYCHO catalogues. Astrometric and photometric star catalogues derived from the ESA HIPPARCOS Space Astrometry Mission*
 Perryman, M. A. C., Lindegren, L., Kovalevsky, J., et al. 1997, *A&A*, 323, L49
 Reid, I. N., Gizis, J. E., & Hawley, S. L. 2002, *AJ*, 124, 2721
 Robin, A., Luri, X., & et al. 2011, submitted to *A&A*
 Robin, A. C., Reylè, C., Derrière, S., & Picaud, S. 2003, *A&A*, 409, 523
 Turon, C. & Perryman, M. A. C. 1999, in *Astronomical Society of the Pacific Conference Series*, Vol. 167, *Harmonizing Cosmic Distance Scales in a Post-HIPPARCOS Era*, ed. D. Egret & A. Heck, 1–12
 van Leeuwen, F. 2007, *A&A*, 474, 653
 van Leeuwen, F. & Fantino, E. 2005, *A&A*, 439, 791

CARBON-ENHANCED METAL-POOR STARS: WITNESSES OF THE FIRST GENERATION OF STARS

T. Masseron¹

Abstract. Carbon-enhanced metal-poor (CEMP) stars are now accepted to be mass-transferred binary member of the first generation of stars. Indeed, the peculiar chemical fingerprints revealed by their spectra represent a unique opportunity to study their now extinct progenitor (basically all low-metallicity stars with $M > 0.8M_{\odot}$).

Keywords: Carbon stars, metal-poor, abundances

1 The method

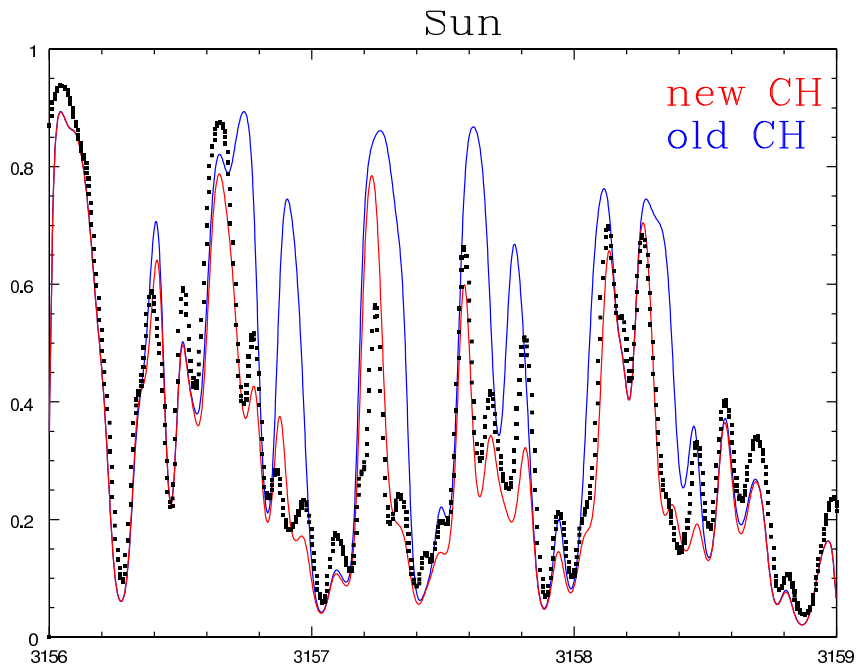


Fig. 1. : Example of synthesis of the Sun spectrum (black squares). The different colored lines show the improvement we made on molecular linelist.

In order to decipher the physics of these first generations of stars, we derive abundances from high resolution and high SNR spectra of a large sample of CEMP stars. For this, we use the radiative transfer code Turbospectrum, and specific stellar atmospheres (MARCS), taking into account the effect of large C enhancement on the atmosphere structure..

¹ Université Libre de Bruxelles, Belgium

One of the critical ingredients of abundance analysis are the input linelists. By using a combination of programs to simulate molecular structure and well selected laboratory measurements, we build new accurate molecular linelists. We show in Fig.1 the results for a part of the C-X band of the CH molecule.

Reciprocally, we also use stellar spectra probing thermodynamical conditions not available on earth to improve molecular constants (notably high rotational levels including predissociation levels).

2 The metal-poor stars zoo

Among metal-poor stars in the Galaxy, $\sim 20\%$ show a high content of carbon, the so-called Carbon-Enriched Metal-Poor (CEMP) stars. It is now clear that most of them have transferred material from an Asymptotic Giant Branch (AGB) star. In particular, AGB stars are known to produced s-process elements (like Ba or Pb).

However, we show in Fig. 2 that many subclasses exists: we do find a subclass of CEMP stars which nicely falls along the s-process predictions, but there are also CEMP stars which show no capture elements enhancement. We observed that these stars tends to have a lower metallicity than other CEMP stars, pointing out that nucleosynthesis of AGB stars may drastically change at very-low metallicity.

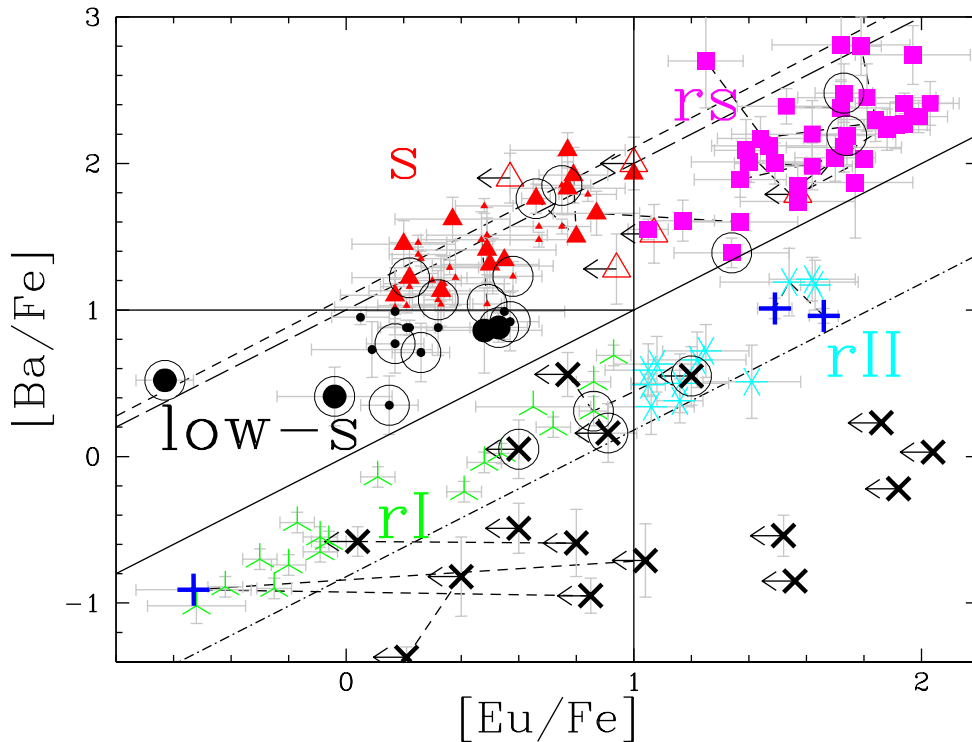


Fig. 2. : Ba vs Eu abundances in metal-poor stars. Lines represent the prediction for pure s-process nucleosynthesis (AGBs) (short and long dashed lines), and pure r-process nucleosynthesis (SNII) (dashed-dotted line). Except black dots, all symbols represent different categories of CEMP stars, according to their content of neutron-capture

In contrast, another subgroup of CEMP stars show a large excess of neutron-capture elements. We claim that another source of neutron is required in order to explain the existence of such stars (possibly the $^{22}\text{Ne}(\alpha, n)^{25}\text{Mg}$).

3 Fluorine

Fluorine is an element very sensitive of the thermodynamical conditions in AGB stars. While C is produced by He burning during the pulses of AGB stars, F is also produced in the He-rich layers of AGB stars, but is dependent on the presence of neutrons in the He intershell. Since the mechanism for making neutrons is still poorly understood, F is a very precious element to constrain the models.

Thanks to the IR high resolution spectrograph CRIRES, we were able to observe the HF lines in sample of CEMP stars (Fig.3). According to the observation of s-process elements, low-metallicity AGB models predict

that the progenitor of CEMP stars should have a mass between $1.2M_{\odot}$ and $2M_{\odot}$. Although we measure mostly upper limits, we did not observe as much Fluorine as expected by the models.

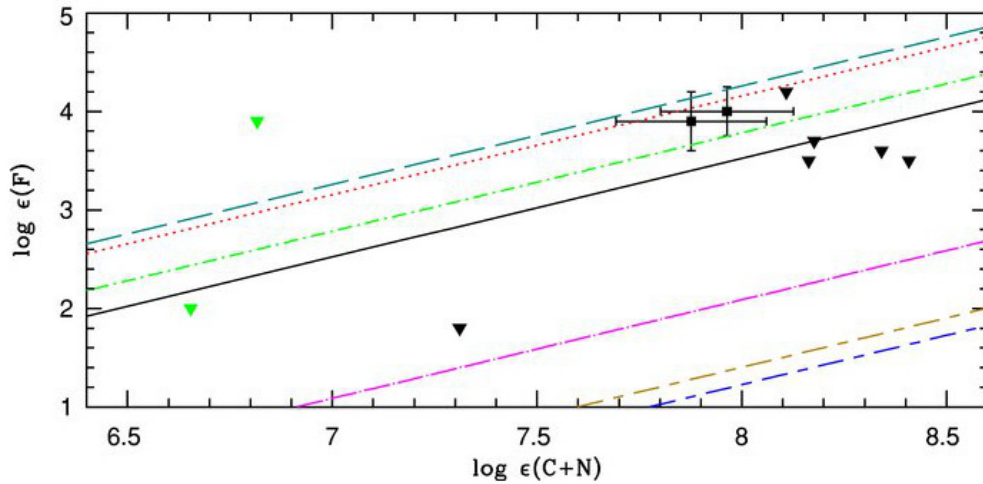


Fig. 3. : black triangles are CEMP stars. Models are from Karakas & Lattanzio (2007) for different masses; solid black line $1.25M_{\odot}$, red dotted line $1.75M_{\odot}$, teal dashed line $2.25M_{\odot}$, green dot-dashed line $2.5M_{\odot}$, magenta dot-dashed line $3.0M_{\odot}$, short-long dashed yellow line $3.5M_{\odot}$, and short-long dashed blue line $4M_{\odot}$.

4 Lithium

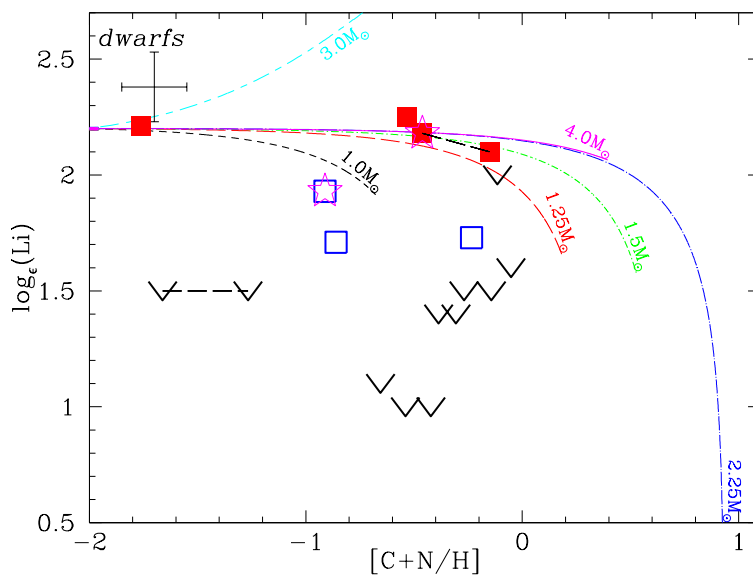


Fig. 4. red squares are CEMP Li-rich stars, blue open squares are Li-poor CEMP stars, black v signs are upper limits. Models are from Karakas & Lattanzio (2010).

While C is produced by AGB stars, Li is generally destroyed. Because CEMP stars have accreted large amount of this AGB material, it was not expected to find CEMP stars with high Li content (close to the Spite plateau). Since then, Li production in AGB stars has been required. However, we demonstrate in Fig.5 that Li-rich stars can naturally be explained by dilution of the AGB yields. In contrast it is more difficult to understand how some CEMP stars can have so low Li content. By looking at the rotation speed of the star, we

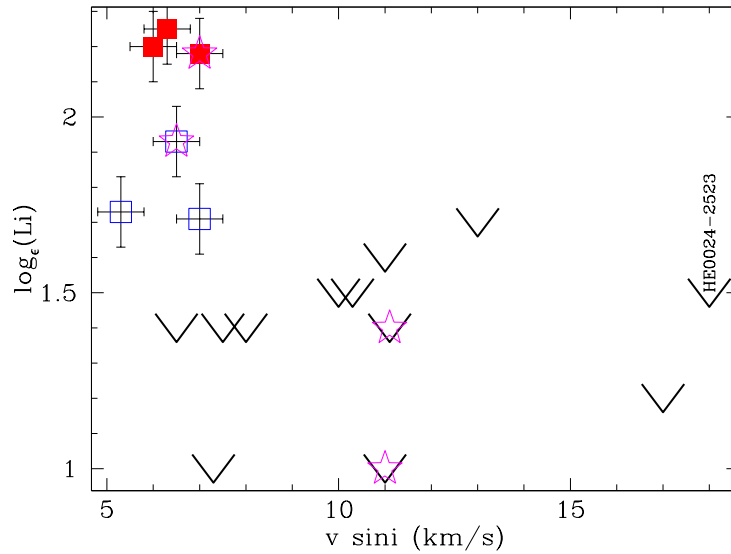


Fig. 5. Li abundance as function of rotational velocity. Red squares are CEMP Li-rich stars, blue open squares are Li-poor CEMP stars, black $v \sin i$ signs are upper limits.

noticed that no fast rotating stars were observed with a high Li content, suggesting that rotation has played a role in the Li destruction.

5 Conclusions

AGB stars at low metallicity show a broad range of nucleosynthetic properties that still need to be understood by the models: it seems that various s-processes occur, but the origin of the neutron source is still not clearly established. Moreover, various mixing mechanisms are expected to occur (thermohaline mixing, canonical extra mixing, hydrogen injection flash, rotation...). The complex interplay of these mechanisms can either lead to the destruction or the production of Li and F. Our observations bring some more constrains to understand AGB stars, but more are needed. Furthermore, there is still a lot of improvement to be made in the analysis and in particular concerning molecular linelists. We plan to build new sets of accurate linelists that could be used for accurate abundance measurements.

References

- Karakas, A., & Lattanzio, J. C. 2007, PASA, 24, 103
- Karakas, A. I. 2010, MNRAS, 403, 1413
- Lucatello, S., Masseron, T., Johnson, J. A., Pignatari, M., & Herwig, F. 2011, ApJ, 729, 40
- Masseron, T., Johnson, J. A., Plez, B., et al. 2010, A&A, 509, A93

SPITZER CHARACTERIZATION OF DUST IN THE IONIZED MEDIUM OF THE LARGE MAGELLANIC CLOUD

D. Paradis^{1,2,3}, R. Paladini³, A. Noriega-Crespo³, G. Lagache⁴, A. Kawamura⁵, T. Onishi⁶ and Y. Fukui⁵

Abstract. Dust emission associated with ionized gas has so far been detected only in our Galaxy, and for wavelengths longer than 60 μm . Spitzer data now offer the opportunity to carry out a similar analysis in the Large Magellanic Cloud, and to separate dust emission into components associated with different phases of the gas, i.e. atomic, molecular and ionized. We perform a correlation study using infrared Spitzer data as part of the Surveying the Agents of a Galaxy's Evolution (SAGE) and IRAS 12-100 μm combined with gas tracers such as the ATCA/Parkes HI data, for the atomic phase, the NANTEN ^{12}CO data, for the molecular phase, and both the SHASSA $\text{H}\alpha$ and the radio Parkes 5 GHz data, for the ionized phase. In particular, we investigate the presence of dust for different physical regimes of the ionized gas, spanning emission measures from 1 pc cm^{-6} (diffuse medium) to 10^3 pc cm^{-6} (HII regions).

Keywords: dust, extinction, HII regions, Magellanic Clouds

1 Introduction

The Large Magellanic Cloud (LMC), located at a distance of 50 kpc has an advantageous almost face-on viewing angle, with small contamination along the line of sight (LOS). Assessing the presence of dust in the ionized gas phase is very important given that the optical properties of dust grains can vary with the properties of the local environment. In the ionized medium, due to the proximity of the ionized gas with UV sources, such as O and B stars, and the cumulative effect of shock fronts, changes in the optical dust properties are indeed expected. For instance, depletion of polycyclic aromatic hydrocarbons (PAHs) has been observed towards individual HII regions. However, this phenomenon does not appear to be systematic. We present a systematic investigation of the dust properties associated with the ionized gas in the LMC. The full description of this analysis is presented in Paradis et al. (2011a).

2 Data

We use the following data set:

- Infrared: Spitzer data as part of the SAGE program (Meixner et al. 2006), from 3.6 to 160 μm , combined with IRAS 12-100 μm ($4'$ angular resolution).
- HI: 21 cm integrated intensity map (W_{HI}), obtained from the combined ATCA ($1'$ Kim et al. 2003) and Parkes data ($4'$ Staveley-Smith et al. 2003). Assuming the gas is optically thin, we derive: $N_{\text{H}} = 1.82 \times 10^{18} W_{\text{HI}}$.

¹ Universite de Toulouse; UPS-OMP, IRAP, Toulouse, France

² CNRS; IRAP, 9 av. du Colonel Roche, BP 44346, 31028, Toulouse, cedex 4, France-Spitzer Science Center, California Institute of Technology, 1200 E. California Blvd, Pasadena, CA 91125, USA

³ Spitzer Science Center, California Institute of Technology, 1200 E. California Blvd, Pasadena, CA 91125, USA

⁴ Institut d'Astrophysique Spatiale, 91405 Orsay, France

⁵ Department of Astrophysics, Nagoya University, Chikusa-ky, Nagoya 464-8602, Japan

⁶ Department of Physical Science, Osaka Prefecture University, Gakuen 1-1, Sakai, Osaka 599-8531, Japan

- CO: $^{12}\text{CO}(J=1-0)$ integrated intensity map (W_{CO}), second survey (2'6, Fukui et al. 2008) obtained with the 4-m radio NANTEN telescope. We compute $N_H = 2X_{\text{CO}}W_{\text{CO}}$, using X_{CO} values deduced from virial masses for each cloud (Fukui et al. 2008).
- H α : SHASSA survey (Gaustad et al. 2001), with an angular resolution of 0'8. We compute $N_H = 1.37 \times 10^{18} I_{\text{H}\alpha} n_e$ (assuming 1R corresponds to an emission measure of $2.25 \text{ cm}^{-6} \text{ pc}$).
- Radio at 5 GHz: Parkes data at a resolution of 5'6 (Filipovic et al. 1995). The data are transformed in H α emission using: $T_b/I_{\text{H}\alpha} = 8.396 \times 10^3 \nu_{\text{GHz}}^2 \nu_{\text{GHz}}^2 T_4^{0.667} 10^{0.029/T_4} (1 + 0.008)$ (Dickinson et al. 2003).

3 Regimes of the ionized gas

We consider three regimes of the ionized gas, from diffuse H $^+$ to bright HII regions, determined using the pixel brightness distribution of the SHASSA map and the Kennicutt & Hodge (1986) catalog of HII regions:

- Case1: diffuse ionized gas $0.8 \text{ R} < \text{H}\alpha < 7 \text{ R}$, $n_e = 0.055 \text{ cm}^{-3}$ (intermediate value from Haffner et al. (2009))
- Case 2: typical HII regions $7 \text{ R} < \text{H}\alpha < 106 \text{ R}$, we derived $n_e = 1.52 \text{ cm}^{-3}$
- Case 3: bright HII regions $106 \text{ R} < \text{H}\alpha < 1000 \text{ R}$, we derived $n_e = 3.98 \text{ cm}^{-3}$

4 Extinction in bright HII regions

The comparison between the SHASSA map and the Parkes data (converted to H α emission) highlights that for 88% of pixels of case 3, the H α -Parkes data are higher than the SHASSA ones, with a median ratio equal to 1.6. To explain such a discrepancy, we invoke extinction as a source of attenuation in the SHASSA map. In our analysis, the factor 1.6 of discrepancy would induce an extinction value in the SHASSA map of 0.51 mag in bright HII regions. Following O'Donnell (1994), Dickinson et al. (2003) estimate the absorption in the H α as $A(\text{H}\alpha) = 0.81A(V)$. The corresponding extinction of LMC bright HII regions in the visible is $A(V)=0.63 \text{ mag}$.

5 Decomposition of the IR emission and modeling

In the LMC, Bernard et al. (2008) evidenced the existence of a large FIR excess with respect to the atomic, molecular and ionized gas phases, which they attributed to either molecular gas with no associated CO emission or to optically thick HI. Following Paradis et al. (2011b), we decompose the IR emission at each wavelength and for each regime, as a function of the atomic, molecular and ionized gas column density:

$$I(\lambda) = a(N_H^{\text{HI}} + N_H^{\text{X}}) + bN_H^{\text{CO}} + cN_H^{\text{H}^+} + d \quad (5.1)$$

with N_H^{X} the column density in the FIR excess component. In the following, we refer to the sum of the atomic and FIR excess components as the atomic phase.

The H α map is used for the three regions as a tracer of the H $^+$ column density, whereas radio map at 5 GHz is used only for case 3 due to its lower sensitivity.

The thermal fraction of the 5 GHz map (f_{th}) has been estimated, using:

$$\frac{S_5}{S_{1.4}} = f_{\text{th}} \left(\frac{\nu_5}{\nu_{1.4}} \right)^{-\alpha_{\text{ff}}} + (1 - f_{\text{th}}) \left(\frac{\nu_5}{\nu_{1.4}} \right)^{-\alpha_{\text{sync}}} \quad (5.2)$$

where S_5 and $S_{1.4}$ are the total flux densities at 5 and 1.4 GHz, and α_{ff} and α_{sync} are the free-free and synchrotron spectral indices, taken equal to 0.1 and 0.6 respectively. We derive an average thermal fraction of 0.85 in bright HII regions of the LMC.

First, we assume a single radiation field along the LOS. We model the spectral energy distributions (SEDs) associated with each phase of the gas using DustEM (Compiègne et al. 2011, see Fig. 2). We impose, for dust emission associated with the atomic and molecular phases, as well as for dust emission associated with the diffuse ionized gas in case 1, the same interstellar radiation field (RF) hardness as for the solar neighborhood (Mathis et al. 1983). However for cases 2 and 3, dust in the ionized phase is associated with typical and bright

HII regions, and therefore it is essentially heated by local hot stars. For these cases, using the GALEV code*, we have generated an UV/visible spectrum of young stellar clusters of 4 Ma. Second, we test our results using a combination of several RF intensities and hardnesses along the LOS. For this purpose we apply the Dale et al. (2001) model that considers a local SED combination by assuming a power-law distribution of dust mass subjected to a given heating intensity.

6 Results

We evidence for the first time dust emission associated with the ionized gas of the LMC. We report:

- A systematic warmer dust temperature in the H⁺ phase compared to the HI and CO phases
- An emissivity in the diffuse H⁺ of 2.3×10^{-26} cm²/H at 160 μm, lower than Galactic values by a factor higher than the metallicity ratio between the two galaxies. This result suggest different properties of dust in the H⁺ gas of the LMC, compared to our Galaxy.
- A significant decrease of the PAH relative abundance in the H⁺ phase of all cases (1, 2, 3) with respect to the HI and CO phases, with a larger difference between the phases for cases 2 and 3. We interpret this result as due to PAH destruction caused by the increased radiation field in the H⁺ phase, although the origin of this phenomenon is still under investigation.
- The survival of the PAHs in the molecular phase. In addition, when one compares bright with typical HII regions, the H⁺ phase shows an enhancement of the very small grains relative abundance by more than a factor of 2.
- An important increase of a near-infrared continuum in the H⁺ phase, which does not seem to correlate with PAH emission.
- A systematic increase of the dust emission going from the diffuse medium to bright HII regions, for all gas components.

References

- Bernard, J.-P., et al. 2008, ApJ, 136, 919
Compiègne, M., et al. 2011, A&A, 525, 103
Dale, D. A., et al. 2001, ApJ, 549, 215
Dickinson, C., Davies, R. D., and Davis, R. J. 2003, MNRAS, 341, 369
Filipovic, M. D. et al. 1995, A&AS, 111, 311
Fukui, Y., et al. 2008, ApJS, 178, 56
Gaustad, J. E., McCullough, P. R., Rosing, W., & van Buren, D. 2001, PASP, 113, 1326
Haffner, L. M., et al. 2009, RvMP, 81, 969
Kennicutt, R. C., & Hodge, P. W. 1986, ApJ, 306, 130
Kim, S., et al. 2003, ApJS, 148, 473
Mathis, J. S., Mezger, P. G., & Panagia, N. 1983, A&A, 128, 212
Meixner, M., et al. 2006, AJ, 132, 2268
O'Donnell, J. E. 1994, ApJ, 422, 158
Paradis, D. et al. 2011a, ApJ, 735, 6
Paradis, D. et al. 2011b, AJ, 141, 43
Staveley-Smith, L., et al. 2003, MNRAS, 339, 87

*available at <http://www.galev.org>

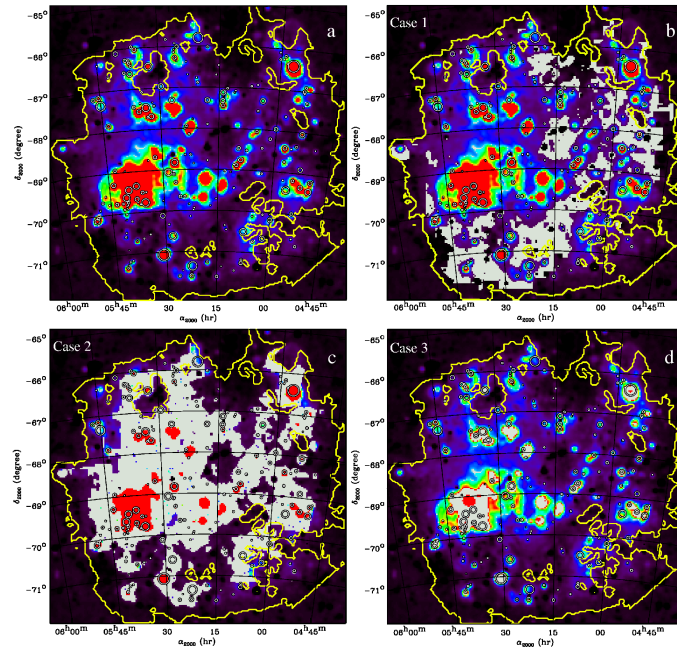


Fig. 1. SHASSA H α map (a) and spatial locations of pixels (in gray) selected for each case: (b) case 1 (diffuse ionized gas), (c) case 2 (typical HII regions), and (d) case 3 (bright HII regions). The overlaid symbols show the HII regions (Kennicutt & Hodge 1986). The range of the maps is [-8; 100] R.

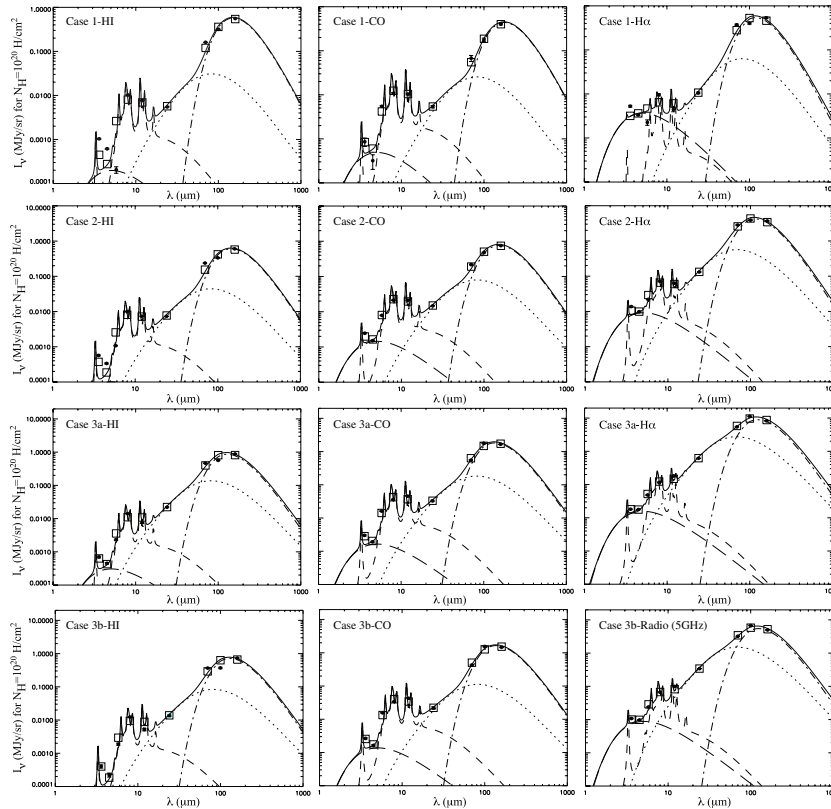


Fig. 2. Results of the fits obtained with the dust emission model (DustEM) assuming a single RF along the LOS. The squares show the fits of the model after applying the color-correction. Different curves denote the contributions from various grain populations: total (solid), big grains (dot-dash), very small grains (dot), polycyclic aromatic hydrocarbons (dash) and a near-infrared continuum (long dash).

GALACTIC DUST PROPERTIES

D. Paradis^{1,2} and the Hi-GAL team

Abstract. Recent studies have shown evidence for variations in the dust emissivity law with temperature and wavelength. A recent dust emission model, called TLS model (for two-level systems), based on the description of the disordered internal structure of the amorphous dust grains has been developed to interpret observations in the far-infrared/submillimeter (FIR/submm) domain. A recent work focusing on the comparison between data of the diffuse interstellar medium seen by FIRAS-WMAP, as well as Archeops compact sources, with the TLS model allowed us to constrain the model parameters characterizing the general Galactic dust properties. Using the newly available Herschel/Hi-GAL data of the inner Galactic plane, we report a 500 μm emissivity excess in the peripheral parts of the Galactic plane, that can reach up to 20% of the emissivity. Results of the TLS modeling indicate significant changes in the dust properties from the central to peripheral parts of the Galactic plane.

Keywords: dust, extinction, infrared, ISM

1 Introduction

The study of the extended far-infrared (FIR) and submillimeter (submm) sky emission is a relatively young subject. This wavelength range is dominated by emission from large silicate-based interstellar grains, that dominate the total dust mass and radiate at thermal equilibrium with the surrounding radiation field. Their emission is often modeled using a modified black body at a given dust temperature and a fixed spectral index (β). The FIR/submm emission is routinely used to infer total gas column density and mass of objects ranging from molecular clouds to entire external galaxies, assuming that dust faithfully traces the gas. The data analysis of balloon (PRONAOS, Archeops) and satellite (FIRAS, WMAP) data has revealed that the FIR/submm emission cannot be explained by a simple extrapolation of the mid-IR emission:

- Dust emissivity appears to be wavelength-dependent with the emission spectrum flattening in the submm as compared to a modified black-body emission (Reach et al. 1995; Finkbeiner et al. 1999; Galliano et al. 2005; Paladini et al. 2007).
- Dust emissivity appears to be temperature-dependent, the emissivity spectra being flatter with the increasing dust temperature (Dupac et al. 2003; Désert et al. 2008).

Similar variations are now seen in laboratory spectroscopic experiments on amorphous dust analogs (Agladze et al. 1996; Mennella et al. 1998; Boudet et al. 2005). In particular, recent studies on three analogs of amorphous silicate Mg_2SiO_4 , MgSiO_3 , and $\text{CaMgSi}_2\text{O}_6$ reveal that this temperature and wavelength dependence of the absorption is observed on all the samples, but disappear when the same samples are annealed until crystallization (Coupeaud et al. 2011).

These analyses indicate that the T_d - β variations are likely to result from intrinsic dust properties that can be reproduced for the first time by a dust emission model such as the two-level systems (TLS) one.

Dust emissivity also appear to be environment-dependent, with an absolute emissivity value in the far-IR increased in cold and dense environments, as seen in the Taurus cloud (Stepnik et al. 2003; Planck Collaboration 2011a).

¹ Université de Toulouse; UPS-OMP, IRAP, Toulouse, France

² CNRS; IRAP, 9 av. du Colonel Roche, BP 44346, 31028, Toulouse, cedex 4, France

2 Evolution of dust properties from diffuse to dense medium

We analyze the dust emission from the outer Galactic plane using DIRBE, Archeops and WMAP data from 100 μm to 3.2 mm. We perform a correlation study of the FIR-mm emission with gas tracers in individual regions, and derive the average equilibrium temperature of large dust grains in both molecular and atomic phases in a set of regions along the Galactic plane. We use this temperature to derive the emissivity spectra for each phase and region.

We show that the emissivity spectra are always steeper in the FIR ($\lambda < 600 \mu\text{m}$) and flatten in the submm and mm. In regions where dust is significantly colder in the molecular phase than in the surrounding atomic medium, we produce an increase in the emissivity by a factor of $\simeq 3$ in the FIR (see Fig. 1, panel A). However, we showed that the emissivity increase is restricted to the FIR range; the emissivity spectra for the dust in the atomic and molecular phases become comparable again in the submm and mm wavelength range.

We interpret the FIR emissivity excess in the molecular clouds containing cold dust as being caused by the coagulation of large grains into fractal aggregates. The fact that the emissivities do reconcile in the submm could be related to the amorphous nature of the grains contained in the aggregates (see the following Section).

The full description of this analysis is presented in Paradis et al. (2009).

3 A model of amorphous dust: the TLS model

The recent TLS model (Mény et al. 2007) is based on the solid-state physics model developed to interpret specific properties of the amorphous solids identified in laboratory data. As a consequence, it is expected to apply with a high degree of universality, and not to be sensitive to the exact chemical nature of the dust. The disordered charge distribution (DCD) part of the model describes the interaction between the electromagnetic wave and acoustic oscillations in the disordered charge of the amorphous material (Vinogradov, 1960; Schlomann, 1964). This charge-disorder is observed on nanometer scale and is described here by a single charge correlation length. The TLS part models the disorder at atomic scale by a distribution of asymmetric double-well potential (ADWP). Each ADWP can be viewed as to close configurations of atoms or group of atoms in the disordered structure (Phillips 1972, 1987; Anderson et al. 1972). The TLS model describes the interaction of the electromagnetic wave with a simple distribution of two-level systems that represent the lowest states (ground states) of the ADWP. Both DCD and TLS phenomena have been first applied by Bösch (1978) to explain the observed temperature dependence of the absorption of some silica-based glasses in the FIR/mm. Three interaction mechanisms, which all depend on temperature, can occur in such a population of TLS sites: a resonant absorption, and two relaxation processes identified as “tunneling relaxation” and “hopping relaxation”.

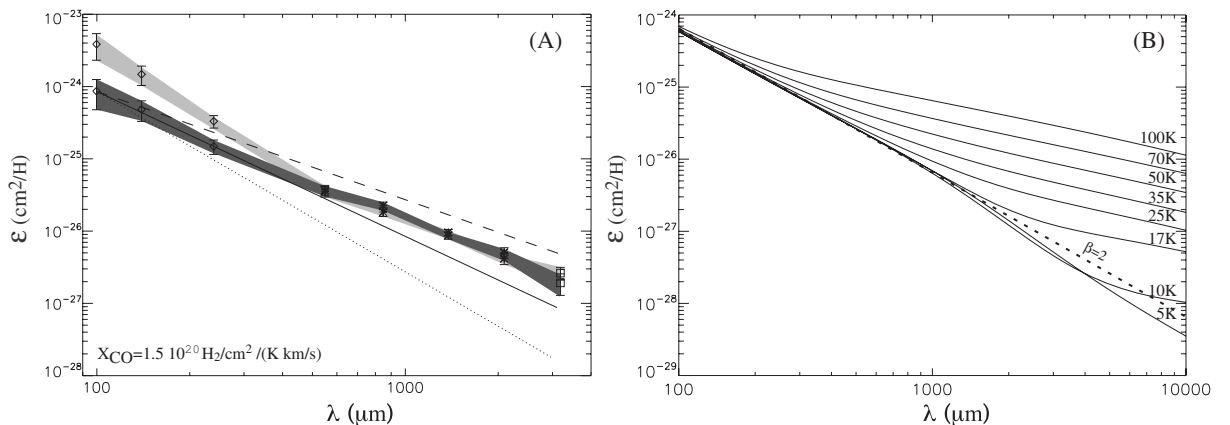


Fig. 1. Left: Panel (A): Median dust emissivity SEDs for regions with dust significantly colder in the molecular phase than in the surrounding atomic medium. The molecular emissivity has been scaled to match that of the atomic phase in the range 550 μm -3 mm. The DIRBE, Archeops and WMAP data correspond to diamond, star and square symbols, respectively. The shaded areas show the $\pm 1\text{-}\sigma$ dispersion around each emissivity SED, in dark and light grey for the atomic and molecular phase. For comparison, power-law spectra with $\beta=1.5$ (dashed), $\beta=2$ (solid) and $\beta=2.5$ (dot) are shown, normalized to the atomic emissivity at 100 μm . **Right:** Panel (B): Predicted emissivity with the TLS model, as a function of wavelength for different temperatures. The dashed line shows a λ^{-2} emissivity power-law.

The TLS model is compared to astrophysical data, such as the FIRAS/WMAP and Archeops data. The FIRAS/WMAP spectrum represents the diffuse interstellar medium in the stellar neighborhood, whereas the Archeops data characterize dust properties in a variety of compact sources, where a significant inverse relationship between the dust temperature and the emissivity spectral index had been shown. We performed a χ^2 minimization to determine standard values for the parameters of the TLS model selected to capture the spectral and temperature variations in the model. These free parameters are the dust temperature (T_{TLS}), the charge correlation length (l_c) that controls the wavelength where the inflection point between the two $\beta = 2$ and $\beta = 4$ ranges occurs, the intensity factor of the TLS processes (A) with respect to the DCD effect, and the intensity factor of the TLS/hopping process (c_Δ). Results indicate that emission in the submm/mm is dominated by the hopping relaxation. According to the model, the BG emission in the FIR/mm domain depends on wavelength and temperature, which is fundamental both for dust mass determination from FIR/submm measurements but also for component separation. Using the best-fit parameters ($T_{TLS} = 17.26$ K, $l_c = 13.4$ nm, $A = 5.81$, and $c_\Delta = 475$) allowing reproduction of both the emission from the diffuse medium and the compact sources, the model predicts significant β variations for temperatures between 5 and 100 K, with a maximum value of 2.6 at 2 mm. The TLS model is presently the only astrophysical model able to predict β variations with temperature and wavelengths, as observed in both observational and laboratory data. The dust emissivity can be seriously underestimated if its variations with temperature and wavelength are not taken properly into account (see Fig. 1, panel B), generally inducing overestimates of the dust mass. We also predict dust emissivities in the IRAS 100 μm , Herschel, and Planck bands for temperatures between 5 and 100 K, which are useful for comparison with the Planck and Herschel data.

The full description of this analysis is presented in Paradis et al. (2011a).

4 Dust properties along the Galactic plane using Hi-GAL data

We investigate variations in the spectral index of the dust emissivity, with temperature and wavelength, in the inner Galactic plane, using Herschel observations in two Hi-GAL ($160 \mu\text{m} < \lambda < 500 \mu\text{m}$) fields, centered at $l = 30^\circ$ and $l = 59^\circ$, acquired during the Herschel Science Demonstration phase, combined with the IRIS 100 μm data, $4'$ angular resolution. We fit the spectral energy distribution (SEDs) for each pixel of the two fields with two independent methods (least-square fit and maximum likelihood using a Monte Carlo Markov Chain algorithm, hereafter MCMC), deriving simultaneously the emissivity spectral index and the dust temperature by adjusting a modified blackbody function to the data. The results are similar with both methods. Using the MCMC method we computed the 68% likelihood contours for each point. We find a T_d - β inverse correlation, with the local variation going from 1.8 to 2.6 for temperatures between 14 and 23 K, shown for the first time in the inner Galactic plane. The median value of β is similar in both fields, equal to 2.3, slightly higher than the usual reference value of 2.

With the newly released Hi-GAL data combined with the IRIS 100 μm data, we perform an analysis of the emissivity variations along the Galactic plane. Changes in the emissivity spectra are interpreted in terms of the TLS model (see Fig. 2). We report:

- A 500 μm emissivity excess with respect to the predictions of a modified black-body model with $\beta=2$, in the peripheral parts of the Galactic plane ($35^\circ < |l| < 70^\circ$) covered by the data. This excess can represent up to 16% to 20% of the total emission. A similar excess has recently been evidenced in the Large Magellanic Cloud (Gordon et al. 2010; Galliano et al. 2011)
- Warmer dust temperatures in the central ($|l| > 35^\circ$) than in the peripheral Galactic regions.
- A flattening of the emissivity spectra in the range 100-500 μm with increasing dust temperature, that does not result from temperature mixture along the line of sight.
- The 500 μm emissivity excess can be explained by an increase in the intensity of the TLS processes, indicating a larger degree of amorphization of the grains in the peripheral parts of the Galactic plane.
- Dust properties along the Galactic plane seem to be different from those of the solar neighborhood, the excess being smaller in the latter than expected from an extrapolation of the Galactic plane behavior.

The full description of this analysis is presented in Paradis et al. (2011b).

5 Conclusions

Understanding emission of the big grains dust component is not easy since it varies with wavelength, temperature and environment. We evidenced variations in the emissivity from diffuse to dense medium, from the solar

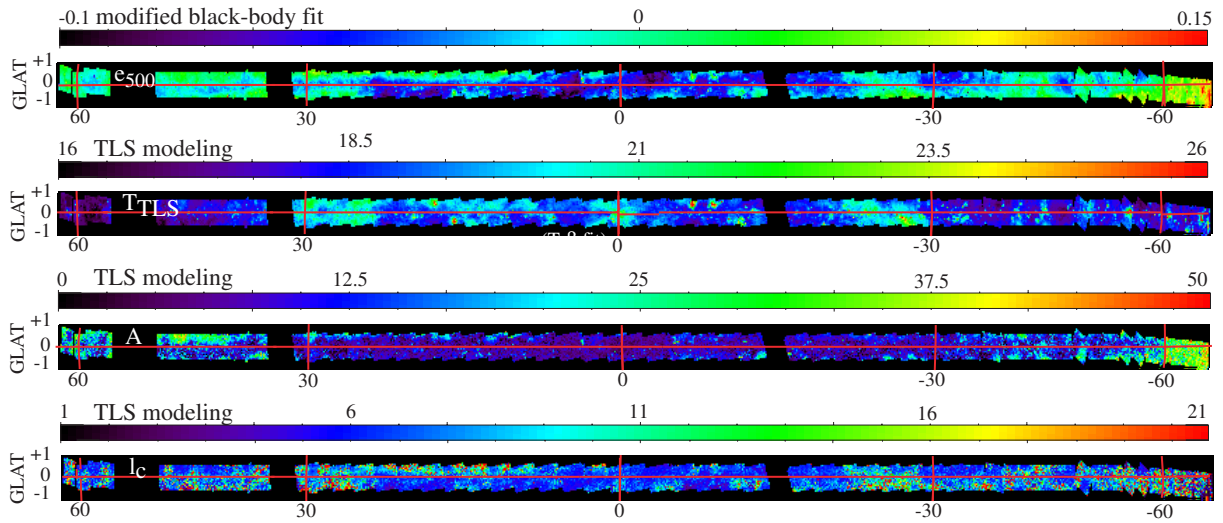


Fig. 2. From top to bottom: 500 μm emissivity excess (e_{500}), and results of the TLS modeling: dust temperature (T_{TLS}) in K, intensity of the TLS processes (A), correlation length (l_c) in nm.

neighborhood to the Galactic plane, and from the central to the peripheral parts of the inner Galactic plane. The presence of submm excess reveals some variations in the optical properties of the interstellar grains. Comparison between astrophysical observations/laboratory data and TLS modeling can lead to deduce more informations on the amorphous state of the grain itself.

References

- Agladze, N. I., Sievers, A. J., Jones, S. A., et al. 1996, *ApJ*, 462, 1026
 Anderson, P. W., Halperin, B. I., & Varma, C. M. 1972, *Phil. Mag.*, 25, 1
 Bösch, M. 1978, *Physical Review Letters*, 40, 879
 Boudet, N., Mutschke, H., Nayral, C., et al. 2005, *ApJ*, 633, 272
 Coupeaud, A., et al. 2011, *A&A*, accepted, arXiv1109.2758
 Désert, F.-X., Macías-Pérez, J. F., Mayet, F., et al. 2008, *A&A*, 481, 411
 Dupac, X., Boudet, N., Giard, M., et al. 2003, *A&A*, 404, L11
 Finkbeiner, D. P., Davis M., Schlegel D.J. 1999, *ApJ*, 524, 867
 Galliano, F., Madden, S. C., Jones, A. P., et al. 2005, *A&A*, 434, 867
 Galliano, F., et al. 2011, *A&A*, accepted
 Gordon, K., et al. 2010, *A&A*, 518, 89
 Mennella, V., Brucato, J. R., Colangeli, L., et al. 1998, *ApJ*, 496, 1058
 Mény, C., et al. 2007, *A&A*, 468, 171
 Paladini, R., et al. 2007, *A&A*, 465, 839
 Paradis, D., Bernard, J.-P., & Mény, C. 2009, *A&A*, 506, 745
 Paradis, D., et al. 2010, *A&A*, 520, 8
 Paradis, D., Bernard, J.-P., Mény, C., & Gromov, V. 2011a, *A&A*, in press, arXiv1107.5179
 Paradis, D., et al. 2011b, *A&A*, submitted
 Phillips, W. 1972, *J. Low Temp. Phys.*, 11, 757
 Phillips, W. 1987, *Rep. Prog. Phys.*, 50, 1657
 Planck Collaboration 2011a, *Planck early results 25*, *A&A*, accepted, arXiv1101.2037
 Reach, W. T., et al. 1995, *ApJ*, 451, 188
 Stepnik, B., Abergel, A., Bernard, J.-Ph., et al. 2003, *A&A*, 398, 551

SPADES: A STELLAR PARAMETERS DETERMINATION SOFTWARE

H. Posbic¹, D. Katz¹, E. Caffau², P. Bonifacio¹, L. Sbordone², A. Gomez¹ and F. Arenou¹

Abstract. With the large amounts of spectroscopic data available today and the very large surveys to come (e.g. Gaia), the need for automatic data analysis software is unquestionable. We thus developed an automatic spectra analysis program for the determination of stellar parameters: radial velocity, effective temperature, surface gravity, micro-turbulence, metallicity and the elemental abundances of the elements present in the spectral range. Target stars for this software should include all types of stars. The analysis method relies on a line by line comparison of the spectrum of a target star to a library of synthetic spectra. The idea is built on the experience acquired in developing the TGMET (Katz et al. 1998, Soubiran et al. 2003), ETOILE (Katz 2001) and Abbo (Bonifacio & Caffau 2003) software. The method is presented and the performances are illustrated with GIRAFFE-like simulated spectra with high resolution ($R = 25000$), with high and low signal to noise ratios (down to $\text{SNR} = 30$). These spectra should be close to what could be targeted by the Gaia-ESO Survey (GCDS).

Keywords: stellar parameters, spectra analysis, Giraffe

1 Introduction

One of the major applications of spectroscopy is the determination of stellar parameters like the radial velocity (V_r), effective temperature (T_{eff}), surface gravity ($\log g$), micro-turbulence (ξ), metallicity ($[\text{Fe}/\text{H}]$) and chemical abundances ($[\text{X}/\text{H}]$). The present and future large spectroscopic surveys are going to significantly increase the number of spectroscopic data to be analysed. A few examples are the Gaia-ESO Survey with about 160000 stars to be observed, Gaia with about 2×10^6 stars to be analysed for chemical abundances (Katz et al. 2004), RAVE with some 400000 stars observed so far (Boeche et al. (2011) and Siebert et al. (2011)) etc. The space mission Gaia will provide the largest survey ever, and that, in the decade to come. To analyse these quantities of data, automatic spectra analysis software is needed. Different families of software exist. A few examples are software like TGMET (Katz et al. (1998) and Soubiran et al. (2003), ETOILE (Katz 2001), MATISSE (Recio-Blanco et al. 2006), Abbo (Bonifacio & Caffau 2003) etc... The work presented is about the development of a new automatic stellar spectra analysis software. In its first version the software will be optimised for medium-resolution Giraffe spectra (VLT) and will thus be tested on Giraffe like spectra. The software is called SPADES (Stellar PArameters DEtermination Software) and is coded with Java.

2 SPADES

2.1 General idea

The software is based on the comparison between observed spectra and a grid of synthetic spectra (with known parameters). Contrary to many existing software, in SPADES, the comparison between spectra is not made over all the spectrum but around pre-selected lines. Another particularity is that the determination of the stellar parameters does not use any equivalent width measures but is based on profile fitting methods. Another important characteristic of SPADES is that it determines elemental abundances. The general idea is as follows:

For each parameter to be determined, one or several methods of determination (diagnostics) are available. One is chosen by the user. The list of diagnostics for each parameter are:

¹ GEPI, Observatoire de Paris, CNRS, Université Paris Diderot, Place Jules Janssen, 92190 Meudon, France

² Zentrum für Astronomie der Universität Heidelberg, Landessternwarte, Königstuhl 12, 69117 Heidelberg, Germany

- V_r : cross-correlation in direct space with a template
- T_{eff} : excitation equilibrium or Balmer lines profile fitting.
- $\log g$: ionization equilibrium or strong lines (e.g. MgIb green triplet) profile fitting.
- $[\text{Fe}/\text{H}]$: Fe lines profile fitting.
- $[\text{X}/\text{H}]$: X lines profile fitting.
- ξ : empiric calibration or nulling the $\Delta W = f(\text{reduced equivalent widths})$ function slope. ΔW being the residuals of the difference between the observed and synthetic line.

The diagnostics so far implemented and tested are detailed in the next section. Each of the parameters, T_{eff} , $\log g$, $[\text{Fe}/\text{H}]$ and ξ atmospheric parameters is determined one by one assuming all the others known. The process is iterated until convergence. The elemental chemical abundances are then determined.

2.2 Diagnostics

2.2.1 Effective temperature : T_{eff}

H α wings fit method. The first step is defining the reference grid to be used: a 1D (in the parameters space) reference spectra grid is defined. This grid varies over T_{eff} only, the other parameters being fixed to their input values. This grid is read or calculated by interpolation based on a pre-calculated reference spectra grid. The analysis is limited to the H α line, more generarely to a spectral range around this line. This range will be now called the ‘‘H α spectral domain’’. For each reference spectrum (T_{eff} value), the H α spectral domain continuum is fitted to the studied H α spectral domain continuum. An example of superposed continuum fitted H α spectral domains is presented in Fig. 1 (Left). The spectral domains differ by their T_{eff} .

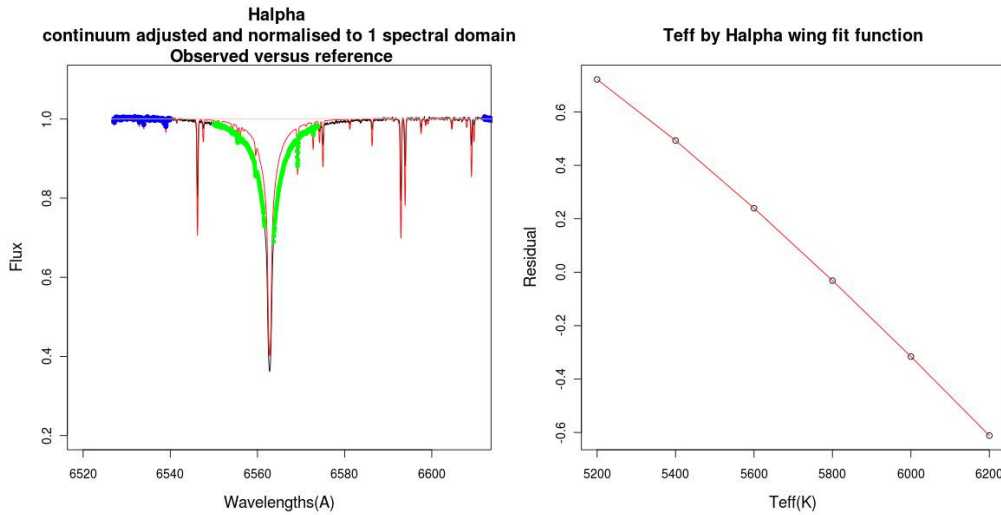


Fig. 1. Left: The reference spectrum H α spectral domain in red is superposed to the studied spectrum H α spectral domain in black. The continuum pixels are in blue. The H α wings pixels are in green. **Right:** The residuals as function of the reference spectra T_{eff} . The result T_{eff} is the value that nulls this function.

The wavelengths ranges used for the continuum fit are pre-defined. The corresponding pixels are in blue. The green pixels represent the H α wings. The wavelength limits of the wings are also pre-defined. Over the H α wings pixels the residual is calculated as: $s = \sum_{\text{pixels}} (x_{\text{obs}} - \tilde{x}_{\text{ref}})$. That is done for all the spectra in the 1D reference spectra grid. $s = f(T_{\text{eff}}(\text{ref}))$ is thus constructed. An example of this function is presented in Fig. 1 (Right). The result T_{eff} is the one that nulls this function.

Excitation equilibrium. In this method a list of pre-selected FeI lines is used. As in the previous method, a 1D (in the parameters space) reference spectra grid is defined with T_{eff} values varying around the input value while the other parameters are fixed to their input values. Around each central wavelength a spectral domain is cut in the reference and observed spectra. The line and continuum limits are determined automatically. For each reference spectrum, the spectral domains around the pre-selected lines are continuum fitted to the continuum of their corresponding spectral domain in the studied spectrum. An example of superposed, continuum fitted spectral domains is given in Fig. 2.

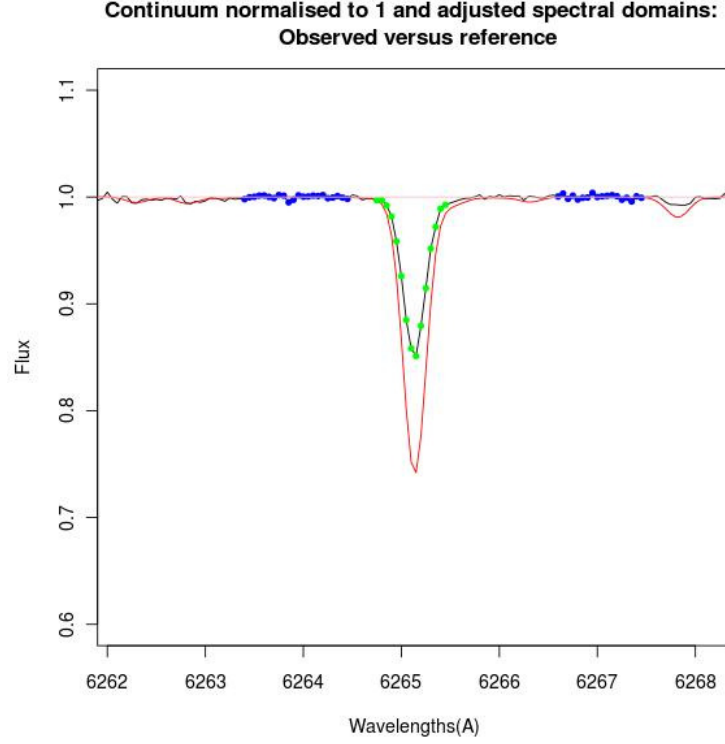


Fig. 2. In red the spectral domain of a FeI line in the reference spectrum superposed to the studied spectral domain of the same line, in black. The studied and the reference spectra are at different T_{eff} s which explains the difference between the line. The continuum pixels are in blue. The line pixels are in green.

For each reference spectral domain, and over the line pixels (green pixels) the residual is measured as such: $\Delta W = \sum_{\text{pixels}} -(x_{\text{obs}} - \tilde{x}_{\text{ref}})$.

This measurement is done for all the used lines. Let ΔW_n be the residual of the n th line. For each reference spectrum, the lines ΔW_n are plotted as a function of the lines respective excitation potentials ξ_n . An example of this function is given in Fig. 3 (Left).

For each reference spectrum (T_{eff} value) the slope a of this function is measured ($\Delta W_n = a * \xi_n + b$). Another function is then constructed: the $a = f(T_{\text{eff}})$ function. An example of this function is presented in Fig. 3 (Right). The result T_{eff} is the one that nulls the $a = f(T_{\text{eff}})$ function.

2.2.2 Gravity: $\log g$

Ionisation equilibrium. In this method the measurement made over the FeI and the FeII lines to be used are: $\Delta W_{\text{FeI}} = \sum_{\text{pixels}} -(x_{\text{obs}} - \tilde{x}_{\text{ref}})$ and $\Delta W_{\text{FeII}} = \sum_{\text{pixels}} -(x_{\text{obs}} - \tilde{x}_{\text{ref}})$.

The diagnostic to be analysed is : $\Delta = \Delta \bar{W}_{\text{FeI}} - \Delta \bar{W}_{\text{FeII}}$ where $\Delta \bar{W}_{\text{FeI}}$ (respectively $\Delta \bar{W}_{\text{FeII}}$) are the mean of the $\Delta W_{\text{FeI},n}$ s (respectively the $\Delta W_{\text{FeII},n}$ s) for all the FeI (respectively the FeII) lines. The result $\log g$ nulls the Δ as a function of the reference spectra $\log g$ function.

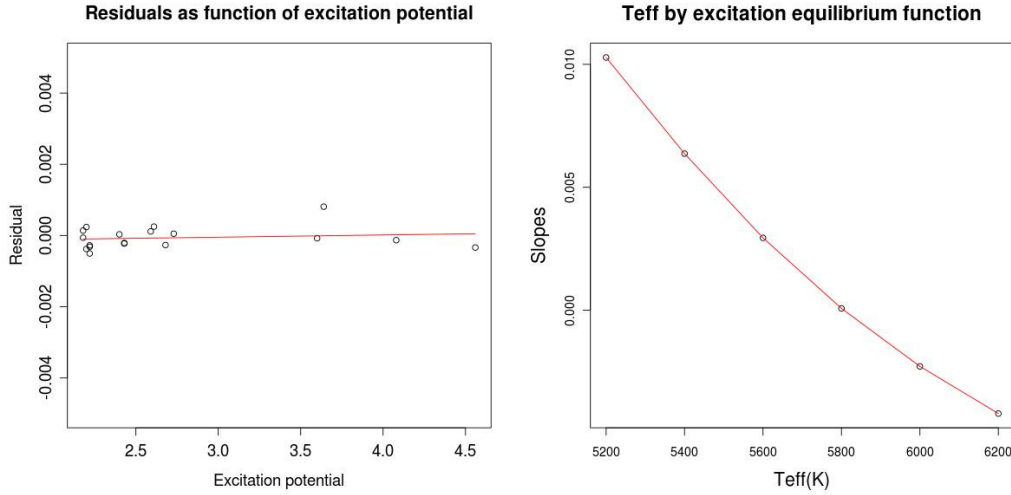


Fig. 3. Left: Line residuals (ΔW_n) as function of excitation potentials ξ_n for the reference spectrum with $T_{\text{eff}} = 5800$ K. **Right:** The slopes such as $\Delta W_n = a * \xi_n + b$ as a function of the reference spectra T_{eff} . The result T_{eff} is the value that nulls this function.

2.2.3 Metallicity and elemental abundances: [X/H]

Profile fit. In this method the measurement over the n lines of the X element to be used is : $s^2 = \sum_{pixels} (x_{obs} - \tilde{x}_{ref})^2 / \sigma^2$. The diagnostic to be analysed over all the X element lines is: $S^2 = \sum_{lines} \sum_{pixels} (x_{obs} - \tilde{x}_{ref})^2 / \sigma^2$. The result [X/H] is the one that nulls the S^2 as function of the reference spectra [X/H] function.

2.3 Tests and performances

SPADES was tested by Monte-Carlo over synthetic spectra with resolution $R = 25000$, effective temperature $T_{\text{eff}} = 5800$ K, gravity $\log g = 4.40$, metallicity $[Fe/H] = -1.0$, with individual abundances of Ca and Ni: $[Ca/H] = 0.0$ and $[Ni/H] = 0.0$. The tests were made for 2 signal to noise ratios (SNR): 30 and 100 (200 reference spectra for each SNR). The values of the dispersions at $1 - \sigma$ of the residuals (difference between the estimated and the real value) for each parameter are as follows (Table 1).

Table 1. Monte-Carlo simulations.

	$SNR = 30$	$SNR = 100$
T_{eff} (K)	31	9
$\log g$	0.14	0.05
[Fe/H] (dex)	0.04	0.0013
[Ca/H] (dex)	0.03	0.009
[Ni/H] (dex)	0.05	0.017

The mean results of these Monte-Carlo runs for each parameter show no bias. The dispersions are acceptable. Actually, for the T_{eff} determination using the $H\alpha$ method, the dispersion is at SNR of 100 (respectively 30) about 10 times (respectively 3 times) smaller than the systematic error (estimated by Cayrel et al. 2011) linked to the physics behind the models used. We note that, of course, the $H\alpha$ line is not always available for use: one reason is that it can simply not be in the spectral domain used, another is that this T_{eff} determination method cannot be used for all stars (cool stars for example). The excitation equilibrium method is then used.

3 Future work

The future work to be done on the software is :

- On the fly reference grid calculation: dynamic call of the SYNTHE software for calculating the reference grid directly from SPADES (completed at the time of writing the proceedings)
- Fix a method for determining micro-turbulence
- Determine the external errors (as opposed to the internal errors determined by Monte-Carlo). One of the methods will be the test on known stars (e.g. Sun)
- In its first version, the software will be fine-tuned to analyze medium to high resolution GIRAFFE spectra of Thick Disk stars .

References

- Boeche, C., Siebert, A., Williams, M., et al. 2011, ArXiv e-prints 1109.5670
- Bonifacio, P. & Caffau, E. 2003, *A&A*, 399, 1183
- Cayrel, R., van't Veer-Menneret, C., Allard, N. F., & Stehlé, C. 2011, *A&A*, 531, A83
- Katz, D. 2001, *Journal of Astronomical Data*, 7, 8
- Katz, D., Munari, U., Cropper, M., et al. 2004, *MNRAS*, 354, 1223
- Katz, D., Soubiran, C., Cayrel, R., Adda, M., & Cautain, R. 1998, *A&A*, 338, 151
- Recio-Blanco, A., Bijaoui, A., & de Laverny, P. 2006, *MNRAS*, 370, 141
- Siebert, A., Williams, M., Siviero, A., et al. 2011, *VizieR Online Data Catalog*, 3265, 0
- Soubiran, C., Bienaymé, O., & Siebert, A. 2003, *A&A*, 398, 141

THE PHYSICAL PARAMETERS OF THE LOW-MASS MULTIPLE SYSTEM LHS1070 FROM SPECTRAL SYNTHESIS ANALYSIS

A. S. Rajpurohit¹, C. Reylé¹, M. Schultheis¹, C. Leinert² and F. Allard³

Abstract. LHS1070 is a nearby multiple systems of low mass stars. It is an important source of information for probing the low mass end of the main sequence, down to the hydrogen-burning limit. The primary of the system consist of a mid-M dwarf and two components are late-M to L dwarf, at the star-brown dwarf transition. It makes it even more valuable to understand the formation of dust in cool stellar atmospheres. This work aims to determine the fundamental parameters of LHS1070 and to test recent model atmospheres. We compared the well calibrated data in the optical and infra-red with synthetic spectra computed from recent cool stars atmosphere models. We derived the physical parameters T_{eff} , radius and $\log g$ for three components of LHS1070. The models which include the formation and settle of dust are able to reproduce and describe the main features of the visible to IR spectra of the components.

Keywords: stars: atmospheres, stars: fundamental parameters, stars: low-mass

1 Introduction

M dwarfs are the most numerous stars in our Galaxy which makes them an important probe for our galaxy as they carry fundamental informations regarding the stellar physics, galactic structure and formation, and its dynamics. In addition the existence of brown dwarfs or planets being discovered and confirmed around M-dwarfs (Butler et al. 2004; Bonfils et al. 2005) plays an important role for the knowledge of the formation of brown dwarfs and planets. The energy distribution in these late type stars is governed by various absorption molecular bands like TiO, CaH, VO in the optical and H₂O and CO bands in the infrared. The presence of these molecular bands dominates the spectrum in the visible and infared. This affects the resulting opacity in the photosphere of these stars and leads to an onset of the dust formation in the photospheric layers (Tsuji et al. 1996a,b; Allard et al. 1998). In particular, the wavelength region from 6300 Å to 9000 Å encompasses a number of TiO and VO bands which are blended with other lines and leaves no window on the true continuum. Because of their complex atmosphere, a reliable way to determine the physical parameters of M-dwarfs is to compare the observed spectra with synthetic spectra. Atmospheric modeling allows us to determine the fundamental reason for such changes in the cool atmosphere and also helps to determine the physical parameters of the M-dwarfs (Bean et al. 2006).

LHS1070 is a low mass multiple system of cool dwarfs discovered by Leinert et al. (1994), with visual magnitude 15. It is located at a distance of 7.72 ± 0.15 pc from the Sun (Costa et al. 2005) and is considered as a member of the old disk population with a probable age of several Ga (Leinert et al. 2001). The spectral type for the A, B and C components was found to be M5.5-M6, M8.5 and M9-M9.5 (Leinert et al. 2000). Components A,B, and C were the faintest stars within 10 pc from the Sun for which dynamical determinations of mass appeared possible. Leinert et al. (2001); Seifahrt et al. (2008) constrained the combined mass of components B and C and showed that their mass is very close to the hydrogen burning minimum mass, in good agreement with the masses of $0.080\text{-}0.083M_{\odot}$ and $0.079\text{-}0.080M_{\odot}$ derived by Leinert et al. (2000) from theoretical mass-luminosity relations (Baraffe et al. 1998; Chabrier et al. 2000).

¹ Université de Franche Comté, Institut UTINAM CNRS 6213, Observatoire des Sciences de l'Univers THETA de Franche-Comté, Observatoire de Besançon, BP 1615, 25010 Besançon Cedex, France.

² Max-Planck-Institut für Astronomie, Königstuhl 17, 69117 Heidelberg, Germany.

³ Centre de Recherche Astrophysique de Lyon, UMR 5574: CNRS, Université de Lyon, École Normale Supérieure de Lyon, 46 allée d'Italie, F-69364 Lyon Cedex 07, France.

The mass range spanned by the components of LHS1070 makes it a valuable system to study, for understanding the formation of dust in the cool atmospheres and the processes that occur at the star/brown dwarf transition. The comparison of the observed spectra of this system with recent atmospheric models helps to determine the stellar parameters (effective temperature, $\log g$, metallicity, radius) and provides an unique opportunity to better understand the lower end of the main sequence which is still poorly understood. LHS1070 is also a testbed to validate and define further developments of the atmospheric models.

2 Model Atmospheres

In this study, we have used the recent new BT-Settl models (Allard et al. 2010) for our analysis of LHS1070. These model atmospheres are computed with the PHOENIX code using hydrostatic equilibrium, convection using the Mixing Length Theory and a mixing length of $1/H_p=2.0$ according to results of radiation hydrodynamics (Ludwig et al. 2006), spherically symmetric radiative transfer, departure from LTE for all elements up to iron, the latest solar abundances by (Asplund et al. 2009), equilibrium chemistry, an important database of the latest opacities and thermochemical data for atomic and molecular transitions, and monochromatic dust condensates refractory indexes. Grains are assumed spherical and non-porous, and their Rayleigh and Mie reflective and absorptive properties are considered. The diffusive properties of grains are treated based on 2-D radiation hydrodynamic simulations, including forsterite cloud formation to account for the feedback effects of cloud formation on the mixing properties of these atmospheres Freytag et al. (2010). For this paper, we use the model grid described as follows: T_{eff} from 2000 K to 4000 K with 100 K step, $\log g = 5.0$ dex, 5.5 dex, $M/H = -1.5$ dex, -1.0 dex, -0.5 dex, 0 dex, +0.3 dex, +0.5 dex.

We have also used the grid of MARCS model atmosphere (Gustafsson et al. 2008). These models are hydrostatic and computed on the assumptions of Local Thermodynamic Equilibrium (LTE), chemical equilibrium, homogeneous plane-parallel stratification, and the conservation of the total flux (radiative plus convective; the convective flux being computed using the local mixing length recipe). The radiation field used in the model generation is calculated by assuming absorption from atoms and molecules by opacity sampling at approximately 100000 wavelength points over the range 1300 Å to 20 μm. This grid spans effective temperatures between $2550 \text{ K} < T_{eff} < 4050 \text{ K}$ in steps of 100 K, surface gravities of $5.0 < \log g(\text{cgs}) < 5.5$ in steps of 0.5 dex, a constant microturbulence of 2 km s^{-1} , and metallicities of $-0.5 < [\text{Fe}/\text{H}] < 0.25$ in steps of 0.25 dex and with an $[\alpha/\text{Fe}] = +0.2$ and +0.1 for the two lowest metallicities, respectively.

The model spectra are converted to absolute fluxes ($\text{erg cm}^{-2} \text{ s}^{-1} \text{ \AA}^{-1}$) at the position of the observer by multiplying with the dilution factor $[r/d]^2$ where the stellar radii are varying from $0.096R_{\odot}$ to $0.142R_{\odot}$ at a step of 0.002 by assuming the distance for the system 7.72 pc (Costa et al. 2005).

3 Physical Parameters Determination and Results

3.1 Effective Temperature and Radius

The effective temperature and radius have been calculated using a χ^2 minimization technique in an automatic interactive way in IDL program. In this technique we first rebin all the synthetic spectra both in optical and infrared to the same resolution as the observed spectra. For all of the observed spectra we then calculate the χ^2 value compared to the grid of the synthetic spectra in the wavelength range between 4500 Å to 2.4 μm. Due to the low S/N ratio of the observed spectra, we excluded the region below 4500 Å. In a second step a 3-D χ^2 map has been obtained for each of the component in the optical and in infrared as a function of temperature and radius. The 3-D χ^2 plot both in optical and in IR shows clearly the parameter space which gives an acceptable solution. We then compared the possible solutions in the optical and IR for each component. The common intersection between the solutions in the optical and infrared were considered as the best physically acceptable solution. The solution was then crossed checked by visual inspection by overplotting them with the observed spectra. The same procedure has been used with both BT-Settl and MARCS model. The derived parameters are given in Table 1. Figure 1 shows the best fit model superimposed to the observed optical and IR spectra for all the three components using BT-Settl and MARCS model.

3.2 Gravity and metallicity

Assuming the stellar radii from theoretical evolutionary model (Baraffe et al. 1998; Baraffe 1999), and the masses computed by Seifahrt et al. (2008), the $\log g$ of the components is found to be close to 5.3. We therefore

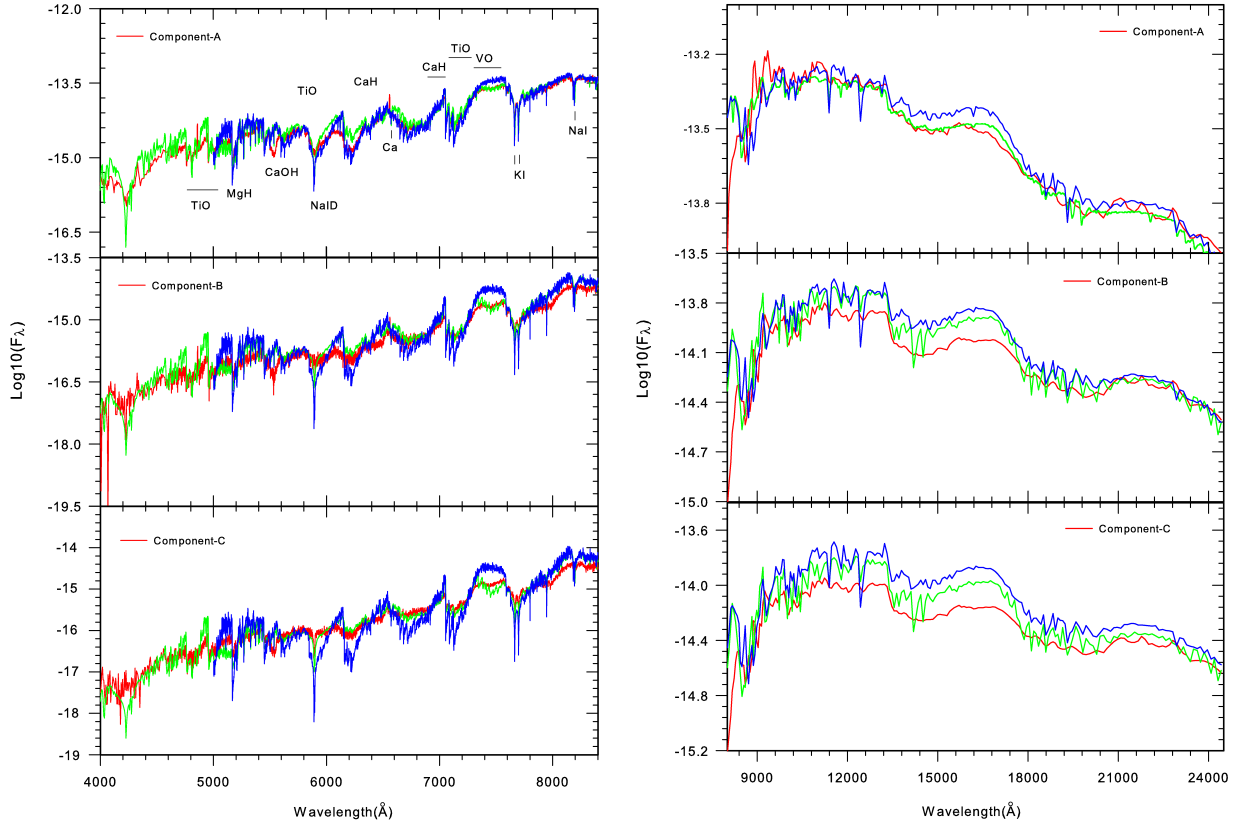


Fig. 1. Optical (left) and Infra-red (right) spectra of all three components. Red: observed spectra. Green: best fit BT-Settl model. Blue: best fit MARCS model. The parameters that give the best fit are given in Table 1.

Table 1. Derived parameters for the LHS1070 system. The uncertainties are drawn from the χ^2 maps and is 100 K for T_{eff} . The metallicity is assumed to be $[m/H] = 0$ and $\log g = 5.0$ to 5.5

Component	Spec. Type	BT-Settl model			MARCS model			
		$[m/H]$	T_{eff} (K)	$\log g$	Radius (R_{\odot})	T_{eff} (K)	$\log g$	Radius (R_{\odot})
A	M5.5-M6	0.0	2900	5.5	0.134 ± 0.005	2900	5.0	0.136 ± 0.005
B	M8.5	0.0	2500	5.5	0.102 ± 0.004	2600	5.0	0.098 ± 0.002
C	M9.5-M9	0.0	2400	5.5	0.098 ± 0.002	2500	5.0	0.100 ± 0.002

restrict our analysis with gravity of 5.0 and 5.5 dex. The surface gravity can be obtained by analyzing the atomic line like K I, Na I and metal hydride like CaH which are gravity sensitive. K I line line 7665 Å and 7699 Å is particularly useful gravity discriminant for M stars. The high density of low-mass stars cause an increase in the gravity and thus the pressure broadening will enhanced the line profiles. Figure 2 (left panel) shows such determination of the gravity for the component A from K I line using both BT-Settl and MARCS model. The strength of line suggests that some important dust opacities yet has to be included into the model. The best fit gives us a $\log g = 5.5$ for the BT-Settl models while $\log g = 5.0$ for the MARCS models. However both values agree within the uncertainties as found by Seifahrt et al. (2008).

The main indicator of the metallicity for all three component is the VO absorption band 7300 Å– 7600 Å which is very well reproduced by the BT-Settl model for the solar metallicity for all the components (see Figure 2, right panel).

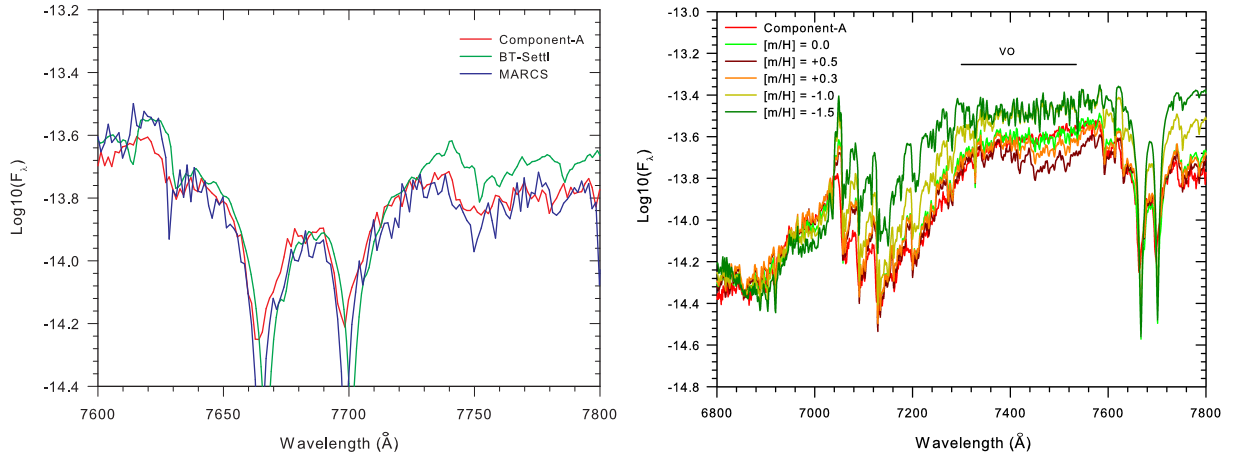


Fig. 2. Left: KI line in the component A (red) compared to the BT-Settl model (green) at $T_{eff} = 2900$ K, $\log g = 5.5$, $R_{\odot} = 0.134$ at solar metallicity along with the MARCS model (blue) at $T_{eff} = 2900$ K, $\log g = 5.0$, $R_{\odot} = 0.136$ at solar metallicity. **Right:** VO band observed in the component A (red) compared to the BT-Settl model at $T_{eff} = 2900$ K, $\log g = 5.5$, $R_{\odot} = 0.134$ at different metallicity

4 Conclusions

This paper presents the results from the spectral synthesis analysis of the LHS1070 triple system. We have determined the physical parameters T_{eff} , $\log g$, metallicity and radius of all the three component by comparing observed spectra with the synthetic spectra computed by BT-settl and MARCS models. The derived parameters agree with those derived using evolutionary models and observed bolometric luminosities (Baraffe et al. 1998; Chabrier et al. 2000). While for the hotter component A the overall agreement between the model and the spectra is satisfactory, we find systematic differences for model B and C. For both components the overall fit is better with the BT-Settl model than the MARCS model. However, we noticed several issues regarding the BT-Settl models. The MgH around 5200 \AA , NaI doublet at around 5900 \AA is far too strong as well as the CaH band at 7000 \AA while the CaOH band is missing. On the other side the TiO and VO band strengths are well reproduced by the models in the NIR part but the calculated fluxes are too high mainly in the J and H band. This may be due to the consideration of too hot deep layers from which the fluxes emerges. This indicates an inaccuracy in the atmosphere structure and also the treatment of the dust grains and opacities in the models as effective temperature decreases which was already proposed by Leggett et al. (2001). There is also clearly a discrepancy in the predicted water bands mainly in the J and H-band visible. Thus LHS1070 can be used as a testbed to validate and define further developments of the atmospheric models.

We acknowledge financial support from "Programme National de Physique Stellaire" (PNPS) of CNRS/INSU, France

References

- Allard, F., Alexander, D. R., & Hauschildt, P. H. 1998, in *Astronomical Society of the Pacific Conference Series*, Vol. 154, *Cool Stars, Stellar Systems, and the Sun*, ed. R. A. Donahue & J. A. Bookbinder, 63
- Allard, F., Homeier, D., & Freytag, B. 2010, *ArXiv e-prints astro-ph.SR 1011.5405*
- Asplund, M., Grevesse, N., Sauval, A. J., & Scott, P. 2009, *ARA&A*, 47, 481
- Baraffe, I. 1999, in *Astronomical Society of the Pacific Conference Series*, Vol. 173, *Stellar Structure: Theory and Test of Connective Energy Transport*, ed. A. Gimenez, E. F. Guinan, & B. Montesinos, p. 111
- Baraffe, I., Chabrier, G., Allard, F., & Hauschildt, P. H. 1998, *A&A*, 337, 403
- Bean, J. L., Sneden, C., Hauschildt, P. H., Johns-Krull, C. M., & Benedict, G. F. 2006, *ApJ*, 652, 1604
- Bonfils, X., Forveille, T., Delfosse, X., et al. 2005, *A&A*, 443, L15
- Butler, R. P., Vogt, S. S., Marcy, G. W., et al. 2004, *ApJ*, 617, 580
- Chabrier, G., Baraffe, I., Allard, F., & Hauschildt, P. 2000, *ApJ*, 542, 464

- Costa, E., Méndez, R. A., Jao, W.-C., et al. 2005, *AJ*, 130, 337
- Freytag, B., Allard, F., Ludwig, H.-G., Homeier, D., & Steffen, M. 2010, *A&A*, 513, A19
- Gustafsson, B., Edvardsson, B., Eriksson, K., et al. 2008, *A&A*, 486, 951
- Leggett, S. K., Allard, F., Geballe, T. R., Hauschildt, P. H., & Schweitzer, A. 2001, *ApJ*, 548, 908
- Leinert, C., Allard, F., Richichi, A., & Hauschildt, P. H. 2000, *A&A*, 353, 691
- Leinert, C., Jahreiß, H., Woitas, J., et al. 2001, *A&A*, 367, 183
- Leinert, C., Weitzel, N., Richichi, A., Eckart, A., & Tacconi-Garman, L. E. 1994, *A&A*, 291, L47
- Ludwig, H.-G., Allard, F., & Hauschildt, P. H. 2006, *A&A*, 459, 599
- Seifahrt, A., Röhl, T., Neuhäuser, R., et al. 2008, *A&A*, 484, 429
- Tsuji, T., Ohnaka, K., Aoki, W., & Nakajima, T. 1996a, *A&A*, 308, L29
- Tsuji, T., Ohnaka, K., Aoki, W., & Nakajima, T. 1996b, *A&A*, 308, L29

SIMULATING THE GALAXY AND APPLICATIONS TO THE PREPARATION OF THE GAIA MISSION

A. C. Robin¹, C. Reylé¹, CU2 and Gaia-DPAC consortium

Abstract. The preparation of the Gaia mission requires simulations of the stellar content of the Galaxy with detailed estimates of the intrinsic properties of the stars, as well as the overall structure of the Galaxy. We present a few distribution in luminosity class and spectral type of the stars visible by Gaia instruments and a new development of the model concerning the populations in the Galactic bulge.

Keywords: Galaxy:stellar content, Galaxy:evolution, Galaxy:structure

1 Introduction

The Gaia mission will give a detailed view, with unprecedented accuracy, of the stellar content of the Galaxy. It will encompass any model that we can make at the time being. However models are still useful to prepare the mission, for providing simulations of the intermediate and final catalogues of the mission, to test algorithms in good conditions before launch, and to provide testbeds for the data analysis methods. In order to achieve Gaia simulations, a coordination unit (CU2) has been established inside the Gaia Data Processing and Analysis Consortium (Gaia-DPAC) in order to provide to other members of the consortium the necessary simulations. CU2 has to implement the simulators which are three at this time : GIBIS, generating images, GASS, generating telemetry data, and GOG for intermediate and final catalogues simulations. All three simulators use two models to simulate the data : the Universe Model and the Instrument Model. One important aspect of the Universe Model concern the stellar content of the Milky Way, which will provide more than 90% of the sources in the Gaia instrument.

CU2 has chosen to base its Galaxy model on the Besançon Galaxy Model (Robin et al. 2003). However the DPAC needed more detailed simulations than in this standard model and improvements have been introduced in the scheme, like the simulation of binary and multiple stars, intrinsic and extrinsic (microlensing) stellar variabilities, simulations of extended objects (HII regions, planetary nebulae) and varying backgrounds (zodiacal light), as well as stars with exoplanets. An overall description of the Universe model can be found in Robin et al. (2011a).

The Gaia simulators have been used to estimate the number of stars of different kinds which are expected in the Gaia telescopes. Examples of these numbers are given here. These numbers are still subject to change before launch because our knowledge evolves and we shall attempt to introduce as much as reality as possible in the simulations in order that people trying to exploit the data can rely on it. The typical usages of these simulations are to test the softwares, in particular the classification schemes, that can be very sensitive to the frequency of the type of objects to classify.

In this paper we summarize the typical star count expectations in the Gaia instruments. In Sect. 2 we present the way the Galaxy stellar content is simulated for the Gaia preparation. In Sect. 3, we show estimations of the numbers and properties of stars that Gaia will see. And in Section 4 we show on-going work for improving the modelling of the Galaxy in the bulge region.

¹ Institut Utinam, CNRS UMR6213, Université de Franche-Comté, Observatoire de Besançon, Besançon, France

Table 1. Number of stars of each luminosity class over 1/8th of the sky up to limiting magnitude $G \leq 20$ and $G_{RVS} \leq 12$. Level 0 concerns single stars only. Level 1 is for objects in star systems with at least two components.

Luminosity class	$G \leq 20$			$G_{RVS} \leq 12$		
	Level 0	Level 1	Total	Level 0	Level 1	Total
Supergiants	14	32	46	14	32	46
Bright giants	15653	54492	70145	6595	21443	28038
Giants	1832214	3236786	5069000	220641	538672	759313
Subgiants	3253211	4526679	7779890	60142	114217	174359
Main Sequence	33223926	33752099	66976025	118576	189104	307680
PreMain sequence	41616	42429	84045	3067	5619	8686
White dwarfs	29140	59881	89021	7	3832	3839
Total	38395774	41672398	80068172	409042	872919	1281961

2 Modelling what Gaia will see

The Universe Model developed for the simulation of the mission is a set of algorithms for computing the positions at any time and observational properties of any objects expected to be observed by the Gaia instruments.

The distributions of these objects and the statistics of observables should be as realistic as possible for simulations to be usable for estimating telemetry, testing software, simulating images, etc. The algorithms have to be optimised in order that the simulations can be performed in reasonable time and can be redone when necessary. The complexity of the model increases with time during the preparation of the mission. The numbers presented here have been obtained from the cycle 10 version of the simulator (2011).

Simulated objects are: solar system objects (planets, satellites, asteroids, comets), Galactic objects (stars, nebulae, stellar clusters, diffuse light), extragalactic objects (galaxies resolved in stars, unresolved but extended galaxies, quasars and active galactic nuclei, supernovae). For each of these simulated objects one needs to have their full 3D spatial distribution together with their spectral characteristics (to be able to compute photometry and spectroscopy, stable or variable in time), and their motions (for astrometric computations and for spectral corrections).

In order to simulate the sky content, the sky is subdivided in small regions with a Hierarchical Triangular Mesh (HTM, see <http://skyserver.org/htm/>). The Universe Model presently uses the 3D extinction model from Drimmel & Spergel (2011). A complete description of the Universe Model used for Gaia simulations can be found in Robin et al. (2011a).

3 Estimations of the stellar content in the Gaia mission

From the Universe Model and from the generators of the final catalog (GOG) it is possible to evaluate the number of each kind of astronomical sources that Gaia will see. We here give a few numbers from a simulation of 1/8th of the sky with version 10 of the simulator. It concerns only stars in the Galaxy, excluding stars in neighbourhood galaxies and other astronomical sources. More up to date numbers for the whole sky will be presented in a forth coming paper (Robin et al., in prep). Table 1 gives the number of stars of each luminosity class and Table 2 the distribution in spectral type. The numbers are given for each hierarchy level. Level 0 concerns single stars only. Level 1 is for objects in star system with at least two components. Numbers are given for two limiting magnitude. At $G < 20$, the stars will have photometry and astrometry measured. At $G_{RVS} \leq 12$, stars will have very accurate radial velocity and abundance measurements from the spectrograph RVS. At the limiting magnitude of the RVS (between 16 and 17 depending on the spectral type) stars will have a rough estimate of the radial velocity and a metallicity index but no elemental abundances.

4 Recent model improvements : the bulge/bar population

Continuing our efforts to improve the realism of the model, and to find constraints on the formation scenario for each of the galactic components, we have turned our eyes towards the bulge/bar region to find out whether it is possible to deduce such constraints from large surveys. The first step is to establish the distribution of the light in 3D from analysis of 2MASS near infrared star counts. The mass distribution will be straightforwardly

Table 2. Number of stars of each spectral type over 1/8th of the sky up to limiting magnitude $G=20$, to $G_{RVS}=17$, and $G_{RVS}=12$. Level 0 concerns single stars only. Level 1 is for objects in star system with at least two components. L dwarf counts are included only up to L5.

Sp. Type	$G \leq 20$			$G_{RVS} \leq 17$			$G_{RVS} \leq 12$		
	Level 0	Level 1	Total	Level 0	Level 1	Total	Level 0	Level 1	Total
O	0	5	5	0	5	5	0	5	5
B	22957	88754	111711	16358	77367	93725	2681	15250	17931
A	424842	1186894	1611736	331214	963217	1294431	20679	66433	87112
F	7490020	9580207	17070227	3415861	5038394	8454255	80922	159564	240486
G	12864111	14079527	26943638	5153553	6186141	11339694	91053	170381	261434
K	12086280	12183767	24270047	4179879	4964899	9144778	176810	408939	585749
M	5477126	4480471	9957597	1549717	1324498	2874215	36211	45288	81499
L	12	12	24	4	7	11	0	0	0
AGB	516	361	877	503	346	849	426	271	697
Other	29910	72400	102310	1682	21028	22710	260	6788	7048
Total	38395774	41672398	80068172	14648771	18575902	33224673	409042	872919	1281961

deduced from it. Further, metallicities and kinematics can be attached to each population to understand the chemo-dynamical history of its formation. For doing so, we extended the approach made by Picaud & Robin (2004) to a wider area of the bulge ($-20^\circ < l < 20^\circ$ and $-10^\circ < b < 10^\circ$). A Monte-Carlo scheme is used to explore the multidimensional space of model parameters. These model parameters are the density function of the bulge population (a triaxial Ferrer ellipsoid defined by 3 scale lengths, 3 orientation angles, 2 parameters for the boxyness, a normalisation factor, and a cutoff radius), plus 2 parameters for the thin disc, which is a really important population in the plane towards the bulge. The thin disc is parametrized by a Einasto (1979) density law, with a scale length, and a scale length for the inner hole, as in Robin et al. (2003). The following equations give the shapes of the fitted bulge population which have been tested : $\rho_S = \rho_0 \operatorname{sech}^2(-R_s)$ or $\rho_E = \rho_0 \exp(-R_s)$ or $\rho_G = \rho_0 \exp(-R_s)^2$ with

$$R_s^{C_\parallel} = \left[\left| \frac{X}{x_0} \right|^{C_\perp} + \left| \frac{Y}{y_0} \right|^{C_\perp} \right]^{C_\parallel/C_\perp} + \left| \frac{Z}{z_0} \right|^{C_\parallel} \quad (4.1)$$

where (X,Y, Z) are the cartesian coordinates in the referential of the triaxial structure (X being the major axis, Y the second axis and the Z the third). The parameters C_\parallel and C_\perp are important to explore a wide range of shapes, from disk to boxy. This allows a great flexibility : one can even have a disk shape in the plane, together with a boxy projection vertically.

The counts are simulated assuming a bulge population of age 8 Ga from Padova isochrones Girardi et al (2002) for different metallicities. The age is not a very sensitive parameter in star counts from broad band photometry. For the simulation we use the Marshall et al (2006) 3D extinction model. The simulated counts are compared with observed counts in bins in the space ($K, J-K$) and a likelihood is computed. While attempting to fit a unique bulge population with a single shape, we realized that the resulting fit was not satisfactory in all the studied region. We then attempted to fit the population with the sum of two ellipsoids and find out a much better global fit over the whole bulge region. The counts and residuals from the data, and from the simulated counts for the 1-ellipsoid model and from the best fit model are given in Figure 1. We clearly see that the best 1-ellipsoid fit does not reproduce enough the boxyness of the bulge region, while the 2-ellipsoid model does.

5 Conclusions and further developments

The Gaia simulator using a Universe Model is able to predict the counts and the properties of the objects that Gaia will see during its mission. The total number will be about 1 billion of stars. This number depends on assumptions in the model, particularly on the assumed binary fraction and on the 3D extinction map. More detailed predictions will be provided in a forthcoming paper (Robin et al., in prep).

In parallel to providing simulations from the standard Galactic model, we attempt to improve the model and particularly towards the bulge region. We presented a new model which reproduces the 2MASS star counts in the region $-20^\circ < l < 20^\circ$ and $-10^\circ < b < 10^\circ$. This model is made of the sum of two Ferrer's ellipsoids, the first

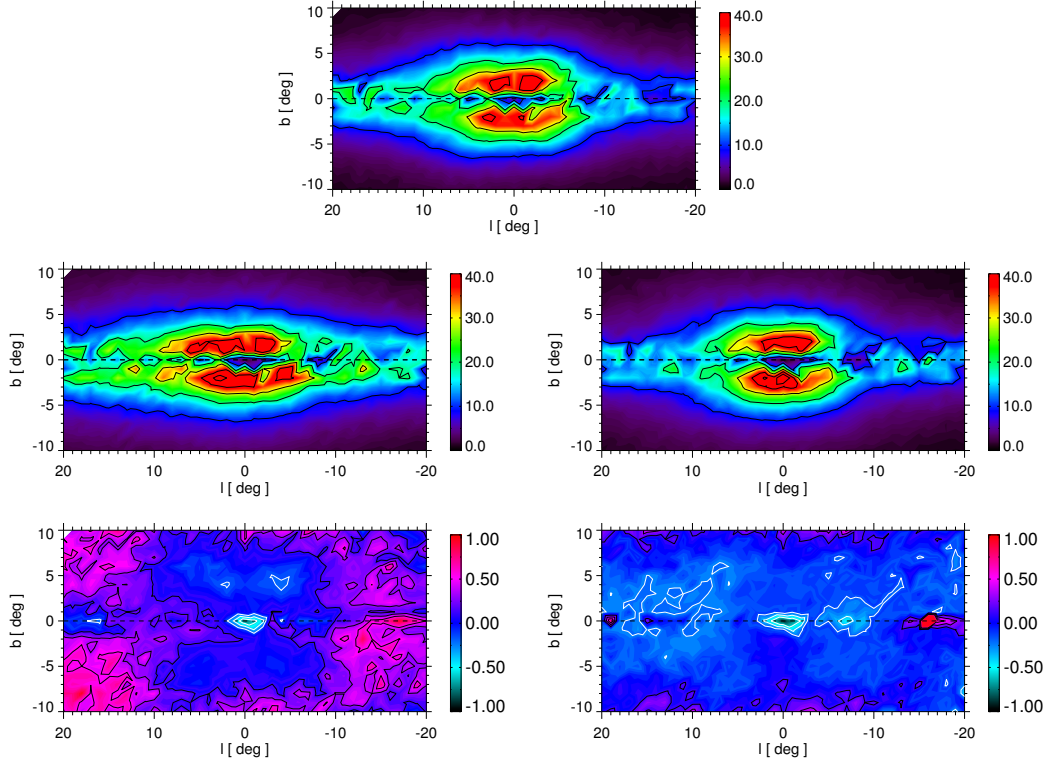


Fig. 1. Star counts up to limiting magnitude K_S from 2MASS data (top) compared with fitted 1 ellipsoid model (middle left), residuals $(N_{mod}-N_{obs})/N_{obs}$ (bottom left), 2-ellipsoids model (middle right) and its residuals (bottom right). In the residual map, contours are drawn at intervals of 20% model overestimate (black) and 20% model underestimate (white). Near the Galactic centre the nuclear bar population is missing in the model and thus appears in the residuals.

ellipsoid having a major axis pointing with an angle of about 13° with the sun-center axis and the scale lengths are 1.46/0.49/0.39 kpc. The second component is less massive (about 4% of the first one) and has larger scale lengths 4.44/1.31/0.80 kpc, but significantly contributes at medium latitudes. The agreement between this new models in terms of colour magnitude diagrams is very good. We also show that assuming that the first ellipsoid is inhabited by a population of solar metallicity and the second ellipsoid is a population of metallicity of -0.35 dex, we can very well reproduce the metallicity gradient which is found in Zoccali et al. (2008) along the minor axis of the bulge. From a preliminary comparison with kinematical data, we find out that the main component is the Galactic bar, and the second component can be either a classical bulge, or a population made from relics of merging, possibly related to the inner thick disc. The complete analysis and discussion can be found in Robin et al. (2011b).

References

- Drimmel, R. and Spergel, D. N., 2001, ApJ 556, 181
 Einasto J., 1979, IAU Symp. 84, The Large Scale Characteristics of the Galaxy, ed. W.B. Burton, p. x
 Ferrers, N. M., 1877, Quart. J. Pure Appl. Math., 14, 1
 Girardi, L., Bertelli, G., Bressan, A., Chiosi, C., Groenewegen, M.A.T., Marigo, P., Salasnich, B., Weiss, A. 2002, A&A, 391, 195
 Marshall D. J., Robin A. C., Reylé C., Schultheis M., Picaud S., 2006, A&A, 453, 635
 Picaud, S., Robin, A.C., 2004, A&A 428, 891
 Robin, A.C., Reylé, C., Arenou, F., et al, 2011, Gaia livelink GAIA-C2-TN-LAOB-AR-004-10
 Robin, A.C., Reylé, C., Derrière, S., Picaud S. 2003, A&A, 409, 523
 Robin, A.C, Marshall, D.J., Schultheis, M., Reylé, C., 2011, A&A, submitted
 Zoccali, M., Hill, V., Lecureur, A., Barbuy, B., Renzini, A., Minniti, D., Gómez, A., Ortolani, S. 2008, A&A, 486, 177

EVOLUTION OF OUR GALAXY AND OTHERS WITH THE HIGH-RESOLUTION VERSION OF THE CODE PÉGASE

B. Rocca-Volmerange¹, A. Sourie¹, A. Karampelas², M. Kontizas² and P. Tsalmanza²

Abstract. With the high performances of the Radial Velocity Spectrograph (RVS) on board of the ESA/Gaia mission, Gaia will detect nuclei and the contrasted zones of a large number of galaxies. With the resolution $R \sim 11500$ and the wavelength domain of the RVS (847nm – 874 nm) the main evolutionary parameter is the metallicity traced by the Ca triplet, Fe and Paschen lines. We propose to use the Munari et al., (2005) library with the galaxy evolution code PÉGASE, to constrain the star formation histories and to solve the degeneracy age-metallicity. High-resolution synthetic spectra might be used for educating the Support Vector Machine (SVM) allowing the automatic classification of observed targets.

Keywords: unresolved galaxies, Galaxy, galaxy nuclei, high resolution, metallicity, Calcium triplet

1 Introduction

For several years, an extended library of synthetic spectra of galaxies (Tsalmanza et al., 2009 and references therein) was built for training and testing the classification system (SVM) at the low resolution ($R \sim 200$) of Gaia prisms (BP/RP instruments). The significant fits of this library with the SDSS observations are shown in Fig. 1 for a series of classical types (elliptical, spiral, irregular) and Quenched Star-Forming Galaxies. The evolution code PÉGASE used for this library, in its available version PÉGASE.2 (www.iap.fr/pegase, Fioc & Rocca-Volmerange 1997), is based on the spectral stellar library BaSeL 2.2 suitable for the low resolution instruments of Gaia.

Then a first version of the code at high resolution: PÉGASE-HR (Le Borgne et al, 2004) was built with the observational stellar library ELODIE (Prugniel & Soubiran, 2004) including metallicity effect. The spectral resolution is $R = 10000$ and the optical range $\lambda = 400\text{--}680$ nm. The ELODIE library takes advantage of a fairly complete coverage of the Hertzsprung-Russell (HR) diagram on the range $[\text{Fe}/\text{H}] = -2$ to $+0.4$. PÉGASE-HR is a tool for exploring signatures of metallicity, age, and kinematics. Unhappily it does not cover the wavelength range of the RVS/Gaia.

We intend to improve the resolution of the synthetic library of galaxies computed with the code PÉGASE, on the wavelength domain of the RVS to interpret observations and to test the coherency at low and high resolutions.

2 The high resolution stellar library

The high resolution stellar library (Munari et al, 2005) is based on Kurucz's codes, extended on the wavelength range from 2500–10500 Å at the resolution of 1 Å/pix. The global library maps the whole HR diagram, but is limited to stars with $T_{eff} > 3500\text{K}$. We extract a selection of parameters (T_{eff} , gravity, $[\text{M}/\text{H}]$ and others). The entire library of synthetic spectra is accessible via the web, gently complemented for a given α/Fe range by R. Sordo and A. Vallenari (private communication). The contribution of cold stars to this library is in development.

¹ Institut d'Astrophysique de Paris, 98bis Bld Arago, 75014 Paris, France

² University of Athens, Greece

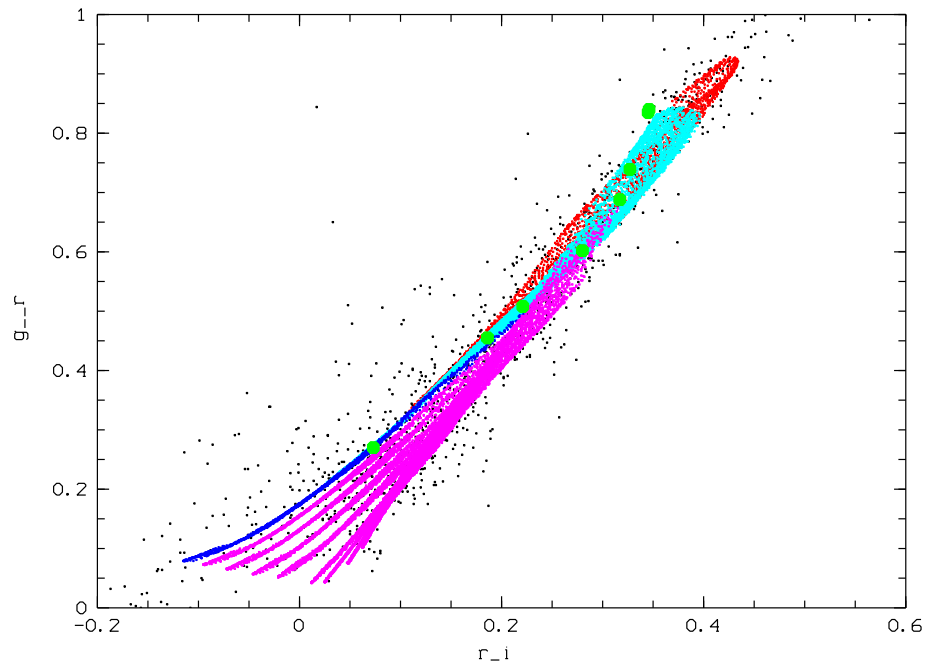


Fig. 1. The synthetic library of galaxies by types for Gaia compared to observations of the SDSS $g - r/r - i$ diagram.

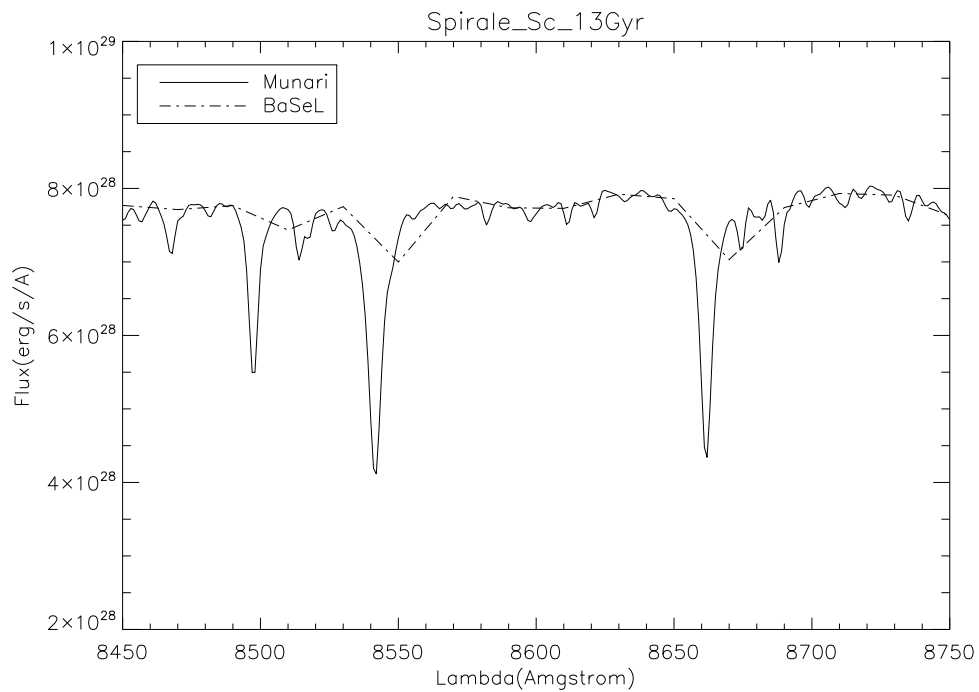


Fig. 2. Sc spiral SEDs at 13 Ga predicted by the code PÉGASE at low and high resolution through the RVS window.

3 Present status of the code PÉGASE-HR2

The new version of PEGASE-HR2, based on the theoretical library described in the previous section computes high- resolution single stellar populations (SSPs) from 10^7 to 2.10^{10} a. Evolution scenarios of galaxies are computed by a combination of SSPs giving predictions of Spectral Energy Distributions (SEDs) by types at all ages. The wavelength domain covers the RVS domain, allowing to follow the evolution of the Calcium triplet, Fe and Paschen H lines. The star formation laws are those adopted for the Gaia synthetic library at low resolution (Tsalmanza et al, 2009). They are fitting at best SEDs of the $z=0$ templates by galaxy types.

After checking the coherency of flux calibration between the code PÉGASE and the library by Munari et al, (2005), we compute SEDs for various galaxy types.

Fig. 2 compares the two SEDs at low and high resolutions for a typical spiral Sc galaxy of 13 Ga old. The lack of cold stars is hard to evaluate but its effect on the equivalent widths of absorption lines will be improved in the near future by a complement of cold star spectra. Predictions are extended to evolved populations from globular clusters, starbursts, spirals Sd to Sa and elliptical galaxies.

References

- Fioc, M., Rocca-Volmerange, B. 1997, A&A, 326, 950
Le Borgne, D., Rocca-Volmerange, B., Prugniel, P., Lançon, A., Fioc, M., Soubiran, C., 2004, A&A, 425, 881
Munari, U., Sordo, R., Castelli, F., Zwitter, T., 2005, A&A, 442, 1127
Prugniel, Ph., Soubiran, C., 2004, arXiv:astro-ph/0409214
Tsalmanza, P., Kontizas, M., Rocca-Volmerange, B., Bailer-Jones, C.A.L., et al., 2009, A&A, 504, 1071

PRELIMINARY DETERMINATION OF THE NON-LTE CALCIUM ABUNDANCE IN A SAMPLE OF EXTREMELY METAL-POOR STARS*

M. Spite¹, F. Spite¹, P. Bonifacio¹, E. Caffau^{1,2}, S. Andrievsky^{1,3}, S. Korotin³, R. Cayrel¹ and P. François¹

Abstract. The abundance ratios of the elements found in the extremely metal-poor stars (EMP) are a test of the yields predicted by the models of supernovae. For precise comparisons, it is of course preferable to avoid the approximation of LTE. The difference of LTE and NLTE profiles is displayed for three strong lines. The NLTE abundances of Ca are derived from the profiles of about 15 Ca I lines in the EMP giants and about 10 lines in the turnoff stars. The improved abundance trends are consistent with a [Ca/Fe] ratio constant vs. [Fe/H], and with a [Ca/Mg] ratio slightly declining when [Mg/H] increases. Also [Ca/Mg] presents a scatter larger than [Ca/Fe]. As far as the comparison with sulfur (another alpha element) is concerned we find that [S/Ca] presents a scatter smaller than [S/Mg].

Keywords: Galaxy:abundances, Galaxy:halo, Galaxy:evolution, Stars:abundances

1 Introduction

In the frame of the ESO Large Program “First Stars” 52 Extremely Metal-Poor Stars “EMP stars” have been observed with the high resolution spectrograph UVES at the ESO-VLT. In this sample 9 turnoff stars and 22 giants have $[\text{Fe}/\text{H}] < -3$.

These stars are the witnesses of the early Galaxy. The metals contained in their atmosphere have been formed by the first supernovae. The aim of this work was to find the chemical composition of the matter in the early Galaxy, to deduce the characteristics of the first supernovae and to constrain the nucleosynthetic processes. The analysis of the stars has been made under the LTE hypothesis and the main results of this analysis have been published in Cayrel et al. (2004) and Bonifacio et al. (2009).

However we have shown that the derivation of accurate element abundances requires that NLTE effects be taken into account (e.g. Andrievsky et al., 2010, 2011, Spite et al. 2011). We present here an attempt to determine the Ca abundance from NLTE computations.

2 Atmospheric parameters

The adopted values of the atmospheric parameters of the stars were discussed in detail in Cayrel et al. (2004) and Bonifacio et al. (2007).

The temperatures were deduced from the color indices, and also, for the turnoff stars, from the profile of the H α wings. The gravity was derived from the ionization equilibrium of iron and titanium (under the LTE hypothesis).

*Based on observations obtained with the ESO Very Large Telescope at Paranal Observatory, Chile (Large Programme “First Stars”, ID 165.N-0276(A); P.I.: R. Cayrel).

¹ GEPI, Observatoire de Paris, CNRS, Univ. Paris-Diderot, France

² Zentrum für Astron. der Univ. Heidelberg, Germany

³ Dept. of Astronomy and Astronomical Observatory, Odessa National Univ., Ukraine

3 NLTE Abundance of Calcium

In our sample of very metal poor stars about 15 Ca I lines and 2 Ca II lines (the 393.3nm and 866.2nm lines) can be measured.

The NLTE profiles of these lines were computed using a modified version of the MULTI code (Carlsson et al., 1986) described by Korotin et al. (1999).

Our model atom contains 70 levels of Ca I, 38 levels of Ca II, and the ground level of Ca III. The fine structure was taken into account for the levels 3d2D and 4p2P* of Ca II. The ionization cross-sections come from TOPBASE. Collisional rates between the ground level and the ten lower levels of Ca I are based on detailed results available from the R-matrix calculations of Samson & Berrington (2001). For Ca II, collisional rates have been found in Meléndez et al. (2007).

Collisions with hydrogen atoms were taken into consideration using the Steenbock & Holweger (1984) formula with a correction coefficient obtained by fitting the synthetic and the observed profiles of the Ca lines in the Sun and in some reference stars (Procyon, HD 122563 and ν Indi). This correction factor was found to be 0.1, in good agreement with Mashonkina et al. (2007).

At low metallicity the influence of the NLTE is very complex and depends on the line considered. In Fig. 1 we present the LTE and NLTE profiles of the 422.6nm line (Ca I) and the 393.3nm (Ca II K) and 866.2nm lines of Ca II for a giant with $[\text{Fe}/\text{H}] \approx -3$.

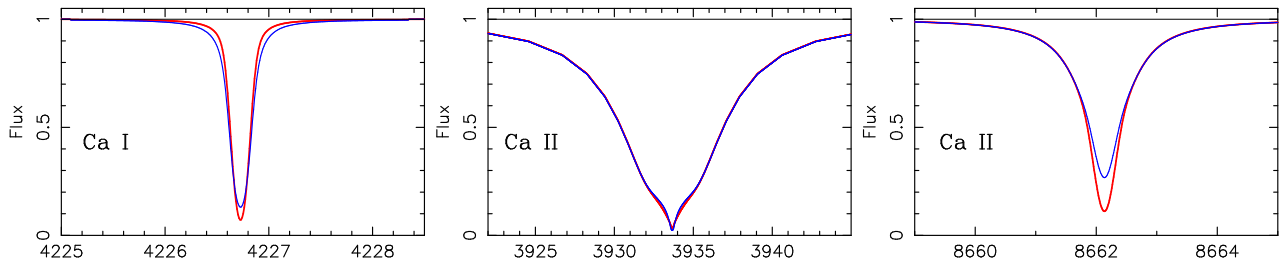


Fig. 1. Profiles of three Ca lines computed for a giant star with $[\text{Fe}/\text{H}] \approx -3$ with LTE (blue) and NLTE (red) hypotheses. **Left:** The profile of the resonance line of Ca I is affected by NLTE effects. The NLTE profile is narrower even in the wings. **Center :** The K Ca II line is practically not affected by NLTE. **Right:** The NLTE correction is important for the strong IR Ca II line, but the wings are not affected and a reliable calcium abundance can be deduced from these wings.

4 Results and Conclusion

The calcium abundance has been derived from about 15 Ca I lines in giants and 10 in dwarfs. In Fig. 2 we present the variation of $[\text{Ca}/\text{Fe}]$ vs. $[\text{Fe}/\text{H}]$ and of $[\text{Ca}/\text{Mg}]$ vs. $[\text{Mg}/\text{H}]$ for our sample of extremely metal-poor stars. (NLTE Mg abundance from Andrievsky et al., 2010).

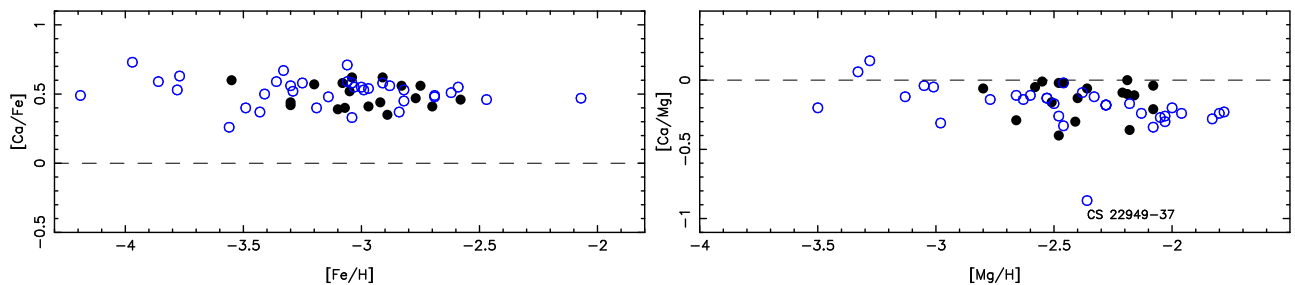


Fig. 2. **Left:** $[\text{Ca}/\text{Fe}]$ vs. $[\text{Fe}/\text{H}]$ and **(Right)** $[\text{Ca}/\text{Mg}]$ vs. $[\text{Mg}/\text{H}]$ at very low metallicity. Black dots, dwarfs, open symbols, giants. The calcium abundance of CS22949-37 is normal but it is Mg-rich and also C-rich, N-rich and O-rich (Depagne et al. 2002).

- In both cases there is a very good agreement between dwarfs and giants.
- In Fig. 2 (right) it seems that there is a slight increase of $[\text{Ca}/\text{Mg}]$ at very low metallicity but this trend is not significant (owing to the larger error on $[\text{Ca}/\text{Fe}]$ and $[\text{Ca}/\text{Mg}]$ at very low metallicity).
- Unexpectedly, the scatter of $[\text{Ca}/\text{Mg}]$ is a little larger than the scatter of $[\text{Ca}/\text{Fe}]$ although Ca and Mg are “ α elements” supposed to be formed in similar processes (unlike Fe).
- In the early Galaxy, if we consider the stars with $[\text{Fe}/\text{H}] < -2.7$: $[\text{Ca}/\text{Fe}] \approx +0.50 \pm 0.10$ dex and $[\text{Ca}/\text{Mg}] \approx -0.15 \pm 0.12$ dex.

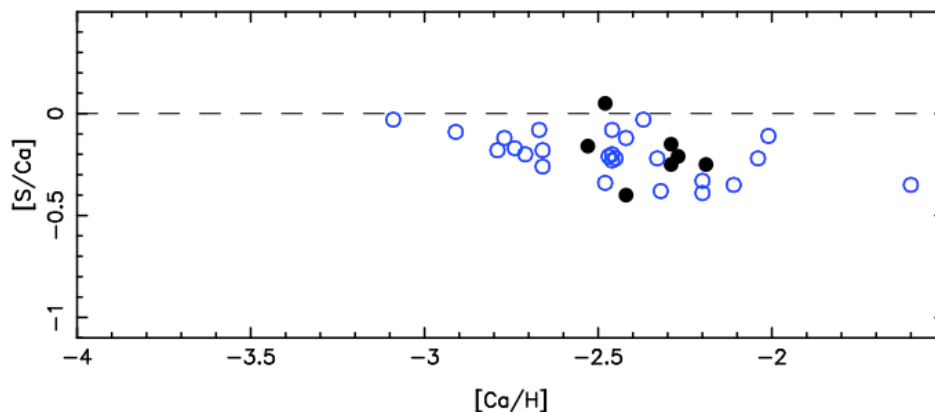


Fig. 3. $[\text{S}/\text{Ca}]$ vs. $[\text{Ca}/\text{H}]$. Symbols like in Fig. 2.

In Fig. 3 we present $[\text{S}/\text{Ca}]$ vs. $[\text{Ca}/\text{H}]$. S is also an “ α element”, its NLTE abundance has been taken from Spite et al. (2011). The correlation between the sulfur and the calcium abundance is very good, the spread of $[\text{S}/\text{Ca}]$ is small, smaller than the spread of $[\text{S}/\text{Mg}]$ (see Spite et al. 2011). This suggests that the production processes of S and Ca are more closely linked than the productions of S and Mg.

References

- Andrievsky S. M., Spite M., Korotin S. A., Spite F., Bonifacio P., Cayrel R. et al. 2010, *A&A*, 509, 88
 Andrievsky S. M., Spite F., Korotin S. A., François P., Spite M., Bonifacio P. et al. 2011, *A&A*, 530, 105
 Bonifacio P., Molaro P., Sivarani T., Cayrel R., Spite M., Spite F., Plez B. et al. 2007, *A&A*, 462, 851
 Bonifacio P., Spite M., Cayrel R., Hill V., Spite F., François P., Plez B. et al. 2009, *A&A*, 494, 1083
 Carlsson M. 1986, *Uppsala Obs. Rep.* 33
 Cayrel R., Depagne E., Spite M., Hill V., Spite F., François P., Plez B., et al. 2004, *A&A*, 416, 117
 Depagne E., Hill V., Spite M., Spite F., Plez B., et al. 2002, *A&A*, 390, 187
 Korotin S.A., Andrievsky S.M., Luck R.E. 1999, *A&A*, 351, 168
 Mashonkina L., Korn A.J., Przybilla N. 2007, *A&A*, 461, 261
 Meléndez M., Bautista M.A., Badnell N.R. 2007, *A&A*, 469, 1203
 Samson A.M., Berrington K.A. 2001, *ADNT*, 77, 87
 Spite M., Caffau E., Andrievsky S. M., Korotin S. A., Depagne E., Spite F., Bonifacio P. 2011, *A&A*, 528, 9
 Steenbock W., & Holweger H. 1984, *A&A*, 130, 319

A.S. GAIA: 2007-2011 AND PERSPECTIVES

C. Turon¹, F. Arenou¹ and M. Haywood¹

Abstract. The Action Spécifique Gaia (A.S. Gaia) has been created mid-2007 by the French National Institute for the Sciences of the Universe (INSU) with the aim of coordinating the French activities related to Gaia, the next ESA cornerstone mission, planned for launch by mid-2013. Various actions have been conducted in order to support 1) studies and ground-based observations mandatory for the calibration of Gaia instruments and for Gaia data analysis and 2) preparatory modelling and observations in view of enhancing the scientific return expected from Gaia data. Perspectives for the coming years are presented.

Keywords: Space observatory, Astrometry, Surveys, Galaxy: structure and evolution, Stars: fundamental parameters, ISM: 3-D structure, Minor planets and asteroids: orbits and fundamental parameters.

1 Introduction

Based on the experience gained with Hipparcos, the first space astrometry mission, launched by ESA in 1989 (Perryman et al. 1997), Gaia, the next ESA cornerstone mission, due for launch in 2013, continues the pioneering tradition of Europe space astrometry (Perryman et al. 2001). However, Gaia will surpass its predecessor by several orders of magnitude in terms of accuracy, limiting magnitude and volume of data. While Hipparcos had a predefined observing program, Gaia will systematically survey the sky, observing all objects brighter than magnitude 20, providing an unbiased view of the sky within a well-defined limit in flux. This combination of a complete census capability with an extreme astrometric accuracy and the simultaneous astrophysical characterisation of the observed objects by multi-epoch spectrophotometric and radial-velocity measurements makes Gaia a unique observatory with a very wide range of science goals. Detailed overviews of these science expectations and of the various questions raised by the huge mass of data expected from Gaia are available, among other references, in the proceedings of the Conference *Gaia at the Frontiers of Astrometry* (Turon et al. 2011).

Gaia is raising two types of challenge: the data processing (devoting one second per star would mean 30 years of data processing ...) and the data scientific exploitation: one billion objects will be repeatedly observed (about 74 observations per objects over the mission duration) with the astrometric, spectrophotometric and spectroscopic instruments on-board Gaia, with an extreme astrometric accuracy and an unprecedented homogeneity. While ESA is funding the satellite in its entirety - including the payload and operations - data reduction is mainly in charge of Member States, as is, of course, the data scientific exploitation. Since 2006, the Gaia Data Processing and Analysis Consortium (DPAC) has been appointed by ESA to process the raw data that will arrive from the Gaia satellite. It is a consortium of over 400 scientists all over Europe, chaired by François Mignard (Observatoire de la Côte d'Azur) and France is its first contributor with about 25 % of the members and manpower. In parallel, in many countries, national structures have been created to coordinate the national activities related to Gaia and prepare their respective astronomical communities for the exploitation of this unique and huge set of data. In France, the Action Spécifique Gaia (A.S. Gaia) has been created mid-2007 by the CNRS National Institute for the Sciences of the Universe (INSU). Also a European network, GREAT= Gaia Research for European Training, is being supported by ESF over the period 2010-2015.

The role of A.S. Gaia is multiple: to prepare the French astronomers, in strong co-operation with European and worldwide colleagues, to best exploit Gaia scientific data in their various domains of application (information about Gaia performance, support to related theory and modelling, support to complementary ground-based observations, including the design of new instrumentations); to support initiatives of dedicated workshops and international meetings; to support ground-based observations required by the Gaia data analysis and not otherwise funded; to represent the French Gaia community towards our National funding authorities and contribute to their roadmaps.

¹ GEPI, Observatoire de Paris, CNRS, Université Paris Diderot ; 5 Place Jules Janssen, 92190 Meudon, France

2 Meetings and workshops

2.1 Plenary meetings

After a kick-off meeting in December 2007, the annual meetings of SF2A are the occasion either of plenary meetings of A.S. Gaia or of common workshops with other *Programmes Nationaux* and other European professional astronomical societies: A.S. Gaia and complementarity with optical surveys (2008); A.S. Gaia and complementarity with asteroseismology (2009); Common workshops 1) *Stellar populations and modelling of the Galaxy: now and after Gaia and complementary ground-based observations*, A.S. Gaia - PNCG, 2) *Resolved Stellar Populations*, SF2A - Società Astronomica Italiana - PNCG - PNPS - A.S. Gaia (2010); Common workshop *Stellar and Interstellar physics for the modelling of the Galaxy and its components*, A.S. Gaia - SF2A - Sociedad Española de Astronomía - PNPS - PNCG - PCMI * (2011). In addition, SF2A plenary meetings have been the occasion to present various domains of application of Gaia: *The Solar System seen by Gaia: new perspectives for asteroid science* by P. Tanga (2008), *Applications de Gaia à la métrologie, la relativité et la physique fondamentale* by F. Mignard (2009), *Gaia : promises and expectations in the field of galactic astronomy* by M. Haywood (2010), and *Stellar physics with Gaia* by B. Plez (2011).

2.2 Topical workshops

Many topical workshops have been organised with the support of A.S. Gaia, in the various fields of application of Gaia data, with the aim of presenting the performance of Gaia astrometry, photometry and spectroscopy. The goals are to make the community well aware of the enormous potential of the mission and to encourage and coordinate efforts in modelling and ground-based observations, including the design of new instruments (for example wide-field multiplex spectrographs) and the establishment of networks of Observatories (e.g. for tracking solar system objects, particularly near-Earth objects), in view of a fruitful scientific exploitation of Gaia data. Information on these workshops, their program and the presentations are available from the A.S. Gaia website (<http://wwwhip.obspm.fr/AS/>).

- 2008: *Reference systems and QSOs*, Bordeaux Observatory, P. Charlot & G. Bourda, 24/10/2008. *Earth-based support to Gaia Solar System science*, Beaulieu sur Mer, P. Tanga & W. Thuillot, 27-28/10/2008.
- 2009: *Multiplex spectroscopy in complement to Gaia*, Nice Observatory, A. Recio-Blanco & V. Hill, 19-20/02/2009. *The Milky Way*, Besançon Observatory, A. Robin, C. Reylé & M. Shulteis, 5-6/11/2009.
- 2010: *Extragalactic Science with Gaia*, Institut d'Astrophysique de Paris, E. Slezak & J. Souchay, 14-16/06/2010. *Milieu Interstellaire*, Paris Observatory, R. Lallement & D. Marshall, 25-26/11/2010. *Gaia Follow-Up Network for the Solar System Objects*, Paris Observatory, W. Thuillot, P. Tanga & D. Hestroffer, 29/11- 01/12/2010 (proceedings: Tanga & Thuillot 2011).
- 2011: *Alertes Gaia*, Institut d'Astrophysique de Paris, M. Dennefeld, 27/05/2011. *Orbiting couples: 'Pas de deux' in the Solar System and the Milky Way*, Paris Observatory, F. Arenou & D. Hestroffer, 10-12/10/2011. *Relevés spectroscopiques en accompagnement à Gaia*, Paris Observatory, P. Bonifacio & C. Babusiaux, 17-18/11/2011.

Beside these workshops and plenary meetings, A.S. Gaia provides some support to a few international conferences organised by French colleagues in France or elsewhere in Europe.

3 Support to ground-based observations

Two categories of ground-based observations, or projects for new instrumentations, are being supported by A.S. Gaia: observations necessary for the data analysis to ensure the precision and accuracy of the future Gaia data (in the context of DPAC) and observations expected to complement Gaia data, with the aim of enhancing the scientific return.

*PNCG = Programme National Cosmologie et Galaxies, PNPS = Programme National de Physique Stellaire, PCMI = Programme National de Physique et Chimie du Milieu Interstellaire

3.1 Ground-based observations in support to Gaia data analysis

A.S. Gaia is supporting two types of ground-based observations in this category: observations for the calibration of the RVS, the Radial Velocity Spectrometer aboard Gaia, and astrometric observations:

- There is no calibration source on board the RVS and the zero-point of radial velocities has to be defined using reference stars and asteroids. The radial velocity stability of these objects must be assured to within 300 m s^{-1} until the end of the mission. 1420 candidate stars were selected and observed in both hemispheres (Crifo et al. 2010). The Northern part (with the Sophie spectrograph at Observatoire de Haute Provence (OHP) and Narval at Observatoire du Pic du Midi) is supported by PNPS and PNCG. The Southern part (with Coralie on the Swiss telescope at La Silla) is supported by A.S. Gaia.
- Astrometric observations of WMAP are performed as a test of the possibility to obtain the position of Gaia on its orbit (also at L2 and with a very similar expected magnitude) with an uncertainty of 150 m in position and 2.5 mm/s in velocity (Taris et al. 2008). Observations of QSOs and compact extragalactic objects are made to enlarge the catalogue of radio sources to be used for aligning the International Celestial Reference System (ICRF) to the Gaia reference system: search for new suitable sources observed in VLBI and observations in the optical wavelengths to detect any variability (Charlot 2011). A.S. Gaia is supporting the observations made in OHP for these two programmes.

3.2 Ground-based observations in support to the preparation of Gaia data scientific exploitation

Most activity in this area is concentrated in two domains: high resolution spectroscopy for galactic archeology (support to observations with existing spectrographs and to the design of new multiplex wide-field spectroscopic instruments), and observations of minor bodies in the Solar System.

- *Galactic archeology.* With its unprecedented astrometric, photometric and spectroscopic survey of all stellar populations, Gaia will revolutionise our knowledge of Galactic and stellar evolution. However, *only* medium resolution spectroscopy ($R = 11\,500$) will be available from the RVS (Radial Velocity Spectrometer) on-board Gaia, and *only* for the brightest 10 million stars, leading to a huge but incomplete knowledge of the abundances and stellar atmospheric parameters. It has long been emphasised that high-resolution spectroscopy would be an essential complement to Gaia data and that Europe should consider the importance of large programmes of ground-based observations using existing instruments, and of designing wide angle high multiplex spectrograph(s) to be mounted on a dedicated ground-based telescope (de Zeeuw & Molster 2007; Turon et al. 2008). This resulted in the setting up of a Working Group on Galactic archeology within the GREAT ESF network, in the proposal of a Gaia-ESO public spectroscopic survey (accepted by ESO in June 2011), and in various projects for new dedicated instrumentations. A.S. Gaia is supporting the participation and contributions of French astronomers to all these actions.
- Observations of minor bodies in the Solar System. Gaia will detect and provide very precise astrometric and photometric measurements for a large number of asteroids. However, a ground-based follow-up is essential to confirm the new detections, to improve the determination of the orbits and to obtain a maximum of information about the physics of the objects observed by Gaia. A Gaia Follow Up Network of Solar System Objects (Gaia-FUN-SSO) is being established, involving observatories of very many countries around the globe (Tanga & Thuillot 2011). In this context, various astrometric, photometric, or spectroscopic observations are considered. This action is accompanied by a theoretical and modelling effort to interpret the results in term of Solar System formation and evolution.

4 Support to modelling and theoretical activities

As for ground-based observations, modelling activities are of two kinds: necessary for data analysis, in the context of DPAC, and in preparation for the exploitation of Gaia data.

4.1 Modelling and theoretical activities in support to Gaia data analysis

Gaia will observe all objects down to magnitude $V = 20$, i.e. a wide variety of stars, solar system bodies, and compact extragalactic objects. To be able to identify, classify and characterise them, it is essential to have a reliable modelling of how these objects will be seen through the Gaia optical system. With one billion objects,

all types of objects, even the rarest, will be observed in large quantity and classification algorithms should be extremely efficient and tested in advance for all possible cases. Many actions in this direction have already been supported by A.S. Gaia during the past four years and these efforts will continue in the coming years.

Among them: modelling of massive atmospheres of hot stars with emission lines with test and improvement of classification algorithms; simulation of globular clusters and multiple star systems and observability with Gaia; estimation of the performance of the RVS for the chemical analysis of giant stars (test on ground-based data); modelling of double stars and estimation of the uncertainties on the astrometric parameters; simulation of the detection and observation of binary asteroids; simulation of the observation of extended objects; development of a library of synthetic spectra of galaxies for the automatic classification of galaxies unresolved by Gaia; simulation and analysis of a catalogue of quasars and AGN for the definition of the Gaia reference system.

4.2 *Modelling and theoretical activities in support to the preparation of Gaia data scientific exploitation*

As already emphasised above, Gaia will observe in a systematic way all objects down to magnitude $V = 20$, thus achieving a complete census of stars in a large part of the Galaxy and of their stellar or planetary companions in the solar neighbourhood. It will provide an unbiased sampling of all stellar populations of the Galaxy, and of the brightest stars in galaxies of the Local Group. Optimum use of this mass of data requires new methods and models and A.S. Gaia has regularly allocated a high priority to such requests. This is also an effort that should be continued in order to obtain a scientific return at the level of the major investment made by France in Gaia preparations.

A list of the various studies supported within this framework is given here: kinematics and modelling of the Galactic bulge; kinematics and structure of the Galactic disk; 3D NETL modelling of stellar chromospheres in order to improve the determination of atmospheric parameters and abundances; calculation of collision rates for the NLTE modelling of stellar atmospheres; modelling of the observation of metal-poor giant stars and test with ground-based measurements; development of criteria for the taxonomic classification and the determination of the absolute magnitude and spectral characteristics of asteroids; modelling of the shape of asteroids from observations of stellar occultations by asteroids; prediction of close encounters of asteroids and determination of their masses; thermophysical modelling of asteroids; observability of comets with Gaia and modelling of the effect of non-gravitational forces on their orbits; preparation of the alignment of ICRF with the Gaia reference system; tests of relativity using Hipparcos, radar and Gaia data.

5 Perspectives

Since 2007, A.S. Gaia has played a strong role in the coordination of actions related to Gaia in France. During that period, the scientific and observational context has changed, with the increasing importance of systematic sky surveys (in photometry up to now) to detect and map halo streams, and of detailed spectroscopic analysis to better understand the evolution of all Galactic stellar populations. Also, the European astronomical community got organised to prepare for the scientific exploitation of Gaia data. The period 2011-2015 will cover the final preparations for the processing of Gaia data, hopefully the launch of the satellite, and the preparation for the first tests on real data. In addition to an increased support to programmes in preparation to Gaia data scientific exploitation, support to actions related to the preparation of the publication of the catalogue will become essential.

References

- Charlot, P. 2011, EAS Publications Series, Volume 45, 345
 Crifo, F., Jasniewicz, G., Soubiran, C. et al. 2010, A&A, 524, A10
 de Zeeuw, P.T. & Molster, F.J. (eds) 2007, Astronet Science Vision for European Astronomy
 Perryman, M.A.C., Lindgren, L. Kovalevsky, J. et al. 1997, A&A, 323, L49
 Perryman, M.A.C., de Boer, K. S., Gilmore, G. et al. 2001, A&A, 369, 339
 Tanga, P. & Thuillot, W. (eds) 2011, Gaia Follow-up Network for the Solar System Objects
 Taris, F. et al. 2008, Proceedings of the Annual meeting of SF2A, C. Charbonnel, F. Combes and R. Samadi (eds), p. 39
 Turon, C., Meynadier, F. & Arenou, F. (Eds) 2011, ELSA Conference 2010: Gaia at the Frontiers of Astrometry, EAS Pub. Series, Vol. 45
 Turon, C., Primas, F., Binney, J. et al. 2008, ESA-ESO WG report No.4, Galactic Populations, Chemistry and Dynamics

Session 04

Atmosphere-Ionosphere coupling: atmospheric electricity (TLEs, TGFs, lightning) and the upper atmosphere physics and chemistry

NATURAL LIGHTNING FLASHES: FROM OBSERVATION TO MODELING

E. Defer¹, T. Farges², C. Barthe³, C. Bovalo³, J.-P. Pinty⁴, M. Chong⁴, S. Soula⁴ and P. Ortéga⁵

Abstract. Different ground-based and space-based sensors are currently used to characterize and locate Earth lightning flashes like VHF mappers, VLF systems with short or long baseline, optical CCD camera and more recently microphone arrays. Concurrent observations with such equipments offer a unique description of the different processes occurring during the life of a lightning flash (triggering phase, leader development and junction phase). While the detection of lightning flashes becomes mature, more challenging investigations are still needed on i) Lightning Nitrogen Oxide (LiNO_x) production and on ii) the modeling of natural lightning discharges, even if "engineer" lightning schemes combined with electrification schemes are already implemented in numerical cloud resolving models. The PEACH project, the Atmospheric Electricity component of the upcoming field experiment HyMeX, will offer a unique opportunity for the European community to document and characterize the Mediterranean lightning activity with observations and modeling from the lightning scale to the regional scale and to gather the French community in preparation for the validation of future space-based missions like TARANIS and MTG-LI and for the interpretation of their lightning observations.

Keywords: Cloud electrification, lightning flashes, LiNO_x, PEACH and HyMeX

1 Introduction

A natural lightning flash is a complex phenomenon composed of successive events, also called flash components, with different physical properties in terms of discharge type and propagation, radio frequency radiation type, current properties, duration. Simultaneous concurrent observations from different techniques sensitive to different properties of the lightning flash are required to characterize and interpret the different processes occurring during a lightning flash and to refine and develop discharge and chemistry modeling schemes. In the following we briefly describe the electrification process and discuss on the types of lightning flashes. Then we describe different techniques to detect and characterize lightning flashes and lightning activity. We then stress out the needs for more investigation on the discharge and chemistry modeling of lightning flashes. Finally we discuss on the Atmospheric Electricity component of the HyMeX project and on the two future space missions offering lightning detection.

2 Electrification processes and lightning occurrence

Optical space-based lightning detection reveals that lightning activity is more often recorded over the continents than over the oceans (Christian & coauthors 2003). Such a feature is explained by stronger updrafts in continental convection inducing a more efficient electrification. Electrical charges are exchanged during non-inductive ice-ice collisions in presence of super-cooled liquid water, the amount and sign of the exchanged charges being dependent on the temperature, the size of the ice particles, the type of hydrometeors and the difference of velocity between the colliding particles. Because the cloud hydrometeors are carrying the electric charges, the transport of the hydrometeors induced by the cloud dynamics leads to the existence of pockets of charges in the

¹ LERMA - CNRS / Observatoire de Paris, France

² CEA, DAM, DIF, France

³ LACy, Université de la Réunion, Saint-Denis, France

⁴ LA - CNRS / Observatoire Midi-Pyrénées, Toulouse, France

⁵ GEPASUD, Université de Polynésie Française, Faa'a, France

clouds and to the installation of an ambient electric field. If the electric is locally intense enough to trigger a discharge, a lightning flash can then propagate in the cloud (intra-cloud, IC) or connect to the ground (cloud-to-ground, CG), if the conditions for the lightning discharges to propagate exist. Lightning activity is then a by-product of the dynamics, the cloud microphysics and the electrification. The monitoring of the lightning activity with lightning locating systems (LLSs) provide key information on the occurrence of the convection but also can offer an idea on the developing and dissipating stages of the thunderstorms: an intensification of the convection is accompanied with a sudden increase of the flash rate; the flash rate often reaches its maximum when the cloud ceases to develop vertically; decaying stage of a storm is often associated with a decrease of the flash rate.

3 Sensing lightning flashes

Lightning flashes can be detected and located by different ground-, air- and/or space-based techniques such as optical (Christian & coauthors 2003) and radio frequency (Krehbiel et al. 2000), acoustics detection (Farges & Blanc 2010) as well as by the measurements of the electrostatic field (Soula & Chauzy 1991). According to the technique employed, different flash components are detected. Time-of-Arrival Very High Frequency (VHF) technique can map the three-dimensional structure of both IC and CG flashes inside and outside the clouds by locating pulsed radiation emitted by different flash components. With VHF detection, the development of the flash can be studied down to the microsecond scale and properties of the lightning flashes (e.g. radiation type and velocity of flash components, flash duration, flash structure, flash vertical and horizontal extends) and of the lightning activity (e.g. flash rate, IC/CG ratio) are available for the entire storm life within the coverage area (250-km diameter) of the lightning VHF network.

Lightning flashes can also be located based on the Low Frequency (LF) and Very Low Frequency (VLF) radiation emitted by some flash components. Short-baseline LF/VLF networks like EUCLID (Schulz et al. 2005) or LINET (Betz et al. 2009) covers Europe and locate CG ground connections and some IC activity. Long-range VLF lightning networks take the advantage of the wave guide between the ground and the ionosphere to locate lightning events at thousands of kilometers. Different long-range VLF networks are currently operated like the UK Met Office ATDnet and the WWLLN networks.

Optical detection is also used to detect and study some properties lightning flashes (e.g. duration, continuous current) even if the radiation is scattered by the cloud, ice particles and rain radiative properties between the flash and the sensor. Acoustic technique can provide the 3D location of the thunder sources. Acoustics offers additional information to investigate the physics of lightning discharges (relation between the temperature inside the lightning channel and the induced acoustic signal) and can be used to monitor and track storms (Farges & Blanc 2010).

All these lightning detection techniques in conjunction with space-based (IR, visible, microwave) cloud imagery and ground-based cloud radar can be used to characterize the flashes, the electrical state of the clouds and the cloud microphysical properties from where originate TLEs (Soula et al. 2011).

4 Electrification, lightning flashes and LiNO_x in cloud resolving models

The French MESO-NH cloud resolving model operates an electrification scheme combined with a lightning flash scheme that helps to understand the complex processes occurring during a storm (Barthe & Pinty 2007). An electrification scheme based on cloud physics and laboratory studies (Takahashi 1978; Saunders et al. 1991; Tsenova et al. 2010) determines the charges exchanged between the hydrometeors (the charges carried by the hydrometeors are produced by elastic shocks between ice particles in the presence of supercooled water) at each model time step. A simplified physics of the positive and the negative ions is included to simulate the screen charges. The ambient electric field is computed over the entire domain of the model by inverting the Gauss equation and a lightning flash is triggered at the location where the ambient electric field exceeds a height-dependent threshold. The lightning flash then develops as a bi-leader that propagates vertically until the electric field drops below a propagation threshold. A pseudo-fractal scheme is then applied to describe the horizontal extension of the flash as a branching tree that fits with the morphology of the lightning flashes. The electrical charges are then partially neutralized at locations along the flash path, The electric field is updated and the process is iterated until no more flash can be triggering during the time step. In addition a production of nitrogen monoxide (LiNO_x) can be computed for application in atmospheric chemistry (Barthe et al. 2007). The electrical scheme has been improved recently (Barthe et al. 2011) to simulate electrified cloud forced by

orography over a large computational domain. This was done for the perspective to simulate real meteorological events and to compare with stroke data collected by lightning flash networks.

5 PEACH, the HyMeX Atmospheric Electricity component

The Projet Electricité Atmosphérique pour la Campagne Hymex (PEACH) project of the Hydrology in the Mediterranean Experiment (HyMeX) aims at performing observational-based and modeling-based studies of the electrical activity in maritime and continental Mediterranean storms (Defer & coauthors 2008, available at <http://ozone.obspm.fr/~defer/Hymex/SciencePlanHymex.lightning.pdf>). Different operational lightning detection networks will be used to record, document and analyze the electrical activity at the storm level, at regional or mesoscale, and at the scale of the Mediterranean basin. The lightning networks selected here are complementary not only on their geographical coverage but also on the fact that they sense different flash components. A VHF Lightning Mapping Array (LMA) will also be deployed. Lightning activity will be related to the microphysics and aerosol contents and also to kinematics properties of the continental and maritime Mediterranean storms as measured by ground-based/airborne instruments deployed during the HYMEX experiment (radar, radiometer, lidar, in situ microphysics probes) and space borne operational sensors. An acoustic sensor array will also be deployed to characterize the infrasonic properties of lightning flashes and will provide a unique description of the lightning flashes by merging concurrent electromagnetic and infrasonic observations. In addition, simulations with the non-hydrostatic mesoscale model MesoNH will be performed to evaluate the model capability in simulating cloud and precipitation fields at the resolved convective scale over a large domain but also to test for the first time and in the context of real meteorological situations, the original electrification-lightning scheme which has been developed in MesoNH and which is dedicated to the very high spatial resolution (1 km scale and less). The PEACH multi-scale studies should then offer potential applications of lightning proxy for hazardous weather detection, nowcasting of flash floods, quantitative rainfall estimation over land and sea and for data assimilation in numerical weather prediction models.

6 TARANIS and MTG-LI missions

The PEACH project will help to organize the community to support the TARANIS mission (Blanc et al. 2007). The TARANIS optical instrument includes 2 cameras and 4 photometers. All sensors are equipped with filters for sprite and lightning differentiation. The filters of cameras are designed for sprite and lightning observations at 762 nm and 777 nm respectively with a sampling frequency of 11 frames per second. One of the photometers will measure precisely the lightning radiance and duration in a wide spectral range from 600 to 900 nm with a sampling frequency of 20 kHz. One of the main contribution of TARANIS to the lightning studies will be the possibility to complement, with TARANIS survey mode, the future geostationary satellite lightning imager data and to quantify the efficiency of global lightning networks (as WWLLN or GLD360) in regions without regional networks, as in Africa. The expertise gained during the PEACH project will help investigate the tropospheric processes related to the TLEs. Indeed high-resolution TLE observations will be performed during the HyMeX project (Soula et al. 2011).

The Meteosat program is the primary European source of geostationary observations over Europe and Africa. One of the new missions selected for The Meteosat Third Generation (MTG) program, with a scheduled launch in 2017, is the Lightning Imagery (LI) mission, detecting continuously over almost the full disc the optical signal radiated by both IC and CG discharges at 777 nm with a spatial resolution around 10 km over Europe. The LI mission is intended to provide a real time lightning detection and location capability in support to Nowcasting (NWC) and Very Short Range Forecasting (VSRF) of severe storm hazards and lightning strike warning. Other applications such as proxy for intensive convection related to ice flux, updraft strength and convective rainfall, for assimilation and for LiNO_x production are envisaged.

7 Conclusions

The analysis performed by the French community involved in Atmospheric Electricity during the PEACH project will serve to prepare the validation of the TARANIS mission. For instance the methodologies and the expertise gained by the French community on the tropospheric lightning flashes will help answer the scientific questions of the TARANIS mission. However more observational- and modeling-based investigations are still needed. For instance the wide set of detectors operating on different principles requires investigations to really understand

what each instrument is sensitive to and to provide a fair assessment on the detection efficiency and location accuracy of the lightning sensors. Such investigations are also important to calibrate instruments and lightning detection networks for a long-term monitoring of the lightning activity as a climate change proxy or to perform studies on the regional, seasonal and diurnal scales. Questions remain on the physical interpretation of the different temporal and spatial multi-scale processes occurring during a lightning flash. The PEACH project with its large battery of sensors will offer a unique description of those processes. The properties of the parent clouds should also be known for both lightning and TLE studies. More work is also required on the modeling. For instance questions remain on the electrification processes as no well-established theory exists yet. In addition multiple parameterizations of the non-inductive process need to be reconciled. The triggering conditions as well as the different multi-scale propagation processes need to be modeled and compared with the typical radiation recorded in radio-frequency, optics and acoustics domains. More works are needed on a good representation of LiNOX with some considerations in plasma kinetic combined with an atmospheric chemistry module.

References

- Barthe, C., Chong, M., Pinty, J.-P., Bovalo, C., & Escobar, J. 2011, Geoscientific Model Development, submitted
- Barthe, C. & Pinty, J.-P. 2007, *J. Geophys. Res.*, 06210
- Barthe, C., Pinty, J.-P., & Mari, C. 2007, *J. Geophys. Res.*, 112, 04302
- Betz, H.-D., Schmidt, K., Laroche, P., et al. 2009, *Atmospheric Research*, 91, 564
- Blanc, E., Lefeuvre, F., Roussel-Dupré, R., & Sauvaud, J. A. 2007, *Advances in Space Research*, 40, 1268
- Christian, H. J. & coauthors. 2003, *J. Geophys. Res.*, 108, 4005
- Defer, E. & coauthors. 2008, Detection, Analysis and Use of The Lightning Activity During The HyMeX Experiment, Science Plan and Implementation Plan
- Farges, T. & Blanc, E. 2010, *J. Geophys. Res.*, 115, A00E31
- Krehbiel, P. R., Thomas, R. J., Rison, W., et al. 2000, *Eos, Trans. American Geophys. Union*, 81, 21
- Saunders, C. P. R., Keith, W. D., & Mitzeva, R. P. 1991, *J. Geophys. Res.*, 96, 11007
- Schulz, W., Cummins, K., Diendorfer, G., & Dorninger, M. 2005, *J. Geophys. Res.*, 110, 9101
- Soula, S. & Chauzy, S. 1991, *J. Geophys. Res.*, 96, 22,327
- Soula, S., van der Velde, O., Montanya, J., et al. 2011, *J. Geophys. Res.*, to appear
- Takahashi, T. 1978, *Journal of Atmospheric Sciences*, 35, 1536
- Tsenova, B., Mitzeva, R. P., & Saunders, C. P. R. 2010, *Atmospheric Research*, 96, 356.

Session 05

Solar-terrestrial relations and space weather

SOHO OBSERVATIONS OF OSCILLATORY MOTIONS IN AN ERUPTIVE FILAMENT: INTENSITY AND VELOCITY VARIATIONS

K. Bocchialini¹, S. Koutchmy² and J. Solomon¹

Abstract. The variations in intensity and velocity inside an eruptive filament, observed on May 30, 2003 with CDS and EIT on-board SOHO, are analysed in the transition region He I line and the coronal Mg X line. Vertical oscillating motions of the filament with damped velocity oscillations before its disappearance are revealed. The link between these oscillations, the flaring regions nearby and the filament eruption is investigated.

Keywords: sun: filaments, prominences, sun: oscillations, sun: atmosphere, sun: cme

1 Introduction

In the context of the initiation of coronal mass ejections and the problem of mass loss related to the physics of coronal neutral sheets and streamers, occurring above lines of solar disc magnetic polarity reversal, we focus our analysis on a single event which occurred at the west limb, on May 30, 2003. We examine the dynamical behaviour of the filament region where reconnection and dissipation of magnetic energy in the turbulent plasma are occurring. The link between the observed oscillatory motions and the eruption occurrence is investigated in detail, using CDS/SOHO measurements, EIT/SOHO images, H α filtergrams with emphasize on synoptic data describing homologous flares.

2 Observations

Fig. 1 shows the general context of the event, in H α and in He II. The successive H α filtergrams taken around the time of the analyzed eruption, show the position of the CDS slit (the black vertical line) used to perform the intensity and the velocity analysis in EUV (He I and Mg X lines). Note the arrow at 9:55 showing a relative short brightening under the filament at the time when a burst was observed in both the He I and the Mg X lines using the CDS/SOHO observations. The EIT/SOHO sequence (He II at 30.4 nm) at 12 minute cadence is used to examine the dynamics of the filament channel several hours before and during the eruption (see Fig. 1, on the right).

The filament is analysed from time series of spectra using a transition region line (He I at 58.43 nm) and a coronal line (Mg X at 60.98 nm), with a 25 s cadence.

In He I line, a strong blue-shifted (Fig. 2) pulse is detected simultaneously with the eruption around 10:00 UT, as shown by the signal in intensity and velocity in both lines on Fig. 3. The oscillations in velocity last roughly one hour and are quickly damped (see Bocchialini et al., 2011). The oscillatory content was investigated using a wavelet analysis and was compared to different models (Bocchialini et al., 2011). Oscillations are clearly observed, in intensity and velocity in the He I line (Fig. 4) and the Mg X line (Fig. 5), with similar periods from a few minutes up to a few tens of minutes, co-temporal with the eruption. In the following, we consider these observations in the light of a more global view of solar activity phenomena.

3 Suggested interpretation

The global context suggests a possible link between several events occurring almost simultaneously as seen in H α (Fig. 6). Several regions flared and/or erupted quasi-simultaneously; such phenomenon was called “sympathetic

¹ Institut d’Astrophysique Spatiale, UMR 8617, Bat. 121, Université Paris 11/CNRS, 91405 Orsay cedex, France

² Institut d’Astrophysique de Paris, UMR 7095, CNRS and UPMC, 98 bis Boulevard Arago, 75014 Paris

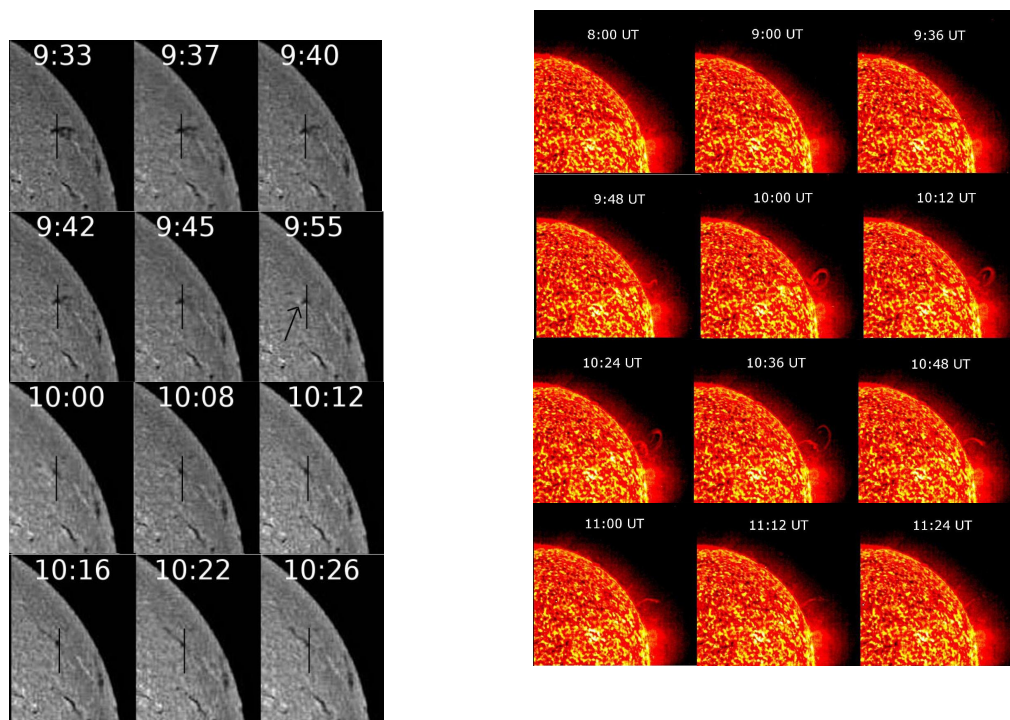


Fig. 1. Left: Successive $H\alpha$ filtergrams taken around the time of the analyzed eruption. **Right:** Successive partial images from the EIT observations to show the context of the filament eruption.

flares” (Schrijver and Title, 2011 and references inside) or homologous flares in the former literature. The link could be supported by the large scale coronal magnetic field as evidenced by the result of the PFSS (Potential Field Source Surface) computed from the underlying measured field. The magnetogram obtained from MDI/SOHO one day before was used, together with a SS (source surface) at 1.4 solar radius. Note the coronal magnetic “channel”, extended in the radial direction, with open field lines near the location of the studied filament eruption red lines on the Fig. 6 on the right).

4 Conclusions

The link between oscillations in a filament and its eruption was investigated. Oscillations are clearly observed, in intensity and velocity in the He I and Mg X lines, with similar periods from a few minutes up to 80 minutes, with a main range from 20 to 30 minutes, simultaneously with the eruption of the filament. The filament exhibits vertical oscillating motions, and the evidence of damped velocity is provided, before its disappearance. The “sympathetic” flares occurring in regions magnetically connected to the observed filament, could be the cause of the oscillations detected, but this scenario is now under investigations (paper in progress). More details concerning the oscillatory behaviour are given in Bocchialini et al. (2011).

The $H\alpha$ images are courtesy of the Kanzelhöhe Observatory and the Meudon Observatory. The CDS, EIT and MDI data are courtesy of SOHO consortia. SOHO is a project of international cooperation between ESA and NASA. Frédéric Baudin, Guillaume Pouget, Lucile Senicour and Ehsan Tavabi helped at different steps of this work.

References

- Bocchialini, K., Baudin, F., Koutchmy, S., Pouget., G., Solomon, J., 2011, A&A, 533, 96
 Schrijver, K., Title, A.L., 2011 JGR, 116, A04108

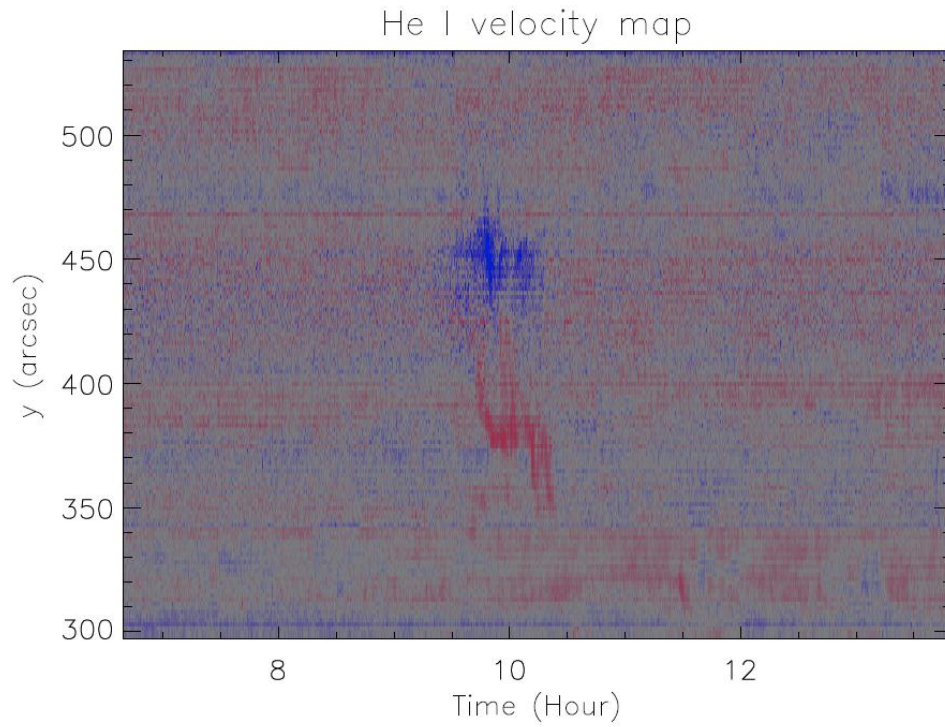


Fig. 2. He I velocity map, as a function of time and along the CDS slit. The filament is located between $y = 409$ and 459 arcsec.

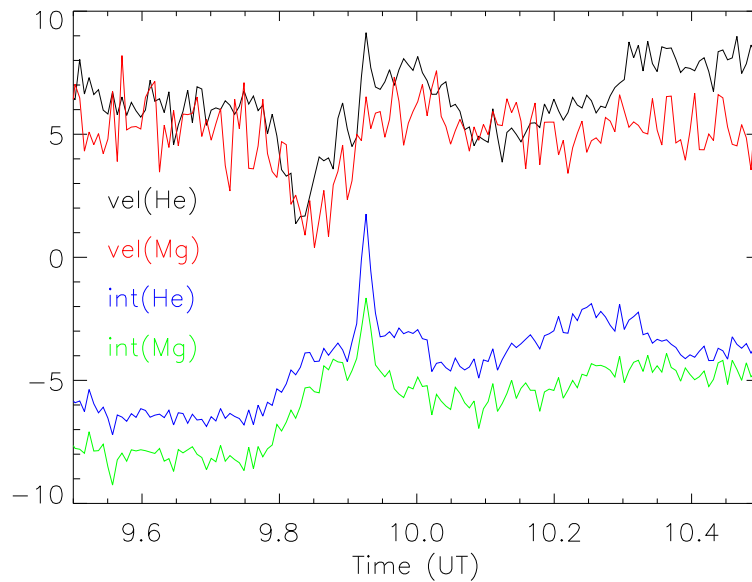


Fig. 3. Velocities and intensities observed during the eruption of the filament between 9:00 UT and 11:00 UT in both the emission lines of He I and Mg X from the CDS observations

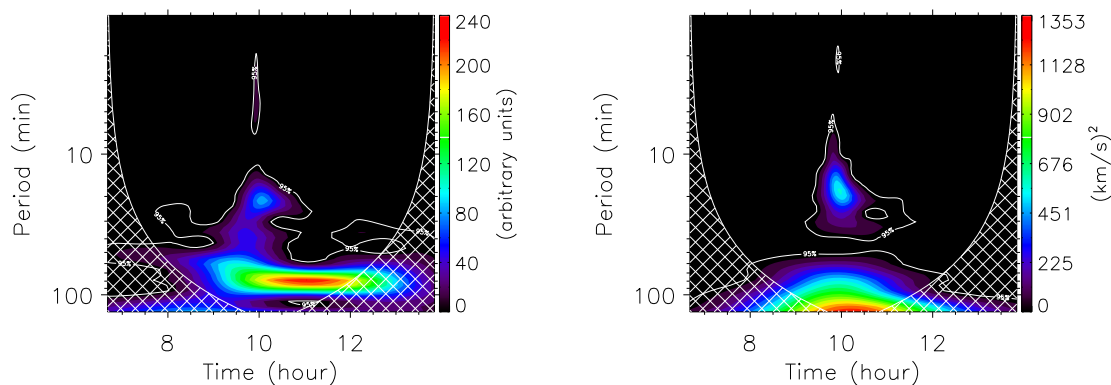


Fig. 4. Wavelet analysis performed in He I using intensities (left) and velocities (right) observed inside the erupting filament during the whole interval of CDS observations. Significant power is within the 95% confidence level contour and outside the hatched cone of influence.

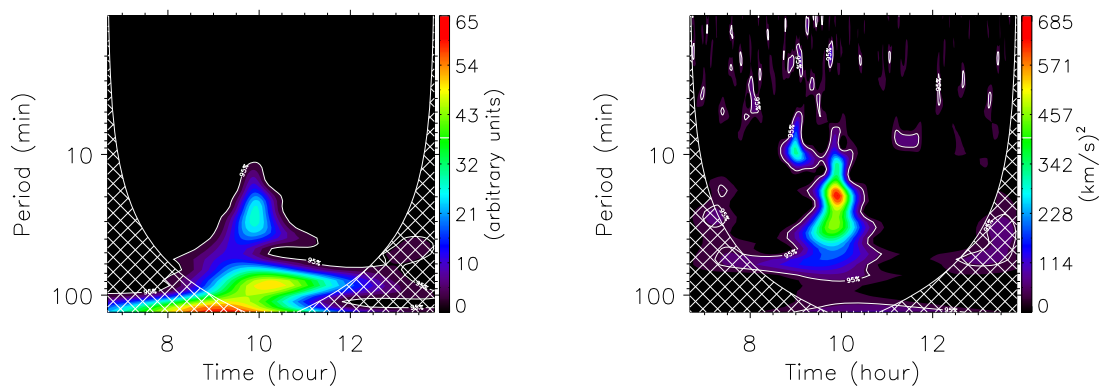


Fig. 5. Wavelet analysis performed in Mg X using intensities (left) and velocities (right) observed inside the erupting filament during the whole interval of CDS observations. Significant power is within the 95% confidence level contour and outside the hatched cone of influence.

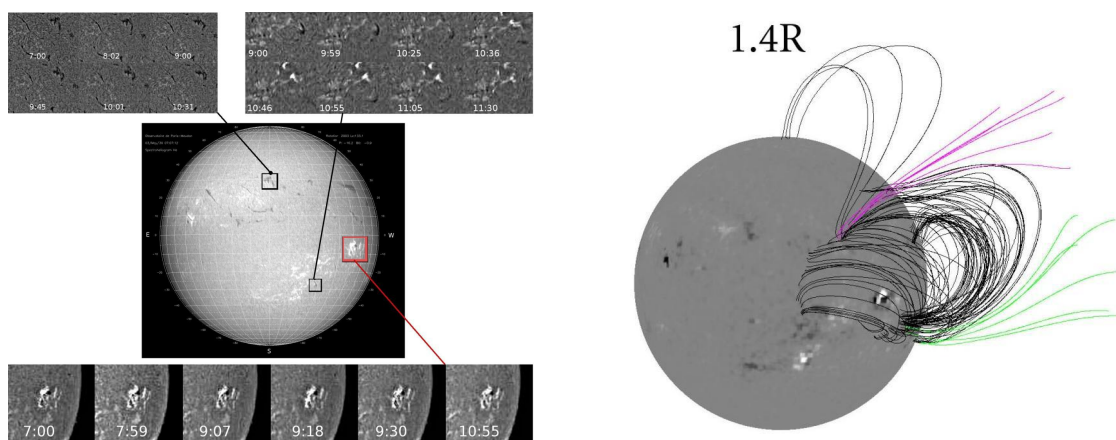


Fig. 6. Left: The global context suggesting a possible link between several events occurring almost simultaneously as seen in H α . **Right:** Extrapolated magnetic field lines using the PFSS approximation. From E. Tavabi et al.

AUTOMATED DETECTION AND TRACKING OF SOLAR AND HELIOSPHERIC FEATURES IN THE FRAME OF THE EUROPEAN PROJECT HELIO

X. Bonnin¹, J. Aboudarham¹, N. Fuller¹, C. Renie¹, D. Perez-Suarez², P. Gallagher², P. Higgins², L. Krista², A. Csillaghy³ and R. Bentley⁴

Abstract. In the frame of the European project HELIO, the Observatoire de Paris-Meudon is in charge of the Heliophysics Feature Catalogue (HFC), a service which provides access to existing solar and heliospheric feature data. In order to create a catalogue as exhaustive as possible, recognition codes are developed to automatically detect and track features. At the time, HFC contains data of filaments, active regions, coronal holes, sunspots and type III radio bursts for a full solar cycle. The insertion of prominences and type II radio bursts should be done in the short term. We present here an overview of some of the algorithms used to populate HFC. The development of such fast and robust techniques also addresses the needs of the Space Weather community in terms of near real-time monitoring capabilities.

Keywords: heliophysics, solar system, virtual observatory, automatic detection, image processing, monitoring, space weather, HELIO, HFC

1 Introduction

The Heliophysics Integrated Observatory, HELIO, is a FP7 European virtual observatory project devoted to solar physics and heliophysics (<http://www.helio-vo.eu/>). At the end of its development, in may 2012, it will supply dedicated tools as well as coordinate access to large amounts of resources available in the different fields covered by heliophysics. To achieve its goals, it is currently deploying a distributed network of services that will help users to efficiently analyse, handle, reach and/or mine relevant data.

One of these services, the Heliophysics Feature Catalogue (HFC), provides access to existing solar and heliospheric features data. Like most of HELIO components, HFC will be accessible through various interfaces such as HELIO Front End*, dedicated workflows, application programming interfaces (API), Solar SoftWare (SSW), or using its own graphical user interface (which can be reached at <http://voparis-helio.obspm.fr/hfc-gui/index.php>). In order to offer the most exhaustive feature database, HFC has been regularly updated with new data, which are extracted from observations by automated recognition codes. These codes use image processing methods developed in the frame of the project (mainly by LESIA in France and TCD in Ireland), or provided by the community itself.

We present here a brief overview of some of the algorithms currently available in HELIO and concerning: active regions and coronal holes observed on SOHO/MDI and SOHO/EIT respectively, solar filament detected and tracked on H α observations of the Meudon spectroheliograms, but also type III solar radio bursts reported on Wind/Waves dynamical spectra. First section is devoted to Solar feature detection and tracking, and Section 2 to heliophysics feature recognition. Section 3 will conclude presenting the future works.

¹ Observatoire de Paris, section de Meudon, LESIA, UMR 8109 CNRS, 92195 Meudon CEDEX, France

² Trinity College Dublin, College Green, Dublin 2, Ireland.

³ Institute of 4D Technologies, FHNW, Steinackerstrass 5, CH-5210 Windisch, Switzerland

⁴ MSSL, University College London, Hombury St. Mary, Dorking, Surrey RH5 6NT, U.K.

*available at <http://helio.i4ds.technik.fhnw.ch/Helio/prototype/explorer>.

2 Recognition of Solar features

2.1 Photospheric Active Regions

The *Solar Monitor Active Region Tracking* (SMART) algorithm (Higgins et al. 2011) allows detection and tracking of active regions (ARs) on solar magnetograms. It has been successfully applied on SOHO/MDI data (Scherrer et al. 1995), and is currently used in the frame of HELIO to provide magnetic and location information to HFC, for a period spanning the entire solar cycle 23. To extract ARs from an image, the SMART method is based on three successive steps: (i) a *segmentation* process (including cleaning process and quiet sun background subtraction) that produces a binary mask of features using threshold technique. (ii) A *characterization* process, which extracts magnetic properties from previous feature masks such as statistical moments of the magnetic field and the minimum and maximum magnetic field values. (iii) a *classification* step that permits to discriminate between various feature types.

Figure 1 shows result of ARs detection by SMART on a SOHO/MDI magnetogram. This image of the Sun, observed on June 10, 2001 at 00:00:01 (UTC) and produced as an output by HFC, presents several ARs localizable thanks to their white line contours. The ARs gravity centers are represented by white dots, and the corresponding NOAA region numbers are given in brackets.

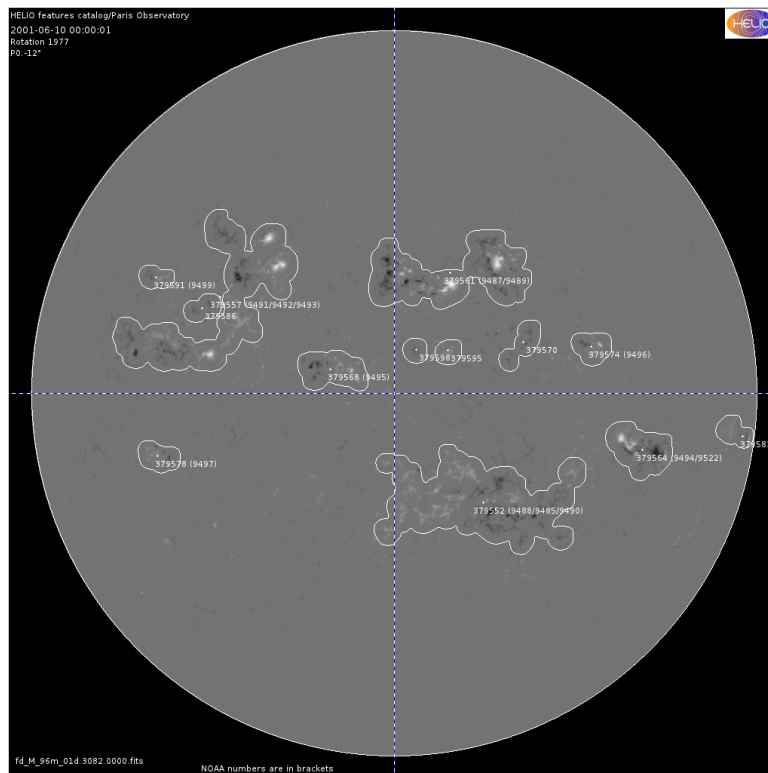


Fig. 1. Magnetogram of the Sun observed on June 10, 2001 at 00:00:01 (UTC) by SOHO/MDI. The strength of line-of-sight magnetic field is represented using gray-scale colors (i.e., white pixels correspond to upward magnetic flux, and dark pixels to downward flux). The contours of detected ARs are indicated by the white lines, and the corresponding gravity centers by white dots. When it is possible, the NOAA region numbers associated with ARs are given in brackets.

2.2 Coronal Holes

The coronal holes (CHs) detection tool applied in HELIO is the *Coronal Hole Automated Recognition and Monitoring* algorithm (CHARM) (Krista & Gallagher 2009). CHARM uses SOHO/EIT (Delaboudinière et al. 1995) 195 Å and SOHO/MDI line-of-sight magnetograms to detect CHs and has the ability to provide real-time high-speed solar wind forecasts at Earth and compare the predictions with *in-situ* solar wind data. The technique used is based on local intensity thresholding. Each EIT image is partitioned and the local intensity

minimum between the quiet Sun and the low intensity regions is extracted. The low intensity regions are distinguished from other regions based on the magnetic field information obtained from SOHO/MDI magnetograms. Figure 2 illustrates the detection of CHs on a Lambert projection representation of a SOHO/EIT 195 Å image of the Sun, observed on January 13, 2008 at 10:00:00 (UTC). The light intensity (represented by green scale) is shown as a function of the heliographic longitude and latitude (in degrees). Contours of the detected CHs are indicated by white lines.

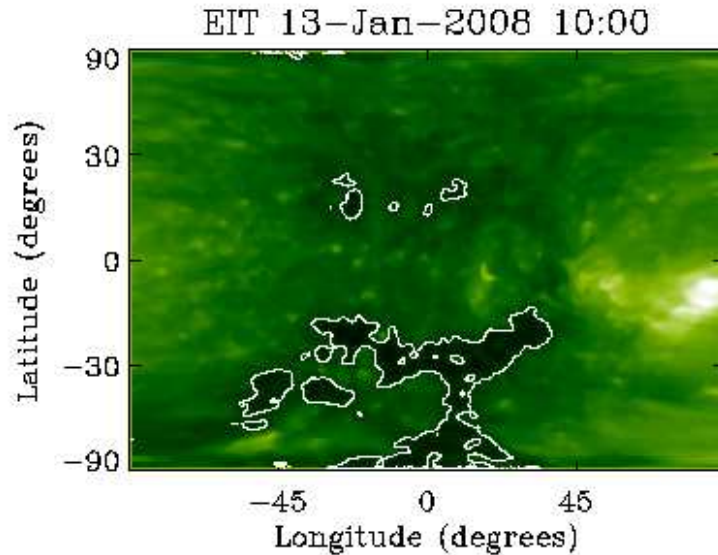


Fig. 2. Lambert projection representation of a SOHO/EIT 195 Å image of the Sun, observed on January 13, 2008 at 10:00:00 (UTC). The light intensity (represented by green scale) is shown as a function of the heliographic longitude and latitude (in degrees). Contours of the detected CHs are indicated by white lines. (Courtesy of L.Krista.)

2.3 Solar filaments

Detection of solar filaments on Halpha images used in HELIO, was previously developed in the frame of the European Grid for Solar Observations (EGSO) FP5 project. It has been successfully applied on Meudon spectroheliograph observations in order to populate HFC. A description of the method can be found in Fuller et al. (2005). To extract filaments parameters, several cleaning processes are first run in order to correct images from defects characteristic of the instrument (which may lead to spurious detections). Then, filament areas are segmented using a region growing method based on local pixels statistics thresholdings. From segmented filaments, a morphological closing operator is applied to merge close regions that could be considered as a single feature. Finally, skeletons of detected filaments are defined using thinning followed by pruned methods (Gonzalez & Woods 2002). Figure 3 presents results of extracted filaments on a Meudon Halpha spectroheliogram.

Automatic tracking of solar filaments has been also developed in order to identify co-rotating features on successive images (bonnin et al., submitted). The algorithm is based on a curve matching method that allows comparison between filaments skeletons, these latter being previously extracted from several successive images by the dedicated recognition code. In order to counterbalance the solar rotation effects, the matching algorithm is applied on a reference frame which rotates with the solar surface at the Carrington speed (i.e., $v \sim 360/27.2753$ degrees/day). On such a reference frame, extracted skeletons of a single co-rotating feature from successive images, will be located at the same coordinates position. A level-of-trust parameter is then computed from each comparison, that will allow to determinate if the tracking is reliable or not. If it is, a unique tracking identification number is allocated to the co-rotating filament on each image. This number will permit, among others, to report in a last step, the filament behaviours (e.g, disappearance before the West limb, *disparitions brusques*, etc.).

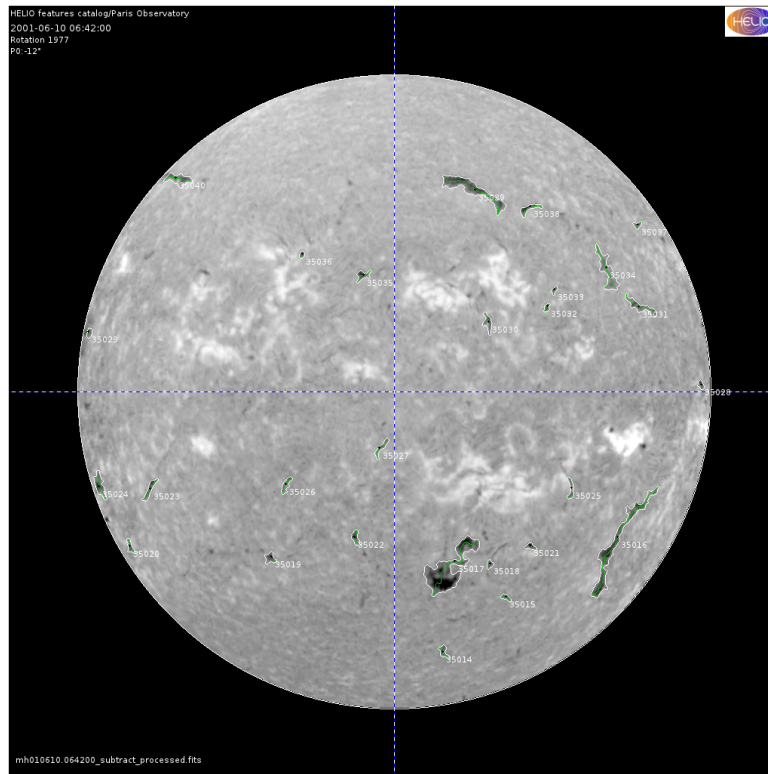


Fig. 3. Halpha image of the Sun observed by the Meudon spectroheliograph on June 6, 2001 at 06:42:00 (UTC). Intensity of light is represented by gray scale colors. Boundaries lines of detected filaments are over-plotted in white, and skeleton lines in green. (This image was produced using the HFC interface.)

3 Recognition of Heliospheric features

3.1 Type III Solar Radio Bursts

In the frame of HELIO, type III solar radio bursts automated recognition is performed by the *RADio Bursts Automated Tracking* (RABAT) algorithm. This algorithm is based on a technique developed by Lobzin et al. (2009) for the coronal type III bursts detection. Although this latter was initially tested on ground based observatories, covering the approximately 10 to 100 MHz frequency range, it can also be successfully applied with minor corrections on space based observatories, for bursts observed below approximately 10 MHz. Hence, from a modified version of the algorithm, daily dynamical spectra produced by Wind/Waves radio experiment (Bougeret et al. 1995) between 1995 and 2011 has been processed. Detection of type III bursts has been realized separately on the $[\sim 0.01, 1 \text{ MHz}]$ and $[\sim 1, 10 \text{ MHz}]$ frequency ranges, corresponding respectively to the RAD1 and RAD2 receivers spectral domains, and using a average time resolution of 60 seconds.

The first processing steps of the tracking technique is quite similar to the ones used by Lobzin et al. (2009), and consists to clean the dynamical spectrum (which can be seen as a 2 dimensions image giving the radio intensity as a function of time and frequency) in order to remove radio interference frequencies (RFI), or time periods of instrument calibration. Interpolated values are allocated to these "bad" pixels, which will be not saved in the final event extraction process. A smoothing filter is also applied to improve signal on noise ratio of the image, and a $1/f$ representation of the dynamical spectrum is used, where type III emissions almost appears as straight lines (since the drifting rate df/dt is proportional to $\sim -0.01f^2$), as illustrated in the left panel of Figure 4.

Then, a binary mask of the cleaned dynamical spectrum is generated, by setting its pixels value to 1 for all the local maxima along time axis at each frequency (all others pixels values are null). On this mask, a type III burst forms a straight line of maxima surrounded by null pixels, as seen in the right panel of Figure 4. These maxima and null pixels correspond respectively to the burst maximal intensities and to the growth and decay

phases, which are drifting with frequency. Using a specific Hough transform and a suitable threshold value, type III bursts main directions can be thus deduced from the binary mask. As HFC stores intensity, location as well morphological information of detected features, a last step is dedicated to extract bursts contours from the dynamical spectrum. These contours are defined by searching the onset and offset times of detected events at each frequency (to filter bad points, fitting processes are applied on onset/offset times versus frequency curves). Finally, as for the others HFC features, bursts boundaries are described using a chain code method.

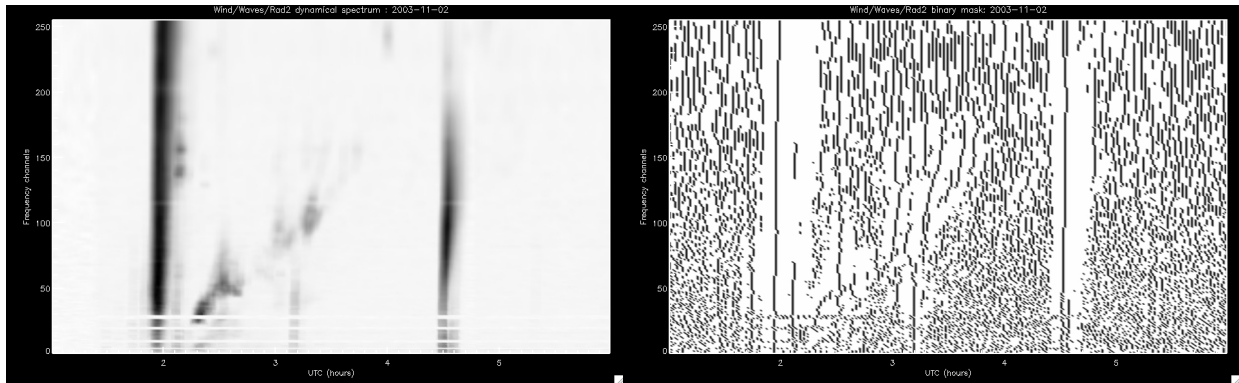


Fig. 4. Left: Zoom on a pre-processed dynamical spectrum of the Wind/Waves Rad2 receiver for the November 2, 2011. The radio flux is showed in gray scale as a function of time and frequency channels ($1/f$ representation). Two type III bursts, which appear as intense (i.e., darker) fast drifting emissions can be seen at about 01:55 and 04:30 respectively (a type II burst, which starts at the same time than the first type III is also visible). **Right:** Corresponding binary mask portion. Type III events can be distinguished from noise by long vertical lines of local maxima, surrounded by null pixels.

4 Future works

We presented here an overview of HELIO/HFC efforts in terms of automated recognition and tracking capabilities. Since the HELIO project is still in progress, this description must be seen as a snapshot of the current development status, which will strongly evolved with the addition of new features data in HFC. Especially, active regions detection will be extended to others available observations and at several wavelengths (e.g. SOHO/EIT and STEREO/EUVI). Sunspots detection (not described here) will be systematically applied on SOHO/MDI as well as SDO/HMI intensity images. Solar filaments algorithm has been successfully tested on Big Bear Solar Observatory (BBSO) data, and should be implemented in the next few months. As previously mentioned, prominences data will be also accessible from HFC. Type III as well as type II bursts detections will be extended to STEREO/Waves and Nançay Decametric Array dataset. Tracking information will be also provided for several features (the SMART algorithm already offers tracking capabilities that will be run in HELIO). Beyond the HFC needs, relevant information, extracted from all these codes, will be used by the HELIO system to provide efficient propagation tools to users, allowing time and space associations between events and features observed on the heliosphere.

HELIO is a Research Infrastructures funded under the Capacities Specific Programme within the European Commission's Seventh Framework Programme (FP7; Project No. 238969).

References

- Bougeret, J.-L., Kaiser, M. L., Kellogg, P. J., et al. 1995, *Space Sci. Rev.*, 71, 231
 Delaboudinière, J.-P., Artzner, G. E., Brunaud, J., et al. 1995, *Sol. Phys.*, 162, 291
 Fuller, N., Aboudarham, J., & Bentley, R. D. 2005, *Sol. Phys.*, 227, 61
 Gonzalez, R. C. & Woods, R. E. 2002, *Digital image processing*, ed. Gonzalez, R. C. & Woods, R. E.
 Higgins, P. A., Gallagher, P. T., McAteer, R. T. J., & Bloomfield, D. S. 2011, *Advances in Space Research*, 47, 2105
 Krista, L. D. & Gallagher, P. T. 2009, *Sol. Phys.*, 256, 87
 Lobzin, V. V., Cairns, I. H., Robinson, P. A., Steward, G., & Patterson, G. 2009, *Space Weather*, 70, S04002
 Scherrer, P. H., Bogart, R. S., Bush, R. I., et al. 1995, *Sol. Phys.*, 162, 129

COMPRESSIBLE TURBULENCE IN ASTROPHYSICS

S. Galtier¹ and S. Banerjee¹

Abstract. It is well known that compressible turbulence is a dominant feature of interstellar clouds; it also plays a non negligible role in the evaluation of the local heating in the solar wind. Nevertheless due to the intrinsic difficulty to include compressible effects in theoretical models almost no serious result exists in compressible turbulence. In this note, we report a recent progress made on compressible isothermal turbulence in the asymptotic limit of a high Reynolds number. Our investigation concludes on the existence of a double inertial range where respectively super- and sub-sonic turbulences happen.

Keywords: Turbulence, solar physics, interstellar medium

1 Introduction

Almost all important results in turbulence concern incompressible fluids (see *e.g.* Frisch 1995). In his third 1941 turbulence paper Kolmogorov derived an exact relation for incompressible isotropic hydrodynamics in terms of third-order longitudinal structure function in the asymptotic limit of a high Reynolds number (Kolmogorov 1941). Because of the rarity of such results the Kolmogorov's universal (4/5s) law has a cornerstone role in the analysis of turbulence: for example, it is the starting point for the prediction of the well known $E(k) \sim k^{-5/3}$ energy spectrum. Extensions have been made of such a result to astrophysical magnetized fluids described in the framework of MHD (Politano & Pouquet 1998) as well as Hall MHD (Galtier 2008).

The previous results are found for incompressible fluids and no universal law of that type has been derived for compressible turbulence which is far more difficult to analyze. The lack of knowledge is such that even basic statements about turbulence like the presence of a cascade, an inertial range and constant flux energy spectra are not well documented. This fact hinders the domain of application of compressible turbulence which ranges from aeronautical engineering to astrophysics. In the latter case, it is believed that highly compressible turbulence controls star formation in interstellar clouds (Elmegreen & Scalo 2004).

In the general case, our knowledge of compressible hydrodynamic turbulence is mainly limited to direct numerical simulations (see *e.g.* Passot et al. 1988; Federrath et al. 2010). The most recent results for super-sonic isothermal turbulence with a grid resolution up to 2048^3 (Kritsuk et al. 2007) reveal that the inertial range velocity scaling deviates substantially from the incompressible Kolmogorov spectrum with a slope of the velocity power spectrum close to -2 and an exponent of the third-order velocity structure function of about 1.3 . Surprisingly, the incompressible predictions are shown to be restored if the density-weighted fluid velocity, $\rho^{1/3}\mathbf{u}$, is used instead of simply the velocity \mathbf{u} . Although a -2 spectrum may be associated with shocks – like in one dimension – it seems that their contribution in three dimensions is more subtle. Generally speaking it is fundamental to establish the equivalent of the 4/5s law for compressible turbulence before going to the more difficult problem of intermittency.

In this note we discuss some recent results on compressible isothermal turbulence obtained by Galtier & Banerjee (2011).

2 Compressible isothermal turbulence

The starting point of our analysis is the three-dimensional compressible hydrodynamics equations which are often used in direct numerical simulations for investigating interstellar turbulence (Kritsuk et al. 2007; Federrath

¹ Univ Paris-Sud, Institut d'Astrophysique Spatiale, UMR 8617, bâtiment 121, F-91405 Orsay, France

et al. 2010). In a recent paper (Galtier & Banerjee 2011), we have derived the equivalent of the Kolmogorov law for compressible structure functions. The main difference with the incompressible case resides in the presence of a new type of term which acts on the inertial range similarly as a source or a sink for the mean energy transfer rate. When isotropy is assumed, compressible turbulence may be described by the relation

$$-\frac{2}{3}\varepsilon_{\text{eff}}r = \mathcal{F}_r(r), \quad (2.1)$$

where \mathcal{F}_r is the radial component of the two-point correlation functions and ε_{eff} is an effective mean total energy injection rate. By dimensional arguments we predict that a spectrum in $k^{-5/3}$ may still be preserved at scales smaller than the sonic scale $1/k_S$ if the density-weighted fluid velocity, $\mathbf{v} \equiv \rho^{1/3}\mathbf{u}$, is used for the spectrum instead of simply the velocity \mathbf{u} . However, at super-sonic scales ε_{eff} becomes space dependent and a $k^{-19/9}$ spectrum may be predicted dimensionally. This result is summarized in Fig. 1: it is a schematic view of the density-weighted energy spectrum. Two regimes are expected according to the scale with a super-sonic turbulence regime at the largest scales and a sub-sonic one at scales smaller than the sonic scale $1/k_S$. This result illuminates some recent high-resolution direct numerical simulations where this behavior was observed (Kritsuk et al. 2007; Federrath et al. 2010).

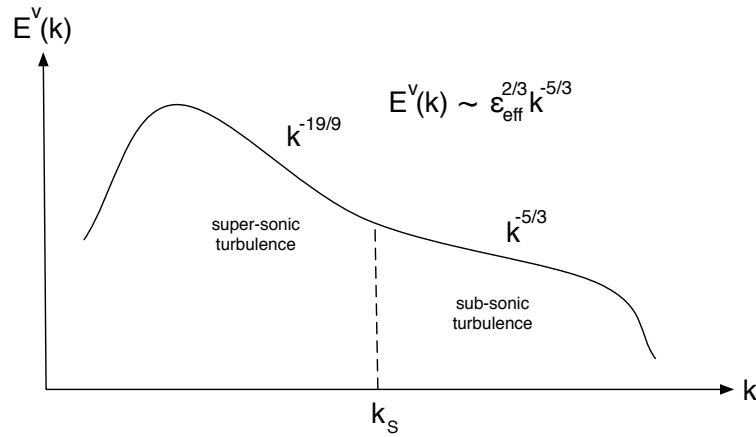


Fig. 1. Schematic view of the spectrum for compressible isothermal turbulence. k_S is the sonic scale.

3 Perspective

We believe that our results on compressible isothermal turbulence are also important in the context of recent observations made with the Herschel telescope (Arzoumanian et al. 2011) which reveal some universality in molecular clouds. Indeed, the interstellar filaments seem to exhibit a universal width of the order of the sonic scale whose origin remains unknown. As proposed by the authors, the answer is certainly hidden in compressible turbulence.

References

- Arzoumanian, D. et al. 2011, *A&A*, 529, L6
- Elmegreen, B.G. & Scalo, J. 2004, *Annu. Rev. Astron. Astrophys.*, 42, 211
- Federrath, C. et al. 2010, *Astron. Astrophys.*, 512, A81
- Frisch, U. 1995, *Turbulence: the legacy of A.N. Kolmogorov* (Cambridge Univ. Press, Cambridge)
- Galtier, S. 2008, *Phys. Rev. E*, 77, R015302
- Galtier, S. & Banerjee, S. 2011, *Phys. Rev. Lett.*, in press
- Kolmogorov, A.N. 1941, *Dokl. Akad. Nauk SSSR*, 32, 16
- Kritsuk, A.G., Norman, M.L., Padoan, P. & Wagner, R. 2007, *Astrophys. J.*, 665, 416
- Passot, T., Pouquet, A. & Woodward, P. 1988, *Astron. Astrophys.*, 197, 228
- Politano, H. & Pouquet, A. 1998, *Phys. Rev. E*, 57, R21

Session 06

The early Earth as a planet in the making

GHOSTS IN SATURN'S RINGS

K. Baillié¹, J.E. Colwell¹ and L.W. Esposito²

Abstract. Using UVIS stellar occultation data, we identified holes in ringlets or plateaus through which we directly observed the star. These "ghosts" are characterized by an isolated peak in photon counts with a height equal to photon counts in places without ring material. We suggest that ghosts are the signatures of ephemeral structures in the rings that could be due to particularly large clumps of material or small moonlets. The usual S-shape around a "propeller" moonlet coincides with the presence of a depletion zone around the clump: these moonlets are probably not massive enough to open full gaps, but could produce azimuthally limited holes in the rings like those seen in the UVIS occultation data. Numerical simulations of the interaction of a moonlet with ring particles have been conducted for different sizes of moonlets and particles, making it possible to extrapolate a relation between the radial extension of the depletion zone and the moonlet Hill radius. This model and our observed ghost widths allowed us to estimate an initial boulder size distribution following a power-law with a cumulative index $Q=0.6 - 0.8$. This boulder size distribution appears not to match the particle size distribution models from Zebker et al., 1985 ($Q=1.75$ in the Cassini Division). Objects up to 15 m were found in the C ring and up to 60 meters in the Cassini Division.

Keywords: saturn, rings, ghosts, boulders, moonlets

1 Observations

We analyze star occultations presenting significant background photon counts (usually higher than 20 photons per integration period). The resolution of our data is of the order of 1 ms, which corresponds to about 1 to 10 m, depending on the geometry of the occultations. We focus on regions of relatively high optical depth such as the C ring and Cassini Division ringlets and we avoid regions presenting local disturbances from known waves or structures. Ghosts behave like holes in a ringlet or plateau through which we directly observe a star: it is therefore characterized by an isolated peak in photon counts with a height equal to the star photon counts in places without ring material (Figure 1). Figure 2 presents the cumulative distribution of these widths in terms of number of data points.

Statistical arguments show that the actual number of our ghosts being cosmic rays should be negligible and we can state with a good confidence that our observed ghosts that are one data point wide are actual structures in the rings.

2 Forming Ghosts: the Propeller Model

In order to understand the interactions between a moonlet and the ring particles, we evaluate the radius of the Hill sphere of a given moonlet of mass $M_{moonlet}$ and of semi-major axis $a_{moonlet}$: $r_H = a_{moonlet} \left(\frac{M_{moonlet}}{3(M_{Saturn} + M_{moonlet})} \right)^{1/3}$, where M_{Saturn} is Saturn's mass. The Hill sphere of a moonlet is the region in which its attraction dominates Saturn's attraction.

Numerical simulations of the interactions between ring particles and a moonlet showed the apparition of a depletion in surface mass density in the neighborhood of the moonlets (Petit & Henon 1988). The chaotic depletion zone where particles are cleared out by the moonlet presents two different lobes due to Keplerian

¹ Department of Physics, University of Central Florida, Orlando, Florida 32816-2385, USA

² Laboratory for Atmospheric and Space Physics, University of Colorado at Boulder, 392 UCB, Boulder, Colorado 80309-0392, USA

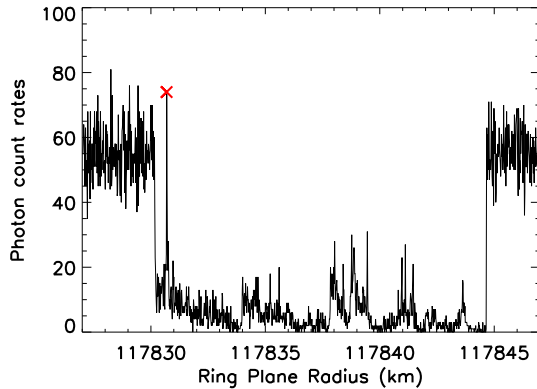


Figure 1. Photon count rates in the Huygens ringlet from the occultation of α Arae, rev. 63. The red cross identifies the position of the detected ghost. Its height matches the background level of the star.

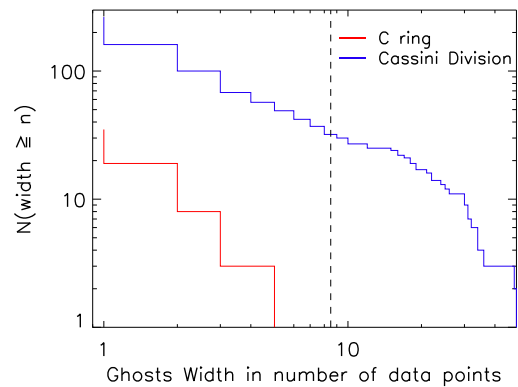


Figure 2. Cumulative width distribution of the detected ghosts in number of data points. The zone at the left of the vertical dashed line delimits the structures that we consider as ghosts with a high confidence.

shear: the inner one is carried forward while the outer one is trailing behind. Spahn & Wiebicke (1989) and Spahn et al. (1992) showed that smaller moonlets will only create localized S-shaped density modulations which radial width scales as r_H for moonlet diameters lower than 3 km and as r_H^2 for larger moonlets (Petit & Henon 1988). Moonlets larger than 2 km in diameter can lead to the formation of complete circumferential structures: diffusion is not strong enough to close the depletion before/after the moonlet, stretching it around the entire ring system. The depletion becomes a gap although the wakes are still visible close to the moonlet. Even larger moonlets (larger than 5 km in diameter) can lead to the formation of an inner ringlet, flanked by gaps. Beyond these gaps, satellite wakes are formed as described in Showalter et al. (1986). Sremčević et al. (2002) estimated that it requires a moonlet with a radius larger than 840 m to open a gap in the B ring. The S-shape of this density modulation is called a "propeller". Lewis & Stewart (2009) determined from numerical simulations that propellers can form only if the mass of the moonlet is at least 30 times higher than the mass of the largest particle in the nearby ring. Indeed, for bigger particles, self-gravity tends to accelerate the damping of the propeller-shaped gaps and prevent the formation of moonlet wakes.

Particles in close-encounters are perturbed and receive a kick in eccentricity proportional to $1/(\Delta a)^2$. In addition, the phases of these particles' orbits are roughly aligned (Showalter & Burns 1982). These now eccentric particles will leave an open space on the outer trailing side and inner leading side of the moonlet. This primary depletion zone has a radial extension of a few Hill radii while its azimuthal extension can be much larger as confirmed in numerical simulations (Figure 3). After a few orbits, the oldest and farthest depletion zones are destroyed by the combined effects of collisions and inter-particle gravitational forces provoking either a damping of the eccentricity, a randomizing of the phases or a scattering of the eccentric particles in the depletion zones. The compression of the streamlines will form the satellite wakes. With the combined effects of collisions and self-gravity, the eccentricity of the wake particles will decrease and the structure will fade. More realistic models involve inter-particle collisions and self-gravity wakes; the latter usually accelerates the damping of the propeller shaped gaps and generally prevents the formation of moonlet wakes.

In our simulations, the boulder stays stable at the center of the simulated box as long as particles are not big enough to change its orbital elements (we verified that this does not happen as long as the particle size radius condition of existence of the depletion zones is respected. It appears that collisions and self-gravity are not playing a key role in the formation of primary propeller signature zones for the initial particle populations described by Zebker et al. (1985) in our regions of interest. However, Lewis & Stewart (2009) showed that self-gravity will generally prevent boulder wakes from forming and will rapidly damp the higher order propeller-shaped gaps. Inputting particles sizes close to the boulder radius will have a similar effect.

We notice that both radial b and azimuthal extensions $r \Delta\phi$ of the primary lobe seem to grow linearly with the boulder radius: $b \approx 3 r_H$, and $r \Delta\phi = (33.4 \pm 2.0)r_H$.

3 Results

We identified 35 ghosts in the C ring plateaus and 265 ghosts in the Cassini Division ringlets and plateaus (mainly in the Huygens Ringlet, the Triple Band and the Cassini Division ramp). No real meaningful spatial distribution can be drawn from our observations since we already selected the places where we were observing. However, we notice that ghosts do not appear in similar locations between occultations. We therefore conclude that these features are not complete circular gaps. In addition, we could estimate an observed radial width W for each of the observed ghosts. The ghosts are a few data points wide, and we can estimate their width by taking the width at half-height of the interpolation of the occultation scan. In first approximation, we measured width ranges for the observed ghosts from 5.4 m to 46.7 m in the C ring and from 1.7 m to 277 m in the Cassini Division.

The UVIS instrument has a constant integration time. However, each occultation has a specific navigation and geometry configuration that changes the spatial resolution in the ring plane. The fact that each occultation has its own resolution introduces a bias in our ghost width measures. In order to estimate the impact of this variability and in order to model the difference between the observable widths and the observed widths, we use a Monte Carlo algorithm designed to model the statistical impact of our occultation resolution variations. This algorithm will evaluate the modeled observed ghost widths from a known particle size distribution. We assume that the particle size distribution in the Cassini Division can be modeled as a power-law. From an arbitrary proportion of the total number of particles, we estimate the corresponding particle radius and model the Hill radius of the boulder and then the width of the ghost that would be created. We assume that this ghost is on a random occultation track, at a random azimuthal distance from the boulder (within the range of the primary open gap) and we estimate what would be measured for its width, given the occultation resolution and based on our interpolated model of the ghost width with respect to the distance from the boulder: this observable width can be zero if the resolution of the occultation is larger than the ghost width. The statistical repetition of this process allows us to determine a cumulative size distribution of the theoretically observed ghost widths. By comparing this distribution with the observed ones, we adjust the initial particle size distribution index in order to match the observable distribution with the observed distribution (by matching both the number of the particles and the shape of the distribution). We estimate that a cumulative power-law index of 0.6 in the C ring and 0.8 in the Cassini Division for the initial particle size distribution will generate ghost-width distributions close to the observed ones. This process happens to provide quite close values between the C ring and the Cassini Division. The difference between these indices is of the same order of magnitude as the difference between the distributions of smaller particles by Zebker et al. (1985): $Q_{Cring} = 2.1$ and $Q_{CD} = 1.75$. From these derived indices, we can estimate that the actual boulder population, that generated our observations, follows a cumulative size distribution not in the prolongation of the one for smaller particles.

4 Discussion

In both the C ring and the Cassini Division, we have been able to identify a population of boulders that would be able to create the ghosts we have observed in UVIS occultation data. These boulders follow less steep power-law distributions than smaller particles, and with similar indices between the C ring and the Cassini Division: 0.6 – 0.8.

Figure 4 compares particle size distributions and boulder size distributions for the C ring and the Cassini Division. Zebker et al. (1985) values for submeter particles were determined with a good accuracy while suprameter particles and in particular upper limits of the distributions were probably overestimated. The boulders appear to not follow the previous trend of the particle size distributions. This is consistent with recent conclusions from Baillié et al. (2011) according to which particles tends to be smaller in the C ring plateaus.

A unique progenitor, big enough to generate the boulder population, would have to be at least 800-m wide for the C ring and at least 2.8-km wide for the Cassini Division. Such small boulders should be able to survive tidal disruption well inside the Roche limit (Goldreich & Tremaine 1982). However, catastrophic disruptions involving cometary collisions would generate a secondary particle population.

In such a scenario, the minor accretion effects would not have allowed the formation of the progenitors in situ. These boulders would have more likely formed outside the main rings and then spiraled inwards by gas drag (Mosqueira & Estrada 2003). They could also be the results of another bigger fragmentation. In addition, we would expect the resulting particle size distribution from a fragmentation process to be steeper than our derived estimations, closer to a power-law distribution with a cumulative index around 3.4 (which is the index obtained for the ejecta of a hammer-destruction of a glacial boulder (Hartmann 1969; Dohnanyi 1969, 1972).

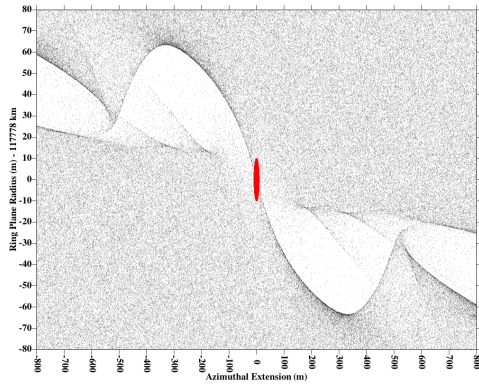


Figure 3. Primary lobes of the propellers created by the interaction of 20-cm radius particles with a 10-m radius boulder. Optical depth is 0.1 and Saturn's direction is towards the bottom.

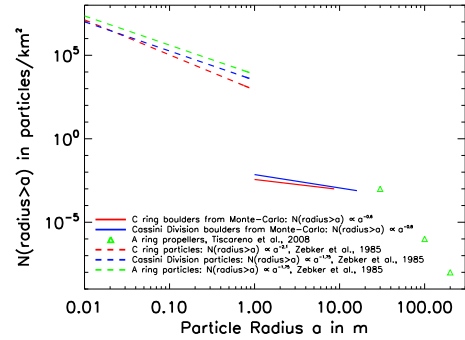


Figure 4. Cumulative particle size distribution for the C ring (red), Cassini Division (blue) and the A ring (green). Submeter particle populations from Zebker et al. (1985) are displayed with dashed lines while the source distribution estimated from the Monte-Carlo algorithm for suprameter particles is displayed in solid lines.

Considering aggregation as the principal effect, it is possible to form temporary aggregates inside the Roche limit (Karjalainen & Salo 2004), which would disturb the encountering particles and clear depletion zones. However, the accretion effects are not predominant in tenuous rings like the C ring or the Cassini Division. In addition, we do not observe any trend in the distribution of our boulder sizes with respect to their distance to Saturn that would strengthen the confidence in this scenario.

This work was supported by NASA through the Cassini Data Analysis Program.

References

- Baillié, K., Colwell, J. E., Esposito, L. W., Sremčević, M., & Lissauer, J. J. 2011, *Icarus* in press
- Dohnanyi, J. S. 1969, *J. Geophys. Res.*, 74, 2531
- Dohnanyi, J. S. 1972, *Icarus*, 17, 1
- Goldreich, P. & Tremaine, S. 1982, *Annual Review of Astronomy and Astrophysics*, 20, 249
- Hartmann, W. K. 1969, *Icarus*, 10, 201
- Karjalainen, R. & Salo, H. 2004, *Icarus*, 172, 328
- Lewis, M. C. & Stewart, G. R. 2009, *Icarus*, 199, 387
- Mosqueira, I. & Estrada, P. R. 2003, *Icarus*, 163, 232
- Petit, J. & Henon, M. 1988, *Astronomy and Astrophysics*, 199, 343
- Showalter, M. R. & Burns, J. A. 1982, *Icarus*, 52, 526
- Showalter, M. R., Cuzzi, J. N., Marouf, E. A., & Esposito, L. W. 1986, *Icarus*, 66, 297
- Spahn, F., Saar, A., Schmidt, S., & Schwarz, U. 1992, *Icarus*, 100, 143
- Spahn, F. & Wiebicke, H. 1989, *Icarus*, 77, 124
- Sremčević, M., Spahn, F., & Duschl, W. J. 2002, *MNRAS*, 337, 1139
- Zebker, H. A., Marouf, E. A., & Tyler, G. L. 1985, *Icarus*, 64, 531

Session 07

Solar physics at the advent of the European Solar
Telescope

RECONSTRUCTION OF THE SOLAR CORONAL MAGNETIC FIELD, FROM ACTIVE REGION TO LARGE SCALE

T. Amari¹, A. Canou¹, F. Delyon¹, J. J. Aly², P. Frey³, F. Alauzet⁴ and SDO/HMI Team⁵

Abstract. The low solar corona is dominated by the magnetic field which is created inside the sun by a dynamo process and then emerges into the atmosphere. This magnetic field plays an important role in most structures and phenomena observed at various wavelengths such as prominences, small and large scale eruptive events, and continuous heating of the plasma, and therefore it is important to understand its three-dimensional properties in order to elaborate efficient theoretical models. Unfortunately, the magnetic field is difficult to measure locally in the hot and tenuous corona. But this can be done at the level of the cooler and denser photosphere, and several instruments with high resolution vector magnetographs are currently available (THEMIS, Imaging Vector Magnetograph (IVM), the Advanced Stokes Polarimeter (ASP), SOLIS, HINODE, Solar Dynamics Observatory (SDO), or will be shortly available by future telescopes such as EST and solar missions as SOLAR-ORBITER. This has lead solar physicists to develop an approach which consists in "reconstructing" the coronal magnetic field from boundary data given on the photosphere. We will discuss some of the issues encountered in solving this problem as well our recent progress and results at the scale of active region scales or the larger one such as full sun scale.

Keywords: solar corona

1 Introduction

The problem of the Reconstruction of the solar coronal magnetic field from solar photospheric boundary data, have been a very active topic of research those last years due to the arrival of high resolution and low noise vector magnetographs on ground such as THEMIS, SOLIS or on board of present solar mission such as HINODE, SDO/HMI and future ones such as EST, as well as SOLAR-ORBITER. We are not willing to present a review of all existing methods (see Aly & Amari (2007); Schrijver et al. (2006)) but will just say for the purpose of this Paper, that the main classes methods are optimisation methods (Wiegelmann 2004) which use all photospheric data and try to minimize a cost function measuring the difference between the computed transverse field and the measured one, those based on magnetohydrodynamics relaxation methods Valori et al. (2005) and on Grad Rubin based method (Sakurai 1981; Amari et al. 1999; Inhester & Wiegelmann 2006; Wheatland 2007). Recently (Amari et al. 2006) presented two methods which attempt to solve the Grad-Rubin Boundary Value Problem (GRBVP), namely XTRAPOL and FEMQ, the first one based on a finite difference approximation and the second one a finite element approximation.

Most of the methods however have addressed the active region scale. With the arrival of SOLIS, and SDO/HMI high resolution, composite vector magnetograms made of several active regions, or embedded in a full disk vector magnetogram of synoptic vector magnetograms become possible. Furthermore vector magnetic fields are also measured on stars at a lower resolution and with different technics, with less accuracy (Donati et al. 2007). This therefore raises the issue of availability of such models at this scale, where the sphericity cannot be negligible. Only very recently extension of reconstruction methods to spherical systems for full sun

¹ CNRS, Centre de Physique Théorique de l'Ecole Polytechnique, F-91128 Palaiseau Cedex, France.amari@cpt.polytechnique.fr

² AIM - Unité Mixte de Recherche CEA - CNRS - Université Paris VII - UMR n° 7158, Centre d'Études de Saclay, F-91191 Gif sur Yvette Cedex, France

³ Laboratoire Jacques Louis Lions, Université Pierre et Marie Curie, 4, place Jussieu, tour 15-25 (3-17), 75005 Paris

⁴ INRIA - Projet Gamma. Domaine de Voluceau - Rocquencourt - B.P. 105.78153 Le Chesnay Cedex (France)

⁵ Stanford University. HEPL Annex, B210.Stanford, CA 94305-4085 USA

scale have been considered. Principally, the optimization methods have been extended to spherical geometry (Wiegelmann 2007). Moreover, either for full disk or synoptic maps strong constraints on spatial resolution are imposed due to the fact that active regions represents only small fraction on the sun surface and therefore neither uniform nor non uniform structured mesh cannot fit such structures in an optimal way..

In the present paper we recall the principles of method we use, show some of our striking results we have obtained at the active region scale. Then we present the extension of our Grad Rubin well posed method to the system of spherical coordinates as well as its current extension to unstructured tetrahedral mesh including the possibility of adaption. As for our cartesian formulation we favor this approach because it correspond to a well posed boundary value problem.

2 The Equilibrium Reconstruction Problem : Boundary Value Problem

In the model we consider, the corona and the photosphere are represented by a domain Ω which can be either the exterior of a sphere or part of it limited in longitude or latitude, or even actually the half-space $\Omega = \{z > 0\}$ and the plane $\partial\Omega = \{z = 0\}$, respectively. Ω is assumed to be filled up with a low beta slightly resistive and viscous plasma embedded in a magnetic field \mathbf{B} which is taken to be force-free and to decrease sufficiently fast to zero at infinity. Therefore, it does obey the equations

$$\nabla \times \mathbf{B} = \alpha \mathbf{B}, \quad (2.1)$$

$$\nabla \cdot \mathbf{B} = 0. \quad (2.2)$$

It results at once from Eqs. (2.1)-(2.2) that the function α satisfies the constraint

$$\mathbf{B} \cdot \nabla \alpha = 0 \quad (2.3)$$

which merely states that α keeps a constant value along any field line.

The set of equations (2.1)-(2.2) has a mixed elliptic-hyperbolic structure. Basically, it can be decomposed into an elliptic part for \mathbf{B} (at α given), and an hyperbolic one for α (at \mathbf{B} given), associated with Eq. (2.3). To solve for the elliptic part, one should give the normal component B_n of the magnetic field on $\partial\Omega$, while to solve for the hyperbolic one, Eq. (2.3) indicates that the value of α should be given on the part $\partial\Omega^+$ of $\partial\Omega$ where $B_n > 0$, say. This leads us to consider the BVP first introduced by Grad & Rubin (1958). It consists of Eq. (2.1)-(2.3) along with the boundary conditions

$$B_n|_{\partial\Omega} = b_0, \quad (2.4)$$

$$\alpha|_{\partial\Omega^+} = \alpha_0, \quad (2.5)$$

where b_0 and α_0 are two given regular functions, and the asymptotic condition

$$\lim_{|\mathbf{r}| \rightarrow \infty} |\mathbf{B}| = 0. \quad (2.6)$$

In the numerical practice, instead of having an unbounded domain we consider the bounded domain Ω_b . Then the asymptotic condition (2.6) is no longer useful and the boundary conditions (2.4)-(2.5) are imposed on the whole $\partial\Omega_b$.

2.1 Principle of the Grad-Rubin method

In the Grad-Rubin method, the BVP above is solved iteratively, with its elliptic and hyperbolic parts being solved successively at each step. More precisely, we look for a sequence $(\mathbf{B}^{(n)}, \alpha^{(n)})$ solution of – BVP-GR hereafter –

$$\mathbf{B}^{(n)} \cdot \nabla \alpha^{(n)} = 0 \quad \text{in} \quad \Omega_b, \quad (2.7)$$

$$\alpha^{(n)}|_{\partial\Omega_b^+} = \alpha_0, \quad (2.8)$$

and

$$\nabla \times \mathbf{B}^{(n+1)} = \alpha^{(n)} \mathbf{B}^{(n)} \quad \text{in} \quad \Omega_b, \quad (2.9)$$

$$\nabla \cdot \mathbf{B}^{(n+1)} = 0 \quad \text{in} \quad \Omega_b, \quad (2.10)$$

$$B_z^{(n+1)}|_{\partial\Omega_b} = b_0. \quad (2.11)$$

The iteration process is initialized by choosing for $\mathbf{B}^{(0)}$ the unique solution of

$$\nabla \times \mathbf{B}^{(0)} = 0 \quad \text{in} \quad \Omega_b, \quad (2.12)$$

$$B_z^{(0)}|_{\partial\Omega_b} = b_0. \quad (2.13)$$

To address the $\text{div } B = 0$ constraint, XTRAPOL uses a vector-potential formulation with a particular gauge defined by $\mathbf{B} = \nabla \times \mathbf{A}$ in Ω_b , with the gauge condition $\nabla \cdot \mathbf{A} = 0$ in Ω_b , and $\nabla_t \cdot \mathbf{A}_t = 0$ on $\partial\Omega_b$, where the subscript t in ξ_t stands for the trace (when it exists) of the tangential component on the boundary of the operator or the field ξ . As noted in Amari et al. (2006), this gauge implies that $\partial_n A_n = 0$ on $\partial\Omega_b$, where $\partial_n f = \hat{n} \cdot \nabla f$.

In the vector potential formulation, the iteration on \mathbf{B} translates into an iteration on \mathbf{A} . $\mathbf{A}^{(n+1)}$ is a vector field belonging to the space $[C^2(\Omega_b) \cup C^1(\partial\Omega_b)]^3$.

The characteristics $(\mathbf{X}; s)$ is a solution of (Amari et al. 2006) $\mathbf{X}' = \mathbf{B}(\mathbf{X})$, with $\mathbf{X}(0) = \mathbf{q}$, for \mathbf{q} given in Ω_b (the prime symbol standing for differentiation with respect to the parameter that runs along the characteristics). Then for any node $\mathbf{q}_h \in \Omega_b$ at which α is defined, one gets α_h as

$$\alpha(\mathbf{q}_h) = \alpha_0(\mathbf{X}_{\partial\Omega_b^+}(\mathbf{q}_h)), \quad (2.14)$$

where $\mathbf{X}_{\partial\Omega_b^+}(\mathbf{q}_h) = \mathbf{X}(\mathbf{q}_h, s_{\partial\Omega_b^+})$ is the intersection of $\{\mathbf{X}(\mathbf{q}; s) : s < 0\}$ with $\partial\Omega_b^+$. Since α_0 is known at nodes that do not in general coincide with $\mathbf{X}_{\partial\Omega_b^+}(\mathbf{q}_h)$, we use an interpolation from its four nearest neighbors. We use a high order Adams-Bashford integration scheme with adaptive step size, which also allows us to capture the ending point of the characteristics defining the limits of the computational box.

One major difference between our Grad-Rubin method and the other methods recalled above, is the fact that those methods uses all the photospheric data as boundary conditions (the three components of the magnetic field), and have therefore to face the ill-posedness of the method, while the Grad-Rubiin method uses α only in one polarity and therefore corresponds to a well posed boundary value problem. However it thus results that the values of α computed in the polarity where it is not imposed, may not match the observed values. Very recently a new approach has been proposed in which the values of α are imposed on the boundary as a weight of the values taken on each polarity. Those are obtained as the solution of an optimization problem such that it minimizes the differences between the computed values and the measured ones in the whole photosphere. This new Grad-Rubin-Optimization-Methods has been shown to give good results with robustness (Amari & Aly 2010).

3 Active Region Scale Scheme

The Grad-Rubin method we have developed above has been successful applied to the modeling of several active regions. In particular it has shown that Twisted Flux Ropes are actually at the origin of several structures observed in the corona using various sources of magnetograms. Using THEMIS we have been able to show for the first time that the emergence of of a twisted flux rope from below the photosphere was associated to a flux rope present in the corona (Canou et al. 2009). Moreover using HINODE, it was possible to show that a Twisted Flux Rope was also at the heart of the magnetic configuration supporting a filament (Canou & Amari 2010) as show on Figure 1.

4 Global and Full Disk Schemes

To face the case of large scale synoptic magnetograms, for which the cartesian geometry used at the active region scale is no longer valid, we have extended the Grad-Rubin Method presented above to the system of spherical coordinates. Such type of magnetograms are now provided by SDO/HMI or SOLIS as shown on Figure 3. Moreover the large amount of data imposes the necessity of developing a numerical which is able to run on massively parallel computers..

The couple of hyperbolic and elliptic BVPs are also valid when Ω_b is a spherical shell comprised between the two spheres $S_0 = \{r = r_0\}$ and $S_1 = \{r = r_1\}$, $\{\mathbf{r} = (x, y, z) \in R^3, r_0 < \|\mathbf{r}\| < r_1\}$, with $r_1 > r_0 > 0$. Moreover compared to the cartesian version, the hyperbolic problem is solved such that for a given point in the domain we use mapping from spherical to cartesian coordinates while going back along the characteristic (Amari et al. 2011a). We have applied successfully our solver to the case of the non linear force free Low and Lou solution (Low & Lou 1991) in spherical geometry as shown on Figure 3.

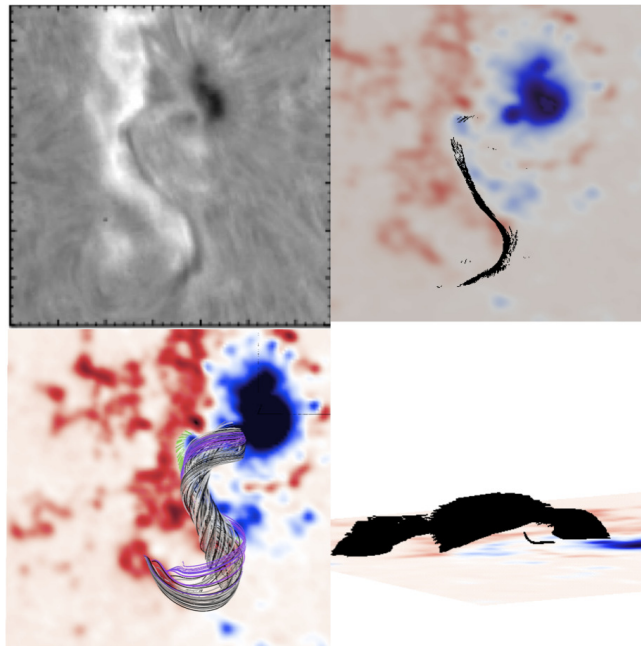


Fig. 1. Comparison of the H- α image taken by SMART (top left panel) on April 29 at 22:10 and the dips corresponding to the non linear force free configuration reconstructed with XTRAPOL (top right panel), in good agreement. A Twisted Flux Rope (bottom left panel) is clearly present and its dips (bottom right panel) exhibit the structure of the observed filament.

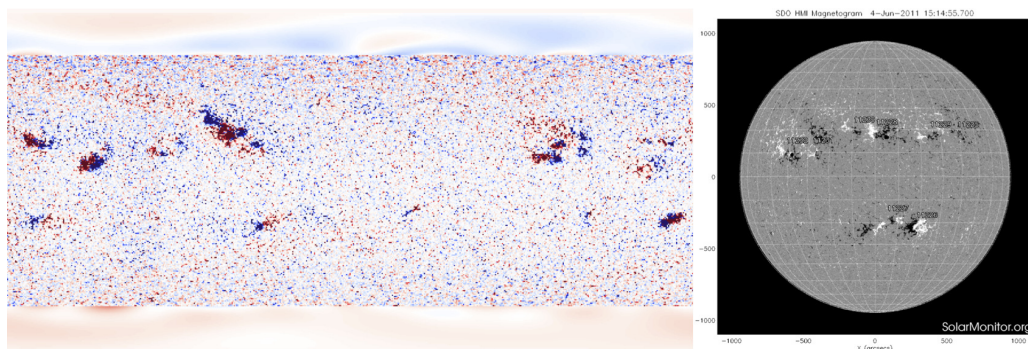


Fig. 2. Example of photospheric magnetic data (photospheric longitudinal field) provided by SDO/HMI for synoptic map (left panel) or full disk (right panel).

The algorithm presented is parallel both for the Elliptic and Hyperbolic problems. We use domain decomposition with the MPI interface on our staggered mesh.

Full disk or synoptic maps impose strong constraints on spatial resolution since active regions represent only a small fraction of the sun surface as shown on Figure 2. Therefore either uniform or non uniform structured mesh cannot fit such structures in an optimal way. For this reason we have recently developed a new approach which consists in extending the Grad-Rubin method to unstructured (tetrahedral) mesh with adaption of the mesh to the solution. This is a quite involving enterprise in which we needed to construct a whole mathematical background including a series of operators such as \mathbf{curl} , $\nabla \cdot$, ∇ on preceding Hilbert Spaces, as well as the boundary value problems on those mesh involving the composition of those operator defined at various locations such as tetrahedra nodes, center, edges, faces (Amari et al. 2011b). We use an adaptation method based on metric computation. Such adaptation can be isotropic or anisotropic. This is used for surface adaptation as well as in the domain during the Grad-Rubin iteration scheme. As seen on Figure 4 this allows to have good surface adaption in the case of synoptic and full disk data. The solution is then computed and the mesh is adapted to the solution in the sense of error targets, in an internal iterative loop during which the solution is

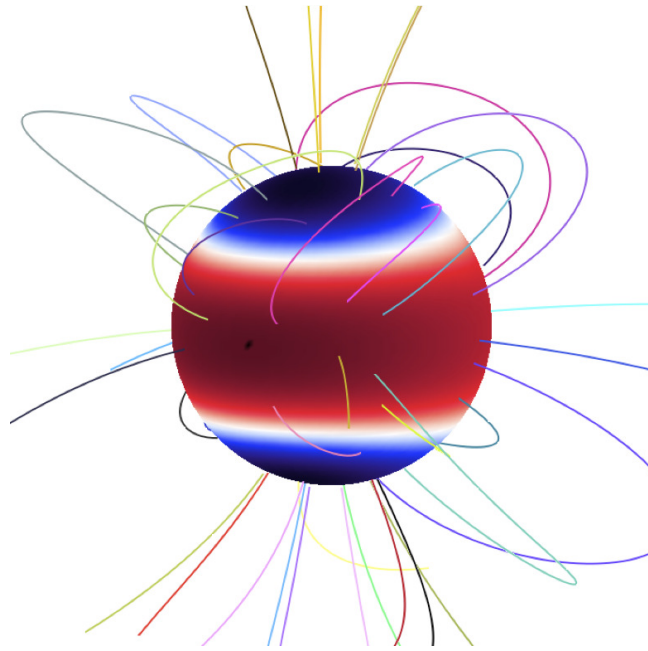


Fig. 3. Field lines of the reconstructed configuration using XTRAPOL in spherical geometry, corresponding to the Low and Lou solution.

computed with the new mesh until adaption is realized. The final solution is obtained in Figure 4 .

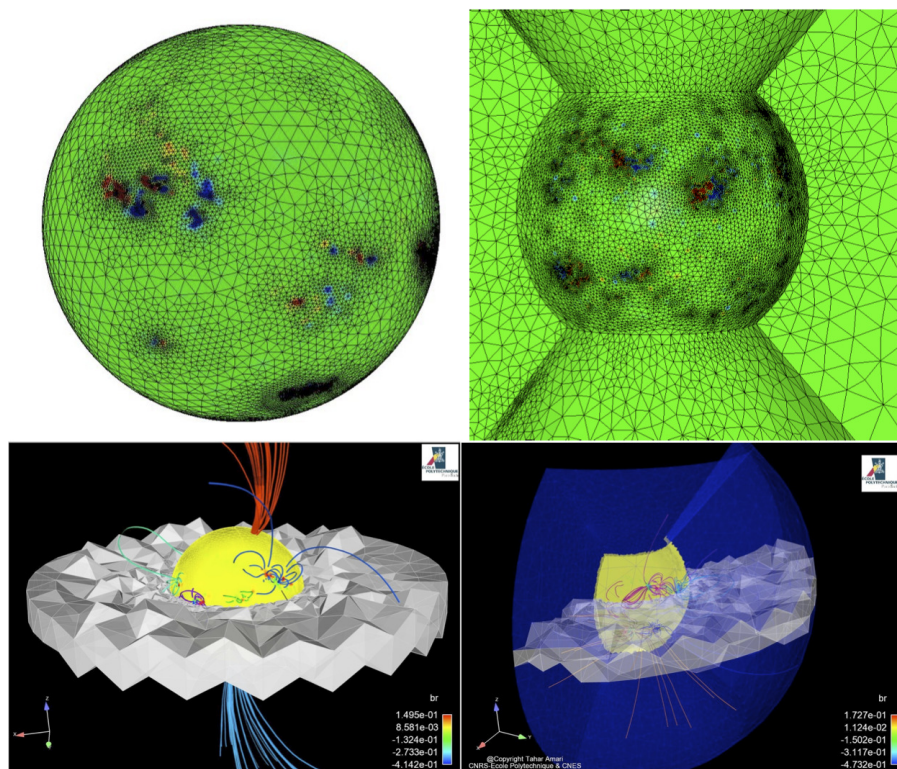


Fig. 4. Resulted mesh obtained after adaption on the photospheric mesh generated after iteration loop for the photospheric synoptic magnetogram (top left panel) and full disk data (right panel). Volume solution and mesh after adaption loop for synoptic case (bottom left panels), and full disk case (bottom right panel).

We acknowledge support from Centre National d'Etudes Spatiales. The numerical simulations performed in this paper have been done on the NEC SX8 supercomputer of the Institute I.D.R.I.S of the Centre National de la Recherche Scientifique.

References

- Aly, J. J. & Amari, T. 2007, *Geophysical and Astrophysical Fluid Dynamics*, 101, 249
- Amari, T. & Aly, J.-J. 2010, *A&A*, 522, A52+
- Amari, T., Aly, J.-J., & Mikic, Z. 2011a, *ApJ*, in press
- Amari, T., Boulmezaoud, T. Z., & Aly, J. J. 2006, *A&A*, 446, 691
- Amari, T., Boulmezaoud, T. Z., & Mikic, Z. 1999, *A&A*, 350, 1051
- Amari, T., Delyon, F., Frey, P., & Aulazet, F. 2011b, *ApJ*, in press
- Canou, A. & Amari, T. 2010, *ApJ*, 715, 1566
- Canou, A., Amari, T., Bommier, V., et al. 2009, *ApJ*, 693, L27
- Donati, J.-F., Jardine, M. M., Gregory, S. G., et al. 2007, *MNRAS*, 380, 1297
- Grad, H. & Rubin, H. 1958, in *Proc. 2nd Intern. Conf. on Peaceful Uses of Atomic Energy*, Vol. 31, United Nations, Geneva, 190–197
- Inhester, B. & Wiegelmann, T. 2006, *Sol. Phys.*, 235, 201
- Low, B. C. & Lou, Y. 1991, *ApJ*, 352, 343
- Sakurai, T. 1981, *Solar Phys.*, 69, 343
- Schrijver, C. J., Derosa, M. L., Metcalf, T. R., et al. 2006, *Sol. Phys.*, 235, 161
- Valori, G., Kliem, B., & Keppens, R. 2005, *Astron. Astrophys.*, 433, 335
- Wheatland, M. 2007, *Solar Phys.*, 245, 251
- Wiegelmann, T. 2004, *Solar Phys.*, 219, 87
- Wiegelmann, T. 2007, *Sol. Phys.*, 240, 227

ADAPTIVE OPTICS SYSTEM PERFORMANCES AND LARGE FIELD OF VIEW SPECTROPOLARIMETRIC OBSERVATIONS

G. Aulanier¹ and G. Molodij¹

Abstract. In the context of the increasing interest for large aperture telescope dedicated to the Sun such as EST or ATST projects, we* present a study to evaluate the adaptive optics system limitations in regard of the scientific requirements expected for magnetic field extrapolations and data-driven MHD simulations of active regions. The questions we address are: what is the size of the field of view at high spatial resolution for a 4 meter class telescope with a spectrograph, what is the impact of the selected spectral domain on the performances in relation to the scientific goals aforementioned ? We show that the visible wavelength domain still remains difficult to explore with ground-based telescope using a classical adaptive optics system. The field of view obtained will be only few arcsecs at diffraction limit for the most part of the observation time.

Keywords: adaptive optics, spectropolarimetry, turbulence

1 Introduction

Solar physics research requires observations of magnetic features in a challenging range from one tenth of an arcsecond, for flux tubes, to a few arc-minutes, for active regions. Another demand on the image compensation system is that the observer should be able to analyze a broad field of view, in order to extrapolate the magnetic field. Even though focused studies of small delta-spots only require relatively small field of views, about 1.6 arcmin in Canou et al. (2009), the typical field of view size required for extrapolation purposes is larger than 2 arcmin: typically 3 to 4 arcmin for emerging active regions, sigmoids and medium-sized filaments (Aulanier & Schmieder 2002; Pariat et al. 2004; Schrijver et al. 2008; Canou & Amari 2010), and even up to 6 arcmin for large filaments, full AR studies and later use the results and initial conditions for MHD simulations (Lionello et al. 2002; Metcalf et al. 2008; Masson et al. 2009). Adaptive optics (AO) is used to recover diffraction-limited resolution with ground-based large telescopes, by compensating in real-time atmospheric turbulence. However, adaptive optics requires a reference source close to the object of interest in order to accurately sense the wavefront disturbed by turbulence. The limitation of the efficiency of the compensation by the adaptive optics is due to the conventional anisoplanatism effect (Fried 1982). The wavefronts incoming from two angular-separated structures on the Sun are different because of the different path through the atmosphere. This effect limits the field of view around the reference source where an efficient correction can be achieved. High image quality is an important requirement for the observation of small solar magnetic features like magnetic flux tubes. Nevertheless, accurate magnetic field topology studies which involve relatively small flux concentrations, need not only a good spatial resolution but also an homogeneous compensation of the terrestrial turbulence effects on an extended field of view. In order to evaluate the limitations due to anisoplanatism, we present useful tools to determine the quality of the measurement of the magnetic field after adaptive optics compensation (Molodij & Aulanier 2011).

2 Analysis of adaptive optics system performances

In this section, we present new simple analytic laws to evaluate both the size of the corrected field of view and the image quality for any classical AO systems and telescope apertures. Theoretical techniques to evaluate the

¹ LESIA-Observatoire de Paris, CNRS, UPMC Univ Paris 06, Univ. Paris-Diderot

*the Guillaumes

effects of anisoplanatism upon the performance of adaptive optics system are detailed in Molodij & Rousset (1997); Molodij & Rayrole (1998); Molodij (2011). The image quality after AO correction is given by Noll (1976) as $\sigma_J^2 \propto (D^2/J)^{5/6}$, and we show that the behavior of the isoplanatic field of view after AO correction is $\theta_{cor} \propto D/\sqrt{J}$, where J is the number of compensated modes and D the telescope aperture. Figure 1 shows the optimal field of view θ_{cor} and the optimal image quality related to the residual phase variance σ_J^2 versus the number of compensated modes J of the AO for three different telescope apertures (1, 2 and 4 meter class telescope). The dashed bottom lines indicate the image quality expected after J compensated modes (the Strehl ratio is $SR = e^{-\sigma^2}$). For instance, conventional "diffraction-limited" aberration level is set at the Strehl ratio of 0.8 ; i.e, a value of $\sigma^2 = 0.2 \text{ rad}^2$ (indicated by the horizontal dotted line in Fig.1). Vertical arrows defined by the intersection of the 80 % Strehl ratio and the σ_J^2 functions give both the maximum order of compensated J of the AO and the isoplanatic patch (intersection of the arrow and θ_{cor} functions). A value θ_{iso} of 5 arcsec is found for the Hufnagel profile (Hufnagel 1974) that has been used to calculate the different terms in the residual wavefront error $\sigma^2(J, \alpha)$. A median value of r_0 at Haleakala site is 9.7 cm, result of 92307 measurements for 651 days from 2002 January to 2004 August, has been derived from the probability exceedance function of r_0 for daytime measurements (Bradley et al. 2006). We remark first that the isoplanatic patch at diffraction after

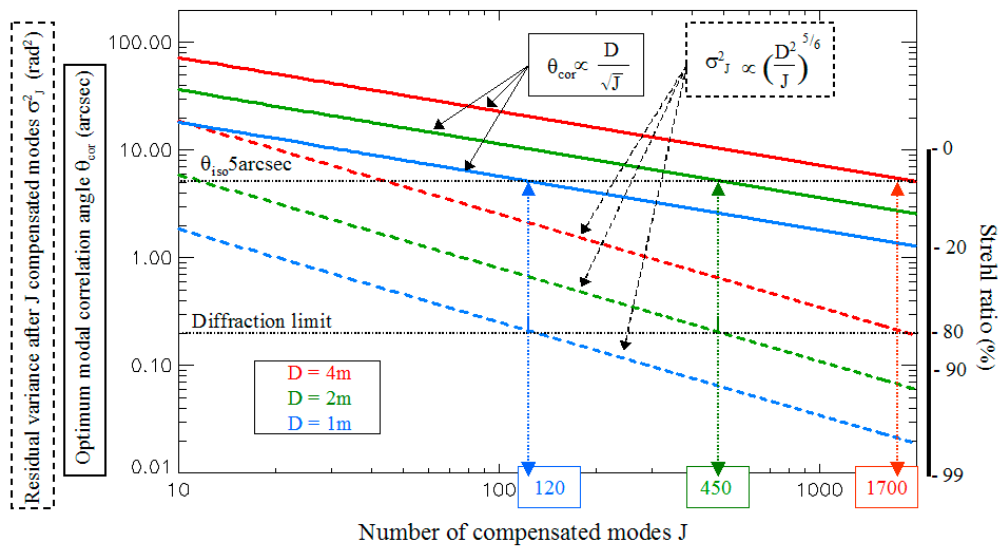


Fig. 1. Optimal field of view θ_{cor} (plain lines) and optimal image quality related to the residual phase variance σ_J^2 (dashed lines) versus the number of compensated modes J of the AO for three different telescope apertures (1, 2 and 4 meter class telescope respectively indicated in blue, green and red). Vertical axis on left shows both the residual phase variance expressed in rad^2 and the optimum field of view (arcsec) in log units. Right vertical axis indicates the Strehl ratio related to the residual phase variance. Notice that the conventional diffraction-limited aberration level is set at the Strehl ratio of 0.8 ; i.e, a value of $\sigma^2 = 0.2 \text{ rad}^2$

AO compensation is independent of the telescope aperture. Secondly, in the case of a 4 meter class telescope, increasing the number of freedom J from 450 actuators up to 1700 does not lead to a considerable increase of the Strehl ratio but reduce 66 % of useful field of view. Figure 2 gives the isoplanatic domain (twice the defined isoplanatic angle θ_{iso}) for $\sigma_0 = 2\pi/5$ corresponding to $\lambda/5$, i.e., a Strehl ratio around 20 %. This arbitrary value of the residual error is the minimum image quality expected for astronomical observations. Figure 2 shows the isoplanatic domains estimated for a 4 meter class telescope after compensation by different adaptive systems from a low-order system after $J = 10$ corrected modes up to $J = 1540$ to reach the diffraction limit in visible wavelength range. We show that the capacity of high order adaptive optics system is suitable for high spatial resolution observations with a severe reduction of the field of view. As expected, the isoplanatic angle θ_{iso} increases with the increase of the observation wavelength. The near infrared spectral domain remains the only possibility to obtain large field of views using classical AO system for a 4 meter class telescope. Examples are the COMEon+ 52 actuators (Léna 1994) or the NAOS 185 actuators system (Lagrange et al. 2003). Two phenomena confer a serious advantage to choose the infra red spectral domain for the magnetometry for large

aperture telescope. The first is due to the higher sensitivity of the IR spectral lines to the Zeeman effect: Zeeman shifts are proportional to $g\lambda^2$ where g is the Landé factor. The second is coming from the properties of the turbulence: the value of the Fried's parameter $r_0 = 10$ cm in the visible wavelength range becomes 60 cm at $2.2 \mu\text{m}$, for instance. Figure 3 shows that the expected isoplanatic field of view is 4 more times larger in the $1.6 \mu\text{m}$ IR band than in the visible range.

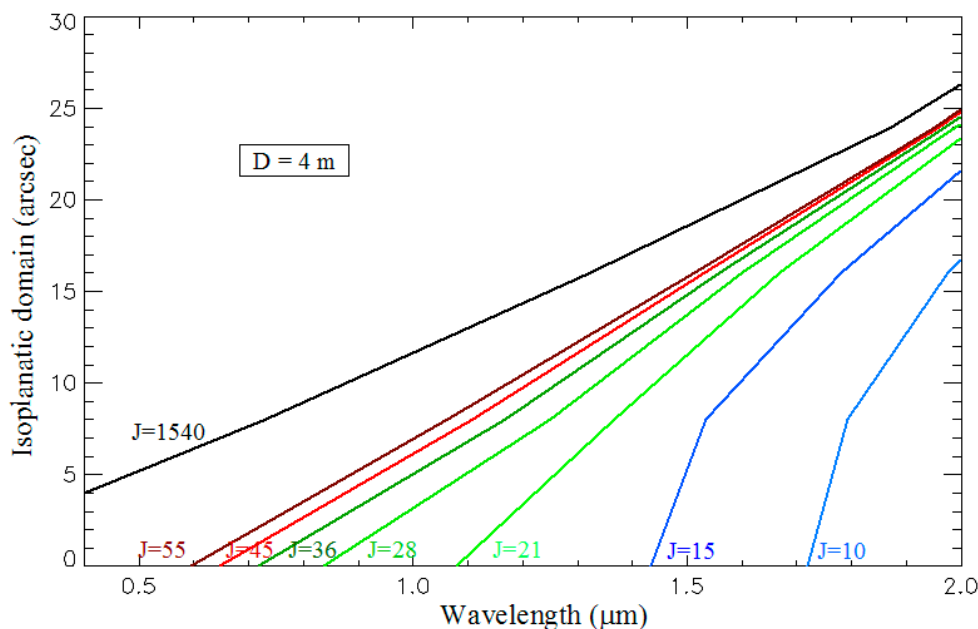


Fig. 2. Isoplanatic domain corresponding to an image quality criterion of $\frac{\lambda}{5}$, versus wavelength, for a 4 meter class telescope after compensation of $J = 10$ up to 1540 modes. Curves are computed with the Hufnagel C_n^2 turbulence profile ($r_0 = 10$ cm @ $\lambda=0.5 \mu\text{m}$).

3 Conclusion

We presented a study to evaluate the adaptive optics system limitations in regard of the scientific requirements expected for magnetic field extrapolations and data-driven MHD simulations large field of views. Questions we addressed are: Can ground based telescopes with adaptive optics systems fulfill the requirements of extrapolations and data-driven MHD simulations? In other words, are large field of views of few arcminutes size accessible at high spatial resolution from the ground? We show that the visible wavelength domain still remains difficult to explore with ground-based telescope using a classical adaptive optics system. The isoplanatic field of view resulting of the compensation of a classical adaptive optics system is only few arcsecs at diffraction limit for usual condition of the atmospheric turbulence. The classical adaptive optics system is unable to reach the required performances in the visible wavelength range in usual conditions of observation. The near infra-red spectral domain remains the only possibility to obtain large field of views using classical AO system for large aperture telescopes. The expected isoplanatic field of view at diffraction is 4 more times larger in the $1.6 \mu\text{m}$ IR band than in the visible range for usual conditions of observation but it still remains to small to cover a whole active region in a single scan passage. Another advantage comes from the higher sensitivity of the IR spectral lines to determine the magnetic flux from spectropolarimetric observations with ground-based observations at $1.56 \mu\text{m}$ (Beck & Rezaei 2009) and at $1.083 \mu\text{m}$ He I (Kuckein et al. 2010) to study the chromospheric dynamics. A 4m class telescope would be well-sized to the only study of the magnetic field dynamics at the granule scale. A question remains on the adequacy of a 4m class by comparison to a 2m class diameter class telescope except to the purpose of collecting more photons.

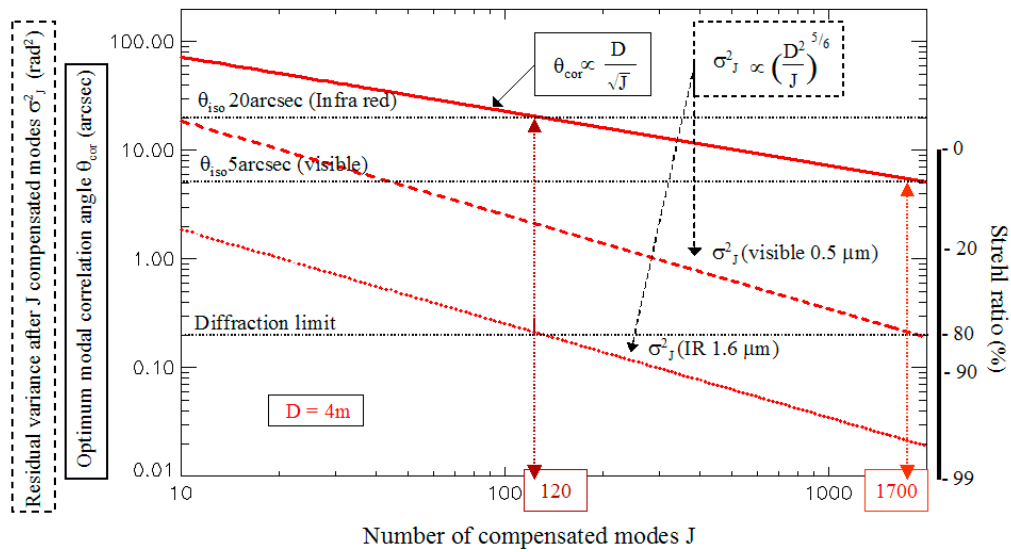


Fig. 3. Comparison of the optimal field of view θ_{cor} (plain lines) and optimal image quality related to the residual phase variance σ_J^2 (dashed lines) versus the number of compensated modes J of the AO for the visible and the infra red spectral domain (4 meter class telescope). Vertical axis on left shows both the residual phase variance expressed in rad^2 and the optimum field of view (arcsec) in log units. Right vertical axis indicates the Strehl ratio related to the residual phase variance.

References

- Aulanier, G., Schmieder, B., 2002, *A & A*, 386, 1106.
- Beck, C., Rezaei, R., 2009, *A&A*, 502, 969.
- Bradley, E.E., Roberts, L.C., Bradford, L.W., Skinner, M.A., Nahestedt, D.A., Waterson, M.F. and Kuhn, J.R., 2006, *P.A.S.P.*, 118, 172.
- Canou, A., Amari, T., Bommier, V., Schmieder, B., Aulanier, G., Li, H., 2009, *Ap.J.*, 693, 27.
- Canou, A., Amari, T., 2010, *Ap.J.*, 715, 1566.
- Fried, D.L., 1982, *J.Opt.Soc.Am.A.*, 72, 52.
- Hufnagel, R.E., 1974, in *Optical Propagation Through Turbulence*, OSA Technical Digest Series, OAS, Washington DC, WA1-1 WA1-4.
- Kuckein, C., Centeno, R., Martinez Pillet, V., 2010, arXiv1001.2434.
- Lagrange, A-M., Chauvin, G., Fusco, T., Gendron, E., Rouan, D., Hartung, M., Lacombe, F., Mouillet, D., Rousset, G., Drossart, P., Lenzen, R., Moutou, C., Brandner, W., Hubin, N., Clenet, Y., Stolte, A., Schoedel, R., Zins, G., Spyromilio, J., 2003, *SPIE* 4841, 860.
- Léna, P., 1994, *SPIE* 2201, 1099.
- Lionello, R., Mikic', Z., Linker, J.A., Amari, T., 2002, *Ap.J.*, 581, 718.
- Masson, S., Pariat, E., Aulanier, G., Schrijver, C. J., 2009, *Ap.J.*, 700, 559.
- Metcalfe, T.R., De Rosa, M.L., Schrijver, C.J., Barnes, G., Van Ballegoijen, A.A., Wiegmann, T., Wheatland, M.S., Valori, G., McTiernan, J.M.: 2008, *Sol. Phys.*, 247, 269.
- Molodij, G., Rousset, G., 1997, *J.Opt.Soc.Am.A.*, 14, 1949.
- Molodij, G. and Rayrole, J., 1998, *Astron.Astrophys.Suppl.Ser.*, 128, 229.
- Molodij, G., *J.Opt.Soc.Am.A.*, 28, 8, 1732, 2011.
- Molodij, G. and Aulanier, A., *Sol.Phys.*, in press.
- Noll, R.J.:1976, *J.Opt.Soc.Am.A.*, 66, 207.
- Pariat, E., Aulanier, G., Schmieder, B., Georgoulis, M. K., Rust, D. M., Bernasconi, P. N., 2004, *Ap.J.*, 614, 1099.
- Schrijver, C.J., De Rosa, M.L., Metcalfe, T., Barnes, G., Lites, B., Tarbell, T., McTiernan, J., Valori, G., Wiegmann, T., Wheatland, M. S., Amari, T., Aulanier, G., Démoulin, P., Fuhrmann, M., Kusano, K., Régnier, S., Thalmann, J. K., 2008, *Ap.J.*, 675, 1637.

MAGNETOHYDRODYNAMICS TURBULENCE: WAVES OR EDDIES?

S. Galtier¹ and B. Bigot²

Abstract. The dynamics of 3D incompressible MHD turbulence is strongly affected by the presence of a large-scale magnetic field \mathbf{B}_0 . In a recent work we have investigated through high-resolution direct numerical simulations this dynamics for a driven turbulence. The analysis reveals a non trivial interaction between the 2D state (eddy turbulence) and the 3D modes (wave turbulence). In particular, it is shown that an initial 2D state without energy is unstable: energy is transferred from the 3D modes to the 2D state with an effectiveness larger for stronger B_0 . In this case, the final state is a mixture of eddy and Alfvén wave turbulence.

Keywords: Turbulence, magnetohydrodynamics, solar physics, Alfvén waves

1 Introduction

A variety of astrophysical plasmas is well described by incompressible MHD turbulence. It is particularly true in solar physics with coronal loops (*e.g.* Galtier, 1999; Buchlin & Velli, 2007) or coronal holes (*e.g.* Bigot, Galtier & Politano, 2008a). It is therefore important to continue the theoretical investigation of MHD turbulence which started half century ago. The first description proposed by Iroshnikov–Kraichnan (1964, 1965 – hereafter IK) is a heuristic model for incompressible MHD turbulence à la Kolmogorov where the large-scale magnetic field fluctuations are supposed to act on small-scales as a uniform magnetic field, leading to counterpropagating Alfvén wave packets whose interactions with turbulent motions produce a slowdown of the nonlinear energy cascade. The typical transfer time through the scales is then estimated as τ_{eddy}^2/τ_A (instead of τ_{eddy} for Navier-Stokes turbulence), where $\tau_{eddy} \sim \ell/u_\ell$ is the eddy turnover time at characteristic length scale ℓ and u_ℓ is the associated velocity. The Alfvén time is the time of collision between two counterpropagating wave packets and is estimated as $\tau_A \sim \ell/B_0$ where B_0 represents the large-scale magnetic field normalized to a velocity ($\mathbf{B}_0 \rightarrow \mathbf{B}_0\sqrt{\mu_0\rho_0}$). Hence, the energy spectrum in $k^{-3/2}$ unlike the $k^{-5/3}$ Kolmogorov one for neutral flows. The weakness of the IKs phenomenology is the apparent contradiction between the presence of Alfvén waves and the absence of a real uniform magnetic field: the external field is supposed to be played by the large-scale magnetic field but its main effect – anisotropy – is not included in the description.

Two fundamental evolutions in MHD turbulence have been made during the last two decades. There are both concerned with anisotropy. The first one is the conjecture that the refined times $\tau_{eddy} \sim \ell_\perp/u_{\ell_\perp}$ and $\tau_A \sim \ell_\parallel/B_0$ (where \perp and \parallel are respectively the perpendicular and parallel directions to the mean magnetic field \mathbf{B}_0) are balanced at all scales (Goldreich & Sridhar, 1995). It leads to the heuristic $k_\perp^{-5/3}$ energy spectrum as well as the relationships $k_\parallel \sim k_\perp^{2/3}$. Whereas the first relation is a trivial consequence of the conjecture, the second prediction reveals a non trivial character of MHD turbulence. The second fundamental evolution is the possibility to handle the effects of a strong B_0 on the MHD dynamics through a rigorous mathematical treatment of wave turbulence which leads asymptotically to a set of integro-differential equations. The exact solution for Alfvén wave turbulence at zero cross-helicity is a k_\perp^{-2} energy spectrum (Galtier et al., 2000). Note that the form of the energy spectrum in the regime of strong turbulence is still the subject of discussions (*e.g.* Galtier et al., 2005; Boldyrev, 2006) although the relationships $k_\parallel \sim k_\perp^{2/3}$ seems to be often verified, whereas the weak turbulence prediction has been obtained recently by two independent set of direct numerical simulations (Bigot et al., 2008b; Perez & Boldyrev, 2008).

¹ Univ Paris-Sud, Institut d’Astrophysique Spatiale, UMR 8617, bâtiment 121, 91405 Orsay, France

² Institut de Mécanique des Fluides, 1 Allée du Professeur Soula, 31400 Toulouse, France

2 2D versus 3D dynamics

In a recent paper (Bigot & Galtier, 2011) we have investigated through high-resolution direct numerical simulations the MHD dynamics for a driven turbulence and in the presence of a uniform magnetic field. In particular, the temporal and spectral properties of the 2D state (eddy turbulence) are investigated. We have shown that if initially the energy contained in the 2D state is set to zero it becomes shortly non negligible in particular when the intensity of B_0 is strong. For our larger B_0 intensity ($B_0 = 15$, with fluctuations b_{rms} of order one) this energy saturates in the stationary phase around 2/3 of the total energy whereas the energy of the 3D modes remains roughly constant. In all situations, the magnetic energy dominates the kinetic energy but it is shown that at large B_0/b_{rms} and in the decay phase the natural state for the 3D modes is the equipartition whereas the 2D state is magnetically dominated.

From a spectral point of view, when the B_0 intensity is strong enough the k_{\perp} -energy spectra are mainly composed at large scales by the 2D state and at small scales by the 3D modes. This situation is similar to rotating turbulence for neutral fluids (Smith & Waleffe, 1999) where in particular the nonlinear transfers are reduced along the rotating rate. However, a detailed analysis of the temporal evolution of the 2D state energy spectra shows that a direct cascade happens whereas for rotating turbulence an inverse cascade is generally evoked. The same remark holds for energy spectra at fixed $k_{\parallel} > 0$ where we observe additionally a pinning effect at large k_{\perp} . According to the value of B_0/b_{rms} scalings close to $k_{\perp}^{-3/2}$, $k_{\perp}^{-5/3}$ or k_{\perp}^{-2} are found which are in agreement with different predictions for eddy and wave turbulence (Galtier et al., 2000; Boldyrev, 2006).

The external force seems to be an important parameter for the dynamics. For example in Perez & Boldyrev (2008) a change of spectral slope was reported for the k_{\perp} -energy spectrum when the intensity of B_0 is modified. In this work the external force was applied at $k_{\parallel} > 0$ and $k_{\perp} = 1, 2$. In Muller et al. (2003) a forcing which kept the ratio of fluctuations to mean field approximately constant was implemented by freezing modes $k \leq 2$ and a spectral slope close $k_{\perp}^{-3/2}$ was reported for $B_0 = 5$. We find that the 2D state is essential at large B_0/b_{rms} since it mainly drives the nonlinear dynamics. The fact that the 2D state was imposed by the forcing has certainly an impact on the nonlinear dynamics since it prevents the natural growth of the 2D state energy at small k_{\perp} .

3 Conclusion

Waves and turbulence are ubiquitous in astrophysical plasmas. The recent detections of Alfvén waves and their interpretation (Cargill & De Moortel, 2011) shows that they are probably the main ingredient to understand the solar corona dynamics. From a theoretical point of view we know that turbulence is also the natural state of the coronal plasma. Then, it is fundamental to better understand the evolution of MHD turbulence and to answer the question: is MHD turbulence is by nature made of waves or eddies ? The latest results reveals that both are present which means that we need to understand both regimes and their mutual interaction.

References

- Bigot, B., Galtier, S. & Politano, H. 2008a, A&A, 490, 325
 Bigot, B., Galtier, S. & Politano, H. 2008b, Phys. Rev. E, 78, 066301
 Bigot, B. & Galtier, S. 2011, Phys. Rev. E, 83, 026405
 Boldyrev, S. 2006, Phys. Rev. Lett., 96, 115002
 Buchlin, É. & Velli, M. 2007, ApJ, 662, 701
 Cargill, P. & De Moortel, I. 2011, Nature, 475, 463
 Galtier, S. 1999, ApJ, 521, 483
 Galtier, S., Nazarenko, S.V., Newell, A.C. & Pouquet, A. 2000, J. Plasma Phys., 63, 447
 Galtier, S., Pouquet, A. & Mangeney, A. 2005, Phys. Plasmas, 12, 092310
 Goldreich, P., & Sridhar, S. 1995, ApJ, 438, 763
 Iroshnikov, P.S. 1964, Soviet Astron., 7, 566;
 Kraichnan, R.H. 1965, Phys. Fluids, 8, 1385
 Müller, W.-C., Biskamp, D. & Grappin, R. 2003, Phys. Rev. E, 67, 066302
 Perez, J.-C. & Boldyrev, S. 2008, ApJ, 672, L61
 Smith, L.M. & Waleffe, F. 1999, Phys. Fluids, 11, 1608

SCATTERING POLARIZATION OF MOLECULAR LINES AT THE SOLAR LIMB

I. Milić¹ and M. Faurobert²

Abstract. Molecular lines formed in the upper photosphere of the Sun show linear scattering polarization, when one observes close to the solar limb. This provides us with a diagnostic tool for measuring weak magnetic fields in the solar photosphere through the differential Hanle effect in these lines. However, in order to interpret polarization ratio measured in different lines of different optical thickness, one has to model accurately enough the line formation processes. Observations performed close to and above the solar limb give access to the still poorly known region of the temperature minimum between the photosphere and the chromosphere. The modeling of such observations requires to account for the spherical geometry of the solar atmosphere. Here we revisit the modeling of molecular solar line scattering polarization in spherical geometry and we investigate its diagnostics potential.

Keywords: line: formation, techniques: spectroscopic, Sun: photosphere, Sun: magnetic fields

1 Introduction

The linear polarization of the solar spectrum, observed close to the solar limb, is due to the scattering of the photospheric radiation field in spectral lines, and to Rayleigh and Thomson scattering in the continuum. Line scattering polarization is modified by collisions and by the Hanle effect of weak magnetic fields. Some weak absorption lines, such as the molecular lines of C₂ and MgH, show relatively large linear scattering polarization at the solar limb (Gandorfer 2000). Molecular lines with different sensitivities to magnetic fields may provide us with a model-independent diagnostics of weak magnetic fields, through the differential Hanle effect (Berdyugina & Fluri 2004; Bommier et al. 2006). However, line polarization rates are also affected by depolarizing collisions and radiative transfer, so the interpretation of the differential Hanle effect in lines with different optical depths requires accurate modeling of the line formation process.

Here we investigate the effect of taking into account the spherical geometry of the solar atmosphere. There are several reasons why this should affect the degree of scattering polarization. The most important one being that at the solar limb, the line of sight intersects only a finite part of the solar atmosphere and crosses a more dilute medium, where scattering processes dominate (see Fig. 1). In the following we consider as test cases the MgH line at 515.98 nm and the C₂ line at 515.96 nm and we compare the results for plane-parallel and spherical geometries. We use FALC and FALX solar models (Fontenla et al. 1990) in order to inspect the effects of different temperature distributions on line and continuum polarization. We solve the polarized radiative transfer problem for the lines and continuum background radiation using a two-level formulation of the line source function, without any approximation regarding the optical thickness of the line forming region. Elastic and inelastic collisions play an important role in the scattering mechanism but their rates are presently poorly known for the molecular lines that we are considering. We use estimates derived by Milić & Faurobert (2011) and Bommier et al. (2006) for these quantities. In Sect. 2 we describe the polarized transfer problem and our method for solving it. Results for the linear polarization in spherical geometry are presented in Sect. 3.

¹ Astronomical observatory Belgrade, Volgina 7, 11060 Belgrade, Serbia

² UMR 6525 H. Fizeau, Université de Nice Sophia Antipolis, CNRS, Observatoire de la Côte d'Azur, Campus Valrose, 06108 Nice, France

2 Radiative transfer

2.1 Transfer equation

In the absence of magnetic field (or in the case of a microturbulent, i.e. weak and unresolved, magnetic field), for axially-symmetric radiation field, only two components of the radiation field Stokes vector are different from zero, so we can write $\hat{I} = (I, Q)^\dagger$ and cast the radiative transfer equation along the ray in following form,

$$\frac{d\hat{I}}{d\tau} = (\phi_\nu + \beta)(\hat{I} - \hat{S}), \quad (2.1)$$

where \hat{S} is the source function vector, τ is line-integrated optical depth along the ray, ϕ_ν the absorption profile and β the continuum-to-line opacity ratio. The total source function vector can be written as a weighted sum of the line and continuum source functions,

$$\hat{S} = \frac{\phi_\nu \hat{S}_l + \beta \hat{S}_c}{\phi_\nu + \beta}. \quad (2.2)$$

Dealing with weak molecular lines, it is reasonable to assume complete redistribution, we also assume here that the line may be modeled with a two-level formalism, so the line source vector is written,

$$\hat{S}_l(\tau, \mu) = (1 - \epsilon) \frac{1}{2} \int_{-\infty}^{\infty} \int_{-1}^1 \hat{P}(\mu, \mu') \hat{I}(\tau, \mu', \nu) d\mu' \phi_\nu d\nu + \epsilon B_t(\tau), \quad (2.3)$$

and the continuum source function as,

$$\hat{S}_c(\tau, \mu) = (1 - \epsilon_c) \frac{1}{2} \int_{-1}^1 \hat{P}(\mu, \mu') \hat{I}(\tau, \mu', \nu) d\mu' + \epsilon_c B_t(\tau), \quad (2.4)$$

where μ and μ' denote respectively the cosines of the heliocentric angles of the outgoing and ingoing radiation propagation direction. The coefficient ϵ is the branching ratio for collisional destruction of line photons. In the continuum source function, $\epsilon_c = \chi_{abs}/(\chi_{sc} + \chi_{abs})$, where χ_{abs} and χ_{sc} denote respectively the absorption and scattering continuum opacities. B_t is the Planck function and $\hat{P}(\mu, \mu')$ is the scattering phase matrix. In the non-magnetic case or in the presence of a microturbulent weak magnetic field, it is given by

$$\hat{P}(\mu, \mu') = \hat{P}_{is} + \frac{3}{8} W_2 W_c W_B \hat{P}_2^0, \quad (2.5)$$

\hat{P}_{is} is the isotropic matrix, and \hat{P}_2^0 , the anisotropic part of the phase matrix, is given by

$$\hat{P}_2^0 = \begin{pmatrix} (\frac{1}{3} - \mu^2)(1 - 3\mu'^2) & (1 - 3\mu^2)(1 - \mu'^2) \\ (1 - \mu^2)(1 - 3\mu'^2) & 3(1 - \mu^2)(1 - \mu'^2) \end{pmatrix} \quad (2.6)$$

W_2 is the intrinsic polarizability, W_c is the collisional depolarization coefficient and W_B the Hanle depolarization coefficient. Neglecting inelastic collisions, we have

$$W_c = \frac{\Gamma_r}{\Gamma_r + D^{(2)}}, \quad (2.7)$$

where Γ_r is the line radiative damping and $D^{(2)}$ is the depolarizing collision rate. In this study we are mainly interested in the effect of spherical geometry on the modeling of scattering polarization in lines and continua observed at the solar limb, so we set $W_B = 1$.

The continuum radiation is not affected by collisional and Hanle depolarization, the relevant phase matrix is the Rayleigh phase matrix $\hat{P} = \hat{P}_{is} + \frac{3}{8} \hat{P}_2^0$. Here, the absorption and scattering opacity in the continuum are derived from the Uppsala package, using FALC and FALX quiet sun models.

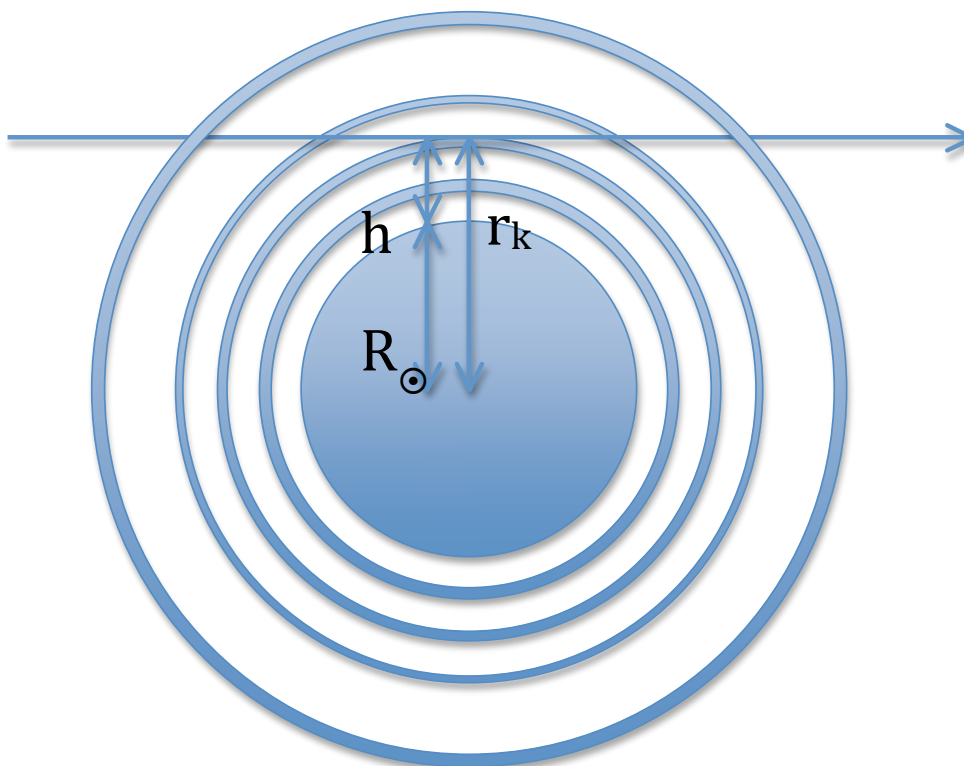


Fig. 1. Geometry of radiative transfer with sphericity taken into account. The line of sight with impact parameter r_k is located at height h above the solar limb, i.e. $r_k = R_\odot + h$.

2.2 Solving the radiative transfer problem in spherical geometry

First, let us notice that, since the solar atmosphere is very thin compared to the solar radius, sphericity effects will be important for very inclined lines of sight only. As they play a negligible role in the angle averaged intensity, level populations and line absorption coefficients may be computed in plane-parallel geometry and the source function for the intensity is weakly affected by sphericity effects. In a first step, we solve the scalar radiative transfer problem for the intensity, neglecting polarization and assuming a plane-parallel geometry. After obtaining self-consistent values for the scalar source function, we take into account polarization and spherical geometry. We start with the assumption $\hat{S} = (S, 0)^\dagger$, where S is the scalar source function computed in the previous step and proceed iteratively, solving in turn the polarized transfer equation and computing the source functions, until convergence. This iterative solution is in essence an ordinary Λ iteration for the polarization, which converges relatively fast, in less than 10 iterations.

When solving the radiative transfer equation in spherical geometry, we avoid the partial differential equation form by using the simpler, "along the ray" approach, as described, for example, by Avrett & Loeser (1984). We compute the scattering integral at each depth point with an angular grid containing both "core-rays" and "surface rays". Core-rays are rays which intersect the solar disk, whereas surface rays go across the limb. The lower boundary condition for core-rays is derived from the diffusion approximation, whereas, for surface-rays, we prescribe a condition of symmetry of the radiation field at the central depth point. In order to get a fine angular mesh at the surface, we use 40 core-rays and as many surface-rays as depth points in the atmospheric model. In the following we consider the line-of-sight limb distance δ , given in arcsec by

$$\delta = \frac{h}{R_\odot} \times 960'', \quad (2.8)$$

where h denotes the altitude of the line of sight with respect to the solar limb. As usual, we define the limb as the point where the continuum limb darkening curve $I(\delta)$ changes its behavior from concave to convex. From our computations we find that the solar limb is located 325 km above the continuum formation height, for both FALC and FALX models. This point is also used to define the solar radius.

2.3 Molecular data

The line integrated opacity, neglecting stimulated emission, is given by

$$\chi = \frac{n_l h \nu}{4\pi} B_{lu}, \quad (2.9)$$

where n_l is the lower level number density and B_{lu} is the Einstein's coefficient of radiative excitation which follows from the coefficient of spontaneous emission A_{ul} .

The MgH line belongs to the Q band of the $A^2\Pi - X^2\Sigma^+(0, 0)$ transition, with $J = 16$, J being the rotational lower level quantum number, the C_2 line belongs to the $P3$ band of the $A^3\Pi_g - X^3\Pi_u$ transition with $J = 26$. The molecular number densities obey the equilibrium equation, given by e.g. by Berdyugina et al. (2003):

$$\frac{n(A)n(B)}{n(AB)} = K_{AB}, \quad (2.10)$$

where, $n(AB)$, $n(A)$ and $n(B)$ are, respectively, the molecule number densities and the constituting atom densities, and K_{AB} is the equilibrium constant. In general, equilibrium constants depend on temperature, partition functions of molecule and constituting atoms and on the dissociation energy of the molecule. Convenient polynomial expressions for equilibrium constants and molecule partition functions are given by Sauval & Tatum (1984). In general, in order to obtain exact molecular number densities, one should take into account all molecules and all constituting atoms and solve a system of non-linear equations as explained by Berdyugina et al. (2003). However, due to relatively high temperatures, molecular densities are small, so when computing the MgH density, we may approximate $n(\text{Mg})$ with the total number density of magnesium derived from its abundance relative to hydrogen. The situation is a bit more complicated when it comes to computing the C_2 density, due to the presence of CO whose number density may be a significant fraction of the total number density of carbon, especially in cool regions of the atmosphere. So we consider both CO and C_2 molecules in equilibrium with atomic carbon and oxygen. Then to compute the line opacity, we assume that for weak molecular lines the population of the lower level of the transition follows the LTE law. We adopt the values of A_{ul} given by Faurobert & Arnaud (2003).

In the case of molecular lines, elastic collisions are mainly due to neutral hydrogen atoms and both electrons and neutral hydrogen contribute to inelastic collisions (Shapiro et al. 2011). As accurate collision rates are presently not available for the molecular lines we are considering here, we use the empirical values derived by Milic & Faurobert (2011) and Bommier et al. (2006).

3 Results and discussion

3.1 Optical paths and line optical depth

We find that both molecules are mostly concentrated in a 200 km wide slab located about 100 km above the base of the photosphere, and that the number density of C_2 is a factor of 10 larger than that of MgH. In case of FALC model, the MgH line center optical thickness, measured along the radial direction, is 0.17 at the base of the photosphere, the C_2 line is thicker, its optical thickness along the radial direction is larger by almost a factor of 3 (≈ 0.45). Radial optical depths computed with the FALX model are very similar, except in the region of the temperature minimum around $z = 500$ km, where molecular densities are larger due to cooler temperatures in the FALX model. Let us now see the behavior of the line optical depths measured along the line-of-sight.

The left panel of Fig. 2 shows the variations of the line-of-sight optical depth as a function of limb distance for both the MgH and C_2 lines and the FALC model. We compare the results obtained in plane-parallel and spherical geometries for lines of sight close to the limb. There is little difference between both geometries when the limb-distance is larger than 5 arcsec, but they differ significantly at smaller limb distances. An important thing to keep in mind is that, in spherical geometry, the optical path does not scale with observing direction as simply as $\Delta\tau_{los} = \Delta\tau/\mu$ (see Fig. 2). It shows a sharp maximum, for both lines, at $\delta \simeq -0.3''$. This value corresponds to the lines of sight which go through the molecular layer. Moving the line of sight outwards, we mainly observe above the molecular layer, as a consequence the line optical depth rapidly goes to zero. In plane-parallel geometry any line of sight always intersect the molecular layer, and the length of its path increases when we go closer and closer to the limb, so that the line optical depths keep increasing. In plane-parallel geometry we cannot model observations performed outside the limb.

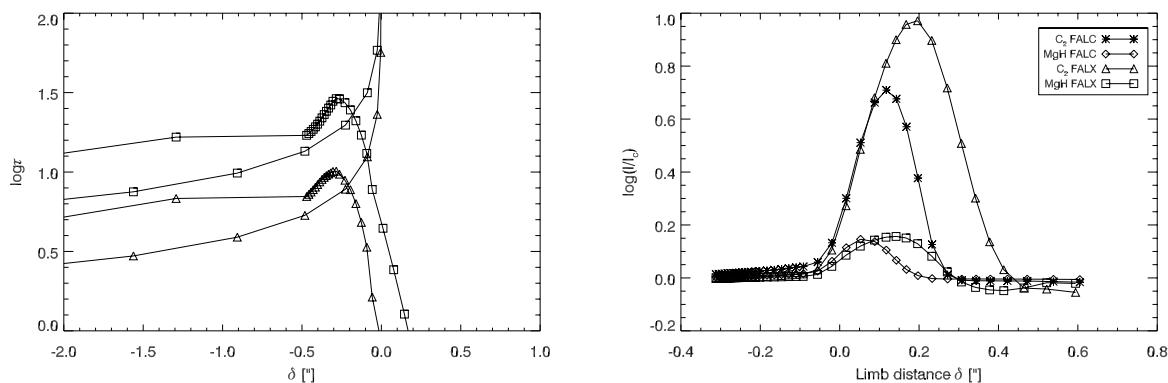


Fig. 2. Left: Comparison of line center optical path for spherical and plane-parallel geometry (triangles for MgH , and squares for C₂). **Right:** Intensity at line center divided by the continuum intensity, in both models as a function of limb distance. When observed above the limb, lines are seen in emission, but quickly disappear.

3.2 Line intensities and scattering polarization.

The right panel of Fig. 2 shows the emergent intensities at line center for the MgH and C₂ lines , for spherical symmetry with FALC and FALX models, as functions of limb distance. Both lines go into emission above the solar limb, for limb distances smaller than 0.4 arcsec, and quickly disappear at larger limb distances. This is consistent with the observations reported by Faurobert & Arnaud (2002). When observed inside the limb both lines are very weak absorption lines. The emission seen above the limb cannot be modeled in plane-parallel geometry.

Figure 3 presents the comparison of the emergent polarization at line centers, as functions of δ , computed in spherical and plane-parallel geometries, with FALC and FALX models. Both geometries give the same results at limb distances larger, in absolute value, than 5", but they differ significantly at smaller limb distances. We notice that the polarization rate shows a maximum, in absolute value, for the lines of sight where the optical path shows a maximum (see Fig. 2). That fact can be qualitatively explained in the following way, as the slab optical thickness increases, the probability that a photon will be scattered in the line increases. So the polarization increases. At larger distance above the limb the line optical depth decreases. This gives rise to the local polarization maximum that we see in Fig. 3. The polarization starts increasing again at larger distance from the limb, where the line has disappeared (see Fig. 2). We then see the continuum polarization only, it increases because continuum scattering opacity increases in the low chromosphere. We notice that with the FALC model, values of the polarization maxima between 2% and 2,5% are consistent with the measurements reported by Faurobert & Arnaud (2002), for the molecular lines seen in emission above the solar limb. With FALX we recover the same general behavior as with the FALC model, but with much larger polarization rates, the maximum reaches values on the order of 10 %. Such large rates have not been observed close to the solar limb.

4 Conclusions

Taking into account the spherical geometry of the solar atmosphere allows us to compute the intensity and scattering polarization of the solar spectrum at the limb. We have found that for our test-case lines of C₂ and MgH, scattering polarization shows maxima of a few percents at about 0.3 arcsec above the limb, where the lines are in emission. The order of magnitude of these polarization maxima are consistent with the observed rates when the FALC quiet sun model is used but the FALX model leads to much larger polarization rates.

The polarization maxima observed at 0.3" above the solar limb correspond to lines of sight crossing the temperature minimum region between the photosphere and the chromosphere. More limb observations are needed to make use of the differential Hanle effect in different molecular lines in order to investigate this region. Such observations require few scattered light in the instrument and good seeing conditions.

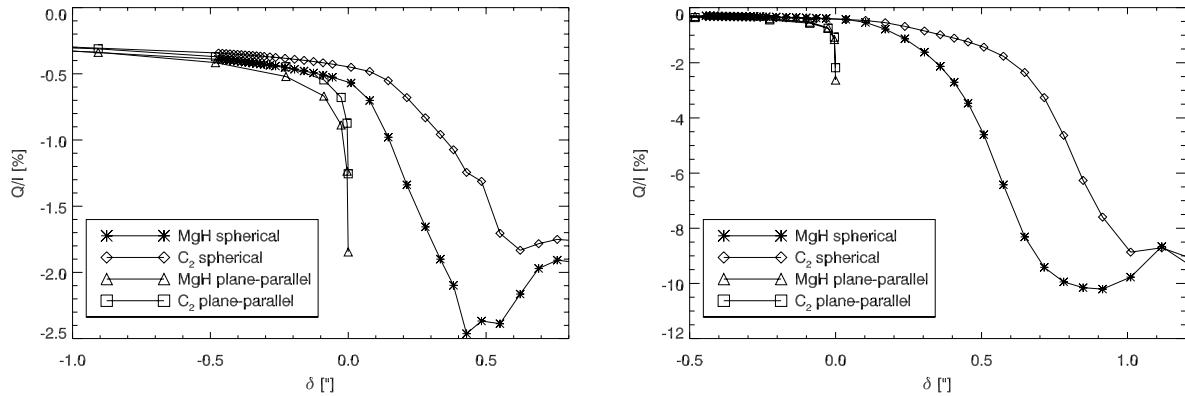


Fig. 3. Linear polarization at line center as a function of limb-distance for the MgH line (asterisks for spherical and triangles for plane-parallel case) and the C_2 line (diamonds for spherical and squares for plane-parallel case). **Left:** FALC model. **Right:** FALX model

References

- Avrett, E. H. & Loeser, R. 1984, Line transfer in static and expanding spherical atmospheres, ed. Kalkofen, W., 341–379
- Berdyugina, S. V. & Fluri, D. M. 2004, *A&A*, 417, 775
- Berdyugina, S. V., Solanki, S. K., & Frutiger, C. 2003, *A&A*, 412, 513
- Bommier, V., Landi Degl’Innocenti, E., Fautrier, N., & Molodij, G. 2006, *A&A*, 458, 625
- Faurobert, M. & Arnaud, J. 2002, *A&A*, 382, L17
- Faurobert, M. & Arnaud, J. 2003, *A&A*, 412, 555
- Fontenla, J. M., Avrett, E. H., & Loeser, R. 1990, *ApJ*, 355, 700
- Gandorfer, A. 2000, *The Second Solar Spectrum: A high spectral resolution polarimetric survey of scattering polarization at the solar limb in graphical representation. Volume I: 4625 Å to 6995 Å*, ed. Gandorfer, A.
- Milic, I. & Faurobert, M. 2011, *A&A*, submitted
- Sauval, A. J. & Tatum, J. B. 1984, *ApJS*, 56, 193
- Shapiro, A. I., Fluri, D. M., Berdyugina, S. V., Bianda, M., & Ramelli, R. 2011, *A&A*, 529, A139+

SIMULATIONS OF THE SOLAR ATMOSPHERE AND SOLAR LIMBS

L. Piau¹, R. F. Stein², S. Melo³, S. Turck-Chièze⁴, G. Thuillier¹ and A. Hauchecorne¹

Abstract. We perform simulations of the solar atmosphere either using the 1D hydrostatic code Atlas12 or the 3D (magneto)hydrodynamic code Stagger. The former numerical tool relies on a phenomenology of convection whereas the later one addresses the surface convection directly and accounts for its dynamical effects. Once the average atmosphere stratification is obtained it is used to perform radiative transfer at specific wavelengths in order to compute the solar limb darkening. We report a ≈ 60 mas shift between inflection point positions of limb profiles computed from 1D and 3D models. This is due to turbulent support present in 3D simulations but not 1D. We further report a slight decrease of the turbulent support when a moderate magnetic field is included in the simulation which suggests that the solar radius should be anti-correlated with the solar activity cycle.

Keywords: Solar atmosphere, Magnetic activity, Simulation, Limb darkening.

1 Introduction

In the few thousands kilometers around the solar surface, temperature and density vary by many orders of magnitude, the medium goes from optically thick to optically thin and from mostly ionized to mostly neutral (Stein & Nordlund 1998). The convective flow is compressible and affected by magnetic activity. All these phenomena make the solar surface difficult to model and to understand. Yet solar and stellar surfaces are important for numerous reasons. Some are related to the interior of the star: surface physics sets the boundary conditions to the stellar structure and evolution. It affects absolute oscillation frequencies (Turck-Chièze, et al. 1997) in a way that remains to investigate (Rosenthal et al. 1999). Some are related to the environment of the star: the dynamics of surface physics has a direct impact on planets atmospheres and likely on their climates.

The work we present here explores the effects of the solar surface dynamics from the point of view of 3D simulations and 1D modelling. We focus on the limb darkening at the edge of the solar disk and at the wavelengths of observation of the SODISM instrument aboard the Picard satellite (215, 393, 535, 607 and 782 nm) and the HMI instrument (617 nm) aboard the SDO satellite. Picard (Thuillier et al. 2006) and SDO (Pesnell et al. 2011) spacecrafts have been launched on June 15 2010 and February 11 2010 respectively to address the solar surface dynamics. For the sake of brevity results only on a few of these wavelengths are reported here. After describing our simulations and method in the next section, we show the effect of turbulent support on limb profiles as deduced from 3D and 1D simulations of the solar atmosphere. Then we show the effect of a moderate horizontal magnetic field entering the simulation domain before concluding.

2 Method

We proceed in two steps. First, we perform a 1D or 3D solar atmosphere calculations adopting the recent Asplund et al. (2009) composition. This provides temperature, mass density, and electron density average stratifications. Subsequently these structures are used to perform radiative transfer for the wavelengths of interest: the wavelengths of current observation by the SODISM instrument aboard Picard satellite and the

¹ LATMOS, 11 Boulevard d'Alembert, 78280 Guyancourt, France

² Michigan State University, Department of Physics & Astronomy East Lansing, MI 48824-2320, USA

³ Canadian Space Agency, 6767 route de l'aéroport, St Huber, Québec, Canada

⁴ CEA/DSM/IRFU/Service d'Astrophysique, CE Saclay, L'Orme des Merisiers, 91191 Gif-sur-Yvette, France

HMI instrument aboard SDO satellite. In both 1D and 3D atmospheres cases the simulation domain starts nearly 1 Mm above Rosseland optical depth τ_{Ross} unity where $\rho \approx 10^{-10} \text{g.cm}^{-3}$ and $\tau_{\text{Ross}} \approx 10^{-7}$. The 1D simulation region extends down to $\tau_{\text{Ross}} = 100$ whereas the 3D simulation extends deeper below the atmosphere at $\tau_{\text{Ross}} \approx 2 \cdot 10^7$.

The 1D atmosphere calculation is made with the `Atlas12` code (Castelli 2005). The version of the code we use relies on the (Canuto, Goldman & Mazzitelli 1996) phenomenology for surface convection where we consider that the characteristic length scale for convection is a fraction of H_p the pressure scale height. We chose $\Lambda = 0.5H_p$ as a characteristic convection length. `Atlas12` does not account for the dynamical effects of convection such as turbulent pressure. It also ignores the magnetic field and its consequences.

The 3D atmosphere calculations are made with the `Stagger` code (Stein & Nordlund 1998). `Stagger` accounts directly for surface convection dynamics and optionally solves the equation of magnetic induction. The simulation domain corresponds to a box of 6 by 6 Mm horizontally and 4 Mm vertically that straddles the solar surface. We solve explicitly the equations of compressible hydrodynamics over 240^3 meshes. The average stratification of a quantity is obtained from a series of 3D snapshots. For a snapshot we consider the horizontal average of the quantity. The vertical profiles that are obtained this way for different snapshots in time are then averaged.

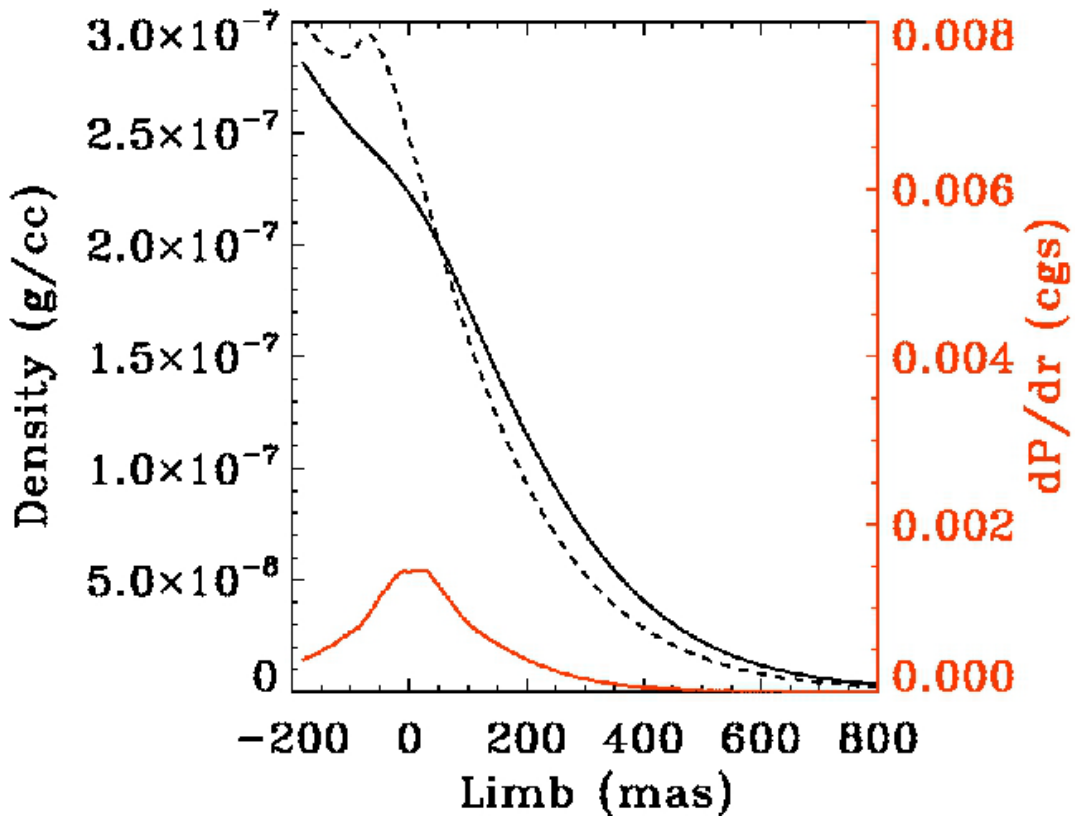


Fig. 1. Density as a function of the distance on the solar limb in milli arcseconds. Solid line: average from 3D simulations. Dashed line: density of the 1D `Atlas12` model. Red line: turbulent pressure gradient as a function of the distance on the limb.

3 Limbs and turbulence

Figure 1 compares the vertical density profile computed from averages of 3D `Stagger` simulations to the 1D density profile obtained with `Atlas12`. The density is given as a function of the angular distance in milliarc second at the edge of the solar disk. The 3D density is above the 1D density in the higher solar atmosphere because the 3D simulations account for the turbulent pressure whose gradient is also shown on Figure 1. The

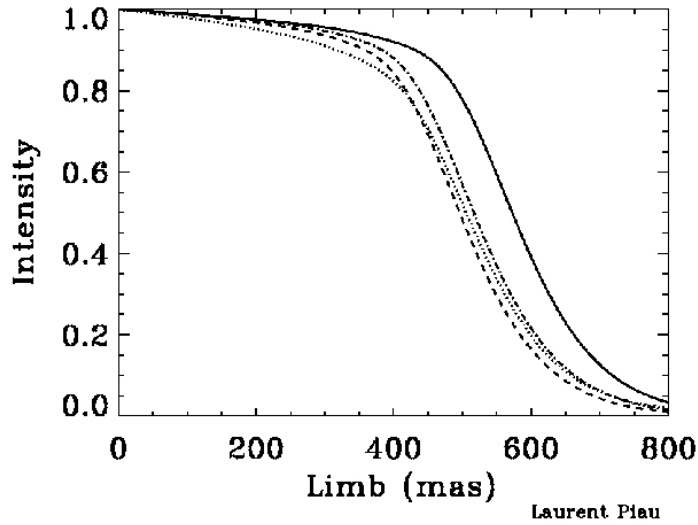


Fig. 2. Light intensity profiles estimated at 782.4 nm from various atmosphere models. The X-axis is the distance on the limb in milli arcseconds. The different tracks correspond to different models and the intensity is normalized to unity at the origin of the X-axis. The solid line comes from our 3D Stagger simulations. The dot-dashed line comes from our 1D Atlas12 model. The other lines are from other 1D atmosphere calculations.

turbulent pressure is given by:

$$P_{\text{turb}} = \rho(\overline{v_z^2} - \bar{v}_z^2) \quad (3.1)$$

with ρ , the density and v_z , the vertical velocity. The gradient of turbulent pressure lifts the atmosphere simulated in 3D but is absent from 1D models which by nature do not include the 3D convective movements.

The 1D/3D shift is to be found again in the Figure 2. There, the darkening profile based on the 3D calculations is pushed away from the limb with respect to the 1D calculations. The 1D based profiles were either computed by us or adapted from the previous work by Thuillier et al. (2011). The origin of the horizontal axis of Figure 2 corresponds to the optical depth unity at 500 nm. The luminosity intensity profiles of the various models have been normalized to one at this origin. The 1D/3D angular shift is about 60 mas at the inflection point of the limb which represents 40 km at the distance of the Sun. These limb profiles illustrate how accurate the limb darkening profiles could constrain the surface turbulent pressure provided one is able to establish the precise direction of optical depth unity at or near 500 nm. This last point clearly is an observational challenge. Besides the shift from 1D to 3D atmosphere models the limb profiles have very similar shapes. In particular we checked that the full width at half maximum of the derivative of a limb profile (the width of the limb) does not depend on the atmosphere model whatever the wavelength that is considered.

4 Magnetic effect

The Stagger code version we use can take into account the magnetic field in the following manner: the plasma injected in the simulation box from below carries a magnetic field of given density and direction. Then the equation of induction is solved over the simulation domain. We report here on the first configuration of magnetic field injected in the domain we have explored. For this configuration, the incoming field is horizontal and 0.25 kiloGauss in intensity. The left panel of Figure 3 shows how the turbulent support changes between the purely hydrodynamical 3D simulation and the magnetohydrodynamical 3D simulation. The peak of gradient of turbulent pressure decreases by 20 percent with respect to the non magnetic simulation. This has the consequence of diminishing the turbulent support to the atmosphere and the right panel of Figure 3 shows how the limb darkening profile changes. We predict that when solar surface magnetism is stronger the solar radius should be smaller by a few tens of milliarcseconds. This conclusion however supposes that the solar activity does not affect the solar radius in regions deeper than the region we simulate and upon which our simulation provide no indications.

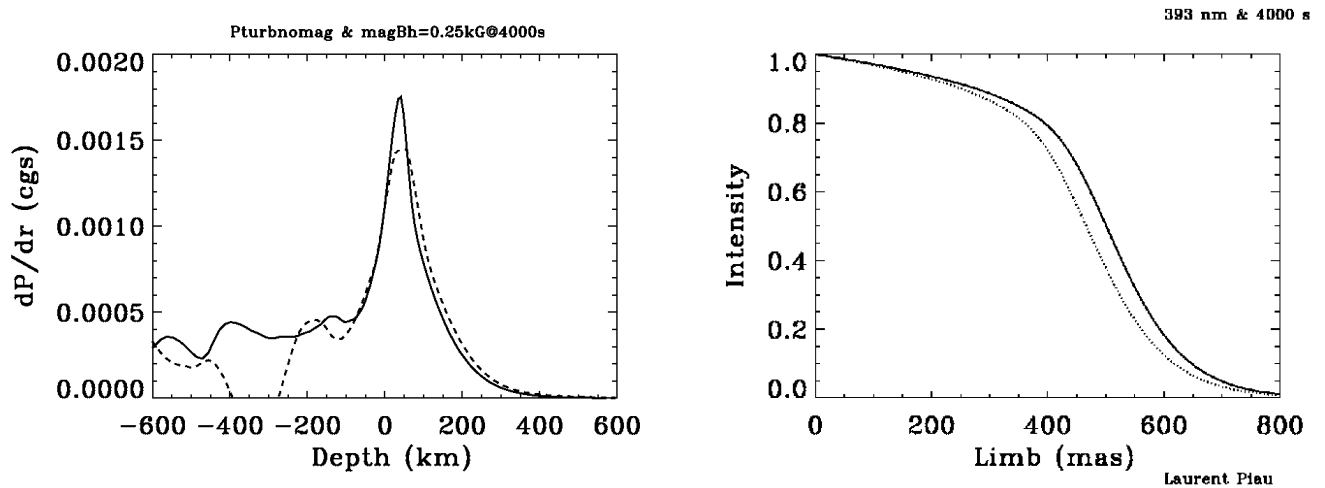


Fig. 3. Left: Turbulent support as a function of altitude in the solar atmosphere. Solid line: no magnetic field, Dashed-line: horizontal incoming magnetic field of 0.25 kG at the bottom of the simulation domain i.e. 3 Mm below Rosseland optical depth unity. **Right:** Light intensity profiles estimated at 393 nm from two Stagger atmosphere 3D models. The X-axis is the distance on the limb in milli arc seconds. The solid line corresponds to the non magnetic simulation. The dotted line corresponds to the magnetic simulation with a 0.25 kG incoming field.

5 Conclusion

We compute 1D hydrostatic and 3D hydrodynamic solar atmosphere models and use these models to compute the average limb profile at specific wavelengths. We then compare the 1D and 3D calculations. While our 1D calculation is in agreement with limb profiles estimated from previous 1D atmospheres, the limb profile estimated from the 3D simulations shows a significant shift with respect to those based on 1D. The shift is due to the turbulent pressure support of the atmosphere and reaches approximately 60 mas at the inflection point position of the limb profile (Figure 2). This suggests that accurate measurements of the limb darkening profile can constrain the dynamics in surface and subsurface solar layers. Further we performed a magnetohydrodynamical simulation. The turbulent support decreases when a moderate horizontal magnetic field of 0.25 kG is carried by the plasma entering the simulation at 3 Mm below the surface (Figure 3). The direct effect is that the atmosphere extension diminishes. Provided the solar radius is estimated from the inflection point position of the limb profile and that activity does not affect the radial mass distribution deeper than 3Mm below the surface, we anticipate a decrease of the solar radius the order of a few 10 of mas when the star goes from the minimum to the maximum of surface activity.

This work has been supported by LATMOS of Centre National de la Recherche Scientifique and the Centre National d'Etudes Spatiales for the scientific return of the Picard mission.

References

- Asplund, M., Grevesse, N. Sauval, A. J. Scott, P., 2009, ARA&A 47, 481
- Canuto, V. M., Goldman, I., Mazzitelli, I., 1996, ApJ, 473, 550
- Castelli, F., 2005, MSAIt, 8, 25
- Pesnell, W. D., B. T. Thompson, and P. C. Chamberlin, 2011, Solar Phys., submitted
- Rosenthal, C. S., Christensen-Dalsgaard, J., Nordlund, A., Stein, R. F., Trampedach, R., 1999, A&A, 351, 689
- Stein, R. F., Nordlund, A, 1998, ApJ, 499, 914
- Thuillier, G., Claudel, J., Djafer, D., Haberreiter, M., Mein, N., Melo, S. M. L., et al., Solar Phys. 268, 125
- Thuillier, G., Dewitte, S., Schmutz, W., 2006, Adv. Space Res. 38, 1792
- Turck-Chièze, et al., 1997, Solar Phys. 175, 247

Session 08

Circumstellar matter with ALMA and HERSCHEL

OBSERVATIONAL STUDIES OF INTERMEDIATE-MASS PROTOSTARS WITH PDBI, 30M, AND HERSCHEL

T. Alonso-Albi¹ and A. Fuente¹

Abstract. The study of intermediate-mass (IM) protostars is important because they provide the link between low-mass and high-mass star formation mechanisms, which are different and not well understood. To advance towards the comprehension of high-mass objects IM protostars are the next natural step. IM and high mass protostars are usually too far to be studied in detail, and their rapid evolution while they are still embedded in the parent cloud makes high-resolution radioastronomy (interferometry) a must. This work shows the most relevant results achieved by our group in the study of circumstellar disks and envelopes around IM protostars during the last few years, using IRAM instruments (30 m radiotelescope at Spain and *Plateau de Bure* interferometer in France) and the NRAO's *Very Large Array* (VLA) interferometer at USA.

Keywords: star formation, pre-main-sequence, intermediate-mass protostars, protoplanetary disks

1 Introduction

IM protostars are objects between 3 and 8 M_{\odot} . We can differentiate two groups of IM protostars: those between 3 and 5 M_{\odot} (the so called Herbig Ae stars, HAe hereafter), and those between 5 and 8 M_{\odot} (Herbig Be stars, HBe hereafter). The formation of HAe stars shows similarities with low-mass or T Tauri stars. In fact, in these objects the mass accretion phase of the protostar occurs prior to (and independently from) its contraction towards the main sequence. The relatively slow evolution during some tenths of million years simplify the study of these objects, since they soon disperse the parent cloud and become visible. In contrast, HBe protostars are usually found in clusters, highly embedded in massive and chemically complex molecular clouds. Their accretion and contraction phases coexist simultaneously, affecting the physical properties and the chemistry of the surrounding circumstellar disk and envelope in much lower time-scales. Even in a sample of (apparently) similar HBe objects we could have each of them at different evolutionary status and evolving with different rates. Since the sample of HBe stars is scarce compared to the HAe or T Tauri ones, the study and comprehension of HBe stars is not easy, but the sensitivity of the instrumentation available today is making this goal feasible.

Our aim is the study of the chemistry in envelopes around IM class 0 protostars, which are the youngest objects detectable at millimeter (mm) wavelengths and where there are still few studies. In more evolved objects (HBe stars that have eroded the cloud to become visible) we are also interested in the properties of their circumstellar disks and the differences between these disks and those around T Tauri stars. The detection frequency, chemistry, and physical properties (mass, size, and grain population) are expected to be different mainly due to the intense UV radiation field (with the contribution of the surrounding objects since clustering is a common phenomenon in IM protostars) and the variability of the central source.

As an aid for the analysis and comprehension of the observations described in the next two sections we developed new tools and models*. We will emphasize two of them that have been used actively in our work: a radiative transfer model that can operate in LTE and slab LVG approximations, and an implementation of the circumstellar disk model by Dullemond et al. (2001).

¹ Observatorio Astronómico Nacional (OAN), Apdo. 112, E-28800 Alcalá de Henares, Madrid. e-mail: t.alonso@oan.es. Presentation available at <http://conga.oan.es/%7Ealonso/sources/presentationSFA2.pdf>.

*Our programs can be installed for any operating system at <http://conga.oan.es/%7Ealonso/doku.php?id=jparsec>. Source code is included and released under GPL license.

2 Observations of envelopes around IM protostars

Continuum observations, coupled with molecular line spectra, allowed us to study the physical and chemical structure of a sample of five IM class 0 protostars (Cep E-mm, Serpens-FIRS 1, CB3, IC1396-N, NGC 7129-FIRS 2). We also observed for comparison the more evolved class I sources S140 and LkH α 234 (see Fig. 1). Crimier et al. (2010) derived the temperature-density profiles based on the SED and the SCUBA maps at 450 μm and 850 μm . Adopting these profiles, Alonso-Albi et al. (2010) modeled the chemistry of these envelopes to fit the radial distribution of the integrated intensity emission of the C ^{18}O 1 \rightarrow 0, N $_2\text{H}^+$ 1 \rightarrow 0 and N $_2\text{D}^+$ 2 \rightarrow 1 lines observed with the IRAM 30 m telescope.

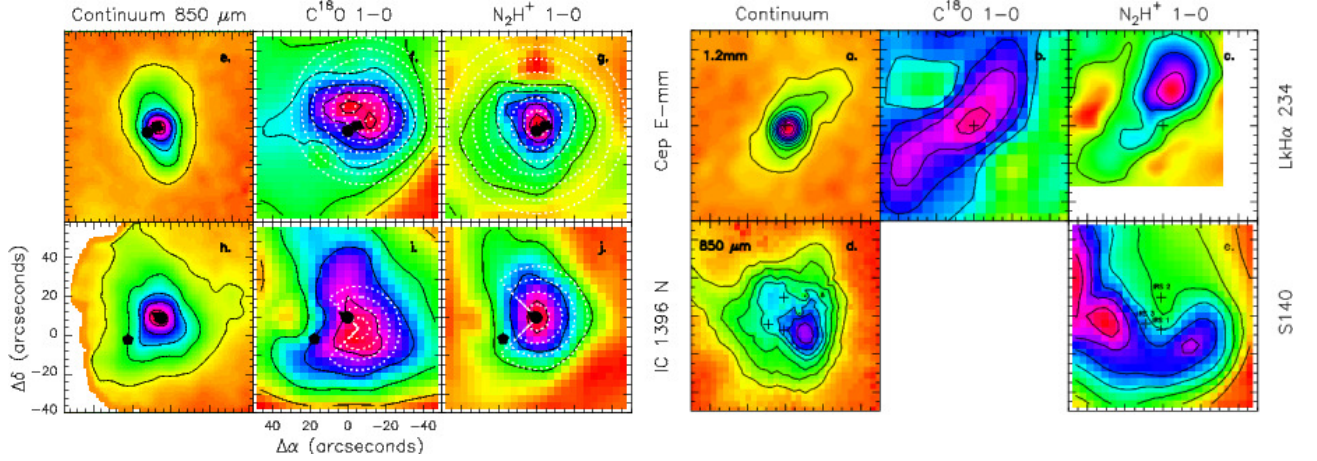


Fig. 1. Left: Observations of C ^{18}O and N $_2\text{H}^+$ towards two of the IM class 0 protostars. White dotted lines represent the different rings considered to obtain the integrated intensity profiles to compare observations and models for different molecules and sources. **Right:** The same observations towards class I objects.

We fitted the radial distribution of the C ^{18}O emission in two steps. First, the C ^{18}O abundance profile is calculated using the chemical code originally described in Caselli et al. (2002), and later updated by Caselli et al. (2008) to include new measurements of the CO and N $_2$ binding energies (Collings et al. 2003; Öberg et al. 2005) and sticking coefficients (Bisschop et al. 2006), and thermal desorption. The density-temperature profiles obtained by Crimier et al. (2010) were used as the physical basis for the chemical model. Once the C ^{18}O abundance profile is derived, we used our radiative transfer model to obtain the emission predicted with this abundance profile to compare with the C ^{18}O observations.

In the standard model (model 1 in Fig. 2), the C ^{18}O abundance decreases inwards the protostellar envelope because of the CO depletion onto grain mantles until the gas and dust reach the CO evaporation temperature, $\approx 20\text{--}25$ K, where the CO is released back to the gas phase and the C ^{18}O abundance sharply increases to $1.6 \cdot 10^{-7}$. Surprisingly, the standard model failed to reproduce the integrated intensity maps of all the IMs. This model assumes that the CO has a binding energy of 1100 K, compatible with CO depleted in a CO-CO matrix. Model 2 assumes a binding energy a 5000 K, compatible with a CO-H $_2\text{O}$ matrix. The radial intensity profiles obtained with both models for C ^{18}O (see first and second panels in the middle in Fig. 2) show that model 1 is more consistent than model 2, so we started from model 1 and we modified it to reduce the C ^{18}O emission in the inner region of the envelope. In three of the sources, NGC 7129-FIRS 2, Cep E-mm and CB3, the C ^{18}O abundance needed to be decreased by a factor of 10 within the CO evaporation region ($T_k > 25$ K) to fit the observations (model 3), both in the absolute values of the integrated intensities and in the slopes of the profiles. These sources were also those with the higher deuterium fractionation, $[\text{N}_2\text{D}^+]/[\text{N}_2\text{H}^+] > 0.01$, and presumably the youngest in our sample. This CO deficiency was interpreted as possible evidence for an active surface chemistry in the protostellar envelope, where CO is efficiently converted in more complex organic molecules, such as CH $_3\text{OH}$. In the other two, Serpens FIRS 1 and IC 1396 N, the observations were fitted by decreasing the C ^{18}O abundance by the same factor but only in the hot core region, $T_k > 100$ K (model 4). In these sources $[\text{N}_2\text{D}^+]/[\text{N}_2\text{H}^+] < 0.01$, and the low C ^{18}O abundance was interpreted to be due to photodissociation. Our results, however, suffered from the limited spatial resolution of the 30 m telescope. Moreover, we were observing low excitation lines whose emission could be dominated by the external part of the envelope, so additional observations of high excitation lines were required to confirm this result.

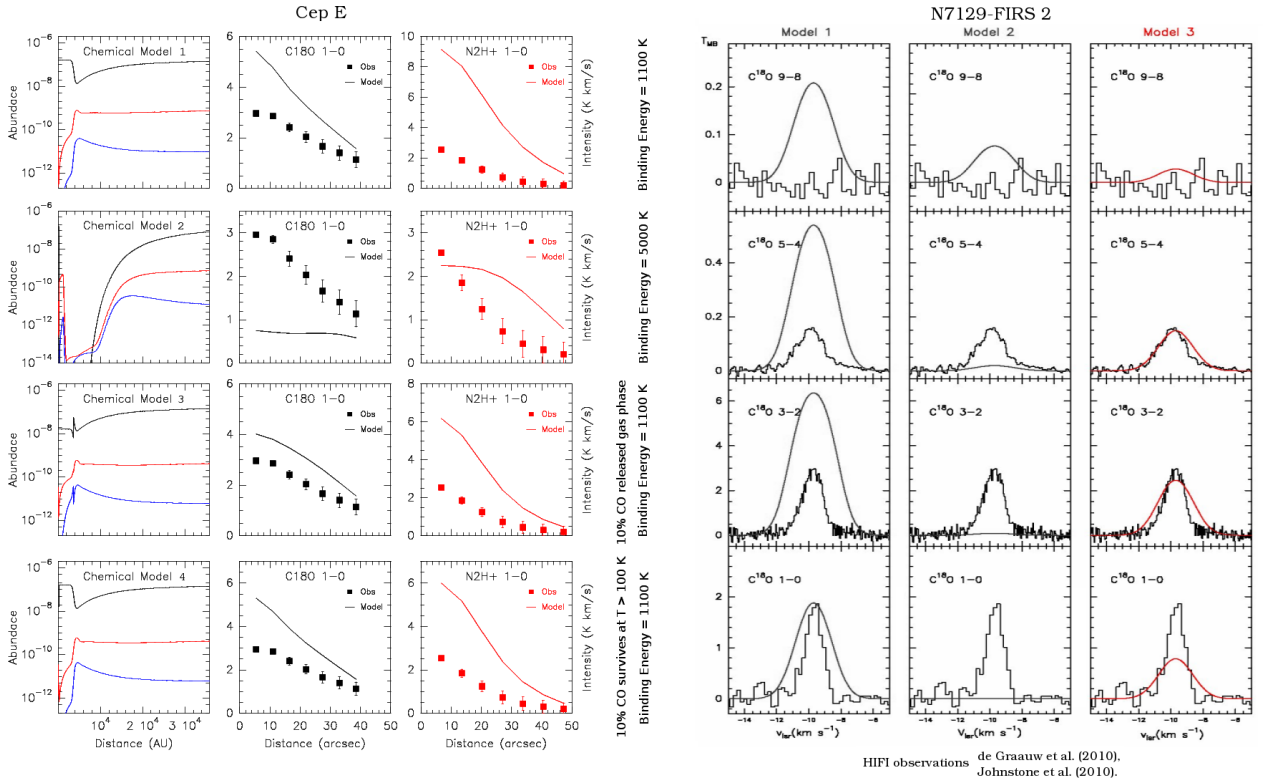


Fig. 2. Left: Sequence of chemical models applied to Cep E until a reasonably fit to observations was found with model 3, that assumes only 10% of CO is released back to gas phase in the inner region ($T > 25$ K). Model 4 assumes that only 10% of CO is not photodissociated in the hot core ($T > 100$ K), and this model was more consistent with observations for IC1396-N and Serpens-FIRS 1. **Right:** Observations and model results of high J CO transitions for NGC 7129-FIRS 2. Model 3 is confirmed to be the most consistent, with some contribution of the cloud to 1 \rightarrow 0 transition.

For the first time, Herschel provided the opportunity to observe the high excitation lines of CO (and isotopes) towards young stellar objects. Combining ground based observations of the $C^{18}O$ J=1 \rightarrow 0 and J=3 \rightarrow 2 lines with the Herschel/HIFI (de Graauw et al. 2010; Johnstone et al. 2010) observations of the $C^{18}O$ J=5 \rightarrow 4 line and J=9 \rightarrow 8 line, Fuente et al. (2011, in preparation) derived the $C^{18}O$ abundance profile across the envelope of the young IM protostar NGC 7129-FIRS 2. The new observations proves that the $C^{18}O$ abundance is $\sim 1.6 \cdot 10^{-8}$ in the inner region of the envelope, corroborating previous results by Alonso-Albi et al. (2010).

3 Observations of circumstellar disks

We carried observations at mm wavelengths in a sample of Herbig Ae/Be stars. In the HBe star R Mon we obtained high angular resolution observations in the continuum and in the ^{12}CO 1 \rightarrow 0 and 2 \rightarrow 1 rotational lines, using the A⁺ configuration of the *Plateau de Bure* interferometer (PdBI) (Fuente et al. 2006). At 1.3 mm the resolution reached $0.7 \times 0.3''$, allowing us to detect the gas rotating around R Mon in molecular lines. We modeled the disk in molecular lines using our radiative transfer model, and found compatible models for a flared and a flat geometry. With this modeling we also estimated dynamically the mass of R Mon itself in $8 M_{\odot}$. Since our ^{12}CO lines were optically thick we needed further observations in an optically thin transition to obtain a more detailed look of the geometry of the disk, so we obtained new observations of ^{13}CO 1 \rightarrow 0 (Alonso-Albi et al. 2007). In Fuente et al. (2006) we concluded that the flat geometry was more probable, since the mass of the disk derived from the model was in very good agreement with the mass estimated from the (optically thin) mm continuum observations. In Alonso-Albi et al. (2007) we confirmed this result, since we tentatively detected ^{13}CO towards R Mon with the expected intensity for a dusty disk of $0.001 M_{\odot}$ (right panel in Fig. 3). The expected result for a flared disk was eight times this value.

The HAe star VV Ser was also observed (Alonso-Albi et al. 2008) with the PdBI in its B configuration, and with the VLA in its D configuration at 44, 22, and 8 GHz (0.7, 1.3, and 3.5 cm). We detected continuum emission

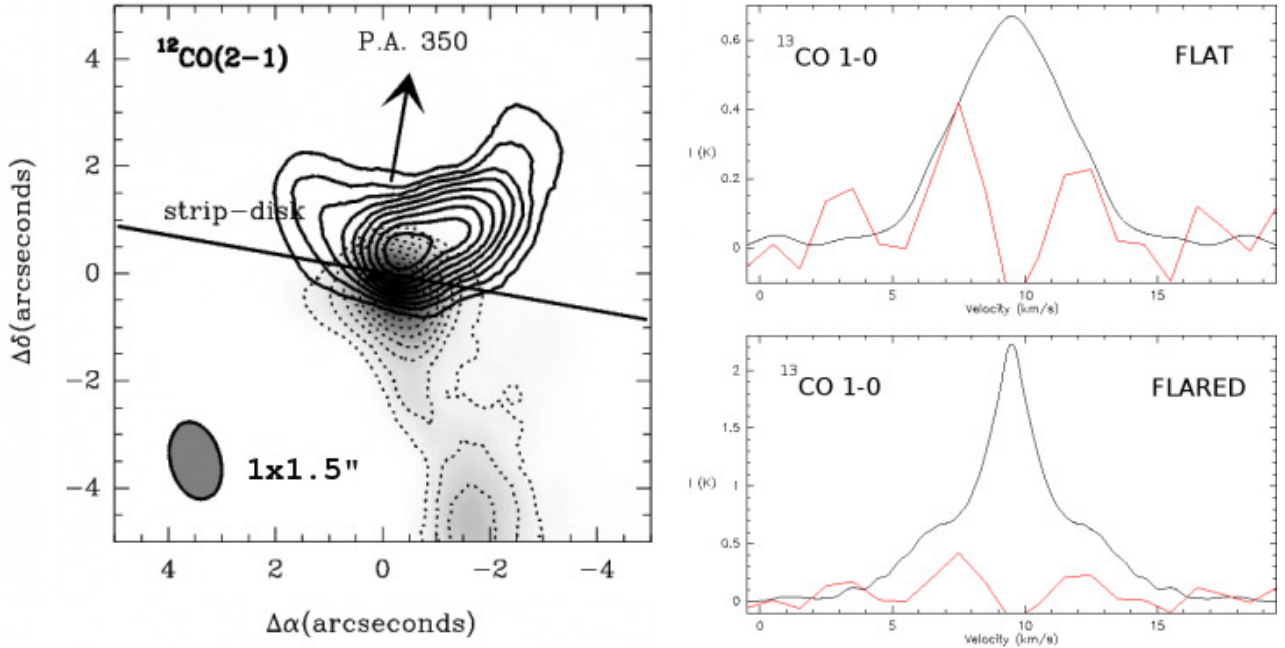


Fig. 3. Left: ^{12}CO 2 \rightarrow 1 observations towards R Mon, with the direction of the outflow and the expected direction of the major axis of the circumstellar disk superimposed. The contours of the emission are separated in a blueshifted component (north) and a redshifted one (south, dotted lines). **Right:** ^{13}CO 1 \rightarrow 0 observations towards R Mon (red), with the predicted intensity from the flared and flat geometries (black). To become optically thick the disk is eight times more massive in the flared model and therefore it predicts an intensity which is inconsistent with observations (Alonso-Albi et al. 2007).

with the PdBI at 1.3 and 2.6 mm, and tentatively with VLA at 7 mm. We did not detect continuum emission at 1.3 or 3.5 cm, neither molecular (^{12}CO) emission. We used our observations and those from Pontoppidan et al. (2007) to complete the SED and we modeled it using our implementation of the Dullemond et al. (2001) circumstellar disk model. We found a disk with an outer radius of only 40 AU, and a mass of dust of $4 \cdot 10^{-5} M_{\odot}$ [†]. This compact and light disk is not usual around low mass objects, where disks usually reach sizes greater than 100 AU. This result and the lack of CO emission was interpreted to be due to the high number of IR sources present around this source (24 in a radius of 0.2 pc according to Testi et al. 1998), that could be responsible of the photoevaporation of the outer part of the disk. The main conclusion of this work was the presence of grains with a maximum size close to 1 cm in the midplane. This result is supported by the flat shape of the SED between 1 and 3 mm, with a spectral index of 0.9. A spectral index below 1 is indicative of grains with a maximum size of 3 mm or larger (Draine 2006).

Alonso-Albi et al. (2009) completed a search for circumstellar disks in a sample of six HBe stars: R Mon, MWC 1080, MWC 137, MWC 297, Z CMa, and LkH α 215. We obtained observations from the PdBI at mm wavelengths and from the VLA at cm wavelengths. We also used MIPS and IRS data from Spitzer for MWC 1080, MWC 297, R Mon, and LkH α 215, and completed the SED using continuum photometry from a variety of catalogs (compiled with data from instruments of different resolutions) using Vizier service. We found excess from the expected level of the free-free emission (derived from VLA observations) in the mm fluxes of four out of the six sources in our sample, only MWC 137 and LkH α 215 showed no trace of a circumstellar disk. A first evident result is that for all HBe sources most of the continuum emission at far IR and sub-mm wavelengths comes from the envelope surrounding the star, so an envelope component must be added to the disk model to account for this flux. As in the case of VV Ser, the spectral index found in these sources was close to unity, which indicates the presence of grains with maximum sizes close to the cm, even for these extremely

[†]Here we specifically mention the *mass of dust* only, in other sections we refer to the *mass of the disk*, which we consider to be 100 times greater due to the gas-to-dust mass ratio.

young sources. From the detailed modeling of the sources (see the top panel in Fig. 4) we found an evolutionary trend from massive and large disks (Z CMa) to mostly dispersed disks (MWC 137). An interesting case was MWC 297, for which we concluded that it is in transition phase between those two extreme status, with a second midplane component that is being dispersed. Details for each source are given in Alonso-Albi et al. (2009).

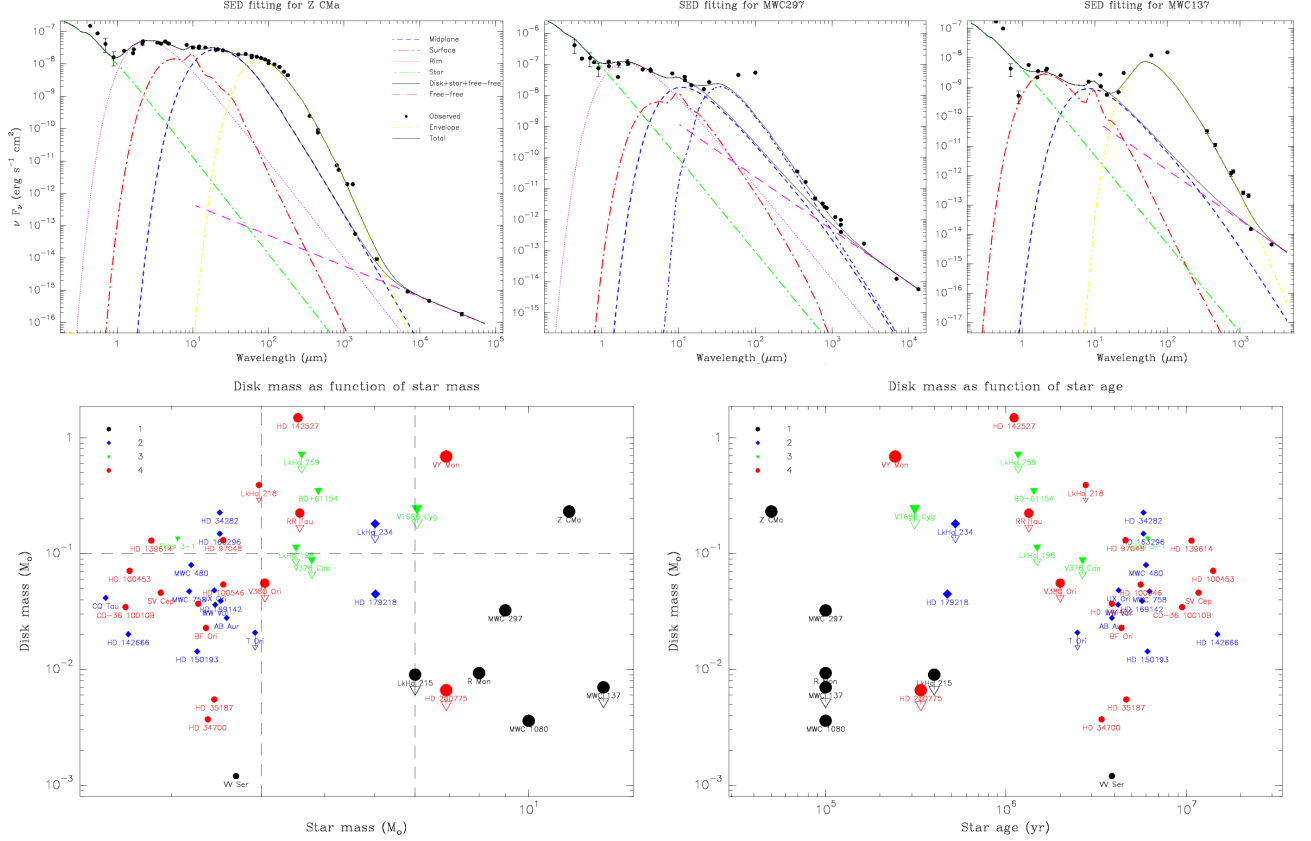


Fig. 4. Top: Detailed modeling of the circumstellar disks around Z CMa, MWC 297, and MWC 137. The evolution is clearly visible from a massive and large disk (Z CMa) with a compact and massive envelope, to an almost inexistent disk with a prominent but partially dispersed envelope (MWC 137). MWC 297 is in transition phase between both status. **Bottom:** Compilation of disk masses against the stellar mass and age. The more the mass of the star the more the mass of the disk, until the stellar mass exceeds 6 M_⊙ and its UV field photoevaporates the disk in very short time scales. The mass of the disks around H Ae stars does not depend on the age of the star.

In Alonso-Albi et al. (2009) we also did a compilation of most detections of circumstellar disks around H Ae and H Be stars from the literature, in order to compare H Be with H Ae sources. We found that the disks around H Ae sources had masses around 0.04 M_⊙, quite independent from the age of the parent star (see the panel at the bottom in Fig. 4). In contrast, disks around H Be sources have much greater dispersion, with values ranging from 0.2 M_⊙ (Z CMa) to 0.003 M_⊙ (MWC 1080) or lower. We concluded that Z CMa and R Mon are the youngest sources in our sample, and the intense UV radiation field produced by B-type stars is responsible for the fast dissipation of the gas and dust in the circumstellar disks around H Be stars, that removes the surface layers in time-scales of about 10⁵ years. Between 3 and 5 M_⊙ we had few sources, so we worked with a new sample of H Ae stars in that range of masses to obtain a better picture for H Ae sources in the limit between H Ae and H Be stars. The studied sources were LkHα 198, BD+61154, RR Tau, and VY Mon (Boissier et al. 2011). In LkHα 198 we did not detect a circumstellar disk, probably due to the effects of the objects in the vicinity (as in VV Ser) since this object is a cluster. For the other sources we found disks with masses of 0.04 M_⊙ or greater, and grains with a maximum size of 1 mm or less, suggesting that although grain growth is proceeding, these disks are less evolved than those around H Be stars. Considering that star ages are around 10⁶ years for H Ae objects and 10⁵ for H Be ones, this result shows that disk evolution is much faster in H Be stars.

4 Conclusions

We carried observations in continuum and molecular lines in a sample of six HBe and five HAe stars. We detected a circumstellar disk in six out of the four HBe sources, and in four out of the five HAe ones. The entire SED was modeled with a disk + envelope (always dominant in sub-mm regime in HBe stars) + free-free emission (to determine the spectral index of the SED in mm wavelengths, and the mass of the disks) model.

The youngest sources (R Mon, Z CMa) still show emission in molecular lines. We modeled the disk around R Mon in ^{12}CO 1 \rightarrow 0 and 2 \rightarrow 1, obtaining a direct estimate of its mass assuming Keplerian rotation. ^{13}CO 1 \rightarrow 0 observations showed the disk is flat.

The spectral index of the dust in mm wavelengths is always < 1 in HBe stars, probably due to the presence of a grain population up to 1 cm in size. Since grain growth occurs even in very young HBe sources, this process seems to be independent from the properties (age, mass) of the HBe source. In case this process happens before photoevaporation gets intense planetesimals around HBe stars would be possible.

The mass of the disks (gas+dust) around HBe sources ranges from $0.2 M_{\odot}$ in extremely young sources (Z CMa) to about $0.003 M_{\odot}$ in more evolved sources (MWC 1080 for instance) or lower, with a high dispersion in the values since the dissipation of the disk occurs in very short timescales.

HAe stars in our sample are older, their disks more massive (with an average value of $0.04 M_{\odot}$), and the grains have not reached cm sizes yet. HAe sources between 3 and $5 M_{\odot}$ show evidences that grain growth is happening, although this process is slower compared with HBe sources.

An important problem is the dependency of the mass of the disks with the mass and age of the stars, and with the effects of the objects in the vicinity. ALMA will provide a more representative sample with more objects in each mass range (up to 5 kpc), and will resolve the disks, allowing detailed chemical studies.

References

- Alonso-Albi, T., Fuente, A., Bachiller, R., et al. 2007, arXiv:astro-ph/0702119
 Alonso-Albi, T., Fuente, A., Bachiller, R., et al. 2008, ApJ, 680, 1289
 Alonso-Albi, T., Fuente, A., Bachiller, R., et al. 2009, A&A, 497, 117
 Alonso-Albi, T., Fuente, A., Crimier, N., et al. 2010, A&A, 518, A52+
 Bisschop, S. E., Fraser, H. J., Öberg, K. I., van Dishoeck, E. F., & Schlemmer, S. 2006, A&A, 449, 1297
 Boissier, J., Alonso-Albi, T., Fuente, A., et al. 2011, A&A, 531, A50+
 Caselli, P., Vastel, C., Ceccarelli, C., et al. 2008, A&A, 492, 703
 Caselli, P., Walmsley, C. M., Zucconi, A., et al. 2002, ApJ, 565, 344
 Collings, M. P., Dever, J. W., Fraser, H. J., McCoustra, M. R. S., & Williams, D. A. 2003, ApJ, 583, 1058
 Crimier, N., Ceccarelli, C., Alonso-Albi, T., et al. 2010, ArXiv e-prints
 de Graauw, T., Helmich, F. P., Phillips, T. G., et al. 2010, A&A, 518, L6+
 Draine, B. T. 2006, ApJ, 636, 1114
 Dullemond, C. P., Dominik, C., & Natta, A. 2001, ApJ, 560, 957
 Fuente, A., Alonso-Albi, T., Bachiller, R., et al. 2006, ApJ, 649, L119
 Johnstone, D., Fich, M., McCoey, C., et al. 2010, A&A, 521, L41+
 Öberg, K. I., van Broekhuizen, F., Fraser, H. J., et al. 2005, ApJ, 621, L33
 Pontoppidan, K. M., Dullemond, C. P., Blake, G. A., et al. 2007, ApJ, 656, 980
 Testi, L., Palla, F., & Natta, A. 1998, A&AS, 133, 81

AN HI 21-CM LINE SURVEY OF EVOLVED STARS

E. Gérard¹, T. Le Bertre² and Y. Libert³

Abstract. The HI line at 21 cm is a tracer of circumstellar matter around AGB stars, and especially of the matter located at large distances (0.1-1 pc) from the central stars. It can give unique information on the kinematics and on the physical conditions in the outer parts of circumstellar shells and in the regions where stellar matter is injected into the interstellar medium. However this tracer has not been much used up to now, due to the difficulty of separating the genuine circumstellar emission from the interstellar one.

With the Nançay Radiotelescope we are carrying out a survey of the HI emission in a large sample of evolved stars. We report on recent progresses of this long term programme, with emphasis on S-type stars.

Keywords: HI line - evolved stars - AGB - circumstellar matter - interstellar matter - individual sources: OP Her, T Cet, R Gem, W And, RS Cnc

1 Introduction

Low- to intermediate-mass stars, at the end of their evolution, become red giants. In this phase they may undergo mass loss at a very large rate ($> 10^{-8} M_{\odot} \text{ yr}^{-1}$), even so large that it has a decisive effect on their late evolution (Olofsson 1999). Observations show that the rate at which this phenomenon develops varies highly from source to source, so that the balance of mass loss as a function of the initial conditions (mass, metallicity, etc.) and of the stage of evolution is presently not well understood.

The HI line at 21 cm is potentially well suited to determine the history of mass loss because hydrogen is the dominant element in AGB outflows and because atomic hydrogen should be protected from photoionization by the surrounding interstellar medium (ISM). However, the dominant species in the atmospheres of AGB stars is expected to be atomic hydrogen only in relatively "warm" red giants with $T_{\text{eff}} > 2500$ K, and by contrast it should be molecular hydrogen in "cool" red giants with $T_{\text{eff}} < 2500$ K (Glassgold & Huggins 1983). Nevertheless molecular hydrogen should be ultimately photodissociated by the interstellar radiation field in the external parts of circumstellar shells (Morris & Jura 1983). The distance at which this happens, is expected to depend mainly on the square root of the mass loss rate, but this needs to be proven. Also molecular hydrogen might survive at larger distance, if the outflows are clumpy. Atomic hydrogen should thus be also a useful tracer of the physical conditions in the outer parts of circumstellar shells and in the regions where stellar matter is injected into the ISM. Therefore, HI spectro-imagery of circumstellar environments is expected to bring a wealth of information on the relations between stars and the ISM.

2 HI surveys

However the detection of red giants in the HI line at 21 cm happens to be difficult partly due to the weakness of the signal, and even more to the competing emission by the ISM on the same lines of sight. Pioneering efforts in the 1980's led to the detection of only two sources, α Ori and Mira (Bowers & Knapp 1987, 1988). This topic was abandoned until we readdressed it in 2001, after the renovation of the Nançay Radio Telescope (NRT). In a first survey we detected HI in about 20 red giants (Gérard & Le Bertre 2006). The high sensitivity to low surface brightness emission, a good spatial resolution in right ascension ($4'$ at 21 cm) and a well-adapted observing technique (position-switch with increasing east-west offset) contributed to this success.

¹ GEPI, Observatoire de Paris

² LERMA, Observatoire de Paris

³ IRAM

The majority of the sources that were detected have a mass loss rate of only a few $10^{-7} M_{\odot} \text{ yr}^{-1}$. Also the majority have a warm central star with $T_{\text{eff}} > 2500$ K. These two results are not independent because, for red giants, there is an inverse correlation between T_{eff} and \dot{M} , with warm sources undergoing a relatively low mass loss rate, as compared to cool sources (with $T_{\text{eff}} \lesssim 2500$ K) that may have rates as large as 10^{-5} to $10^{-4} M_{\odot} \text{ yr}^{-1}$. The line profiles of our detected H I sources are generally narrower than the CO line profiles, implying a slowing down of stellar outflows by surrounding material. The emissions are extended, indicating shell sizes on the order of 1 pc, and suggesting the possibility of tracing the history of mass loss over a few 10^5 years (see following section).

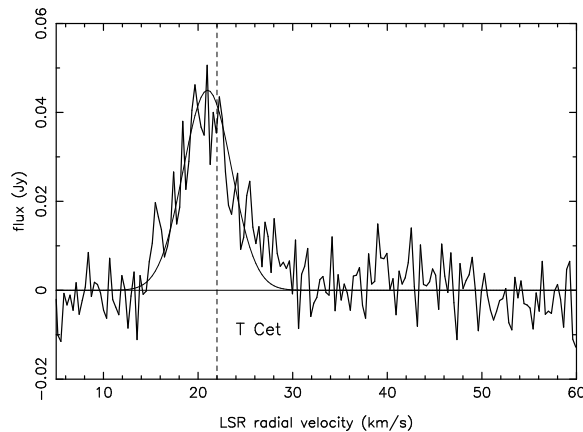


Fig. 1. H I spectrum of T Cet. The vertical dashed line marks the radial velocity determined from circumstellar CO lines by Ramstedt et al. (2009). The thin line is a gaussian fit to the H I profile.

In collaboration with L.D. Matthews, the most promising sources are then imaged with the Very Large Array (VLA; e.g. Matthews et al. 2008, 2011). These images allow us to study in more detail the geometry of the circumstellar shells which tend to exhibit signatures of ISM interaction due to the motion of the central stars with respect to the local ISM (Villaver et al. 2003; Libert et al. 2008).

The observation of H I in cool sources ($T_{\text{eff}} \lesssim 2500$ K) is more difficult because atomic hydrogen is not expected to peak on the central star, but rather to be found only at some distance as a daughter species of molecular hydrogen. For nearby sources we therefore need to cover large areas on the sky in order to detect the putative H I emission (that may or may not be present depending on the history of mass loss, clumping,...). Although more difficult to study, we cannot ignore these sources which may in fact dominate the replenishment of the interstellar medium by stellar matter (Sedlmayr 1994).

It thus appears necessary to survey systematically evolved stars for their H I emission. We have already performed systematic observations of a sample of 60 carbon stars (Gérard et al. 2011), and presently study a sample of 20 S-type stars, i.e. AGB stars with a photospheric C/O abundance ratio close to 1 or slightly less, mainly selected from the work of Ramstedt et al. (2009). These authors have obtained CO radio observations that allow them to derive accurate radial velocities which, for us, are a useful guide to identify the circumstellar H I lines.

In Fig. 1, we show the H I profile of T Cet, a S-type semi-regular variable (SRb), with a mass loss rate of $0.4 \cdot 10^{-7} M_{\odot} \text{ yr}^{-1}$ (for a distance of 240 pc, Ramstedt et al. 2009). The H I line is slightly offset in velocity ($\sim 1 \text{ km s}^{-1}$) with respect to the CO lines. As usual, this offset is towards the zero-velocity of the local standard-of-rest (LSR) frame which suggests a dragging of the circumstellar envelope by the ambient ISM (Gérard & Le Bertre 2006). In Fig. 2 (left), we show the spectrum of OP Her, an irregular variable (Lb) of type S for which no radio CO detection has been reported. Famaey et al. (2005) give a LSR radial velocity of 29.5 km s^{-1} , whereas we find an H I line centered at 27 km s^{-1} .

T Cet and OP Her are rather warm sources at high galactic latitudes, and we easily detect their H I emissions. On the other hand the S-type Mira variable R Gem is barely detected in H I (Fig. 2 right), although it is a strong CO emitter, with a substantial mass loss rate ($4.4 \cdot 10^{-7} M_{\odot} \text{ yr}^{-1}$, for a distance of 710 pc, Ramstedt et al. 2009). As its radial velocity is large (-60 km s^{-1}), confusion remains weak, and we could obtain a marginal detection of ~ 7 mJy. We presently do not fully understand the reason for the weakness of the H I emission of many Miras. Hydrogen could be mainly in molecular form, and preserved from photo-dissociation in the outer layers of their circumstellar shells (self-shielding in high density regions?). Alternatively the duration of the

mass loss phenomenon could be too short to allow for the presence of a detectable quantity of atomic hydrogen. It is noteworthy that, in their IRAS survey of evolved stars, Young et al. (1993) found that Mira variables tend to have been losing mass for a shorter period than semi-regular variables, and have smaller infrared diameters. This questions the often cited argument that semi-regular variables might evolve into Mira variables.

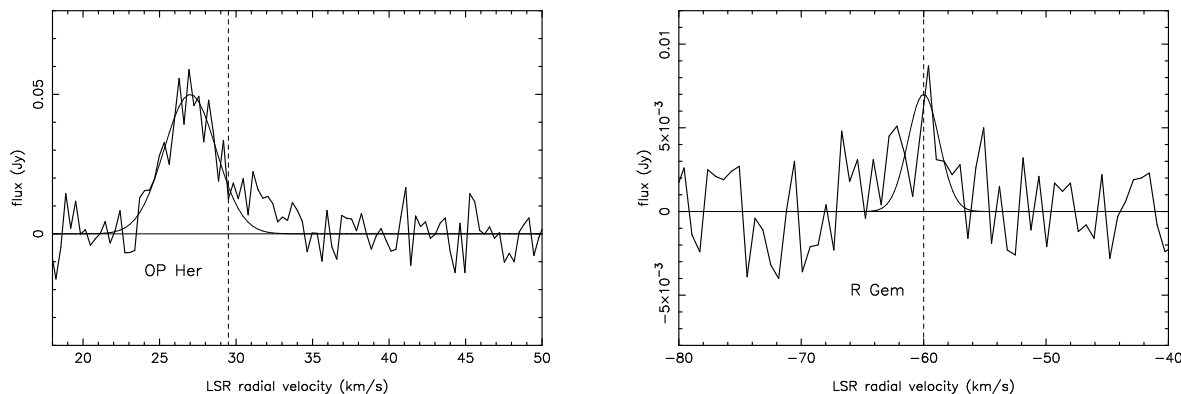


Fig. 2. Left: H I spectrum of OP Her. The vertical dashed line marks the stellar radial velocity from Famaey et al. (2005). **Right:** H I spectrum of R Gem. The vertical dashed line marks the radial velocity determined from circumstellar CO lines by Ramstedt et al. (2009). The thin lines are gaussian fits to the H I profiles.

3 Detailed studies of individual sources

In our first H I survey (Gérard & Le Bertre 2006) we found that, in general, the emissions of nearby sources are extended, indicating shell sizes on the order of 1 pc, and suggesting the possibility of tracing the history of mass loss over a few 10^5 years. Also, the H I emissions are sometimes spatially shifted w.r.t. to the central stars in a direction that is often opposite to that of the proper motion. Using the VLA, a “head-tail” morphology has been found in several cases (Matthews & Reid 2007; Matthews et al. 2008, 2011). Thus it appears that, in H I at 21 cm, we are probing a region that is shaped by the motion of the star relative to the ISM. Even though the NRT has a large beam ($4'$ in right ascension and $22'$ in declination at 21 cm) compared to the VLA ($\sim 1'$ in the D-configuration), the circumstellar environments of many sources can be resolved. In the extreme case of Mira, a 2-degree long tail has been discovered in the far ultra-violet by the satellite GALEX (Martin et al. 2007). In that case the H I emission extends clearly beyond the VLA primary beam, and observations with a large size single dish antenna are needed to detect H I in the tail (Matthews et al. 2008). It is in such regions that stellar matter is expected to be injected into the ISM, and observations at high spectral resolution of the H I line at 21 cm allow us to constrain the kinematics in this kind of fascinating, but barely studied, environment.

In Fig. 3, we show the spectra obtained on and around W And, a Mira variable of type S, with a mass loss rate of $1.7 \cdot 10^{-7} M_{\odot} \text{ yr}^{-1}$ (for a distance of 280 pc, Ramstedt et al. 2009). In the left panel, the position-switch spectra obtained at $\pm 4'$ and at $\pm 6'$ are almost indistinguishable. Thus the source does not appear to be extended in right ascension (diameter size $\leq 4'$). On the other hand the maximum of H I emission is clearly offset south ($\sim 5'$) because the fluxes obtained on the star position and at $11'$ south are almost the same (Fig. 3, right panel).

There is also a practical reason for mapping individual sources. The confusion with interstellar emission can be so intricate that a large size map around the target is needed in order to isolate the genuine circumstellar emission. For example an extended mapping around RScnc, a S-type semi-regular variable (SRc), by Libert et al. (2010), revealed a structure of $\sim 18'$ that we could separate from the underlying ISM emission.

4 Conclusion and future work

The 21-cm H I emission from evolved stars brings unique information on the kinematics and the physical conditions in the external regions of circumstellar shells. However, it is weak, especially in cool sources where molecular hydrogen may dominate, and its observation often suffers from confusion by the ISM emission. More work is needed to understand the formation of H I lines in circumstellar environments, and to assess the potential contribution of H I studies to the physics of circumstellar shells around evolved stars.

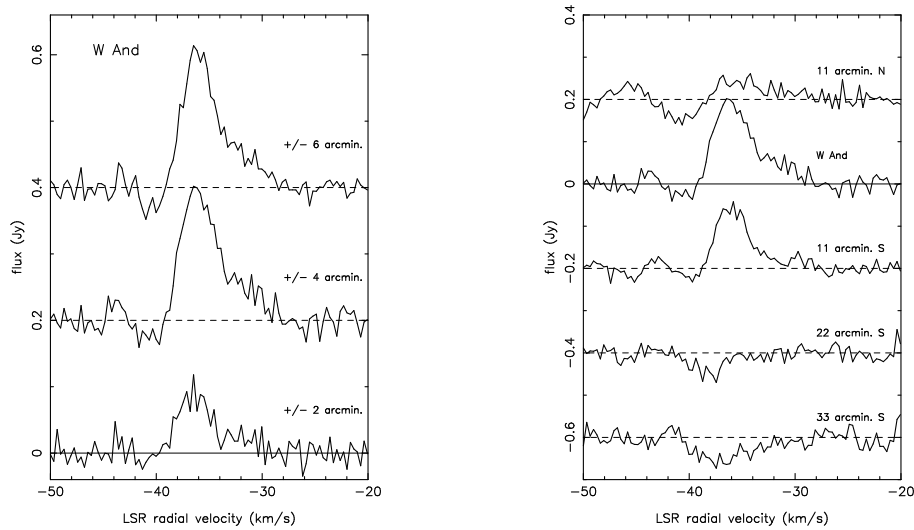


Fig. 3. Left: W And spectra obtained in the position-switch mode with the star centered (“on”) and the off-positions taken in the east-west direction at $\pm 2'$, $\pm 4'$, and $\pm 6'$. For clarity the spectra have been successively shifted by 0.2 Jy. **Right:** position-switch spectra ($\pm 4'$) with the central beam placed at $+11'$ (half a beam, north), on source (as on the left panel), $-11'$ (half a beam, south), $-22'$ (one beam, south), and $-33'$ (one and half beam, south).

The Square Kilometre Array (SKA) would be ideal to study these weak and extended sources. In the H I line at 21 cm it will be able to image nearby circumstellar environments at all scales needed to probe the history of mass loss and the interaction of stellar outflows with the ISM. Nevertheless, using the observational strategy that we have developed with the NRT we can already begin to explore this field. The EVLA offers also the promising possibility to study these sources at the sub-arcminute scale, as well as will soon the SKA precursors (ATA, MeerKAT, etc.) that are under construction.

Acknowledgements

We are grateful to Drs L.D. Matthews and J.M. Winters for fruitful discussions. We thank the PCMI for financial support. The Nançay Radio Observatory is the Unité scientifique de Nançay of the Observatoire de Paris, associated as Unité de Service et de Recherche (USR) No. B704 to the French Centre National de la Recherche Scientifique (CNRS). The Nançay Observatory also gratefully acknowledges the financial support of the Conseil Régional de la Région Centre in France.

References

- Bowers, P.F., & Knapp, G.R., 1987, ApJ, 315, 305
 Bowers, P.F., & Knapp, G.R., 1988, ApJ, 332, 299
 Famaey, B., Jorissen, A., Luri, X., et al., 2005, A&A, 430, 165
 Gérard, E., & Le Bertre, T., 2006, AJ, 132, 2566
 Gérard, E., Le Bertre, T., & Libert, Y., 2011, Proc. “Why Galaxies Care About AGB Stars II”, in press
 Glassgold, A.E., & Huggins, P.J., 1983, MNRAS, 203, 517
 Libert, Y., Le Bertre, T., Gérard, E., & Winters, J.M., 2008, Proc. “SF2A-2008”, p. 317
 Libert, Y., Winters, J.M., Le Bertre, T., Gérard, E., & Matthews, L.D., 2010, A&A, 515, A112
 Martin, D.C., Siebert, M., Neill, J.D., et al., 2007, Nature, 448, 780
 Matthews, L.D., Libert, Y., Gérard, E., Le Bertre, T., Johnson, M.C., & Dame, T.M., 2011, AJ, 141, id. 60
 Matthews, L.D., Libert, Y., Gérard, E., Le Bertre, T., & Reid, M.J., 2008, ApJ, 684, 603
 Matthews, L.D., & Reid, M.J., 2007, AJ, 133, 2291
 Morris, M., & Jura, M., 1983, ApJ, 264, 546
 Olofsson, H., 1999, IAU Symposium n° 191, p. 3
 Ramstedt, S., Schöier, F.L., & Olofsson, H., 2009, A&A, 499, 515
 Sedlmayr, E., 1994, IAU Colloquium n° 147, p. 163
 Villaver, E., García-Segura, G., & Manchado, A., 2003, ApJ, 585, L49
 Young, K., Phillips, T.G., & Knapp, G.R., 1993, ApJ, 409, 725

MOLECULAR EMISSION IN CHEMICALLY ACTIVE PROTOSTELLAR OUTFLOWS

B. Lefloch^{1,2}

Abstract. Protostellar outflows play an important role in the dynamical and chemical evolution of cloud through shocks. The *Herschel Space Observatory* (HSO) brings new insight both on the molecular content and the physical conditions in protostellar shocks through high spectral and angular resolution studies of the emission of major gas cooling agents and hydrides. The Herschel/CHESS key-program is carrying out an in depth study of the prototypical shock region L1157-B1. Analysis of the line profiles detected allows to constrain the formation/destruction route of various molecular species, in relation with the predictions of MHD shock models. The Herschel/WISH key-program investigates the properties and origin of water emission in a broad sample of protostellar outflows and envelopes. Implications of the first results for future studies on mass-loss phenomena are discussed.

Keywords: ISM: astrochemistry, individual objects: L1157, ISM: molecules, ISM: jets, outflows, stars: formation

1 Introduction

Outflows are the most spectacular manifestation of the mass-loss phenomena which take place along the protostellar evolution, from the very early, embedded Class 0 to the late Class II phase, when the parental cocoon is dispersed. Three main types of mass-loss phenomena have been identified from their observational signatures : a) highly collimated jets of hot ($T > 1000$ K), partly ionized/atomic material, which propagate at velocities (typically several hundreds of km s^{-1}), detected at optical and near-IR wavelengths; b) outflow cavities of cold (10 K) molecular gas, propagating at low-velocity ($\sim 10 \text{ km s}^{-1}$), detected at millimeter wavelengths; c) bullets of molecular gas moving at extremely high-velocities (EHV), comparable to the optical jet, also detected at millimeter wavelengths. The presence of a protostellar wide-angle wind, which would accompany the launch of a highly-collimated jet remains debated. The outflow cavities and the EHV bullets are understood in the framework of the jet-driven bowshock model as the result of the shock interaction of the high-velocity jet powered by the newly-born star with the parental cloud.

There is now large observational evidence that indeed outflows play an important in the chemical evolution of the cloud. Abundance enhancements of several orders of magnitude have been reported for various molecular species, e.g. SiO, SO, and CH₃OH in "chemically active" outflows (see e.g. Bachiller et al. 2001). More recently, complex organic molecules have been reported in L1157 (Arce et al. 2008; Codella et al. 2009). The formation route of these species, either gas phase or dust grain chemistry, remains strongly debated. Large differences in molecular abundances are observed not only between sources at different evolutionary stages but also between regions of the same flow (e.g. B1 and B2, Fig. 1), that remain unexplained. The recent instrumental developments at millimeter wavelengths now permit to undertake outflow millimeter line surveys at a reasonable cost so to explore in a systematic way their molecular content.

An important point is to determine whether the shock accelerating the outflow is a purely hydrodynamical discontinuity ("J-type" shock), or a continuous, non-dissociative("C-type") shock with a magnetic precursor where ions are decoupled from the neutral fluid. Indeed, the physical and dynamical conditions implied by C- and J-type shocks are very different. C-shocks are predicted to play an important role in the gas chemical evolution through the temperature and density changes resulting from the activation of endothermic reactions, ionization, and dust sputtering in the ion-neutral drift zones.

¹ CNRS-INSU, Institut de Planétologie et d'Astrophysique de Grenoble (IPAG), UMR5274, Grenoble, F-38041, France

² Centro de Astrobiología, INTA-CSIC, Crta Torrejón km 4, 28856 Torrejón de Ardoz, Madrid, Spain

The study of the H_2 rovibrational line emission at near- and mid-IR wavelengths has proven very successful, and could bring indirect evidence for MHD shocks in protostellar outflows (see e.g. Cabrit et al. 2003). The limited spectral resolution prevents any detailed study of the shock dynamics, however. The great promise of the *HSO* was precisely to give access to the emission of the major gas cooling agents in the submillimeter and far-infrared domain, CO and H_2O , at an angular resolution comparable to that of the largest ground-based telescopes. The high-spectral resolution of the heterodyne instrument HIFI permits to study the dynamics and to reconstruct the thermal profile in the shocked gas. Thanks to its unprecedented sensitivity, *Herschel* permits to search for the presence of hydrides, which play an important role in the chemical networks and the synthesis of more complex molecules. By probing the whole CO ladder from $J_{\text{up}} = 4$ ($E_{\text{up}} = 55.3$ K) up to $J_{\text{up}} = 45$ ($E_{\text{up}} = 5120$ K), *Herschel* is expected to establish the link between the cold gas of the outflow cavities detected in the millimeter range and the hot shocked gas detected at near-infrared wavelengths.

2 Peering into the protostellar shock L1157-B1

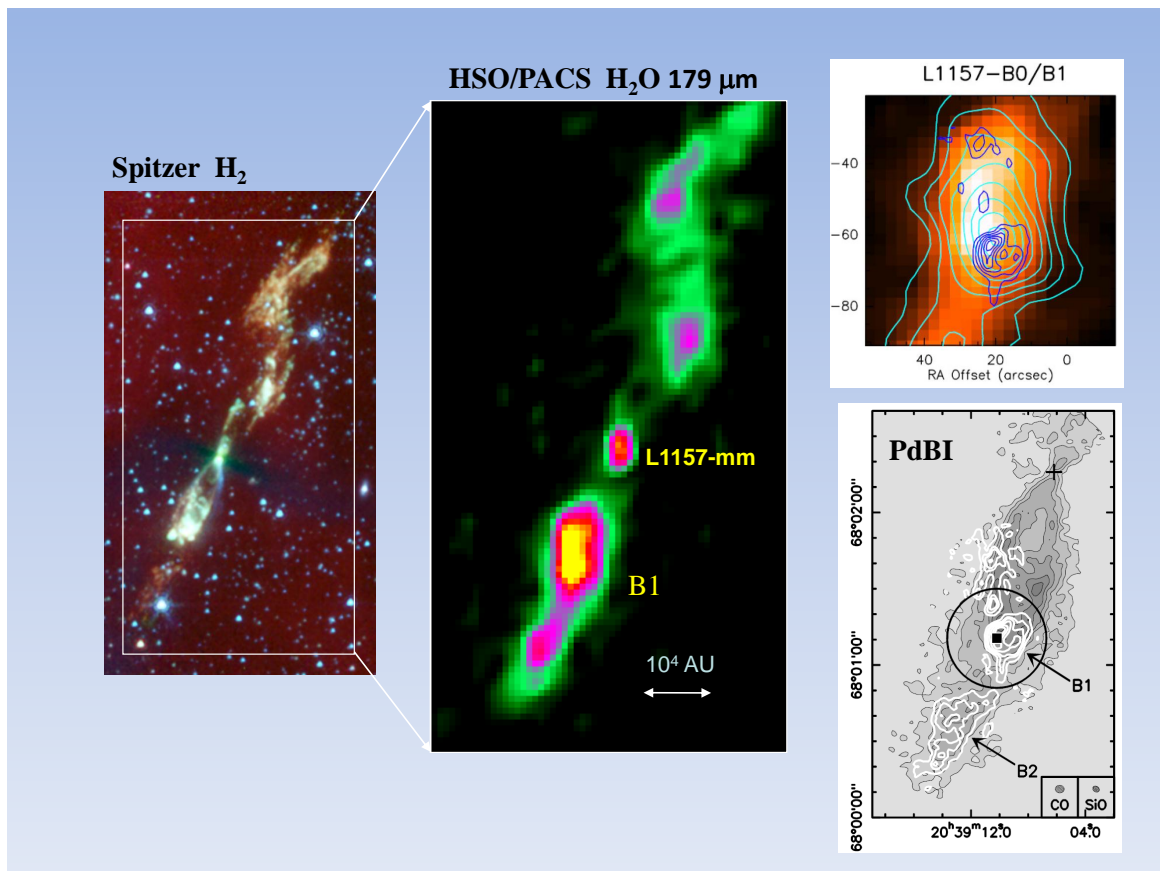


Fig. 1. Molecular gas emission in the prototypical outflow L1157. *Left:* H_2 as seen with Spitzer/IRAC (Neufeld et al. 2009); *middle:* $\text{H}_2\text{O } 2_{12} - 1_{01}$ as seen with PACS (Nisini et al. 2010). *Bottom right:* CO 1-0 (greyscale) and SiO 2-1 (white contours) as seen with the PdBI (Gueth et al. 1996). *Top right:* Comparison of $\text{H}_2\text{O } 2_{12} - 1_{01}$ (color scale) and SiO 2-1 emissions at IRAM 30m and PdBI (light and dark blue contours, respectively) in the direction of B1.

The outflow from the Class 0 protostar IRAS20386+6751 ($L = 4 - 10 L_{\odot}$) in the L1157 cloud ($d = 440$ pc) is probably the best studied protostellar outflow at millimeter and far-infrared wavelengths (see Fig. 1; also Codella et al. 2009 and references therein). Mapping of the Southern lobe with the PdBI by Gueth et al. (1996) revealed two cavities associated with subsequent ejection episodes in the (precessing) protostellar jet. Bright millimeter line emission was detected at the position of the shocks B1 and B2, coinciding with the apex of the cavities (Fig. 1; Bachiller et al. 2001).

L1157-B1 was observed with the three instruments onboard *HSO* in the course of the guaranteed-time key-

project CHESS, dedicated to the exploration of molecular complexity in star-forming regions (Ceccarelli et al. 2010). A full spectrum was obtained in the submillimeter range ($672 - 192\mu\text{m}$) with SPIRE and in the far-infrared range ($55 - 200\mu\text{m}$) with PACS (Benedettini et al. 2011). The whole spectrum is dominated by the CO line emission (the transitions from $J_{\text{up}} = 4$ up to $J_{\text{up}} = 22$ were detected) and, to a lesser extent, by a few lines of H₂O OH and OI. Estimating the luminosity of these various tracers, it comes out that the gas cooling is dominated by H₂ and CO.

About 20 molecular species were identified from the CHESS survey (Codella et al. 2010; Lefloch et al. 2011 in prep). A few hydrides were detected for the time in outflows, like HCl (Codella et al. 2011). The analysis of the molecular line profiles shows that the emission arises from two physically distinct regions (Figs. 1-2; also Lefloch et al. 2010) : a compact ($\sim 7''$), CO and H₂O rich region, of high-excitation, emitting at high-velocity (HVC); an extended ($\sim 20''$), molecular-rich region (LVC), of lower excitation, emitting at low-velocity. This is illustrated by the comparison of the profiles of the CO transitions from $J_{\text{up}} = 5$ up to $J_{\text{up}} = 13$ in Fig. 2, which have been scaled so to match the emission in the high-velocity gas (HVC). One observes a decrease of the CO line intensity in the low-velocity range (LVC) as a function of J_{up} . There is an excellent agreement between the profiles of the high-J CO lines ($J_{\text{up}} \geq 13$ and $E_{\text{up}} > 500$ K) and the SiO line arising from the HVC, as mapped at the PdBI (Fig. 2). This implies that these tracers are probing the same region of the shock. The physical conditions in the HVC were obtained from a simple modelling of the CO spectral distribution in the Large-Velocity Gradient approach. The complementarity of PACS and HIFI is essential in this kind of analysis : the fit to the whole data set favors gas temperatures (~ 600 K) and densities $n(\text{H}_2) \simeq 10^5 \text{ cm}^{-3}$. The CO flux distribution of the high-velocity component (filled circles and triangles in the top right panel in Fig. 2) is well accounted for by a J-type shock propagating into gas of density $n(\text{H}_2) \simeq 10^4 \text{ cm}^{-3}$ with a shock velocity $V_s \simeq 10 \text{ km s}^{-1}$. Interestingly, the CO flux distribution of the LVC (empty triangles in the top right panel in Fig. 2) is well accounted for by a steady-state magnetized (C-type) shock.

The high spectral resolution of HIFI permits to derive both the physical *and* chemical structure of the shock region from the molecular line profiles. The ratio of the H₂O $1_{10} - 1_{01}$ to CO 5-4 line intensity shows a continuous increase as a function of velocity, consistent with an increase of the H₂O abundance in the higher-excitation gas of the HVC in the shock. Lefloch et al. (2010) estimated an increase of one to two orders of magnitude in the H₂O abundance between the LVC and the HVC. A similar behaviour was observed between water and NH₃ (Fig. 2). Unlike NH₃ which is produced only from dust grain chemistry, H₂O can form very efficiently in the gas phase, as soon as T_{kin} exceeds 220 K. Viti et al. (2011) argue that the increase of the H₂O/NH₃ intensity ratio actually reflects the destruction of NH₃ in the gas phase, via the reaction $\text{NH}_3 + \text{H} \rightarrow \text{NH}_2 + \text{H}_2$, which has an energy barrier of 4000 K. The authors' modelling shows that this reaction is activated when T_{kin} reaches about 3500 K in the gas, which, then, allows them to constrain the density and velocity of the shock. Observations of other shock regions have just been completed with Herschel and should allow to test the suggestion of Viti et al. over a wide range of shock parameters.

The H₂O $2_{12} - 1_{01}$ line at $179\mu\text{m}$ was mapped with PACS in the WISH program (Fig. 1). The H₂O emission is spatially correlated with that of the H₂ pure rotational lines (Fig. 1; Neufeld et al. 2009), and corresponds well with the peaks of other shock-produced molecules such as SiO and NH₃ along the walls of the outflow cavity, where low-velocity shocks are observed (see Fig. 1, top right panel). In contrast with these species, H₂O is also strong at the source position itself. The analysis of the H₂O $179\mu\text{m}$ emission line, combined with existing Odin and SWAS data, shows that water originates in warm compact shocked clumps of few arcsec in size, where the water abundance is of the order of 10^{-4} , i.e., close to that expected from high-temperature chemistry.

3 Water in Protostellar Outflows

The importance of water as a physical diagnostic stems from the orders of magnitude variations in its gas phase abundance between warm and cold regions. Although thermal lines of H₂O cannot be observed from ground, a few masing lines are however accessible under "dry" atmospheric conditions. The p-H₂O $3_{13} - 2_{20}$ line at 183.3 GHz is especially interesting as it arises from a level rather low in energy ($E_{\text{up}} \simeq 205$ K). The difficulties of these observations are such* that only few protostellar sources have been surveyed up to know.

Cepe E is an intermediate-mass Class 0 protostar of luminosity $L \sim 75 L_{\odot}$ where the p-H₂O $3_{13} - 2_{20}$ was recently detected (Fig. 3; Lefloch et al. 2011). Emission was detected in the direction of the protostar only. Like in L1157-B1, one observes a strong similarity between the line profiles of SiO 2-1, as observed with the PdBI, and

*the atmospheric opacity can vary a lot on short timescales.

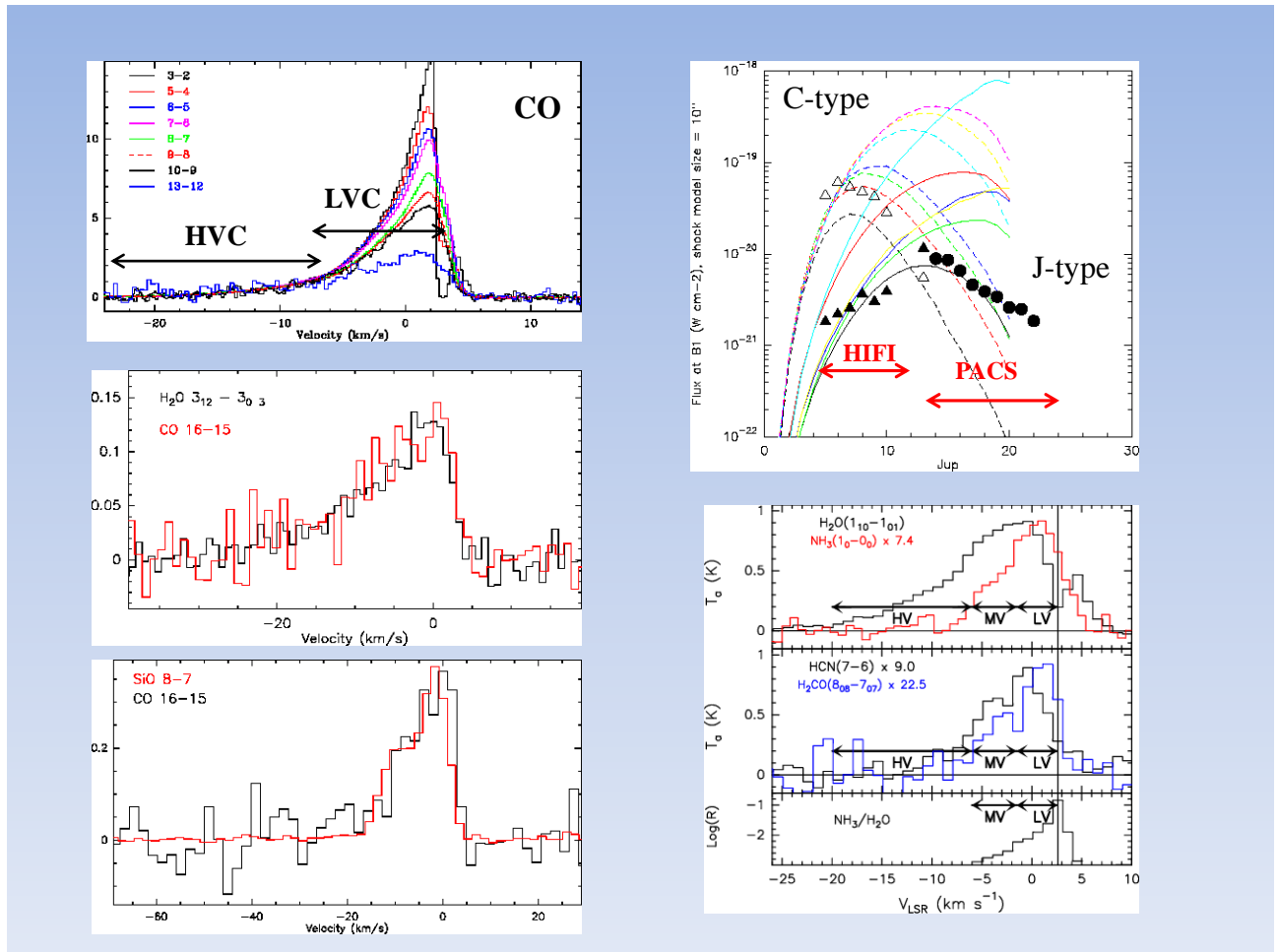


Fig. 2. **Left:** CO line emission detected with HIFI towards L1157-B1 (top;); comparison with shock tracers SiO 8-7 (bottom) and H₂O 3₁₂ - 3₀₃ (middle). (Lefloch et al. 2011, in prep). **Top right:** Comparison of the HVC CO fluxes obtained with PACS and HIFI with steady-state J-type (C-type) shock models in solid (dashed) contours (see Lefloch et al. 2011; Flower & Pineau des Forets 2010). **Bottom right:** ground-state transition of o-H₂O 557 GHz, NH₃, HCN(7-6) and H₂CO line profile observed in the same spectral band (Codella et al. 2010).

H₂O. Comparison with the SiO interferometric maps shows that the H₂O emission arises from high-velocity clumps (size $\sim 10^3$ AU) of dense ($n \sim 10^6$ cm⁻³) and hot ($T \sim 200$ K) gas, with a mass of a few $10^{-4} M_{\odot}$, probably tracing internal shocks in the jet. The water abundance derived ($\sim 10^{-4}$) is indeed consistent with that expected from gas phase chemistry. No emission was detected from the hot corino region itself.

The nature and the physical conditions of the H₂O emission in protostellar environments is one of the main goals of the WISH key-program (van Dishoeck et al. 2011). Observation of the ground state transition of o-H₂O 1₁₀ - 1₀₁ at 557 GHz towards a large sample of protostars shows that the emission is dominated by the emission of the outflow, from the early Class 0 to the Class I (Kristensen et al. 2010). The emission reaches velocities up to 40 - 50 km s⁻¹, although the line is somewhat narrower for evolved sources. The derived abundances are typically $\sim 10^{-4}$. In the chemically active outflow L1448-mm, Herschel/HIFI detected the presence of water bullets, similar to those detected in Cep E with the IRAM 30m, which appear to have formed from atomic oxygen in the high-velocity jet (Kristensen et al. 2011). Interestingly, determination of the water abundance in the inner protostellar envelope from H₂¹⁸O line observations yields values of a few $\sim 10^{-6}$, well below the 10^{-4} measured in outflows (Visser et al., in prep).

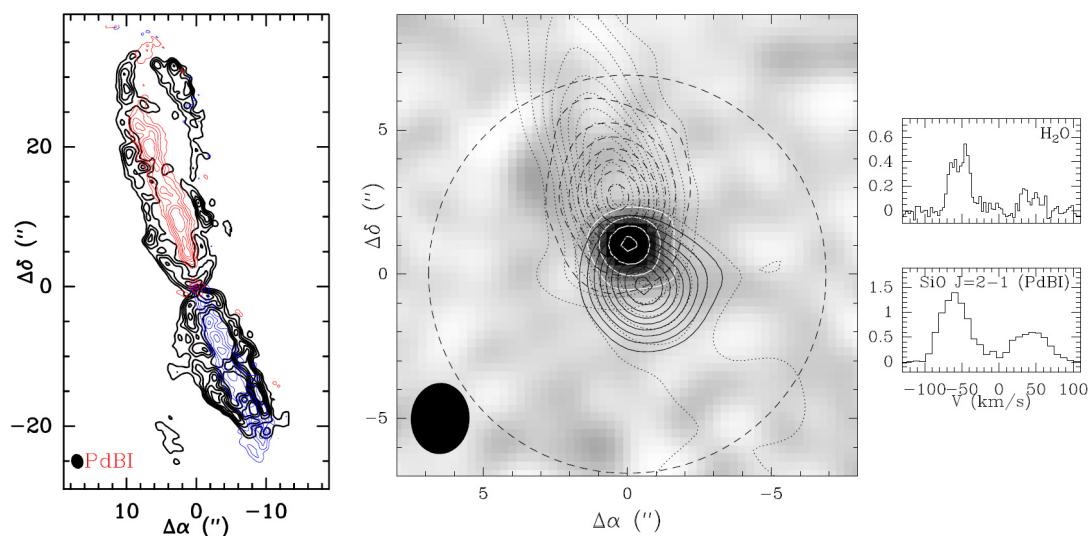


Fig. 3. **Left:** CO 2-1 emission in the Cep E protostellar outflow (black contours) and jet (red/blue contours). (*middle*) SiO 2-1 emission map as observed with the PdBI at 2'' resolution. The jet emission is drawn in thin dotted contours; the SiO 2-1 emission integrated in the velocity range of H₂O emission is drawn in thick contours; the IRAM 30m beam at 183 GHz is drawn in dashed. **Right:** Comparison of the average SiO 2-1 (PdBI) and H₂O (IRAM 30m) line profiles observed towards the core (Lefloch et al. 2011).

4 Conclusions

The studies on H₂O line emission with Herschel and ground based telescopes have clearly established the importance of outflows and shocks in the chemical evolution of molecular clouds *and* protostellar envelopes. Systematic studies on the archetypal shock region L1157-B1 suggest that H₂O and other shock tracers like e.g. SiO actually display a very similar behaviour, an important result which should be established on a large source sample. Analysis of the molecular line emission detected with Herschel gives access to the structure of the shock region L1157-B1 with unprecedented detail, and in a rather consistent way despite the complexity of the region itself. A relatively simple picture emerges, with evidence for two shocks : a C-type shock, associated with the low-velocity, low-excitation gas in the wings of the bow, and a J-type, located close to the apex of the outflow cavity. The observational evidence for strong outflow shocks and efficient water production in the inner protostellar region opens new perspectives on the chemical complexity observed in these regions, attributed up to now to the evaporation of the ice mantles in the hot corino region, as a consequence of heating by the accretion luminosity. The characterization of these shocks should permit to better understand the origin of molecules in protostellar jets, and to discriminate between the various jet launch mechanisms, which will remain out of reach even to the next generation of millimeter interferometers (ALMA, NOEMA).

It is my pleasure to thank the CHESS team, and my collaborators in the outflow group G. Busquet, M. Benedettini, S. Cabrit, C. Ceccarelli, J. Cernicharo, E. Caux, C. Codella, B. Nisini, M. Salez, K. Schuster, M. Vasta. This work has been supported by l'Agence Nationale pour la Recherche (ANR), France (project FORCOMS, contracts ANR-08-BLAN-022) and the Centre National d' Etudes Spatiales (CNES).

References

- Arce, H., Santiago-García, J., Jørgensen, J.K., et al., 2008, ApJ, 681, L21
- Bachiller, R., Pérez Gutiérrez, M., Kumar, M. S. N., 2001, A&A, 372, 899
- Raga, A., Cabrit, S. 1993, A&A, 278, 267
- Cabrit, S., Flower, D. R., Pineau des Forêts, G., et al., 2004, ApSS, 292, 501
- Codella, C., Benedettini, M., Beltrán, M. T., et al., 2009, A&A, 507, L25
- Codella, C., Lefloch, B., Ceccarelli, C., et al., 2010, A&A, 518, L112
- Codella, C., Ceccarelli, C., Bottinelli, S., et al., 2011, in press

- Flower, D.R., Pineau des Forets, G., 2010, MNRAS, 406, 1745
- Gueth, F., Guilloteau, S., Bachiller, R., 1996, A&A, 307, 891
- Gusdorf, A., Pineau Des Forêts, G.; Cabrit, S., Flower, D. R., 2008, A&A, 490, 695
- Kristensen, L.E., Visser, R., van Dishoeck, E. F, et al., 2010, A&A, 521, L30
- Kristensen, L.E., van Dishoeck, E. F., Tafalla, M., et al, 2011, A&A, 531, L1
- Lefloch, B., Codella, C., Cabrit, S., et al., 2010, A&A, 518, L113
- Lefloch, B., Benedettini, M., Cabrit, S., et al., 2011, The Molecular Universe, Proceedings of the IAU Symposium 280, Toledo, Spain, May 30-June 3, 2011
- Lefloch, B., Cernicharo, J., Pacheco, S., Ceccarelli, C., 2011, A&A, 527, L3
- Neufeld, D., Nisini, B., Giannini, T., et al., 2009, ApJ, 706, 170
- Nisini, B., Benedettini, M., Codella, C., et al., 2010, A&A, 518, L120
- van Dishoeck, E.F., Kristensen, L. E., Benz, A. O., 2011, PASP, 123, 138
- Viti, S., Jimenez-Serra, I., Yates, J. A., et al., 2011, ApJ, 740, L3

STRIPPING A DEBRIS DISK BY GRAVITATIONAL INTERACTION WITH AN INNER PLANET

E. Morey¹ and J.-F. Lestrade¹

Abstract. Debris disks are detected through scattered light or thermal emission of their dust, produced by collisions or erosion of planetesimals. The rate of collisions depends on the number density of planetesimals and on the dynamical excitation and geometry of the disk. We have studied a debris disk gravitationally perturbed by a single inner planet, by using a numerical integration over a large parameter space for both the orbital elements of the planet and the disk geometry. We discuss our findings in the context of observed orbital elements for exoplanets and plausible disk geometries.

We have studied whether or not a disk can be significantly disrupted, and stripped of its planetesimals, because of this interaction. We have focused on how the depletion of the disk depends on the masses of the central star and planet. We have found that this dependence is not monotonous, except for low mass stars.

Keywords: circumstellar disks, extrasolar planetary systems

1 Introduction

According to theory, a debris disk is made of planetesimals which are the left over of the processes that have formed planets, in the inner part of the system, during the first 10 Myrs. Afterwards, planets can dynamically excite the disk (Mustill & Wyatt 2009), or even can strip it of its planetesimals, as in the Nice model with Neptune and Uranus put on eccentric orbits when Jupiter and Saturn went through a MMR (Gomes et al. 2005). The fraction of planetesimals stripped off the disk depends on the planet orbital parameters (semi-major axis and eccentricity) and mass, as well as on the central star mass and disk properties (inner and outer radii, thickness, and radial distribution of planetesimals). We have undertaken a search of the parameter space of this problem.

A large variety of eccentricities and masses have been found among the ~ 700 exoplanets discovered since 1995. For example, their eccentricities range from 0 to 0.97 (17% have high eccentricities > 0.4 , see Fig. 1) and their masses ($m \sin i$) range from 3 Earth masses to more than 10 Jupiter masses. These planets are strongly biased toward small orbital radii because of the radial velocity technique and transit observations used for most of the discoveries. Hence, we use instead the Solar System as a guide for plausible orbital radii.

In this first report, we present our study on how the fraction of planetesimals stripped off a disk depends on the masses of the star and planet, non-monotonously according to our finding.

2 Methodology

We have numerically integrated the motion of planetesimals in the disk under the sole influence of the gravitational forces of the central star and the planet ; i.e. the restricted three body problem for the non self-gravitating disk. We use a leapfrog integration scheme. The time step (0.5 day) was adopted after various convergence tests.

¹ LERMA, Observatoire de Paris, 61 avenue de l'Observatoire, 75014 Paris, France

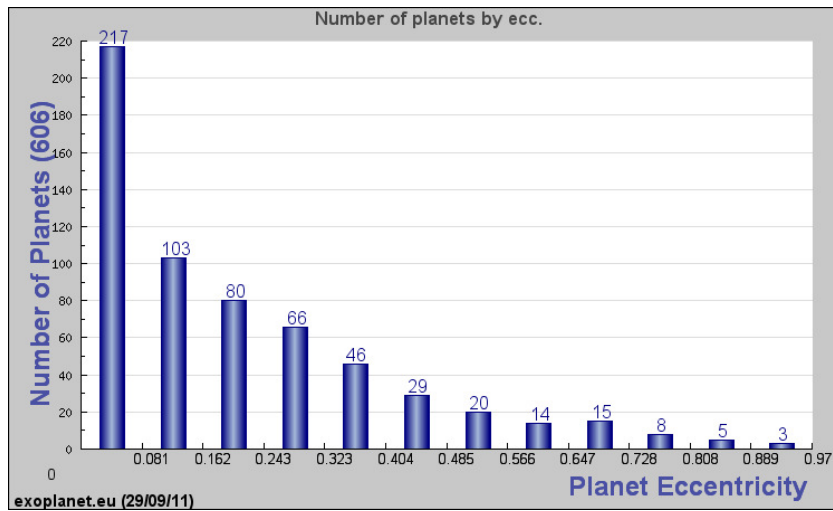


Fig. 1. Histogram of eccentricity of currently known exoplanets (<http://exoplanet.eu/>).

The disk is made of 1000 massless particles, sufficient in number to properly estimate the fraction of planetesimals that leave the system on unbound orbits. Our result below is based on integrations over 100 Myrs. A few integrations were run over 200 Myrs and 500 Myrs to probe the longer term evolution which is not significant except for low mass planets (see Fig 2).

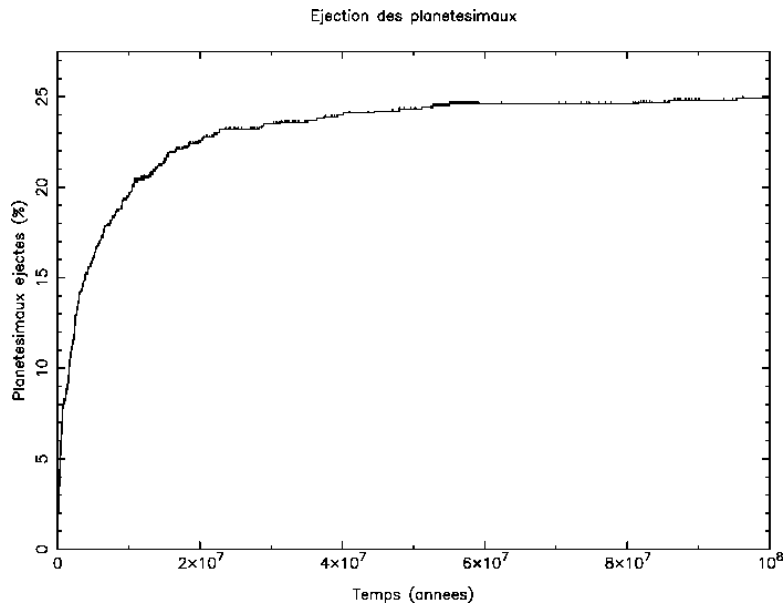


Fig. 2. Ejection fraction of planetesimals, according to time, for a disk surrounding a solar mass star and a Jupiter mass planet orbiting at $a = 20$ AU with $e = 0.5$ ($m_{pl}/m_* = 10^{-3}$). For lower ratio m_{pl}/m_* , the curve saturates less rapidly over 100 Myrs and may underestimate the final ejection fraction by 10-20%.

The initial edges of the disk are set at 30 and 80 AU. Integrations are carried out in a three-dimensional space : the thickness of the initial disk is 1 AU at the inner edge, and 2.8 AU at the outer edge (opening angle = 2°). The planetesimals in the disk are initially set on circular orbits. The surface density of planetesimals decreases as $1/r$.

3 Results and discussion

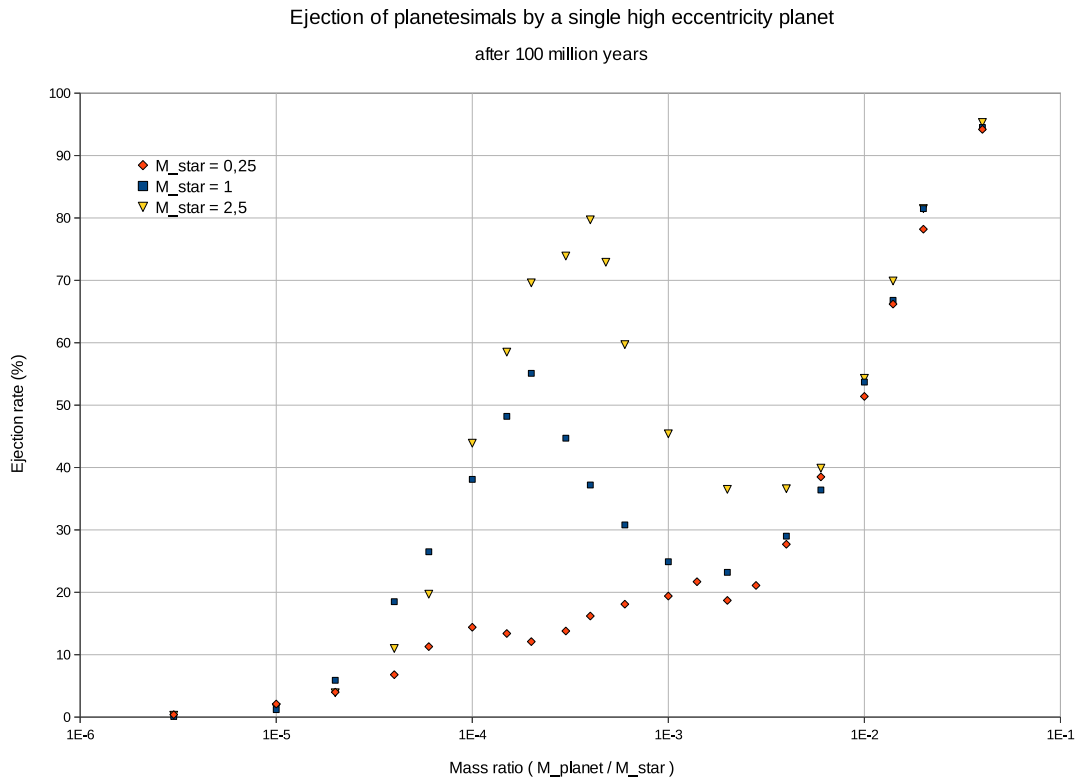


Fig. 3. Fractions of planetesimals stripped off a disk versus the ratio of planet and star masses, after 100 Myrs, by a single planet at $a = 20$ AU and with $e = 0.5$. The apoapsis of the planet is located at 30 AU of the star, which corresponds to the inner edge of the disk. The outer edge is placed at 80 AU. Three star masses are adopted : 2.5, 1, and 0.25 solar mass (spectral types : A, G and M). Each point corresponds to a full integration of 100 Myrs.

Current results are shown on Fig. 3. For each of the three star masses (A, G, M spectral types), the points delineate three regions :

1. for low mass ratios ($m_{pl}/m_* < 2.10^{-5}$), the ejection fraction asymptotically vanishes, as expected because the low planet mass cannot perturb the disk sufficiently.
2. for high mass ratios ($m_{pl}/m_* > 6.10^{-3}$), the ejection fraction depends solely on the mass ratio, and the disk can be completely stripped for the most massive planets.
3. for the intermediate range $2.10^{-5} < m_{pl}/m_* < 6.10^{-3}$, the ejection fraction depends on the masses of the star and planet, independently. In this range, there is an enhancement of the stripping which is counter-intuitive ; for example, a Jupiter mass planet strips the disk more efficiently around an A star (peaking at $\sim 80\%$) than around a G or a M star ($\sim 25\%$). Similarly, a six Jupiter mass planet around an A star ejects less planetesimals than a one Jupiter mass planet around the same star (36% vs 80%). In this intermediate range, for the same mass ratio, the higher the star mass is, the higher the ejection fraction is.

4 Conclusion and perspectives

We have shown that the ejection fraction in a debris disk perturbed by an inner eccentric ($e = 0.5$) planet is clearly not monotonous as a function of m_{pl}/m_* . The enhanced ejection fraction of planetesimals for relatively

low m_{pl}/m_* could make debris disks around A star less frequently observable. Current observational data show the opposite trend ($\sim 30\%$ of A stars have observable disks, $\sim 15\%$ for F, G and K stars, and 5% for M stars), however this trend is not corrected for observational bias (it is easier to detect “cold” dust in disks around A stars, than “very cold” dust in disks around M stars).

We are currently in the process of studying the analytical justification (mean motion resonances, orbit precession, . . .) for this numerical result.

E. Morey PhD work is funded by a Fondation CFM-JP Aguilar grant.

References

- Gomes, R., Levison, H. F., Tsiganis, K., & Morbidelli, A. 2005, *Nature*, 435, 466
Mustill, A. J. & Wyatt, M. C. 2009, *MNRAS*, 399, 1403

Session 10

Stellar physics (PNPS)

THEORETICAL ANALYSIS OF THE HE₂ LINE AT 585 Å

N. F. Allard^{1,2}, F. X. Gadéa³, A. Monari³ and B. Deguilhem³

Abstract. Pressure broadening by molecular hydrogen and helium is one of the major broadening mechanism in the atmosphere of brown dwarfs. He(1 ¹S)-He(2 ¹P) collisional line profiles are determined in a unified theory of spectral line broadening using very recent *ab initio* potential energies. Results are reported for the conditions prevailing in brown dwarf atmospheres.

Keywords: line: profiles, stars: low mass, brown dwarfs, stars: atmospheres

1 Introduction

A unified theory of spectral line broadening has been developed to calculate neutral atom spectra given the interaction and radiative transition moments for relevant states of the radiating atom with other atoms in its environment. Complete details and the derivation of the theory are given in Allard et al. (1994, 1999). The interatomic interactions are the main physical quantities needed for a good understanding of collisional processes, they are now computed with high accuracy.

2 Molecular potentials

The *ab initio* computation of the adiabatic potential energy curves of He₂ have been carried out using the MOLPRO 2009 package *. A huge Multi Reference Configuration Interaction (MRCI) has been performed starting from a very large Multi Configuration Self Consistent Field (MCSCF). The MCSCF calculation involved 26 active orbitals and a very large basis set (called basis E) composed of 118 orbitals for each He atom (21s, 12p, 8d, 3f). For the lowest quintet state this approach was shown (Deguilhem 2009) to be very effective compared to full CI results, leading to differences much less than a tenth of a wavenumber.

We have also checked that using orbitals optimised from state averaged or the ones of the quintet state, lead to almost identical results, a strong indication that we are very close to the full CI results.

Therefore the main limitation in the accuracy of these adiabatic potential curves resides in limitation due to the finite basis set used, however considering the quality of the basis set this error appears to be small.

There are 2 transitions which contribute to the $1s\ ^1S \rightarrow 2p\ ^1P$ line profile:

$$\begin{aligned} 1s\ X^1\Sigma_g^+ &\rightarrow 2p\ F^1\Pi_u \quad \text{noted } (X - F) \\ 1s\ X^1\Sigma_g^+ &\rightarrow 2p\ D^1\Sigma_u^+ \quad \text{noted } (X - D). \end{aligned}$$

The involved molecular potentials are shown in Fig. 1.

¹ Observatoire de Paris, GEPI, UMR 8111, CNRS, 61, Avenue de l'Observatoire, F-75014 Paris, France

² Institut d'Astrophysique de Paris, F-75014 Paris, UMR 7095, CNRS, 98bis Boulevard Arago, F-750014 Paris, France

³ Laboratoire de Physique Quantique, UMR5626, CNRS, Université Paul Sabatier, 118 route de Narbonne, F-31400 Toulouse, France

*<http://www.molpro.net>.

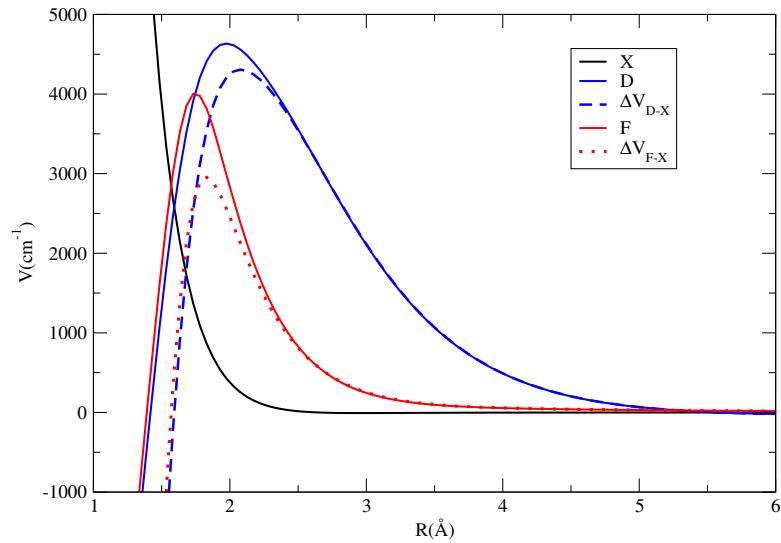


Fig. 1. *Ab initio* potential energy curves and the corresponding energy differences of the $1s\ ^1S \rightarrow 2p\ ^1P$ line.

3 Theoretical spectra

In radiative collision transitions it is the difference potential between the final and initial states that determines the frequency and the energy emitted or absorbed by a single photon. The shape of the line wing is sensitive to $\Delta V(R)$, the difference between the ground and excited state interaction potential. For the transitions $X \rightarrow D$ and $X \rightarrow F$ the difference potential maxima are respectively 4300 and 3000 cm^{-1} (Fig. 1) which lead to far blue satellite respectively at 4000 cm^{-1} (571.4 Å) and 2600 cm^{-1} (576 Å) (Fig. 2).

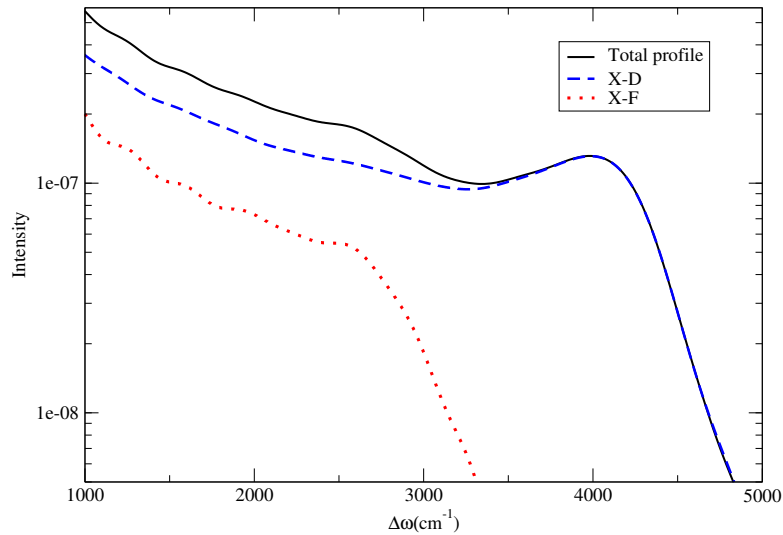


Fig. 2. Individual components of the blue far wing compared to the total one ($T=1000\text{ K}$ and $n_{\text{He}}=10^{19}\text{ atoms cm}^{-3}$).

The unified profile, including the core of the line (Fig. 3), is asymmetrical and contributes only in the UV part. It is not correct to use Lorentzian profiles in the far wings, as is the standard practice in most stellar atmosphere work.

The cores are formed in the uppermost, lowest density atmospheric layers still dominated by He and H_2 collisions. Since in a model atmosphere calculation, the resulting line profile is the integration of the flux in all layers from the deepest to the uppermost, it is important that the centers be adequately represented, i.e., they can be non-Lorentzian at the high densities of the innermost layers, while Lorentzian in the upper atmosphere but with different widths than predicted by the hydrogenic van der Waals approximation usually used for the

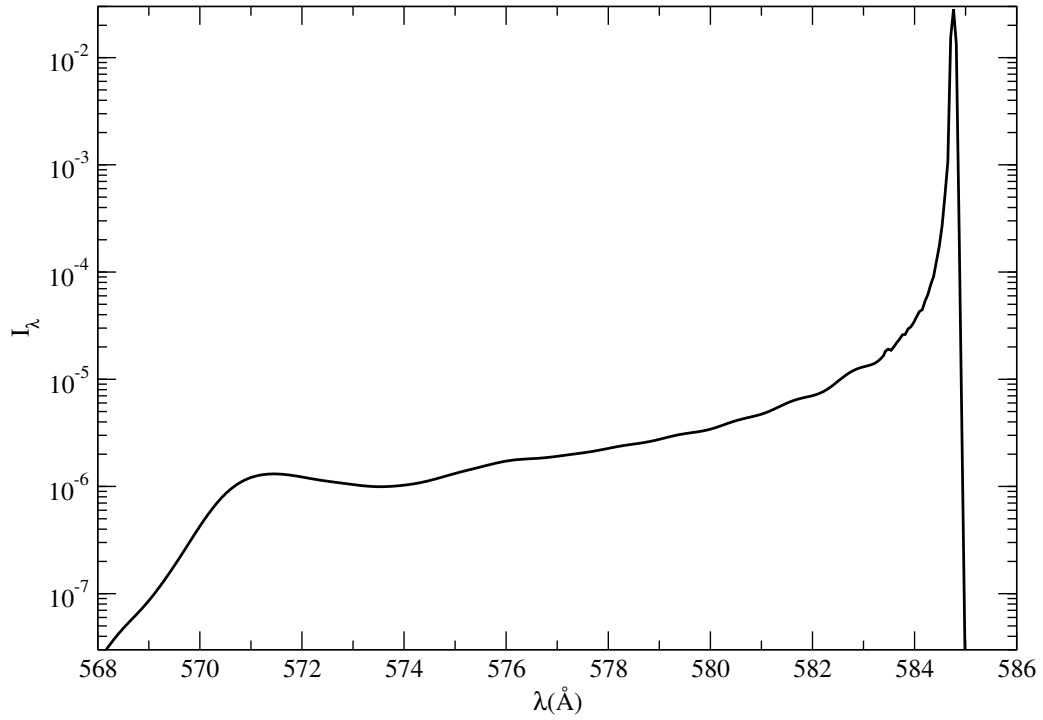


Fig. 3. Unified profile for $T=1000$ K and $n_{\text{He}}=10^{20}$ atoms cm^{-3} .

Table 1: Variation with temperature of the full width at half maximum and shift (10^{-20} $\text{cm}^{-1}/\text{cm}^{-3}$)

Line parameters	1000 K	2000 K	3000 K	4000 K	5000 K	6000 K
w_{imp}	2.44	2.6	2.77	2.86	2.97	3.12
d_{imp}	0.47	0.75	0.89	1.11	1.16	1.32

cores. At low densities, pressure broadening and shift of spectral lines are described by the well-known impact theory of Lindholm (1945). The variation of the impact width (full width at half maximum) and shift versus the temperature is given in Table 1.

One of us (NFA) would like to acknowledge PNPS for the financial support which allows the collaboration with the Laboratoire de Physique Quantique in Toulouse.

References

- Allard, N. F., Koester, D., Feautrier, N., & Spielfiedel, A. 1994, *A&A Suppl.*, 200, 58
 Allard, N. F., Royer, A., Kielkopf, J. F., & Feautrier, N. 1999, *Phys. Rev. A*, 60, 1021
 Deguilhem, B. 2009, in Ph. D. thesis (Toulouse, France: Université Paul Sabatier)
 Lindholm, E. 1945, *Ark. Fys. A*, 32, 1

ABSORPTION PROFILES OF THE POTASSIUM $4S - 4P$ AND $4P - 5S$ LINES PERTURBED BY HELIUM

N. F. Allard^{1,2}

Abstract. An accurate determination of the complete profile including the extreme far wing is required to model the contribution of strong alkali resonance lines to brown dwarf spectra. A unified theory of collisional line profiles has been applied for the evaluation of the absorption coefficients of potassium perturbed by helium. Results are reported here from the optical range to the near-infrared.

Keywords: line: profiles - stars: low mass, brown dwarfs - stars: atmospheres

1 Introduction

Pressure broadening by molecular hydrogen and helium is one of the major broadening mechanism in the atmosphere of brown dwarfs. The optical spectra of L and T -type dwarfs exhibit a continuum dominated by the far wings of the absorption profiles of the Na $3s - 3p$ and K $4s - 4p$ doublet perturbed by molecular hydrogen and helium. Model atmosphere, synthetic spectra and color predictions rely on knowledge of the far wings of alkali resonance lines in the presence of high densities of H_2 and He (Allard et al. 2003, 2007a).

One of the improvements upon previous calculations of (Allard et al. 2003) is the use of *ab initio* K–He potentials instead of pseudo-potentials of Pascale (1983) which lead to a K–He line satellite at 6930 Å much too far to the blue. Laboratory spectra of K with He (Kielkopf & Allard 2008a,b) agree exceptionally well with the semi-classical profiles based on molecular potentials of Santra & Kirby (2005). The comparison with theoretical profiles establishes the accuracy of the interaction potentials, which are difficult to compute *a priori*. This work is now extended to the $4p - 5s$ transitions. In theoretical spectra models of T dwarfs the KI doublet at 1.24/1.25 μm is seen for values of T_{eff} at 700 K and above. These lines of excited KI have been identified in T dwarfs (Strauss et al. 1999; Tsvetanov et al. 2000).

2 Theoretical spectra

In Allard et al. (2003) we presented the first application of the absorption profiles of sodium and potassium perturbed by helium and molecular hydrogen to the modeling of brown dwarfs. Line profiles were calculated in a unified line shape semi-classical theory (Allard et al. 1994, 1999) using pseudo-potentials of Pascale (1983) (hereafter labelled P83). For the specific study of the $D1$ ($P_{1/2}$) and $D2$ ($P_{3/2}$) components we need to take the spin-orbit coupling of the alkali into account. This is done using an atom-in-molecule intermediate spin-orbit coupling scheme, analogous to the one derived by Cohen & Schneider (1974). The degeneracy is partially split by the coupling and the distinction between $D1$ and $D2$ results.

Our approach requires accurate theoretical molecular potentials to describe the interaction between radiator and perturber. *Ab initio* calculations have now been reported by Santra & Kirby (2005) (hereafter labelled SK05). We compare in Fig. 1 potentials computed by Pascale (1983) and Santra & Kirby (2005) including spin-orbit coupling.

It is seen that the major difference with respect to SK05 is that Pascale’s potentials are systematically less repulsive than theirs, the state mostly affected being state B which starts to deviate from SK05 as soon as

¹ Observatoire de Paris, GEPI, CNRS, UMR 8111, Université Denis Diderot, 61, Avenue de l’Observatoire, F-75014 Paris, France

² Institut d’Astrophysique de Paris, CNRS, UMR 7095, Université Pierre et Marie Curie, 98bis Boulevard Arago, F-750014 Paris, France

$R < 5$ nm when decreasing the separation. This difference on the B state strongly affects the blue satellite position.

Blue satellite bands in alkali-He/H₂ profiles are correlated with maxima in the excited B state potentials and can be predicted from the maxima in the difference potentials ΔV for the B - X transition (Allard et al. (2003, 2005); Allard & Spiegelman (2006); Allard et al. (2007b); Zhu et al. (2005, 2006); Alioua & Bouledroua (2006); Alioua et al. (2008); Christova et al. (2008)). The difference potential, $\Delta V(R)$, is given by

$$\Delta V(R) \equiv V_{e'e}[R(t)] = V_{e'}[R(t)] - V_e[R(t)], \quad (2.1)$$

and represents the difference between the electronic energies of the quasi-molecular B - X transition.

New K-He semi-classical line absorption profiles have been done using these last potentials, they were presented in (Kielkopf & Allard 2008a,b).

The $P_{1/2}$ ($D1$) line is due to a simple isolated $A \Pi_{1/2}$ state, the line profile for the $D1$ line is totally asymmetric. Whereas the $P_{3/2}$ ($D2$) line comes from the $A \Pi_{3/2}$ and $B \Sigma_{1/2}$ adiabatic states arising from the $4p$ $P_{3/2}$ atomic state. The interaction potentials lead to far wing line profiles with a K-He satellite at about 700 nm on the blue side of the D -lines, and a monotonically decreasing wing on the red side. While the Pascale pseudopotentials overestimated the displacement of the He satellite from the line Allard et al. (2003), newer potentials of (Santra & Kirby 2005) predict a K-He satellite that matches the one observed in laboratory spectra of Kielkopf & Allard (2008a,b). Such comparisons provide a critical test of the calculated molecular potentials and the relevance of the theoretical approach which has been used. Opacity tables of alkali perturbed by He and molecular hydrogen can be obtained from *.

This work is now extended to the excited states. We had to use pseudo-potential of Pascale (1983) for the $4p - 5s$ transition as *ab initio* potentials are not available. The potential difference curves for the $4p - 5s$ transition are presented in Fig. 2. We report calculations done for the $4s - 4p$, $4p - 5s$ lines for $T_{\text{eff}} = 1000$ K for a fixed helium density ($n_{\text{He}} = 1 \times 10^{21} \text{ cm}^{-3}$). They are presented in Fig. 3.

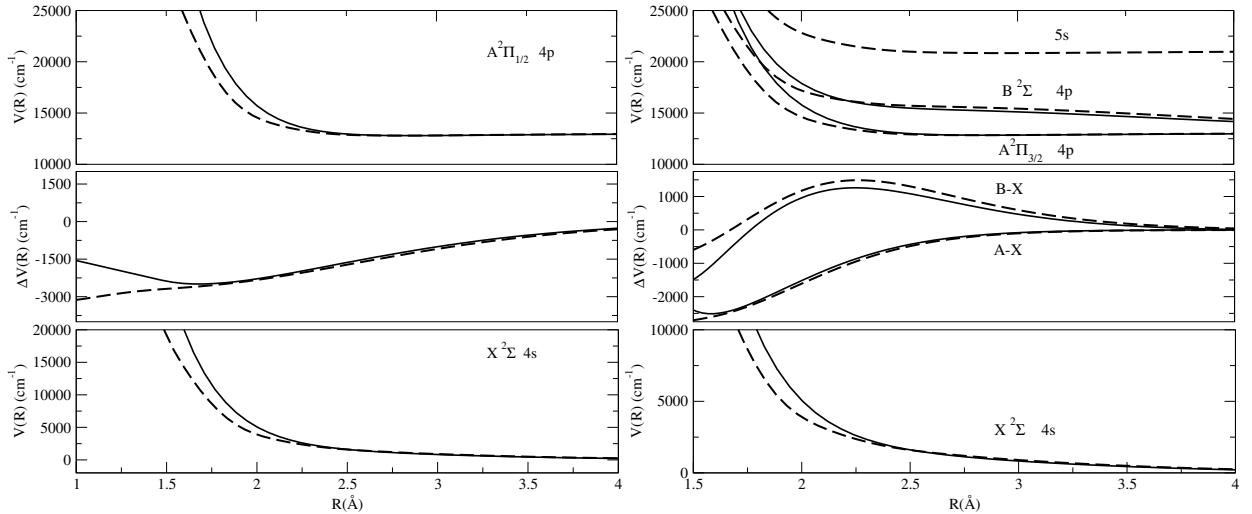


Fig. 1. Potential curves for the K-He molecule of P83 (dashed curves) compared to SK05 (full line).

We would like to thank J. Babb for making available the *ab initio* K-He potentials of (Santra & Kirby 2005) used in Zhu et al. (2006).

References

- Alioua, K. & Bouledroua, M. 2006, Phys. Rev A, 74, 032711
 Alioua, K., Bouledroua, M., Allouche, A. R., & Aubert-Frécon, M. 2008, J. Phys. B: At. Mol. Opt. Phys., 41, 175102
 Allard, F., Allard, N. F., Homeier, D., et al. 2007a, A&A, 474, L21

*<http://mygepi.obspm.fr/~allard/>.

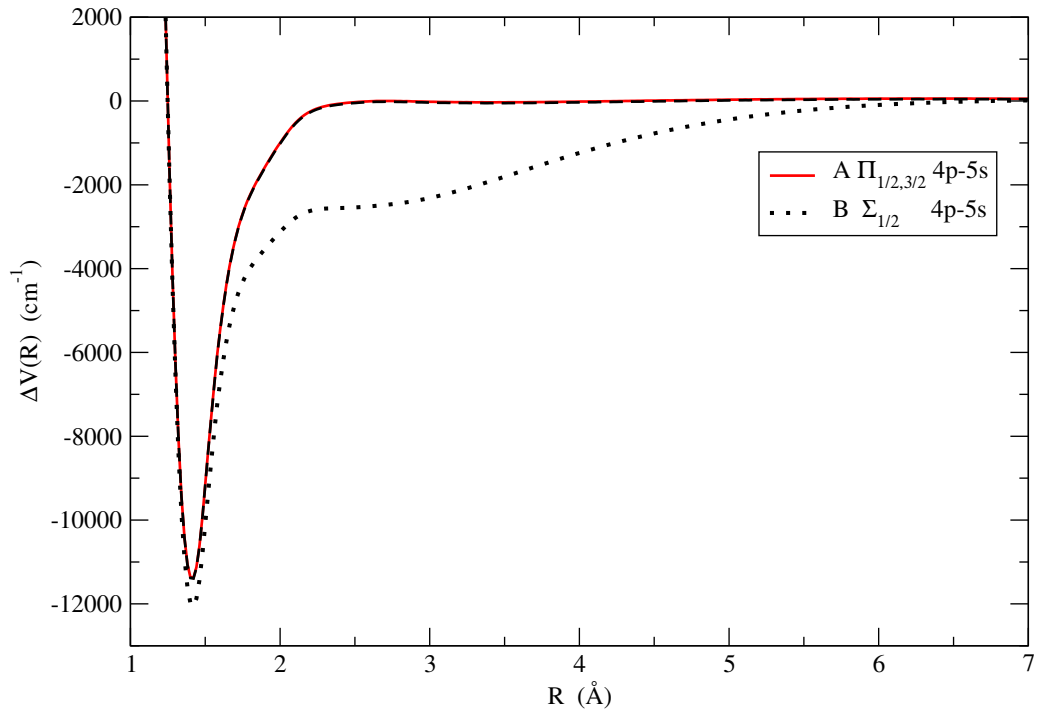


Fig. 2. Potential difference curves of the $4p - 5s$ transition of the K-He molecule.

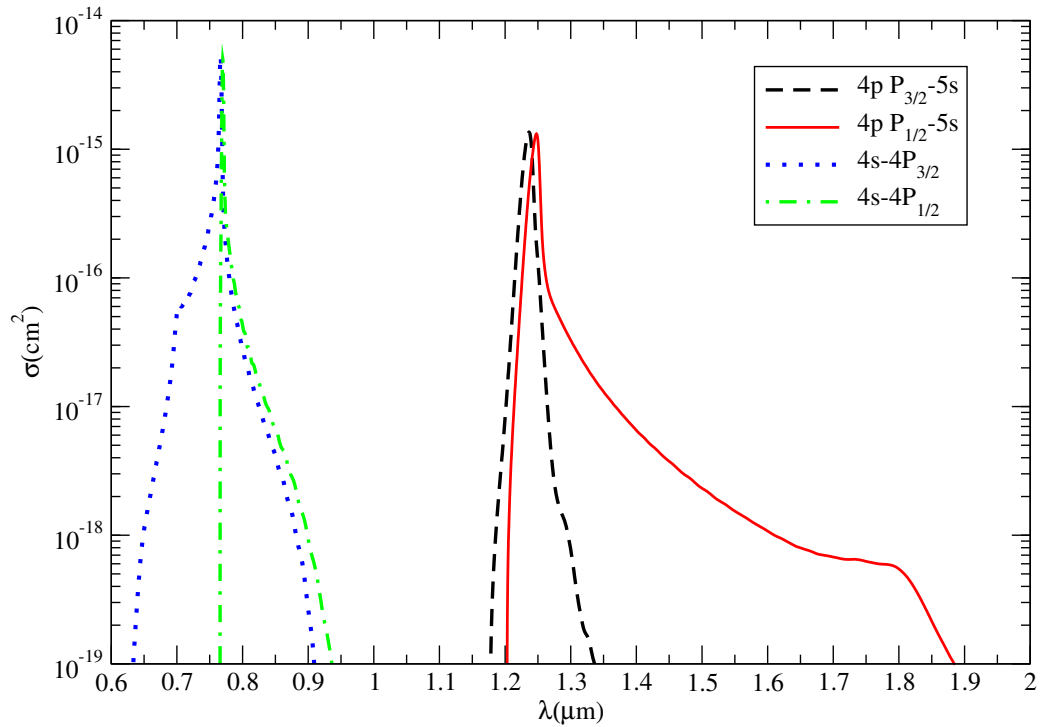


Fig. 3. Absorption cross section of the $4s - 4p$, $4p - 5s$ lines. ($T = 1000\text{K}$, $n_{\text{He}} = 1 \times 10^{21} \text{ cm}^{-3}$).

Allard, N. F., Allard, F., Hauschildt, P. H., Kielkopf, J. F., & Machin, L. 2003, A&A, 411, 473

Allard, N. F., Allard, F., & Kielkopf, J. F. 2005, A&A, 440, 1195

Allard, N. F., Koester, D., Feautrier, N., & Spielfiedel, A. 1994, A&A Suppl., 200, 58

Allard, N. F., Royer, A., Kielkopf, J. F., & Feautrier, N. 1999, Phys. Rev. A, 60, 1021

- Allard, N. F. & Spiegelman, F. 2006, *A&A*, 452, 351
- Allard, N. F., Spiegelman, F., & Kielkopf, J. F. 2007b, *A&A*, 465, 1085
- Christova, M., Allard, N. F., Kielkopf, J. F., Allard, F., & Homeier, D. 2008, in 19th International Conference on Spectral Line Valladolid, Spain, June 16-20, 2008 (New York: AIP Conference Proceeding)
- Cohen, J. S. & Schneider, B. 1974, *J. Chem. Phys.*, 61, 3230
- Kielkopf, J. F. & Allard, N. F. 2008a, *Bull. Am. Astron. Soc.*, 40, 186
- Kielkopf, J. F. & Allard, N. F. 2008b, in 19th International Conference on Spectral Line Valladolid, Spain, June 16-20, 2008 (New York: AIP Conference Proceeding)
- Pascale, J. 1983, *Phys. Rev. A*, 28, 632
- Santra, R. & Kirby, K. 2005, *J. Chem. Phys.*, 123, 214309
- Strauss, M. A., Fan, X., & Gunn, J. E. 1999, *ApJ*, 522, L61
- Tsvetanov, Z. I., Golimowski, D. A., & Zheng, W. 2000, *ApJ*, 531, L61
- Zhu, C., Babb, J. F., & Dalgarno, A. 2005, *Phys. Rev. A*, 71, 052710
- Zhu, C., Babb, J. F., & Dalgarno, A. 2006, *Phys. Rev. A*, 73, 012506

CRITICAL LAYERS FOR INTERNAL WAVES IN STELLAR RADIATION ZONES

L. Alvan¹ and S. Mathis¹

Abstract. Internal waves are candidates for explaining stellar radiation zone angular velocity profiles, for example in the Sun. The equation describing the adiabatic and inviscid propagation of such waves is singular at a “critical level” where the fluid rotation frequency is proportional to the wave frequency. Here, we propose a generalization of previous studies to the stellar, spherical case. We resolve the problem by three methods, depending on the value of the Richardson number at the critical level Ri_c and our results can be divided into two cases. If $(l(l+1)/m^2) Ri_c$ is larger than $1/4$, waves are attenuated by a factor depending on Ri_c as they pass through a critical level. If $(l(l+1)/m^2) Ri_c$ is less than $1/4$, the basic flow is then unstable and the wave can be reflected with a coefficient larger than 1. In the latter case, the process is called over-reflection.

Keywords: internal gravity waves, critical layers, angular momentum transport

1 Introduction

Internal waves have been invoked as a source of mixing for chemicals (Press 1981; Schatzman 1996), before being used to explain the evolution of angular velocity (Goldreich & Nicholson 1989; Charbonnel & Talon 2005) due to the transport of angular momentum they induce. Later, Barker & Ogilvie (2010) studied internal waves approaching the center of a solar type star. The behaviour of such waves at a critical level has mainly been studied in Geophysics with 2D cartesian coordinates (Booker & Bretherton 1967; Lindzen 1985; Ringot 1998). This work is a generalization to the stellar, spherical case.

2 Waves in differentially rotating stars

2.1 Hypotheses

As a first approach we consider a perfect fluid (no viscosity and heat conduction). We neglect the Coriolis and Lorentz forces too and assume that the angular velocity Ω depends only on depth : $\Omega(r, \theta) = \Omega(r)$, justified by the fact that differential rotation in latitude is severely limited through hydrodynamical instabilities (Zahn 1992).

Then, we define the local frequency $\sigma(r) = \sigma_c + m\Delta\Omega(r)$ caused by the Doppler shift due to the differential rotation. σ_c is the excitation frequency of the wave and $\Delta\Omega(r) = \Omega(r) - \Omega_c$ is the difference between the local angular velocity and the one at the base of the convective zone or the top of the convective core, where internal gravity waves are excited. Waves are prograde if $m < 0$ and retrograde if $m > 0$ (m corresponds to a Fourier expansion along the longitudinal direction).

¹ Laboratoire AIM, CEA/DSM-CNRS-Université Paris Diderot, IRFU/SAP, F-91191 Gif-sur-Yvette Cedex, France; lucie.alvan@cea.fr, stephane.mathis@cea.fr

2.2 System of linearized equations

We solve the adiabatic and inviscid system composed by :

$$\begin{cases} \text{Equation of motion} & D_t \vec{u} = -\frac{\vec{\nabla} p'}{\bar{\rho}} + \frac{\rho'}{\bar{\rho}} \vec{g}, \\ \text{Continuity equation} & D_t \rho' + \vec{\nabla} \cdot (\bar{\rho} \vec{u}) = 0, \\ \text{Energy equation} & D_t \left(\frac{\rho'}{\bar{\rho}} - \frac{1}{\Gamma_1} \frac{p'}{\bar{p}} \right) + \left(\frac{d \ln \bar{p}}{dr} - \frac{1}{\Gamma_1} \frac{d \ln \bar{p}}{dr} \right) u_r = 0, \end{cases} \quad (2.1)$$

where \vec{u} is the fluctuation of velocity associated with the wave, p and ρ the pressure and the fluid density, \vec{g} the acceleration due to gravity, $\Gamma_1 = \frac{\partial \ln \bar{p}}{\partial \ln \bar{\rho}}$ the adiabatic exponent and $D_t = \partial_t + \Omega \partial_\varphi$. Mean values are denoted by \bar{X} and the associated fluctuations by X' .

The stratification of the studied radiation zone is described with the Brunt-Väisälä frequency : $N^2 = -g \left(\frac{1}{\bar{\rho}} \frac{\partial \bar{p}}{\partial r} - \frac{1}{\Gamma_1 \bar{p}} \frac{\partial \bar{p}}{\partial r} \right)$ where we neglect the perturbation of the gravitational field (Cowling approximation). We introduce the wave's Lagrangian displacement $\vec{\xi} = \xi_v \vec{e}_r + \vec{\xi}_h$ and following the method proposed by Zahn et al. (1997), we define $\xi_v = \hat{\xi}_{v;l,m}(r) Y_{l,m}(\theta, \varphi) e^{i\sigma c t}$ ($Y_{l,m}$ are the usual spherical harmonics) and $\Psi_{l,m}(r) = \bar{\rho}^{1/2} r^2 \hat{\xi}_{v;l,m}(r)$ to obtain a differential equation of second order for the vertical velocity :

$$\frac{d^2 \Psi_{l,m}}{dr^2} + k_v^2(r) \Psi_{l,m} = 0, \quad (2.2)$$

where k_v is the vertical wavenumber whose expression near the critical layer is :

$$k_v^2 = \left(\frac{N^2}{\sigma^2} - 1 \right) \frac{l(l+1)}{r^2} \underset{r \rightarrow r_c}{\approx} \frac{l(l+1)}{m^2} \frac{Ri_c}{(r - r_c)^2}. \quad (2.3)$$

In cartesian 2D coordinates the equivalent of this equation is called TGS (Taylor, Goldstein and Synge) and we will use this name again. From this point, we use the expression of k_v near the critical layer defined by $r = r_c$ where $\sigma(r_c) = \sigma_c + m \Delta \Omega(r_c) = 0$. The TGS equation is singular at this point.

3 Resolution of the TGS equation

The original contribution of this work is related to the resolution of the TGS equation in the spherical case. Most of the time people use the WKBJ approximation. In spherical coordinates, the Richardson number is $Ri = \frac{N^2}{r^2 \Omega'^2(r)}$ and we denote it Ri_c when we evaluate it at the critical level $r = r_c$. After some calculation it appears that the WKBJ method is available only in the case where $\frac{l(l+1)}{m^2} Ri_c \gg \frac{1}{4}$, that is to say if the shear is weak before the stratification.

3.1 Case 1 : $\frac{l(l+1)}{m^2} Ri_c \geq \frac{1}{4}$

Another method is available in the whole domain $\frac{l(l+1)}{m^2} Ri_c \geq \frac{1}{4}$. It is called the Frobenius method and the solution are the same as those obtained with the WKBJ method. Nevertheless we have to cut the physical domain into two parts to avoid the singularity in $r = r_c$. Then, it is possible to connect the solutions with the method employed by Booker & Bretherton (1967). The global solution is of the form :

Above the critical layer ($r > r_c$) :

$$\Psi_{l,m+} = C |r - r_c|^{\frac{1}{2}} \left(1 + i \sqrt{q_{l,m} - \frac{1}{4}} \right) + D |r - r_c| \left(1 - i \sqrt{q_{l,m} - \frac{1}{4}} \right), \quad (3.1)$$

and below the critical layer ($r < r_c$) :

$$\Psi_{l,m-} = -iC |r - r_c|^{1+i\nu_{l,m}} e^{-\pi\nu_{l,m}} - iD |r - r_c|^{1-i\nu_{l,m}} e^{+\pi\nu_{l,m}}, \quad (3.2)$$

where $\nu_{l,m} = \sqrt{\frac{l(l+1)}{m^2} Ri_c - \frac{1}{4}}$.

We observe two phenomenon as the wave passes through the critical level :

- a **phase difference** of $-\frac{\pi}{2}$,
- an **attenuation** by a factor $e^{-\pi \sqrt{\frac{l(l+1)}{m^2} Ri_c - \frac{1}{4}}}$ which is equivalent to the factor found by Booker & Bretherton (1967) in cartesian coordinates. This factor is represented in the figure 1.

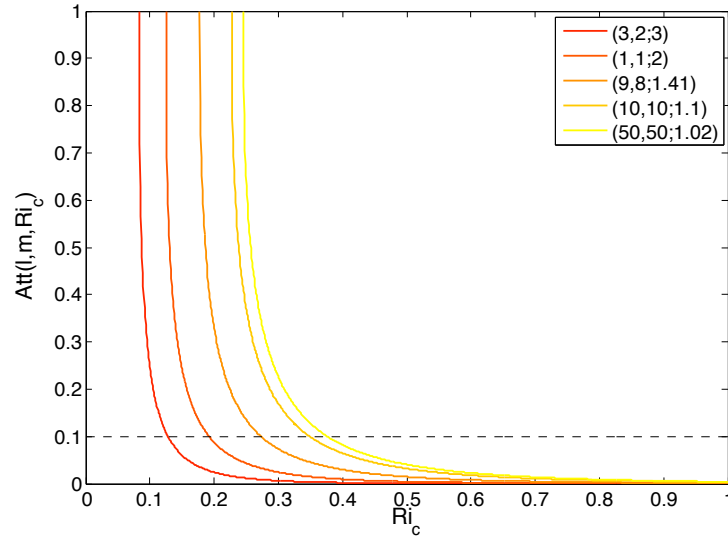


Fig. 1. Attenuation's rate $Att=e^{-\pi\sqrt{\frac{l(l+1)}{m^2}Ri_c-\frac{1}{4}}}$ for different values (l,m) as a function of Ri_c . For each plot, the minimal value of Ri_c is $\frac{m^2}{4l(l+1)}$. Legend : $(l,m;\frac{l(l+1)}{m^2})$.

3.2 Case 2 : $\frac{l(l+1)}{m^2} Ri_c < \frac{1}{4}$

In this case, the Frobenius method is available but not physically acceptable. That the reason why we introduce new variables : $\mu_{l,m} = \sqrt{\frac{1}{4} - \frac{l(l+1)}{m^2} Ri_c}$ and $X = \frac{l(l+1)}{r_c^2}(r - r_c)$. The TGS equation becomes :

$$\frac{d^2\Psi_{l,m}}{dX^2} + \left(\frac{\frac{1}{4} - \mu_{l,m}^2}{X^2} - 1\right) \Psi_{l,m} = 0, \tag{3.3}$$

and the solutions are combinations of **modified Bessel functions** :

$$\Psi_{l,m-}(X) = X^{\frac{1}{2}} [K_1 I_{\mu_{l,m}}(X) + K_2 I_{-\mu_{l,m}}(X)] . \tag{3.4}$$

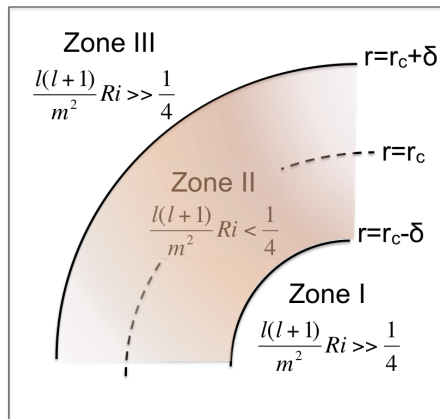


Fig. 2. Expected profile of the area around the critical layer.

Lindzen & Barker (1985) have studied this case in 2D cartesian coordinates. We employ the same method to calculate the reflection and transmission coefficients of the wave passing through the critical layer. Let assume

that the area around the critical layer has the profile described on the figure 2. A wave created in the first zone can be described by the system above.

$$\begin{cases} \text{zone I : } & \Psi_1(r) = e^{-ik_v r} + R e^{ik_v r}, \\ \text{zone II : } & \Psi_2(r) = (r - r_c)^{1/2} [K_1 I_\mu(k_h(r - r_c)) + K_2 I_{-\mu}(k_h(r - r_c))], \\ \text{zone III : } & \Psi_3(r) = T e^{ik_v r}. \end{cases}$$

The constants K_1 , K_2 , R and T are determined by the requirements that Ψ and $\frac{d\Psi}{dr}$ should be continuous at $r = \pm\delta$ (continuity of displacement and stresses). We obtain the figure 3 which show that $|R|$ and $|T|$ are greater than one if Ri_c is small enough. These graphs are similar to those obtained in the cartesian case by Lindzen (1985). In this case, waves are taking supplementary energy from the unstable shear. Let us point out that the expressions of R and T are independent of the sign of m .

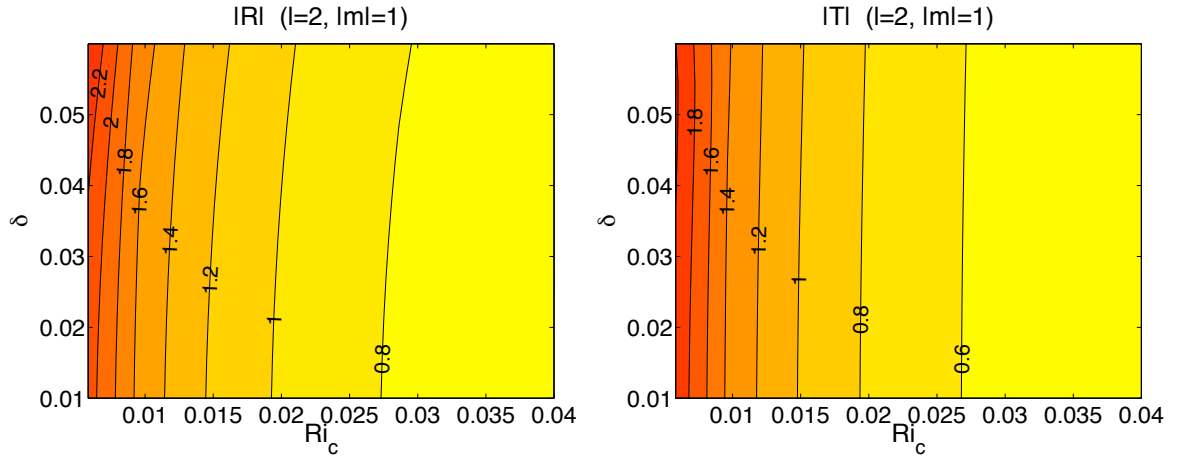


Fig. 3. Left: Reflection coefficient as a function of Richardson number Ri_c and width δ of the region where $\frac{l(l+1)}{m^2} Ri_c < \frac{1}{4}$, for $l=2$ and $|m|=1$. **Right:** Transmission coefficient for the same example.

4 Conclusion

If the Richardson number at the critical layer satisfies $\frac{l(l+1)}{m^2} Ri_c > \frac{1}{4}$, the corresponding internal gravity wave passing through the layer is attenuated by the factor $\exp(-\pi \sqrt{\frac{l(l+1)}{m^2} Ri_c - \frac{1}{4}})$. But in the case where $\frac{l(l+1)}{m^2} Ri_c < \frac{1}{4}$, an over-reflection occurs. Extension of the previous analysis to a non perfect fluid show that the absorption mechanism is not dependent on viscosity or other dissipative processes. Moreover, work is in progress to implement these theoretical results in the dynamical stellar evolution code STAREVOL (Siess et al. 2000; Palacios et al. 2003; Decressin et al. 2009).

References

- Barker, A. J. & Ogilvie, G. I. 2010, MNRAS, 404, 1849
- Booker, J. & Bretherton, F. 1967, J. Fluid Mech., 27, 513
- Charbonnel, C. & Talon, S. 2005, Science, 309, 2189
- Decressin, T., Mathis, S., Palacios, A., et al. 2009, A&A, 495, 271
- Goldreich, P. & Nicholson, P. D. 1989, ApJ, 342, 1079
- Lindzen, R. Barker, A. 1985, J. Fluid Mech., 151, 189
- Palacios, A., Talon, S., Charbonnel, C., & Forestini, M. 2003, A&A, 399, 603
- Press, W. 1981, ApJ, 245, 286
- Ringot, O. 1998, PhD thesis, Université Paris VII
- Schatzman, E. 1996, Sol. Phys., 169, 245
- Siess, L., Dufour, E., & Forestini, M. 2000, A&A, 358, 593

Zahn, J.-P. 1992, *A&A*, 265, 115

Zahn, J.-P., Talon, S., & Matias, J. 1997, *A&A*, 322, 320

CHARACTERISATION OF SPH NOISE IN SIMULATIONS OF PROTOPLANETARY DISCS

S. E. Arena¹, J.-F. Gonzalez¹ and E. Crespe¹

Abstract. We have started a characterization of the noise in SPH (Smoothed Particle Hydrodynamics) simulations of the gas component of protoplanetary discs. The main goal is the determination of the properties of the fluctuating velocity field in order to compare them to those proper both to standard incompressible Kolmogorov turbulence and to compressible supersonic turbulence. A controlled fluctuating velocity field with turbulence-like properties is very important in the context of the theories of pre-planetary formation where the dynamics of dust, driven by that of the gas, is the crucial point.

Keywords: protoplanetary discs, turbulence, numerical simulations

1 Introduction

While the general picture of planet formation is rather well understood, the early phase leading from mm/cm-sized dust grains to the formation of km-sized pre-planetesimals is still highly debated.

The growth of pre-planetesimals is believed to develop in the discs around Classical T Tauri stars. These discs are usually called protoplanetary discs (abbreviated in PPD) and composed mainly of gas in quasi-keplerian rotation around the central star. Only a small fraction of the total mass of the discs (about 1%-2%) is made of dust grains, which are the seeds of pre-planetesimals. Dust grains are coupled to the gas at different degrees of strength depending on their size. Two main mechanisms are the direct consequence of this coupling: radial drift and vertical settling. In addition the action of turbulence on the dynamics of dust is expected to be of relevant importance. It can have two competing effects, mediated by gas drag: stirring up and diffusing dust particles, preventing their agglomeration; or trapping them inside eddies, favoring their agglomeration. Here we focus on the mechanism of turbulence.

Current observations have not yet reached the resolution necessary to directly detect turbulence and study its effects. However, the measured values of mass accretion rates onto the central star ($\dot{M}_0 \approx 10^{-8} M_\odot/\text{yr}$; Hartmann et al. 1998; Andrews et al. 2009) and the estimated life time of discs (around 10^7 yr; see e.g. Armitage 2007) imply a kinematic viscosity much larger than the molecular viscosity in PPD ($20 \text{ m}^2\text{s}^{-1}$; see e.g. Armitage 2007). Shakura & Sunyaev (1973) noted that turbulence can provide an effective viscosity able to justify these data.

Given the complex interplay between dust and gas, the problem can be only addressed by numerical simulations. In this work we focus mainly on the study of the fluctuating velocity field of gaseous discs evolved by means of Smoothed Particle Hydrodynamics (SPH) simulations. Our aim is to clarify if the numerical noise intrinsically present in SPH simulations of accretion discs can mimic the effects of turbulence and to what extent. A set of SPH simulations of a gaseous disc with different numerical and physical parameters has been performed. For each simulated disc we have studied both the magnitude and the structure of the fluctuations present in the velocity field. The resulting properties of such fluctuations have been compared to the typical behaviour of turbulence and to results from grid based simulations available in the literature.

¹ Université de Lyon, Lyon, F-69003, France; Université Lyon 1, Observatoire de Lyon, 9 avenue Charles André, Saint-Genis Laval, F-69230, France; CNRS, UMR 5574, Centre de Recherche Astrophysique de Lyon; École Normale Supérieure de Lyon, Lyon, F-69007, France

2 The disc model, the code and the simulations

The reference disc model A Classical T Tauri disc of mass $M_{\text{disc}} = 0.01 M_{\text{star}}$ orbiting around a one solar mass star ($M_{\text{star}} = M_{\odot}$) is considered. It extends from 20 to 400 AU, it is characterized by a surface density radial profile given by $\Sigma(r) = \Sigma_0(r/r_0)^{-p}$ and it is locally isothermal with a sound speed radial profile $c_s(r)$ given by $c_s^2(r) = c_{s_0}^2(r/r_0)^{-q}$. The semi-thickness H of the disc is related to the sound speed and to the angular velocity Ω by $H(r) = c_s(r)/\Omega(r)$. Note that the sound speed coefficient c_{s_0} and the sound speed exponent $q/2$ determine respectively the semi-thickness of the disc and its radial dependence $H(r) \propto r^{(3-q)/2}$.

The reference values we adopt in the following are $p = 3/2$ and $q = 3/4$ typical of the Minimum Mass Solar Nebula. The disc is slightly flared with $H(r)/r = 0.05$ at $r = 100$ AU. The evolution of the disc is followed for about 10 orbits (at 100 AU) after numerical thermalisation has been reached.

The code We use the two-phase SPH code described in Barrière-Fouchet et al. (2005). The two phases represent gas and dust that interact via aerodynamic drag. The gas is described by Euler equations and artificial viscosity is used to model physical viscosity as described in Meglicki et al. (1993). Here we consider only the gas phase because we are interested in the modeling of gas turbulence. The smoothing length h is variable and is derived from the density ρ : $h = h_0(\rho_0/\rho)^{1/3}$, in order to guarantee a roughly constant number of neighbours. The kernel is a cubic-spline.

The Monaghan & Gingold (1983) artificial viscosity is implemented. Here we recall this formulation because the two parameters α and β are relevant for the following study: $\Pi_{ij} = (-\alpha \bar{c}_{ij} \mu_{ij} + \beta \mu_{ij}^2) / \bar{\rho}_{ij}$ when $\mathbf{v}_{ij} \cdot \mathbf{r}_{ij} < 0$ and zero otherwise; \mathbf{r}_{ij} and \mathbf{v}_{ij} are respectively the relative distance and relative velocity. The overlined quantities are averages between particle i and its neighbouring particle j : $\bar{c}_{ij} = (c_i + c_j)/2$, $\bar{\rho}_{ij} = (\rho_i + \rho_j)/2$, $\bar{h}_{ij} = (h_i + h_j)/2$. Finally, $\mu_{ij} = \bar{h}_{ij} \mathbf{v}_{ij} \cdot \mathbf{r}_{ij} / (\mathbf{r}_{ij}^2 + \bar{h}_{ij}^2 \eta^2)$, with $\eta^2 = 10^{-2}$.

The internal units of the code are set in order to have the gravitational constant $G=1$ and are: 1 M_{\odot} for mass, 100 AU for length and $10^3/2\pi$ yr for the time. In the following, all the results are expressed in code units.

The simulations We have performed two groups of simulations. Simulations in the first group are identified by the AV name followed by the relative number: the two Artificial Viscosity parameters α and β are changed. Simulations from AV1 to AV5 are characterized by $\alpha = 0.1$ and $\beta = 0, 0.2, 0.5, 2, 10$ respectively. Simulations AV6 and AV7 have $(\alpha, \beta) = (1, 0)$ and $(\alpha, \beta) = (1, 2)$ respectively. Simulations AV8 has $(\alpha, \beta) = (0, 10)$ and AV10 has $(\alpha, \beta) = (5, 0)$. All the other parameters are those of the reference model. In the second group we have two simulations: DP1 where the parameter of the Disc Profile of the sound speed is changed in $q = 1.5$ and DS1 where, in addition, the coefficient of the Disc Sound speed is increased at $c_{s_0} = 0.1$. For simulations in this group we have taken the standard values for the artificial viscosity parameters: $(\alpha, \beta) = (1, 2)$.

All discs are sampled by $2 \cdot 10^5$ particles and initially evolved for about 9 orbits (at 100 AU) in order to reach numerical thermalisation. The face-on and edge-on view of the surface density profile of four of the simulated discs are displayed in Fig. 1.

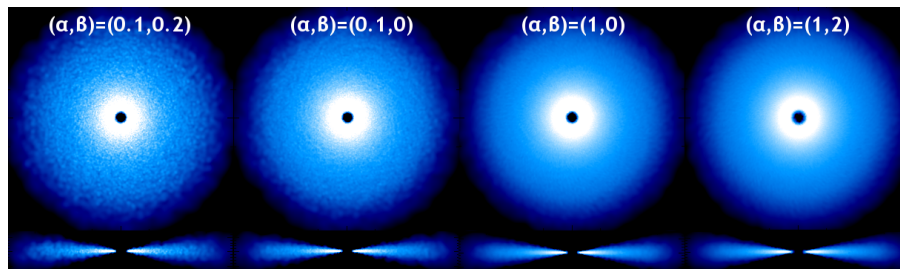


Fig. 1. The simulations: face-on and edge-on view of the surface density for simulations AV1, AV2, AV6, AV7 (from left to right).

3 Magnitude of SPH noise

A. Central mass accretion rate and turbulent viscosity estimated by α_{ss} In accretion disc theory, the observed central mass accretion rate \dot{M}_0 is connected to the turbulent viscosity coefficient ν_{T} . The latter is

parametrised by the dimensionless quantity α_{ss} by means of the scale height and the sound speed: $\nu_{\text{T}} = \alpha_{\text{ss}} c_s H$ (Shakura & Sunyaev 1973). For protoplanetary discs $\dot{M}_0 \approx 10^{-8} M_{\odot}/\text{yr}$ and $\alpha_{\text{ss}} \approx 10^{-2}$ (Hartmann et al. 1998; King et al. 2007). The central mass accretion rate measured in our simulations is displayed in the left plot of Fig. 2: for all simulations we found values consistent with the reference values from observations. In addition, the plot shows that larger artificial viscosity parameters lead to larger accretion rates onto the central star.

Following Fromang & Nelson (2006) we computed the α_{ss} parameter starting from Reynolds stress: $\alpha_{\text{RS}} = \langle u_r u_{\theta} \rangle / \langle P / \rho \rangle$, where P and ρ are respectively the pressure and density of the gas, u_r and u_{θ} are the velocity fluctuations in the radial and azimuthal directions and the symbol $\langle \cdot \rangle$ represents average quantities. The result displayed in the right plot of Fig. 2 shows that the behaviour of α_{RS} is very sensitive to the numerical noise. For sufficiently large α and β (e.g. simulations AV7 and AV9) the modulus of α_{RS} correlates with the central mass accretion rate and is in agreement with the value of 10^{-3} found by Fromang & Nelson (2006). In the other cases, the value of α or β is too low and the consequent noise breaks this correlation. The negative values of α_{RS} are due to the dominant outward flow in the region around the midplane, which characterizes the mechanism of meridional circulation present in these models.

A general view of the flow in the disc is given by colour plots of the radial velocity field in face-on sections of the discs. In Fig. 3 a transition from a chaotic to a more regular flow structure is visible comparing simulation AV1 with AV7.

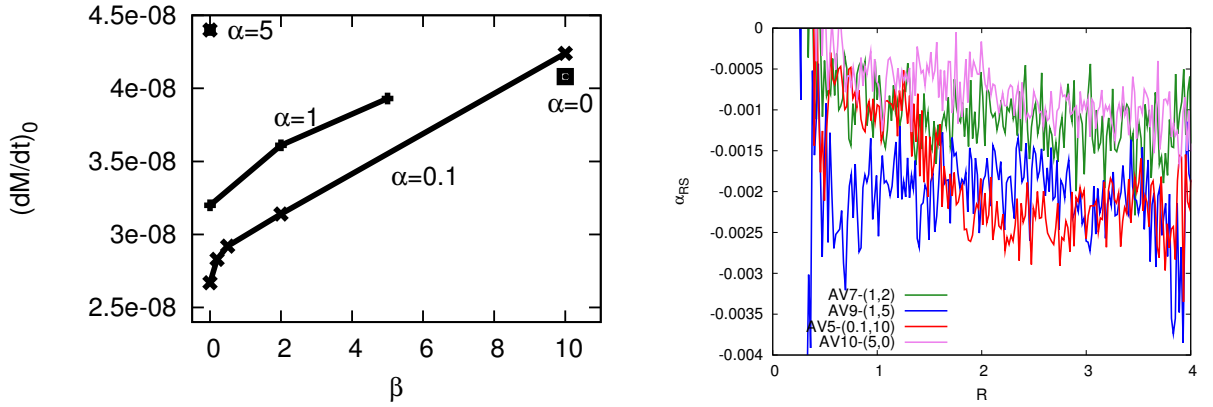


Fig. 2. Magnitude of SPH noise. **Left:** central mass accretion rate \dot{M}_0 in unit of M_{\odot}/yr . **Right:** radial profile of α_{RS} , which gives an estimate of α_{ss} based on Reynolds stress.

B. Vertical diffusion coefficient Following Fromang & Papaloizou (2006) we computed the turbulent diffusion coefficient D_{T} starting from the vertical velocity correlation function $S_{zz}(t) = \langle v_z[z(z_0, t), t] v_z(z_0, 0) \rangle$: $D_{\text{T}}(t) = \int_0^t S_{zz}(t') dt'$, where the zero refers to quantities at the initial time $t = 0$, z is the vertical position of each particle and v_z the vertical component of velocity.

The evolution with time of the diffusion coefficient D_{T} (in units of $c_s H$), measured at the intermediate radial position $r = 1.82$, is shown in Fig. 4 for all simulations. Results at different locations are qualitatively similar. The diffusive mechanism is correctly represented by large artificial viscosity parameters (α, β). More viscous and less extended discs are less diffusive. For the usually adopted combinations of parameters $(\alpha, \beta) = (1, 2)$, $D_{\text{T}}/(c_s H) \approx 5 \cdot 10^{-3}$ is in agreement with the value found by Fromang & Papaloizou (2006) in their MHD local shearing box stratified simulations.

4 Structure of SPH noise

Power spectrum Since the system is not homogeneous, we compute the power spectrum for each component of velocity along a ring located at different radii from the central star and at several altitudes: $P(k) = |\hat{u}_i(k)|^2$, where $\hat{u}_i(k)$ is the Fourier transform of the i component of the velocity fluctuation vector. In the two reference cases considered, the power spectrum is given by a power law: $P(k) \sim k^{\delta}$, with $\delta = -5/3$ in the incompressible

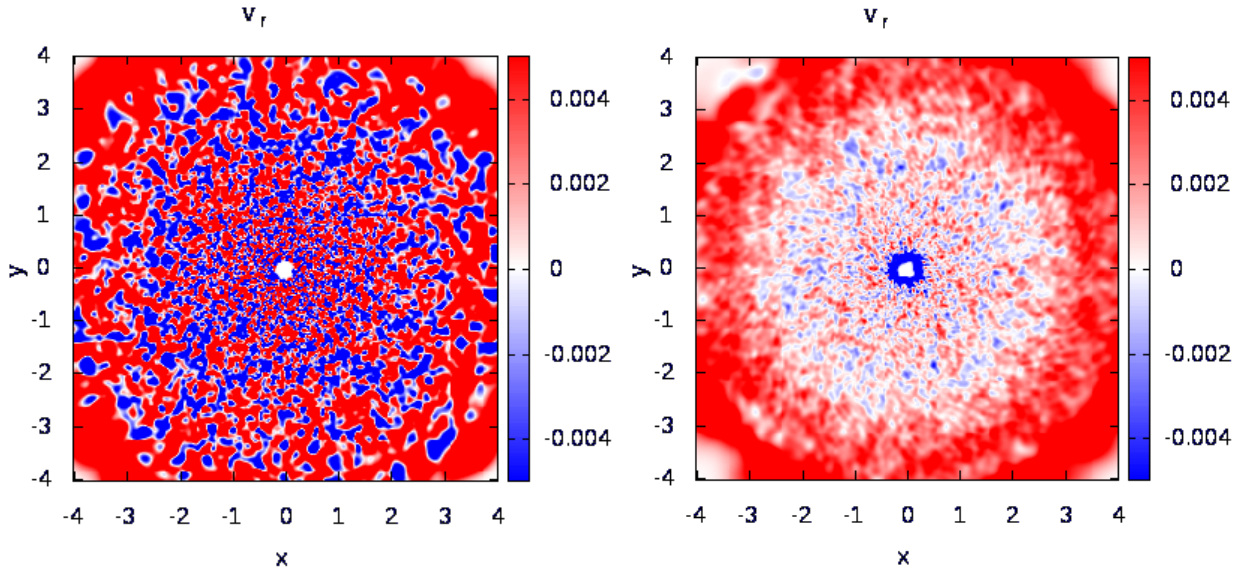


Fig. 3. The face-on view of the cross section of the radial velocity field of the disc for simulation AV1 (left) and AV7 (right) shows the transition from a chaotic to an ordered and more regular flow.

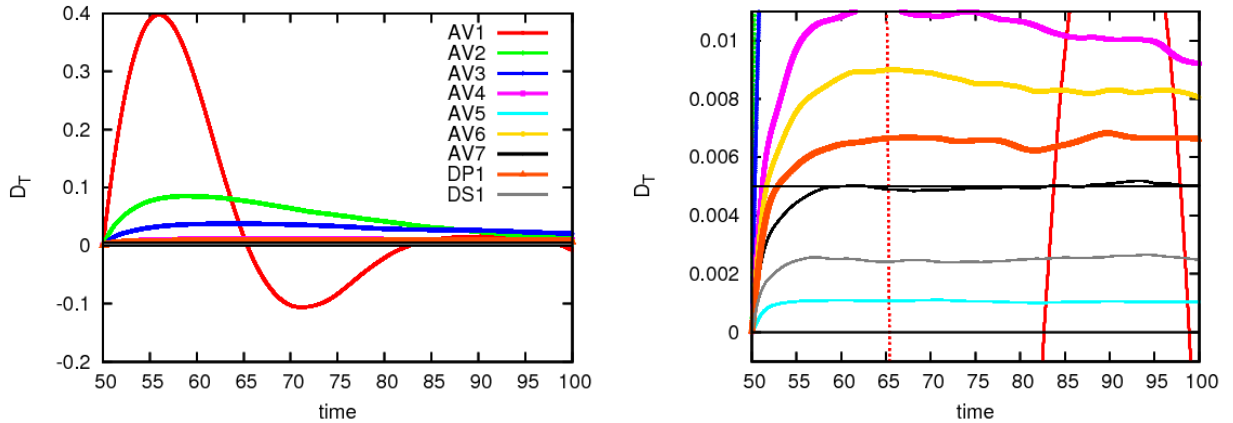


Fig. 4. Magnitude of SPH noise. The turbulent diffusion coefficient $D_T(t)$. The right panel represents an enlargement of the y-axis in order to better distinguish the curves that refers to simulations from AV4 to DS1.

Kolmogorov (1941) case and $\delta \approx -1.75, -2$ in the compressible supersonic case (e.g. see Price & Federrath 2010).

Figure 5 shows that when the artificial viscosity term is weak (low α and low β) a clear cascade is not identified (see left panel). However, larger (α, β) pairs lead to a cascade that is limited by the vertical extension of the disc at small wave numbers and by the resolution at high wave numbers. The exponent of the observed cascade is close to that of the compressible supersonic case mainly for the radial component for intermediate values of the artificial viscosity parameters (see middle panel), in the other cases, azimuthal and vertical components and increasing artificial viscosity, it tends to approach that of the Kolmogorov case (see right panel).

An increase in resolution, artificial viscosity and sound speed leads to more extended cascades. The features observed for the power spectrum are qualitatively preserved at different radial and vertical positions inside the disc.

Intermittency Highly turbulent flow are characterized by *intermittency*. This feature is highlighted by the exponent of the structure function and higher order moments of probability distribution functions (PDF) of several quantities such as density and velocity. We have analysed the 3rd (skewness S) and the 4th (kurto-

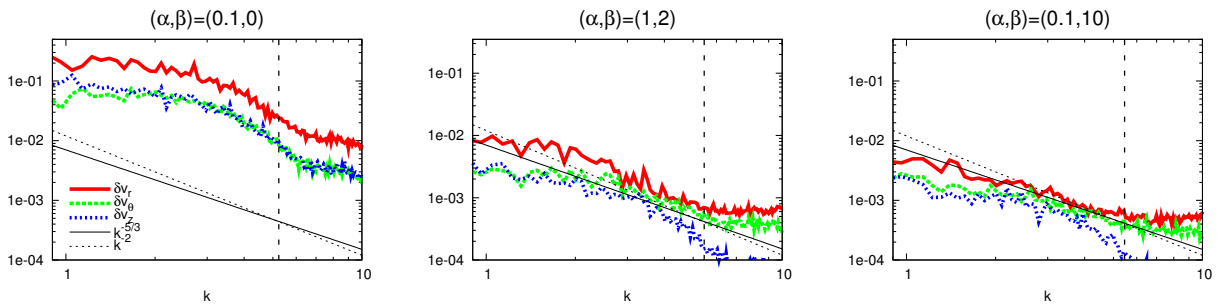


Fig. 5. Structure of SPH noise. Power Spectrum of velocity fluctuations: radial, azimuthal and vertical components are represented with solid red, dashed green and blue dotted lines respectively. The vertical long dashed line represents the resolution limit. The solid and the dotted black lines represent the Kolmogorov and the $\delta = -2$ slope of the power spectrum, respectively.

sis K) moment: no significant deviation from the gaussian values has been observed, indicating absence of intermittency.

5 Conclusions

The noise in SPH simulations, called here SPH noise, can be considered as the numerical noise filtered by the model chosen for the implementation of artificial viscosity. SPH noise produces a fluctuating field that depends both qualitatively and quantitatively on the artificial viscosity term.

Simulations with significantly large (α, β) parameters, among those considered, have given encouraging results. In this case, the Monaghan & Gingold (1983) artificial viscosity implementation partially mimics the effects of a physical turbulent viscosity: an energy cascade is present, accretion and turbulent diffusion are reproduced (but inversely related); however intermittency is not present.

Further investigation is necessary before studying the effect of highly turbulent gas on the dynamics of dust grains.

This research was supported by the Agence Nationale de la Recherche (ANR) of France through contract ANR-07-BLAN-0221. Figure 1 has been done using SPLASH Price (2007).

References

- Andrews, S. M., Wilner, D. J., Hughes, A. M., Qi, C., & Dullemond, C. P. 2009, *ApJ*, 700, 1502
 Armitage, P. J. 2007, *ArXiv Astrophysics e-prints*, arXiv:astro-ph/0701485
 Barrière-Fouchet, L., Gonzalez, J., Murray, J. R., Humble, R. J., & Maddison, S. T. 2005, *A&A*, 443, 185
 Fromang, S. & Nelson, R. P. 2006, *A&A*, 457, 343
 Fromang, S. & Papaloizou, J. 2006, *A&A*, 452, 751
 Hartmann, L., Calvet, N., Gullbring, E., & D'Alessio, P. 1998, *ApJ*, 495, 385
 King, A. R., Pringle, J. E., & Livio, M. 2007, *MNRAS*, 376, 1740
 Kolmogorov, A. 1941, *Akademiia Nauk SSSR Doklady*, 30, 301
 Meglicki, Z., Wickramasinghe, D., & Bicknell, G. V. 1993, *MNRAS*, 264, 691
 Monaghan, J. & Gingold, R. 1983, *Journal of Computational Physics*, 52, 374
 Price, D. J. 2007, *PASA*, 24, 159
 Price, D. J. & Federrath, C. 2010, *MNRAS*, 406, 1659
 Shakura, N. I. & Sunyaev, R. A. 1973, in *IAU Symposium, Vol. 55, X- and Gamma-Ray Astronomy*, ed. H. Bradt & R. Giacconi, 155–+

PLANETARY MIGRATION IN WEAKLY MAGNETIZED TURBULENT DISCS

C. Baruteau¹, S. Fromang², R. P. Nelson³ and F. Masset⁴

Abstract. In laminar viscous disc models, the migration of protoplanets embedded in their nascent protoplanetary discs may be directed inwards or outwards, depending on the relative magnitude of the Lindblad and corotation torques. The long-term evolution of the corotation torque is intimately related to diffusion processes inside the planet's horseshoe region. This communication examines the properties of the corotation torque in discs where magnetohydrodynamic (MHD) turbulence develops as a result of the magnetorotational instability (MRI), considering a weak initial toroidal magnetic field. We show that the differential Lindblad torque takes very similar values in MHD turbulent and laminar viscous discs, and there exists an unsaturated corotation torque in MHD turbulent discs.

Keywords: accretion discs, magnetohydrodynamics (MHD), turbulence, methods: numerical, planetary systems: planet-disc interactions, planetary systems: protoplanetary discs

1 Introduction

By combining models of planetary formation and migration, and models of protoplanetary discs, planet population syntheses (e.g., Ida & Lin 2008; Mordasini et al. 2009) have shown that the reproduction of the mass-period diagram of known exoplanets is particularly sensitive to the magnitude of the tidal torque driving the migration of forming protoplanets, known as type I migration. The latter has been intensively studied in two-dimensional (2D) non-magnetized, laminar viscous disc models. In such models, the tidal torque comprises the differential Lindblad torque and the corotation torque. The differential Lindblad torque corresponds to the angular momentum carried away by the spiral density waves the planet generates in the disc (see illustration in Fig. 1). Alone, it would drive type I migration on timescales typically $\leq 10^5$ yrs, shorter than the timescale for giant planet formation (e.g., Ward 1997). The corotation torque corresponds to the exchange of angular momentum between the planet and the fluid elements inside its horseshoe region. The magnitude of the corotation torque is powered by advection-diffusion of gas vortensity and entropy inside the horseshoe region. Alone, it would drive migration inwards or outwards, depending on the background density and temperature profiles.

A lot of efforts have been recently put forward to derive simple and accurate expressions for the Lindblad and corotation torques (Masset & Casoli 2010; Paardekooper et al. 2011). The question that we address here is to what extent these predictions, which are based on viscous disc models, still hold in the presence of MHD turbulence arising from the MRI, a likely source of turbulence in protoplanetary discs.

2 Physical model and numerical setup

We explore the properties of the tidal torque between a planet and its nascent protoplanetary disc, wherein turbulence is driven by the non-linear development of the MRI. The key point we address is whether an unsaturated corotation torque exists and can be maintained in the long term in such turbulent discs. For this purpose, we performed 3D MHD simulations with the NIRVANA and RAMSES codes, adopting a simple disc model with a locally isothermal equation of state, and neglecting non-ideal MHD effects as well as vertical stratification.

¹ DAMTP, University of Cambridge, Wilberforce Road, Cambridge CB30WA, United Kingdom

² Laboratoire AIM, CEA/DSM-CNRS-Université Paris Diderot, IRFU/SaP, CEA/Saclay, 91191 Gif-sur-Yvette, France

³ Astronomy Unit, Queen Mary University of London, Mile End Road, London E1 4NS, United Kingdom

⁴ Instituto de Ciencias Físicas, Universidad Nacional Autónoma de México, Apdo. Postal 48-3, 62251-Cuernavaca, Morelos, México

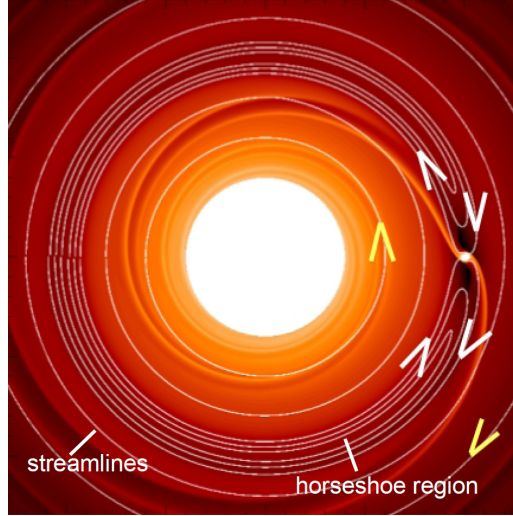


Fig. 1. Disc density perturbed by a few Earth-mass planet. Streamlines in the frame corotating with the planet are overplotted by solid curves.

Table 1. Disc, grid and planet parameters used in the MHD simulations

Parameter	Value	Remarks
Radial resolution	320 cells in $R \in [1; 8]$	
Azimuthal resolution	480 cells in $\varphi \in [0; \pi]$	15-20 cells per H at planet location
Vertical resolution	40 cells in $z \in [-0.3; 0.3]$	
Initial magnetic field	Toroidal, set up in $R \in [1.5; 5]$	
Plasma β -parameter	$\beta = 50$ (NIRVANA), $\beta = 400$ (RAMSES)	
Aspect ratio	$h = H/R = 0.1$ at $R = 3$	
Planet mass	$M_p = 3 \times 10^{-4} M_\star$	$M_p/(h^3 M_\star) = 0.3$ at planet location
Planet location	$R_p = 3, \varphi_p = \pi/2, z_p = 0$	(planet subject to type I migration)
Planet's softening length	$\varepsilon = 0.2H(R_p)$	
Frame	Corotating with $R = R_p$	
Radial boundary condition	Wave-killing zones in $R \in [1; 1.5]$ and $R \in [7; 8]$	

No explicit kinematic viscosity is included. When included, the planet remains on a fixed circular orbit, and the tidal torque exerted by the disc on the planet is measured as a time series. To get a steady-state density profile, the initial density profile is reinforced on 20 planet orbits. The key parameters used in the simulations are summarized in Table 1. For more details about the numerical setup, the reader is referred to Baruteau et al. (2011). For comparison, results with 2D viscous disc models without magnetic field, having otherwise the same disc and planet parameters as in the 3D MHD models are also presented below.

3 Results of simulations

3.1 Disc model with an inner cavity (planet trap)

In locally isothermal discs, the corotation torque can be particularly large in disc regions where the density gradient is positive, and for this reason we performed a sequence of simulations with the planet located in a turbulent disc with an inner cavity. The planet orbits in the transition region between the outer high-density disc and the inner low-density cavity, a region often referred to as a planet trap (Masset et al. 2006). The sequence was initiated with a preliminary viscous 1D run aimed at obtaining a steady-state density profile with an inner cavity. This run was used to construct a 3D cylindrical disc model into which a purely toroidal magnetic field was introduced throughout the disc. This magnetized disc model was evolved until MHD turbulence was fully developed before inserting the planet.

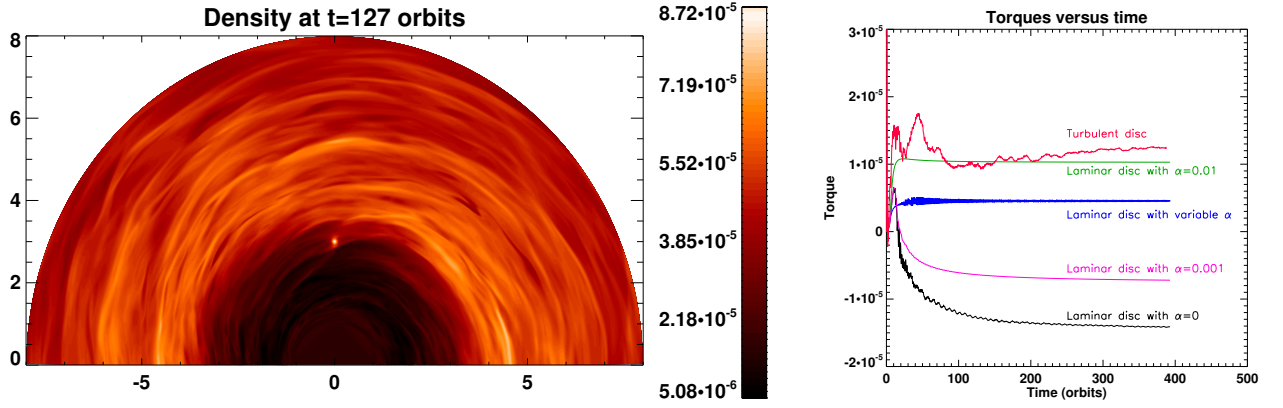


Fig. 2. Left: disc midplane density obtained with the cavity run of § 3.1. The planet is located at $x = 0$, $y = 3$. Right: running time-averaged torque obtained with the turbulent cavity model. Torques of laminar disc models with similar density profile and various viscosities at the planet location are superimposed for comparison.

The disc's midplane density obtained 127 orbits after the planet insertion is displayed in the left panel of Fig. 2, where we can see the planet sitting at the edge of the cavity. The time-averaged alpha viscous parameter associated with the turbulent stress is $\langle \alpha \rangle \approx 0.02$ near the planet. The running time-average of the torque exerted by the disc on the planet is shown by the red curve in the right panel of Fig. 2. The results of 2D laminar simulations with different viscosities are depicted for comparison. The time-averaged turbulent torque remains positive, indicating that the corotation torque is sustained at a value close to its maximum, unsaturated value throughout the simulation. These results strongly suggest that a planet trap maintained in a turbulent protoplanetary disc can be effective in preventing the large scale migration of embedded protoplanets.

3.2 Disc models with a power-law density

To provide a more quantitative comparison between the results of MHD turbulent and viscous disc models, we consider in this section two disc models where the initial profiles of the disc density (ρ_0) and temperature (T_0) are power-law functions of radius. In Model 1, $\rho_0 \propto R^{-1/2}$ and $T_0 \propto R^{-1}$. In Model 2, $\rho_0 \propto R^{-3/2}$ and T_0 is uniform. In the absence of magnetic field and turbulence, the corotation torque would vanish in Model 2, but not in Model 1. Although it is uncertain how a toroidal magnetic field modifies the dependence of the corotation torque with density and temperature gradients, the tidal torque values obtained in both models can hint whether MHD turbulence impacts the differential Lindblad torque and the corotation torque.

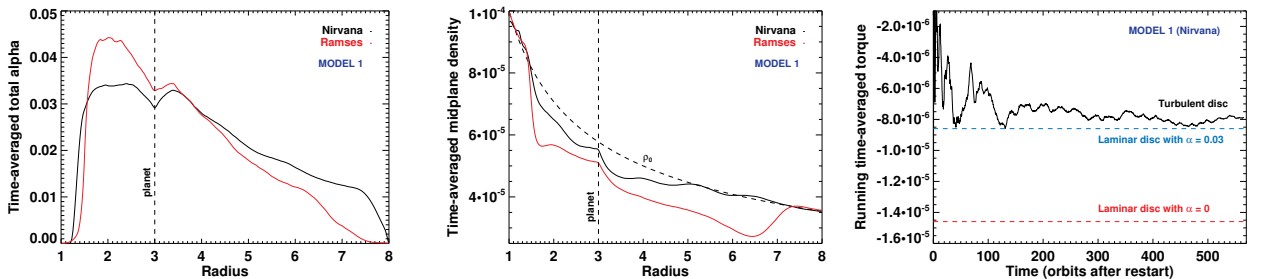


Fig. 3. Results obtained with disc Model 1 in § 3.2: radial profiles of the alpha viscous parameter (left) and midplane density (middle), time-averaged over 100 orbits. Right: Running time-averaged torque. The stationary torques of 2D non-magnetized laminar disc models (inviscid and viscous) are overplotted, in which the profiles of ρ_0 and α correspond to their time-averaged MHD counterpart.

The key results obtained with Model 1 are summarized in Fig. 3. The left panel shows the time-averaged profile of the total alpha viscous parameter obtained with both codes. At the planet location, $\langle \alpha \rangle \sim 0.03$, a value that translates into an averaged diffusion timescale across the planet's horseshoe region that is slightly

longer than the horseshoe U-turn timescale. The corotation torque is thus expected to adopt a value close to that predicted by linear theory. The middle panel displays the azimuthally- and time-averaged disc midplane density. The fact the initial density is restored over 20 local orbital periods implies that we get a stationary density profile slightly reduced compared to the initial one, depicted by a dashed curve. The right panel shows the running time-averaged turbulent torque, along with the final torque obtained in 2D inviscid ($\alpha = 0$) and viscous ($\alpha = 0.03$) non-magnetic disc models. The running time-averaged turbulent torque reaches a stationary value after ~ 200 orbits, and is in decent agreement with the torque of the laminar disc model with similar viscous alpha parameter near the planet. Although not shown here, similar results were obtained with Model 2, as well as a remarkably good overall agreement between the results of both codes.

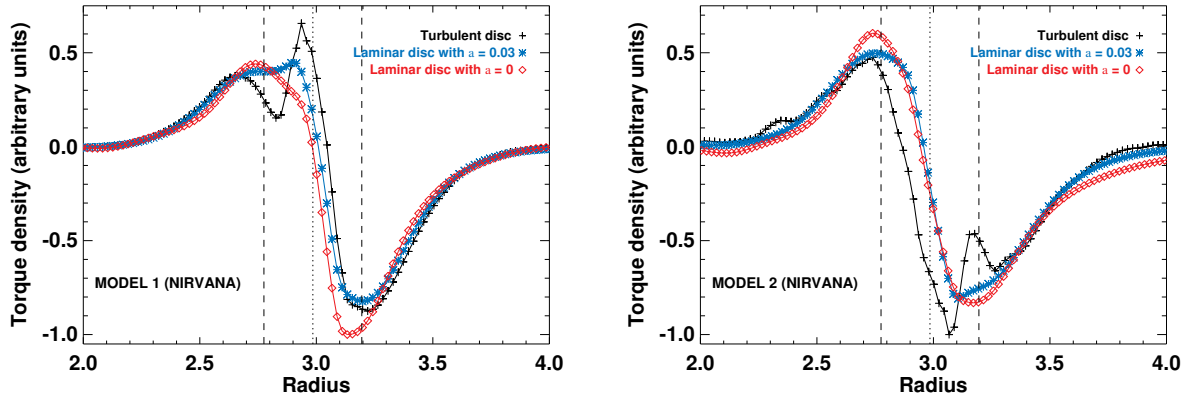


Fig. 4. Torque density distribution time-averaged over 100 orbits. The (stationary) torque distributions of inviscid and viscous disc models are overplotted. The dashed lines show the approximate location of the separatrices of the planet's horseshoe region.

To gain insight into the similar torque values of the turbulent and viscous disc models, we show in Fig. 4 the time-averaged torque distribution of the turbulent torque, and the stationary torque distribution of the inviscid and viscous models. The planet is located at $R = 3$ and the vertical dashed lines show the approximate location of the separatrices of its horseshoe region. We see that outside the horseshoe region, the very good agreement between the turbulent and laminar torque distributions shows that, on time average, the differential Lindblad torque is essentially unchanged by the full development of MHD turbulence. Inside the horseshoe region, however, the different torque distributions highlight the existence of an additional corotation torque in weakly magnetized discs. Interestingly, the additional corotation torque takes negative values in the \sim inner half of the horseshoe region, and positive values in the outer half. This approximately symmetric distribution conspires to make the additional torque have a very small net amplitude, which accounts for the good agreement between the turbulent and viscous total torques shown in the right panel of Fig. 3. The properties of this new corotation torque, in particular its dependence with the strength and gradient of the background toroidal magnetic field, will be presented in a future study.

References

- Baruteau, C., Fromang, S., Nelson, R. P., & Masset, F. 2011, *A&A*, 533, A84+
- Ida, S. & Lin, D. N. C. 2008, *ApJ*, 685, 584
- Masset, F. S. & Casoli, J. 2010, *ApJ*, 723, 1393
- Masset, F. S., Morbidelli, A., Crida, A., & Ferreira, J. 2006, *ApJ*, 642, 478
- Mordasini, C., Alibert, Y., Benz, W., & Naef, D. 2009, *A&A*, 501, 1161
- Paardekooper, S., Baruteau, C., & Kley, W. 2011, *MNRAS*, 410, 293
- Ward, W. R. 1997, *Icarus*, 126, 261

PLANETS FORMED BY GRAVITATIONAL INSTABILITY SHOULD RAPIDLY MIGRATE INWARD

C. Baruteau¹, F. Meru² and S.-J. Paardekooper¹

Abstract. The observation of massive exoplanets at large orbital separation from their host star challenges theories of planetary formation. A possible formation mechanism involves the fragmentation of massive protoplanetary discs into clumps. While the conditions for fragmentation have been extensively investigated, little is known of the subsequent evolution of these giant planet embryos, in particular their expected orbital migration. We examine in this communication the interaction between a single planet and the gravitoturbulent disc it is embedded in, following the assumption that the planet has formed by gravitational instability. We show that such planets should rapidly migrate towards the inner parts of protoplanetary discs, regardless of the planet mass.

Keywords: accretion, accretion discs, turbulence, methods: numerical, planetary systems: formation, planetary systems: protoplanetary discs

1 Introduction

Planets observed a few tens of au away from their host star are thought to be potential candidates for the formation scenario based on the gravitational instability (GI) of massive protoplanetary discs. A few numerical studies have observed that clumps could drift inwards (e.g., Mayer et al. 2002), some of them having focused on the early phases of disc formation and evolution following the collapse from the prestellar core stage (e.g., Machida et al. 2011). In a recent paper (Baruteau et al. 2011), we have shown that the interaction between a planet and the fully gravitoturbulent disc it is embedded in leads to the rapid inward migration of the planet. Our model and results of simulations are summarized below.

2 Physical model

We investigate the tidal interaction between a massive planet and the protoplanetary disc it formed in through the GI scenario. Two-dimensional hydrodynamical simulations were carried out for this purpose. Our study does not address the formation of the planet after the fragmentation stage. We consider instead an already formed single planet embedded in its nascent gravitoturbulent disc. We first set up a quasi steady-state disc, in which shock heating arising from the gravitoturbulence, modeled with a von Neumann-Richtmyer artificial bulk viscosity, is balanced by cooling. A simple but common prescription is used for the disc cooling, where the ratio of the cooling timescale to orbital period is taken to be a constant, denoted by β . Since we require the disc to be in a gravitoturbulent state, but we do not require fragmentation, we simulated various disc models with $\beta \geq 15$. In the following, results are shown for $\beta = 30$.

3 Results of simulations

Before inserting the planet, our model comprises an $\approx 0.25M_{\odot}$ disc around a star of fixed mass $M_{\star} = M_{\odot}$, spanning a radial range $20 < r < 250$ au. The radial profile of the surface density is $\approx 15 \text{ g cm}^{-2} (r/100 \text{ au})^{-3/2}$, and that of the temperature ≈ 10 K throughout the disc. The time-averaged radial profile of the alpha viscous

¹ DAMTP, University of Cambridge, Wilberforce Road, Cambridge CB30WA, United Kingdom

² Institut für Astronomie und Astrophysik, Universität Tübingen, Auf der Morgenstelle 10, 72076 Tübingen, Germany

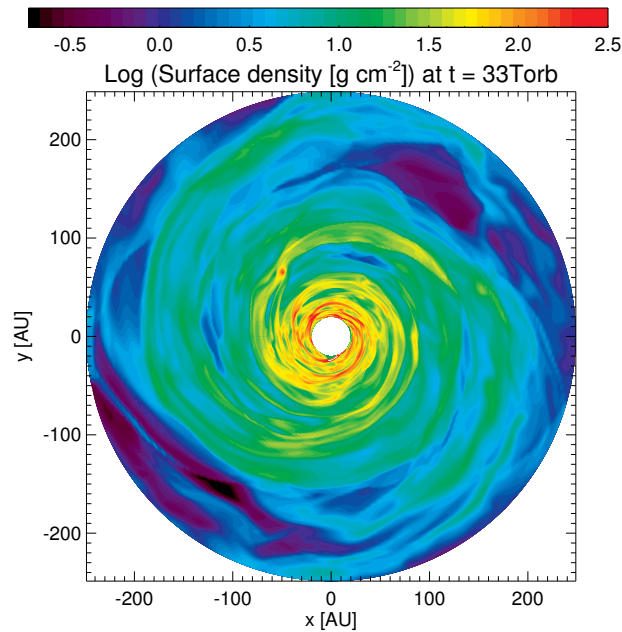


Fig. 1. Disc’s surface density obtained in a restart simulation with $\beta = 30$, where a Jupiter-mass planet has been introduced at 100 au. Results are displayed three orbits after the restart time. The planet is now located at about 80 au from the central star (at $x \sim -50$ au, $y \sim 60$ au).

parameter associated with gravitoturbulence, $\langle\alpha\rangle$, is also approximately uniform ($\langle\alpha\rangle \approx 2.5\%$). The above density and temperature profiles result from the fact the disc reaches a quasi steady-state with uniform profiles of its Toomre- Q and $\langle\alpha\rangle$ parameters.

Simulations were restarted with including a single planet at 100 au. We considered three planet masses about the typical initial mass of a clump formed by GI (Boley et al. 2010): a Saturn-mass planet, a Jupiter-mass planet and 5 Jupiter-mass planet (for more details, see Baruteau et al. 2011). For each planet mass, a series of eight runs was performed with varying the planet’s azimuth at restart. Fig. 1 displays the gas surface density in one of the restart runs with the Jupiter-mass planet, and we see that the density perturbation due to the planet is comparable to the turbulent density perturbations.

The time evolution of the planets orbital separation is depicted in Fig. 2. The net trend coming out of our results is that planets migrate inwards very rapidly, despite the stochastic kicks due to gravitoturbulence. The averaged migration timescale is typically shorter than 10^4 years, regardless of the planet mass. Smaller planets are more sensitive to stochastic kicks, but also migrate inwards very fast. Stochastic kicks may be directed inwards or outwards depending on the density turbulent fluctuations inside the planet’s horseshoe region. They can be seen as an effective, *temporary* type III migration feature coming on top of the inward migration due to the background disc–planet tidal torque.

Because their formation and migration timescales are shorter than their gap-opening timescale (partly because of the disc’s vigorous turbulence), planets do not have time to open a dip or a gap around their orbit in our model. They are therefore not subject to the type II and *runaway* type III migration regimes. The comparison of our results with those of equivalent laminar disc models shows that the averaged torque driving the net inward migration in gravitoturbulent discs is actually very similar to the one leading to type I migration in the absence of turbulence. We interpret the rapid inward migration in our model as due to an increasing radial profile of the disc entropy in a steady state, which yields a large negative horseshoe drag adding up to the negative differential Lindblad torque. We argue that in discs with uniform Toomre- Q profiles and cooling-to-orbital timescale ratios, rapid inward migration should be a generic expectation for planets formed by GI.

4 Concluding remarks

We have shown that massive planets formed at large separation from their star by GI are unlikely to stay in place, and should rapidly migrate towards the inner parts of protoplanetary discs, regardless of the planet mass.

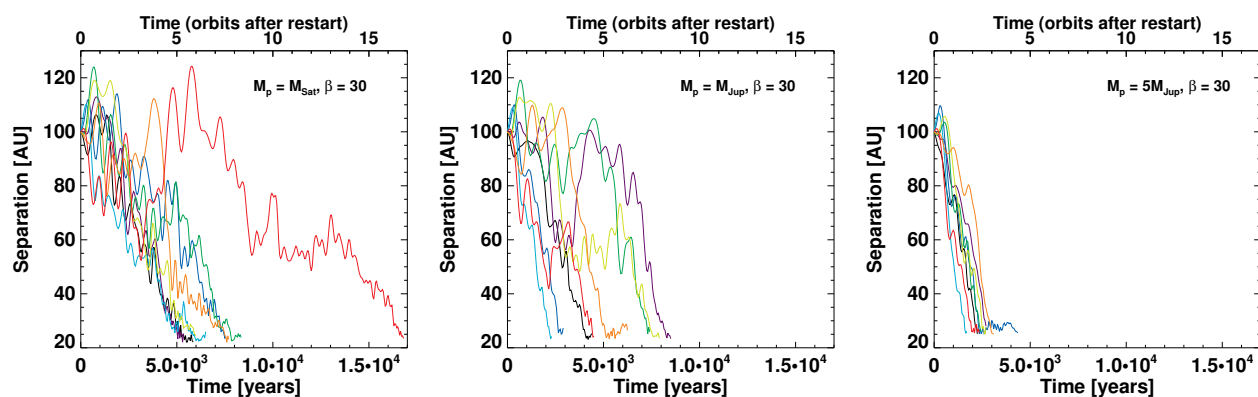


Fig. 2. Time evolution of the orbital separation of a Saturn-mass planet (left column), a Jupiter-mass planet (middle column), and a 5 Jupiter-mass planet (right column) in a gravitoturbulent disc with $\beta = 30$. Time is displayed in years (bottom x-axis), and in orbital periods at 100 au (top x-axis). Results are obtained for eight evenly-spaced planet's azimuths at restart.

Such planets are not necessarily to reach the very vicinity of their host star. The inner parts of protoplanetary discs should indeed be too hot to be gravitationally unstable, and other sources of turbulence, such as the magnetorotational instability, could prevail, changing the background disc profiles as well as the amount of turbulence. It is thus possible that the rapid type I migration of planets formed by GI slows down in the disc inner parts and results in the formation of a gap. Although the formation of several planets by GI and their mutual interactions could change the above picture, we speculate that the planets in the HR 8799 system (Marois et al. 2010) could have formed by GI, if the fastest migrating planet slows down or stalls its migration in the disc inner parts, and that the (possibly sequential) convergent migration of the outer planets leads to their capture into mean-motion resonance.

References

- Baruteau, C., Meru, F., & Paardekooper, S.-J. 2011, *MNRAS*, 416, 1971
 Boley, A. C., Hayfield, T., Mayer, L., & Durisen, R. H. 2010, *Icarus*, 207, 509
 Machida, M. N., Inutsuka, S., & Matsumoto, T. 2011, *ApJ*, 729, 42
 Marois, C., Zuckerman, B., Konopacky, Q. M., Macintosh, B., & Barman, T. 2010, *Nature*, 468, 1080
 Mayer, L., Quinn, T., Wadsley, J., & Stadel, J. 2002, *Science*, 298, 1756

NUMERICAL MODELLING OF THE ACCRETION COLUMN IN MAGNETIC CATAclySMIC VARIABLES

C. Busschaert^{1,2}, C. Michaut¹, E. Falize^{1,2}, B. Loupiaz², A. Ravasio³, A. Dizière³, H. C. Nguyen¹
and M. Koenig³

Abstract. Numerical simulations of the accretion column in magnetic cataclysmic variables are presented along with the experimental principle of laboratory experiment from the POLAR project. The main focus of the project is to design and diagnose an exact scaled accretion column using powerful lasers. These measurements allow the testing of the astrophysical models of accretion processes present in magnetic cataclysmic variables.

Keywords: laboratory astrophysics, magnetic cataclysmic variables, radiative shocks, accretion, scaling laws

1 Introduction

Modern high-energy density facilities allow to bring up matter, reproducibly, to extreme states of density, temperature and velocity which are relevant to astrophysical environments (Remington et al. 2006). In the context of the POLAR project (Falize et al. 2011b) new similarity experiments are realized in order to study the formation and the dynamics of accretion shocks in magnetic cataclysmic variables (mCVs).

The mCVs are semi-detached binary systems containing an accreting magnetic white dwarf which accretes matter from a late type Roche-lobe filling secondary star (Warner 1995). They are divided into two main sub-classes according to the magnetic field intensity (Cropper et al. 2002): the intermediate polar or DQ Her star which has $1 \text{ MG} < B < 10 \text{ MG}$ and the polar or AM Her star with $B > 10 \text{ MG}$. In polar stars, the magnetic field is so strong that it prevents the formation of an accretion disc. The accreted gas is confined to stream flowing along the magnetic field line onto the pole of white dwarf (Wu 2000).

We developed a theoretical model of radiative optically thin shocks which can be easily confronted with observations from polars since the radiation of those objects comes mainly from an area near the white dwarf surface: the base of the accretion column where many spectroscopic clues indicate the presence of radiating shocks. However the size scales associated with the accreted shock are smaller than the white dwarf radius. Consequently it is impossible for now to resolve this zone by direct observations (Hoogerwerf et al. 2006). In order to explore more precisely what happens in the column, we can use an adapted scaling law which allows to reproduce with powerful laser a diagnosable accretion column.

At first, we will detail the model and numerical results obtained with the code HYDRO-COOL for the accretion column at the astrophysical scale and then we will detail how to build a model of those objects in the laboratory.

2 Analytical model of the accretion column and numerical study

During the accretion process in polars, the matter is directed along the magnetic field lines toward the magnetic pole(s) of the white dwarf. When the flow hits the surface of the star at supersonic velocity, a reverse shock is created and propagates upward in the accretion column until a position on the order of 100-1000 km above the surface (see Fig. 1).

The shock's height, x_s , is determined by radiative processes which occur in the post-shock region. Indeed,

¹ LUTH, Observatoire de Paris, CNRS, Université Paris-Diderot, 92190 Meudon, France

² CEA-DAM-DIF, F-91297 Arpaçon, France

³ LULI Ecole Polytechnique, CNRS, UPMC, Route de Saclay, 91128 Palaiseau, France

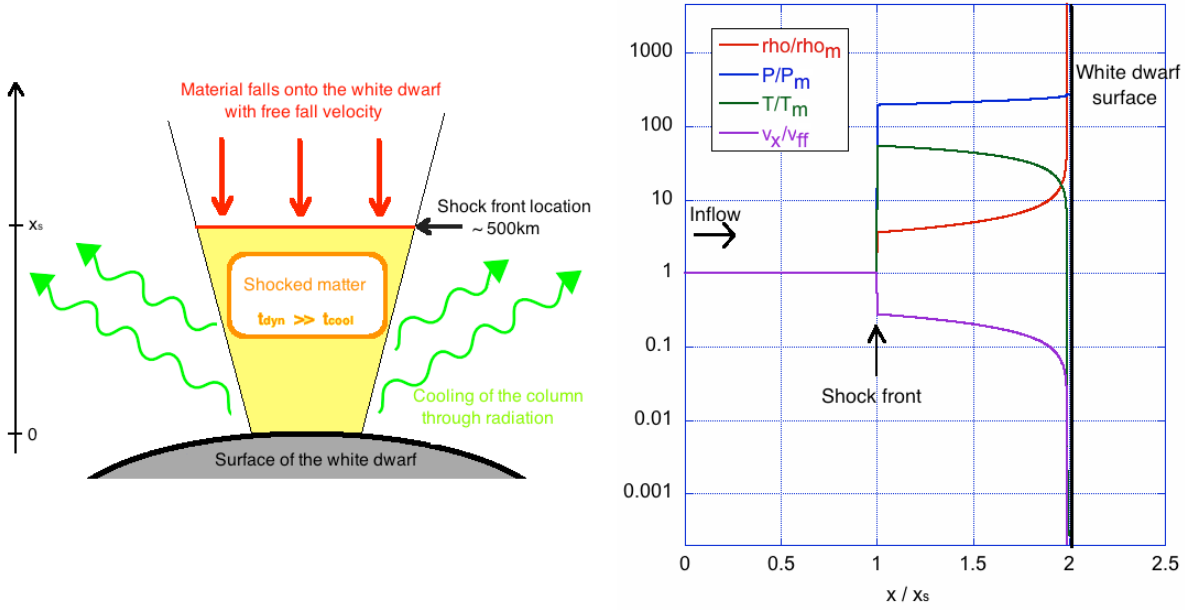


Fig. 1. Left: the model of accretion column in polars: free-falling material hits the surface of the white dwarf. A shock is created and propagates upward in the accretion column until a position on the order of 100 km above the surface. **Right:** typical normalized profile for temperature, density, pressure and velocity in the column.

the loss of energy implies a decrease of temperature toward the white dwarf, accompanied by a densification and a decrease of velocity (see Fig. 1). The shock position is then settled given that the fluid needs enough time to cool and slow down before reaching the surface. We describe this post-shock region by considering 1D hydrodynamical equations with a source term in the energy conservation equation $\Lambda(\rho, T) = \Lambda_0 \rho^\alpha T^\beta$, where $\rho, T, \Lambda_0, \alpha, \beta$ are respectively the density, temperature and three constants (Chevalier & Imamura 1982; Falize et al. 2009b):

$$\frac{\partial \rho}{\partial t} + \frac{\partial}{\partial x}(\rho v) = 0 \quad (2.1)$$

$$\frac{\partial}{\partial t}(\rho v) + \frac{\partial}{\partial x}(\rho v^2 + P) = 0 \quad (2.2)$$

$$\frac{\partial E}{\partial t} + \frac{\partial}{\partial x}[v(E + P)] = -\Lambda(\rho, T) \quad (2.3)$$

where t, x, v and E are respectively time, position, velocity and total energy of the fluid with $E = \rho e + 1/2 \rho v^2$, e being the internal energy of the fluid. We then assumed that the plasma is optically thin which is a good approximation since considering typical parameters for the system we found that the horizontal optical depth is approximately of $\tau = 8 \cdot 10^{-2}$ (Frank et al. 2002). As long as the magnetic field is lower than 50 MG and the accretion rate higher than $1 \text{ g} \cdot \text{cm}^{-2} \cdot \text{s}^{-1}$ the main cooling process is bremsstrahlung and its exact cooling function corresponds to $\alpha = 2, \beta = 0,5$ (Rybicki & Lightman 1979). For higher magnetic field and/or lower accretion rate, we need to take into account the cyclotron cooling whose cooling function can also be approximated as a power law (Chanmugam et al. 1985; Saxton et al. 1998).

For such power law form cooling function, complete analytical solution exists in the stationary regime (Chevalier & Imamura 1982; Falize et al. 2009b). In particular, we use them as one of our initial conditions in our time-dependant simulations. Otherwise, as initial conditions, we launch the fluid in our simulation box to observe the appearance of the shock and its evolution. Similar results are obtained with those two different initial conditions at long time.

Numerical simulations are made thanks to HYDRO-COOL which is a 2D hydrodynamical code developed at LUTH (Michaut et al. 2010). The code is based on a MUSCL-Hancock scheme; the Riemann problem is computed by a HLLC or a HLLC solver depending on the conditions of the simulation case; the source term

is included in the scheme using the Strang splitting method and calculated thanks to a Runge-Kutta method. Assuming that cooling is mainly due to bremsstrahlung, we found similar results as Imamura et al. (1984) and Strickland & Blondin (1995) using similar boundary conditions: the position of the shock front is unstable and oscillates with a characteristic timescale of the order of the cooling timescale right behind the shock (see Fig. 2). Thus the origin of the oscillations seems to be a cooling instability which occurs in the shocked region: if the shock front is displaced toward (resp. away from) the white dwarf, the fluid has too little time (resp. too much) to cool down, there is too much (resp. not enough) thermal energy in the shocked region, pressure increases (resp. decreases) and drives the shock away from (resp. toward) the white dwarf. This oscillation induces a variation in luminosity of those objects which could correspond to optical quasi periodical oscillations observed in some polars (Larsson 1989).

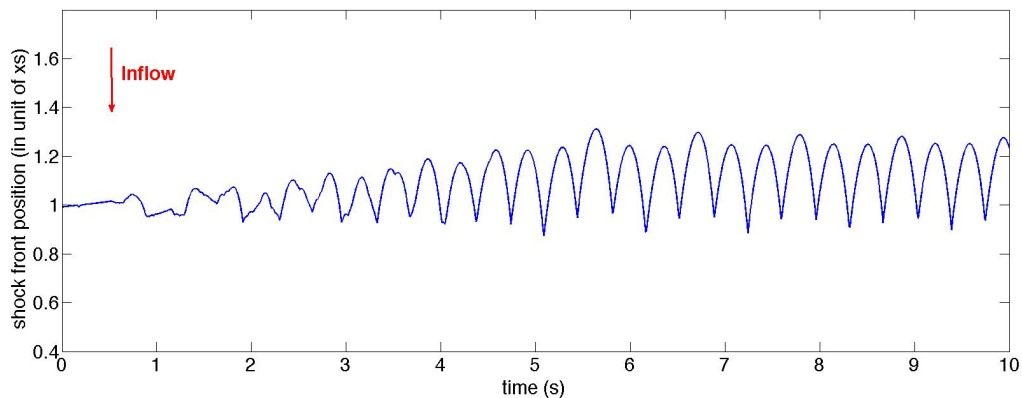


Fig. 2. Variation of the position of the shock front in unit of the stationary position x_s with time for an accretion column cooled by bremsstrahlung. The system is in an overstable regime and the oscillations rapidly reach a saturated amplitude.

3 Similarity and scaling laws

The distance between the shock front and the surface of the white dwarf is very small (on the order of 100 km) compared to the radius of the white dwarf (on the order of 10^4 km), thus it is impossible to observe directly the structure of the accretion column. A new point of view is to create a model of the column in the laboratory thanks to powerful lasers in order to test our model.

It was proved that exact scaling laws exist for different accretion column regimes -one temperature with bremsstrahlung and/or cyclotron cooling (Falize et al. 2009a, 2011c) and two temperatures (Falize et al. 2011a); the number of free parameters depending on the degree of similarity we choose. For example, following the Aizu model (Aizu 1973), in the case of an accretion column dominated by bremsstrahlung cooling considering the absolute similarity – leaving the equations invariant and allowing a rescaling of all physical quantities – the scalability properties of the column are the following:

$$x/\tilde{x} = B/A^2; t/\tilde{t} = \sqrt{B/A^3}; v/\tilde{v} = \sqrt{B/A}; \rho/\tilde{\rho} = A; P/\tilde{P} = B; T/\tilde{T} = B/A,$$

where A and B are two free parameters linking the physical quantities of the astrophysical and laboratory systems respectively with and without tilde.

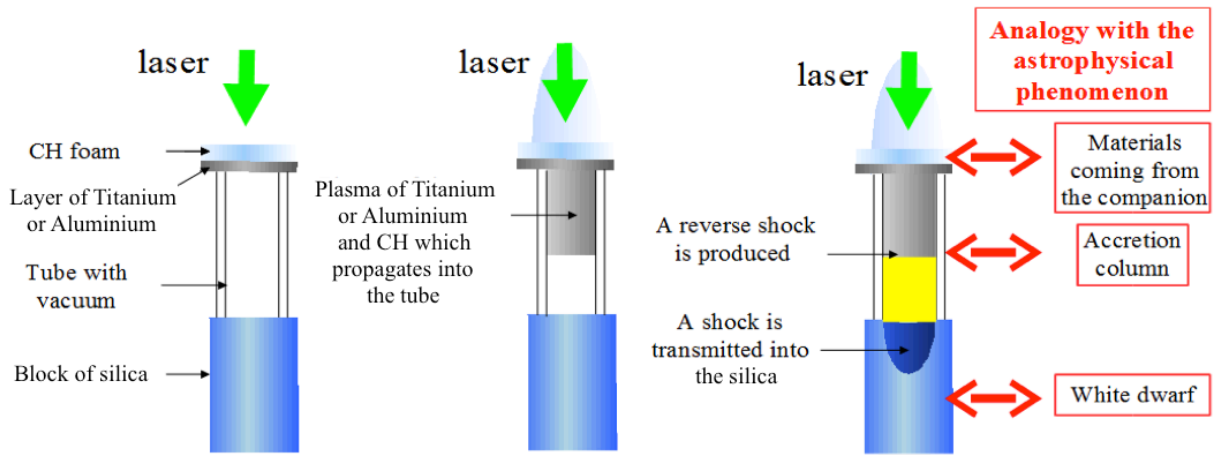
According to this scaling law, it is possible to reproduce the accretion column phenomenon in the laboratory since the needed regime is achievable (see Table 1). Moreover, one can notice that the typical length of the post-shock region, 10^{-3} cm, is large enough to be well diagnosed in the laboratory.

Based on this scaling law, an experimental principle was designed and is described in Fig. 3 (Falize et al. 2011a). The laser impacts on a pusher, creating a plasma which propagates into the tube toward an obstacle. The parallel with the astrophysical case is immediate: the expanding plasma corresponds to the material falling on the white dwarf which is itself modeled by the obstacle, and the collimation role of the magnetic field is played by the tube.

Table 1. Typical scale of the two systems of interest: the astrophysical and laboratory accretion columns

	x (cm)	t (s)	v (cm/s)	ρ (g/cm ³)	T (K)
Astrophysical system	10^7	1	$5 \cdot 10^8$	10^{-8}	10^8
Laboratory system	0.1	10^{-7}	$5 \cdot 10^7$	10^{-2}	10^6

For now, one experiment has taken place using the laser LULI2000 (Ecole Polytechnique - LULI) with different compositions of the target pusher in order to test the experimental principle. We did observe the flow propagating into the tube until the collision against the obstacle, and we observed the reverse shock (Falize et al. 2012).

**Fig. 3.** Experimental principle

4 Conclusions and Perspectives

In this work, we showed our preliminary numerical simulations at the astrophysical scale. In order to test our code HYDRO-COOL, we retrieved former results using different initial conditions and boundary conditions. We are currently improving the code in order to take into account more ingredients in our model such as multiple cooling processes or being able to modify the geometry of the column.

We also presented the theoretical bases of the experimental setup which aims at producing a model of the accretion column in the laboratory. The first experiment allowed us to test our target design and to diagnose the plasma flow propagation through the tube. In future work, we plan to improve the target design in order to reach more relevant regimes and improve similarity with astrophysical scaled phenomenon.

References

- Aizu, K. 1973, Progress of Theoretical Physics, 50, 344
 Chanmugam, G., Langer, S. H., & Shaviv, G. 1985, ApJ, 299, L87
 Chevalier, R. A. & Imamura, J. N. 1982, ApJ, 261, 543
 Cropper, M., Ramsay, G., Hellier, C., et al. 2002, RSPTA, 360, 1951
 Falize, E., Bouquet, S., & Michaut, C. 2009a, Ap&SS, 322, 107
 Falize, E., Dizière, A., & Loupiau, B. 2011a, Ap&SS, 138
 Falize, E., Loupiau, B., Ravasio, A., et al. 2011b, Ap&SS, 80
 Falize, É., Michaut, C., & Bouquet, S. 2011c, ApJ, 730, 96
 Falize, E., Michaut, C., Cavet, C., et al. 2009b, Ap&SS, 322, 71

- Falize, E., Ravasio, A., Loupiau, B., et al. 2012, *High Energy Density Physics*, 8, 1
- Frank, J., King, A., & Raine, D. J. 2002, *Accretion Power in Astrophysics: Third Edition*
- Hoogerwerf, R., Brickhouse, N. S., & Mauche, C. W. 2006, *ApJ*, 643, L45
- Imamura, J. N., Wolff, M. T., & Durisen, R. H. 1984, *ApJ*, 276, 667
- Larsson, S. 1989, *A&A*, 217, 146
- Michaut, C., Nguyen, H. C., & di Menza, L. 2010, *Ap&SS*, 320
- Remington, B. A., Drake, R. P., & Ryutov, D. D. 2006, *Review of Modern Physics*, 78, 755
- Rybicki, G. B. & Lightman, A. P. 1979, *Radiative processes in astrophysics*, 393
- Saxton, C. J., Wu, K., Pongracic, H., & Shaviv, G. 1998, *MNRAS*, 299, 862
- Strickland, R. & Blondin, J. M. 1995, *ApJ*, 449, 727
- Warner, B. 1995, *Cambridge Astrophysics Series*, 28
- Wu, K. 2000, *Space Sci. Rev.*, 93, 611

THE ROSSBY WAVE INSTABILITY IN 2D VISCOUS PROTOPLANETARY DISCS

E. Crespe¹, J.-F. Gonzalez¹ and S. E. Arena¹

Abstract. To form meter-sized pre-planetesimals in protoplanetary discs, dust aggregates have to collide at velocities lower than a threshold so that they are not destroyed during the collision. Dust grains are affected by the gas through aerodynamic drag, therefore its study is relevant in determining the grain growth evolution. The Rossby Wave Instability (RWI, non-axisymmetric instability, Lovelace et al. 1999; Lovelace & Hohlfield 1978), may solve this problem by the formation of vortices where dust particles can accumulate, collide at low velocity and stick together (Barge & Sommeria 1995). We study the development of the RWI in a 2D viscous disc using the Smoothed Particle Hydrodynamics (SPH) method. We show that Rossby Vortices can form and survive in the disc for a few thousand years. The instability is triggered by a “*jump*” in the radial surface density profile caused by the presence of a dead zone in the protoplanetary disc.

1 Introduction

The formation of preplanetesimals is the first step of planetary formation. Current models and experiments of grain growth do not explain how grains can reach sizes larger than ≈ 1 m. The existence of the “radial-drift barrier” introduced by Weidenschilling (1977), the “fragmentation-barrier” and the “bouncing-barrier”, presented by Güttler et al. (2010) and Zsom et al. (2010), are the current limits of the first steps of planetary formation. Barge & Sommeria (1995) suggested the existence of vortices in protoplanetary discs that could develop and exist for hundreds of years. In their center, grains could accumulate and stop their inner migration, leading to easier growth thanks to smaller relative velocities. Indeed, it is well known that dust grains tend to accumulate in pressure maxima. This condition can be satisfied if the gas density is locally higher as in anticyclonic vortices. The Rossby Wave Instability may solve this problem as it generates Rossby Vortices where dust particles can accumulate. Lyra et al. (2008, 2009) underline the fact that vortices trap the dust in their center, creating embryos of various sizes in approximately a hundred years.

We will first briefly describe the Rossby Wave Instability (RWI) and its trigger mechanism. Then we present the Smoothed Particle Hydrodynamics (SPH) approach, the α artificial viscosity and numerical setup. Section 4 details the results obtained from the 2D simulation of gas only, and conclusions of this work are presented in Section 5.

2 The Rossby Wave Instability

The Rossby Wave Instability in protoplanetary discs was first introduced by Lovelace et al. (1999), after the previous work of Lovelace & Hohlfield (1978). They presented the necessary criterion to develop the instability (see Section 2.1). Tagger (2001) presented an analytical study of this instability reminding the fact the Vortices should be destroyed by the differential rotation of the nebula. He showed that the RWI can be maintained thanks to the coupling between density waves and Rossby waves at the corotation radius. Numerical simulations performed by Li et al. (2000) showed that a “*bump*” or a “*jump*” in the radial density profile can trigger the instability. Varnière & Tagger (2006) used this method showing that an overdensity can naturally result from the presence of a dead zone (DZ) in the disc. The accretion is slower in the DZ than in the inner or outer part of the disc, therefore (1) at the DZ’s outer edge, gas coming from the outer disc accumulates and (2) at the DZ’s inner edge, the gas in the DZ is accreted more slowly than matter present in the inner disc. Finally both configurations produce an overdensity such that the RWI can develop.

¹ Université de Lyon, Lyon, F-69003, France; Université Lyon 1, Villeurbanne, F-69622, France; CNRS, UMR 5574, Centre de Recherche Astrophysique de Lyon, École Normale Supérieure de Lyon, 46 allée d’Italie, F-69364 Lyon cedex 07, France; Observatoire de Lyon, 9 avenue Charles André, F-69561 Saint Genis Laval cedex, France

2.1 Instability criterion

A necessary criterion to develop the RWI in the disc is to have an extremum of the quantity \mathcal{L} (Lovelace et al. 1999; Lovelace & Hohlfield 1978):

$$\mathcal{L} = \frac{\Sigma \Omega}{\kappa^2} \frac{P}{\Sigma \gamma} = \left(\frac{(\nabla \times \mathbf{v})_z}{\Sigma} \right)^{-1} \quad \text{for an isothermal disc,} \quad (2.1)$$

where Ω is the orbital time, κ the epicyclic frequency, γ the adiabatic index, P the pressure, Σ the surface density and \mathbf{v} is the gas velocity.

3 SPH simulations

We use a 2D SPH code (Barrière-Fouchet et al. 2005) that models an unmagnetized protoplanetary disc containing only gas around a one-solar mass star. We implement a dead zone (DZ) to examine how SPH simulations can develop the RWI. The DZ is created by introducing a radial dependence in the α artificial viscosity profile. We study the resulting effects on the surface density profile $\Sigma(r)$.

3.1 α artificial viscosity

To run the simulations, we use the standard artificial viscosity of Gingold & Monaghan (1983) introduced to avoid interpenetration of SPH particles during shocks and parametrized by two parameters: α and β . The α parameter is linked to the Shakura & Sunyaev (1973) α_{ss} parameter (Megllicki et al. 1993), which represents the turbulent viscosity of the gas and is responsible for the mass accretion rate onto the central star.

3.2 Disc model

The disc extends from 0.1 AU to 15 AU and the dead zone from 1 AU to 5 AU. The temperature and surface density profiles follow $\Sigma \propto r^{-p}$ and $T \propto r^{-q}$ with $p=3/2$, $q=3/4$. The initial state is made of 500,000 gas particles in a 2D near-equilibrium disc that relaxes to a stationary disc in a few years. We let the disc evolve over 1600 years. The standard artificial viscosity is parametrized by $\alpha = \alpha(r)$ and $\beta = 0$ (Section 3.1). The code units are: $1 M_{\odot}$, 7.5 AU, $(7.5)^{3/2}$ yr, $G=1$.

3.3 Dead Zone profile

To create an artificial dead zone in the disc, we introduce a radial variation in the α artificial viscosity (Section 3.1). We use the profile of Varnière & Tagger (2006) so that the viscosity varies like:

$$\begin{cases} \alpha = a_0 (\epsilon + \text{atan}(\delta_r(-r + r_{\text{in}}^{\text{DZ}}))) & \text{if } r \leq r_{\text{in}}^{\text{DZ}}, \\ \alpha = a_0 \epsilon & \text{if } r_{\text{in}}^{\text{DZ}} < r < r_{\text{out}}^{\text{DZ}}, \\ \alpha = a_0 (\epsilon + \text{atan}(\delta_r(r - r_{\text{out}}^{\text{DZ}}))) & \text{if } r \geq r_{\text{out}}^{\text{DZ}}, \end{cases} \quad (3.1)$$

where $r_{\text{in}}^{\text{DZ}} = 1$ AU is the inner edge of the dead zone, $r_{\text{out}}^{\text{DZ}} = 5$ AU is the outer edge of DZ, $\delta_r = 50$ is the slope of the viscosity profile at the edges of the DZ, $\epsilon = 10^{-5}$ is the residual viscosity in the DZ and $a_0 = 10^4$. Figure 1 gives the representation of the artificial viscosity profile in the disc.

4 Results from gas simulations - Evidences of the RWI

4.1 Density fluctuations

Figure 2 shows the density fluctuations ($\rho - \langle \rho \rangle$) at four different times during the disc evolution. At early times, the viscosity profile does not permit to have a strong enough maximum in the density profile. The accumulation of gas at the edges of the dead zone produces an overdensity satisfying the \mathcal{L} -criterion. At early times, the simulation shows the formation of many vortices. After about 100 years, they merge in five dominant vortices evolving near the dead zone's outer-edge. As long as the dead zone remains in the disc, the vortices can exist.

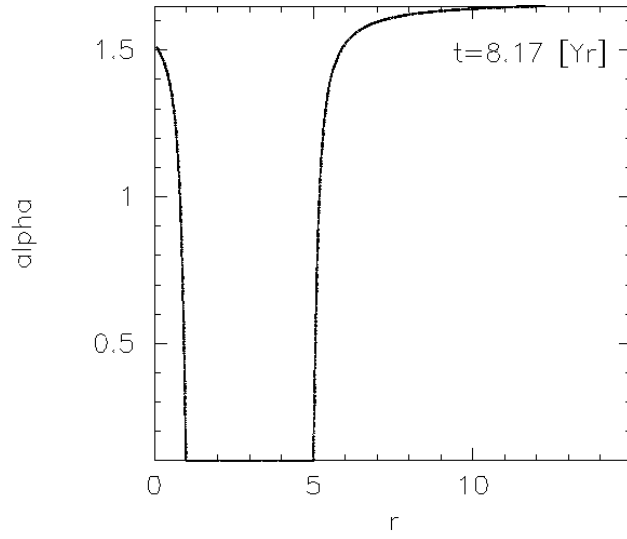


Fig. 1: Radial profile of the artificial viscosity α in our SPH simulation of the disc. $\alpha \in [0.1; 1.7]$. The radius is in AU.

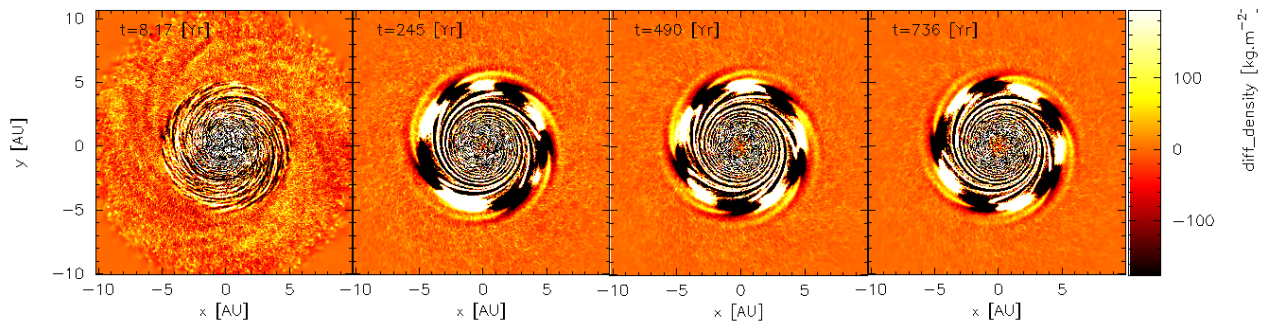


Fig. 2: Map of the density fluctuations near 5 AU. From left to right: 8.17, 245, 490 and 736 years.

4.2 Time evolution of the density

The radial surface density profile (Figure 3) shows the accretion of matter across the edges of the dead zone that allows to validate the \mathcal{L} -criterion.

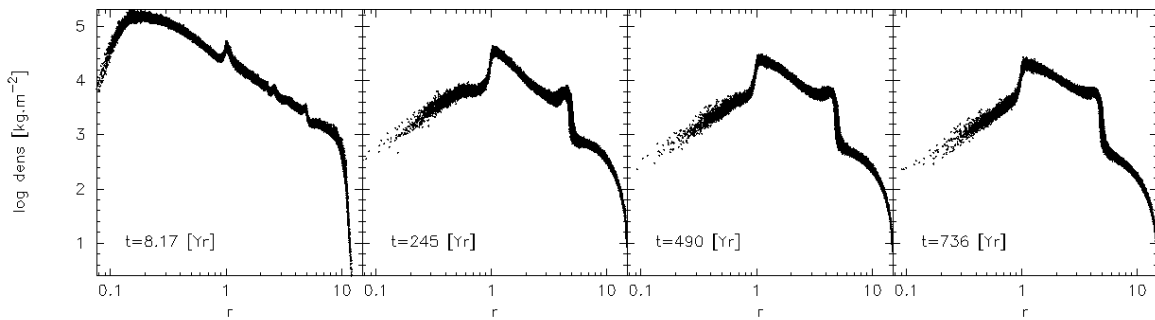


Fig. 3: Evolution of the radial density profile with time : 8.17, 245, 490 and 736 years. The radius r is in AU.

4.3 Vorticity

Figure 4a and 4b show the vorticity ($\omega_z = (\nabla \times \mathbf{v})_z$) of the SPH particles in the disc. One sees five anticyclonic vortices coupled with five cyclonic vortices that appear less resolved (as can be seen in Figure 4b showing a close up of a vortex near 5 AU). The mode $m=5$ is dominant during all the simulation. No more merging of vortices is appreciable after the early evolution (Section 4.1).

4.4 Velocity field

In Figure 4c and 4d, the plot of the non-axisymmetric part of the gas velocity ($\mathbf{v}_{\text{gas}} - \mathbf{v}_{\text{K}}$, where \mathbf{v}_{K} is the Keplerian velocity) highlights the presence of cyclonic ($\Omega_{\text{vortices}} \equiv +\Omega_{\text{K}}$) and anticyclonic ($\Omega_{\text{vortices}} \equiv -\Omega_{\text{K}}$) vortices (near the outer edge of the DZ) and density waves. One clearly sees the rotation of the gas particles around underdensities (Figure 4d).

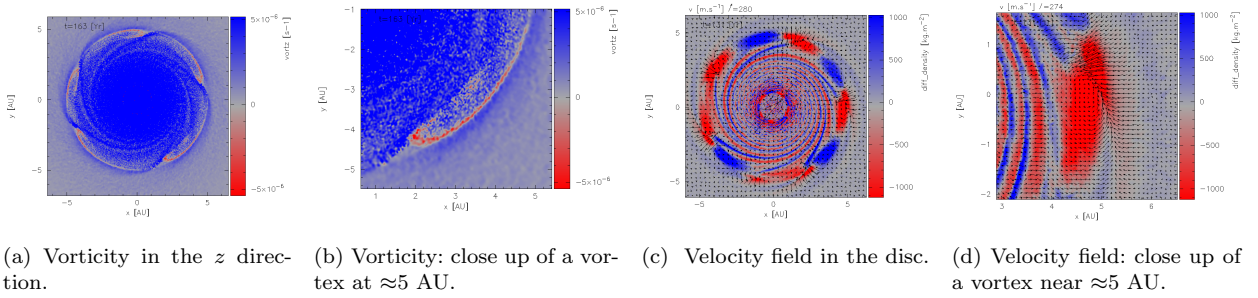


Fig. 4: **Vorticity plot (a,b)**: Blue: cyclonic (positive) vorticity and red: anticyclonic (negative) vorticity. **Velocity plot (c,d)**: Colors represent the differential density, the non-axisymmetric part of the velocity field is superimposed.

5 Conclusions

The presence of a dead zone in the disc (Varnière & Tagger 2006) is a good tool to obtain an overdensity that allows the development of the Rossby Wave Instability. The presence of a viscosity in the disc, that is modeled by the use of the radial variation of the α artificial viscosity, is not an obstacle to the existence of the RWI. Velocity and vorticity plots clearly show the presence of Rossby Vortices that survive during a few thousand years. A mode $m=5$ is dominant during all the simulation. Other works show various evolution and merging of vortices from higher modes ($m=4,6$) to lower ones ($m=3,2$) (Varnière & Tagger 2006; Lyra et al. 2008, 2009). A comparison between Lagrangian (SPH) and Eulerian methods should be considered. Further work to investigate the growth of modes, the behaviour of dust in the 2D viscous disc in the presence of vortices and the growth of the RWI in a 3D viscous disc is in progress.

This research was partially supported by th Programme National de Physique Stellaire and the Programme National de Planétologie of CNRS/INSU, France, and the Agence Nationale de la Recherche (ANR) of France through contract ANR-07-BLAN-0221. The authors wants to thank P. Varnière and H. Méheut for useful comments and discussions.

References

- Barge, P. & Sommeria, J. 1995, A&A, 295, L1
 Barrière-Fouchet, L., Gonzalez, J.-F., Murray, J. R., Humble, R. J., & Maddison, S. T. 2005, A&A, 443, 185
 Gingold, R. A. & Monaghan, J. J. 1983, MNRAS, 204, 715
 Güttler, C., Blum, J., Zsom, A., Ormel, C. W., & Dullemond, C. P. 2010, A&A, 513, A56+
 Li, H., Finn, J. M., Lovelace, R. V. E., & Colgate, S. A. 2000, ApJ, 533, 1023
 Lovelace, R. V. E. & Hohlfield, R. G. 1978, ApJ, 221, 51
 Lovelace, R. V. E., Li, H., Colgate, S. A., & Nelson, A. F. 1999, ApJ, 513, 805
 Lyra, W., Johansen, A., Klahr, H., & Piskunov, N. 2008, A&A, 491, L41

- Lyra, W., Johansen, A., Zsom, A., Klahr, H., & Piskunov, N. 2009, *A&A*, 497, 869
- Meglicki, Z., Wickramasinghe, D., & Bicknell, G. V. 1993, *MNRAS*, 264, 691
- Shakura, N. I. & Sunyaev, R. A. 1973, *A&A*, 24, 337
- Tagger, M. 2001, *A&A*, 380, 750
- Varnière, P. & Tagger, M. 2006, *A&A*, 446, L13
- Weidenschilling, S. J. 1977, *MNRAS*, 180, 57
- Zsom, A., Ormel, C. W., Güttler, C., Blum, J., & Dullemond, C. P. 2010, *A&A*, 513, A57+

NUMERICAL SIMULATIONS OF MAGNETIC RELAXATION IN ROTATING STELLAR RADIATION ZONES

V. Duez¹

Abstract. I detail the results of simulations of magnetic relaxation, as is assumed to happen in stellar radiation zones. While previous studies focused on the description of static equilibria, rotation is here included in the numerical setup which substantially modifies the outcome of the simulations. In particular, magnetic equilibria are found, whose configuration remain stable over diffusive timescales. Their privileged axis are inclined with respect to the rotation axis. The stationary internal flows and the dependence of the final equilibrium state on the rotation rate are described. Implications on stellar evolution are discussed.

Keywords: stars: magnetic fields, magnetohydrodynamics (MHD)

1 Introduction

Spectropolarimetric observations routinely reveal the presence of magnetic fields at the surface of a substantial proportion of early type stars, in particular of the chemically peculiar ones. It is thus clear that magnetism is somehow linked with their evolution as it potentially modifies microscopic transport processes, as well as macroscopic ones by interfering with rotation and meridional flows. Besides, current stellar evolution models including all known hydrodynamic transport processes still present difficulties in explaining many observed features, among which internal solar rotation profile recovered from helioseismology, chemical abundances anomalies in intermediate as well as massive stars (nitrogen enrichments in slowly rotating massive stars, hydrogen in type II supernovae progenitors, etc.). However, the details of the interplay between magnetic and hydrodynamic processes remain uncertain, not to say totally understood.

It is clear that these magnetic fields often display large-scale organized features, since observations can in general be interpreted in terms of an inclined (the “oblique rotator”) dipole model Bagnulo et al. (2002); Donati & Landstreet (2009) with lower contributions of the higher multipoles, though smaller scale features are mostly unresolved. But the way such a large-scale magnetic equilibrium is reached, starting from a field certainly organized on much smaller scales, still lacks of a coherent theoretical frame.

I here present the results of numerical simulations, in order to model the relaxation process occurring from an initial stochastic magnetic field presumably of primordial origin or being the result of a dynamo having occurred earlier, during the convective pre-main-sequence phase and to decipher the physical processes at work during the formation of large-scale equilibrium magnetic field in a stratified region. In both cases, it is taken for granted that the initial field is organized initially on much smaller scales than the final equilibrium; this latter one appears to be a minimum-energy state in agreement with the hydrodynamical constraints on the system. For the first time, rotation is included in the numerical set-up.

2 Numerical Set-up

2.1 Implementation

Use is made of the STAGGER code Nordlund & Galsgaard (1995); Gudiksen & Nordlund (2005), a high-order finite-difference Cartesian MHD code which uses a “hyper-diffusion” scheme. A modest resolution of 128^3 is used here, and is sufficient since one does not need to resolve turbulent features. The code includes Ohmic as well

¹ Argelander Institut für Astronomie, Universität Bonn, Auf dem Hügel 71, D-53121 Bonn, Germany

as thermal and kinetic diffusion. Using Cartesian coordinates avoids problems with singularities and simplifies the boundary conditions: periodic boundaries are used here. The rotation is implemented through the Coriolis acceleration only, while the centrifugal acceleration is not taken into account to avoid undesired effects arising from the enhanced rotation rate used in the simulation. However, the hierarchy between sound crossing time (τ_s), Alfvén crossing time (τ_A), rotation period (T) and Ohmic diffusive timescale (τ_η) is still well-preserved: $\tau_s \ll \tau_A, T \ll \tau_\eta$. The magnetic energy is kept fixed throughout the different runs; in contrast the rotation rate changes from one run to another, in order to cover a wide range of values spanning from $T \ll \tau_A$ (this is the case e.g. for a typical Ap star, where $\tau_A \simeq 10$ yrs and $T \simeq 100$ days), to $T \gg \tau_A$ (which can easily be reached for slowest rotating stars, assuming the inner field strength is two orders of magnitude higher than that at the surface).

2.2 Initial conditions

The star is modeled as a self-gravitating ball of ideal gas ($\gamma = 5/3$) with radial density and pressure profiles initially obeying the polytropic relation $P \propto \rho^{1+(1/n)}$, with index $n = 3$. This approximates a stably stratified radiation zone of an early-type, main sequence star. The influence of a convective core is neglected: owing the high turbulent diffusivity the large scale field penetrates this region easily – it is assumed to be unaffected.

I start from an initial normal distribution for the magnetic energy distribution: $|B| = B_0 \exp(-r^2/2B_w^2)$ with the scale parameter $B_w = 0.35 R_*$; $|B|^2, B_0, R_*$ and r being respectively the magnetic energy, the central magnetic field intensity, the stellar radius and the radius. This distribution and the initial seed for the random distribution in the direction of the stochastic field are chosen so that the resulting field in the non-rotating case is a simple nested torus, to deal with the simplest case. The influence of rotation on the development of non-axisymmetric configurations resulting from different initial conditions will be explored in a forthcoming work.

3 Results

3.1 General comments

Including rotation, a set of stationary MHD equilibria similar to the one obtained in the non-rotating case is obtained. Fig. 1a shows the representation of the perpendicular dipole resulting from the relaxation in the slowly rotating regime. The field lines (perpendicular to \mathbf{B}) are drawn. The final magnetic configuration is a twisted torus, with a strong toroidal component inside the star while the magnetic field lines in the vicinity of the stellar surface (not shown here) match with a quasi dipolar, potential field at the surface and are thus constrained to be poloidal in all cases. The differences between the static and the stationary equilibrium with rotation are twofolds: (i) the inclination β between the rotation axis and the magnetic privileged axis (torus revolution axis) $\mathbf{B} = \int_V \mathbf{r} \times \mathbf{B} dV$ varies as a function of the rotation rates, (ii) the internal flows and the differential rotation regime are modified.

3.2 Settling of the equilibrium

The evolution covering approximately 40 rotation periods (up to $t = 600$ in arbitrary units) happens in three consecutive phases: (i) the relaxation itself for $0 \leq t \leq 120$; (ii) the stationary evolution once the field has reached the relaxed state for $120 \leq t \leq 450$; (iii) the diffusive limit for $450 \leq t \leq 600$.

Relaxation phase In this first phase, the system evolves from small scale to large scale coherence. The ideal MHD invariants are no longer conserved, since during this phase the magnetic diffusivity η plays a key role in helping the system to organize into a larger scale equilibrium: larger angular modes structures are first smoothed out since $\delta\mathbf{B}/\delta t \simeq -\eta m^2 \mathbf{B}$ in the limit of high azimuthal numbers m .

Stationary evolution During the second phase, some ideal MHD invariants are indeed conserved: magnetic helicity, and higher order invariants are conserved such as the mass enclosed in magnetic flux surfaces. This last invariant was shown by Chandrasekhar & Prendergast (1958) to be conserved in the ideal MHD, axisymmetric case. A closer analysis (to be published in a separate work) reveals that in the rotating stationary case, the equilibrium can still be identified using the same analytical tools as in the static case. It is found that it is of linear, non-force-free type.

Furthermore, inner flows reach a steady state. I detail here the slowly rotating case. Fig. 1b shows cross sections of the poloidal magnetic field lines (isocontours) and of the angular frequency $\Omega = v_\varphi/(r \sin \theta)$ (color scale), toroidally averaged (in frame associated with the magnetic field, here with a quasi-perpendicular inclination). One can readily notice a departure to the Ferraro state (Ferraro 1954), with the presence of two counter rotating poloidal flows. Therefore, though on azimuthal average responsible for a solid-body rotation (as was predicted by Moss 1989), these flows mainly concentrated deep inside the star may be responsible for an extra-mixing mechanism associated with the presence of a large-scale magnetic field. This is to be observed in parallel to the recent results obtained from the VLT-Flames Survey, showing nitrogen enrichments in intrinsically slowly rotating massive stars requiring additional sources of extra-mixing (Brott et al. 2011).

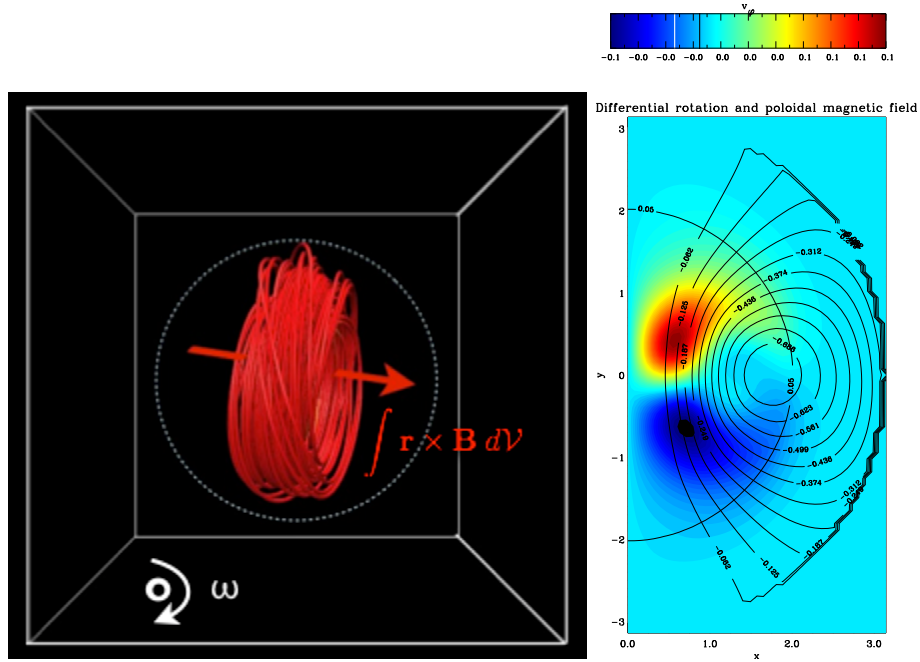


Fig. 1. Left: Three-dimensional representation of magnetic field lines for the perpendicular rotator (dashed line: stellar surface). **Right:** cross-section in the magnetic reference frame (toroidal average) of the azimuthal velocity v_φ (color scale) and the poloidal flux function $\Psi r \sin \theta$ such that the poloidal field is tangent to Ψ in any point (isocontours). All quantities are normalized to their maximum.

Diffusive limit The third and last phase of the simulation corresponds to the diffusive limit: the neutral line migrates in direction of the surface; the high poloidal field component reaches the surface and the flux is lost from the star. In this limit, the invariants are no longer conserved.

3.3 Final state: magnetic dipole inclination

It is interesting to evaluate the dependency of the inclination angle β , as some tendencies have been reported following recent observations on Ap stars Bagnulo et al. (2002); Mathys (2008). Large inclinations ($\beta \rightarrow 90^\circ$) seem to arise in fast rotators ($T < 100$ d); slow rotators ($100 \text{ d} < T < 1000$ d) display a tendency to axisymmetry ($\beta \rightarrow 0^\circ$) while for very slow rotators ($T > 1000$ d) β increases again. Fig. 2a shows the evolution of this angle β as a function of the rotation rate imprinted to the model for seven simulations covering seven different rotation rates spanning approximately $8 \tau_A$. For high rotation rates, the inclination angle goes to 0° , while for low rotation rates, the final state tends to a perpendicular rotator ($\beta \rightarrow 90^\circ$). On Fig. 2b is plotted the final inclination angle as a function of the rotation rate. Two distinct behaviours emerge. One below $\Omega = 0.75$, where the final inclination angle decreases linearly from 90° to 0° i.e. from the perpendicular dipole to the aligned one, and above this value a saturated regime with β in the vicinity of 0° .

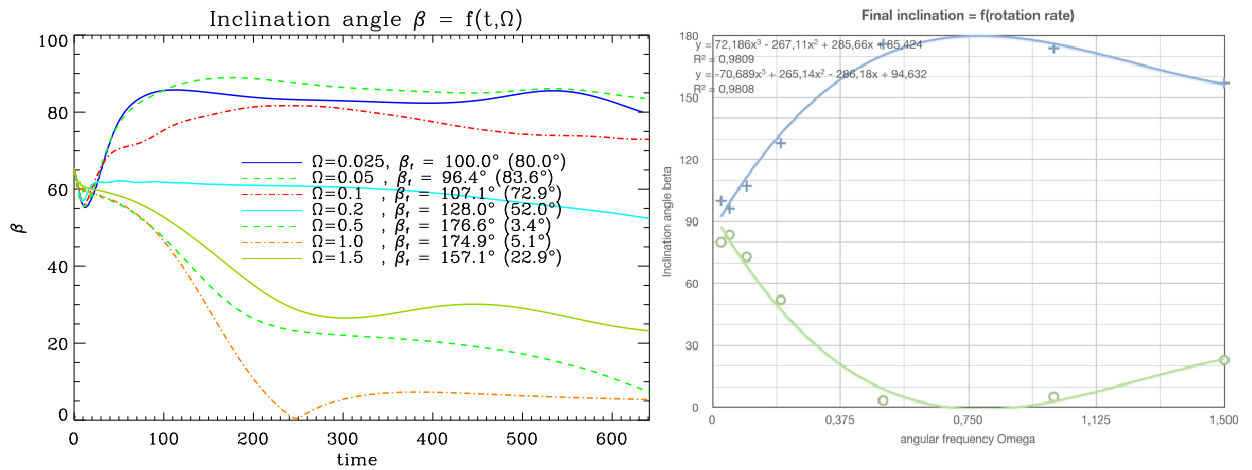


Fig. 2. **Left:** temporal evolution of the angle β (modulo 180°; actual values given in legend) between the rotation and the magnetic privileged axis. **Right:** final inclination angle β (and modulo 180°) as a function of the rotation rate.

4 Conclusion and perspectives

It has been shown how the numerical relaxation method can be used as a test-case tool to understand magnetic configurations evolution in early-type, main sequence stars. It provides informations about the equilibrium state between differential rotation and meridional flows, which will be important when implementing MHD transport processes in upcoming stellar evolution codes including magnetic fields. In the cases explored here, magnetic dipoles, presenting a toroidal component inside the star result from the relaxation process. Their inclination with respect to the magnetic field depends of the rotation rate: for the simulations performed it is found that slower rotators give perpendicular dipoles while faster rotators give aligned dipoles. Some ideal MHD invariants are shown to be conserved during the relaxed phase, although this still happens in a resistive regime. These invariants are described and allows to identify the type of equilibrium obtained: it shares many similarities with the static equilibria described in recent literature. However, poloidal flows are observed, especially in the slowly rotating case, although the star remains on average in a solid-body rotation regime. These flows might be responsible for an extra source of mixing.

References

- Bagnulo, S., Landi Degl'Innocenti, M., Landolfi, M., & Mathys, G. 2002, *A&A*, 394, 1023
- Brott, I., Evans, C. J., Hunter, I., et al. 2011, *A&A*, 530, A116
- Chandrasekhar, S. & Prendergast, K. H. 1958, in *IAU Symposium, Vol. 6, Electromagnetic Phenomena in Cosmical Physics*, ed. B. Lehnert, 46–+
- Donati, J.-F. & Landstreet, J. D. 2009, *ARA&A*, 47, 333
- Ferraro, V. C. A. 1954, *ApJ*, 119, 407
- Gudiksen, B. V. & Nordlund, Å. 2005, *ApJ*, 618, 1020
- Mathys, G. 2008, *Contributions of the Astronomical Observatory Skalnaté Pleso*, 38, 217
- Moss, D. 1989, *MNRAS*, 236, 629
- Nordlund, Å. & Galsgaard, K. 1995, *A 3D MHD code for Parallel Computers*, Tech. rep., <http://www.astro.ku.dk/~aaake/papers/95.ps.gz>

INFRARED EXCESS AND EXTENDED EMISSION AROUND CEPHEIDS

A. Gallenne¹, P. Kervella¹ and A. Mérand²

Abstract. We present new thermal IR photometry and spectral energy distributions (SEDs) of the classical Cepheids W Sgr, Y Oph and FF Aql, using newly obtained *VISIR* thermal IR photometric measurements. We used the BURST mode of the instrument to get diffraction-limited images at 8.59, 11.25 and 11.85 μm . For these three stars, the SEDs show an IR excess at long wavelengths. These excesses are likely extended emissions surrounding the stars linked to a possible mass loss mechanism. We also detected a spatially extended emission around W Sgr and Y Oph while we do not resolve the circumstellar envelope of FF Aql.

Keywords: Stars: circumstellar matter, Stars: variables: Cepheids, Infrared: stars

1 Introduction

The discovery of circumstellar envelopes (CSEs) around several Galactic Cepheids is an indication that many Cepheids, if not all, are surrounded by CSEs. These CSEs have an effect on the infrared surface brightness technique (IRSB) since the Cepheid appears brighter and also on interferometric measurements since the star appears larger than it really is. It is therefore necessary to quantify this excess in order to estimate the bias on the distance. This circumstellar material is also important in the context of Cepheid mass-loss since it may play a significant role in the problem of the Cepheid mass discrepancy (see e.g. Neilson et al. 2010a). The infrared excess could be linked to a mass-loss mechanism generated by shocks between different layers of the Cepheid's atmosphere during the pulsation cycle. A correlation between the period and the envelope flux (relatively to the star) was proposed by Mérand et al. (2007). A Cepheid with a larger pulsation period would have a larger IR excess. On the other hand, from photometry on a larger sample of Cepheids, Neilson et al. (2010b) reach the opposite conclusion. It is thus essential to study these CSEs to quantify their contribution and to understand how they form.

We present new observations of three Classical Cepheids, W Sgr, Y Oph and FF Aql, with the *VISIR* instrument from the VLT. We present the data analysis using aperture photometry applied to our images and we study the spectral energy distribution (SED) of these three stars. We also look for a spatially resolved component using a Fourier technique analysis.

2 Observation and data reduction

The observations were carried out during May 2008 using the BURST mode of *VISIR* to obtain the best spatial resolution. Series of observations were obtained in three filters: PAH1, PAH2 and SiC (respectively $8.59 \pm 0.42 \mu\text{m}$, $11.25 \pm 0.59 \mu\text{m}$ and $11.85 \pm 2.34 \mu\text{m}$). The classical chopping–nodding technique was applied to correct for instrumental artefacts and background thermal emission.

Our first step in the data reduction process consisted of a classical subtraction of the chopped and nodded images in order to remove the thermal background and in storing them in data cubes that contain thousands of frames. To have the best diffraction-limited images, we selected 50% of the best frames according to the brightest pixel (as tracer of the Strehl ratio). We then proceeded to a precentering (at a integer pixel level), a spatial resampling by a factor of 4 using a cubic spline interpolation and a fine recentering using a Gaussian

¹ LESIA, Observatoire de Paris, CNRS UMR 8109, UPMC, Université Paris Diderot, 5 Place Jules Janssen, F-92195 Meudon, France

² European Southern Observatory, Alonso de Córdova 3107, Casilla 19001, Santiago 19, Chile

fitting (at a precision level of a few milliarcseconds). The resulting cubes were then averaged to get the final image used in the data analysis process. This raw data processing has already been used and has proven its efficiency (see e.g. Kervella & Domiciano de Souza 2007; Kervella et al. 2009; Gallenne et al. 2011). The efficiency of the cube mode vs. the standard long exposure mode is discussed in Kervella & Domiciano de Souza (2007).

3 Spectral energy distribution

We carried out a classical aperture photometry on our final average images to assess the flux density for each star in each filter. Photometric templates from Cohen et al. (1999) were used to have an absolute calibration of the flux density, taking into account the filter transmission and the airmass correction from Schütz & Sterzik (2005). We have then collected additional photometric measurements from $0.4 \mu\text{m}$ to $100 \mu\text{m}$ to analyse the spectral energy distribution of our Cepheids.

As they are pulsating stars, the SEDs vary during the pulsation cycle and we have to take into account the phase of pulsation when retrieving the data. To estimate the magnitudes at our phase of pulsation we retrieved the B, V, J, H and K light curves from the literature when available, that we plotted as a function of phase. We then applied the Fourier decomposition technique (see e.g. Ngeow et al. 2003) to estimate the value at our phase. At longer wavelength, there are no existing light curves, we then chose to use the amplitude of the light curves A_λ (that is decreasing with wavelengths) as additional uncertainties on the magnitude due to the phase mismatch. Based on the estimated J, H and K amplitudes of 51 Galactic Cepheids from Laney & Stobie (1993), we chose as additional uncertainties on the magnitude for $1 < \lambda < 3.5 \mu\text{m}$, the values 0.1 mag for W Sgr and FF Aql and 0.2 mag for Y Oph, and for $\lambda > 3.5 \mu\text{m}$ we chose 0.05 mag for the three stars.

The photospheric emission was modelled with tabulated stellar atmosphere models obtained with the ATLAS9 simulation code from Castelli & Kurucz (2003). We have chosen a grid which was computed for solar metallicity and a turbulence velocity of 2 km s^{-1} . We then interpolated this grid in order to compute spectra for any effective temperature and any surface gravity. The spectrum was multiplied by the solid angle of the stellar photosphere, $\pi\theta_{\text{LD}}^2/4$, where θ_{LD} is the limb-darkened angular diameter. We adjusted the photometric data to the model taking into account the spectral response of each instrument. We assume that there is no detectable excess (5% or less) below $2.2 \mu\text{m}$ and all the photometric measurements bluer than the K band are used to fit the angular diameter and the effective temperature.

All flux densities $< 3 \mu\text{m}$ are corrected for interstellar extinction $A_\lambda = R_\lambda E(B - V)$ using the total-to-selective absorption ratios R_λ from Fouqué et al. (2003) and Hindsley & Bell (1989), and the color excess $E(B - V)$ from Fouqué et al. (2007). Fluxes in any other longer wavelengths are not corrected for the interstellar extinction, which we assume to be negligible.

3.1 FF Aql

We selected $\log g = 2.05$ from Luck et al. (2008) as fixed parameter. The adjusted SED is presented in Fig. 1. The B and V values were taken from light curves of Berdnikov (2008) and Moffett & Barnes (1984). The J, H and Ks photometry are from Welch et al. (1984). We also added photometric values from the Infrared Array Camera (*IRAC*: 3.6, 4.5, 5.8 and $8 \mu\text{m}$) and the Multiband Imaging Photometer (*MIPS*: $24 \mu\text{m}$) installed in the *Spitzer* space telescope (Marengo et al. 2010). We also use broadband photometry from the Infrared Astronomical Satellite (*IRAS*: 12 and $25 \mu\text{m}$, Helou & Walker 1988), from the *AKARI* satellite *IRC* point source catalogue (9 and $18 \mu\text{m}$, Ishihara et al. 2010) and from the Midcourse Space Experiment (*MSX*: 8.28, 12.13, 14.65, 21.34 μm , Egan & Price 1996; Egan et al. 2003).

Our best-fit values are $\theta_{\text{LD}} = 0.86 \pm 0.03 \text{ mas}$ and $T_{\text{eff}} = 5890 \pm 235 \text{ K}$. The SED is plotted in Fig. 1 (black solid curve). This fitted effective temperature is only 3% smaller than the value from Luck et al. (2008) ($6062 \pm 43 \text{ K}$) at this phase of pulsation. The angular diameter is in excellent agreement with the $0.86 \pm 0.17 \text{ mas}$ from Groenewegen (2007).

We fitted to this star a second component assuming it follows a simple greybody distribution of the form :

$$F_\lambda = \beta B_\lambda(T_d)$$

where $B_\lambda(T_d)$ is the Planck function at dust temperature T_d and β contains the informations about the solid angle and the total emissivity. Our best greybody model with a temperature $T_d = 556 \pm 177 \text{ K}$ and $\beta = 1.50 \pm 0.54 \text{ mas}^2$ is plotted in Fig. 1 (the solid green curve).

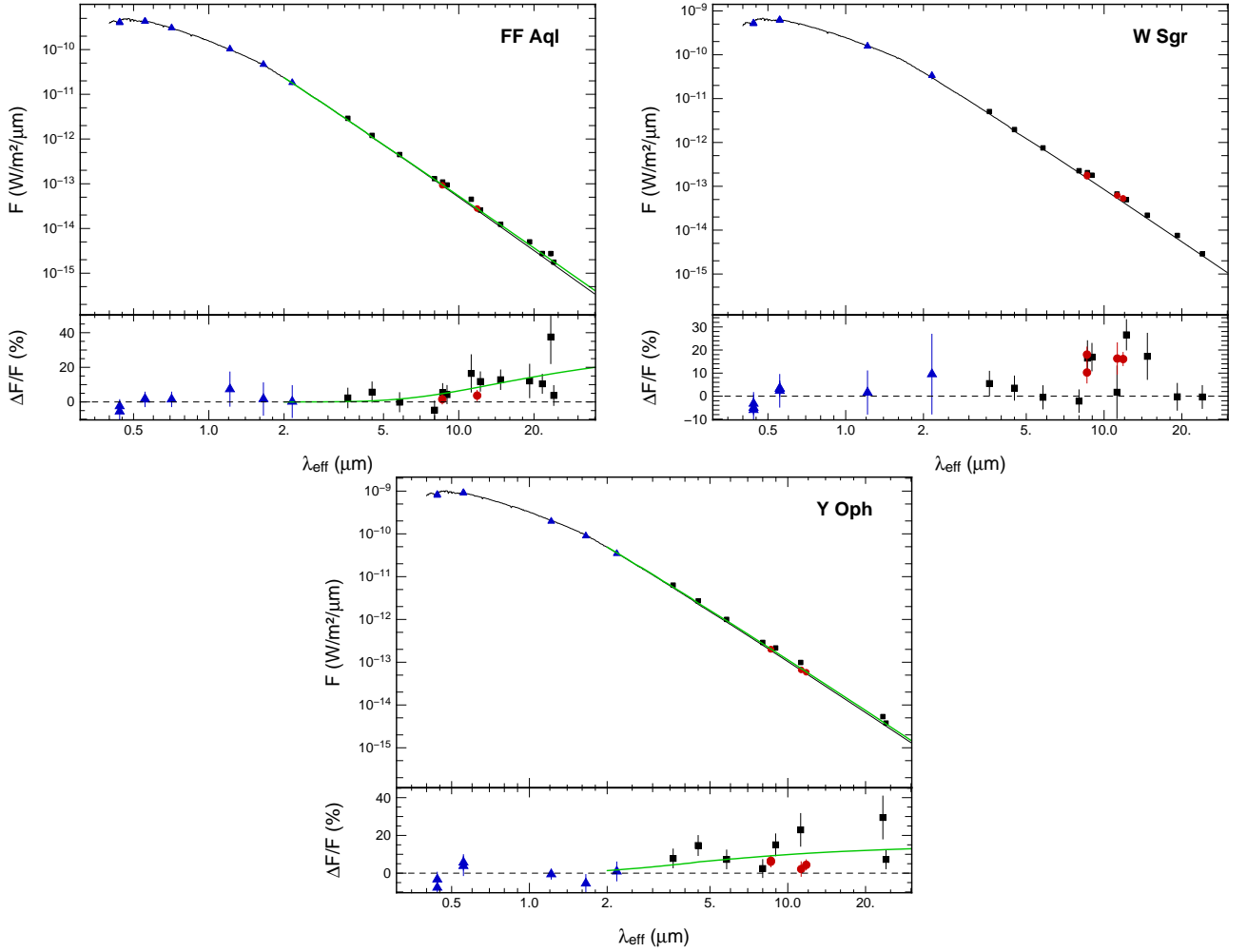


Fig. 1. Synthetic spectra of the classical Cepheid FF Aql, W Sgr and Y Oph (solid line) with the photometric measurements taken from the literature. The blue triangles are the points used to fit the SED. Our measurements are presented with the red circles while the black squares are the other photometric data. On the lower panel is plotted the excess flux density relatively to the photospheric emission. The green curve represents the greybody model.

3.2 W Sgr

The B and V photometry are from Kervella et al. (2004) and Berdnikov (2008). The other irradiances are from *DENIS* (J, K_s), *Spitzer* (3.6, 4.5, 5.8, 8 and $24 \mu\text{m}$ from Marengo et al. 2010), *IRC* (9 and $18 \mu\text{m}$), *MSX* (8.28, 12.13, 14.65, $21.34 \mu\text{m}$) and the $12 \mu\text{m}$ photometry from *IRAS*. The SED is plotted in Fig. 1.

Our fitted effective temperature $T_{\text{eff}} = 5623 \pm 162 \text{ K}$ is in agreement at a 2% level with $T_{\text{eff}} = 5535 \pm 51 \text{ K}$ from Luck & Andrievsky (2004) around the same phase with an effective gravity from the same author of 1.7. We found an angular diameter $\theta_{\text{LD}} = 1.14 \pm 0.06 \text{ mas}$ that is about 15% and 1.7σ smaller than the one measured by interferometry by Kervella et al. (2004) ($1.31 \pm 0.04 \text{ mas}$) at this phase of pulsation. Conversely our estimate is in agreement with the mean diameter from Bersier et al. (1997) who found $\theta_{\text{LD}} = 1.17 \pm 0.11 \text{ mas}$ based on photometry. However Kervella et al. (2004) used a limb darkened diameter to model their data and the presence of an extended emission could overestimate the angular diameter.

Spitzer's values are consistent with the blackbody radiation adjusted by Marengo et al. (2010). However our *VISIR* photometry shows an excess of $\pm 15\%$. The same trend is observed from *IRC* (at $9 \mu\text{m}$) and *MSX* (at 8.28, 12.13 and $14.65 \mu\text{m}$). This could be an evidence of a particular dust composition.

Table 1. Fitted parameters of the $\Psi(\nu, \rho_\lambda, \alpha_\lambda)$ function.

Stars	Filter	ρ (")	α (%)
W Sgr	PAH1	1.14 ± 0.39	3.8 ± 0.6
	PAH2	1.19 ± 0.37	9.1 ± 1.5
	SiC	1.03 ± 0.50	8.3 ± 2.4
Y Oph	PAH1	0.71 ± 0.12	15.1 ± 1.4
	PAH2	1.02 ± 0.52	7.5 ± 2.3
	SiC	0.54 ± 0.46	6.2 ± 4.1

3.3 Y Oph

We retrieved the B, V data from Berdnikov (2008) and Moffett & Barnes (1984). The J, H, K photometry is from Laney & Stoble (1992) and Kervella et al. (2004). The plot of the spectral energy distribution is shown in Fig. 1. The other fluxes are from *Spitzer* (3.6, 4.5, 5.8, 8 and 24 μm from Marengo et al. 2010), *IRC* (9 μm) and the 12 μm and 25 μm photometry from *IRAS*.

The best fitted parameters are $\theta_{\text{LD}} = 1.24 \pm 0.05$ mas and $T_{\text{eff}} = 5870 \pm 387$ K with $\log g \sim 1.8$ (Luck et al. 2008). Luck et al. (2008) also give an effective temperature at our phase of $T_{\text{eff}} = 5800 \pm 148$ K that is in good agreement with our value. Our fitted angular diameter and the value $\theta_{\text{LD}} = 1.24 \pm 0.01$ mas measured by Mérand et al. (2007) at this phase of pulsation is also good.

We detected a likely infrared emission from our *VISIR* measurements. This result is consistent with Mérand et al. (2007) where a CSE has been found around this star in the K band with a relative contribution of $5.0 \pm 2.0\%$. The greybody model of Equ. 3.1 was fitted for wavelengths larger than 3 μm . The best-fitted parameters are $T_{\text{d}} = 1009 \pm 183$ K and $\beta = 1.39 \pm 0.23$ mas². Y Oph seems to have a hot circumstellar envelope that could be located close to the star and heated by its radiations.

4 Spatially resolved emission

We search for spatially extended emission using a Fourier technique, similar in its principle to the calibration technique used in long baseline interferometry. This method was already used and validated by Kervella et al. (2009); Kervella & Domiciano de Souza (2006). The principle is to divide the Fourier transform modulus of the image of the Cepheid (I_{cep}) by that of the calibrator image (I_{cal}) to obtain a calibrated visibility function $\Psi(\nu_x, \nu_y)$, with (ν_x, ν_y) denoting the angular spatial frequencies.

We then compute the ring median of Ψ , i.e. the median for a given spatial frequency radius ν over all azimuths (where $\nu^2 = \nu_x^2 + \nu_y^2$). The function $\Psi(\nu)$ obtained is equivalent to a visibility in interferometry. The error bars on Ψ were estimated by the quadratic sum of the dispersion of the PSF calibrator's Fourier modulus over the night and the rms dispersion of the calibrated Ψ function over all azimuth directions for each spatial frequency. A deviation from a central symmetry will not be detected and any departure will be included in the error bars.

Defining a model of a point-like star surrounded by a Gaussian shaped CSE and taking its Fourier transform, it is possible to retrieve the CSE intensity distribution. This type of model was already used by Kervella et al. (2009) and Kervella & Domiciano de Souza (2006) with the $\Psi(\nu)$ function

$$\Psi(\nu, \rho_\lambda, \alpha_\lambda) = \frac{1}{1 + \alpha_\lambda} \left[1 + \alpha_\lambda \exp \left(-\frac{(\pi \rho_\lambda \nu)^2}{4 \ln 2} \right) \right]$$

where the Gaussian CSE is defined with a FWHM ρ_λ and a relative flux $\alpha_\lambda = f_{\text{cse}}(\lambda)/f_\star(\lambda)$, i.e the ratio of the flux of the envelope to the photospheric flux. We set $V_\star = 1$ since the star is unresolved by *VISIR*.

We applied the fit using a classical χ^2 minimization to all the final images. We did not detect spatially resolved emission for FF Aql. For W Sgr and Y Oph that show a resolved component, the fitted parameters are presented in Table 1 with the Ψ function plotted in Fig. 2.

For FF Aql, an upper limit of ~ 265 mas can be set for the extension of the CSE based on the telescope resolution.

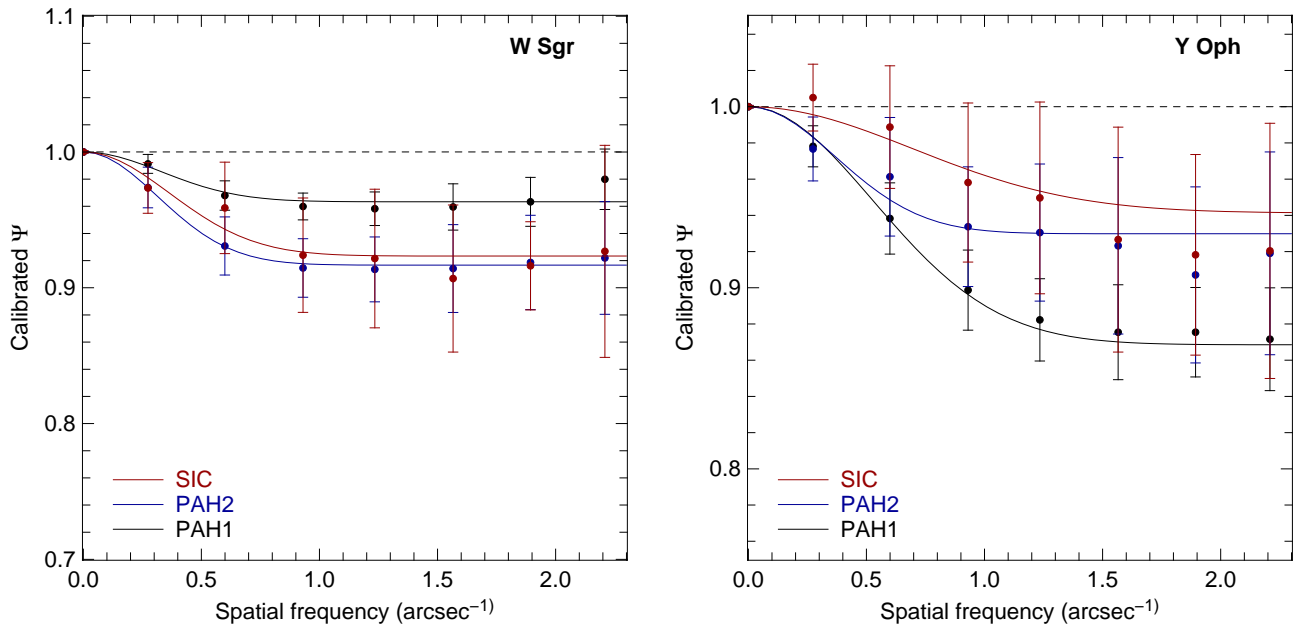


Fig. 2. Fit of a Gaussian CSE + unresolved point source model to the Ψ functions of our Cepheids. The dashed curve is here for a reference as an unresolved star.

5 Conclusions

We presented new thermal IR photometry and spectral energy distributions of 3 classical Cepheids. We detected infrared excess around all of them. This confirms that the presence of circumstellar material around Classical Cepheids is a widespread phenomenon. The origin of these CSEs is not well understood. Their presence could be linked to mass loss from the star. It has been suggested that the IR excess is caused by dust formed in a wind from the Cepheids (Kervella et al. 2006). From a radiative-driven wind model including pulsation and shock effects Neilson & Lester (2008) concluded that radiative driving is not sufficient to account for the observed IR excesses and proposed that the mass loss could be driven by shocks generated in the atmosphere by the pulsation of the star. Other observational evidences were provided with IR excess detections from *IRAS* observations by Deasy (1988) who estimated mass loss rates ranging from 10^{-10} to $10^{-6} M_{\odot} \text{ yr}^{-1}$.

Mérand et al. (2007) showed for the classical Cepheids a likely correlation between the pulsation period and the CSE flux (relative to the photosphere) in the *K* band. We found the same trend at $8.6 \mu\text{m}$, in which the longer periods have larger excesses. However a larger sample of Cepheids is needed to confirm this correlation.

The current status of high angular resolution observations indicate that CSEs are present around all Cepheids, and that the brightness of these envelopes is increasing with the pulsation period of the star. The nature of these envelopes is currently unknown. However, several observation techniques, over a broad range of wavelengths, have the potential to bring new informations about their composition and the mechanisms about their creation. For Cepheids, the CSEs represent a potential source of bias for the distance scale. Their contribution in the infrared could significantly affect the calibrations of the Period-Luminosity relations, as they are often based on the infrared surface brightness variant of the Baade-Wesselink method.

We received the support of PHASE, the high angular resolution partnership between ONERA, Observatoire de Paris, CNRS, and University Denis Diderot Paris 7. This work made use of the SIMBAD and VIZIER astrophysical database from CDS, Strasbourg, France and the bibliographic informations from the NASA Astrophysics Data System. Data processing for this work have been done using the Yorick language which is freely available at <http://yorick.sourceforge.net/>. This research is based on observations with AKARI, a JAXA project with the participation of ESA.

References

- Berdnikov, L. N. 2008, VizieR Online Data Catalog: II/285, originally published in: Sternberg Astronomical Institute, Moscow, 2285
- Bersier, D., Burki, G., & Kurucz, R. L. 1997, *A&A*, 320, 228

- Castelli, F. & Kurucz, R. L. 2003, in IAU Symposium, Uppsala University, Sweden, Vol. 210, Modelling of Stellar Atmospheres, ed. N. Piskunov, W. W. Weiss, & D. F. Gray (ASP), 20
- Cohen, M., Walker, R. G., Carter, B., et al. 1999, AJ, 117, 1864
- Deasy, H. P. 1988, MNRAS, 231, 673
- Egan, M. P. & Price, S. D. 1996, AJ, 112, 2862
- Egan, M. P., Price, S. D., Kraemer, K. E., et al. 2003, VizieR Online Data Catalog: V/114. Originally published in: Air Force Research Laboratory Technical Report AFRL-VS-TR-2003-1589 (2003), 5114, 0
- Fouqué, P., Arriagada, P., Storm, J., et al. 2007, A&A, 476, 73
- Fouqué, P., Storm, J., & Gieren, W. 2003, in Stellar Candles for the Extragalactic Distance Scale, ed. D. Alloin & W. Gieren, Vol. 635, 21–44
- Gallenne, A., Mérand, A., Kervella, P., & Girard, J. H. V. 2011, A&A, 527, A51
- Groenewegen, M. A. T. 2007, A&A, 474, 975
- Helou, G. & Walker, D. W., eds. 1988, IRAS catalogue, Vol. 7 (STI)
- Hindsley, R. B. & Bell, R. A. 1989, ApJ, 341, 1004
- Ishihara, D., Onaka, T., Kataza, H., et al. 2010, A&A, 514, A1
- Kervella, P., Bersier, D., Mourard, D., et al. 2004, A&A, 428, 587
- Kervella, P. & Domiciano de Souza, A. 2006, A&A, 453, 1059
- Kervella, P. & Domiciano de Souza, A. 2007, A&A, 474, L49
- Kervella, P., Mérand, A., & Gallenne, A. 2009, A&A, 498, 425
- Kervella, P., Mérand, A., Perrin, G., & Coudé Du Foresto, V. 2006, A&A, 448, 623
- Laney, C. D. & Stobie, R. S. 1993, MNRAS, 260, 408
- Laney, C. D. & Stobie, R. S. 1992, A&AS, 93, 93
- Luck, R. E. & Andrievsky, S. M. 2004, AJ, 128, 343
- Luck, R. E., Andrievsky, S. M., Fokin, A., & Kovtyukh, V. V. 2008, AJ, 136, 98
- Marengo, M., Evans, N. R., Barmby, P., et al. 2010, ApJ, 709, 120
- Mérand, A., Aufdenberg, J. P., Kervella, P., et al. 2007, ApJ, 664, 1093
- Moffett, T. J. & Barnes, III, T. G. 1984, ApJS, 55, 389
- Neilson, H. R., Cantiello, M., & Langer, N. 2010a, ArXiv e-prints
- Neilson, H. R. & Lester, J. B. 2008, ApJ, 684, 569
- Neilson, H. R., Ngeow, C., Kanbur, S. M., & Lester, J. B. 2010b, ApJ, 716, 1136
- Ngeow, C., Kanbur, S. M., Nikolaev, S., Tanvir, N. R., & Hendry, M. A. 2003, ApJ, 586, 959
- Schütz, O. & Sterzik, M. 2005, in High Resolution Infrared Spectroscopy in Astronomy, ed. H. U. Käuffl, R. Siebenmorgen, & A. Moorwood, Proceedings of an ESO Workshop held at Garching, Germany, 104–108
- Welch, D. L., Wieland, F., McAlary, C. W., et al. 1984, ApJS, 54, 547

SPEC3D: A THREE-DIMENSIONAL RADIATIVE TRANSFER CODE FOR ASTROPHYSICAL AND LABORATORY APPLICATIONS

L. Ibgui¹, I. Hubeny², T. Lanz³ and C. Stehlé¹

Abstract. We have developed a generic three-dimensional radiative transfer code, SPEC3D, aimed at post-processing 3D radiation magnetohydrodynamics simulations. SPEC3D solves the monochromatic 3D radiative transfer equation. The numerical approach and the major features of the code are presented. The wide range of applications includes the modeling of a number of astrophysical objects and structures, such as accretion shocks around young stellar objects, stellar and exoplanets atmospheres, cosmological structures, but also the modeling of laboratory astrophysics experiments such as magnetohydrodynamics jets and radiative shocks.

Keywords: radiative transfer, quantitative spectroscopy, methods: numerical, laboratory astrophysics, shock waves

1 Introduction

Radiation is a major component of many astrophysical objects. First, radiation is a probe of the physical state: the medium is analyzed through the observed spectra. Second, radiation is often strong enough to have a significant contribution to the momentum and energy budget of the medium.

With the considerable progress in computing power, it is now possible to build three-dimensional numerical models that couple the contributions of fluid dynamics, radiation, and magnetic field (if strong enough). Many 3D radiation hydrodynamics or radiation magnetohydrodynamics codes have been developed over the past few years. The treatment of radiative transfer is simplified, since such models consider the moments of the specific intensity and some kind of a closing relation between them. On the other hand, an efficient code that solves the monochromatic radiative transfer equation (RTE) is required, either to provide exact closing relations for the radiation hydrodynamics, or, more importantly, in order to compute radiation for snapshots of hydrodynamic simulations, and thus to provide a tool to analyze the physical properties of a radiating object. Several three-dimensional radiative transfer codes have been developed over the last few years (see Carlsson 2009 for a review).

We present here a generic 3D radiative transfer code, SPEC3D. We assume local thermodynamic equilibrium (LTE), and consider the time-independent form of the RTE. In § 2, we describe the formal solution solver, which applies the short-characteristics method (Kunasz & Auer 1988) in a 3D Cartesian grid, and which is coupled with efficient piecewise cubic Bezier interpolations (Auer 2003). Other features of the code are summarized in § 3. We finally present a first application to the modeling of radiative shocks experiments in § 4, which is relevant to the understanding of accretion shocks in classical T Tauri Stars.

2 3D short-characteristics

2.1 Overview of the method

The short-characteristics method can be summarized as follows. We consider a grid for which the thermophysical properties (temperature, density, velocity) are known from a prior (magneto)hydrodynamics simulation. We use

¹ LERMA, Observatoire de Paris, CNRS, UMPIC, 5, place J.Janssen, 92195 Meudon Cedex, France

² Department of Astronomy, Steward Observatory, The University of Arizona, 933 N.Cherry Ave, Tucson, AZ 85721-0065, USA

³ Department of Astronomy, University of Maryland, College Park, MD 20742-2421, USA

the integral form of the formal solution of the RTE as described hereafter. For a given direction of propagation, we consider each ray that emerges from each point of the grid. There is one ray per grid point per direction. We determine the intersection of each ray with the closest face of the corresponding upwind cubic cell. The line segment joining the intersection point with the grid point is called the short-characteristic (SC). The integral form of the RTE is then solved along this short-characteristic. There is one short-characteristic per grid point per direction. Fig. 1 shows an example of a short-characteristic defined in a 3D cartesian grid. We want to determine in the observer's frame the specific intensity in point 2 for a direction defined by polar angle θ and azimuthal angle φ . Point 1 is the intersection of the considered ray with the upwind cubic cell. We call it upwind endpoint. The short-characteristic is here defined by the line segment joining point 1 and point 2.

Let us introduce the following notations. $I(\mathbf{r}, \mathbf{n}, \nu, t)$ is the specific intensity at position \mathbf{r} for a radiation propagating in direction \mathbf{n} with frequency ν , at time t . Let us note $\chi(\mathbf{r}, \mathbf{n}, \nu, t)$ the absorption coefficient, and ds the elementary path length along the direction of propagation \mathbf{n} . The optical depth from position s_1 to position s_2 may be written as

$$\tau_{12} = \tau_{s_1 \rightarrow s_2} = \int_{s_1}^{s_2} \chi(\mathbf{r}, \mathbf{n}, \nu, t) ds \quad (2.1)$$

Let us note $I_2 = I(\mathbf{r}_2, \mathbf{n}, \nu, t)$ and $I_1 = I(\mathbf{r}_1, \mathbf{n}, \nu, t)$. The integral form of the RTE may be written along the short-characteristic joining point 1 to point 2, as

$$I_2 = I_1 e^{-\tau_{12}} + \int_0^{\tau_{12}} S(\tau) e^{-(\tau_{12}-\tau)} d\tau \quad (2.2)$$

where $S(\tau)$ is the source function $S(\mathbf{r}, \mathbf{n}, \nu, t)$.

Therefore, we can infer the specific intensity at point 2 if we know the following quantities: the specific intensity in point 1, I_1 , the source function along the short-characteristic from point 1 to point 2, and the absorption coefficient along the short-characteristic (in order to deduct the optical depth between point 1 and point 2). However, by the very nature of the problem, the source function and the absorption coefficients are specified only at the grid points. Therefore, we are essentially free to define laws of variation of these quantities along the short-characteristics, typically as low-order polynomials. Moreover, the following quantities at the upwind endpoint (point 1), intensity I_1 , optical depth τ_1 , and source function S_1 , have to be interpolated from the values in the neighbor grid points. We detail in next subsection the mathematical functions that we have adopted.

2.2 Cubic Bezier interpolations

Because of the numerous required interpolations, the short-characteristics method is known to be numerically diffusive, whether linear or second order polynomial laws be employed. Therefore, an efficient interpolation law has to be adopted. Following a suggestion by Auer (2003), we adopt Bezier cubic interpolation laws with specific adjustments.

The Bezier cubic interpolant is a polynomial of degree 3, $B(x)$, which is defined between two values of a given function $f(x)$, (x_1, f_1) and (x_2, f_2) , so that it matches the values of the function at both ends, $B(x_1) = f_1$ and $B(x_2) = f_2$, and whose derivatives at both ends, $B'(x_1)$ and $B'(x_2)$ are free values to be adjusted depending on the context. Now, we introduce a constraint of monotonicity to $B(x)$, in order to ensure its positivity between the extremal points x_1 and x_2 . This results in a range of permitted values for the derivative on the left end, $B'(x_1)$, and for the derivative on the right end, $B'(x_2)$. We choose to match the derivatives at both ends with the derivatives of the function, $B'(x_1) = f'_1$ and $B'(x_2) = f'_2$, if possible, i.e., as long as the monotonicity of the interpolant $B(x)$ is guaranteed. Such a procedure suppresses the spurious extrema encountered with a parabolic interpolation law, while ensuring a much better fit to the interpolated function than a linear or a quadratic law could provide.

Going back to the short-characteristics method, the Bezier cubic interpolant is used as an approximate of the source function between the upwind endpoint 1 and point 2 (see Fig. 1). Now, if one knows the source function value at only two points, S_1 and S_2 , then the only possibility to estimate the derivatives at both ends is to assume that they are identical and that they equal the value of the slope of the line that joins S_1 and S_2 ; one can then show that Bezier interpolant reduces to linear interpolation. It is therefore necessary, in order to increase the precision of the interpolation, to define a third point along the short-characteristic defined by point 1 and point 2. This is why we define the downwind endpoint, point 3, which is the intersection of this short-characteristic with the downwind cubic cell. Therefore, it is possible to specify a Bezier cubic interpolant

between point 1 and point 2, by defining the derivative at point 1 as the slope of the line that joins point 1 and point 2. Several possibilities exist for the estimate of the derivative at point 2, using the values at points 1, 2 and 3. The same procedure is applied for the determination of the absorption coefficient along the short-characteristic. More details will be available in a forthcoming paper.

Another issue is the determination of the physical quantities at point 1 and point 3, which are generally not grid points. To this end, we define Bezier cubic interpolants on the edges of the intersected face. Note that, while the source function and the absorption coefficients are known at each point of the grid, the specific intensity is known only in the upwind cubic cells of the current grid point that is being processed. Therefore, the sweeping of the grid must follow the direction of propagation of the radiation, to ensure that the upwind specific intensities are known before we determine the new specific intensity at a given grid point. Again, more details will soon be available in a forthcoming paper.

3 SPEC3D: major features

We have developed and validated (specifically with comparisons with well-tested 1D codes) a radiative transfer code, called SPEC3D, that determines the monochromatic formal solution of the radiative transfer equation in a three-dimensional geometry. It applies the short-characteristics method with cubic Bezier interpolations, as summarized in the preceding section. We have incorporated the possibility to define periodic boundary conditions. The user can also specify pre-defined boundary conditions. We take into account the Doppler shift of the lines. Based on the determination of the monochromatic specific intensity at each point of the grid and for each direction, the code uses Gaussian quadratures to determine the resulting moments, the mean intensity $J(\nu, x, y, z)$, the flux vector in the three directions, $F_x(\nu, x, y, z)$, $F_y(\nu, x, y, z)$, $F_z(\nu, x, y, z)$, and the six components of the radiation pressure tensor P_{xx} , P_{yy} , P_{zz} , P_{xy} , P_{xz} , P_{yz} , which all depend on (ν, x, y, z) .

4 Applications of SPEC3D

SPEC3D is a generic radiative transfer code that can be applied to simulate numerous astrophysical objects and structures, e.g., accretion shocks around young stellar objects, stellar and exoplanets atmospheres, cosmological structures. It can also be used to simulate experiments relevant to astrophysics such as magnetohydrodynamics jets and radiative shocks.

We show here a simulation of an experimental radiative shock. Such studies are an important step toward a correct modeling of spectroscopic signatures of accretion shocks in classical T Tauri Stars (Stehlé et al. 2010). Fig. 2 shows the monochromatic radiative flux in the direction of propagation of the shock, z -direction, $F_z(x, y, z, \nu)$, as calculated by SPEC3D. The radiative shock is generated in a tube full of Xenon, with a rectangular section of $1 \times 1 \text{ cm}^2$, and with the following upstream conditions: fluid velocity = 60 km s^{-1} , pressure = 7 bar, temperature = 1 eV. The lateral walls have a zero albedo: the photons can freely escape from these walls. SPEC3D post processes the hydrodynamics results provided by Matthias González* and generated by the three-dimensional radiation hydrodynamics code HERACLES (González et al. 2007). The fluid is assumed to be ideal. The objective here is to show the 3D effects of the radiation. Realistic simulations with real gas effects will be shown in a forthcoming paper (L. Ibgui, M. González et al. 2011, in preparation). The absorption coefficients are derived from an opacity database, which is based on the Screened Hydrogenic Model (Eidmann 1994; Michaut et al. 2004).

Left panel of Fig. 2 represents the flux F_z along z -axis at the center of the sections perpendicular to z -axis, for a frequency ν corresponding to an energy of $h\nu = 296 \text{ eV}$: $F_z(x = 0.5 \text{ cm}, y = 0.5 \text{ cm}, z, h\nu = 296 \text{ eV})$. The red curve represents the 3D model and the blue curve represents the 1D model (for a 1D model, the flux is obviously the same one at any point of a given section perpendicular to z -axis). The position of the hydrodynamics shock is $z = 0.10 \text{ cm}$. The radiative precursor is distinctly identified in the upstream gas (González et al. 2009 show typical profiles of a 1D radiative shock). This figure clearly reveals the difference between a 1D model and a 3D model. The maximum value of the flux F_z , reached at around $z = 0.12 \text{ cm}$, is smaller when the 3D model is applied (7.3 versus $7.7 \text{ erg}^{-1} \text{ cm}^{-2} \text{ Hz}^{-1}$) and the flux's extension in z -direction is smaller when the 3D model is applied. This is due to the lateral radiative losses, which are taken into account by SPEC3D. This result underlines the fact that a radiative shock cannot be correctly understood without considering a 3D radiative transfer model. This is also naturally a critical point for the modeling of accretion columns in T Tauri stars.

*AIM, CEA/DSM/IRFU, CNRS, Université Paris Diderot, 91191 Gif-sur-Yvette, France

Right panel of Fig. 2 represents the flux F_z at a given position in the radiative precursor $z = 0.22$ cm, $F_z(x, y, z = 0.22 \text{ cm}, h\nu = 296 \text{ eV})$. A behavior of the flux, whose value decreases as one approaches the borders, due to lateral radiative losses, is another manifestation of a 3D nature of radiative shocks.

5 Conclusions

We have presented a new generic three-dimensional radiative transfer code, SPEC3D, that solves the monochromatic 3D radiative transfer equation in Cartesian coordinates. Currently, we assume local thermodynamic equilibrium (LTE), and a time-independent situation, but both these simplifications will be removed in the future development of the code. We have employed the 3D short-characteristics method, known to be faster than the long-characteristics method, combined with performant cubic Bezier interpolation techniques.

We have shown a preliminary application to the modeling of laboratory generated radiative shocks. We have demonstrated the necessity to account for the 3D radiative transfer in 3D radiative shock structures.

We intend to apply our code to a large variety of astrophysical objects and structures, such as accretion shocks around young stellar objects, stellar and exoplanet atmospheres, cosmological structures, but also for laboratory astrophysics to study magnetohydrodynamics jets and radiative shocks.

The authors are grateful to Matthias González (AIM, CEA/DSM/IRFU, CNRS, Université Paris Diderot, 91191 Gif-sur-Yvette, France) for providing the 3D hydrodynamics results of the ideal gas shock wave simulation, which were used as an input for the radiative transfer code SPEC3D. The work is supported by French ANR, under grant 08-BLAN-0263-07.

References

- Auer, L. 2003, in *Astronomical Society of the Pacific Conference Series*, Vol. 288, *Stellar Atmosphere Modeling*, ed. I. Hubeny, D. Mihalas, & K. Werner, 3
- Carlsson, M. 2009, *Mem. Soc. Astron. Italiana*, 80, 606
- Eidmann, K. 1994, *Laser and Particle Beams*, 12, 223
- González, M., Audit, E., & Huynh, P. 2007, *A&A*, 464, 429
- González, M., Audit, E., & Stehlé, C. 2009, *A&A*, 497, 27
- Kunasz, P. & Auer, L. H. 1988, *Journal of Quantitative Spectroscopy and Radiative Transfer*, 39, 67
- Michaut, C., Stehlé, C., Leygnac, S., Lanz, T., & Boireau, L. 2004, *European Physical Journal D*, 28, 381
- Stehlé, C., González, M., Kozlova, M., et al. 2010, *Laser and Particle Beams*, 28, 253

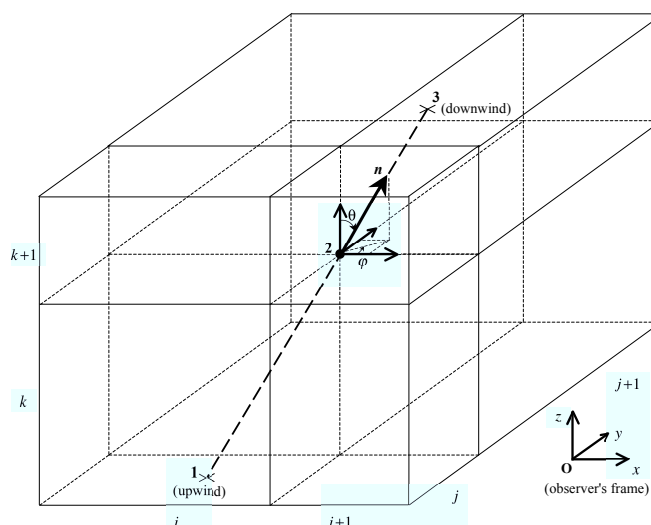


Fig. 1. The short-characteristics method illustrated with an example of a 3D cartesian grid. The specific intensity is calculated in point 2, for a radiation propagating from point 1 (upwind endpoint) to point 3 (downwind endpoint). The direction \mathbf{n} of the ray is defined by polar angle θ and azimuthal angle φ . The short-characteristic is defined by the line joining point 1 and point 2. The radiative transfer equation is solved in its integral form along this short-characteristic. The cell numbers around point 2 are $i, i+1$ in x -direction, $j, j+1$ in y -direction, and $k, k+1$ in z -direction.

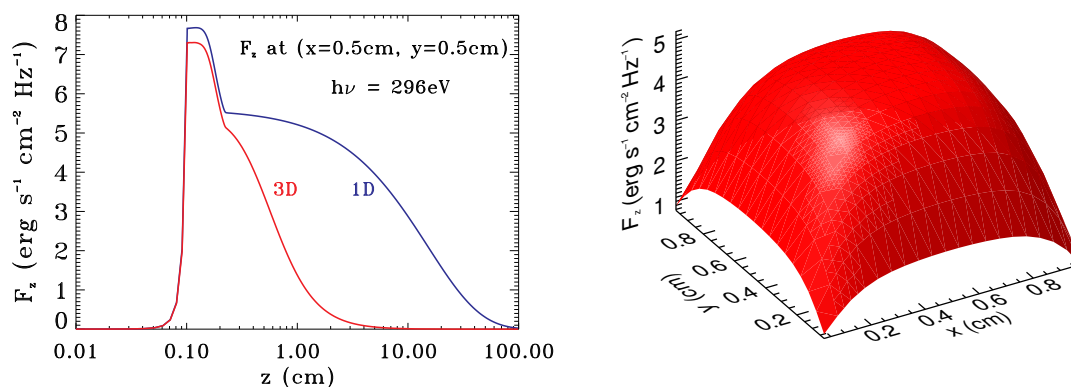


Fig. 2. Left: Monochromatic radiative flux in z -direction, $F_z(x=0.5\text{ cm}, y=0.5\text{ cm}, z, h\nu=296\text{ eV})$, at the center of the planes perpendicular to z -axis, emitted by a radiative shock propagating in z -direction. It is a pure Xenon flow in a cell with a rectangular section of $1 \times 1\text{ cm}^2$. The hydrodynamics simulation makes the assumption of an ideal gas, with the following upstream conditions: fluid velocity = 60 km s^{-1} , pressure = 7 bar, temperature = 1 eV. We display the results of two hydrodynamics and radiative transfer models: the one-dimensional model is depicted by the blue curve, the three-dimensional model is represented by the red curve. See text for comments. **Right:** The same monochromatic radiative flux, but at a given z -position, $F_z(x, y, z=0.22\text{ cm}, h\nu=296\text{ eV})$. The 3D effects are clearly demonstrated by a non-constant behavior of the flux, which is due to lateral radiative losses.

ANGULAR MOMENTUM TRANSPORT IN STELLAR INTERIORS

S. Mathis¹

Abstract. In this short article we review the advances that have been obtained in the global modelling of angular momentum transport in stellar interiors during the last years. First, we consider the couplings between differential rotation and the large-scale meridional circulation and shear-induced turbulence this induces. Then, we describe the state of the art of our understanding of transport mechanisms in presence of a fossil magnetic field. Next, we show how rotation and magnetic fields are now taken into account in the study of internal waves. Finally, we emphasize that it becomes necessary to get a complete picture of the interaction of stars with their environment.

Keywords: MHD, turbulence, stars: evolution, stars: rotation, stars: magnetic fields

1 Context

Stars are dynamical rotating and magnetic objects. So, rotation and magnetic fields modify their evolution as well as their interactions with their environment. For example, differential rotation induces "non-standard" mixing processes, which modify their life time, their late stages of evolution, their nucleosynthetic properties and the resulting chemical enrichment of the close interstellar medium. Since, more and more observational constraints are obtained thanks to asteroseismology, interferometry, and spectropolarimetry, it is thus necessary to construct stellar models that account for transport processes both on dynamical and secular time-scales. This short article addresses the most recent progresses that have been achieved for the modelling of secular exchanges of angular momentum in stellar interiors. Therefore, we focus on mechanisms acting in stellar radiation zones while the reader could refer to Brun (2011) for a review on dynamical time-scales and on convective regions.

2 Differential rotation and associated large-scale meridional circulation and shear-induced turbulence

The first processes that should be understood are the differential rotation and the associated large-scale meridional circulation and shear-induced turbulence. A global understanding of their couplings have been obtained in Deressin et al. (2009). First, viscous turbulent transport, stellar winds, and structural adjustments induce meridional currents. Then, these latter advect heat that leads to latitudinal gradients of temperature. Because of the associated baroclinic torque, a new differential rotation profile is built which can be understood looking at the so-called thermal-wind equation and the transport loop is closed. However, these three mechanisms, if applied to the Sun and low-mass stars, are unable to reproduce the angular velocity profile of the radiative core of the Sun and the light elements mixing (Turck-Chièze et al. 2010; Talon & Charbonnel 2005). Therefore, other processes such as magnetic fields or internal waves excited by penetrative convection or tides if there is a close companion must be studied.

3 Magnetic fields

The main admitted hypothesis for magnetic field origin in stellar radiation zones is the one of a fossil field. Fossil fields are thus believed to originate from the trapping of the interstellar magnetic field flux during star formation. If the initial field is a small-scale turbulent field, we have to understand and predict the topology of the resulting field after the birth of the radiative region, which impacts the angular momentum transport. As

¹ Laboratoire AIM, CEA/DSM-CNRS-Université Paris Diderot, IRFU/SAP, F-91191 Gif-sur-Yvette Cedex, France; stephane.mathis@cea.fr

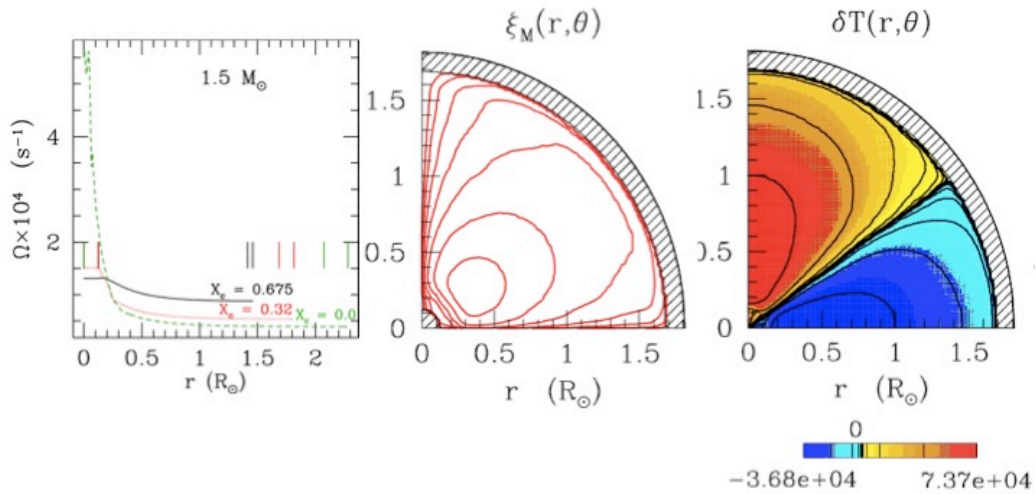


Fig. 1. Evolution of a rotating $1.5 M_\odot$ star with a solar metallicity and an initial surface velocity of 100 km.s^{-1} . **Left:** the angular velocity profile is given for different stages of the evolution of the star on its main-sequence; X_c is the central fraction of mass in Hydrogen. **Middle:** Stream lines of the meridional circulation for $X_c = 0.32$; the red color indicates that the circulation is extracting angular momentum towards the surface where it is carried by the stellar wind. **Right:** Baroclinic temperature profile at the same stage. (Adapted from Decressin et al. (2009)).

described in Neiner, Alécian & Mathis and in Duez contributions in this proceeding, this problem is related to the turbulent MHD relaxation processes, in which a turbulent magnetic field is converted into a large-scale one due to a selective decay of the ideal MHD invariants. The case of high-beta stellar radiation zone plasmas has been studied both theoretically (Duez & Mathis 2010) and numerically (Braithwaite & Spruit 2004; Braithwaite & Nordlund 2006; Braithwaite 2008). Resulting non force-free relaxed states minimize the total energy for given magnetic helicity and fluid invariants due to the stable stratification of stellar radiation zones. Roughly axisymmetric dipolar twisted configurations are obtained if the initial magnetic energy is confined near the center (Braithwaite & Nordlund 2006; Duez & Mathis 2010) while one obtains non-axisymmetric fields in the case where this is distributed in the whole radiation zone (Braithwaite 2008). The field is then organized on large-scale, mixed (poloidal and toroidal), non force-free configurations, which are stable as it has been demonstrated by Braithwaite (2009) and Duez et al. (2010).

Once the initial non force-free magnetic configuration (axi or non-axisymmetric) has been established, this interacts with differential rotation. Then, two cases are possible as described by Spruit (1999). In the first case, if the field is strong, the rotation becomes uniform on magnetic surfaces due to Alfvén waves phase mixing, which damps the differential rotation; in the axisymmetric case this leads to the Ferraro’s state where the angular velocity is frozen in the poloidal field lines and to a uniform rotation in the non-axisymmetric case (the oblique rotators case for example; see Moss 1992). In the second case, if the field is weak, it could first become axisymmetric if it is non-axisymmetric because of rotational smoothing and then, because of phase mixing, this leads to the Ferraro’s state (Strugarek et al. 2011). This picture could be modified by magnetic instabilities, if during the first step of the phase mixing, the residual differential rotation on each magnetic surface is able to generate a strong toroidal component of the field that becomes unstable and if this instability becomes able to trigger a dynamo action through an α -effect; this question remains open (Zahn et al. 2007). Let us now take into account the meridional circulation. To understand its interaction with the other dynamical processes (the differential rotation and the shear induced turbulence) in presence of a fossil magnetic field, we shall adopt the picture of rotational transport as described in §2. and generalise it to the magnetic case. As in the purely hydrodynamical case, meridional circulation in radiation zones are driven by applied torques (internal like the Lorentz torque or external like those induced by stellar winds), structural adjustments during stellar evolution, and turbulent transport. In the case where all these sources vanish, the meridional circulation dies after an Eddington-Sweet time and the star settles in a baroclinic state described by the thermal wind equation. If we apply this picture to the case of radiation zones with a fossil magnetic field, we thus understand that the meridional circulation (if we consider a star without structural adjustments and external torques) will be mainly driven by the residual magnetic torque until the phase mixing leads the star to a torque-free state (see fig. 2). Then, the meridional circulation advection of angular momentum balances the residual Lorentz torque (see Mestel et al. 1988; Mathis

& Zahn 2005).

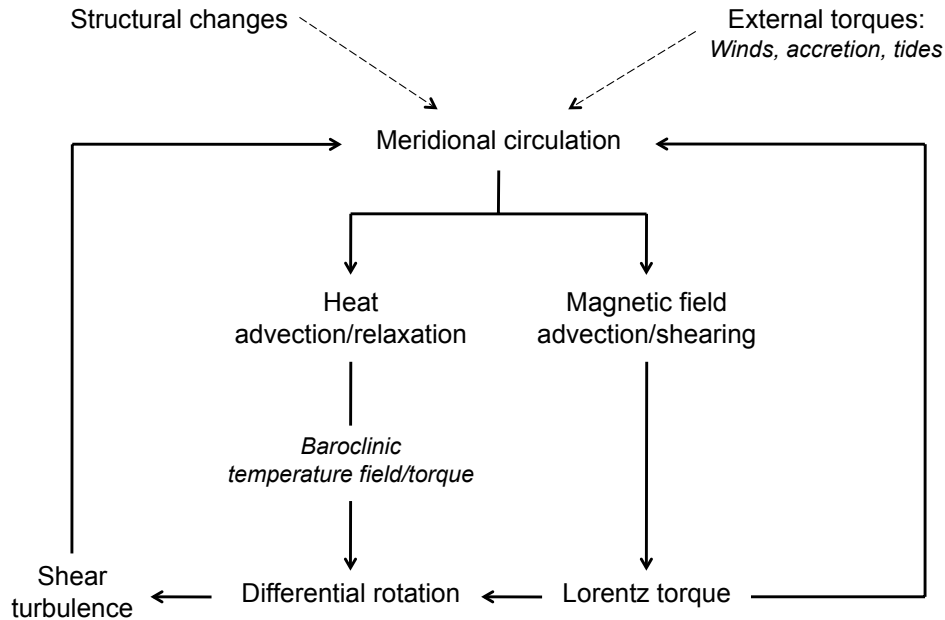


Fig. 2. Transport loop in stellar radiation zones in presence of large-scale magnetic fields.

4 Internal waves

The last transport mechanism that should be studied is the action of internal waves propagating in stably stratified radiation zones and which are excited by turbulent convective flows at the radiation/convection borders. Indeed, these transport angular momentum (of same sign of the energy flux for prograde waves and of the opposite one for retrograde waves), which is deposited where waves are dissipated because of diffusion processes or where these reach their critical layers where their frequency is proportional to the local angular velocity (see Alvan & Mathis in this proceeding). Then, if differential rotation is initially present, a net flux of angular momentum is transported because of the Doppler effect that affects the respective diffusive damping rates acting on pro- and retrograde waves. This transport, combined with the strong horizontal shear-induced turbulence is therefore seen as a candidate to explain the observed quasi uniform rotation rate of the solar radiative core as well as the mixing in low-mass stars (Talon & Charbonnel 2005). However, progresses should be obtained in the description of waves excitation by turbulent convection and on the impact of rotation and magnetic fields on waves structure, dissipation and associated transport of angular momentum.

This is the reason why the modification of their structure and dissipation by the (differential) rotation has been studied with taking into account the Coriolis acceleration (Mathis et al. 2008; Mathis 2009). Then, depending on the ratio between excited frequencies (σ_c) and the inertial frequency (2Ω , where Ω is the angular velocity), waves are propagating at all latitudes in the super-inertial regime ($\sigma_c > 2\Omega$) while these are trapped in an equatorial belt below a given critical latitude in the sub-inertial one ($\sigma_c < 2\Omega$) (see fig. 3 in the general case of a given differential rotation). This thus modifies the transmission of the energy coming from turbulent convective flows which may be thus reduced in this latter. Moreover, the thermal diffusion is enhanced and waves are thus damped close to their excitation region. This leads, combined with the equatorial trapping, to a weaker efficiency of the angular momentum transport as soon as the ratio $\sigma_c/2\Omega$ diminishes.

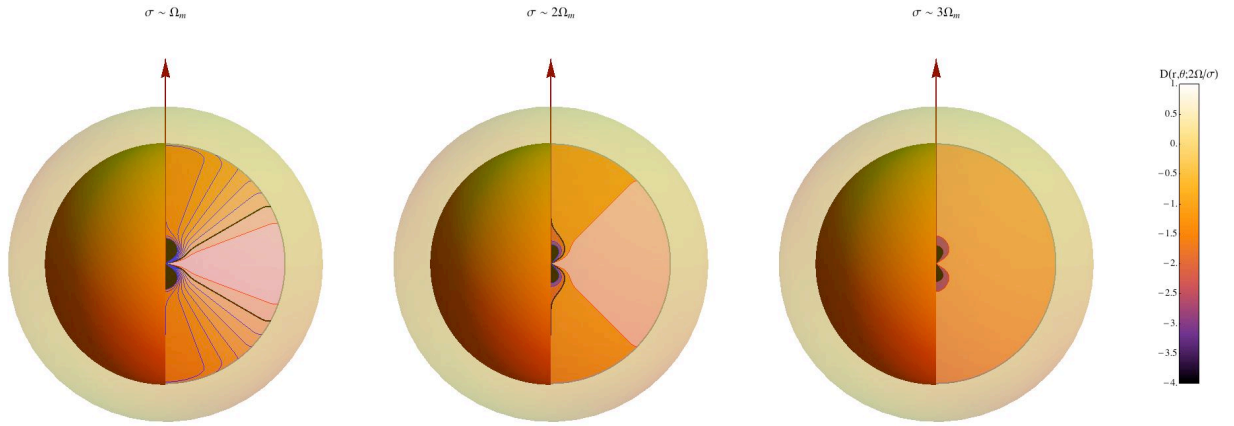


Fig. 3. We consider here a solar-twin star with an external convective envelope and a radiative core. The rotation profile in this latter is flat (i.e. $\Omega = \Omega_m$) for $r \in [0.2R, 0.7R]$, where R is the stellar radius. In the central region, Ω increases until $\Omega = 5\Omega_m$ in the center. Finally, at the radiation/convection border we choose the same differential rotation that in the Solar tachocline. Regions with reds contours correspond to those where waves are propagative while polar and central regions with blue contours correspond to "dead" zones for waves propagation. We choose three frequencies ($\sigma = \{\Omega_m, 2\Omega_m, 3\Omega_m\}$) that shows that for frequency below $2\Omega_m$ equatorial trapping phenomena appear. The black line corresponds to the critical surface (the critical latitude in the case of uniform rotation) at the level of which the wave propagation regime changes. The central region is always a non-propagative region because of the central rapid rotation. D is a function of σ , Ω , and the gradients of Ω . Its definition is given in Mathis (2009).

Then, the bottom of convective envelopes in solar-type stars as well as the top of convective cores in massive stars are the seat of dynamo action. For example, the tachoclines are believed to be the place of the large-scale toroidal magnetic field storage (Browning et al. 2006). Moreover, as it has been discussed in §3., stellar radiation zones may host fossil magnetic fields. We thus have to also account for the magnetic field action on internal waves dynamics, which become Magneto-Gravito-Inertial waves because of the three restoring forces: i.e. the buoyancy force, the Coriolis acceleration, and the Lorentz force. The first studies have been devoted to the case of waves dynamics with an axisymmetric toroidal field (Mathis & de Brye 2011). In this case, waves become vertically trapped as soon as $1 - m^2 \omega_A^2 / \sigma_c^2 < 0$, where we introduce the Alfvén frequency ω_A and the wave azimuthal order m . Moreover, waves are submitted to the same equatorial trapping phenomenon that in the hydrodynamical case of gravito-inertial waves. The main difference in the magnetic case is that this trapping due to the combined action of the Coriolis acceleration and the Lorentz force is different for pro- and retrograde waves because of this latter. Then, the horizontal trapping of prograde waves is stronger than those of retrograde waves. Finally, waves thermal diffusion become stronger as soon as magnetic field amplitude increases. The efficiency of the induced transport of angular momentum is thus a function of the rotation and of the magnetic field amplitude as shown in fig. 4. This decreases as soon as vertical and horizontal trappings modifies waves dynamics, with a net bias in favor of retrograde waves.

5 Coupling the star with its environment

As it has been emphasized in previous sections, applied torques on stars modify internal transport processes; for example these generate large-scale meridional circulations. Therefore, one must get a coherent physical modeling of the interaction of the star with its environment when treating its rotational evolution. First, stellar winds must be carefully studied as a function of the stars rotation rate and their magnetic field topology and amplitude (see for example Pinto et al. 2011). Furthermore, if stars host a planetary system, the coupling with the protoplanetary disk (Matt & Pudritz 2005) as well as tidal interactions should be taken into account. For this latter, the equilibrium tide associated to the hydrostatic adjustment of the star to the tidal excitation leads to a net torque applied on the external convective envelopes of solar-type stars (Zahn 1966), while internal waves are excited by the tidal potential at the radiation/convection borders and are able to transport angular momentum in the same way that those excited by the turbulent penetrative convection (this is the dynamical tide; see Zahn 1975).

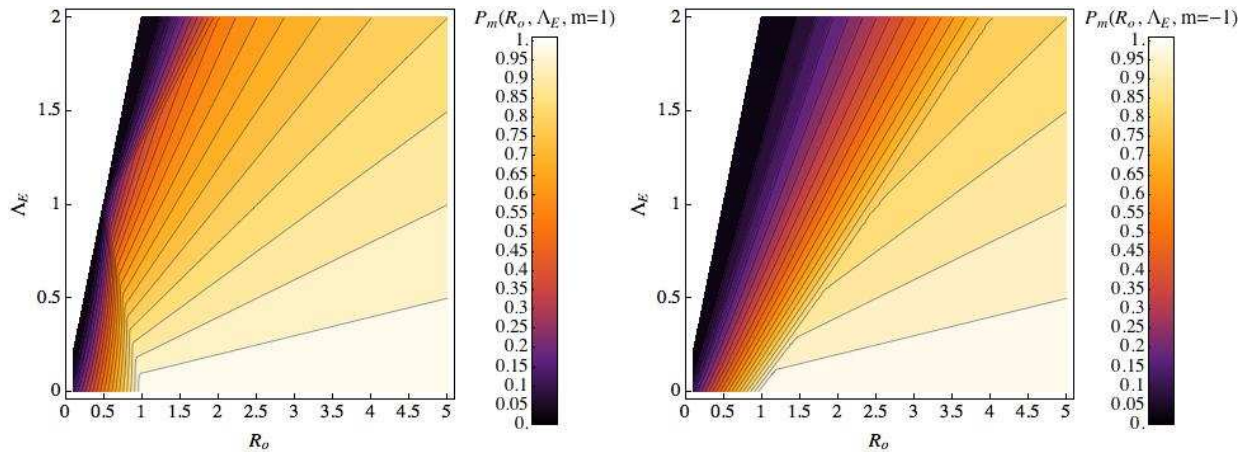


Fig. 4. Efficiency of the transmission of energy coming from convective regions to internal waves as a function of their Rossby and Elsasser numbers ($R_o = \frac{\sigma_c}{2\Omega}$, $\Lambda_E = \frac{\omega_A^2}{\sigma_c \Omega}$) for a given couple of retrograde ($m = 1$) and prograde ($m = -1$) waves.

We acknowledge PNPS (CNRS/INSU) for the constant support to this work.

References

- Braithwaite, J. 2008, MNRAS, 386, 1947
 Braithwaite, J. 2009, MNRAS, 397, 763
 Braithwaite, J. & Nordlund, Å. 2006, A&A, 450, 1077
 Braithwaite, J. & Spruit, H. C. 2004, Nature, 431, 819
 Browning, M. K., Miesch, M. S., Brun, A. S., & Toomre, J. 2006, ApJ, 648, L157
 Brun, A. S. 2011, in EAS Publications Series, Vol. 44, EAS Publications Series, ed. H. Wozniak & G. Hensler, 81–95
 Decressin, T., Mathis, S., Palacios, A., et al. 2009, A&A, 495, 271
 Duez, V., Braithwaite, J., & Mathis, S. 2010, ApJ, 724, L34
 Duez, V. & Mathis, S. 2010, A&A, 517, A58+
 Mathis, S. 2009, A&A, 506, 811
 Mathis, S. & de Beye, N. 2011, A&A, 526, A65+
 Mathis, S., Talon, S., Pantillon, F.-P., & Zahn, J.-P. 2008, Sol. Phys., 251, 101
 Mathis, S. & Zahn, J.-P. 2005, A&A, 440, 653
 Matt, S. & Pudritz, R. E. 2005, ApJ, 632, L135
 Mestel, L., Tayler, R. J., & Moss, D. L. 1988, MNRAS, 231, 873
 Moss, D. 1992, MNRAS, 257, 593
 Pinto, R. F., Brun, A. S., Jouve, L., & Grappin, R. 2011, ApJ, 737, 72
 Spruit, H. C. 1999, A&A, 349, 189
 Strugarek, A., Brun, A. S., & Zahn, J.-P. 2011, A&A, 532, A34+
 Talon, S. & Charbonnel, C. 2005, A&A, 440, 981
 Turck-Chièze, S., Palacios, A., Marques, J. P., & Nghiem, P. A. P. 2010, ApJ, 715, 1539
 Zahn, J. P. 1966, Annales d’Astrophysique, 29, 489
 Zahn, J.-P. 1975, A&A, 41, 329
 Zahn, J.-P., Brun, A. S., & Mathis, S. 2007, A&A, 474, 145

LONG-TERM MAGNETIC MONITORING OF 19 SUN-LIKE STARS

A. Morgenthaler^{1,2}, P. Petit^{1,2}, J. Morin³, M. Aurière^{1,2} and B. Dintrans^{1,2}

Abstract. A sample of 19 Sun-like stars, probing masses between 0.7 and 1.4 solar mass and rotation rates between 1 and 3 solar rotation rate, was regularly observed using the NARVAL spectropolarimeter at Telescope Bernard Lyot (Pic du Midi, France) since 2006. The data sets enable us to monitor the rotational and long-term evolution of indirect activity indicators such as the width of several magnetically-sensitive spectral lines, the radial velocities, the line asymmetry of intensity line profiles and the chromospheric emission in the cores of the Ca II H and H α lines. In the same time, the Zeeman-Doppler Imaging allowed us to study the reconstructed large-scale photospheric magnetic field. I will present the main results of this monitoring, which includes the observations of several polarity reversals and magnetic cycles, and the highlight of links between some of our computed quantities and some fundamental parameters of the stars.

Keywords: stars: atmospheres - stars: low-mass - stars: magnetic field - stars: solar-type

1 Introduction

Sun-like stars are characterized by convective envelopes in which large-scale plasma flows (related, in particular, to radial and latitudinal differential rotation and to the Coriolis force) are able to trigger a global dynamo (Parker 1955). This continuous generation of a large-scale field is related to surface variability affecting a wide range of temporal and spatial scales, including quasi-periodic polarity reversals associated to magnetic cycles. Recent numerical models, in particular global MHD simulations, are able to mimic some characteristics of this cyclic behavior for Sun-like stars (Ghizaru et al. 2010; Brown et al. 2011). In addition to numerical computations, spectropolarimetry now enables us to perform direct measurements of surface magnetic fields and follow the long-term temporal evolution of large-scale magnetic geometries. So far, it allowed the observation in Sun-like stars of one global polarity switch (Petit et al. 2009) and of a full magnetic cycle (Fares et al. 2009).

Our aim is to study the long-term variations of the magnetic field properties of a sample of solar-type stars. Our observed sample includes 19 FGK-type stars on the main sequence, monitored since 2007. We probe here stellar masses between 0.6 and 1.4 solar mass, and rotation periods between 3.4 and 43 days.

After a brief description of the instrumental setup, data reduction and multi-line extraction of Zeeman signatures, we explain the reconstruction technique of the large-scale topology of the stars. We then highlight three representative examples of different types of variability observed in our sample. We finally discuss the results derived from our measurements.

2 Instrumental setup, data reduction, and extraction of the Zeeman signatures

We use data from the NARVAL spectropolarimeter (Aurière 2003), installed at Telescope Bernard Lyot (Pic du Midi, France). The instrumental setup is strictly identical to the one described by Petit et al. (2008). The spectrograph unit of NARVAL benefits from a spectral resolution of 65,000 and covers the whole wavelength domain from near-ultraviolet (370 nm) to near-infrared (1,000 nm). Thanks to the polarimetric module, NARVAL can provide intensity, circularly or linearly polarized spectra. In the present study, we restrict the measurements to Stokes V.

¹ Université de Toulouse, UPS-OMP, Institut de Recherche en Astrophysique et Planétologie, Toulouse, France

² CNRS, Institut de Recherche en Astrophysique et Planétologie, 14 Avenue Edouard Belin, F-31400, Toulouse, France

³ Dublin Institute for Advanced studies, School of Cosmic Physics, 31 Fitzwilliam Place, Dublin 2, Ireland

The circularly polarized spectra allow the detection of large-scale photospheric magnetic fields, thanks to the Zeeman effect. However, when observing cool dwarfs, the signal-to-noise ratio of circularly polarized spectra produced by NARVAL is not sufficiently high to reach the detection threshold of typical Zeeman signatures (which amplitude does not exceed $10^{-4}I_c$ for low-activity stars, where I_c is the continuum intensity). To solve this problem, we calculate from the reduced spectrum a single, cross-correlated photospheric line profile using the Least-Squares-Deconvolution (LSD) multi-line technique (detailed by Donati et al. 1997; Kochukhov et al. 2010). Thanks to the large number of available photospheric lines in cool stars (several thousands in the spectral domain of NARVAL), the noise level is reduced by a factor of about 30 with respect to the initial spectrum.

3 Magnetic mapping

To reconstruct the surface magnetic geometry of the stars, we use the technique of Zeeman-Doppler Imaging (ZDI). This tomographic inversion technique is based on the modelling of the rotational modulation of the circularly polarized signal (Semel 1989). The time series of polarized signatures are iteratively compared to artificial profiles corresponding to a synthetic magnetic geometry, until the best fit is obtained between the model and the observations (Donati & Brown 1997; Donati et al. 2006). ZDI enables to recover, to some extent, the location of magnetic regions, as well as the strength and orientation of the magnetic vector in magnetic spots. The application of this technique to cool stars with low $v \sin i$ is described by Petit et al. (2008). The resulting maps for the three stars presented here are illustrated in Fig. 1, 2 and 3.

4 Results

Since the monitoring began a few years ago, long-term changes in the magnetic properties become observable in some of our targets. The magnetic quantities derived from ZDI exhibit temporal fluctuations over a wide range of timescales, due to rotational modulation and longer-term magnetic trends. Three representative examples of the different kinds of stellar variability we observed is described hereafter.

4.1 Short magnetic cycle : HD 78366

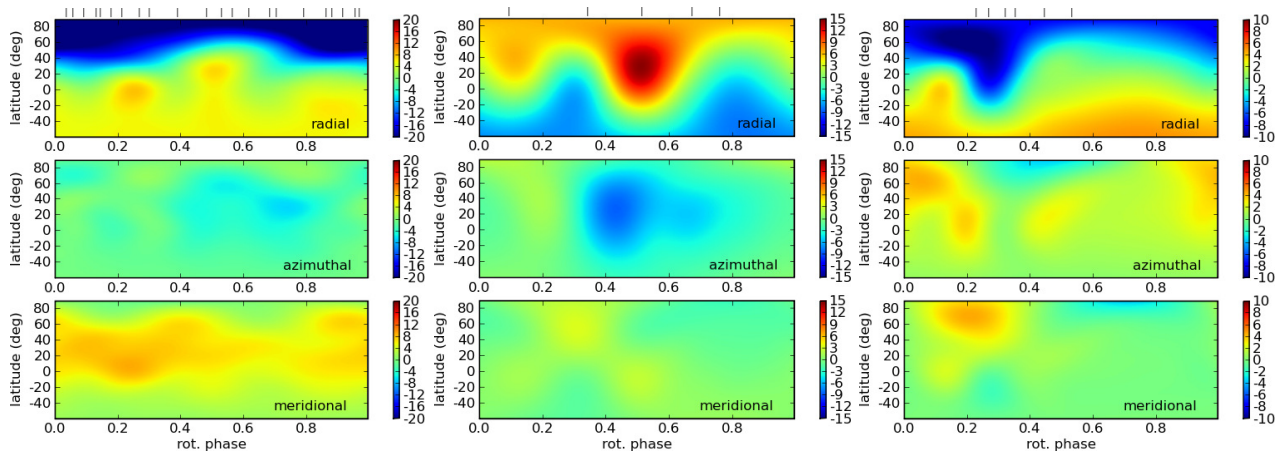


Fig. 1. Magnetic maps of HD 78366, derived from 2008.09, 2010.04 and 2011.08 observations (from left to right). For each data set, the 3 charts illustrate the field projection onto one axis of the spherical coordinate frame with, from top to bottom, the radial, azimuthal, and meridional field components. The magnetic field strength is expressed in Gauss.

A simple type of variability is observed for HD 78366. This target is slightly more massive than the Sun and rotates about two times faster. The data sets of this object are collected over three distant seasons. The corresponding magnetic maps are shown in Fig. 1. We observe two polarity switches, especially visible in the polar area of the radial field component, which is of negative polarity in 2008.09, positive in 2010.04 (and associated at that time with a more complex magnetic field geometry), and negative again in 2011.08. After the two observed polarity reversals, the magnetic field retrieves its initial configuration. Assuming that the magnetic variability of this star is not much faster than the temporal sampling imposed by the right ascension

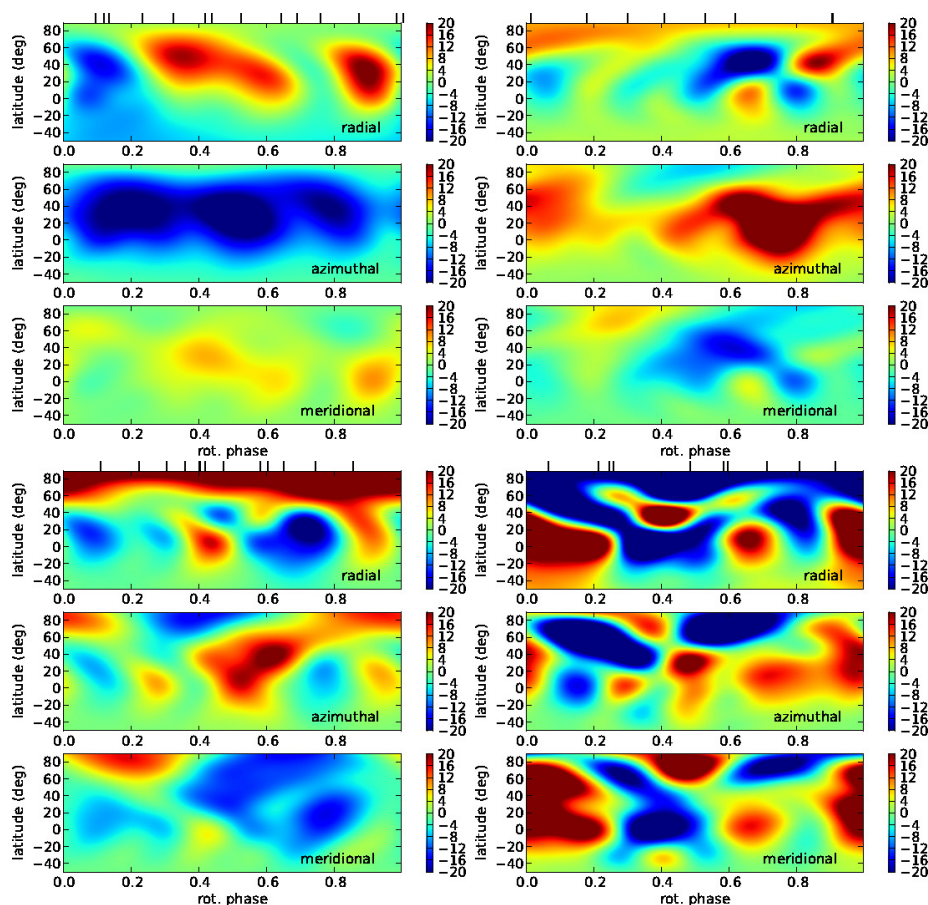


Fig. 2. Same as Fig. 1 for HD 190771, for 2007.59, 2008.67, 2009.47 and 2010.50 data sets (from left to right and top to bottom).

of the star (visible only during winters), this first time-series suggests that HD 78366 may obey to a magnetic cycle of about three years.

4.2 Fast polarity reversals : HD 190771

A more complex type of variability is illustrated by HD 190771. It has a mass similar to the Sun's, but has a rotation period of 8.8 days. In Fig. 2, we plot the magnetic maps derived for this star. A polarity reversal is visible on the strong azimuthal component between 2007.59 and 2008.67 (Petit et al. 2009). Between 2008.67 and 2009.47, the magnetic geometry changed in a different manner : the magnetic field which was mainly toroidal in 2008.67 became mostly poloidal in 2009.47. A second polarity reversal took place between 2009.47 and 2010.50, this time on the radial field component. In this case, the two successive polarity switches do not imply that the initial magnetic state is reached again, so that the observed variability is not taking the form of a cycle.

4.3 Fast and complex variability : ξ Bootis A

Finally, another, more complex type of variability is observed with ξ Boo A, the less massive and most rapidly rotating star of our three examples. It was observed at seven epochs, for which the magnetic field geometry was derived (Morgenthaler et al. 2011). Here we highlight two results of this long-term monitoring.

The first one refers to the 2007.59 and 2008.09 data sets (top part of Fig. 3). We observe that within a six months interval, the intensity of the magnetic field decreased by about 50% and that the magnetic geometry, which was quite simple in 2007.59 with an aligned dipole and a prominent ring of azimuthal field, became more complex and less axisymmetric in 2008.09, with a less pronounced toroidal surface component.

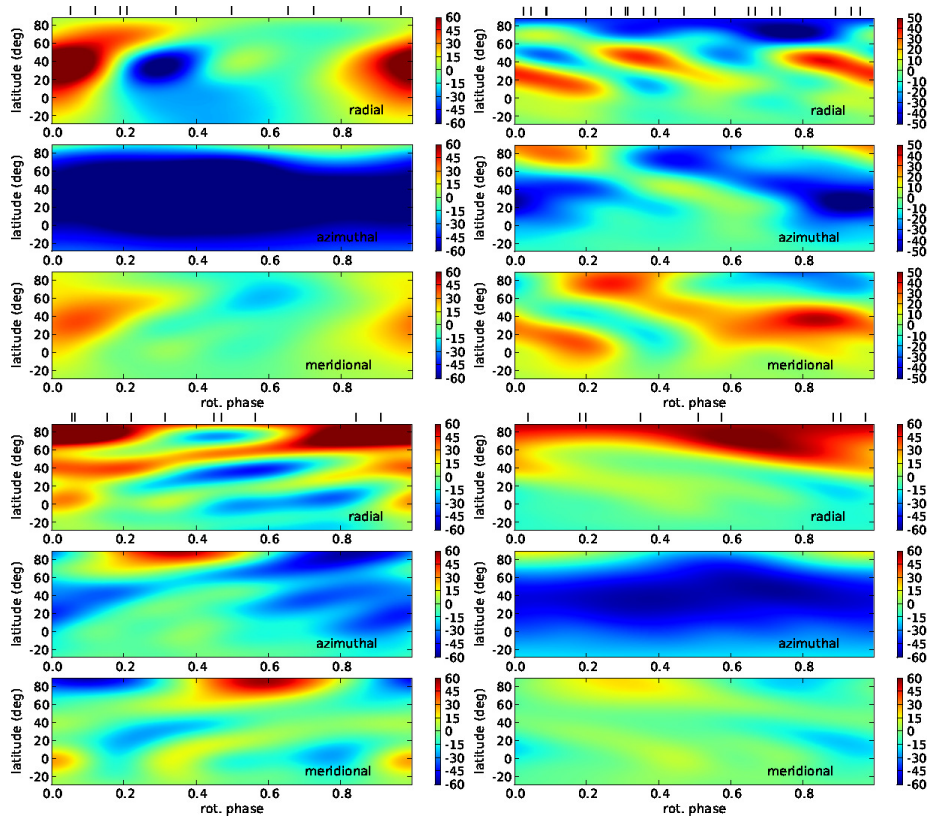


Fig. 3. Same as Fig. 1 for ξ Bootis A, for 2007.59, 2008.09, 2010.48 and 2010.59 data sets (from left to right and top to bottom).

The second example is visible in the set of observations collected during the summer of 2010, which we decided to split in two subsets (2010.48 and 2010.59) to take into account the fast variations of the Zeeman signatures over this short timespan. In the corresponding magnetic maps (bottom part of Fig. 3), the most striking evolution is a sharp increase of the azimuthal magnetic field.

ξ Boo A is therefore submitted to fast and complex surface changes that are different from those of the two previous stars, and reminiscent of the complex behavior of other rapid rotators observed in the past (e.g. Donati et al. 2003).

5 Discussion

All stars of our sample show variability over the four years of our monitoring, but of different types. Stars which show at least one field reversal over this timespan have in common a fast rotation period (at least twice the solar one) and masses equal or slightly larger than that of the Sun. We note that the solar-type star τ Bootis, which is not part of our sample but which is reported to be affected by a short magnetic cycle of two years at most (Fares et al. 2009), shares also these mass and rotation properties. We stress also that active stars with masses below our lower mass boundary (in particular, mid-M dwarfs with masses just below the fully convective limit) are reported to possess strong, simple and stable surface magnetic fields (Morin et al. 2008a,b).

τ Boo and HD 78366 were also observed at Mount Wilson as chromospherically active stars. For τ Boo, Baliunas et al. (1995) report a cycle of twelve years, versus two years from spectropolarimetry. Concerning HD 78366, periods of six and twelve years were identified using the Mount Wilson time-series, against about three years in our investigation. We therefore note that, at least for these two examples, the cycle lengths derived by chromospheric activity seem to be longer than those derived by spectropolarimetry. We suggest that this apparent discrepancy may be linked to the different temporal sampling inherent to the two approaches, so that the sampling adopted at Mount Wilson may not be sufficiently tight to unveil short activity cycles.

Future observations of our target list will allow us to investigate longer timescales of the stellar magnetic

evolution. The sample includes several solar twins (Petit et al. 2008) which have not shown cycles yet, and which will help us to determine how small departures from the solar fundamental parameters may affect the characteristics of magnetic cycles. More generally, a regular monitoring of our targets over more than one decade will enable us to determine more precisely the relation between the length/occurrence of magnetic cycles and the rotation/mass of Sun-like stars.

This research made use of the POLLUX database (<http://pollux.graal.univ-montp2.fr>) operated at LUPM (Université Montpellier II - CNRS, France, with support of the PNPS and INSU). We are grateful to the staffs of TBL for their efficient help during the many nights dedicated to this observing project.

References

- Aurière, M. 2003, in EAS Publications Series, Vol. 9, EAS Publications Series, ed. J. Arnaud & N. Meunier, 105–+
- Baliunas, S. L., Donahue, R. A., Soon, W. H., et al. 1995, *ApJ*, 438, 269
- Brown, B. P., Miesch, M. S., Browning, M. K., Brun, A. S., & Toomre, J. 2011, *ApJ*, 731, 69
- Donati, J. & Brown, S. F. 1997, *A&A*, 326, 1135
- Donati, J., Semel, M., Carter, B. D., Rees, D. E., & Collier Cameron, A. 1997, *MNRAS*, 291, 658
- Donati, J.-F., Collier Cameron, A., Semel, M., et al. 2003, *MNRAS*, 345, 1145
- Donati, J.-F., Howarth, I. D., Jardine, M. M., et al. 2006, *MNRAS*, 370, 629
- Fares, R., Donati, J., Moutou, C., et al. 2009, *MNRAS*, 398, 1383
- Ghizaru, M., Charbonneau, P., & Smolarkiewicz, P. K. 2010, *ApJ*, 715, L133
- Kochukhov, O., Makaganiuk, V., & Piskunov, N. 2010, *A&A*, 524, A5+
- Morgenthaler, A., Petit, P., Saar, S., et al. 2011, *ArXiv*
- Morin, J., Donati, J.-F., Forveille, T., et al. 2008a, *MNRAS*, 384, 77
- Morin, J., Donati, J.-F., Petit, P., et al. 2008b, *MNRAS*, 390, 567
- Parker, E. N. 1955, *ApJ*, 122, 293
- Petit, P., Dintrans, B., Morgenthaler, A., et al. 2009, *A&A*, 508, L9
- Petit, P., Dintrans, B., Solanki, S. K., et al. 2008, *MNRAS*, 388, 80
- Semel, M. 1989, *A&A*, 225, 456

EVIDENCE FOR DYNAMO BISTABILITY AMONG VERY LOW MASS STARS

J. Morin¹, X. Delfosse², J.-F. Donati³, E. Dormy⁴, T. Forveille², M. M. Jardine⁵, P. Petit³ and M. Schrunner⁴

Abstract. Dynamo action in fully convective stars is a debated issue that also questions our understanding of magnetic field generation in partly convective Sun-like stars. During the past few years, spectropolarimetric observations have demonstrated that fully convective objects are able to trigger strong large-scale and long-lived magnetic fields. We present here the first spectropolarimetric study of a sample of active late M dwarfs (M5-M8) carried out with ESPaDOnS@CFHT. It reveals the co-existence of two distinct types of magnetism among stars having similar masses and rotation rates. A possible explanation for this unexpected discovery is the existence of two dynamo branches in this parameter regime, we discuss here the possible identification with the weak *vs* strong field bistability predicted for the geodynamo.

Keywords: dynamo, stars: magnetic fields, stars: low-mass, planets and satellites: magnetic fields, techniques: spectropolarimetry

1 Introduction

In cool stars, which possess a convective envelope, magnetism is thought to be constantly regenerated against ohmic decay by dynamo effect. For Sun-like stars the interface layer between the inner radiative zone and the outer convective envelope is generally thought to play a major role in the dynamo processes (see e.g., Charbonneau 2010). Since fully-convective stars – either main sequence stars below $0.35 M_{\odot}$ (i.e. with spectral type later than $\sim M4$) or young T Tauri stars – do not possess such an interface layer, generation of magnetic field in their interiors is often thought to rely on a non-solar-type dynamo. However, the precise mechanism and the properties of the resulting magnetic have been a debated issue (Durney et al. 1993; Chabrier & Küker 2006; Dobler et al. 2006; Browning 2008).

Two main complementary approaches are successfully applied to study magnetic fields close to the fully-convective transition. On the one hand, by modelling Zeeman broadening of photospheric spectral lines it is possible to assess the magnetic field averaged over the visible stellar disc (e.g., Reiners & Basri 2006). This method is therefore able to probe magnetic fields regardless of their complexity but provides very little information about the field geometry. On the other hand, the Zeeman-Doppler imaging technique models the evolution of polarization in spectral lines during at least one rotation period in order to reconstruct a map of the large-scale component of the vector magnetic field on the stellar photosphere.

Spectropolarimetric studies of a sample of M0–M4 dwarfs, conducted with ESPaDOnS and NARVAL, have revealed for the first time a strong change in large-scale magnetic topologies occurring close to the fully-convective boundary. Stars more massive than $0.5 M_{\odot}$ exhibit large-scale fields of moderate intensity featuring a significant toroidal component and a strongly non-axisymmetric poloidal component, with evolution happening on a timescale of less than 1 yr (Donati et al. 2008, D08). For those in the range 0.25 – $0.50 M_{\odot}$ much stronger large-scale fields are observed, which are dominated by the axial dipolar component and show only very limited evolution over successive years (Morin et al. 2008a,b, M08a,b). Comparisons of these large-scale magnetic field

¹ Dublin Institute for Advanced Studies, School of Cosmic Physics, 31 Fitzwilliam Place, Dublin 2, Ireland

² Université. J. Fourier (Grenoble 1)/CNRS; Laboratoire d’Astrophysique de Grenoble (LAOG, UMR 5571); F-38041 Grenoble, France

³ IRAP-UMR 5277, CNRS & Univ de Toulouse, 14 av E Belin, F-31400

⁴ MAG (ENS/IPGP), LRA, Ecole Normale Supérieure, 24 Rue Lhomond, 75252 Paris Cedex 05, France

⁵ School of Physics and Astronomy, Univ. of St Andrews, St Andrews, Scotland KY16 9SS, UK

measurements with X-ray activity indices or with measurements of the total magnetic field (i.e. at all spatial scales) derived from the analysis of Zeeman broadening of FeH molecular lines, suggest that fully-convective stars are much more efficient at generating large-scale magnetic field than partly-convective ones (D08, Reiners & Basri 2009).

2 Surface magnetic fields of late M dwarfs

A sample of 11 active M dwarfs with masses significantly below the fully-convective boundary ($0.08 < M_{\star} < 0.21 M_{\odot}$ or spectral types M5–M8) has been observed with the ESPaDOnS spectropolarimeter (Morin et al. 2010, hereafter M10). Below $0.15 M_{\odot}$, we observe two radically different categories of large-scale magnetic fields: either a strong and steady almost dipolar field (hereafter SD, similar to stars in the range 0.15 – $0.5 M_{\odot}$); or a weaker multipolar, non-axisymmetric field configuration undergoing dramatic evolution on a timescale of at most 1 yr (hereafter WM). However the two groups of objects cannot be separated in a mass-rotation diagram, see Fig. 1. No object is observed to evolve from one type of magnetism to the other during the survey (some objects were observed for 4 years). In terms of large-scale magnetic field values, a gap exists between these two types of magnetism, with no object with $200 < B_V < 900 G$ in this mass range, see Fig. 3. Both stars hosting weak multipolar (WM) or strong dipolar (SD) fields have very strong total magnetic fields (2–4 kG). No systematic correlation is found between the type of large-scale magnetic topology and the total magnetic field B_I (see Fig. 2). Hence, the two different types of magnetic field configurations are only detected when considering the large-scale component (probed by spectropolarimetry, and which represents 15–30 % of the total flux in the SD regime, but only a few percent in the WM regime) and not the total magnetic flux derived from unpolarised spectroscopy. This unexpected observation may be explained in several different ways: for instance, another parameter than mass and rotation period (such as age) may be relevant, two dynamo modes may be possible or stars may switch between two states in this mass range, etc.

3 Weak and strong field dynamos: from the Earth to the stars

In this section we briefly detail one of the hypothesis that could explain the observation of two groups of late M dwarfs with very different magnetic properties: the fact that two different dynamo modes could genuinely operate in stars having very similar mass and rotation. We focus here on the weak *vs* strong field dynamo bistability, initially proposed for the geodynamo. The underlying idea is that both, magnetic fields and rotation, taken separately tend to inhibit convection, but that if both effects are combined the impeding influences of the Lorentz and of the Coriolis forces may be reduced, allowing convection to set on at lower Rayleigh number and to develop on larger length scales (Chandrasekhar 1961). This led Roberts (1978) to conjecture that in a rapidly rotating system, for magnetic fields stronger than a threshold value, the Lorentz force would enhance convection and hence dynamo action, resulting in a runaway growth of the magnetic field. The corresponding bifurcation diagram is depicted on Fig. 3. On the weak-field branch the Lorentz force is balanced by viscous or inertial terms in the momentum equation, this force balance requires small-spatial scales. On the strong field branch, however, the magnetic field strength is set by a balance between Lorentz and Coriolis forces, which requires larger spatial scales, this is the magnetostrophic regime. A similar bifurcation diagram, but based on the fact that magnetic buoyancy would be negligible close to the dynamo onset has been proposed for stars by Weiss & Tobias (2000).

We now briefly discuss the identification between WM (SD) magnetism and weak-field (strong-field) dynamo regime, the reader is referred to Morin et al. (2011) for a more detailed discussion. The usual control parameter in the weak *vs* strong field dynamo scenario described above is the Rayleigh number, which measures the energy input relative to forces opposing the motion. Mass can be used as a good proxy for the available energy flux in M dwarfs, Fig. 2 can therefore be interpreted as a bifurcation diagram for the amplitude of the large scale magnetic field versus a control parameter measuring the energy input. In order to compare the driving of convection with the impeding effect of rotation, we can use $M_{\star} \times P_{\text{rot}}^2$ as a rough proxy for the Rayleigh number (see Fig. 2) based on rotation rather than diffusivities (e.g., Christensen & Aubert 2006).

First, in the SD regime the magnetic field strength has to be compatible with a Lorentz–Coriolis force balance. We note that this balance is valid spatial large-scales for which the Coriolis term is predominant over inertial terms in the momentum equation, in qualitative agreement with the observation that only the large-scale component of the magnetic field exhibits a bimodal distribution. This magnetostrophic force balance roughly

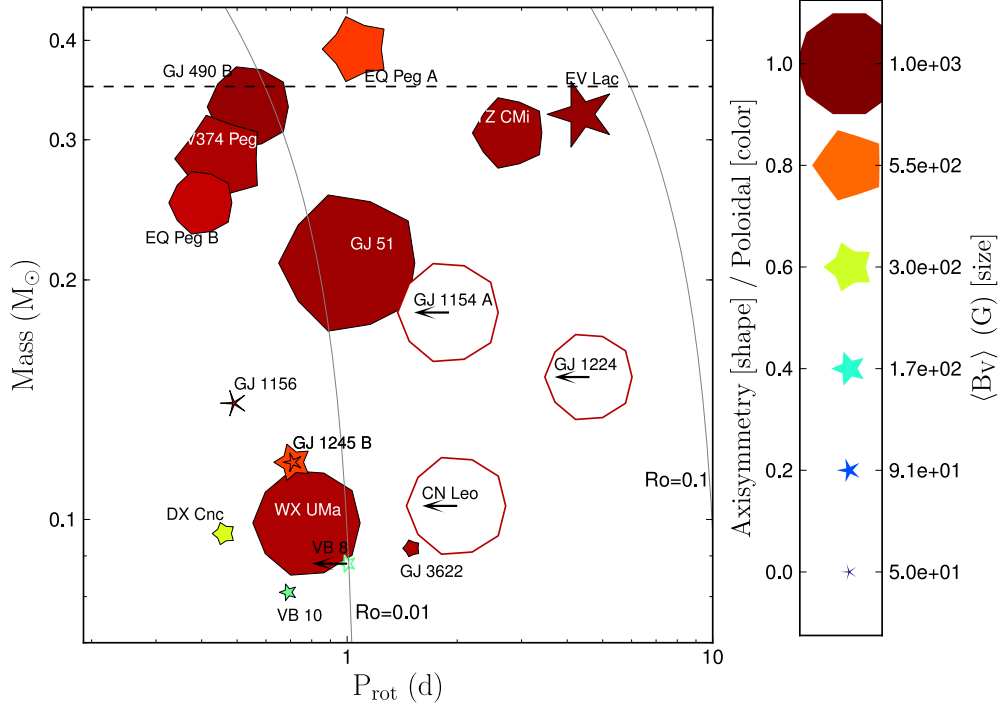


Fig. 1. Mass–period diagram of fully-convective stars derived from spectropolarimetric data and Zeeman-Doppler Imaging (ZDI). Symbol size represents the reconstructed magnetic energy, the color ranges from blue for a purely toroidal to red for a purely poloidal field, and the shape depicts the degree of axisymmetry from a sharp star for non-axisymmetric to a regular decagon for axisymmetric. For a few stars of the sample Morin et al. (2010) could not perform a definite ZDI reconstruction, in these cases only an upper limit of the rotation period is known and the magnetic flux is extrapolated, those objects are depicted as empty symbols. The theoretical fully-convective limit is depicted as a horizontal dashed line. Thin solid lines represent contours of constant Rossby number $Ro=0.01$ (left) and 0.1 (right), as estimated in Morin et al. (2010).

corresponds to an Elsasser number of order unity, i.e. :

$$\Lambda = \frac{B^2}{\rho\mu\eta\Omega} \sim 1, \quad (3.1)$$

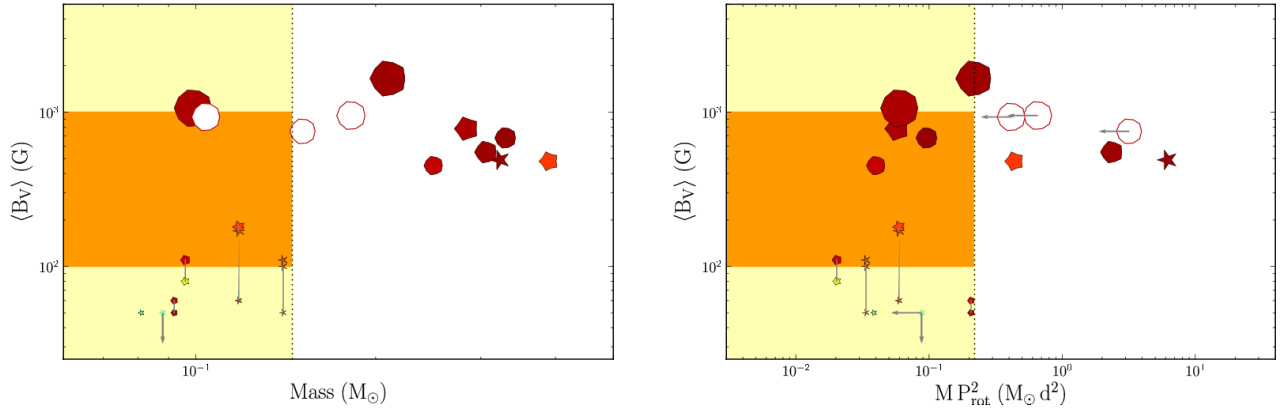


Fig. 2. Average large-scale magnetic fluxes of fully-convective stars derived from spectropolarimetric data and Zeeman-Doppler Imaging (ZDI), as a function of mass (**left panel**) and mass $\times P_{\text{rot}}^2$ (**right panel**). Symbols are similar to those used in the mass–period diagram (see Fig. 1). For stars in the WM regime symbols corresponding to different epochs for a given star are connected by a vertical grey line. The yellow region represents the domain where bistability is observed and the orange one separates the two types of magnetic fields identified (see text).

where B is the magnetic field strength, ρ the mass density, μ the magnetic permeability, η the magnetic diffusivity and Ω the rotation rate. With a few assumptions described in Morin et al. (2011), we find that the order of magnitude of the expected magnetic field strength on the strong field branch is set by:

$$B_{sf} \sim 6 \left(\frac{M_\star}{M_\odot} \right)^{1/2} \left(\frac{R_\star}{R_\odot} \right)^{-1} \left(\frac{L_\star}{L_\odot} \right)^{1/6} \left(\frac{\eta_\odot}{\eta_{\text{ref}}} \right)^{1/2} \left(\frac{P_{\text{rot}}}{1 \text{ d}} \right)^{-1/2} \text{ kG} \quad (3.2)$$

Where η_\odot is a reference value for the magnetic diffusivity in the solar convection zone, and $\eta_{\text{ref}} = 10^{11} \text{ cm}^2 \text{ s}^{-1}$. Taking stellar radius and luminosity for the stellar mass in the range $0.08 - 0.35 M_\odot$ from Chabrier & Baraffe (1997) main sequence models, and η_\odot in the range $10^{11} - 3 \times 10^{12} \text{ cm}^2 \text{ s}^{-1}$ (e.g., Rüdiger et al. 2011), we derive surface values in the strong field regime in the range 2–50 kG, compatible with the order of magnitude of measured B_V values. More conclusively, the gap in terms of B_V between the two branches depends on the ratio of inertia to Coriolis force in the momentum equation and can be estimated with:

$$\frac{B_{wf}}{B_{sf}} = Ro^{1/2}, \quad (3.3)$$

which is of the order of 10^{-1} for stars of our sample in the bistable domain, in good agreement with the typical ratio of large-scale magnetic fields measured between the WM and SD groups of stars (see Fig. 2).

We note that according to the Chabrier & Baraffe (1997) main sequence models, the product of the terms depending on stellar mass, radius and luminosity in the expression of B_{sf} is almost constant in the mid-to-late M dwarf regime. The expected magnetic field strength on the strong field branch hence almost scales with $\Omega^{1/2}$. This is not in contradiction with the fact all the stars in our sample belong to the so-called saturated regime of the rotation–activity relation. Indeed $B_{sf} \propto \Omega^{1/2}$ (derived from $\Lambda \sim 1$) should apply here to the large scale field alone, which is only a fraction of the total magnetic field of the stars (between 15 and 30 %). If a small scale dynamo operates, it does not need to follow the same dependency. Finally, the weak dependency of the large-scale magnetic field on stellar rotation predicted for stars in the strong-field regime cannot be ruled out by existing data and should be further investigated.

4 Conclusions

We present here the main results of the first spectropolarimetric analysis of a sample of active late M dwarfs (more thoroughly detailed in Morin et al. 2010). In particular we report the co-existence of two radically different types of magnetism – strong and steady dipolar field (SD) as opposed to weaker multipolar field evolving in time (WM) – for stars with very similar masses and rotation periods. One of the foreseen hypothesis to explain these observations is the genuine existence of two types of dynamo in this parameter regime, i.e. bistability.

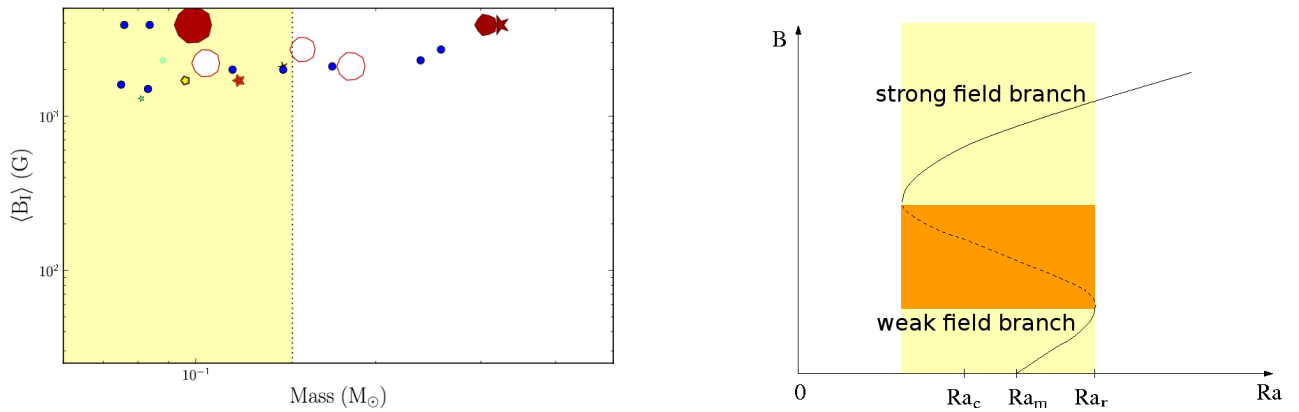


Fig. 3. Left: Total magnetic fluxes of fully-convective stars measured from unpolarised spectra of FeH lines. The values are taken from Reiners et al. (2009) and Reiners & Basri (2010), whenever 2MASS near infrared luminosities (Cutri et al. 2003) and Hipparcos parallaxes (ESA 1997) are available to compute the stellar mass from the Delfosse et al. (2000) mass–luminosity relation. Whenever spectropolarimetric data are available the properties of the magnetic topology are represented as symbols described in Fig. 2. Else small blue symbols are used, upward (downward) triangles represent lower (upper) limits. **Right:** Anticipated bifurcation diagram for the geodynamo (adapted from Roberts 1988). The magnetic field amplitude is plotted against the Rayleigh number. The bifurcation sequence is characterized by two branches, referred to as weak and strong field branches. The yellow and orange regions have the same meaning as in Fig. 2. Ra_c is the critical Rayleigh number for the onset of non-magnetic convection. The weak field regime sets in at Ra_m , and the turning point associated with the runaway growth corresponds to $Ra = Ra_r$.

We show that the weak *vs* strong field dynamo bistability is a promising framework. The order of magnitude of the observed magnetic field in stars hosting a strong dipolar field, and more conclusively the typical ratio of large-scale magnetic fields measured in the WM and SD groups of stars are compatible with theoretical expectations. We argue that the weak dependency of the magnetic field on stellar rotation predicted for stars in the strong-field regime cannot be ruled out by existing data and should be further investigated. We do not make any prediction on the extent of the bistable domain in terms of stellar parameters mass and rotation period, this issue shall be investigated by further theoretical work, and by surveys of activity and magnetism in the ultracool dwarf regime.

A dynamo bistability offers the possibility of hysteretic behavior. Hence the magnetic properties of a given object depend not only on its present stellar parameters but also on their past evolution. For instance, for young objects episodes of strong accretion can significantly modify their structure and hence the convective energy available to sustain dynamo action (Baraffe et al. 2009) initial differences in rotation periods of young stars could also play a role. Because stellar magnetic fields are central in most physical processes that control the evolution of mass and rotation of young stars (in particular accretion-ejections processes and star-disc coupling, e.g., Bouvier 2009; Gregory et al. 2010), the confirmation of stellar dynamo bistability could have a huge impact on our understanding of formation and evolution of low mass stars.

References

- Baraffe, I., Chabrier, G., & Gallardo, J. 2009, *ApJ*, 702, L27
 Bouvier, J. 2009, in *EAS Publications Series*, Vol. 39, *EAS Publications Series*, ed. C. Neiner & J.-P. Zahn, 199–209
 Browning, M. K. 2008, *ApJ*, 676, 1262
 Chabrier, G. & Baraffe, I. 1997, *A&A*, 327, 1039
 Chabrier, G. & Küker, M. 2006, *A&A*, 446, 1027
 Chandrasekhar, S. 1961, *Hydrodynamic and hydromagnetic stability* (Oxford: Clarendon, 1961)
 Charbonneau, P. 2010, *Living Reviews in Solar Physics*, 7, 3
 Christensen, U. R. & Aubert, J. 2006, *Geophysical Journal International*, 166, 97
 Cutri, R. M., Skrutskie, M. F., van Dyk, S., et al. 2003, *2MASS All Sky Catalog of point sources*
 Delfosse, X., Forveille, T., Ségransan, D., et al. 2000, *A&A*, 364, 217
 Dobler, W., Stix, M., & Brandenburg, A. 2006, *ApJ*, 638, 336

- Donati, J.-F., Morin, J., Petit, P., et al. 2008, MNRAS, 390, 545
- Durney, B. R., De Young, D. S., & Roxburgh, I. W. 1993, Solar Physics, 145, 207
- ESA. 1997, VizieR Online Data Catalog, 1239, 0
- Gregory, S. G., Jardine, M., Gray, C. G., & Donati, J. 2010, Reports on Progress in Physics, 73, 126901
- Morin, J., Donati, J., Petit, P., et al. 2010, MNRAS, 407, 2269
- Morin, J., Donati, J.-F., Forveille, T., et al. 2008a, MNRAS, 384, 77
- Morin, J., Donati, J.-F., Petit, P., et al. 2008b, MNRAS, 390, 567
- Morin, J., Dormy, E., Schrunner, M., & Donati, J. . 2011, ArXiv e-prints
- Reiners, A. & Basri, G. 2006, ApJ, 644, 497
- Reiners, A. & Basri, G. 2009, A&A, 496, 787
- Reiners, A. & Basri, G. 2010, ApJ, 710, 924
- Reiners, A., Basri, G., & Browning, M. 2009, ApJ, 692, 538
- Roberts, P. H. 1978, Rotating fluids in geophysics, ed. Roberts, P. H. & Soward, A. M.
- Roberts, P. H. 1988, Geophys. Astrophys. Fluid Dyn., 44, 3
- Rüdiger, G., Kitchatinov, L. L., & Brandenburg, A. 2011, Sol. Phys., 269, 3
- Weiss, N. O. & Tobias, S. M. 2000, Space Sci. Rev., 94, 99

PROGRESS ON MAGNETISM IN MASSIVE STARS (MIMES)

C. Neiner¹, E. Alecian¹, S. Mathis² and the MiMeS collaboration

Abstract. We present the MiMeS project, which aims at studying all aspects of magnetism in massive stars to understand their characteristics, origin, incidence, evolution, and impact on other physical processes. We show examples of recent observational results obtained within this project on pulsating B stars (β Cephei and SPB stars) as well as Herbig Ae/Be stars. Recent theoretical progress obtained within MiMeS on the configuration and stability of magnetic fields is also summarized.

Keywords: stars: early-type, stars: magnetic fields

1 The MiMeS project

The Magnetism in Massive Stars (MiMeS) project represents a comprehensive, multidisciplinary strategy to address the big questions related to the complex and puzzling magnetism of massive stars.

MiMeS has been awarded “Large Program” status with the high resolution spectropolarimeters Espadons at the CFHT (Hawaii), Narval at TBL (France), and HarpsPol at ESO (Chile), resulting in a total of ~ 1500 hours of allocated observing time from late 2008 through early 2013. This large amount of time is being used to acquire an immense database of sensitive measurements of polarized and unpolarized spectra of massive stars, providing magnetic fields measurements for hundreds of massive stars. This database is combined with a wealth of new and archival complementary data (e.g. optical photometry, UV and X-ray spectroscopy) as well as theoretical work, and applied to address the 4 main scientific objectives of the MiMeS project:

- to identify and model the physical processes responsible for the generation of magnetic fields in massive stars
- to study the physics of atmospheres, winds, envelopes, and magnetospheres of massive stars
- to identify the role of magnetic field in the rotational evolution of massive stars
- to understand the impact of magnetic fields on the evolution of massive stars and origin of the magnetic fields of neutron stars and magnetars

The MiMeS collaboration includes over 60 scientists from all around the world and in particular from France and Canada. To address the general problems expressed by the MiMeS science drivers, we have devised a two-component observing program that allows us to obtain basic statistical information about the magnetic properties of the overall population of massive stars (the Survey Component), while simultaneously providing detailed information about the magnetic fields and related physics of individual objects (the Targeted Component). See more details in Wade & the MiMeS Collaboration (2010). In addition, theoretical work and simulations are being developed to interpret the data.

2 Recent observational results

Observational results have been obtained within the MiMeS project on all types of massive stars: OB stars, Of?p stars, β Cephei stars, Slowly Pulsating B (SPB) stars, Be stars, Herbig Ae/Be stars,... Here we concentrate on recent results obtained for pulsating B stars and Herbig Ae/Be stars.

¹ LESIA, Observatoire de Paris, CNRS UMR 8109, UPMC, Université Paris Diderot; 5 place Jules Janssen, 92190 Meudon, France

² Laboratoire AIM, CEA/DSM - CNRS - Université Paris Diderot, IRFU/Service d’Astrophysique, CEA-Saclay, 91191 Gif-sur-Yvette Cedex, France

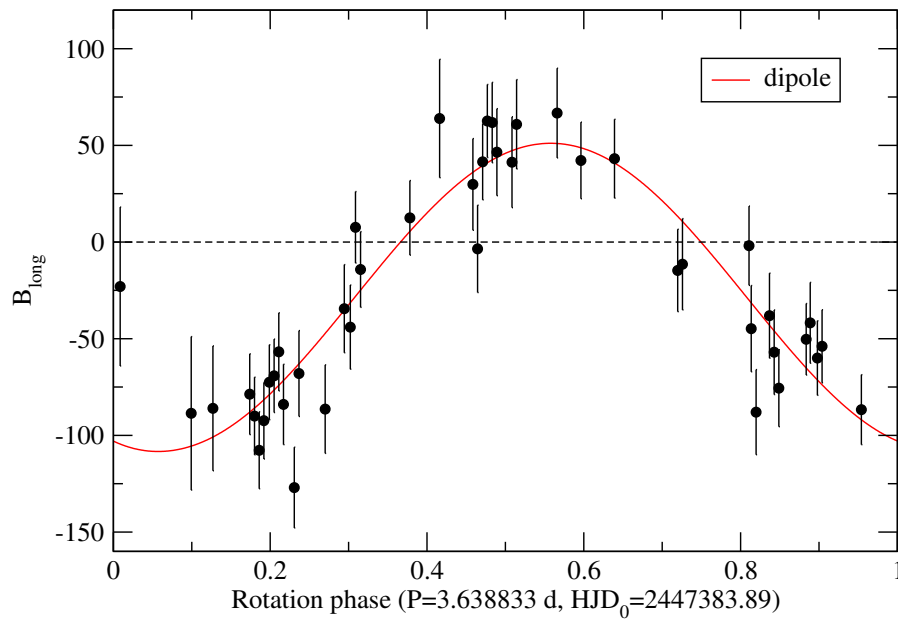


Fig. 1. Longitudinal magnetic field curve of the β Cephei star V2052 Oph obtained from Narval measurements within the MiMeS project. A dipole fit is superimposed. Adapted from Neiner et al. (2011).

2.1 Pulsating B stars

Before MiMeS, a direct magnetic signature had been detected in only very few pulsating stars of β Cephei or SPB type. β Cep itself was the first β Cephei star for which a Zeeman signature had been directly detected (Henrichs et al. 2000). Direct signatures had also been reported for ζ Cas (Neiner et al. 2003a) and ξ^1 CMa (Silvester et al. 2009; Fourtune-Ravard et al. 2011). Other magnetic β Cep or SPB stars have been suggested (e.g. Hubrig et al. 2009) but further observations rejected those possible detections (e.g. Silvester et al. 2009).

Within MiMeS a direct magnetic signature has been observed for 3 new magnetic pulsating B stars: 16 Peg (Henrichs et al. 2009), σ Lup (Henrichs et al. 2011), and V2052 Oph (Neiner et al. 2011). Note that V2052 Oph was already considered magnetic thanks to indirect evidences (Neiner et al. 2003b) but no direct signature had been detected until recently. Its longitudinal field curve folded in phase with the stellar rotation period is shown in Fig. 1.

The few detections and statistical results obtained within MiMeS show that magnetic fields do exist in pulsating B stars but are present in only $\sim 16\%$ of these stars (Grunhut et al. 2011) at the level of detection that can currently be reached. The fields are usually dipolar with an intensity B_{pol} of a few hundreds of Gauss. Some of the magnetic pulsating B stars also show spots of enhanced chemical abundance at their surface (e.g., V2052 Oph, see Neiner et al. 2011).

2.2 Herbig Ae/Be stars

Many indirect evidences of magnetic fields are observed in Herbig Ae/Be (HAeBe) stars. Highly ionised species, such as NV or OVI, are observed in emission in the spectra of HAeBe stars, and rotational modulation of the UV wind lines has been observed in some HAeBe stars (e.g. Catala et al. 1991). Moreover, X-ray emission has also been reported in HAeBe stars and are believed to come from very high-temperature regions close to the stellar surface, such as hot corona or chromosphere. Finally, non-thermal radio observations of a few HAeBe stars have also been reported (Skinner et al. 1993) suggesting a magnetic origin.

For all these reasons, HAeBe stars have been assumed to host magnetic fields. Until recently, however, only one marginal detection in HD 104237 had been reported (Donati et al. 1997). It is only with the emergence of the new generation of spectropolarimeters ESPaDOnS and Narval that a large survey of HAeBe stars could be performed, leading to the detection of 8 additional magnetic stars, i.e., an incidence of $\sim 6\%$ of magnetic HAeBe stars (e.g. Alecian et al. 2009). Following the survey, one more magnetic HAeBe star has been discovered,

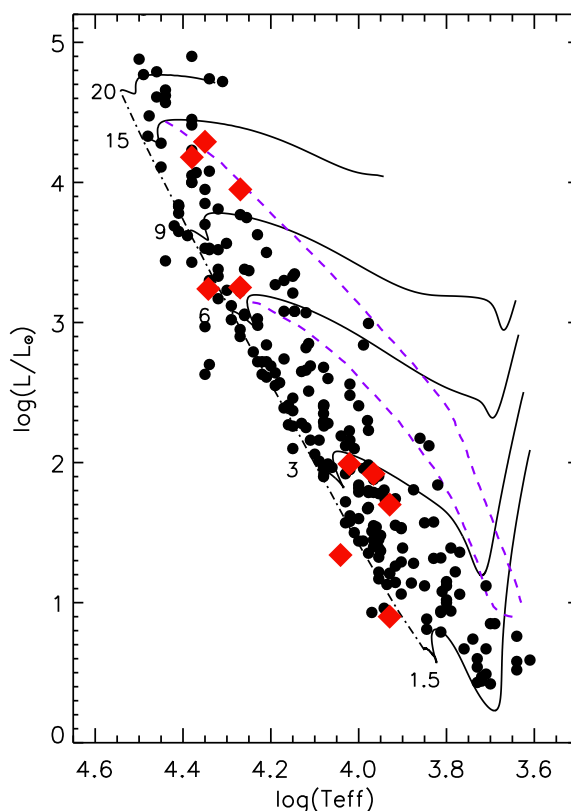


Fig. 2. Hertzsprung-Russell diagram of the Herbig Ae/Be stars for which the magnetic field was measured. Red diamonds indicate the 10 known magnetic HAeBe stars. Evolutionary tracks are superimposed (solid black lines). Purple dotted lines are the birthlines. Taken from Alecian et al. (2012).

bringing the total to 10 (see their position in the HR diagram in Fig. 2).

The incidence of magnetic field in HAeBe stars should be compared with the $\sim 5\%$ of main sequence A/B stars that possess strong magnetic fields, organised on large scales, and stable over many years (Donati & Landstreet 2009). The spectropolarimetric survey of HAeBe stars has thus brought very strong arguments in favour of the fossil origin of the magnetic field in A/B stars, by discovering that their progenitors also possess strong magnetic fields organised on large scales, stable on many years and with the same incidence. A fossil link has therefore been established between the PMS and the MS phases of intermediate- and high-mass stars.

3 Recent theoretical work

The physics of magnetic fields in massive stars is not well understood. However, since observed fields have large-scale, quasi-static, stable configurations, which are not correlated with the star's characteristics such as rotation, the favored hypothesis is a fossil origin. Three main theoretical questions have to be addressed: i) what are the configurations of such fields and how are they born? ii) what are the necessary conditions to achieve large-scale organized stable magnetic configurations as observed in massive stars and how can one explain the dichotomy observed in the stellar population (some stars are magnetic and the others not)? iii) how are fossil fields coupled with other dynamical processes in massive star interiors such as differential rotation and what is their impact on stellar evolution? Until now, the MiMeS collaboration has mainly focused on the first two questions which constitute the first step to tackle the third question.

First, fossil fields are believed to originate from the trapping of the interstellar magnetic field flux during stellar formation. If the initial field is a small-scale turbulent field, we have to understand how it is converted into large-scale organized stable configurations as those observed at the surface of massive stars. This problem is related to the turbulent MHD relaxation processes, in which a turbulent magnetic field is converted into a large-scale one due to a selective decay (with different time-scales) of the ideal MHD invariants (the magnetic

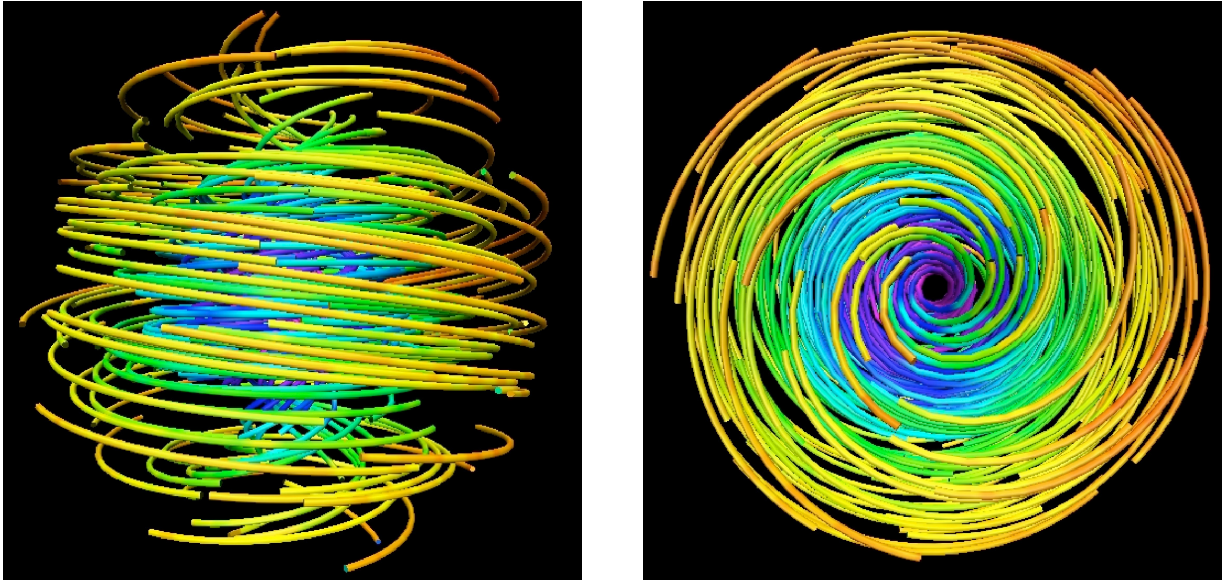


Fig. 3. Semi-analytical stable relaxed axisymmetric magnetic configuration seen from the equator (left panel) and from the pole (right panel). Colors scale with the density. Taken from Duez et al. (2010) (courtesy ApJ).

energy and the magnetic helicity). These processes have been first studied in experimental plasma physics where resulting relaxed states are those of minimum magnetic energy for a given magnetic helicity (Taylor 1954). Then, the case of high- β stellar radiation zone plasmas has been studied both theoretically (Duez & Mathis 2010) and numerically (Braithwaite & Spruit 2004; Braithwaite & Nordlund 2006; Braithwaite 2008). Resulting non force-free relaxed states are more complex and minimize the total energy for a given magnetic helicity and fluid invariants due to the stable stratification of stellar radiation zones. Moreover, roughly axisymmetric dipolar twisted configurations are obtained if the initial magnetic energy is confined near the stellar center (Braithwaite & Nordlund 2006; Duez & Mathis 2010) whereas one obtains non-axisymmetric fields when it is distributed in the whole radiation zone (Braithwaite 2008). The field is then organized on large-scale, mixed (poloidal and toroidal), stable, non force-free configurations, which are in magnetohydrostatic equilibrium. The study of the impact of rotation on such relaxation mechanisms is ongoing (see Duez, Braithwaite & Mathis, these proceedings).

Once relaxed magnetic configurations are obtained, one has to test their stability. It has been demonstrated in the 70's that purely poloidal or toroidal magnetic configurations are unstable (Tayler 1973; Markey & Tayler 1973). These theoretical results have recently been verified using 3-D MHD numerical simulations (see e.g., Brun 2007). Thus, stable magnetic configurations should be of mixed type (Tayler 1980; Braithwaite 2009) thanks to the stabilization of each component by the other; this is precisely the case of known relaxed configurations. To study the stability of relaxed mixed configurations we use direct 3-D MHD numerical simulations in which the obtained configurations are submitted to general perturbations. This numerical method is used because of the lack of general results by the analytical method, which is very efficient to demonstrate instability but not stability. This type of simulations applied to axisymmetric relaxed configurations obtained by numerical simulations (Braithwaite & Nordlund 2006) and by theoretical studies (Duez & Mathis 2010) concluded on the stability of those configurations (Braithwaite 2009; Duez et al. 2010), a major result for the magnetism of massive stars (see Fig. 3) that should be extended to other and more general configurations.

Theoretical results are then used to understand observed magnetic topologies. Moreover, these constitute a strong basis to get a coherent picture of magnetic massive stars internal dynamical processes and evolution (Mathis & Zahn 2005). Finally, these will be used in 3-D MHD modelling of massive stars environment by MiMeS collaborators (Townsend et al. 2007).

4 Conclusions

The MiMeS project allows to obtain rapid progress on the study of magnetic fields in massive stars. The new observations provide critical constraints on the configuration, strength, and incidence of magnetic fields in massive stars. This allows for the development and testing of new models and theories.

Based on observations obtained at the Canada-France-Hawaii Telescope (CFHT) which is operated by the National Research Council of Canada, the Institut National des Sciences de l'Univers of the Centre National de la Recherche Scientifique of France, and the University of Hawaii, as well as on observations obtained using the Narval spectropolarimeter at the Observatoire du Pic du Midi (France), which is operated by the Institut National des Sciences de l'Univers (INSU). We thank the Programme National de Physique Stellaire (PNPS) for their support to MiMeS.

References

- Alecian, E., Wade, G. A., Catala, C., et al. 2009, MNRAS, 400, 354
- Alecian, E., Wade, G. A., Catala, C., et al. 2012, MNRAS, to be submitted
- Braithwaite, J. 2008, MNRAS, 386, 1947
- Braithwaite, J. 2009, MNRAS, 397, 763
- Braithwaite, J. & Nordlund, Å. 2006, A&A, 450, 1077
- Braithwaite, J. & Spruit, H. C. 2004, Nature, 431, 819
- Brun, A. S. 2007, Astronomische Nachrichten, 328, 1137
- Catala, C., Czarny, J., Felenbok, P., Talavera, A., & The, P. S. 1991, A&A, 244, 166
- Donati, J.-F. & Landstreet, J. D. 2009, ARA&A, 47, 333
- Donati, J.-F., Semel, M., Carter, B. D., Rees, D. E., & Collier Cameron, A. 1997, MNRAS, 291, 658
- Duez, V., Braithwaite, J., & Mathis, S. 2010, ApJ, 724, L34
- Duez, V. & Mathis, S. 2010, A&A, 517, A58
- Fourtune-Ravard, C., Wade, G. A., Marcolino, W. L. F., et al. 2011, in IAU Symposium 272, ed. C. Neiner, G. Wade, G. Meynet, & G. Peters, 180
- Grunhut, J. H., Wade, G. A., & the MiMeS Collaboration. 2011, ArXiv e-prints 1108.2673
- Henrichs, H. F., de Jong, J. A., Donati, D.-F., et al. 2000, in Magnetic Fields of Chemically Peculiar and Related Stars, ed. Y. V. Glagolevskij & I. I. Romanyuk, 57
- Henrichs, H. F., Kolenberg, K., Plaggenborg, B., et al. 2011, in IAU Symposium 272, ed. C. Neiner, G. Wade, G. Meynet, & G. Peters, 192
- Henrichs, H. F., Neiner, C., Schnerr, R. S., et al. 2009, in IAU Symposium 259, 393
- Hubrig, S., Briquet, M., De Cat, P., et al. 2009, Astronomische Nachrichten, 330, 317
- Markey, P. & Tayler, R. J. 1973, MNRAS, 163, 77
- Mathis, S. & Zahn, J.-P. 2005, A&A, 440, 653
- Neiner, C., Alecian, E., Briquet, M., et al. 2011, A&A, submitted
- Neiner, C., Geers, V. C., Henrichs, H. F., et al. 2003a, A&A, 406, 1019
- Neiner, C., Henrichs, H. F., Floquet, M., et al. 2003b, A&A, 411, 565
- Silvester, J., Neiner, C., Henrichs, H. F., et al. 2009, MNRAS, 398, 1505
- Skinner, S. L., Brown, A., & Stewart, R. T. 1993, ApJS, 87, 217
- Tayler, R. J. 1973, MNRAS, 161, 365
- Tayler, R. J. 1980, MNRAS, 191, 151
- Taylor, R. L. 1954, Science, 119, 780
- Townsend, R. H. D., Owocki, S. P., & Ud-Doula, A. 2007, MNRAS, 382, 139
- Wade, G. A. & the MiMeS Collaboration. 2010, ArXiv e-prints 1012.2925

THE FLUID EQUILIBRIUM TIDE IN STARS AND GIANT PLANETS

F. Remus^{1,2,3}, S. Mathis^{2,4} and J.-P. Zahn¹

Abstract. Many extrasolar planets orbit very close to their parent star, so that they experience strong tidal interactions; by converting mechanical energy into heat, these tides contribute to the dynamical evolution of such systems. This motivates us to seek a deeper understanding of the processes that cause tidal dissipation, which depend both on the internal structure and the physical properties of the considered bodies. Here, we examine the equilibrium tide, i.e. the hydrostatic adjustment to the tidal potential, in a rotating fluid planet or star. We derive the adiabatic velocity field induced by the tidal perturbation and discuss in particular how the quality factor Q characterizing the dissipation is linked with the turbulent viscosity of convection zones. Finally, we show how the results may be implemented to describe the dynamical evolution of the system.

Keywords: stars: binaries (including multiple): close, stars: planetary systems

1 Introduction

When an extrasolar planet orbits very close to its host star, both components experience strong tidal interactions, which govern their orbital evolution. The dynamical evolution of a binary system is driven by the conversion of its mechanical energy into heat. Provided the system loses no angular momentum, it tends to the state of minimum energy in which the orbits are circular, the rotation of the components is synchronized with the orbital motion, and the spins are aligned. However, in very close systems of star-planet kind, such final state cannot be achieved: instead, the planet spirals toward the star and may eventually be engulfed by it (Hut 1981; Levrard et al. 2009). To predict the fate of a binary system, one has to identify the dissipative processes that achieve the conversion of kinetic energy into thermal energy, from which one may then draw the characteristic times of circularization, synchronization and spin alignment. Before reviewing these processes, let us recall the two types of tides which operate in stars and in the fluid parts of giant planets. The *equilibrium tide* designates the large-scale flow induced by the hydrostatic adjustment of the star in response to the gravitational force exerted by the companion (Zahn 1966a). On the other hand, the *dynamical tide* corresponds to the eigenmodes (gravity, inertial, or gravito-inertial waves) that are excited by the tidal potential (Zahn 1975; Goldreich & Nicholson 1989; Ogilvie & Lin 2004; Goodman & Lackner 2009; Rieutord & Valdettaro 2010; Barker & Ogilvie 2010). These tides experience two main dissipative mechanisms: turbulent friction in convective regions and thermal dissipation acting on the gravito-inertial modes excited in radiative zones.

We shall focus here on the equilibrium tide acting in the convective envelopes of solar type stars or giant planets.

2 Description of the problem

2.1 The system

We consider a system consisting of two bodies A and B, of mass m_A and m_B , and we undertake to describe the tide exerted by B on A, which we assume to be in fluid state, i.e. a star or a giant planet. Due to their mutual attraction, they move in elliptic orbits around their common center of mass, but it is often convenient to choose

¹ LUTH, Observatoire de Paris, CNRS, Université Paris Diderot, 92195 Meudon, France

² Laboratoire AIM, CEA/DSM, CNRS, Université Paris Diderot, IRFU/SAP, 91191 Gif-sur-Yvette, France

³ IMCCE, Observatoire de Paris, CNRS, UPMC, USTL, 75014 Paris, France

⁴ LESIA, Observatoire de Paris, CNRS, Université Paris Diderot, UPMC, 92195 Meudon, France

an inertial reference frame \mathcal{R}_A whose origin is placed at the center of A (designated by the same letter) and whose axes $\{\mathbf{X}, \mathbf{Y}, \mathbf{Z}\}$ are fixed in space. We assume that all spins are aligned along the $(A\mathbf{Z})$ axis; therefore the position of B is entirely determined by the three following keplerian elements: the semi-major axis a of the relative orbit of B around A, its eccentricity e , and its true anomaly ν . The mean motion of B is denoted ω .

2.2 The tidal potential

The tidal force exerted by B on A derives from a potential, which may be expanded in spherical harmonics using the Kaula transform (Kaula 1962). Considering binary systems that are separated enough to allow the companion to be treated as a point mass (this approximation has been discussed by Mathis & Le Poncin-Lafitte 2009), the tidal potential U takes then, in this quadrupolar approximation, the following form:

$$U(r, \theta, \varphi) = -\frac{1}{4} \frac{m_B}{m_A + m_B} \omega^2 r^2 \sum_l G_{2,0,l-2}(e) P_2^2(\cos \theta) \cos(2\varphi - l\omega t), \quad (2.1)$$

where (r, θ, φ) are the spherical coordinates attached to the inertial reference frame \mathcal{R}_A , and the functions $G_{2,0,l-2}(e)$ are polynomials in e whose lowest power is $|l-2|$. Each term of this expansion acts with a proper tidal frequency $\sigma = l\omega - 2\Omega$. The tidal potential (2.1) induces in the star (or the giant planet) pressure and density perturbations and a modified velocity field which obeys the classical equations of Navier-Stokes, mass conservation, Poisson and entropy.

3 The adiabatic and dissipative equilibrium tides

Treating the tides as a small amplitude perturbation of the hydrostatic structure of the object, we may separate the problem in two parts:

- first, an *adiabatic system* (I) in phase with the perturbing potential U (eq. 2.1) : it corresponds to the adiabatic tide, i.e. the star's response to the tidal excitation, ignoring all dissipative processes.
- second, a *dissipative system* (II) in quadrature with the perturbing potential : it corresponds to the star's response due to the dissipative processes (here, the turbulent friction due to the convective motions).

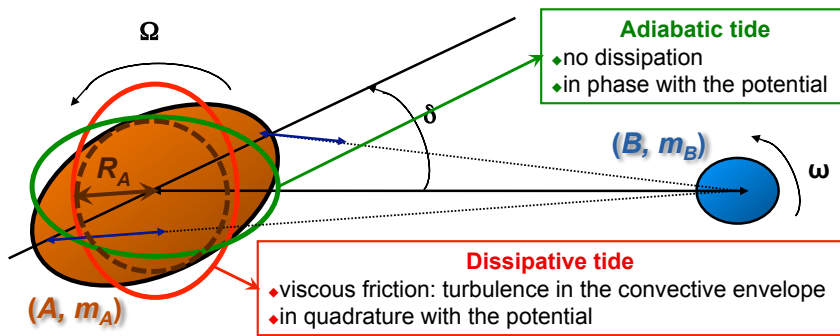


Fig. 1. Tidal interactions in a binary system. Body B exerts a tidal force on body A, which adjusts itself with a phase lag δ , because of internal friction. This adjustment may be split in an adiabatic component, which is in phase with the tide, and a dissipative one, which is in quadrature.

4 The adiabatic tide

First of all, each body suffers a deformation due to its hydrostatic adjustment to the tidal perturbation described by an adiabatic response potential ϕ_I . This adjustment is quantified by the second-order Love number $k_2 = \phi_I(R_A)/U(R_A)$, where ϕ_I and U are taken at the surface of the planet. In the absence of dissipation, this deformation induces a velocity field (represented in Fig. 2), which is in phase with the tidal potential and thus does not lead to a net exchange of angular momentum.

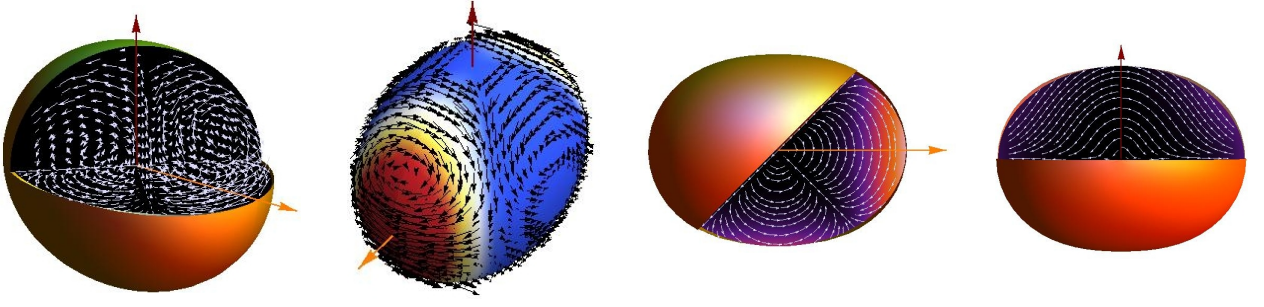


Fig. 2. Representations of the total (poloidal and toroidal) adiabatic equilibrium tide velocity field. The red and orange arrows respectively indicate the direction of the primary rotation axis and of the line of centers. **First:** 3-D view of the total (poloidal and toroidal) adiabatic equilibrium tide velocity field (white arrows). **Second:** Representation of this velocity field at the surface of the primary (black arrows); the color-scaled background represents the normalized tidal potential intensity (blue and red for the minimum and maximum values respectively). **Third:** View of the velocity field (white arrows) in its equatorial plane of symmetry; the color-scaled background represents the velocity value (black and orange for the minimum and maximum values respectively). **Fourth:** View of the velocity field (white arrows) in its meridional plane of symmetry; the color-scaled background represents the velocity value (black and purple for the minimum and maximum values respectively).

5 The dissipative tide

We assume that the convective motions and the tidal flow are separated enough in temporal and spatial scales that their interaction can be described by an eddy viscosity η acting on the tidal velocity field. We use here the prescription of Zahn (1989) for the turbulent viscosity. In convective regions, viscous friction acts on the adiabatic tide velocity field and leads to a redistribution of mass, which is no longer in phase with the tidal potential (Zahn 1966b, 1989). This process is at the origin of the tidal dissipation in solar-type stars and giant planets; it is quantified by the ratio k_2/Q , where Q is the tidal dissipation factor. k_2/Q is a function of tidal frequency, as shown in Fig. 3.

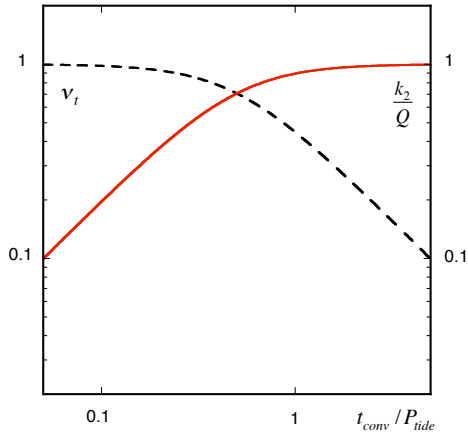


Fig. 3. The two regimes of turbulent dissipation. As long as the local convective turn-over time remains shorter than the tidal period ($t_{\text{conv}} < P_{\text{tide}}$), the turbulent viscosity ν_t (in black dashed line) is independent of the tidal frequency, and the inverse quality factor k_2/Q (in red continuous line) varies proportionally to the tidal frequency (σ_l) (so does also the tidal lag angle). When $t_{\text{conv}} > P_{\text{tide}}$, ν_t varies proportionally to the tidal period, whereas k_2/Q does no longer depend on the tidal frequency. ν_t and k_2/Q have been scaled by the value they take respectively for $t_{\text{conv}}/P_{\text{tide}} \rightarrow 0$ and $\rightarrow \infty$.

6 Dynamical evolution

Due to dissipation, the tidal torque has non-zero average over the orbit, and it induces an exchange of angular momentum between each component and the orbital motion. This exchange governs the evolution of the semi-major axis and the eccentricity of the orbit, and that of the angular velocity of each component (see for example Mathis & Le Poncin-Lafitte 2009). Depending on the initial conditions and on the planet/star mass ratio, the system evolves either to a stable state of minimum energy (where all spins are aligned, the orbits are circular and the rotation of each body is synchronized with the orbital motion) or the planet tends to spiral into the parent star. For simplicity, we give here the results for the coplanar case, where the orbital and rotational

spins are aligned. The evolution of the semi-major axis a , of the eccentricity e and of the angular velocity Ω of component A (I_A denotes its moment of inertia), is governed by the following equations:

$$\begin{aligned} \frac{1}{t_{\text{sync}}} &\equiv -\frac{1}{(\Omega - \omega) I_A} \frac{d(I_A \Omega)}{dt} = \frac{1}{(\Omega - \omega) I_A} \frac{8\pi \mathcal{G} m_B^2 R^5}{5 a^6} \sum_l \left\{ \frac{k_2(\sigma_l)}{Q(\sigma_l)} [\mathcal{H}_l(e)]^2 \right\}, \\ \frac{1}{t_{\text{circ}}} &\equiv -\frac{1}{e} \frac{de}{dt} = \frac{1}{\omega} \frac{1 - e^2}{e^2} \frac{4\pi \mathcal{G} m_B R^5}{5 a^8} \sum_l \left\{ \left[2 \left(1 - \frac{1}{\sqrt{1 - e^2}} \right) + (l - 2) \right] \frac{k_2(\sigma_l)}{Q(\sigma_l)} [\mathcal{H}_l(e)]^2 \right\}, \\ \frac{1}{a} \frac{da}{dt} &= -\frac{2}{\omega} \frac{4\pi \mathcal{G} m_B R^5}{5 a^8} \sum_l \left\{ l \frac{k_2(\sigma_l)}{Q(\sigma_l)} [\mathcal{H}_l(e)]^2 \right\}, \end{aligned}$$

where: $\mathcal{H}_l(e) = \left(\frac{15}{32\pi} \right)^{1/2} G_{2,0,l-2}(e)$.

7 Conclusion

We have rigorously separated equilibrium and dynamical tides (pseudo-resonances, present in Zahn 1966a, have been removed). We also have confirmed the divergence-free property of the tidal velocity field (critized by Scharlemann 1981). The results obtained here are valid even if the components are far from synchronism and evolve on highly elliptical orbits. This work represents a consistent treatment of the equilibrium tide, taking into account the hydrodynamical properties of the considered body. That allowed us to get the equations of the dynamical evolution of the system in function of a dissipative quality factor Q depending on the tidal frequency. Those results have been presented in a submitted article (Remus et al. 2011). The next work will integrate differential rotation and obliquity of the axis of rotation.

The authors thank V. Lainey, C. Le Poncin-Lafitte, A.-S. Brun, S. Udry, R. Mardling and A. Triaud for fruitful discussions during this work, which was supported in part by the Programme National de Planétologie (CNRS/INSU), the EMERGENCE-UPMC project EME0911, and the CNRS *Physique théorique et ses interfaces* program.

References

- Barker, A. J. & Ogilvie, G. I. 2010, MNRAS, 404, 1849
- Goldreich, P. & Nicholson, P. D. 1989, ApJ, 342, 1075
- Goodman, J. & Lackner, C. 2009, ApJ, 696, 2054
- Hut, P. 1981, A&A, 99, 126
- Kaula, W. M. 1962, AJ, 67, 300
- Levrard, B., Winisdoerffer, C., & Chabrier, G. 2009, ApJ, 692, L9
- Mathis, S. & Le Poncin-Lafitte, C. 2009, A&A, 497, 889
- Ogilvie, G. I. & Lin, D. N. C. 2004, ApJ, 610, 477
- Remus, F., Mathis, S., & Zahn, J.-P. 2011, A&A, submitted
- Rieutord, M. & Valdetaro, L. 2010, Journal of Fluid Mechanics, 643, 363
- Scharlemann, E. T. 1981, ApJ, 246, 292
- Zahn, J. P. 1966a, Annales d'Astrophysique, 29, 313
- Zahn, J. P. 1966b, Annales d'Astrophysique, 29, 489
- Zahn, J.-P. 1975, A&A, 41, 329
- Zahn, J.-P. 1989, A&A, 220, 112

THE EQUILIBRIUM TIDE IN VISCOELASTIC PARTS OF PLANETS

F. Remus^{1,2,3}, S. Mathis^{2,4}, J.-P. Zahn¹ and V. Lainey³

Abstract. Earth-like planets have viscoelastic mantles, whereas giant planets may have viscoelastic cores. As for the fluid parts of a body, the tidal dissipation of such solid regions, gravitationally perturbed by a companion body, highly depends on the tidal frequency, as well as on the rheology. Therefore, modelling tidal interactions presents a high interest to provide constraints on planet properties, and to understand their history and their evolution. Here, we examine the equilibrium tide in the solid core of a planet, taking into account the presence of a fluid envelope. We explain how to obtain the different Love numbers that describe its deformation. Next, we discuss how the quality factor Q depends on the chosen viscoelastic model. Finally, we show how the results may be implemented to describe the dynamical evolution of planetary systems.

Keywords: planetary systems, dynamical evolution and stability

1 Introduction

Since 1995 a large number of extrasolar planets have been discovered with a large diversity of physical parameters (Santos & et al. 2007). Quite naturally the question arose whether these planets could allow the development of life. Among the conditions which determine the habitability, i.e. the presence of liquid water, many are closely linked with the rotational and orbital elements of the planetary system. How these evolve in time depends mainly on the tidal interactions between the host star and the planet(s); these are very strong in close systems, and they can even modify the structure of the components by internal heating. Provided the system loses no angular momentum, it tends to the state of minimum energy in which the orbits are circular, the rotation of the components is synchronized with the orbital motion, and the spins are aligned. However, in very close systems of star-planet kind, such final state cannot be achieved: instead, the planet spirals toward the star and may eventually be engulfed by it (Hut 1981; Levrard et al. 2009). To predict the fate of a binary system, one has to identify the dissipative processes that achieve the conversion of kinetic energy into heat, from which one may then draw the characteristic times of circularization, synchronization and spin alignment. The extrasolar planets may be classified in two groups: giant planets with a potential rocky core, and telluric planets made of solid and fluid layers. Since tidal mechanism is closely related with the internal structure, one has to investigate its effects on each kind of materials that may compose a planet. The purpose of this study is to determine the tidal dissipation in the solid parts of planets (viscoelastic cores of giant planets & viscoelastic layers of Earth-like planets).

2 The system

Two-layer model. We will consider as a model a two-bodies system where the component A, rotating at the angular velocity Ω , has a viscoelastic core of shear modulus μ , made of ice or rock, surrounded by a fluid envelope, such as an ocean, stretching out from core's surface (of mean radius R_c) up to planet's surface (of mean radius R_p). Both core and envelope are considered homogeneous, with constant density ρ_c and ρ_o respectively. This model is represented on the left panel of Fig. 1.

¹ LUTH, Observatoire de Paris, CNRS, Université Paris Diderot, 92195 Meudon, France

² Laboratoire AIM, CEA/DSM, CNRS, Université Paris Diderot, IRFU/SAP, 91191 Gif-sur-Yvette, France

³ IMCCE, Observatoire de Paris, CNRS, UPMC, USTL, 75014 Paris, France

⁴ LESIA, Observatoire de Paris, CNRS, Université Paris Diderot, UPMC, 92195 Meudon, France

Configuration. We undertake to describe the tide exerted by B (of mass m_B) on the solid core of A, when moving in an elliptic orbit around A, with eccentricity e , at the mean motion ω . Since no assumption is made on the B's orbit, we need to define an inclination angle I to determine the position of the orbital spin of B with respect to the total angular momentum of the system (in the direction of Z_R) which defines an inertial reference plane (X_R, Y_R), perpendicular to it. The spin axis of A then presents an obliquity ε with respect to Z_R . Refer to the right panel of Fig. 1 for a synthetic representation of the system configuration.

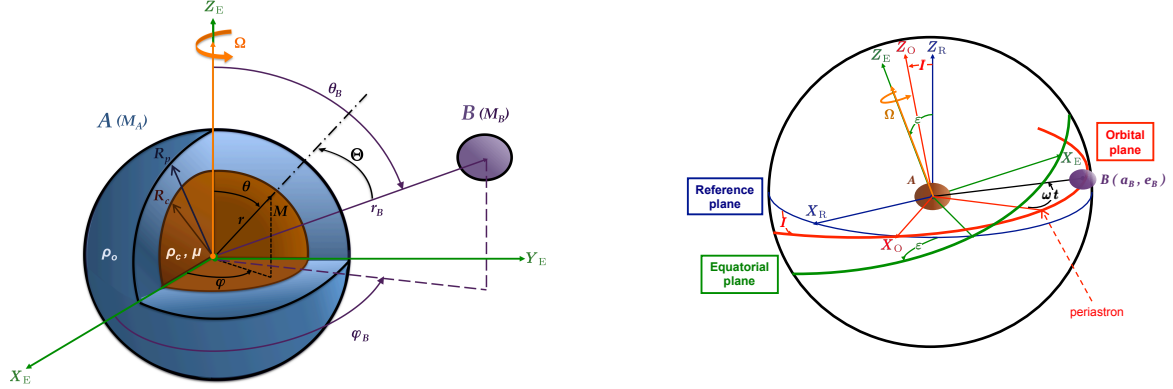


Fig. 1. **Left:** the system is composed by a two-layer main component A, with an homogeneous and incompressible solid core and an homogeneous static fluid envelope, and a point-mass perturber B orbiting around A. **Right:** B is supposed to move on an elliptical orbit, inclined with respect to the inertial reference plane (X_R, Y_R). The equatorial plane of A (X_E, Y_E) is also inclined with respect to this same reference plane.

We follow the methodology of Dermott (1979).

3 Tidal dissipation

3.1 Definition

In presence of dissipation, there is a lag between the line of centers and the tidal bulge. Then, the response ϕ' of the body to the tidal potential U defines the second order complex Love number \tilde{k}_2 whose real part corresponds to the purely elastic deformation, while its imaginary part accounts for dissipation (Biot 1954, see also Tobie 2003 and Henning et al. 2009). U is developed on spherical harmonics (Y_2^m), each term having a large range of tidal frequencies $\sigma_{2,m,p,q} = (2-2p+q)\omega - m\Omega$, for $(m, p, q) \in \llbracket -2, 2 \rrbracket \times \llbracket 0, 2 \rrbracket \times \mathbb{Z}$, resulting from the expansion of U on the Keplerian elements using the Kaula transform (Kaula 1962, see also Mathis & Le Poncin-Lafitte 2009).

This dissipation is quantified by the *quality factor* Q (see for example Tobie 2003):

$$Q^{-1}(\sigma_{2,m,p,q}) = -\frac{\text{Im} \tilde{k}_2(\sigma_{2,m,p,q})}{|\tilde{k}_2(\sigma_{2,m,p,q})|}, \quad \text{where} \quad \tilde{k}_2(\sigma_{2,m,p,q}) = \frac{\phi'(\sigma_{2,m,p,q})}{U(\sigma_{2,m,p,q})}. \quad (3.1)$$

Note that expression (3.1) depends on the tidal frequency $\sigma_{2,m,p,q}$.

3.2 Role of the fluid shell

In absence of a fluid shell surrounding the solid core, *i.e.* in the case where the planet is completely solid, the second order Love number, then denoted by \tilde{k}_2^θ , is expressed by:

$$\tilde{k}_2^\theta(\sigma_{2,m,p,q}) = \frac{3}{2} \frac{1}{1 + \bar{\mu}(2, m, p, q)}, \quad (3.2)$$

where quantity $\bar{\mu}$, called the *complex effective shear modulus*, is linked with the anelasticity and the gravity of the planet's core.

Acting as an overload on the solid core, the fluid shell, previously deformed by the tide, increases the tidal deformation of the core's surface. The second order Love number \tilde{k}_2 takes then a different form than in the fully-solid case. Thus, the

tidal dissipation rate may be expressed in terms of the complex effective shear modulus $\bar{\mu} \equiv \bar{\mu}_1 + i\bar{\mu}_2 = 19\mu/(2\rho_c g_c R_c)$, whatever the chosen rheological model, as:

$$Q(\sigma_{2,m,p,q}) = \sqrt{1 + \frac{9}{4\alpha^2 A^2 D^2} \left\{ 1 + \frac{[B + \bar{\mu}_1(\sigma_{2,m,p,q})] \left[\frac{2\alpha C}{3} + \bar{\mu}_1(\sigma_{2,m,p,q}) \right]}{\bar{\mu}_2(\sigma_{2,m,p,q})} \right\}^2}, \quad (3.3)$$

where α , A , B , C and D account for the planet rheology through the ratios of radii R_c/R_p and densities ρ_o/ρ_c .

In 2004, Ogilvie & Lin studied tidal dissipation in rotating giant planets with solid cores, resulting from the excitation of inertial waves in the convective region by the tidal potential. They obtained a decrease of the effective quality factor $Q_{\text{eff}} = (R_p/R_c)^5 Q$, which measures the dissipation of the whole planet, associated to the fluid equilibrium tide of a fully convective planet (except for a small solid core): from $Q_{\text{eff}} = 10^6$ to $Q_{\text{eff}} = 10^5$.

Since the composition of giant planets cores is weakly constrained (Guillot 2005), we explore in Fig. 2 a large field of values of the visco-elastic parameters considering the Maxwell rheological model.

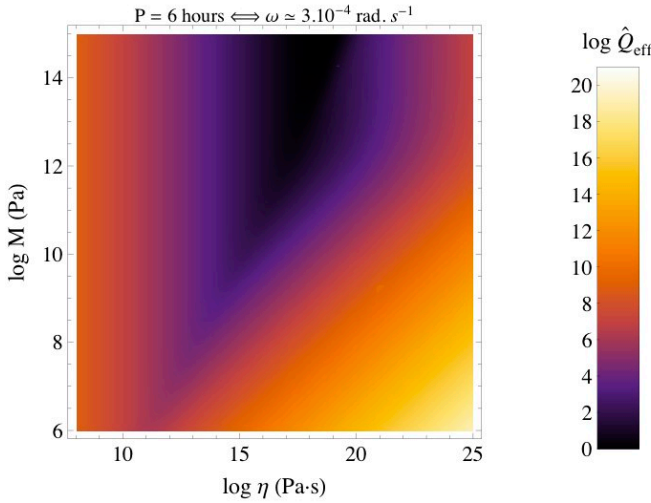


Fig. 2. Dissipation quality factor Q_{eff} in function of the viscoelastic parameters M and η , of a Saturn-like two-layers planet, using the Maxwell model.

The present two-layer model proposes an alternative process to reach such a dissipation (the region above the second contour line $Q_{\text{eff}} = 10^5$, in light purple), and even more depending on the viscosity η and the stiffness M (the region above the first contour line $Q_{\text{eff}} = 10^4$, in dark purple). These results are obtained for a Saturn-like planet with a planet radius $R_p = 9.140 \times R_{\oplus}$, a core radius $R_c = 0.2 \times R_p$, a core mass $M_c = 11 \times M_{\oplus}$ and a fluid envelope density $\rho_o = 0.1 \times \rho_c$ (Guillot et al. 1995; Guillot 1999; Dermott 1979; Tobie 2003).

To explain the tidal dissipation observed in giant planets of our proper Solar System (eg. $Q_{\text{Jupiter}} = 3.56 \pm 0.56 \times 10^4$ determined by Lainey et al. 2009, see also Lainey et al. 2011, for Saturn), all processes have to be taken into account.

4 Dynamical evolution

Due to dissipation, the tidal torque has non-zero average over the orbit, and it induces an exchange of angular momentum between each component and the orbital motion. This exchange governs the evolution of the semi-major axis a , the eccentricity e of the orbit, the inclination I of the orbital plane, of the obliquity ε and that of the angular velocity of each component (see for example Mathis & Le Poncin-Lafitte 2009). Depending on the initial conditions and on the planet/star mass ratio, the system evolves either to a stable state of minimum energy (where all spins are aligned, the orbits are circular and the rotation of each body is synchronized with the orbital motion) or the planet tends to spiral into the parent star. The evolution of the semi-major axis a , of the eccentricity e , of the inclination I , of the obliquity ε and of the angular velocity Ω (\bar{I}_A denotes the moment of inertia of A), is governed by the following equations, derived from Mathis & Le

Poncin-Lafitte (2009) and Remus et al. (2011):

$$\begin{aligned}
\frac{1}{t_{\text{sync}}} &\equiv -\frac{1}{(\Omega - \omega) \bar{I}_A} \frac{d(\bar{I}_A \Omega)}{dt} = \frac{1}{(\Omega - \omega) \bar{I}_A} \frac{8\pi \mathcal{G} M_B^2 R_{\text{eq}}^5}{5 a^6} \sum_{m,j,p,q} \left\{ \frac{|\tilde{k}_2(\sigma_{2,m,j,p,q})|}{\hat{Q}(\sigma_{2,m,j,p,q})} [\mathcal{H}_{m,j,p,q}(e, I, \varepsilon)]^2 \right\}, \\
\frac{1}{t_{\text{circ}}} &\equiv -\frac{1}{e} \frac{de}{dt} = \frac{1}{\omega} \frac{1-e^2}{e^2} \frac{4\pi \mathcal{G} M_B R_{\text{eq}}^5}{5 a^8} \sum_{m,j,p,q} \left\{ \left[(2-2p) \left(1 - \frac{1}{\sqrt{1-e^2}} \right) + q \right] \frac{|\tilde{k}_2(\sigma_{2,m,j,p,q})|}{\hat{Q}(\sigma_{2,m,j,p,q})} [\mathcal{H}_{m,j,p,q}(e, I, \varepsilon)]^2 \right\}, \\
\frac{1}{t_{\text{align}_A}} &\equiv -\frac{1}{\varepsilon} \frac{d\varepsilon}{dt} = \frac{1}{\varepsilon \sin \varepsilon} \frac{d(\cos \varepsilon)}{dt} = \frac{1}{\varepsilon \sin \varepsilon} \frac{1}{\bar{I}_A \Omega_A} \frac{4\pi \mathcal{G} M_B^2 R_{\text{eq}}^5}{5 a^6} \sum_{m,j,p,q} \left\{ (j+2 \cos \varepsilon) \frac{|\tilde{k}_2(\sigma_{2,m,j,p,q})|}{\hat{Q}(\sigma_{2,m,j,p,q})} [\mathcal{H}_{m,j,p,q}(e, I, \varepsilon)]^2 \right\}, \\
\frac{1}{t_{\text{align}_{\text{Obs}}}} &\equiv -\frac{1}{I} \frac{dI}{dt} = \frac{1}{I \sin I} \frac{d(\cos I)}{dt} = \frac{1}{I \sin I} \frac{1}{\omega} \frac{1}{\sqrt{1-e^2}} \frac{4\pi \mathcal{G} M_B^2 R_{\text{eq}}^5}{5 a^8} \\
&\quad \times \sum_{m,j,p,q} \left\{ [j + (2q-2) \cos I] \frac{|\tilde{k}_2^F(\sigma_{2,m,j,p,q})|}{\hat{Q}(\sigma_{2,m,j,p,q})} [\mathcal{H}_{m,j,p,q}(e, I, \varepsilon)]^2 \right\}, \\
\frac{1}{a} \frac{da}{dt} &= -\frac{2}{\omega} \frac{4\pi \mathcal{G} M_B R_{\text{eq}}^5}{5 a^8} \sum_{m,j,p,q} \left\{ (2-2p+q) \frac{|\tilde{k}_2^F(\sigma_{2,m,j,p,q})|}{\hat{Q}(\sigma_{2,m,j,p,q})} [\mathcal{H}_{m,j,p,q}(e, I, \varepsilon)]^2 \right\},
\end{aligned}$$

where $\mathcal{H}(e, I, \varepsilon)$ is proportional to the product of Kaula's functions that intervene in the expansion of the tidal potential in spherical harmonics, and R_{eq} is the equatorial radius of A (in general, $R_{\text{eq}} \neq R_p$).

5 Conclusion

Our preliminary evaluations confirm the results of Dermott (1979), and they reveal a much higher dissipation in the solid cores of planets than that found by Ogilvie & Lin (2004) for the fluid envelop of a planet having a small solid core. These results seem to be in good agreement with observed properties of Saturn's system (Lainey et al. 2011).

This work was supported in part by the Programme National de Planétologie (CNRS/INSU), the EMERGENCE-UPMC project EME0911, and the CNRS *Physique théorique et ses interfaces* program.

References

- Biot, M. A. 1954, *Journal of Applied Physics*, 25, 1385
Dermott, S. F. 1979, *Icarus*, 37, 310
Guillot, T. 1999, *Planet. Space Sci.*, 47, 1183
Guillot, T. 2005, *Annual Review of Earth and Planetary Sciences*, 33, 493
Guillot, T., Chabrier, G., Gautier, D., & Morel, P. 1995, *ApJ*, 450, 463
Henning, W. G., O'Connell, R. J., & Sasselov, D. D. 2009, *ApJ*, 707, 1000
Hut, P. 1981, *A&A*, 99, 126
Kaula, W. M. 1962, *AJ*, 67, 300
Lainey, V., Arlot, J.-E., Karatekin, Ö., & van Hoolst, T. 2009, *Nature*, 459, 957
Lainey, V., Karatekin, O., Desmars, J., et al. 2011, submitted
Lévard, B., Winisdoerffer, C., & Chabrier, G. 2009, *ApJ*, 692, L9
Mathis, S. & Le Poncin-Lafitte, C. 2009, *A&A*, 497, 889
Ogilvie, G. I. & Lin, D. N. C. 2004, *ApJ*, 610, 477
Remus, F., Mathis, S., & Zahn, J.-P. 2011, *A&A*
Santos, N. C. & et al. 2007, in JENAM-2007, "Our Non-Stable Universe"
Tobie, G. 2003, Master's thesis, Université Paris 7 - Denis Diderot

Session 12

High energy and cosmic phenomena (PCHE)

ULTRA FAST VARIABILITY MONITORING WITH CTA

J. Biteau¹ and B. Giebels¹

Abstract.

After three decades of small scale research, very high energy (> 100 GeV) gamma-ray astronomy emerged in 1989 with the detection of the Crab nebula by the Whipple observatory, Arizona, USA. In the '90s, French researchers improved the temporal and spatial sampling of the atmospheric showers initiated by gamma rays, with experiments such as ASGAT, Themistocle, Celeste and CAT. Only a handful of TeV sources had been seen in 2000, the Crab nebula (the standard candle in this field) and five extragalactic sources, mostly detected during flaring periods. The advent of stereoscopy (simultaneous monitoring of a shower with several telescopes) established the domain with observatories such as HEGRA and now H.E.S.S., in which French laboratories are involved. This enabled the detection of > 100 sources and the ability to sample light curves down to the minute time scale during exceptional outbursts, such as the flares of the blazar PKS 2155-304 in July 2006. During the next decade, the first large gamma ray observatory, CTA, will probe the sky above 50 GeV with tens of telescopes. The sensitivity and low-energy threshold of this array will allow the probing of blazar ultra fast variability during exceptional outbursts. We show with simulations that CTA timing capabilities would enable us to resolve the behaviour of PKS 2155-304 down to the second timescale, thus raising puzzling questions on the engine responsible for the TeV emission.

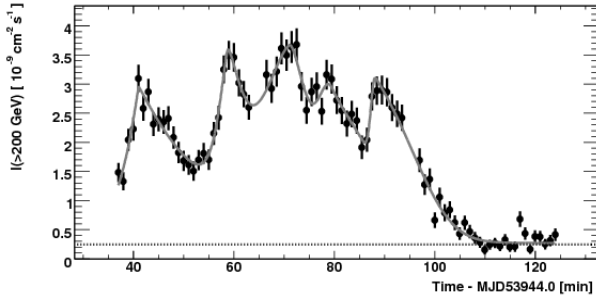
Keywords: high energy astrophysical phenomena, variability, galaxies: active, BL Lacertae objects: individual: PKS 2155-304

1 Introduction

Characteristic variability time scales of Active Galactic Nuclei (AGN) provide constraints on the properties of the emitting region. Assuming that the whole region of size R coherently emits the TeV γ rays, the causality argument yields a low bound on the minimum variability time scale $t_{var} > R/c \times (1+z)/\delta$, where δ and z are the Doppler factor and redshift of the studied region. Assuming that R scales with the Schwarzschild radius $R_S = 2GM/c^2$ of the supermassive black hole, one can derive a lower limit on the Doppler factor. Such constraints have been established by Aharonian *et al.* (2007) for the exceptional outbursts of PKS 2155–304 monitored by H.E.S.S. in July 2006. To derive proper variability time scales, the lightcurve shown on Fig. 1 was fitted with a series of generalized asymmetric gaussian peaks $I(t) = A \exp[-(|t - t_{max}|/\sigma_{r,d})^\kappa]$, where t_{max} is the time of the burst's maximum intensity A ; σ_r and σ_d are the rise ($t < t_{max}$) and decay ($t > t_{max}$) time constants, respectively; and κ is a measure of the burst's sharpness. σ_r and σ_d being highly correlated with κ , the appropriate rise and decay times from half to maximum amplitude are then computed as $\tau_{r,d} = [\ln 2]^{1/\kappa} \sigma_{r,d}$. The peak finding and fitting procedure reveals that during MJD 59344 the flux of PKS 2155–304 is well described by a series five bursts above a constant term (see the table in Fig. 1, extracted from Aharonian *et al.*, 2007).

The shortest rise time during these outbursts is $\tau_r = 67 \pm 44$ s (fifth peak), with a large uncertainty due to the minute temporal binning. Conservatism impose to chose the shortest significant rise time as $\tau_{r, HESS} = 173 \pm 28$ s (first peak), corresponding to a lower limit on the Doppler factor $\delta > 60 - 120$, for a black hole mass ranging in $1 - 2 \times 10^9 M_\odot$. Variability can also be investigated in the Fourier space. A structure function analysis of this lightcurve as well as the contiguous nights (Superina, 2008 - Abramowski *et al.*, 2010) shows that the Power Spectral Density (PSD) of the underlying stochastic process is well described by a power law $P_\nu \propto \nu^{-2}$. The high frequency part of the spectrum is almost flat above a frequency ν_{max} , i.e. dominated by the measurement uncertainty power, which would be lowered if the flux was measured with more statistics. Thus an improvement of the instrumental sensitivity would enable the probing of higher frequencies and bring better constraints on the shortest time scale visible in such a light curve.

¹ Laboratoire Leprince-Ringuet, Ecole Polytechnique, CNRS/IN2P3, F-91128 Palaiseau, France



t_{\max} [min]	A [$10^{-9} \text{ cm}^{-2} \text{ s}^{-1}$]	τ_r [s]	τ_d [s]	κ
41.0	2.7 ± 0.2	173 ± 28	610 ± 129	1.07 ± 0.20
58.8	2.1 ± 0.9	116 ± 53	178 ± 146	1.43 ± 0.83
71.3	3.1 ± 0.3	404 ± 219	269 ± 158	1.59 ± 0.42
79.5	2.0 ± 0.8	178 ± 55	657 ± 268	2.01 ± 0.87
88.3	1.5 ± 0.5	67 ± 44	620 ± 75	2.44 ± 0.41

Fig. 1. Left: Integral flux of PKS 2155–304 above 200 GeV during the first hours of MJD 59344. The data are binned in 1 min intervals. **Right:** Results of the best χ^2 fit of the superposition of five bursts and a constant to the H.E.S.S. data. The constant term is $0.27 \pm 0.03 \times 10^{-9} \text{ cm}^{-2} \text{ s}^{-1}$ ($1.1 I_{\text{Crab}}$) *Extracted from Aharonian et al., 2007.*

2 Simulation of the lightcurves

2.1 Estimation of the flux

To estimate the flux that CTA would monitor, we first have to take into account the decrease of the energy threshold from $E_{\min \text{ HESS}} \sim 200 \text{ GeV}$ to $E_{\min \text{ CTA}} \sim 50 \text{ GeV}$ that would result in an increase of the integral flux above the threshold by a factor:

$$\Phi_{\text{CTA}}(t) = \Phi_{\text{HESS}}(t) \times \frac{\int_{E_{\min \text{ CTA}}}^{E_{\max \text{ CTA}}} F(E) dE}{\int_{E_{\min \text{ HESS}}}^{E_{\max \text{ HESS}}} F(E) dE} \quad (2.1)$$

where $E_{\max \text{ HESS}}$ and $E_{\max \text{ CTA}}$ are the maximum photon energies detectable by H.E.S.S. and CTA, reasonably approximated here as $+\infty$. $F(E)$, the photon spectrum - sometimes written dN/dE - is derived from the Synchrotron Self Compton (SSC) model fitted to the data of PKS 2155–304 during the 2008 multi wavelength campaign (Sanchez & Giebels, 2009 - Aharonian et al., 2009). $\Phi_{\text{HESS}}(t)$ is the lightcurve shown on Fig. 1, reasonably approximated by the series of bursts described in the introduction.

The energy dependency of the flux is fully accounted for in Eq. (2.1), but the modeling of the time dependency requires knowledge on the small timescales behaviour of the flux and is thus related to the high frequency part of the PSD. If the temporal binning of the lightcurve monitored with CTA (resp. H.E.S.S.) is T_{CTA} (resp. T_{HESS}), then the highest frequency accessible for a given sampling (Nyquist frequency) will go from $\nu_{\text{Nyq HESS}} = 1/2T_{\text{HESS}}$ to $\nu_{\text{Nyq CTA}} = 1/2T_{\text{CTA}}$. The variability contained in the frequency range $[\nu_{\text{Nyq HESS}}, \nu_{\text{Nyq CTA}}]$, the extended part of the PSD, must be added to the lightcurve. Let us call the inverse Fourier transform of this extension $\Psi(t)$, then Eq. (2.1) becomes:

$$\Phi_{\text{CTA}}(t) = (\Phi_{\text{HESS}}(t) + \Psi(t)) \times \frac{\int_{E_{\min \text{ CTA}}}^{+\infty} F(E) dE}{\int_{E_{\min \text{ HESS}}}^{+\infty} F(E) dE} \quad (2.2)$$

To simulate $\Psi(t)$, a certain temporal behaviour must be assumed. On one hand, we assume no additional variability above the maximum frequency for which the H.E.S.S. PSD is significantly above the measurement noise level. Then, $\Psi(t)$ represents the measurement noise fluctuations. On the other hand, the PSD can be modeled as a continuous power law, even for frequencies above $\nu_{\max \text{ HESS}}$. Then $\Psi(t)$ Fourier transform is the extension of the H.E.S.S. PSD :

$$P(\nu) = \begin{cases} 0 & \text{if } \nu < \nu_{\max \text{ HESS}} \\ \nu^{-2} & \text{if } \nu \geq \nu_{\max \text{ HESS}} \end{cases} \quad (2.3)$$

where $\nu_{\max \text{ HESS}} \sim 1.6 \times 10^{-3} \text{ Hz}$ is the frequency for which the PSD of the HESS lightcurve is dominated by the measurement noise level. We use Timmer and König's method (1995) to simulate lightcurves associated to $P(\nu)$. One of the realizations is shifted to have a null mean and finally stretched to have a proper variance. The amplitude of the stretch is determined by the Parseval's theorem: the variance of the lightcurve points equals the area below the PSD. That is to say, if the PSD is described by a power law of Fourier index α :

$$V(\Phi_{\text{CTA}}) = V(\Phi_{\text{HESS}}) \times \frac{\int_{\nu_0}^{\nu_{\max \text{ CTA}}} \nu^{-\alpha} d\nu}{\int_{\nu_0}^{\nu_{\max \text{ HESS}}} \nu^{-\alpha} d\nu} \quad (2.4)$$

where ν_0 is the inverse of the lightcurve duration and $\nu_{max\ CTA}$ the frequency for which the PSD of the simulated CTA lightcurve is dominated by the measurement level noise, reasonably approximated by the associated Nyquist frequency ^{*}.

2.2 Estimation of the error on the flux and determination of the sampling rate

The estimation of the uncertainty on the flux in each time bin is of uttermost importance since it is directly related to the sampling rate. Assuming that the number of collected photons N_γ during a time T is Poisson distributed, the error on the integrated flux is $\sigma_{\Phi(> E_{min})} = \Phi(> E_{min})/\sqrt{N_\gamma}$.

To compute the integral flux above a threshold energy $\Phi(> E_{min})$, one has to take into account the energy dependency of the collection area, $A(E)$ obtained from simulations described by Bernlöhr (2008) / CTA consortium (2010), and weigh it by the energy distribution of the incoming photons $F(E)$:

$$\Phi(> E_{min}) = \frac{N_\gamma}{\left[\int_{E_{min}}^{+\infty} A(E)F(E)dE / \int_{E_{min}}^{+\infty} F(E)dE \right] \times T}. \quad (2.5)$$

The uncertainty on the integral flux is then :

$$\sigma_{\Phi(> E_{min})} = \sqrt{\frac{\Phi(> E_{min})}{\left[\int_{E_{min}}^{+\infty} A(E)F(E)dE / \int_{E_{min}}^{+\infty} F(E)dE \right] \times T}} \quad (2.6)$$

The last missing parameter in Eq. (2.6) is the temporal binning T , which is chosen so that the mean significance of CTA lightcurve points equals the one of H.E.S.S. lightcurve points.

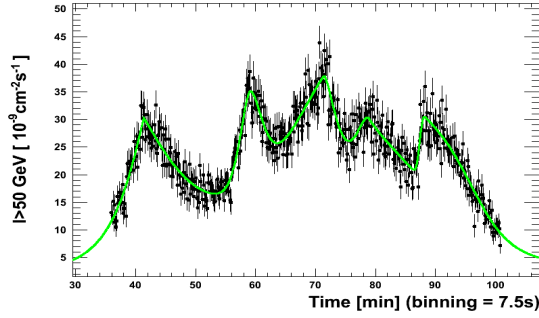
3 Results

The lightcurve simulated in case of no extension of the PSD is shown in Fig. 2. The increase of collection area and decrease of energy threshold allows a temporal binning of few seconds vs a minute for the H.E.S.S. lightcurve. The analysis performed on the H.E.S.S. lightcurve by Aharonian *et al.* (2007) was applied to the CTA simulated one. This light curve was fitted with a series of bursts, detected with a peak finder, added to a constant term. The value of the latter parameter is fixed to $2.7 \times 10^{-9} \text{ cm}^{-2} \text{ s}^{-1}$, in agreement with the fit performed on H.E.S.S. data[†]. Each peak of the lightcurve shown in Fig. 2 is directly comparable to one of the H.E.S.S. lightcurve, since there is not any distortion by an additional variance. H.E.S.S. and CTA average rise/decay time resolution $\sigma_t = \langle \sigma_\tau / \tau \rangle$ during the outburst can be derived from each table, yielding $\sigma_t(\text{H.E.S.S.}) = 38\%$ and $\sigma_t(\text{CTA}) = 17\%$. This resolution improvement implies a significant measurement of the fifth peak rising time $\tau_{r\ CTA} = 60 \pm 18$ s, approximately three times smaller than $\tau_{r\ HESS} = 173 \pm 28$ s. Considering $\tau_{r\ CTA}$ as an upper limit on the variability time scale would yield a Doppler factor $\delta > 200 - 400$.

In the case where variability is added above $\nu_{max\ HESS}$, the function $\Psi(t)$ can be derived from simulations, with power above the measurement noise level up to $\nu_{max\ CTA} \sim 10^{-2}$ Hz. One of the realization is used to obtain the simulated lightcurve $\Phi_{CTA}(t)$ shown in Figure 3. The addition of variance in the Fourier space yield substructures in the temporal space, the second and fourth peaks in this case, which could not have been resolved by H.E.S.S.. The shortest significant rising time tabulated in Fig. 3, $\tau_{r\ CTA} = 25 \pm 4$ s, is approximately seven times smaller than $\tau_{r\ HESS}$, corresponding to a Doppler factor $\delta > 450 - 900$, quite unusual within the currently favored acceleration schemes (Blandford, 2005). The large Doppler factor derived would certainly question the causality argument and the interpretation of such a lightcurve in terms of bursts.

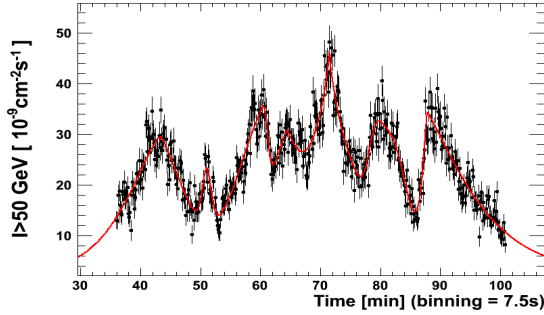
^{*}The PSD is a steep power law, which makes the variance in $[\nu_{max\ CTA}, \nu_{Nyq\ CTA}]$ negligible compared to the one in $[\nu_{max\ H.E.S.S.}, \nu_{max\ CTA}]$.

[†] C_{CTA} and C_{HESS} being the constant terms of each light curves, we fixed $C_{CTA} = C_{HESS} \times \int_{E_{min\ CTA}}^{+\infty} F(E)dE / \int_{E_{min\ HESS}}^{+\infty} F(E)dE$.



t_{\max} [min]	A [$10^{-9} \text{ cm}^{-2} \text{ s}^{-1}$]	τ_{r} [s]	τ_{d} [s]	κ
41.4	26.7 ± 1.5	208 ± 13	452 ± 80	1.11 ± 0.17
59.1	16.8 ± 2.0	111 ± 14	138 ± 18	1.69 ± 0.63
71.5	32.7 ± 1.0	541 ± 106	186 ± 38	1.38 ± 0.27
78.8	23.8 ± 1.8	182 ± 36	784 ± 122	1.58 ± 0.81
88.3	11.9 ± 1.1	60 ± 18	513 ± 65	2.65 ± 0.40

Fig. 2. Left : Simulated integral flux of PKS 2155–304 above 50 GeV as CTA would monitor it. This simulation corresponds to the case where no additional variability is present above $\nu_{\max \text{ HESS}}$. The data are binned in 7.5 seconds intervals. **Right :** Results of the best χ^2 fit of the superposition of five bursts and a constant to the simulated CTA data. The constant term is fixed to $2.7 \times 10^{-9} \text{ cm}^{-2} \text{ s}^{-1}$.



t_{\max} [min]	A [$10^{-9} \text{ cm}^{-2} \text{ s}^{-1}$]	τ_{r} [s]	τ_{d} [s]	κ
43.3	25.7 ± 1.1	202 ± 13	147 ± 13	1.42 ± 0.15
51.0	10.9 ± 1.6	32 ± 8	34 ± 6	1.85 ± 0.44
60.4	17.5 ± 2.0	210 ± 19	37 ± 8	2.19 ± 0.35
64.4	15.1 ± 2.0	124 ± 27	60 ± 11	1.32 ± 0.28
71.5	43.7 ± 1.6	74 ± 9	80 ± 6	0.80 ± 0.11
80.5	18.3 ± 1.7	108 ± 17	177 ± 17	2.99 ± 0.43
87.8	26.8 ± 1.8	25 ± 4	235 ± 12	1.27 ± 0.10

Fig. 3. Left : Simulated integral flux of PKS 2155–304 above 50 GeV as CTA would monitor it. This simulation correspond to the case where variability is added above $\nu_{\max \text{ HESS}}$, assuming a PSD $P_{\nu} \propto \nu^{-2}$. The data are binned in 7.5 seconds intervals. **Right :** Results of the best χ^2 fit of the superposition of seven bursts and a constant to the simulated CTA data. The constant term is fixed to $2.7 \times 10^{-9} \text{ cm}^{-2} \text{ s}^{-1}$.

4 Conclusions

In July 2006, the H.E.S.S. collaboration observed an exceptional outburst of the blazar PKS 2155-304. The lightcurve sampling, limited by the instrumental sensitivity, revealed significant variations down to three minutes, imposing a Doppler factor above 60-120. The simulation of this dramatic outburst as it would be observed with the low energy threshold and the large collection area of CTA allows us to show that a gain of a factor ten on the sampling rate is achievable. Two scenarios of ultra-fast variability are investigated, each of them imposing a Doppler factor of several hundreds, quite unusual within the current blazar paradigm. The observation of such events with CTA will certainly raise puzzling questions on the mechanisms responsible for the TeV emission of blazars and will help to unravel their mysteries.

References

- Abramowski *et al.* (H.E.S.S. Collaboration), 2010, A&A, 520, A83
 Aharonian F. *et al.* (H.E.S.S. Collaboration), 2007, ApJ 664, L71
 Aharonian F. *et al.* (H.E.S.S. & Fermi LAT collaborations) 2009, ApJL, 696, L150
 Bernlöhner K., Astropart. Phys., 2008, 30, 149
 Blandford R.D., 2005, Probing the Physics of AGN, ASP Conference Proceedings, San Francisco, Vol. 224, 499
 CTA Consortium, 2010, arXiv:astro-ph/1008.3703
 Sanchez D. and Giebels B., 2009, arXiv:0912.5152v1
 Superina G., 2008, PhD thesis, Ecole Polytechnique
 Timmer J., König M., 1995, A&A, 300, 707

SEARCH FOR LORENTZ INVARIANCE VIOLATION WITH AGNS: A PROSPECT FOR CTA

J. Bolmont¹ and A. Jacholkowska¹

Abstract. In the recent years, many results have been published about a possible violation of Lorentz Invariance in the frame of Quantum Gravity (QG) models measuring time delays in the arrival times of very high energy (VHE, >100 GeV) gamma-ray photons from distant flaring active galaxies. These photons have been detected by the current ground-based VHE Cherenkov detectors (HESS, MAGIC, VERITAS) and so far, no deviations in the speed of light in vacuum have been seen either for linear or for quadratic scales. The new generation of ground-based instruments "the Cherenkov Telescope Array" (CTA) will be able to probe deeper into this area due to its increased sensitivity (one order of magnitude better than the current detectors) and broader energy range (above 10 GeV). Based on a maximum likelihood technique, a quantitative study is presented of the potential of CTA to detect possible QG effects. In addition, different array configurations are compared in an attempt to maximize the sensitivity to Lorentz Invariance Violation (LIV) effects.

Keywords: CTA, active galaxies, quantum gravity, Lorentz invariance violation

1 Quantum Gravity and Lorentz Invariance Violation

The search for a quantum theory of gravitation is one of the outstanding tasks of modern physics (Amelino-Camelia 2008). As an important consequence of the time-space discretization, Lorentz Invariance Violation (LIV) may appear as predicted in some models of Loop Quantum Gravity (Alfaro et al. 2002; Gambini & Pullin 1999) or String Theory (Ellis et al. 1999). The tiny effects in the photon propagation from distant astrophysical sources as Active Galactic Nuclei (AGNs) or Gamma-ray Bursts (GRBs) would add-up producing deviations in the value of the velocity of light (Amelino-Camelia 1998). These deviations could be represented by linear and quadratic terms in the so-called dispersion relation:

$$c^2 p^2 = E^2 (1 \pm \xi(E/M) \pm \zeta(E/M)^2 \pm \dots), \quad (1.1)$$

where M is the Quantum Gravity energy scale (in principle close to the Planck scale) and ξ and ζ are positive parameters.

In this paper a search for LIV with photons emitted in flares of AGN is being presented as a prospect for the future Cherenkov Telescope Array (CTA) (CTA Consortium 2010). In section 2, the performance of the different possible array configurations, currently under evaluation with Monte Carlo simulations, are compared with the aim of maximizing the sensitivity to LIV effects. Then in section 3, the effect of potentially improved statistical accuracy due to both increased sensitivity and better energy coverage is evaluated.

2 Comparison of array configurations

The energy lever-arm ΔE is determined in order to compare the different array configurations, following to the spectrum simulation of a power law with EBL absorption (Mazin 2008) (for a redshift $z = 0.03$) and a break at 100 GeV representing the maximum of the Inverse Compton peak. The spectrum is then convoluted with the effective areas of different array configurations. Finally, the mean energy for low ($E < E_{lim}$) and high

¹ LPNHE, Université Pierre et Marie Curie Paris 6, Université Denis Diderot Paris 7, CNRS/IN2P3, 4 Place Jussieu, F-75252, Paris Cedex 5, France

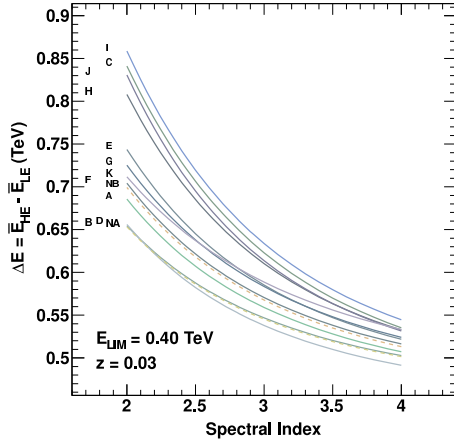


Fig. 1. Parameter ΔE as a function of the spectral index for all arrays considered in CTA Monte Carlo simulations. The configurations A to K are studied for Southern array and configurations NA and NB for the Northern array. The configurations have different layouts and number of telescopes CTA Consortium (2010).

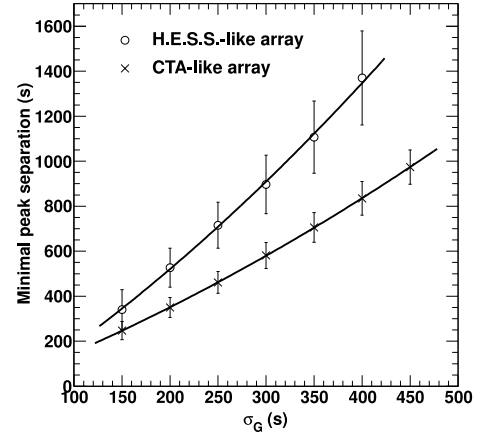


Fig. 2. Minimal distinguishable separation of the two peaks as a function of their width, in case of a H.E.S.S.-like (open circles) and a CTA-like measurement (crosses).

($E > E_{lim}$) energy bands are computed and the difference $\Delta E = \bar{E}_{HE} - \bar{E}_{LE}$ is deduced. This way of comparing the different array configurations does not depend on the method used to compute the time lags.

Fig. 1 shows the parameter ΔE as a function of the spectral index for all arrays considered in CTA Monte Carlo simulations. E_{lim} is chosen to be optimal while preserving the highest statistics at high energies. This value is almost stable regardless of the array or spectral index used and lies around 500 GeV. Arrays which maximize ΔE are J, C, H, I for the Southern site and NB for the Northern array. The same ranking is obtained for the quadratic difference ΔE^2 .

3 Effect of increased statistics

3.1 The analysis procedure

Here a likelihood fit procedure, as described in detail by Abramowski et al. (2011) and Martinez & Errando (2009), is used to measure the energy dependent time lags. This method makes use of individual photon information (energy and detection time) and requires a parameterization of both the light curve and the spectrum. The light curve is parameterized (function F_S) at low energies where the time lags are supposed to be negligible and the measured spectrum (Λ) is parameterized in the full energy range of the instrument. Then the probability density function (pdf) is given by:

$$P(t, E) = \int_0^\infty A(E_S) \Lambda(E_S) G(E - E_S, \sigma(E_S)) F_S(t - \tau_l E_S) dE_S, \quad (3.1)$$

where A is the acceptance of the detector and G takes into account the energy resolution of the detector, considered here to be 10%. After normalizing the pdf, the parameter τ_l (here for the linear correction to the dispersion relation of Eq. 1.1) is obtained by minimizing $-\ln(L)$ where

$$L = \prod_{\text{all photons}} P(t, E). \quad (3.2)$$

A toy Monte Carlo software developed for PKS 2155-304 analysis (Abramowski et al. 2011) is used to simulate various sets of photons with given time and energy distributions. The injected lags range from -60 s TeV^{-1} to 60 s TeV^{-1} in steps of 20 s TeV^{-1} for the linear case and from -60 s TeV^{-2} to 60 s TeV^{-2} in steps of 20 s TeV^{-2}

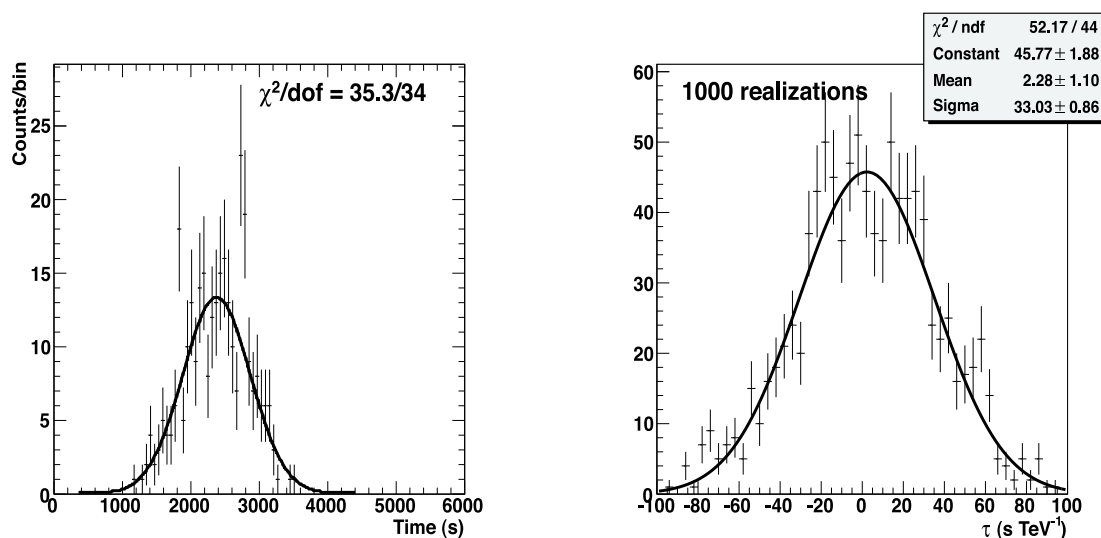


Fig. 3. **Left:** realization of a light curve with 300 photons and a binning of 60 s (H.E.S.S. case). The fit with a Gaussian curve leads to $\chi^2/\text{dof} = 35.3/34$. **Right:** distribution of the minimum of the likelihood for 1000 realizations of the lightcurve. The distribution is fitted with a Gaussian curve.

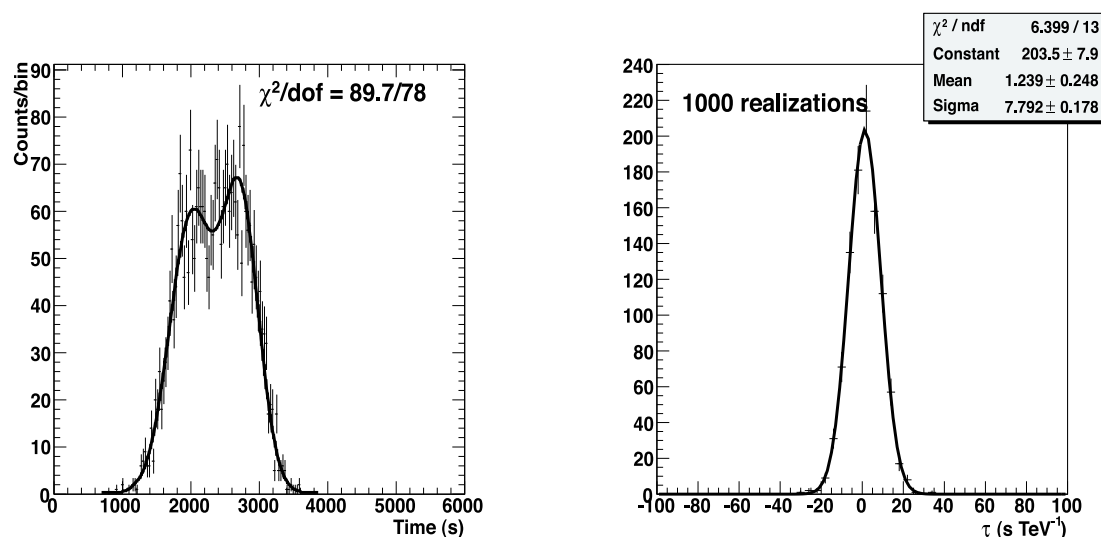


Fig. 4. **Left:** the flare of Fig. 3 (left) with 3000 photons and a binning of 30 s (CTA case). The fit with a double Gaussian curve leads to $\chi^2/\text{dof} = 89.7/78$. **Right:** distribution of the minimum of the likelihood for 1000 realizations of the lightcurve. The distribution is fitted with a Gaussian curve.

for the quadratic case. For each injected lag, 1000 realizations of the lightcurve are simulated. The obtained distribution of reconstructed lags is a Gaussian with standard deviation σ_τ . The mean dispersion $\bar{\sigma}_\tau$ is found as a standard deviation when fitting the distribution of Fig. 4 (right) and represents the calibrated error value used in further computation of the limits on LIV.

3.2 Peak separation capabilities

The likelihood fit procedure requires the measured light curve to be parameterized at low energies. As the error σ_τ is smaller when the spikes of the light curve are narrower, the peak separation capability is essential: a single peak seen by present day experiments could be observed with sub-structures with an instrument as CTA, which would in turn increase the performance of the analysis. In this section, this issue is studied using simple

hypotheses.

A list of 3000 photons is generated randomly with energies following a power law distribution with index $\Gamma = 2.8$ and a time distribution chosen to be the sum of two Gaussian functions, which have the same standard deviation σ_G and the separation between the peaks is varied from 0 to 1400 s. The time distribution is fitted with one or two Gaussian functions. The bin width of the light curve is set to 60 s for H.E.S.S./MAGIC and to 30 s for CTA. The minimal peak separation is then obtained when $\chi^2/\text{dof} = 1.5$.

Fig. 2 (previous page) shows the minimal peak separation necessary to distinguish the two spikes as a function of σ_G . For example, for two spikes of width $\sigma_G = 300$ s, a separation of at least 900 s is needed for H.E.S.S./MAGIC and only 500 s for CTA.

In order to quantify the effect of this result on the limits on M_{LIV} , the likelihood was computed for $\sigma_G = 300$ s and a peak separation of 700 s.

As an example of this type of studies, Fig. 3 shows the fit of a realization of the light curve (left) and the distribution of likelihood minima for 1000 realizations (right) for an injected lag of 0 s TeV^{-1} and for 300 photons. The fit of the lightcurve with a single Gaussian curve gives a good value of $\chi^2/\text{dof} = 35.3/34$.

Fig. 4 shows the same plots for 3000 photons. The two peaks are clearly visible and the light curve is fitted with the sum of two Gaussian functions. The lag reconstruction precision is improved by a factor of 5.

3.3 Lag reconstruction precision

In this section, the simulated time distribution of photons is considered to be a Gaussian curve with a standard deviation of σ_P . The energy distribution follows a power law $E^{-\Gamma}$ with index $\Gamma = 3.4$ (corresponding to PKS 2155-304 data recorded by H.E.S.S. in 2006 flare Aharonian et al. (2007)).

As expected, the average error $\bar{\sigma}_\tau$ on the reconstructed lag as a function of the number N_L of photons included in the likelihood fit computation (*ie* photons in the energy range of 0.3–10 TeV) follows the relation:

$$\bar{\sigma}_\tau \sim 1/\sqrt{N}. \quad (3.3)$$

In addition, and as already pointed out by Abramowski et al. (2011), when the width of the light curve peak σ_P increases, $\bar{\sigma}_\tau$ increases as well. This is related to the fact that the error on the lag is strongly dependent on the variability amplitude of the source.

As a conclusion at this step, it is expected that a flare like the one of PKS 2155-304 in July 2006 would lead to an error of <1 s TeV^{-1} (considering systematic and statistical effects) with CTA.

4 Discussion

The simulations performed for this work show that CTA will greatly improve the sensitivity of photon propagation studies with respect to LIV effects. Considering the fact that the sensitivity will be ten times higher than the one of present-day experiments and that the energy range covered will be much larger, the Planck scale will be easily reached for the “linear” models, comforting the present *Fermi* and H.E.S.S. results (Abdo et al. 2009a,b; Abramowski et al. 2011). In case of a flare as the one of Mkn 501 seen by MAGIC, Planck scale will be reached for the linear correction to the dispersion relations while a flare as the one seen by H.E.S.S. with PKS 2155-304 would largely exceed this value. The main increase in sensitivity will be reflected in the LIV scale in case of the “quadratic” models where a new range of detection will emerge. In particular, taking into account the best array configurations of section 2, the limits for the quadratic term of the dispersion relation should be higher than 10^{12} GeV.

Another important question for future studies is how many AGN flares will be observed by CTA. Of all flares observed so far, only three had enough statistics and high variability to be used for search of LIV. It is expected that CTA will detect tens of AGN flares per year, especially in the so-called “survey pointing mode” where each telescope points at different locations of the sky, allowing a higher probability to detect transient events. This will allow to increase the sensitivity to LIV effects by use of stacking procedures.

We gratefully acknowledge the support of GdR PCHE in France.

References

Abdo, A. A., Ackermann, M., Arimoto, M. et al. (Fermi LAT Collaboration) 2009, Science Express, 02/19/2009

- Abdo, A. A., Ackermann, M., Arimoto, M. et al. (Fermi LAT Collaboration) 2009, *Nature*, 462, 331
- Abramowski, A., Acero, F., Aharonian, F. et al. (H.E.S.S. Collaboration) 2011, *Astropart. Phys.*, 34, 738
- Aharonian, F., Akhperjanian, A. G., Bazer-Bachi, A. R., et al. (H.E.S.S. Collaboration) 2007, *ApJL*, 664, L71
- Albert, J., Aliu, E., Anderhub, H. et al. (MAGIC Collaboration) 2007, *ApJ*, 669, 862
- Albert, J., Aliu, E., Anderhub, H. et al. (MAGIC Collaboration) 2008, *Phys. Lett. B*, 668, 253
- Alfaro, J., Morale-Técotl, H. A. & Urrutia, L. F. 2002, *Phys. Rev. D*, 65, 103509
- Amelino-Camelia, G., Ellis, J., Mavromatos, N. E. et al. 1998, *Nature*, 395, 525
- Amelino-Camelia, G. 2008, arXiv:0806.0339
- CTA Consortium 2010, arXiv:1008.3703, <http://www.cta-observatory.org>
- Ellis, J., Mavromatos, N. E. & Nanopoulos, D. V. 1999, *Phys. Rev. D*, 61, 027503
- Gambini, R. & Pullin, J. 1999, *Phys. Rev. D*, 59, 124021
- Martinez, M. & Errando, M. 2009, *Astropart. Phys.*, 31, 226
- Mazin, D. 2008, in *Science with the New Generation of High Energy Gamma-Ray Experiments*, eds. Scineghe

DATA ANALYSIS METHOD FOR THE SEARCH OF POINT SOURCES OF GAMMA RAYS WITH THE HAGAR TELESCOPE ARRAY

R. J. Britto¹, B. S. Acharya¹, G. C. Anupama², P. Bhattacharjee³, V. R. Chitnis¹, R. Cowsik^{2,4}, N. Dorji¹, S. K. Duhan¹, K. S. Gothe¹, P. U. Kamath², P. K. Mahesh², J. Manoharan², B. K. Nagesh¹, N. K. Parmar¹, T. P. Prabhu², S. K. Rao¹, L. Saha⁴, F. Saleem², A. K. Saxena², S. K. Sharma¹, A. Shukla², B. B. Singh¹, R. Srinivasan², G. Srinivasulu², P. V. Sudersanan¹, D. Tsewang², S. S. Upadhy¹ and P. R. Vishwanath²

Abstract. The High Altitude GAMMA-Ray (HAGAR) experiment is the highest altitude atmospheric Cherenkov sampling array, set up at 4300 m amsl in the Himalayas (Northern India). It constitutes 7 telescopes, each one with seven 90 cm-diameter mirrors, a field of view of 3 degrees, and was designed to reach a relatively low threshold (currently around 200 GeV) with quite a low total mirror area (31 m²). In order to remove the strong isotropic background of charged cosmic rays, data are collected by tracking separately ON-source followed by OFF-source regions, or vice-versa. Typical observations period is about 30-40 min. ON-OFF data pairs are then selected according to quality parameters such as stability of the trigger rate and the comparison of average trigger rates between ON and OFF-source data sets. Signal extraction from point sources is done by performing analysis cuts on the count rate excess, rejecting off-axis events. Validation of method and systematics are evaluated through the analysis of fake sources (OFF-OFF pairs) located at similar declination as the observed point sources. Spurious signal, if any, would show up in this study.

Keywords: gamma rays: atmospheric Cherenkov technique, methods: data analysis, telescopes: HAGAR

1 Introduction

When a cosmic gamma-ray photon enters the Earth atmosphere, it causes a shower of relativistic particles. These particles initiate a spherical wavefront of blue-UV Cherenkov light which originates mostly from the shower maximum region (at about 10 km a.s.l. at 100 GeV). This wavefront has a width of few nanoseconds and forms on the ground a pool of light with a diameter of about 200 metres. Sampling the Cherenkov light using fast PMTs and recording precise relative arrival time between the detectors are the key for the detection of gamma rays at GeV energies, using wavefront sampling detectors. Located at 4270 m amsl in the Ladakh region of the Himalayas, in Northern India (Latitude: 32°46'45" N, Longitude: 78°58'36"E), the HAGAR experiment is a Cherenkov sampling array of 7 telescopes, each one built with 7 para-axially mounted 0.9 m-diameter mirrors, giving a total reflective area of ~31 m² (Fig. 1a).

Other characteristics are: $f/D \sim 1$; fast Photonis UV sensitive photomultipliers (PMTs) XP 2268B at the focus of each mirror and with a field of view of 3°17'; data recorded for each event: relative arrival time of shower front at each PMT accurate to 0.25 ns using TDCs; total charge at each mirror recorded using 12 bit QDCs; absolute event arrival time accurate to μ s. For trigger generation, the 7 pulses of PMTs of a given telescope are linearly added to form one telescope pulse, called *royal sum* pulse. HAGAR operates with a trigger logic designed to significantly reject random triggers due to night sky background (NSB), as well as some of the cosmic ray events. Thus, a coincidence of any 4 telescope pulses above a preset threshold out of 7 royal sum pulses, within a resolving time of 150 to 300 ns, generates a trigger pulse (Chitnis et al. 2009).

¹ Tata Institute of Fundamental Research, Homi Bhabha Road, Mumbai 400 005, India

² Indian Institute of Astrophysics, Sarjapur Road, 2nd Block, Koramangala, Bangalore 560 034, India

³ Saha Institute of Nuclear Physics, 1/AF, Bidhannagar, Kolkata 700 064, India

⁴ Now at Washington University, St Louis, MO 63130, USA

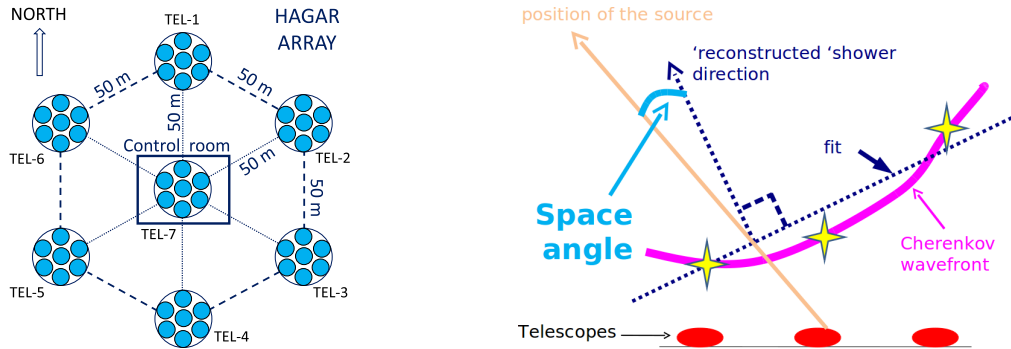


Fig. 1. (a) The HAGAR telescope array. (b) Illustration of the space angle fitting procedure.

Several sources are observed with HAGAR (Chitnis et al. 2011). We give in brackets the duration in hours of the ON-source observations up to June 2011: Galactic sources: Crab Nebula and pulsar (117), Geminga pulsar (76), X-ray binary LSI +61 303 (26), MGRO 2019+37 (15); and extragalactic sources—blazars: Markarian 421 (86) and 501 (49), 1es2344+514 (80), and 3C454.3 (15). Also we have started to regularly observe some Fermi pulsars.

2 Signal extraction procedure

The analysis of HAGAR data is based on the estimation of the arrival angle of the incident atmospheric shower w.r.t. the source direction. This angle—called space angle—is obtained for each event by measuring relative arrival times of the shower at each telescope. This allows us to fit the arriving spherical Cherenkov wavefront, using plane front approximation. The normal to this plane gives the reconstructed shower direction (Fig. 1b). Precise time calibration of the optoelectronic chain is then required, as well as an accurate pointing of telescopes (Chitnis et al. 2009). Time calibration is achieved first by computing TDC differences between pairs of telescopes from fix angle runs (*i.e.* using real cosmic-ray events) where the time-offsets are calculated, using information on the pointing direction, coordinates of telescopes, and on the transit time of each channel through the electronic chain. The TDC differences between pairs of telescopes from fix angle runs yield the calculation of what we call “ T_0 ’s” (say “t-zeros”), which are the relative time offsets for each telescope. These offsets are to be used in the analysis to ensure a valid estimation of the relative timing differences in the arrival of the Cherenkov signal on the telescopes. As we require a timing precision of 1 ns, the accuracy of the calculation of T_0 ’s is fundamental. We have found that the computation of a set of T_0 ’s is dependent on the nature of trigger. We require that at least 4 telescopes out of 7 get a signal above a preset threshold, which leads to 64 possible combinations for the trigger: events which trigger Tel. 1,2,3,4, events which trigger Tel. 1,2,3,5, etc. (Britto et al. 2011a).

Space angle (Ψ) is then computed by fitting the arriving spherical Cherenkov wavefront, using plane front approximation. For each event, the value of the χ^2 of the fit and other fit parameters are given, and the number of telescopes with valid TDC information, *i.e.* participating in the trigger, is written. Thus are defined four types of events, based on the *Number of Triggered Telescopes* (NTT), viz. events with NTT=4, NTT=5, NTT=6 and NTT=7.

Events with $\chi^2 \geq (\text{mean} + 1\sigma)$ are rejected, where χ^2 is the parameter of plane front fit. Further we reject events with space angle greater than 7° , as these are mostly due to bad fits (noise, chance triggers, etc.). Space angle distribution is plotted for each pair and each event type.

In order to remove isotropic emission due to cosmic rays, source observation region (ON) is compared with OFF-source region at same local coordinates on the sky, but at a different time (before or after tracking the source region for about 30-50 mins). However, atmospheric conditions change during observation time, reflected by variations on the trigger rate readings. This add systematics in our analysis. Normalisation of background events of both the ON and OFF source data sets is done by comparing number of events at large space angles, where no significant gamma-ray signal is expected. This yield a ratio, called *normalisation constant* “C”. The normalisation region (NR) of Ψ is defined as the range from the FWHM cut (say Ψ_{cut}) to 7 deg (Fig. 2a). The ON-OFF excess is then computed as the normalised excess below Ψ_{cut} . However, two difficulties arise in the use of C. First, we assume that no signal at all is present in the NR. The second difficulty is that the number

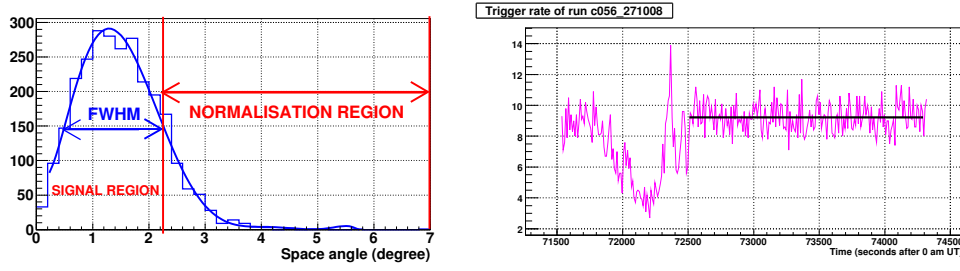


Fig. 2. (a) Illustration of the cuts we perform to define the normalisation region on the space angle distribution of OFF-source data sets. Cut is shown for $NTT=7$. (b) Raw trigger rate versus time for a run with a rate stable after 72500 seconds: only the stable part of the run was kept. Each bin corresponds to a duration of 10 seconds.

of events in the NR is small, which induces some statistical error on C . Therefore, our results are given through two ways of computing C . The first method is the basic ratio:

$$C1 = \frac{N_{ON}^{(NR)}}{N_{OFF}^{(NR)}}. \quad (2.1)$$

The second method is a χ^2 minimisation of the bin per bin $N_{ON}^{(NR)} - C2 \times N_{OFF}^{(NR)}$ expression:

$$\chi_k^2 = \sum_{i=\Psi_{cut}}^7 (N_{ON}^{(NR)} - C2_k \times N_{OFF}^{(NR)})^2 \quad (2.2)$$

where $C2_k$ varies from 0.5 to 2.0 with a step (k) of 0.001. The size of the i bin is 0.1 deg.

3 Data selection

Data selection is done using some parameters which characterize good quality data, in order to reduce systematics as much as possible. Our selection is done both run-wise and pair-wise. Runs with high value of the trigger rate are laid aside for future analysis, as they were taken under different conditions. We first reject acquisitions whose trigger rate is non stable and whose defaults in timing information are identified. We show in Fig. 2b an example of a trigger rate plot as a function of time of a run, where only the stable part of the plot can be selected. The stability of the trigger rate of each run is quantified using one variable, called R_{stab} , defined as the RMS of the rate on the square root of its mean. For perfect poissonian fluctuations, this variable is expected to be equal to 1. Run rejection is done for $R_{stab} \geq 1.5$. Also, stability of the mean rates of events remaining after analysis cut is verified by $R_{stab} \leq 1.2$.

Pair selection is then done by constraining several parameters. One of our selection parameters is the relative difference of the *One Fold* rate (rate of triggers due to one or more telescopes which is recorded as monitoring information) between ON and OFF source runs. This parameter is related to the night sky background rate. Its value is imposed to be less than 15 %, otherwise the pair is rejected. Due to changes in the HAGAR hardware, the *One Fold* rate was not monitored for most of the dark region acquisitions presented in next section. An other criterion for selection is on the ON/OFF absolute difference of the average trigger rate. This difference is imposed to be less than 2.5 Hz. These previous criteria are designed to control dramatic changes in atmospheric conditions, night sky brightness, acquisition threshold, etc., within a pair. During the pair processing, ratio of events for each telescope are computed and constrained to be between 0.75 and 1.25 for at least 6 telescopes, for the analysis of data from dark regions. A cut on the value of C is required in the same range. Then, a cut is imposed to reject data sets with a hour angle greater than 2.5 hours (39 deg. of zenith angle).

4 Analysis and results of data from sky dark regions

Crab nebula, standard candle of the γ -ray astronomy, is used to calibrate the instrument and optimize hadronic rejection. As previously mentioned, our current analysis method is built upon the estimation of the space angle of both the ON and OFF data sets, and on a proper evaluation of the normalisation constant C (computed to

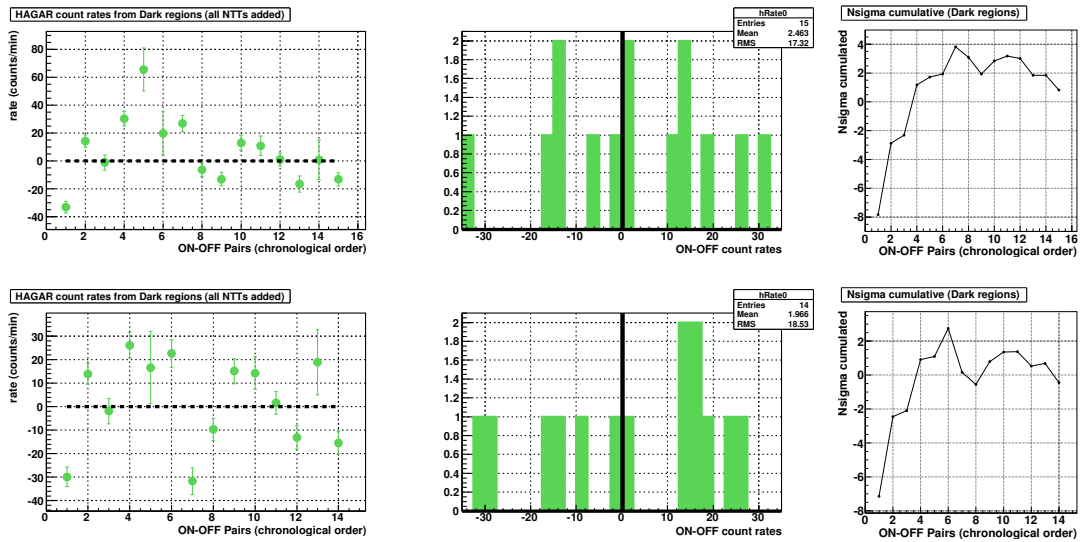


Fig. 3. Pair by pair count rates for the selected dark region data set, computed using C1 (top), and C2 (bottom).

Data sets	C	no. of pairs sel./ini.	duration	N_σ
Dark	1	15*/26	6.5 h	0.8
	2	14*/26	6.4 h	-0.4

Table 1. Summary of results obtained from the 3 data sets. (*) indicates that two pairs share a common “OFF 1” run respectively in two occurrences.

balance differences in comic-ray triggers between ON and OFF data sets). However, signal extraction can be confirmed if background fluctuation between ON and OFF-axis source is not dominant, so an important step in the validation of the analysis method is to observe and analyse data by comparing two sets of OFF-source regions (called *dark regions* or *fake sources*), located at a similar declination as of Crab nebula ($\simeq 22^\circ$). Out of the initial 26 pairs, we have selected up to 15 pairs, corresponding to 6.5 hours of data. An excess with a significance of 0.82 and -0.44σ (for excess computed with C1 and C2 respectively) is seen, which is compatible with zero (Fig. 3 & Tab. 1). This indicates that systematic effects due to sky and time differences during observations are not dominant in our data/analysis.

5 Conclusions

Observations with the HAGAR telescope array are regular since September 2008. Several Galactic and extragalactic sources are observed. Analysis of dark regions and regions containing a bright blue star show us that, under appropriated data selection and analysis cuts, we can perform the analysis of gamma-ray point sources (Britto et al. 2011b).

R. J. Britto would like to thank the organizers of the SF2A conference and the PCHE group for providing financial support to attend the conference. We thank J. K. Chabukswar and G. Raman for their participation in the data selection work, the local staff at Hanle, and all members of our institutes and visiting students who have contributed towards the design, fabrication and testing of telescopes and data acquisition systems of HAGAR.

References

- Britto, R. J. et al, Proc. of the 22nd ECRS, Astrophys. Space Sci. Trans., 2011a, 8, 1-5
 Britto, R. J. et al., 2011b, these proc.
 Chitnis, V. R. et al, Proc. of the 31st ICRC, 2009, OG 2.7, Paper # 0696
 Chitnis, V. R. et al, Proc. of the 32st ICRC, 2011, OG 2.5, paper # 1089

STATUS OF THE HIMALAYAN GAMMA-RAY OBSERVATORY (HIGRO) AND OBSERVATION WITH HAGAR AT VERY HIGH ENERGIES

R. J. Britto¹, B. S. Acharya¹, G. C. Anupama², N. Bhatt³, P. Bhattacharjee⁴, S. Bhattacharya³, V. R. Chitnis¹, R. Cowsik^{2,5}, N. Dorji¹, S. K. Duhan¹, K. S. Gothe¹, P. U. Kamath², R. Koul³, P. K. Mahesh², J. Manoharan², A. Mitra³, B. K. Nagesh¹, N. K. Parmar¹, T. P. Prabhu², R. C. Rannot³, S. K. Rao¹, L. Saha⁴, F. Saleem², A. K. Saxena², S. K. Sharma¹, A. Shukla², B. B. Singh¹, R. Srinivasan², G. Srinivasulu², P. V. Sudersanan¹, A. K. Tickoo³, D. Tsewang², S. S. Upadhya¹, P. R. Vishwanath² and K. K. Yadav³

Abstract. High Altitude GAMMA Ray (HAGAR) telescope array, which is the first stage of Himalayan Gamma Ray Observatory (HIGRO), has been successfully installed at Hanle in Himalayas and has been collecting science data since September, 2008. In last three years, we have observed several sources including Galactic objects like Crab Nebula, Geminga, LSI+61 303 and some of the Fermi detected pulsars as well as extragalactic objects including Mkn 421, Mkn 501, 1ES2344+514, 3C454.3 etc. Analysis of data on all these sources is underway. Preliminary results include detection of Crab Nebula and Mkn 421 during its flare in February, 2010. Upper limits are given for several pulsars. In the second phase of HIGRO, Major Atmospheric Cherenkov Experiment (MACE), a 21 m-imaging telescope, will be installed at Hanle, next to HAGAR.

Keywords: gamma rays: atmospheric Cherenkov technique, methods: data analysis, telescopes: HAGAR

1 Introduction

Located at 4270 m amsl in the Ladakh region of the Himalayas, in Northern India (Latitude: 32°46'45" N, Longitude: 78°58'36" E), the Himalayan Gamma Ray Observatory (HIGRO) is the highest altitude ground-based gamma-ray observatory using the atmospheric Cherenkov technique. Phase 1 of HIGRO is the HAGAR experiment, operating with the full array since 2008. HAGAR is a sampling array of 7 telescopes, each one built with 7 para-axially mounted 0.9 m-diameter mirrors, giving a total reflective area of $\sim 31 \text{ m}^2$. Relative arrival time of Cherenkov shower front at each mirror is recording using TDCs and Flash ADCs, in order to obtain a timing precision as good as 1 ns, to sample the Cherenkov flash. Technical details as well as analysis procedure are given in companion paper (Britto et al. 2011), referred as *Paper I* hereafter.

In order to remove isotropic emission due to cosmic rays, source observation region (ON) is compared with OFF-source region at same local coordinates. The analysis of data is based on the arrival angle estimation of the incident atmospheric shower w.r.t. the source direction. This angle—called space angle—is obtained for each event by measuring relative arrival times of the shower at each telescope. Signal is extracted after rejecting large space angle events, and following the process of normalisation of ON/OFF background events (at large space angle), to balance night sky background differences between both data samples (Paper I). As the process of computing the normalisation constant 'C' is difficult due to the lack of statistics in the normalisation region, C is computed through two methods, as explained in Paper I. This gives the C1 and C2 values of C respectively.

¹ Tata Institute of Fundamental Research, Homi Bhabha Road, Mumbai 400 005, India

² Indian Institute of Astrophysics, Sarjapur Road, 2nd Block, Koramangala, Bangalore 560034, India

³ Bhabha Atomic Research Centre, Trombay, Mumbai 400 085, India

⁴ Saha Institute of Nuclear Physics, 1/AF, Bidhannagar, Kolkata 700 064, India

⁵ Now at Washington University, St Louis, MO 63130, USA

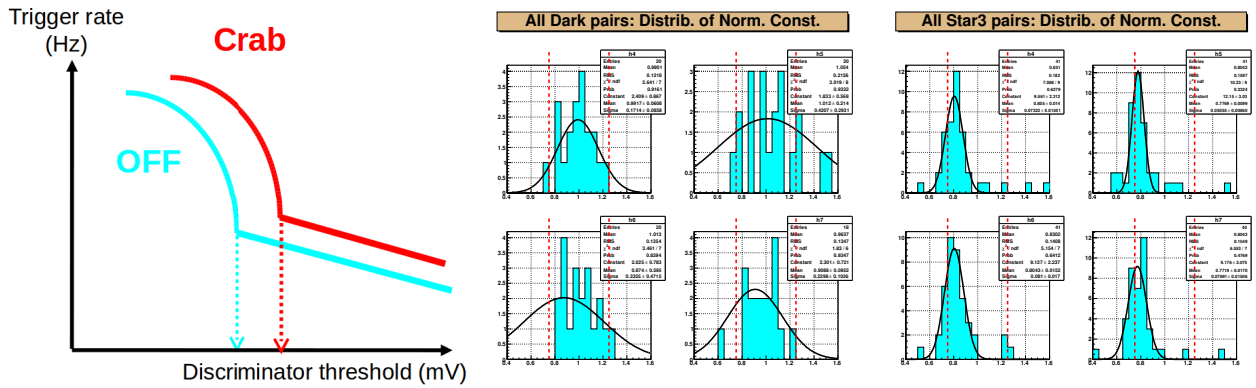


Fig. 1. (a) Representation of the Crab ON/OFF trigger rate versus hardware energy threshold. (b) Distribution of normalisation constants “C2” for “dark regions”. (c) Distribution of normalisation constants “C1” for “star3” runs. From left to right and top to bottom of (b) and (c) respectively, are normalisation constants for NTT=4, 5, 6 and 7. The dashed red vertical lines delimitate the accepted range of C for dark region pairs (Paper I).

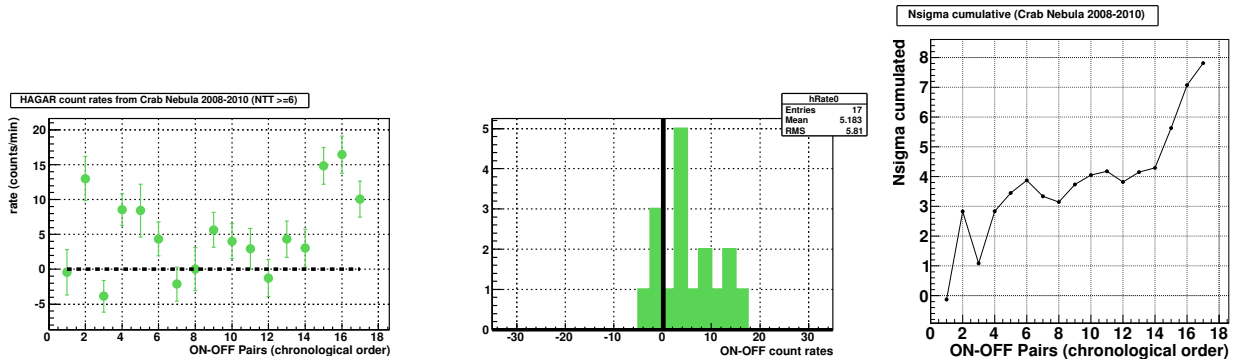


Fig. 2. Pair by pair count rates, computed using C1, for the selected data set of Crab Nebula 2008-2011.

2 A bright star in the field of view of Crab Nebula

The Crab Nebula is located at 67.5' from a star of magnitude 3. This star is within the FOV of the PMT during observations of Crab Nebula. As we keep PMT rates at 5 kHz for both ON and OFF runs, hardware energy threshold of Crab runs is higher than for off-source runs, as illustrated in Fig. 1(a). We need to verify if our analysis method could be biased by the presence of this bright star. So we performed acquisitions of so-called “star3” pairs, where we keep this bright star (or a star of similar magnitude and colour) in the field of view (FOV) of HAGAR, but with the Crab Nebula outside FOV. Due to these ON/OFF differences in trigger rates, we had to redefine the pair selection related to the ON/OFF ratio of events per telescope and the normalisation constant values. The mean values of normalisation constant are around 1 for “dark regions” (Fig. 1b), but systematically below 1 for “star 3” pairs (Fig. 1c).

The ranges for the normalisation constant were constrained to be within 0.65-0.95, as the mean value is around 0.8 (Fig. 1c). Results based on a minimum of 4 triggered telescopes ($NTT \geq 4$) gives an artefact of signal. By keeping $NTT \geq 6$, we increase the energy threshold and significantly reject low energy events. Out of the initial 47 pairs, we have selected 11 pairs, corresponding to 7.2 hours of data. No excess is seen (significance less than 2.0σ , which is compatible with zero (Tab. 1). This indicates that systematic effects induced by a much brighter FOV during observations are to be considered in our data/analysis, and can be balanced by an appropriate event selection.

3 Analysis of the data from Crab Nebula

Since Sep. 2008, more than 120 hours of data have been collected from Crab Nebula. Using an event selection procedure, similar to the one of “star 3” data analysis, we perform the analysis of 10.4 hours of Crab Nebula data from the period 2008-2011.

Data sets	C	no. of pairs sel./ini.	duration	Count rate	N_σ	N_σ/\sqrt{h}
Dark	1	15(-)/26	6.5 h	-	0.8	-
	2	14(-)/26	6.4 h	-	-0.4	-
Star3	1	11/47	7.2 h	-	1.4	-
	2	11/47	7.2 h	-	2.0	-
Crab	1	17/153	10.4 h	5.1 ± 0.7	7.8	2.4
	2	20/153	12.6 h	5.7 ± 0.6	9.5	2.7

Tab. 1. Summary of results obtained from the 3 data sets used to report our results on Crab Nebula. Dark region results are described in Paper I. (-) indicates that two pairs share a common “OFF 1” run respectively in two occurrences. $NTT \geq 4$ for ‘dark’ pairs; $NTT \geq 6$ for “star3” and “Crab” pairs.

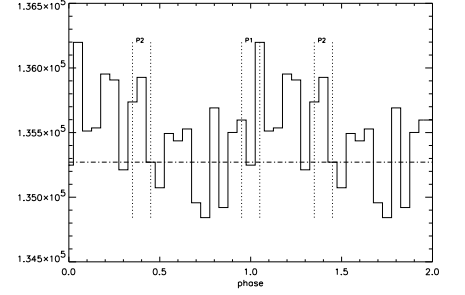


Fig. 3. Phase histogram for Crab pulsar.

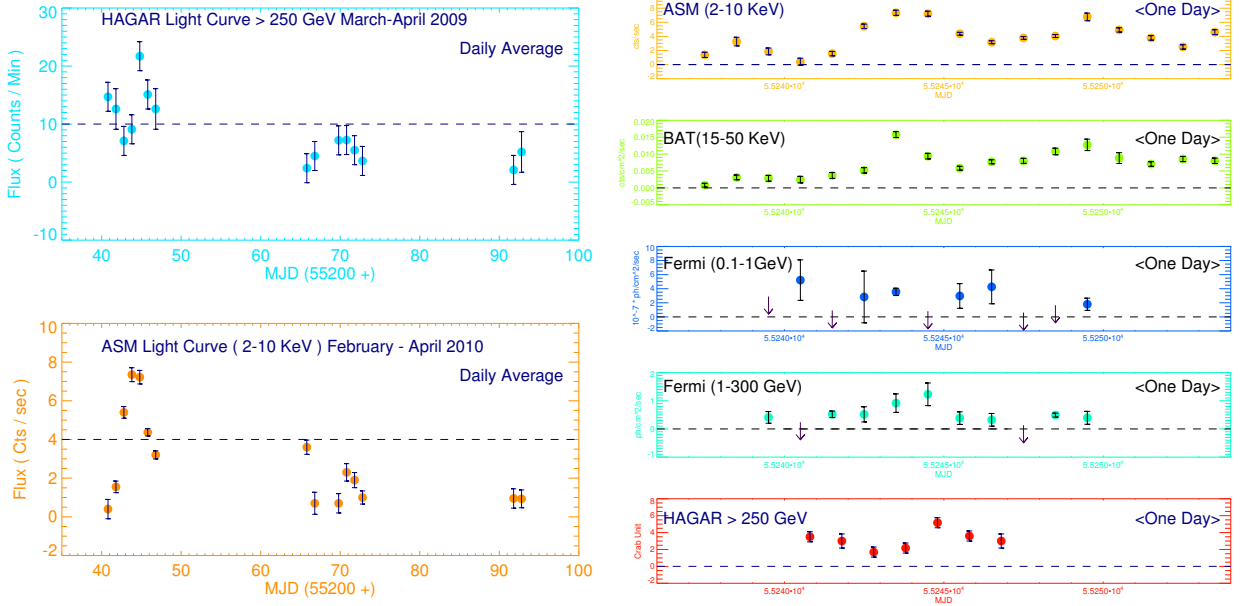


Fig. 4. *Left:* Daily average light curve of Mrk421 during Feb.-Apr. 2010. *Right:* Daily average light curve of Mrk421 during Feb. 2010.

An excess at 7.8σ ($2.4\sigma/\sqrt{h}$) is reported, corresponding to $5.1 \pm 0.7 \text{ counts min}^{-1}$, while computing the excess using C1. An excess of 9.5σ ($2.7\sigma/\sqrt{h}$), corresponding to $5.7 \pm 0.6 \text{ counts min}^{-1}$, is obtained based on 12.6 hours of data and using the normalisation constant C2 (Fig. 2 and Tab. 1). However, these values seem overestimated while comparing with our simulations, which predict $1.3 \text{ gamma}/\sqrt{h}$ and $2.6 \text{ counts min}^{-1}$ for vertical showers for a 1 Crab flux (Saha et al. 2011).

4 Study of pulsars

Search for pulsed emission at the known period has been carried out for several pulsars (Singh et al. 2011). Phase histogram for Crab pulsar is shown folded over rotation period (33 ms) for two cycles in Fig. 3. The

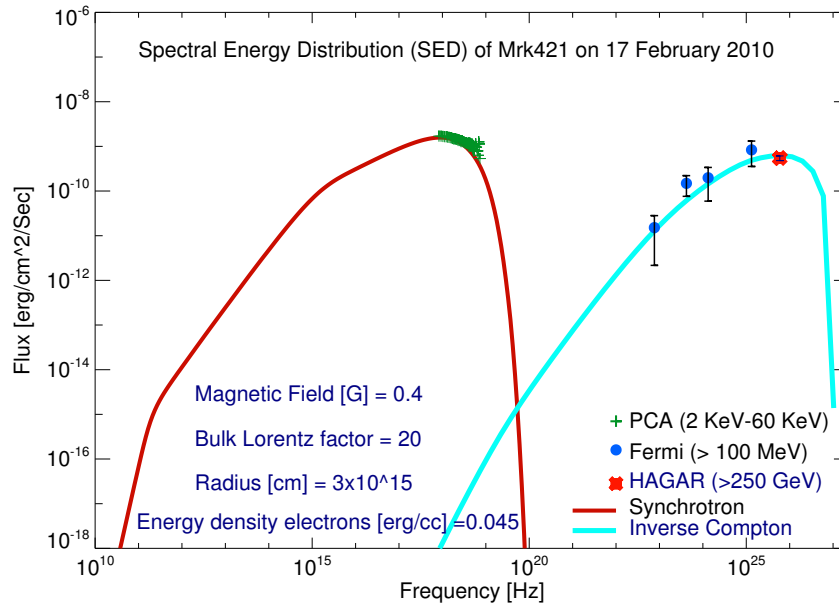


Fig. 5. Spectral Energy Distribution of Mrk421 of 17 February, 2010.

monthly timing ephemeris of the Crab pulsar were extracted from Jodrel Bank crabtime data base*. From HAGAR data, no evidence for pulsed emission was seen at energies above 200 GeV. Time averaged 3σ upper limits on pulsed component of gamma ray flux are estimated. For Crab pulsar, the estimated upper limit is $1.5 \times 10^{-11} \text{ ph cm}^{-2} \text{ s}^{-1}$. The upper limit for Geminga pulsar is $3.6 \times 10^{-11} \text{ ph cm}^{-2} \text{ s}^{-1}$. Three Fermi detected pulsars, viz. J0357+32, J0633+0632 and J2055+2539 are being observed with HAGAR. These pulsars have high confidence pulsed emission, rotational energy loss rate and flat emission spectrum. Preliminary analysis indicate that there is no evidence of pulsed emission from any of these sources in our data at energies above 200 GeV.

5 Analysis of the data from Markarian 421 during its high activity state

HBL BL Lac AGN Markarian 421 (Mkn 421, $z=0.031$) has been observed during its high activity state, in Feb.-Apr. 2010 (Shukla et al. 2011). Data analysis was performed on data with a zenith angle less than 6 deg. The analysis method is similar to the one described in Paper I, but as the source is far from the Galactic plane, sky is darker and so selection cuts are less tight. We report an excess of $13.4 \pm 1.05 \text{ count min}^{-1}$ at 12.7σ based on 479 minutes of data during February 2010.

We show on Fig. 4 (left) daily light curve of Mkn 421 during the high state of the X-ray and gamma ray from February to April 2010. It's clearly seen that source was in brightest state in the month of February in both Gamma rays and X-rays. Activity of the source has reduced in the months of March and April but it was still brighter than its quiescent level flux. On Fig. 4 (right) is shown quasi-simultaneous light curves of Mrk 421, during Feb. 2010, as obtained in X-ray and gamma ray bands, using archived data from other observatories together with the present data. The light curves are plotted with one day binning (daily average) in the above figure. One zone homogeneous SSC model (Krawczynski et al. 2004) is fitted to the X-ray and gamma data to obtain the SED (Fig. 5). This model assumes a spherical blob of radius R and uniform magnetic field B , moving with respect to the observer with the Lorentz Factor δ which is filled with a homogeneous non-thermal electron population. Best fit SED is obtained for the parameters given in Fig. 5.

*<http://www.jb.man.ac.uk/pulsar/crab.html>

6 Major Atmospheric Cherenkov Experiment

The Major Atmospheric Cherenkov Experiment (MACE) is a 21 m-imaging Cherenkov telescope which is expected to be installed at Hanle by 2012, next to the HAGAR array (Koul et al. 2005, 2011). It will have the following characteristics: a total reflective area of $\sim 330 m^2$ from 356 mirror panels; f/1.2 m; FOV of $4^\circ \times 4^\circ$, a 1088 pixel camera. The energy threshold is expected to be below 30 GeV. The sensitivity of MACE is expected to be comparable to the MAGIC one. Simultaneous observations with HAGAR are expected, in such a way that the same event can be detected by both the experiments. Foundations for the first imaging telescope and building of the control room of MACE at Hanle are well advanced. Installation of MACE is now going on in Hyderabad (South India), but with a limited number of mirror and PMTs. This will allow a phase of calibration and observations of Crab Nebula for a few months before the instrument is shifted to Hanle. We also expect at least a second similar imaging element to be installed next to the first element by 2014 or 2015, to perform stereoscopic observations (MACE II project).

7 Conclusions

The analysis of data from regions containing a bright blue star shows us that we can perform the analysis of gamma-ray point sources while balancing cosmic ray triggers and acquisition threshold differences. The preliminary results obtained from Crab Nebula give encouraging perspective for the study of gamma-ray point sources with the HAGAR telescope array. We report detection of Mkn 421 during its high activity state, and give upper limit on several pulsars. Furthermore, improvement of the method and development of new analysis softwares are still under going. The differences between Monte Carlo simulations and data regarding the strength of the signal (rate of gamma rays per minute) need to be probed further.

R. J. Britto would like to thank the organizers of the SF2A conference and the PCHE group for providing financial support to attend the conference. We thank J. K. Chabukswar and G. Raman for their participation in the data selection work, the local staff at Hanle, and all members of our institutes and visiting students who have contributed towards the design, fabrication and testing of telescopes and data acquisition systems of HAGAR.

References

References

- Britto, R. J. et al., 2011, these proc.
- Koul, R., Kaul, R. K., Mitra, A. K. et al., Proceedings of the 29st ICRC, Vol. 5, 243-246, 2005
- Koul, R. et al, 2011, Proc. of the 32st ICRC, 2011
- Krawczynski H. et al., 2004, ApJ, 601, 151
- Saha, L. et al., Proc. of the 32st ICRC, 2011, OG 2.5, paper # 1129
- Shukla A. et al., Proc. of the 32st ICRC, 2011, OG 2.3, paper # 977
- Singh B. B. et al., Proc. of the 32st ICRC, 2011, OG 2.2, paper # 276

THE W49 REGION AS SEEN BY H.E.S.S.

F. Brun¹, M. de Naurois¹, W. Hofmann², S. Carrigan², A. Djannati-Ataï³, S. Ohm^{2,4,5} and H.E.S.S. Collaboration⁶

Abstract. The W49 region hosts a star forming region (W49A) and a supernova remnant interacting with molecular clouds (W49B). The $10^6 M_{\odot}$ Giant Molecular Cloud W49A is one of the most luminous giant radio HII region in our Galaxy and hosts several active, high-mass star formation sites. The mixed-morphology supernova remnant W49B has one of the highest radio surface brightness of all the SNRs of this class in our Galaxy. Infrared observations evidenced that W49B is interacting with molecular clouds and Fermi recently reported the detection of a coincident bright, high-energy gamma-ray source. Observations by the H.E.S.S. telescope array resulted in the significant detection of VHE gamma-ray emission from the W49 region, compatible with gamma-ray emission from the SNR W49B. The results, the morphology and the origin of the VHE gamma-ray emission are presented in the multi-wavelength context and the implications on the origin of the signal are discussed.

Keywords: gamma rays, W49, H.E.S.S.

1 Introduction

The W49 region is a prime candidate to observe with ground-based Cherenkov telescopes such as H.E.S.S. since it hosts a star forming region (W49A) and a mixed morphology supernova remnant interacting with molecular clouds (W49B).

W49A is one of the most luminous giant HII region in the Galaxy (Smith et al. 1978). In the core (~ 15 pc) of this $10^6 M_{\odot}$ Giant Molecular Cloud of 100 pc in total extension (Simon et al. 2001), ~ 30 ultra-compact HII regions, each hosting at least one massive star (earlier than B3) are resolved in radio (de Pree et al. 1997). From the proper motion of the strong H_2O masers it hosts, the distance of W49A is estimated to be 11.4 ± 1.2 kpc (Gwinn et al. 1992).

The progenitor of W49B is thought to be a super-massive star that created a wind-blown bubble in a dense molecular cloud in which the explosion occurred (Keohane et al. 2007) as revealed by IR and X-ray observations. The detection of Mid-IR lines from shocked molecular hydrogen is an evidence that W49B is interacting with molecular clouds (Reach et al. 2006). From HI absorption analyses, its distance was estimated to be ~ 8 kpc (Radhakrishnan et al. 1972). More recent VLA observations show that W49B could be associated with W49A (Brogan & Troland 2001), extending the range of possible distances for this object ($8 \text{ kpc} < D < 12 \text{ kpc}$). Its age is estimated to be between 1 kyr and 4 kyrs (Pye et al. 1984; Hwang et al. 2000). In Radio, the supernova remnant shell is resolved with a size of $\sim 4'$. W49B is also detected by the Fermi-LAT at a level of 38σ with 17 months of data (Abdo et al. 2010).

The discovery of VHE γ -rays from the W49 region is reported in the next section. These preliminary results are then discussed.

¹ Laboratoire Leprince-Ringuet, Ecole Polytechnique, CNRS/IN2P3, Palaiseau, France

² Max Planck Institut für Kernphysik, Heidelberg, Germany

³ APC - AstroParticule Cosmologie, CNRS/IN2P3 - Univ Paris 7 - Observatoire de Paris - CEA, Paris, France

⁴ School of Physics & Astronomy, University of Leeds, UK

⁵ Department of Physics & Astronomy, University of Leicester, UK

⁶ <http://www.mpi-hd.mpg.de/hfm/HESS>.

2 H.E.S.S. Observations and Analysis Results

H.E.S.S. is an array of four 13 m diameter imaging Cherenkov telescopes situated in the Khomas Highlands in Namibia at an altitude of 1800 m above sea level (see e.g. Bernlöhner et al. 2003; Funk et al. 2004). The standard H.E.S.S. run selection procedure was used to select observations taken under good weather conditions. This resulted in a dataset comprising 60 hours of observations (live time) on W49B and W49A. Data were analysed using the *Model Analysis* as described in de Naurois & Rolland (2009). This analysis was performed on W49A and W49B, using the standard cuts which include a minimum charge of 60 photoelectrons resulting in an energy threshold of ~ 260 GeV. The analysis regions were defined a-priori as circles of 0.1° centered on the nominal position of W49A ($l = 43.17^\circ, b = 0.0^\circ$) and W49B ($l = 43.27^\circ, b = -0.19^\circ$). The results presented below were also confirmed by independent analyses such as those described in Ohm et al. (2009) or Becherini et al. (2011).

Figure 1 shows the resulting excess map smoothed to the H.E.S.S. Point Spread Function (PSF) (68% containment radius $R_{68} = 0.066^\circ$). An excess of 191 VHE γ -rays is detected towards W49B by H.E.S.S. with a statistical significance of 8.8σ using an integration radius of 0.1° . An excess of VHE γ -rays is also detected in the direction of W49A with a significance of more than 4.4σ . The best fit position of the TeV emission is found to be ($l = 43.258^\circ \pm 0.008^\circ, b = -0.188^\circ \pm 0.01^\circ$) assuming point-like emission. As shown on Figure 2, this is well coincident with the brightest radio part of the W49B remnant and with the GeV emission fitted position ($l = 43.251^\circ - b = -0.168^\circ$, with an error radius of 0.024° at 95% C.L. (Abdo et al. 2010)).

The TeV excess visible towards W49A is in good coincidence with the densest part of the molecular cloud as observed by the ^{13}CO Galactic Ring Survey (Jackson et al. 2006) as can be seen on Figure 2.

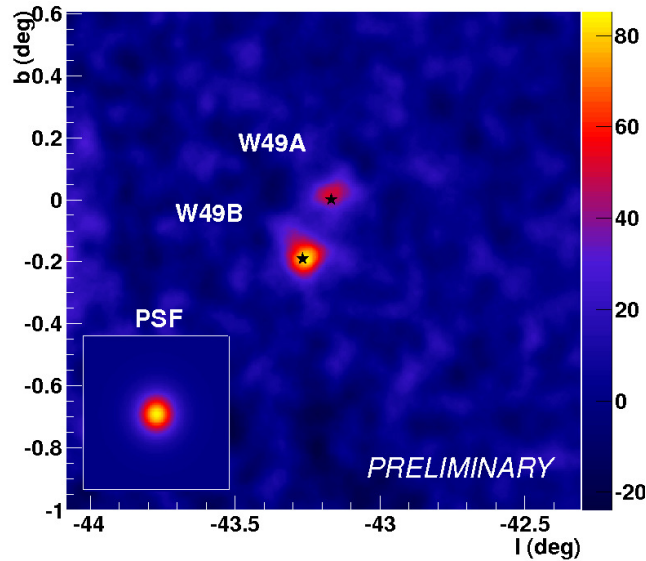


Fig. 1. H.E.S.S. excess map of the W49 region obtained with the Model Analysis. The map is smoothed to the H.E.S.S. PSF shown in the caption. The stars marks W49B and W49A nominal positions.

The differential energy spectrum of the VHE γ -ray emission towards W49B was derived above the energy threshold of 260 GeV selecting the events inside a circular region of 0.1° around the supernova remnant nominal position. The spectrum obtained for W49B is well described ($\chi^2/dof = 39.6/38$) by a power-law model defined as $dN/dE = N_0(E/1\text{TeV})^{-\Gamma}$ with $\Gamma = 3.1 \pm 0.3_{stat} \pm 0.2_{syst}$ and $N_0 = 2.3 \pm 0.4_{stat} \pm 0.6_{syst} 10^{-13} \text{ cm}^{-2}\text{s}^{-1}\text{TeV}^{-1}$. This corresponds to an integral flux above 1 TeV of $1.1 \pm 0.3_{stat} \pm 0.3_{syst} 10^{-13} \text{ cm}^{-2}\text{s}^{-1}$, equivalent to $\sim 0.5\%$ of the Crab nebula flux above the same energy. As can be seen on Figure 3, the GeV (Abdo et al. 2010) and TeV gamma-ray spectra are in remarkably good agreement.

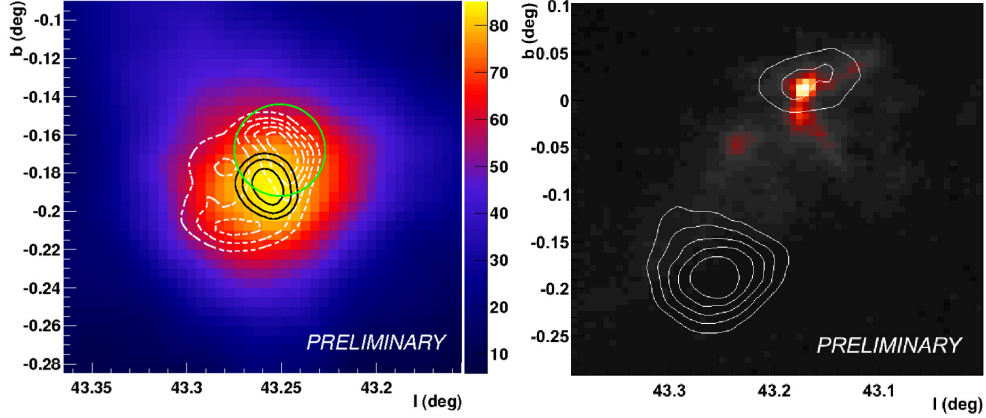


Fig. 2. Left: Detail of Figure 1 centered on W49B. The black contours are the error contours at 68%, 95% and 99% of the fitted position assuming point-like emission. The green circle is the Fermi-LAT fitted position at 95% C.L. The white contours show the radio emission as seen by NVSS. **Right:** Integrated Map of the $^{13}\text{CO}(J = 1 - 0)$ Galactic Ring Survey between $v_{LSR} = 0$ km/s and 20 km/s. This velocity range corresponds to the distance to W49A. The white contours are from the H.E.S.S. excess map shown in Figure 1.

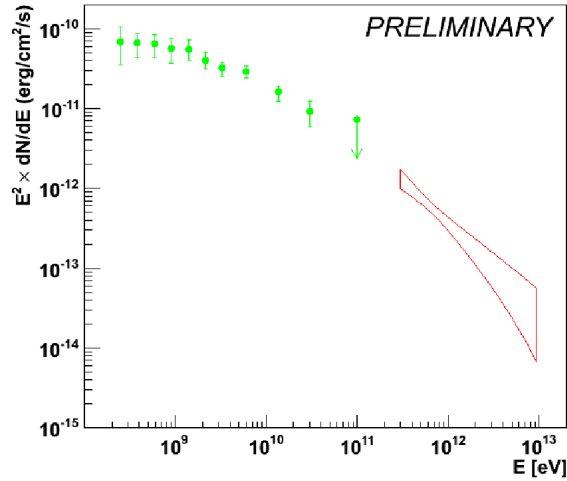


Fig. 3. Combined GeV and TeV energy spectrum obtained by the Fermi-LAT (green) and H.E.S.S. (red). The H.E.S.S. spectrum was extracted from a circular region of 0.1° around the nominal position of W49B.

3 Interpretations

3.1 W49B

The most straight forward interpretations for the origin of the signal are particle acceleration either by a pulsar or by the SNR shock. No observations suggest the presence of a pulsar or pulsar wind nebula in W49B. The spatial coincidence of the TeV emission with the brightest part of the radio shell and GeV emission points toward emission from particle accelerated at the shock as predicted, for instance by the diffusive shock acceleration theory (DSA) (e.g. Drury 1983)

Since the shock is observed to be interacting with the molecular cloud in which the supernova exploded, very-high energy γ -ray emissions from the decay of π^0 mesons is expected to be enhanced proportionally to the target mass. Furthermore, the large GeV gamma-ray luminosity (Abdo et al. 2010) of $\sim 10^{36}$ erg s $^{-1}$ seems to

be difficult to explain with IC scattering only. The detection of W49B at GeV and TeV emission is therefore a rather compelling argument in favour of a hadronic nature of the accelerated particles. More detailed studies are in progress to understand and constrain the emission processes in W49B.

3.2 W49A

Star forming regions are potential acceleration sites of VHE particles. This can, for instance, occur at the shocks created by the strong winds of the numerous massive stars they generally host. Recently, the presence of two expanding shells as well as gas ejections were found in W49A (Peng et al. 2010). The shells seem to have a common origin in the cloud core and a total kinetic energy of $\sim 10^{49}$ ergs. The gas ejections are likely to have the same origin as the expanding shells and a total energy of $\sim 10^{50}$ ergs.

4 Conclusion

The W49 region was observed by the H.E.S.S. telescope array, yielding ~ 60 h of good quality data. This led to the significant detection of TeV gamma-ray emission coincident with the supernova remnant W49B at a significance level of 8.8σ . The position of the emission is compatible with the brightest part of the radio emission from the SNR as well as with the GeV emission. Energy spectra in the GeV and TeV bands are in very good agreement. Given the very high GeV luminosity and the fact that the SNR is interacting with dense material, a hadronic scenario is favored.

These observations also resulted in evidence for gamma-ray emission in the direction of the star forming region W49A. Analyses are still ongoing in order to confirm this promising preliminary result.

The support of the Namibian authorities and of the University of Namibia in facilitating the construction and operation of H.E.S.S. is gratefully acknowledged, as is the support by the German Ministry for Education and Research (BMBF), the Max-Planck-Society, the French Ministry for Research, the CNRS-IN2P3 and the Astroparticle Interdisciplinary Programme of the CNRS, the U.K. Particle Physics and Astronomy Research Council (PPARC), the IPNP of the Charles University, the South African Department of Science and Technology and National Research Foundation, and by the University of Namibia. We appreciate the excellent work of the technical support staff in Berlin, Durham, Hamburg, Heidelberg, Palaiseau, Paris, Saclay, and in Namibia in the construction and operation of the equipment.

This publication makes use of molecular line data from the Boston University-FCRAO Galactic Ring Survey (GRS). The GRS is a joint project of Boston University and Five College Radio Astronomy Observatory, funded by the National Science Foundation under grants AST-9800334, AST-0098562, AST-0100793, AST-0228993, & AST-0507657.

References

- Abdo, A. A., Ackermann, M., Ajello, M., et al. 2010, *ApJ*, 722, 1303
- Becherini, Y., Djannati-Ataï, A., Marandon, V., Punch, M., & Pita, S. 2011, *Astroparticle Physics*, 34, 858
- Bernlöhr, K., Carrol, O., Cornils, R., et al. 2003, *Astroparticle Physics*, 20, 111
- Brogan, C. L. & Troland, T. H. 2001, *ApJ*, 550, 799
- de Naurois, M. & Rolland, L. 2009, *Astroparticle Physics*, 32, 231
- de Pree, C. G., Mehringer, D. M., & Goss, W. M. 1997, *ApJ*, 482, 307
- Drury, L. O. 1983, *Reports on Progress in Physics*, 46, 973
- Funk, S., Hermann, G., Hinton, J., et al. 2004, *Astroparticle Physics*, 22, 285
- Gwinn, C. R., Moran, J. M., & Reid, M. J. 1992, *ApJ*, 393, 149
- Hwang, U., Petre, R., & Hughes, J. P. 2000, *ApJ*, 532, 970
- Jackson, J. M., Rathborne, J. M., Shah, R. Y., et al. 2006, *ApJS*, 163, 145
- Keohane, J. W., Reach, W. T., Rho, J., & Jarrett, T. H. 2007, *ApJ*, 654, 938
- Ohm, S., van Eldik, C., & Egberts, K. 2009, *Astroparticle Physics*, 31, 383
- Peng, T.-C., Wyrowski, F., van der Tak, F. F. S., Menten, K. M., & Walmsley, C. M. 2010, *A&A*, 520, A84+
- Pye, J. P., Becker, R. H., Seward, F. D., & Thomas, N. 1984, *MNRAS*, 207, 649
- Radhakrishnan, V., Goss, W. M., Murray, J. D., & Brooks, J. W. 1972, *ApJS*, 24, 49
- Reach, W. T., Rho, J., Tappe, A., et al. 2006, *AJ*, 131, 1479
- Simon, R., Jackson, J. M., Clemens, D. P., Bania, T. M., & Heyer, M. H. 2001, *ApJ*, 551, 747
- Smith, L. F., Biermann, P., & Mezger, P. G. 1978, *A&A*, 66, 65

PROSPECTS FOR DARK MATTER SEARCHES WITH CTA

P. Brun¹

Abstract. CTA is the next generation of ground-based Cherenkov telescopes, it will allow a deeper look into the gamma-ray sky in the 10 GeV-100 TeV range. Beside the conventional physics program, the CTA instrument will be adapted to search further for particle dark matter. Under the assumption that dark matter is made of new particles, their annihilations are required to reproduce the correct dark matter abundance in the Universe. This process is expected to occur in dense regions of our Galaxy such as the Galactic center, dwarf galaxies and other types of sub-haloes. High-energy gamma-rays are produced in dark matter particle collisions and could be detected by CTA. Here we recall the pros and cons of the Cherenkov telescope technique and illustrate the different strategies that are foreseen.

Keywords: CTA, gamma-ray astronomy, dark matter

1 Particle dark matter and the γ -ray sky

The cosmological standard model stipulates that 84% of the matter in the Universe is non-baryonic. This is motivated by different probes on various scales (Spergel et al. (2007)). In an independent way, models beyond the standard model of particle physics predict the existence of new massive stable particles that have the required properties to make up the cosmological non-baryonic matter, dubbed dark matter (DM) in the following. In this scenario, the current cosmological DM density is set by their annihilation rate in the early Universe. This provides a natural value for the annihilation cross section of $\langle\sigma v\rangle \sim 3 \times 10^{-26} \text{ cm}^3\text{s}^{-1}$, where $\langle\sigma v\rangle$ is the velocity-weighted annihilation cross-section. In the standard picture, the stars of our Galaxy lie in a thin disk of ~ 20 kpc radius, which is dipped into a spherical DM halo of scale a factor of ~ 10 larger. Some of the DM particles happen to collide within the halo, producing standard model particles. This exotic production of standard model particles is associated with the emission of γ -rays with energies of the order of the DM particle mass. The considered weakly interacting massive particle (WIMP) being related to electroweak physics, its mass is expected to range between 100 GeV and a few TeV. In this paper, we focus on two widely studied targets where DM annihilations could occur in an efficient way: dwarf galaxies and DM clumps in the Galactic halo.

2 Cherenkov telescopes now and then

The basic idea of running ground based telescopes to observe cosmic γ -rays is to use the atmosphere as a calorimeter. When a high energy particle hits the top of the atmosphere, it induces a cascade of secondary particles. At TeV energies, that cascade is fully contained in the atmosphere, and it produces a flash of Cherenkov photons. Hadronic and electromagnetic particles produce different types of cascades. While hadrons induce irregular particle showers, electrons, positrons and γ -rays produce a more even shower. The projection of Cherenkov flash cone on the ground is a disk of order 250 m diameter. From any place inside this disk, the atmospheric shower is observable, should one use a sensitive enough instrument. Ground-based γ -ray observatories use this principle to measure γ -ray induced Cherenkov light, as sketched on the left panel of Fig. 1. Large dishes are used to collect enough photons, those are focused on very sensitive cameras equipped with photomultipliers. To gain in angular resolution, energy resolution and background subtraction, several telescopes are used simultaneously to observe the event, thus getting a stereoscopic view of the particle cascade. The cameras are

¹ CEA, Irfu, Centre de Saclay, F-91191 Gif-sur-Yvette, France

able to integrate the signal very quickly and to resolve the image of the atmospheric showers, in order to fight against different types of backgrounds: night sky background, hadronic cosmic ray induced showers, electrons and positrons induced showers, and diffuse gamma-rays. The different methods for background rejection allow an efficient reconstruction of gamma-ray sources, as long as its extension is smaller than the $\sim 5^\circ$ field of view of the telescope arrays (see Brun (2011) and references therein).

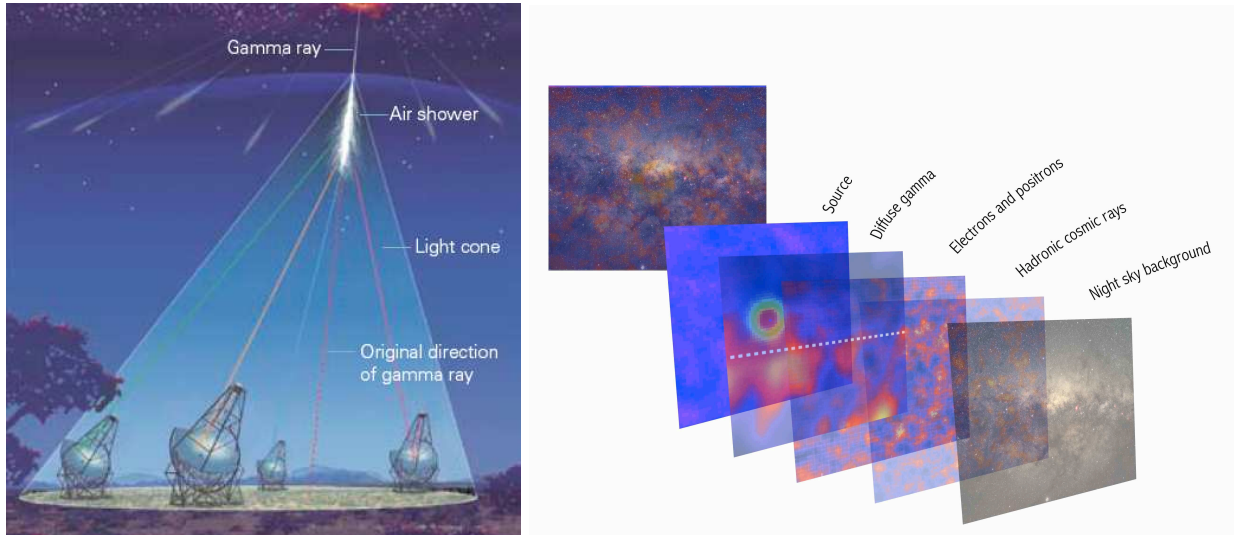


Fig. 1. Left: Principle of the Cherenkov telescopes, several telescopes measure the Cherenkov flash induced by the initial γ -ray (image from Völk & Bernlöhr (2009)). **Right:** Schematic representation of the different layers of background that Cherenkov astronomers have to suppress to obtain a image of the TeV sources (image from Brun (2011)).

There are now three main telescope arrays running in the world, MAGIC and VERITAS in the northern hemisphere, and HESS in the southern hemisphere. All of those performed observation of potential DM targets such as dwarf galaxies or globular clusters. Next generation of Cherenkov observatories will involve tens of telescopes. For instance, the CTA project intends to built up two arrays –one in each hemisphere– made of more than 50 telescopes each (CTA-consortium (2010)). The gain in sensitivity with respect to current generation instruments is of order an order of magnitude and the angular resolution will be better by a factor 2 to 3. CTA will allow observing more deeply the sources, and also to perform surveys of the sky in a more efficient way than it is done today, with sub-arrays pointing in distinct regions of the sky simultaneously.

3 Current observations of dwarf galaxies and limits on dark matter parameters

At the moment, Cherenkov observatories have performed observation of selected targets. Some of those are listed on the skymap of Fig. 2. For each of the selected targets, the DM density has been inferred from stellar dynamics within the object. Once the DM content of the target is modeled, the annihilation rate is determined by the mass and the annihilation cross-section of the WIMP. The absence of detection of any signal gives constraints on these two parameters. Fig. 3 displays some limits from Magic, Veritas, Whipple and HESS, as well as a comparison with a limit from Fermi. Some of these results account for the uncertainty on the DM profile of the target and present a band instead of a single line. In the best case, current limits on the annihilation cross section reach $10^{-22} \text{ cm}^3/\text{s}$ around $m = 1 \text{ TeV}$, still 4 orders of magnitude above the value of $10^{-26} \text{ cm}^3/\text{s}$ corresponding to thermally produced WIMPs.

4 Prospects for CTA with the observation of Sagittarius dwarf galaxy

The Sagittarius dwarf galaxy has been observed by HESS to derive constraints on the DM particle properties. The results are presented in Aharonian et al. (2008a), they correspond to XX h of observation. In Viana et al. (2011), these results have been extrapolated to 50 h of observations and the expected sensitivity of the CTA array has been used to compute future constraints. These two results are displayed in Fig. 4. Different halo modeling and observation times have been used to drive the CTA constraints, that is why the predictions spread

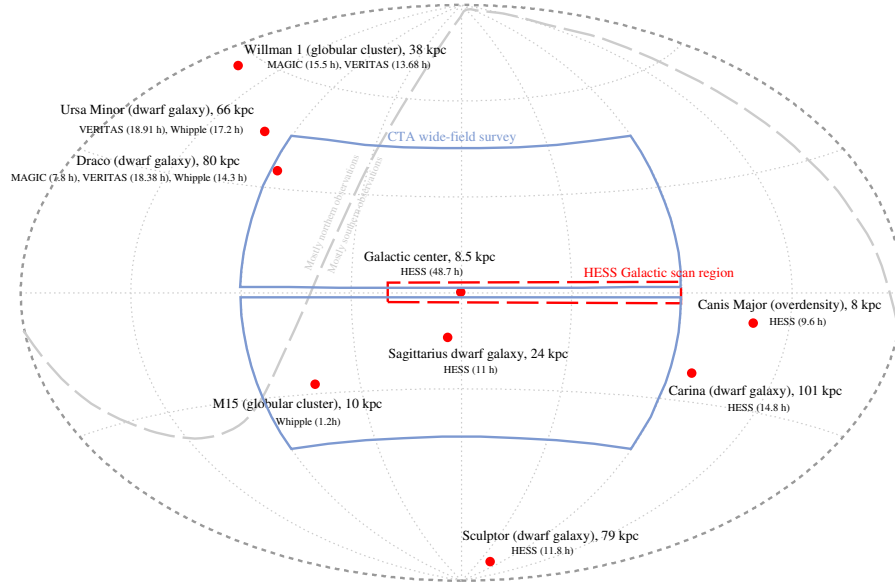


Fig. 2. Sky map with positions of some observed DM targets and scan regions both observed (red) and foreseen (blue).

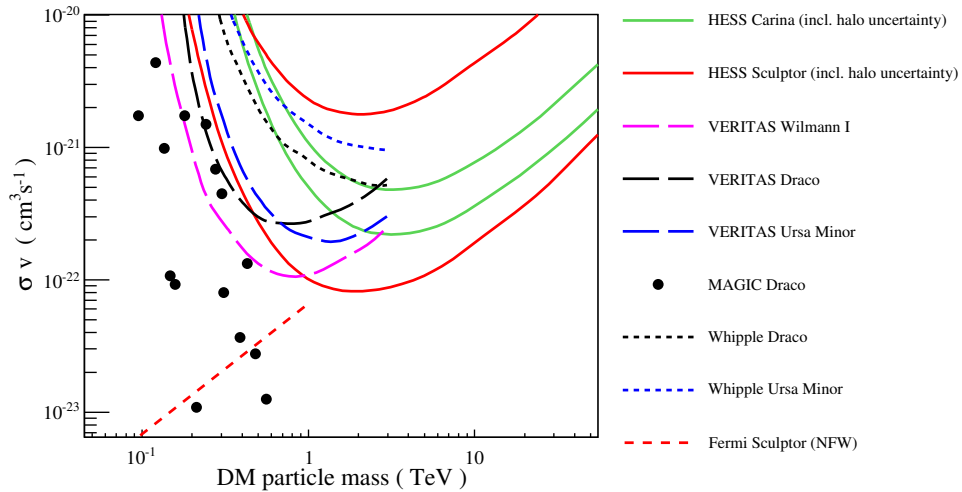


Fig. 3. Current constraints on DM particle from observations of selected targets

over an order of magnitude or so, reaching $\sim 10^{-24}$ cm^3/s at best. In Viana et al. (2011), we also considered possible conventional signal from Sagittarius dwarf galaxy: signal from a possible central intermediate mass black hole and collective emission from millisecond pulsars (MSP). Indeed the main limitation comes from MSPs, because the M54 globular cluster lies in the center of Sagittarius dwarf. The signal from MSPs should be observable with more sensitivity. As it would overcome an eventual DM signal, this defines a no-go line for the sensitivity to DM annihilations, at the level of 10^{-25} cm^3/s , one order of magnitude above the region of interest for thermal WIMPs. Therefore we conclude that Sagittarius dwarf galaxy might not be the best target for indirect detection.

5 Wide-field searches for clumps with HESS and CTA

One possibility to avoid possible conventional signal from the baryonic content of the targets is to search for the most primitive sub-haloes that our Galaxy harbors. N-body simulations such as *Via Lactea* (Diemand

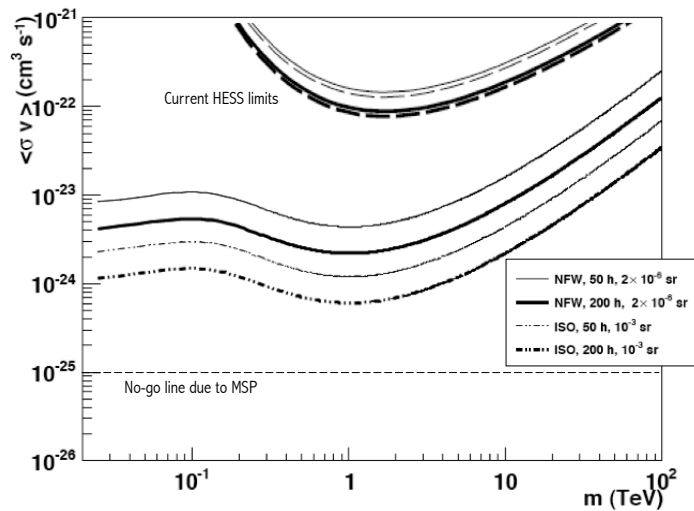


Fig. 4. Current and projected constraints on DM particle parameters from the observation of Sagittarius dwarf galaxy

et al. (2008)) predict a large number of DM sub-haloes in Milky-Way sized haloes. Those clumps which never accreted no baryon are supposed to be very dense in their center and in principle cannot be detected directly other than via their DM annihilations. As the position of these objects are unknown, we rely on cosmological structure formation simulations to estimate the probability to have a given clump at a given position in the sky. Then, the probability to observe it with a Cherenkov telescope is the convolution of the sensitivity of the instrument and the size of the field of view that is used. It turns out that in the typical $5^\circ \times 5^\circ$ field of view of current Cherenkov telescopes, the probability to have a sufficiently bright clump is very low. In order to make this technique more sensitive, one has to use large surveys. The HESS array of Cherenkov telescopes performed a survey of the Galactic plane. Data from this survey has been used to build up a sensitivity map in a $\pm 3^\circ$ latitude and $-30^\circ / + 90^\circ$ longitude window in Aharonian et al. (2008b) (red rectangle on Fig. 2). This sensitivity map has been compared to predictions from *Via Lactea* in Brun et al. (2011). The absence of clump candidates in the HESS survey leads to the exclusion curves that are presented in the left panel of Fig. 5. The sensitivity map for the Galactic scan has been extrapolated to CTA, the exclusion curves in the no detection hypothesis are shown in the right panel of Fig. 5 (dashed curves). The projected constraints for CTA in the case of a Galactic scan are still an order of magnitude above the region of interest. The only way of reaching this region is to take advantage of an ambitious quarter sky survey with CTA. Notice that such a survey may be performed independently of MD searches. The suggested survey appears as blue contours on Fig. 2. In the no detection hypothesis, the thermal WIMPs annihilation cross section is reached within 6 years.

6 Conclusions

Some results regarding DM searches towards known targets with Cherenkov telescopes are reviewed. In the case of the observation of Sagittarius dwarf galaxy with CTA, it is shown that conventional physics processes could curb searches for DM. Alternative methods are proposed, based on blind searches for DM clumps, it is shown that an ambitious survey of a quarter of the sky with CTA could give the required sensitivity to reach thermally produced WIMPs.

References

- Aharonian, F. et al. 2008a, *Astropart. Phys.*, 29, 55, erratum-ibid.33:274,2010
- Aharonian, F. et al. 2008b, *Phys. Rev.*, D78, 072008
- Brun, P. 2011, FFP11 proceedings
- Brun, P., Moulin, E., Diemand, J., & Glicenstein, J.-F. 2011, *Phys. Rev.*, D83, 015003
- CTA-consortium. 2010, arXiv:1008.3703
- Diemand, J. et al. 2008, *Nature*, 454, 735

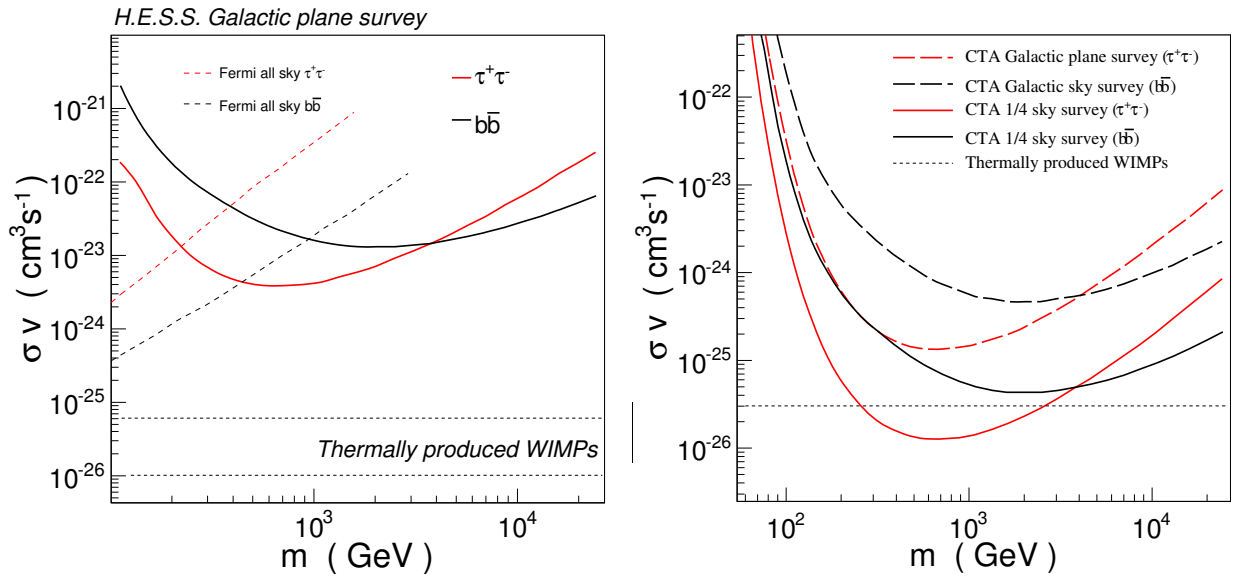


Fig. 5. Current constraints from the HESS Galactic scan (left) and CTA projection for a Galactic scan and a 1/4-sky survey (right).

Spiegel, D. et al. 2007, *Astrophys. J. Suppl.*, 170, 377

Viana, A., Medina, M. C., Peñarrubia, J., et al. 2011, Submitted

Völk, H. & Bernlöhr, K. 2009, *Experimental Astronomy*, 25, 173

LEPTO-HADRONIC MODELLING OF BLAZAR EMISSION

M. Cerruti¹, A. Zech¹, C. Boisson¹ and S. Inoue²

Abstract. The characteristic double-bumped spectral energy distribution (SED) of blazars is explained by either leptonic or hadronic models. In the former, Inverse Compton emission dominates the emission of the high energy bump, while proton synchrotron emission and proton-gamma interactions dominate it in the latter.

We present a new stationary lepto-hadronic code that evaluates both the leptonic and the hadronic interactions. Apart from the modelling of the SED produced in a leptonic or hadronic model, the code permits the study of interesting mixed lepto-hadronic scenarios, where both processes contribute significantly to the high energy bump.

A first application to data from the high frequency peaked BL Lac object PKS 2155-304 is discussed.

Keywords: radiative transfer, BL Lacertae objects, gamma rays

1 Introduction

The spectral energy distribution (SED) of blazars is characterized by two non-thermal emission bumps, the first one peaking in the optical or in X-rays, the second one peaking in γ -rays. The origin of this emission is generally ascribed to a region of high density, filled with a magnetic field and moving in a relativistic jet aligned to the line-of-sight.

While there is a general consensus that the low energy bump is due to synchrotron emission from electrons and positrons in the emitting region, the origin of the high energy emission is interpreted differently in leptonic or hadronic models. In the first scenario, the emission is entirely dominated by leptons, which produce the high energy bump through inverse Compton scattering off the synchrotron photons themselves (Synchrotron-Self-Compton, SSC) or off an external photon field. In the hadronic scenario the high energy bump is usually attributed entirely to proton synchrotron emission or photo-hadronic interactions.

We have developed a lepto-hadronic code that reproduces both “extreme” scenarios and also allows the study of mixed scenarios with characteristic signatures in the high energy band.

2 Code development

2.1 Leptonic processes

The framework of our model is the stationary one-zone SSC code developed by Katarzyński et al. (2001). A spherical region (characterized by its radius R) moves in the relativistic jet with Doppler factor δ : it is filled with a homogenous magnetic field B and a primary electron population $n_e(\gamma=E/(mc^2))$, which is parametrised by a broken power law (defined by the two slopes $\alpha_{1,2}$, the Lorentz factors $\gamma_{e,min}$, $\gamma_{e,break}$, $\gamma_{e,max}$ and the normalization factor K_e at $\gamma = 1$).

The leptonic part of the original code has been improved as follows :

¹ Laboratoire Univers et Théories (LUTH), Observatoire de Paris, CNRS, Université Paris Diderot, Meudon, France

² Institute for Cosmic Ray Research, University of Tokyo, Kashiwa, Japan

- The synchrotron emission is evaluated computing the exact integration over pitch angles. The approximation used by Katarzyński et al. (2001) is valid only in the energy range of interest if the emitting particles are e^\pm .
- The internal absorption due to γ - γ pair production is evaluated using the parametrization for the cross-section given by Aharonian et al. (2008), instead of a δ -function. The pair injection rate from γ - γ interactions is computed following Aharonian et al. (1983). A stationary distribution of secondary e^\pm pairs (1st generation), taking into account synchrotron cooling, is evaluated following Inoue & Takahara (1996). Synchrotron emission from the stationary pair distribution is evaluated as well.
- The absorption induced by the extra-galactic background light (EBL) on TeV photons is evaluated using the EBL model by Franceschini et al. (2008).

2.2 Hadronic processes

The spherical emitting region is filled with a primary proton population $n_p(\gamma)$, parametrized by a power law with slope α_p , normalization factor K_p at $\gamma = 1$ and minimal and maximal Lorentz factor $\gamma_{p,min}$ and $\gamma_{p,max}$. The proton synchrotron emission is corrected for internal $\gamma - \gamma$ absorption and the associated first generation pair spectrum is evaluated as described above.

In hadronic scenarios, an important role is played by photo-hadronic interactions. They have been computed using the Monte Carlo code *SOPHIA* (Mücke & Protheroe 2001).

The target photon field is composed by the synchrotron radiation from primary electrons and from the protons themselves. The energy of the interacting protons is corrected for synchrotron losses following Mücke & Protheroe (2001). The *SOPHIA* code is then called for 10 sampled proton energies. The distributions of the generated particles ($\gamma, e^\pm, p, n, \nu_{e,\mu}, \bar{\nu}_{e,\mu}$) are summed and normalized to the number of protons in the blob suffering p - γ interactions.

The spectra of the generated e^\pm are corrected for radiative cooling to arrive at a steady-state solution. Synchrotron emission from secondary leptons and from the first generation pair spectrum from γ - γ interactions is then evaluated.

μ^\pm can emit synchrotron radiation before decaying into e^\pm . They are retrieved from *SOPHIA*, and, in a first approximation, their synchrotron emission is evaluated without considering the competition between synchrotron photon emission and decay into e^\pm .

3 Application to PKS 2155-304 data

As a first test of our code, we have reproduced the SED of a bright high frequency peaked blazar for different scenarios. Fig. 1 shows an application to the data from the 2008 multiwavelength campaign on the blazar PKS 2155-304 (Aharonian et al. 2009). This data set represents at this time one of the most complete simultaneous SEDs of a TeV blazar: the shape of the high energy bump is fully characterized by the Fermi and H.E.S.S. data. PKS 2155-304 has been found to be in a low activity state during the campaign. In the interpretations presented here, the emission from the blob explains only the X-ray to γ -ray emission, assuming that from radio to visible light the emission from the extended jet dominates.

We report the modelling of the SED in three different scenarios : a pure SSC leptonic model, a proton synchrotron dominated hadronic model and a third, mixed, scenario in which both the synchrotron emission from protons and the inverse Compton component contribute to the high energy bump.

The modelling of the SED for the three different cases is shown in Fig. 1, and the model parameters are given in Table 1. The first scenario (top left in Fig. 1), is a standard SSC model, assuming a low magnetic field (75 mG), far from equipartition; the synchrotron emission from secondary particles from γ - γ pair production is more than three order of magnitude below the primary synchrotron emission. The second scenario (top right in Fig. 1) is a proton synchrotron dominated hadronic model, in which the inverse Compton component is almost three order of magnitude lower than the proton synchrotron emission; μ -cascade emission contributes (even though at $\sim 1\%$ only) to the high energy bump; the magnetic field value is much higher (80 G) than in the SSC case, in order to have a significant contribution from protons; the presence of protons significantly

increases the luminosity of the jet (equal to 10^{46} ergs s^{-1}). The last case (bottom in Fig. 1) is an example of a mixed lepto-hadronic scenario, in which both inverse Compton and proton synchrotron emission contribute to the high energy bump; the magnetic field value is small (0.22 G), but the jet luminosity is high, given the high value of the emitting region size (ten times the value assumed for the proton synchrotron model).

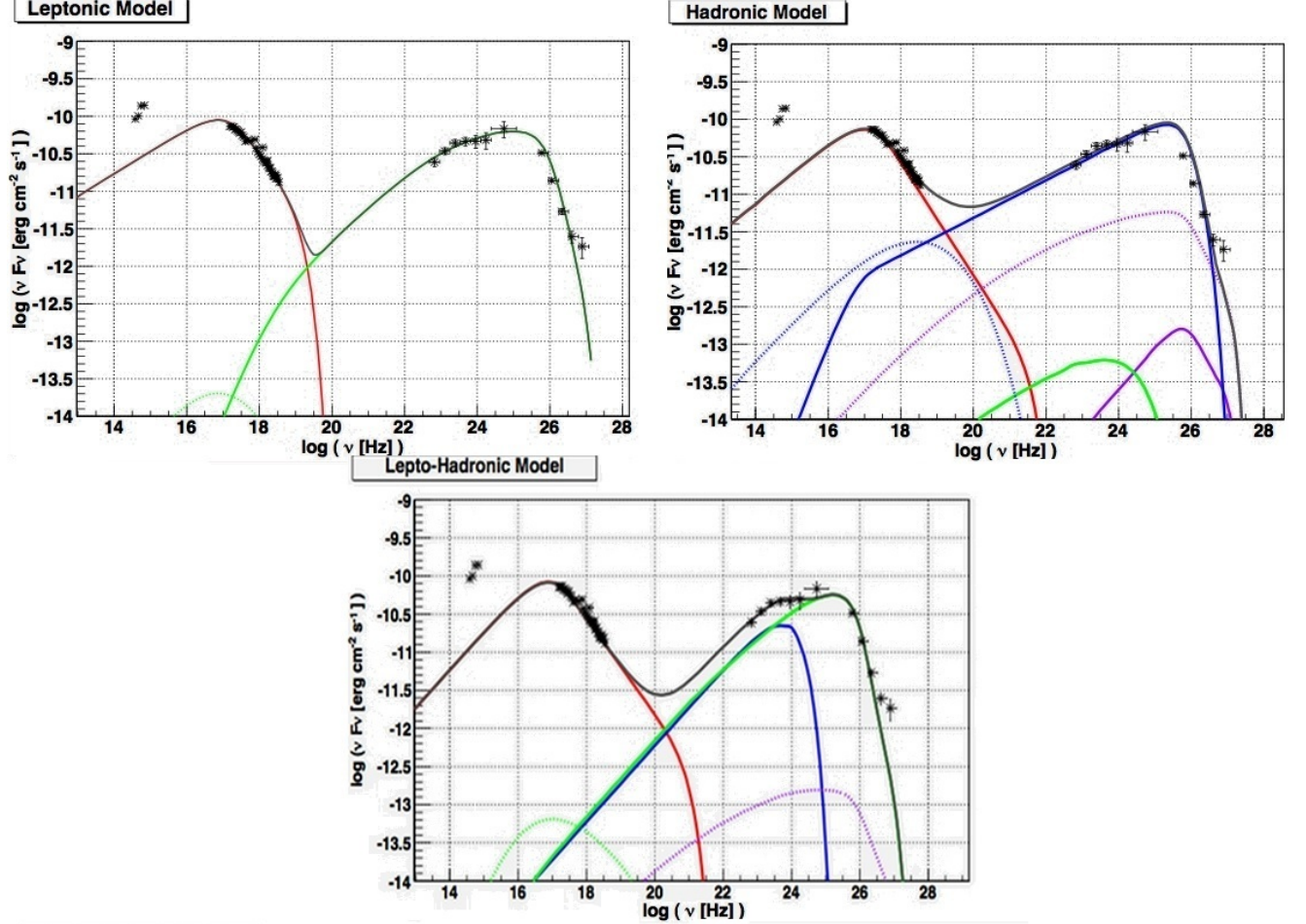


Fig. 1. Modelling of PKS2155-304 in three different scenarios. Colour code is as follow : primary electron synchrotron emission - red; inverse Compton emission - green; proton synchrotron emission - blue; muon synchrotron emission - violet. Dotted lines represent the synchrotron emission from the secondary pairs from γ - γ pair production. *Top left*: pure SSC model; *top right*: proton synchrotron dominated model; *bottom*: mixed lepto-hadronic scenario.

4 Conclusions

The code presented here permits to reproduce the observed blazar SED in different scenarios, spanning a wide parameter space: a leptonic or a hadronic solution can be found assuming different physical conditions (magnetic field, density and distribution of primary particles) in the blob. In addition, mixed lepto-hadronic scenarios naturally arise in this framework.

The increasing data quality at high energies, provided by *Fermi* in the GeV range, and by current and planned Cherenkov telescopes in the TeV range, will hopefully help to evaluate contributions from both leptons and hadrons. The next step towards a more realistic emission model would be a time-dependent lepto-hadronic code, which could take into account constraints from the observed variability from blazars.

	SSC	Proton synch	Mixed
θ	1°	1°	1°
δ	30	30	30
$\gamma_{e,min}$	5×10^2	1×10^3	1×10^3
$\gamma_{e,break}$	1.2×10^5	4×10^3	6×10^4
$\gamma_{e,max}$	1×10^6	5×10^5	5×10^6
$\alpha_{e,1}$	2.4	2.2	2.0
$\alpha_{e,2}$	4.32	4.5	4.25
K_e	7×10^4	3.1×10^3	6.7×10^3
u_e	1.1×10^{-2}	4.8×10^{-4}	1.0×10^{-2}
$\gamma_{p,min}$	-	1×10^5	1×10^5
$\gamma_{p,max}$	-	5×10^9	1×10^{10}
α_p	-	2.5	2.0
$\eta = K_p/K_e$	-	4.8×10^4	8
u_p	-	1.4×10^3	9.2×10^2
R_{src}	1.7×10^{16}	5.0×10^{14}	4.8×10^{15}
B	0.075	80	0.22
u_B	2.2×10^{-4}	2.5×10^2	2×10^{-3}
L_{jet}	8×10^{43}	1×10^{46}	5×10^{47}

Table 1. The table shows the different parameters used in the modelling of the PKS 2155-304 SED for the three different scenarios (SSC, synchrotron proton and mixed scenario) plotted in Figs. 1 to 3. Common values of redshift $z = 0.116$, Doppler factor $\delta = 30$ and viewing angle $\theta = 1^\circ$ have been used. The normalization parameter $K_{e,p}$ is in units of cm^{-3} , and represents the number density of the primary particle distribution at $\gamma = 1$; the size of the emitting region R_{src} is in cm; the magnetic field in gauss. The energy densities $u_{e,p,B}$ are given in ergs cm^{-3} ; the jet luminosity is in ergs s^{-1} . In the evaluation of the jet luminosity the cold proton content of the jet has been included (following Sikora et al. (2009)).

The authors wish to thank Anita Reimer for providing the latest version of the SOPHIA code, and H el ene Sol for very useful discussions.

References

- Aharonian, F., Akhperjanian, A. G., Anton, G., et al. 2009, ApJ, 696, L150
 Aharonian, F. A., Atoian, A. M., & Nagapetian, A. M. 1983, Astrofizika, 19, 323
 Aharonian, F. A., Khangulyan, D., & Costamante, L. 2008, MNRAS, 387, 1206
 Franceschini, A., Rodighiero, G., & Vaccari, M. 2008, A&A, 487, 837
 Inoue, S. & Takahara, F. 1996, ApJ, 463, 555
 Katarzyński, K., Sol, H., & Kus, A. 2001, A&A, 367, 809
 Mücke, A. & Protheroe, R. J. 2001, Astroparticle Physics, 15, 121
 Sikora, M., Stawarz, L., Moderski, R., Nalewajko, K., & Madejski, G. M. 2009, ApJ, 704, 38

COLLECTIVE EXCITATIONS IN THE NEUTRON STAR INNER CRUST

L. Di Gallo¹, M. Oertel¹ and M. Urban²

Abstract. We study the spectrum of collective excitations in the inhomogeneous phases in the neutron star inner crust within a superfluid hydrodynamics approach. Our aim is to describe the whole range of wavelengths, from the long-wavelength limit which can be described by macroscopic approaches and which is crucial for the low-energy part of the spectrum, to wavelengths of the order of the dimensions of the Wigner-Seitz cells, corresponding to the modes usually described in microscopic calculations. As an application, we will discuss the contribution of these collective modes to the specific heat in comparison with other known contributions.

Keywords: collective modes, neutron star crust, pasta phases, specific heat

1 Neutron star cooling and the inner crust

It has been known for a long time that within the different structures inside a neutron star we can find superfluid and superconducting ones. The first observational indications were the glitches, and more recently observations of the surface thermal emission have been discussed in this context. The latter is an observable, which depends on heat transport properties and is thus very sensitive to the superfluid and superconducting character of the different structures inside the star. The properties of the crust thereby influence the cooling behavior mainly during the first 50-100 years, the crust thermalisation epoch (Gnedin et al. 2001). During this stage the core evacuates heat by strong neutrino cooling and the crust is not yet thermalized with the cold core. The outer crust and the envelope have high thermal conductivity such that the inner crust matter plays an essential role.

The inner crust is composed of nuclear clusters, unbound neutrons and ultrarelativistic electrons. Close to the core, probably nuclear clusters start to deform, from an almost spherical shape, they could form tubes or slabs immersed in homogeneous neutron rich matter at the different densities (Ravenhall et al. 1983). These phases are commonly called the nuclear pasta. In this work we focus on these inhomogeneous phases in the inner crust.

2 Superfluid hydrodynamics approach

The spectrum of collective excitations shall be discussed within a superfluid hydrodynamics approach. Here we mention only the main ideas, more details can be found in Di Gallo et al. (2011). The advantage of the approach is that the wavelengths are not limited to the size of the Wigner-Seitz cell as in standard microscopic (quasiparticle random-phase approximation, QRPA) calculations (Khan et al. 2005). Our aim is to describe also the low-energy part of the spectrum, which is determined by modes whose wavelengths are longer than the periodicity of the inhomogeneous structure. These modes can give important contributions to thermal properties (Aguilera et al. 2009; Pethick et al. 2010; Cirigliano et al. 2011). However, in contrast to Pethick et al. (2010); Cirigliano et al. (2011), we are not only interested in the long wavelength limit, but we want to study more in detail the effect of the inhomogeneous structure on the excitations. This means in particular that the phase of the superfluid order parameter, the density variations and the velocities characterizing the collective modes are not plane waves, but have a more complicated spatial dependence.

¹ Laboratoire Univers et Théories, CNRS/Observatoire de Paris/Université Paris Diderot, 5 place Jules Janssen, 92195 Meudon, France

² Institut de Physique Nucléaire, CNRS-IN2P3/Université Paris Sud, 91406 Orsay cedex, France

Let us summarize the assumptions on which our approach is based. First of all, we neglect temperature effects. This assumption is justified if we consider temperatures well below the superfluid energy gap, $T \ll 1$ MeV. Under this assumption, neutrons and protons form two superfluids, while the normal-fluid component made of thermally broken pairs is absent. Furthermore, we assume that the Cooper pairs are not broken by the excitation of the collective modes themselves, i.e., the excitation energies should not exceed the pairing gap of 1 MeV. Finally, the use of superfluid hydrodynamics is only valid if all spatial variations, those corresponding to the inhomogeneous structures and the wavelengths of the collective modes under consideration, are larger than the coherence length of the Cooper pairs.

At the present stage of our work, we shall completely neglect the Coulomb interaction between the protons. As long as we focus on the neutron modes, this is acceptable, but one should nevertheless keep in mind that the neutron modes are coupled to the lattice phonons which cannot be described without Coulomb interaction.

For completeness, we mention that we use a non-relativistic framework because all relevant velocities are much smaller than the speed of light.

The hydrodynamic equations can be derived from local conservation laws. Particle number conservation for neutrons and protons leads to two continuity equations, while energy and momentum conservation give the Euler equations. The acceleration of the fluids, described by the Euler equations, depends on the fluid densities through the equation of state (EOS). The latter depends on the nuclear interaction. Following Avancini et al. (2009), we use a relativistic mean-field (RMF) model, the so-called DDH δ model, to calculate the EOS. For the study of collective modes, it is sufficient to linearize the hydrodynamic equations around stationary equilibrium.

In the case of uniform matter, one easily obtains in this way an eigenvalue problem for two coupled sound modes. Due to the nuclear interaction (including entrainment), these modes do not describe pure proton or neutron waves, but combinations of both.

3 Collective modes in a periodic slab structure

In our model, the inhomogeneous phases we are interested in are described as mixed phases where a neutron gas (phase 1) coexists with a dense phase (phase 2) containing protons and neutrons. Inside each phase, the densities are supposed to be constant, with a sharp interface at the phase boundaries. Although this is a crude approximation, it contains the essential features of the structure of the inner crust.

Since the densities are discontinuous at the phase boundaries, the hydrodynamic equations have to be supplemented by appropriate boundary conditions. The first condition is that the pressure must be continuous, i.e., at a given point of the interface, the pressures in phase 1 and phase 2 must be equal: $P_1 = P_2$. The second condition is that the interface remains well defined, i.e., the normal components of the velocities of neutron fluid in phase 1 and of the neutron and proton fluids in phase 2 must be equal: $v_{\perp n1} = v_{\perp n2} = v_{\perp p1}$.

We will restrict ourselves to the simplest geometry which is a structure of periodically alternating slabs with different proton and neutron densities (“lasagna” phase), see Fig. 1.

The equilibrium properties, i.e., the densities n_{n1} , n_{p1} , n_{n2} and n_{p2} , and the slab thicknesses L_1 and L_2 , are input parameters taken from Avancini et al. (2009).

The excitations are then obtained by solving in each slab the linearized hydrodynamic equations together with the boundary conditions at the interfaces between neighboring slabs. In addition, the periodicity of the structure is taken into account by the Floquet-Bloch boundary condition $\vec{v}_A(\vec{r} + \vec{R}, t) = e^{i\vec{q}\cdot\vec{R}} \vec{v}_A(\vec{r}, t)$ where \vec{q} is the Bloch momentum and R_z must be a multiple of L . Here we have written the Bloch condition for the neutron ($A = n$) and proton ($A = p$) velocities, but analogous equations exist for the other oscillating quantities (deviations of the chemical potentials, densities, and pressure from their equilibrium values).

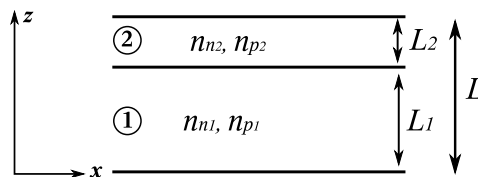


Fig. 1. Diagram representing the 1D (lasagna) structure.

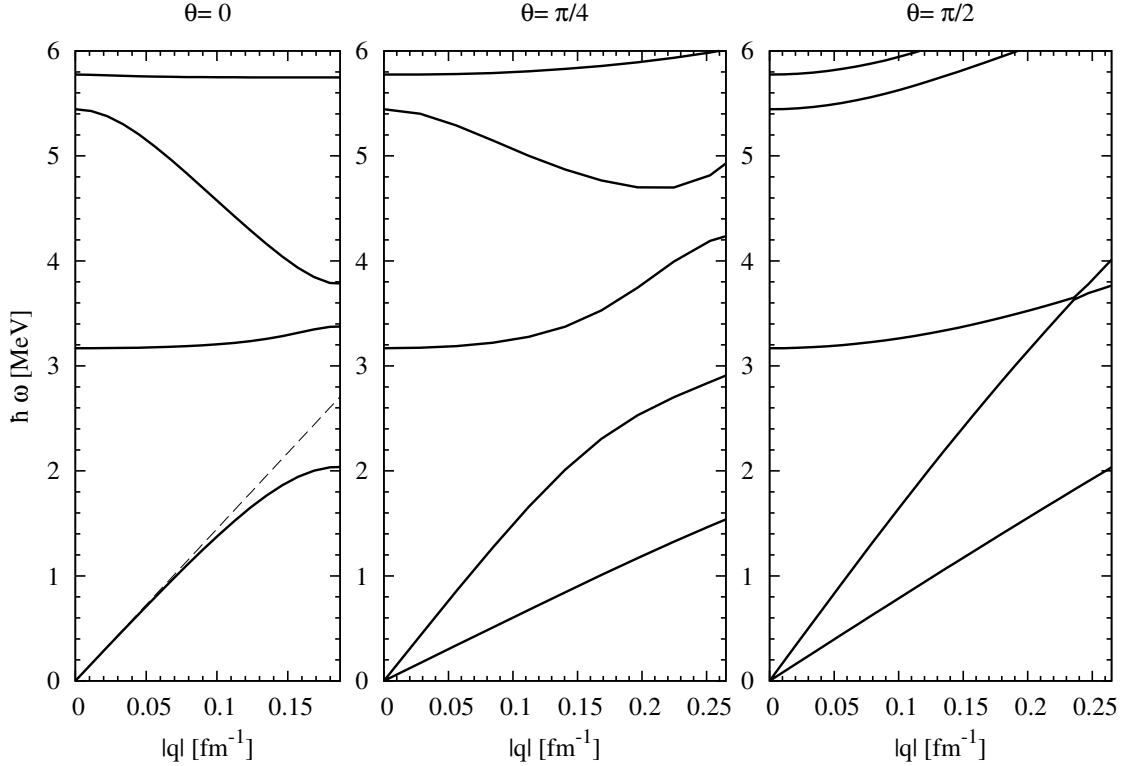


Fig. 2. Dispersion relations for waves propagating in different directions, from left to right: perpendicular to the interface, angle of $\pi/4$ and parallel to the interface.

4 Excitation spectrum

After working out the explicit equations, one obtains a 6×6 linear system of equations for the amplitudes of forward and backward running waves in the two slabs 1 and 2. The excitation spectrum of the eigenmodes is obtained by looking for those values of the frequency ω for which this system has a non-trivial solution (i.e., for which the determinant of the matrix vanishes). The frequencies depend, of course, on the Bloch momentum \vec{q} .

As an example, the spectrum as a function of $q = |\vec{q}|$ is displayed in Fig. 2 for different angles θ between \vec{q} and the z axis. The total baryon number density is chosen to be $n_B = 0.48n_0$, corresponding to a lasagna-type structure in the model of Avancini et al. (2009).

In the case $\theta = 0$, one observes one acoustic mode (having $\omega = 0$ for $q = 0$) and several optical ones (having $\omega > 0$ for $q = 0$). The slope of the acoustic one in the long wavelength limit ($q \rightarrow 0$) corresponds to an average sound velocity. The discrete spectrum of the optical modes at the point $q = 0$ is what one can obtain within the Wigner-Seitz approximation with periodic boundary conditions. However, the coupling between different Wigner-Seitz cells makes the energies q dependent, resulting in a continuous spectrum. In the case $\theta \neq 0$, a second acoustic mode appears. This mode describes an excitation of the denser phase with neutrons and protons moving out of phase. Since this mode penetrates only weakly into the neutron gas, its energy is almost independent of q_z , i.e., it is approximately proportional to $q \sin \theta$.

5 Application to specific heat

In the case of superfluidity, due to the pairing energy, the contribution of individual fermions (protons, neutrons) to the specific heat c_V is strongly suppressed ($\propto e^{-\Delta/T}$ since it costs energy of the order of Δ to break a pair). However, superfluidity induces collective low-energy excitations, for homogeneous matter these are called Bogoliubov-Anderson modes. In our case they correspond to the acoustic modes. From Fig. 3 it can be seen that indeed, for a typical temperature of 10^9 K, the contribution of the collective modes to c_V is much more

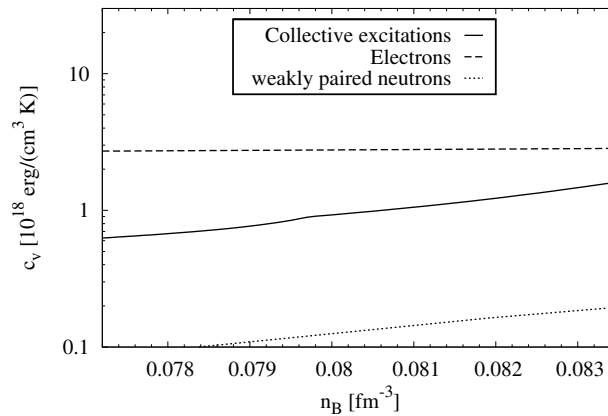


Fig. 3. Different contributions to the specific heat as a function of density for the lasagna-type structure at a temperature of $T = 10^9$ K.

important than that of the individual neutrons (even if we assume that the latter are only weakly paired, dotted line) and comparable to that of the electrons (dashed line). At low temperatures, only the electrons and the acoustic modes contribute. While the electron contribution to the specific heat is linear in T , the contribution of the collective modes in homogeneous matter follows a T^3 law. In the slab structure, however, the second acoustic branch discussed in the preceding section gives a contribution proportional to T^2 . At higher temperatures, the deviations from a linear dispersion relation become important, and also the optical modes start to contribute. However, one should keep in mind that, as mentioned in the beginning, our approach is in principle only valid at energies (and temperatures) below ~ 1 MeV ($\sim 10^{10}$ K).

6 Summary and outlook

In order to determine the thermal properties of the neutron star inner crust, the entire excitation spectrum has to be known. We have considered collective excitations taking into account the effects of superfluidity. With our approach, we try to build a bridge between the long wavelength limit ($|\vec{q}| \ll \pi/L$) of Pethick et al. (2010); Cirigliano et al. (2011) and the microscopic QRPA approaches (Khan et al. 2005) applying the Wigner-Seitz approximation ($|\vec{q}| > L$).

Our results for the slab structure (lasagna phase) show that the collective modes can give important contributions to the specific heat. For typical temperatures during the crust thermalization epoch, in particular the lowest lying acoustic mode(s) are important for the thermal properties.

Because of a couple of very restrictive simplifications, the present work has to be seen as an exploratory study which we plan to improve in the next future. In particular, it seems very important to include the Coulomb interaction between the protons. In addition, it will be necessary to consider more complicated geometries (2D tubes/rods, 3D droplets/bubbles) in order to be able to describe the entire inner crust.

The collective excitations are in fact not only interesting in the context of the specific heat. It could also be interesting to study their effect on neutrino-matter interactions.

References

- Aguilera, D. N., Cirigliano, V., Pons, J. A., Reddy, S., & Sharma, R. 2009, *Phys. Rev. Lett.*, 102, 091101
 Avancini, S. S., Brito, L., Marinelli, J. R., et al. 2009, *Phys. Rev. C*, 79, 035804
 Cirigliano, V., Reddy, S., & Sharma, R. 2011, arXiv:1102.5379
 Di Gallo, L., Oertel, M., & Urban, M. 2011, *Phys. Rev. C* 84, 045801, arXiv:1107.4209
 Gnedin, O. Y., Yakovlev, D. G., & Potekhin, A. Y. 2001, *Mon. Not. R. Astron. Soc.*, 324, 725
 Khan, E., Sandulescu, N., & Giai, N. V. 2005, *Phys. Rev. C*, 71, 042801
 Pethick, C. J., Chamel, N., & Reddy, S. 2010, *Prog. Theor. Phys. Suppl.*, 186, 9
 Ravenhall, D. G., Pethick, C. J., & Wilson, J. R. 1983, *Phys. Rev. Lett.*, 50, 2066

SELF-CONSISTENT SPECTRA FROM GRMHD SIMULATIONS WITH RADIATIVE COOLING: A LINK TO REALITY FOR SGR A*

S. Drappeau¹, S. Dibi¹, J. Dexter², S. Markoff¹ and P. C. Fragile³

Abstract. Cosmos++ (Anninos et al., 2005) is one of the first fully relativistic magneto-hydro-dynamical (MHD) codes that can self-consistently account for radiative cooling, in the optically thin regime. As the code combines a total energy conservation formulation with a radiative cooling function, we have now the possibility to produce spectra energy density from these simulations and compare them to data. In this paper, we present preliminary results of spectra calculated using the same cooling functions from 2D Cosmos++ simulations of the accretion flow around Sgr A*. The simulation parameters were designed to roughly reproduce Sgr A*'s behavior at very low (10^{-8} - 10^{-7} M_{\odot}/yr) accretion rate, but only via spectra can we test that this has been achieved.

Keywords: Sgr A*, MHD, radiation mechanisms: general, plasmas, radiative transfer, diffusion, acceleration of particles.

1 Methodology

Given some characteristics like temperature, mass density and magnetic pressure from the simulation, we can generate broad-band spectra with emission coming from Bremsstrahlung, Synchrotron and Compton effects. These signatures can then be compared to data (Fig. 1).

Simulation characteristics are time-averaged over one stable orbits (2.5-3.5 cycle) before generating a spectrum. We obtain then a steady-state emission spectrum to compare to data. Up-to-now, thirteen models have been simulated, set by the following parameters space:

1. Cooling = [ON, OFF]
2. $\dot{M} = 10^{[-8,-9]} M_{\odot}/\text{yr}$
3. $\frac{T_i}{T_e} = [1, 3, 10]$
4. Spin factor = [0, 0.5, 0.7, 0.9, 0.9]
5. Magnetic field configuration = [1, 4] -loop

The reference simulation has been chosen to have the following parameters:

1. Cooling = ON
2. $\dot{M} = 10^{-9} M_{\odot}/\text{yr}$
3. $\frac{T_i}{T_e} = 3$
4. Spin factor = 0.9
5. Magnetic field configuration = 4-loop

¹ Sterrenkundig Instituut ‘Anton Pannekoek’, Universiteit van Amsterdam, Postbus 94249, 1090GE Amsterdam, The Netherlands

² Theoretical Astrophysics Center, Dept. of Astronomy, University of California, Berkeley, CA 94720-3411, USA

³ Dept. of Physics & Astronomy, College of Charleston, Charleston, USA

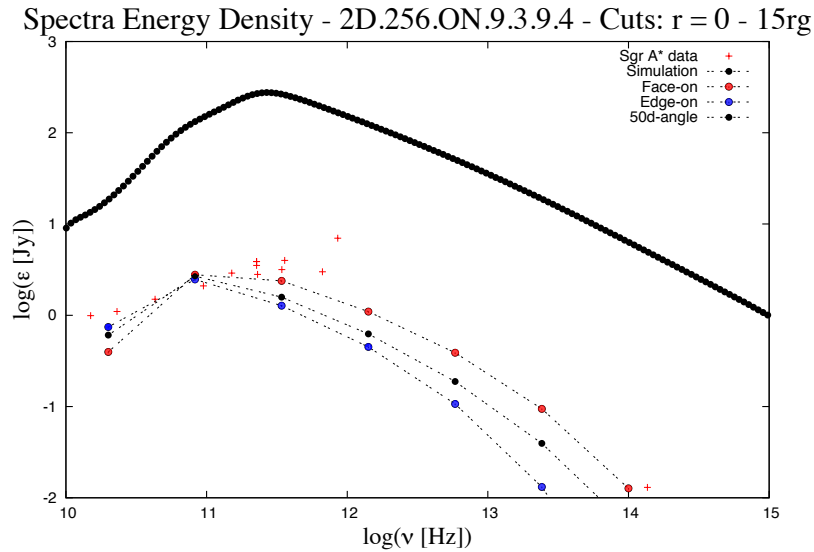


Fig. 1. Sgr A* data (*plus symbol and line*) from Melia & Falcke (2001). We show here synchrotron emission from the reference simulation B4S9T3M9C without taking into account inclination and grav. redshift (*line of black filled-circle*) followed by SEDs of the same simulation with three different angles of inclination: edge-on (*blue filled-circle*), 50 deg (*black filled-circle*) and face-on (*red filled-circle*)

2 Preliminary results

This work is still in development. Further simulations of Sgr A* are ongoing. But from our first results we can already draw some interesting conclusions:

1. Synchrotron emission is higher than expected. It is also broader. This divergence between models and data might come from the fact that we didn't take into account *inclination* considerations, *gravitational redshift* from region close to the black hole and *Doppler effect*.
2. Bremsstrahlung emission is too faint, as expected, most of the X-rays are dominated by cooler bremsstrahlung emission from the outer radii (e.g. Quataert (2002)), a part of the accretion disk which is not simulated presently.
3. Turning on cooling routines seems to have more effects on simulations with high accretion rate.
4. Tuning black hole spin to maximum generates too much magnetic field, hence too much emission.
5. Tuning temperature ration T_i/T_e to 10 gets us closer to data.
6. So does tuning magnetic field configuration to 4-loop.

3 Conclusion

These spectra show Dibi et al. (see proceedings article, this volume) first set of runs are a good start in modeling Sgr A* even though they are generating too much power. We have great expectations in model B4S9T10M9 and it will be interesting to see how its spectrum behave when inclination and gravitational redshift effects will be taken into account.

S.D. acknowledge support from a Netherlands Organization for Scientific Research (NWO) Vidi Fellowship. S.M. also acknowledges support from The European Community Seventh Framework Programme (FP7/2007-2013) under grant agreement number ITN 215212 Black Hole Universe.

References

- Anninos, P., Fragile, P. C. & Salmonson, J. D. 2005, *ApJ*, 635, 723
Blumenthal, G. R. & Gould, R. J. 1970, *Review of Modern Physics*, 42, 237
Esin, A. A., Narayan, R., Ostriker, E. & Yi, I. 1996, *ApJ*, 465, 312
Fragile, P. C. & Meier, D. L. 2009, *ApJ*, 693, 771
Mahadevan, R., Narayan, R. & Yi, I. 1996, *ApJ*, 465, 327
Melia, F. & Falcke, H. 2001, *araa*, 39, 309
Quataert, E. 2002, *ApJ*, 575, 855
Stepney, S. & Guilbert, P. W. 1983, *MNRAS*, 204, 1269

DETECTION OF A RELATIVISTIC IRON LINE IN MXB 1728–34 WITH *XMM-NEWTON*

E. Egron¹, T. Di Salvo², L. Burderi¹, A. Papitto¹, L. Barragán³, T. Dauser³, J. Wilms³, A. D’Aì²,
A. Riggio¹, R. Iaria² and N. R. Robba²

Abstract. We analyzed an *XMM-Newton* observation of the low-mass X-ray binary and atoll source MXB 1728–34. The source was in a low-luminosity state during the *XMM-Newton* observation, corresponding to a bolometric X-ray luminosity of $5 \times 10^{36} d_{5.1 \text{ kpc}}^2 \text{ erg s}^{-1}$. The 1–11 keV X-ray spectrum of the source, obtained combining data from all the five instruments on-board *XMM-Newton*, is well fitted by a Comptonized continuum. Evident residuals are present at 6–7 keV, which are ascribed to the presence of a broad iron emission line. This feature can be equally well fitted by a relativistically smeared line or by a self-consistent, relativistically smeared reflection model. Under the hypothesis that the iron line is produced by reflection from the inner accretion disk, we can infer important information on the physical parameters of the system, such as the inner disk radius, $R_{\text{in}} = 25 - 100 \text{ km}$, and the inclination of the system, $44^\circ < i < 60^\circ$.

Keywords: line: formation, line: identification, stars: neutron, stars: individual: MXB 1728–34, X-ray: binaries, X-ray: general

1 Introduction

Broad iron emission lines in the energy range 6.4–6.97 keV have been detected in high-energy resolution spectra of many X-ray sources containing a compact object, such as active galactic nuclei (e.g., Tanaka et al. 1995; Fabian et al. 2000) and X-ray binary systems containing a stellar-mass black hole (e.g., Miller et al. 2002; Miller 2007, for a review), or a weakly-magnetized neutron star (e.g., Bhattacharyya & Strohmayer 2007; Cackett et al. 2008; Di Salvo et al. 2009; Papitto et al. 2009; Iaria et al. 2009; D’Aì et al. 2009, and references therein). Identified with fluorescent $K\alpha$ transition of iron at different ionization states, these lines are generally interpreted in terms of reflection of the central hard X-ray emission on the accretion disk (Fabian et al. 1989). Under this hypothesis, these lines are made broad and asymmetric by Doppler and relativistic effects induced by the Keplerian motion in the accretion disk near the compact object. The shape of the line is therefore an almost unique proxy of the innermost accretion disk close to the compact object (see Reynolds & Nowak 2003, for a review), and, in particular, on the inner disk radius. It also indicates the inclination angle of the system and the ionization state of the reflecting matter. Other reflection components like absorption edges and the Compton hump, which are usually observed between 20–40 keV, are also expected to result from photoelectric absorption and Compton scattering of the main Comptonization continuum on the accretion disk matter.

MXB 1728–34 (4U 1728–34, GX 354–0) is a low-mass X-ray binary containing a weakly magnetized accreting neutron star. The optical counterpart of this “galactic bulge” source has not been identified yet, owing to the high optical extinction toward the Galactic center. Discovered in 1976 with the Small Astronomy Satellite SAS-3 (Lewin et al. 1976; Hoffman et al. 1976), this source belongs to the so-called atoll class (Hasinger & van der Klis 1989) and shows frequent type-I X-ray bursts (e.g., Basinska et al. 1984) that are caused by thermonuclear flashes on the neutron star surface.

¹ Dipartimento di Fisica, Università degli Studi di Cagliari, SP Monserrato-Sestu, KM 0.7, Monserrato, 09042 Italy

² Dipartimento di Scienze Fisiche ed Astronomiche, Università di Palermo, via Archirafi 36, Palermo, 90123, Italy

³ Dr. Karl Remeis-Sternwarte and Erlangen Centre for Astroparticle Physics, Friedrich-Alexander-Universität Erlangen-Nürnberg, Sternwartstrae 7, 96049 Bamberg, Germany

Spectral analysis of MXB 1728–34 has been performed in the past using data from different satellites, such as *Einstein* (Grindlay & Hertz 1981), *SAS-3* (Basinska et al. 1984), *EXOSAT* (White et al. 1986), *SIGMA* (Claret et al. 1994), *ROSAT* (Schulz 1999), and more recently using *BeppoSAX* (Piraino et al. 2000; Di Salvo et al. 2000), *ASCA* (Narita et al. 2001), *RXTE*, *Chandra* (D’Ai et al. 2006), *INTEGRAL* (Falanga et al. 2006), and *XMM-Newton* (Ng et al. 2010).

A broad emission line at 6.7 keV has been often detected in the X-ray spectra of this source and has been interpreted as emission from highly ionized iron (e.g., Di Salvo et al. 2000). The large width of the line suggests that it could come from an ionized inner accretion disk (Piraino et al. 2000), or alternatively it could be emitted from a strongly ionized corona. D’Ai et al. (2006) have proposed an alternative model to describe the iron line region using two absorption edges associated with ionized iron instead of a Gaussian line.

We present a spectral analysis of high-energy resolution data taken by *XMM-Newton* on 2002 October 3 using all five X-ray instruments on-board this satellite. The EPIC-pn data have already been published by Ng et al. (2010), in a ‘catalog’ paper dedicated to the study of the iron line in 16 neutron star LMXBs observed by *XMM-Newton*. Here we present a different approach to the analysis of these data, because we fitted for the first time the *XMM-Newton* data of MXB 1728–34 with a self-consistent modeling of the continuum emission and of the reflection component. We also tried several models to fit the iron line profile, such as diskline or relline, which are different from the models proposed by Ng et al. (2010) (Gaussian or Laor). All our results favor the relativistic nature of the line profile. We simultaneously fitted the spectra from all five X-ray instruments on-board *XMM-Newton*, while the pn data alone are analyzed by Ng et al. (2010). For more detailed informations about this work, see Egron et al. (2011).

2 Observation and data reduction

MXB 1728–34 was observed by *XMM-Newton* on 2002 October 3 for a total on-source observing time of 28 ks. The 1.5 – 12 keV lightcurve of the All Sky Monitor (ASM) on-board *RXTE* extracted within ~ 450 days the *XMM-Newton* observation indicates that the source was not in a high activity state, because it shows an average count rate of about 3 counts/s.

The *XMM-Newton* data were processed using the Science Analysis Software v. 9. The EPIC-pn camera was operated in timing mode to prevent photon pile-up. We created a calibrated photon event file using the pn processing tool EPPROC. We used the task EPFAST to correct rate-dependent CTI effects in the event list. The source spectrum was extracted from a rectangular area, covering all pixels in the Y direction, and centered on the brightest RAWX column (RAWX=38), with a width of 13 pixels around the source position. We selected only events with PATTERN ≤ 4 (single and double pixel events) and FLAG=0 as a standard procedure to eliminate spurious events. We extracted the background away from the source (in the RAWX = 6 – 18). We also checked that pile-up did not affect the pn spectrum using the task EPATPLOT. The total count rate registered by EPIC-pn CCDs was around 110 count/s, and was 64 count/s in the 2.4–11 keV range, slightly increasing (by 5%) during the observation.

The MOS data were also taken in timing mode and processed with the routine EMPROC to produce calibrated event list files. The source spectra were extracted from a rectangular box centered on RAWX=320 (MOS1), and on RAWX=308 (MOS2), selecting an area 30 pixels wide around the source position, and covering 722 pixels on the Y (PHA) direction. Only events corresponding to PATTERN ≤ 12 and FLAG= 0 were selected, corresponding to standard filters. The background spectra were extracted far from the source, centered on the column RAWX= 240. We checked that the MOS spectra were not affected by pile-up. The count rates were estimated to be around 30 counts/s for each MOS unit (20 counts/s considering 2.4–11 keV energy range).

Spectral channels of EPIC-pn and MOS spectra were rebinned to have three channels per energy resolution element and at least 25 counts per energy channel.

The two RGS were operated in the standard spectroscopy mode. The RGS data were processed using the RGSPROC pipeline to produce calibrated event list files, spectra and response matrices. The count rates measured by RGS1 and RGS2 were around 2.5 and 3.5 counts/s, respectively. The RGS data were rebinned to provide a minimum of 25 counts per energy channel.

3 Spectral analysis

Data were fitted by using XSPEC (Arnaud 1996) v.12.5.1. All uncertainties are given at the 90% confidence level ($\Delta\chi^2 = 2.706$). We simultaneously fitted the broad band energy spectra of the source obtained from all five

instruments. Considering the best calibration ranges of the different detectors, the data analysis from EPIC-pn, MOS1 and MOS2 cameras was restricted to the energy range 2.4–11 keV. This excluded the region around the detector Si K-edge (1.8 keV) and the mirror Au M-edge (2.3 keV) that could affect our analysis. We only used the RGS1 and RGS2 data between 1–2 keV to constrain the softest band.

The different cross calibrations of the five instruments were taken into account by including normalizing factors in the model. These factors were fixed to 1 for pn and kept free for the other instruments.

We first fitted the continuum with a thermal Comptonized model using COMP TT (Titarchuk 1994), modified at low energy by the interstellar photoelectric absorption modeled by PHABS. The $\chi^2/\text{d.o.f.}$ of the fit was large, 1732/903. We then tried to add a blackbody component (BBODY model) to improve the fit. The addition of this component turned out not to be statistically significant, thus we decided not to include the blackbody in our model.

With respect to this continuum model, an excess was present in the residuals between 5.5 and 8 keV, probably indicating the presence of iron discrete features. The fit was improved by adding a broad iron emission line, modeled by a simple Gaussian line (Model 1), centered at 6.6 keV with the σ parameter frozen at 0.6 keV. With the addition of the Gaussian, the fit gave a $\chi^2/\text{d.o.f.} = 1489/901$ (resulting in a significant improvement of the fit, with a $\Delta\chi^2 = 243$ for the addition of two parameters).

We then tried to substitute the Gaussian at 6.6 keV with a diskline profile and obtained a slightly better result with a $\chi^2/\text{d.o.f.} = 1463/899$. Owing to the large uncertainties on the outer radius of the disk and on the inclination of the system if they were let free, we froze the first one at $1000 R_g$ and the inclination at 60° (the source does not show any dip in its lightcurve, implying $i < 60^\circ$). The improvement of the fit corresponds to $\Delta\chi^2 = 26$ for the addition of two parameters (the F-test gives a probability of chance improvement of about 10^{-4}).

To assess the significance of the relativistic line smearing on a statistical basis, we used another statistical method based on the posterior predictive p values described by Hurkett et al. (2008). For simplicity, we restricted our data to two instruments (pn and MOS2). These data were fitted with Model 1 and Model 2, respectively. We obtained an improvement of the fit corresponding to a $\Delta\chi^2$ of 18 for the addition of two parameters when we substituted Model 1 with Model 2. Then, we simulated 200 pn and MOS2 spectra according to Model 1, which were fitted in a second step using Model 2. The $\Delta\chi^2$ was registered for each simulation. Among the 200 simulations, we twice found a $\Delta\chi^2$ higher than 18. So the probability of chance improvement we gain from these simulations is 1%, which agrees with the 0.75% calculated by the F-test performed on the real data restricted to two instruments. Therefore, we can conclude that the diskline model is to be preferred because it gives a probability of chance improvement of the fit of about 10^{-4} using all instruments.

This model gives an estimate of the inner radius of the disk $R_{\text{in}} \sim 18 R_g$ ($R_g = GM/c^2$ is the gravitational radius). Fixing the inclination to lower values (i.e. $i < 60^\circ$), worse χ^2 were obtained with the other diskline parameters drifting toward lower R_{in} , higher rest-frame energies, and higher emissivity indices in absolute value. We searched for an absorption edge in the energy range 7–10 keV, but none was significantly detected.

To fit the iron line, we also used a new model for a relativistically distorted diskline, called RELLINE* (Dauser et al. 2010), which calculates line profiles taking into account all relativistic distortions in a disk around the compact object. We also fixed the outer radius of the disk and the inclination of the system to the same values used in the diskline model. The $\chi^2/\text{d.o.f.}$ obtained in these conditions is 1464/899. The best-fit line parameters obtained in this way are perfectly consistent with those obtained using the diskline model. In particular this model (Model 3) estimates the inner radius of the disk to be $R_{\text{in}} \sim 19 R_g$.

We tried an alternative model for the iron features (see D’Ai et al. 2006) using two absorption edges (instead of an emission line), which are found at 7.50 keV ($\tau \sim 0.06$) and 8.49 keV ($\tau \sim 0.06$), associated to mildly and highly ionized iron, respectively. The $\chi^2/\text{d.o.f.}$ for this fit is 1519/899 (which has to be compared to 1489/901 that we obtained fitting the iron line with a Gaussian (Model 1) or to 1463/899 that we obtained fitting the iron line with a diskline (Model 2)). Therefore this model gives a worse fit of the iron features than the previous ones.

In order to test the consistency of the broad iron line with a reflection component, we fitted the data using REFLION, a self-consistent reflection model including both the reflection continuum and the corresponding discrete features (Ross & Fabian 2005), in addition to a thermally Comptonized continuum modeled with NTHCOMP, by Zdziarski et al. (1996), and extended by Zycki et al. (1999)), instead of COMP TT. The $\chi^2/\text{d.o.f.}$ was 1555/901, without the inclusion of relativistic smearing. Because the iron line was found to be significantly

*[urlhttp://www.sternwarte.uni-erlangen.de/research/relline/](http://www.sternwarte.uni-erlangen.de/research/relline/).

broad in the previous models (Model 1, 2, and 3), we added the relativistic smearing using the RDBLUR component. The addition of this component to the model constitutes Model 5 and led to a $\chi^2/\text{d.o.f.} = 1466/899$. The decrease of the χ^2 for the addition of the relativistic smearing was $\Delta\chi^2 = 89$ for the addition of two parameters (corresponding to an F-test probability of chance improvement of $\sim 10^{-12}$). Assuming that iron has a solar abundance and freezing the emissivity betor index to -2.8 (value obtained with the diskline model) and the ionization parameter $\xi = L_X/(nr^2)$ to 660 (this parameter tends to take high values but is unstable during the fit, which is why we preferred to freeze it), where L_X is the ionizing X-ray luminosity, n is the electron density in the reflector, and r the distance of the reflector to the emitting central source, the inner radius was estimated again to be $20 R_g$ and a lower limit to the inclination angle was found to be 44° . In Fig. 1 we plot the residuals obtained with this self-consistent reflection model in comparison with the continuum and the RELLINE model using the EPIC-pn data.

The residuals found with respect to the different models described above do not show any evident systematic trend; the large χ^2 could be due to mismatches in the cross-calibration between the different instruments (for more details, see the cross-calibration document available on the *XMM-Newton* webpage[†]) or to unresolved and unfitted features.

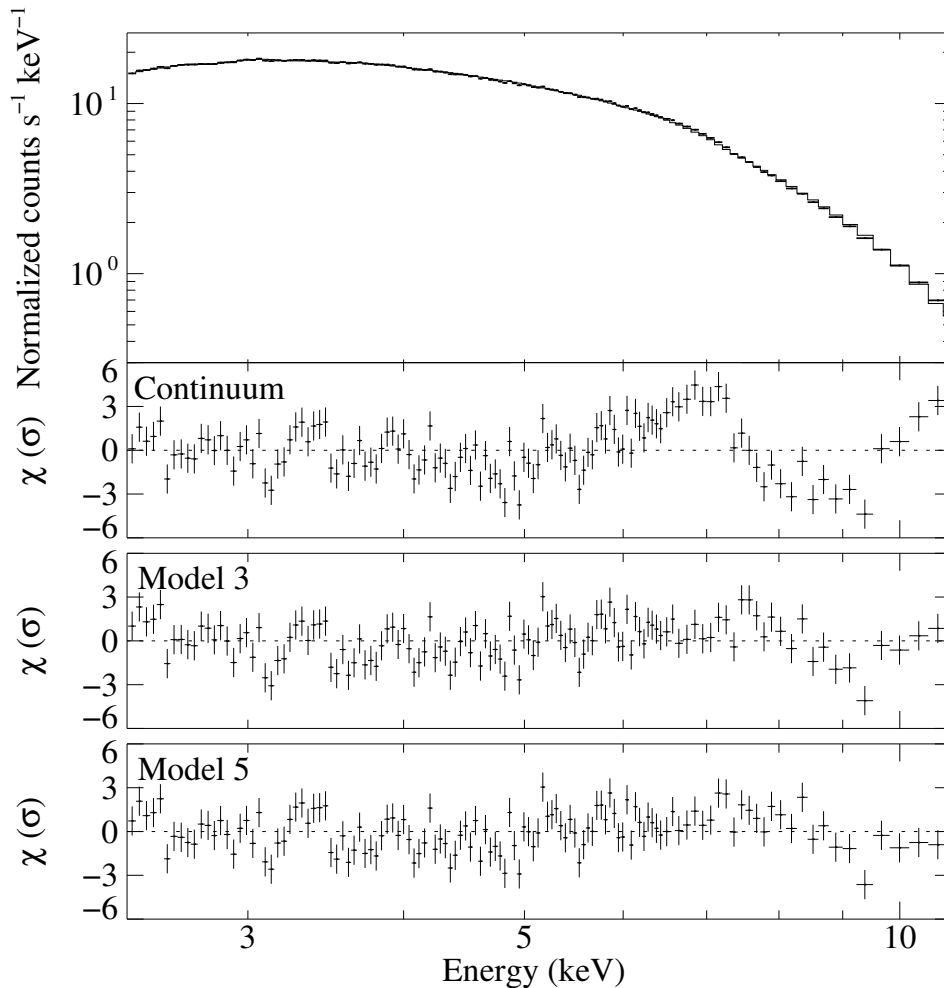


Fig. 1. Top: EPIC-pn data points of MXB 1728–34 in the range 2.4–11 keV. **Bottom:** Residuals (data-model) in unit of sigmas for the continuum, for Model 3 including a relativistic line (RELLINE), and for Model 5 using a relativistic reflection component (REFLION), respectively. Data were rebinned for graphical purposes.

[†]<http://xmm2.esac.esa.int/docs/documents/CAL-TN-0052.ps.gz>.

4 Discussion

We performed a spectral analysis of MXB 1728–34 observed by *XMM-Newton* on 2002 October 3 in the 1–11 keV energy range. The best-fit continuum model consists of an absorbed Comptonized component; the addition of a soft blackbody component does not improve the fit significantly. With respect to this continuum model, evident residuals are present at 6–8 keV, which can be fitted either by a relativistic line (such as diskline or RELLINE) or by a self-consistent relativistic reflection model.

4.1 The continuum emission

The X-ray spectra of black-hole and neutron star in X-ray binaries are generally described by models that include a soft/thermal and a hard/Comptonized component; the electron temperature of the Comptonized component significantly decreases when the source transits from the hard to the soft state while its optical depth increases. We chose a continuum that consists of an absorbed Comptonization model (COMPTT or NTHCOMP) because these models gave the best fit to the broad-band (0.1–200 keV) *BeppoSAX* spectrum of MXB 1728–34 (Piraino et al. 2000; Di Salvo et al. 2000).

Usually a soft blackbody component is required to fit the broad band X-ray spectra of LMXBs, most frequently interpreted as emitted by an accretion disk. This component is not significantly detected in the *XMM-Newton* spectrum. This may be ascribed to the relatively low X-ray luminosity of the source during the *XMM-Newton* observation, specially in the soft band. The bolometric X-ray flux in the range 0.1–150 keV also implies a bolometric X-ray luminosity of $L_X \sim 5 \times 10^{36} d_{5.1}^2 \text{ erg s}^{-1}$, corresponding to 2% of the Eddington luminosity, that is $L_{\text{Edd}} = 2.5 \times 10^{38} \text{ erg s}^{-1}$ for a $1.4 M_{\odot}$ neutron star (e.g., van Paradijs & McClintock 1994). Indeed, during the high/soft state the disk is expected to be very close to the compact object, while in the low/hard state the disk should be truncated far from the compact object, and therefore its contribution is expected to be less important.

We conclude that the blackbody component is just too weak to be detected. This agrees with the results obtained from the fit of the iron feature with a reflection model. This indicates that the inner accretion disk is probably truncated far from the neutron star ($R_{\text{in}} > 25 \text{ km}$), and with a relatively high value for the system inclination with respect to the line of sight estimated at $44^\circ < i < 60^\circ$, which would further reduce the disk luminosity with respect to the Comptonized component in the hypothesis that the last one has a spherical geometry around the compact object.

4.2 The iron line emission

Recently Ng et al. (2010) and Cackett et al. (2010) presented a spectral analysis of a sample of neutron star LMXBs observed by *XMM-Newton* and *Suzaku*, respectively, with particular interest in the iron discrete features in these sources. While Cackett et al. (2010) conclude that Fe K line profiles are well fitted by a relativistic line model for a Schwarzschild metric in most cases and imply a narrow range of inner disk radii (6–15 GM/c^2), Ng et al. (2010) conclude there is no evidence for asymmetric (relativistic) line profiles in the *XMM-Newton* data, although the line profiles (fitted with a simple Gaussian or a laor model) again appear to be quite broad, with Gaussian sigmas ranging between 0.17 up to 1.15 keV.

We tried different models to fit the iron line profile. Although a Gaussian line provides an acceptable fit of the line profile, we tried to physically interpret its large width using models for a relativistically smeared line in an accretion disk.

Using the diskline profile (Model 2), we find the line centroid energy at 6.45 keV, compatible with a fluorescent $K\alpha$ transition from mildly ionized iron Fe I–XX. The inner radius is in the range 12–21 R_g . The line profile appears therefore to be significantly broad and compatible with a diskline profile. The results obtained by using a relativistic line profile corresponding to Model 3, which uses the more recent RELLINE instead of diskline, are perfectly consistent with the diskline model. The inner radius is estimated to be in the range 15–22 R_g .

The line profile can be equally well fitted using a self-consistent relativistic reflection model (Model 5). The addition of the RDBLUR component significantly improves the χ^2 . This indicates that the line is indeed broad, and that the width of the line agrees with a relativistic smearing in the disk. The value of the inner radius is again consistent with that found using a diskline or a relline profile, even if the uncertainty is larger ($R_{\text{in}} = 13\text{--}43 R_g$). For a neutron star mass of $1.4 M_{\odot}$, the inner disk radius is in the range 25–100 km from the neutron star center, and so the disk would be truncated quite far from the neutron star surface. The inclination angle

of the system with respect to the line of sight is found to be $> 44^\circ$, which is still compatible with the absence of dips in its lightcurve (which implies $i < 60^\circ$).

We therefore favor the interpretation of the iron feature as a broad and relativistic emission line produced in the accretion disk, because this gives a better fit of the *XMM-Newton* spectrum and very reasonable values of the reflection parameters.

This work was supported by the Initial Training Network ITN 215212: Black Hole Universe funded by the European Community.

References

- Arnaud, K. A. 1996, in ASP Conf. Ser. 101: Astronomical Data Analysis Software and Systems V, 17
- Basinska, E. M., Lewin, W. H. G., Sztajno, M., Cominsky, L. R., & Marshall, F. J. 1984, ApJ, 281, L337
- Bhattacharyya, S. & Strohmayer, T. E. 2007, ApJ, 664, L103
- Cackett, E. M., Miller, J. M., Ballantyne, D. R., et al. 2010, ApJ, 720, L205
- Cackett, E. M., Miller, J. M., Bhattacharyya, S., et al. 2008, ApJ, 674, L415
- Claret, A., Goldwurm, A., Cordier, B., et al. 1994, ApJ, 423, L436
- D'Ai, A., Di Salvo, T., Iaria, R., et al. 2006, A&A, 448, 817
- D'Ai, A., Iaria, R., Di Salvo, T., Matt, G., & Robba, N. R. 2009, ApJ, 693, L1
- Dauser, T., Wilms, J., Reynolds, C. S., & Brenneman, L. W. 2010, MNRAS, 409, 1534
- Di Salvo, T., D'Ai, A., Iaria, R., et al. 2009, MNRAS, 398, 2022
- Di Salvo, T., Iaria, R., Burderi, L., & Robba, N. R. 2000, ApJ, 542, L1034
- Egron, E., Di Salvo, T., Burderi, L., et al. 2011, A&A, 530, A99
- Fabian, A. C., Iwasawa, K., Reynolds, C. S., & Young, A. J. 2000, PASP, 112, 1145
- Fabian, A. C., Rees, M. J., Stella, L., & White, N. E. 1989, MNRAS, 729
- Falanga, M., Gotz, D., Goldoni, P., et al. 2006, A&A, 458, 21
- Grindlay, J. E. & Hertz, P. 1981, ApJ, 247, L17
- Hasinger, G. & van der Klis, M. 1989, A&A, 225, 79
- Hoffman, J. A., Lewin, W. H. G., Doty, J., et al. 1976, ApJ, 210, L13
- Hurkett, C. P., Vaughan, S., Osborne, J. P., et al. 2008, ApJ, 679, L587
- Iaria, R. and D'Ai, A., di Salvo, T., Robba, N. R., et al. 2009, A&A, 505, 1143
- Lewin, W. H. G., Clark, G., & Doty, J. 1976, iauc, 2922, 1
- Miller, J. M. 2007, ARA&A, 45, 441
- Miller, J. M., Fabian, A. C., Wijnands, R., et al. 2002, ApJ, 570, L69
- Narita, T., Grindlay, J. E., & Barret, D. 2001, ApJ, 547, L420
- Ng, C., Diaz Trigo, M., Cadolle Bel, M., & Migliari, S. 2010, A&A, 522, A96
- Papitto, A., Di Salvo, T., D'Ai, A., et al. 2009, A&A, 493, 39
- Piraino, S., Santangelo, A., & Kaaret, P. 2000, A&A, 360, 35
- Reynolds, C. S. & Nowak, M. A. 2003, Phys. Rep., 377, 389
- Ross, R. R. & Fabian, A. C. 2005, MNRAS, 358, 211
- Schulz, N. S. 1999, ApJ, 511, L304
- Tanaka, Y., Nandra, K., Fabian, A. C., et al. 1995, Nature, 375, 659
- Titarchuk, L. 1994, ApJ, 434, L570
- van Paradijs, J. & McClintock, J. E. 1994, A&A, 290, 133
- White, N. E., Peacock, A., Hasinger, G., et al. 1986, MNRAS, 218, 129
- Zdziarski, A. A., Johnson, W. N., & Magdziarz, P. 1996, MNRAS, 283, 193
- Zycki, P. T., Done, C., & Smith, D. A. 1999, MNRAS, 309, 561

THERMAL EVOLUTION OF NEUTRON STARS AND CONSTRAINTS ON THEIR INTERNAL PROPERTIES

M. Fortin¹, J. L. Zdunik², P. Haensel² and J. Margueron³

Abstract. Neutron stars, the end point of the life of massive stars, are cosmic laboratories for various fields of physics, in particular for nuclear physics of cold and dense matter. The very high densities inside neutron stars can not be reproduced on Earth. Nevertheless, modeling the thermal evolution of both isolated and accreting neutron stars enables to put constraints on the poorly known composition, structure, superfluid and thermal properties of their interior.

Keywords: Neutron stars, cooling, dense matter, equation of state, superfluidity

1 Introduction

Neutron stars are the remnant of the gravitational collapse of $\sim 8 - 10M_{\odot}$ stars after a supernova event. They have a mass $\sim 1 - 2M_{\odot}$, a radius ~ 10 km and a magnetic field up to $\sim 10^{15}$ G. They are relativistic objects sustained by the strong interaction. Their extreme properties make them celestial laboratories for general relativity, magnetohydrodynamics, nuclear physics, superfluidity and superconductivity, . . .

Their average density $\sim 10^{15}$ g cm⁻³ is unreachable in terrestrial laboratories so neutron stars offer a unique possibility to understand and constraint the properties of cold and dense matter.

2 Structure of a neutron star

Figure 1 schematically shows the structure of a NS. The surface of a neutron star is surrounded by an atmosphere which is a thin layer of plasma at the origin of the electromagnetic radiation. Below the envelope, the outer envelope or outer crust is made of a gas of electrons e and a lattice of ions Z . The neutrons n start to drip out of the nuclei at $\rho_{\text{ND}} \simeq 4 \times 10^{11}$ g cm⁻³. This point defines the boundary between the outer and inner crust. The matter of the latter is composed of electrons, free neutrons that may be superfluid and a lattice of very neutron-rich atomic nuclei. At the core-crust interface, when $\rho \sim 0.5\rho_0$ with $\rho_0 = 2.8 \times 10^{14}$ g cm⁻³ the nuclear saturation density, the nuclei disappear. The inner core consists of neutrons, protons, electrons and probably muons μ and the nucleons are likely to be superfluid. Deeper in the neutron star is the inner core whose composition is still unknown and is the subject of active research. Various theories predict the appearance of hyperons (baryons with a least one strange quark), the formation of condensates of particles such as pions or kaons, or the phase transition to deconfined quark matter.

The composition and the superfluid properties of the matter inside neutron stars are some of the many mysteries of these objects.

3 Thermal evolution of isolated neutron stars

3.1 Thermal history

A neutron star is born hot in a core-collapse supernova explosion, with a temperature $\sim 10^{11}$ K. In about a hundred years, it cools by neutrino emission in the core and by the heat diffusion in the crust. Therefore, the

¹ LUTH, Observatoire de Paris, 5 Place Jules Janssen, F-92195 Meudon, France

² N. Copernicus Astronomical Center, Polish Academy of Sciences, Bartycka 18, PL-00-716 Warszawa, Poland

³ Institut de Physique Nucléaire, IN2P3-CNRS, and Université Paris-Sud, F-91406 Orsay, France

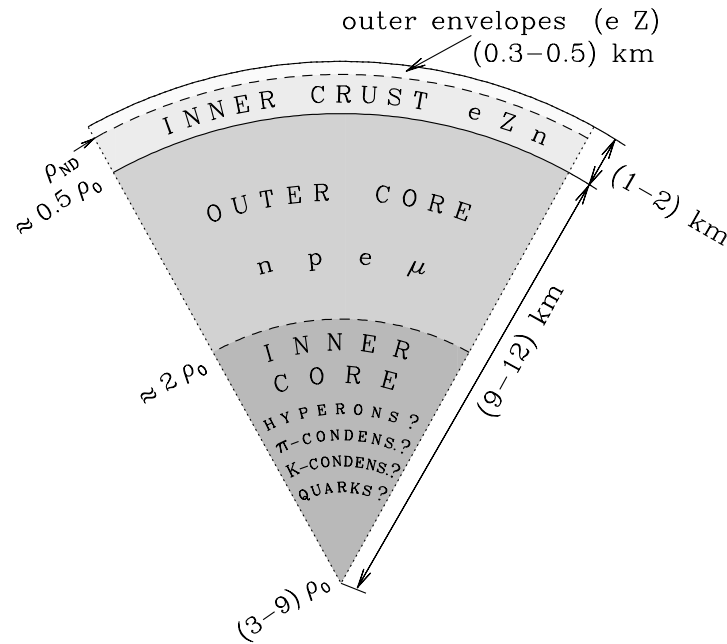


Fig. 1. Structure of a neutron star. From Haensel et al. (2007).

evolution of the surface temperature is connected with the properties and the thermal state of the crust. Later, the temperature inside the core and the crust equilibrates and the cooling of the whole neutron star is driven by the neutrino emission from the core. The thermal state reflects the properties of the core. Finally, after few ten thousand years, the cooling is dominated by the emission of photons at the surface. Therefore, depending on the age of the isolated neutron star whose temperature is determined, one can constraint the physics in different regions of the star.

3.2 Constraining superfluidity with observations

The theoretical modeling of the thermal evolution of an isolated neutron star shows that the cooling depends on the properties of crust, in particular the superfluidity of free neutrons in the inner-crust (Lattimer et al. 1994; Gnedin et al. 2001). Therefore a precise description of the thermal behavior of these neutrons is necessary to simulate the cooling.

New calculations of the superfluid properties of the free neutrons in the crust have been performed taking into account the influence of the surrounding nuclei (Fortin et al. 2010). Simulations of the cooling of a neutron star show that the presence of superfluid neutrons in the inner crust fastens the cooling, as compared to normal neutrons, for the first hundred years and that including the effects of the nuclei has a non-trivial influence on the thermal evolution.

Analyzing archival Chandra X-ray Observatory data, Ho & Heinke (2009) show that the compact object in Cassiopeia A supernova remnant is a neutron star with a carbon atmosphere and a surface temperature $T_s \sim 2 \times 10^6$ K. This is the first determination of the composition of the atmosphere of an isolated neutron star. Spectral fits of ~ 10 years of Chandra observations of CasA neutron star with a carbon atmosphere model reveal that the temperature of the neutron star decreases (Heinke & Ho 2010). For the first time, the cooling of an isolated neutron star is directly observed. So far, only the temperature at one instant in time of neutron stars with different ages and different masses were known. Modeling the thermal evolution of CasA neutron star that is ~ 330 years-old, Shternin et al. (2011) and Page et al. (2011) conclude that the protons in the core are superfluid and superconducting. They also put constraints on the superfluid properties of the neutrons in the core and the associated neutrino emissivity. The future monitoring of CasA neutron star offers exciting perspectives.

4 Thermal evolution of quasi-persistent X-ray transients

A subclass of accreting neutron stars, the so-called quasi-persistent X-ray transients (QPXRTs), also enables to constrain the properties of the matter inside neutron stars.

In the active phase, with $L \sim 10^{36-39}$ erg s $^{-1}$, the neutron star accretes matter from a low-mass companion during years to decades before accretion stops (when $L < 10^{34}$ erg s $^{-1}$). In the deep crustal heating scenario (Brown et al. 1998), the accreted matter undergoes a series of nuclear reactions (Haensel & Zdunik 2008) while it sinks deeper into the crust under the weight of the newly-accreted material. The reactions produce heat that is at the origin of the thermal relaxation observed just after accretion stops, shown in figure 2.

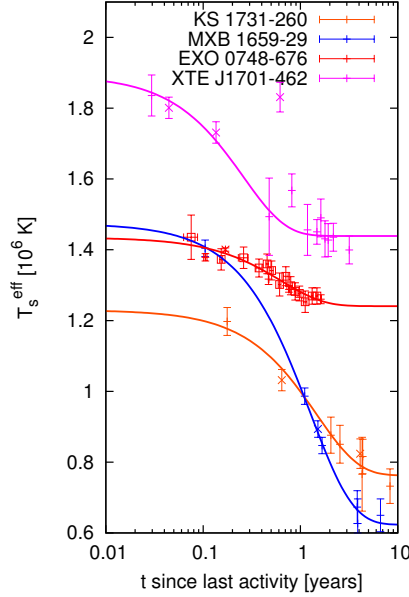


Fig. 2. Thermal relaxation of the four quasi persistent X-ray transients. The temperature as seen by an observer at infinity is plotted versus the time since the source turns to quiescence. The solid lines show the best-fit of the observations by an exponential decay. Observations from Cackett et al. (2010, 2008); Degenaar et al. (2011); Fridriksson et al. (2011).

The modeling of the thermal relaxation after accretion stops depends on the accretion rate, the composition and mass of the neutron star and the microphysical input.

The thermal relaxation of KS 1731 – 260 excludes a very efficient neutrino process, the so-called DURCA process, in the core and is consistent with moderate neutrino emissivity and a crystalline crust with superfluid neutrons (Shternin et al. 2007). The thermal relaxations of KS 1731 – 260 and MXB 1659 – 29 are consistent with the presence of nuclides with different charge numbers at a given density (Brown & Cumming 2009). These two sources have a relaxation time scale τ , after accretion stops, of the order of 500 days (table 1). There are two more QPXRTs whose thermal relaxation has not been successfully modeled yet : EXO 0748 – 676 and XTE J1701 – 462 with much shorter relaxation time scales (~ 200 and 100 days respectively). These suggest that there exist heat sources at densities lower than the ones that have been considered so far in the models of deep crustal heating. Moreover, XTE J1701 – 462 exhibits in the relaxation stage a sudden increase in temperature that is believed to originate from a sudden spur of accretion.

Source	τ (d)
KS 1731 – 260	540 ± 125
MXB 1659 – 29	465 ± 35
EXO 0748 – 676	230 ± 60
XTE J1701 – 462	95 ± 15

Table 1. Relaxation time scales τ in days of the QPXRTs obtained by a fit of the observations with an exponential decay.

Future work intend to take into account a precise description of the microphysical properties (composition, thermal properties) in the outer part of the neutron star together with an up-to-date model of atmosphere for an accreting neutron star Fortin et al. (2012). The burning of the accreted matter at low density will be taken into account for the first time. Preliminary results show that the thermal relaxation of all four sources can be reproduced by our model. Moreover the thermal evolution of an accreting neutron star in the accreting phase will be calculated. The model can enable to put constraints on the properties of the outer parts of neutron stars and is to be later extended to study the other neutron star transients.

5 Conclusions

The properties of the matter inside neutron stars are poorly-known since the high densities inside them can not be reproduced on Earth. Nevertheless, modeling the thermal evolution of isolated and accreting neutron stars enables to put constraint on the physics of cold and dense matter, in particular on the superfluid properties, the neutrino processes and the composition.

This work was partially supported by the Polish MNiSW grant no. N N203 512 838 and the LEA Astrophysics Poland-France (Astro-PF). MF acknowledges Observatoire de Paris and European Science Foundation 'The New Physics of Compact Stars' fellowship program.

References

- Brown, E. F., Bildsten, L., & Rutledge, R. E. 1998, *ApJ*, 504, L95
Brown, E. F. & Cumming, A. 2009, *ApJ*, 698, 1020
Cackett, E. M., Brown, E. F., Cumming, A., et al. 2010, *ApJ*, 722, L137
Cackett, E. M., Wijnands, R., Miller, J. M., Brown, E. F., & Degenaar, N. 2008, *ApJ*, 687, L87
Degenaar, N., Wolff, M. T., Ray, P. S., et al. 2011, *MNRAS*, 412, 1409
Fortin, M., Grill, F., Margueron, J., Page, D., & Sandulescu, N. 2010, *Phys. Rev. C*, 82, 065804
Fortin, M., Zdunik, J. L., & Haensel, P. 2012
Fridriksson, J. K., Homan, J., Wijnands, R., et al. 2011, *ApJ*, 736, 162
Gnedin, O. Y., Yakovlev, D. G., & Potekhin, A. Y. 2001, *MNRAS*, 324, 725
Haensel, P., Potekhin, A. Y., & Yakovlev, D. G., eds. 2007, *Astrophysics and Space Science Library*, Vol. 326, Neutron Stars 1 : Equation of State and Structure
Haensel, P. & Zdunik, J. L. 2008, *A&A*, 480, 459
Heinke, C. O. & Ho, W. C. G. 2010, *ApJ*, 719, L167
Ho, W. C. G. & Heinke, C. O. 2009, *Nature*, 462, 71
Lattimer, J. M., van Riper, K. A., Prakash, M., & Prakash, M. 1994, *ApJ*, 425, 802
Page, D., Prakash, M., Lattimer, J. M., & Steiner, A. W. 2011, *Physical Review Letters*, 106, 081101
Shternin, P. S., Yakovlev, D. G., Haensel, P., & Potekhin, A. Y. 2007, *MNRAS*, 382, L43
Shternin, P. S., Yakovlev, D. G., Heinke, C. O., Ho, W. C. G., & Patnaude, D. J. 2011, *MNRAS*, 412, L108

ACCURATE BLACK HOLE MASS MEASUREMENTS FOR THERMAL AGNS AND THE ORIGIN OF THE CORRELATIONS BETWEEN BLACK HOLE MASS AND BULGE PROPERTIES

C. M. Gaskell¹

Abstract. A simple refinement is proposed to the Dibai method for determining black hole masses in type-1 thermal AGNs. Comparisons with reverberation mapping black hole masses and host galaxy bulge properties suggest that the method is accurate to ± 0.15 dex. Contrary to what was thought when the $M_{\bullet} - \sigma_{*}$ relationship was first discovered, it does not have a lower dispersion than the $M_{\bullet} - L_{bulge}$ relationship. The dispersion in the $M_{\bullet} - L_{host}$ relationship for AGNs decreases strongly with increasing M_{\bullet} or L_{bulge} . This is naturally explained as a consequence of the $M_{\bullet} - bulge$ relationships being the result of averaging due to mergers. Simulations show that the decrease in dispersion in the $M_{\bullet} - L_{bulge}$ relationship with increasing mass is in qualitative agreement with being driven by mergers. The large scatter in AGN black hole masses at lower masses rules out significant AGN feedback. A non-causal origin of the correlations between black holes and bulges explains the frequent lack of supermassive black holes in late-type galaxies, and the lack of correlation of black hole mass with pseudo-bulges.

Keywords: Black hole physics, galaxies: active, quasars: emission lines, galaxies: bulges, galaxies: formation, galaxies: evolution

1 Introduction

Dibai (1977) introduced the estimation of the masses, M_{\bullet} , of supermassive black holes (SMBHs) in type-1 thermal AGNs (i.e., high accretion rate AGNs seen close to pole-on – see Antonucci 1993, 2011) from the optical luminosity and the FWHM of the $H\beta$ line. Because of its ease of use, the “Dibai method” (also known as the “photoionization method” or the “single-epoch method”) is by far the most widely used method of SMBH mass determination. The assumptions in the Dibai method are discussed in Bochkarev & Gaskell (2009). For a recent review of AGN SMBH determinations see Marziani & Sulentic (2011). The Dibai method assumes that the broad-line region (BLR) is gravitationally bound and that AGNs have similar continuum shapes and structures so that the size of the $H\beta$ emitting region can be estimated from the luminosity. For checking these assumptions and calibrating the method, reverberation mapping has been crucial. Cross-correlation of line and continuum time series (Lyutyi & Cherepashchuk 1972; Cherepashchuk & Lyutyi 1973; Gaskell & Sparke 1986) yields effective radii of the line-emitting regions, and velocity-resolved reverberation mapping shows that the gas is gravitationally bound (Gaskell 1988).

A long-standing question in AGN research has been whether the masses of SMBHs are correlated with the masses of their host galaxies. Until the mid-1990s it was generally assumed that an SMBH was an incidental and perhaps accidental addition to a galaxy – discovering an SMBH in a galaxy was considered worthy of a press release! A notable exception to this assumption was Zasov & Dibai (1970) who discovered a correlation between the brightness of AGNs and their host galaxies. Dibai (1977) subsequently found an apparent correlation between AGN luminosity and M_{\bullet} . Taken together these findings implied that M_{\bullet} and L_{host} were correlated. The tacit assumption of the 1980s, though, was that any correlation between M_{\bullet} and L_{host} was the result of selection effects (because only a bright host could be seen in a bright AGN). This attitude began to change when Kormendy (1994) discovered that the masses of inactive SMBHs seemed to be correlated with the luminosity,

¹ Centro de Astrofísica de Valparaíso y Departamento de Física y Astronomía, Universidad de Valparaíso, Av. Gran Bretaña 1111, Valparaíso, Chile

L_{bulge} , of the bulge of the host galaxy. Further work (notably Magorrian et al. 1998) verified that there was indeed a $M_{\bullet} - L_{bulge}$ relationship* but also showed that there was substantial scatter in it. In trying to understand the origin of the relationship it is important to know how much of this scatter is the result of observational and modeling errors, and how much is intrinsic.

2 Improving the Dibai method

Masses determined from reverberation mapping (Gaskell 1988) have been considered the “gold standard” of AGN BH mass determinations because the effective radius is estimated relatively directly. Comparing reverberation mapping masses, M_{rev} , with masses from the most widely-used version of the Dibai method ($M_{Dibai} \propto FWHM^2 L^{0.5}$) gives a dispersion of ± 0.37 dex (see Fig. 1a). It is known that BLR line profile shapes vary from object to object and that the shape is a function of line width (see Gaskell 2009b for a review of the BLR). It is therefore reasonable to ask whether the Dibai method can be refined. Gaskell (2010a) has suggested improving the Dibai method by introducing an extra line width term. Fig. 1b shows M_{new} , the masses determined from Eq. 1 of Gaskell (2010a), compared with reverberation masses. This gives a relative dispersion of ± 0.22 dex. An F -test shows that the improvement is significant at the 99.8% level.

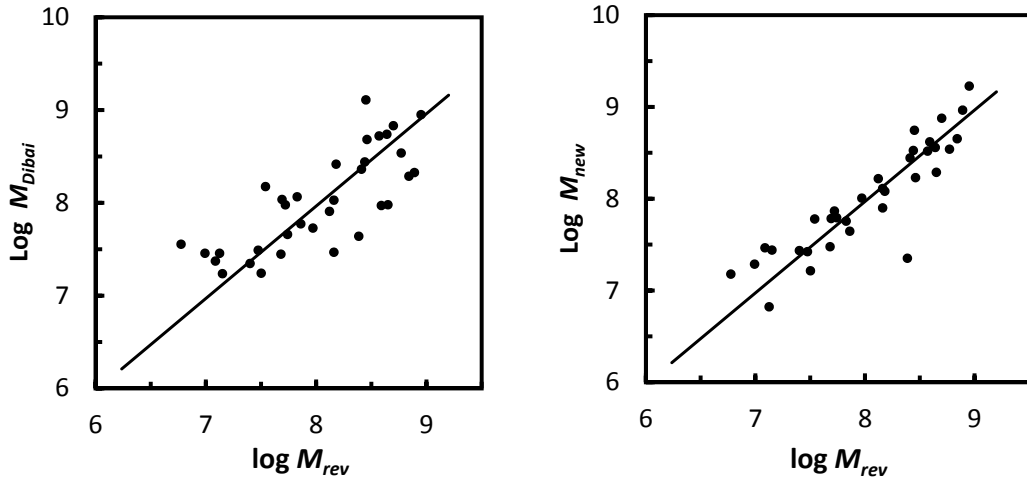


Fig. 1. Left: Correlation between masses, M_{rev} , measured from reverberation mapping and masses, M_{Dibai} , estimated using from $FWHM^2 L_{AGN}^{0.5}$. **Right:** improvement when M_{Dibai} is replaced with M_{new} , the mass estimated using Eq. 1 of Gaskell (2010a). $H\beta$ line widths, L_{AGN} , and M_{rev} are from the compilation of Vestergaard & Peterson (2006).

The ± 0.22 dex includes errors from both reverberation mapping and from using Eq. 1 of Gaskell (2010a). From inspection of the Vestergaard & Peterson (2006) compilation of reverberation-mapping black hole estimates, the rms error in M_{rev} is ± 0.12 dex due to measuring error alone. To this should be added an additional, unknown, error caused by the off-axis nature of the continuum variability (see Gaskell 2010b). Because of this, reverberation mapping gives different time delays for different continuum events. The effect of this on the error budget for M_{rev} still needs to be evaluated.

Denney et al. (2009) have used repeated measurements of the same object to estimate the error in the Dibai method due to measuring error. They get an error of ± 0.10 dex and, taking into account additional effects, they believe the combined error is ± 0.12 to 0.16 dex. The rms error in M_{new} will be similar. These error estimates do not take into account possible random or systematic object-to-object differences in the scaling.

Since there could be unknown random or systematic sources of error in determination of M_{\bullet} by each method, and some of these (such as orientation effects) could be the same for both M_{rev} and M_{new} , it is important to have an external check. The correlations between M_{\bullet} , L_{bulge} , and the stellar velocity dispersion, σ_* , offer such a check.

*The correlation is with *bulge* luminosity (Kormendy et al. 2011), but the L_{host} measured by Zasov & Dibai (1970) would have been dominated by L_{bulge} .

3 The $M_{\bullet} - L_{host}$ relationship for AGNs

Bentz et al. (2009) have presented host galaxy bulge luminosities for most of the AGNs with high-quality reverberation mapping mass estimates. Fig. 2a shows the host luminosities compared with masses estimated from $\text{FWHM}^2 L^{0.5}$. Fig. 2b shows the $M_{\bullet} - L_{bulge}$ relationship when the masses are estimated using Eq. 1 of Gaskell (2010a). As is expected from Fig. 1, the scatter in the $M_{\bullet} - L_{bulge}$ relationship is reduced. The interesting thing is that *it is only the scatter at the high-mass end that is reduced*.

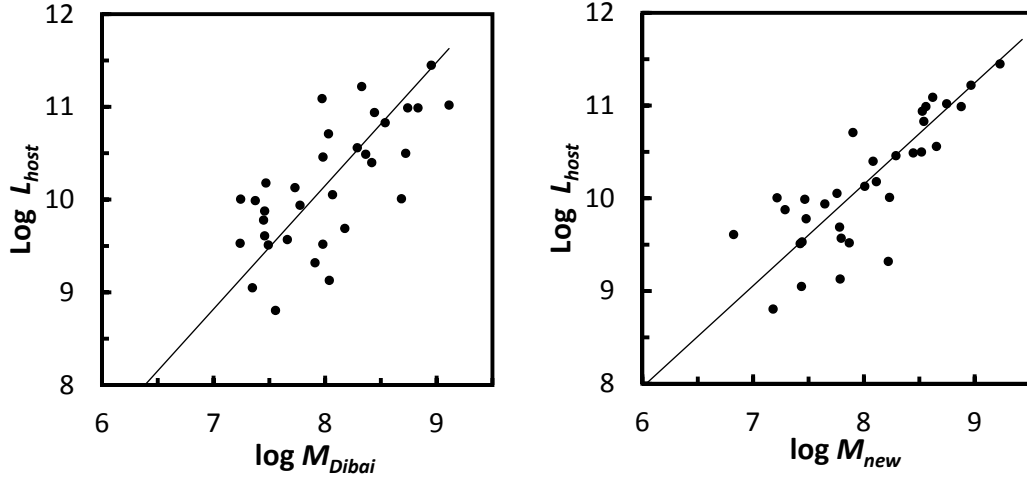


Fig. 2. The improvement in the AGN $M_{\bullet} - L_{host}$ relationship when going from using the standard $M_{Dibai} \propto \text{FWHM}^2 L^{0.5}$ masses (left) to the masses, M_{new} , of Gaskell (2010a) (right).

Fig. 3a shows the comparison of residuals from the $M_{\bullet} - L_{bulge}$ and $M_{\bullet} - \sigma_*$ relationships for the AGNs with σ_* available. The first thing to note is that the scatter in both axes is comparable. Given that the excitement over the discovery of the $M_{\bullet} - \sigma_*$ relationship was that it was supposed to be significantly tighter than the $M_{\bullet} - L_{bulge}$ relationship (see Fig. 2 of Gebhardt et al. 2000), this is perhaps surprising, but making a similar plot for the compilation of non-BLR mass determinations in Gültekin et al. (2009) (see Fig. 3b) shows that non-BLR galaxies now have comparable scatter about the $M_{\bullet} - L_{bulge}$ and $M_{\bullet} - \sigma_*$ relationships too.

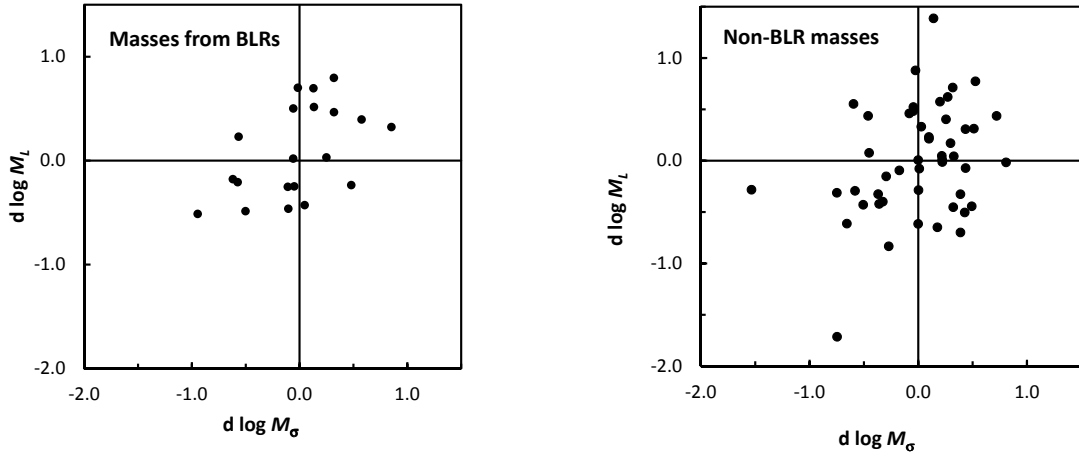


Fig. 3. $d \log M_L$, the residuals from the $M_{\bullet} - L_{bulge}$ relationship, versus $d \log M_{\sigma}$, the residuals from the $M_{\bullet} - \sigma_*$ relationships. The left frame is for the M_{new} estimates for the AGNs discussed here and the right frame shows data from Gültekin et al. (2009).

Since M_{\bullet} appears on both axes in Fig. 3, if there are large errors in the mass determinations they will introduce a direct correlation into the residuals. No strong correlations can be seen. The slight elongation in Fig. 3a corresponds to possible scatter in M_{new} of about 0.28 dex.

In Fig. 2b it can be seen that the scatter in the $M_{\bullet} - L_{bulge}$ relationship declines with increasing mass. Fig. 4 shows the scatter in the $M_{\bullet} - L_{host}$ relationship as a function of L_{host} .

There are several conclusions that can be drawn from Fig. 4.

1. The scatter for the highest luminosity bin (± 0.14 dex) is remarkably small. It is comparable to the Denney et al. (2009) estimate of the measuring error. This thus provides good support for the accuracy of the approach proposed in Gaskell (2010a).
2. Since the M_{new} determinations seem accurate, the substantial scatter at low luminosities must be *intrinsic*.

It is possible that there is some unknown additional source of error causing the increase in dispersion in Fig. 4 at low masses, but a similar trend has already been reported for a different sample for the dispersion in the $M_{\bullet} - \sigma_{*}$ relationship (Gaskell 2009a). Furthermore, the wide dispersion in M_{\bullet} found from highly-accurate maser measurements of yet another sample (Greene et al. 2010) provides additional strong independent support for the large increase in scatter in M_{\bullet}/L_{host} at low masses being real.

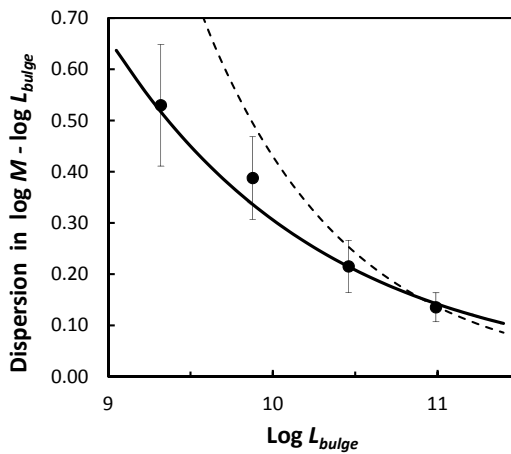


Fig. 4. The scatter in the AGN $M_{\bullet} - L_{host}$ relationship as a function of bulge luminosity. The AGNs have been divided equally into four L_{host} bins. The dotted line shows the expected $n^{-1/2}$ reduction in the scatter if a galaxy forms as a result of mergers of n units with Gaussian distributions of M_{\bullet} and L_{stars} . The solid line shows the result of simulations using a log-normal initial distribution of black hole mass to stellar mass ratio. (Figure adapted from Gaskell 2010a)

4 The origin of $M_{\bullet} - L_{host}$ relationship

It has long been recognized that mergers will influence correlations between M_{\bullet} and bulge properties. For example, Haehnelt & Kauffmann (2000) pointed out that mergers move galaxies along the bulge/SMBH scaling relationships. Peng (2007) discussed how mergers might affect the bulge/SMBH scaling relationships and made the important point that SMBH–bulge scaling relationships will emerge, independent of the initial conditions and detailed physics, simply because of averaging and that “random merging of galaxies that harbor random black hole masses tends to strengthen rather than weaken a preexisting, linear, correlation.” Gaskell (2010c) provided the first observational evidence that merging alone is indeed the origin of the $M_{\bullet} - L_{host}$ relationship and further proposed that a preexisting correlation is neither necessary nor desirable. If we assume that initially M_{\bullet} and the stellar luminosity of each galactic building block have independent normal distributions, then, if we merge n building blocks, L_{bulge} is proportional to n and the scatter in the M_{\bullet}/M_{bulge} ratio goes down as $n^{-1/2} = L_{bulge}^{-1/2}$. This is shown in Fig. 4 as the dotted line. This is probably too steep a decrease in the scatter.[†] However, a $n^{-1/2}$ decrease is only true for a normal distribution of initial values of M_{\bullet} and stellar luminosity. The actual distributions are almost certainly highly non-Gaussian. Simulations were therefore run starting with a more likely log–normal distribution. These gives the solid curve in Fig. 4.

Several important conclusions follow from these results:

[†]I say “probably” because the right-most point must be somewhat too high because of measuring error, and selection effects (not observing very weak AGNs with small SMBHs) could well be lowering the dispersion at low luminosities.

1. The M_{\bullet} measurements *require* a large scatter in M_{\bullet}/L_{stars} in the initial merging units — a scatter greater than that for the least massive galaxies in the sample, where the $\pm 2\sigma$ scatter is already a factor of ~ 300 .
2. Because of this, detectable SMBHs in *Sc/Sd* galaxies are going to be rare.
3. Intermediate mass black holes (IMBHs) in globular clusters will also be very rare.
4. As pointed out in Gaskell (2010c), the huge scatter in M_{\bullet}/L_{stars} in the initial merging units *excludes* fine-tuning of M_{\bullet} or L_{bulge} or else the subsequent scatter in larger galaxies would be much lower than observed.
5. Fine-tuning via AGN feedback that significantly reduces scatter at any subsequent stage is also excluded. This is not saying, of course, that an AGN has zero effect on its host galaxy — only that it does not *significantly* affect SMBH–bulge relationships.
6. The averaging due to mergers will only produce an SMBH–bulge relationship in *classical bulges* — not in pseudo-bulges which grow through secular processes. This has indeed been found to be the case (Kormendy et al. 2011).
7. The model explains why M_{\bullet} is systematically higher at a given σ_* in classical bulges than in pseudo bulges (Graham 2008; Hu 2008; Graham et al. 2011), because, in classical bulges, M_{\bullet} is dominated by the highest M_{\bullet} in last merger.

The simulations discussed in Gaskell (2010c) and here are purely for “dry” mergers (those without star formation), but SMBHs certainly grow through the accretion of gas as do the stellar populations of galaxies. I believe that including star-forming “wet” mergers will not substantially alter the conclusions for two reasons: firstly, at the high-mass end we are dealing with galaxies becoming “red and dead”. Mergers between them will effectively be dry. The second reason why wet mergers will not have a large effect on Fig. 4 is that they are most important at the low mass end where the scatter is already large. There are two main possibilities here: either the stellar population and the SMBH grow roughly proportionately or they do not. The former gives the same result as dry mergers, while the latter can increase the dispersion in the M_{\bullet}/L_{stars} ratio. However, as mentioned, this dispersion is already very large, so the effect on Fig. 4 will be negligible. Jahnke & Macciò (2011) have recently performed more elaborate simulations including prescriptions for star formation, black hole growth, and disk-to-bulge conversion, and they have affirmed the conclusions of Gaskell (2010c).

5 Conclusions

A slight modification to the Dibai method seems to significantly increase the accuracy of BH mass estimates. Using these new mass estimates the scatters about the $M_{\bullet} - L_{bulge}$ and $M_{\bullet} - \sigma_*$ relationships are comparable (contrary to what was thought when the $M_{\bullet} - \sigma_*$ relationship was discovered). These mass estimates imply that there is a strong decrease in the dispersion of the $M_{\bullet} - L_{host}$ relationship for higher mass black holes and hosts. This is qualitatively consistent with the BH–bulge relationships being *solely a consequence of mergers and not having an underlying physical cause*. The dispersion at the low mass end is too high to allow any significant causal relationship between black hole and bulge masses.

I am grateful to John Kormendy and Jenny Greene for useful discussions. This research has been supported by US National Science Foundation grants AST 03-07912 and AST 08-03883, NASA grant NNH-08CC03C, and grant 32070017 of the GEMINI-CONICYT Fund.

References

- Antonucci, R. 1993, *ARA&A*, 31, 473
 Antonucci, R., 2011, *Astron. & Astrophys. Transactions*, in press. [arXiv:1101.0837]
 Bentz, M. C., Peterson, B. M., Pogge, R. W., & Vestergaard, M. 2009, *ApJ. Lett.*, 694, L166
 Bochkarev, N. G., & Gaskell, C. M. 2009, *Ast. Lett.*, 35, 287
 Cherepashchuk, A. M., & Lyutyi, V. M. 1973, *Ap. Lett.*, 13, 165
 Denney, K. D., Peterson, B. M., Dietrich, M., Vestergaard, M., & Bentz, M. C. 2009, *ApJ*, 692, 246
 Dibai, É. A. 1977, *Soviet Astron. Lett.*, 3, 1

- Gaskell, C. M. 1988, *ApJ*, 325, 114
- Gaskell, C. M. 2009a, *ApJ*, submitted [arXiv:0908.0328]
- Gaskell, C. M. 2009b, *New Ast. Rev.*, 53, 140
- Gaskell, C. M. 2010a, *IAU Symp.*, 267, 203
- Gaskell, C. M. 2010b, *ApJ*, submitted [arXiv:1008.1057]
- Gaskell, C. M. 2010c, *Am. Inst. Phys. Conf. Ser.*, 1294, 261
- Gaskell, C. M. & Sparke, L. S. 1986, *ApJ*, 305, 175
- Gebhardt, K., et al. 2000, *ApJ. Lett.*, 539, L13
- Graham, A. W. 2008, *ApJ*, 680, 143
- Graham, A. W., Onken, C. A., Athanassoula, E., & Combes, F. 2011, *MNRAS*, 412, 2211
- Greene, J. E., Peng, C. Y., Kim, M., et al. 2010, *ApJ*, 721, 26
- Gültekin, K., et al. 2009, *ApJ*, 698, 198
- Haehnelt, M. G., & Kauffmann, G. 2000, *MNRAS*, 318, L35
- Hu J., 2008, *MNRAS*, 386, 2242
- Jahnke, K., & Macciò, A. V. 2011, *ApJ*, 734, 92
- Kormendy, J. 1994 in *The Nuclei of Normal Galaxies: Lessons from the Galactic Center*, eds. R. Genzel & A. I. Harris (Dordrech: Kluwer Academic Publishers), p. 379
- Kormendy, J., Bender, R., & Cornell, M. E. 2011, *Nature*, 469, 374
- Lyu'tyi, V. M., & Cherepashchuk, A. M. 1972, *Astron. Tsirk.*, 688, 1
- Magorrian, J. et al. 1998, *AJ*, 115, 2285
- Marziani, P., & Sulentic, J. W. 2011, *New Ast. Rev.* in press [arXiv:1108.5102]
- Peng, C.-Y. 2007, *ApJ*, 671, 1098
- Vestergaard, M., & Peterson, B. M. 2006, *ApJ*, 641, 689
- Zasov, A. V. & Dibai, E. A. 1970, *Soviet Ast.*, 14, 17

MODELING X-RAY POLARIMETRY WHILE FLYING AROUND THE MISALIGNED OUTFLOW OF NGC 1068

R. W. Goosmann¹ and G. Matt²

Abstract. In contrast to the standard unified model, the ionized outflow in the nucleus of the Seyfert-2 galaxy NGC 1068 is claimed to be tilted with respect to the symmetry axis of the dusty torus. We compute the broad-band X-ray spectrum and polarization emerging from multiple reprocessing in an asymmetric model setup of NGC 1068. Considering different azimuthal viewing directions, we show that the slope of the polarization angle between the soft X-ray and the hard X-ray bands allows us to distinguish a clock-wise from a counter clock-wise tilt of the wind with respect to the torus axis. We also find that equatorial scattering in the outer accretion flow has a minor impact on the X-ray polarization of typical Seyfert-2 nuclei.

Keywords: Galaxies: active, Galaxies: Seyfert, Galaxies: individual: NGC 1068, Radiative transfer, Polarization, Scattering

1 Introduction

Accreting supermassive black holes in thermal active galactic nuclei (AGN) are known to redirect a large fraction of the accretion flow into strong outflows. Neither the ejection mechanism nor the geometry of these winds are well-constrained yet. According to the unified scheme of AGN (Antonucci 1993) the wind in type-2 objects – those that do not show broad Balmer emission lines – should be seen from the side, in contrast to type-1 objects where the wind is observed in transmission. The standard unified model is assumed to be axis-symmetric, but there has been a recent claim by Raban et al. (2009) that the ionized wind in the well-studied Seyfert-2 galaxy NGC 1068 is misaligned with respect to the axis of the dusty torus and the accretion disk.

Raban et al. (2009) infer the ejection direction of the outflow in NGC 1068 somewhat indirectly; the authors implicitly assume that the more distant narrow line region is aligned with the wind base situated much closer to the black hole. In Goosmann & Matt (2011) we present a model of the expected X-ray polarization of NGC 1068 and we argue that a soft X-ray polarization measurement would unambiguously constrain the flow direction (projected on the plane of the sky) at the wind base. We further show how the tilting angle of the wind with respect to the torus axis can be constrained by broad-band X-ray polarimetry.

So far, we have only presented spectra and polarization properties at one azimuthal viewing angle. In this note, we therefore consider a more general viewing direction toward the asymmetric model setup of NGC 1068.

2 Modeling results for different azimuthal viewing directions

Our modeling is carried out using the latest version of the radiative transfer code STOKES. The code and the model are described in more detail in Goosmann & Matt (2011) and we summarize the setup in Fig. 1 and the parameters in Table 1. The model comprises an irradiated accretion disk, a dusty torus and a bi-conical outflow with an angular offset of 18° with respect to the torus axis. We investigate two cases that either include an equatorial scattering disk (model B) or not (model A). A primary spectrum with a power-law shape $F_E \propto E^{-\alpha}$ and $\alpha = 1$ is assumed. The spectrum cuts off at 1 keV and 100 keV. We introduce a Cartesian coordinate system with the z -axis being the common symmetry axis of the torus and the accretion disk. All reprocessing

¹ Observatoire astronomique de Strasbourg, Section Hautes Energies, 11 Rue de l'Université, 67000 Strasbourg, France

² Dipartimento di Fisica, Università degli Studi Roma Tre, Via della Vasca Navale 84, I-00146 Roma, Italy

irradiated accretion disk	dusty torus	bi-conical, polar outflow	flared disk
on-axis source at height 0.0001 pc $R_{\text{disk}} = 0.0004$ pc $h_{\text{disk}} = 3.25 \times 10^{-7}$ pc vertical opt. depth > 600 neutral reprocessing	$R_{\text{min}} = 0.1$ pc $R_{\text{max}} = 0.5$ pc half-open. ang. = 60° equat. opt. depth = 750 neutral reprocessing	$R_{\text{min}} = 0.3$ pc $R_{\text{max}} = 1.8$ pc half-open. ang. = 40° , tilted by 18° radial opt. depth = 0.3 electron scattering	$R_{\text{min}} = 0.02$ pc $R_{\text{max}} = 0.04$ pc half-open. ang. = 20° radial opt. depth = 1 electron scattering

Table 1. Parameters of the model components. The primary X-ray source subtends a half-angle of $\sim 75^\circ$ with the disk. For the polar outflow, the half-opening angle is measured with respect to its symmetry axis, while for the flared disk the half-opening angle is taken with respect to the equatorial plane. Model B includes the flared disk, model A does not.

regions are centered on the coordinate origin and the wind axis is tilted inside the yz -plane leaning towards the positive y -axis. The observer's inclination and the tilting angle of the outflow are measured from the z -axis. The azimuthal viewing angle, ϕ , is taken inside the xy -plane with respect to the negative y -axis. In Goosmann & Matt (2011), ϕ was set to $\sim 90^\circ$, which corresponds to the view shown in Fig. 1.

The results for the models A and B are shown in Figs. 2 and 3. The inclination $i \sim 18^\circ$ features a type-1 object, at $i \sim 63^\circ$ the line-of-sight lies just below the torus horizon, while $i \sim 76^\circ$ and $i \sim 87^\circ$ represent type-2 objects. We cover half a round in azimuth at $\phi = 35^\circ$, $\phi = 80^\circ$, $\phi = 125^\circ$, and $\phi = 170^\circ$; we extend the results to a full round for the polarization angle ψ . For $\psi = 0^\circ$, the polarization is perpendicular to the z -axis; it rotates clock-wise with rising ψ until it is aligned with the projected z -axis at $\psi = 90^\circ$.

The spectral flux does not depend strongly on ϕ , which is due to the system's still limited divergence from axis-symmetry. But the polarization below 10 keV is very sensitive to scattering in the tilted outflow and ψ shows a systematic behavior as one goes around in azimuth. At an extreme type-2 view, the soft X-ray polarization is strictly perpendicular to the projected wind axis (at the type-1 inclination, the polarization partly is very low and the Monte Carlo results suffer a bit from insufficient statistics).

Above 10 keV, Compton scattering in the dusty torus and the accretion disk competes with the electron scattering in the wind. The polarization angle shows some dependency on this competition around 30 keV. Note that when comparing ψ at azimuthal viewing angles that are symmetric with respect to the yz -plane one can derive in which direction the wind is leaning: if it is rotated clock-wise (counter clock-wise) with respect to the z -axis, the polarization angle increases (decreases) with photon energy (this relation inverts should ψ be defined in the opposite direction).

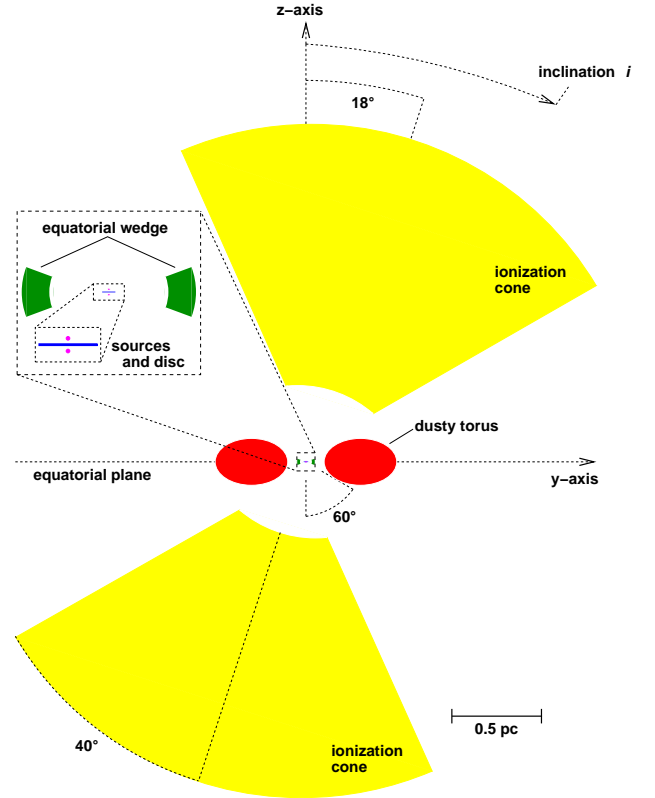


Fig. 1. Edge-on view ($i = 90^\circ$) of our model setup at the azimuthal viewing angle $\phi = 90^\circ$ (see Goosmann & Matt 2011, for more details).

The equatorial scattering disk has a significant impact on the X-ray polarization only at type-1 viewing angles. Since the equatorial scattering modifies the irradiation pattern of the inner torus surfaces, one could suspect that the hard X-ray polarization at type-2 viewing angles should be different when the flared disk is included. Careful comparison between model A and model B shows that there are indeed minor shifts in the polarization spectra at type-2 view; but the effect turns out to be rather weak. At type-1 view or at the limit of a type-1/type-2 view, the flared disk produces strong polarization at a different polarization angle than the outflow. This is visible in both polarization features (percentage and position angle). Note that the presence of the flared disk also increases the total soft X-ray flux by scattering primary photons into the line-of-sight.

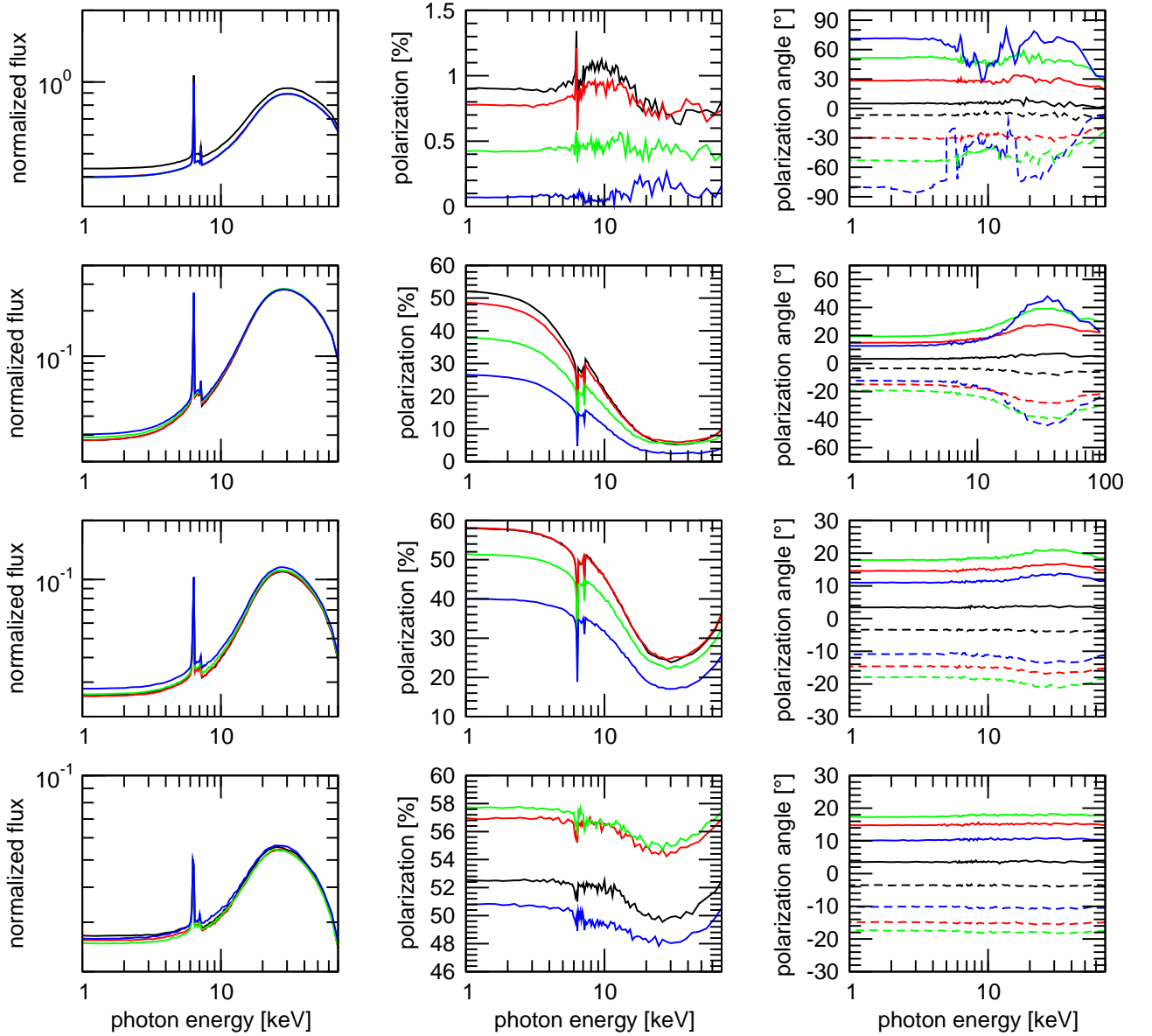


Fig. 2. Results for Model A (no equatorial scattering disk). From top to bottom the panels represent the inclinations $i \sim 18^\circ$, $i \sim 63^\circ$, $i \sim 76^\circ$, and $i \sim 87^\circ$. We plot the spectral flux (left), the polarization percentage (middle), and the polarization angle ψ (right) at four azimuthal angles (half a round) measured from the negative y -axis: $\phi = 35^\circ$ (blue), $\phi = 80^\circ$ (green), $\phi = 125^\circ$ (red), and $\phi = 170^\circ$ (black). The spectral flux is always normalized to the source flux emitted into the same line-of-sight. The polarization angle ψ is shown also for the symmetric azimuth $\phi' = -\phi$ (dashed lines). For $\psi = 0^\circ$, the polarization is perpendicular to the z -axis; it rotates clock-wise with rising ψ .

3 Summary and conclusions

We have added new results to our previous modeling of the X-ray polarization induced by complex reprocessing in NGC 1068. Presuming that the double-conical outflow is tilted with respect to the symmetry axis of the dusty torus, we explore the polarization results at different azimuthal viewing angles and inclinations of the observer; it turns out that in particular the behavior of the polarization position angle as a function of photon energy can help to determine the viewing direction towards the asymmetric model. However, this rather requires broad-band polarimetry capability, which is already technically feasible (Tagliaferri et al. 2011) and hopefully will be included in a future X-ray mission.

An equatorial scattering region situated between the accretion disk and the inner edge of the dusty torus has

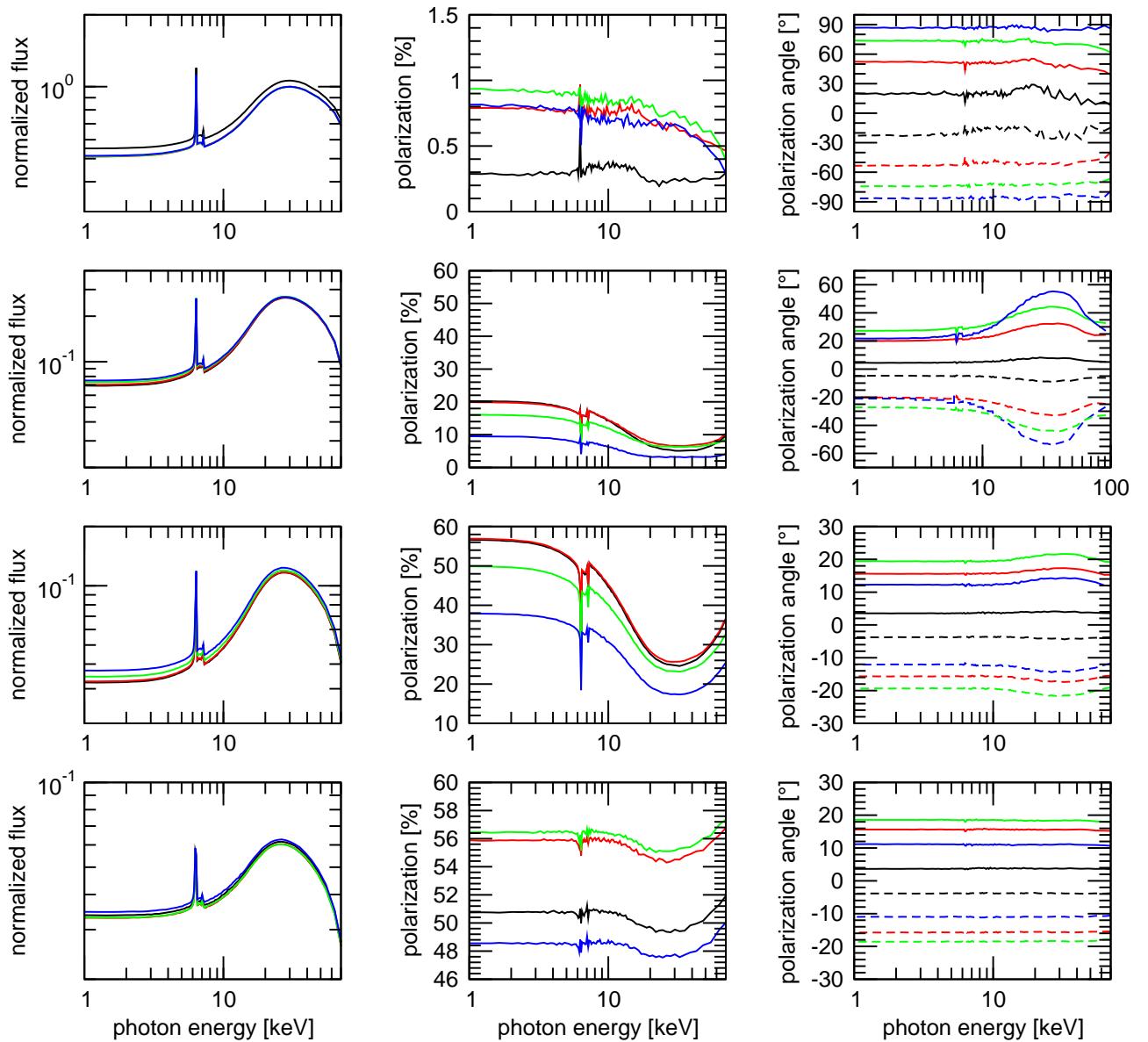


Fig. 3. The same denominations as for Fig. 2, but for model B that includes scattering inside an equatorial, flared disk.

an impact in particular at type-1 or limiting type-1/type-2 viewing angles. The equatorial scattering increases the total soft X-ray flux and modifies the polarization in competition with other reprocessing regions. At type-2 viewing angles, the effect of equatorial scattering is minor. The soft X-ray polarization of X-ray bright AGN can soon be probed with the *NASA* GEMS mission (Kallman et al. 2010) to be launched in 2014.

We are grateful to the French *GdR* PCHE for supporting this research.

References

- Antonucci, R. 1993, *ARA&A*, 31, 473
 Goosmann, R. W. & Matt, G. 2011, *MNRAS*, 415, 3119
 Kallman, T. R., Swank, J. H., & GEMS Team. 2010, in *Bulletin of the American Astronomical Society*, Vol. 42, AAS/High Energy Astrophysics Division #11, 737+
 Raban, D., Jaffe, W., Röttgering, H., Meisenheimer, K., & Tristram, K. R. W. 2009, *MNRAS*, 394, 1325
 Tagliaferri, G., Hornstrup, A., Huovelin, J., et al. 2011, *Experimental Astronomy*, 37

FERMI LARGE AREA TELESCOPE OBSERVATIONS OF GAMMA-RAY PULSARS

L. Guillemot¹, the Fermi LAT Collaboration, the LAT Pulsar Timing Consortium and the LAT Pulsar Search Consortium

Abstract. Since Fermi was launched in June 2008, its main instrument, the Large Area Telescope (LAT), has observed the gamma-ray sky with unprecedented sensitivity, establishing pulsars as the largest gamma-ray source class in the Galaxy and enabling a considerable advance in our understanding of their high-energy emission properties. The number of known gamma-ray pulsars is approaching a hundred, including pulsars discovered in blind searches of the Fermi LAT data, and a population of gamma-ray millisecond pulsars. Supporting radio observations have been key to the success of pulsar studies with Fermi. As an example, searches for radio pulsars in Fermi sources with no known counterparts yielded a burst of discoveries of new millisecond pulsars, with more than thirty detections of these particularly interesting objects to date. We review Fermi LAT observations of gamma-ray pulsars and the multi-wavelength follow-up of pulsars discovered in Fermi unidentified sources.

Keywords: gamma rays: general, pulsars: general

1 Introduction

The Large Area Telescope (LAT), is the primary instrument on the *Fermi* observatory launched on 11 June 2008, is a pair conversion telescope sensitive to gamma-ray photons with energies between 20 MeV and more than 300 GeV. With its large field of view > 2 sr, large effective collecting area of ~ 6500 cm² at 1 GeV and normal incidence, and improved angular resolution of 0.8° at 1 GeV, the LAT represents a major improvement compared to previous gamma-ray observatories, such as EGRET. Moreover, gamma-ray photons are time-stamped with an accuracy better than $1 \mu\text{s}$, so that it can observe sharp structures in gamma-ray pulse profiles of pulsars accumulated over several years. Finally, *Fermi* operates in survey mode, allowing the LAT to cover the sky uniformly and detect many previously unknown sources. A detailed description of the LAT and of its performances can be found in Atwood et al. (2009) and Abdo et al. (2009a). Gamma-ray pulsations have been firmly detected for 88 pulsars so far, and this number is expected to increase as the *Fermi* mission continues. In this paper we summarize the results of pulsar observations with the LAT during its first two and a half years of activity and the results of searches for new pulsars in gamma-ray sources with no known associations. We finally discuss the prospects for the coming years.

2 Fermi LAT observations of pulsars

2.1 Known pulsars

Seven pulsars had been detected in gamma rays with high significance by EGRET and COMPTEL on the CGRO observatory (see Thompson 2004, for a review) before *Fermi* and AGILE were launched, plus another few marginal detections, including that of the millisecond pulsar (MSP) PSR J0218+4232 (Kuiper et al. 2000). All seven pulsars had been detected as sources of pulsed gamma-ray emission by phase-folding the photon arrival times using pulsar “ephemerides” (giving astrometric, rotational and binary parameters as a function of time) obtained from radio and X-ray pulsar timing measurements. A pulsar timing campaign involving several large radio telescopes around the world as well as X-ray telescopes has therefore been organized in the context of the *Fermi* mission, to monitor the best candidates for detection in gamma rays on a regular basis (see Smith

¹ Max-Planck-Institut für Radioastronomie, Auf dem Hügel 69, D-53121, Germany

et al. 2008). While the initial list of pulsars to be observed in radio and X-rays for *Fermi* comprised 224 pulsars with spin-down luminosities $\dot{E} = 4\pi^2 I \dot{P} / P^3 \geq 10^{34} \text{ erg s}^{-1}$ (where P denotes the rotational period, \dot{P} its time derivative, and I is the moment of inertia of the neutron star, typically assumed to be $10^{45} \text{ g cm}^{-2}$), more than 700 objects with a wide range of properties are now monitored, allowing the *Fermi* LAT to study the gamma-ray properties of a wide variety of pulsars.

Because of their brightness, pulsars detected in gamma rays before the launch of *Fermi* were prime targets for studies with unprecedented details with the LAT. Observations of the brightest steady gamma-ray source in the sky, the Vela pulsar, resulted in the discovery of a third component between the two main peaks, shifting to larger rotational phases with increasing energy (Abdo et al. 2009d, 2010a). Detailed phase-resolved spectroscopy revealed important variations of the spectral properties (photon index and exponential cutoff energy) across the pulse profile. Complex behaviors of the spectral properties as a function of rotational phase have also been observed for the other EGRET pulsars (see Abdo et al. 2010d,f), giving us an insight into gamma-ray emission mechanisms in pulsar magnetospheres.

Pulsed gamma-ray emission has also been detected for 27 other known “normal pulsars” (with rotational periods P of more than a few tens of ms) and 27 MSPs ($P < 30$ ms), including many MSPs that were discovered in *Fermi* unassociated sources (see Section 2.3), in two and a half years of data taking (see for example Abdo et al. 2009c, 2010c). The gamma-ray spectra of pulsars from both populations are well fit with exponentially cutoff power laws with typical cutoff energies in the GeV range. As is observed for EGRET pulsars, the gamma-ray pulse profiles of these pulsars is typically composed of two sharp peaks separated by 0.4 to 0.5 rotations, with the first gamma-ray peak lagging the main radio emission component by 0.1 – 0.2 rotations, or one broad gamma-ray peak offset from the main radio peak by $\sim 0.4 - 0.6$ rotations. Exceptions to this trend exist, in particular for gamma-ray MSPs: the MSP PSR J1231–1411 shows three gamma-ray peaks (Ransom et al. 2011), and radio and gamma-ray peaks in close alignment have been observed for a small population of MSPs (Abdo et al. 2010b; Guillemot et al. 2011). For both pulsar populations, light curve and spectral shapes match well the predictions of models placing the high-energy emission at high altitude in the magnetosphere, such as the *Two Pole Caustic* (TPC) Dyks & Rudak (2003) or *Outer Gap* (OG) models Cheng et al. (1986).

2.2 Searching for new pulsars in the LAT data

Blind searches of the gamma-ray data are necessary for finding gamma-ray pulsars that are very faint or quiet in the radio and X-ray domains. Attempts to discover pulsars in the data recorded by EGRET by means of blind searches were unsuccessful (see e.g. Chandler et al. 2001), mainly because of the sparseness of the data and because of the irregularities in the rotation of pulsars as a function of time (the “timing noise”). In spite of the large leap in sensitivity compared to EGRET, the LAT data are still sparse; with a few hundreds of photons recorded over several months for a typical gamma-ray pulsar. Long integration times are required to detect gamma-ray pulsations with high significance, which makes traditional Fourier methods time- and computer-intensive. The “time-differencing technique” (Atwood et al. 2006) was developed to address this problem. With this technique, pulsations are searched in the differences between arrival times, which reduces the computational cost dramatically. This technique has proven to be very efficient, with the discovery of 27 new pulsars so far Abdo et al. (2009b); Saz Parkinson et al. (2010).

Many of the gamma-ray pulsars discovered in blind searches of the LAT data are associated with previously unidentified EGRET sources. Several are associated with supernova remnants or pulsar wind nebulae. Their gamma-ray properties (light curves and spectra) are similar to those of other gamma-ray pulsars, however their discovery provides the opportunity to constrain the ratio of radio-loud to radio-quiet pulsars, which is an important discriminator of theoretical models of emission from pulsars. Searches for pulsed radio signal from the LAT-discovered pulsars have been conducted at several large radio telescopes around the world and resulted in only three detections up to now, with very low radio fluxes (Abdo et al. 2010e; Camilo et al. 2009). The small number of radio detections reported so far indicates that many of the new gamma-ray pulsars could be truly radio-quiet.

2.3 New millisecond pulsars found in Fermi LAT sources

The Second *Fermi* LAT catalog (2FGL; Abdo et al. 2011) contains 1873 sources detected by the LAT over 24 months between 100 MeV and 100 GeV. In these 1873 sources, 576 ($\sim 30\%$) are “unassociated”: they are not associated with sources known at other wavelengths. Some of these unassociated sources exhibit gamma-ray emission properties that resemble those of known gamma-ray pulsars: lack of flux variability and spectra with

sharp cutoffs at 1 – 10 GeV, and could thus hide unknown radio and gamma-ray pulsars that could have been missed by past surveys for pulsars for different reasons (sensitivity, binary motion, dispersion and scintillation, insufficient sky coverage, *etc.*). Searches for radio pulsars at the positions of EGRET sources were challenging, as the EGRET error boxes were several times larger than typical radio telescope beams, so that many radio pointings were necessary to cover the gamma-ray sources entirely (see e.g. Champion et al. 2005). In contrast, gamma-ray sources are typically localized to within a few arc minutes, which is comparable in size to radio telescope beams. Because of this dramatic enhancement in localization accuracy, *Fermi* can “point” radio telescopes to unknown pulsars, and 33 Galactic disk MSPs have so far been discovered at the positions of LAT unassociated sources, at the Parkes, Nançay, Effelsberg, Green Bank and GMRT telescopes (Cognard et al. 2011; Keith et al. 2011; Ransom et al. 2011). Figure 1 shows the locations of the new MSPs. These > 30 new MSP detections represent a significant increase in the number of known Galactic disk MSPs (~ 70 objects known prior to *Fermi*), which opens important prospects for a number of studies involving MSPs, including searches for gravitational waves with millisecond pulsar timing, neutron star mass measurements, tests of theories of gravity, pulsar formation and evolutions scenarios, and many other areas. As the LAT continues to accumulate data, it will detect additional gamma-ray sources with no known associations, while further improving the localization of the sources that are already detected. In addition, no strong correlation between the radio and gamma-ray fluxes of pulsars discovered in LAT unassociated sources has been observed. It is thus expected that *Fermi* will continue to point radio telescopes to new radio pulsars.

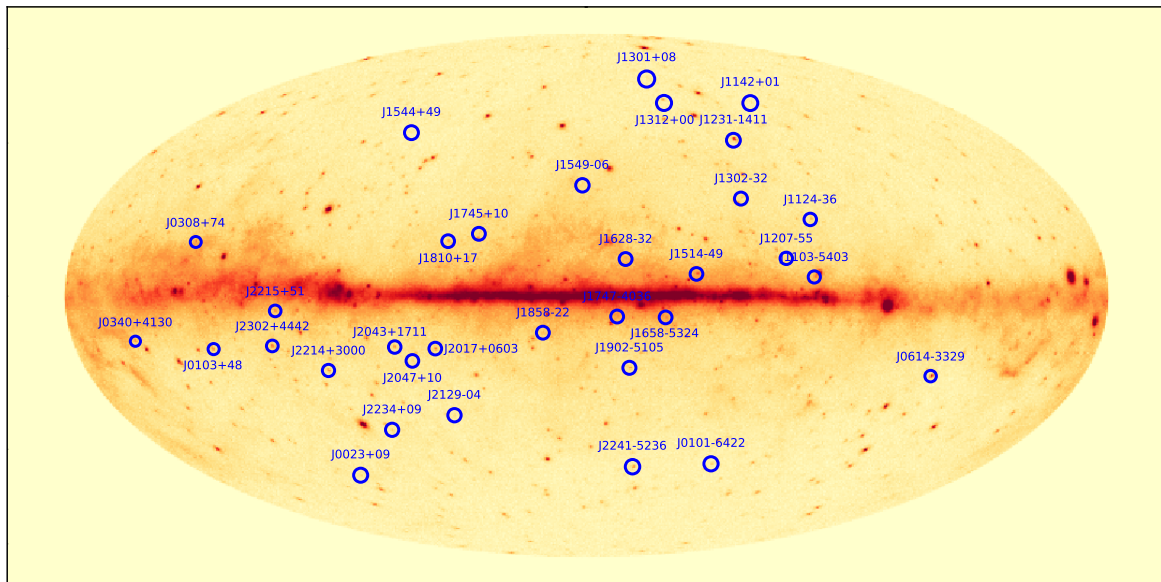


Fig. 1. Sky map of the gamma-ray data taken by the *Fermi* LAT during its first two years of operation and above 0.1 GeV, in Galactic coordinates. Blue circles indicate the 33 new MSPs discovered at radio wavelengths at the position of LAT sources with no known association, as of June 2011. *Credit: Paul S. Ray.*

2.4 Which pulsars are we seeing?

Figure 2 shows the classical period (P) – period derivative (\dot{P}) diagram with the ~ 2000 currently known pulsars. Pulsars detected in gamma rays with the *Fermi* LAT are shown as colored symbols. As can be seen from Figure 2, pulsars detected in gamma rays tend to have the largest values of the spin-down luminosity \dot{E} . Nevertheless, a number of high \dot{E} pulsars have not been detected in gamma rays with the LAT, which could be due to several reasons. The pulsars may simply be faint or too distant, so that additional LAT data is required to detect them. Emission geometry is also a possibility: some pulsars with large \dot{E} values may be bright gamma-ray pulsars, with beams that do not point toward the Earth. Detailed geometrical studies of individual objects, helped by radio polarization measurements giving access to pulsar orientation angles (angle between the rotation axis and

the magnetic axis of the pulsar, α , and between the rotation axis and the observer's line-of-sight, ζ) might help understand the causes of non-detection.

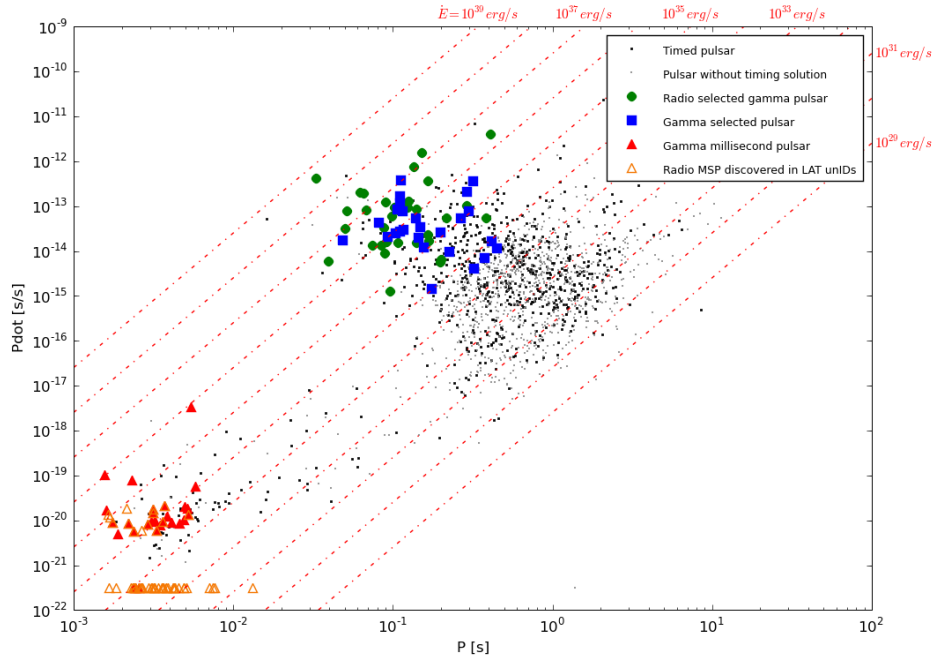


Fig. 2. Period – period derivative diagram for the ~ 2000 currently known pulsars. Red triangles and green circles indicate millisecond and normal pulsars so far detected with the *Fermi* LAT using radio ephemerides, while pulsars discovered in a blind search of the LAT data are shown as blue squares. The new MSPs discovered at radio wavelengths in LAT unassociated sources are indicated by empty triangles. For several of these new objects the period derivative is currently unknown; for these pulsars \dot{P} was set to $10^{-21.5}$ in this diagram. *Credit: Denis Dumora and David A. Smith.*

3 Conclusions and prospects

Two and a half years after *Fermi* was launched, the LAT has detected pulsed gamma-ray emission from 88 pulsars, including normal pulsars and MSPs detected by phase-folding the data with radio or X-ray ephemerides, and normal pulsars discovered in the LAT data with blind search techniques. Many radio MSPs have been discovered in *Fermi* unassociated sources, opening prospects for a wide range of physics and astrophysics. In the next few years the LAT will continue to accumulate gamma-ray data, so that the number of known gamma-ray pulsars will soon reach the symbolic threshold of 100 objects, a major step forward in pulsar astronomy and high-energy astrophysics.

Important questions concerning gamma-ray emission from pulsars remain to be answered. The relationship between the gamma-ray luminosity and the spin-down luminosity \dot{E} is badly known, in particular because of large uncertainties in the distances of many gamma-ray pulsars. VLBI parallax measurements for *Fermi* pulsars are being undertaken and will hopefully yield accurate distance measurements, which should help constrain the fraction of spin-down luminosity that is converted into gamma-ray emission. It is also important to understand the non-detection in gamma rays of some highly energetic pulsars. Another prospect for the coming years is the search for gamma-ray emission from other types of pulsars. Young binaries such as LS I +61 303 may hide gamma-ray pulsars that could be detected with blind search techniques. Also, some of the unassociated *Fermi* sources may be radio-quiet MSPs. Most MSPs ($\geq 75\%$) have binary orbits, making blind searches in the gamma-ray data very challenging. Nevertheless, extending blind searches of the LAT data to isolated MSPs may help uncover the hidden population of radio-quiet MSPs, which would improve our understanding of pulsar emission mechanisms.

The *Fermi* LAT Collaboration acknowledges support from a number of agencies and institutes for both development and the operation of the LAT as well as scientific data analysis. These include NASA and DOE in the United States, CEA/Irfu and IN2P3/CNRS in France, ASI and INFN in Italy, MEXT, KEK, and JAXA in Japan, and the K. A. Wallenberg Foundation, the Swedish Research Council and the National Space Board in Sweden. Additional support from INAF in Italy and CNES in France for science analysis during the operations phase is also gratefully acknowledged.

References

- Abdo, A. A., Ackermann, M., Ajello, M., et al. 2010a, *ApJ*, 713, 154
- Abdo, A. A., Ackermann, M., Ajello, M., et al. 2010b, *ApJ*, 712, 957
- Abdo, A. A., Ackermann, M., Ajello, M., et al. 2009a, *Astroparticle Physics*, 32, 193
- Abdo, A. A., Ackermann, M., Ajello, M., et al. 2009b, *Science*, 325, 840
- Abdo, A. A., Ackermann, M., Ajello, M., et al. 2009c, *Science*, 325, 848
- Abdo, A. A., Ackermann, M., Ajello, M., et al. 2010c, *ApJS*, 187, 460
- Abdo, A. A., Ackermann, M., Ajello, M., et al. 2010d, *ApJ*, 720, 272
- Abdo, A. A., Ackermann, M., Ajello, M., et al. 2010e, *ApJ*, 711, 64
- Abdo, A. A., Ackermann, M., Atwood, W. B., et al. 2009d, *ApJ*, 696, 1084
- Abdo, A. A., Ajello, M., Antolini, E., et al. 2010f, *ApJ*, 720, 26
- Abdo, A. A. et al. 2011, *ApJS* (submitted), astro-ph/1108.1435v1
- Atwood, W. B., Abdo, A. A., Ackermann, M., et al. 2009, *ApJ*, 697, 1071
- Atwood, W. B., Ziegler, M., Johnson, R. P., & Baughman, B. M. 2006, *ApJ*, 652, L49
- Camilo, F., Ray, P. S., Ransom, S. M., et al. 2009, *ApJ*, 705, 1
- Champion, D. J., McLaughlin, M. A., & Lorimer, D. R. 2005, *MNRAS*, 364, 1011
- Chandler, A. M., Koh, D. T., Lamb, R. C., et al. 2001, *ApJ*, 556, 59
- Cheng, K. S., Ho, C., & Ruderman, M. 1986, *ApJ*, 300, 500
- Cognard, I., Guillemot, L., Johnson, T. J., et al. 2011, *ApJ*, 732, 47
- Dyks, J. & Rudak, B. 2003, *ApJ*, 598, 1201
- Guillemot, L., Johnson, T. J., Venter, C., et al. 2011, *ApJ* (submitted)
- Keith, M. J., Johnston, S., Ray, P. S., et al. 2011, *MNRAS*, 414, 1292
- Kuiper, L., Hermsen, W., Verbunt, F., et al. 2000, *A&A*, 359, 615
- Ransom, S. M., Ray, P. S., Camilo, F., et al. 2011, *ApJ*, 727, L16
- Saz Parkinson, P. M., Dormody, M., Ziegler, M., et al. 2010, *ApJ*, 725, 571
- Smith, D. A., Guillemot, L., Camilo, F., et al. 2008, *A&A*, 492, 923
- Thompson, D. J. 2004, in *Astrophysics and Space Science Library*, Vol. 304, *Cosmic Gamma-Ray Sources*, ed. K. S. Cheng & G. E. Romero, 149–+

GRB LORENTZ FACTOR CONSTRAINTS IN THE FERMI-LAT ERA

R. Hascoët¹, F. Daigne^{1,2}, R. Mochkovitch¹ and V. Venmin¹

Abstract. Recent detections of GeV photons in a few GRBs by Fermi-LAT have led to strong constraints on the bulk Lorentz factor in GRB outflows. To avoid a large $\gamma\gamma$ optical depth, minimum values of the Lorentz factor have been estimated to be as high as 800-1200 in some bursts. Here we present a detailed calculation of the $\gamma\gamma$ optical depth taking into account both the geometry and the dynamics of the jet. In the framework of the internal shock model, we compute light curves in different energy bands and the corresponding spectrum and we show how the limits on the Lorentz factor can be significantly lowered compared to previous estimates.

Our detailed model of the propagation of high energy photons in GRB outflows is also appropriate to study many other consequences of $\gamma\gamma$ annihilation in GRBs: (i) the $\gamma\gamma$ cutoff transition in a time-integrated spectrum is expected to be closer to a power-law steepening of the spectrum than to a sharp exponential decay; (ii) the temporal evolution of the $\gamma\gamma$ opacity during a burst favors a delay between the MeV and GeV light curves; (iii) for complex GRBs, the $\gamma\gamma$ opacity suppress the shortest time-scale features in high energy light curves (above 100 MeV). Finally we also consider GRB scenarii where MeV and GeV photons are not produced at the same location, showing that the $\gamma\gamma$ opacity could be further lowered, reducing even more the constraint on the minimum Lorentz factor.

Keywords: gamma-ray bursts, GRB 080916C, radiative transfer, non thermal radiation mechanisms

1 Introduction

The compactness problem. The short time scales observed in GRBs (down to a few ms) can be used to deduce an upper limit on the size of the emitting region producing γ -rays. This information combined with the huge isotropic γ -ray luminosities deduced from the measured redshifts imply huge photon densities. Then the simplest assumption of an emission produced by a plasma radiating isotropically with no macroscopic motion predicts that γ -ray photons should not escape due to $\gamma\gamma$ annihilation $\gamma\gamma \rightarrow e^+e^-$. This is in contradiction with the observed GRB spectra which are non-thermal and extend well above the rest-mass electron energy $m_e c^2 \approx 511$ keV. Observation and theory can be reconciled by assuming that the emitting material is moving at ultra-relativistic velocities (Rees 1966). This is mainly due to the relativistic beaming. First the relativistic beaming implies that the observer will see only a small fraction of the emitting region: the constraint on the size of the emitting region is now less severe. Second, the collimation of photons in the same direction reduce the number of potential interactions. Finally the typical $\gamma\gamma$ interaction angle becoming small the photon energy threshold for pair production becomes higher. This theoretical context combined with the observational data gives the possibility to estimate a minimum Lorentz factor Γ_{\min} for the emitting outflow in GRBs (Lithwick & Sari 2001) or directly a Lorentz factor estimate if the $\gamma\gamma$ cutoff is clearly identified in the spectrum (see Ackermann et al. (2011)).

Severe constraints on the Lorentz factor from Fermi-LAT observations. Since the launch of Fermi in June 2008, the LAT instrument has detected high energy photons above 10 GeV in a few GRBs. The observed γ -ray spectrum often remains consistent with a Band function covering the GBM and LAT spectral ranges without any evidence of a high energy cutoff, that could be identified as a signature of $\gamma\gamma \rightarrow e^+e^-$. This

¹ UPMC Univ Paris 06, UMR 7095, Institut d'Astrophysique de Paris, F-75014, Paris, France
CNRS, UMR 7095, Institut d'Astrophysique de Paris, F-75014, Paris, France

² Institut Universitaire de France

extension by Fermi of the observed spectral range upper bound from 10 MeV (e.g. BATSE) to 10 GeV implies constraints on Γ_{\min} which are much more severe than the ones obtained previously. In a few cases Γ_{\min} has been estimated to be of the order of 1000 (for example: GRB 080916C – $\Gamma_{\min} = 887$ Abdo et al. (2009), GRB 090510 – $\Gamma_{\min} = 1200$ Ackermann et al. (2010)). These extreme values put severe constraints on the physics of the central engine which should be able to strongly limit the baryon load in the outflow.

However these Γ_{\min} values were obtained from a simplified “single zone” model where the space and time dependencies are averaged out. The motivation of this work is to develop a detailed approach taking into account a more realistic treatment of the dynamics.

Computing the $\gamma\gamma$ optical depth. The kernel of our study is the calculation of the $\gamma\gamma$ opacity created by a spherical flash. It is then possible to model the case of a propagating radiating spherical front (representing for example a shock wave) by the succession of many spherical flashes. One of the critical step is the exact calculation of the photon density n_{Ω} taking into account all the relativistic effects. Before dealing with more complex dynamical configurations within the internal shock framework, the validity of our numerical approach was tested on a simple single-pulse case with a comparison to the previous semi-analytic study of Granot et al. (2008) (see Hascoët et al. (2011) for more details).

2 Application to Internal Shocks

2.1 Internal shocks within a relativistic outflow

The model is applied to the internal shock model, where the whole prompt γ -ray emission is produced by electrons accelerated by shock waves propagating within a relativistic variable outflow. We model the dynamics via a multiple shell model where the successive collisions between shells mimic the propagation of shock waves (Daigne & Mochkovitch 1998). Each collision produces an elementary spherical flash: the simulated light curves are the result of the sum of all flashes. For each high energy photon, the $\gamma\gamma$ opacity is computed by an integration made from its emission location to the observer taking into account the exact radiation field n_{Ω} produced by all the collisions in the outflow. A previous study of the $\gamma\gamma$ opacity in internal shocks was made by Aoi et al. (2010). However the prescription used to compute $\tau_{\gamma\gamma}$ was still approximate, using the local physical conditions of the outflow where the high energy photon is emitted and applying them to an average formula of $\tau_{\gamma\gamma}$ (as can be found in Lithwick & Sari (2001); Abdo et al. (2009); Ackermann et al. (2010)).

2.2 Minimum Lorentz factor in GRB outflows – The case of GRB 080916C

The first natural application of our model is the estimate of the minimum bulk Lorentz factor Γ_{\min} in GRB outflows, obtained from the constraint $\tau_{\gamma\gamma}(E_{\text{HE,max}}) \simeq 1$, where $E_{\text{HE,max}}$ is the highest photon energy detected in the burst. To illustrate this aspect with an example, we applied our approach to the case of one of the four brightest GRBs detected in the GeV range by *Fermi*, i.e. GRB 080916C. The results are shown in Fig. 1. Using our numerical model, a synthetic GRB was generated, which reproduces the main observational features: the total radiated isotropic γ -ray energy ($E_{\text{iso}} = 8.8 \times 10^{54}$ ergs between 10 keV and 10 GeV), the spectral properties (E_p , α , β parameters of the Band function*), the envelop of the light curve and a short time-scale variability of 0.5 s in the observer frame. The study is focused on the most constraining time bin (time bin 'b'), during which the highest observed photon energy was $E_{\text{HE,max}} = 3$ GeV (16 GeV in the source rest frame): for this reason, only time bins 'a' and 'b' are reproduced in the synthetic GRB. These two intervals correspond to 32 % of the total radiated isotropic equivalent energy. The minimum mean Lorentz factor $\bar{\Gamma}_{\min}$ is obtained by requiring that $\tau_{\gamma\gamma}(E_{\text{HE,max}}) \leq 1$ (see Fig. 1, lower panel). With the detailed calculation, we find a minimum mean Lorentz factor $\bar{\Gamma}_{\min} = 340$, i.e. a factor 2.6 lower than the value $\bar{\Gamma}_{\min} = 887$, which was obtained from an approximate “single zone” model (Abdo et al. 2009). Even more remarkable, the whole initial distribution of the Lorentz factor used in this model of GRB 080916C (from 170 to 700) remains below the “minimum” value of the Lorentz factor derived from single zone models (see Fig. 1, upper left panel).

*We use the values given by Abdo et al. (2009) for time bin 'b'.

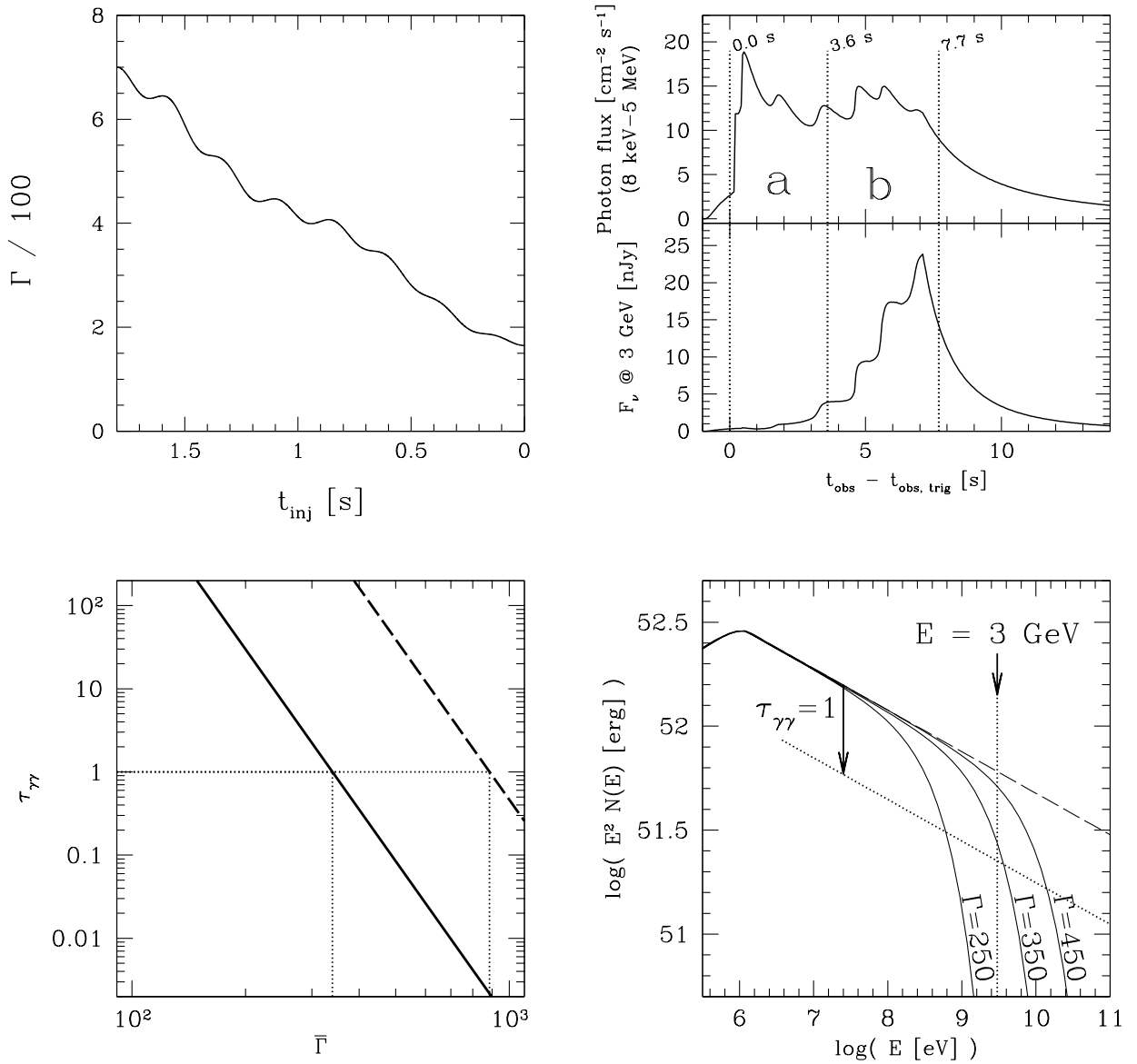


Fig. 1. Minimum Lorentz factor for GRB 080916C. The two first panels are plotted for the limit case leading to $\tau_{\gamma\gamma}(3\text{ GeV}) = 1$ in time bin 'b', i.e. for a mean Lorentz factor $\bar{\Gamma} = \bar{\Gamma}_{\text{min}} = 340$. *Upper left panel:* initial Lorentz factor distribution in the outflow. *Upper right panel:* γ -ray light curves in the GBM/BGO band (8 keV – 5 MeV, top) and at 3 GeV (bottom). The light curves are plotted as a function of $t_{\text{obs}} - t_{\text{obs, trig}}$, where $t_{\text{obs, trig}}$ is the observer time of the first detected photons. *Lower left panel:* evolution of $\tau_{\gamma\gamma}$ at $E_{\text{HE}} = 3$ GeV against the mean Lorentz factor in the outflow $\bar{\Gamma}$, following our detailed modeling (solid line) and using the average formula from Abdo et al. (2009) (dashed line). *Lower right panel:* time integrated spectrum over time bin 'b' for different mean Lorentz factors (the relative shape of the initial Lorentz factor distribution is kept the same) and reference spectrum without $\gamma\gamma$ annihilation (dashed line). [figure from Hascoët et al. (2011)]

2.3 Is the delayed onset of the GeV emission a signature of the $\gamma\gamma$ opacity ?

The high energy emission (above 100 MeV) detected by *Fermi* in a few bright GRBs often shows a delayed onset compared to the softer γ -ray emission (below 5 MeV). The analysis by Zhang et al. (2011) indicates that such a delayed onset is present in at least 7 in a sample of 17 GRBs detected by *Fermi*-LAT. This feature seems to be common to long and short GRB classes and its origin is debated (Granot et al. 2010). Among the proposed explanations (see e.g. Zou et al. 2009; Li 2010; Toma et al. 2009), the possibility that this delayed

onset is induced by a $\gamma\gamma$ opacity temporal evolution effect has already been discussed by Abdo et al. (2009): as the shock wave producing the γ -ray emission expands to larger radii, the opacity seen by the high energy photons evolve from an optically thick to an optically thin regime. The model developed in the present study is well appropriate to investigate this possibility in more details. The synthetic burst used in Fig. 1 to model bins 'a' and 'b' of GRB 080916C gives an example of a delayed onset at 3 GeV induced by an evolving $\gamma\gamma$ opacity. The first pulse is produced at lower radii and in lower Lorentz factor material and is therefore strongly absorbed. For this reason, it is almost suppressed in the 3 GeV light curve, whereas the second pulse is well visible. Note that the model reproduces simultaneously the onset delay of $\simeq 5$ s at high energy, and the short timescale variability of $\simeq 0.5$ s at low energy.

3 Conclusions

The detailed $\gamma\gamma$ opacity calculation model presented in these proceedings is appropriate and accurate to study many aspects and consequences of $\gamma\gamma$ annihilation in GRBs. In the present work we focus on the internal shock model and consider the consequences and signatures that $\gamma\gamma$ opacity could have in GRB observations. The model was validated by comparing our results to a previous semi-analytical study by Granot et al. (2008).

- It is shown how a detailed calculation can predict minimum Lorentz factors Γ_{min} which are lower by a factor of 2-3 compared to a simplified "single zone" model where space and time dependencies are averaged out.
- The temporal evolution of $\tau_{\gamma\gamma}$ during a burst could favor a delay between the MeV and GeV light curves.

Other effects (Hascoët et al. 2011) can be studied with our model:

- The $\gamma\gamma$ cutoff transition can be characterized in time-integrated spectra. It is usually closer to a power-law steepening than to a sharp exponential cutoff. The exact shape of the transition strongly depends on the details of the GRB dynamics.
- For complex GRBs, the $\gamma\gamma$ opacity could suppress the shortest time-scale features in high energy light curves (above 100 MeV).
- If MeV and GeV photons are not produced at the same location (see e.g. Bošnjak et al. (2009); Zou et al. (2011)), $\tau_{\gamma\gamma}$ could be further lowered, reducing even more the constraint on Γ_{min} .

This work is partially supported by the French Space Agency (CNES). R.H.'s PhD work is funded by a Fondation CFM-JP Aguilar grant.

References

- Abdo, A. A. et al. 2009, *Science*, 323, 1688
- Ackermann, M., Asano, K., Atwood, W. B., et al. 2010, *ApJ*, 716, 1178
- Ackermann, M. et al. 2011, *ApJ*, 729, 114
- Aoi, J., Murase, K., Takahashi, K., Ioka, K., & Nagataki, S. 2010, *ApJ*, 722, 440
- Bošnjak, Ž., Daigne, F., & Dubus, G. 2009, *A&A*, 498, 677
- Daigne, F. & Mochkovitch, R. 1998, *MNRAS*, 296, 275
- Granot, J., Cohen-Tanugi, J., & do Couto e Silva, E. 2008, *ApJ*, 677, 92
- Granot, J. et al. 2010, to appear in the Proceedings of "The Shocking Universe - Gamma-Ray Bursts and High Energy Shock phenomena", Venice (Italy), September 14-18, 2009, eprint arXiv:1003.2452.
- Hascoët, R., Daigne, F., Mochkovitch, R., & Vennin, V. 2011, submitted to *MNRAS*, eprint arXiv:1107.5737
- Li, Z. 2010, *ApJ*, 709, 525
- Lithwick, Y. & Sari, R. 2001, *ApJ*, 555, 540
- Rees, M. J. 1966, *Nature*, 211, 468
- Toma, K., Wu, X.-F., & Mészáros, P. 2009, *ApJ*, 707, 1404
- Zhang, B.-B., Zhang, B., Liang, E.-W., et al. 2011, *ApJ*, 730, 141
- Zou, Y., Fan, Y., & Piran, T. 2011, *ApJ*, 726, L2+
- Zou, Y.-C., Fan, Y.-Z., & Piran, T. 2009, *MNRAS*, 396, 1163

MODELING THE POLARIZATION OF RADIO-QUIET AGN: FROM THE OPTICAL TO THE X-RAY BAND

F. Marin¹ and R. W. Goosmann¹

Abstract. A thermal active galactic nucleus (AGN) consist of a powerful, broad-band continuum source that is surrounded by several reprocessing media with different geometries and compositions. Here we investigate the expected spectropolarimetric signatures in the optical/UV and X-ray wavebands as they arise from the complex radiative coupling between different, axis-symmetric AGN media. Using the latest version of the Monte-Carlo radiative transfer code STOKES, we obtain spectral fluxes, polarization percentages, and polarization position angles. In the optical/UV, we assume unpolarized photons coming from a compact source that are reprocessed by an optically-thick, dusty torus and by equatorial and polar electron-scattering regions. In the X-ray band, we additionally assume a lamp-post geometry with an X-ray source irradiating the accretion disk from above. We compare our results for the two wavebands and thereby provide predictions for future X-ray polarimetric missions. These predictions can be based on present-day optical/UV spectropolarimetric observations. In particular, we conclude that the observed polarization dichotomy in the optical/UV band should extend into the X-ray range.

Keywords: galaxies: active - galaxies: Seyfert - polarization - radiative transfer

1 Introduction

Since the early observations by Fath (1909), active galactic nuclei (AGN) have been intensively observed at all possible wavelengths using ground-based and space telescopes. The core of an AGN cannot be resolved by current optical instruments. In addition to that we find that in type-2 objects (those with narrow optical emission lines) the central engine is hidden by optically thick dust blocking most of the light. According to the unified scheme of AGN (Antonucci 1993), the obscuring dust is distributed anisotropically and in type-1 AGN, which show broad optical emission lines, the central region is directly visible. This anisotropic distribution of absorbing and scattering media in AGN must induce a net polarization that we can exploit in order to investigate the complex radiative coupling between the innermost components of AGN. In fact, spectropolarimetry is a unique tool to probe the unresolvable parts of AGN thanks to two more independent observables it adds: the percentage and the position angle of polarization. So far, spectropolarimetry observations could be performed from the radio to the optical/UV band, but with the launch of the GEMS satellite (Kallman et al. 2010) the first X-ray polarization data of bright AGN is soon going to be in reach.

To interpret the data, polarization modeling of the radiative interplay between different AGN components is necessary. Such modeling has been conducted previously by a number of authors (see e.g. Kartje 1995; Smith et al. 2004; Wolf & Henning 1999; Goosmann & Matt 2011). For computational reasons, some models are restricted to a single-scattering approach following the suggestion by Henney & Axon (1995) about the predominance of first-order scattering in optically thick media. But one should bear in mind that this argument does not necessarily hold for the multiple scattering between several non-absorbing, electron-scattering components. Also, previous modeling is most often limited to a given waveband.

In this research note, we present a composite, multiple-scattering and reprocessing model of AGN from which spectropolarimetric fluxes are computed simultaneously in the optical/UV and in the X-ray band. Our model setup is based on the classical, axis-symmetric unified scheme of AGN (Urry & Padovani 1995) and we are particularly interested in the polarization properties as a function of wavelength and viewing direction.

¹ Observatoire astronomique de Strasbourg, Section Hautes Energies, 11 Rue de l'Université, 67000 Strasbourg, France

irradiated accretion disk	flared disk	dusty torus	polar outflows
(only present for X-rays) $R_{\text{disk}} = 0.0004$ pc $h_{\text{disk}} = 3.25 \times 10^{-7}$ pc vertical optical depth >600 neutral reprocessing	$R_{\text{min}} = 0.02$ pc $R_{\text{max}} = 0.04$ pc half-opening angle = 20° equat. optical depth = 1 electron scattering	$R_{\text{min}} = 0.1$ pc $R_{\text{max}} = 0.5$ pc half-opening angle = 60° equat. optical depth = 750 Mie scattering/neutral reprocessing	$R_{\text{min}} = 0.3$ pc $R_{\text{max}} = 1.8$ pc half-opening angle = 40° vertical optical depth = 0.03 electron scattering

Table 1. Parameters of the different model components. The accretion disk is only present when modeling the X-ray range. The elevated primary X-ray source is located on the disk axis and subtends a half-angle of 76° with the disk. Note that for the polar outflow, the half-opening angle is measured with respect to the vertical, symmetry axis of the torus, while for the flared-disk the half-opening angle is taken with respect to the equatorial plane.

When observing the optical polarization of AGN, a dichotomy is found for the polarization angle (Antonucci 1983): at type-2 viewing angles, the position angle of the polarization is most often directed perpendicularly to the central radio structure; at type-1 viewing angles, the polarization vector favors a direction that is aligned with the (projected) radio axis. Assuming that the radio structure is stretched along the symmetry axis of the torus, our modeling allows us to test if we can reproduce this observed dichotomy. In the following, we define *parallel* (or *perpendicular*) polarization according to the preferentially observed polarization angle of *type-1* (or *type-2*) AGN. When plotting our results, we distinguish parallel polarization by adding a negative sign to the polarization percentage.

2 Modeling the unified scheme of AGN

2.1 Model setup for the AGN structure

We investigate the radiative coupling between different axis-symmetric emission and reprocessing regions: the inner and outer parts of the accretion disk, the obscuring equatorial dust region, and double-conical outflows along the polar direction.

We consider a compact continuum source of unpolarized photons being emitted isotropically according to a power-law $F_\nu \propto \nu^{-\alpha}$ with index $\alpha = 1$. For the optical/UV part ($1600 \text{ \AA} - 8000 \text{ \AA}$) we assume the continuum source to be very compact and quasi point-like. For the X-ray range ($1 \text{ keV} - 100 \text{ keV}$), we adopt a lamp-post geometry and include X-ray reprocessing of the primary radiation by the underlying disk. The primary source is located at low height on the disk axis subtending a large solid angle with the disk.

The source region is surrounded by a geometrically and optically thin scattering annulus with a flared shape. This radiation-supported wedge plays a major role as it produces a parallel polarization signature in type-1 view by electron scattering (see e.g. Chandrasekhar 1960, Angel 1969, Antonucci 1984, Sunyaev & Titarchuk 1985). At larger radius an optically thick, elliptical dusty torus surrounds the system. It shares the same symmetry plane as the flared disk and is responsible for the optical obscuration at type-2 views. The torus funnel supposedly collimates a mildly-ionized, optically thin outflow stretched along the symmetry axis of the system. The polar wind has an hourglass shape and is centered on the photon source. Parameters defining the shape and the composition of the three/four reprocessing regions are summarized in Table 1. The dust model used for the torus at optical/UV wavelengths is based on a prescription for Galactic dust as described in Goosmann & Gaskell (2007). In the X-ray band, we assume neutral reprocessing for the torus and for the accretion disk. Details of this reprocessing model can be found in Goosmann & Matt (2011).

2.2 The radiative transfer code STOKES

We apply the latest version of the Monte-Carlo code STOKES (www.stokes-program.info). For details on the code, consult Goosmann & Gaskell (2007) and Goosmann & Matt (2011). It conducts radiative transfer in complex emission and reprocessing environments and includes the treatment of polarization. The calculations include multiple scattering, an angle-dependent analysis in 3D, and different dust models. The STOKES code computes the total flux spectrum, the polarization angle, the percentage of polarization, and the polarized flux. The reprocessing physics depends on the energy band considered. Electron and Mie scattering are assumed in the optical/UV waveband; Compton scattering and neutral reprocessing predominate in the X-ray range.

We compute the spectropolarimetric flux as a function of wavelength or photon energy at a given polar viewing angle, i , that is measured with respect to the symmetry axis of the system.

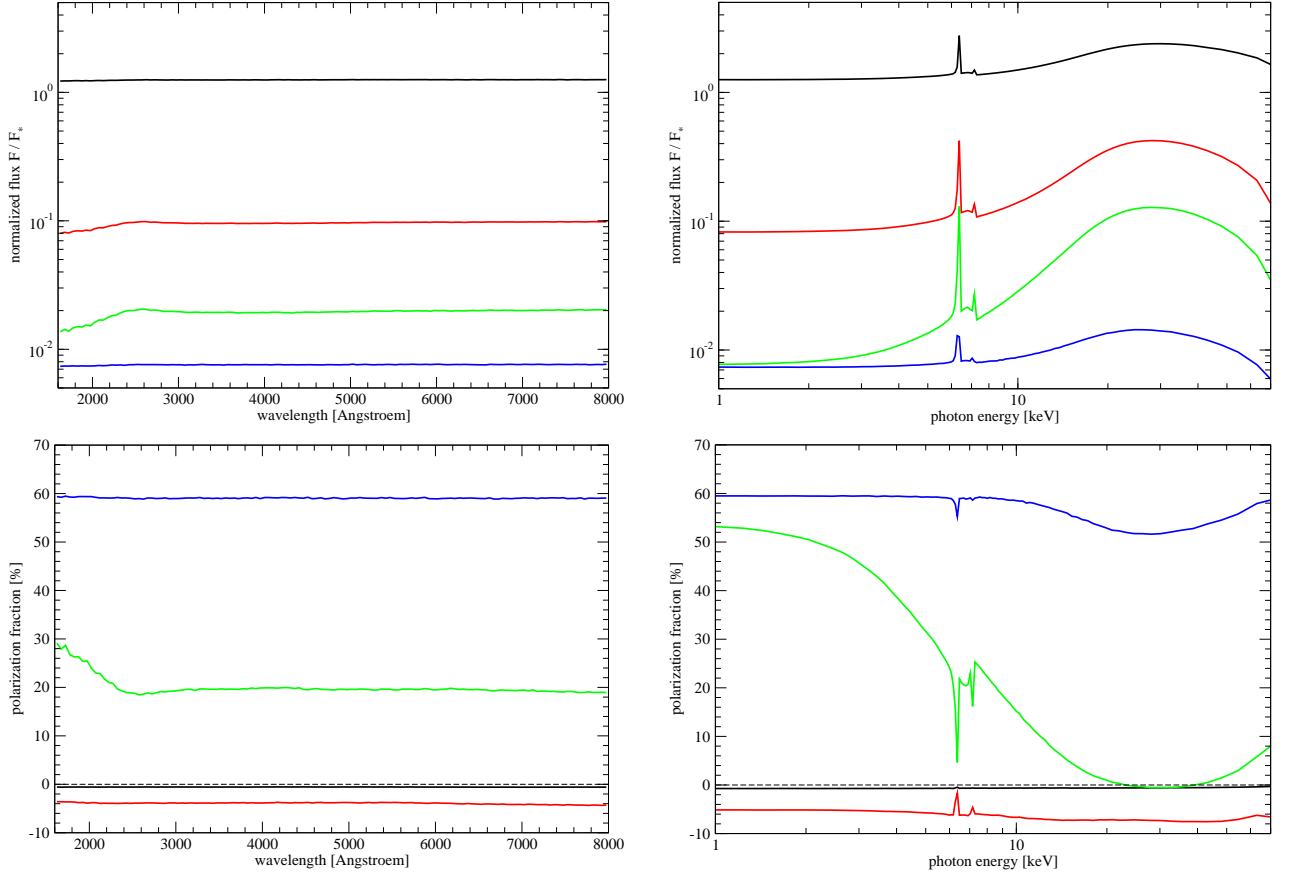


Fig. 1. Modeling the radiative coupling between the different axis-symmetric reprocessing regions. The normalized spectral flux is shown in the top panels, the polarization properties are shown below. A negative P denotes a “type-1” polarization (parallel to the projected symmetry axis) and a positive P stands for a “type-2” polarization (perpendicular to the axis). The transition at $P = 0$ is indicated by dashed lines. Four different viewing angles, i , are considered: a face-on view at $i \sim 18^\circ$ (black), a line-of-sight just below the torus horizon at $\cos i = 0.63^\circ$ (red), an intermediate type-2 view at $i \sim 76^\circ$ (green), and an edge-on view at $i \sim 87^\circ$ (blue). Left: optical/UV energy band. Right: X-ray band.

3 Results

In the top panels of Fig. 1, we present the total flux, F , for the two wavebands considered. The fluxes are normalized to the pure source flux, F_* , that would emerge along the same line-of-sight if there were no scattering media. The results for the polarization percentage, P , and for the polarization angle are combined in the bottom panels of Fig. 1. We adopt a sign convention for the polarization percentage that is recalled in the figure caption.

3.1 Results for the optical/UV band

At face-on and edge-on view, the optical flux is wavelength-independent indicating that electron-scattering in the equatorial flared-disk and in the polar outflows dominates. At intermediate viewing-angles, the impact of the wavelength-dependent dust scattering emerges, mostly around the λ_{2175} feature in the UV. This little bump at 2175 \AA in the flux spectrum is due to scattering by carbonaceous dust in the torus.

The model reproduces the observed polarization dichotomy. The signature of the flared-disk is visible exceeding the effects of the polar outflow and producing low degrees of parallel polarization towards face-on viewing angles. At higher inclination, the equatorial scattering is hidden by the dusty torus and polar scattering dominates causing perpendicular polarization. The variations of P with wavelength at intermediate viewing angles indicate that the dusty torus also has a significant impact on the polarization. The rise in P towards the UV at $i \sim 73^\circ$ is a combined effect of multiple scattering inside the torus funnel and of the wavelength-dependent polarization phase function that is associated with Mie scattering by Galactic dust.

3.2 Results for the X-ray band

The X-ray spectrum shows typical features of neutral reprocessing – the iron $K\alpha$ and $K\beta$ fluorescence lines at 6.4 keV and 7.1 keV and their absorption edges, the Compton hump, and strong soft X-ray absorption at intermediate viewing angles are prominent spectral features. The fluorescent line emission and the Compton reflection hump around 30 keV are present at every line of sight.

An important result of our modeling is that we predict a polarization dichotomy also for the X-ray band. At all viewing directions below the torus horizon, P is positive implying perpendicular polarization. But towards a face-on view, the electron scattering in the equatorial flared disk predominates and produces a net parallel polarization. A peculiar feature appears at $i \sim 73^\circ$, where P changes from positive to mildly negative values around the Compton hump. This behavior is due to the competition between parallel and perpendicular polarization emerging from different reprocessing regions of the model. Around 30 keV, the effect of the flared disk becomes less important than the Compton scattering in the other regions. Explaining this behavior in detail is not trivial as several factors have to be taken into account, one of them being the angle-dependent scattering phase function. But also, the energy-dependence of the electron scattering cross-section has an effect as it favors soft X-ray photons to scatter more than hard X-ray photons. Higher energy photons therefore pass more easily through the optically thin, equatorial scattering region without interacting. This partly explains the disappearance of the parallel polarization at higher photon energy. A more detailed discussion about the X-ray polarization signature of isolated and coupled reprocessing regions is going to be provided elsewhere.

4 Summary and conclusions

We have applied the latest version of the STOKES radiative transfer code to examine the complex reprocessing between different, axis-symmetric media of an active nucleus. We provide simultaneous results for the optical/UV and for the X-ray wavebands and we trace the spectral flux and the polarization as a function of photon wavelength. The observed optical/UV polarization dichotomy is successfully reproduced and an analogous dichotomy is predicted for the X-ray range.

This work is carried out in anticipation of the forthcoming age of X-ray polarimetry. The NASA space telescope GEMS (Kallman et al. 2010) is planned to be launched in 2014 and will be entirely dedicated to X-ray polarimetry. The satellite will observe X-ray sources in the 2–10 keV band allowing us to test the soft X-ray part of our modeling results for the brightest AGN. Note that a next generation, broad-band X-ray polarimeter is technically feasible (Tagliaferri et al. 2011) and could even observe polarization up to 35 keV. Such observations include the X-ray polarization of the Compton hump and thus put even stronger constraints on the validity of our modeling results.

The authors are grateful to Martin Gaskell at the University of Valparaíso in Chile for his great help.

References

- Angel, J. R. P. 1969, ApJ, 158, 219
- Antonucci, R. 1993, ARA&A, 31, 473
- Antonucci, R. R. J. 1983, Nature, 303, 158
- Antonucci, R. R. J. 1984, ApJ, 281, 112
- Chandrasekhar, S. 1960, Radiative transfer, ed. S. Chandrasekhar
- Fath, E. A. 1909, Popular Astronomy, 17, 504
- Goosmann, R. W. & Gaskell, C. M. 2007, A&A, 465, 129
- Goosmann, R. W. & Matt, G. 2011, MNRAS, 415, 3119
- Henney, W. J. & Axon, D. J. 1995, ApJ, 454, 233
- Kallman, T. R., Swank, J. H., & GEMS Team. 2010, in Bulletin of the American Astronomical Society, Vol. 42, AAS/High Energy Astrophysics Division #11, 737–+
- Kartje, J. F. 1995, ApJ, 452, 565
- Smith, J. E., Robinson, A., Alexander, D. M., et al. 2004, MNRAS, 350, 140
- Sunyaev, R. A. & Titarchuk, L. G. 1985, A&A, 143, 374
- Tagliaferri, G., Hornstrup, A., Huovelin, J., et al. 2011, Experimental Astronomy, 98
- Urry, C. M. & Padovani, P. 1995, PASP, 107, 803
- Wolf, S. & Henning, T. 1999, A&A, 341, 675

NEUTRINO TRANSPORT IN GRAVITATIONNAL SUPERNOVÆ SIMULATIONS : A SIMPLIFIED TREATMENT VIA A LEAKAGE SCHEME

B. Peres¹, J. Novak¹ and M. Oertel¹

Abstract. We present a leakage scheme, a simplified model for the treatment of the neutrinos in core collapse supernovæ simulations. In the leakage scheme, the neutrinos are considered either fully at equilibrium with the fluid or streaming out freely. This approach is a quite rough approximation compared to a full transport scheme (Boltzmann solver), but it is much less CPU time consuming and hence is well suited, e.g., for parameter studies. This scheme has been written for CoCoNuT, a general relativistic hydrodynamics code which uses Godunov type methods.

Keywords: supernova, neutrino, numerical methods

1 Introduction

A core collapse supernova is the explosion of a massive star (roughly more than $8M_{\odot}$). At the end of its life, a massive star has onion-like layers of nuclei, the most massive being at the center. Unless the star is very close to $8M_{\odot}$ the core is composed of iron-like nuclei and the explosion is triggered by it reaching the Chandrasekhar mass ($\simeq 1.4M_{\odot}$), when the degeneracy pressure of the electrons cannot balance the gravitation anymore.

The core collapses and loses degeneracy pressure as there are more and more electron captures with increasing density. Above $\rho \simeq 2.10^{14} \text{ g cm}^{-3}$ strong interaction becomes repulsive. The collapsing core bounces, leaving a central compact object (proto-neutron star or black hole).

This bounce creates a pressure wave that becomes a shock propagating outwards. It loses a huge amount of energy photodissociating iron nuclei and soon stalls. Since we observe supernovæ, we know the shock has to revive. The ingredients implied to make the shock propagate again are still under investigation, and may involve neutrino heating, hydrodynamic instabilities (SASI, see Blondin et al. (2003), Foglizzo et al. (2007)), convection, magnetic field, general relativistic effects, ...

2 Leakage scheme

The leakage scheme is a way to avoid the computation of the neutrino distribution function, which would be done by solving the transport equation (this equation depends on time and 6 dimensions in phase space if no symmetry is assumed, and is often referred to as Boltzmann equation). Instead, the neutrinos are considered fully at equilibrium with the fluid (they enter the fluid equations) when trapped, and streaming freely when untrapped (they leave the simulation and remove some energy from the fluid). New fluid equations are implemented in the trapped regime, to satisfy the lepton number conservation. To create neutrinos three neutrino processes are considered : electron capture, pair production by electron positron annihilation and pair production by plasmon decay. Neutrino energies are averaged so that they only have a mean energy (grey scheme). Additional processes are considered to compute the neutrino mean free path : scattering off neutrons, scattering off nuclei, scattering off protons and absorption on neutrons (the latter is not relevant for neutrinos other than ν_e).

¹ Laboratoire Univers et Théories (LUTH), CNRS / Observatoire de Paris / Université Paris-Diderot

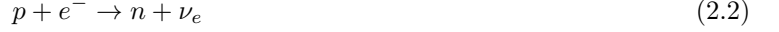
2.1 Neutrino processes

2.1.1 Electron capture on free protons

Electron captures lower the electron density n_{e^-} . In CoCoNuT, we evolve the electron fraction Y_e

$$Y_e = \frac{n_{e^-} - n_{e^+}}{n_b} \quad (2.1)$$

The electron capture on free protons



is treated as in Bruenn (1985) (eq. B12)

$$\frac{\partial Y_e}{\partial t} = \frac{1}{\rho} \frac{4\pi c}{8\pi^3 (\hbar c)^3} \int_0^\infty w^2 dw \left(j(w)[1 - f_\nu(w)] - \frac{f_\nu(w)}{\lambda(w)} \right) \quad (2.3)$$

Where w is the neutrino energy, $f_\nu(w)$ is the distribution function of the neutrinos*, and $j(w)$ and $1/\lambda(w)$ are respectively the emissivity and absorptivity, defined by eqs. C13 and C15 of Bruenn (1985), with an extra $|V_{ud}|^2$ term. This CKM matrix term describes the mixing of mass eigenstates and gauge eigenstates of the quarks entering the hadronic matrix element (n ; p).

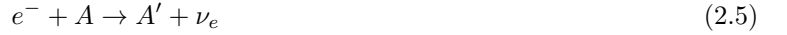
Contrary to Bruenn (1985), we compute the integration every time for η_{np} and η_{pn} , the nucleon final state Pauli blocking, to avoid approximation problems.

$$\eta_{np} = \frac{2}{(2\pi\hbar c)^3} \int d^3p f_n(E)(1 - f_p(E)) \quad (2.4)$$

η_{pn} can be found by interchanging $n \leftrightarrow p$. $f_n(E)$ and $f_p(E)$ are Fermi-Dirac distribution functions with $E = p^2/2m$.

2.1.2 Electron capture on nuclei

The electron capture on nuclei



can be treated similarly, except that it requires the calculation of the corresponding emissivity $j(w)$ and absorptivity $1/\lambda(w)$, eq. C.27 and C.29 from Bruenn (1985).

2.1.3 Pair production

The pair production from electron positron annihilation



is implemented following Ruffert et al. (1996) (eq. B8-10 and B16).

The pair production from plasmon decay



is implemented following Ruffert et al. (1996) (eq. B11, B12 and B17).

2.2 Neutrinosphere

2.2.1 Effective chemical potentials

The neutrinosphere is computed as in Ruffert et al. (1996), with effective chemical potentials. $\mu_\nu = 0$ if the neutrinos are free streaming, $\mu_\nu = \mu_\nu^{eq} = \mu_e + \mu_p - \mu_n$ if the neutrinos are totally trapped. In the intermediate regime, the effective chemical potential is calculated as

$$\mu_\nu = \mu_\nu^{eq}(1 - \exp(-\tau)), \quad (2.8)$$

where τ is the optical depth defined in the next subsection. This is a self-consistent problem which we solve iteratively. The effective chemical potential is taken into account in the calculation of the electron capture and pair production rate, too.

*since we do not compute distribution functions in the leakage scheme, we have to assume that it is a Fermi-Dirac distribution.

2.2.2 Optical depth calculation

For each process considered (scattering off neutrons, scattering off nuclei, scattering off protons and absorption on neutrons), we compute a cross section, following Ruffert et al. (1996) and Rosswog & Liebendörfer (2003). The corresponding opacity is roughly proportionnal to the square of the neutrino energy.

This opacity (or inverse mean free path $1/\lambda$) is then integrated over a radial path to get the optical depth. With general relativistic corrections (within conformal flatness condition) this gives

$$\tau(r) = \int_r^\infty \frac{1}{\lambda} \frac{dr}{\frac{\alpha}{\phi^2} - \beta^r} \quad (2.9)$$

where α is the lapse, β^r is the radial part of the shift vector and ϕ is the conformal factor. The radius of the neutrinosphere R_ν is defined as $\tau(R_\nu) = 2/3$. The neutrinosphere is the limit which separates the two regimes (trapped at $r < R_\nu$, free streaming at $r > R_\nu$).

The neutrino escape time is then (from Ruffert et al. (1996))

$$t_{esc} = \frac{3(r - R_\nu)}{c} \tau(r) \quad (2.10)$$

2.3 Energy treatment

Neutrinos have a mean energy computed as

$$\langle \epsilon \rangle = T \frac{F_5(\eta_e)}{F_4(\eta_e)} \quad (2.11)$$

with T the fluid temperature, and F_5 and F_4 Fermi integrals defined by

$$F_k(\eta) = \int_0^\infty \frac{x^k dx}{1 + \exp(x - \eta)} \quad (2.12)$$

The energy removed is then $\langle \epsilon \rangle Y_\nu / t_{esc}$ if the neutrinos are trapped and $\langle \epsilon \rangle R$ if the neutrinos are free streaming (R is the total neutrino production rate).

In the regime where neutrinos are trapped, a neutrino pressure term that has to be taken into account, too (from Dimmelmeier et al. (2008)).

$$P_\nu = \frac{T^4}{6\pi^2(\hbar c)^3} F_3(\eta_\nu) \quad (2.13)$$

3 Behavior during a simulation

3.1 Collapse and bounce

Starting with a progenitor from Heger and Woosley (see, e.g., Heger et al. (2005)), we run a simulation using CoCoNuT (see, e.g., Dimmelmeier et al. (2005)) with spherical symmetry, equation of state by Lattimer and Swesty (Lattimer & Swesty (1991)) and the leakage scheme. The collapse is induced by an initial velocity gradient.

At collapse, only electron captures are significant. The central density increases as free streaming neutrinos escape from the core. At a density of about 2.10^{12} g cm⁻³ neutrinos become trapped in the fluid. At about 5.10^{14} g cm⁻³, the core bounces and the central density stabilises at 3.10^{14} g cm⁻³, slightly above nuclear matter saturation density, creating the proto-neutron star. The central electron fraction at this time is 0.26 to 0.28, in good agreement with Liebendörfer (2005).

3.2 After bounce

The shock propagates outwards but loses a lot of energy by photodissociating heavy nuclei. It stalls at about 80 to 100km from the center. Pair production becomes non negligible because of the very high temperatures reached in this area (several MeV).

In these simulations the shock cannot revive because there is no neutrino heating and no convection or hydrodynamic instability (that would require more than one dimension).

The proto-neutron star contracts to compensate the energy loss by pair production and electron capture, such that the central temperature remains relatively constant. Together with the mass still falling onto the proto-neutron star, this slowly makes the shock move back to the center of the star (see Figure 1).

We then reach a point where the shock is at the edge of the proto-neutron star, which continues to contract as matter still falls on it. The only possible behavior is that the proto-neutron star collapses into a black hole. This is not yet visible on Figure 1 .

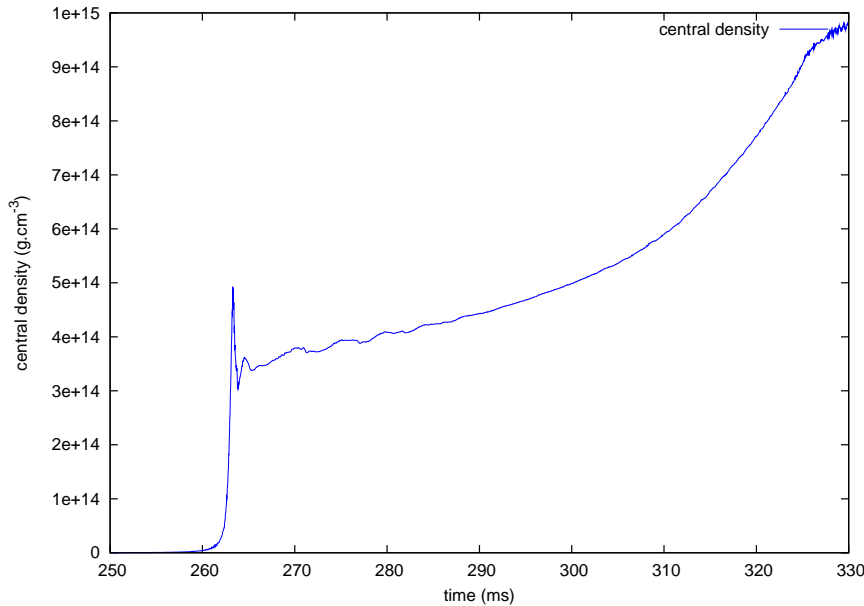


Fig. 1. Central density as a function of time

4 Conclusions

The leakage scheme is an approximation for the neutrino treatment in core collapse supernovæ. It is computationally cheap compared to a Boltzmann solver but comes with some drawbacks. The leakage does not reproduce well the intermediate regime, where the neutrinos are not in equilibrium with the fluid but not yet free streaming either. This is the regime where the shock stalls, and consequently the leakage scheme implies too much deleptonization behind the shock.

Being aware of these approximations, the leakage scheme can be sufficient for some applications, in particular parameter studies where one cannot afford to use a Boltzmann solver.

References

- Blondin, J. M., Mezzacappa, A., & DeMarino, C. 2003, *ApJ*, 584, 971
- Bruenn, S. W. 1985, *ApJS*, 58, 771
- Dimmelmeier, H., Novak, J., Font, J. A., Ibáñez, J. M., & Müller, E. 2005, *Phys. Rev. D*, 71, 064023
- Dimmelmeier, H., Ott, C. D., Marek, A., & Janka, H.-T. 2008, *Phys. Rev. D*, 78, 064056
- Foglizzo, T., Galletti, P., Scheck, L., & Janka, H.-T. 2007, *ApJ*, 654, 1006
- Heger, A., Woosley, S. E., & Spruit, H. C. 2005, *ApJ*, 626, 350
- Lattimer, J. M. & Swesty, F. D. 1991, *Nuclear Physics A*, 535, 331
- Liebendörfer, M. 2005, *ApJ*, 633, 1042
- Rosswog, S. & Liebendörfer, M. 2003, *MNRAS*, 342, 673
- Ruffert, M., Janka, H.-T., & Schaefer, G. 1996, *A&A*, 311, 532

PARTICLE TRANSPORT AT RELATIVISTIC SHOCKS

I. Plotnikov¹

Abstract. Relativistic shocks structure studied in recent analytical works and large Particle-In-Cell (PIC) simulations reports the existence of strong self-generated magnetic fields at the proximity of the shock front. These fields are generated by plasma instabilities (e.g. Weibel instability) and are turbulent on plasma skin depth scale. In this proceeding we present the study of particle transport in microturbulent isotropic magnetic field $\delta\vec{B}$ in the presence of external mean field \vec{B}_0 , assuming $\langle\delta B^2\rangle \gg B_0^2$. The expression of parallel (D_{\parallel}) and transverse (D_{\perp}) diffusion coefficients are found. We find that D_{\parallel} evolves as the square of particle energy and D_{\perp} saturates when particle reduced rigidity ρ is greater than $\delta B/B_0$. Application to relativistic shocks upstream and downstream regions shows that the acceleration by Fermi mechanism is possible only for the range of particle rigidities where $1 < \rho < \delta B/B_0$.

Keywords: Turbulence, magnetic fields, particle diffusion

1 Introduction

High energy radiation from astrophysical objects as hot-spots of Active Galactic Nuclei (AGN) and Gamma Ray Bursts (GRBs) is usually explained by accelerated charged particles at relativistic shocks. In the case of GRBs external shock front attains Lorentz factors up to several hundreds ($\Gamma_s \sim 100$), providing an unique source involving ultra-relativistic blastwaves. It is logically expected that relativistic effects play an essential role in shock physics. For example, strong magnetic fields $> 10^{-4}\text{G}$ in preshocked region are inferred from observations, difficult to explain as the ISM or ambient field strength (Li & Waxman 2006), but seem to be produced by the shock itself.

As supported by PIC simulations (Sironi & Spitkovsky 2011) relativistic shocks produce strong self-generated magnetic fields mediated by Weibel (filamentation) instability. Typical variation scale of such fields corresponds to plasma skin depth ($\sim 10^5$ m in the ISM). Larmor radius of individual particles with relativistic thermal energy $\Gamma_s m_p c^2$ in the downstream region appears to be always larger than this scale. Particle acceleration should be possible as long as the external magnetisation remains low, and produce non-thermal particle distribution with power-law tail $s = -2.24$. There are, however, no evidence of acceleration up to Very High Energies in relativistic shocks. In order to investigate particle acceleration we study the effects of intense small-scale turbulence on particle transport, adopting test-particle approximation. In following sections we present a study of transport of charged particles in intense small-scale turbulence and apply the results to constrain diffusive acceleration mechanism at relativistic shocks.

2 Particle trajectories

We consider particles with Larmor radius R_L greater than the magnetic field coherence length l_c . As astrophysical environments are always magnetised we superpose an external constant field \vec{B}_0 along z direction on turbulent self-generated field $\delta\vec{B}$, isotropic. To illustrate in simplest way the behaviour of particles in small-scale magnetic turbulence we consider three different cases: regular magnetic field alone $B_0\vec{e}_z$, purely turbulent field with coherence length l_c smaller than the particle Larmor radius R_L , and two fields together with $\delta B \gg B_0$ and $R_L/l_c \gg 1$. In Fig. 1 field structure (top panel) and corresponding particle trajectories (bottom panel) are presented. Constant field \vec{B}_0 produces the well-known helical particle trajectory (left column). $\delta\vec{B}$ alone

¹ UJF-Grenoble 1/CNRS-INSU, Institut de Planétologie et d'Astrophysique de Grenoble (IPAG) UMR 5274, 38041 Grenoble, France

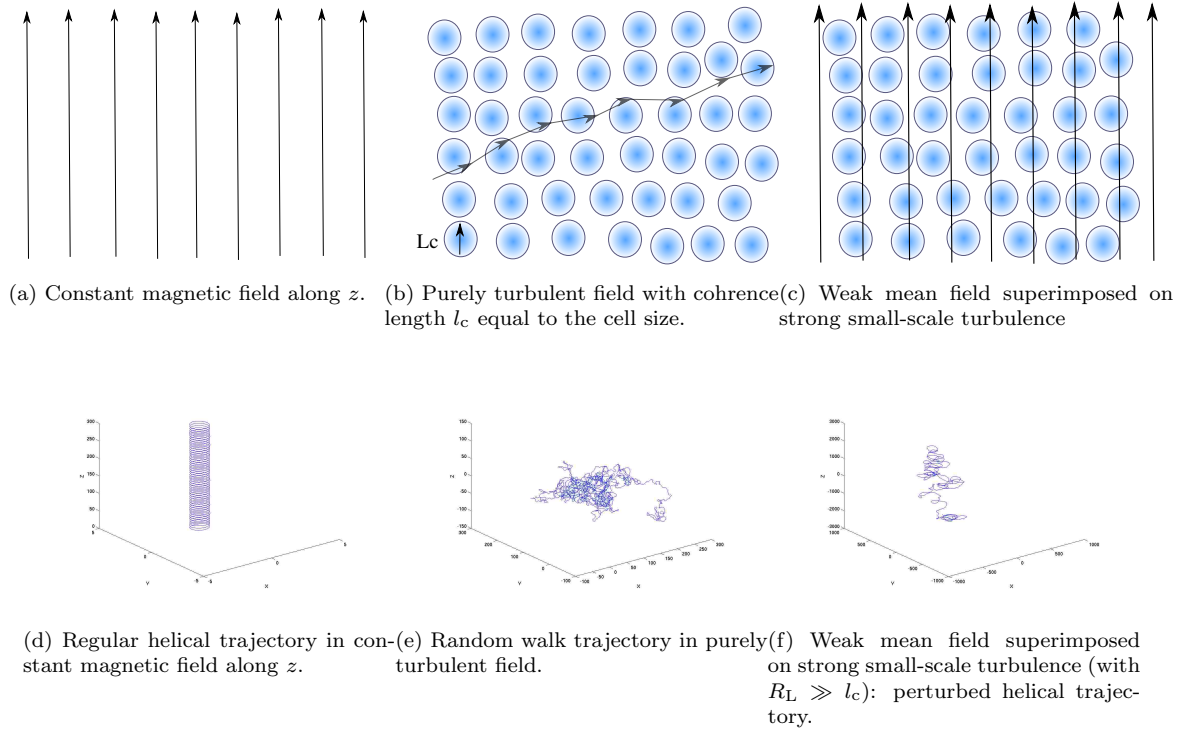


Fig. 1: Example of three magnetic field structures (on the top panel) and corresponding particle trajectories (on the bottom panel).

produces isotropic “random walk” trajectories (middle column). The superposed \vec{B}_0 and $\delta\vec{B}$ produce a moderately perturbed helical trajectory (right column). It is interesting to note that the trajectory is not isotropic despite that $\langle\delta B^2\rangle/B_0^2 \gg 1$. It illustrates the effect of smallness of l_c compared to R_L . Hence, one cannot neglect the mean field, even very weak in comparison to $\delta\vec{B}$.

3 Transport in small-scale turbulence: theory and simulations

Only one physical assumption is necessary to deduce transport coefficients when $R_L \gg l_c$: scattering time is greater than turbulent field coherence time $\tau_s \gg \tau_c$. Consider random rotations from $\delta\vec{B}$ field and regular deflexion in (x, y) plane from \vec{B}_0 field. Then one may obtain diffusion coefficients expressions as (Plotnikov et al. 2011)

$$D_{\parallel} = \frac{c^2}{3\nu_s}, \quad D_{\perp} = \frac{c^2}{3} \frac{\nu_s}{\omega_{L|0}^2 + \nu_s^2}, \quad \text{where } \nu_s = \frac{2c}{3\eta\rho^2}, \quad (3.1)$$

where the subscripts \parallel and \perp signify respectively parallel and transverse to \vec{B}_0 , ν_s is the angular scattering frequency, $\omega_{L|0}$ is the Larmor pulsation in B_0 field only ($\omega_{L|0} = qB_0/\gamma mc$), ρ is the particle reduced rigidity and $\eta = \langle\delta B^2\rangle/(\langle\delta B^2\rangle + B_0^2)$ is the field degree of turbulence.

When $\rho \gg 1$, $\omega_{L|0} \gg \nu_s$, so as $D_{\perp} \simeq c^2/3\nu_s/\omega_{L|0}^2 = 2cl_c/9B_0^2 + \langle\delta B^2\rangle/B_0^2$. Hence it is independent of particle energy and governed by turbulence strength only.

Numerical Monte-Carlo simulations were performed in the same spirit as in Casse et al. (2002). Numerical scheme consists in integrating a large number of trajectories in random $\delta\vec{B}$ realization. Then statistical estimates of D_{\parallel} and D_{\perp} were obtained as the mean square of displacements from initial particle position divided by Δt . We explored the range of rigidities going from 1 to 10^2 and turbulence degree $\langle\delta B^2\rangle/B_0^2$ was varied between 1 and 10^4 . Results are presented in Fig. 2 were parallel (left side) and perpendicular (right side) diffusion coefficient are plotted as function of numerical rigidity $\rho' = 2\pi R_L/L_{\max}$, where $L_{\max} \simeq 10l_c$. As expected, $D_{\parallel} \propto \rho'^2$ independently of turbulence level. For $\rho' < \sqrt{\langle\delta B^2\rangle/B_0^2}$, $D_{\perp} \propto \rho'^2$ until it reaches the plateau

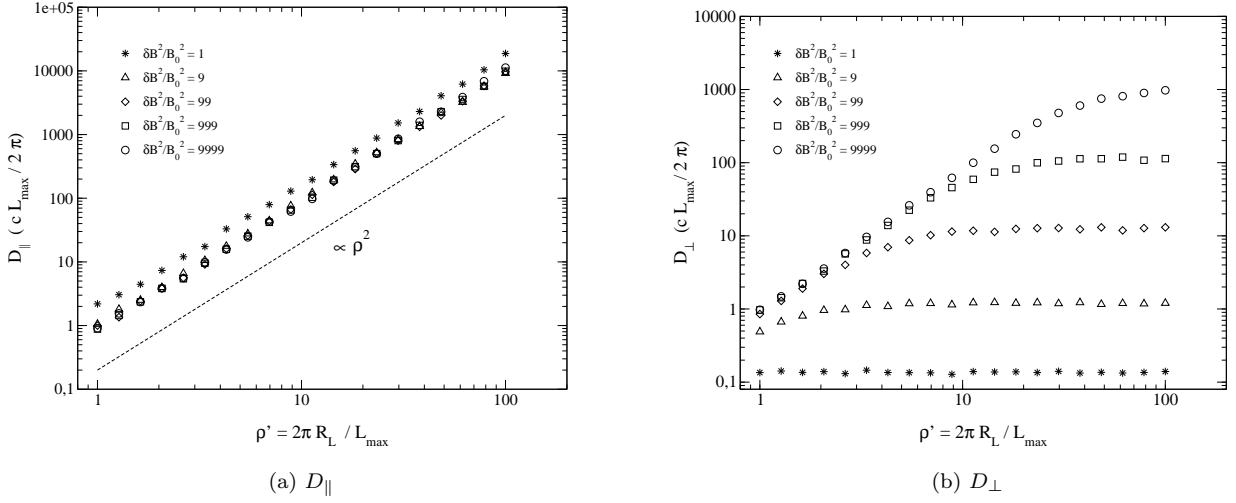


Fig. 2: Diffusion coefficients D_{\parallel} (left panel) and D_{\perp} (right panel) as function of reduced rigidity ρ' . The symbols correspond to various turbulence degrees $\langle \delta B^2 \rangle / B_0^2$ going from 1 to 10^4 as indicated. $D_{\parallel} \propto \rho'^2$ independently of turbulence level. For $\rho' < \sqrt{\langle \delta B^2 \rangle / B_0^2}$, $D_{\perp} \propto \rho'^2$ until it reaches the plateau at $\rho' \sim \sqrt{\langle \delta B^2 \rangle / B_0^2}$.

at $\rho' \sim \sqrt{\langle \delta B^2 \rangle / B_0^2}$. Both are in agreement with equations 3.1. Systematic presentation of the theory and simulations of this transport regime can be found in Plotnikov et al. (2011). At this point we can examine first-order Fermi acceleration mechanism when only small-scale turbulence is considered.

4 Application to upstream and downstream of relativistic shocks

The natural way to apply transport process is to consider two co-moving frames: upstream (unshocked medium, Laboratory frame) and downstream (shocked medium).

4.1 Upstream

In the upstream region the shock front move with the speed $V_{s|u} \simeq c(1 - 1/\Gamma_S^2)$, very close to the light speed. Particles coming from downstream region are rapidly caught up by the shock front. The distribution function is consequently highly anisotropic, confined to the loss cone $\Delta\theta \simeq 2/\Gamma_S$ (Achterberg et al. 2001)

As argued in Lemoine et al. (2006) when only B_0 is present or when particles experiences large-scale turbulence with $\rho < 1$, acceleration process cannot take place due to field correlation between upstream and downstream region. If the field is turbulent on small scales ($R_L > l_c$) then the correlation disappears and diffusive acceleration is working. In the latter case, mean field deflective effect dominates over small-scale turbulence when ρ is large and returns are governed mostly by B_0 . The acceleration process may be quenched when $\rho \gg 1$, as in the case of pure B_0 field. This is illustrated in Fig. 3 where phase space plots of entering (red dots) an escaping to downstream (blue dots) particles in three cases are plotted. Regular B_0 field deflects particles to the left (left panel, see also Achterberg et al. 2001). When small-scale turbulence is present and $\rho' \sim 1$ the distribution is isotropic in velocity space (middle panel) so that the acceleration is operative. With increasing energy $\rho' > \delta B / B_0$ and the turbulent field is no more able to isotropize the distribution. Particle residence time in the upstream region (t_{ups}) is then : $\bar{t}_L / \Gamma_S < t_{\text{ups}} < t_{L|0} / \Gamma_S$. Were \bar{t}_L and $t_{L|0}$ are Larmor periods in the rms field and mean field alone, respectively. Lower limit applies when ρ is close to 1 and the upper limit applies when B_0 governs particle returns.

4.2 Downstream

Shock front speed in the downstream comoving frame is $V_{s|d} \simeq c/3$. Shock compression of upstream magnetic field makes B_0 to be always perpendicular to the shock normal, therefore diffusive returns are governed by the transverse diffusion coefficient. Residence time is estimated as $t_{\text{dow}} \simeq 18D_{\perp}/c^2$. As result of D_{\perp} saturation at highest energies, diffusive return time attains a finite value.

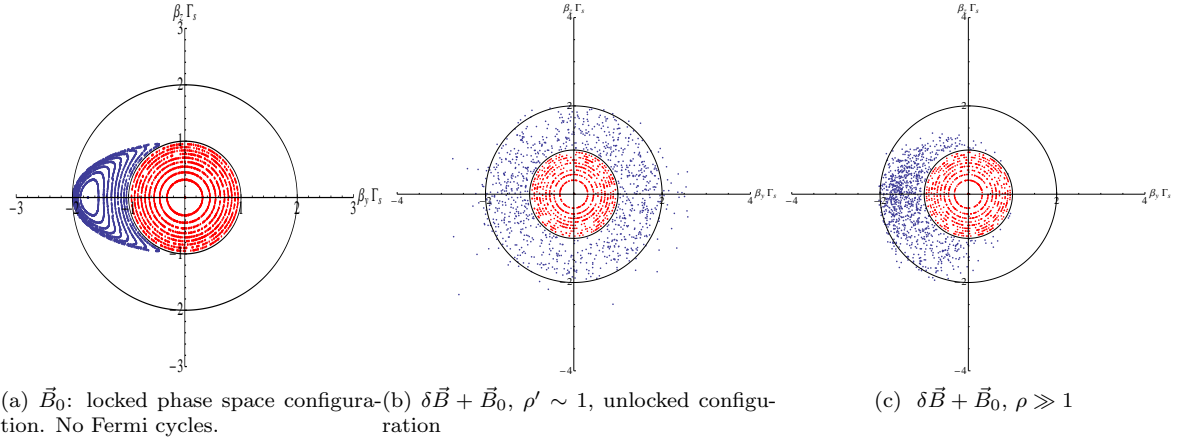


Fig. 3: Three plots of upstream velocity space in shock front plane: $\beta_y \Gamma_S$ vs $\beta_z \Gamma_S$. Shock front propagates along x direction. Red dots: entry from downstream. Blue dots: escape to downstream.

These results are in qualitative agreement with direct simulations of Niemiec et al. (2006) of particle acceleration including small-scale intense magnetic fields in the downstream region. When B_0 and large-scale compressed field are present these authors observed acceleration cut-off.

Diffusive acceleration is not effective enough to span several orders of magnitude in energy. Small-scale turbulence is effective at the beginning of the process. But if the external medium is magnetised the acceleration process is quenched rapidly.

5 Conclusion

In this proceeding a study of particle transport in small-scale intense magnetic turbulence was presented. We found that:

- When particle energy is high (e.g. $\rho \gg 1$), B_0 is kinematically important, and the particle transport is anisotropic, even if $\delta B^2 \gg B_0^2$, as illustrated in Fig. 1. The diffusion coefficients (Eq.3.1) have been derived with a theory that is exact in the limit of a short correlation time $\tau_c \ll \tau_s$.
- Diffusive shock acceleration in small-scale turbulence appears to be effective only when $1 < \rho < \sqrt{\delta B^2 / B_0^2}$.

Conclusions about acceleration performances might be modified if coherence length of the turbulence grows with time, additional source of magnetic turbulence on large scale is present in downstream region.

References

- Achterberg, A., Gallant, Y. A., Kirk, J. G., & Guthmann A. W. 2001, MNRAS 328, 393
 Casse, F., Lemoine, M., & Pelletier, G. 2002, Phys. Rev. D, 65, 023002
 Lemoine, M., Pelletier, G., & Revenu, B. 2006, ApJL, 645, 129
 Li, Z., & Waxman, E. 2006, ApJ, 651, 328
 Niemiec, J., Ostrowski, M., Pohl, M. 2006, ApJ, 650, 1020
 Plotnikov, I., Pelletier, G., Lemoine, M., 2011, A&A, 532, 68
 Sironi, L., & Spitkovsky, A. 2011, ApJ, 726, 75

SOME RECENT RESULTS OF THE CODALEMA EXPERIMENT

A. Rebai¹ and the CODALEMA collaboration²

Abstract. Codalema is one of the experiments devoted to the detection of ultra high energy cosmic rays by the radio method. The main objective is to study the features of the radio signal induced by the development in the atmosphere of extensive air showers (EAS) generated by cosmic rays in the energy range of 10^{16} - 10^{18} eV. After a brief presentation of the detector features, the main results obtained are reported (emission mechanism, lateral distribution of the electric field, energy calibration, etc.). The first studies of the radio wave front curvature are discussed as new preliminary results.

Keywords: UHECR, radiodetection, antennas, radio emission mechanism, EAS

1 Introduction

A century after the discovery of cosmic rays, several fundamental issues related to the nature and the origin of ultra high energy cosmic rays (UHECR) remain unanswered, despite intensive experimental efforts. The main difficulty opposing the progress is due to the extremely low flux of UHECR (1 particle/km²/century at 10^{20} eV) and the present performances of particle detectors arrays and fluorescence telescopes (Abraham et al. 2010; Abbasi et al. 2010). In the recent decade, the measurement of the radio counterparty of EAS becomes a promising technique. Many scientific collaborations like CODALEMA in France (Ardouin et al. 2009) and LOPES in Germany (Apel et al. 2010) have demonstrated the feasibility of this method to deduce the EAS features. The potentialities of the radiodetection resides in several advantages, among them may be mentioned: the operating duty cycle close to 100%, the sensitivity to the shower longitudinal development in the atmosphere and the mechanical robustness, the simplicity and the low cost of the antennas. The CODALEMA experiment is installed at the radio observatory site (Nançay, 47.3°N, 2.1°E and 137 m above sea level). Its main goal is to improve the pioneer experimental results (Allan 1971), taking advantage of ultrafast electronic devices and a quiet radio environment from anthropic transmitters in the detection bandwidth (Ardouin et al. 2006). From the phenomenological point of view, CODALEMA has made progress in the understanding of radio signal origin, showing that the geomagnetic field is the main actor in radio signal emission via the geomagnetic mechanism (Ardouin et al. 2009), and showing recently the contribution of a second emission mechanism due to the shower negative charge excess (Marin 2011). This contribution reports on the last results of the experiment CODALEMA with updated data set, recalling the observations of the north-south asymmetry and of the energy correlation. Finally the reconstruction method of the radio wavefront radius of curvature is presented.

2 Experimental situation

The CODALEMA experiment is made of two main arrays of detectors. The first array is built with 24 short active dipoles antennas distributed on a cross geometry with dimensions 400 m by 600 m. This apparatus is used to study the EAS radio counterpart. The dipole antenna is made by two radiator arms each 60 cm long at a height of 1.2 m. The antenna design was optimized to reach an almost isotropic pattern. Low noise amplifier (LNA) is used to amplify the electric signal. It is conceived to be sensitive to the radio galactic background and is linear over a wide frequency band from 0.1 MHz up to 230 MHz. The second apparatus is a ground-based particle detector array formed by 17 plastic scintillators placed on a square with 340 m side. It measures the primary particle energy and provides the trigger signal to the other detector arrays. The entire acquisition system (DAQ) is triggered by the passage of secondary particles in coincidence through each of the five central scintillators.

¹ SUBATECH IN2P3-CNRS/Université de Nantes/École des Mines de Nantes France

² LESIA, Observatoire de Paris-Meudon France - Station de Radioastronomie de Nançay France

3 A North-South asymmetry: a geomagnetic effect signature in the production of the radio signal

CODALEMA is the first experience which has reported a large and stable asymmetry in counting rates between showers coming from north and south (Ardouin et al. 2009; Ravel 2010). This asymmetry has been interpreted as a signature of the geomagnetic field effect in the radio signal emission process. The local geomagnetic field \vec{B} is the main cause of this asymmetry through the action of Lorentz force on the secondary charged particles via the $\vec{v} \wedge \vec{B}$ term. We find that among the 2030 events detected in coincidences with the two arrays: 1708 events coming from the north and 322 coming from the south (see Fig. 1, left). The respective ratio equal to 0.188 is consistent with the value of 0.17 obtained with a previous statistic used in (Ardouin et al. 2009). A pure statistical effect is excluded with 15σ . One can enhance here on the fact that this asymmetry is stable over time and with different data samples.

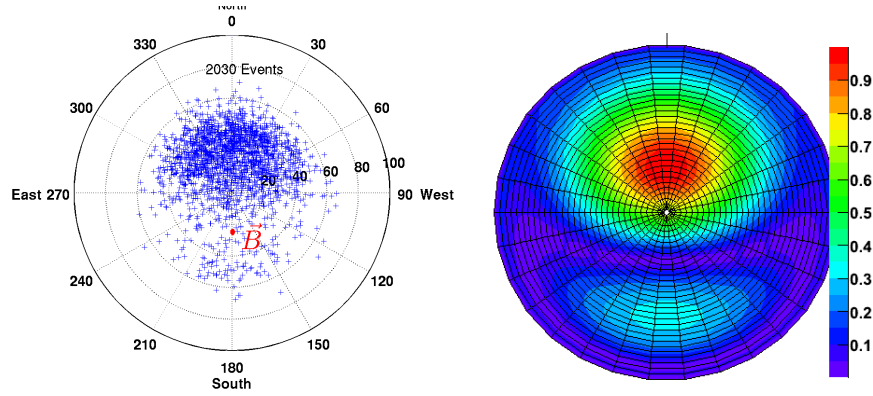


Fig. 1. Left: A plot sky showed the arrival directions distribution of detected EAS events. The red dot indicates the local geomagnetic field ($\theta = 27^\circ, \phi = 0^\circ$). **Right:** Sky map of the geomagnetic model theoretical prediction based on the projection of the product $\vec{v} \wedge \vec{B}$ on the East-West direction multiplied by the trigger coverage map. The colormap is normalized to 1.

4 Energy calibration of the Codalema antenna array

The energy of the primary particle E_p is one of the most important parameters for studying EAS. To avoid the use of the particles detectors array, the radio technique must demonstrate its ability to estimate the primary particle energy with the information given by the radio signal alone. In this perspective, a study of the correlation between the shower energy and the electric field created at the shower axis E_0 is the natural way to determine the energy calibration response of the antenna array. In this goal, after sampling the particles density at ground a NKG lateral distribution is deduced to measure the total number of charged particles N_e (mostly electrons and positrons) in the shower front. The energy E_p is deduced from the constant intensity cuts method (CIC). The procedure gives a relative error equal to 30%. The electric field E_0 is determined by the lateral distribution function (LDF). The Allan formula has been used to fit the radio LDF with an exponential law (Fig. 2) following this formula:

$$E_i = E_0 \exp \left(- \frac{\sqrt{(x_i - x_c)^2 + (y_i - y_c)^2} - ((x_i - x_c) \cos(\phi) \sin(\theta) + (y_i - y_c) \sin(\phi) \sin(\theta))^2}{d_0} \right),$$

where, θ and ϕ are respectively zenithal and azimuthal angles reconstructed by a planar fit. This fit has four free parameters E_0 , the LDF decay distance d_0 and the radio-shower core coordinates on the ground (x_c, y_c) , providing the antennas coordinates (x_i, y_i) and the radio filtered pulse amplitude E_i for each antennas. The error on E_0 has been estimated through a Monte Carlo analysis. It consist of repeating the LDF fit with E_i values, randomly selected from gaussian probability density function centred on the measured values E_i and a gaussian standard deviation σ_i took as the RMS of measured radio noise on the antenna. This Monte Carlo method enables to explore the entire phase space and thus to estimate the E_0 error on a by event basis. At the end of the procedure a statistical error less than 22 % is deduced. A linear regression is then used to deduce the

correlation coefficients in the (E_p, E_0) plan, assuming some hypothesis: (i) The two variables are represented on a linear scale. (ii) Gaussian errors are used on both observables. (iii) The two observables E_p and E_0 are assumed to be independent, to cancel the nonlinear covariance term. Results of this procedure is presented on Fig. 3.

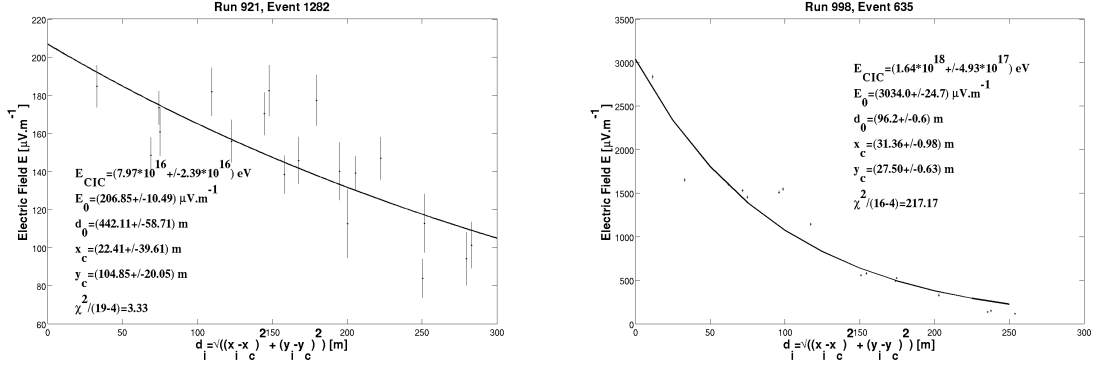


Fig. 2. Radio lateral distributions reconstructed from antenna signals. The full line show the result of an exponential law fit (Allan formula). **Left:** We show the lateral distribution of an event detected by 19 antennas. The primary particle energy is estimated to $E_p = 7.97 \cdot 10^{16}$ eV. Error bars correspond to the radio galactic background. In this example, the signal amplitudes are close to the noise level. **Right:** We show the lateral distribution of an other event, detected by 16 antennas, with larger energy $E_p = 1.64 \cdot 10^{18}$ eV. In this case, error bars are small compared to signals.

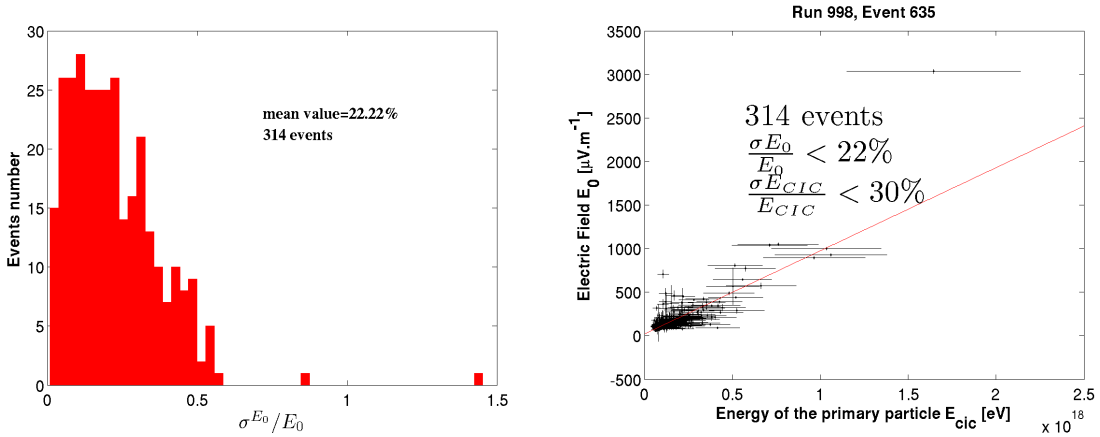


Fig. 3. Left: E_0 statistical errors $\frac{\sigma E_0}{E_0}$ histogram of the LDF fit method. **Right:** Fit of the correlation between the primary particle energy E_p and the electric field at the shower axis E_0 . This study strongly depends on both E_p and E_0 errors.

It shows that the electric field created at the shower axis E_0 is clearly correlated with the primary particle energy E_p following the relationship $E_0 = a E_p + b$. This correlation shows that the radio signal emitted by EAS seems coherent. An energy calibration relationship can be deduced, with the following form $E_R = (1/a) E_0 - (b/a)$ which allows to have a radio estimation E_R of the energy through the radio method once we have measured E_0 . It is conceivable that for a future autonomous antennas array, we can measure the primary particle energy only with a pure radio observable.

5 Radius of curvature reconstruction with CODALEMA

Because theoretical developments indicate that the radio signal shape depends on the shower longitudinal development, it is waited that the wavefront shape provides information on the nature of the primary particle. In the first step of the CODALEMA's analysis, the wavefront was assimilated to a plan determined by a simple planar fit using the arrival times and locations of each tagged antenna. More detailed studies indicates today (Fig. 4.

Left) that the measured wavefront differs slightly from the plan in most cases and that it exhibits a curved geometry, favoring the idea of a privileged center for the radio emission during the shower development (Rebai 2010; Schroder 2011). To take into account of these experimental observations, one of the simplest hypothesis is to assume that the maximum of the filtered pulse is linked to a radio signal emission center located along the shower axis. This leads to define a curvature radius R_c . Several modelisations suggest that this observable could then be related to the shower maximum, X_{max} , which is directly correlated to the UHECR chemical composition. This possibility has been investigated using the present data. Our fitting method is based on the fit of the residue between the real wavefront determined by arrivals times distribution and the planar wavefront. A parabolic dependence is used to account for the difference. Results of the calculations are presented in Fig. 4. The distribution of the R_c presents a maximum at 4 km in global agreement with the waited characteristic altitude of the emission maximum. However, the tail of the distribution extends up to 20 km. A present time, the physical interpretation of this long tail is not well understood. This may be due both to a poor estimate of arrival time and to a biased assessment of the estimated error on its time measurement, an arrival time error of 10 ns is used. Improvement of these points are underway.

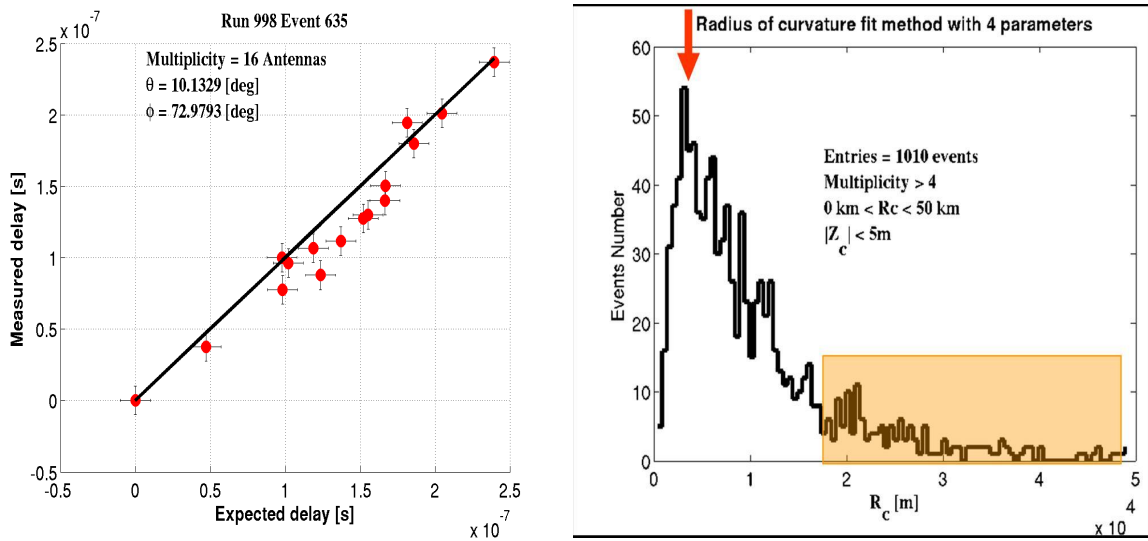


Fig. 4. Left: Expected delay versus measured delay. The black line presents the plane wave fit, Despite the 10 ns error bars on both axes, many points are located far from the line, which shows that the wavefront differs from a plane. **Right:** The histogram of the radius of curvature R_c distribution for 1010 selected events. The distribution maximum is located at 4 km.

6 Conclusions

Codalema is installed in a radio quiet environment. This advantage has enabled very high accuracy radio signal measurements and several progress in the understanding of the radio emission mechanisms like the geomagnetic field effect or the energy calibration method. A method for the wavefront radius of curvature reconstruction has been presented. The first analysis of the radius of curvature presented shows extremely interesting perspectives with the aim of determining the cosmic rays nature. The deduced location of the emission point are in a satisfactory agreement (for radii less than 10 km) with the waited values, but for the larger curvatures the values remain poorly understood. Unfortunately the low timing accuracy (<10 ns) may limit the analysis with current data. The current array extension which uses standalone radio stations to reach a larger array (1.5 km^2) will increased the available statistic and improve our interpretations.

This work has been made a part under a grant from Région Pays de la Loire. The author wishes to thank the CNRS (Centre national de la recherche scientifique) for funding his work. The author likes to thank the SF2A week organizers for their hospitality.

References

- Abbasi, R. U., Abu-Zayyad, T., Al-Seady, M., et al. 2010, *Phys. Rev. Lett.*, 104, 161101
- Abraham, J., Abreu, P., Aglietta, M., et al. 2010, *Phys. Rev. Lett.*, 104, 091101
- Allan, H. 1971, *Progress in Elementary Particles and Cosmic Ray Physics*, 10, 169
- Apel, W., Arteaga, J., Asch, T., et al. 2010, *Astroparticle Physics*, 32, 294
- Ardouin, D., Belletoile, A., Berat, C., et al. 2009, *Astroparticle Physics*, 31, 192
- Ardouin, D., Charrier, D., Dallier, R., et al. 2006, *Astroparticle Physics*, 26, 341
- Marin, V. 2011, in *International Cosmic Ray Conference ICRC*
- Ravel, O. 2010, *Nuclear Instruments and Methods in Physics Research Section A: Accelerators, Spectrometers, Detectors and Associated Equipment*,
- Rebai, A. 2010, *Proceedings Journées Jeunes Chercheurs*, 159
- Schroder, F. G. 2011, PhD thesis

OPTICAL FOLLOW-UP OF HIGH ENERGY NEUTRINOS DETECTED BY THE ANTARES TELESCOPE

M. Vecchi¹, M. Ageron¹, C. Akerlof², I. Al Samarai¹, S. Basa³, V. Bertin¹, M. Boer⁴, J. Brunner¹, J. Busto¹, D. Dornic⁵, A. Klotz⁶, F. Schüssler⁷, B. Vallage⁷ and W. Zheng²

Abstract. The ANTARES Collaboration has completed in 2008 the deployment of what is currently the largest high energy cosmic neutrino detector in the Northern hemisphere, covering a volume of about 0.01 km^3 . To enhance the sensitivity of the ANTARES detector to transient sources, such as Gamma Ray Bursts (GRBs), Core Collapse Super Novae (CCSN), flaring active galactic nuclei (AGN) and microquasars, a method based on coincident observations of neutrinos and optical signals has been set up. The observation is triggered whenever a high energy singlet or a burst of neutrinos event in space and time coincidence is detected by the ANTARES telescope: the selection of events is such that alerts are sent with a frequency of about twice per month. The system is operational since 2009 and since then, about 40 alerts have been sent to the telescopes network, about 30 of them being followed. The optical follow-up system will be described and first results on the optical images analysis searching for GRBs will be presented.

Keywords: Neutrino astronomy, Transient Sources, Optical Follow-up

1 Introduction

The production of high-energy neutrinos has been proposed for several kinds of astrophysical sources, such as gamma-ray bursts, supernova remnants, active galactic nuclei and microquasars, in which the acceleration of hadrons may occur. Transient sources offer a unique opportunity to detect high energy neutrinos, the background of atmospheric muons and neutrinos being strongly reduced in the narrow observation time window. For example, several authors predict the emission of neutrinos in correlation with multi-wavelength signals, e.g. the Fireball model of GRBs (see Piran 1999).

The ANTARES Collaboration has completed in May 2008 the deployment of a neutrino telescope that is located about 2500 meters deep, offshore Toulon, France (see Ageron 2011a). The PMTs are arranged on 12 detection lines, each comprising up to 25 triplets of PMTs (floors), regularly distributed on 350 m, the lowest floor being located at 100 m above the sea bed. The main goal of the experiment is to search for neutrinos of astrophysical origin, by detecting high energy muons ($\geq 100 \text{ GeV}$) induced by their neutrino charged current interaction in the vicinity of the detector. Due to the large background from downgoing cosmic ray induced muons, the detector is optimised for the detection of upgoing neutrino induced muon tracks.

In this paper, the implementation and the first results of a strategy for the detection of transient sources of high energy neutrinos is presented. This method, earlier proposed in Kowalski & Mohr (2007), is based on the optical follow-up of selected neutrino events very shortly after their detection by the ANTARES neutrino telescope. The alert system is known as “TAToO” (Telescopes and ANTARES Target of Opportunity) and it is described in Ageron (2011b).

¹ CPPM, CNRS/IN2P3, Université de la Méditerranée, 163 avenue de Luminy, 13288 Marseille Cedex 09, France

² Randall Laboratory of Physics, Univ. of Michigan, 450 Church Street, Ann Arbor, MI, 48109-1040, USA

³ LAM, BP8, Traverse du siphon, 133376 Marseille Cedex 12, France

⁴ OHP, 04870 Saint Michel de l’Observatoire, France

⁵ IFIC, Edificios Investigacion de Paterna, CSIC-Universitat de Valencia, Apdo. de correos 22085 Valencia, Spain

⁶ IRAP, 9 avenue du Colonel Roche, BP44346, 31028 Toulouse Cedex 4, France

⁷ CEA-IRFU, Centre de Saclay, 91191 Gif-Sur-Yvette, France

2 ANTARES neutrino alerts

Several theoretical models predict the production of high energy neutrinos with energies higher than 1 TeV from transient sources like GRBs and Core Collapse Supernovae (see for example Waxman & Bahcall 1997; Ando & Beacom 2005). Under certain conditions, multiplet of neutrinos can be expected, as discussed in Razzaque & et al. (2005). Two online neutrino trigger criteria are currently implemented in the TAToO alert system: the detection of at least two neutrino induced muons coming from similar directions within a predefined time window, and the detection of a single high energy neutrino induced muon.

A basic requirement for the coincident observation of a neutrino and an optical counterpart is that the pointing accuracy of the neutrino telescope should be at least comparable to the field of view of the optical telescopes, namely TAROT and ROTSE (see Boer & et al. 1999; Akerlof & et al. 2003), having a field of view of about $2^\circ \times 2^\circ$.

To select the events which might trigger an alert, a fast and robust algorithm is used to reconstruct the ANTARES events (see Aguilar & et al 2011). The principle is to minimize a χ^2 which compares the times of selected hits with the expectation from a Cherenkov signal of a muon track. The resulting direction of the reconstructed muon track is available within about 10 ms and the obtained minimal χ^2 is used as fit quality parameter to remove mis-reconstructed tracks. This algorithm uses a simplified detector geometry, that does not take into account the actual shape of the detector as well as the storeys orientation and lateral extension. Neutrino events selection criteria have been established on the basis of Monte Carlo simulations of both signal and background events. Figure 1 shows the angular resolution of the online algorithm as a function of the neutrino energy. This resolution is defined as the median of the space angular difference between the direction of the incoming neutrino and the reconstructed neutrino-induced muon. For neutrinos with an energy higher than a few tens of TeV, an angular resolution of 0.4 degree is achieved.

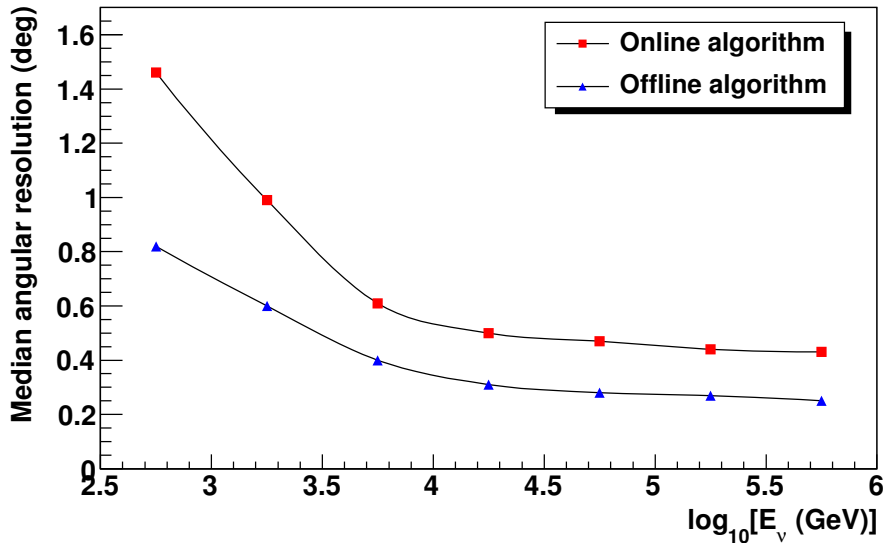


Fig. 1. Angular resolution obtained for both online and offline reconstructions as a function of the neutrino energy.

2.1 Multi-neutrino trigger

The typical signature of the transient emission of high energy neutrinos is expected to be a neutrino burst, i.e. a multiplet of neutrino events originating from the source in a short time window. A trigger for this event type is implemented as the detection of two upgoing events reconstructed with at least two lines in a 15 minutes time window with a maximum angular difference of 3° . The time window was optimized to include most predictions of the neutrino emission by various models for transient sources. The 3° angular window was selected to match the convolution of the track reconstruction angular resolution and the field of view of the robotic optical telescopes ($\approx 2^\circ \times 2^\circ$). The accidental coincidence rate due to background events, from two

uncorrelated upgoing atmospheric neutrinos, is estimated to be 7×10^{-3} coincidences per year with the full ANTARES detector. With such a small background, the detection of a doublet (triplet) in ANTARES would have a significance of about 3 (5) sigma.

2.2 High energy event trigger

Since the spectrum of cosmic neutrinos is expected to be harder than that of atmospheric neutrinos, a cut on the reconstructed energy could efficiently reduce the atmospheric neutrino background, while keeping most of the signal events. The selection of the alert candidates is based on two simple energy estimators: the number of storeys used in the track fit and the total amplitude (in photoelectrons) of the hits in the storeys.

The event selection for the high energy trigger has been tuned on atmospheric neutrinos in order to obtain a false alarm rate of about 25 alerts per year. This rate was agreed between ANTARES and the optical telescope collaborations. A requirement of at least 20 storeys on at least three lines and an amplitude greater than 180 photoelectrons will select around 25 high energy events per year (for the full configuration of the ANTARES detector). Simulations performed using an E^{-2} energy spectrum for signal events indicate energies higher than 10 TeV for the single high energy trigger. Figure 2 shows the estimation of the point spread function for a typical high energy neutrino alert. Around 70% of the events are contained in the field of view of a typical robotical telescope ($\approx 2^\circ \times 2^\circ$).

With a larger delay (few minutes after the time of the burst), an additional reconstruction algorithm is used to refine the result of the online strategy. This algorithm has been developed to search for point-like sources of high energy neutrinos (see Heijboer, A. J. 2004). Simulations indicate that, with this algorithm, ANTARES reaches an angular resolution smaller than about $0.3\text{-}0.4^\circ$ for neutrino energies above 10 TeV (curve labeled 'offline algorithm' in Figure 1).

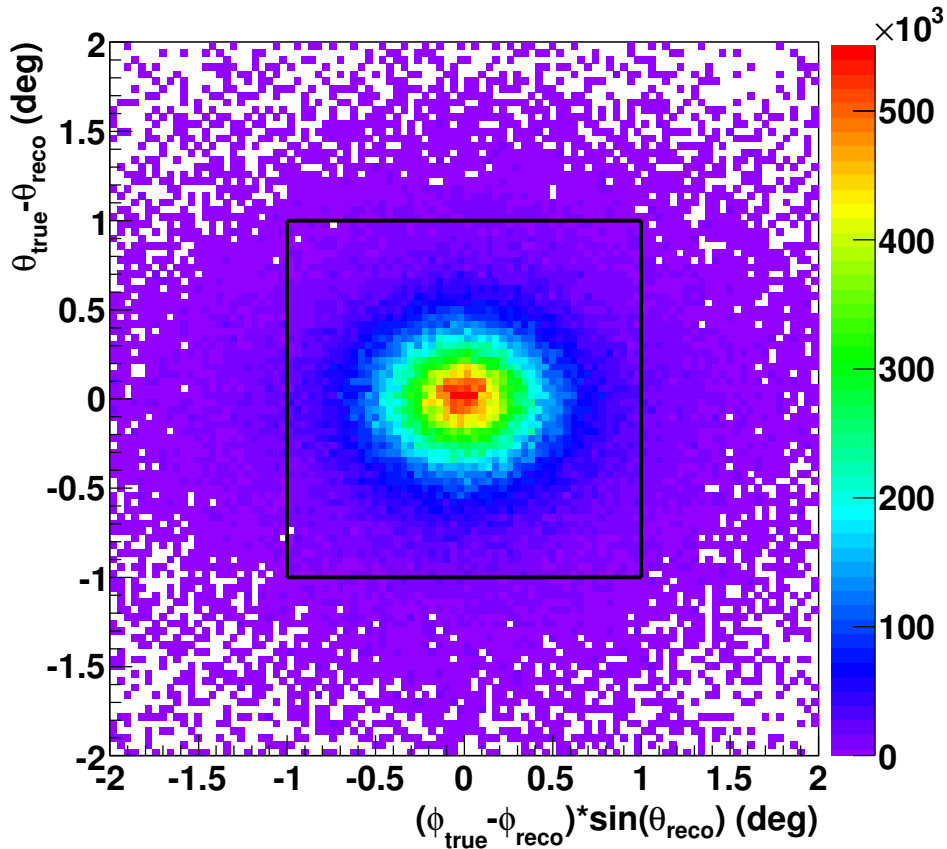


Fig. 2. Bi-dimensional angular resolution. The black square corresponds to the TAROT telescope field of view ($\approx 2^\circ \times 2^\circ$).

3 Observation strategy of the robotical telescopes

ANTARES is organizing a follow-up program in collaboration with the TAROT and ROTSE telescopes. The TAROT network is composed of two 25 cm optical robotic telescopes located at Calern (France) and La Silla (Chile). The ROTSE network is composed of four 45 cm optical robotic telescopes located at Coonabarabran (Australia), Fort Davis (USA), Windhoek (Namibia) and Antalya (Turkey). The main advantages of these instruments are the large field of view, namely about 2×2 square degrees, and their very fast positioning time (less than 10s). These telescopes are perfectly tailored for such a program. Thanks to the location of the ANTARES telescope in the Northern hemisphere (42.79 degrees latitude), all the six telescopes are used for the optical follow-up program. Depending on the neutrino trigger settings, the alert are sent at a rate of about one or two times per month. With the current settings, the connected telescopes can start taking images with a latency of the order of one minute with respect to the neutrino event (T_0).

To be sensitive to a wide range of transient sources, the TAToO observational strategy is composed of a real time observation, optimized to search for GRBs, followed by several observations during the following month, optimized to search for longer phenomena like CCSN. For the prompt observation, 6 images with an exposure of 3 minutes and 30 images with an exposure of 1 min are taken respectively by the first available TAROT and ROTSE telescopes. The integrated time has been defined in order to reach an average magnitude of about 19. For each delayed observation, six images are taken at $T_0+1, +2, +3, +4, +5, +6, +7, +9, +15, +27$ days after the trigger for TAROT (8 images for ROTSE the same days plus T_0+16 and T_0+28 days).

4 Optical image analysis

Once the images are collected, they are automatically dark subtracted and flat-fielded at the telescope site. Once the data are copied from the telescopes, an offline analysis is performed combining the images from all sites. This off-line program is composed by three main steps: astrometric and photometric calibration, subtraction between each image and a reference one and light curve determination for each variable candidates. The choice of the reference image is based on quality criteria such as the limiting magnitude and the seeing. For the GRB search, the reference is chosen amongst the follow-up observations (few days after the alert) where no GRB signal is expected anymore, while for SN search, we consider the first night observation, or we use images of an additional observation, performed few months later, to have a better quality, in absence of a SN signal.

The ROTSE pipeline has been applied to five alerts from which optical images have been recorded during the first 24 hours after the neutrino alert sending. The minimum delay between the neutrino detection and the first image is around 70 s. No object has been found for which the light curve is compatible with a fast time decreasing signal.

5 Conclusions

The method used to search for an optical counterpart of candidate neutrino events detected by the ANTARES telescope has been presented. The TAToO system is able to trigger the observation with a network of optical telescopes within one minute from the detection of the neutrino candidate, with an precision on the alert position that is better than one degree. The quasi-online availability of a refined direction further improves the quality and efficiency of the alert system.

The alert system is operational since February 2009, and as of October 2011, about 40 alerts have been sent, all of them triggered by the high energy selection criterium. No doublet trigger has been recorded yet. After a commissioning phase in 2009, almost all alerts had an optical follow-up in 2010, and the live time of the system over this year is equal to the one of the ANTARES telescope, namely 87%. These numbers are consistent with the expected trigger rate, after accounting for the duty cycle of the neutrino telescope. The image analysis of five 'prompt' observations has not permitted to discover a GRB afterglow associated to the high energy neutrino. The analysis of the rest of the images to look for the light curve of a core collapse SN is still on-going.

The optical follow-up of neutrino events significantly improves the perspective for the detection of transient sources. A confirmation by an optical telescope of a neutrino alert will not only provide information on the nature of the source but also improve the precision of the source direction determination in order to trigger other observatories (for example very large telescopes for redshift measurement). The program for the follow-up of ANTARES neutrino events is already operational with the TAROT and ROTSE telescopes and results based on analysis of the optical images will be presented in a forthcoming paper. This technique could be extended to observations in other wavelength regimes such as X-ray or radio.

This work has been financially supported by the GdR PCHE in France.

References

- Ageron, M. e. 2011a, submitted to N.I.M. A, [arXiv:1104.1607](#)
Ageron, M. e. 2011b, submitted to Astropart. Phys., [arXiv:1103.4477](#)
Aguilar, J. & et al. 2011, Astropart. Phys., 34 I9, 652
Akerlof, C. & et al. 2003, Public. Astron. Soc. Pac., 115, 132
Ando, S. & Beacom, J. 2005, Phys. Rev. Lett., 95, 061103
Boer, M. & et al. 1999, Astron. Astrophys. Suppl. Ser., 138, 579
Heijboer, A. J. 2004, PhD thesis, Amsterdam University, Amsterdam, The Netherlands
Kowalski, M. & Mohr, A. 2007, Astropart. Phys., 27, 533
Piran, T. 1999, Phys. Rept., 314, 575
Razzaque, S. & et al. 2005, Phys. Rev. Lett., 94, 109903
Waxman, E. & Bahcall, J. 1997, Phys. Rev. Lett., 78, 2292

THE GALACTIC CENTER REGION VIEWED BY H.E.S.S..

A. Viana^{1,2}

Abstract. The Galactic center region is the most active region in the Milky Way harboring a wealth of photon sources at all wavelengths. H.E.S.S. observations of the Galactic Center (GC) region revealed for the first time in very high energy (VHE, $E > 100$ GeV) gamma-rays a detailed view of the innermost 100 pc of the Milky Way and provided a valuable probe for the acceleration processes and propagation of energetic particles near the GC. H.E.S.S. has taken more than 180 hours of good-quality observations toward the GC region since the experience started in 2003. A strong and steady gamma-ray source has been detected coincident in position with the supermassive black hole Sgr A*. Besides the central pointlike source, a diffuse emission extended along the Galactic Plane has been detected within about 1° around the GC. An accurate analysis of the Galactic center region suggests that the diffuse emission may dominate highest energy end of the overall GC source spectrum. I will review the current VHE view by H.E.S.S. of the GC region and briefly discuss the theoretical models which explain VHE gamma-ray emissions of the central source and the diffuse emission.

Keywords: galactic center, gamma-ray astronomy, Sgr A*, supermassive black hole, diffuse emission, cosmic rays

1 Introduction

The Galactic Center (GC) region harbours a variety of potential sources of high-energy radiation including the supermassive black hole Sagittarius (Sgr) A* of $2.6 \times 10^6 M_\odot$ (Schodel et al. 2002), and a number of supernova remnants, among them the Sgr A East remnant of a giant supernova explosion which happened about 10000 years ago. The Galactic Center was therefore a prime target for observations with Imaging Atmospheric Cherenkov telescopes (IACTs), and detection of very high energy (VHE, $E > 100$ GeV) gamma rays was reported by The CANGAROO (Tsuchiya et al. 2004), VERITAS (Kosack et al. 2004), H.E.S.S. (Aharonian et al. 2004) and MAGIC (Albert et al. 2006) from the direction of the Galactic Center (GC). The nature of this source is still unknown. The H.E.S.S. observations of the GC region led to the detection of a point-like source of VHE gamma-rays at the gravitational center of the Galaxy (HESS J1745-290), compatible with the positions of the supermassive black hole Sgr A*, the supernova remnant (SNR) Sgr A East, and the plerion G359.95-0.04. A larger exposure of the region in 2004 revealed a second source: the supernova remnant G0.9+0.1 (Aharonian et al. 2005). The subtraction of these two sources revealed a ridge of diffuse emission extending along the Galactic plane for roughly 2° (Fig. 1).

2 The H.E.S.S. instrument

The H.E.S.S. (High Energy Stereoscopic System) experiment is an array of four identical imaging atmospheric Cherenkov telescopes located in the Khomas Highland of Namibia ($23^\circ 16' 18''$ South, $16^\circ 30' 00''$ East) at an altitude of 1800 m above sea level. Each telescope has an optical reflector consisting of 382 round facets of 60 cm diameter each, yielding a total mirror area of 107 m^2 . The Cherenkov light, emitted by charged particles in the electromagnetic showers initiated by primary gamma rays, is focused on cameras equipped with 960 photomultiplier tubes, each one subtending a field-of-view of 0.16° . The large field-of-view ($\sim 5^\circ$) permits survey coverage in a single pointing. The direction and the energy of the primary gamma rays are reconstructed by the stereoscopic technique.

¹ CEA, Irfu, Centre de Saclay, F-91191 Gif-sur-Yvette, France

² on behalf of the H.E.S.S. collaboration

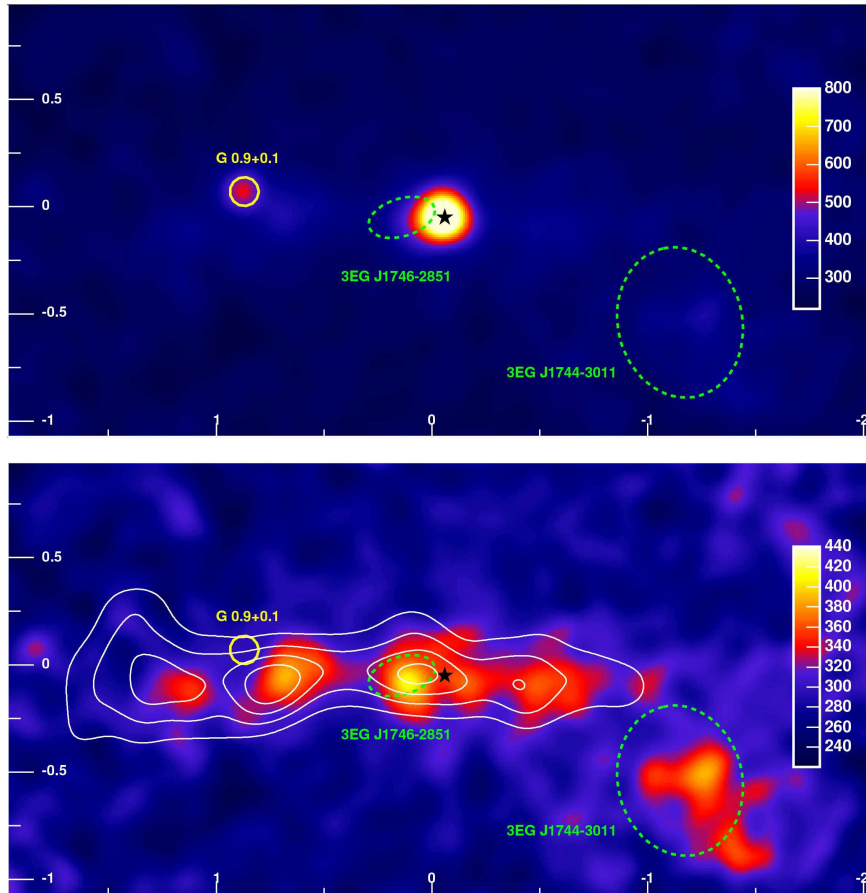


Fig. 1. VHE gamma-ray images of the GC region. Top: gamma-ray count map, bottom: the same map after subtraction of the two dominant point sources, showing an extended band of gamma-ray emission. White contour lines indicate the density of molecular gas, traced by its CS emission. The position and size of the composite SNR G0.9+0.1 is shown with a yellow circle. The position of Sgr A* is marked with a black star. Figure extracted from Aharonian et al. (2006).

3 HESS J1745-290: counterparts and spectrum

In December 2004, H.E.S.S. reported the detection of VHE gamma rays from the center of our Galaxy, at the time based on data obtained with the first two H.E.S.S. telescopes during 16h of observations in 2003. Within the – at the time unprecedented – precision of $30''$ in RA and Dec, the location of the source HESS J1745-290 was consistent with the Galactic gravitational center, and the spectrum of gamma rays was consistent with a power law up to 10 TeV. Towards identifying the origin of the gamma rays, a multi-year effort was invested aimed at improving the pointing position of the H.E.S.S. telescopes. After a careful investigation of the pointing systematics of the H.E.S.S. telescopes, the systematic error on the centroid position was reduced from $30''$ to $6''$ per axis, with a comparable statistical error – by far the best source location achieved in gamma rays so far (Acero et al. 2010). The thus determined source position is within $8'' \pm 9''_{\text{stat}} \pm 9''_{\text{sys}}$ from Sgr A*, well consistent with the location of the black hole and the pulsar wind nebula (PWL) G359.95-0.04, but it excludes Sgr A East remnant as the main counterpart of the VHE emission at the level of $5-7\sigma$, depending on the assumed position of the VHE emission in Sgr A East (Fig. 2, left; see Acero et al. 2010, for more details).

Using 93h of data on the central source accumulated in the years 2004, 2005 and 2006, the energy spectrum of the gamma rays was measured with high precision, revealing an energy break or cutoff in the spectrum around 15 TeV (Fig. 2, right). No signs of variability has been found (Aharonian et al. 2009). Different mechanisms have been suggested to explain the broadband spectrum of the GC. Firstly, the stochastic acceleration of electrons interacting with the turbulent magnetic field in the vicinity of Sgr A*, as discussed by Liu et al. (2006), has been advocated to explain the millimeter and sub-millimeter emission. This model would also reproduce the IR

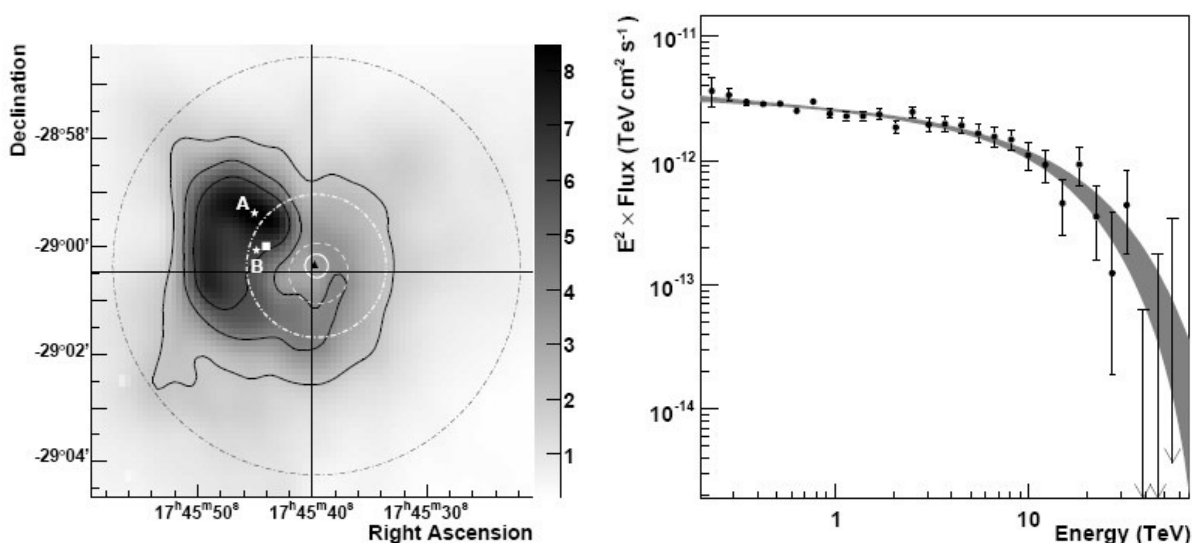


Fig. 2. Left: 90 cm VLA radio flux density map of the innermost 20 pc of the GC, showing emission from the supernova remnant Sgr A East. The crossing lines show the position of the Galactic Center Sgr A*. The 68% CL error contour for the position of the gamma ray source HESS J1745-290 is given by the small white circle. The white stars marked A and B denote the position of the radio maximum and the centroid of a radio emission from Sgr A East, respectively. Figure extracted from Acero et al. (2010). **Right:** Energy spectrum of gamma rays from HESS J1745-290 as determined from the data sets obtained in the years 2004, 2005 and 2006. The shaded band shows the best fit to data for a power law with an exponential cutoff. Figure extracted from Aharonian et al. (2009).

and X-ray flaring. In addition, it assumes that charged particles are accreted onto the black hole, and predicts the escape of protons from the accretion disk and their acceleration (Liu et al. 2006). These protons produce π^0 mesons by inelastic collisions with the interstellar medium in the central star cluster of the Galaxy. The cut-off energy found in the gamma-ray spectrum could reflect a cut-off $E_{cut,p}$ in the primary proton spectrum. In that case, one would expect a cut-off in the gamma-ray spectral shape at $E_{cut} \simeq E_{cut,p}/30$. The measured value of ~ 15 TeV would correspond in this scenario to a cut-off energy in the primary proton spectrum between 100-400 TeV depending on the strength of the exponential cut-off. Energy-dependent diffusion models of protons to the outside of the central few parsecs of the Milky Way (Aharonian & Neronov 2005) are alternative plausible mechanisms to explain the TeV emission observed with the H.E.S.S. instrument. They would lead to a spectral break as in the measured spectrum due to competition between injection and escape of protons outside the vicinity of the GC.

4 The diffuse emission from the Galactic Center Ridge

In order to search for much fainter emission, an analysis of the GC region was made (Aharonian et al. 2006) subtracting the best fit model for point-like emission at the position of HESS J1745-290 and the SNR G0.9+0.1. Two significant features are apparent after subtraction: extended emission spatially coincident with the unidentified EGRET source 3EGJ1744-3011 and emission extending along the Galactic plane for roughly 2° . The latter emission is not only clearly extended in longitude l , but also significantly extended in latitude b (beyond the angular resolution of H.E.S.S.) with a characteristic root mean square (rms) width of 0.2° , as can be seen in Fig. 1. The reconstructed gamma-ray spectrum for the region $-0.8^\circ < l < 0.8^\circ$, $|b| < 0.3^\circ$ (with point-source emission subtracted) is well described by a power law with photon index $\Lambda = 2.29 \pm 0.07_{stat} \pm 0.20_{sys}$ (Fig. 3).

Given the plausible assumption that the gamma-ray emission takes place near the center of the Galaxy, at a distance of about 8.5 kpc, the observed rms extension in latitude of 0.2° corresponds to a scale of ≈ 30 pc. This value is similar to that of interstellar material in giant molecular clouds in this region, as traced by their CO emission and in particular by their CS emission (Tsuboi et al. 1999). At least for $|l| < 1^\circ$, a close match between the distribution of the VHE gamma-ray emission and the density of dense interstellar gas is found (see Aharonian et al. 2006, for more details). The close correlation between gamma-ray emission and

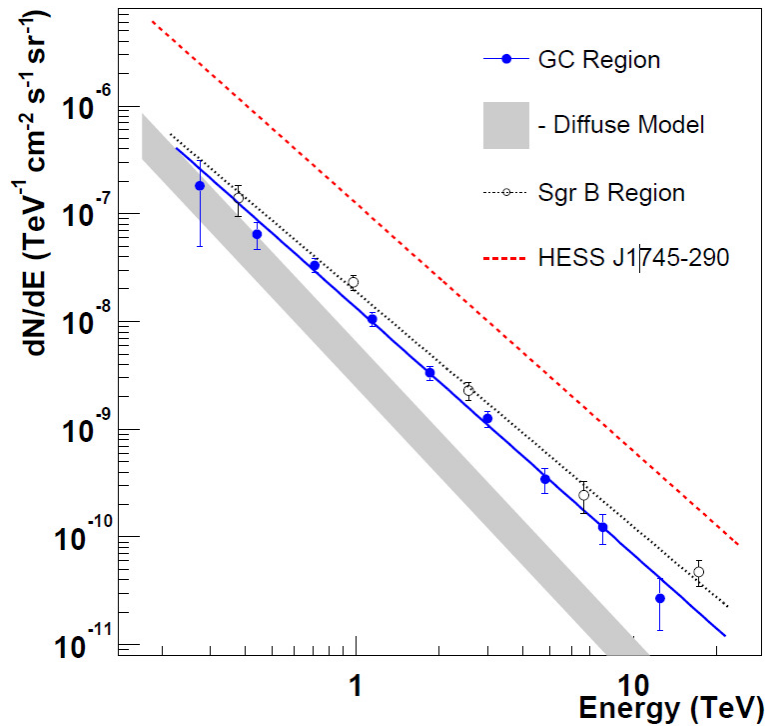


Fig. 3. Gamma-ray flux per unit solid angle in the GC region (data points), in comparison with the expected flux assuming a cosmic-ray spectrum as measured in the solar neighbourhood (shaded band). The strongest emission away from the bright central source HESS J1745-290 occurs close to the Sagittarius B complex of giant molecular clouds. The energy spectrum of this region is shown using open circles. The 2006 spectrum of the central source HESS J1745-290 is shown for comparison (using an integration radius of 0.14°). Figure extracted from Aharonian et al. (2006).

available target material in the central 200 pc of our galaxy is a strong indication for an origin of this emission in the interactions of CRs. The hardness of the gamma-ray spectrum and the conditions in those molecular clouds indicate that the cosmic rays giving rise to the gamma-rays are likely to be protons and nuclei rather than electrons. Since in the case of a power-law energy distribution the spectral index of the gamma-rays closely traces the spectral index of the CRs themselves, the measured gamma-ray spectrum implies a CR spectrum near the GC with a spectral index close to 2.3, significantly harder than in the solar neighbourhood (where an index of 2.75 is measured). Given the probable proximity and young age of particle accelerators, propagation effects are likely to be less pronounced than in the Galaxy as a whole, providing a natural explanation for the harder spectrum which is closer to the intrinsic CR-source spectra. In addition, the key experimental facts of a harder than expected spectrum, and a higher than expected TeV flux, imply that there is an additional young component to the GC cosmic-ray population above the CR 'sea' which fills the Galaxy. This is the first time that such direct evidence for recently accelerated (hadronic) CRs in any part of our galaxy has been found.

The observation of a deficit in VHE emission at $l = 1.3^\circ$ relative to the available target material (see Fig. 2, bottom) suggests that CRs, which were recently accelerated in a source or sources in the GC region, have not yet diffused out beyond $|l| = 1^\circ$. Therefore the central CRs accelerators would only have been active in the GC for the past 10,000 years. The fact that the diffuse emission exhibits a photon index which is the same – within errors – as that of HESS J1745-290 suggests that the underlying astrophysical emitter of HESS J1745-290 could be the source in question. Within the $1'$ error box of HESS J1745-290 are two compelling candidates for such a CR accelerator. The first is the SNR Sgr A East with its estimated age around 10 kyr. The second is the supermassive black hole Sgr A* which may have been more active in the past (Aharonian & Neronov 2005).

5 Conclusions

Observations with H.E.S.S. provide a very sensitive view of this interesting region. With the recent data from the H.E.S.S. instrument, a rich VHE gamma-ray morphology becomes evident, giving strong indication for the

existence of a cosmic ray accelerator within the central 10 pc of the Milky Way. Future observations with more sensitive instruments such as CTA will significantly improve our knowledge about the GC region at VHE energies.

References

- Acero, F. et al. 2010, MNRAS, 402, 1877
Aharonian, F. & Neronov, A. 2005, *Astrophys.J.*, 619, 306
Aharonian, F. et al. 2004, *Astron.Astrophys.*, 425, L13
Aharonian, F. et al. 2005, *Astron.Astrophys.*, 432, L25
Aharonian, F. et al. 2006, *Nature*, 439, 695
Aharonian, F. et al. 2009, *Astron.Astrophys.*, 503, 817
Albert, J. et al. 2006, *Astrophys.J.*, 638, L101
Kosack, K. et al. 2004, *Astrophys.J.*, 608, L97
Liu, S.-M., Melia, F., Petrosian, V., & Fatuzzo, M. 2006, *Astrophys.J.*, 647, 1099
Schodel, R., Ott, T., Genzel, R., et al. 2002, *Nature*, 419, 694
Tsuboi, M., Handa, T., & Ukita, N. 1999, *ApJS*, 120, 1
Tsuchiya, K. et al. 2004, *Astrophys.J.*, 606, L115

Session 15

Gravitation, reference, astronomy, and metrology
(AS-GRAM)

UPDATED ORBIT OF APOPHIS WITH RECENT OBSERVATIONS

D. Bancelin¹, F. Colas¹, W. Thuillot¹, D. Hestroffer¹ and M. Assafin²

Abstract. Asteroid Apophis (previously designed 2004 MN4) was first discovered in June 2004. From its first observations, Apophis was revealed to be a special study case in as much as, it reached the level 4 of Torino scale with a high probability of collision in 2029. New observations eliminated all danger for 2029. But, because of a deep close encounter in 2029 (~38000 km), the asteroid will be put on a chaotic-like orbit and some risks of collision in 2036 occur if the asteroid goes through a very small region called keyhole. Now, its orbit is quite well known and thanks to additional observations, the risk for the short term seems to disappear. But what about the long term? As far as the Earth-impact threat study is concerned, the deep 2029-close encounter is an opportunity for space missions towards Apophis. With our technologies, to deflect an asteroid, we can only act from the source. Many deflection missions were studied, from the hardest (nuclear weapons), to the softest (shadow mission). But in order to prepare such missions, we have to be sure that the asteroid is really on an impact trajectory. Moreover, if it is the case, we have to be sure that it won't be put on the trajectory of other keyholes. To this aim, we need a good knowledge of the 2029 region uncertainty and we will analyse the impact of the new observations of March 2011.

Keywords: PHAs, Apophis, b-plane, keyhole, ellipse uncertainty, astrometry

1 Introduction

Near-Earth Asteroids (NEAs) are objects orbiting near the Earth orbit. They are transient bodies that come from the Main Belt Asteroids (MBA). They are generally transported through an interplay of collisions, non-gravitational forces drift and secular resonance, among other sources. NEAs are generally classified into four dynamical families: the Apollos and Atens asteroids that cross twice the orbit of the Earth; the Amors and Atras which orbiting respectively above and under the Earth's orbit. Among those four categories, some of them can become threatening for the Earth. They are called Potentially Hazardous Asteroids (PHAs) because they can come very close to the Earth. Those objects are characterized by a MOID < 0.05 AU (Minimum Orbit Intersection Distance (Gronchi 2005)) which acts as a warning indicator and an absolute magnitude $H < 22$. Objects in this category will be under surveillance and will need special monitoring.

Among the known PHAs, asteroid (99942) Apophis is the more emblematic. It belongs to the Aten family and it is the closest approacher to the Earth in as much as it will pass at about 38000 km from the Earth's center in April 2029. It will pass below the position of geosynchronous orbit and will be visible to naked eye. Apophis became a study case since its discovery in that, it remained dangerous for few days because of a possible impact with the Earth in 2029, with an unprecedented probability estimated to 2.7%. Since, additional observations ruled out every possibility of impact in 2029 but others remain in the future. The most popular one is the 2036-threat, but at the epoch of October 7th 2009, chances of crashing were estimated at 1/250000 by the Sentry/JPL website*.

The last observation of Apophis was done in 2008. After a long period of unfavorable conditions for observations, Apophis has been re-observed in March 2011 at Pic du Midi observatory (French Pyrenean) and Magdalena Ridge Observatory (New Mexico). We report here the new orbit obtained from the adjustment of all data available at MPC[†] and new sketch of impacts for the next century. We will also discuss on other sources of uncertainty remaining on Apophis's orbit.

¹ Institut de Mécanique Céleste et de Calcul des Éphémérides, 77 Avenue Denfert-Rochereau 75014 Paris, France

² Universidade Federal do Rio de Janeiro, Observatorio do Valongo, Ladeira Pedro Antonio 43, CEP 20.080 - 090 Rio De Janeiro RJ, Brazil

*<http://neo.jpl.nasa.gov/risk/>

†<http://www.minorplanetcenter.net/>

2 2029-close encounter study

During the 2029-close encounter, the gravitational perturbation of the Earth will be so important that the trajectory of Apophis will be very altered. As a matter of fact, the perturbation will be so deep that Apophis will move from the Aten (defined by the semi-major axis $a < 1.0$ and aphelion $Q > 0.983$) to the Apollo family (defined by $a > 1.0$ and perihelion $q \leq 1.017$) (Fig. 1).

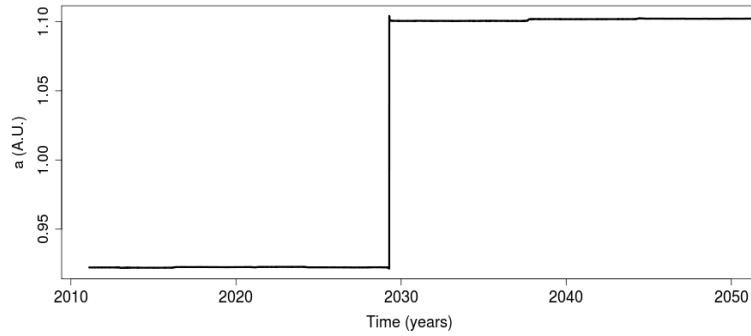


Fig. 1. Time evolution of the semi-major axis of Apophis. The deep close encounter in 2029 will lead to a dynamical change on Apophis's dynamic. It will go from the Aten family ($a < 1.0$) to the Apollo family ($a > 1.0$).

Because of this strong deflection, Apophis 2029-post orbit will be chaotic-like. As a matter of fact, a small change on the initial orbital elements or on the dynamical model used will lead to a certain uncertainty on Apophis's location after 2029. We do expect both asteroid and the Earth to meet again in the future after k revolution of Apophis around the Sun and after h years. Those encounters are called *resonant return* (Valsecchi et al. 2003) and are defined by:

$$k \times T_{ap} = h \times T_{\oplus}$$

where T_{ap} is the 2029-post period of Apophis and T_{\oplus} the period of the Earth. Using this relation, we can find the date of resonant return and the 2029-post period range of Apophis associated. Tab. 1 shows some resonant returns some years after the encounter.

Table 1. Resonant returns after the 2029-close approach. The period range correspond to the 2029-post period that Apophis should have in order to meet Earth again.

Year	Resonance	2029-post period range [days]
2034	4:5	[456.2:456.9]
2035	6:5	[437.9:438.6]
2036	7:6	[425.7:426.5]
2037	8:7	[417.1:417.8]
2038	9:8	[410.5:411.3]
2046	17:15	[413.6:414.3]
2048	19:17	[407.9:408.6]
2051	22:19	[422.5:423.3]

As observations contain errors (assumed as gaussian), the orbital elements obtained from the least-squares method will be given with their uncertainties provided by the covariance matrix. This matrix gives the 6-dimensions region of confidence of the orbital elements. When this region is small, this region can be approximate to an ellipsoid. When propagating this covariance matrix, it is possible to estimate the uncertainty related to the distance of closest approach in 2029. To better represent this uncertainty, we can study the geometry of

the close encounter in the b-plane[‡] (Valsecchi et al. 2003). This plane better represents the state of an asteroid approaching the Earth. It passes through the Earth's center and is perpendicular to the geocentric velocity of the asteroid. Thus, the object will have two geocentric coordinate (ξ, ζ) and the projection of the ellipsoid uncertainty in this plane is an ellipse centered on the nominal value of (ξ, ζ) . Its semi-major and semi-minor axis are given respectively by the $3\sigma_\zeta$ and $3\sigma_\xi$ standard deviations. Thus, the distance of closest approach is given by $\sqrt{\xi^2 + \zeta^2}$. Besides, while some resonant returns lead only to close approaches, others can lead to collision. Using Monte Carlo technique for sampling virtual asteroids (VAs) in the region of confidence, each VAs propagated can become virtual impactors (VIs) if they can reach a distance close or less to the Earth radius. To estimate the risk of collision, it is thus possible to find the region in the sky where all VIs have to pass in order to collide the Earth in the future. Those regions are called *keyholes*. They are narrow regions and the most famous keyhole of Apophis is the 600 meters 2036-keyhole. Keyholes can be primary when they are the consequence of one close encounter, and secondary when they are the consequences of two consecutive close encounters. VIs can also impact at both ascending or descending node. Thus, it is possible to map the uncertainty region and the location of the keyholes' center in the 2029-b-plane. Fig. 2 shows the 3σ ellipse uncertainty which size is $(3\sigma_\xi; 3\sigma_\zeta) = (12; 73)$ km. The distance of close approach is ~ 38080 km and the position of keyholes are also indicated.

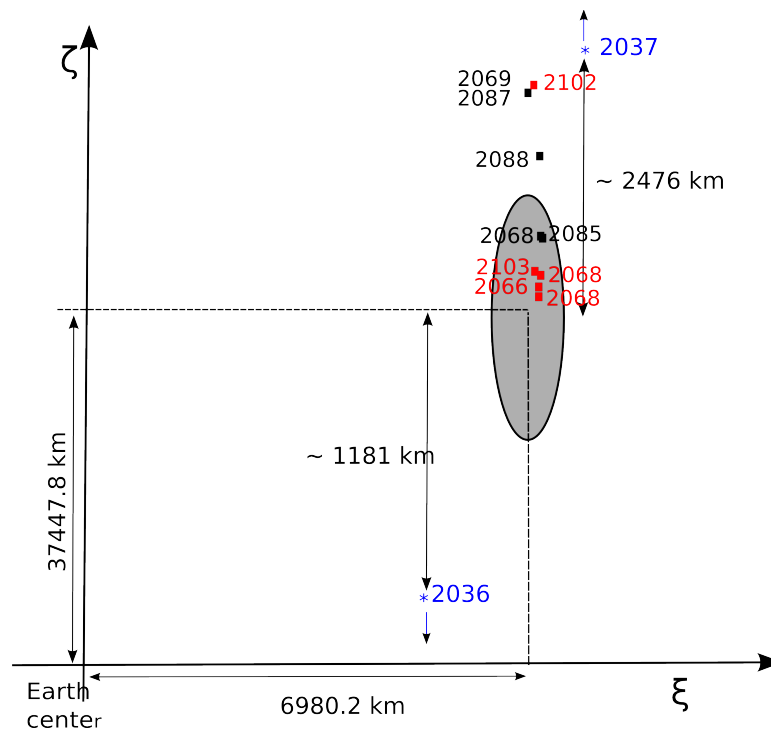


Fig. 2. 2029-b-plane of Apophis. The coordinates of the ellipse's center are indicated as well as the location of the center of primary (★) and secondary keyholes leading to collision at ascending node (■) and descending node (■). The position of the famous 2036-keyhole is also indicated.

The size of the ellipse uncertainty, its position and the location of keyholes depend on the observations available, their accuracy and the data arc length. Of course, keyhole have fixed position and when new observational data are added, the position of the ellipse can shift and thus get closer or go away from some keyholes. The next section will treat this case for the new optical data of March 2011. The dynamical model used for all computations includes all planets, the Moon, relativistic perturbations and the gravitational perturbations of Ceres, Pallas, and Vesta. The numerical integration was performed with a Lie series integrator (Bancelin et al. 2011).

[‡]Also called target plane

3 Observations of March 2011

Apophis was observed at Pic du Midi Observatory located in the French Pyrenean mountain (altitude 2800 m) with a 1meter telescope. The conditions of observation were quite challenging because, the asteroid was visible in the sky with a magnitude of 21 with a high velocity ~ 2.7 arcsec/min and according to the IMCCE website[§], the solar elongation was around 49° . A preliminary astrometry of the CCD images was made using Astrometrica Tool[¶] and the mostly used USNO-B1.0 catalog was chosen for the positions reduction. A new orbital solution and covariance matrix was thus provided using OrbFit package^{||} and thus, the propagation of this new solution and the matrix will give us the new position of the asteroid and the ellipse uncertainty in the 2029-b-plane. On Fig. 3 are represented both ellipses computed without March 2001 data (blurred ellipse) and with March data (solid ellipse). One can see that the new ellipse is upper-shifted and there is no overlap between those ellipses. As a matter of fact, our results show that Apophis seems to pass ≈ 600 km further that the distance previously computed. Besides, those new observations enable to reduce the uncertainty of the ellipse which size is $(3\sigma_\xi; 3\sigma_\zeta) = (9; 46.5)$ km.

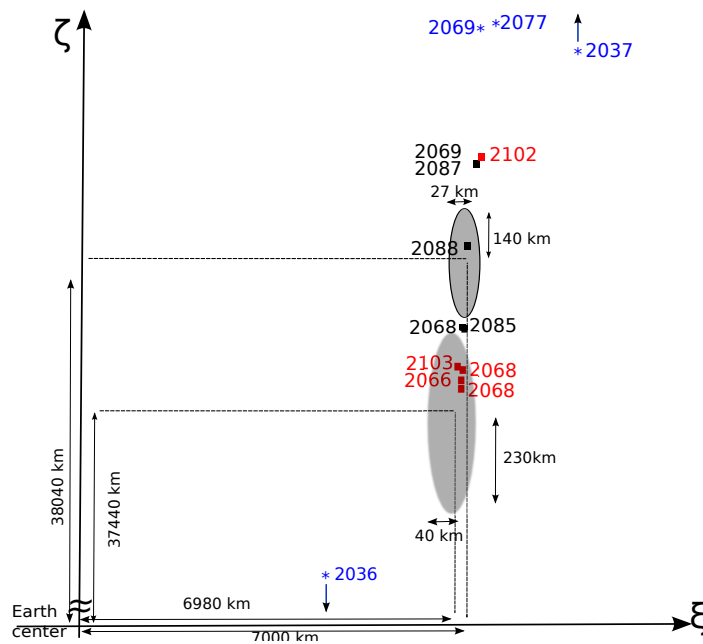


Fig. 3. 2029-b-plane of Apophis. The blurred ellipse was computed using data spanning 2004-2008 and the solid one was computed using 2004-2008 data and March 2011 observations.

Because of this, Apophis seems to move away from 2036-keyhole and to get closer to 2037-keyhole. The new relative positions of those keyholes are indicated in Tab. 2.

Table 2. Relative positions of 2036 and 2037 keyholes from the nominal ellipse center, without and without March 2011 observations.

	Without March data	With March data
2036	1181 km	1781 km
2037	2476 km	1875 km

This new scenario gives a new sketch for impact probabilities because of the vicinity of other keyholes. Tab. 3 gives the relative distance of the center of the closest keyholes from the center of the ellipse as well as there size

[§]<http://www.imcce.fr>
[¶]<http://www.astrometrica.at/>
^{||}<http://adams.dm.unipi.it/orbfit/>

(when it can be determined) and the related impact probability. When the size is set to < 1 it means that only one impact point has been found.

Table 3. Position of the closest keyholes from the center of the ellipse uncertainty. Their size are also indicated as well as their impact probabilities. The color code is the same as on Fig. 1

	Distance from ellipse center (km)	Keyhole size (m)	Impact probability
2068	250	< 1	9.5e-08
2068	500	40	1.1e-06
2069	355	90	1.6e-06
2069	700	110	1.0e-06
2077	730	65	9.5e-08
2085	250	< 1	9.5e-08
2087	355	< 1	9.5e-08
2088	42	< 1	9.5e-08

4 Uncertainties

Those results can raise some questions. Because of the lack of overlap between the two ellipses, we can wonder if strong non-gravitational forces do not act on this asteroid or if other sources of uncertainty remains on its orbit.

4.1 Yarkovsky effect

The main non-gravitational effect acting on small bodies is Yarkovsky effect (Vokrouhlický et al. 2000). Yarkovsky effect leads to a variation of the semi-major axis in a long timescale: Because of the difference of temperature at the surface of the asteroid, the infrared emission, from the surface, of the absorbed solar radiation is anisotropic. This leads to a recoil force affecting the orbital motion of the asteroid. The main effect lies on a secular drift of the semi-major axis (increasing or decreasing depending on the value of the spin obliquity). Objects with diameter ≤ 20 km are sensitive to Yarkovsky effect. Its impact on Apophis's orbit has already been studied in Chesley (2006) and Giorgini et al. (2008). Those authors concluded on a displacement on the position of Apophis in 2029 at about 300 km in distance. But, regarding our results, Yarkovsky alone can not explain the shift of ~ 600 km in distance in 2029.

4.2 Catalog biases

Chesley et al. (2010) showed that biases exist in stellar catalog, especially in the widely used USNO-B1.0 catalog (used for our astrometric reduction) and proposed a method to remove them from astrometric measurements. This method has been recently implemented in the OrbFit package in order to remove the biases in (α, δ) . An exercise has to be done in order to estimate the impact of such treatment using the new observations.

5 Conclusions

The new observations of March 2011 enable to rule out the possibility of collision with the Earth in 2036. But the important shift found allow us to think that strong non gravitational forces act on this asteroid. Besides, some other uncertainties may participate in this moving. As mentioned in the previous section, a debiased treatment has to be done on the astrometric data. Other areas may also be exploited. We can consider an other independent software for the astrometric reduction and also an improvement of the dynamical model used (i.e. including J_2 or J_4 of the Earth).

The authors are grateful to F. Vachier and M. Birlan for the astrometric reduction of Apophis's observations and also to L. Magana, undergraduate trainee at IMCCE for her work on the observations planning.

References

- Bancelin, D., Hestroffer, D., & Thuillot, W. 2011, *Celestial Mechanics*, submitted
- Chesley, S. R. 2006, in *IAU Symposium*, Vol. 229, *Asteroids, Comets, Meteors*, ed. L. Daniela, M. Sylvio Ferraz, & F. J. Angel, 215–228
- Chesley, S. R., Baer, J., & Monet, D. G. 2010, *Icarus*, 210, 158
- Giorgini, J. D., Benner, L. A. M., Ostro, S. J., Nolan, M. C., & Busch, M. W. 2008, *Icarus*, 193, 1
- Gronchi, G. F. 2005, *Celestial Mechanics and Dynamical Astronomy*, 93, 295
- Valsecchi, G. B., Milani, A., Gronchi, G. F., & Chesley, S. R. 2003, *A&A*, 408, 1179
- Vokrouhlický, D., Milani, A., & Chesley, S. R. 2000, *Icarus*, 148, 118

RELATIVISTIC ASTROMETRY AND TIME TRANSFER FUNCTIONS

S. Bertone¹ and C. Le Poncin-Lafitte¹

Abstract. Given the extreme accuracy reached by future space astrometry missions, one needs a global relativistic modeling of observations. Indeed, a consistent definition of the astrometric observables in the context of General Relativity is essential to find unique stellar coordinates. This is usually done explicitly by solving the null geodesic equations which describe the trajectory of a photon from its emission by a celestial object to its reception by a moving observing satellite. However, we show here that this task can be avoided if one uses the recently developed formalism of the time transfer functions. We describe a possible approach to the reconstruction of the source coordinates from the knowledge of the reception coordinates with this new method.

Keywords: space astrometry, relativity

1 Introduction

Future space astrometry missions, such as Gaia (Perryman et al. 2001; Bienayme & Turon 2002) and SIM, will provide large astrometric catalogs with some microarcseconds (μas) accuracy on positions, parallaxes and proper motions of celestial objects. However it is nowadays well known that μas astrometry requires a precise relativistic modeling of astrometric parameters. Several of these modelings have been developed during the last decade, such as GREM (Klioner 2003) or RAMOD (de Felice et al. 2006), and they are based on the determination of the light trajectory from the emitting celestial object up to the observing satellite by solving the null geodesic equations. However it has been recently demonstrated that this task is not mandatory and can be replaced with advantages by another approach based on the calculation of the time transfer functions (Le Poncin-Lafitte et al. 2004; Teyssandier & Le Poncin-Lafitte 2008). In this article we illustrate how to build an astrometric modeling with the use of this alternative formalism.

This paper is organized as follows. In section 2 we give the notations used in this article. In section 3 we set up the astrometric problem by introducing a moving observer receiving a light ray from a distant celestial object. Then in section 4, we give the expression of the covariant components of a tangent vector to the light ray received by the observer. In section 5 we deal with the expression of Solar System's gravitational potential, a key point to calculate the light deflection. By introducing a *three zones* modeling, we show how to take into account the motion of planets during the propagation of the light ray from an emitting star to the observing satellite. Finally, we present some concluding remarks in section 6.

2 Notations and conventions

Throughout this work, c is the speed of light in vacuum and G is the Newtonian gravitational constant. The Lorentzian metric of space-time V_4 is denoted by g . We adopt the signature $(+ - - -)$. We suppose that space-time is covered by some global coordinates system $x^\alpha = (x^0, \mathbf{x})$, with $x^0 = ct$ and $\mathbf{x} = (x^i)$, centered on the Solar System barycenter. Greek indexes run from 0 to 3, and Latin indexes from 1 to 3. Moreover, we assume that the curves of equations $x^i = \text{const}$ are timelike, at least in the neighborhood of the chosen observer. This condition means that $g_{00} > 0$ in the vicinity of the observer. Any ordered triple is denoted by a bold letter. In order to distinguish the triples built with the spacelike contravariant components of a vector from the ones built with covariant components, we systematically use the notation $\mathbf{a} = (a^1, a^2, a^3) = (a^i)$ and $\underline{\mathbf{b}} = (b_1, b_2, b_3) = (b_i)$.

¹ Observatoire de Paris - SYRTE, CNRS/UMR8630, 77 Av. de l'Observatoire, 75014 Paris, France

3 Set up of the astrometric problem

Let us consider a timelike observer. Along its worldline we introduce a comoving tetrad of four vectors $E_{\hat{\mu}}^{\alpha}$ where index (μ) is only the tetrad index running from 0 to 3, to enumerate the four 4-vectors, while index α is a normal tensor index. We postulate that $E_{(0)}^{\alpha}$ is a timelike vector strictly equal to the unit four-velocity u^{α} of the satellite. When the observer receives a light ray from a distant object, one can characterize its spacetime direction by a null vector $k^{\mu} = (k^0, k^i)$ tangent to the incoming light ray. Its unit spacelike direction \tilde{k}^{μ} relative to the hyperplane orthogonal to u^{α} is then given by (Teyssandier & Le Poncin-Lafitte 2006)

$$\tilde{k}^{\mu} = \frac{k^{\mu}}{u^{\nu}k_{\nu}} - u^{\mu}. \quad (3.1)$$

It is now straightforward to calculate the three director cosines $\cos \phi_{(a)}$ formed by each spacelike vector $E_{(a)}^{\alpha}$ (here index (a) runs from 1 to 3) with \tilde{k}^{μ} , as follows

$$\cos \phi_{(a)} = -\frac{E_{(a)}^0 + \hat{k}_i E_{(a)}^i}{u^0 (1 + \hat{k}_i \beta^i)}, \quad (3.2)$$

where $\beta^i = v^i/c$, v^i being the coordinate velocity of the observer, and $\hat{k}_i = k_i/k_0$ will be called in the following the deflection functions. We immediately deduce from equation (3.2) that the knowledge of the ratio k_i/k_0 fully characterizes the light ray at the reception point and so it is mandatory to determine completely the astrometric director cosines. However, most of relativistic modelings are dealing with an explicit integration of the light ray equations to calculate this ratio, even if these calculations may be very complicated. Thus, our purpose is now summarized by this question: *if we do not determine the light ray trajectory from its emission to its reception, what can we do instead?* The answer lies in the basic properties of a null geodesic connecting two point-events, in particular the relationship between time delay and deflection of light.

4 The covariant components of the tangent vector

Let us consider that spacetime is globally regular with the topology $\mathbb{R} \times \mathbb{R}^3$ and that it is without horizon, which is admissible in the context of practical space astrometry within the Solar System. Henceforth, we are working with a barycentric coordinates system (BCRS). In this section, we consider only one deflecting body of spatial position \mathbf{x}_p and we suppose the existence of a unique light ray connecting two point-events $x_A = (ct_A, \mathbf{x}_A)$ and $x_B = (ct_B, \mathbf{x}_B)$. By convention x_A and x_B denote the emission point and the reception point of the photon, respectively. In addition we put $R_{AB} \equiv R = |\mathbf{x}_B - \mathbf{x}_A|$ as illustrated in figure 1.

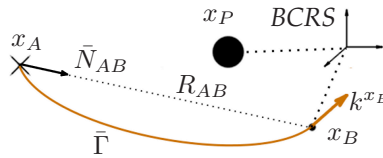


Fig. 1. Illustration of a light deflection experiment.

Working at the post-Newtonian approximation of General Relativity and considering the metric tensor recommended by the International Astronomical Union (Soffel et al. 2003), we obtained an expression of the deflection functions \hat{k}_i at reception point by calculating the derivatives of the time transfer functions as follows (Bertone & Le Poncin-Lafitte 2011)

$$\begin{aligned} \hat{k}_i = & -N^i \\ & -\frac{(\gamma+1)}{c^2} \int_0^1 \left[W N^i + (1-\lambda) R \frac{\partial W}{\partial x^i} \right]_{z_{\pm}^{\alpha}(\lambda)} d\lambda \\ & + \frac{4}{c^3} \int_0^1 \left[W^i - \frac{(\gamma+1)}{4} (1-\lambda) R N^i \frac{\partial W}{\partial t} \right. \\ & \left. + (1-\lambda) R \left(\mathbf{N} \cdot \frac{\partial \mathbf{W}}{\partial x^i} \right) \right]_{z_{\pm}^{\alpha}(\lambda)} d\lambda + \mathcal{O}(c^{-4}), \end{aligned} \quad (4.1)$$

where γ is a PPN parameter (Will 1993) and the integral is taken along the Minkowskian line of sight

$$z_-(\lambda) = (ct_B - \lambda R, \mathbf{x}_B - \lambda R \mathbf{N}), \quad (4.2)$$

with $\mathbf{N} = \{N^i\} = (\mathbf{x}_B - \mathbf{x}_A)/R$, W and \mathbf{W} being the gravitational potentials studied in the next section.

5 Towards a "three zones" modeling

Here we assume the Solar System as an isolated system of N deflecting bodies, thus we neglect gravitational perturbations due to the galaxy, dark matter, the emitting star itself, etc. Then, potentials W and \mathbf{W} are generated only by the Solar System bodies and can be written

$$W(t, \mathbf{x}) = \sum_{p=0}^N \frac{GM_p}{r_p} \left[1 - \sum_{n=2}^{\infty} J_n \left(\frac{r_e^p}{r_p} \right)^n P_n \left(\frac{\mathbf{k}_p \cdot \mathbf{x}}{r_p} \right) \right], \quad (5.1)$$

$$\mathbf{W}(t, \mathbf{x}) = \sum_{p=0}^N \frac{GM_p \mathbf{v}_p}{r_p} \left[1 - \sum_{n=2}^{\infty} J_n \left(\frac{r_e^p}{r_p} \right)^n P_n \left(\frac{\mathbf{k}_p \cdot \mathbf{x}}{r_p} \right) \right], \quad (5.2)$$

where P_n are the Legendre polynomials, $r_p = |\mathbf{x} - \mathbf{x}_p(t)|$ is the spatial distance between the light signal and the perturbing body p at time t ; \mathbf{k}_p , M_p , J_n^p and r_e^p denote the unit vector along the axis of symmetry, the mass, the mass multipole moments and the equatorial radius of body p , respectively.

To calculate the total deflection of light, we need to know the motion of Solar System bodies from the emission to the reception of the light ray. But if the light is coming from a star, it is quite impossible to give a simple analytical expression of that motion and we have to use an ephemeris. That is why we propose a *three zones* modeling, as illustrated on figure 2, to deal with this problem:

- **internal zone:** let us introduce a fictitious point-event $x_C = (ct_C, \mathbf{x}_C)$ on the light world line. Spatial distance of x_C from Solar System barycenter is supposed to be small, such as 100 astronomical units. The deflection functions \hat{k}_i at x_B is known since the satellite has observed a celestial object. Then, one uses equation (4.1) to compute x_C when we consider the potentials given by equations (5.1) and (5.2). $t_C - t_B$ is a small time interval, so we can approximate the motion of Solar System bodies by a straight line of equation

$$\mathbf{x}_p(t) = \mathbf{x}_p^B - (t - t_B) \mathbf{v}_p^B, \quad (5.3)$$

where \mathbf{x}_p^B and \mathbf{v}_p^B are the position and the velocity of body p at time t_B , respectively. In this case, we can derive an analytical formula for equation (4.1).

- **external zone:** we introduce another fictitious point-event $x'_C = (ct'_C, \mathbf{x}'_C)$ on the light world line. Here x'_C is assumed to be very far from the Solar System in such a way that its gravitational field can be approximated by a Schwarzschild's metric. This very well known problem has an analytical solution which can be obtained easily with the time transfer functions (Le Poncin-Lafitte & Teysandier 2008).
- **third zone:** this zone is introduced to enable a smooth transition between the internal and external zones. To achieve this, we want to find a criterion to match the deflection functions at x_C and x'_C , respectively. A possible choice is to stipulate that the angular distance between them must be one tenth below the desired astrometric accuracy.

6 Conclusion

In this article, we have presented a relativistic modeling for high precision space astrometry, valid in the Post-Newtonian approximation. This approach allows us to take advantage of a simple motion law for the bodies during the light propagation through the Solar System, i.e. the internal zone. We also outline a matching procedure between this zone and an additional external area where Solar System bodies are supposed at rest. In this work, light deflection is obtained as a boundary value problem solved by the use of the time transfer functions and consequently a complete solution of the light ray trajectory is avoided.

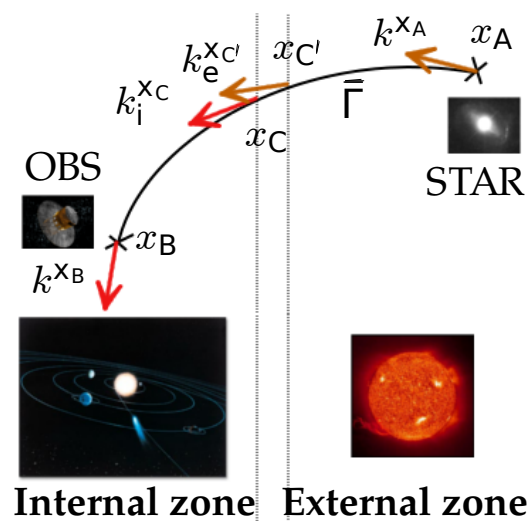


Fig. 2. The *three zones* modeling.

References

- Bertone, S. & Le Poncin-Lafitte, C. 2011, *Memorie della Societa' Astronomica Italiana*, to be submitted
- Bienayme, O. & Turon, C. 2002, *EAS Publications Series*, 2
- de Felice, F., Vecchiato, A., Crosta, M. T., Bucciarelli, B., & Lattanzi, M. G. 2006, *Astrophysical Journal*, 653, 1552
- Klioner, S. A. 2003, *Astronomical Journal*, 125, 1580
- Le Poncin-Lafitte, C., Linet, B., & Teyssandier, P. 2004, *Classical and Quantum Gravity*, 21, 4463
- Le Poncin-Lafitte, C. & Teyssandier, P. 2008, *Physical Review D*, 77, 044029
- Perryman, M. A. C., de Boer, K. S., Gilmore, G., et al. 2001, *Astronomy and Astrophysics*, 369, 339
- Soffel, M., Klioner, S. A., Petit, G., et al. 2003, *Astronomical Journal*, 126, 2687
- Teyssandier, P. & Le Poncin-Lafitte, C. 2006, *ArXiv General Relativity and Quantum Cosmology e-prints*
- Teyssandier, P. & Le Poncin-Lafitte, C. 2008, *Classical and Quantum Gravity*, 25, 145020
- Will, C. M. 1993, *Theory and Experiment in Gravitational Physics*, ed. C. M. Will

STATISTICAL ANALYSIS ON THE UNCERTAINTY OF ASTEROID EPHEMERIDES

J. Desmars^{1,2}, D. Bancelin², D. Hestroffer² and W. Thuillot²

Abstract. The large number of asteroids allows a statistical analysis especially for their orbital uncertainty. It presents a particular interest for Near-Earth asteroids in order to estimate their close approach from Earth and eventually their risk of collision. Using ASTORB and MPCORB databases, we analyse the different uncertainty parameters (CEU, U) and highlight relations between the uncertainty parameter and the characteristics of the asteroid (orbital arc, absolute magnitude, ...).

Keywords: Asteroids, Ephemerides, Dynamics, Databases

1 Introduction

Since February 2010, the number of discovered asteroids exceeds 500 000. The large number of asteroids allows a statistical analysis particularly about their orbital uncertainty. There are currently four main databases for asteroids orbital elements: Minor Planet Center, Lowell Observatory, JPL and Pisa University. We specifically deal with two of these databases: ASTORB (Bowell 2011) and MPCORB (Minor Planet Center 2011a). As from April 26, 2011, a total of 550 293 asteroids are compiled in ASTORB and 550 468 in MPCORB. Both databases provide similar parameters such as name/number of the asteroid, osculating elements, magnitude and information on observations (number, length of the orbital arc) and specific information about the uncertainty (Desmars et al. 2011).

2 Uncertainty Parameters

The two databases provide parameters about ephemerides uncertainty. Only one for MPCORB which is the U parameter and five for ASTORB which are the CEU, CEU rate, PEU and the two greatest PEU.

The U parameter provided by MPCORB is a integer value between 0 (very small uncertainty) and 9 (extremely large uncertainty). It is determined by computing first the RUNOFF parameter:

$$RUNOFF = (dT * e + \frac{10}{P} dP) \frac{k_0}{P} * 3600 * 3 \quad (2.1)$$

where dT is the uncertainty in the perihelion time (in days), e is the eccentricity, P is the orbital period (in years), dP is the uncertainty in the orbital period (in days) and k_0 is the Gaussian constant (in degrees). RUNOFF can be considered as the in-orbit longitude runoff in arcseconds per decade. Finally, U is deduced from RUNOFF by:

$$U = \text{INT} \left(\frac{\ln(RUNOFF)}{C_0} \right) + 1 \quad (2.2)$$

where $C_0 = \ln(648000)/9$. The quality of the orbit can be quickly determined. But it would have be preferable to provide the RUNOFF parameter which represents a difference in longitude (a physical value).

The ASTORB database provides five parameters related to ephemeris uncertainty:

¹ Shanghai Astronomical Observatory, Chinese Academy of Sciences, 80 Nandan Road Shanghai 200030, China

² Institut de Mécanique Céleste et de Calcul des Éphémérides - Observatoire de Paris, UMR 8028 CNRS, 77 avenue Denfert-Rochereau, 75014 Paris, France

- **Current Ephemeris Uncertainty (CEU):** absolute value of the current 1-ephemeris uncertainty expressed in arcsec. The date of CEU is also provided.
- **Rate of change of CEU** (noted CEU rate) given in arcsec/day
- **Peak ephemeris Uncertainty (PEU):** the next peak of ephemeris uncertainty from the date of CEU. The date of PEU is also given.
- **Greatest PEU:** the first parameter is the greatest PEU in 10 years after the date of CEU and the second one is the greatest PEU in 10 years after the date of next PEU.

3 Comparison of the parameters

The U parameter can be compared to the CEU and its rate of change. Fig. 1 shows a correlation between CEU, rate of change of CEU and U parameter. Asteroids with a low U have also a low CEU and CEU rate.

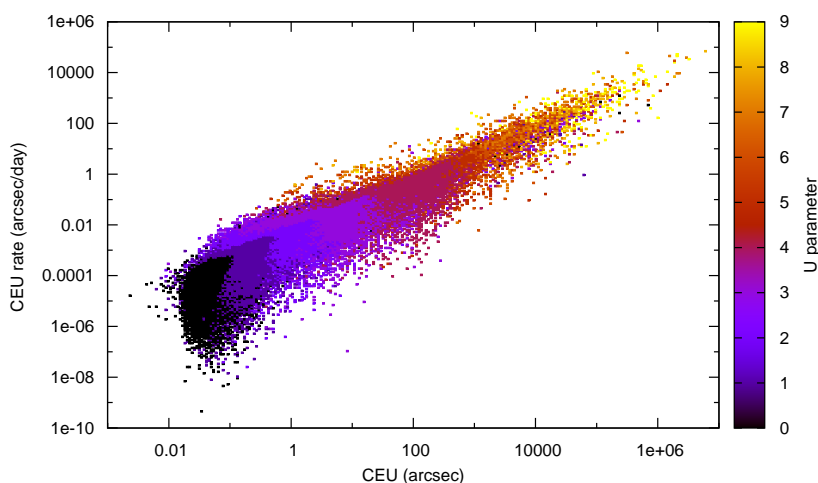


Fig. 1. CEU, CEU rate and U parameter for asteroids in common to the ASTORB and MPCORB databases.

All the parameters seem to be equivalent. The measure of the uncertainty can be provided by only one of these parameters. Nevertheless, one of these parameters could sometimes be missing. Another problem is that some asteroids have a bad parameter U ($U > 6$) and a good CEU ($CEU < 1$ arcsec) and conversely.

To clarify the situation, we have computed our own uncertainties for 4 groups of specific objects. These four groups have been defined considering good and bad U or CEU and two objects in each group have been selected. For each object, we have estimated the accuracy of the ephemerides using two statistical methods of non linear extrapolation.

These methods are based on Monte Carlo process in order to create clones of initial parameters from the nominal orbit, representing the region of possible motion. The first one, Monte Carlo using the Covariance Matrix (MCCM), consists in adding a random noise on each initial condition using the covariance matrix. The second one, Bootstrap Resampling (BR) consists in a random resampling of the observations (Desmars et al. 2009). For this test, we have computed 1000 clones of each representative asteroid and then calculated the standard deviation at the date of CEU, on angular separation, which represents the angular deviation of an orbit to the nominal one.

Table 1 gives the comparison between U parameter, CEU and standard deviation provided by clones of nominal orbit with two different methods. For these representative asteroids, the CEU is often close to the standard deviation computed whereas U parameter is misestimated for at least four representative asteroids.

Table 1. Comparison of U, CEU and standard deviation in discordant cases as obtained by clones of nominal orbit with two methods.

	U (mpcorb)	CEU (") (astorb)	σ_{MCCM} (") (our work)	σ_{BR} (") (our work)
2002GM5	9	56 000	55 297	46 934
2006LA	9	100 000	66 185	70 395
2000RH60	5	0.24	0.144	0.171
2003FY6	6	0.76	0.226	0.313
2007WD5	0	1 200	6 812	13 393
1995WZ13	0	5 400	0.122	1.751
4321 Zero	0	0.036	0.019	0.034
31824 Elatus	0	0.24	0.150	0.129

Moreover, the U parameter provides a number which is not related to a physical value (a distance or an angle).

In light of Table 1 and Fig. 1, the CEU seems to be a good parameter in order to estimate the accuracy and predictability of an asteroid orbit as CEU is quickly computable, precise and providing a physical value (an angle). Nevertheless, for some extreme cases (when only few observations are available or for Earth-approaching asteroids), the CEU can be misestimated (Minor Planet Center 2011b). This parameter is not perfect and could be improved for poor observed asteroids.

4 Relations between CEU and orbital arc

The decreasing of the CEU seems obviously related to the increasing of the orbital arc. In this context, we have tried to find a relation between this two parameters (Fig. 2). In this figure, four groups of asteroids can be identified using their orbital arc:

- arc < 10 days
- 10 days \leq arc < 250 days
- 250 days \leq arc < 8000 days
- 8000 days \leq arc

For each group, linear regression can be computed and we have an empirical relation between the value of CEU and the length of orbital arc:

$$\log(CEU) = a \log(arc) + b \quad (4.1)$$

where a and b are given in Fig. 2 for each groups.

If the orbital arc is smaller than 10 days, the CEU is very large and does not much improve when the length of arc becomes greater. Between 10 and 250 days, the CEU is clearly improved if the length of arc increases. For asteroids with an orbital arc between 250 and 8 000 days, the CEU is smaller than 100 arcsec and is still much improved when the length of arc becomes greater. If the orbital arc is greater than 8 000 days, then the CEU is not much improved and reaches its typical minimum value (about 0.1-0.2 arcsec).

5 Conclusion

The best parameter of uncertainty provided by asteroid databases seems to be CEU because it is quickly computable, precise and related to a physical value. An empirical relation between CEU and the orbital arc of the asteroid has also been highlighted.

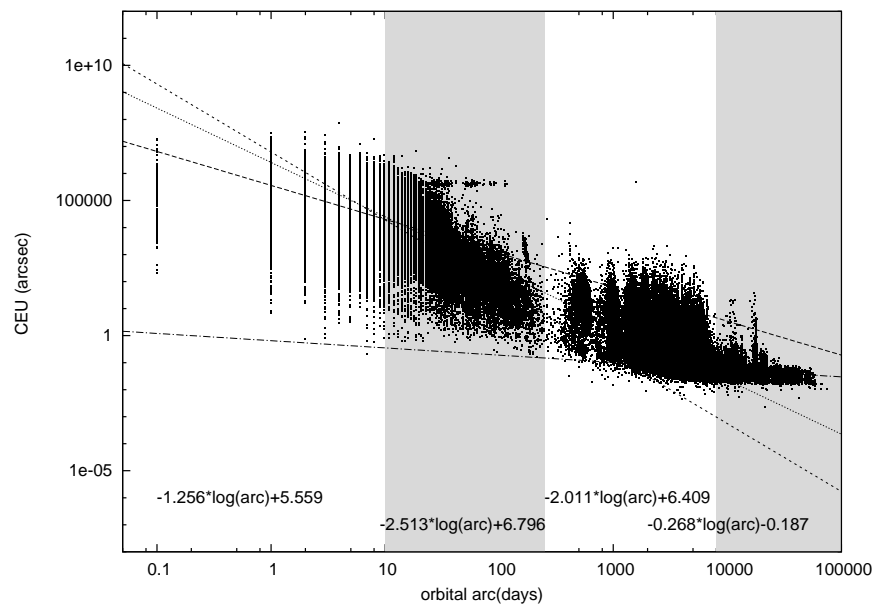


Fig. 2. Relations between the length of orbital arc and CEU.

This study was supported by contract ESA/22885/09/F/MOS/100409-R from European Space Agency. The authors are grateful to Pascal Rosenblatt (ORB, Brussels) for fruitful discussions and valuable help.

References

- Bowell, E. 2011, The asteroid orbital elements database, <ftp://ftp.lowell.edu/pub/elgb/astorb.html>
- Desmars, J., Arlot, S., Arlot, J., Lainey, V., & Vienne, A. 2009, *A&A*, 499, 321
- Desmars, J., Bancelin, D., Hestroffer, D., & Thuillot, W. 2011, Asteroid Ephemerides, Report ESA/22885/09/F/MOS/100409-R
- Minor Planet Center. 2011a, MPCORB database, <http://minorplanetcenter.net/iau/MPCORB.html>
- Minor Planet Center. 2011b, Uncertainty parameter U, <http://www.minorplanetcenter.net/iau/info/UValue.html>

ANALYTICAL EXPRESSION OF THE POTENTIAL GENERATED BY A MASSIVE INHOMOGENEOUS STRAIGHT SEGMENT

N.-E. Najid¹ and E. Elourabi²

Abstract. Potential calculation is an important task to study dynamical behavior of test particles around celestial bodies. Gravitational potential of irregular bodies is of great importance since the discoveries of binary asteroids, this opened a new field of research. A simple model to describe the motion of a test particle, in that case, is to consider a finite homogeneous straight segment. In our work, we take this model by adding an inhomogeneous distribution of mass. To be consistent with the geometrical shape of the asteroid, we explore a parabolic profile of the density. We establish the closet analytical form of the potential generated by this inhomogeneous massive straight segment. The study of the dynamical behavior is fulfilled by the use of Lagrangian formulation, which allowed us to give some two and three dimensional orbits.

Keywords: Potential, Inhomogeneous-distribution, Asteroids.

1 Introduction

The discovery of irregular small bodies and binary asteroids like Ida and Doctyl, gave a rise to the potential calculation. Many attempts have been made to approximate the potential. Riaguas et al. (1999) proposed a homogeneous straight segment. In Elipe et al. (2003) described the motions around (433) Eros with the same homogeneous model. A harmonic polyhedron was used by Werner and Scheeres for asteroid 4769 Castalia in Werner et al. (1997) and Werner. (1994). Ellipsoids, material points and double material segment was used by Przemyslaw et al. (2003) and Przemyslaw et al. (2006), as the model of irregular elongated bodies. In our work we give a new idea to models the potential generated by an elongated body. We consider a straight massive segment with variable density. To be consistent with the geometrical aspect of the asteroid, we use a parabolic profile. Our work generalize that of Riaguas et al. (1999). In the first part of this work, we establish the closet forme of the potential generated by an inhomogeneous massive straight segment. In the second part we study the dynamical behavior of a test particle in the field of the straight segment. We conclude in the last part by the numerical resolution of the differential equations of motion. In this part we show some orbits in two and three dimension.

2 Potential calculation

We consider an inhomogeneous straight segment of length $2l$ and mass M which lies along the $(x - axis)$, with a parabolic profile of linear mass density expressed by $\lambda(x) = -ax^2 + b$ in which a and b are linked by $a < \frac{b}{l^2}$ and $M = -\frac{2}{3}al^3 + 2bl$. At a point P , the gravitational potential generated by the segment is :

$$U(P) = -G \int \frac{dm}{r} \quad (2.1)$$

Where G is the gravitational constant. r is the distance between P and the infinitesimal mass dm located at H with abscissa x_H in the segment. Fig.1.

Let us consider an inertial reference frame $(Oxyz)$, and let \mathbf{r}_1 , and \mathbf{r}_2 be the position vectors of the end points

¹ Equipe Mécanique Statistique et Astronomie - Laboratoire de Physique Théorique et Appliquée Université Hassan II Ain Chock- Faculté des Sciences Ain Chock BP 5366 Maârif Casablanca Morocco.

² Equipe Mécanique Statistique et Astronomie - Laboratoire de Physique Théorique et Appliquée Université Hassan II Ain Chock- Faculté des Sciences Ain Chock BP 5366 Maârif Casablanca Morocco.

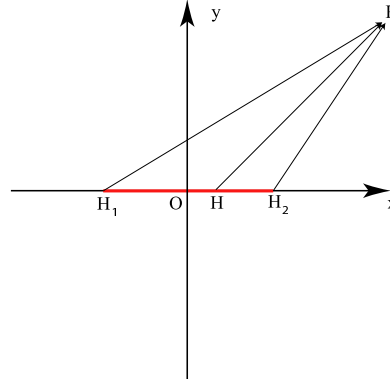


Fig. 1. Straight segment .

H_1 and H_2 of the straight segment. We define $\nu = \frac{1}{2}(1 + \frac{xH}{l})$ as a new variable of integration with $0 \leq \nu \leq 1$. After calculation we obtain

$$U(r_1, r_2) = 4al^2G \int_0^1 \frac{\nu^2 - \nu - \frac{b-al^2}{4al^2}}{\sqrt{\nu^2 + \nu \left(\frac{r_2^2 - r_1^2 - 4l^2}{4l^2} \right) + \frac{r_1^2}{4l^2}}} d\nu \quad (2.2)$$

After a laborious calculation and simplification we achieve the closet expression of the potential generated at P :

$$U(r_1, r_2) = \frac{G}{32l^2} \left(A_1 + A_2 \ln \left(\frac{r_2 + r_1 - 2l}{r_2 + r_1 + 2l} \right) \right) \quad (2.3)$$

Where

$$A_1 = 16al^3 (r_2 + r_1) + 12al (r_2 - r_1) (r_1^2 - r_2^2)$$

and

$$A_2 = 8al^2 (r_2 + r_1)^2 - 16al^2 r_1 r_2 - 3a (r_1 - r_2)^2 (r_2 + r_1)^2 - 16al^4 + 32bl^2$$

We define $s = r_2 + r_1$, $d = r_1 - r_2$ and $p = r_2 r_1$ as an auxiliaries functions depending only on distances r_1 and r_2 of the particle to the end points of the segment. The expression of Eq. (2.3) reduce to :

$$U(P) = -\frac{G}{32l^2} \left\{ 12alsd^2 - 16al^3s + [8l^2a (s^2 - 2p) - 3as^2d^2 - 16l^4a + 32bl^2] \ln \left(\frac{s + 2l}{s - 2l} \right) \right\} \quad (2.4)$$

Eq. (2.4) represent the gravitational potential generated by an inhomogeneous straight segment with a quadratic profile of density, this expression is our main result, to have more details and study about, (see Najid et al. 2011). The case of constant density (Riaguas et al. 1999) is a particular situation of Eq. (2.4), if we put $a = 0$ and $b = \frac{M}{2l} = \lambda$. We obtain the expression (1) in Riaguas et al. (1999).

3 Dynamical study

We plane to study the dynamical behavior of a test particle, with unit mass, located at P in the field of the inhomogeneous straight segment. $R(O, x, y, z)$ is the sidereal referential frame, with the cylindrical coordinates (ρ, θ, x) as in Fig. 2. The differential equations of motion corresponding to ρ , x and θ are given by

$$\ddot{\rho} = \rho\dot{\theta}^2 + \frac{G}{32l^2p} \left(A_3 - \frac{4l\rho s}{s^2 - 4l^2} A_4 \right) \quad (3.1)$$

$$\ddot{x} = \frac{Ga}{16l^2p} \left(A_5 + A_6 \ln \left(\frac{s + 2l}{s - 2l} \right) - \frac{2l(xs - ld)}{s^2 - 4l^2} A_7 \right) \quad (3.2)$$

$$\rho^2\dot{\theta} = \Lambda = cste \quad (3.3)$$

Where

$$A_3 = 32al^2p\rho \ln \left(\frac{s + 2l}{s - 2l} \right) - 4al\rho s (3d^2 + 4l^2)$$

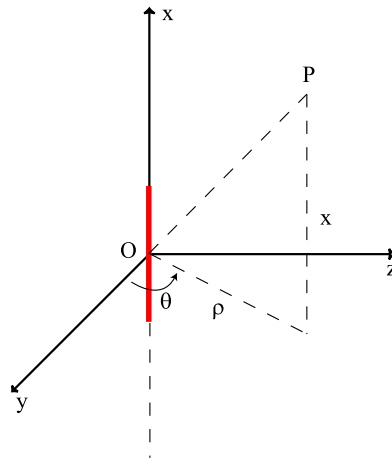


Fig. 2. Sidereal referential and the cylindrical coordinates.

$$A_4 = 8l^2 a (s^2 - 2p) - 3as^2d^2 - 16l^4a + 32bl^2$$

$$A_5 = 2l (xs - ld) (3d^2 - 4l^2) + 12lsd (ls - xd)$$

$$A_6 = s (xs - ld) (8l^2 - 3d^2) - 8l^2x (s^2 - 2p) + 8l^3sd - 3s^2d (ls - xd)$$

and

$$A_7 = 8l^2 (s^2 - 2p) - 3s^2d^2 - 16l^4 + \frac{32bl^2}{a}$$

The case of homogeneous profile of density, $a = 0$ and $b = \lambda = \frac{M}{2l}$, lead to the equations

$$\ddot{\rho} = \frac{\Lambda^2}{\rho^3} - \frac{2\mu s \rho}{p (s^2 - 4l^2)} \qquad \ddot{x} = -\frac{2\mu x}{sp}$$

We obtain the equation (3) as in Riaguas et al. (1999). In our case of inhomogeneous straight segment Eqs (3.1), (3.2) and (3.3) are strongly non linear and coupled. It need a deep numerical treatment. In fact, it is out of view to plane to work it out in an analytical way.

4 Numerical integration

To have a deep insight about the dynamical behavior of the test particle in the field of the inhomogeneous straight segment, we have to solve Eqs. (3.1), (3.2) and (3.3). In this system of differential equations the unknowns are ρ , θ and x . We derive some curves both, in the plan and in the space.

Fig. 3, Fig. 4 and Fig. 5 give some orbits in the plan and in the space corresponding to different initial conditions. We notice, in a qualitative point of view, the existence of many behavior , we obtain the state: collision, confined and not confined. More analysis about the curves below are developed in Najid et al. (2011).

5 Conclusion

In this work, we established the analytical expression of the potential generated by a straight segment with a quadratic profile of its density. This potential model in an accurate manner celestial elongated bodies in the solar system. We derived some curves (trajectories) both in two and three dimensions. They gave an overview of the dynamical behavior of massless test particle. A deep study is fulfilled in Najid et al. (2011) by using the Poincaré surface of section. After the achievement of the dynamical behavior of a test particle in the field of that segment, fixed in space, we plane, in a next future, to study the case where the segment is in rotation.

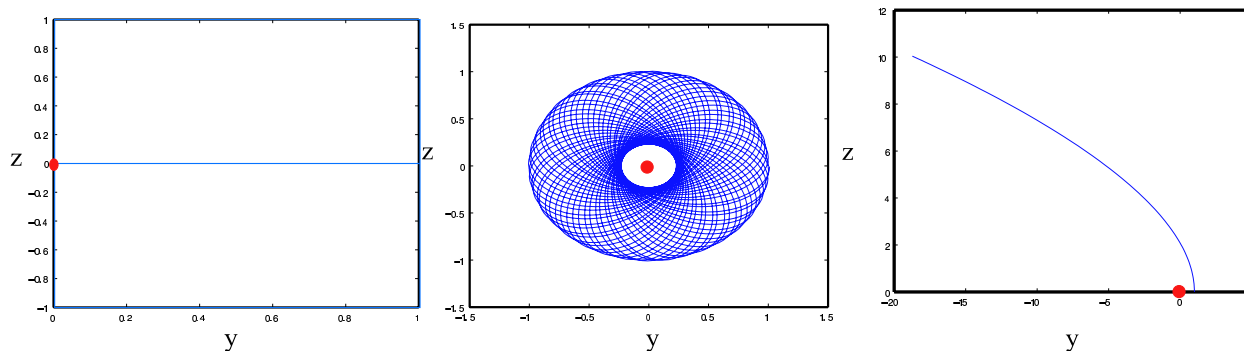


Fig. 3. Trajectories in the plan yz .

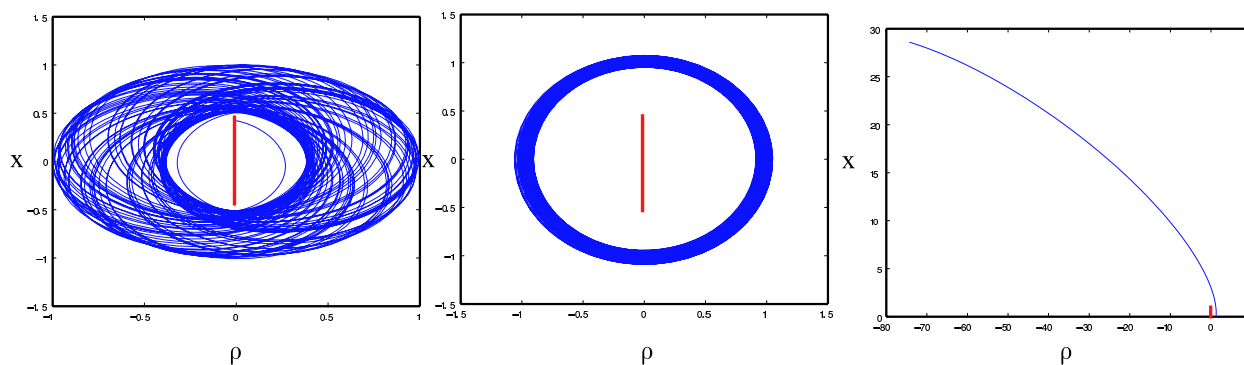


Fig. 4. Trajectories in the plan $x\rho$.

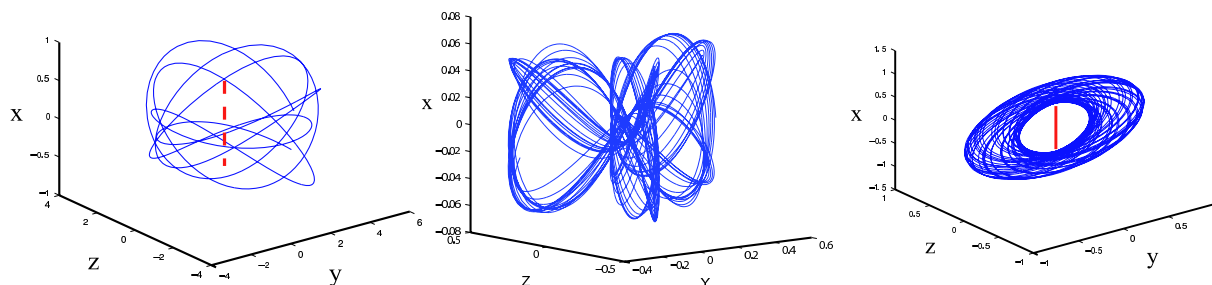


Fig. 5. Trajectories in the space.

References

- Riaguas, A., Elife, A., & Lara, M. 1999, *Celest.Mech.Dyn. Astr.*, 169, 178
 Elife, A., & Lara, M. 2003, *The journal of Astronautical Sciences* V.51, 391, 404
 Werner, R.A., & Scheeres, D.J. 1997, *Celest.Mech.Dyn.Astr.*, 313, 343
 Werner R.A. 1994, *Celest.Mech.Dyn.Astr.*, 253, 278
 Przemyslaw, B., & Slawomir, B., 2003, *Celest.Mech.Dyn.*, 131, 141
 Przemyslaw, B., Slawomir, B. & Przemyslaw, J. 2006, *Celest.Mech.Dyn.*, 31, 48
 Najid, N.-E., Elourabi, E., & Zegoumou, M. 2011, *Research in Astronomy and Astrophysics*, 345, 352

IN-FLIGHT CALIBRATION OF THE MICROSCOPE SPACE MISSION INSTRUMENT: DEVELOPMENT OF THE SIMULATOR

E. Hardy¹, A. Levy¹, G. Métris², A. Robert³, M. Rodrigues¹ and P. Touboul¹

Abstract. The space mission MICROSCOPE aims at testing the Equivalence Principle (EP) with an accuracy of 10^{-15} . The test is based on the precise measurement delivered by a differential electrostatic accelerometer onboard a drag-free microsatellite which includes two cylindrical test masses submitted to the same gravitational field and made of different materials. The accuracy of the measurement exploited for the EP test is limited by our knowledge of the physical parameters of the instrument. The on-ground evaluation of these parameters is not precise enough. An in-orbit calibration is therefore needed to finely characterize these instrumental parameters in order to correct the measurements. The calibration procedures have been proposed and their analytical performances have been evaluated. In addition, a software simulator including models of the instrument and the satellite drag-free system has been developed. After an overall presentation of the MICROSCOPE mission, this paper will focus on the description of the simulator used to confirm and validate the specific procedures which are planned to determine in-orbit the exact values of the driving parameters of the instrument.

Keywords: MICROSCOPE, test of the Equivalence Principle, space accelerometer, calibration, simulator

1 Introduction

The MICROSCOPE space mission aims at testing the Equivalence Principle (EP), which states the Universality of Free Fall: ‘the acceleration of an object in a gravitational field is independent of its composition’. This is equivalent to the proportionality between the inertial mass, which quantifies the resistance to a modification of the motion by any force, and the gravitational mass, which quantifies the gravitational force. The Universality of Free Fall has been tested throughout the centuries with an improving accuracy. Sophisticated torsion-balances, and more recently the Lunar Laser Ranging method, have lead to an accuracy of a few 10^{-13} (Will (2006)). However, the unification theories which try to merge gravitation with the three other fundamental interactions expect a violation of the EP below 10^{-14} . For this reason and others, the MICROSCOPE mission will test this principle with the accuracy of 10^{-15} . To achieve this goal, the payload of the MICROSCOPE satellite is a differential electrostatic accelerometer which includes two cylindrical test masses made of different materials. The test is based on the precise measurement of the difference of gravitational acceleration between the two test masses while they are submitted to the same gravitational field. The accuracy of the measurement exploited for the EP test is limited by our knowledge of the physical parameters of the instrument. These parameters are partially estimated by means of ground tests or during the integration of the instrument in the satellite. However, these evaluations are not sufficient and an in-orbit calibration is needed in order to correct the measurements of the effects of these parameters. We have defined calibration procedures and evaluated their analytical performances: they are compatible with the accuracy objectives. We have developed a software simulator including models of the instrument and the satellite drag-free system in order to validate numerically these procedures.

After an overall presentation of the MICROSCOPE mission, the interest of an in-flight calibration and the corresponding procedures will be explained. The structure of the calibration simulator used to validate them will then be described.

¹ ONERA, 29 avenue de la Division Leclerc F-92322 Châtillon, France

² Université de Nice Sophia-Antipolis, Centre National de la Recherche Scientifique (UMR 6526), Observatoire de la Côte d’Azur, Géoazur, Avenue Copernic 06130 Grasse, France

³ CNES, 18 avenue Edouard Belin 31401 Toulouse, France

2 Overview of the MICROSCOPE project

2.1 The space mission

MICROSCOPE is a 200 kg microsatellite developed by CNES to orbit around the Earth for a one year mission. The onboard payload is constituted of two differential electrostatic accelerometers developed by ONERA, each one being composed of two concentric cylindrical test masses controlled to be on the same orbit by the accelerometer electronics channels thanks to capacitive detection methods and electrostatic actuations. A difference measured between the forces applied to maintain two masses of different composition on the same trajectory will indicate a violation of the EP.

There are several advantages to perform the experiment in space. The experiment can last for several orbits. Moreover, the environment is much less disturbed and a drag-free system (SCAA) allows compensating perturbations to maintain the satellite on a geodesic trajectory. Another important advantage is to be able to use the Earth instead of the Sun as source of the gravity field, allowing increasing the signal by more than three orders of magnitude. Lastly, the frequency and the phase of the signal to be detected are very well known.

2.2 Principle of an electrostatic accelerometer

An electrostatic accelerometer is composed of a cylindrical free mass surrounded by electrodes. Control loops maintain the mass motionless and centred in the cage.

The electrode set around the mass allows both measurement of its position and control of its six degrees of freedom with electrostatic forces generated by voltages applied on it. The electrical potential of the mass is maintained to a constant level in order to generate linear actuation forces, and a sine wave pumping signal is also applied to the mass for the capacitive position detection. This position is obtained from the measurement of the capacitance variations of two symmetric electrodes with respect to the mass: along the \vec{X} sensitive axis, the opposite variations of the recovering surfaces between the proof mass and the cylindrical electrodes located at the two mass extremities generate opposite variations of both capacitances when the mass is moving.

3 The in-orbit instrument calibration

3.1 The measurement principle

The ideal measurement of the inertial sensor would be the acceleration $\vec{\Gamma}_{App,k}$ applied to the proof mass k to keep it at the centre of the electrostatic cage. This applied acceleration corresponds to the difference between the acceleration of the satellite and the acceleration of the mass, since the purpose is to maintain it motionless. The accelerations can be decomposed into a gravitational part and non-gravitational parts applied on the satellite and the mass k , respectively $\frac{\vec{F}_{NGsat}}{M_{I sat}}$ and $\frac{\vec{F}_{NGk}}{m_{Ik}}$:

$$\vec{\Gamma}_{App,k} = \left(\frac{M_{gsat}}{M_{I sat}} - \frac{m_{gk}}{m_{Ik}} \right) \vec{g}(O_{sat}) + (T - I) \overrightarrow{O_k O_{sat}} + \frac{\vec{F}_{NGsat}}{M_{I sat}} - \frac{\vec{F}_{NGk}}{m_{Ik}}$$

where M_{gsat} and m_{gk} are the gravitational masses of the satellite and the proof mass k , $M_{I sat}$ and m_{Ik} their inertial masses, O_{sat} and O_k their centres of mass, T is the Earth gradient gravity tensor and I the inertia tensor.

The instrument is not perfect: therefore the measured acceleration is not exactly equal to the applied acceleration. Some parameters of the instrument limit the measurement accuracy: the bias $\vec{B}_{0,k}$, the noise $\vec{\Gamma}_{n,k}$, the sensitivity matrix $[M_k]$ and the quadratic diagonal matrix $[K_{2,k}]$:

$$\vec{\Gamma}_{mes,k} = \vec{B}_{0,k} + [M_k] \vec{\Gamma}_{App,k} + [K_{2,k}] \vec{\Gamma}_{App,k}^2 + \vec{\Gamma}_{n,k}$$

The components of $\vec{\Gamma}_{App,k}^2$ are defined as the square values of the components of $\vec{\Gamma}_{App,k}$.

The EP violation parameter, $\delta = \frac{m_{g2}}{m_{I2}} - \frac{m_{g1}}{m_{I1}}$, appears in the differential mode measurement along \vec{X} , the ultrasensitive instrument axis of revolution; $\Gamma_{mes,dx}$ is the half difference between the accelerations measured for the two test masses:

$$\Gamma_{mes,dx} = \frac{1}{2} K_{1cx} \delta g_x(O_{sat}) + \frac{1}{2} \begin{bmatrix} K_{1cx} \\ \eta_{cz} + \theta_{cz} \\ \eta_{cy} - \theta_{cy} \end{bmatrix}^t [T - I] \begin{bmatrix} \Delta_x \\ \Delta_y \\ \Delta_z \end{bmatrix} + \begin{bmatrix} K_{1dx} \\ \eta_{dz} + \theta_{dz} \\ \eta_{dy} - \theta_{dy} \end{bmatrix}^t (\vec{\Gamma}_{resaf} + \vec{C})$$

$$+ 2K_{2cxx}(\Gamma_{app,d} + b_{1dx})(\Gamma_{resdf,x} + C_x - b_{0cx}) + K_{2dxx}((\Gamma_{app,d} + b_{1dx})^2 + (\Gamma_{resdf,x} + C_x - b_{0cx})^2)$$

The parameters arising in this equation are those of the sensitivity matrix: the scale factor K_1 , the coupling parameter η and the misalignment parameter θ , the off-centring between the two proof masses Δ and the quadratic factor K_2 ; the indices c and d referring respectively to the common (half sum) and differential (half difference) parameters. b_{0c} is the common read-out bias, and $-b_{1d}$ gathers the differential parasitic forces. We define $\Gamma_{app,d}$ so that $\Gamma_{App,d} = \Gamma_{app,d} + b_{1d}$. C is the drag-free command and Γ_{resdf} the drag-free loop residue. In first approximation, $\Gamma_{App,cx}$ is equal to $\Gamma_{mes,cx} - b_{0cx}$. Since $\Gamma_{mes,c}$ is the input of the SCAA, $\Gamma_{App,cx}$ can be approximated by $\Gamma_{resdf,x} + C_x - b_{0cx}$.

3.2 The calibration process

Error sources such as mechanical defects, magnetic effects or thermal effects limit the measurement accuracy. In the previous expression of the differential measurement, three groups of errors explicitly appear: the defects between the satellite and the instrument, encompassing the off-centring and common parameters, the defects between the two sensors, encompassing the differential parameters, and quadratic non linearities. The contributions of the 10 parameters included in these three groups have been evaluated, corresponding to the best possible performances for the realization of the instrument. The results clearly exceed the specifications (Levy et al. (2010) and Guiu (2007)). That is why in-orbit calibration sessions are necessary.

These calibration sessions will allow to estimate the driving parameters with a better accuracy and thus to correct the measurement. The idea is to create a signal which amplifies the effect of the parameter, so that the corresponding term in the measurement equation becomes predominant. For example, to increase the accuracy on the knowledge of the off-centring parameter $K_{1cx}\Delta_y$ from $20\mu\text{m}$ to $2\mu\text{m}$, the oscillation of the satellite around its Z axis is forced through the drag-free command; the resulting angular acceleration amplifies the term we are interested in. Similarly, the satellite oscillates along the X axis to reach an accuracy of 10^{-4} on the knowledge of the differential scale factor K_{1dx} . Other appropriate methods are used to reach an accuracy of $0,1\mu\text{m}$ for the off-centring parameters along X and Z, and 10^{-3} rad for the misalignment angles. To reduce the stochastic error of the parameter estimation, induced by the instrument noises and the stochastic variations of the measurement acceleration components, the calibration duration for each parameter is fixed to 10 orbits, also compatible with the mission duration according to the foreseen number of in orbit calibration phases.

The analytical evaluation of the accuracy reached by means of these calibration procedures is compatible with the specifications when developing the expression of the exploited measurement at first order (Levy et al. (2010)). These procedures were therefore implemented in a simulator including a model of the satellite and its payload in order to validate them numerically.

4 The calibration simulator

The calibration simulator has been developed with Simulink and recreates the drag-free loop including, as shown in figure 1, a model of the satellite dynamics, the frame dynamics, the six-axes accelerometer, the SCAA (Attitude and Altitude Control System) and the stellar sensor. The parameters we want to calibrate are set to initial realistic random values. The calibration sessions correspond to movements of the satellite imposed by the calibration procedures: angular or linear oscillation of the satellite, oscillation of the proof-masses, or a combination of several of these movements. These signals are injected as secondary inputs in the accelerometer and in the SCAA. The structure of the simulator will now be detailed.

First of all, the ‘dynamics of the satellite’ block outputs the acceleration of the satellite, which corresponds to the thrust delivered by the propulsion system added to the non-gravitational external forces, mainly the atmospheric drag and the solar pressure. These accelerations come from a data file provided by OCA and representing the non gravitational accelerations for a specific trajectory and orientation of the satellite.

The acceleration at the centre of the cage of the instrument is then deduced from the acceleration of the satellite centre of mass by the ‘dynamics of the frame’ block. This process accounts for effects of the Earth gravity gradient and the rotation of the satellite, which arise due to the offset between the centres of mass of the satellite and of the sensor cage.

For the model of the instrument, only one of the two differential accelerometers is represented, constituted of an external and an internal proof mass. In a first stage, the applied acceleration on each mass is calculated. To this end, the acceleration at the centre of the cage of the inertial sensor is expressed as the acceleration at the centre of mass of the proof mass by accounting for the Earth gravity gradient and inertia effects induced by

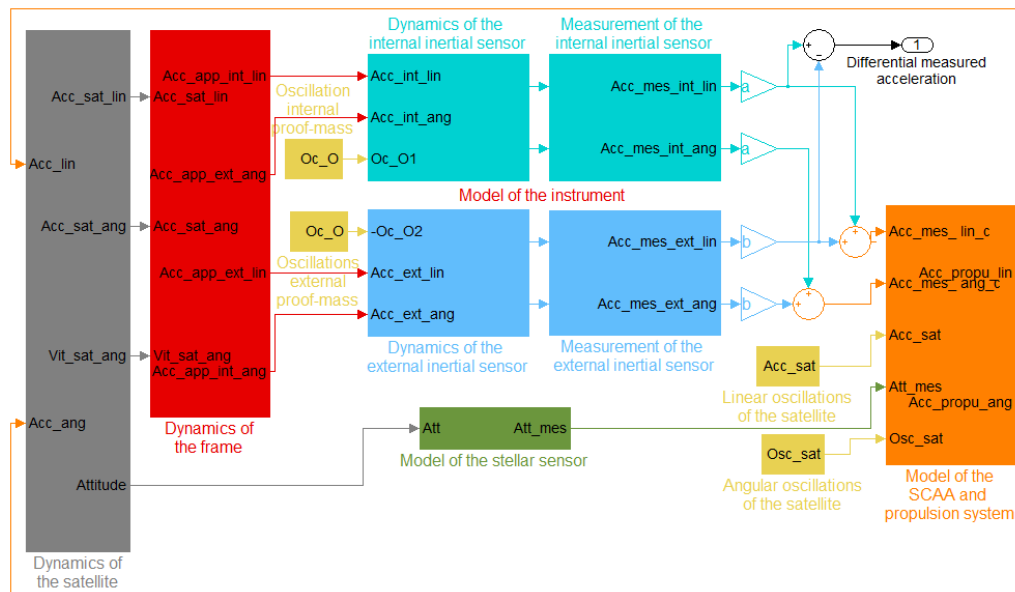


Fig. 1. Scheme of the calibration simulator

the offset between the centres of mass of the sensor cage and of the proof mass. Moreover, for some calibration procedures the masses have to move, which results in an additional Coriolis effect. In a second stage, the measurement error due to the instrument defects is simulated, with a bias, a sensibility matrix, quadratic terms and noise. The outputs of the ‘instrument’ block are the differential acceleration, used for the scientific experiment, and the common mode acceleration, which becomes the input of the SCAA block.

The SCAA computes the acceleration to be applied to the satellite to compensate for surface perturbations and thereby minimizes the non-gravitational acceleration measured by the inertial sensors. The angular and linear compensating accelerations are computed from the common acceleration measured by the instrument thanks to the SCAA third-order transfer functions (provided by CNES in charge of this sub-system). The computation of the angular compensating acceleration uses the attitude of the satellite measured by the stellar sensor in addition to the angular acceleration measured by the instrument in order to reach a better accuracy at low frequencies and reject the angular acceleration offsets. The computed compensating acceleration is then applied by the propulsion system: the cold gas thrusters control the six degrees-of-freedom of the satellite.

5 Conclusions

Prior to any calibration of the MICROSCOPE instrument, the measurement accuracy is not compatible with the accuracy objectives for the EP test. To correct the measurement, an in-flight calibration has to be performed. The relevant parameters to be calibrated have been determined and an appropriate calibration method has been proposed for each of them. The numerical results of the analytical error budget for the calibration process are compatible with the mission specifications. A simulator was therefore developed to validate these procedures. It includes a model of the instrument and of the drag-free system.

The next step is the comparison of the results of the simulator with the analytical evaluation. An appropriate data processing protocol will thus be needed. Moreover, a simulator dedicated to the sessions for the EP test has been developed at OCA. We aim to simulate the entire mission scenario thanks to the association of these two simulators.

The authors wish to thank the MICROSCOPE teams at CNES, OCA and ZARM for the technical exchanges. This activity has received the financial support of Onera.

References

Guiu, E. 2007, PhD Thesis, University of Nantes

Levy, A., Touboul, P., Rodrigues, M., Métris, G., & Robert, A. 2010, SF2A-2010: Proceedings of the annual Meeting of the French Society of Astronomy and Astrophysics

Will, C. 2006, Living Reviews Relativity, 9

TESTING GRAVITATION IN THE SOLAR SYSTEM WITH RADIO SCIENCE EXPERIMENTS

A. Hees^{1,2}, P. Wolf², B. Lamine³, S. Reynaud³, M. T. Jaekel⁴, C. Le Poncin-Lafitte², V. Lainey⁵
and V. Dehant¹

Abstract. The laws of gravitation have been tested for a long time with steadily improving precision, leading at some moment of time to paradigmatic evolutions. Pursuing this continual effort is of great importance for science. In this communication, we focus on Solar System tests of gravity and more precisely on possible tests that can be performed with radio science observations (Range and Doppler). After briefly reviewing the current tests of gravitation at Solar System scales, we give motivations to continue such experiments.

In order to obtain signature and estimate the amplitude of anomalous signals that could show up in radio science observables because of modified gravitational laws, we developed a new software that simulates Range/Doppler signals. We present this new tool that simulates radio science observables directly from the space-time metric. We apply this tool to the Cassini mission during its cruise from Jupiter to Saturn and derive constraints on the parameters entering alternative theories of gravity beyond the standard Parametrized Post Newtonian theory.

Keywords: tests of general relativity, radio science

1 Introduction

Testing General Relativity (GR) is a long standing and worthy effort in the scientific community. From a theoretical point of view, different attempts to quantize gravity or to unify it with other fundamental interactions predict deviations from GR. From an observational point of view, cosmological data can not be explained by the combination of GR and the standard model of particles, requiring the introduction of Dark Matter and Dark Energy. Since these two dark components have not been observed directly, cosmological observations can be a hint that the gravitation theory differs from the Einstein theory of gravity.

Within the solar system, GR is very well confirmed by different types of experiments: tests of the weak equivalence principle, Post-Newtonian constraints or fifth-force searches. In Sec. 2, we briefly recall the solar system constraints on the gravitation theory and we give motivations to go beyond these stringent constraints. In this communication we focus on the possibility to test gravity with radio science measurements (Range and Doppler). In order to study the impact of alternative theories of gravity on radio science observables, we present a software that simulates Range and Doppler signals directly from the space time metric (and from the initial conditions of the bodies considered). This approach allows one to simulate signals in any metric theory. This software is presented in Sec. 3 as well as some simulations about the Cassini mission.

¹ Royal Observatory of Belgium, Avenue Circulaire, 3, 1180 Bruxelles, Belgium

² LNE-SYRTE, Observatoire de Paris

³ Laboratoire Kastler Brossel, Paris

⁴ Laboratoire de Physique Théorique de l'ENS

⁵ IMCCE, Observatoire de Paris

2 Solar system constraints on gravity

2.1 Basis of General Relativity

General Relativity is built on two main principles. The first one, the Equivalence Principle, gives to gravitation a geometric nature. This principle implies that gravity can be identified to space-time geometry which is described by a metric tensor $g_{\mu\nu}$. Since freely falling test masses follow the geodesics of this metric, their motion is independent of their composition. This universality of free fall can be parametrized by a parameter η , defined as the relative difference between the accelerations of two test bodies. The universality of free fall has then been tested to an impressive level of $\eta < 10^{-13}$ by Lunar Laser Ranging (Williams et al. 2009) and by torsion pendulum (for a review see Adelberger et al. 2009). Let us note that even if this principle is one of the best tested in physics some theoretical models coming from unification theories may still produce deviations below the current constraints (Damour & Polyakov 1994), justifying the necessity to perform more accurate experiments like Microscope (Touboul & Rodrigues 2001) or STEP missions (Mester et al. 2001). The Equivalence Principle also defines the behavior of ideal clocks which is independent of their constitution and which measures a geometrical quantity $\tau = \int \sqrt{g_{\mu\nu} dx^\mu/ds dx^\nu/ds} ds$, a point which is also very well tested.

While the first building block of GR postulates the existence of a metric tensor that determines the trajectory of freely falling bodies (the geodesics) and the behavior of clocks, the second building block concerns the form of the metric tensor. The metric tensor is determined through field equations, which in the case of GR, are the Einstein equations

$$G_{\mu\nu} = R_{\mu\nu} - \frac{1}{2}g_{\mu\nu}R = \frac{8\pi G}{c^4}T_{\mu\nu}, \quad (2.1)$$

$G_{\mu\nu}$ is Einstein curvature tensor, $R_{\mu\nu}$ and R are Ricci and scalar curvatures (these are derived from the metric), G is Newton constant, c the speed of light and $T_{\mu\nu}$ the stress-energy tensor. These equations allow one to determine the metric tensor from the energy and matter contents of space-time.

If one considers the solar system and only the Sun's gravitational contribution, the metric tensor can be written as an expansion of the Newton potential $\phi_N = -\frac{GM}{rc^2}$ (where M is the mass of the central body and r a radial coordinate)

$$ds^2 = (1 + 2\phi_N + 2\phi_N^2 + \dots)c^2 dt^2 - (1 - 2\phi_N + \dots)d\vec{x}^2. \quad (2.2)$$

This expansion is justified since the value of the Newton potential in the solar system is always smaller than $\phi_N < 10^{-6}$. The metric (2.2) is written in isotropic coordinates.

The previous two principles produce important effects that need to be taken into account for high precision astrometry or for space missions: first, the dynamic is different from Newton gravity (one major consequence is the advance of planet perihelia) ; then, the propagation of light is affected ; finally clocks measure a proper time which is different from coordinate time t appearing in the metric. All these effects need to be modeled for space missions in addition to other classical effects. As a consequence, space missions constitute an excellent laboratory to test gravity.

2.2 Solar system tests of General Relativity

Gravity tests allow one to compare measurements with the predictions made by some theoretical framework. Within the solar system, two important frameworks have been developed: the Parametrized Post Newtonian formalism fully described in Will (1993) and the fifth force search fully described in Talmadge et al. (1988); Adelberger et al. (2009). Both formalisms embed GR metric within a wider class of specifically parametrized metric.

The PPN formalism extends the metric (2.2) by introducing Post Newtonian Parameters in expansion (2.2). In the simplest case, two parameters are introduced and the metric describing a spherical and static sun becomes

$$ds^2 = (1 + 2\phi_N + 2\beta\phi_N^2 + \dots)c^2 dt^2 - (1 - 2\gamma\phi_N + \dots)d\vec{x}^2. \quad (2.3)$$

Testing GR with PN formalism consists in measuring the PPN parameters γ and β and comparing the experimental results with their GR value ($\gamma = \beta = 1$). Thirty years of precise experiments have constrained PPN

parameters very closely around GR (for a review, see Will 2006). In particular, the observation of the Shapiro delay of the Cassini probe during a solar conjunction in 2002 gives the best constraint on the γ PPN parameter known to date (Bertotti et al. 2003)

$$\gamma - 1 = (2.1 \pm 2.3) \times 10^{-5}. \quad (2.4)$$

This constraint is confirmed by deflection measurement with VLBI (Lambert & Le Poncin-Lafitte 2009) or tracking Mars orbiter (Konopliv et al. 2011). The present best constraint on the β parameter comes from the solar system ephemerides (assuming the γ parameter to be given by (2.4)) (Fienga et al. 2011)

$$\beta - 1 = (-4.1 \pm 7.8) \times 10^{-5}. \quad (2.5)$$

Other type of experiments also confirmed this constraint like Lunar Laser Ranging (Williams et al. 2009) or Mars orbiter tracking (Konopliv et al. 2011).

The other type of formalism often used in solar system tests of gravity, the fifth-force search, consists in a search of the dependence of the Newton potential ϕ_N with the radial coordinate. This formalism parametrizes deviations from the Newtonian potential with a Yukawa potential, justified by unification models. More precisely the scale dependence of the Newton potential modifies the temporal part of the metric

$$g_{00} = 1 + 2\phi_N \left(1 + \alpha e^{-r/\lambda}\right) + 2\phi_N^2 = [g_{00}]_{GR} + 2\phi_N \alpha e^{-r/\lambda}. \quad (2.6)$$

The α parameter characterizes the amplitude of the deviation with respect to the Newtonian potential and the λ parameter is a range related to the mass of the new particle that would mediate this fifth interaction. These parameters have been tested in a very wide range (see Fig. 31 of Konopliv et al. 2011). In particular, the α parameter is constrained to a very high level of accuracy ($\alpha < 10^{-10}$) at Earth-Moon and Sun-Mars distances. From this picture, we can also see that windows remain open at very short distances and at very large distances.

2.3 Is it necessary to go beyond these tests ?

From the arguments presented in last section, one may wonder if it is necessary to continue to go beyond the present constraints on the gravitation theory. The answer is positive for several reasons. Firstly, there exist theoretical models predicting deviations smaller than the current constraints. For example, a tensor-scalar theory of gravity can naturally be attracted towards GR by a cosmological mechanism (Damour & Nordtvedt 1993) and lead to a deviation of the γ parameter smaller than the Cassini constraint. Another example is given by the chameleon field (Khoury & Weltman 2004) where deviations of GR are hidden in region of high density (in the solar system) and remain smaller than current constraints.

Then, it appears interesting to search for deviations in regions where no test has been performed so far. For example, a fifth force may be searched at very small range or at very large range where stringent constraints are missing. Let us mention that not all alternative theories of gravity are entering the PPN or fifth-force framework. It would be instructive to extend these frameworks to include new types of deviations. To illustrate this, we consider two alternative theories of gravity that do not enter the PPN or fifth-force formalism.

Such a first alternative theory of gravity is provided by *Post-Einsteinian Gravity (PEG)* (Reynaud & Jaekel 2005; Jaekel & Reynaud 2005, 2006a,b). This theory is based on a non local extension of Einstein field equations, as suggested by radiative corrections. Phenomenologically in the solar system, the space time metric can be parametrized by two radial dependent potentials $\delta\Phi_N(r)$ and $\delta\Phi_P(r)$

$$g_{00} = 1 + 2\phi_N + 2\phi_N^2 + 2\delta\Phi_N \quad (2.7)$$

$$g_{ij} = \delta_{ij} (-1 + 2\phi_N + 2\delta\Phi_N - 2\delta\Phi_P). \quad (2.8)$$

This parametrization extends the PPN formalism by replacing parameters by functions.

The second example considered in this communication concerns a particular effect due to MOND theory. In Blanchet & Novak (2011), it is shown that MOND induces within the solar system an *External Field Effect*. This effect is modeled by a quadrupolar contribution to the Newtonian potential

$$\phi_N = -\frac{GM}{rc^2} - \frac{Q_2}{2c^2} x^i x^j \left(e_1 e_j - \frac{1}{3} \delta_{ij} \right) \quad (2.9)$$

e_i is a unitary vector pointing towards the galactic center and $2.1 \cdot 10^{-27} \text{ s}^{-2} \leq Q_2 \leq 4.1 \cdot 10^{-26} \text{ s}^{-2}$ is the value of the quadrupole moment whose value depends on the MOND function.

These examples show that there are motivations to improve current tests of gravity but also to look at situations previously untested. This can be done by considering theories not entering the traditional frameworks or looking in regions of parameters where strong constraints are missing.

3 Range and Doppler simulations

In this work we focus on the possibility to perform gravity tests with radio science measurements. This kind of test has already been very successful when deriving the PPN γ constraint with Cassini (see previous section). In order to provide estimation of the order of magnitude and of the signature that an alternative theory of gravity produces on radio science signals (Range and Doppler), we have developed a software that simulates these signals. In order to allow for a wide class of alternative theories of gravity, Range and Doppler are simulated directly from the space-time metric $g_{\mu\nu}$. This means that it is very easy to change the gravitation theory by changing the metric.

Since GR and the alternative theories of gravity we consider are covariant, we are free to choose the coordinates to work with (gauge freedom). On the other hand, observations are covariant quantities (or gauge independent). Therefore, it is very important to produce simulations that are also covariant. In radio science, covariant quantities are based on proper time (time given by ideal clocks). The Range is defined as the difference between the reception proper time and the emission proper time and the Doppler is defined as the ratio of the received proper frequency over the emitted proper frequency. Three different steps are needed to simulate these quantities: the derivation and integration of the equations of motion, the derivation and integration of the equations of proper time and the computation of time transfer in curved space-time. These three steps are computed from the space-time metric by methods described in Hees et al. (2011). Finally in order to investigate the observables of an alternative theory of gravity in the Range and Doppler data we perform a least-squares fit in GR on the different parameters (initial conditions and masses of the bodies) and search for identifiable signatures in the residuals.

In the following, as an example, we present simulations of a two-way Range and Doppler signals for Cassini spacecraft from June 2002 during 3 years (when the probe was between Jupiter and Saturn). A simplified model is built with the Sun, the Earth and Cassini spacecraft. We successively consider Post-Einsteinian Gravity and MOND External Field Effect.

3.1 Post-Einsteinian Gravity (PEG)

As a simplified preliminary study, we focus on the effects of the potential $\delta\Phi_P(r)$ on the radio science signals. Indeed, the potential $\delta\phi_N$ is already very tightly constrained (from fifth force measurement). We consider a series expansion of this potential, that is to say we suppose the spatial part of the metric to be modified as

$$g_{ij} = [g_{ij}]_{GR} - 2\delta_{ij} \left(\chi_1 r + \chi_2 r^2 + \delta\gamma \frac{GM}{c^2 r} \right) \quad (3.1)$$

M is the Sun mass, $\delta\gamma = \gamma - 1$ is related to the PPN parameter and χ_1 and χ_2 are parameters characterizing deviations due to linear and quadratic terms in the metric.

We performed different simulations with different values for the three PEG parameters. For example, Fig. 1 represents the Range and Doppler residuals due to the presence of a PPN γ deviation of $\delta\gamma = \gamma - 1 = 10^{-5}$. The three peaks occur at solar conjunctions. The signal due to the conjunctions is not absorbed at all by the fit of the initial conditions. The simulated data are comparable with real data obtained in Bertotti et al. (2003).

To summarize the simulations performed, Fig. 2 represents the maximal Doppler residuals due to PEG theories of gravity (parametrized by their values of χ_1 , χ_2 and $\delta\gamma = \gamma - 1$). By requesting the maximal residuals to be smaller than the Cassini precision on Doppler signal (10^{-14}), we can estimate an upper limit for the PEG parameters: $\chi_1 < 10^{-23} m^{-1}$, $\chi_2 < 2 \cdot 10^{-33} m^{-2}$ and $\delta\gamma < 3 \cdot 10^{-5}$ (which is very similar to the real estimation (2.4)).

3.2 MOND External Field Effect

In the framework of MOND theory, Blanchet & Novak (2011) have shown that there exists an effect in the Solar System, the External Field Effect (EFE), which is modeled by a quadrupole contribution (see Sec. 2.3).

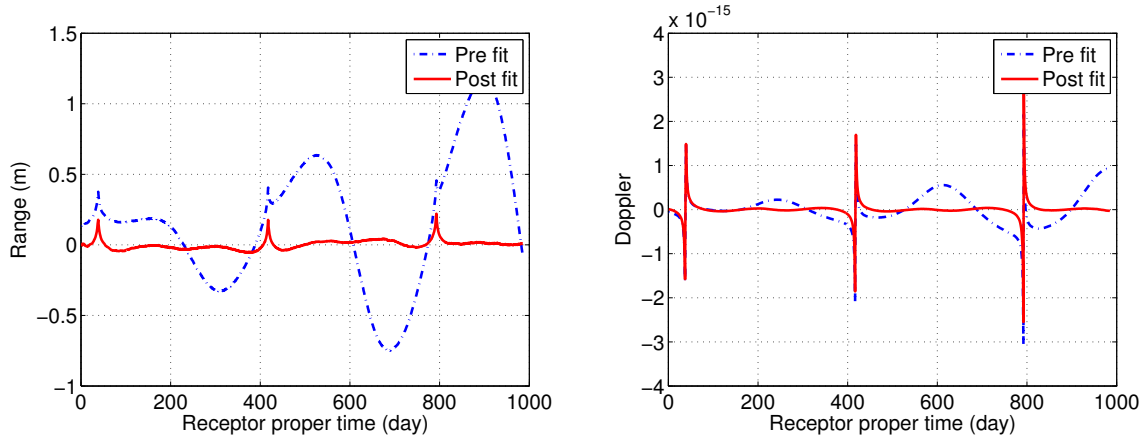


Fig. 1. Representation of the Range (left) and Doppler (right) signals due to a PEG theory of gravity with $\delta\gamma = \gamma - 1 = 10^{-5}$. The blue (dashed) lines represent the direct difference between simulations in GR and simulations in the alternative theory of gravity (with the same parameters). The red (continuous) lines represent the residuals after the least-square analysis (the observable signals).

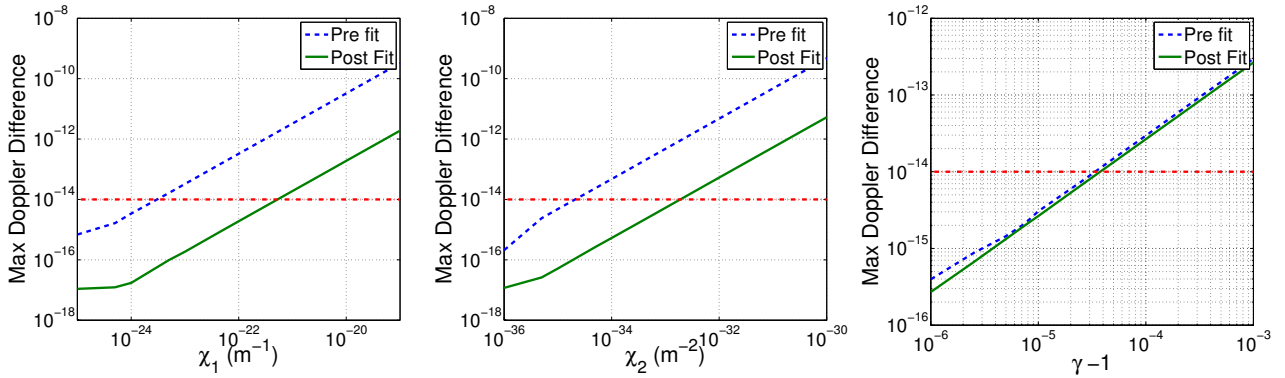


Fig. 2. Representation of the maximal Doppler signal due to PEG theory (parametrized by the three parameters χ_1 , χ_2 , $\delta\gamma$) for the Cassini mission. The blue (dashed) lines represent the direct difference between the Doppler in alternative theories and GR (with the same parameters) while the green (continuous) lines represent the maximal residuals that can be observed after the least-square analysis. The red lines represent the Doppler Cassini accuracy.

Results of our simulations for this effect are given in Fig. 3 where Range and Doppler residuals due to the EFE with $Q_2 = 4.1 \cdot 10^{-26} \text{ s}^{-2}$ (the maximal value allowed by the theory) are represented. The residuals are below the Cassini accuracy (10^{-14} in Doppler). Therefore, the Cassini arc considered here appears to be insufficient to provide a satisfactory test of MOND EFE. Note that this may be improved by considering other arcs or a dedicated space mission.

4 Conclusions

Starting from the basis of GR, we have presented current gravity tests performed in the Solar System. We have given motivations to increase the accuracy of the current constraints and to look at situations previously untested. In this context, we have presented a new software that performs radio science simulations from the space-time metric. With this tool, we are able to simulate any space mission in any alternative metric theory of gravity and to give the signature of an hypothetical alternative theory of gravity on the Range and/or on the Doppler. As examples, we have presented simulations of the Cassini mission in PEG theory of gravity and with the MOND External Field Effect. For the PEG theory, constraints have been derived for the parameters entering the expression of the spatial part of the metric. For the MOND EFE, we have shown that the predicted effect is too small to be detected with the considered arc of the Cassini mission.

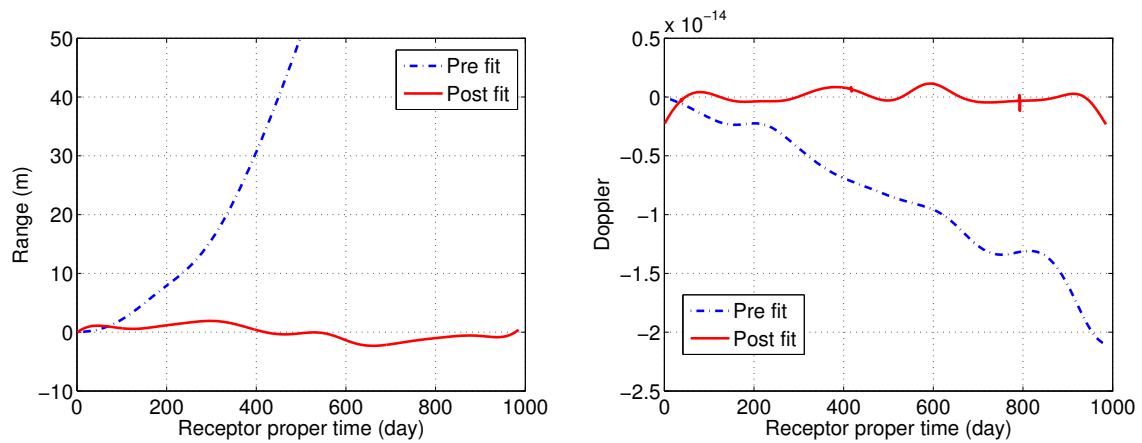


Fig. 3. Representation of the Range (left) and Doppler (right) signals due to the MOND External Field Effect with $Q_2 = 4.1 \cdot 10^{-26} \text{ s}^{-2}$. The blue (dashed) lines represent the direct difference between simulations in GR and simulations in the alternative theory of gravity (with the same parameters). The red (continuous) lines represent the residuals after the least-square analysis (the observable signals).

In the future, further simulations can be done for other theories and other (future and past) space missions to answer the following question: can a particular theory of gravity be observed with Range/Doppler measurements of a specific mission ?

A. Hees is research fellow from FRS-FNRS (Belgian Fund for Scientific Research) and he tanks FRS-FNRS for financial support.

References

- Adelberger, E. G., Gundlach, J. H., Heckel, B. R., Hoedl, S., & Schlamminger, S. 2009, *Progress in Particle and Nuclear Physics*, 62, 102
- Bertotti, B., Iess, L., & Tortora, P. 2003, *Nature*, 425, 374
- Blanchet, L. & Novak, J. 2011, *MNRAS*, 412, 2530
- Damour, T. & Nordtvedt, K. 1993, *Physical Review Letters*, 70, 2217
- Damour, T. & Polyakov, A. M. 1994, *General Relativity and Gravitation*, 26, 1171
- Fienga, A., Laskar, J., Kuchynka, P., et al. 2011, *Celestial Mechanics and Dynamical Astronomy* (ArXiv:1108.5546), 11, 363
- Hees, A., Wolf, P., Lamine, B., et al. 2011, *Proceedings of "Rencontres de Moriond 2011 - Gravitation Session"*
- Jaekel, M.-T. & Reynaud, S. 2005, *Classical and Quantum Gravity*, 22, 2135
- Jaekel, M.-T. & Reynaud, S. 2006a, *Classical and Quantum Gravity*, 23, 777
- Jaekel, M.-T. & Reynaud, S. 2006b, *Classical and Quantum Gravity*, 23, 7561
- Khoury, J. & Weltman, A. 2004, *Physical Review Letters*, 93, 171104
- Konopliv, A. S., Asmar, S. W., Folkner, W. M., et al. 2011, *Icarus*, 211, 401
- Lambert, S. B. & Le Poncin-Lafitte, C. 2009, *A&A*, 499, 331
- Mester, J., Torii, R., Worden, P., et al. 2001, *Classical and Quantum Gravity*, 18, 2475
- Reynaud, S. & Jaekel, M.-T. 2005, *International Journal of Modern Physics A*, 20, 2294
- Talmadge, C., Berthias, J.-P., Hellings, R. W., & Standish, E. M. 1988, *Physical Review Letters*, 61, 1159
- Touboul, P. & Rodrigues, M. 2001, *Classical and Quantum Gravity*, 18, 2487
- Will, C. M. 1993, *Theory and Experiment in Gravitational Physics*, ed. Will, C. M.
- Will, C. M. 2006, *Living Reviews in Relativity*, 9
- Williams, J. G., Turyshev, S. G., & Boggs, D. H. 2009, *International Journal of Modern Physics D*, 18, 1129

THE FIRST MEASUREMENT OF THE GALACTIC ABERRATION BY THE VLBI

S. B. Lambert¹

Abstract. This paper reports on the detection of the Galactic aberration in astrometric measurements of quasar positions by very long baseline radio interferometry (VLBI). The Galactic aberration effect shows up as a dipole component in the quasar proper motion field, oriented towards the Galactic center. The dipole amplitude is in good agreement with theoretical predictions.

Keywords: Astrometry, Techniques: interferometric, Galaxies: radio sources, Galaxies: active

The main component of the Solar System acceleration is due to its motion around the Galactic center. This acceleration produces a slight aberration of 5 to 6 milliseconds of arc per year (mas/yr) to the positions of distant bodies (e.g., Kovalevsky (2003)). This effect, known as secular aberration drift, was recently detected for the first time in geodetic and astrometric very long baseline interferometry (VLBI) measurements at 2 and 8 GHz by Titov, Lambert & Gontier (2011). This paper constitutes a summary of the former article which gives more technical details.



Fig. 1. Radio telescopes involved in 24 hour geodetic VLBI sessions since 1979 (<http://ivsopar.obspm.fr>).

Astrometric and geodetic VLBI is the cornerstone of highly accurate measurements of the time variable Earth's orientation and the establishment of terrestrial and celestial reference frames. Since 1979, the technique makes use of radio telescopes reported worldwide (Figure 1). About thirty of these radio telescopes are regularly involved in 24-hour sessions scheduled bi-weekly for more than twenty years. Since 1998, the International VLBI Service for Geodesy and Astrometry (IVS, Schlüter & Behrend (2007)) coordinates astrometric and geodetic VLBI observations from scheduling to analysis (<http://ivscc.gsfc.nasa.gov>). The SYRTE department at

¹ Observatoire de Paris/SYRTE, CNRS/UMR8630, UPMC, 75014 Paris, France

the Paris Observatory hosts an IVS analysis center and an IVS data center (<http://ivsopar.obspm.fr>) whose jobs are to run operational analysis of the latest VLBI observations and to make publicly (and continuously) available the full VLBI observational data base together with analysis results.

The analysis of the full observational data base, consisting of about seven million delays at 2 and 8 GHz recorded over thirty years, allows one to obtain time series of absolute coordinates of hundreds of compact extragalactic radio sources with an accuracy better than 0.1 mas. Figure 2 displays two examples of these time series which reflect changes in the structure of the body.

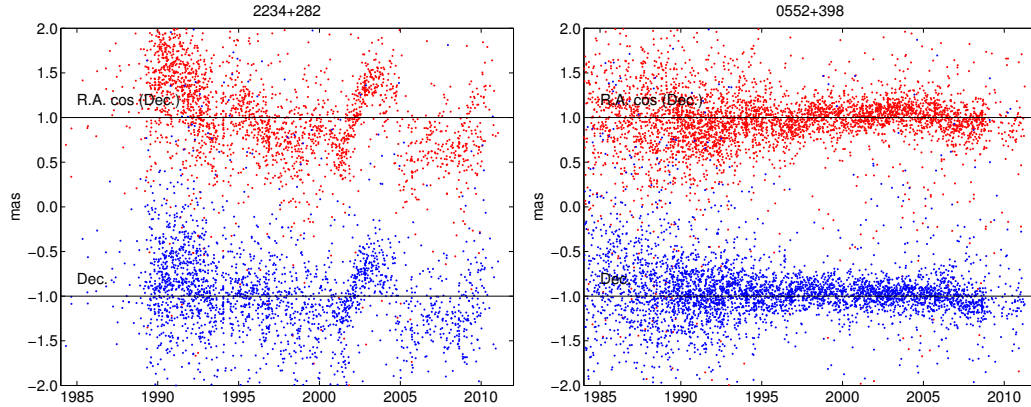


Fig. 2. Offsets of radio sources 2234+282 and 0552+398 to their respective ICRF2 positions.

The proper motion of the radio sources can then be computed as the slope of the series. However, this slope can be contaminated by reference frame effects if the analysis is done incorrectly. Indeed, during the analysis of delays, the analysts must impose minimal constraints of no-net rotation to avoid degeneracy of the system of equations, and to tie the radio sources to a reference frame (for instance the ICRF2 of Ma et al. (2009)). However, the constraint must be sufficiently loose to avoid masking the aberration effect. This point is the key point of the study. Previous studies that failed in finding the aberration used too tight constraints and obtained biased proper motions.

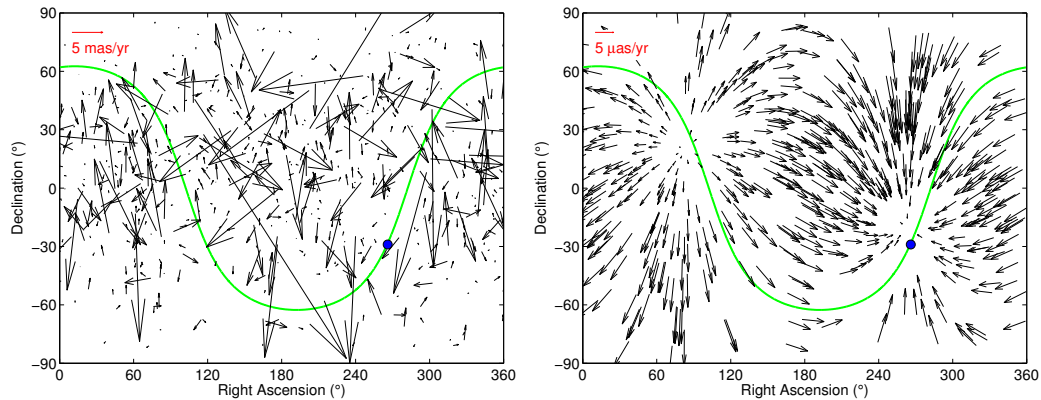


Fig. 3. Estimated proper motions of 555 radio sources (left) and adjusted dipole component (right). Note the drastic change in the scale.

The leftmost Fig. 3 displays the estimated proper motions of 555 radio sources fitted over 1990–2010. Through these proper motion we adjusted vector spherical harmonic coefficients of degree 2 (see for example Mignard & Morando (1990)) including a spheroidal (or dipolar) component, a toroidal (or global rotation) component, and a quadrupolar part. Before any adjustment, about 40 sources showing strong proper motion due to violent changes in the structure were removed from the sample. The quasar 2234+282 is among them. The dipole component is plotted in the right panel of Fig. 3.

The dipole of amplitude 6.4 ± 1.5 mas/yr is in good agreement with theoretical predictions and constitutes the first direct measurement of the Galactic aberration of distant bodies. It shows that VLBI has now accumu-

lated accurate enough data to detect the Galactocentric acceleration through its effect on distant radio source positions. It turns out that the current definition of the celestial reference frame as epochless and based on the assumption that quasars have no detectable proper motions (Feissel & Mignard (1998)) should be mitigated. In the future, VLBI realizations of the celestial reference system should correct source coordinates for this effect, possibly by providing source positions, together with a corrective formula. The origin of the quadrupole remains unclear at this stage. It is certainly affected by Sun-atmosphere interactions along the ecliptic and needs more observations to identify systematics. It is especially interesting because the quadrupole amplitude is linked to the energy density of gravitational waves of period larger than 30 years Gwinn et al. (1997). The marginal quadrupolar amplitude found in our study is 6.4 ± 3.6 mas/yr and allows us to say that the upper limit of the gravitational wave energy density is $0.0042h^{-2}$.

References

- Feissel, M., & Mignard, F. 1998, *A&A*, 331, 33
Gwinn, C. R., Eubanks, T. M., Pyne, T., et al. 1997, *ApJ*, 485, 87
Kovalevsky, J. 2003, *A&A*, 404, 743
Ma, C., Arias, E. F., Bianco, G., et al. 2009, In: A. L. Fey et al. (Eds.), *International Earth Rotation and Reference Systems Service (IERS) Technical Note 35*, Bundesamt für Kartographie und Geodäsie, Frankfurt am Main
Mignard, F., & Morando, B. 1990, In: N. Capitaine, & S. Débarbat (Eds.), *Proc. Journées 1990 Systèmes de Référence Spatio-Temporels*, Observatoire de Paris, 151
Schlüter, W., & Behrend, D. 2007, *J. Geod.*, 81, 479
Titov, O., Lambert, S. B., & Gontier, A.-M. 2011, *A&A*, 529, A91

MEASURING THE ABSOLUTE NON-GRAVITATIONAL ACCELERATION OF A SPACECRAFT: GOALS, DEVICES, METHODS, PERFORMANCES

B. Lenoir¹, B. Christophe¹ and S. Reynaud²

Abstract. Space provides unique opportunities to test gravitation. By using an interplanetary spacecraft as a test mass, it is possible to test General Relativity at the Solar System distance scale. This requires to compute accurately the trajectory of the spacecraft, a process which relies on radio tracking and is limited by the uncertainty on the spacecraft non-gravitational acceleration.

The Gravity Advanced Package (GAP) is designed to measure the non-gravitational acceleration without bias. It is composed of an electrostatic accelerometer supplemented by a rotating stage. This article presents the instrument and its performances, and describes the method to make unbiased measurements. Finally, it addresses briefly the improvement brought by the instrument as far as orbit reconstruction is concerned.

Keywords: electrostatic accelerometer, bias rejection, colored noise, Allan variance, non-gravitational acceleration, General Relativity, orbit reconstruction

1 Introduction

With the ever-increasing precision of measurements, space has become a privileged place to test the two fundamental theories which emerged during the 20th century: General Relativity and Quantum Theory. In addition to providing a very clean environment, it opened new ways of testing these theories: as an example of interest for this article, precise navigation of interplanetary spacecrafts allows probing the scale dependence of gravitation at the Solar System distance scale (Jaekel & Reynaud 2006).

Even if most experimental tests support General Relativity (Will 2006), there are still open windows for deviations. Indeed, the fact that these two fundamental theories are difficult to reconcile suggest that General Relativity may not be the final description of gravitation. The reason is that gravitation is the only interaction not having a quantum description. The validity of the Newton potential has been extensively tested for distances between the millimeter and the characteristic size of planetary orbits (Fischbach & Talmadge 1999). But there remain open windows outside this distance range for violations of the inverse square law (Adelberger et al. 2003, Fig. 4): below the millimeter or for distances of the order or larger than the Solar System characteristic size.

Long range tests are performed using the motion of planets and interplanetary probes. Monitoring of the Moon and Mars delivers high precision tests of the validity of General Relativity at these distances (e.g. Kolosnitsyn & Melnikov 2004; Williams et al. 1996). However, the navigation data of the Pioneer probes show a discrepancy with respect to the predictions of General Relativity (Anderson et al. 1998, 2002a; Lévy et al. 2009). This discrepancy can be described as an anomalous acceleration directed toward the Sun with a roughly constant amplitude of approximately $8 \times 10^{-10} \text{ m.s}^{-2}$. The origin of this anomaly is yet unexplained despite a huge effort of the scientific community (Turyshev & Toth 2010, and references therein): it may be an experimental artifact as well as a hint of considerable importance for fundamental physics (Brownstein & Moffat 2006; Jaekel & Reynaud 2005). At larger scales, the rotation curves of galaxies and the relation between redshift and luminosities of supernovae are accounted for by introducing respectively “dark matter” and “dark energy”, which represent 25 % and 70 % of the energy content of the Universe (Frieman et al. 2008). Since these dark components have been introduced on the basis of gravitational observations solely, the hypothesis that General Relativity is not a correct description of gravitation at these scales needs to be considered (Carroll et al. 2004).

¹ Onera – The French Aerospace Lab, 29 avenue de la Division Leclerc, F-92322 Châtillon, France.

² Laboratoire Kastler Brossel (LKB), ENS, UPMC, CNRS, Campus Jussieu, F-75252 Paris Cedex 05, France.

It is therefore essential to test gravitation at all distance scales. To this extent, several mission concepts have been proposed to improve the experiment made by the Pioneer probes (Anderson et al. 2002b; Bertolami & Paramos 2007; Johann et al. 2008; Christophe et al. 2009, 2011; Wolf et al. 2009). In many proposals, the addition of an accelerometer being able to measure without bias the non-gravitational acceleration of the spacecraft is central. ESA included this idea in the roadmap for fundamental physics in space (ESA 2010) and recommended the development of accelerometer compatible with spacecraft tracking at the 10 pm.s^{-2} level. This article presents such an instrument, called the Gravity Advanced Package (Lenoir et al. 2011b). First, a description of the instrument and its performances is given. Then, the method used to make absolute measurement is described (Lenoir et al. 2011a). Finally, the expected improvements of the orbit reconstruction process using the instrument are briefly discussed.

2 The Gravity Advanced Package

The Gravity Advanced Package is an important technological upgrade for future fundamental physics missions in space. It is composed of two subsystems: MicroSTAR is a three-axis electrostatic accelerometer (Josselin et al. 1999) based on Onera's experience (Touboul et al. 1999; Touboul & Rodrigues 2001), and the Bias Rejection System is a rotating stage with piezo-electric actuator used to rotate MicroSTAR around its x axis. The accelerometer aims at measuring the non-gravitational acceleration of the spacecraft but other quantities are also measured. In fact, MicroSTAR measures the components of the vector \mathbf{a} on its three orthogonal measurement axis called x , y and z :

$$\mathbf{a} = \frac{1}{m_S} \mathbf{F}_{ext \rightarrow S}^{\text{NG}} + \dot{\boldsymbol{\Omega}} \wedge \mathbf{l} + \boldsymbol{\Omega} \wedge (\boldsymbol{\Omega} \wedge \mathbf{l}) - \left(\frac{1}{m_A} + \frac{1}{m_S} \right) \mathbf{F}_{S \rightarrow A}^{\text{G}} + \left(\frac{1}{m_S} \mathbf{F}_{ext \rightarrow S}^{\text{G}} - \frac{1}{m_A} \mathbf{F}_{ext \rightarrow A}^{\text{G}} \right) \quad (2.1)$$

where m_S and m_A are the masses of the satellite and the proof mass respectively, $\mathbf{F}_{ext \rightarrow S}^{\text{NG}}$ is the non-gravitational force acting on the spacecraft, $\boldsymbol{\Omega}$ is the rotation vector of the instrument with respect to a Galilean reference frame, \mathbf{l} is the vector between the center of mass of the satellite and the instrument (lever arm), $\mathbf{F}_{S \rightarrow A}^{\text{G}}$ is the gravity of the spacecraft, and the last term in parenthesis is the gravity gradient expressed in term of acceleration, $\mathbf{F}_{ext \rightarrow S}^{\text{G}}$ and $\mathbf{F}_{ext \rightarrow A}^{\text{G}}$ being the gravitational forces acting on the satellite and the proof mass respectively. All these additional terms can be removed (Lenoir et al. 2011b).

Of course, the measurement is plagued by scale ($\delta k_{1\nu}$) and quadratic factors ($k_{2\nu}$), by bias (b_ν) and by noise (n_ν), such that the actual measurement on the axis $\nu \in \{x; y; z\}$ is :

$$m_\nu = (1 + \delta k_{1\nu}) a_\nu + k_{2\nu} a_\nu^2 + b_\nu + n_\nu \quad (2.2)$$

where a_ν is the projection of \mathbf{a} on the axis ν .

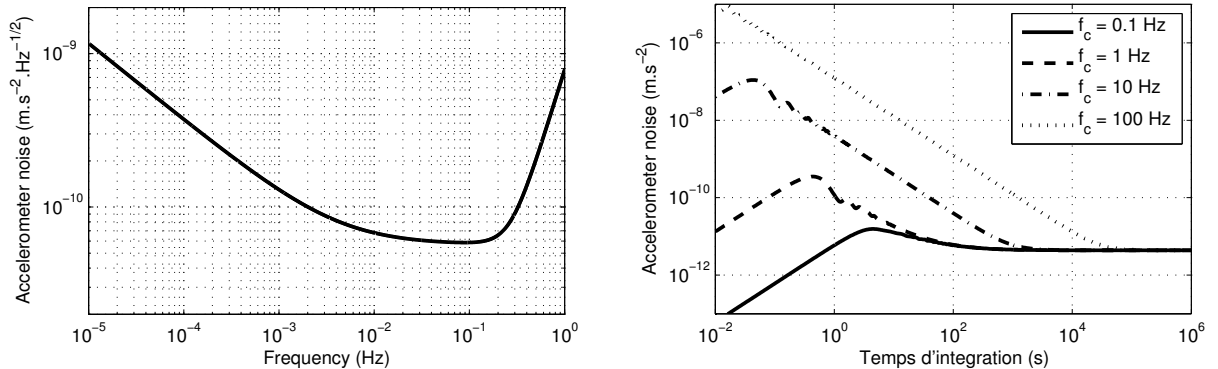


Fig. 1. Left: Square-root of the power spectrum density of the accelerometer noise. **Right:** Square-root of the Allan variance of the accelerometer noise. The curves are plotted for different cut-off frequencies. The oscillations for $2\pi\tau f_c < 1$ are not described by the simplified formula (2.4).

The measurement noise is characterized by the following power spectrum density (Lenoir et al. 2011b) for a

measurement range of $1.8 \times 10^{-4} \text{ m.s}^{-2}$ (cf. fig. 1):

$$S_n(f) = \left(5.7 \times 10^{-11} \text{ m.s}^{-2}.\text{Hz}^{-1/2}\right)^2 \times \left[1 + \left(\frac{f}{4.2 \text{ mHz}}\right)^{-1} + \left(\frac{f}{0.27 \text{ Hz}}\right)^4\right] \quad (2.3)$$

The characterization of the noise can also be given in term of Allan variance $A(\tau, f_c)$, where f_c is the cut-off frequency. A simplified expression of the Allan variance (AVAR) (Allan 1966) for $2\pi\tau f_c \gg 1$ is:

$$A_n(\tau, f_c) = \left(5.7 \times 10^{-11} \text{ m.s}^{-2}.\text{Hz}^{-1/2}\right)^2 \times \left[\frac{1}{2\tau} + 2 \ln(2) \times 4.2 \text{ mHz} + \frac{f_c^3}{3\pi^2\tau^2} \times (0.27 \text{ Hz})^{-4}\right] \quad (2.4)$$

Figure 1 shows the dependence of Allan variance with respect to integration time and cut-off frequency without the $2\pi\tau f_c \gg 1$ approximation.

The Bias Rejection System rotates the accelerometer around the x axis of a monitored angle called θ . Assuming that the quadratic factors are equal to zero and that the scale factors are perfectly known*, the quantities measured along the axis y and z are :

$$\begin{cases} m_y = [\cos(\theta)a_Y + \sin(\theta)a_Z] + b_y + n_y \\ m_z = [-\sin(\theta)a_Y + \cos(\theta)a_Z] + b_z + n_z \end{cases} \quad (2.5a)$$

$$(2.5b)$$

with a_μ ($\mu \in \{Y; Z\}$) being the components of the acceleration in the reference frame of the spacecraft.

3 Method to remove the bias of the electrostatic accelerometer from the measurements

The method for removing the bias of the instrument consists in flipping MicroSTAR. The underlying idea is that when $\theta = 0$ rad, the accelerometer measures the quantities $m_y = a_Y + b_y$ and $m_z = a_Z + b_z$, and when $\theta = \pi$ rad, it measures $m_y = -a_Y + b_y$ and $m_z = -a_Z + b_z$. Subtracting these measurements allows recovering the external signal without bias, under the assumption that they are constants. The complete method, which can handle time variations of the external signal and of the bias, is described in (Lenoir et al. 2011a). It is shown in particular that the modulation signal, i.e. the time variation of θ , must fulfill some conditions in order to correctly remove the bias from the measurement (cf. eq. (3.1)).

The modulation signal is supposed to be periodic, τ being the period. Moreover, the measurements used for data post-processing are the ones made when the angle θ is constant with time and only two positions are considered: 0 rad and π rad (so that assuming $k_{2\nu} = 0$ is not restrictive). On the contrary, the measurements made when the accelerometer is rotating are not used because they may be spoiled by unwanted signal (vibration, fictitious acceleration). The duration of the rotation per period is called T_M and will be referred to as the masking duration.

Assuming that the signal to measure and the bias are affine functions of time for each modulation period (which is correct if τ is small compared to the characteristic variation time of the signal and the bias), the conditions for completely removing the bias from the measurements read

$$\int_{-\tau/2}^{\tau/2} m(t) \cos(\theta(t)) dt = \int_{-\tau/2}^{\tau/2} t m(t) \cos(\theta(t)) dt = \int_{-\tau/2}^{\tau/2} t^2 m(t) \cos(\theta(t)) dt = 0 \quad (3.1)$$

where $m(t)$ is equal to 0 when the accelerometer is rotating and 1 when it is not. These conditions allow deriving the time variation of the angle θ , which is shown in figure 2 (left). The pattern depends on the ratio of the masking duration T_M and the period τ , as shown by figure 2 (right).

With such a signal and after post-processing, it is possible to recover the mean of the external signal without bias over a modulation period τ . It is possible to characterize these unbiased measurements in term of noise. The level of noise depends on the modulation period τ and the masking time T_M but is approximately white as shown by figure 3 (left). For $\tau = 600$ s and $T_M = 200$ s, the uncertainty on the unbiased measurements is $4.2 \times 10^{-12} \text{ m.s}^{-2}$ (this value is the integral of the power spectrum density shown in fig. 3 (left)). This allows reaching a precision of 1 pm.s^{-2} for an integration time of three hours.

*These assumptions are made for simplicity purpose. The complete treatment of the problem is presented in (Lenoir et al. 2011a).

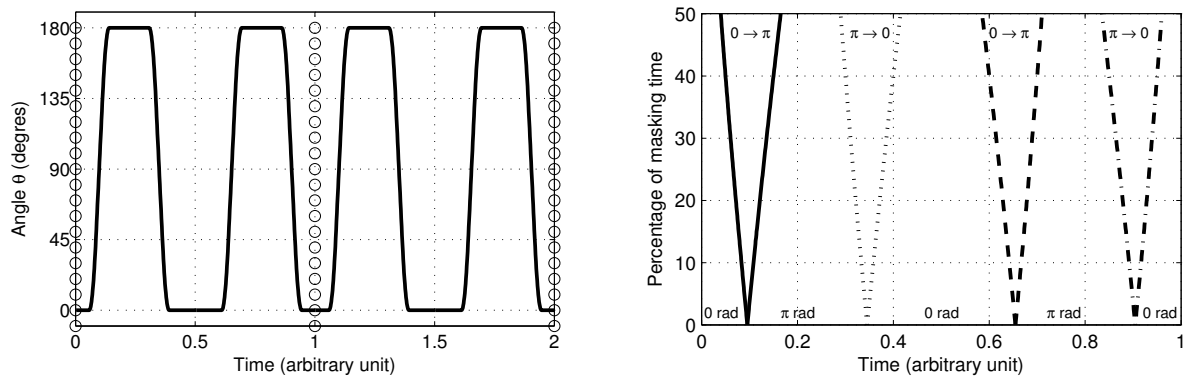


Fig. 2. Left: Modulation signal (-) for a masking duration representing 33.33 % of the modulation period $\tau = 1$ arbitrary unit. Two periods are represented, separated by circles (\circ) **Right:** The figure describes how the modulation signal changes when the ratio T_M/τ changes (one period is represented). The abscissa is time and the ordinate is T_M/τ expressed in percentage. The curves indicate the values of the angle θ : between two curves of the same style θ changes, between the curves (-) and (\cdot) and between the curves (- -) and (- \cdot) $\theta = \pi$ rad, and $\theta = 0$ rad elsewhere.

4 Improvement of orbit reconstruction

As mentioned in the introduction, the Gravity Advances Package (GAP) aims at improving the orbit reconstruction of interplanetary probes so as to test the theories of gravitation. So far, models have been used to correct for the non-gravitational acceleration of the spacecrafts. But the computed orbit is then subject to errors due to uncertainties or inaccuracies in the models. By providing unbiased measurements of the non-gravitational acceleration in the orbit plane, the GAP enhances orbit reconstruction: it removes parameters to be fitted, it measures the fluctuation of the non-gravitational acceleration, and it removes correlations.

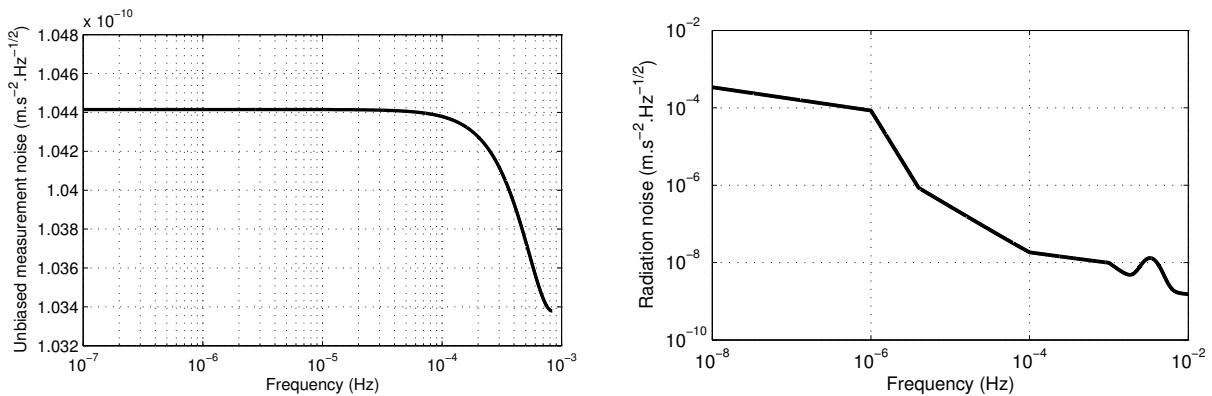


Fig. 3. Left: Square root of the power spectrum density of the unbiased measurements obtained after post-processing for a modulation period $\tau = 600$ s and a masking duration $T_M = 200$ s. **Right:** Square root of the power spectrum density of the solar radiation pressure noise (Fröhlich & Lean 2004) in term of acceleration for a spacecraft with a ballistic coefficient of $0.1 \text{ m}^2.\text{kg}^{-1}$ at 10 AU of the Sun (Biesbroek 2008). The bump at 3 mHz corresponds to the 5-minute oscillations of the Sun.

There are several sources for the non-gravitational acceleration, the main ones being the direct solar radiation pressure and the anisotropic thermal radiation of the spacecraft. Figure 3 illustrates the interest of the GAP as far as the fluctuations of the non-gravitational acceleration are concerned. The power spectrum density of the unbiased measurement noise is compared to the noise on the radiation pressure expressed in term of acceleration. Whereas these fluctuations are not taken into account in the models, it shows that the GAP allows measuring them with a very high precision.

5 Conclusions

The Gravity Advances Package, designed to improve the tests of gravitation at the Solar System distance scale, displays performances which will allow improving the accuracy of orbit reconstruction significantly. Indeed, with a carefully designed calibration signal for the rotating stage, it is possible to remove completely the bias of the electrostatic accelerometer and to obtain the mean non-gravitational acceleration of the spacecraft with no bias and a precision of 1 pm.s^{-2} for an integration time of three hours. This expected precision will allow reaching the 10 pm.s^{-2} level for spacecraft tracking recommended by ESA. To do so, the accelerometer measurements will have to be taken into account during the orbit reconstruction process.

The authors are grateful to CNES for its financial support.

References

- Adelberger, E., Heckel, B., & Nelson, A. 2003, *Annu. Rev. Nucl. Part. Sci.*, 53
- Allan, D. 1966, *Proceedings of the IEEE*, 54, 221
- Anderson, J., Laing, P., Lau, E., et al. 1998, *Phys. Rev. Lett.*, 81, 2858
- Anderson, J., Laing, P., Lau, E., et al. 2002a, *Phys. Rev. D*, 65, 082004
- Anderson, J., Nieto, M., & Turyshev, S. 2002b, *Mod. Phys. Lett. A*, 17, 875
- Bertolami, O. & Paramos, J. 2007, *Int. J. Mod. Phys. D*, 16, 1611
- Biesbroek, R. 2008, *Laplace : Assessment of the Jupiter Ganymede Orbiter*, CDF Study Report CDF-77(A), ESA
- Brownstein, J. R. & Moffat, J. W. 2006, *Class. Quantum Grav.*, 23, 3427
- Carroll, S., Duvvuri, V., Trodden, M., & Turner, M. 2004, *Phys. Rev. D*, 70, 043528
- Christophe, B., Andersen, P. H., Anderson, J. D., et al. 2009, *Exp. Astron.*, 23, 529
- Christophe, B., Spilker, L., Anderson, J., et al. 2011, arXiv:1106.0132 [gr-qc]
- ESA. 2010, *A Roadmap for Fundamental Physics in Space*, available at [2010/08/23]: <http://sci.esa.int/fprat>
- Fischbach, E. & Talmadge, C. 1999, *The search for non-Newtonian gravity* (New York: Springer)
- Frieman, J. A., Turner, M. S., & Huterer, D. 2008, *Annu. Rev. Astro. Astrophys.*, 46, 385
- Fröhlich, C. & Lean, J. 2004, *Astron. Astrophys. Rev.*, 12, 273
- Jaekel, M. T. & Reynaud, S. 2005, *Mod. Phys. Lett. A*, 20, 1047
- Jaekel, M. T. & Reynaud, S. 2006, *Class. Quantum Grav.*, 23, 7561
- Johann, U. et al. 2008, in *Astrophysics and Space Science Library*, Vol. 349, *Lasers, Clocks and Drag-Free Control*, ed. H. Dittus, C. Lämmerzahl, & S. Turyshev (Springer), 577–604
- Josselin, V., Touboul, P., & Kielbasa, R. 1999, *Sens. Actuators, A*, 78, 92
- Kolosnitsyn, N. I. & Melnikov, V. N. 2004, *Gen. Relativ. Gravitation*, 36, 1619
- Lenoir, B., Christophe, B., & Reynaud, S. 2011a, arXiv:1105.4979 [physics.ins-det]
- Lenoir, B., Lévy, A., Foulon, B., et al. 2011b, *Adv. Space Res.*, 48, 1248
- Lévy, A., Christophe, B., Bério, P., et al. 2009, *Adv. Space Res.*, 43, 1538
- Touboul, P., Foulon, B., & Willemenot, E. 1999, *Acta Astronaut.*, 45, 605
- Touboul, P. & Rodrigues, M. 2001, *Class. Quantum Grav.*, 18, 2487
- Turyshev, S. M. & Toth, V. T. 2010, *Living Reviews in Relativity*, 13, available at [2010/10/13]: <http://www.livingreviews.org/lrr-2010-4/>
- Will, C. 2006, *Living Reviews in Relativity*, 9, available at [2010/01/08]: <http://www.livingreviews.org/lrr-2006-3>
- Williams, J., Newhall, X., & Dickey, J. 1996, *Phys. Rev. D*, 53, 6730
- Wolf, P., Bordé, C. J., Clairon, A., et al. 2009, *Exp. Astron.*, 23, 651

GETEMME: A MISSION TO EXPLORE THE MARTIAN SATELLITES

C. Le Poncin-Lafitte¹ and the GETEMME core team²

Abstract. GETEMME (Gravity, Einstein’s Theory, and Exploration of the Martian Moons’ Environment) is a proposition of mission towards martian’s moons. The spacecraft will initially rendezvous with Phobos and Deimos in order to carry out a comprehensive mapping and characterization of the two satellites and to deploy passive laser retro-reflectors on their surfaces. In the second stage of the mission, the spacecraft will be transferred into a lower 1500-km Mars orbit, to carry out routine laser range measurements to the Phobos and Deimos reflectors. Also, asynchronous two-way laser ranging measurements between the spacecraft and stations of the ILRS (International Laser Ranging Service) on Earth are foreseen. An onboard accelerometer will ensure a high accuracy for the spacecraft orbit determination. The inversion of all range and accelerometer data will allow us to determine or improve dramatically on a host of dynamic parameters of the Martian satellites system. From the complex motion and rotation of Phobos and Deimos we will obtain clues on internal structures and the origins of the satellites. Also, crucial data on the time-varying gravity field of Mars related to climate variation and internal structure will be obtained. Ranging measurements will also be essential to improve on several parameters in fundamental physics, such as the Post-Newtonian parameter β as well as time-rate changes of the gravitational constant and the Lense-Thirring effect. Measurements by GETEMME will firmly embed Mars and its satellites into the Solar System reference frame.

Keywords: space mission, Mars, planetology, relativity

1 Mission scenario

GETEMME (Gravity, Einstein’s Theory, and Exploration of the Martian Moons’ Environment) is an interplanetary mission to Mars and its two satellites Phobos and Deimos consisting of one spacecraft with four embedded landers. The Spacecraft will fly to Mars with an electric propulsion system.

After 700 days of flight GETEMME will rendezvous with Deimos, stay in orbit for three months and fly to Phobos afterwards. During these rendezvous phases two passive landers will be deployed on each moon. We assume a baseline of the lander’s delivery from a low (few radii) Phobos or Deimos orbit and ”dropping” the packages by ejection, reducing orbital velocity as shown in figure 1. The Landers will undergo an unpowered, uncontrolled (but pre-calculated) free fall (touchdown velocity of the order of 8 m/s for Phobos and 5 m/s for Deimos) to a selected landing site (within a 1-km landing error ellipse). The touchdown is damped by crushables. Uprightening is carried out automatically by opening the shell cover or the lever arm, thereby also removing the protective cover hat from the reflector optics. A maximum surface slope of between 30° and 45° can be tolerated with the baseline reflector design, thus, no active pointing is foreseen. Two landing sites will be chosen each for Phobos and Deimos, near the equator, approx. 20° east and west of the sub-Martian point, sub-Martian latitude $\pm 5^\circ$, (corresponding to an error ellipse semimajor axis of about 1 km on Phobos and 0.5 km on Deimos). The proposed Lander design is based on a shell-like structure that protects all electronics (as well as the reflectors) during impact with crushable shock absorbers and opens after landing.

Then the spacecraft will finally travel to a circular Mars orbit and stay there for one Martian year for scientific operations. The mission will be completed after at least 2 years of nominal operations. An onboard accelerometer will ensure highly accurate spacecraft orbit determination. Major part of scientific operations will be devoted

¹ SYRTE, Obs. de Paris, CNRS/UMR8630, 77 Av. Denfert Rochereau, 75014 Paris, France

² J. Oberst, V. Lainey, V. Dehant, P. Rosenblatt, S. Ulamec, J. Biele, H. Hoffmann, K. Willner, U. Schreiber, N. Rambaux, P. Laurent, A. Zakharov, B. Foulon, L. Gurvits, S. Murchie, C. Reed, S. Turyshev, B. Noyelles, J. Gil, M. Graziano, R. Kahle, V. Klein, A. Pasewaldt, A. Schlicht, J. Spurmann, M. Wählisch, K. Wickhusen

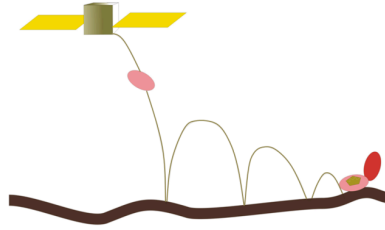


Fig. 1. Delivery scheme of Landers on the Martian Moons.

to ranging measurement between the spacecraft and the landed reflectors. We adopt a ranging schedule, where the orbiter is in a suitable position for successful range measurements to the reflectors within incidence angles of $\pm 10^\circ$ from the vertical (taking into account uncertainties in surface tilt and the reflector orientations on Phobos and Deimos). At 1500 km above ground the orbiter will move 8.3 times around Mars per 24 hour. It will therefore be in opposition to Phobos every 280 minutes and to Deimos every 190 minutes. Ranging will be carried in selected time slots. A measurement interval will last at least 15 minutes for Phobos and 50 minutes for Deimos. The total number of ranging measurements to all 4 reflectors is 1 000 000 (measurement goal). Earth ranging can generally be performed more than 8 times per 24 hours, with one measurement interval lasting approx. 135 minutes. We anticipated the use of multiple Earth stations to warrant ranging measurements not disrupted by the rotational cycle. The total number of ranging measurements is 500 000.

2 Mission objectives

2.1 Planetology of martian's system

Monitoring the satellite orbits accurately is a powerful way to quantify physical parameters related to interior. As an example, tidal dissipation inside Mars provides a phase lag between the tidal bulge and the line of sight Mars-satellite. Such lag induces a torque that provides exchange of angular momentum between rotation of the primary body Mars and orbital motion of the tide raising satellite. Benefitting from equatorial orbits, the tracking of the GETEMME spacecraft will provide high accuracy estimates for the tidal Love numbers k_2 , k_3 and the dissipation factor Q at Solar, Phobos, and Deimos tidal frequencies. The quantification of these parameters and their dependence on frequency will be a major step for solving the origin and fate of the Martian moons, as well as improving our knowledge of the interior of Mars (Mignard 1981; Efroimsky & Lainey 2007). Similar parameters for Phobos and Deimos will be derived by the study of the moon rotations. The gravity field

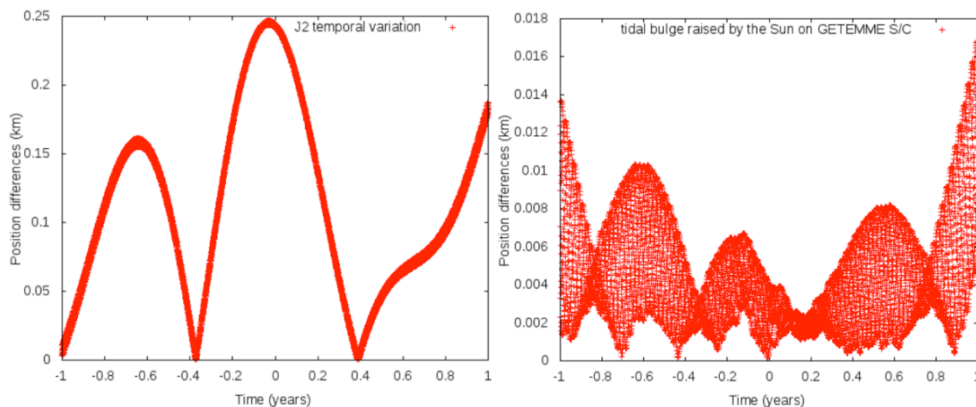


Fig. 2. Left: post-fit residuals with/without temporal variations of Mars J_2 over 2 years after fitting initial state vectors of GETEMME S/CCaption of the left panel. **Right:** post-fit residuals with/without the Solar tidal bulge raised on Mars over 2 years after fitting initial state vectors of GETEMME S/C.

of Mars undergoes temporal variations. During one Mars year, CO_2 sublimates from the North polar cap to the atmosphere, condenses at the South polar cap, and vice versa. Thanks to the equatorial orbits of Phobos,

Deimos and GETEMME spacecraft, this CO_2 cycle will be accurately measured. Annual and semi-annual seasonal variations of low-degree harmonics as well as length of day variations will be greatly constrained (see figure 2 - left). Estimated to be on the order of 10^{-11} yr^{-1} , the secular variation of J_2 will also be known with an accuracy of 1.5×10^{-17} after two years of data. This effect is observed on the Earth and has been attributed to the relaxation of the mantle released from ice loads of the ice age. If detected on Mars, such effect will bring important information on the past climate of Mars, as well as on Mars interior. The quantification of Mars nutation and Chandler wobble, with possible free core nutation (FCN) signal may provide strong input for the interior modeling, including the size of the Martian core.

2.2 Relativity tests

Ranging data, provided by GETEMME, will also drastically lead to a major improvement of the Martian satellites' ephemerides (Lainey et al. 2007). At the centimeter level of accuracy, General Relativity has to be used to describe correctly the motions of the two moons and the impact of curvature on the light propagation. By using the first parameterized post-Newtonian (PPN) approximation of General Relativity (Will 1993), GETEMME data can give new highlights on several of the ten PPN parameters, in particular PPN β which plays an important role in the relativistic perihelion's precession formula. Hence, when using the GETEMME ranging dataset to build new precise ephemerides of Phobos and Deimos around Mars, one can measure with high precision their periapsis precession. Then, a local determination of PPN beta can be performed and this result will improve actual determination usually obtained in the gravitational field of the Sun, e.g. by using planetary ephemerides (Fienga et al. 2010).

Another relativistic effect can be constraint by GETEMME ranging data. Indeed Lense-Thirring precession is a relativistic correction to the precession of a gyroscope near a large rotating mass such as the Earth, i.e. a gravitomagnetic frame-dragging effect. It is a prediction of General Relativity consisting of secular precessions of the longitude of the ascending node and the argument of pericenter of a test particle freely orbiting a central spinning mass endowed with a specified angular momentum. This effect have been detected by observing the motion of geodetic LAGEOS satellite around the Earth at the level of 10^{-1} (Ciufolini & Pavlis 2004) and a space project named LARES (Ciufolini et al., 2010) has been recently proposed to reach a determination at the level of $10^{-2/-3}$. With GETEMME, we can detect this effect because we are sensitive to this relativistic precession of Phobos and Deimos orbits due to the rotation of Mars. As illustrated on figure 3, one can expect a detection of this effect at the level of accuracy of 10^{-4} .

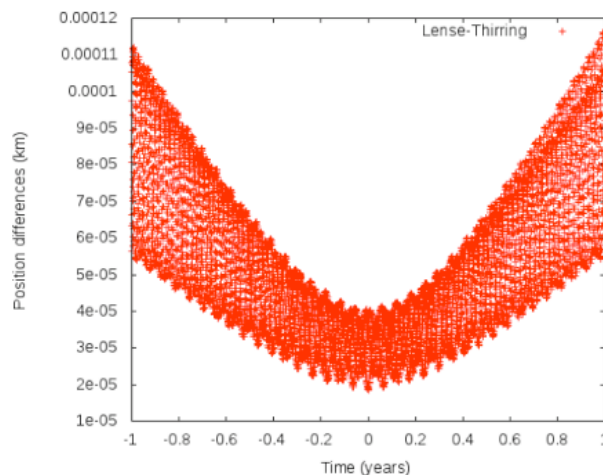


Fig. 3. post-fit residuals with/without the Lense-Thirring effect due to Mars rotation over 2 years after fitting initial state vectors of GETEMME S/C.

References

Efroimsky, M. & Lainey, V. 2007, *Journal of Geophysical Research (Planets)*, 112, E12003

- Fienga, A., Laskar, J., Kuchynka, P., et al. 2010, in IAU Symposium, Vol. 261, IAU Symposium, ed. S. A. Klioner, P. K. Seidelmann, & M. H. Soffel, 159–169
- Lainey, V., Dehant, V., & Pätzold, M. 2007, *Astronomy and Astrophysics*, 465, 1075
- Mignard, F. 1981, *Moon and Planets*, 24, 189

DEVELOPMENT OF TECHNIQUES TO STUDY THE DYNAMIC OF HIGHLY ELLIPTICAL ORBITS

G. Lion¹ and G. Métris¹

Abstract. Many spacecrafts are or will be placed in highly eccentric orbits around telluric planets of the Solar system. Such eccentricities allow to cover a wide range of altitudes, mainly for planetology purposes. There are also orbits with very high eccentricity around the Earth, especially the GTO (Geostationary Transfer Orbit) and orbits of some space debris. In this case, the motion is strongly perturbed by the luni-solar attraction. For various reasons which will be recalled, the traditional tools of celestial mechanics are not well adapted to the particular dynamic of highly eccentric orbits. Therefore, it is necessary to develop specific techniques for this configuration. This concerns numerical as well as analytical tools. We will show how to construct the expression of the disturbing function due to the presence of an external body, well-suited for highly eccentric orbits. Expansion of the elliptic motion in closed-form by using Fourier series in multiple of the eccentric anomaly will be presented. On the other hand, classical methods of numerical integration have often a poor efficiency. We will show the interest of geometric integrators and in particular the variational integrators.

Keywords: Third-body, disturbing function, Hansen-like coefficients, elliptic motion, high eccentricity, closed-form, variational integrators

1 Introduction

When dealing with highly elliptical orbits, we have to face several difficulties. Due to the fact that such orbits cover a wide range of altitudes, the hierarchy of the perturbations acting on the satellite changes with the position on the orbit. At low altitude, the oblateness of the Earth (the so called J_2 effect) is the dominant perturbation while at high altitude the luni-solar perturbation acceleration can reach or exceed the order the J_2 acceleration. This particular configuration requires to develop adapted strategies to propagate the orbit by means of analytical theories from the one hand and numerical integration on the other hand.

From the analytical point of view, the traditional theories of celestial mechanics are not well adapted to this particular dynamic. On the one hand, analytical solutions are quite generally expanded into power series of the eccentricity and so limited to quasi-circular orbits. On the other hand, the time-dependency due to the motion of the third body is almost always neglected.

Regarding the numerical methods, the traditional integrators can be numerically unstable for high eccentricity if a moderate step size is chosen due to the very fast variation of the perturbation around the perigee. If the step size is taken extremely small this implies large round-off errors and high CPU cost. Experiments show that even numerical integrators with variable step size does not solve perfectly this problem.

The paper is organized as follows. In Section 2, we propose a new expression of the disturbing function of the third-body problem which is in closed form with respect to the satellite eccentricity and still permits to construct an analytical theory of the motion. We will show that the use of the eccentric anomaly instead of the mean anomaly as fast angular variable fulfills this requirement. In Section 3, we give an overview of the variational integrators and we will see the interest of using such methods rather than classical integrators for orbital mechanics problems.

¹ Université de Nice Sophia-Antipolis, Centre National de la Recherche Scientifique (UMR 6526), Observatoire de la Côte d'Azur, Géoazur, Avenue Nicolas Copernic 06130 Grasse, France

2 Third-body problem

2.1 Expression of the disturbing function of the third-body problem

Let us consider a satellite of position vector $\mathbf{r} = r\mathbf{u}$ orbiting a central body and a third body of position vector $\mathbf{r}' = r'\mathbf{u}'$, with \mathbf{u} and \mathbf{u}' unit vectors. The disturbing function R of the third-body problem can be expressed into spherical coordinates (r, ϕ, λ) using the traditional expansion in Legendre polynomials $P_n(x)$ as follow

$$R = \frac{\mu'}{r'} \sum_{n \geq 2} \left(\frac{r}{r'}\right)^n P_n(\mathbf{u} \cdot \mathbf{u}'), \quad (2.1)$$

where $\mu' = \mathcal{G}m'$, m' being the mass of the third body and \mathcal{G} the gravitational constant.

In order to construct an analytical theory, it is more suitable to express (2.1) as function of orbital elements (semi-major axis a , eccentricity e , inclination I , argument of perigee ω , longitude of the ascending node Ω and mean anomaly M) or equivalent variables. From several works as Kaula (1962), Giacaglia & Burša (1980), Lane (1989) or yet Brumberg (1995), we were able to obtain a general expression of the disturbing function into Hill-Whittaker canonical variables: $r, \dot{r}, \theta = \omega + \nu, G = \sqrt{\mu a(1 - e^2)}, \Omega$ and $H = G \cos I$, with ν the true anomaly:

$$R = \frac{\mu'}{a'} \sum_{n \geq 2} \sum_{m=-n}^n \sum_{m'=-n}^n \sum_{p=0}^n \sum_{p'=0}^n \left(\frac{a}{a'}\right)^n \left(\frac{r}{a}\right)^n \left(\frac{a'}{r'}\right)^{n+1} \mathcal{D}_{n,m,m',p,p'} \exp i(\Psi_{n,m,p} - \Psi'_{n,m',p'}), \quad (2.2a)$$

$$\mathcal{D}_{n,m,m',p,p'}(I, I', \varepsilon) = (-1)^{m-m'} \frac{(n-m')!}{(n+m)!} \tilde{F}_{n,m,p}(I) \tilde{F}_{n,m',p'}(I') U_{n,m,m'}(\varepsilon), \quad (2.2b)$$

$$\Psi_{n,m,p} = (n-2p)\theta + m\Omega, \quad (2.2c)$$

$$\Psi'_{n,m',p'} = (n-2p')\theta' + m'\Omega', \quad (2.2d)$$

where the \tilde{F} -functions are related to the Kaula's inclination functions (see Kaula (1961)), ε is the obliquity and the U -functions are to the Wigner formula (see Sneeuw (1992)) giving the components of the rotation matrix between equatorial to ecliptic plane related.

In order to have a perturbation fully expressed in orbital elements, we expand the functions of the elliptical motion $(r/a)^n \exp i\nu$ and $(a'/r')^{n+1} \exp i\nu'$ into Fourier series with respect to an angular variable and coefficients which depend of the eccentricity. Quite generally, these functions are expanded in multiples of the mean anomaly as follow (see for example Kaula (1962), Giacaglia (1974))

$$\left(\frac{r}{a}\right)^n \exp im\nu = \sum_{s=-\infty}^{\infty} X_s^{n,m}(e) \exp isM, \quad (2.3)$$

where the $X_s^{n,m}$ are the so-called Hansen coefficients. In the general case, the series (2.3) always converge as Fourier series but can converge rather slowly (see e.g Brumberg & Brumberg 1999). Only in the particular case where e is small, the convergence is fast thanks to the d'Alambert property which ensure that $e^{|k-q|}$ can be factorized in $X_q^{n,k}(e)$. That is why the method is reasonably efficient for most of the natural bodies (in particular the Sun and the Moon) but can fail for satellites moving on orbits with high eccentricities. In this case, Fourier series of the eccentric anomaly E , are much more efficient :

$$\left(\frac{r}{a}\right)^n \exp im\nu = \sum_{s=-\infty}^{\infty} Z_s^{n,m} \exp isE, \quad (2.4)$$

where the Z -functions are called the Hansen-like coefficients. Expressions of these coefficients are given in Brumberg & Fukushima (1994) and can be computed using recurrence relations (see Lion & Métris (2011)). Using this development, we have the double advantage when $0 \leq |m| \leq n$ (which occurs in the third-body problem) that these coefficients admit a closed-form representation and that the sum (2.4) is exactly limited to $s = \pm n$ (coefficients are null for $|s| > n$).

Using the Fourier series (2.3) and (2.4) we show in Lion et al. (2011) that the disturbing function R takes the form:

$$R = \sum_{n \geq 2} \sum_{m=-n}^n \sum_{m'=-n}^n \sum_{p=0}^n \sum_{p'=0}^n \sum_{q=-n-1}^{n+1} \sum_{q'=-\infty}^{+\infty} \frac{a}{r} \mathcal{A}_{n,m,m',p,p',q,q'} \exp i\Theta_{n,m,m',p,p',q,q'}, \quad (2.5a)$$

$$\mathcal{A}_{n,m,m',p,p',q,q'} = \frac{\mu'}{a'} \left(\frac{a}{a'}\right)^n \mathcal{D}_{n,m,m',p,p'}(I, I', \varepsilon) Z_q^{n+1,n-2p}(e) X_{q'}^{-n-1,n-2p'}(e') , \tag{2.5b}$$

$$\Theta_{n,m,m',p,p',q,q'} = \tilde{\Psi}_{n,m,p,q} - \tilde{\Psi}'_{n,m',p',q'} , \tag{2.5c}$$

$$\tilde{\Psi}_{n,m,p,q} = qE + (n - 2p)\omega + m\Omega , \tag{2.5d}$$

$$\tilde{\Psi}'_{n,m',p',q'} = q'M' + (n - 2p')\omega' + m'\Omega' . \tag{2.5e}$$

2.2 Lie transformations perturbation method

The idea is to use a perturbative method based on the time-dependent Lie transform Deprit (1969) in order to obtain an approximated analytical solution of the third-body problem. Because the canonical variable $h = \omega$ is not ignorable and g is not automatically removed in the same time that the fast angle $l = M$ after a canonical transformation (contrary to the J_2 problem case), our initial Hamiltonian \mathcal{H}_0 of order 0 contains not only the keplerian energy, but also the secular part of the J_2 problem. The disturbing function R belongs to the hamiltonian \mathcal{H}_1 of order 1. In that way, \mathcal{H}_0 depends of the three momenta L, G and H which will allow to eliminate the three conjugate angles l, g and h from the transformed hamiltonian. Next, we use the homological equation providing the Lie generator W and the new Hamiltonian \mathcal{K} at first order. The new Hamiltonian \mathcal{K} is taken such as it does not depend on any angular variable. The Lie generator W_1 is obtained by solving a PDE involving variables which are linear with time and the eccentric anomaly which is not linear with time. Solution of W_1 can be computed with by means of two different methods. If we seek a separable solution of the PDE we find the exact solution involving Anger and Weber functions. The other method is to solve the PDE by means of a recursive process which may be more suitable for our analytical theory.

3 Variational integrators

3.1 Philosophy

Variational integrators derive from a discrete version of the least action principle. Instead of a continuous path $q(t)$ for $t \in [t_i, t_f]$, we consider a discrete path $q : \{t_0 = t_i, t_1, \dots, t_k, \dots, t_N = t_f\}$ where $k, N \in \mathbb{N}$, q_k being an approximation to $q(t_k)$. Hence, the Lagrangian $L(q, \dot{q}, t)$ of the system is approximated on each time interval $[t_h, t_{k+1}]$ by a discrete Lagrangian $L_d(q_k, q_{k+1}, h)$, with $h = t_{k+1} - t_k$ being the time interval. For conservatives systems, we just compute the principle of discrete stationary action, which gives the discrete Euler-Lagrange (DEL) equations and the discrete Hamilton equations (see West (2004)):

$$p_k = -D_1 L_d(q_k, q_{k+1}) \quad , \quad p_{k+1} = D_2 L_d(q_k, q_{k+1}), \tag{3.1}$$

where $D_i L$ denotes the derivative of L with respect to the i slot. For (q_k, p_k) known, we can compute q_{k+1} then p_{k+1} .

In case of dissipative or forced systems, the discrete action can be modified by adding the non-conservative force and using the Lagrange d'Alembert principle.

The variational integrators preserve the geometric structure of the mechanical system. This has two consequences. Firstly, the schemes are symplectic and so, we have a good energy behaviour for equal time steps. Secondly, momenta and symmetries are conserved (via the discrete Noether's theorem). More over, one can obtain higher-order methods by using higher-order quadrature to approximate the Lagrangian (e.g, Gauss-Lobatto) as our variational integrator RKN6 tested in the following section.

3.2 Numerical tests for conservative system

To illustrate the performance of the variational integrators we consider the keplerian problem which is a simple and an integrable system. The Lagrangian describing this problem is

$$L(q, \dot{q}) = \frac{1}{2} \dot{q}^T \dot{q} - V(q) \quad \text{and} \quad V(q) = -\frac{\mu}{\|q\|} , \tag{3.2}$$

where $q = q(t) \in \mathbb{R}^2$ is the trajectory of body orbiting the primary body (Earth) and μ is the gravitational parameter. The equations of motion are given by the Euler-Lagrange equations and the trajectories of this conservative system have two conserved quantities: the energy of the system and the total angular momentum.

So, the easiest way to check on the reliability of integration schemes is to watch the behavior of these conserved quantities. The algorithms for which we present results are:

- RK6: Explicit Runge-Kutta 6-order, with fixed stepsize $h=20s$ and $h=60s$.
- Symmetric RKN6*: Symmetric and reversible Runge-Kutta Nyström 6-order, using the 4-stage Lobatto IIIA[†] method, with fixed stepsize $h=60s$ (see Cash & Girdlestone (2006)).
- Variational RKN6: Variational Runge-Kutta Nyström 6-order, using the Gauss-Lobatto quadrature rules with a 4-stage Lobatto IIIA method and a fixed stepsize $h=60s$. This integrator was built from the papers of Farr & Bertschinger (2007) and Farr (2009).
- Ode113: variable order Adams-Bashforth-Moulton (PECE) solver in Matlab with adaptative stepsize.

As initial conditions, we have chosen an highly elliptical orbit with: $a = 36890.683$ km, $e = 0.8$. The integration is performed over 325 days corresponding to 400 orbits.

The relative error in the energy for each integrators is plotted in Fig. 1. As expected, we can see that the classical integrators RK6 and ode113 do not preserve the energy of the system, even if ode113 uses an adaptative stepsize. The variational RKN6 preserves better energy than the symmetric and reversible RKN6.

Results for the relative error in the total angular momentum behaviour lead to the same conclusion. The standard integrators have a divergent angular momentum, while the others it is conserved with at most the finite fluctuations.

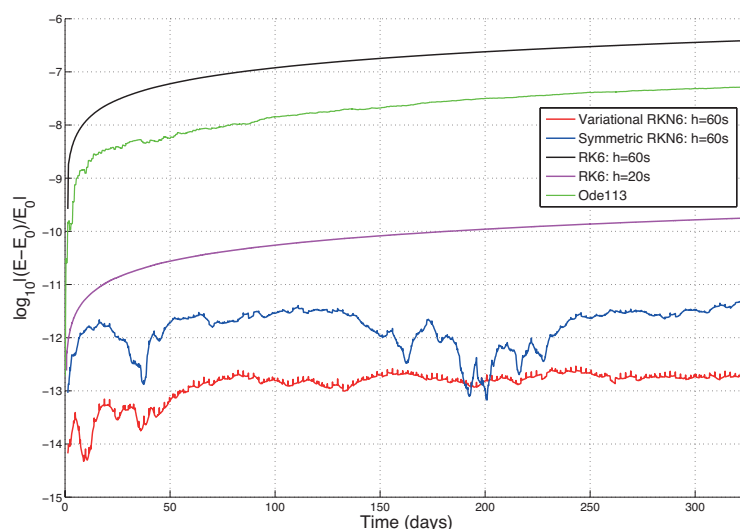


Fig. 1. Relative error in the energy behaviour of integrators for a conservative system

Conservation properties are not the only indicators for the quality of integrators. The amount of computational resources consumed in this process is equally important, as any algorithm can be trimmed to produce highly accurate results. Using for the variational integrators a predictor of high order simply derived from finite difference methods, we have reduced up to 35 percent the number of function evaluation.

References

- Brumberg, E. V. & Fukushima, T. 1994, *Celest. Mech. & Dyn. Astron.*, 60, 69
 Brumberg, V. A. 1995, *Analytical Techniques of Celestial Mechanics* (New York: Springer)
 Brumberg, V. A. & Brumberg, E. V. 1999, *Advances in Astronomy and Astrophysics*, Vol. 3, *Celestial Dynamics at High Eccentricities* (Gordon and Breach)

*Source code available on http://www2.imperial.ac.uk/~jcash/GI_software/readme.php.

[†]The Lobatto IIIA are collocation methods symmetric and symplectic (see Hairer et al. (2002)).

- Cash, J. R. & Girdlestone, S. 2006, *J. Numer. Anal., Ind. & Appl. Math.*
- Deprit, A. 1969, *Celest. Mech.*, 1, 12
- Farr, W. M. 2009, *Celest. Mech. & Dyn. Astron.*, 103, 105
- Farr, W. M. & Bertschinger, E. 2007, *Astron. J.*, 663, 1420
- Giacaglia, G. E. O. 1974, *Celest. Mech.*, 9, 239
- Giacaglia, G. E. O. & Burša, M. 1980, *Stud. Geophys. & Geod.*, 24, 1
- Hairer, E., Lubich, C., & Wanner, G. 2002, *Springer Series in Computational Mathematics, Vol. 31, Geometric Numerical Integration : Structure-Preserving Algorithms for Ordinary Differential Equations*, 2nd edn. (Springer-Verlag)
- Kaula, W. M. 1961, *Geophys. J. Intern.*, 5, 104
- Kaula, W. M. 1962, *Astron. J.*, 67, 300
- Lane, M. T. 1989, *Celest. Mech. & Dyn. Astron.*, 46, 287
- Lion, G. & Métris, G. 2011, *Celest. Mech. & Dyn. Astron.*, submitted
- Lion, G., Métris, G., & Deleflie, F. 2011, *Celest. Mech. & Dyn. Astron.*
- Sneeuw, N. 1992, *Manuscr. Geod.*, 17, 117
- West, M. 2004, PhD thesis, California Institute of Technology

ACES-PHARAO : MICROWAVE LINK DATA PROCESSING

F. Meynadier¹, P. Delva¹, C. Le Poncin-Lafitte¹, P. Laurent¹ and P. Wolf¹

Abstract. The Atomic Clocks Ensemble in Space (PHARAO-ACES mission, Salomon et al. (2007)), which will be installed on board the International Space Station, uses a dedicated two-way microwave link in order to compare the timescale generated on board with those provided by many ground stations disseminated on the Earth. Phase accuracy and stability of this long range link will have a key role in the success of the PHARAO-ACES experiment.

The SYRTE is heavily involved in the design and the development of the data processing software : from theoretical modelling and numerical simulations to the development of a software prototype. Our team is working on a wide range of problems that need to be solved in order to achieve high accuracy in (almost) real time.

In this poster we present some key aspects of the measurement, as well as the current status of the software's development.

Keywords: Atomic clocks, time transfer, fundamental physics experiments.

1 The ACES mission and its microwave link

The ACES payload includes a caesium atomic clock (PHARAO) and an active hydrogen maser (SHM) which will provide a frequency reference with an expected performance around 10^{-16} in stability and accuracy. It will also include a GNSS receiver (for precise orbit determination) and two dedicated links for time comparison, one in the optical domain and the other in the microwave range.

The primary aim of the microwave link is to compare two clock signals : one is on the ground and the other is provided by the ACES payload on board of the ISS. The method that will be used is an asynchronous two way radio link with an additional downlink (at a different frequency, to derive the ionospheric delay, see fig. 2).

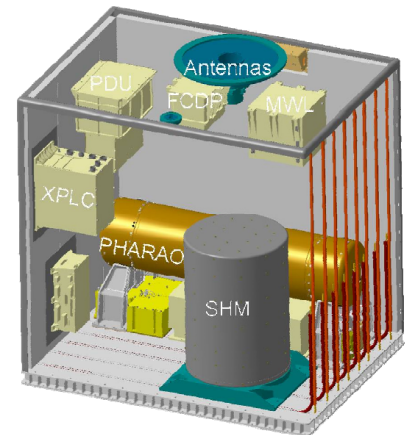


Fig. 1. The ACES payload

Time transfer is achieved by using a Pseudo-Random Noise code on the signal's carrier. Higher resolution is achieved by measuring the carrier phase of the signal. Multiple effects need to be taken into account in order to recover the clocks desynchronisation : both stations are moving during signal propagation, the troposphere and the ionosphere induce different types of delays, instrumental delays have to be calibrated and relativistic effects will come into play.

¹ LNE / Syrte – Observatoire de Paris, CNRS, UPMC Univ Paris 06, UMR8630, F-75005, Paris, France

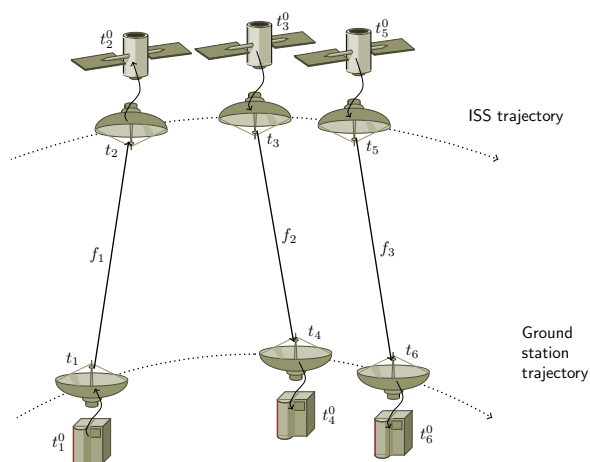


Fig. 2. The MicroWave Link (MWL) : one uplink (f_1 , Ku-Band) and two downlinks (f_2 , Ku and f_3 , S-Band). MWL hardware developed by TimeTech GmbH. Both stations move during the signal exchange, and both have their own proper time, so a particular frame is chosen for coordinate time.

2 Two-way measurement principle

A simple one-way measurement consists in comparing the time displayed by two distant clocks, by measuring the time interval between the reception of a given tick and the generation of the same tick by the local clock. The result is a time interval $\Delta\tau = \tau_{\text{production}} - \tau_{\text{reception}}$, in the local clock's proper time. In order to recover the clocks desynchronization from this delay, one needs to model all other effects that contribute to $\Delta\tau$. The following figures exhibit the basic methods used to encode the time data on the signal, yet recovering the full resolution thanks to carrier-phase measurements.

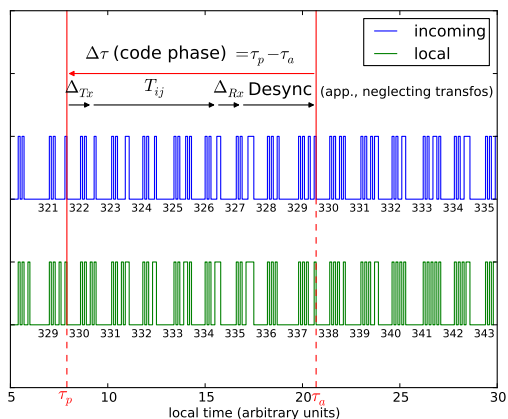


Fig. 3. Basic concept of code-phase measurement. For clarity, a simplistic encoding is used here (in reality a PRN code is used).

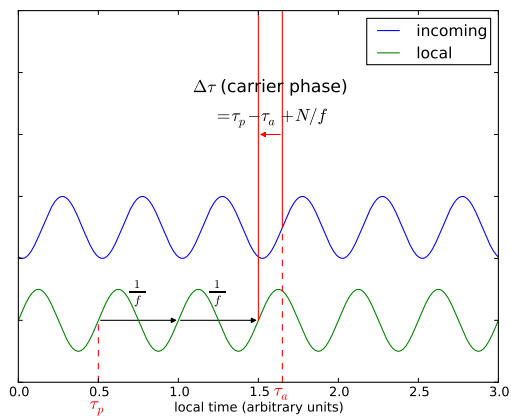


Fig. 4. Basic concept of carrier-phase measurement. For full temporal resolution is recovered, the phase ambiguity has to be resolved.

The two-way measurement aims at minimizing uncertainties by performing two symmetrical one-way measurements (i.e. one from ground to space, the other from space to ground) : when subtracting the $\Delta\tau$ obtained

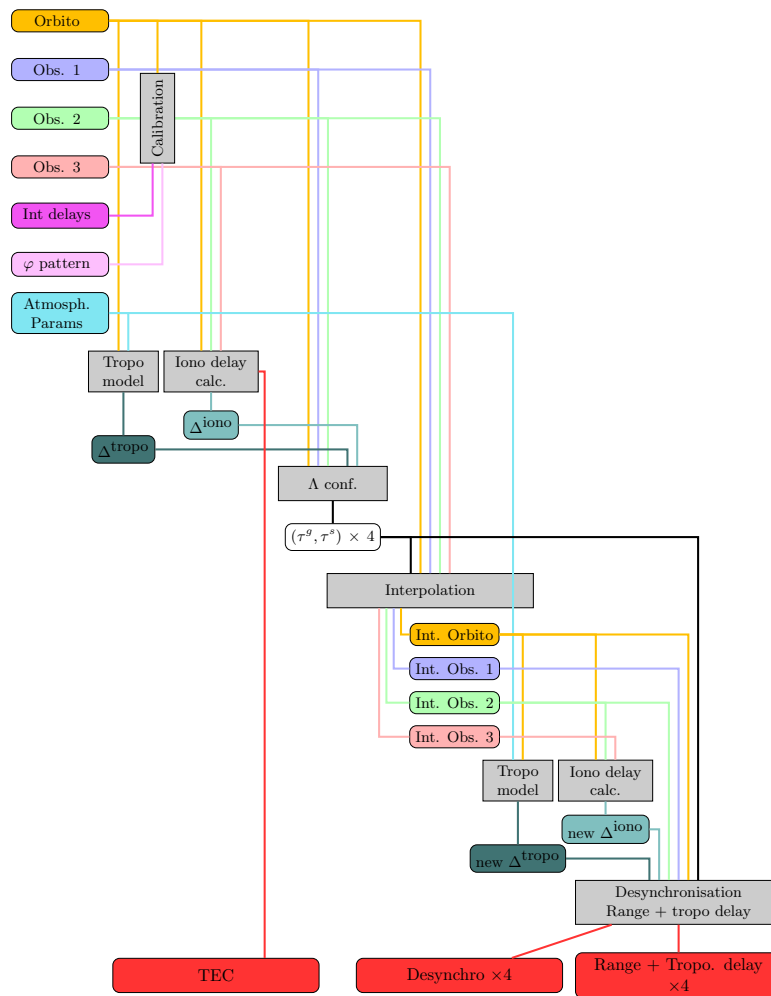


Fig. 5. Overall flowchart of the data processing software. Inputs are in the top-left corner and scientific products are at the bottom (red squares).

in each case, some major contributions (e.g. the range) cancel out at first order and the resulting desynchronisation determination is less model-dependant. A third (much lower) frequency allows to determine the ionospheric delay (and thus the total electron content).

3 Data processing software

Our team is currently developing a prototype of the data processing software. It will be used :

- as a guideline for Astrium who will implement the industrial-grade data processing in the ACES ground segment
- by our team, to achieve the highest possible accuracy in post-processing.

The core algorithm is based upon Loïc Duchayne’s PhD thesis (Duchayne 2008). Its top-level flowchart is reproduced on Fig. 5

First, observables are calibrated and corrected for various systematic effects that are monitored during the mission. Then a model of the atmosphere is applied in order to correct for the delay that is induced by those layers.

One of the key aspects of this algorithm is the calculation of the Λ configuration : as downlink and uplink signals series each have their own timescale and do not coincide *a priori*, we have to interpolate one of the series in order to get a coherent measurement. The Λ configuration is a particular interpolation that ensures that

the uplink signal reception coincides with the downlink signal emission (i.e. $t_2 = t_3$ on fig. 2, so the f_1 and f_2 signals form a Λ -shaped figure). This reduces the impact of the ISS's orbitography uncertainty, which is orders of magnitude less accurately known than the ground station's positions (Duchayne et al. 2009).

4 First results

We have designed and implemented the algorithm that recovers $\Delta\tau$ from raw MWL data, i.e. T_i and n_i couples as explained in this figure :

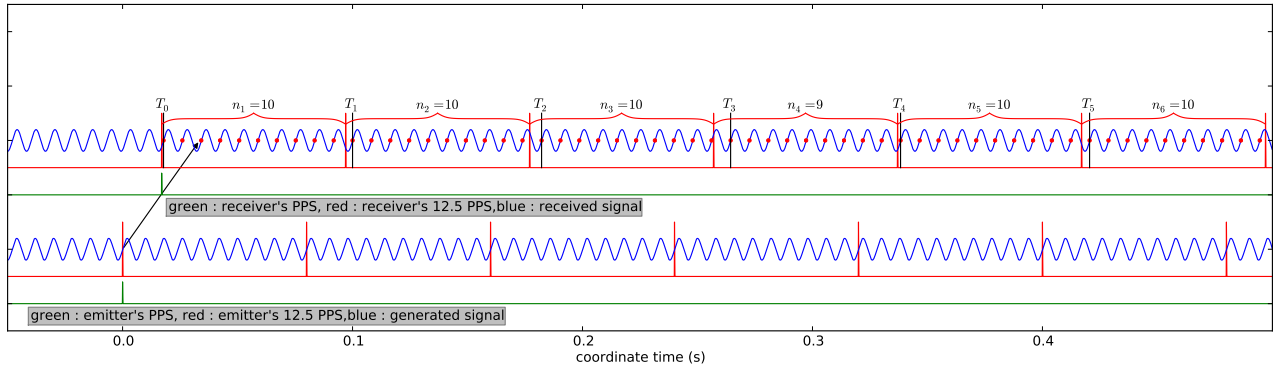


Fig. 6. A simplified diagram representing how the measurement is actually made.

Fig. 6 shows a carrier (in blue) when generated (lower part of the graph) and when received (upper part of the graph), with a slight shift and a varying frequency because of Doppler effects. Time scales (in red and green) are also different for the emitter and the receiver. Ascending zero-crossings are materialized by a red dot. For each 80 ms interval of the receiver's proper time, we get T (the date of the first zero crossing) and n , the number of zero-crossings in the previous interval.

In such a (simplified) configuration, in the receiver's time frame we get :

$$\Delta\tau(T_i) = \Delta\tau(T_{i-1}) + \frac{n_i}{f_{Tx}} - (T_i - T_{i-1})$$

where f_{Tx} is the frequency of the carrier. Note that, compared to this diagram, the carrier's frequency is much higher, so it is not used directly and we get a beatnote instead : this introduces another term in the equation.

5 Simulations

Our team also develops in parallel a data simulation software. Development is as independent as possible in order to identify possible bugs or misunderstandings in the data processing software.

A first version of the simulation software is already delivering test datasets that are useful for evaluating the orders of magnitudes for the various effects that come into play. Those first batches are currently used to test and validate the first working modules of the data processing software, and will serve as "test cases" throughout the code's development.

As an illustration, fig. 7 shows a simulation of the signal's frequency based on real ISS orbitography.

References

- Duchayne, L. 2008, PhD thesis, Observatoire de Paris, France
 Duchayne, L., Mercier, F., & Wolf, P. 2009, A&A, 504, 653
 Salomon, C., Cacciapuoti, L., & Dimarcq, N. 2007, International Journal of Modern Physics D, 16, 2511

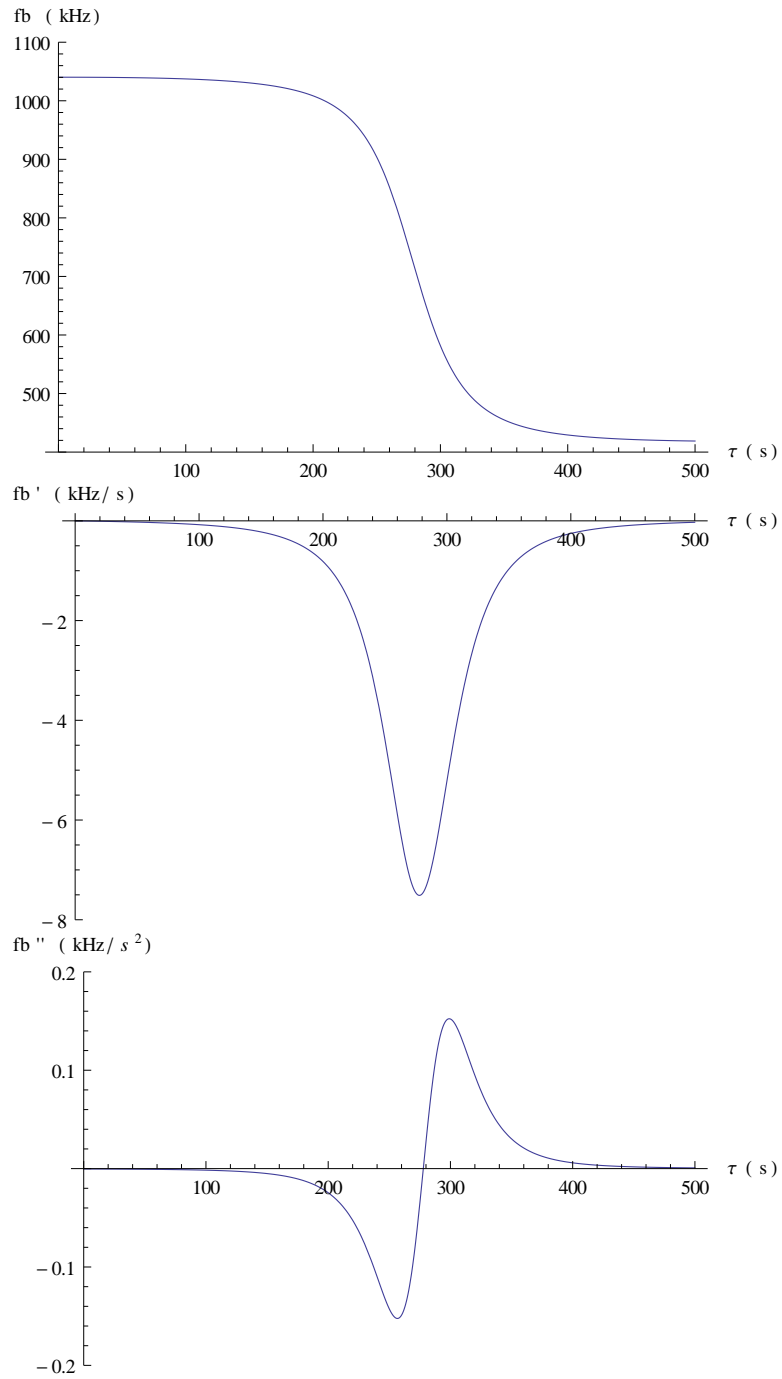


Fig. 7. The (simulated) beatnote frequency and its derivatives on board the satellite over a passage of the ISS.

THE GRAVITATIONAL POTENTIAL OF AXIALLY SYMMETRIC BODIES FROM A REGULARIZED GREEN KERNEL

A. Trova¹, J.-M. Huré¹ and F. Hersant¹

Abstract. The determination of the gravitational potential inside celestial bodies (rotating stars, discs, planets, asteroids) is a common challenge in numerical Astrophysics. Under axial symmetry, the potential is classically found from a two-dimensional integral over the body's meridional cross-section. Because it involves an improper integral, high accuracy is generally difficult to reach. We have discovered that, for homogeneous bodies, the singular Green kernel can be converted into a regular kernel by direct analytical integration. This new kernel, easily managed with standard techniques, opens interesting horizons, not only for numerical calculus but also to generate approximations, in particular for geometrically thin discs and rings.

Keywords: Gravitation, Methods: analytical, Celestial mechanics

1 Introduction

According to Newton's law, the potential ψ associated with two point masses at a relative distance δr from each other diverges as $\delta r \rightarrow 0$. As a result, for any continuous body, the gravitational potential is obtained by integrating a function which diverges everywhere in the inside. The expansion of the Green kernel into Legendre polynomials (which circumvent this singularity problem), as usually done, leads to numerical oscillations due to truncations (Clement 1974). When the body is axially symmetric, the integration over the polar angle ϕ results in the well known expression (e.g. Durand 1953):

$$\psi(R, Z) = -G \int_{\text{volume}} \frac{\rho(\vec{r}')}{|\vec{r} - \vec{r}'|} da dz a d\phi \longrightarrow -2G \int_{\text{section}} \rho(a, z) \sqrt{\frac{a}{R}} k \mathbf{K}(k) da dz \quad (1.1)$$

where \mathbf{K} is the complete elliptic integral of the first kind, k is the modulus, with $(a + R)^2 + (z - Z)^2 = 4aR/k^2$. The singularity is still present here since $|\vec{r} - \vec{r}'| \rightarrow 0$ now corresponds to $k \rightarrow 1$. Figure 1 shows the logarithmic divergence of the function $\mathbf{K}(k)$ near unity. Unfortunately, there is no way to obtain a more advanced form for the above bidimensional integral, except for a few special cases. For instance, in the absence of any radial density gradient, the integration along the radial direction can be performed analytically. This fundamental result, described in Durand (1953) and rediscovered in the astrophysical context by Lass & Blitzler (1983), is:

$$\psi(R, Z) = -G \int_{\text{boundary}} \rho(z) \left[4\sqrt{aR} \frac{\mathbf{E}(k)}{k} + \frac{a^2 - R^2 - (z - Z)^2}{\sqrt{aR}} k \mathbf{K}(k) - (z - Z)\Omega \right] dz \quad (1.2)$$

where \mathbf{E} is the complete elliptic integral of the second kind, and Ω is the solid angle sustained by the disc (radius a , altitude z) when seen from point (R, Z) . Actually, this expression is nothing but the total potential due to a collection of infinitely thin circular plates (i.e. discs) piled up along the z -direction (see Fig. 2a). This kind of formula is therefore well suited not only for homogeneous bodies but also for inhomogeneous bodies such that $\partial_a \rho = 0$. The integrand in Eq.(1.2) being regular, there is no difficulty to get accurate potential values.

There is apparently no equivalent form of Eq.(1.2) corresponding to bodies having zero vertical density gradients. In other words, the potential due to a semi-infinite homogeneous cylinder might not exist in a closed form. This question is the subject of a longstanding debate. As a matter of fact, the potential and forces due

¹ Université de Bordeaux, CNRS, LAB, Bordeaux, France

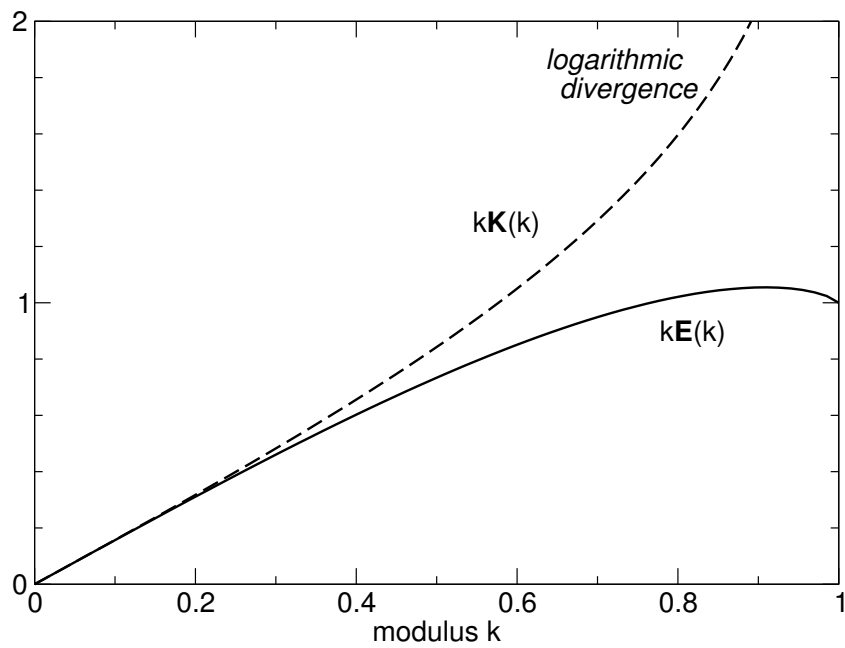


Fig. 1. Part of the initial Green kernel $k\mathbf{K}(k)$ and part of the new regular kernel $k\mathbf{E}(k)$; see Eqs.(1.1) and (2.1).

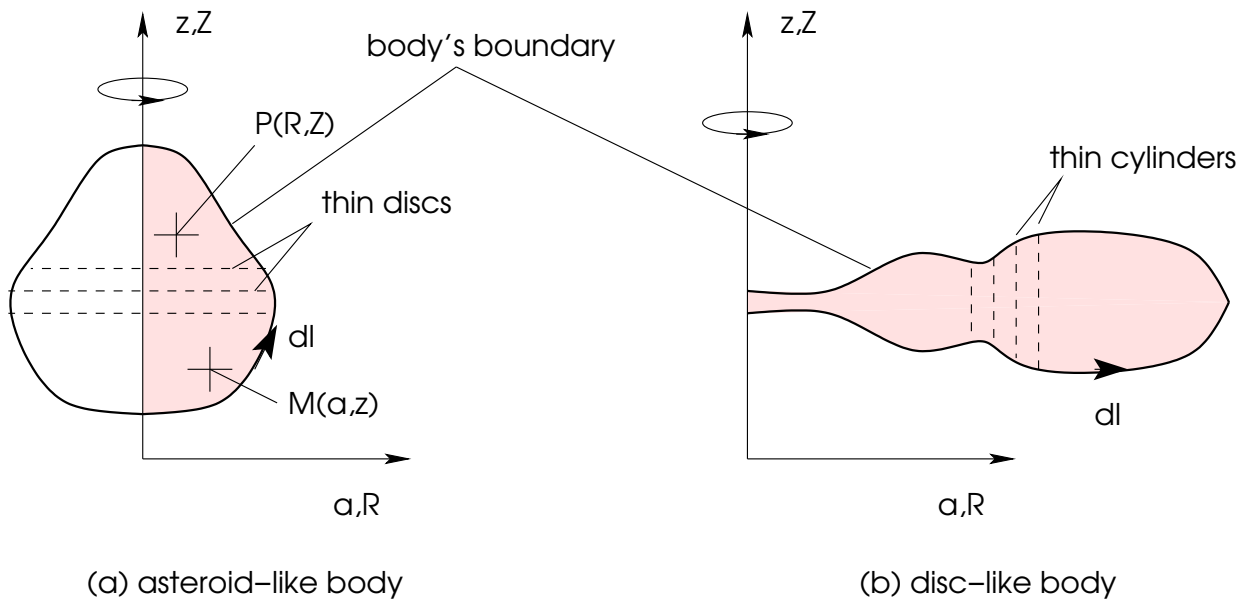


Fig. 2. Two different configurations of axially symmetric bodies, with their geometrical cross-section where $\rho \neq 0$ (shaded zone) and boundary (bold).

to charged, toroidal structures are required in many contexts of research including Biology, Electromagnetism and Plasma physics. In his remarkable textbook, Durand (1953) mentions that “[...] *Le calcul analytique de l’intégrale du potentiel paraît difficile [...]*”. He can only give a solution in the form of infinite series involving Legendre polynomials. This series is however an alternate series which poorly converges, as usually observed (Clement 1974). A constant and careful bibliographic search shows that this question is still open.

2 A new regularized kernel ?

After some effort and investment in integral calculus involving elliptic integrals, we have recently discovered a simple way to bypass the singularity of Green kernel precisely in the case where $\partial_z \rho = 0$. The result is based on the derivation of this following new definite integral:

$$\int k\mathbf{K}(k)dz = \int k\mathbf{E}(k)dz + (z - Z)k \left[\mathbf{K}(k) - m'^2\mathbf{\Pi}(m, k) \right], \tag{2.1}$$

where $\mathbf{\Pi}(m, k)$ is the complete elliptic integral of the third kind, $m = 2\sqrt{aR}/(a + R)$ is the characteristic, and m' is its complementary (i.e. $m'^2 + m^2 = 1$). All the details of the derivation will be presented in a forthcoming paper. The first term in the right-hand-side of Eq.(2.1) is fully regular since $\mathbf{E}(k) \in [\frac{\pi}{2}, 1]$. Figure 1 compares the two kernels $k\mathbf{K}(k)$ and $k\mathbf{E}(k)$. The second term is also fully regular: the divergence of the \mathbf{K} - and $\mathbf{\Pi}$ -functions as k and m approach unity is cancelled out by the presence of the two vanishing factors m' and $(z - Z)$. The potential of any vertically homogeneous axially symmetric body is then found from the expression:

$$\psi(R, Z) = -2G \int_{\text{boundary}} \rho(a)\sqrt{\frac{a}{R}} \left\{ (z - Z)k \left[\mathbf{K}(k) - m'^2\mathbf{\Pi}(m, k) \right] \right\} da - 2G \int_{\text{section}} \rho(a)\sqrt{\frac{a}{R}} k\mathbf{E}(k) dz da \tag{2.2}$$

This expression is exact. It is interpreted as the total potential due to a collection of infinitely thin (semi-infinite) coaxial cylinders* side by side along the a -direction (see Fig. 2b). In some sense, Eqs.(1.2) and (2.2) are complementary: the use of the one or the other depends on the shape of the body and on its density structure as well.

3 Note on Green's theorem for fully homogeneous bodies

For fully homogeneous bodies, we have $\partial_a \rho = \partial_z \rho = 0$, and so Eqs.(1.2) and (2.2) are formally equivalent. The ability to integrate analytically Eqs.(1.2) or (2.2) must be considered (this is for instance possible for the homogeneous sphere). In this purpose, the conversion of the double integral in the right-hand-side of Eq.(1.1) into a line (or contour) integral is possible by using Green's theorem, provided the kernel is the curl of a certain field \vec{F} . Actually, for any vector field $\vec{F}(F_a, F_z)$, Green's theorem writes in the present context:

$$\int_{\text{section}} \nabla \times \vec{F} da dz \cdot \vec{u}_\phi = \oint_{\text{boundary}} \vec{F} \cdot d\vec{\ell} \tag{3.1}$$

where $d\vec{\ell}$ is an infinitesimal displacement along the boundary (oriented counter-clockwise). This powerful approach is stressed in Ansorg et al. (2003) who compute new figures of equilibrium and bifurcations from the Maclaurin sequence. Indeed, they have determined a vector \vec{F} such that:

$$\sqrt{\frac{a}{R}} k\mathbf{K}(k) \propto \nabla \times \vec{F} \cdot \vec{u}_\phi = \frac{\partial F_z}{\partial a} - \frac{\partial F_a}{\partial z} \tag{3.2}$$

and so, from Eq.(1.1), they immediately get the potential, namely:

$$\psi(R, Z) \propto \int_{\text{boundary}} (F_a da - F_z dz). \tag{3.3}$$

This allows to derive the potential everywhere in space through a single integral, which is numerically very advantageous. In practice, it seems however difficult to reach high accuracy when the potential is required just onto the boundary (or contour), and so the numerical treatment must still be faced with care (Ansorg et al. 2003).

*For finite size bodies, one must subtract the contribution of two semi-infinite cylinders, after shifting the one with respect to the other.

4 Concluding remarks

The new, regular kernel appearing in Eq.(2.2) is a substitute for the genuine Green kernel whose singularity avoids, from the numerical point of view, any direct treatment. This kernel is particularly interesting in the context of geometrically thin discs and rings. For such objects actually, the radial and vertical structures are often decoupled (Shakura & Sunyaev 1973) and the density of gas is uniform in the direction perpendicular to the equatorial plane (but variable in radius). The formula is indeed helpful at the numerical level even for axially symmetric bodies having radial and vertical density gradients in the framework of the splitting method (Huré 2005). It is also useful at the theoretical level, for instance to derive reliable approximations for the mid-plane gravitational potential and acceleration. In this case for instance, we have $k \approx m$ at the first order in $z/(a + R)$. Thus, we have simply:

$$\int_{\text{section}} \rho(a) \sqrt{\frac{a}{R}} k \mathbf{E}(k) dz da \approx \int_{\text{boundary}} \Sigma(a) \sqrt{\frac{a}{R}} m \mathbf{E}(m) da \quad (4.1)$$

where Σ is the local surface density. More generally, it would be interesting to convert the section integral in Eq.(2.2) into a contour integral via Green's theorem. This question is currently under study.

References

- Ansorg, M., Kleinwächter, A., & Meinel, R. 2003, MNRAS, 339, 515
 Clement, M. J. 1974, ApJ, 194, 709
 Durand, E. 1953, Electrostatique. Vol. I. Les distributions (Paris: Masson)
 Huré, J.-M. 2005, A&A, 434, 1
 Lass, H. & Blitzler, L. 1983, Celestial Mechanics, 30, 225
 Shakura, N. I. & Sunyaev, R. A. 1973, A&A, 24, 337

TOWARDS CONSTRAINING THE CENTRAL BLACK HOLE'S PROPERTIES BY STUDYING ITS INFRARED FLARES WITH THE GRAVITY INSTRUMENT

F. H. Vincent^{1,2,3}, T. Paumard¹, G. Perrin¹, E. Gourgoulhon², F. Eisenhauer³ and S. Gillessen³

Abstract. The ability of the near future second generation VLTI instrument GRAVITY to constrain the properties of the Galactic center black hole is investigated. The Galactic center infrared flares are used as probes of strong-field gravity, within the framework of the hot spot model according to which the flares are the signature of a blob of gas orbiting close to the black hole's innermost stable circular orbit. Full general relativistic computations are performed, together with realistic observed data simulations, that lead to conclude that GRAVITY could be able to constrain the black hole's inclination parameter.

Keywords: Galaxy: center, Black hole physics

1 Introduction

The existence of a supermassive black hole coincident with the radio source Sgr A* at the center of our Galaxy is highly probable, as advocated by decades of observations (see Ghez et al. 2008; Gillessen et al. 2009, for the most recent). Moreover, Sgr A* exhibits outbursts of radiation, hereafter flares, in the millimeter, infrared and X-ray wavelengths (see Trap et al. 2011, and references therein, for the most recent observations). No consensus has yet been reached regarding the physical nature of these flares. Different models have been proposed in the literature: adiabatic expansion of a synchrotron-emitting blob of plasma (Yusef-Zadeh et al. 2006), heating of electrons in a jet (Markoff et al. 2001), Rossby wave instability in the disk (Tagger & Melia 2006), or a clump of matter heated by magnetic reconnection orbiting close to the innermost stable circular orbit (ISCO) of the black hole (Hamaus et al. 2009). To be tested, this last model, hereafter hot spot model, requires an astrometric precision at least of the order of the angular radius of the ISCO, which is a few times the Schwarzschild radius of the black hole, i.e. a few times $10 \mu\text{as}$.

Such a precision will be within reach of the near future GRAVITY instrument (Eisenhauer et al. 2008). Vincent et al. (2011b) have shown that GRAVITY will be able of putting in light the motion of a spot orbiting on the ISCO of a Schwarzschild black hole, however without taking into account any relativistic effect. The aim of this paper is to determine, in the framework of a full general relativistic treatment, the ability of GRAVITY to get information on the properties of the central black hole by giving access to the astrometry of near infrared flares.

2 Observing a hot spot orbiting around Sgr A*

The hot spot model used here is developed by Hamaus et al. (2009). The central black hole is assumed to be surrounded by a magnetized accretion disk. Due to differential rotation, the magnetic field lines are stretched, which leads to reconnection events that violently heat some part of the disk, giving rise to a hot sphere of synchrotron emitting plasma orbiting around the black hole on some circular orbit at a radius $r \gtrsim r_{\text{ISCO}}$. The sphere is assumed to emit isotropically and to have a radius $r_{\text{sph}} = 0.5 M$, where M is the black hole's mass (this value is consistent with the constraint on the spot's radius given by Gillessen et al. 2006). Due

¹ LESIA, Observatoire de Paris, CNRS, Université Pierre et Marie Curie, Université Paris Diderot, 5 place Jules Janssen, 92190 Meudon, France

² LUTH, Observatoire de Paris, CNRS, Université Paris Diderot, 5 place Jules Janssen, 92190 Meudon, France

³ Max-Planck-Institut für Extraterrestrische Physik, 85748 Garching, Germany

to differential rotation, the sphere is distorted and finally forms an arc. The so-called hot spot is thus made of the superimposition of the initial sphere and of the arc resulting from its stretching. In order to take into account the heating and cooling phases due to the reconnection event, the sphere's and the arc's emission are multiplied by a gaussian temporal modulation. For the simulations, the arc is modeled as the sum of nearby spheres over one complete period around the black hole. Moreover, the arc's emitted intensity is modulated by an azimuthal gaussian that allows to peak the emission on the initial sphere's position. The parameters describing the hot spot are thus the standard deviations of these gaussian modulations, $\sigma_{\uparrow,\text{sph}}$ and $\sigma_{\uparrow,\text{arc}}$ for the heating modulations of the sphere and the arc, $\sigma_{\downarrow,\text{sph}}$ and $\sigma_{\downarrow,\text{arc}}$ for their cooling modulations, σ_{azimuth} for the arc's azimuthal modulation. One last parameter is added, the ratio ρ_I of the sphere's mean luminosity to the arc's mean luminosity. This last parameter allows the bright sphere to dominate the emission. In all the following computations, these parameters will be maintained at the following values:

$$\begin{aligned}\sigma_{\text{azimuth}} &= 2\pi \\ \rho_I &= 60 \\ \sigma_{\uparrow,\text{sph}} &= 0.5 t_{\text{per}}, & \sigma_{\downarrow,\text{sph}} &= t_{\text{per}} \\ \sigma_{\uparrow,\text{arc}} &= 0.5 t_{\text{per}}, & \sigma_{\downarrow,\text{arc}} &= t_{\text{per}}\end{aligned}\tag{2.1}$$

where t_{per} is the period of the orbit. A general study taking into account the variations of these parameters goes beyond the scope of this work. However, the strongest hypothesis in the perspective of the following astrometric analysis is the big value of the parameter ρ_I . If this parameter is smaller, the sphere does not dominate the total emission, and the motion of the photocenter of the object is much attenuated, making it difficult, if not impossible, for an instrument to measure it. Nevertheless, let us note that the value of ρ_I fitted on observed data by Hamaus et al. (2009) (see their Table 2) is even higher than the value used here.

The radius of the circular orbit of the hot spot and the black hole's spin parameter can be constrained by the near infrared observations of flares already obtained. These observations show a pseudo-periodic variability of the light curve that varies between around 20 min and around 40 min (Genzel et al. 2003; Dodds-Eden et al. 2010). In the framework of the hot spot model, these pseudo-periodicities correspond to the orbiting period of the spot around the black hole. Figure 1, representing the evolution of the orbital period around the central black hole as a function of the radius normalized by the ISCO radius or the Schwarzschild radius r_S , immediately lead to the conclusion that the black hole's spin parameter a and hot spot's orbiting radius r must satisfy:

$$\begin{aligned}a &\gtrsim 0.5, \\ 2r_S &\lesssim r \lesssim 3.5r_S.\end{aligned}\tag{2.2}$$

The computation of the hot spot trajectory around the black hole, as well as the simulation of its observed appearance for an observer on Earth is computed by means of the ray-tracing algorithm GYOTO* (Vincent et al. 2011a).

3 Towards constraining the inclination of the central black hole

In this section, we wish to investigate the impact of the black hole's inclination on the GRAVITY astrometric simulated data. The impact of the spin parameter will not be investigated, and it is thus fixed to $a = 0.7M$, in agreement with the lower bound given in Eq. 2.2. Moreover, the radius of the circular orbit of the hot spot is fixed to its highest possible value (see Eq. 2.2): $r = 3.5r_S$. One last parameter that has a strong impact on the astrometric data is the maximum magnitude of the hot spot. It is fixed to $m_K = 13$. These values are optimistic as the hot spot is very bright and evolves on a large trajectory. However, these values are not unrealistic as the brightest flare observed to date had a maximum magnitude of $m_K = 13.5$ (Dodds-Eden et al. 2011), and the orbital radius of the hot spot investigated in Sect. 3.3.2 of Hamaus et al. (2009) is fitted to a value close to $3.5r_S^\dagger$. Moreover, as will be stressed below, only one flare observed with such parameters would

*Freely available at the following URL: <http://gyoto.obspm.fr>

[†]Let us note that the central black hole's mass used in Hamaus et al. (2009) differs from the mass used to obtain Figure 1 thus changing the timescale.

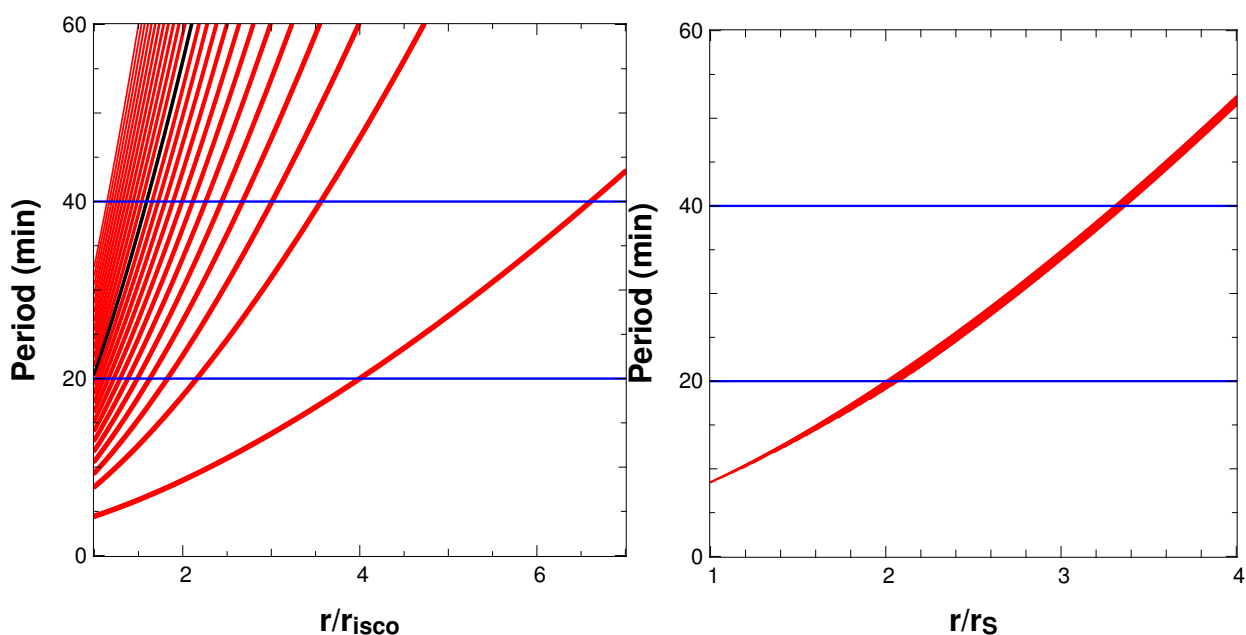


Fig. 1. Left: Circular orbital period around a Kerr black hole of mass $4.31 \cdot 10^6 M_{\odot}$ with spin parameter between 0 (top left curve) to 1 (down right curve), as a function of the orbital radius in units of the ISCO radius. The blue horizontal lines correspond to the range of observed pseudo periods: typically between 20 and 40 min. The black curve corresponds to spin 0.5: spins $\lesssim 0.5$ are not able of accounting for the smallest observed pseudo period of flares of ≈ 20 min. **Right:** Same as left panel, but as a function of the orbital radius in units of the Schwarzschild radius of the black hole. The curves are truncated for values of r smaller than the corresponding ISCO.

allow getting interesting information on the central black hole. These values are not assumed to be standard hot spot parameters.

The theoretical trajectory of the hot spot projected on the observer's screen and the observed flux being known by using the GRAVITY code, it is possible to simulate accurately the hot spot's astrometric positions that would be obtained by GRAVITY (see Vincent et al. 2011b, for the description of this procedure). Fig. 2 shows the simulation of such an observation by GRAVITY, with two different values of the inclination parameter. Let us stress that the error bars appearing on this figure take into account all sources of noise that will affect a real GRAVITY observation (see Vincent et al. 2011b).

Fig. 2 shows clearly that the dispersion of the retrieved positions depends strongly on the inclination: the smaller the inclination, the bigger the dispersion. Building upon this result, we have investigated the ability to get an information on the inclination parameter of the black hole by computing the dispersion of the retrieved positions. This was done within the framework of a Monte Carlo analysis, by computing the dispersion values in the x and y directions corresponding to the horizontal and vertical directions of the observer's screen, for a number of simulated observations.

Fig. 3 represents the bidimensional histograms of the retrieved positions in the x and y directions, for three different values of the inclination. The histograms corresponding to the three values of inclination, 20° , 40° and 60° , span different values of the dispersion. Thus, if one considers one given night of observation satisfying the above assumption on the flare's maximum magnitude and orbital radius (which can be tightly constrained from the measured orbital period, see Fig. 1, right panel), the inclination parameter can be constrained by computing the dispersion of the retrieved positions found by GRAVITY on this given night. For instance, if the dispersion in both direction is found to be $10 \mu\text{as}$, Fig. 3 excludes at 3σ any inclination values $\gtrsim 40^\circ$. This constraint could be refined by choosing a finer sampling of the inclination parameter.

4 Conclusion

Within the framework of the hot spot model for the Galactic center infrared flares, we have shown that, provided one bright enough ($m_K = 13$ at maximum) flare with a large enough ($r \approx 3.5 r_S$) orbital radius is observed, the

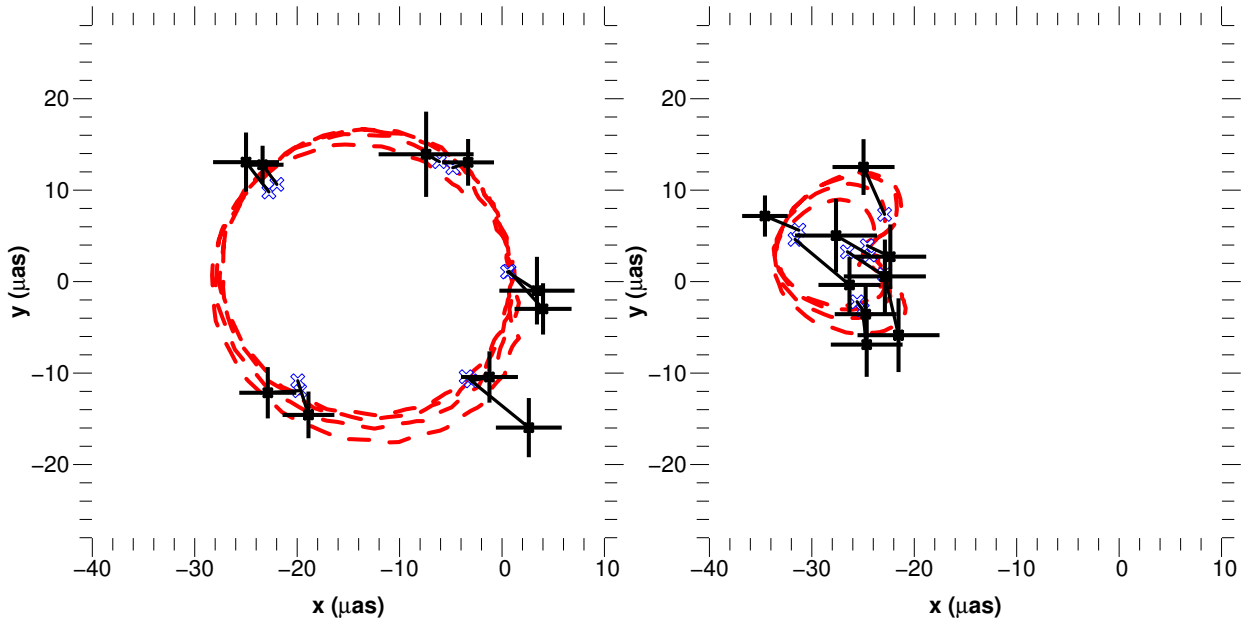


Fig. 2. Left: GRAVITY observation simulation of a hot spot circularly orbiting at a radius $r = 3.5 r_S$ around a Kerr black hole of spin parameter 0.7 seen under an inclination of 20° . The maximum magnitude of the flare is $m_K = 13$. The hot spot's parameters are given in Eq. 2.1. The red dashed line is the theoretical projected trajectory as computed by GYOTO. The black error bars are simulations of GRAVITY astrometric data (the size of the error bar is a function of the hot spot's magnitude at the time of observation), the instrument integrates during 100 s for each data point. Each black retrieved position is linked to the corresponding real position of the spot along its orbit (in blue). **Right:** Same as left panel, but with an inclination parameter of 60° .

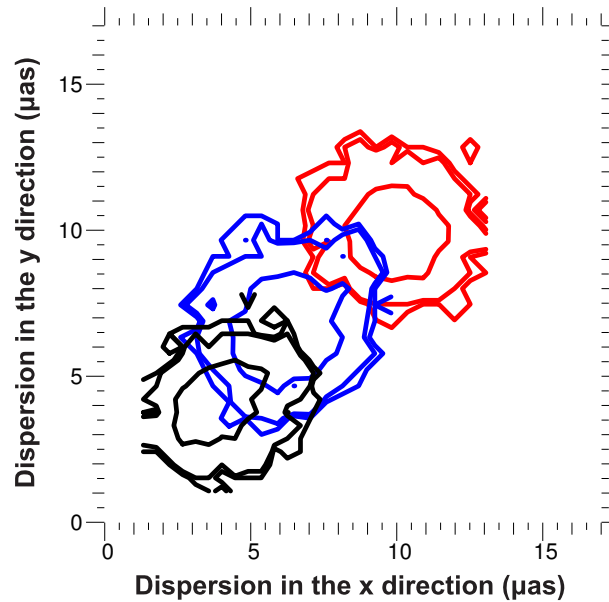


Fig. 3. 2-dimensional histograms of the dispersion of the retrieved position in the two horizontal (x) and vertical (y) directions of the observer's screen. The hot spot parameters are the same as in Fig. 2, with an inclination parameter of 20° (red), 40° (blue) and 60° (black). The contours include respectively (innermost to outermost) 68%, 95% and 99% of the dispersion values obtained in the Monte Carlo procedure.

GRAVITY instrument would be able of constraining the inclination parameter of the central black hole. As no

consensus has yet emerged on the value of this important parameter, such a measure would allow progressing towards a better understanding of the innermost Galactic center.

This work was supported by grants from Région Ile-de-France.

References

- Dodds-Eden, K., Gillessen, S., Fritz, T. K., et al. 2011, *ApJ*, 728, 37
- Dodds-Eden, K., Sharma, P., Quataert, E., et al. 2010, *ApJ*, 725, 450
- Eisenhauer, F., Perrin, G., Brandner, W., et al. 2008, in *SPIE Conference Series*, Vol. 7013
- Genzel, R., Schödel, R., Ott, T., et al. 2003, *Nature*, 425, 934
- Ghez, A. M., Salim, S., Weinberg, N. N., et al. 2008, *ApJ*, 689, 1044
- Gillessen, S., Eisenhauer, F., Quataert, E., et al. 2006, *ApJ*, 640, L163
- Gillessen, S., Eisenhauer, F., Trippe, S., et al. 2009, *ApJ*, 692, 1075
- Hamaus, N., Paumard, T., Müller, T., et al. 2009, *ApJ*, 692, 902
- Markoff, S., Falcke, H., Yuan, F., & Biermann, P. L. 2001, *A&A*, 379, L13
- Tagger, M. & Melia, F. 2006, *ApJ*, 636, L33
- Trap, G., Goldwurm, A., Dodds-Eden, K., et al. 2011, *A&A*, 528, A140
- Vincent, F. H., Paumard, T., Gourgoulhon, E., & Perrin, G. 2011a, *Class. Quantum Grav.*, in press, gr-qc/1109.4749
- Vincent, F. H., Paumard, T., Perrin, G., et al. 2011b, *MNRAS*, 412, 2653
- Yusef-Zadeh, F., Roberts, D., Wardle, M., Heinke, C. O., & Bower, G. C. 2006, *ApJ*, 650, 189

Session 16

Discussions EJSM JGO after Decadal Survey US:
towards a new mission scenario?

QUANTIFYING THE MEASUREMENT REQUIREMENTS NEEDED TO UNDERSTAND THE ORIGIN OF THE GALILEAN SATELLITE SYSTEM

O. Mousis¹, J. H. Waite² and J. I. Lunine³

Abstract. One of the primary science objectives of the JUPiter ICy moon Explorer (JUICE) mission is to characterize the origin and evolution of the Galilean satellites. Here we discuss the observational tests that could be performed via a Ion and Neutral Mass Spectrometer (INMS) aboard the JUICE mission and that would shed light on the formation circumstances of the Galilean satellite system.

Keywords: Origin of Jupiter and its satellite system, Cosmochemistry, Spacecraft missions

1 Introduction

The history of the Jovian system can be divided into three main phases: the formation of Jupiter, the formation of its satellite system and its secular evolution to its present day state. Three different sets of formation conditions can be considered regarding the Galilean satellite system: 1) unaltered building blocks from the protosolar nebula (Mousis & Gautier 2004; Horner et al. 2008), 2) altered materials where a significant fraction of the volatile components have outgassed before the formation process (Mousis et al. 2009a), and 3) building blocks that were vaporized in the subnebula of Jupiter before coalescing in the formation process, i.e. the Jupiter mini-solar system formation scenario (Prinn & Fegley 1981). Cassini has shown that the Saturn system seems to fall largely into category 2 (Waite et al. 2009; Mousis et al. 2009b) but the size of Jupiter and its relative distance from the Sun may favor process 3 for the Galilean satellites. Here we discuss the observational tests that could shed light on the formation circumstances of the Galilean satellite system.

2 Key measurements

Figure 1 displays the different key observations that could constrain the origin of the Galilean satellite system. These measurements are divided into two categories: determinations of the noble gas abundances and measurements of the isotopic ratios.

2.1 Noble gas abundances

INMS measurement of the ratios of the noble gases in the satellite environments, particularly Ar, Kr and Xe would allow comparison with bodies that likely formed in the solar nebula, such as comets, and thereby constrain whether the material from which the icy satellites formed was primarily circumsolar or circum-Jovian.

2.2 Isotopic ratios

The deuterium-to-hydrogen ratio in water, compared to that of the well-determined primordial value and that in terrestrial ocean water, gives an indication of the extent to which water in planetesimals experienced elevated temperatures for durations sufficient for re-equilibration with the surrounding hydrogen-rich gas (Horner et al.

¹ Université de Franche-Comté, Institut UTINAM, CNRS/INSU, UMR 6213, Observatoire des Sciences de l'Univers de Besançon, France

² Space Science and Engineering Division, Southwest Research Institute, San Antonio, TX 78228, USA

³ CRSR, Cornell University, Ithaca, NY 14853, USA

2008). Measurement of the ratios of noble gases to CH_4 and the $^{12}\text{C}/^{13}\text{C}$ and D/H ratios provides constraints on the origin of any methane that might be present either primordially or as a product of hydrothermal reactions in the interiors of Europa and Ganymede (Jehin et al. 2009; Mousis et al. 2009c). The origin of methane as primordial or a later product of internal processing would provide a supplementary constraint on the temperature history of the disk.

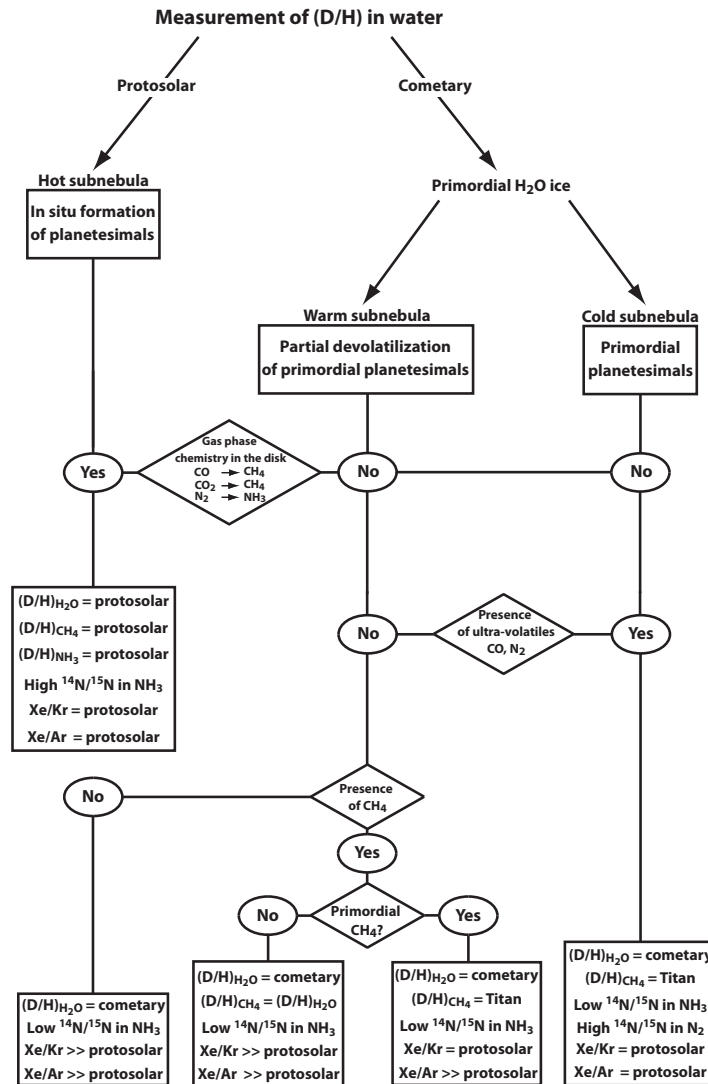


Fig. 1. Observational tests derived from different formation scenarios.

References

- Horner, J., Mousis, O., Alibert, Y., Lunine, J. I., & Blanc, M. 2008, *Planet. Space Sci.*, 56, 1585
- Jehin, E., Manfroid, J., Hutsemékers, D., Arpigny, C., & Zucconi, J.-M. 2009, *Earth Moon and Planets*, 105, 167
- Mousis, O., & Gautier, D. 2004, *Planet. Space Sci.*, 52, 361
- Mousis, O., Lunine, J. I., Thomas, C., et al. 2009a, *ApJ*, 691, 1780
- Mousis, O., Lunine, J. I., Waite, J. H., et al. 2009b, *ApJ*, 701, L39
- Mousis, O., Lunine, J. I., Pasek, M., et al. 2009c, *Icarus*, 204, 749
- Prinn, R. G., & Fegley, B., Jr. 1981, *ApJ*, 249, 308
- Waite, J. H., Jr., Lewis, W. S., Magee, B. A., et al. 2009, *Nature*, 460, 487

O.M. acknowledges support from CNES.

References

Author Index

- Abe, L., 107
Abouadarham, J., 373
Acharya, B. S., 535, 539
Adami, C., 101
Ageron, M., 615
Akerlof, C., 615
Al Samarai, I., 615
Alauzet, F., 389
Albrecht, M., 119
Aldering, G., 179
Alecian, E., 509
Alecian, G., 253
Alimi, J.-M., 9
Allard, F., 339
Allard, N. F., 267, 435, 439
Alonso-Albi, T., 413
Alvan, L., 443
Aly, J. J., 389
Amari, T., 389
Andrievsky, S., 353
Aniano, G., 119
Ansoorge, W., 107
Antilogus, P., 179
Antoja, T., 287
Anupama, G. C., 535, 539
Aragon, C., 179
Arena, S. E., 449, 469
Arenou, F., 303, 333, 357
Argentini, S., 107
Ashley, M. C. B., 107
Assafin, M., 629
Athanassoula, E., 135
Aubert, D., 77
Aulanier, G., 395
Aurière, M., 497

Baillié, K., 383
Balcells, M., 161
Balkowski, C., 153
Ball, N., 153
Balland, C., 55, 73
Balmès, I., 59
Balogh, M. L., 153
Baltay, C., 179
Bancelin, D., 263, 629, 639
Banerjee, S., 379
Barragán, L., 567
Barthe, C., 363
Baruteau, C., 455, 459
Basa, S., 615
Bazin, C., 203
Belyaev, A. K., 283

Benoist, C., 185
Bentley, R., 373
Bertin, E., 101
Bertin, V., 615
Bertoldi, F., 119
Bertone, S., 635
Beust, H., 3
Bhatt, N., 539
Bhattacharjee, P., 535, 539
Bhattacharya, S., 539
Bienaymé, O., 311
Bigot, B., 399
Bijaoui, A., 311
Biteau, J., 525
Bitsakis, T., 81
Blakeslee, J. P., 153, 175
Bocchialini, K., 369
Boer, M., 615
Boissier, S., 153
Boisson, C., 555
Bolmont, J., 529
Bongard, S., 179
Bonifacio, P., 333, 353
Bonnin, X., 373
Boone, F., 141, 161
Boselli, A., 153
Bouhou, B., 63
Bouillot, V., 9
Bournaud, F., 153
Bovalo, C., 363
Braine, J., 275
Britto, R. J., 535, 539
Brun, F., 545
Brun, P., 549
Brunner, J., 615
Bryson, I., 107
Burderi, L., 567
Busschaert, C., 463
Busto, J., 615
Buton, C., 179

Côté, P., 153
Caffau, E., 333, 353
Canou, A., 389
Canto, A., 179
Cardiel, N., 161
Carignan, C., 153
Carlberg, R. G., 153
Carrigan, S., 545
Castander, F. J., 69
Cayrel, R., 267, 353
Cellier-Holzem, F., 73

- Cerruti, M., 555
Chapman, S. G., 153
Chardin, J., 77
Charmandaris, V., 81
Chauvin, G., 3
Chemin, L., 271
Childress, M., 179
Chitnis, V. R., 535, 539
Chong, M., 363
Chotard, N., 179
Christophe, B., 663
Colas, F., 629
Colwell, J.E., 383
Copin, Y., 179
Corasaniti, P.-S., 59
Courteau, S., 153
Couvidat, S., 257
Cowsik, R., 535, 539
Crespe, E., 449, 469
Crida, A., 15
Crifo, F., 271
Csillaghy, A., 373
Cuby, J. G., 161
Cucciati, O., 85
Cuillandre, J. C., 153
- D'Ai, A., 567
Daigne, F., 593
Dale, D., 119
Dalton, G., 107
Dasyra, K. M., 91
Dauser, T., 567
David, C., 107
Davidge, T. J., 153
Davies, G. R., 207
de Barros, S., 95
Defer, E., 363
Deguilhem, B., 435
Dehant, V., 653
Deheuvels, S., 211
Delfosse, X., 503
Delva, P., 679
Delyon, F., 389
Demarco, R., 175
Demers, S., 153
Desmars, J., 639
Dexter, J., 563
de Laverny, P., 311
de Naurois, M., 545
Di Gallo, L., 559
Dib, S., 235, 275
Dibi, S., 563
Dintrans, B., 215, 497
Dizière, A., 463
Di Salvo, T., 567
Djannati-Atai, A., 545
- Domínguez-Tenreiro, R., 157
Doménech-Moral, M., 157
Donati, J.-F., 503
Dorji, N., 535, 539
Dormy, E., 503
Dornic, D., 615
Douspis, M., 21
Dréan, G., 295
Draine, B., 119
Drappeau, S., 563
Duc, P.-A., 153
Duez, V., 475
Duhan, S. K., 535, 539
Durrell, P. R., 153
Durret, F., 101, 147
- Egami, E., 141
Egron, E., 567
Eisenhauer, F., 689
Elourabi, E., 643
Emsellem, E., 153
Engelbracht, C., 119
Epchtein, N., 107
Erben, T., 153
Esau, I., 107
Esposito, L.W., 383
- Fakhouri, H. K., 179
Falize, E., 463
Famaey, B., 303
Farges, T., 363
Faurobert, M., 401
Feautrier, N., 283
Ferrarese, L., 153
Ferrari, C., 111
Ferrière, E., 153
Figueras, F., 287
Floquet, M., 231
Flores, H., 135
Ford, H., 175
Fortin, M., 573
Forveille, T., 503
Fossati, L., 307
Fouquet, S., 135
Fragile, P. C., 563
Fraix-Burnet, D., 115
François, P., 353
Frey, P., 389
Fromang, S., 455
Fuente, A., 413
Fukui, Y., 325
Fuller, N., 373
- Gérard, E., 419
Gadéa, F. X., 435
Galamez, M., 119

- Gallagher, P., 373
 Gallego, J., 161
 Gallenne, A., 479
 Galtier, S., 379, 399
 Gangler, E., 179
 García, R. A., 207, 257
 Garzón, F., 161
 Gaskell, C. M., 577
 Gastine, T., 215
 Gaudin, N., 291
 Gavazzi, G., 153
 Gavazzi, R., 153
 Georgantopoulos, I., 91
 Giebels, B., 525
 Gillessen, S., 689
 Gilmore, G., 311
 Gomez, A., 333
 Gonzalez, J.-F., 449, 469
 Goosmann, R. W., 583, 597
 Gothe, K. S., 535, 539
 Goupil, M.-J., 249
 Gourgoulhon, E., 689
 Guédé, C., 295
 Guennou, L., 125
 Guillemot, L., 587
 Guillout, P., 303
 Guitou, M., 283
 Guittet, M., 299
 Guzmán, R., 161
 Gwyn, S. D. J., 153
- Haensel, P., 573
 Haider, M., 101
 Halbwachs, J.-L., 303
 Hammer, F., 135
 Hardy, E., 647
 Hascoët, R., 593
 Hauchecorne, A., 407
 Hauschildt, P., 235
 Hayes, M., 129, 161
 Haywood, M., 299, 357
 Hees, A., 653
 Helmi, A., 311
 Hersant, F., 685
 Hestroffer, D., 263, 271, 629, 639
 Higgins, P., 373
 Hill, V., 311
 Hinz, J., 119
 Hoekstra, H., 153
 Hofmann, W., 545
 Holden, B. P., 175
 Hsiao, E. Y., 179
 Hubeny, I., 485
 Hudelot, P., 153, 161
 Huertas-Company, M., 153, 175
 Huré, J.-M., 685
- Iaria, R., 567
 Ibgui, L., 485
 Ilbert, O., 85, 153
 Illingworth, G., 175
 Inoue, S., 555
- Jacholkowska, A., 529
 Jaekel, M. T., 653
 Jardine, M. M., 503
 Jasniewicz, G., 271
 Jee, M. J., 175
 Jordán, A., 153
- Kamath, P. U., 535, 539
 Karampelas, A., 349
 Katz, D., 271, 333
 Kavelaars, J. J., 153
 Kawamura, A., 325
 Kennicutt, R., 119
 Kern, P., 27
 Kerschhaggl, M., 179
 Kervella, P., 235, 479
 Klotz, A., 615
 Kneib, J.-P., 141, 161
 Kniazev, A. Y., 37
 Kodama, T., 175
 Koenig, M., 463
 Kontizas, M., 349
 Kordopatis, G., 311
 Korotin, S., 353
 Koul, R., 539
 Koutchmy, S., 203, 369
 Kowalski, M., 179
 Krista, L., 373
 Kılıçoğlu, T., 307
- Lagache, G., 325
 Laganá, T. F., 101, 147
 Lagrange, A.-M., 3
 Lainey, V., 519, 653
 Lambert, S. B., 659
 Lamine, B., 653
 Lamy, P., 203
 Lançon, A., 153
 Langlois, M., 107
 Lanz, T., 485
 Laporte, N., 141, 161
 Laurent, P., 679
 Lawrence, J. S., 107
 Le Borgne, J. F., 161
 Le Poncin-Lafitte, C., 635
 LeBlanc, F., 253
 Lebreton, Y., 295, 303
 Lefloch, B., 423
 Leinert, C., 339
 Lemoine, M., 39

- Lenoir, B., 663
Lestrade, J.-F., 429
Levy, A., 647
Le Bertre, T., 419
Le Fèvre, O., 85
Le Poncin-Lafitte, C., 653, 669, 679
Libert, Y., 419
Lignières, F., 249
Lima Neto, G. B., 147
Lion, G., 673
Lochard, J., 249
Loken, S., 179
Loupias, B., 463
Lunine, J. I., 697
Luri, X., 315
- Mérand, A., 479
Métris, G., 673
Métris, G., 647
MacArthur, L., 153
Mahesh, P. K., 535, 539
Manoharan, J., 535, 539
Margueron, J., 573
Marin, F., 597
Markoff, S., 563
Martínez-Serrano, F. J., 157
Martin, J.-M., 37
Martinet, N., 147
Masseron, T., 321
Masset, F., 455
Mathis, S., 443, 491, 509, 515, 519
Mathur, S., 221
Matt, G., 583
Maurogordato, S., 185
McConnachie, A. W., 153
McLaughlin, D., 153
Mei, S., 153, 175
Mellier, Y., 153, 161
Melo, S., 407
Meru, F., 459
Meynadier, F., 679
Michaut, C., 463
Mihos, J. C., 153
Milić, I., 401
Milkeraitis, M., 153
Mitra, A., 539
Mochkovitch, R., 593
Mohanty, S., 275
Molodij, G., 395
Monari, A., 435
Monier, R., 307
Moreno, E., 287
Morey, E., 429
Morgenthaler, A., 497
Morin, J., 497, 503
Mosser, B., 225
- Mousis, O., 697
Muñoz, R., 153
- Nagesh, B. K., 535, 539
Najid, N.-E., 643
Nakata, F., 175
Neiner, C., 231, 509
Nelson, R. P., 455
Nguyen, H. C., 463
Noriega-Crespo, A., 325
Novak, J., 601
Nugent, P., 179
- Obreja, A., 157
Oertel, M., 559, 601
Ohm, S., 545
Onishi, T., 325
Ordenovic, C., 311
Ortége, P., 363
- Paardekooper, S.-J., 459
Paech, K., 179
Pain, R., 179
Paladini, R., 325
Papitto, A., 567
Paradis, D., 325, 329
Parmar, N. K., 535, 539
Paumard, T., 689
Pecontal, E., 179
Pelló, R., 141, 161
Pelletier, G., 39
Peng, C., 153
Peng, E. W., 153
Pereira, R., 179
Peres, B., 601
Perez-Suarez, D., 373
Perlmutter, S., 179
Perrin, G., 689
Petit, P., 497, 503
Piau, L., 235, 257, 275, 407
Pichardo, B., 287
Pinty, J.-P., 363
Planesas, P., 169
Plez, B., 47
Plotnikov, I., 605
Pope, A., 91
Posbic, H., 333
Postman, M., 175
Pourbaix, D., 303
Prabhu, T. P., 535, 539
Prieto, M., 161
Puech, M., 135
Pustilnik, S. A., 37
Puzia, T. H., 153
- Rabinowitz, D., 179

- Raichoor, A., 175
 Rajpurohit, A. S., 339
 Rannot, R. C., 539
 Rao, S. K., 535, 539
 Ravasio, A., 463
 Rebai, A., 609
 Recio-Blanco, A., 311
 Reese, D. R., 249
 Remus, F., 515, 519
 Renie, C., 373
 Rettura, A., 175
 Reylé, C., 339, 345
 Reynaud, S., 653, 663
 Richard, J., 141, 161
 Rieutord, M., 249
 Rigault, M., 179
 Riggio, A., 567
 Robba, N. R., 567
 Robert, A., 647
 Robin, A. C., 345
 Rocca-Volmerange, B., 349
 Rodrigues, M., 135, 647
 Romero-Gómez, M., 287
 Rosati, P., 175
 Rostagni, F., 185
 Roudier, T., 241
 Roussel, H., 119
 Rovilos, M., 91
 Runge, K., 179
- Saha, L., 535, 539
 Salabert, D., 245
 Saleem, F., 535, 539
 Samadi, R., 249
 Sawicki, M., 153
 Saxena, A. K., 535, 539
 Sbordone, L., 333
 Scalzo, R., 179
 Scarlata, C., 129
 Schüssler, F., 615
 Schade, D., 153
 Schaerer, D., 95, 141, 161
 Schrinner, M., 503
 Schultheis, M., 299, 339
 Semelin, B., 197
 Serna, A., 157
 Shankar, F., 175
 Sharma, S. K., 535, 539
 Shukla, A., 535, 539
 Simard, L., 153
 Singh, B. B., 535, 539
 Smadja, G., 179
 Solomon, J., 369
 Soubiran, C., 271
 Soula, S., 363
 Sourie, A., 349
- Spielfiedel, A., 283
 Spite, F., 353
 Spite, M., 353
 Srinivasan, R., 535, 539
 Srinivasulu, G., 535, 539
 Stanford, S. A., 175
 Stark, D. P., 95
 Stehlé, C., 267, 485
 Stein, R. F., 407
 Suárez, J. C., 249
 Sudersanan, P. V., 535, 539
- Tanaka, M., 175
 Tao, C., 179
 Taylor, J. E., 153
 Théado, S., 253
 Thomas, R. C., 179
 Thuillier, G., 407
 Thuillot, W., 263, 629, 639
 Tickoo, A. K., 539
 Tonry, J. L., 153
 Touboul, P., 647
 Tresse, L., 85, 161
 Trova, A., 685
 Tsalmantza, P., 349
 Tsewang, D., 535, 539
 Tully, R. B., 153
 Turck-Chièze, S., 257, 407
 Turon, C., 315, 357
- Udry, S., 271
 Upadhyya, S. S., 535, 539
 Urban, M., 559
- Valenzuela, O., 287
 Vallage, B., 615
 van Driel, W., 153
 van Waerbeke, L., 153
 Van't Veer-Menneret, C., 267
 Vauclair, S., 253
 Vauglin, I., 107
 Vecchi, M., 615
 Vennin, V., 593
 Viana, A., 621
 Villa, F., 191
 Vincent, F. H., 689
 Vishwanath, P. R., 535, 539
 Vollmer, B., 153
 Vonlanthen, P., 197
- Waite, J. H., 697
 Walter, F., 119
 Wang, J. L., 135
 Weaver, B. A., 179
 Weiss, A., 119
 White, R. L., 175

Wilms, J., 567
Wilson, C. D., 153
Wolf, P., 653, 679
Woods, D., 153
Wozniak, H., 291
Wu, C., 179
Wyse, R. F. G., 311

Yadav, K. K., 539
Yang, Y. B., 135

Zahn, J.-P., 515, 519
Zdunik, J. L., 573
Zech, A., 555
Zheng, W., 615
Zoccali, M., 311